STATE OF THE CLIMATE IN 2021

Special Supplement to the
Bulletin of the American Meteorological Society
Vol. 103, No. 8, August 2022

Cover credits:

Flames and smoke from wildfires above the Fraser River Valley near Lytton, British Columbia, Canada, on 2 July 2021. Photographer: James MacDonald/Bloomberg ©2021 Bloomberg Finance LP - Getty

Photograph of the South Pole sunrise in September 2021. Photo taken by Jeffrey Keller, USAP/PAE, Preventative Maintenance Foreman, Colorado Springs, Colorado.

How to cite this document:

Citing the complete report:
Blunden, J. and T. Boyer, Eds., 2022: "State of the Climate in 2021". *Bull. Amer. Meteor. Soc.*, **103** (8), Si–S465, https://doi.org/10.1175/2022BAMSStateoftheClimate.1

Special Supplement to the *Bulletin of the American Meteorological Society*, Vol. 103, No. 8, August 2022 https://doi.org/10.1175/2022BAMSStateoftheClimate.1

Corresponding author: Full report: Jessica Blunden / jessica.blunden@noaa.gov

STATE OF THE CLIMATE IN 2021

TABLE OF CONTENTS

ABSTRACT—J. BLUNDEN AND T. BOYER

In 2021, the dominant greenhouse gases released into Earth's atmosphere continued to increase. The annual global average carbon dioxide (CO_2) concentration was 414.7 ± 0.1 ppm, an increase of 2.6 ± 0.1 ppm over 2020, the fifth-highest growth rate since the start of the instrumental record in 1958. This brings the concentration of CO_2 to, once again, the highest in the modern record and ice core records dating back 800,000 years. The growth rate for methane (CH_4) was the highest on record and the third highest for nitrous oxide (N_2O), contributing to new record high atmospheric concentration levels for both gases.

Weak-to-moderate La Niña conditions were present in the eastern equatorial Pacific during most of 2021, a continuation from 2020. La Niña tends to dampen temperatures at the global scale; even so, the annual global surface temperature across land and oceans was still among the six highest with records dating as far back as the mid-1800s. While La Niña conditions contributed to Australia's coldest year since 2012, New Zealand and China each reported their warmest year on record. Europe reported its second-hottest summer on record, after 2010. A provisional new European maximum temperature record of 48.8°C was set in Sicily (Italy) on 11 August. In North America, exceptional heat waves struck the Pacific Northwest, leading to a new Canadian maximum temperature record of 49.6°C, set at Lytton, British Columbia, on 29 June, breaking the previous national record by over 4°C. In the United States, Furnace Creek in Death Valley, California, reached 54.4°C on 9 July—equaling the temperature measured at that location in 2020, which was the hottest temperature measured on Earth since 1931. The effects of warming temperatures were apparent across the Northern Hemisphere, where lakes were frozen 7.3 fewer days on average. Lake Erken, in Sweden, lost the most ice cover during the 2021 winter, with 61 days less ice cover compared to the 1991–2020 normal in response to an anomalously warm winter. The average growing season was six days longer than the 2000–20 base period. In Kyoto, Japan, full bloom dates for a native cherry tree species, *Prunus jamasakura*, were the earliest in the entire record, which began in AD 801, breaking the previous earliest date set in the year 1409.

While fewer in number and locations than record high temperatures, record cold was also observed in various locales during the year. In Spain, a new all-time national minimum temperature record of –34.1°C was set on 6 January at Clot del Tuc de la Llança in the Pyrenees. Slovenia reported a national low temperature record of –20.6°C for the month of April, set at station Nova vas Bloka.

Over Antarctica, a persistently strong and stable polar vortex helped maintain the second longest-lived ozone hole on record (shorter only than 2020), which did not close until 23 December, and contributed to the coldest extended winter on record at the South Pole. But on the northeastern Antarctic Peninsula, Esperanza and Marambio stations received persistent warm northerly winds, contributing to their warmest (tied) and second-warmest years on record, respectively.

Across the global cryosphere, glaciers lost mass for the 34th consecutive year, and permafrost temperatures continued to reach record highs at many high latitude and mountain locations. In the high northern latitudes, the Arctic as a whole (poleward of 60°N), observed its coolest year since 2013, but 2021 was still the 13th-warmest year in the 122-year record. Extreme heat events occurred during the summer. Related to the western North American heat waves, a temperature of 39.9°C was recorded in Fort Smith, Northwest Territories, Canada, on 30 June, the highest temperature ever recorded north of 60°N. A widespread melt event on the Greenland Ice Sheet on 14 August—the latest on record—coincided with the first observed rainfall in the 33-year record at the Summit Station (3216 m a.s.l.).

The seasonal Arctic minimum sea ice extent, typically reached in September, was the 12th-smallest extent in the 43-year record; however, the amount of multiyear ice—ice that survives at least one summer melt season—remaining in the Arctic at this time was the second lowest on record, indicating the Arctic's sustained transition to a younger, thinner ice cover. The oldest ice, more than four years old, has declined by 94% since the start of the record. While the rate of decline in minimum sea ice extent over the 2010–21 period has slowed compared to previous decades, Arctic sea ice volume continues to rapidly shrink.

Across the world's oceans, global mean sea level was record high for the 10th consecutive year, reaching 97.0 mm above the 1993 average when satellite measurements began, an increase of 4.9 mm over 2020. Globally-averaged ocean heat content was also record high in 2021, while the global sea surface temperature cooled compared to 2019 and 2020 due to the ongoing La Niña conditions in the tropical Pacific. Still, approximately 57% of the ocean surface experienced at least one marine heatwave in 2021.

A total of 97 named tropical storms were observed during the Northern and Southern Hemisphere storm seasons, well above the 1991–2020 average of 87, but well below the record

104 named storms of 1992. In the North Atlantic, 21 tropical cyclones formed, the third most for the basin, behind the record 30 cyclones in 2020 and 28 in 2005. There were seven Category 5 tropical cyclones across the globe—four in the western North Pacific and one each in the South Indian Ocean, Australian region, and the Southwest Pacific. Super Typhoon Rai was the third costliest typhoon in the history of the Philippines, causing about $1 billion (U.S. dollars) in damage and more than 400 deaths. While not reaching Category 5 status, Hurricane Ida was the most impactful storm in the Atlantic. At $75 billion (U.S. dollars) in damage, Ida was the costliest U.S. disaster of 2021 and the fifth most expensive hurricane on record (since 1980).

As is typical, some areas around the world were notably dry in 2021 and some were notably wet. In August, 32% of global land areas were experiencing some level of drought, a new record high. A "mega-drought" continued in central Chile for the 12th consecutive year, becoming the longest drought in the historical record in the region. Drought intensified and expanded through most of the western United States and elsewhere along a large stretch of northeastern Siberia and the Far East region of Russia, which led to unprecedented wildfires. Most of the Middle East, from Türkiye to Pakistan, also saw an intensification of drought conditions. In parts of equatorial East Africa, the annual total rainfall was the lowest on record, leading to three consecutive failed rainy seasons that resulted in one of the worst threats to food security in 35 years for more than 20 million people in the region..

Conversely, on 20 July, a 1-hour precipitation total of 201.9 mm was recorded in Zhengzhou—capital of Henan province in central China and home to more than 10 million people—the highest hourly precipitation on record for mainland China. On 4 October, a new European 12-hour rainfall record was set in Rossiglione (northwest Italy), with a total of 740.6 mm, which was more than 50% of its annual average of 1270 mm. Following months of above-average rain, the Rio Negro River at Manaus (central Brazilian Amazon) rose and remained above its emergency threshold for a total of 91 days, reaching a record high level of 30.02 m on 16 June. The overflow of the river caused damaging floods that surpassed the "once-in-a-century" Amazon flood in 2012.

STATE OF THE CLIMATE IN 2021

INTRODUCTION

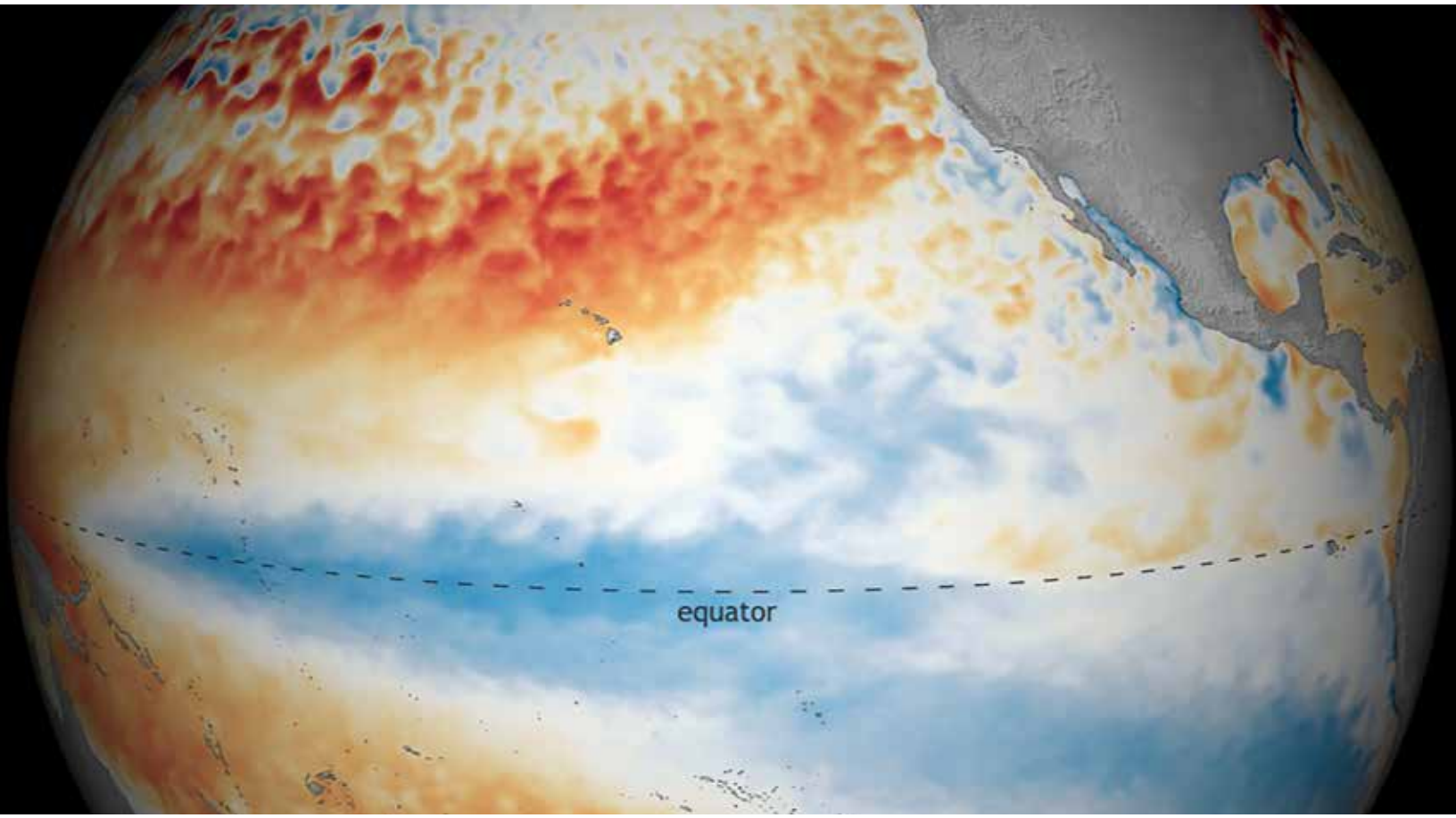

Sea surface temperature anomaly in the Pacific Ocean, December 2021 from NOAA Coral Reef Watch. Credits: NOAA Climate.gov, based on data from NOAA Coral Reef Watch

Citing this chapter: Boyer, T., J. Blunden, and R. J. H. Dunn., 2022: Introduction [in "State of the Climate in 2021"]. *Bull. Amer. Meteor. Soc.,* **103** (8), S1–S9, https://doi.org/10.1175/2022BAMSStateoftheClimate_Intro.1.

Special Supplement to the *Bulletin of the American Meteorological Society*, Vol.103, No. 8, August 2022

The Introduction is one chapter from the *State of the Climate in 2021* annual report. Compiled by NOAA's National Centers for Environmental Information, *State of the Climate in 2021* is based on contributions from scientists from around the world. It provides a detailed update on global climate indicators, notable weather events, and other data collected by environmental monitoring stations and instruments located on land, water, ice, and in space. The full report is available from https://doi.org/10.1175/2022BAMSStateoftheClimate.1.

Corresponding author, Introduction: Jessica Blunden / jessica.blunden@noaa.gov

STATE OF THE CLIMATE IN 2021

Introduction

Editors

Jessica Blunden

Tim Boyer

Chapter Editors

Freya Aldred

Peter Bissolli

Kyle R. Clem

Howard J. Diamond

Matthew L. Druckenmiller

Robert J. H. Dunn

Catherine Ganter

Nadine Gobron

Gregory C. Johnson

Rick Lumpkin

Ademe Mekonnen

John B. Miller

Twila A. Moon

Marilyn N. Raphael

Ahira Sánchez-Lugo

Carl J. Schreck III

Richard L. Thoman

Kate M. Willett

Zhiwei Zhu

Technical Editor

Laura Ohlmann

BAMS Special Editor for Climate

Michael A. Alexander

American Meteorological Society

Editor and Author Affiliations (alphabetical by name)

Blunden, Jessica, NOAA/NESDIS National Centers for Environmental Information, Asheville, North Carolina
Boyer, Tim, NOAA/NESDIS National Centers for Environmental Information, Silver Spring, Maryland
Dunn, Robert, J. H., Met Office Hadley Centre, Exeter, United Kingdom

Editorial and Production Team

Allen, Jessicca, Graphics Support, Cooperative Institute for Satellite Earth System Studies, North Carolina State University, Asheville, North Carolina
Hammer, Gregory, Content Team Lead, Communications and Outreach, NOAA/NESDIS National Centers for Environmental Information, Asheville, North Carolina
Love-Brotak, S. Elizabeth, Lead Graphics Production, NOAA/NESDIS National Centers for Environmental Information, Asheville, North Carolina
Misch, Deborah J., Graphics Support, Innovative Consulting and Management Services, LLC, NOAA/NESDIS National Centers for Environmental Information, Asheville, North Carolina
Ohlmann, Laura, Technical Editor, Innovative Consulting and Management Services, LLC, NOAA/NESDIS National Centers for Environmental Information, Asheville, North Carolina
Riddle, Deborah B., Graphics Support, NOAA/NESDIS National Centers for Environmental Information, Asheville, North Carolina
Veasey, Sara W., Visual Communications Team Lead, Communications and Outreach, NOAA/NESDIS National Centers for Environmental Information, Asheville, North Carolina

1. INTRODUCTION—T. Boyer, J. Blunden, and R. J. H. Dunn

The complexity of Earth's climate system was evident in 2021, as illustrated on the report's cover, with the South Pole experiencing its coldest winter on record (Sidebar 6.1), averaging –61.0°C from April through September, juxtaposed against a record high temperature for Canada of 49.6°C in the town of Lytton, northeast of Vancouver, on 29 June (Sidebar 7.1). Conditions, including a stable polar vortex and clear skies, contributed to the cold at the South Pole. A persistent high-pressure ridge over western North America, clear skies, and drought conditions contributed to 'Hell on Earth' in western Canada, to quote the title of the sidebar. However, while the year did include extremes, 2021 was overall marked more by trends ameliorated, rather than enhanced, by shorter-term phenomena, most notably the 'double dip' La Niña which persisted through the year. While ocean heat content steadily increased year over year, reaching a new high in 2021 (section 3c), indicative of steadily increasing heat in Earth's system, the annual global surface temperature was fifth or sixth highest on record (depending on the dataset referenced; section 2b) and the annual Arctic surface air temperature was the lowest since 2013 (section 5b). Chapter 3 describes the 2021 El Nino-Southern Oscillation (ENSO) state (begun in 2020) as a typical double dip La Niña, a strong La Niña interrupted (in terms of sea surface temperature threshold) by an oceanic Kelvin wave, followed by a return to La Niña conditions (Hu et al. 2014). Chapter 4 does not use the terminology but does describe the downwelling oceanic Kelvin wave which temporarily disrupted the cool near-surface waters as seen in Fig. 4.9. La Niña conditions favor enhanced Atlantic storm activity; however, in 2021, the number of named hurricanes in this basin was at the long-term mean (seven; section 4g2). Madden-Julian Oscillation (MJO) activity was low in the first part of 2021, typical for a La Niña period, with higher activity during the period of weaker/below-threshold La Niña. Other variability of note in 2021, affecting tropical and extratropical events, includes the first (weakly) negative Indian Ocean dipole since 2016 (section 4f). The complexity and evolution of Earth's climate system is cataloged here in the *State of the Climate in 2021* due to the continued dedication and efforts of the 531 authors from 66 countries representing their colleagues and contributors from universities and agencies around the globe.

"Climate is what you expect, weather is what you get" is an aphorism whose roots date back to a Mark Twain compilation of school children's sayings in the mid-1800s, but what to expect in a changing climate? The answer from the World Meteorological Organization (WMO 2007) is the climate normal—a 30-year average of a given climate variable. Since its first formalization in 1956, the climate normal has evolved into a representation of a particular mean state of a changing climate (Arguez and Vose 2011), where the differences from the previous decade's normal are assumed to be due to long-term trends. For the *State of the Climate in 2021*, many variables discussed are now compared to the most recent 1991–2020 climate normal rather than a 1981–2010 climate normal. For some variables, a 1991–2020 climate normal is not yet available or not used. For other variables, there are not yet 30 years of data for comparison; for example, mean global sea level relies on an altimeter record beginning in 1993. Given that the decadal change in the climate normal is, roughly speaking, simply a shift in the frame of reference, yearly rankings for climate variables are not affected. The status of 2021 as the sixth (or fifth) warmest year on record, as measured by global mean surface temperature, will not change regardless of whether the 1981–2010 or 1991–2020 climate normal is used as a reference. Similarly, magnitudes of year-to-year differences will not be affected, though the frame of reference has changed, in some cases significantly. For example, the annual mean surface air temperature in the Arctic is more than 0.6°C higher in the 1991–2020 climate normal than in the 1981–2010 climate normal with attendant adjustments to the reference frame of the time series of anomalies (Fig. 5.1). In 2020/21 NH lakes froze 3.8 days

later and thawed 3.5 days early vs. the 1991–2020 mean, the second shortest freeze period on record (section 2c4). In 2019/20, in comparison, NH lakes froze over 3 days later/5.5 days earlier vs. the 1981–2010 mean, third shortest on record (Sharma and Woolway 2021). A careful reading of the particular climate normal is needed to properly interpret the quantification of the climate variables in relation to interannual change. This is particularly important in variables, such as classification of ENSO conditions, which rely on a threshold value related to the mean. In fact, the trend in sea surface temperatures in the Nino-3.4 region (L'Heureux et al. 2013) necessitates a 30-year climate normal, which is modified every five years to calculate the threshold value for the Oceanic Niño Index (ONI). Without this more frequent climate normal adjustment, ENSO events defined by the ONI would not always match the physical realities of ENSO formation and consequences.

The layout of the *State of the Climate in 2021* is similar to previous years. Following this introduction (Chapter 1), Chapter 2 catalogs global climate, Chapter 3 the oceans, Chapter 4 the tropics, Chapters 5 and 6 the high latitudes (Arctic and Antarctic, respectively), and Chapter 7 other specific regions of the globe (North America, Central America/Caribbean, South America, Africa, Europe, Asia, and Oceania). Finally, Chapter 8 is a listing of many (though not all) datasets used in the various sections of the *State of the Climate in 2021* and a link to dataset access and further information. Datasets are listed by essential climate variables, with a reference to chapter(s) in which the particular dataset was used. Most of the datasets are readily downloadable by the reader who would like to reproduce the results found in this report or investigate further.

Time series of major climate indicators are again presented in this introductory chapter. Many of these indicators are essential climate variables, originally defined by the World Meteorological Organization's Global Climate Observing System (GCOS 2003) and updated again by GCOS (2010). As their name indicates, these variables are essential for a full understanding of the changing climate system. However, some of them are not available on the immediate timescales of this report, and others, particularly those dealing with the living world, are outside the scope of this report.

Essential Climate Variables—T. BOYER, J. BLUNDEN, AND R. J. H. DUNN

The following variables are considered fully monitored in this report, in that there are sufficient spatial and temporal data, with peer-reviewed documentation to characterize them on a global scale:

- Surface atmosphere: air pressure, precipitation, temperature, water vapor, wind speed and direction
- Upper atmosphere: Earth radiation budget, temperature, water vapor, wind speed and direction
- Atmospheric composition: carbon dioxide, methane and other greenhouse gases, ozone
- Ocean physics: ocean surface heat flux, sea ice, sea level, surface salinity, sea surface temperature, subsurface salinity, subsurface temperature, surface currents, surface stress
- Ocean biogeochemistry: ocean color
- Ocean biogeosystems: plankton
- Land: albedo, river discharge, snow

The following variables are considered partially monitored, in that there is systematic, rigorous measurement found in this report, but some coverage of the variable in time and space is lacking due to observing limitations or availability of data or authors:

- Atmospheric composition: aerosols properties, cloud properties, precursors of aerosol and ozone
- Upper atmosphere: lightning
- Ocean physics: subsurface currents
- Ocean biogeochemistry: inorganic carbon
- Land: above-ground biomass, anthropogenic greenhouse gas fluxes, fire, fraction of absorbed photosynthetically active radiation, glaciers, groundwater, ice sheets and ice shelves, lakes, permafrost, soil moisture
- Surface atmosphere: surface radiation budget

The following variables are not yet covered in this report, or are outside the scope of it.

- Ocean physics: sea state
- Ocean biogeochemistry: nitrous oxide, nutrients, oxygen, transient tracers
- Ocean biogeosystems: marine habitat properties
- Land: anthropogenic water use, land cover, land surface temperature, latent and sensible heat fluxes, leaf area index, soil carbon

Acknowledgments

The editors thank the BAMS editorial staff, in particular Bryan Hanssen, who provided technical guidance, oversaw publication of the report, and continues to help us shepherd the report into a digital publishing era; Liz Wright, who provided peer review support; and Nicole Rietmann, who oversaw the hundreds of citations and references this year; and the NCEI Graphics team for facilitating the construction of the report and executing the countless number of technical edits needed. We thank our technical editor Laura Ohlmann for her dedication and attention to detail. We also express our gratitude to Michael Alexander, who served as the AMS special editor for this report. Finally, we thank all of the authors and chapter editors who provide these valuable contributions each year, always with an aim to improve and expand their analyses for the readers.

Plate 1.1. Global (or representative) average time series for essential climate variables through 2021. Anomalies are shown relative to the base period in parentheses although base periods used in other sections of the report may differ. The numbers in the parentheses in the lower left or right side of each panel indicate how many in situ (red), reanalysis (blue), and satellite (orange), datasets are used to create each time series in that order. (a) NH polar stratospheric ozone (Mar); (b) SH polar stratospheric ozone (Oct); (c) surface temperature; (d) night marine air temperature; (e) lower tropospheric temperature; (f) lower stratospheric temperature; (g) extremes (warm days [solid] and cool days [dotted]); (h) Arctic sea ice extent (max [solid]) and min [dashed]); (i) Antarctic sea ice extent (max [solid] and min [dashed]); (j) glacier cumulative mean specific balance; (k) NH snow cover extent; (l) NH lake ice duration; (m) Mauna Loa apparent transmission; (n) lower stratospheric water vapor; (o) cloudiness; (p) total column water vapor – land; (q) total column water vapor – ocean; (r) upper tropospheric humidity; (s) specific humidity – land; (t) specific humidity – ocean; (u) relative humidity – land; (v) relative humidity – ocean; (w) precipitation – land; (x) precipitation – ocean; (y) ocean heat content (0–700 m); (z) sea level rise; (aa) tropospheric ozone; (ab) tropospheric wind speed at 850 hPa for 20°–40°N; (ac) land wind speed; (ad) ocean wind speed; (ae) biomass burning; (af) global land evaporation; (ag) soil moisture; (ah) terrestrial groundwater storage; (ai) fraction of absorbed photosynthetically active radiation (FAPAR); (aj) land surface albedo – visible (solid) and infrared (dashed).

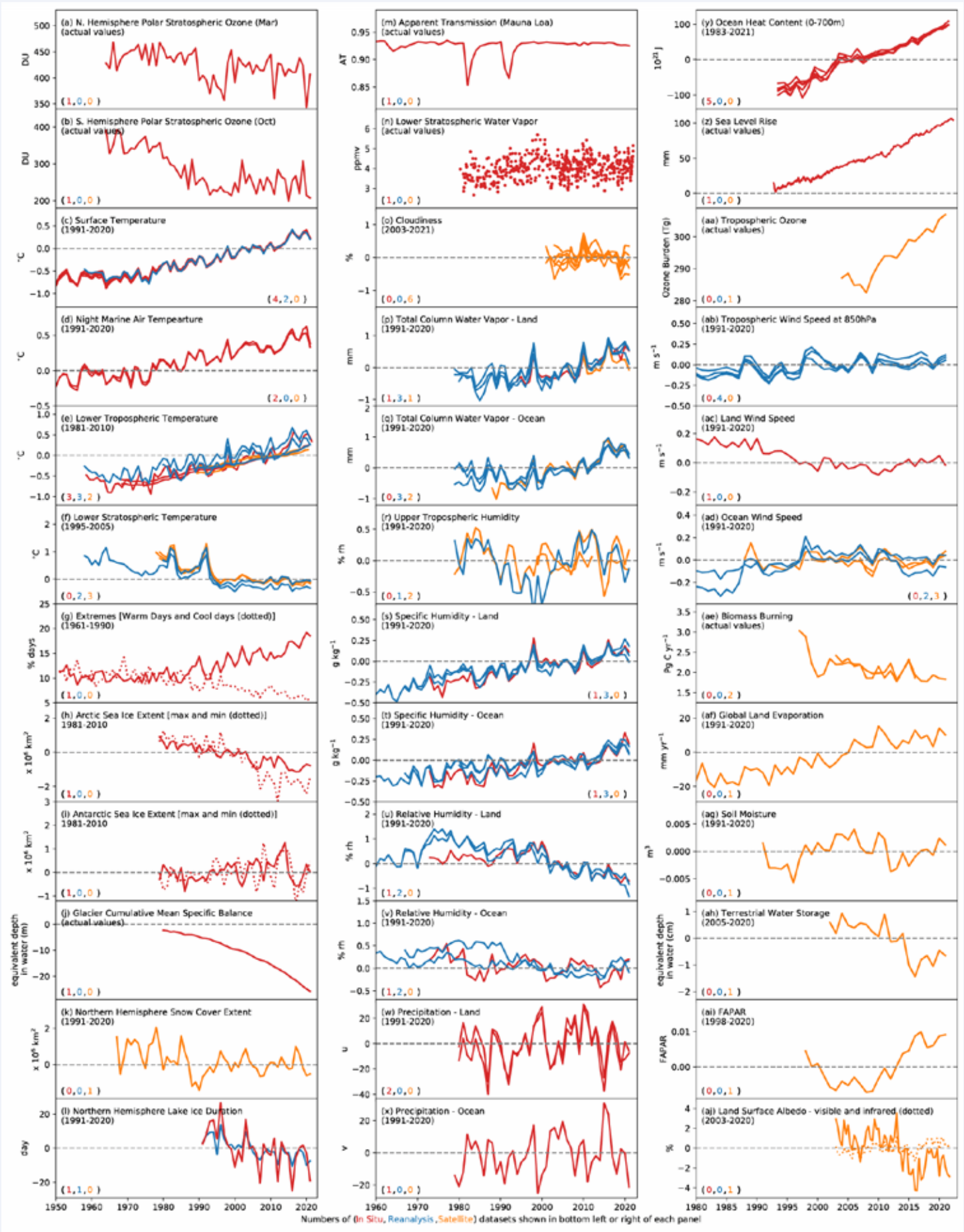
(a) N. Hemisphere Polar Stratospheric Ozone (Mar) (actual values)
DU
(1,0,0)
(b) S. Hemisphere Polar Stratospheric Ozone (Oct) (actual values)
DU
(1,0,0)
(c) Surface Temperature (1991-2020)
°C
(4,2,0)
(d) Night Marine Air Tempearture (1991-2020)
°C
(2,0,0)
(e) Lower Tropospheric Temperature (1981-2010)
°C
(3,3,2)
(f) Lower Stratospheric Temperature (1995-2005)
°C
(0,2,3)
(g) Extremes [Warm Days and Cool days (dotted)] (1961-1990)
% days
(1,0,0)
(h) Arctic Sea Ice Extent [max and min (dotted)] 1981-2010
x 10⁶ km²
(1,0,0)
(i) Antarctic Sea Ice Extent [max and min (dotted)] 1981-2010
x 10⁶ km²
(1,0,0)
(j) Glacier Cumulative Mean Specific Balance (actual values)
equivalent depth in water (m)
(1,0,0)
(k) Northern Hemisphere Snow Cover Extent (1991-2020)
x 10⁶ km²
(0,0,1)
(l) Northern Hemisphere Lake Ice Duration (1991-2020)
day
(1,1,0)
(m) Apparent Transmission (Mauna Loa) (actual values)
AT
(1,0,0)
(n) Lower Stratospheric Water Vapor (actual values)
ppmv
(1,0,0)
(o) Cloudiness (2003-2021)
%
(0,0,6)
(p) Total Column Water Vapor - Land (1991-2020)
mm
(1,3,1)
(q) Total Column Water Vapor - Ocean (1991-2020)
mm
(0,3,2)
(r) Upper Tropospheric Humidity (1991-2020)
% rh
(0,1,2)
(s) Specific Humidity - Land (1991-2020)
g kg⁻¹
(1,3,0)
(t) Specific Humidity - Ocean (1991-2020)
g kg⁻¹
(1,3,0)
(u) Relative Humidity - Land (1991-2020)
% rh
(1,2,0)
(v) Relative Humidity - Ocean (1991-2020)
% rh
(1,2,0)
(w) Precipitation - Land (1991-2020)
u
(2,0,0)
(x) Precipitation - Ocean (1991-2020)
v
(1,0,0)
(y) Ocean Heat Content (0-700m) (1983-2021)
10²² J
(5,0,0)
(z) Sea Level Rise (actual values)
mm
(1,0,0)
(aa) Tropospheric Ozone (actual values)
Ozone Burden (Tg)
(0,0,1)
(ab) Tropospheric Wind Speed at 850hPa (1991-2020)
m s⁻¹
(0,4,0)
(ac) Land Wind Speed (1991-2020)
m s⁻¹
(1,0,0)
(ad) Ocean Wind Speed (1991-2020)
m s⁻¹
(0,2,3)
(ae) Biomass Burning (actual values)
Pg C yr⁻¹
(0,0,2)
(af) Global Land Evaporation (1991-2020)
mm yr⁻¹
(0,0,1)
(ag) Soil Moisture (1991-2020)
m³
(0,0,1)
(ah) Terrestrial Water Storage (2005-2020)
equivalent depth in water (cm)
(0,0,1)
(ai) FAPAR (1998-2020)
FAPAR
(0,0,1)
(aj) Land Surface Albedo - visible and infrared (dotted) (2003-2020)
%
(0,0,1)
Numbers of (In Situ, Reanalysis, Satellite) datasets shown in bottom left or right of each panel

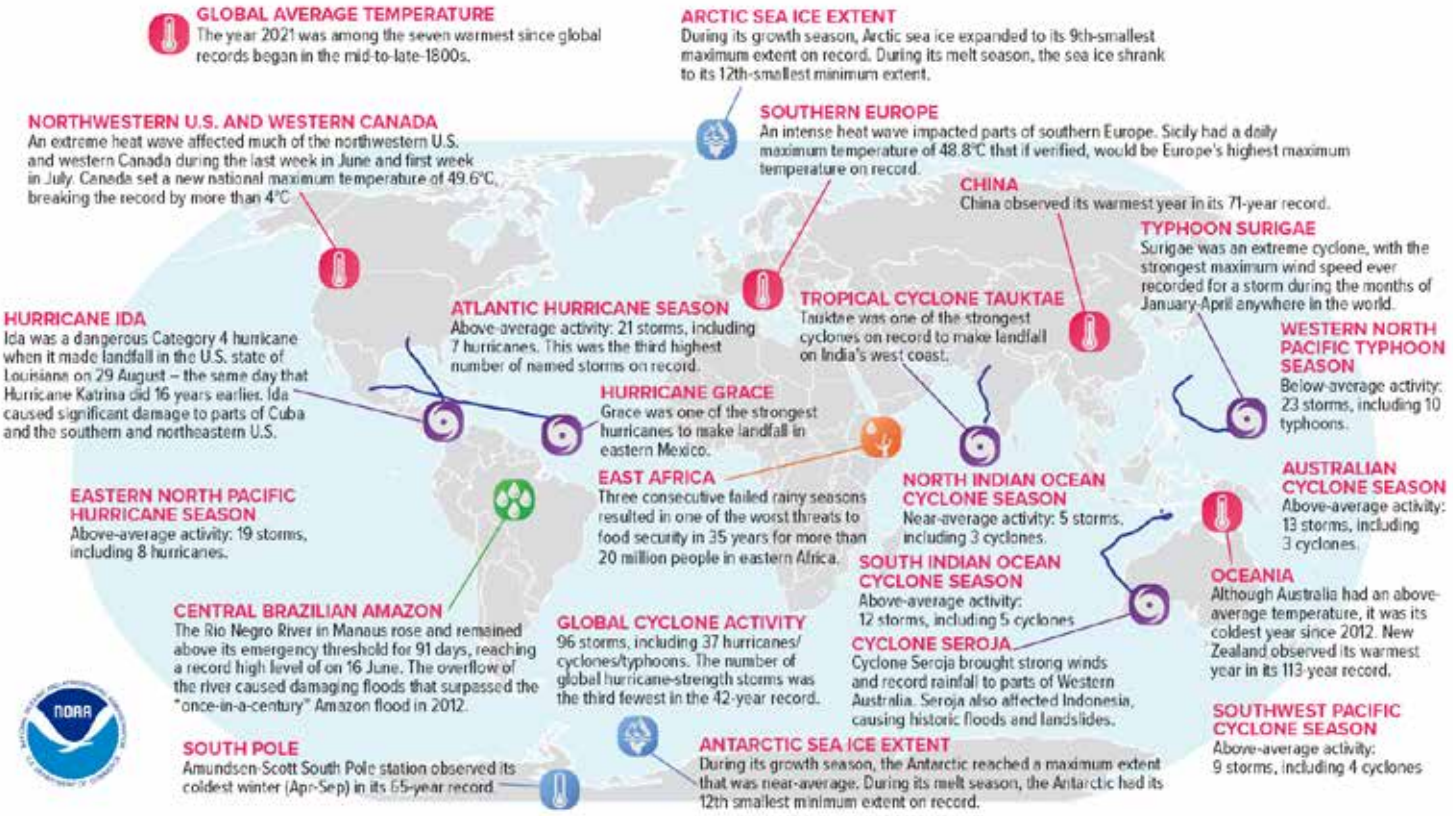

Fig. 1.1. Geographical distribution of selected notable climate anomalies and events in 2021.

References

Arguez, A., and R. S. Vose, 2011: The definition of the standard WMO climate normal: The key to deriving alternative climate normals. *Bull. Amer. Meteor. Soc*., **92**, 699–704, https://doi.org/10.1175/2010BAMS2955.1.

GCOS, 2003: The second report on the adequacy of the global observing system for climate in support of the UNFCCC. WMO/TD 1143, GCOS-82, 85 pp., https://library.wmo.int/doc_num.php?explnum_id=3931.

——, 2010: Implementation plan for the Global Observing System for Climate in Support of the UNFCCC. WMO Tech. Doc. WMO/TD-1523, 186 pp. [Available online at www.wmo.int/pages/prog/gcos/Publications/gcos-138.pdf.]

Hu, Z.-Z., A. Kumar, Y. Xue, and B. Ja, 2014: Why were some La Niñas followed by another La Niña? *Climate Dyn.*, **42**, 1029–1042, https://doi.org/10.1007/s00382-013-1917-3.

L'Heureux, M. L., D.C. Collins, and Z.-Z. Hu, 2013: Linear trends in sea surface temperature of the tropical Pacific Ocean and implications for the El Niño-Southern Oscillation. *Climate Dyn*, **40**, 1223–1236, https://doi.org/10.1007/s00382-012-1331-2.

Sharma, S., and R. I. Woolway, 2021: Lake ice, [in "State of the Climate in 2020"]. *Bull. Amer. Meteor. Soc.*, **102** (8), S48–S51, https://doi.org/10.1175/BAMS-D-21-0098.1.

WMO, 2007: The role of climatological normals in a changing climate. WMO/TD-1377, WCDMP-61, World Meteorological Organization, 130 pp., https://library.wmo.int/index.php?lvl=notice_display&id=16659.

STATE OF THE CLIMATE IN 2021

GLOBAL CLIMATE

R. J. H. Dunn, F. Aldred, N. Gobron, J. B Miller, and K. M. Willett, Eds.

Special Online Supplement to the *Bulletin of the American Meteorological Society*, Vol. 103, No. 8, August 2022

doi:10.1175/BAMS-D-22-0092.1

Corresponding author: Robert Dunn / robert.dunn@metoffice.gov.uk

STATE OF THE CLIMATE IN 2021
Global Climate

Editors

Jessica Blunden
Tim Boyer

Chapter Editors

Freya Aldred
Peter Bissolli
Kyle R. Clem
Howard J. Diamond
Matthew L. Druckenmiller
Robert J. H. Dunn
Catherine Ganter
Nadine Gobron
Gregory C. Johnson
Rick Lumpkin
Ademe Mekonnen
John B. Miller
Twila A. Moon
Marilyn N. Raphael
Ahira Sánchez-Lugo
Carl J. Schreck III
Richard L. Thoman
Kate M. Willett
Zhiwei Zhu

Technical Editor

Laura Ohlmann

BAMS Special Editor for Climate

Michael A. Alexander

American Meteorological Society

Cover credit:
Caption: Lightning discharges appear in various colours depending on the scatter of light inside the thundercloud and in the atmosphere. The intracloud lightning discharges in the centre of the thundercloud appear to be white with a bluish tint, and the cloud-to-ground discharge below appears to be orange. The right hand side of the thundercloud exhibits a green tint that is attributed to the unique composition of hydrometeors inside the thundercloud.

The photo was taken in the late evening of 10 September 2013, near Tarragona in northeastern Spain.

Global Climate is one chapter from the State of the Climate in 2021 annual report and is available from https://doi.org/10.1175/BAMS-D-22-0092.1. Compiled by NOAA's National Centers for Environmental Information, *State of the Climate in 2021* is based on contributions from scientists from around the world. It provides a detailed update on global climate indicators, notable weather events, and other data collected by environmental monitoring stations and instruments located on land, water, ice, and in space.
The full report is available from https://doi.org/10.1175/2022BAMSStateoftheClimate.1

How to cite this document:

Citing the complete report:
Blunden, J. and T. Boyer, Eds., 2022: "State of the Climate in 2021". *Bull. Amer. Meteor. Soc.*, **103** (8), Si–S465 https://doi.org/10.1175/2022BAMSStateoftheClimate.1

Citing this chapter:
Dunn, R. J. H., F. Aldred, N. Gobron, J. B Miller, and K. M. Willett, Eds., 2022: Global Climate [in "State of the Climate in 2021"]. *Bull. Amer. Meteor. Soc.*, **103** (8), S11–S142, https://doi.org/10.1175/BAMS-D-22-0092.1.

Citing a section (example):
Cornes, R. C., T. Cropper, R. Junod, and E. C. Kent, 2022: Night marine air temperature [in "State of the Climate in 2021"]. *Bull. Amer. Meteor. Soc.*, **103** (8), S31–S33, https://doi.org/10.1175/BAMS-D-22-0092.1.

Editor and Author Affiliations (alphabetical by name)

Ades, Melanie, European Centre for Medium-Range Weather Forecasts, Reading, United Kingdom
Adler, Robert, CMNS-Earth System Science Interdisciplinary Center, University of Maryland, College Park, Maryland
Aldred, Freya, Met Office Hadley Centre, Exeter, United Kingdom
Allan, R. P., Department of Meteorology and National Centre for Earth Observation, University of Reading, Reading, United Kingdom
Anderson, John, Department of Atmospheric and Planetary Science, Hampton University, Hampton, Virginia
Anneville, Orlane, National Research Institute for Agriculture, Food and Environment (INRAE), CARRTEL, Université Savoie Mont Blanc, Thonon les Bains, France
Aono, Yasuyuki, Graduate School of Life and Environmental Sciences, Osaka Prefecture University, Sakai, Osaka, Japan
Argüez, Anthony, NOAA/NESDIS National Centers for Environmental Information, Asheville, North Carolina
Arosio, Carlo, University of Bremen, Bremen, Germany
Augustine, John A., NOAA Global Monitoring Laboratory, Boulder, Colorado
Azorin-Molina, Cesar, Centro de Investigaciones sobre Desertificación, Spanish National Research Council (CIDE, CSIC-UV-Generalitat Valenciana), Climate, Atmosphere and Ocean Laboratory (Climatoc-Lab), Moncada, Valencia, Spain
Barichivich, Jonathan, Instituto de Geografía, Pontificia Universidad Católica de Valparaíso, Valparaíso, Chile and Climatic Research Unit, School of Environmental Sciences, University of East Anglia, Norwich, United Kingdom
Basu, Aman, York University, Toronto, Canada
Beck, Hylke E., Joint Research Centre of the European Commission, Ispra, Italy and GloH2O, Almere, the Netherlands
Bellouin, Nicolas, University of Reading, Reading, United Kingdom
Benedetti, Angela, European Centre for Medium-Range Weather Forecasts, Reading, United Kingdom
Blagrave, Kevin, York University, Toronto, Canada
Blenkinsop, Stephen, School of Engineering, Newcastle University, Newcastle-upon-Tyne, United Kingdom
Bock, Olivier, Université de Paris Cité, Institut de physique du globe de Paris, CNRS, IGN, F-7500 Paris, France
Bodin, Xavier, Laboratoire EDYTEM, CNRS/Université Savoie Mont-Blanc, Le Bourget-du-Lac, France
Bosilovich, Michael G., Global Modeling and Assimilation Office, NASA Goddard Space Flight Center, Greenbelt, Maryland
Boucher, Olivier, Sorbonne Université, Paris, France
Bove, Gerald, University of the Virgin Islands, St. Thomas, U.S. Virgin Islands
Buechler, Dennis, University of Huntsville Alabama, Huntsville, Alabama
Buehler, Stefan A., Meteorologisches Institut, Centrum für Erdsystem- und Nachhaltigkeitsforschung (CEN), Fachbereich Erdsystemwissenschaften, Universität Hamburg, Hamburg, Germany
Carrea, Laura, Department of Meteorology, University of Reading, Reading, United Kingdom
Chang, Kai-Lan, Cooperative Institute for Research in Environmental Sciences, University of Colorado Boulder; and NOAA Chemical Sciences Laboratory, Boulder, Colorado
Christiansen, Hanne H., Geology Department, University Centre in Svalbard, Longyearbyen, Norway
Christy, John R., The University of Alabama in Huntsville, Huntsville, Alabama
Chung, Eui-Seok, IBS Center for Climate Physics, South Korea
Ciasto, Laura M., NOAA Climate Prediction Center, College Park, Maryland
Coldewey-Egbers, Melanie, DLR (German Aerospace Center) Oberpfaffenhofen, Wessling, Germany
Cooper, Owen R., Cooperative Institute for Research in Environmental Sciences, University of Colorado, Boulder, Colorado; and NOAA Chemical Sciences Laboratory, Boulder, Colorado
Cornes, Richard C., National Oceanography Centre, Southampton, United Kingdom
Covey, Curt, Lawrence Livermore National Laboratory, Livermore California
Cropper, Thomas, National Oceanography Centre, Southampton, United Kingdom
Crotwell, Molly, Cooperative Institute for Research in Environmental Sciences, University of Colorado, Boulder, Colorado; and NOAA Global Monitoring Laboratory, Boulder, Colorado
Cusicanqui, Diego, Université Grenoble Alpes, Institut de Géosciences de l'Environnement (IGE), Grenoble, France
Davis, Sean M., NOAA Chemical Sciences Laboratory, Boulder, Colorado
de Jeu, Richard A. M., Planet Labs, Haarlem, The Netherlands
Degenstein, Doug, University of Saskatchewan, Saskatoon, Saskatchewan, Canada
Delaloye, Reynald, Department of Geosciences, University of Fribourg, Fribourg, Switzerland
Donat, Markus G., Barcelona Supercomputing Centre, Barcelona, Spain and Catalan Institution for Research and Advanced Studies (ICREA), Barcelona, Spain
Dorigo, Wouter A., TU Wien, Vienna, Austria
Dunn, Robert J. H., Met Office Hadley Centre, Exeter, United Kingdom
Durre, Imke, NOAA/NESDIS National Centers for Environmental Information, Asheville, North Carolina
Dutton, Geoff S., Cooperative Institute for Research in Environmental Sciences, University of Colorado, Boulder, Colorado; and NOAA Global Monitoring Laboratory, Boulder, Colorado
Duveiller, Gregory, Max Planck Institute for Biogeochemistry, Jena , Germany
Elkins, James W., NOAA Global Monitoring Laboratory, Boulder, Colorado
Estilow, Thomas W., Rutgers University, Piscataway, New Jersey
Fedaeff, Nava, National Institute of Water and Atmospheric Research (NIWA), New Zealand
Fereday, David, Met Office Hadley Centre, Exeter, United Kingdom
Fioletov, Vitali E., Environment and Climate Change Canada, Toronto, Canada
Flemming, Johannes, Copernicus Department, European Centre for Medium-Range Weather Forecasts, Reading, United Kingdom
Foster, Michael J., Cooperative Institute for Meteorological Satellite Studies, Space Science and Engineering Center, University of Wisconsin-Madison, Madison, Wisconsin
Frith, Stacey M., Science Systems and Applications, Inc., Lanham, Maryland; and NASA Goddard Space Flight Center, Greenbelt, Maryland
Froidevaux, Lucien, Jet Propulsion Laboratory, California Institute of Technology, Pasadena, California
Füllekrug, Martin, University of Bath, Bath, United Kingdom
Garforth, Judith, Woodland Trust, Grantham, United Kingdom
Garg, Jay, SSAI, Hampton, Virginia
Gentry, Matthew, Cooperative Institute for Research in Environmental Sciences, University of Colorado, Boulder, Colorado; and NOAA Global Monitoring Laboratory, Boulder, Colorado
Gobron, Nadine, European Commission Joint Research Centre, Ispra, Italy
Goodman, Steven, Thunderbolt Global Analytics, Huntsville, Alabama
Gou, Qiqi, Hydro-Climate Extremes Lab (H-CEL), Ghent University, Ghent, Belgium
Granin, Nikolay, Siberian Branch of Russian Academy of Sciences, Irkutsk, Russia
Guglielmin, Mauro, Department of Theoretical and Applied Science, Insubria University, Italy
Hahn, Sebastian, TU Wien, Vienna, Austria
Haimberger, Leopold, Department of Meteorology and Geophysics, University of Vienna, Vienna, Austria

Editor and Author Affiliations (alphabetical by name)

Hall, Brad D., NOAA Global Monitoring Laboratory, Boulder, Colorado
Harris, Ian, National Centre for Atmospheric Science (NCAS), University of East Anglia, Norwich, United Kingdom; and Climatic Research Unit, School of Environmental Sciences, University of East Anglia, Norwich, United Kingdom
Hemming, Debbie L., Met Office Hadley Centre, Exeter, United Kingdom; and Birmingham Institute of Forest Research, Birmingham University, Birmingham, United Kingdom
Hirschi, Martin, ETH Zürich, Zürich, Switzerland
Ho, Shu-pen (Ben), Center for Satellite Applications and Research, NOAA, College Park, Maryland
Holzworth, Robert, University of Washington, Seattle, Washington
Hrbáček, Filip, Department of Geography, Masaryk University, Brno, Czech Republic
Hubert, Daan, Royal Belgian Institute for Space Aeronomy (BIRA-IASB), Brussels, Belgium
Hulsman, Petra, Hydro-Climate Extremes Lab (H-CEL), Ghent University, Ghent, Belgium
Hurst, Dale F., Cooperative Institute for Research in Environmental Sciences, University of Colorado Boulder, Boulder, Colorado; NOAA Global Monitoring Laboratory, Boulder, Colorado
Inness, Antje, European Centre for Medium-Range Weather Forecasts, Reading, United Kingdom
Isaksen, Ketil, Norwegian Meteorological Institute, Oslo, Norway
John, Viju O., EUMETSAT, Darmstadt, Germany
Jones, Philip D., Climatic Research Unit, School of Environmental Sciences, University of East Anglia, Norwich, United Kingdom
Junod, Robert, Earth System Science Center (ESSC), University of Alabama in Huntsville, Huntsville, Alabama
Kääb, Andreas, Department of Geosciences, University of Oslo, Norway
Kaiser, Johannes W., Centre for Agrometeorological Research (ZAMF), German Meteorological Service (DWD), Braunschweig, Germany
Kaufmann, Viktor, Institute of Geodesy, Working Group Remote Sensing and Photogrammetry, Graz University of Technology, Graz, Austria
Kellerer-Pirklbauer, Andreas, Institute of Geography and Regional Science, Cascade – The Mountain Processes and Mountain Hazards Group, University of Graz, Graz, Austria
Kent, Elizabeth C., National Oceanography Centre, Southampton, United Kingdom
Kidd, Richard, Earth Observation Data Centre (EODC), Vienna, Austria
Kim, Hyungiun, Moon Soul Graduate School of Future Strategy and Department of Civil and Environmental Engineering, Korea Advanced Institute of Science and Technology, Daejeon, Korea
Kipling, Zak, European Centre for Medium-Range Weather Forecasts, Reading, United Kingdom
Koppa, Akash, Hydro-Climate Extremes Lab (H-CEL), Ghent University, Ghent, Belgium
L'Abée-Lund, Jan Henning, Norwegian Water Resources and Energy Directorate, Oslo, Norway
Lan, Xin, Cooperative Institute for Research in Environmental Sciences, University of Colorado, Boulder, Colorado; NOAA Global Monitoring Laboratory, Boulder, Colorado
Lantz, Kathleen O., NOAA Global Monitoring Laboratory, Boulder, Colorado
Lavers, David, European Centre for Medium-Range Weather Forecasts, Reading, United Kingdom
Loeb, Norman G., NASA Langley Research Center, Hampton, Virginia
Loyola, Diego, DLR (German Aerospace Center) Oberpfaffenhofen, Wessling, Germany
Madelon, Remi, CESBIO (Université Toulouse 3, CNES, CNRS, INRAE, IRD), Toulouse, France
Malmquist, Hilmar J., Icelandic Museum of Natural History, Reykjavík, Iceland
Marszelewski, Wlodzimierz, Nicolaus Copernicus University in Toruń, Toruń, Poland
Mayer, Michael, University of Vienna, Vienna, Austria; and European Centre for Medium-Range Weather Forecasts, Reading, United Kingdom
McCabe, Matthew F., Division of Biological and Environmental Sciences and Engineering, King Abdullah University of Science and Technology, Thuwal, Saudi Arabia
McVicar, Tim R., CSIRO Land and Water, Canberra, Australian Capital Territory; and Australian Research Council Centre of Excellence for Climate Extremes, Sydney, New South Wales, Australia
Mears, Carl A., Remote Sensing Systems, Santa Rosa, California
Menzel, Annette, TUM School of Life Sciences, Technical University of Munich, Freising, Germany; and Institute for Advanced Study, Technical University of Munich, Garching, Germany
Merchant, Christopher J., Department of Meteorology, University of Reading, Reading, United Kingdom
Miller, John B., NOAA Global Monitoring Laboratory, Boulder, Colorado
Miralles, Diego G., Hydro-Climate Extremes Lab (H-CEL), Ghent University, Ghent, Belgium
Montzka, Stephen A., NOAA Global Monitoring Laboratory, Boulder, Colorado
Morice, Colin, Met Office Hadley Centre, Exeter, United Kingdom
Mösinger, Leander, TU Wien, Vienna, Austria
Mühle, Jens, Scripps Institution of Oceanography, University of California, San Diego, La Jolla, California
Nicolas, Julien P., European Centre for Medium-Range Weather Forecasts, Reading, United Kingdom
Noetzli, Jeannette, WSL Institute for Snow and Avalanche Research SLF, Davos-Dorf, Switzerland and Climate Change, Extremes and Natural Hazards in Alpine Regions Research Center CERC, Davos Dorf, Switzerland
Nõges, Tiina, Estonian University of Life Sciences, Tartu, Estonia
Noll, Ben, National Institute of Water and Atmospheric Research (NIWA), New Zealand
O'Keefe, John, The Harvard Forest, Harvard University, Petersham, Massachusetts
Osborn, Tim J., Climatic Research Unit, School of Environmental Sciences, University of East Anglia, Norwich, United Kingdom
Park, Taejin, NASA Ames Research Center, Moffett Field, California; Bay Area Environmental Research Institute, Moffett Field, California
Pellet, Cecile, Department of Geosciences, University of Fribourg, Fribourg, Switzerland
Pelto, Maury S., Nichols College, Dudley, Massachusetts
Perkins-Kirkpatrick, Sarah E., University of New South Wales, Canberra, Australia
Phillips, Coda, Cooperative Institute for Meteorological Satellite Studies, Space Science and Engineering Center, University of Wisconsin-Madison, Madison, Wisconsin
Po-Chedley, Stephen, Program for Climate Model Diagnosis and Intercomparison, Lawrence Livermore National Laboratory, Livermore, California
Polvani, Lorenzo, Columbia University, New York, New York
Preimesberger, Wolfgang, TU Wien, Vienna, Austria
Price, Colin, Tel Aviv University, Tel Aviv, Israel
Pulkkanen, Merja, Finnish Environment Institute SYKE, Helsinki, Finland
Rains, Dominik G., Hydro-Climate Extremes Lab (H-CEL), Ghent University, Ghent, Belgium
Randel, William J., National Center for Atmospheric Research (NCAR), Boulder, Colorado

Rémy, Samuel, HYGEOS, Lille, France
Ricciardulli, Lucrezia, Remote Sensing Systems, Santa Rosa, California
Richardson, Andrew D., School of Informatics, Computing, and Cyber Systems and Center for Ecosystem Science and Society, Northern Arizona University, Flagstaff, Arizona
Robinson, David A., Rutgers University, Piscataway, New Jersey
Rodell, Matthew, Hydrological Sciences Laboratory, NASA Goddard Space Flight Center, Greenbelt, Maryland
Rodríguez-Fernández, Nemesio J., CESBIO, Université Toulouse 3, CNES, CNRS, INRAE, IRD, Toulouse, France
Rosenlof, Karen H., NOAA Chemical Sciences Laboratory, Boulder, Colorado
Roth, Chris, University of Saskatchewan, Saskatoon, Canada
Rozanov, Alexei, University of Bremen, Bremen, Germany
Rutishäuser, This, Swiss Academy of Sciences (SCNAT), Bern, Switzerland
Sánchez-Lugo, Ahira, NOAA/NESDIS National Centers for Environmental Information, Asheville, North Carolina
Sawaengphokhai, Parnchai, Science Systems and Applications, Inc. (SSAI), Hampton, Virginia
Schenzinger, Verena, Medical University of Innsbruck, Innsbruck, Austria
Schlegel, Robert W., Sorbonne Université, CNRS, Villefranche-sur-mer, France
Schneider, Udo, Global Precipitation Climatology Centre, Deutscher Wetterdienst, Offenbach, Germany
Sharma, Sapna, York University, Toronto, Ontario, Canada
Shi, Lei, NOAA/NESDIS National Centers for Environmental Information, Asheville, North Carolina
Simmons, Adrian J., European Centre for Medium-Range Weather Forecasts, Reading, United Kingdom
Siso, Carolina, Cooperative Institute for Research in Environmental Sciences, University of Colorado, Boulder CO USA, and NOAA Global Monitoring Laboratory, Boulder, Colorado
Smith, Sharon L., Geological Survey of Canada, Natural Resources Canada, Ottawa, Canada
Soden, Brian J., University of Miami Rosenstiel School of Marine and Atmospheric Science (RSMAS), Key Biscayne, Florida
Sofieva, Viktoria, Finnish Meteorological Institute (FMI), Helsinki, Finland
Sparks, Tim H., Poznań University of Life Sciences, Poznań, Poland
Stackhouse, Jr., Paul W., NASA Langley Research Center, Hampton, Virginia
Stauffer, Ryan, NASA Goddard Space Flight Center, Greenbelt, Maryland
Steinbrecht, Wolfgang, German Weather Service (DWD), Hohenpeissenberg, Germany
Steiner, Andrea K., Wegener Center for Climate and Global Change, University of Graz, Graz, Austria
Stewart, Kenton, State University of New York at Buffalo, Buffalo, New York
Stradiotti, Pietro, TU Wien, Vienna, Austria
Streletskiy, Dimitri A., George Washington University, Washington, D.C.
Telg, Hagen, Cooperative Institute for Research in the Environmental Sciences, University of Colorado, Boulder, Colorado
Thackeray, Stephen J., Centre for Ecology and Hydrology, Lancaster, United Kingdom
Thibert, Emmanuel, Université Grenoble Alpes, INRAE, UR ETGR, Grenoble, France
Todt, Michael, Cooperative Institute for Research in the Environmental Sciences, University of Colorado, Boulder
Tokuda, Daisuke, Institute of Industrial Science, The University of Tokyo, Tokyo, Japan
Tourpali, Kleareti, Aristotle University, Thessaloniki, Greece
Tye, Mari R., National Center for Atmospheric Research, Boulder, Colorado
van der A, Ronald, Royal Netherlands Meteorological Institute (KNMI), DeBilt, The Netherlands
van der Schalie, Robin, Planet Labs, Haarlem, The Netherlands
van der Schrier, Gerard, Royal Netherlands Meteorological Institute, De Bilt, The Netherlands
van der Vliet, Mendy, Planet Labs, Haarlem, The Netherlands
van der Werf, Guido R., Faculty of Science, Vrije Universiteit Amsterdam, Amsterdam, Netherlands
van Vliet, Arnold., Environmental Systems Analysis Group, Wageningen University & Research, the Netherlands
Vernier, Jean-Paul, National Institute of Aerospace/NASA Langley Research Center, Hampton, Virginia
Vimont, Isaac J., Cooperative Institute for Research in Environmental Sciences, University of Colorado Boulder; and NOAA Global Monitoring Laboratory, Boulder, Colorado
Virts, Katrina, University of Huntsville, Huntsville, Alabama
Vivero, Sebastiàn, Department of Geosciences, University of Fribourg, Fribourg, Switzerland
Vömel, Holger, Earth Observing Laboratory, National Center for Atmospheric Research, Boulder, Colorado
Vose, Russell S., NOAA National Centers for Environmental Information, Asheville, North Carolina
Wang, Ray H. J., Georgia Institute of Technology, Atlanta, Georgia
Weber, Markus, University of Bremen, Bremen, Germany
Wiese, David, Jet Propulsion Laboratory, California Institute of Technology, Pasadena, California
Wild, Jeanette D., ESSIC/University of Maryland, College Park, Maryland; and NOAA Climate Prediction Center, College Park, Maryland
Willett, Kate M., Met Office Hadley Centre, Exeter, United Kingdom
Williams, Earle, Massachusetts Institute of Technology, Cambridge, Massachusetts
Wong, Takmeng, NASA Langley Research Center, Hampton, Virginia
Woolway, R. I., School of Ocean Sciences, Bangor University, Menai Bridge, Anglesey, Wales
Yin, Xungang, NOAA National Centers for Environmental Information, Asheville, North Carolina
Yuan, Ye, TUM School of Life Sciences, Technical University of Munich, Freising, Germany
Zhao, Lin, School of Geographical Sciences, Nanjing University of Information Science and Technology, Nanjing, China
Zhou, Xinjia, Center for Satellite Applications and Research, NOAA, College Park, Maryland
Ziemke, Jerry R., Goddard Earth Sciences Technology and Research, Morgan State University, Baltimore, Maryland; and NASA Goddard Space Flight Center, Greenbelt, Maryland
Ziese, Markus, Global Precipitation Climatology Centre, Deutscher Wetterdienst, Offenbach am Main, Germany
Zotta, Ruxandra M., TU Wien, Vienna, Austria

Editorial and Production Team

Allen, Jessicca, Graphics Support, Cooperative Institute for Satellite Earth System Studies, North Carolina State University, Asheville, North Carolina

Camper, Amy, Graphics Support, Innovative Consulting and Management Services, LLC, NOAA/NESDIS National Centers for Environmental Information, Asheville, North Carolina

Hammer, Gregory, Content Team Lead, Communications and Outreach, NOAA/NESDIS National Centers for Environmental Information, Asheville, North Carolina

Love-Brotak, S. Elizabeth, Lead Graphics Production, NOAA/NESDIS National Centers for Environmental Information, Asheville, North Carolina

Misch, Deborah J., Graphics Support, Innovative Consulting and Management Services, LLC, NOAA/NESDIS National Centers for Environmental Information, Asheville, North Carolina

Ohlmann, Laura, Technical Editor, Innovative Consulting and Management Services, LLC, NOAA/NESDIS National Centers for Environmental Information, Asheville, North Carolina

Riddle, Deborah B., Graphics Support, NOAA/NESDIS National Centers for Environmental Information, Asheville, North Carolina

Veasey, Sara W., Visual Communications Team Lead, Communications and Outreach, NOAA/NESDIS National Centers for Environmental Information, Asheville, North Carolina

2. Table of Contents

2. Table of Contents

*Please refer to Chapter 8 (Relevant datasets and sources) for a list of all climate variables and datasets used in this chapter for analyses, along with their websites for more information and access to the data.

2. GLOBAL CLIMATE

R. J. H. Dunn, F. Aldred, N. Gobron, J. B. Miller, and K. M. Willett, Eds.

a. Introduction—R. J. H. Dunn, F. Aldred, N. Gobron, J. B Miller, and K. M. Willett

In 2021, both social and economic activities began to return towards the levels preceding the COVID-19 pandemic for some parts of the globe, with others still experiencing restrictions. Meanwhile, the climate has continued to respond to the ongoing increase in greenhouse gases and resulting warming. La Niña, a phenomenon which tends to depress global temperatures while changing rainfall patterns in many regions, prevailed for all but two months of the year. Despite this, 2021 was one of the six-warmest years on record as measured by global mean surface temperature with an anomaly of between +0.21° and +0.28°C above the 1991–2020 climatology.

Lake surface temperatures were their highest on record during 2021. The number of warm days over land also reached a new record high. Exceptional heat waves struck the Pacific Coast of North America, leading to a new Canadian maximum temperature of 49.6°C at Lytton, British Columbia, on 29 June, breaking the previous national record by over 4°C. In Death Valley, California, the peak temperature reached 54.4°C on 9 July, equaling the temperature measured in 2020, and the highest temperature recorded anywhere on the globe since at least the 1930s. Over the Mediterranean, a provisional new European record of 48.8°C was set in Sicily on 11 August. In the atmosphere, the annual mean tropospheric temperature was among the 10 highest on record, while the stratosphere continued to cool.

While La Niña was present except for June and July, likely influencing Australia's coolest year since 2012 and wettest since 2016, other modes of variability played important roles. A negative Indian Ocean dipole event became established during July, associated with a warmer east and cooler west Indian Ocean. Northern Hemisphere winters were affected by a negative phase of the North Atlantic Oscillation at both the beginning and end of 2021. In the Southern Hemisphere, a very strong positive Southern Annular Mode (also known as the Antarctic Oscillation) contributed to New Zealand's record warm year and to very cold temperatures over Antarctica. Land surface winds continued a slow reversal from the multi-decadal stilling, and over the ocean wind speeds were at their highest in almost a decade.

La Niña conditions had a clear influence on the regional patterns of many hydrological variables. Surface specific humidity and total column water vapor over land and ocean were higher than average in almost all datasets. Relative humidity over land reached record or near-record low saturation depending on the dataset, but with mixed signals over the ocean. Satellite measurements showed that 2021 was the third cloudiest in the 19-year record. The story for precipitation was mixed, with just below-average mean precipitation falling over land and below-average mean precipitation falling over the ocean, while extreme precipitation was generally more frequent, but less intense, than average. Differences between means and extremes can be due to several factors, including using different indices, observing periods, climatological base reference periods, and levels of spatial completeness. The sharp increase in global drought area that began in mid-2019 continued in 2021, reaching a peak in August with 32% of global land area experiencing moderate or worse drought, and declining slightly thereafter.

Arctic permafrost temperatures continued to rise, reaching record values at many sites, and the thickness of the layer which seasonally thaws and freezes also increased over 2020 values

in a number of regions. It was the 34th-consecutive year of mass balance loss for alpine glaciers in mountainous regions, with glaciers on average 25 m thinner than in the late 1970s. And the duration of lake ice in the Northern Hemisphere was the fourth lowest in situ record dating back to 1991.

The atmospheric concentrations of the major long-lived greenhouse gases, CO_2, CH_4, and N_2O, all reached levels not seen in at least the last million years and grew at near-record rates in 2021. La Niña conditions did not appear to have any appreciable impact on their growth rates. The growth rate for CH_4, of 17 ppb yr^{-1}, was similar to that for 2020 and set yet another record, although the causes for this post-2019 acceleration are unknown presently. Overall, CO_2 growth continues to dominate the increase in global radiative forcing, which increased from 3.19 to 3.23 W m^{-2} (watts per square meter) during the year. In 2021, stratospheric ozone did not exhibit large negative anomalies, especially near the poles, unlike 2020, where large ozone depletions appeared, mainly from dynamical effects. The positive impact of reductions in emissions of ozone depleting substances can be seen most clearly in the upper stratosphere, where such dynamical effects are less pronounced.

It was the fourth-lowest fire year since global records began in 2003, though extreme regional fire activity was again seen in North America and also in Siberia; as in 2020, the effects of wildfires in these two regions led to locally large regional positive anomalies in tropospheric aerosol and carbon monoxide abundance.

Vegetation is responding to the higher global mean temperatures, with the satellite-derived measures for the Northern Hemisphere for 2021 rated among the earliest starts of the growing season and the latest end of the season on record. The first bloom date for cherry trees in Kyoto, Japan, broke a 600-year record set in 1409.

This year we welcome a sidebar on the global distribution of lightning, which has been recently declared an essential climate variable (ECV) by the Global Climate Observing System (GCOS).

Time series and anomaly maps from many of the variables described in this chapter can be found in Plates 1.1 and 2.1. As with other chapters, many of the sections have moved from the previous 1981–2010 to the new 1991–2020 climatological reference period, in line with WMO recommendations (see Chapter 1). This is not possible for all datasets, as it is dependent on their length of record or legacy processing methods. While anomalies from the new climatology period are not so easily comparable with previous editions of this report, they more clearly highlight deviations from more recent conditions.

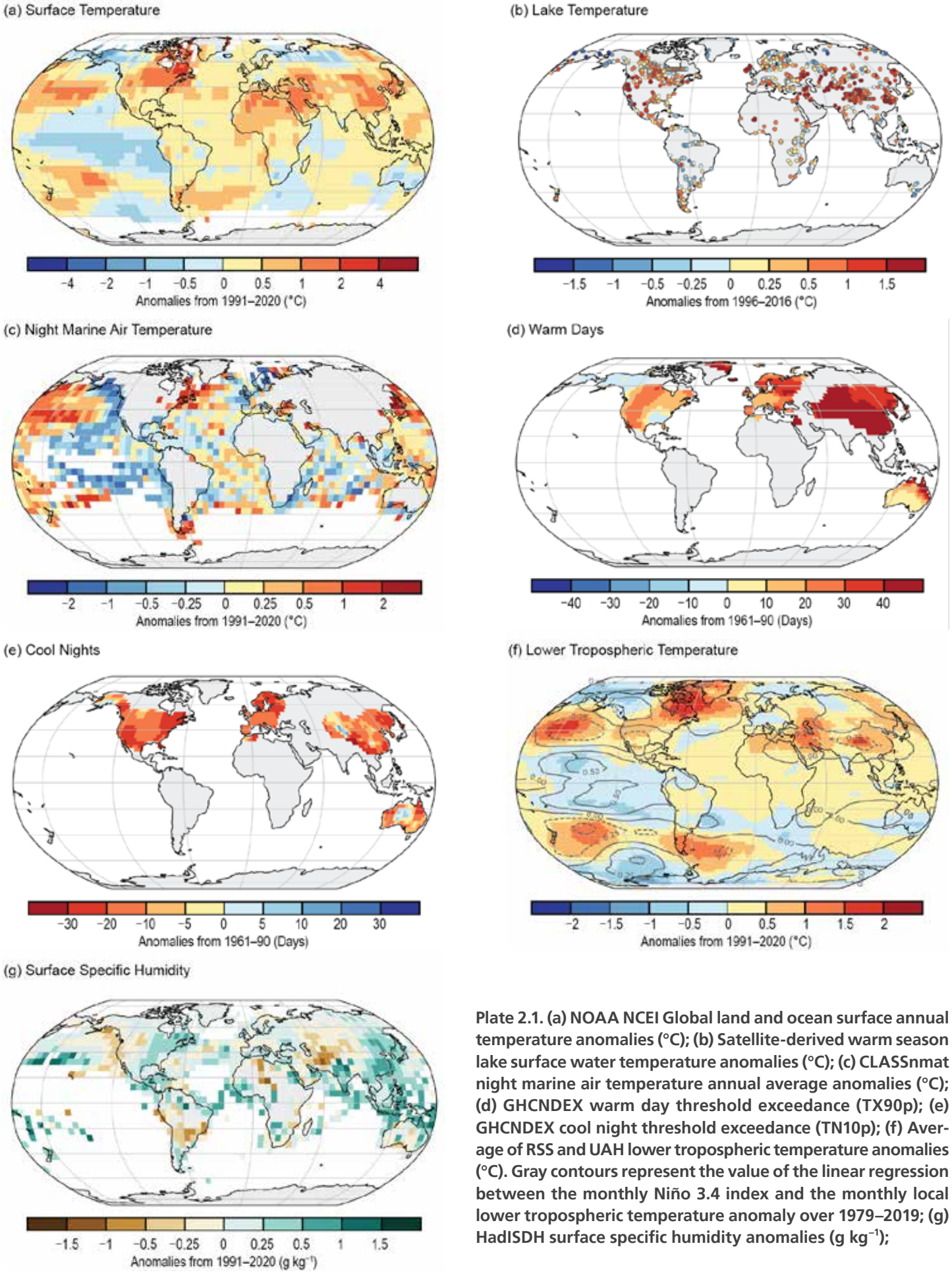

Plate 2.1. (a) NOAA NCEI Global land and ocean surface annual temperature anomalies (°C); (b) Satellite-derived warm season lake surface water temperature anomalies (°C); (c) CLASSnmat night marine air temperature annual average anomalies (°C); (d) GHCNDEX warm day threshold exceedance (TX90p); (e) GHCNDEX cool night threshold exceedance (TN10p); (f) Average of RSS and UAH lower tropospheric temperature anomalies (°C). Gray contours represent the value of the linear regression between the monthly Niño 3.4 index and the monthly local lower tropospheric temperature anomaly over 1979–2019; (g) HadISDH surface specific humidity anomalies (g kg^{-1});

(h) Surface Relative Humidity

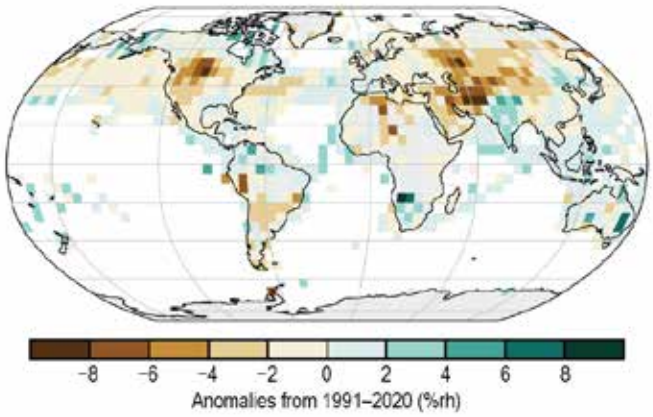

(i) Total Column Water Vapor

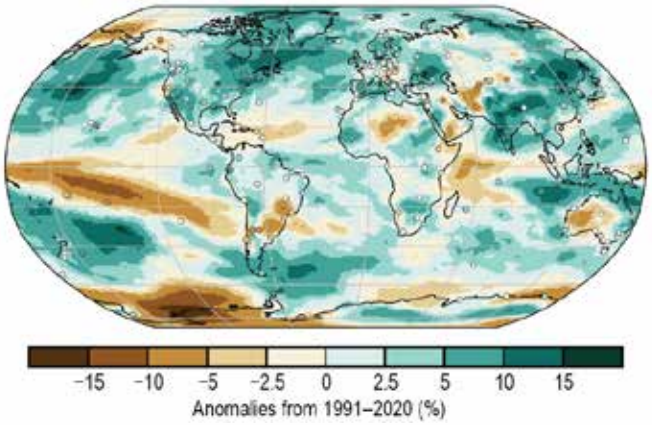

(j) Upper Tropospheric Humidity

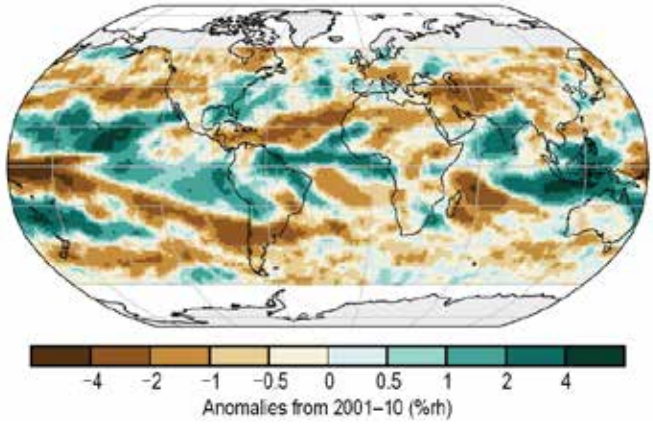

(k) Precipitation

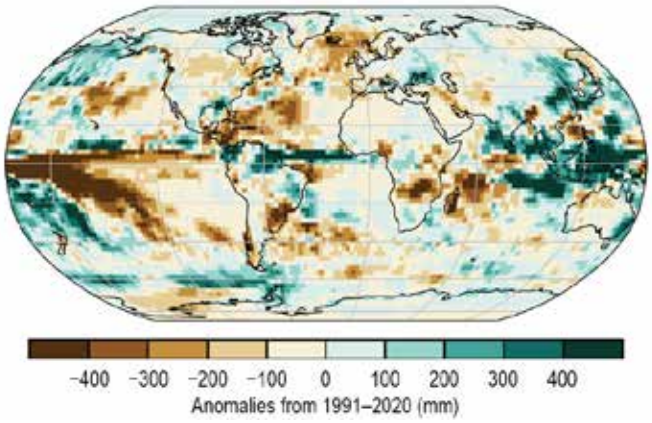

(l) Rx1day Anomalies

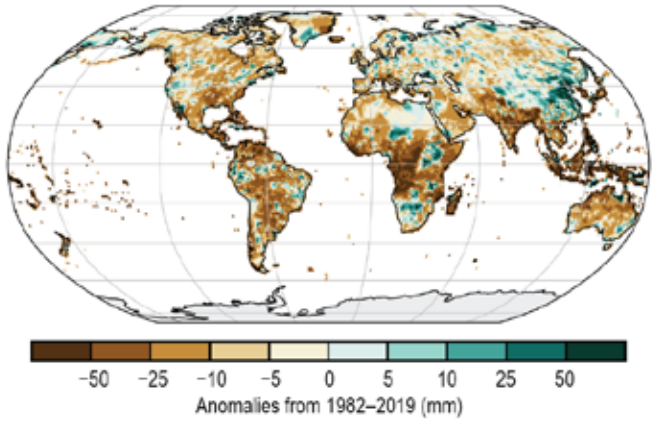

(m) Cloudiness

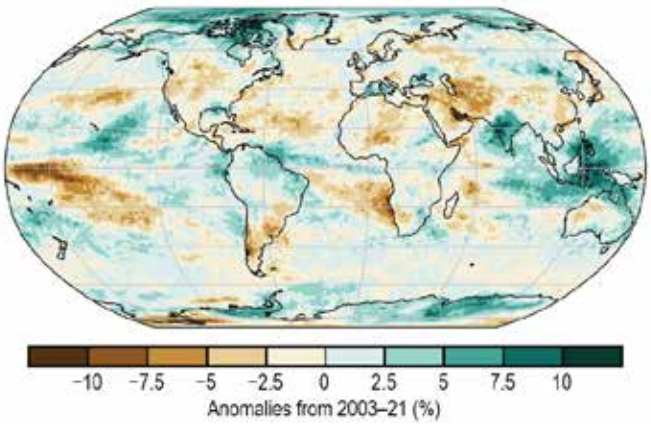

(n) Runoff

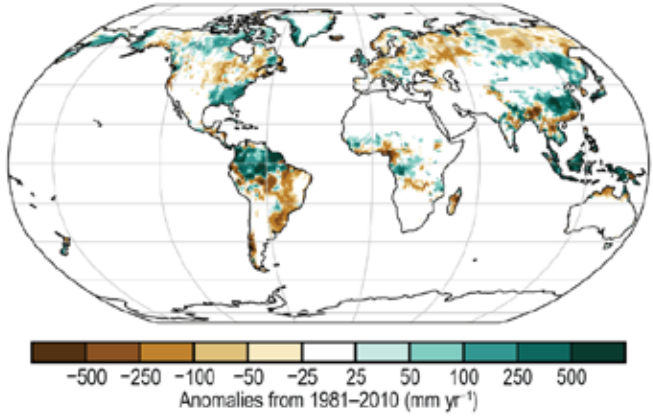

Plate 2.1. (cont.) (h) HadISDH surface relative humidity anomalies (%rh); (i) MERRA2 TCWV anomalies (%). Data from GNSS stations are plotted as filled circles; (j) "All sky" microwave-based UTH anomalies (%rh); (k) GPCP v2.3 annual mean precipitation anomalies (mm yr^{-1}); (l) GPCC maximum 1-day (Rx1day) annual precipitation anomalies (mm); (m) MODIS Aqua C6.1 cloud fraction annual anomalies (%); (n) ELSE (Ensemble Land State Estimator) global distribution of runoff anomalies (mm yr^{-1});

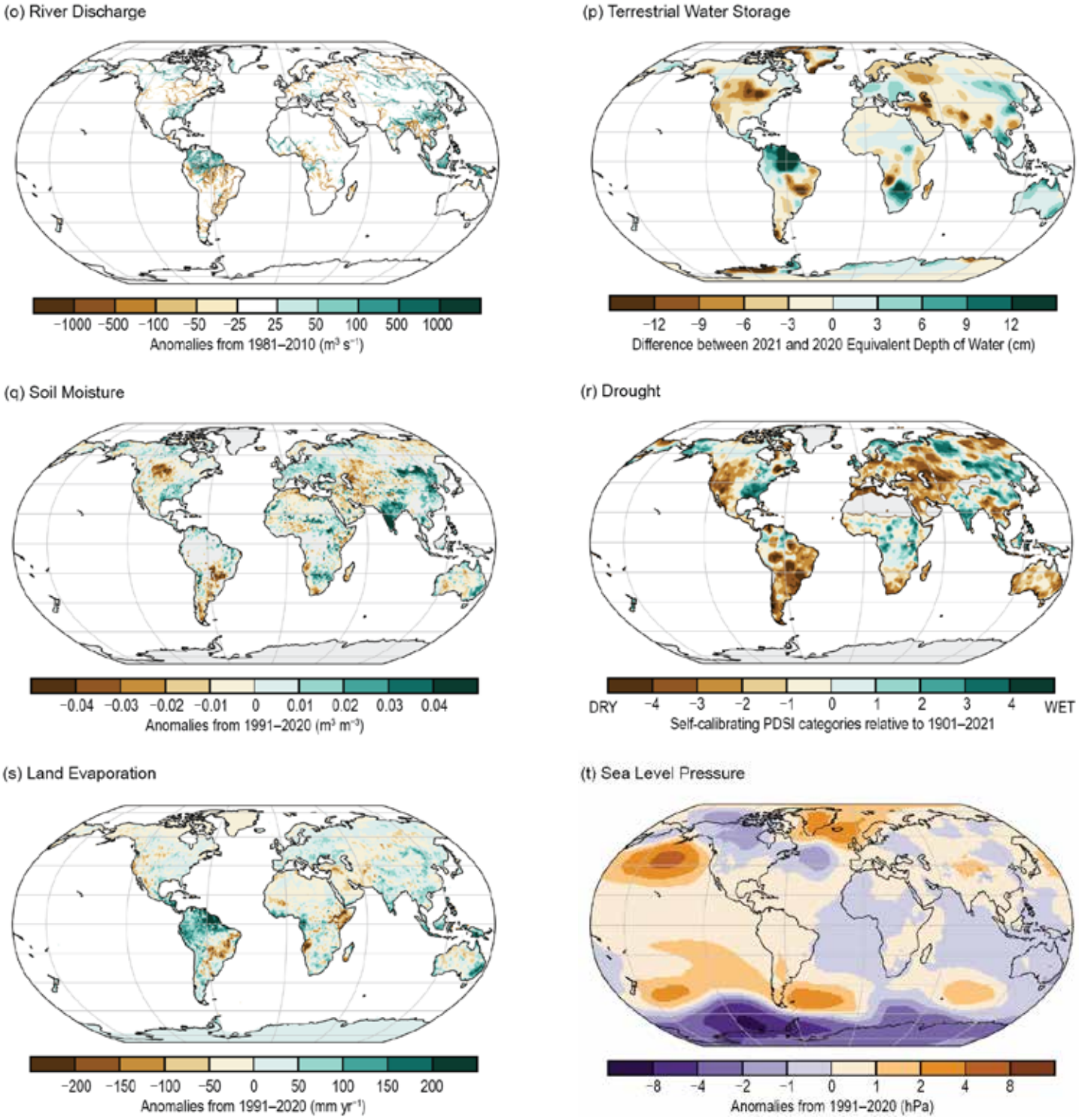

Plate 2.1. (cont.) (o) ELSE global distribution of river discharge anomalies ($m^3 s^{-1}$); (p) GRACE and GRACE-FO difference in annual-mean terrestrial water storage between 2021 and 2020 (cm); (q) ESA CCI average surface soil moisture anomalies ($m^3 m^{-3}$); (r) Mean scPDSI for 2021. Droughts are indicated by negative values (brown), wet episodes by positive values (green); (s) GLEAM land evaporation anomalies (mm yr^{-1}); (t) ERA5 sea level pressure anomalies (hPa);

(u) Surface Winds

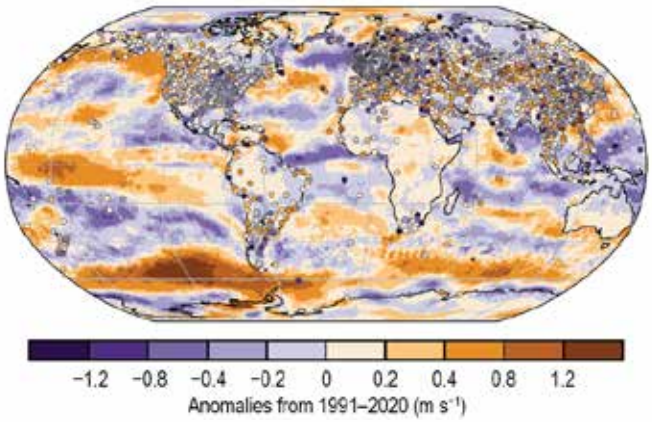

(v) Upper Air (850-hPa) Eastward Winds

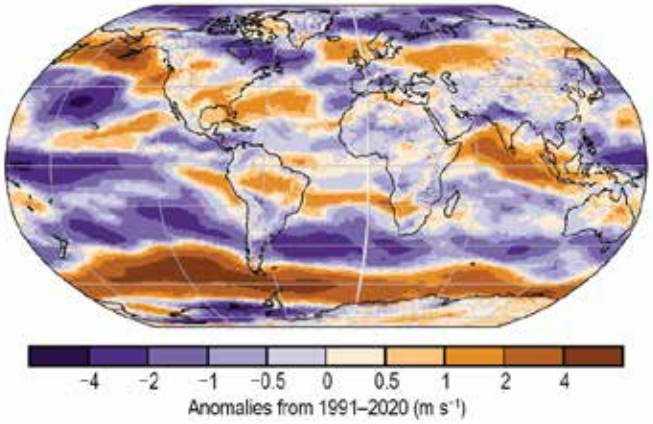

(w) Total Aerosol

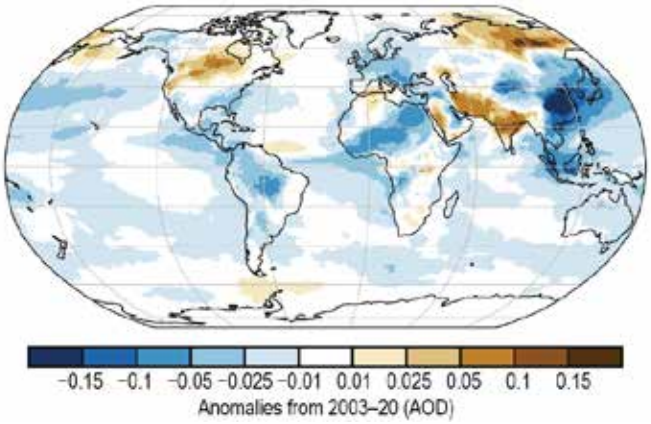

(x) AOD Ratio

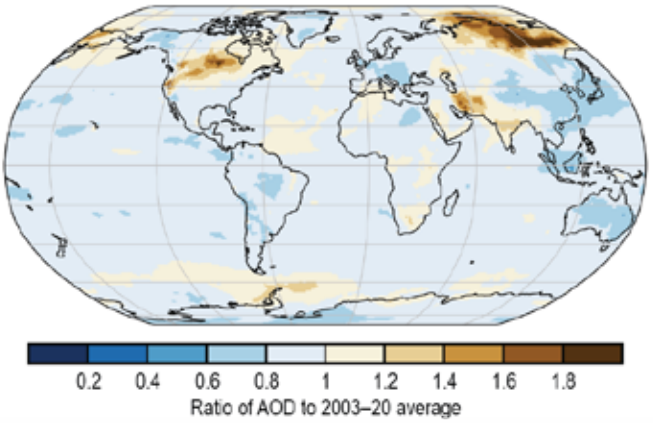

(y) Extreme Aerosol Days

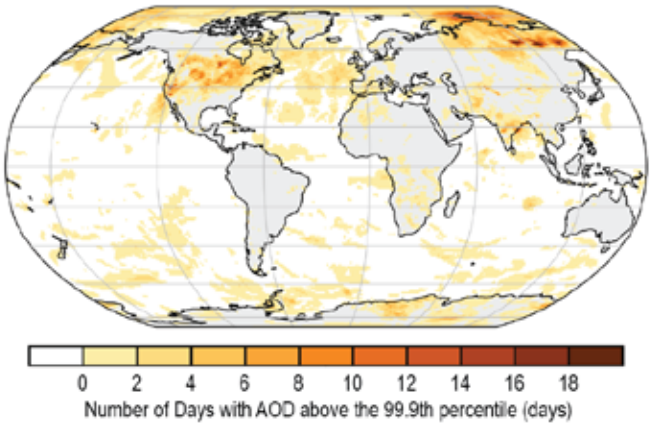

(z) Stratospheric (Total Column) Ozone

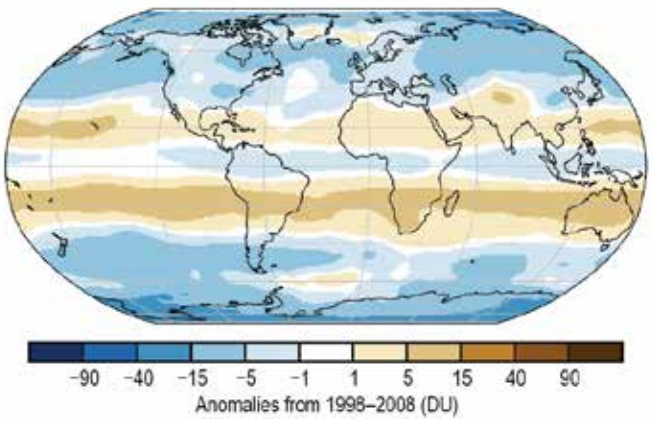

(aa) OMI/MLS Tropospheric Column Ozone

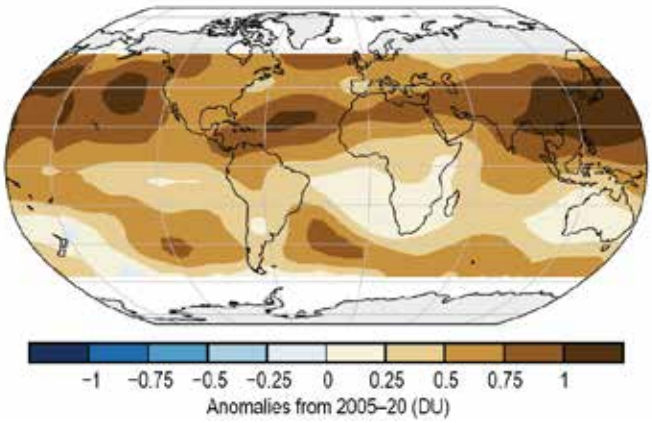

Plate 2.1. (cont.) (u) Surface wind speed anomalies (m s^{-1}) from the observational HadISD3 dataset (land, circles), the ERA5 reanalysis output (land, shaded areas), and RSS satellite observations (ocean, shaded areas); (v) ERA5 850-hPa eastward wind speed anomalies (m s^{-1}); (w) Total aerosol optical depth (AOD) anomalies at 550 nm; (x) Ratio of total AOD at 550 nm in 2021 relative to 2003–20; (y) Number of days with AOD above the 99.9th percentile. Areas with zero days appear as the white/gray background; (z) GOME-2C total column ozone anomalies relative to the 1998–2008 mean from GSG merged dataset (DU); (aa) OMI/MLS tropospheric ozone column anomalies for 60°S–60°N (DU);

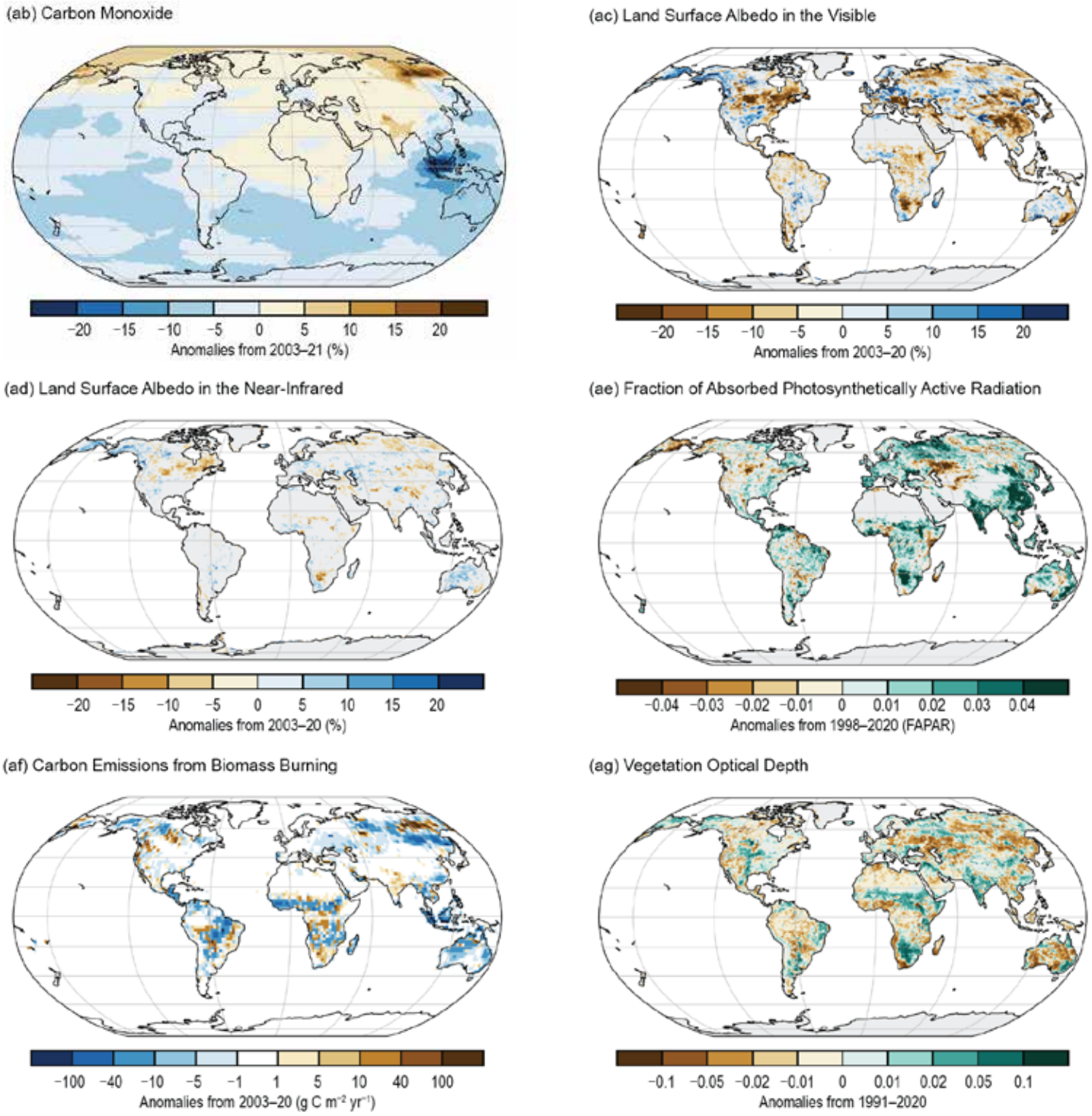

Plate 2.1. (cont.) (ab) CAMS reanalysis total column CO anomalies (%); (ac) Land surface visible broadband albedo anomalies (%); (ad) Land surface near-infrared albedo anomalies (%); (ae) FAPAR anomalies; (af) GFASv1.4 carbonaceous emission anomalies (g C m^{-2} yr^{-1}) from biomass burning; (ag) VODCA Ku-band VOD anomalies.

b. Temperature

1. GLOBAL SURFACE TEMPERATURE—A. Sánchez-Lugo, C. Morice, J. P. Nicolas, and A. Argüez

The year 2021 was among the seven warmest years since global records began in the mid-to-late 1800s, with a temperature departure between +0.21° and +0.28°C, according to six global temperature datasets (Table 2.1). Depending on the dataset, 2021 was either the fifth, sixth, or equal with 2018 as sixth-warmest year on record (Fig. 2.1). These datasets consist of four independent global in situ surface temperature analyses (NASA-GISS, Lenssen et al. 2019; HadCRUT5, Morice et al. 2021; NOAAGlobalTemp, Zhang et al. 2019; Berkeley Earth, Rhode and Hausfather 2020) and two global atmospheric reanalyses (ERA5, Hersbach et al. 2020, Bell et al. 2021; JRA-55, Kobayashi et al. 2015).

Table 2.1. Temperature anomalies (°C) and uncertainties (where available) for 2021 (1991–2020 base period). Where uncertainty ranges are provided, the temperature anomalies correspond to the central values of a range of possible estimates. Uncertainty ranges represent a 95% confidence interval. Note that for the HadCRUT5 column, land values were computed using the CRUTEM.5.0.1.0 dataset (Osborn et al. 2021), ocean values were computed using the HadSST.4.0.1.0 dataset (Kennedy et al. 2019) and global land and ocean values used the HadCRUT.5.0.1.0 dataset.

Global	NASA-GISS	HadCRUT5	NOAA GlobalTemp	Berkley Earth	ERA5	JRA-55
Land	+0.40	+0.32 ± 0.11	+0.41 ± 0.14	+0.35 ± 0.03	+0.41	+0.33
Ocean	+0.14	+0.19 ± 0.06	+0.15 ± 0.16	—	+0.22	+0.16
Land and Ocean	+0.24 ± 0.05	+0.22 ± 0.03	+0.22 ± 0.15	+0.24 ± 0.03	+0.28	+0.21

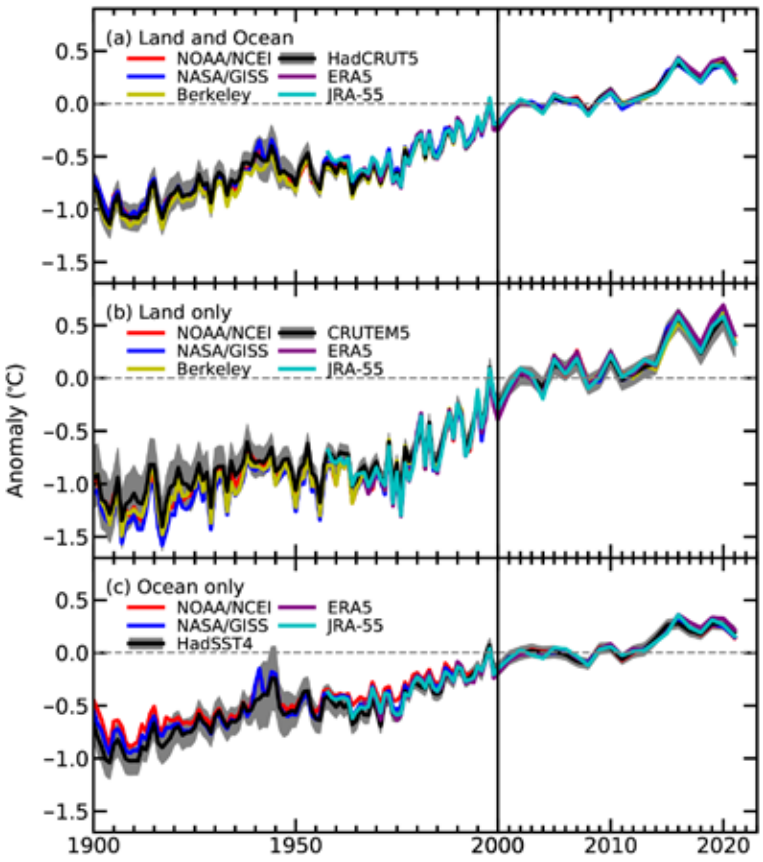

Fig. 2.1. Global average surface air temperature anomalies (°C; 1991–2020 base period). In situ estimates are shown for NOAA/NCEI (Zhang et al. 2019), NASA-GISS (Lenssen et al. 2019), Berkeley Earth (Rhode and Hausfather 2020), HadCRUT5 (Morice et al. 2021), CRUTEM5 (Osborn et al. 2021), and HadSST4 (Kennedy et al. 2019). Reanalysis estimates are shown from ERA5 (Hersbach et al. 2020), including from the preliminary ERA5 back-extension (Bell et al. 2021) for 1967–2021, and JRA-55 (Kobayashi et al. 2015). Please note change in x-axis scale pre/post 2000.

The six datasets all agree that the last seven years (2015–21) were the seven warmest years on record. Similarly, the datasets agree that the global average surface temperature has increased at an average rate of 0.08°–0.09°C decade^{-1} since 1880 and at a rate more than twice as high since 1981 (0.18°–0.20°C decade^{-1}, depending on the dataset).

The year began with a cold phase of the El Niño-Southern Oscillation (ENSO; see section 4b), also known as La Niña, across the eastern and central tropical Pacific Ocean, helping cool global temperatures slightly. The month of February had the smallest temperature anomaly of the year for the globe and was the coldest February since 2014, with global temperatures close to the 1991–2020 base period. La Niña dissipated by June, but re-emerged in August. With the exception of February, each month during 2021 had a global temperature that was above the 1991–2020 average.

While it is common, and arguably expected, for each newly completed year to rank as a top 10 warmest year (see Arguez et al. 2020), the global annual temperature for 2021 was considerably lower than we would expect due to the secular upward trend alone, with trend-adjusted anomalies registering between the 10th and 40th percentiles (depending on the dataset) following the Arguez et al. (2020) approach. These relatively cool conditions observed in 2021 are generally consistent with the typical cooling influence of La Niña. Moreover, trend-adjusted anomalies for 2021 are similar to the values recorded over the relatively cool years from 2011 to 2014, a period that also predominantly exhibited cooler-than-normal ENSO index values.

The year 2021 was characterized by above-average temperatures across much of the globe (Plate 2.1a; Appendix Figs. A2.1–A2.4), in particular across a large swath of North America (from the western United States to far northeastern Canada), as well as a region spanning northern Africa, western and central Asia, and into eastern Asia. Average to below-average temperatures prevailed across the central and eastern tropical Pacific Ocean and across parts of northwestern North America, Scandinavia, northern Russia, southern Africa, southern Australia, and parts of the southern oceans. Averaged as a whole, the global land-only surface air temperature for 2021 ranked among the sixth highest in the six datasets with a temperature departure of +0.32° to +0.41°C. The globally averaged SST was either sixth or seventh highest on record at +0.14° to +0.22°C, depending on the dataset.

Even though each dataset might differ slightly on the annual rankings and anomalies, it is worth noting that these differences are small and that, overall, temperature anomalies for each dataset are in close agreement (for more details see Simmons et al. 2017, 2021; Morice et al. 2021). Global atmospheric reanalyses use a weather prediction model to combine information from a range of satellite, radiosonde, aircraft, and other in situ observations to reconstruct historical weather and climate across the whole globe. While reanalyses may show regional differences from in situ surface temperature analyses because of regional model biases and changes in the observation network, they have been shown to agree well in well-observed regions (Simmons et al. 2017, 2021). Here, the data from ERA5 and JRA-55 are processed as described in Sanchez-Lugo et al. (2021).

2. LAKE SURFACE WATER TEMPERATURE—L. Carrea, C. J. Merchant, and R. I. Woolway

In 2021, the worldwide averaged satellite-derived lake surface water temperature (LSWT) warm-season anomaly was +0.60°C with respect to the 1996–2016 baseline, the highest since the beginning of the record in 1995, comparable with 2016. The mean LSWT trend during 1995–2021 is +0.24° ± 0.01°C decade^{-1} (Fig. 2.2a), broadly consistent with previous analyses (Woolway et al. 2017, 2018; Carrea et al, 2019, 2020, 2021). The warm-season anomalies for each lake are shown in Plate 2.1b, with 78% having positive (i.e., above-average temperature) and 22% negative (i.e., below-average) anomalies.

Globally, distinct regions of coherent above- and below-average LSWT anomaly can be seen. Almost half (45%) of the observed lakes show LSWT anomalies exceeding +0.5°C, with 3% having anomalies higher than +3°C. The highest positive anomalies were located across the Tibetan Plateau, in the northwest United States, and in the Middle East and Pakistan. Negative anomalies

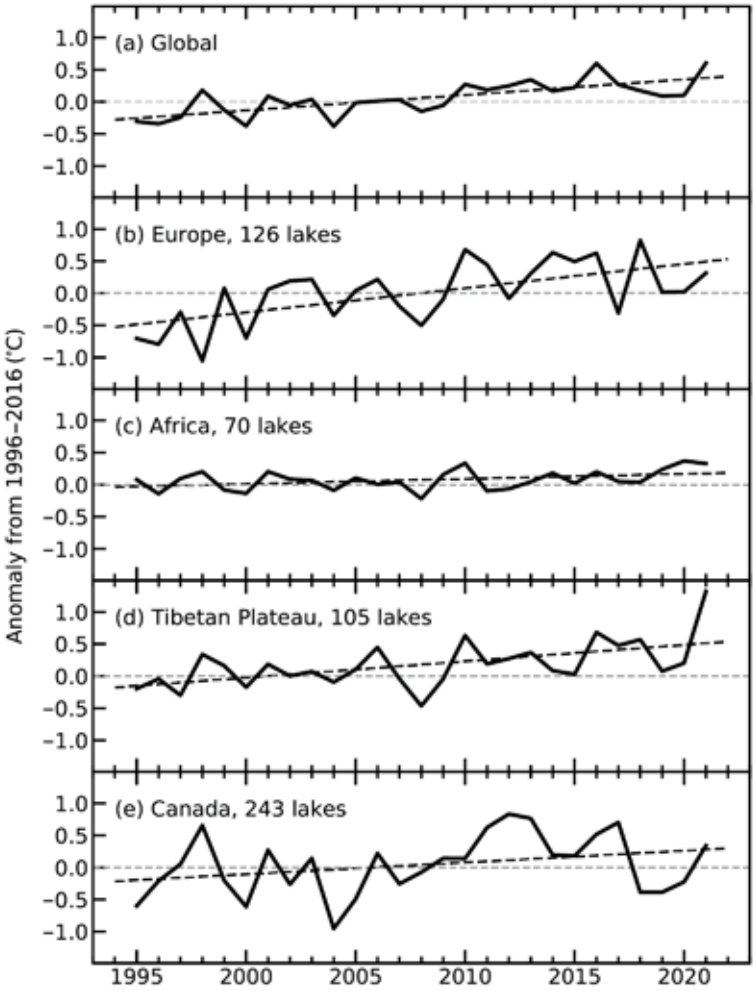

Fig. 2.2. Annual time series of satellite-derived warm-season lake surface water temperature anomalies (°C; 1996–2016 base period) from 1995 to 2021 for (a) more than 900 lakes distributed globally, (b) Europe, (c) Africa, (d) Tibet, and (e) Canada.

were mostly in South America (except Patagonia), Australia, and in high northern latitudes, including Alaska, Greenland, and eastern Russia (Plate 2.1b). Two lakes in the latter region had the most negative anomalies (below –3°C).

Four regions are considered in more detail: Canada, Europe, Tibet, and Africa (Fig. 2.3). The warm-season (July–September) LSWT anomalies calculated from the satellite data are consistent with the averaged surface air temperature (SAT) anomalies and show a warming tendency (from 1995) of +0.38° ± 0.03°C decade^{-1} in Europe and +0.18° ± 0.03°C decade^{-1} in Canada (Figs. 2.2b,e). In Africa, the tendency is closer to neutral (+0.08° ± 0.01°C decade^{-1}), while in Tibet the warming tendency has increased with respect to the previous years due to the exceptionally positive 2021 anomaly (Figs. 2.2c,d). In the Tibetan area, all but two lakes had positive anomalies in 2021, with an average of +1.3°C. This is exceptionally high for the region, being 3.8 times the standard deviation of the average anomalies (1996–2016) and the highest on record. In Europe, below-average anomalies in northern Europe (29 lakes) are less prevalent than above-average anomalies (97 lakes), with an average anomaly of +0.31°C. In Africa, 74% of the 70 lakes recorded positive anomalies. Several of the highest anomalies occurred north of the equator, contributing to an average continental anomaly of +0.33°C. In Canada, 80% of the lakes had positive anomalies, with an average LSWT anomaly of +0.34°C. The 2021 warm-season anomalies for Lakes Superior, Michigan, and Huron were computed using both in situ measurements and satellite data. The 2021 in situ anomalies were +3.36°C, +1.47°C, and +1.00°C, and the satellite were +2.49°C (the highest on record), +0.85°C, and +0.99°C, respectively. The differences are mostly because the in situ measurements are taken at only some sites on the lake while the satellite observations

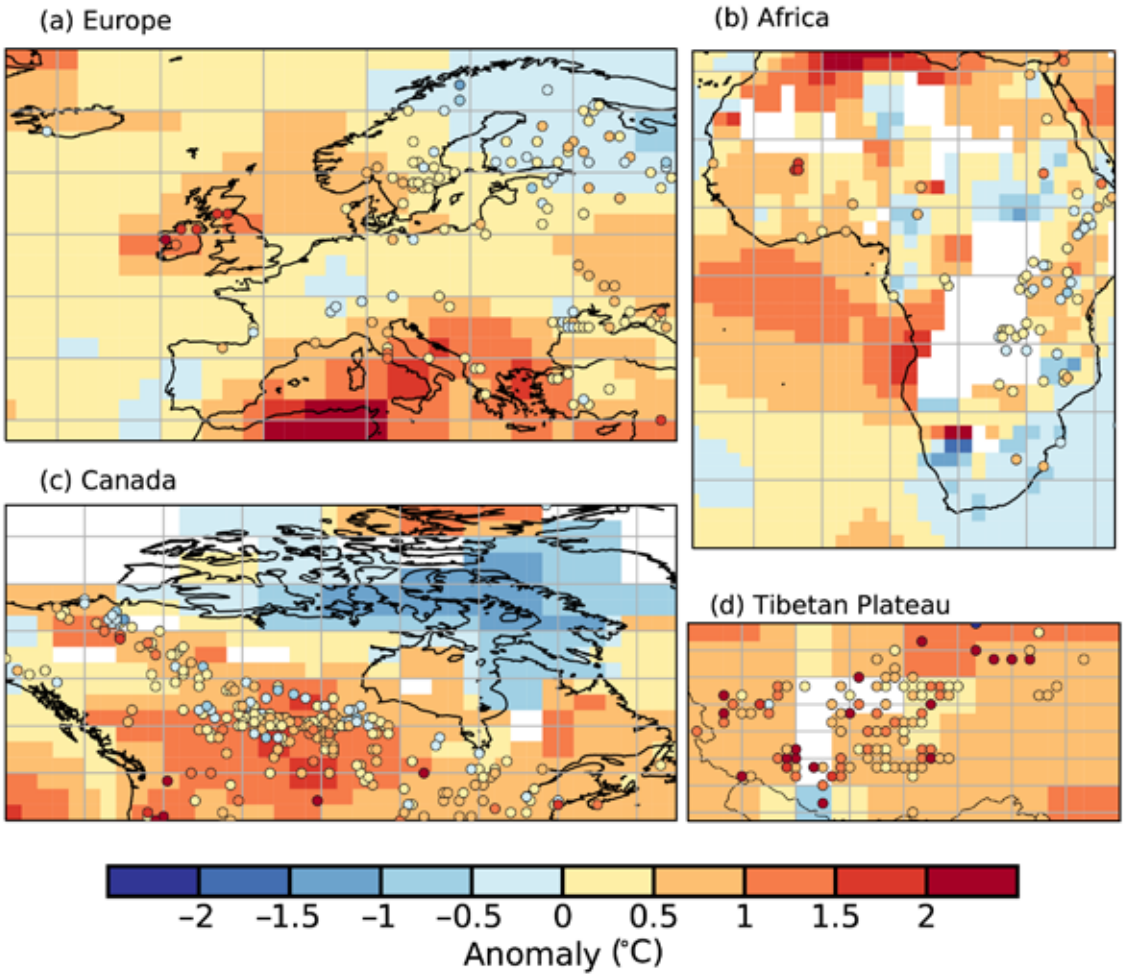

Fig. 2.3. Individual lake temperature anomalies (°C, colored dots) and 2-m air temperature anomalies (°C) in 2021 in (a) Europe, (b) Africa, (c) Canada, and (d) Tibet. These values were calculated for the warm season (Jul–Sep in the extratropical NH; Jan–Mar in the extratropical SH; Jan–Dec in the tropics) with reference to the 1996–2016 base period.

cover the whole lake. The spatial distribution of 2021 anomalies for these lakes (Appendix Fig. A2.5) all have positive values, but with strong variation across each of the lakes. The LSWT warm-season averages for midlatitude lakes are computed for summers, (July–September [JAS] in the extratropical Northern Hemisphere and January–March [JFM] in the extratropical Southern Hemisphere) and whole-year averages (January–December) are presented for tropical lakes (within 23.5° of the equator). LSWT time series were derived from satellite observations from the series of Along Track Scanning Radiometers (ATSRs), the Advanced Very High Resolution Radiometers (AVHRRs) on MetOp A and B (1996–2019), and the Sea and Land Surface Temperature Radiometers (SLSTRs) on Sentinel3A and 3B (2019–2021). The retrieval method of MacCallum and Merchant (2012) was applied on image pixels filled with water according to both the inland water dataset of Carrea et al. (2015) and a reflectance-based water detection scheme. The satellite-derived LSWT data are spatial averages for each of a total of 963 lakes, for which high quality temperature records were available in 2021. The satellite-derived LSWT data were validated with in situ measurements with a good agreement (average satellite minus in situ temperature difference less than 0.5°C). Lake-wide average surface temperatures have been shown to give a more representative picture of LSWT responses to climate change than single-point measurements (Woolway and Merchant 2018). The averaged surface air temperature was calculated from the GHCN v4 (250-km smoothing radius) data of the NASA GISS surface temperature analysis (Hansen et al. 2010; GISTEMP Team 2022). The in situ data for the Great Lakes were collected by the NOAA National Data Buoy Center.

3. NIGHT MARINE AIR TEMPERATURE—R. C. Cornes, T. Cropper, R. Junod, and E. C. Kent

Globally gridded datasets of night marine air temperature (NMAT) provide a useful and independent comparison against sea surface temperature (SST) data. Air temperature values have been recorded onboard vessels for centuries and continue to the present through the Voluntary Observing Ship (VOS) network. These observations can be used to construct global datasets of marine air temperature back to at least 1900. While temperature values are recorded throughout the day and night on these ships, only the nighttime observations are currently used to construct the gridded values due to the heating bias that arises in the daytime data, as a result of the superstructure of the ship.

Global mean temperature anomalies calculated from the two gridded NMAT datasets (CLASSnmat, Cornes et al. 2020 and UAHNMAT, Junod and Christy 2020) show a marked cooling in 2021 compared to 2020 but also relative to values over the last decade (Fig. 2.4). For CLASSnmat, the average global temperature anomaly (relative to the 1961–90 average) during 2021 was +0.38°C, a value comparable to that recorded in 2006. As such, 2021 was only the 13th highest in the series, which dates back to 1880. For UAHNMAT, the global mean anomaly value was +0.33°C in 2021; this is also the 13th highest annual mean temperature in its 1900–2021 record. These values contrast with the HadSST4 sea surface temperature dataset (Kennedy et al. 2019), which shows that 2021 was the fifth highest in the 1850–2021 period, with a global average anomaly of

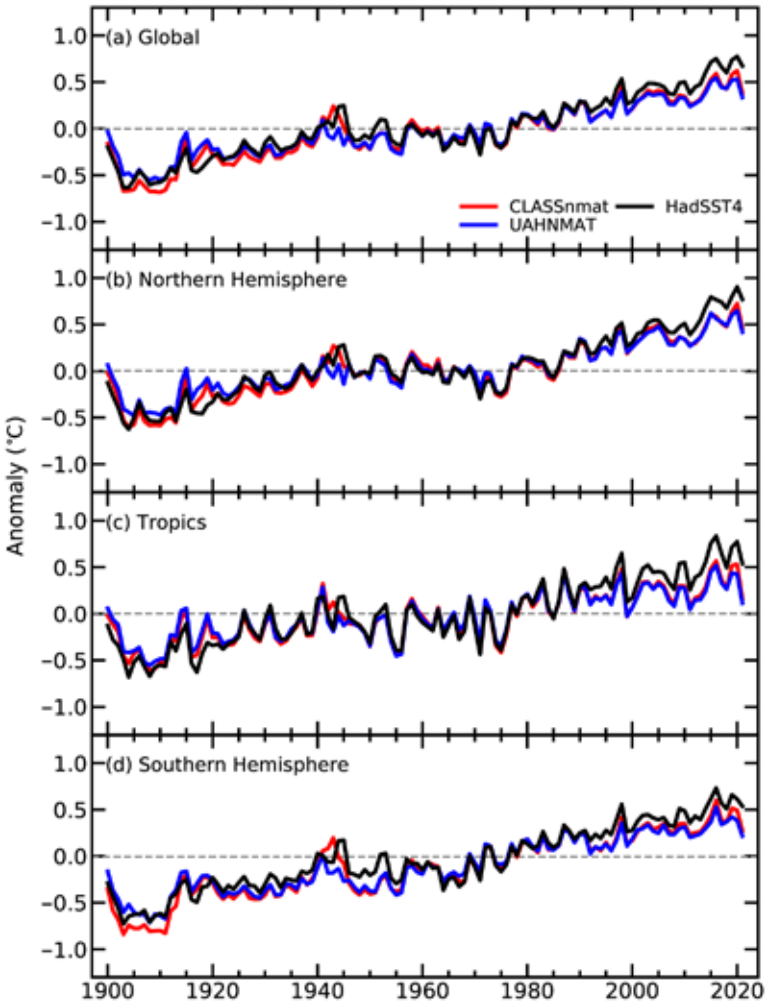

Fig. 2.4. Annual mean temperature anomalies (°C; 1961–90 base period) calculated from the CLASSnmat, UAHNMAT, and HadSST4 datasets averaged over four domains. The tropics is defined as the latitude range 20°S–20°N and the Northern (Southern) Hemisphere is defined as north (south) of 0°. The averages only include values that are common to all three datasets for a given year, and since UAHNMAT are only available after 1900, only values for the period 1900–2021 are plotted.

Table 2.2. Annual average temperature anomalies (°C) across four regions for 2021 for the CLASSnmat, UAHNMAT, and HadSST4 datasets (1961–90 base period). The values in parentheses indicate the ranking (1 = highest) of these values over the period 1900–2021.

	Global	Northern Hemisphere	Southern Hemisphere	Tropics
CLASSnmat2.1	+0.38 (13)	+0.46 (11)	+0.27 (17)	+0.16 (31)
UAHNMAT	+0.33 (13)	+0.42 (11)	+0.22 (25)	+0.11 (38)
HadSST4	+0.67 (5)	+0.77 (4)	+0.54 (7)	+0.54 (10)

+0.67°C. A similar difference of about −0.3°C in the 2021 NMAT averages, relative to HadSST4, is seen across other large-scale regions (Table 2.2). In this comparison of the three datasets, co-located gridded data are used to avoid any complication to the analysis from differing global coverage. In particular, the NMAT datasets have poor coverage south of 40°S.

The principal reason for the lower temperature anomalies during 2021, compared to recent years, is the extended La Niña conditions that were present during the year (see section 4b). Historically, the NMAT data show a clear response to La Niña conditions, with a pattern across the Pacific that is similar in form and magnitude to that observed in the SST data (Figs. 2.5a–c). However, differences are apparent in the NMAT data compared to SST beyond the typical La Niña pattern and is the reason for the lower global average anomalies in the two NMAT datasets for 2021 compared to 2020 (Figs. 2.5d–f). The negative temperature anomalies in the central Pacific are more widespread in NMAT compared to SST, and the two nodes of positive anomalies in the North and southwestern Pacific are not clearly defined in either NMAT dataset. In addition, while positive anomalies for 2021 are evident in most grid cells in the SST data across the Atlantic and Indian Oceans, these are much weaker in the NMAT datasets, and there are many more grid cells in these regions with negative anomalies. Some of these regional differences can be explained by different data availability in the SST and NMAT datasets. Most notably, across the southern Pacific there is greater uncertainty in the NMAT values because there are few ship observations in the region; this is mitigated in the SST through the use of drifting buoy measurements in the grid cell averages. However, this does not fully explain the differences seen in these results as there is relatively good observational coverage in the NMAT datasets across the North Atlantic.

The data used in Fig. 2.5 were detrended, prior to averaging, in order to remove the long-term trend from the data by calculating the residuals from a linear regression fit to the data per grid cell. This detrending allows the response of the SST and NMAT data to La Niña conditions to be compared more directly. Over approximately the last 50 years, global mean NMAT has increased at a slower rate than SST (Fig. 2.4; Cornes et al. 2021); this accounts for the difference in rankings in the NMAT datasets compared to HadSST4. The reasons for this trend-differential are not well understood, and work is ongoing to determine if this is a true feature of the data or an artifact in the NMAT and/or SST datasets. It is also not clear if the interannual variability, and notably the relatively cool conditions observed during 2021, is related to this difference in long-term trends since taking into account this trend differential, the −0.3°C offset between NMAT and SST in 2021 was unusually large.

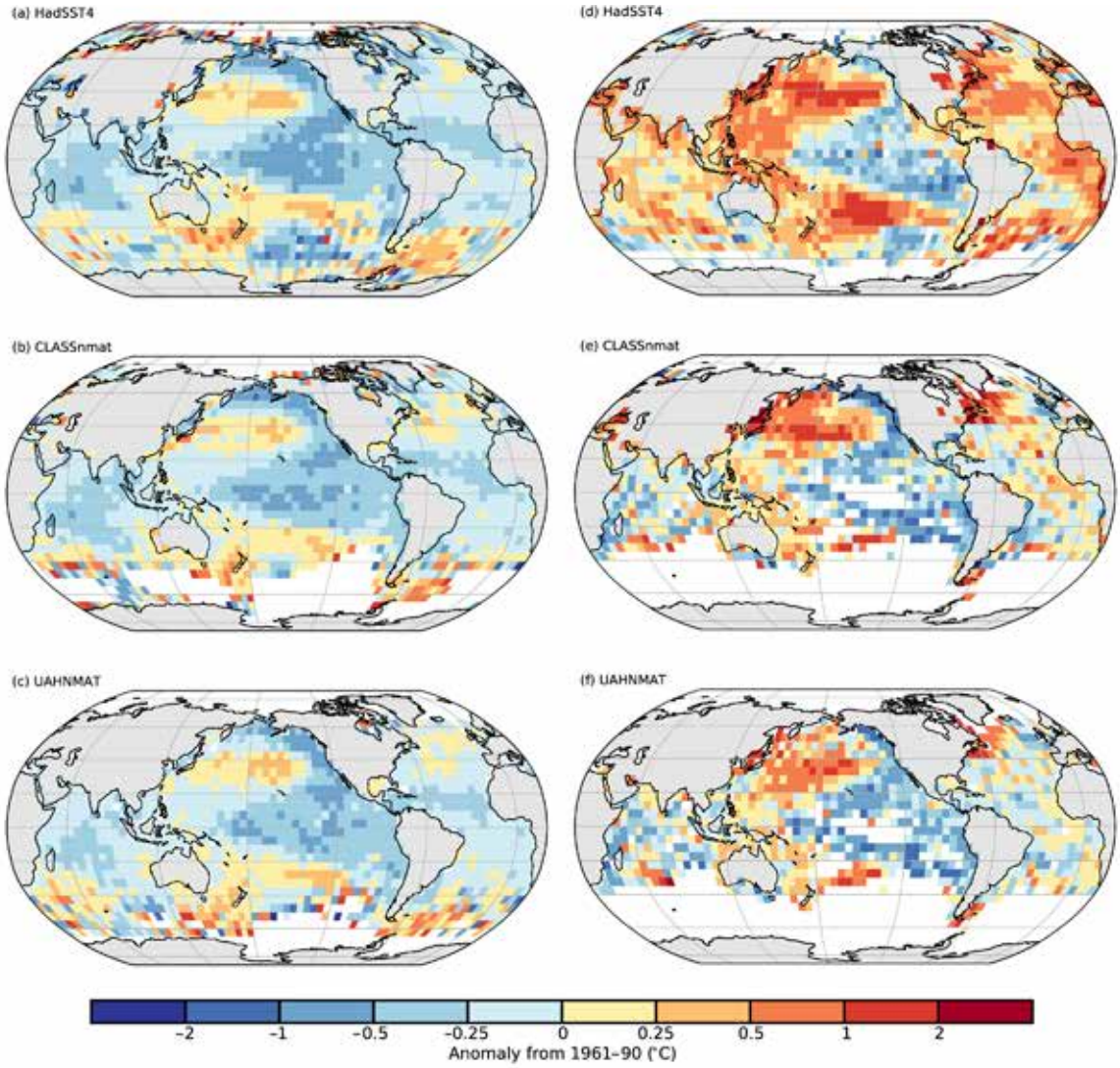

Fig. 2.5. Average detrended temperature anomalies (°C) in the HadSST4, CLASSnmat, and UAHNMAT datasets calculated as (a–c) the mean of nine years between 1955 and 2000 in the year following a La Niña event and (d–f) for the year 2021. The years used in (a–c) are 1955, 1956, 1965, 1971, 1974, 1976, 1989, 1999, and 2000. Grid-cell values are marked missing if there are fewer than five months complete per year. In (a–c), grid-cells are marked as missing if there are fewer than five of the nine years complete.

4. LAND AND SURFACE MARINE TEMPERATURE EXTREMES—R. J. H. Dunn, M. G. Donat, R. W. Schlegel, and S. E. Perkins-Kirkpatrick

The average number of warm days (TX90p, Table 2.3) over land was the second most on record, according to the observational dataset GHCNDEX (Donat et al. 2013; Fig. 2.6, using the 1961–90 reference period), with 68 days, though we note the incomplete spatial coverage. The average number of cool nights (TN10p) was 22, which was 14 fewer than the expected average, but not at record values. The expected values for these two indices are 36.5 days over the reference period, which is used in their calculation. The average values of the spatially complete reanalysis dataset ERA5 (Hersbach et al. 2020, using the 1981–2010 reference period) over land are similar to those from GHCNDEX, and TX90p was at its third highest value at 65.6 days, after 2016 and 2020 (Fig. 2.6). The spatial patterns of these indices (Plates 2.1d,e; Appendix Fig. A2.6) show especially high numbers of warm days over Africa and Asia and relatively low numbers over Australia, which also had high numbers of cool nights in 2021. Below we describe some of the low and high temperature events of 2021 in more detail (see also WMO 2022), primarily from the global north where these details were more readily available.

Table 2.3. WMO Extremes indices from the Expert Team for Climate Change Detection and Indices (ETCCDI) used in this section and their definitions (Zhang et al. 2011). In GHCNDEX, these indices are calculated using 1961–90 as the reference period, and thus these anomalies use the same period. As a result of their construction, comparison, or conversion to other base periods is not simple (Dunn and Morice 2022).

Index	Name	Definition
TX90p	Number of warm days	Number of days in a year where the daily maximum temperature was above the 90th percentile of the 1961–90 values.
TN10p	Number of cool nights	Number of days in a year where the daily minimum temperature was below the 10th percentile of the 1961–90 values.

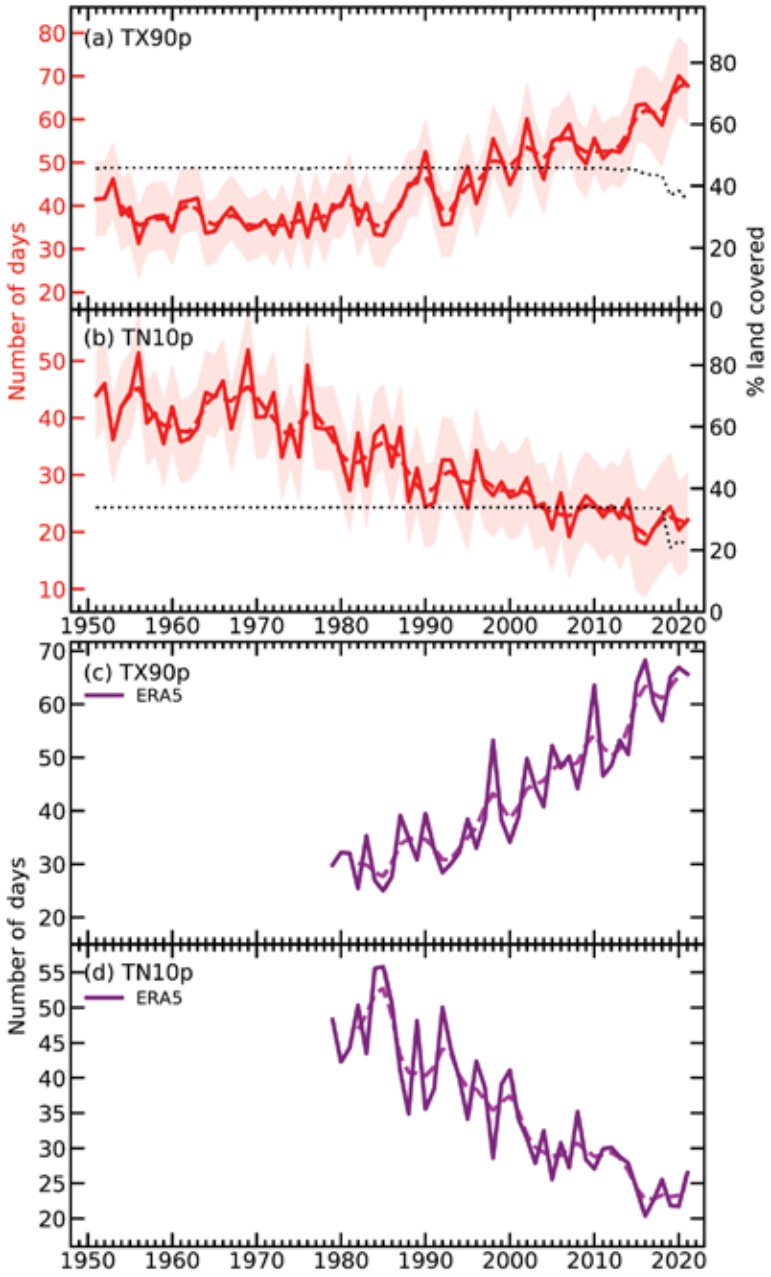

Fig. 2.6. Timeseries of (a),(c) number of warm days (TX90p) and (b),(d) number of cool nights (TN10p) from GHCNDEX (a),(b) and ERA5 (c),(d). The dashed lines show the smoothed behavior from a binomial filter, and the coverage uncertainty (following Brohan et al. 2006) is shown by the shading in (a) and (c). The dotted black lines in (a),(b) show the percentage of land grid boxes with sufficient temporal coverage over the record which have data in each year.

During 2021 there were a number of notable cold periods, starting with the after effects of a major storm on the Iberian Peninsula in January, with widespread temperatures below –20°C in northeast Spain, and a new national record of –34.1°C set on 6 January at Clot del Tuc de la Llança (Appendix Table 2.1). In February, North America was affected by two major winter storms, leading to the coldest event across the continental United States in more than 30 years, reaching as far south as northern Mexico. Heating demand placed strain on the electrical power grid in Texas, resulting in up to 10 million people without power, and there were over 200 direct and indirect deaths related to this event (see section 7b2 for details).

Following a warm end to March, Europe had an abnormally cold April, with record low minimum temperatures for the month (Appendix Table 2.1). Western North America experienced exceptional heat waves during June and July. Temperatures of above 40°C occurred over a large area in June, with maximum temperatures more than 15°C above average. Lytton (British Columbia, Canada) reached 49.6°C on 29 June, a new Canadian national record 4.6°C above the previous record (Appendix Fig. A2.7; see Sidebar 7.1 for details). On 9 July, Death Valley (California) recorded 54.4°C, equaling the temperature measured in 2020 as the highest temperature on Earth since at least the 1930s. Many other stations reported new maximum records from these two events.

The Mediterranean region experienced a number of record-setting heatwaves in July and August, and a station near Syracuse, Sicily (Italy), recorded a provisional new European maximum temperature record of 48.8°C on 11 August (Appendix Table 2.1). On 5 July, Lapland (Finland) recorded 33.6°C in Kevo, the hottest day in the region for over a century; it was the second warmest summer (JJA) average in the 120-year Finnish national record (see section 7f for details). Around the Arabian Gulf, a high temperature of 50.4°C was recorded at Dammam, Saudi Arabia, on 31 July. Also, during July, and coinciding with the delayed 2020 Olympic Games, a heatwave over Japan broke all-time records at numerous stations (see Sidebar 7.4 for details). In the Southern Hemisphere, New Zealand recorded its warmest year on record, which included its warmest June on record, 2°C higher than the 1981–2010 average (see Sidebar 7.5 for details).

Analyzing data from NOAA OISST v2.1 (Huang et al. 2021), 57% of the surface of the ocean experienced at least one marine heatwave (MHW, Hobday et al. 2016) in 2021 (Fig. 2.7b), and 25% experienced at least one marine cold-spell (MCS, Fig. 2.7d). Category 2 Strong MHWs (Hobday et al. 2018) were the most common (28%) for the eighth consecutive year, whereas Category 1 Moderate MCSs have remained the most common (20%) since 1985. The ocean experienced a global average of 49 MHW days (13 MCS days), which is fewer than the 2020 average of 58 days (14 days) and the 2016 record of 61 days (1982 record of 27 days, Figs. 2.7a,c). This daily average equates to 13% (4%) of the surface of the ocean experiencing a MHW (MCS) on any given day (Figs. 2.7a,c). The equatorial Pacific and Southern Oceans showed a noticeable lack of MHWs in 2021 while experiencing nearly complete MCS coverage. Heat anomalies in the equatorial Pacific Ocean are tightly linked with ENSO, which was in a La Niña state most of the year (see section 2e1), a continuation from 2020. The relationship between extreme events in the Southern Ocean and broad climate indices is complex and still poorly understood, making this an opportune avenue of future research. Note that with the Hobday et al. (2016) MHW definition the long-term trend is not removed before detecting events. This means that warming (cooling) areas will generally experience more (fewer) MHWs in the present than in the past, with the inverse observed for MCSs.

GHCNDEX (Donat et al. 2013) is based on the daily GHCND dataset (Menne et al. 2012). The extremes indices developed by the former ETCCDI (WMO Expert Team in Climate Change Detection and Indices, Zhang et al. 2011) are calculated for each station and then interpolated onto a regular 2.5° grid. Reduced spatial coverage in the most recent years (Fig. 2.6) arises because of late arriving data; hence for complete global land coverage we also use the ERA5 reanalysis (Hersbach et al. 2020), not including the preliminary release of the 1950–78 data. The shorter temporal coverage means a different reference period needs to be used (1981–2010), which can lead to differences when comparing recent trends (Dunn et al. 2020; Yosef et al. 2021; Dunn and Morice 2022).

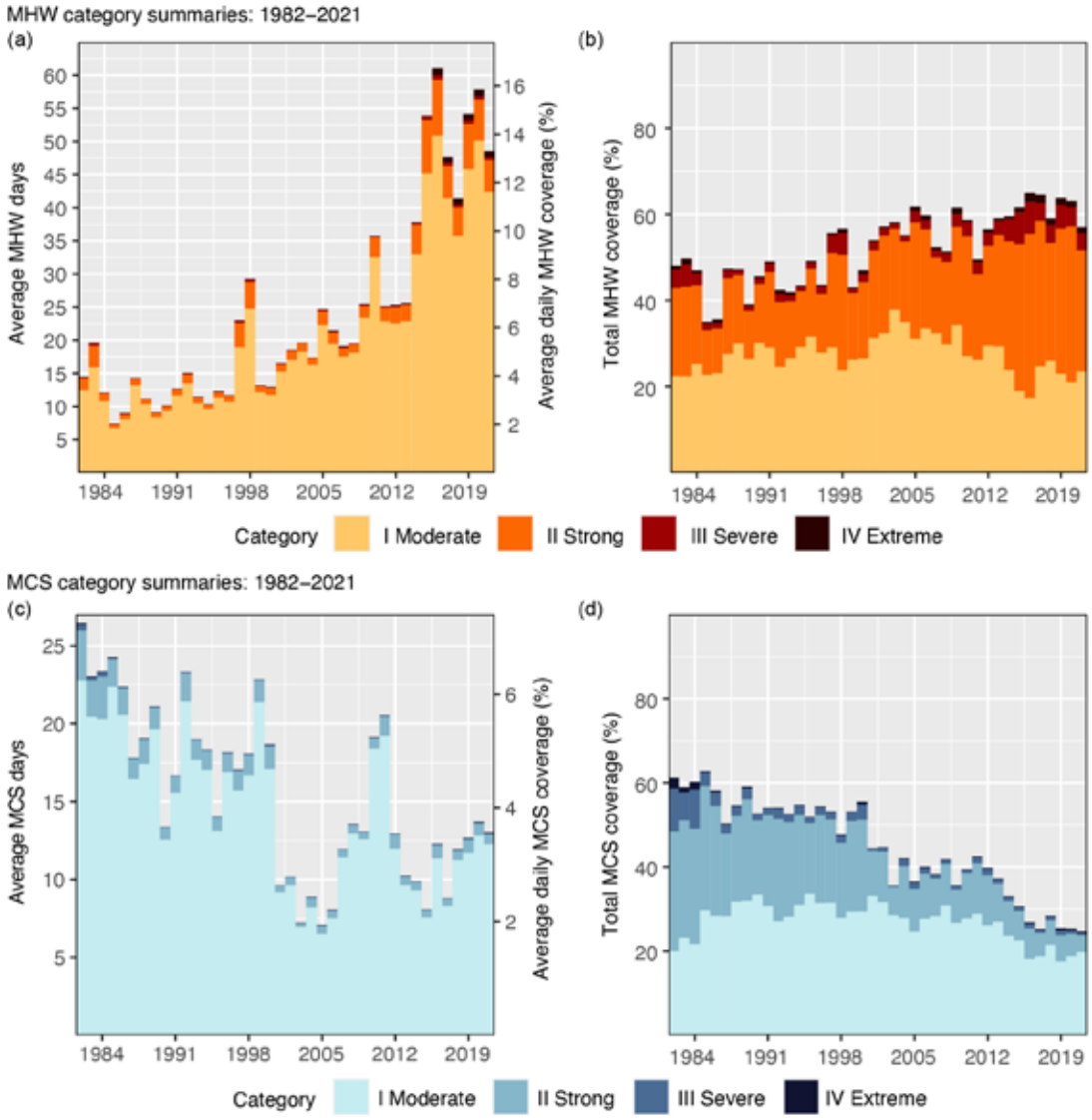

Fig. 2.7. Annual global marine heatwave (MHW; a,b) and marine cold-spell (MCS; c,d) occurrence from NOAA OISST using a climatology base period of 1982–2011. (a),(c) The average count of MHW/MCS days experienced over the surface of the ocean in 2021 (left y-axis), also expressed as the percent of the surface of the ocean experiencing a MHW/MCS on any given day (right y-axis). (b),(d) Total percent of the surface area of the ocean that experienced an MHW/MCS at some point during the year. The values shown are for the highest category of MHW/MCS experienced at any point.

5. TROPOSPHERIC TEMPERATURE—S. Po-Chedley, J. R. Christy, L. Haimberger, and C. A. Mears

The 2021 global lower-tropospheric temperature (LTT) was approximately 0.25°C higher (0.14°–0.34°C, depending on dataset) than the long-term climatological (1991–2020) average. This places 2021 among the 10 warmest years on record (since 1958) despite La Niña conditions during most of 2021, which typically reduce the temperature of the troposphere.

Earth's tropospheric temperature is influenced by several natural factors such as volcanic eruptions, solar variability, and internal climate variability. Anthropogenic emissions of greenhouse gases and aerosols also affect LTT and collectively contribute to long-term warming of the global troposphere (Table 2.4). Since August of 2020, the El Niño-Southern Oscillation (ENSO) has largely been in a La Niña state (Fig. 2.8; see section 4b), which corresponds to below-average central and eastern tropical Pacific Ocean SSTs and reduced tropical and global average tropospheric temperatures. The background warming trend and La Niña conditions combined in 2021 to create a global LTT that was higher-than-average, but not record-breaking (Fig. 2.9).

Table 2.4. Temperature trends (°C decade^{-1}) for global lower tropospheric temperature (LTT) and tropical tropospheric temperature (TTT) over the period 1958–2021 and 1979–2021, respectively. NASA MERRA-2 data begins in 1980. UW (Po-Chedley et al. 2015) and NOAA STAR (Zou and Wang 2011) data do not produce LTT products.

		LTT (90°S–90°N)		TTT (20°S–20°N)	
Start Year		**1958**	**1979**	**1958**	**1979**
Radiosonde	NOAA/RATPACvA2	0.18	0.22	0.17	0.19
	RAOBCOREv1.9	0.168	0.18	0.14	0.16
	RICHv1.9	0.18	0.20	0.18	020
Satellite	UAHv6.0	—	0.13*	—	0.13
	RSS v4.0	—	0.21	—	0.17
	UWv1.0	—	—	—	0.17
	NOAA STAR v4.1	—	—	—	0.23
Reanalyses	ERA5	—	0.18	—	0.16
	JRA-55	0.17	0.18	0.16	0.15
	NASA/MERRA-2	—	0.19	—	0.18
	Median	**0.18**	**0.19**	**0.17**	**0.17**

*The vertical sampling in UAH LTT is slightly different from other datasets and results in temperature trends that are approximately 0.01°C decade^{-1} smaller than other datasets.

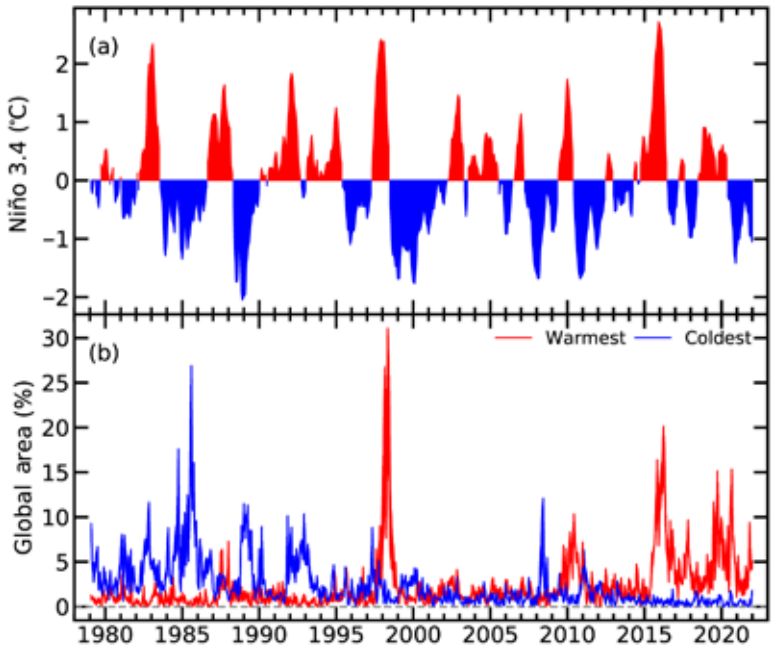

Fig. 2.8. (a) Sea surface temperature anomalies (°C, 1991–2020 base period) in the Niño 3.4 region in the central equatorial Pacific. Prolonged positive anomalies in red are associated with El Niño events; the reverse is true for La Niña events (in blue). (b) Fraction of Earth (%) with record high (red) and low (blue) monthly LTT values. The width of the line represents the difference between the UAH and RSS datasets.

The LTT anomaly pattern in 2021 is typical of La Niña conditions (Plate 2.1f; Yulaeva and Wallace 1994). Although La Niña events tend to reduce globally averaged LTT, some regions are associated with above-average LTT (Plate 2.1f), and approximately 5% of the planet experienced its highest annual mean LTT since 1979 (Fig. 2.8). Regions of record low annual mean LTT were sparse and represented less than 1% of global area (Fig. 2.8). Areas experiencing record high temperatures included the Pacific Ocean midlatitudes, the southwest Atlantic Ocean, the Middle East,

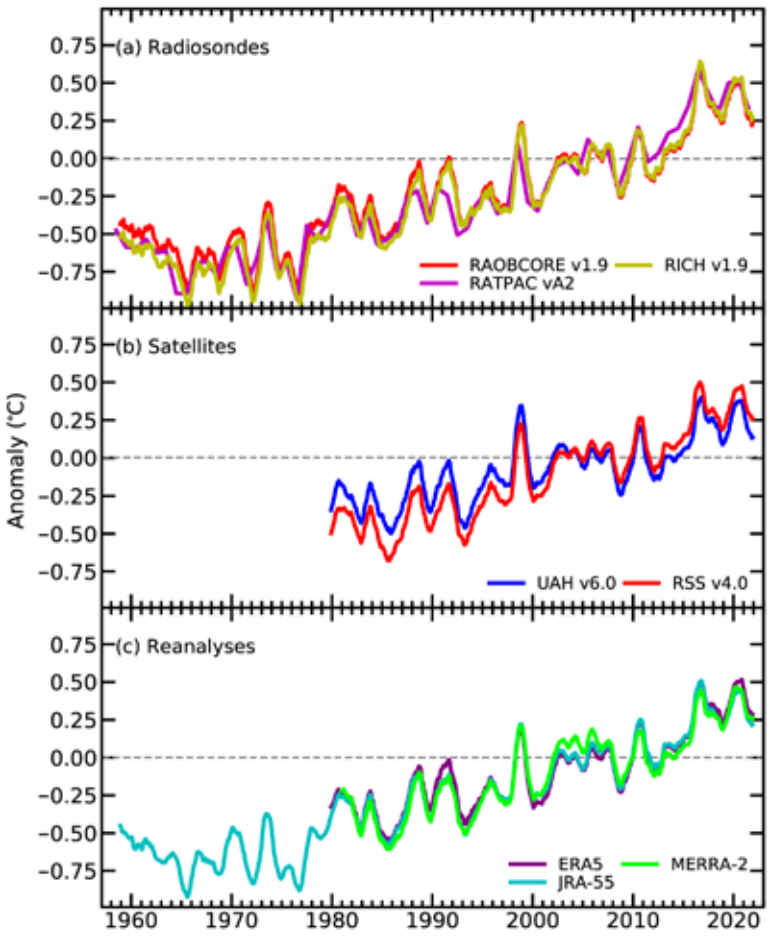

Fig. 2.9. Monthly average LTT anomalies (°C) for (a) radiosonde, (b) satellite, and (c) reanalysis datasets. Time series are smoothed using a 12-month running average. Annual averages are displayed for the RATPAC dataset. Anomalies are with respect to a 1991–2020 base period.

southwest China, and northeastern Canada. In contrast, the tropical eastern Pacific Ocean, regions along the West Antarctic coastline, and northwest Canada and Alaska exhibited below-average tropospheric temperatures in 2021.

Datasets of atmospheric temperature change are derived from balloon-based radiosonde measurements (RATPAC vA2, RICH v1.9, and RAOBCORE v1.9), satellite-based microwave sounding observations (RSS v4, UAH v6, UW v1, and NOAA STAR v4.1), and atmospheric reanalysis products (MERRA-2, ERA5, and JRA-55). Each dataset is constructed with different strategies to remove biases, resulting in slightly different time series. In the ERA5 and MERRA-2 reanalysis datasets, 2021 was the fifth-warmest year on record for global LTT (Hersbach et al. 2020; Gelaro et al. 2017). 2021 was the sixth-warmest year in the RATPAC, RICH, and RSS datasets (Free et al. 2005; Mears and Wentz 2016; Haimberger et al. 2012) and eighth in the JRA-55, RAOBCORE, and UAH datasets (Kobayashi et al. 2015; Spencer et al. 2017). In general, observations of the global LTT (Fig. 2.9) and tropical tropospheric temperature (TTT) have similar interannual variations, but exhibit non-negligible structural uncertainty for long-term trends, which range from 0.13° to 0.23°C decade^{-1} since 1979 (Table 2.4). The estimated trend uncertainty for individual satellite datasets is approximately 0.04°C decade^{-1} and the uncertainty in converting level temperatures to synthetic satellite brightness temperatures is approximately 0.02°C decade^{-1} (Po-Chedley et al. 2021).

Efforts to intercompare and understand differences across tropospheric temperature datasets is ongoing (Steiner et al. 2020). For example, Christy et al. (2018) compares radiosonde and satellite-based measurements of tropospheric temperature and concludes that satellite datasets likely have spurious warming over the 1990s. On the other hand, this analysis also documents unexplained

cooling in satellite datasets over the early 2000s. This latter finding is consistent with recent work by Zou et al. (2021), who note that existing satellite datasets underestimate tropospheric temperature trends relative to a new post-2002 dataset, which relies on observations from the most recent generation of microwave sounding instruments and/or satellites in stable sun-synchronous orbits. Consistent with physical expectations, recent research shows that climate models exhibit a close coupling between atmospheric moistening and warming in the tropics. If model simulations are sufficiently accurate, relationships between distinct geophysical fields (e.g., water vapor and sea surface temperature observations) may be used to investigate potential observational biases in tropospheric temperature datasets (Santer et al. 2021). As a result of collective efforts to better understand and intercompare existing observational datasets, records of tropospheric warming are continually evolving and improving.

6. STRATOSPHERIC TEMPERATURE—W. J. Randel, C. Covey, L. Polvani, and A. K. Steiner

Global mean temperatures in the lower, middle, and upper stratosphere for 2021 were similar to 2020. The long-term trend, however, is multi-decadal cooling of the upper stratosphere and warming of the troposphere due to anthropogenic CO_2 increases. Shorter-term climate variations from both natural and anthropogenic sources (e.g., Australian bushfires in 2020) are also evident in the record but were not prominent in 2021. The Antarctic stratospheric polar vortex was strong and persistent in 2021, while the Arctic was disturbed by a major stratospheric warming event early in the year. The stratospheric quasi-biennial oscillation (QBO) progressed normally in 2021, in contrast to disruptions in 2016 and 2020.

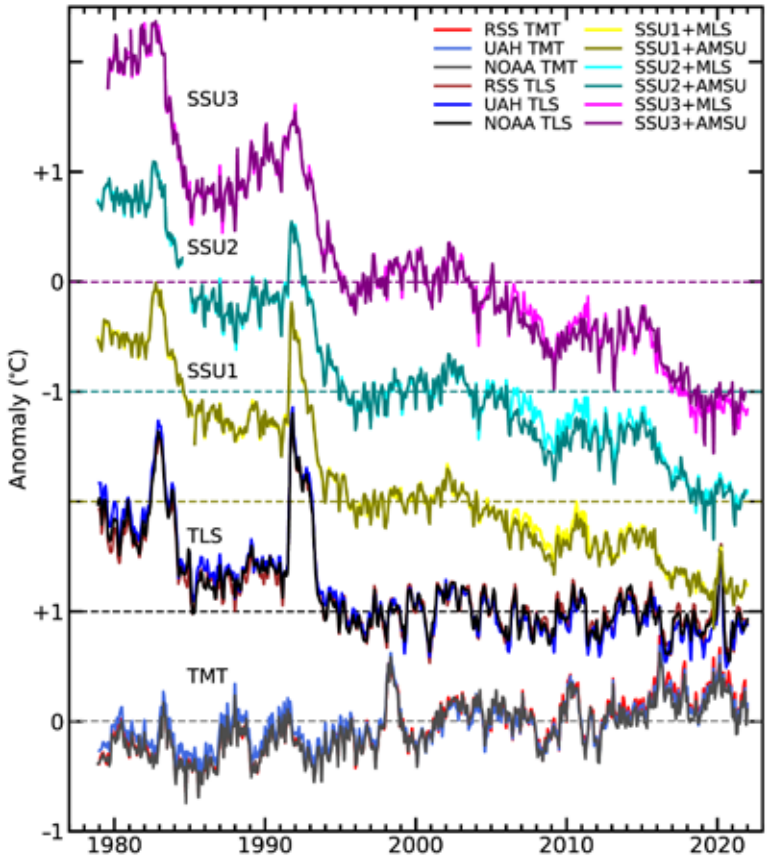

Fig. 2.10. Monthly global temperature anomalies (°C) from the middle troposphere to upper stratosphere (bottom to top). Middle and upper stratosphere data are from the Stratospheric Sounding Unit (SSU), representing thick-layer averages centered near 30, 38, and 45 km (SSU1, SSU2 and SSU3, respectively). Lower stratosphere temperatures (TLS) are ~13–22-km layer averages from satellite microwave measurements. Middle troposphere (TMT) data are ~0–10-km layer averages, and are included for comparison. Each time series has been normalized to zero for the period 1995–2005, and curves are offset for clarity.

Time series of global monthly temperature anomalies from the middle troposphere to the upper stratosphere based on satellite measurements are shown in Fig. 2.10. As discussed in Steiner et al. (2020), the middle and upper stratosphere data are merged products combining infrared emission measurements (Stratospheric Sounding Unit [SSU] 1, 2, 3 from 1979 to 2006) with more recent satellite data from microwave and infrared limb sounders for a continuous record. Merged datasets from microwave emission measurements provide layer-averaged temperatures for the lower stratosphere (TLS) and for the middle troposphere (TMT). In addition to long-term stratospheric cooling (due to CO_2 increase and stratospheric ozone changes) and tropospheric warming due to greenhouse gas increases (section 2b5), transient variations arise from a variety of causes including ENSO (e.g., large El Niño events in 1997 and 2016) and large volcanic eruptions (e.g., in 1982 and 1991). Transient warming in the lower stratosphere (TLS) in early 2020 was caused by stratospheric aerosol injections from the large Australian bushfires (Yu et al. 2021; Rieger et al. 2021; Stocker et al. 2021). However, no such events are apparent in the global average time series for 2021.

Independent measurements of temperatures between altitudes of ~10–30 km are available from occultations of GPS radio signals since 2002 (Steiner et al. 2020; Gulev et al. 2021). Figure 2.11 shows the resulting temperature trends for the period 2002–21 as a function of latitude and altitude. The results clearly differentiate warming in the troposphere from weak cooling over much of the lower to middle stratosphere. A more complicated situation occurs in the Southern Hemisphere subtropics, where warming extends across the tropopause into the lower stratosphere.

The long-term stratospheric cooling caused by rising greenhouse gas concentrations has led to a substantial contraction of the stratosphere over the last decades (Pisoft et al. 2021). Moreover, an increase of the tropopause height by about 50 m decade^{-1} was observed over the Northern Hemisphere with radiosonde data, confirmed with GPS radio occultation (Meng et al. 2021). The increase is found to be due to tropospheric warming and stratospheric cooling over the period 1980–2000, while the continuous rise after 2000 results primarily from enhanced tropospheric warming.

Unlike 2020, when the stratospheric winter polar vortices were unusually strong and undisturbed in both hemispheres, the Arctic polar vortex was disrupted by a major sudden stratospheric warming early in 2021 (Lee 2021). The Antarctic polar vortex was relatively cold and persistent in

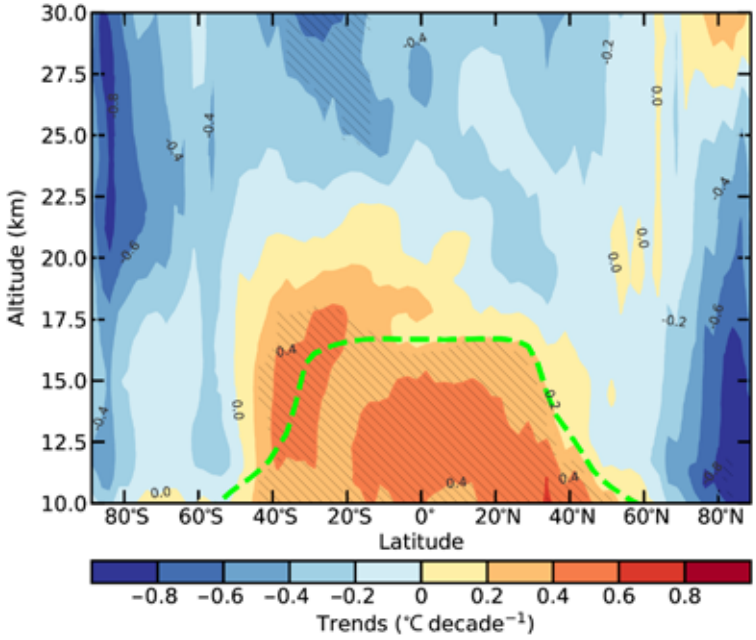

Fig. 2.11. Latitude–height section of temperature trends (°C decade^{-1}) derived from GPS radio occultation measurements over the period 2002–21 (updated from Steiner et al. 2020). Thick dashed line denotes the time average tropopause. Hatching denotes trends that are significant at 2-sigma uncertainty.

2021, coinciding with a large ozone hole persisting until December (sections 2g4, 6h). The equatorial stratosphere's quasi-biennial oscillation progressed in 2021 as it usually has for more than half a century: downward-propagating easterly and westerly wind regimes and accompanying temperature variations, with a mean periodicity of somewhat more than two years. This regular downward propagation from the upper to lower stratosphere was interrupted in both 2016 and 2020, but more regular evolution appeared to resume at the end of 2020 with an easterly phase propagating downward from the middle stratosphere (https://acd-ext.gsfc.nasa.gov/Data_services/met/qbo/qbo.html).

c. Cryosphere

1. PERMAFROST TEMPERATURE AND ACTIVE LAYER THICKNESS—J. Noetzli, H. H. Christiansen, M. Guglielmin, F. Hrbáček, K. Isaksen, S. L. Smith, L. Zhao, and D. A. Streletskiy

Permafrost—ground material remaining at or below 0°C for at least two consecutive years—is a key component of the cryosphere in high-latitude and high-altitude regions. Global permafrost temperatures have increased for several decades, with regional variability in magnitude and shorter-term fluctuations related to meteorological variations (Biskaborn et al. 2019; Etzelmueller et al. 2020; Haberkorn et al. 2021). Observed warming rates close to the depth of the zero annual amplitude (DZAA)—where annual temperature fluctuations become negligible—were in the range of a few tenths °C decade^{-1} (Smith et al. 2022). They were largest (0.3°–0.8°C decade^{-1}) at sites in continuous permafrost or at highest elevations with low permafrost temperatures. Warmer and ice-rich permafrost warms more slowly due to latent heat uptake during ice melt (< 0.3°C decade^{-1}). Changes in active layer thickness (ALT)—the thickness of the layer above the permafrost that freezes and thaws annually—relate to annual atmospheric and snow conditions. ALT was greater in 2021 than in 2020 in some polar regions and generally above average of available records for all observed permafrost regions.

Permafrost temperatures in 2021 across the Arctic regions were the highest on record at many sites (see section 5h); however, at some Arctic sites (e.g., northwestern North America, Nordic region, and northern Russia) lower permafrost temperatures than in the previous years were observed, related to lower air temperatures. ALT could not be fully reported for some Arctic regions due to continued COVID-related travel restrictions. In northern Alaska, ALT was below the 2009–18 average, while it was among the largest values on record in Alaska Interior and on average more than 30 cm greater than in 1995. Greenland also reported its greatest ALT since 1995. Northern European Russia and western and eastern Siberia had lower ALT compared to 2020, but was greater than average, while in central Siberia it was greater than 2020.

On James Ross Island, northeastern Antarctic Peninsula, permafrost temperatures in 2021 were the second highest (–5.0°C) since the record began in 2011. The ground temperature at 75 cm increased by 0.9°C over the period 2011–21 (Hrbáček et al. 2021). ALT has increased here by 12 cm decade^{-1} reaching 66 cm in 2021, which was 6 cm above average. At Rothera Point, permafrost temperature below the DZAA has remained stable since 2009.

Mountain permafrost accounts for approximately one-third of the global area underlain by permafrost (Hock et al. 2019). Data are primarily available from the European Alps, the Nordic region, and the Qinghai-Tibetan Plateau (QTP). Ranges of permafrost temperature and warming rates are similar to those observed in the Arctic, but with high spatial variability due to the complex topography. Significant ALT increase by meters were documented at sites in the European Alps over the past two decades (Etzelmueller et al. 2020; Haberkorn et al. 2021; PERMOS 2022), with considerable loss of ground ice (Mollaret et al. 2019). Ground temperatures close to the surface were lower in 2021 than 2020 in the European Alps (PERMOS 2022; Pogliotti et al. 2015; Magnin et al. 2015) due to a long period of snow cover and lower atmospheric temperatures (e.g., MeteoSwiss 2022). This resulted in ALT that were often lower in 2020 and a general decrease in rock glacier velocity (section 2c2). For many sites, permafrost temperatures at 20-m depth—where they react

to longer term trends—continued to increase in 2021 and reached record levels (Fig. 2.12). This is also true for the Nordic mainland; on Juvvasshøe in southern Norway, 2021 was the eighth consecutive year (since 2014) with record permafrost temperatures (Noetzli et al. 2021a; Etzelmüller et al. 2020). ALT at sites in the Nordic countries in 2021 were greater than or close to the maximum of 2020. In Svalbard, however, permafrost temperatures at 10-m depth continued to decrease due to cold winters in 2019–21 (Christiansen et al. 2021), but were still above the long-term average (Fig. 2.12). Permafrost temperatures in the QTP in central Asia increased at six sites from 2005 to 2020: 0.45°C decade^{-1} at 10-m depth and 0.24°C decade^{-1} at 20-m depth (Fig. 2.13; Zhao et al. 2020, 2021). Along the Qinghai-Tibet Highway (Kunlun mountain pass), an ALT increase was observed with a mean of 19.4 cm decade^{-1} for the period 1981–2020 (Fig. 2.14).

Long-term observation of permafrost relies on field observations of ALT, permafrost temperatures, and, since 2021, on rock glacier velocity (Streletskiy et al. 2021; Pellet et al. 2021). International data are collected by the Global Terrestrial Network for Permafrost (GTN-P) as part of the Global Climate Observing System (GCOS). Permafrost temperatures are logged in boreholes reaching at least the DZAA, with a measurement accuracy assumed to be 0.1°C (Biskaborn et al. 2019; Noetzli et al. 2021b; Streletskiy et al. 2021). ALT is determined by mechanical probing where possible (accuracy of ~1 cm) and otherwise interpolated from borehole temperature measurements. The global coverage of permafrost monitoring sites is sparse and particularly limited in regions such as Siberia, central Canada, Antarctica, and the Himalayan and Andes Mountains.

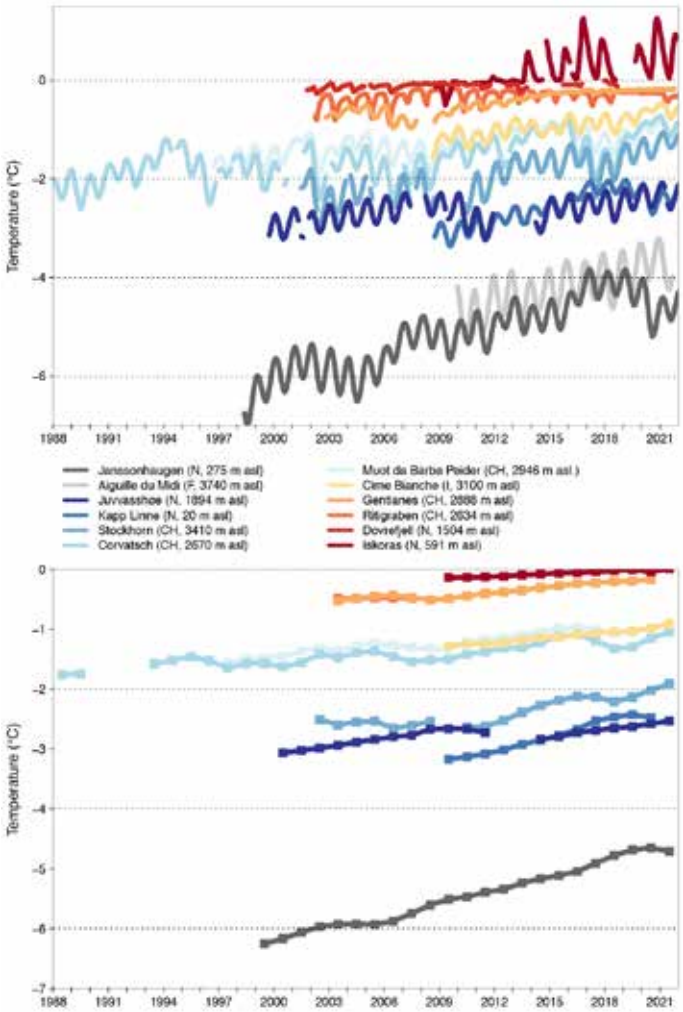

Fig. 2.12. Permafrost temperature (°C) measured in boreholes in the European Alps and the Nordic countries at a depth of (a) ca. 10 m (monthly means) and (b) 20 m (annual means). (Data sources: Switzerland: Swiss Permafrost Monitoring Network PERMOS; Norway: Norwegian Meteorological Institute and the Norwegian Permafrost Database NORPERM; France: updated from Magnin et al. 2015; Italy: updated from Pogliotti et al. 2015.)

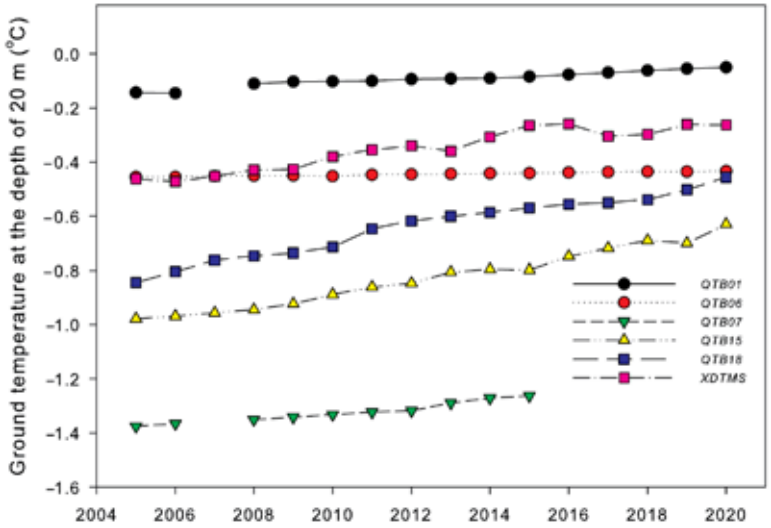

Fig. 2.13. Permafrost temperature (°C) measured in boreholes along the Qinghai-Xizang Highway on the Tibetan Plateau at 2-m depth for the period 2005–20. (Source: Cryosphere Research Station on Qinghai-Xizang Plateau, CAS.)

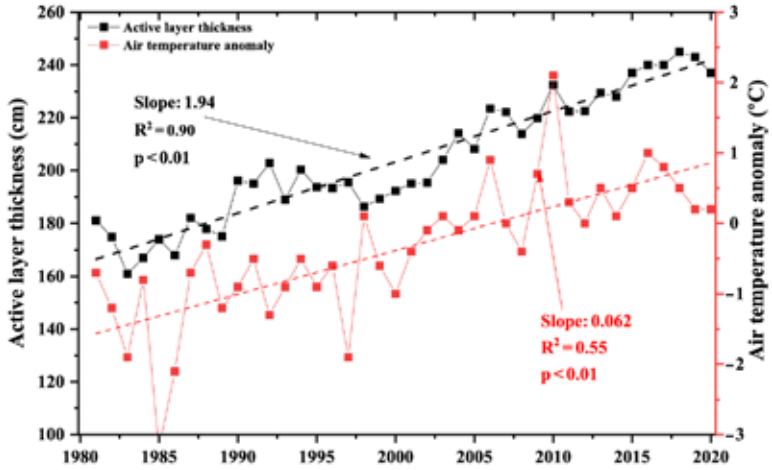

Fig. 2.14. The active layer thickness (cm) and air temperature anomalies (°C) in the permafrost zone along the Qinghai-Tibet Highway during the period 1981–2020. The air temperature anomaly is estimated relative to the base period 1981–2010. (Source: Cryosphere Research Station on Qinghai-Xizang Plateau, CAS.)

2. ROCK GLACIER VELOCITY—C. Pellet, X. Bodin, D. Cusicanqui, R. Delaloye, A. Kääb, V. Kaufmann, J. Noetzli, E. Thibert, S. Vivero, and A. Kellerer-Pirklbauer

Rock glaciers are debris landforms generated by the creep of frozen ground (permafrost) found in most mountain ranges worldwide (RGIK 2021). Changes in their velocities are mostly related to the evolution of ground temperature and liquid water content between the permafrost table and the shearing horizon at depth: the closer to 0°C, the faster the rock glacier is able to move (Cicoira et al. 2019; Frauenfelder et al. 2003; Staub et al. 2016). In 2021, the variable rock glacier velocity (RGV) was adopted as a new associated product to the essential climate variable (ECV) permafrost by GCOS and the Global Terrestrial Network for Permafrost (GTN-P, Streletskiy et al. 2021), given the global occurrence of active rock glaciers and their sensitivity to changes in ground temperature.

RGVs, observed in several mountain ranges across the globe, have been increasing since the 1950s, with regional variability in magnitude and marked interannual variability. Observed rates of increase are largest since 2010 and record high velocities have been recorded since 2015. These changes are consistent with interannual variations of permafrost temperatures (cf. section 2c1), to which rock glacier velocities have been shown to respond synchronously (Cusicanqui et al. 2021; Kääb et al. 2007; Kellerer-Pirklbauer and Kaufmann 2012; Staub et al. 2016; Vivero et al.

2021). Regionally, RGVs follow the same interannual behavior despite variable size, morphology, and velocity range (e.g., Delaloye et al. 2010; Kääb et al. 2021; Kellerer-Pirklbauer et al. 2018; PERMOS 2019).

RGVs in the European Alps have increased by a factor of between 2 and 10 from the 1980s to 2021 (Fig. 2.15b). This acceleration was temporarily interrupted at most sites during 2004–06 and 2016–18, coinciding with a decrease in permafrost temperatures, mainly resulting from snow-poor winters, which enabled more efficient ground cooling due to the later onset of an insulating snow cover (Noetzli et al. 2018; PERMOS 2019). Compared to 2020, RGVs decreased in 2021, e.g., at Gemmi/Furggentälti (Switzerland, –26%), Grosses Gufer (Switzerland, –24%), and Laurichard (France, –4%), whereas RGVs increased at Dösen (Austria, +19%) and Hinteres Langtalkar (Austria, +35%) to record values (Fig. 2.15b). The velocity decrease at Swiss and French sites is consistent with lower air temperatures compared to 2020 (Fig. 2.15a) as well as a long-lasting snow cover in spring and a relatively late thickening of the snow cover in autumn, which led to lower ground temperatures (cf. section 2c1). Different behaviors of the rock glaciers between the Western and Eastern Alps in 2021 might be related to differences in precipitation and temperature, particularly in December 2020 (warmer east), January 2021 (drier east), and July 2021 (warmer and less humid east), in addition to the influence of local topo-climatic factors.

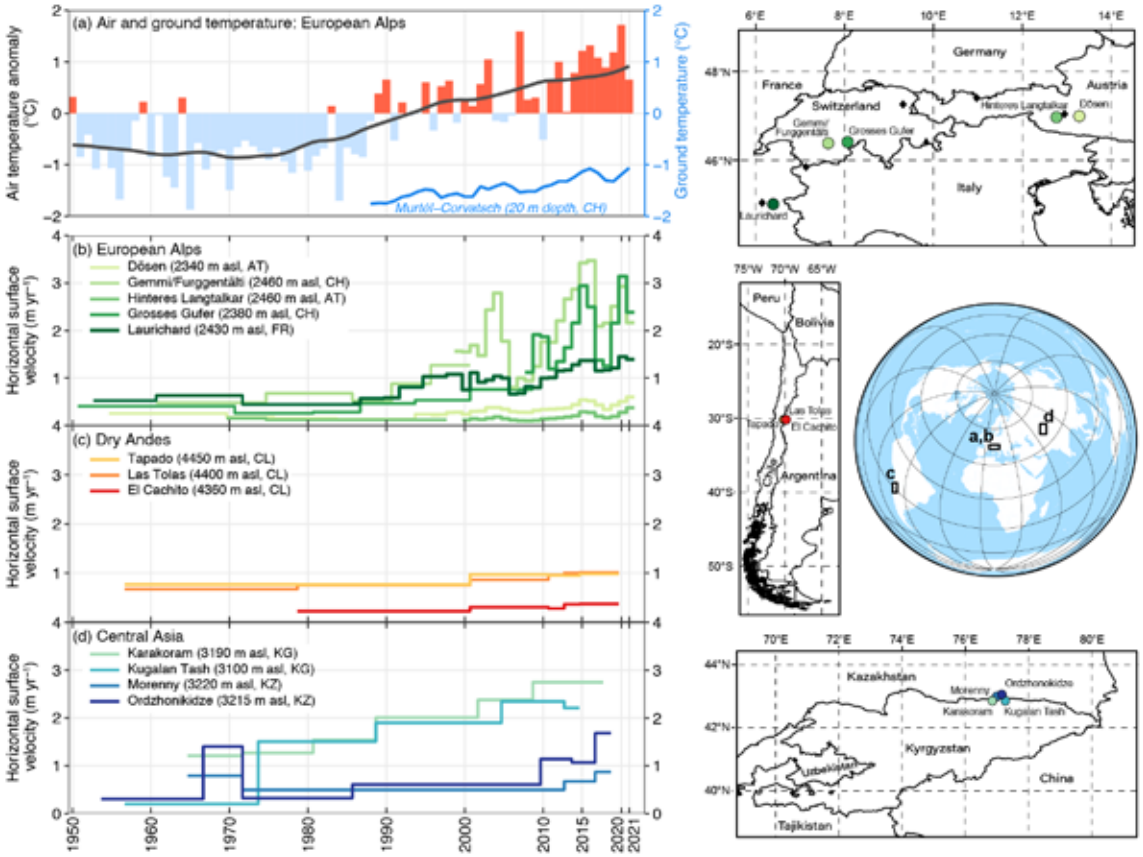

Fig. 2.15. (a) Rock glacier velocity and climate: air and ground temperature (°C) in the European Alps. Rock glacier velocities (m yr^{-1}) at selected sites in (b) the European Alps, (c) the Dry Andes (adapted from Vivero et al. 2021), and (d) central Asia (adapted from Kääb et al. 2021). Rock glacier velocities based on in situ geodetic surveys or photogrammetry in the context of long-term monitoring. In-situ permafrost temperature measured at 20-m depth (blue line) at Murtèl Corvatsch (black triangle on Europe map) and air temperature: composite anomaly to the 1981–2010 average (bars) and composite 20-year running mean (solid line) at Besse (FR), Grand Saint-Bernard (CH), Saentis (CH), Sonnblick (AT), and Zugspitze (D, black diamonds on Europe map). (Data sources: Météo France, Deutscher Wetterdienst [DWD], MeteoSwiss, Zentralanstalt für Meteorologie und Geodynamik [ZAMG], Swiss Permafrost Monitoring Network [PERMOS], University of Fribourg, University of Graz, Graz University of Technology, Université Grenoble Alpes [INRAE], University of Oslo.)

There are few long-term in situ measurements of RGVs outside of the European Alps. However, an increasing number of studies exploit the potential of archival aerial photographs and high-resolution satellite data to reconstruct RGVs (e.g., Cusicanqui et al. 2021; Eriksen et al. 2018). The velocities of three rock glaciers observed in the Dry Andes in South America showed slow velocities from 1950 to 2000, followed by a steady acceleration since the 2000s (Fig. 2.15c), consistent with the climatic conditions observed in the region (Vivero et al. 2021).

RGVs observed in Central Asia since the 1950s do not show a uniform picture (Fig. 2.15d; Kääb et al. 2021). The Karakoram and Kugalan Tash (Kyrgyzstan) RGVs steadily increased since the 1960s, whereas at Ordzhonikidze and Morenny (Kazakhstan) high velocities were observed during the second half of the 1960s, then low velocities until 2010, and increasing velocities in recent years. All RGVs have increased since the start of the observations and accelerated since 2010, which is consistent with increasing air temperatures and with the acceleration reported in the European Alps and Dry Andes.

Long-term RGV time series are reconstructed using multi-temporal aerial or optical satellite images. Horizontal displacements are computed based on feature tracking, 2D ortho-image matching algorithms or digital elevation model matching. The resulting accuracy strongly depends on the spatial resolution of the aerial images and on the image quality. Surface displacements are averaged for a cluster of points selected within areas, representative of the flow field and indicative of the downslope movement of the rock glacier (RGIK 2022). Annual rock glacier velocities are measured using terrestrial geodetic surveys performed each year at the same time (usually at the end of summer). The positions are measured for a number of selected boulders (10–100 per landform) with an average accuracy in the range of mm to cm (Delaloye et al. 2008; PERMOS 2019).

3. ALPINE GLACIERS—M. Pelto

In the hydrological year 2020/21, observed World Glacier Monitoring Service (WGMS) reference glaciers experienced a mass balance loss of –900 mm water equivalent (mm w.e.), compared to –700 mm w.e. in 2019/20. From 1970 to 2021 the eight most negative mass balance years were all recorded after 2010. A value of –1000 mm w.e. per year represents a mass loss of 1000 kg m^{-2} of ice, or an annual glacier-wide thickness loss of about 1100 mm yr^{-1}.

Figure 2.16 illustrates glacier mass balance for the WGMS global reference glaciers with more than 30 years of data for the period 1970 to 2020. Global values are calculated using a single value (averaged) for each of 19 mountain regions in order to avoid a bias to well observed regions. In 2021, a negative annual mass balance was reported from 31 of the 32 reference glaciers reported to the WGMS as of 1 June 2022. The mean annual mass balance of the 32 reference glaciers reporting

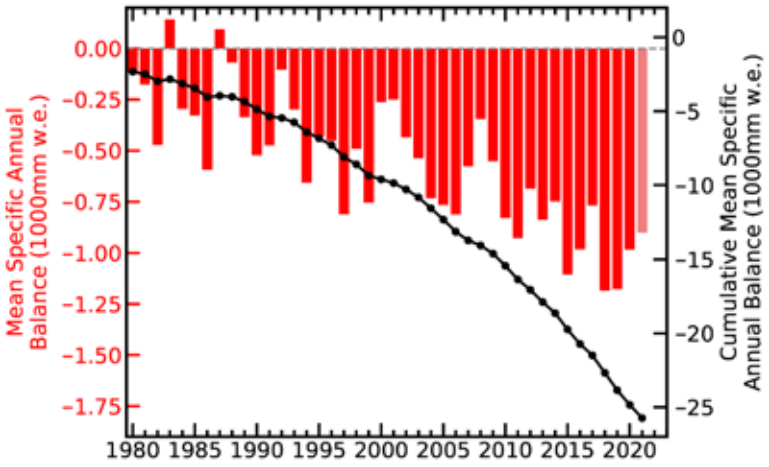

Fig. 2.16. Global annual glacier mass balance of WGMS reference glacier network in mm water equivalent (w.e.), with annual values (red bars, left axis) and cumulative amounts since 1979 (black dots, right axis). Lighter shading for 2021 is used as the final values for that year were not yet available at time of publication.

is –900 mm w.e., which includes data from 12 nations on four continents (not final regionally-averaged global value; there are 42 reference glaciers in total). This will make 2021 the 34th consecutive year with a global alpine mass balance loss and the 13th consecutive year with a mean global mass balance below –500 mm w.e.

The rate of thinning increased from –527 mm yr^{-1} for 2000–09 to –896 mm yr^{-1} for 2010–19 (WGMS 2021). This agrees well with the satellite survey of 200,000 alpine glaciers by Huggonet et al. (2021) who identified a thinning rate excluding ice sheet peripheral glaciers of 360 ± 210 mm yr^{-1} in 2000 to 690 ± 150 mm yr^{-1} in 2019. Alpine glaciers lost a mass of 267 ± 16 Gt yr^{-1} from 2000 to 2019, equivalent to 21 ± 3% of the observed global sea level rise (Huggonet et al. 2021). More frequent and intense heat waves continue to take a toll on alpine glaciers (Pelto et al. 2021, 2022).

All 17 reporting glaciers in the Alps had a negative mass balance averaging –682 mm in 2021. In Austria in 2020, of the 92 glaciers with annual terminus observations, 85 (93.4%) withdrew and seven remained stationary (Lieb and Kellerer-Pirklbauer 2021). This retreat trend continued in 2021, with another year of mass balance loss. In Norway, the six reporting glaciers all had a negative mass balance, yielding an average mass balance of –671 mm in 2021. On Svalbard, the mean loss of the four reporting glaciers was –227 mm. Iceland completed surveys of nine glaciers; all nine had negative balances, with a mean mass balance of –1160 mm.

In western Canada and Washington (United States) all 14 glaciers observed in 2021 had a negative mass balance averaging –1635 mm. The exceptional heat wave during late June and early July in western North America (section 2b4; Sidebar 7.1) set the stage for the large glacier mass loss (Pelto et al. 2022; Fig. 2.17). In Alaska, three of the four glaciers measured had a negative mass balance, with a mean annual balance of –528 mm. In South America, 2021 mass balance data were reported from three glaciers in Argentina, two glaciers in Chile, and one in Colombia; all were negative with a mean of –861 mm. This is greater than the 2000–18 average loss observed in the Andes of –720 ± 220 mm yr^{-1} (Dussaillant et al. 2019). In High Mountain Asia, 15 of 18 glaciers reported negative balances in 2021. The average mass balance was –468 mm. Early winter of 2021 was warm and dry across the Himalayan region. This was capped off by record warmth in the Mount Everest region, leading to the snow line on glaciers rising and snow-free glaciers up to 6000 m (Pelto et al. 2021), illustrating that the ablation season no longer always ends when winter begins. The importance of winter conditions was further noted by Potocki et al. (2022) who reported on an ice core drilled on South Col Glacier, on Mount Everest at 8020 m a.s.l., revealing a contemporary sublimation driven thinning of ~2000 mm yr^{-1}.

Fig. 2.17. Easton Glacier in Washington state in August 2021, with less than 10% snowcover and one month left in the ablation season.

4. LAKE ICE—S. Sharma, R. I. Woolway, A. Basu, K. Blagrave, G. Bove, N. Granin, J. H. L'Abée-Lund, H. J. Malmquist, W. Marszelewski, T. Nõges, M. Pulkkanen, and K. Stewart

In the 2020/21 winter, lake ice phenology (timing of ice-on and ice-off) across the Northern Hemisphere (NH, calculated from Copernicus Climate Change Service [C3S] ERA5 [Hersbach et al. 2020]) continued to exhibit later ice-on dates, earlier ice-off dates, and shorter seasonal ice cover, thus continuing the pattern observed in recent decades (Sharma and Woolway 2021). Relative to the 1991–2020 base period, NH lakes froze, on average, 3.8 days later, thawed 3.5 days earlier, and ice duration was over 7 days shorter (Figs. 2.18, 2.19). The regional variations in ice duration were consistent with NH winter air temperature anomalies. Most notably, some regions in North America, such as western Canada, experienced below-average air temperatures, which resulted in longer-than-average ice duration. Conversely, eastern Canada and many regions in Eurasia experienced warmer-than-average conditions that resulted in shorter-than-average ice duration (Fig. 2.18d).

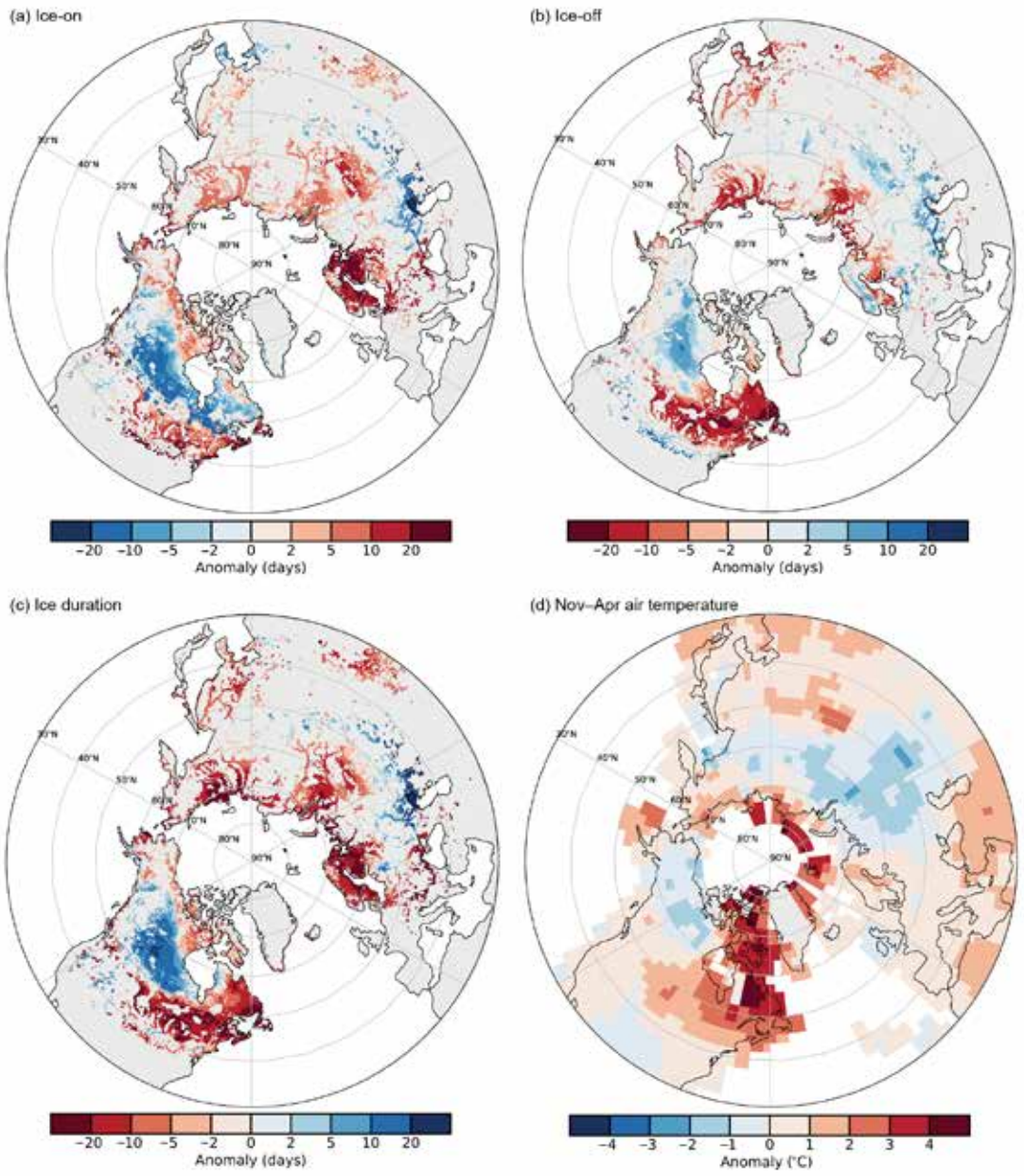

Fig. 2.18. Anomalies (days) in 2021 in (a) ice-on (positive = later), (b) ice-off (negative = earlier), and (c) ice duration for lakes across the NH (negative = shorter), and (d) surface air temperature anomalies (°C) for the NH cold season (Nov–Apr average), the time of year in which lakes typically freeze. The base period is 1991–2020. (Sources: ERA5, GISTEMP.) The winter season for 2021 generally refers to the time between the end of autumn 2020 and the start of spring 2021.

Based on in situ ice phenological records from 110 lakes in North America (NA), Europe, and Asia, ice-on was 11 days later, ice-off was 7.5 days earlier, and there were 19 fewer days of ice cover over the 2020/21 winter season, on average, relative to 1991–2020 (Fig. 2.19). For NA lakes, ice-on averaged 5 days later and ice-off was 11 days earlier. For European lakes, ice-on was 17 days later, ice-off was 3 days earlier, totaling 20 days less ice cover in the winter of 2021 relative to the 1991–2020 base period. Lake Erken, in Sweden, lost the most ice cover during the 2021 winter, with 61 days less ice cover compared to the 1991–2020 normal in response to an anomalously warm winter in 2021 in the region. Analysis of ice phenology trends during 1991–2021 suggest that ice-on date is 4.1 days later per decade, ice-off date is 2.2 days earlier per decade, and ice duration

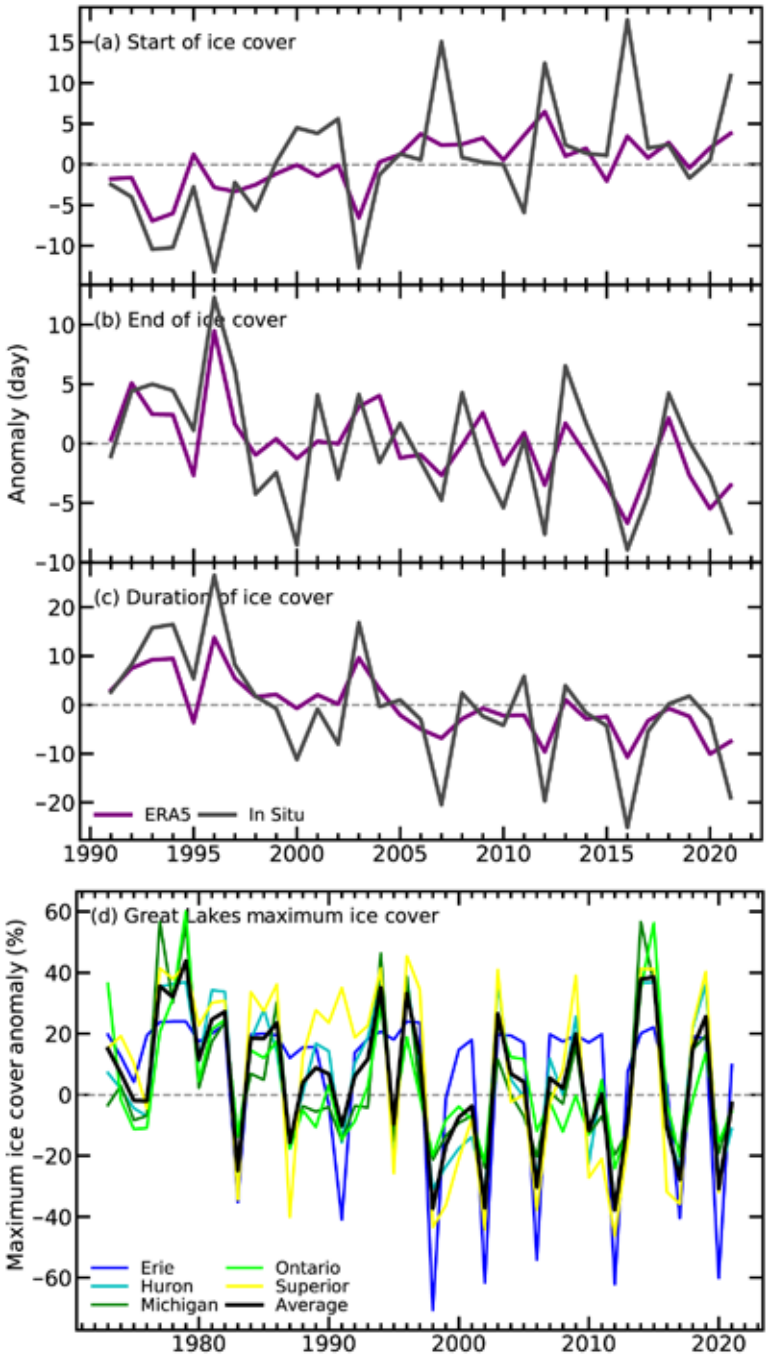

Fig. 2.19. (a) Lake ice-on, (b) ice-off, and (c) ice duration anomalies from 1980 to 2021 derived from in situ observations and ERA5 reanalysis. (d) Anomalies in Great Lakes maximum ice cover extent (%) for 1973–2021. The black line shows the average anomaly for all of the Great Lakes, whereas the lines in color show individual lakes (Erie, Michigan, Superior, Ontario, Huron). Base period is 1991–2020. The winter season for 2021 generally refers to the time between the end of autumn 2020 and the start of spring 2021.

is 6.8 shorter per decade on average for these 110 lakes. In 2021, the Laurentian Great Lakes had 2.9% less maximal ice coverage relative to 1991–2020. The deeper and most northern lakes all had less maximal ice coverage, of which Lake Huron was the most anomalous with 11.6% less ice coverage in 2021. Lake Erie, the shallowest lake, was the exception, with 9.7% more ice coverage in 2021 (Fig. 2.19d). Since 1973, the Laurentian Great Lakes have been losing on average 4.3% (95% confidence interval: 0.5, −9.1) of ice coverage per decade. Lake Superior is losing the most ice coverage per decade of all the Great Lakes (7.0% per decade). In fact, Lake Superior is one of the world's fastest warming lakes (O'Reilly et al. 2015; Sharma et al. 2021) and has lost over 60 days of ice cover since 1857 (Sharma et al. 2021; Wang et al. 2021).

To estimate the timing of ice-on and ice-off and, ultimately, the duration of winter ice cover across NH lakes, ice simulations from the ERA5 reanalysis product (Hersbach et al. 2020) were analyzed following the methods of Grant et al. (2021). We obtained in situ ice phenology for 110 lakes: Canada (5), United States (53), Estonia (2), Finland (27), Iceland (1), Norway (18), Poland (1), Sweden (1), Russia (1), and Japan (1). In addition, we obtained annual maximum ice cover (%) data for each of the Laurentian Great Lakes from 1973 to 2020 (https://www.glerl.noaa.gov/data/ice/). Surface air temperature data for the NH cold season (November–April average) were downloaded from the NASA GISS surface temperature analysis (Lenssen et al. 2019; GISTEMP Team 2022). To create the time series figure, the ERA5 data were averaged across all 0.25° grids and consisted of a much larger sample size relative to the in situ data where the anomalies were averaged across 110 lakes.

5. NORTHERN HEMISPHERE CONTINENTAL SNOW COVER EXTENT—D. A. Robinson and T. W. Estilow

Annual snow cover extent (SCE) over Northern Hemisphere (NH) lands averaged 24.3 million km^2 in 2021. This is 0.6 million km^2 less than the 1991–2020 mean and 0.8 million km^2 below the mean over a 52-year period of record (Fig. 2.20; Table 2.5), marking the seventh least extensive cover on record. Monthly SCE in 2021 ranged from a maximum of 46.8 million km^2 in January to a minimum of 2.5 million km^2 in August.

The year began with NH SCE ranking in the middle tercile of the 55-year record, although North America (NA) SCE was fourth most extensive on record in February. NA quickly lost SCE in March, falling to 47th most extensive, while Eurasia (EUR) remained well below average. These conditions persisted throughout spring, with May having the 52nd most extensive SCE on record and June 47th most extensive.

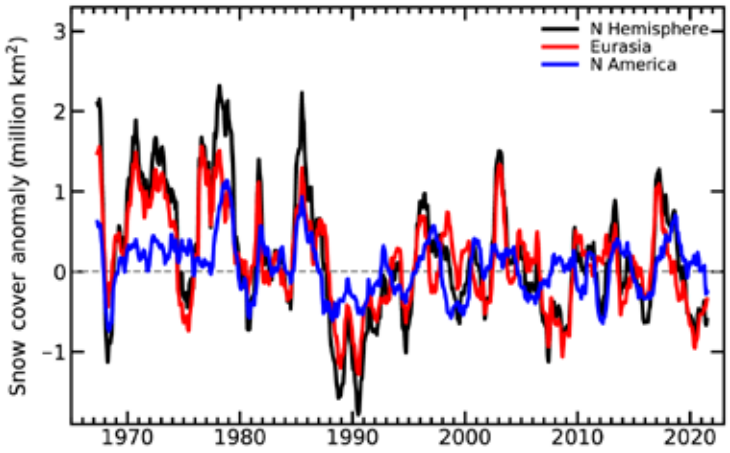

Fig. 2.20. 12-month running anomalies (million km^2) of monthly SCE over NH lands as a whole (black) and EUR (red), and NA (blue) separately, plotted on the seventh month using values from Nov 1966 to Dec 2021. Anomalies are calculated from NOAA snow maps. Mean NH SCE is 25.1 million km^2 for the full period of record. Monthly means for the period of record are used for nine missing months during 1968, 1969, and 1971 in order to create a continuous series of running means. Missing months fall between Jun and Oct. Data from Estilow et al. (2015).

Table 2.5. Monthly and annual climatological information on NH, EUR, and NA SCE between Nov 1966 and Dec 2021. Included are the numbers of years with data used in the calculations, NH means, standard deviations, 2021 values, and rankings. Units: million km^2. 1968, 1969, and 1971 have one, five, and three missing months respectively, thus are not included in the annual (Ann) calculations. NA includes Greenland. Ranks are from most to least extensive.

	Years of data	NH Mean	Std. Dev.	2021	2021 NH rank	2021 Eurasia rank	2021 N Am. rank
Jan	55	47.1	1.5	46.8	32	36	28
Feb	55	46.0	1.8	46.1	22	42	4
Mar	55	40.4	1.9	38.6	44	42	47
Apr	55	30.5	1.7	28.8	45	40	46
May	55	19.1	2.0	16.2	53	51	45
Jun	54	9.4	2.5	6.2	46	52	42
Jul	52	3.9	1.2	2.8	43	44	39
Aug	53	3.0	0.7	2.5	40	42	30
Sep	53	5.4	0.9	5.6	22	30	13
Oct	54	18.6	2.7	18.1	28	22	46
Nov	56	34.3	2.1	35.4	18	9	44
Dec	56	43.7	1.8	44.5	17	13	26
Ann	**52**	**25.1**	**0.8**	**24.3**	**46**	**44**	**41**

NA picked up some early autumn snow, contributing to its 13th most extensive September cover. This ranking fell to 46th most extensive in October, when EUR and the NH ranked in the middle tercile. NH November and December SCE fell near the boundary of the highest and middle tercile, mainly due to above-average SCE in EUR where November ranked ninth most extensive and December 13th most extensive. Following an average snow cover in January, SCE over the contiguous United States was fifth most extensive in February and below-average every other month thereafter in 2021.

SCE is calculated at the Rutgers Global Snow Lab (GSL) from daily SCE maps produced by meteorologists at the U.S. National Ice Center, who rely primarily on visible satellite imagery to construct the maps. Maps depicting daily, weekly, and monthly conditions, anomalies, and climatologies may be viewed at the GSL website (https://snowcover.org).

d. Hydrological cycle

1. SURFACE HUMIDITY—K. M. Willett, D. A. Lavers, M. Bosilovich, and A.J. Simmons

Global mean specific humidity (q) in 2021 was lower compared to 2020, although remaining well above the 1991–2020 average in all datasets (+0.07 to +0.18 g kg^{-1} for q_{land}, +0.07 to +0.20 g kg^{-1} for q_{ocean}) except for ERA5, which placed global q_{land} just below average at −0.01 g kg^{-1} (Figs. 2.21a–d). For global mean relative humidity (RH), 2021 was less saturated than 2020 in all datasets over land (–1.32 to −0.70 %rh) (Figs. 2.21e,f). Both JRA-55 and ERA5 show a large difference between 2020 and 2021, placing 2021 as the least saturated year on record (since 1958 and 1967, respectively) by a large margin (−0.23 %rh and −0.45 %rh, respectively). It was the second driest year on record after 2019 in HadISDH. Over oceans, RH remained mixed with HadISDH and JRA-55 behaving similarly, placing 2021 RH_{ocean} at +0.20 and +0.16 %rh above the 1991–2020 average, respectively, which is slightly above 2020, while ERA5 dropped below average at −0.09 %rh, continuing a short drying trajectory since 2019.

Spatially, missing data regions of HadISDH (Plate 2.1g) over much of northwestern, central, and eastern Africa are regions that showed strong negative q anomalies in ERA5, indicating that the water vapor content was lower than average (Appendix Fig. A2.8). This might explain the discrepancy in global land averages between ERA5 and HadISDH. Central Africa is a key region for differences between the reanalyses, with MERRA-2 (Appendix Fig. A2.9) showing strong high water vapor content anomalies there and more expansive high water vapor content anomalies generally, likely contributing to the MERRA-2 high 2021 q_{land} anomaly. Other discrepancies are notable over western Australia where HadISDH shows an isolated suspect highwater vapor content anomaly, and over northern Colombia and Venezuela where MERRA-2 shows strong low water vapor content anomalies. Over the ocean, MERRA-2 and ERA5 are in good agreement. The HadISDH higher global mean q_{ocean} anomaly for 2021 is missing many of the low water vapor content anomaly regions of the central eastern Pacific and Southern Hemisphere more generally, the former being associated with the La Niña conditions. Positive and negative anomalies are broadly

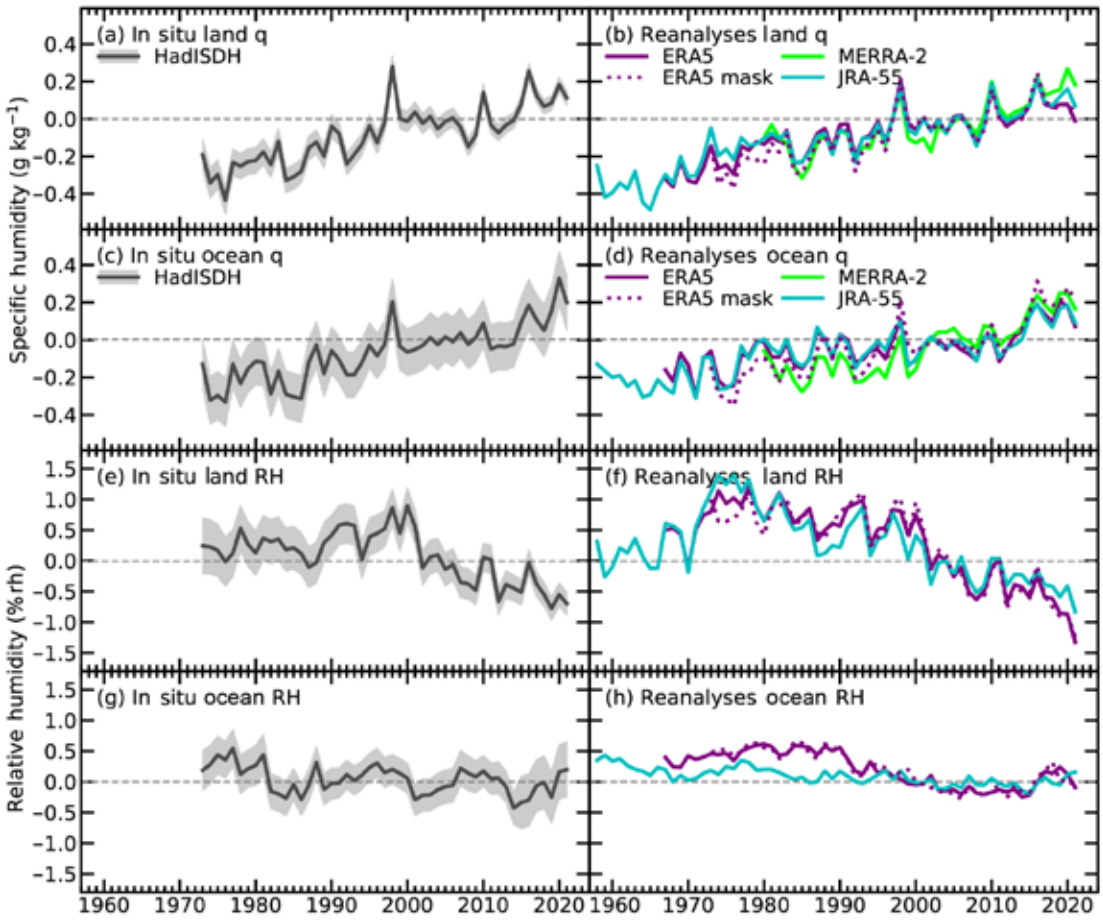

Fig. 2.21. Global average surface humidity annual anomalies (1991–2020 base period). For the in-situ datasets 2-m surface humidity is used over land and ~10-m over the oceans. For the reanalysis 2-m humidity is used over the whole globe. For ERA5 ocean series-only points over open sea are selected. ERA5 mask is a version of ERA5 that spatially matches the coverage of HadISDH. 2-sigma uncertainty is shown for HadISDH capturing the observation, gridbox sampling and spatial coverage uncertainty. (Sources: HadISDH [Willett et al. 2013, 2014, 2020]; ERA5 [Hersbach et al. 2020]; JRA-55 [Kobayashi et al. 2015]; MERRA-2 [Gelaro et al. 2017].)

similar between RH (Plate 2.1h; Appendix Figs. A2.10, A2.11) and q but with the central Eurasian and western North American anomalies more expansive for RH_{land}, and RH_{ocean} anomalies more muted than those for q_{ocean}, q_{land}, and RH_{land} generally.

In terms of long-term trends (Table 2.6), all datasets continue to show long-term increasing water vapor over land and ocean (+0.04 to +0.10 g kg^{-1} decade^{-1}), while the air over land has become less saturated (−0.23 to −0.45 %rh decade^{-1}). This means that the water vapor content of the air has increased more slowly than the water vapor carrying capacity of the air, which increases exponentially with temperature. The trend magnitudes for q are similar over land and ocean for each dataset. HadISDH and MERRA-2 show similar larger trends in q (+0.09 to +0.10 g kg^{-1} decade^{-1},

Table 2.6. Global average decadal trends for the period 1979–2021 fitted using ordinary least squares regression. The 90th percentile confidence intervals are shown in parentheses, fitted using AR(1) correction following Santer et al. (2008). Trends shown in bold are considered significantly different from a zero trend, in which the confidence intervals do not cross the zero line. Units are g kg^{-1} decade^{-1} for q and %rh decade^{-1} for RH.

Variable	HadISDH	ERA5	ERA5 masked to HadISDH	MERRA-2 (1980–2020)	JRA-55
Land q	**0.09 (0.02)**	**0.05 (0.01)**	**0.07 (0.01)**	**0.09 (0.02)**	**0.06 (0.01)**
Land RH	**−0.23 (0.08)**	**−0.45 (0.06)**	**−0.44 (0.08)**	NA	**−0.33 (0.04)**
Ocean q	**0.09 (0.01)**	**0.04 (0.02)**	**0.08 (0.02)**	**0.10 (0.02)**	**0.04 (0.01)**
Ocean RH	−0.03 (0.04)	**−0.18 (0.08)**	**−0.18 (0.07)**	NA	**−0.04 (0.02)**

respectively), while ERA5 and JRA-55 show more moderate trends (+0.04 to +0.06 g kg^{-1} decade^{-1}, respectively). While all datasets show a negative trend for RH_{ocean}, these trends are small, relatively widespread (−0.03 to −0.18 %rh decade^{-1}), and not considered to be significant for HadISDH. We conclude that there is large uncertainty in whether there is any real change in RH_{ocean}.

Agreement between the monitoring products in terms of both long-term trajectories and year-to-year variability is generally good (Fig. 2.21), with the exception of RH_{ocean}. Greater discrepancy over ocean is expected given the sparse observing network available from the Voluntary Observing Ships (VOS; https://www.vos.noaa.gov/vos_scheme.shtml) that make up the HadISDH record and the difference in methodological approaches between datasets. For example, ERA5 does not incorporate any in situ near-surface temperature or dew point temperature measurements over ocean, whereas HadISDH, MERRA-2, and JRA-55 do. The uncertainty range estimated for HadISDH is larger over ocean than over land, reflecting both the larger observational uncertainty since 2015, when digitized ship metadata provision ended, and larger spatial coverage uncertainty compared to over land. For RH_{land}, ERA5 is consistent with JRA-55 whereas for RH_{ocean} it is not.

Despite the good agreement generally over land, the reanalyses have diverged since 2018. ERA5 masked to the HadISDH spatial coverage differs little from the complete ERA5 anomaly time series (dashed lines in Fig. 2.21), especially over the last 30 years. Global trends in the masked versus complete ERA5 for *q* are closer to, but still less than, those from HadISDH (Table 2.6), but practically identical for RH. Interestingly, masked and complete ERA5 RH_{land} and RH_{ocean} anomalies are persistently more saturated than HadISDH pre-1990. Simmons et al. (2021) note an increase in the number of temperature observations, particularly those sampling different hours of the day around between 1988 and 1990; however, it is not clear how this would lead to biases in RH.

2. TOTAL COLUMN WATER VAPOR—C. A. Mears, J. P. Nicolas, O. Bock, S. P. Ho, and X. Zhou

In 2021, global land and ocean averages of total column water vapor (TCWV) were above the 1991–2020 climatological averages, but were generally lower than the 2015–20 period which showed high vapor values. This is not surprising because La Niña conditions, which were present for most of the year, have a cooling effect on global surface and tropospheric temperatures, thus lowering the water-holding capacity of the global atmosphere. In reanalysis output, where time series are available for the entire 1979–2021 period, 2021 was the fourth (MERRA-2, anomaly = 0.477 kg m^{-2}), seventh (ERA5, anomaly = 0.264 kg m^{-2}), and eighth (JRA55, anomaly = 0.383 kg m^{-2}) highest vapor year since 1979. Time series of global averages agree well in all datasets (Fig. 2.22). Part of the discrepancy between the Global Navigation Satellite System (GNSS) time series and reanalysis over land is due to the limited spatial sampling afforded by the GNSS network. While TCWV decreased sharply from 2020 to 2021 globally and over ocean in all the datasets used in this assessment, there is substantial spread in the amount of this decrease over land.

The global map of TCWV anomalies from MERRA-2 (presented as percent of annual mean values to show extratropical changes more clearly) for 2021 (Plate 2.1i) reveals large low vapor anomalies in the eastern South Pacific, with low vapor anomalies close to the equator along a northwest–southeast oriented band and high vapor anomalies farther south. This pattern denotes the southwest displacement of the South Pacific Convergence Zone (SPCZ) that is typically associated with La Niña conditions (Brown et al. 2020). Prominent low vapor anomalies also occurred over West Antarctica and the adjacent sector of the Southern Ocean. Much of the rest of the globe showed wet anomalies, with the largest relative values observed over the Maritime Continent, South and East Asia, the northern Pacific, the southwest Atlantic, and eastern Canada, which correspond to regions with positive anomalies in surface temperature and lower tropospheric temperature (Plates 2.1.a,f). While the 2020/21 and 2021/22 boreal winters were both marked by La Niña conditions, the pattern of low vapor in the tropical Pacific along the SPCZ region was significantly more pronounced than what has been typically observed during La Niña events since 1980, and during the previous La Niña winter in 2017/18 (Fig. 2.23).

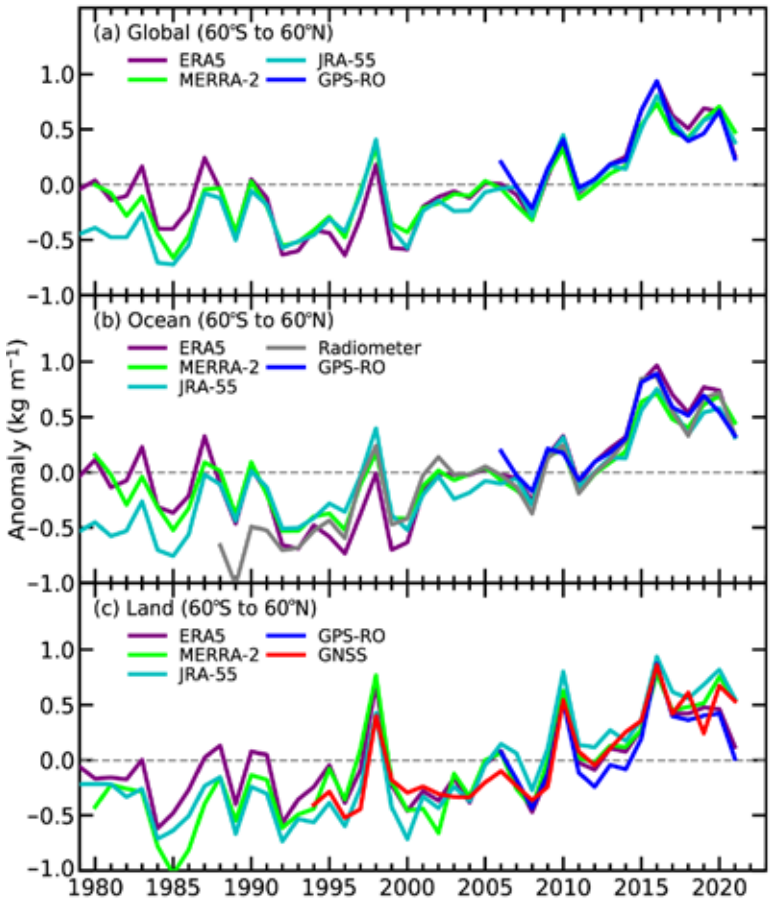

Fig. 2.22. Time series of yearly-mean TCWV anomalies (kg m^{-1}) from reanalysis, GPS-RO, GNSS, and satellite radiometers. All averages are over latitudes from 60°S to 60°N.

This assessment of global TCWV is based on data from three global reanalysis products: ERA5 (Hersbach et al. 2020), MERRA-2 (Gelaro et al. 2017), and JRA-55 (Kobayashi et al. 2015), as well as measurements made by satellite-borne microwave radiometers over the ocean (RSS Satellite; Mears et al. 2018), Global Positioning System–Radio Occultation (GPS-RO) observations from the COSMIC, Metop-A, -B, and -C and COSMIC2 satellite missions (satellite RO; Ho et al. 2020a,b, 2010a,b; Teng et al. 2013; Huang et al. 2013), and from ground-based GNSS stations (Bock 2020). The RSS satellite measurements are only available over the ocean, while GNSS stations are generally located on land. GPS-RO is available for both land and ocean. All three reanalyses assimilate satellite microwave radiometer and GPS-RO data and are therefore not fully independent from these two datasets. Ground-based GNSS measurements are not assimilated and are thus independent.

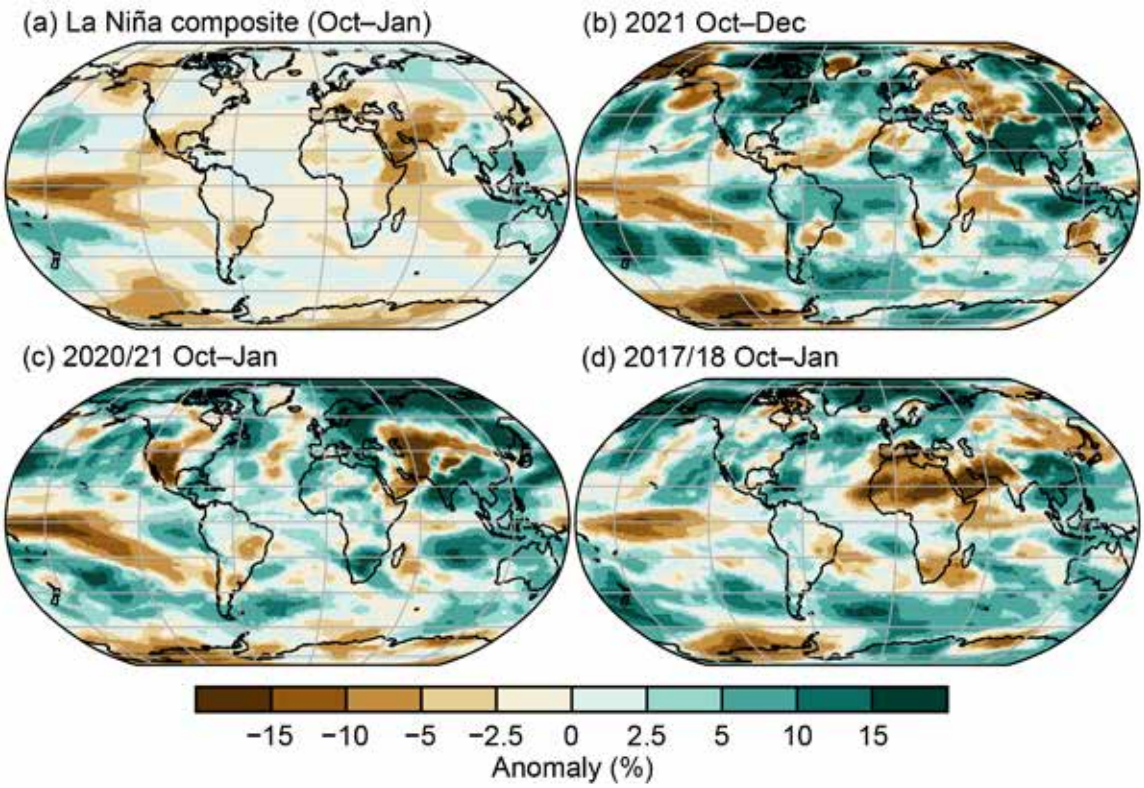

Fig. 2.23. Maps of TCWV anomalies (%) during La Niña events from the MERRA2 reanalysis. (a) Mean anomaly for the previous 12 La Niña seasons (Oct–Jan for 1983, 1984, 1988, 1995, 1998, 1999, 2005, 2007, 2010, 2011, 2017, and 2020). (b) Oct–Dec 2021 and (c) Oct–Jan 2020/21 anomalies. The La Niña periods highlighted in (b) and (c) show substantial drying south of the equator in the tropical Pacific, a feature less prominent in (d) Oct–Jan 2017/18 and in the composite in (a).

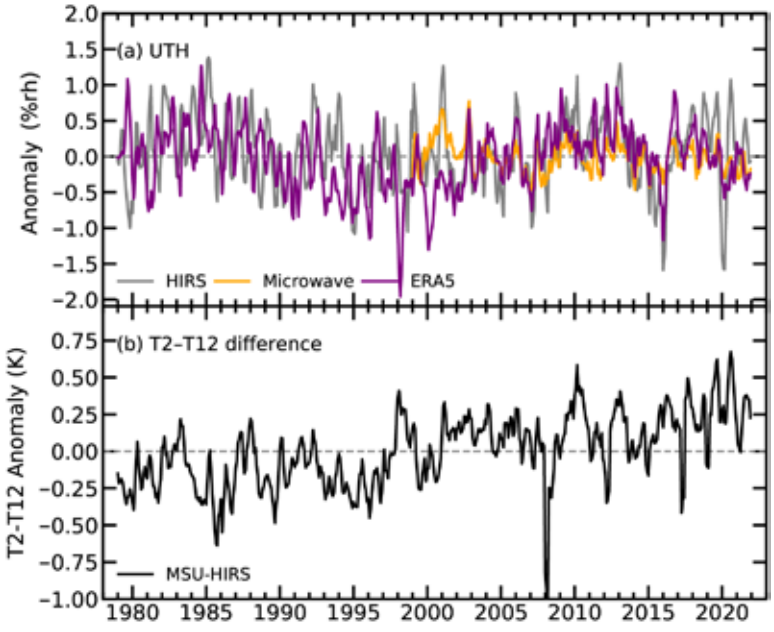

Fig. 2.24. (a) Time series of upper tropospheric humidity anomalies (%rh) from three datasets (see text for details). The anomalies are computed for area averaged data using the base period 1991–2020. (b) Difference (K) between the temperature and water vapor brightness temperature measurements in the upper troposphere.

3. UPPER TROPOSPHERIC HUMIDITY—V. O. John, L. Shi, E.-S. Chung, R. P. Allan, S. A. Buehler, and B. J. Soden

Upper tropospheric humidity (UTH) was slightly below the 1991–2020 average in 2021. Figures 2.24a,b show the monthly time series of the humidity datasets and a difference time series between the temperature and water vapor brightness temperature measurements in the UT, respectively. The large-scale relative humidity in the upper troposphere remains roughly constant, as expected from theoretical considerations (Ingram 2010); however, moistening in terms of the water vapor content of the UT is clearly evident from the lower panel. Here, there is a positive trend in the difference between T2 (brightness temperature of MSU Channel 2/AMSU-A Channel 5, which is sensitive to the UT temperature) and T12 (brightness temperature of HIRS Channel 12, which is sensitive to the UT water vapor). The trend in T2 and T12 indicates that the

emission level of the HIRS water vapor channel is shifting higher due to an increase in water vapor over time, while the emission level of the temperature sounding channel located in the 60-GHz oxygen absorption band remains unchanged, because the oxygen concentration does not change over time (Chung et al. 2016).

Water vapor is the strongest greenhouse gas in the atmosphere. Therefore, monitoring of water vapor in the upper troposphere (UT), owing to the cold temperature there, is crucial to determine one of the strongest positive feedback factors to the anthropogenic warming of the climate system (Coleman and Soden 2021). Three of the four datasets used in this work to monitor changes of water vapor in the UT are satellite based: 1) infrared based upper tropospheric humidity (UTH) derived from HIRS measurements starting in the late 1970s (Shi and Bates 2011), 2) microwave-based UTH derived from AMSU-B and MHS measurements starting in the late 1990s (Chung et al. 2013), and 3) mid-to-upper tropospheric temperature derived from MSU/AMSU-A measurements starting in the late 1970s (Zou and Wang 2011). The fourth dataset is relative humidity in the UT from the ERA5 reanalysis (Hersbach et al. 2020).

The agreement among the three UTH datasets is fairly good; the correlations of the HIRS and ERA5 data with the microwave data during their common period (1999–2021), are 0.6 and 0.5, respectively, despite their differences. For example, satellite data represent a layer average UTH with one satellite sampling the same location over Earth only two times a day while ERA5 data represent the 400-hPa level RH with hourly sampling. The microwave data have almost all-sky sampling while the HIRS data sample have only clear-sky conditions; this sampling difference is one reason for the higher interannual variability in the HIRS data as illustrated in John et al. (2011). In recent years, the HIRS data behave differently from the other two datasets: the mean value of UTH anomaly during 2021 for the HIRS data is 0.08 %rh, while for the microwave and the ERA5 data it is −0.15 and −0.18 %rh, respectively. This difference is due to the degradation in the quality of recent HIRS instruments (e.g., on board NOAA-19). The HIRS instrument era is slowly coming to an end and these instruments will soon be replaced by hyperspectral instruments, such as Infrared Atmospheric Sounding Interferometer (IASI). For the last three years (2019–21), simulated HIRS data from IASI spectra have been used in the creation of HIRS UTH data.

Plate 2.1j shows the 2021 anomaly map for the microwave UTH data. The patterns of the anomalies relate to large-scale weather conditions, with positive (negative) UTH anomalies associated with wetter (drier) conditions at the surface. This is due to the fact that one of the main drivers of UTH is convection; therefore, UTH is useful for monitoring changes in large-scale dynamics in the atmosphere. Clear La Niña patterns are visible, with positive anomalies over the Maritime Continent, India, and parts of Brazil and a strong dry signal in the western equatorial Pacific (centered near the data line). Prevailing drought conditions over the western United States are also reflected in the anomaly patterns. The patterns also reveal flooding conditions in northern Brazil and continued drought conditions over much of southern Brazil, Paraguay, Uruguay, and northern Argentina. Drought patterns in parts of the Horn of Africa, including Somalia, and in southern Madagascar are also clearly depicted.

4. PRECIPITATION—R. S. Vose, R. Adler, U. Schneider, and X. Yin

Precipitation over global land areas in 2021, as estimated from two different monitoring products, was slightly below the 1991–2020 long-term average (Fig. 2.25a). In particular, the global precipitation total anomaly according to the gauge-based product from the Global Precipitation Climatology Centre (GPCC; Becker et al. 2013) was −7.55 mm for 2021, and the blended gauge-satellite product from the Global Precipitation Climatology Project (GPCP; Adler et al. 2018) was −5.87 mm. The good agreement between the two products is in contrast to 2020, when GPCC depicted less precipitation than average whereas GPCP depicted slightly more than average. Given the modest discrepancy in 2020, it is not clear whether the global land surface was wetter in 2021 compared to 2020.

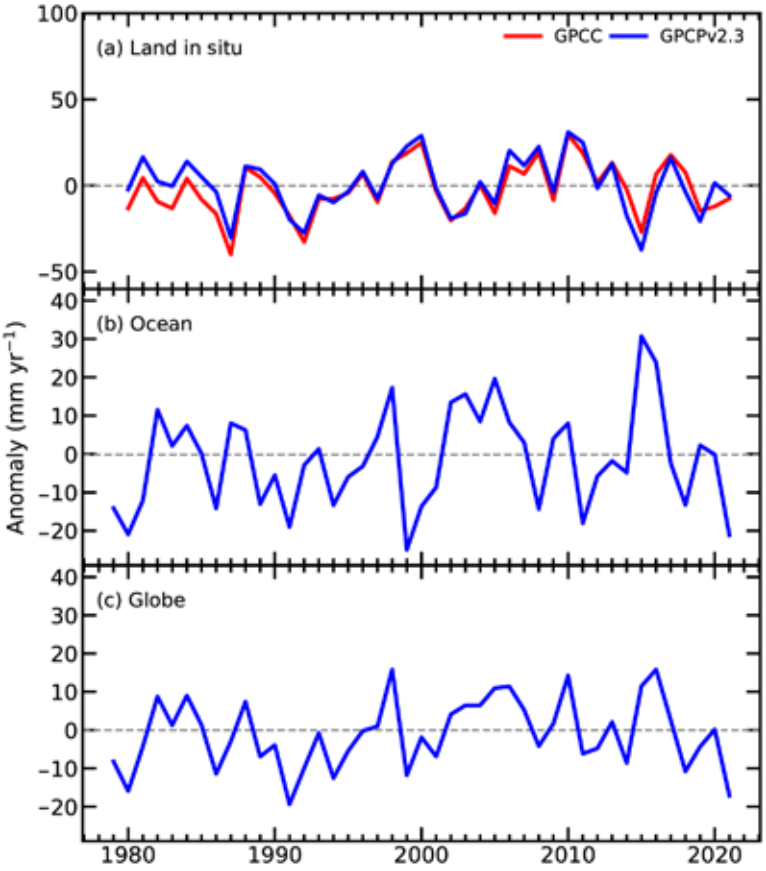

Fig. 2.25. Globally averaged precipitation anomalies (mm yr^{-1}) relative to the 1991–2020 base period over (a) land areas, (b) ocean areas, and (c) the globe. Land and ocean time series were created using a proportional land/sea mask at the 1° × 1° resolution scale.

Over the global oceans (Fig. 2.25b), the precipitation anomaly was –21.17 mm, and the global anomaly (Fig. 2.25c) was –17.07 mm, according to the GPCP product, both of which were substantial decreases from the previous year. Overall, the GPCP product ranks 2021 as the third-lowest year for precipitation in both the global and ocean records, which begin in 1979, after 1991 and 1999, respectively.

In many parts of the world, precipitation anomaly patterns in 2021 were consistent with the 'typical' La Niña pattern. For example, La Niña is often associated with more precipitation than average falling across southern Asia southeastward across the Maritime Continent and into the South Pacific Ocean. Northern South America and the equatorial Atlantic Ocean also tend to have above-average precipitation during La Niña. In contrast, much of the central Pacific Ocean near and south of the equator tends to receive much less precipitation than average, as do the eastern North Pacific and North Atlantic Oceans. However, in 2021 some areas exhibited patterns that ran counter to a 'canonical' La Niña event; for instance, La Niña usually means additional rainfall to Australia, but the anomaly map for 2021 shows a mixed pattern with expected abundant rainfall in the southeast and along the northern coast, but general dry conditions in the outback. In fact, the global land precipitation being below average is somewhat unusual compared to recent La Niña years when it was above average.

Over global land areas, the largest high precipitation anomalies in 2021 were across northern South America and eastern China, and the largest low precipitation anomalies were over central America, southeastern South America, the Middle East, southeastern Africa, and northern Australia (Plate 2.1k). Over the global oceans, a broad swath of large high precipitation anomalies extended from the eastern Indian Ocean to the Maritime Continent and then southeastward across the tropical western Pacific Ocean. The equatorial Atlantic Ocean and parts of the equatorial Pacific Ocean also received much more precipitation than average, as did part of the Southern Ocean near South America. In contrast, large low precipitation anomalies were apparent over much of the central Pacific Ocean south of the equator as well as over the western Indian Ocean, and to a somewhat lesser extent, over parts of the North Pacific and North Atlantic Oceans. Rainfall excesses helped to fuel frequent flood conditions, such as in Indonesia, Malaysia, and surrounding countries, as well as in northern South America and eastern Brazil. The dry anomalies were associated with continuing drought conditions over much of the southern half of South America and eastern Africa. See also section 2d5 and Chapter 7 for detailed information on region-specific extreme precipitation events.

5. LAND-BASED PRECIPITATION EXTREMES—S. Blenkinsop, M. R. Tye, M. G. Bosilovich, M. G. Donat, I. Durre, D. Lavers, A. J. Simmons, and M. Ziese

Overall, 2021 saw above-average frequencies of heavy and very heavy 24-hour precipitation (Figs. 2.26c,d) across several large regions but below-average intensities for the most extreme events in most areas (Plate 2.1l). Long-term changes in global precipitation extremes are difficult to quantify due to the local nature of events and sparse observations. These difficulties, such as different observing and reference periods and assessing means vs. totals, explain some of the discrepancies between extreme precipitation indices and below-average mean precipitation in 2021 (section 2d4). Using a combination of observational and reanalysis products, we summarize national-scale temporal variability of extreme precipitation indices (Table 2.7; NOAA 2022a).

Across the contiguous United States, the area experiencing a high proportion of precipitation from the highest 10th percentile 1-day events (NOAA Climate Extremes Index component 4; NOAA 2022b) was substantially above average, at 18.5%, the sixth largest area in the 112-year record

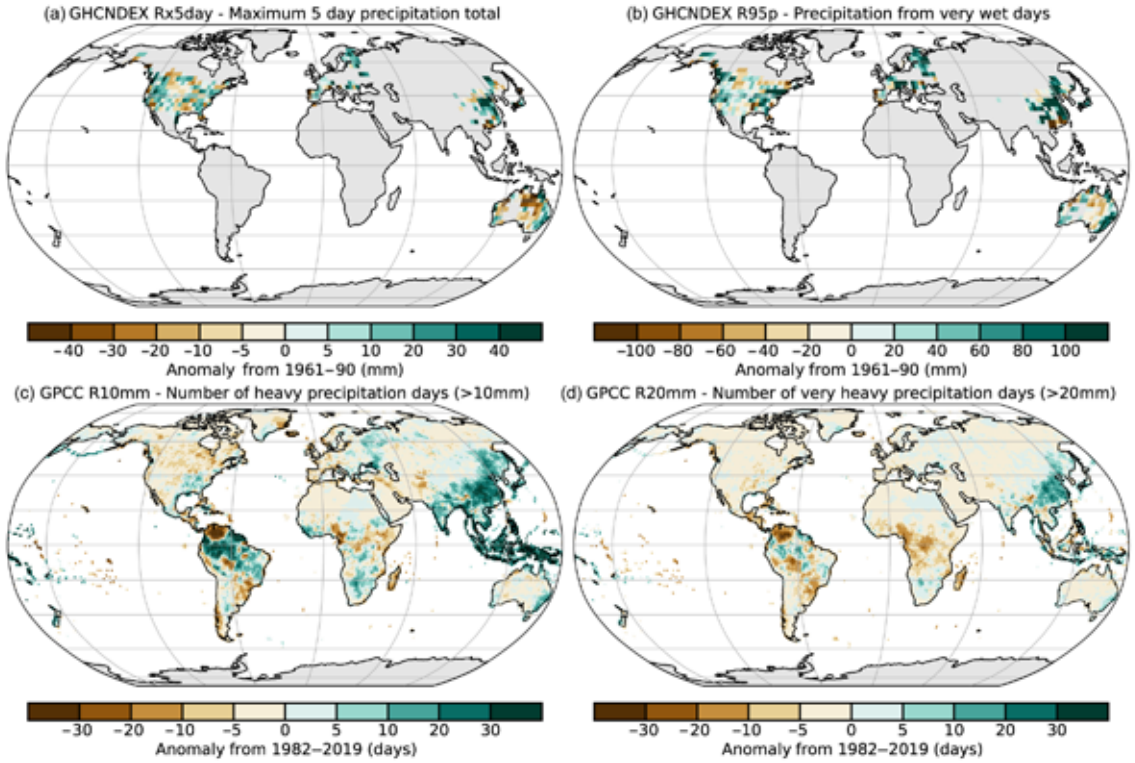

Fig. 2.26. Anomalies of 2021 indices: (a) Rx5day and (b) R95p (mm) derived from the in situ-based GHCNDEX relative to a 1961–90 baseline (Donat et al. 2013) and (c) R10mm and (d) R20mm (GPCC) relative to a 1982–2019 baseline.

Table 2.7. Indices used in this section and their definitions. Indices are expressed as anomalies relative to a baseline climatology which varies between data products.

Index	Name	Definition
Rx1day	Maximum 1-day precipitation	Annual maximum 1-day precipitation amount (mm)
Rx5day	Maximum 5-day precipitation	Annual maximum consecutive 5-day precipitation amount (mm)
R10mm	Heavy precipitation days	Count of days where daily precipitation total > 10mm (days)
R20mm	Very heavy precipitation days	Count of days where daily precipitation total > 20mm (days)
R95p	Total precipitation from very wet days	Total precipitation from days where the daily precipitation total exceeds the climatological baseline wet day 95th percentile
10th Percentile 1-day	NOAA Climate Extremes Index Component 4 (NOAA 2022a)	The percentage area of the United States experiencing extreme precipitation on days where the total daily precipitation exceeds the historical record (1910–present) baseline wet day 90th percentile, per year, winter (DJF), spring (MAM), summer (JJA), or autumn (SON) season

(Fig. 2.27a), while the same index for the autumn season indicated the largest area on record (17.4%). GHCNDEX (Donat et al. 2013; section 2b4) highlights several clusters of positive Rx1day and Rx5day (Fig. 2.26a; Table 2.7) anomalies in North America. Several storms occurred in California (Appendix Table A2.2), partly related to the clustering of strong Pacific storms in October, including a "bomb cyclone" and an exceptional atmospheric river that affected California and Oregon coasts (NOAA 2021a). Parts of Washington State experienced another atmospheric river event in mid-November, which caused record rainfall in around 20 locations in British Columbia (Canada), resulting in flooding and landslides (see section 7b1, Sidebar 7.1). In August, Hurricane Ida (Category 4) was the most significant storm to affect the eastern United States during the North Atlantic season, moving northeast after landfall in Louisiana, breaking the hourly observed rainfall record in New York City (WMO 2021b; NOAA 2021b).

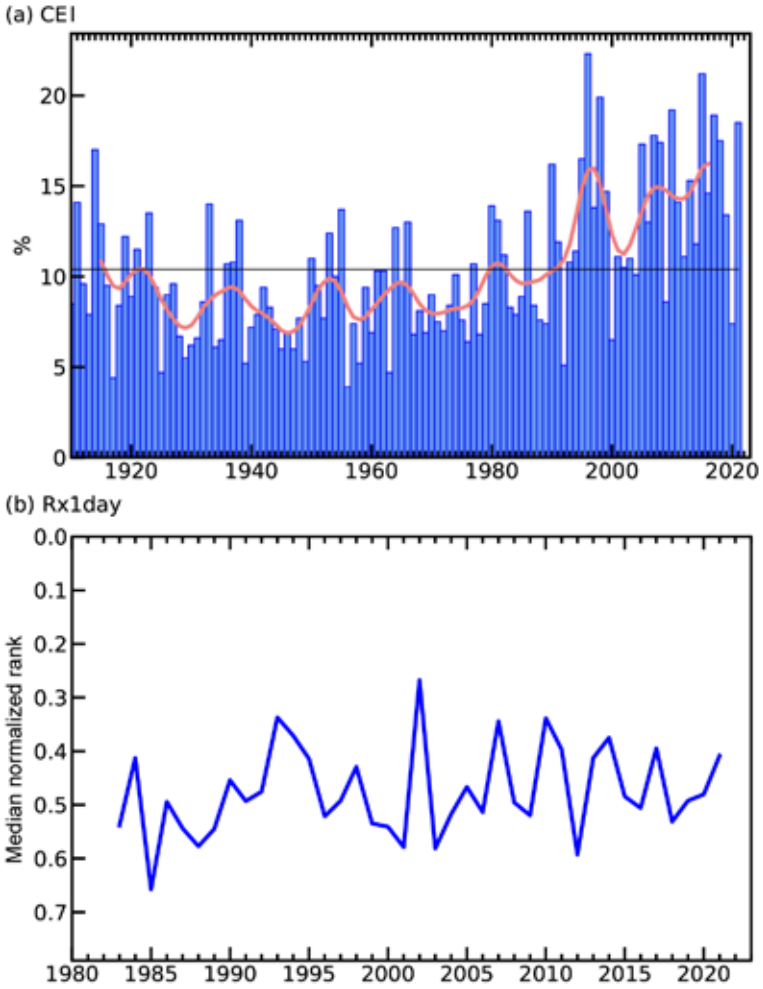

Fig. 2.27. (a) Annual percentage (%) of the contiguous United States with a much-greater-than-normal proportion of precipitation derived from extreme (highest 10th percentile) 1-day precipitation events for the period 1910–2021 (NOAA 2022a). The solid red line denotes a smoothed Gaussian filter, and the horizontal black line denotes the series mean. Note that methodological changes introduced after 2005 means that this series may produce higher values after this date. (b) Median normalized rank of annual Rx1day values for Europe. The annual rank of the Rx1day value at each gauge relative to its own record is derived from the European Climate and Assessment Dataset (Klein Tank et al. 2002) and is normalized by gauge length. The median of all the gauge normalized ranks is then calculated for each year, with low values denoting a higher median rank. Only gauges with at least 50 years of data were used to calculate the annual ranking statistics, and only years for which at least 5000 gauges returned an index value are shown.

Rain gauges from the European Climate and Assessment Dataset (Klein Tank et al. 2002) indicate 2021 was an average year for R10mm, R20mm, and Rx5day for Europe, but above average for Rx1day (Fig. 2.27b) and R95p, the latter ranking 9th and 11th, respectively, in the 39-year record. A cutoff low-pressure system contributed to severe flooding in western Germany and neighboring countries in mid-July (section 7f3; ECMWF 2021), with 18 (12) new Rx1day (Rx5day) records set in GHCNDEX. The 24-hour and 48-hour accumulations over western Germany were the highest in the 140-year record (Junghänel et al. 2021) and caused severe flooding. A rapid attribution study calculated an increased likelihood of such 1-day accumulations (factor of 1.2–9) in the region today compared to a 1.2°C cooler climate (Else 2021). Positive Rx1day anomalies (GPCC, Plate 2.1l) over Sweden and adjacent areas also saw six gauges in GHCNDEX with new records, including the city of Gävle (SMHI 2021).

The GPCC (Schamm et al. 2013) and GHCNDEX data show positive anomalies corresponding to a prolonged period of heavy rain in eastern parts of New South Wales, Australia, in late March, with some areas recording more than 500 mm of rain in 48 hours (Floodlist 2021b) and more than 50 new daily records for March (Bureau of Meteorology 2021a). More than 60 daily records were broken for November across New South Wales and Queensland, with widespread flooding

(Bureau of Meteorology 2021b,c). Combined, these contributed to considerable positive anomalies of R10mm and R20mm (Figs. 2.26c,d).

The datasets examined here are broadly consistent over southeast Asia in showing above-average frequencies of rainfall extremes, although the GPCC data show below-average intensities in Rx1day (Plate 2.1l). Cyclone Seroja produced 15 new monthly records for April over Western Australia (Bureau of Meteorology 2021d), after generating significant accumulations over Timor, Indonesia, and Singapore (WMO 2021b; Floodlist 2021c). Farther north, Cyclone Surigae brought record rainfall to the Philippines (NOAA 2021c) and parts of Cambodia and Vietnam (Floodlist 2021d,e) in April. An area of positive anomalies over northern and eastern China appears consistent across indices and datasets (Plate 2.1l, Figs. 2.26a–d), reflecting a series of extreme rainfall events; Typhoon In-fa generated several days of heavy rain in Henan Province in mid-July. Nearby Shanxi and Shaanxi Provinces also saw over 60 gauges reporting record accumulations in October (Floodlist 2021f) as moisture was transported from the South China Sea and Bay of Bengal.

Many areas with significant events in 2021 also have positive anomalies in GHCNDEX R95p (Fig. 2.26b), showing the important contribution of extremes to total precipitation. In GPCC, R95p also shows a strong contribution from extreme events over parts of Brazil and southern Africa. The R10mm and R20mm indices for GPCC (Figs. 2.26c,d) and ERA5 (Hersbach et al. 2020) show positive anomalies over northern Brazil and neighboring nations, associated with prolonged rainfall during May and June and again at the end of the year. Above-average Rx1day is also apparent over southeastern Brazil, which experienced widespread flooding early in the year (Plate 2.1l). Above-average R10mm and R20mm frequencies are also evident over several southern African nations (Figs. 2.26c,d). Tropical Cyclone Eloise was followed by several weeks of heavy rainfall at the start of 2021, with Beira, Mozambique, receiving close to its average total January precipitation in 24 hours (NOAA 2022c). Prolonged heavy rain in the summer also resulted in above-average values over southern Sudan and northern Uganda, contrasting with much of central Africa (Plate 2.1l).

Please refer to Chapter 7 (Regional Climates) for more details about precipitation events around the world.

6. CLOUDINESS—C. Phillips and M. J. Foster

The average global cloud fraction, as measured by MODIS *Aqua* C6.1 (Platnick et al. 2015), was 67.67% in 2021. This makes 2021 the third-cloudiest year in the 19-year *Aqua* satellite record, after 2010 and 2020. La Niña occurred over most of the past three years, though not all years with similar Niño-3.4 index values were associated with such positive cloud anomalies. Being a single satellite in a sun-synchronous orbit, MODIS *Aqua* data is limited to two global observations per day. *Terra* MODIS might have been included to add better representation, but electronics issues beginning in October 2020 forced degradation of the cloud products, so it must be omitted (Platnick 2022). Prior to those issues, the *Terra* global cloud anomaly had excellent correlation with *Aqua*, so single day and night observations seem to be sufficient. The annual anomalies for CERES-*Aqua*-MODIS (Trepte et al. 2010; Minnis et al. 2008), PATMOS-x v6.0 (Heidinger et al. 2013), MISR (Di Girolamo et al. 2010), CLARA-A2.1 (Karlsson et al. 2017, 2020, 2021), and PATMOD (MODIS *Aqua* processed with PATMOS-x cloud algorithms, unpublished) have been included for comparison; however, they have differed from MODIS *Aqua* C6.1 significantly in recent years (Fig. 2.28). For the sake of simplicity, the following analysis will focus on MODIS *Aqua* C6.1.

This MODIS record exhibits a small increasing trend in global cloudiness since the record began in 2003. The main positive contributing regions are the poles and the tropics, which are partially offset by negative trends in the subtropics and midlatitudes (Fig. 2.29). This trend makes especially cloudy years like 2021 more likely, though the rank for 2021 is unchanged in the detrended data.

Plate 2.1m shows a map of the average cloudiness anomaly in 2021. Naturally, regional anomalies are much larger than global anomalies, frequently on the order of 5%. The pattern of increased cloudiness in the western Pacific and reduced cloudiness in the central Pacific is common during

La Niña conditions, resulting from the invigoration of convection over high sea surface temperatures (SST) and suppression of convection over cool SSTs. Conversely, other cloud regimes like the marine stratocumulus of the eastern Pacific can exhibit an inverse relationship, with lower SSTs correlated with more cloudiness (Loeb et al. 2018b). Note the opposite signs of cloud and SST anomalies in the eastern Pacific contrasted with aligned signs in the western Pacific (Plate 2.1a).

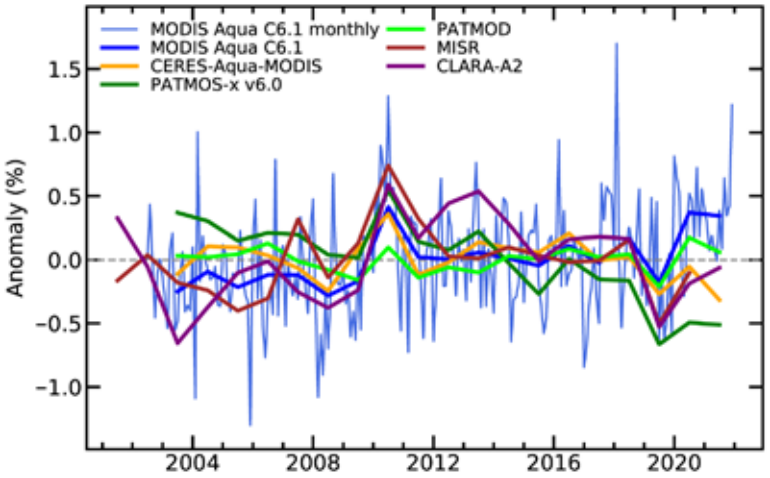

Fig. 2.28. Global average cloud fraction anomaly (%) relative to the 2003–21 reference period. PATMOS-x v6.0 anomalies were computed by backfitting a grid of joint seasonal-diurnal cloudiness models for all satellites simultaneously and taking the smoothed residual.

In addition to the typical La Niña pattern in the Pacific in 2021, several regions experienced their highest percentage of cloudiness in the record, notably the Indian subcontinent, the Canadian Arctic, and part of East Antarctica. All of these locations were also anomalously cloudy in 2020. On the other hand, the southeast Atlantic near the coast of Africa has had a negative anomaly since 2018 and had a record minimum in 2021. While these regional anomalies are not the largest values seen in Plate 2.1m, they are highlighted here after inspecting their time series and considering their z-score (standard deviations from the mean) to ensure that they were truly cloud fraction outliers in 2021.

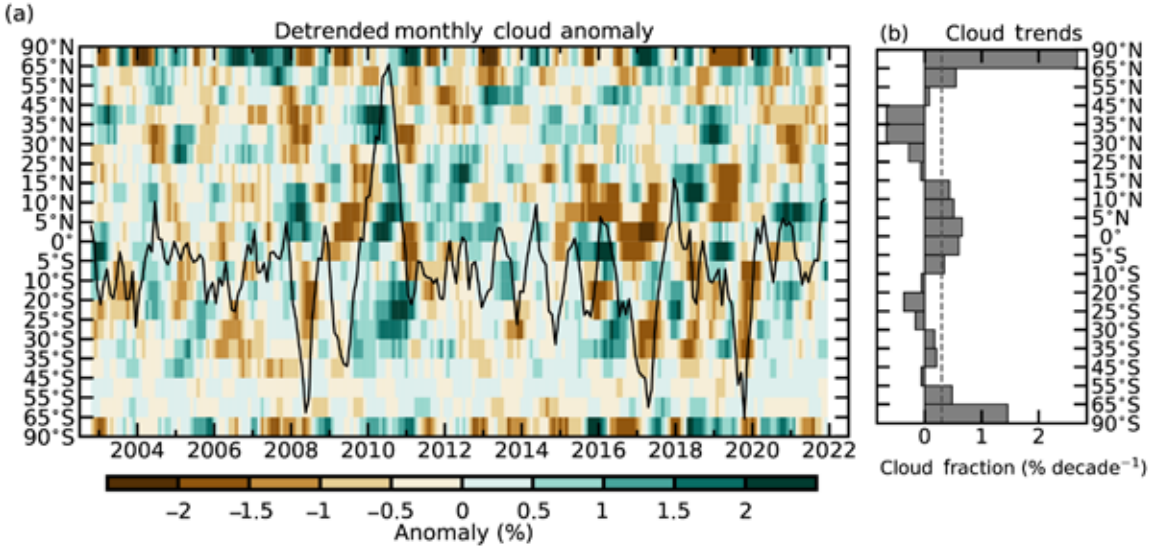

Fig. 2.29. (a) Zonal mean cloud fraction anomaly (%) from MODIS *Aqua* C6.1 with 20 latitude bands partitioned to have approximately equal area. Monthly anomalies are relative to the mean of all identical months between 1 Jul 2002 and 31 Jan 2022. Individual bands were detrended with trends computed using the complete years from 2003 through 2021. The detrended anomaly was then smoothed by a 6-month centered rolling mean filter. The smoothed detrended global anomaly is superimposed for reference as a black line, detached from any y-axis. (b) The extracted trends in cloud fraction (% decade^{-1}, aligned gray bars) for the period 2003–21 and the global mean trend (vertical dotted black line).

Clouds reduce both net infrared (IR) emission and solar absorption, and many factors influence the relative balance that determines the sign of the overall cloud radiative effect (section 2f1). The presented regional anomaly in total cloud fraction best describes the solar absorption component, e.g., positive cloud fraction anomalies suggest negative solar absorption anomalies. Calculating the change in full radiative balance would require information, such as independently estimating the changes in height-partitioned cloud fraction, which is difficult with passive satellite observations, due to obscuration from higher clouds. Direct observations of the radiation budget at the top-of-atmosphere are examined in section 2f1.

7. RIVER DISCHARGE AND RUNOFF—H. Kim and D. Tokuda

For five years consecutive years (since 2017), global average runoff has been greater than the 1981–2010 average. Runoff in 2021 was the 11th greatest (~84th percentile) in the 64-year record dating to 1958. It was slightly less than the 2020 average, which had the third greatest runoff (~97th percentile; Fig. 2.30); however, there were significant differences in global distributions of runoff (Plate 2.1n) and discharge (Plate 2.1o) anomalies compared to those of 2020.

Rivers in northern South America, such as the Amazon and Orinoco, experienced a strong wet phase of above-average discharge, after a relatively dry phase (below-average discharge) the previous year. In the Amazon, such a shift was particularly notable in the Rio Negro and Rio Solimoes, while Rio Madeira and Rio Tapajos have stayed drier than the 1981–2010 reference period. In Africa, the Nile has shifted into a dry phase, while the Congo, Niger, and Zambezi have stayed in the same phase as 2020. Northern North America had less water than in 2020, and the midwest and northeastern United States became drier than average, leading to less discharge. Northern Europe and western Siberian regions were drier than in 2020. Discharge in many European rivers, including the Dnieper, Don, Loire, Northern Dvina, Rhone, Rhine, Seine, and Volga, was below average. However, it is worth nothing that, in spite of the below-normal annual discharge, there was a devastating flood disaster in Europe, including the Ahr Valley, a tributary of Rhine River, in July 2021. The Danube discharged more freshwater into the Black Sea than usual. Compared to the prior year, most regions in Asia did not show noticeable changes except for southern China (e.g., the vicinity of the Pearl River), Indochina (e.g., the Mekong and Chao Phraya) and the Indus River region, where those regions experienced severe drought and thus had less discharge.

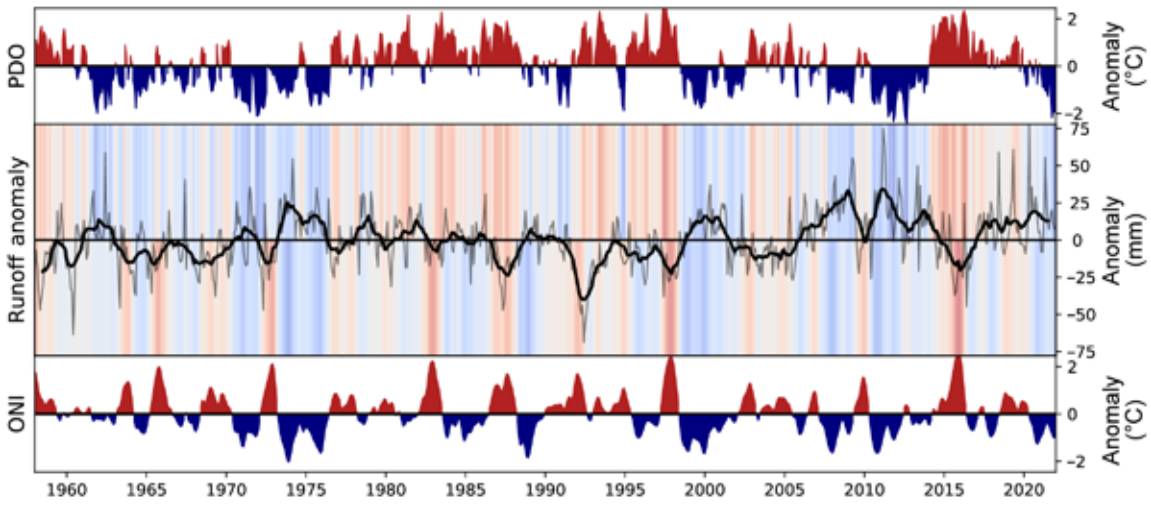

Fig. 2.30. Interannual variability of the Oceanic Niño Index (ONI; lower, °C), the Pacific Decadal Oscillation (PDO; upper, °C), and global runoff (middle; mm; thick line is 12-month moving average). The ONI and PDO are shaded red (positive phase) or blue (negative phase). Shading above and below the zero-line of global runoff is proportional to the PDO and ONI, respectively.

Runoff is a local residue of the water budget to be integrated along pathways turning into discharge, which is the most important freshwater resource to humanity. The El-Niño Southern Oscillation (ENSO) and Pacific Decadal Oscillation (PDO; Zhang et al. 1997) are well-known factors that influence global freshwater discharge (e.g., Kim and Tokuda 2020, 2021). Figure 2.30 depicts the long-term fluctuation of the total runoff and those climate modes. Positive and negative phases of ENSO and PDO correspond to drier and wetter conditions of global freshwater discharge, with ENSO and PDO accounting for around 47% of the total variance. The interannual variability and climatology of freshwater discharge into the major oceans are shown in Fig. 2.31 for the Pacific, Atlantic, Arctic, and Indian basins, where they receive 85% of global freshwater discharge, of which the drainage area reaches 75% of the total land surface area. The Pacific Ocean has received an increasing amount of freshwater discharge during the last two decades, reaching a record maximum in 2021, with above-average discharge throughout the entire year. Freshwater discharge into the Atlantic Ocean remained in a positive phase due to an anomalously large discharge during boreal summer (June–September). The Arctic Ocean received less discharge in 2021, and its month-to-month variability was near-average; however, there is an increasing trend present over the entire analysis period beginning in 1958. An increasing trend is also found in the

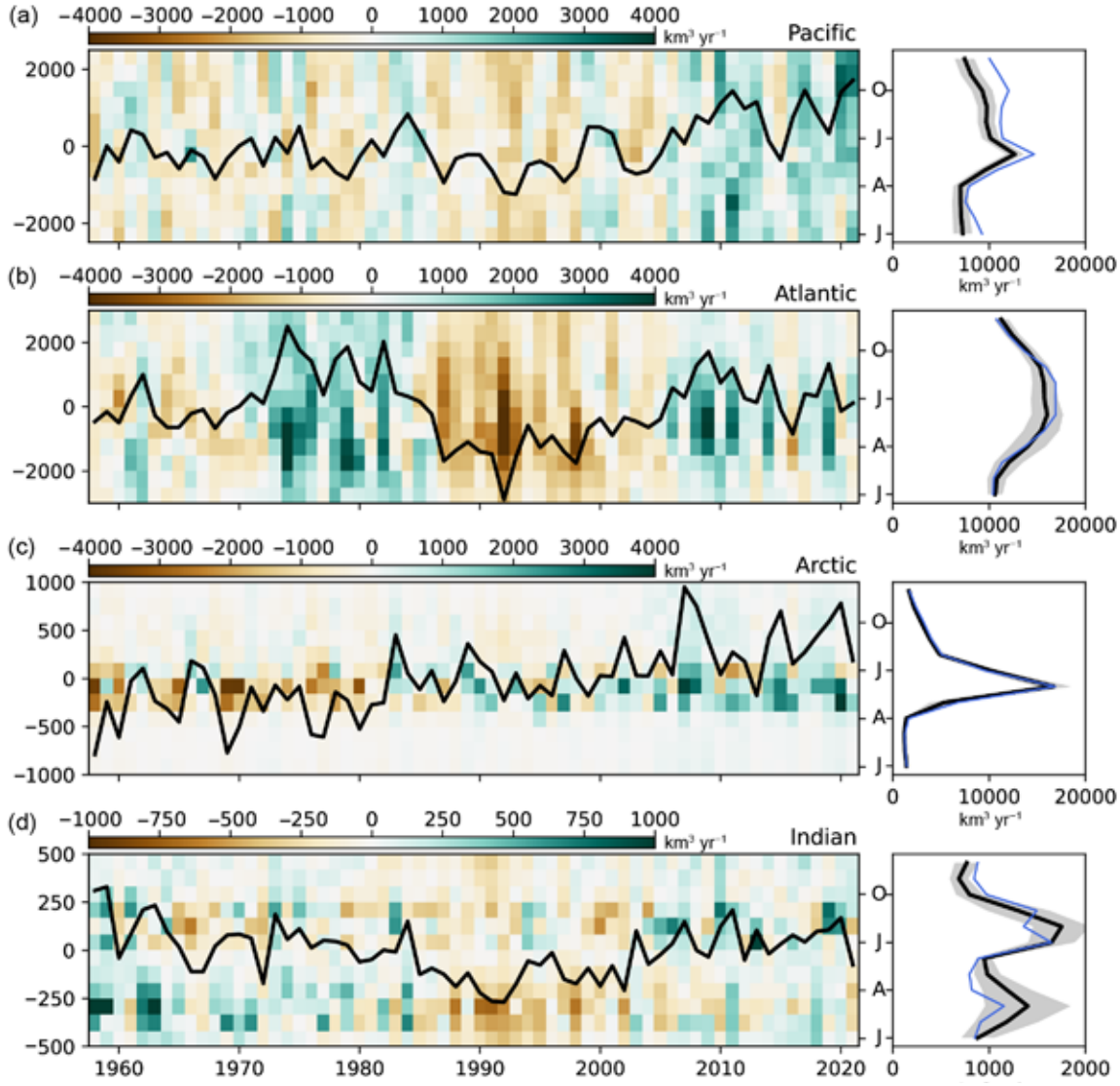

Fig. 2.31. (a–d, left panels) Interannual variability of freshwater discharge (km^3 yr^{-1}) to global ocean basins. The black line and vertical shaded boxes indicate the annual mean and monthly anomaly, respectively. (a–d, right panels) Seasonality of freshwater discharge (km^3 yr^{-1}) to global ocean basins. The thick black line, thin blue line, and gray shade indicate long-term climatology, seasonal variation during 2021, and 1 std. dev. of long-term variability, respectively.

Indian Ocean, but it is weaker and shorter, beginning around 1990. The Indian Ocean received slightly less discharge on average in 2021, with a less-than-normal amount occurring during the first wet season of the year.

The time series of natural variability-only estimates of global runoff and discharge were generated using global off-line hydrologic simulations by the Ensemble Land State Estimator (ELSE; Kim et al. 2009) on a 1° grid and a large-scale river routing and flood inundation model Catchment-based Macro-scale Floodplain (CaMa-Flood; Yamazaki et al. 2011) on a 30-minute drainage direction map (DDM30; Döll and Lehner 2002). The World Ocean Atlas 2018 (Garcia et al. 2019) was used to separate the freshwater discharge into each oceanic basin. The atmospheric boundary conditions were created based on the Japanese global atmospheric reanalysis (JRA-55; Kobayashi et al. 2015), and the Global Precipitation Climatology Centre (GPCC) Monitoring Product version 2020 (Schneider et al. 2020) was used to adjust bias in the reanalysis precipitation field.

8. GROUNDWATER AND TERRESTRIAL WATER STORAGE—M. Rodell and D. Wiese

Changes in terrestrial water storage (TWS), which is the sum of groundwater, soil moisture, surface water, snow, and ice, have been measured on regional to global scales by the Gravity Recovery and Climate Experiment (GRACE) and GRACE Follow On (GRACE-FO) satellite missions on a monthly basis since 2002 (Tapley et al. 2004; Landerer et al. 2020). Interannual changes tend to be dominated by snow and ice at high latitudes and in alpine regions, by surface water in the wet tropics, and by groundwater elsewhere (Getirana et al. 2017).

Plate 2.1p displays observed changes in mean annual TWS between 2021 and 2020 as equivalent heights of water in cm. Changes in TWS were mixed across Eurasia. Most of western Europe continued to recover from the 2019 drought, while Scandinavia in the north dried (lost TWS) after a wet 2020. Copious rain increased TWS in southern India, where it was already elevated at the start of the year. To the east, the Indochina peninsula recovered from drought, receiving abundant rainfall from Typhoon Surigae (see section 4g5). Northeastern China also gained water, while drought afflicted areas south and west of the Caspian Sea. In Australia, TWS increased along the northern and southeastern coasts. Droughts in Africa caused TWS decreases in Angola and Madagascar, while TWS increased rapidly in Zimbabwe and adjacent areas at the start of 2021, including a 2-m increase in the level of Lake Kariba. In North America, TWS declines extended from southern California into southern Canada, regions where drought conditions prevailed, and across to the Great Lakes region, where declines exceeded 12 cm equivalent height of water in some parts. However, TWS in the center of the continent (including the Great Lakes region) had been elevated since 2019, when record flooding occurred, and the decrease in 2021 was largely a return to more typical conditions. Northern South America gained a massive amount of water, with increases exceeding 12 cm over a large area, but TWS declined in southern Brazil. Time series of zonal mean and global mean monthly TWS anomalies, after removing the seasonal cycle, are plotted in Figs. 2.32 and 2.33, respectively. TWS declines

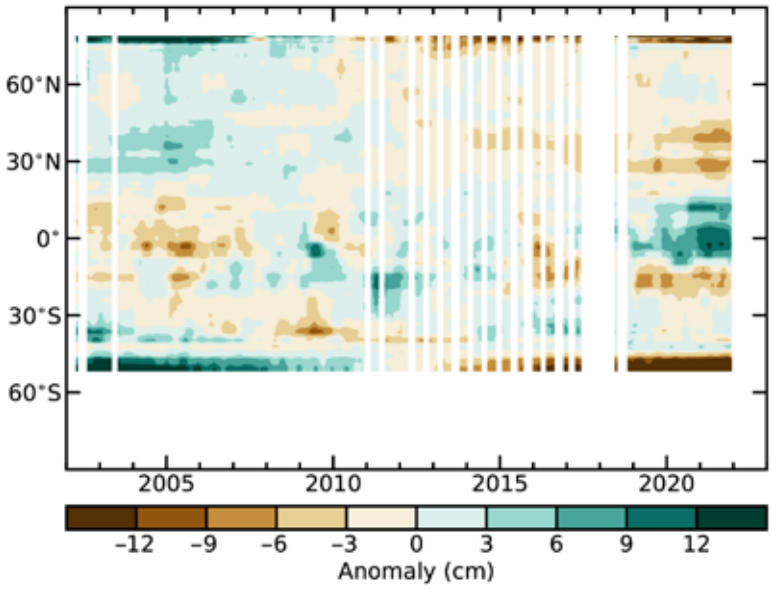

Fig. 2.32. Zonal means of terrestrial water storage anomalies, excluding those in Antarctica, Greenland, the gulf coast of Alaska, and polar islands, in cm equivalent height of water, based on gravity observations from GRACE and GRACE-FO. The anomalies are relative to a 2003–20 base period.

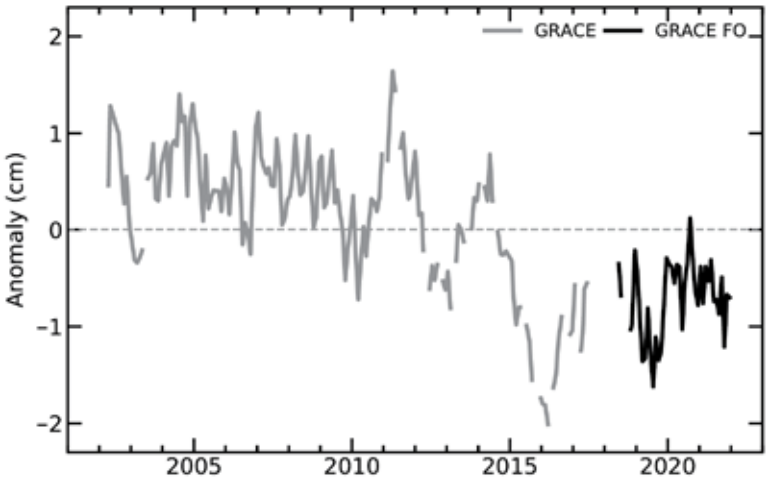

Fig. 2.33. Global average terrestrial water storage anomalies from GRACE (gray) and GRACE-FO (black), in cm equivalent height of water, relative to a 2003–20 base period.

in Antarctica, Greenland, the Gulf Coast of Alaska, and polar islands are attributed to ice sheet and glacier ablation as opposed to meteorological variations, so those regions were excluded from the calculations for Figs. 2.32 and 2.33. However, the effects of additional high latitude ice mass losses remain. The large TWS increase, seen straddling the equator in Fig. 2.32, corresponds to the massive wet anomaly in northern South America. The TWS decline just south of 30°N is due almost entirely to long-term groundwater depletion in northern India (Rodell et al. 2018), exacerbated by a drought just east of that area in 2021 (section 2d10). The TWS decline near 40°N mainly reflects drought across the western and central United States, drought stretching from Turkey to the Caspian Sea (including water level declines in that sea), and long-term groundwater depletion associated with agricultural irrigation in the North China Plain (Rodell et al. 2018). Droughts in southern Brazil and Angola caused the TWS decline near 15°S. Overall, global-scale TWS variability in 2021 was muted compared with past years (Plate 2.1p). Owing to the scarcity of in situ TWS measurement records, we relied on TWS data derived from GRACE and GRACE-FO satellite observations of Earth's time-varying gravity field. Uncertainty in the derived TWS anomalies is heterogeneous, but as a point of reference, uncertainty in monthly TWS anomalies is typically around 1–2 cm equivalent height of water at 500,000 km^2 and larger scales (Wiese et al. 2016).

9. SOIL MOISTURE

—R. van der Schalie, W. Preimesberger, P. Stradiotti, M. van der Vliet, L. Mösinger, N. J. Rodríguez-Fernández, R. Madelon, S. Hahn, M. Hirschi, R. Kidd, R. A. M. de Jeu, and W. A. Dorigo

Soil moisture plays a key role in land–atmosphere interaction due to its defining effect on boundary conditions for energy and water fluxes (Seneviratne et al. 2010). In 2021, global satellite-observed soil moisture recorded wetter-than-usual conditions (Fig. 2.34). Note that wetter/drier within this section refers to higher/lower soil moisture volumes in the first centimeters of the soil as compared to the 1991–2020 reference period. The discrepancy between NH and SH, as recorded in 2020 (van der Schalie et al. 2021), was strongly reduced, with NH continuing to be wetter-than-usual and SH observing near-neutral conditions. Given that North America and central Asia experienced dry conditions, the wet conditions in Europe, eastern Asia, and the Indian subcontinent more than compensated for that in the NH average. For the SH, widespread dry

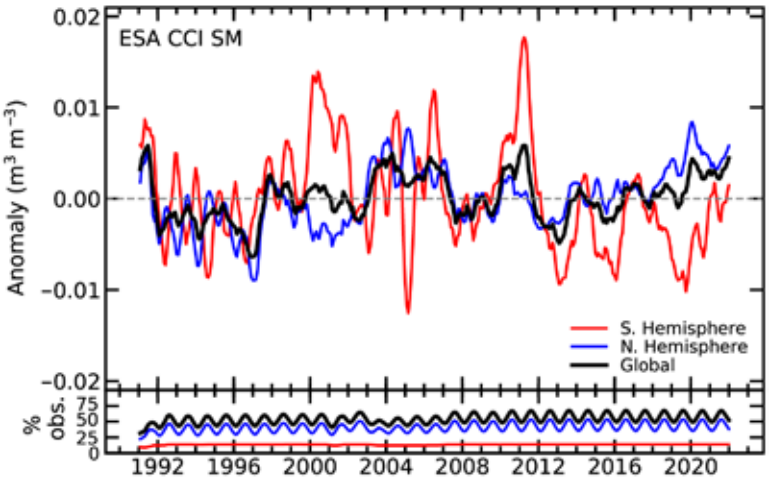

Fig. 2.34. Time series of global (black), NH (blue), and SH (red) monthly surface soil moisture anomalies for the period 1991–2021 (upper, m^3 m^{-3}; 1991–2020 base period) and the valid retrievals as a percentage of total global land surface (lower, %). Data are masked where no retrieval is possible or where the quality is not assured and flagged due to dense vegetation, frozen soil, radio frequency interference, and so forth. (Source: ESA CCI Soil Moisture.)

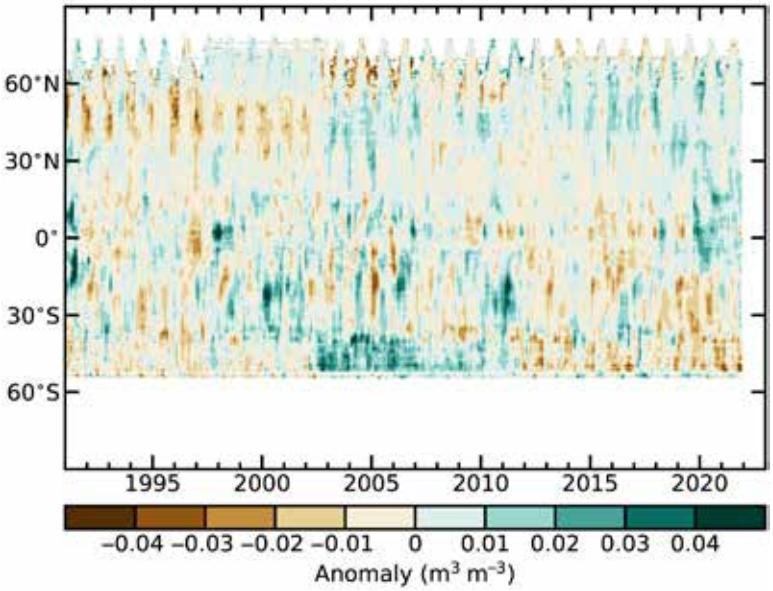

Fig. 2.35. Time–latitude diagram of monthly surface soil moisture anomalies ($m^3 m^{-3}$; 1991–2020 base period). Data are masked where no retrieval is possible or where the quality is not assured and flagged due to dense vegetation, frozen soil, radio frequency interference, and so forth. (Source: ESA CCI Soil Moisture.)

conditions in central to southern South America are balanced out by wet anomalies seen in other regions.

These findings are clearly shown in Fig. 2.35, where NH and equatorial latitudes show positive anomalies since early 2020. South of 15°S in the SH, consistent negative anomalies have been present since at least 2018, moving closer to neutral conditions in 2021. More detailed maps of the spatial distribution are shown in Plate 2.1o (average for 2021) and Appendix Fig. A2.12 (monthly).

Linked to the La Niña conditions in winter, part of North America (Mexico) started the year with mostly negative anomalies (Appendix Fig. A2.12). These negative anomalies expanded northward to the western and central United States and Canada during the first four months of the year. The dry conditions in the Canadian Prairies and Montana intensified during an extreme heatwave that occurred in June and July (Philip et al. 2021; section 2b4). The wetter-than-normal autumn that followed eased the anomalies, resulting in close-to-normal conditions at the end of the year. The southeastern United States recorded a widespread positive anomaly over 2021, caused by above-normal precipitation (NOAA 2022e; section 2d4).

In 2021, the southern half of South America mostly saw a continuation (van der Schalie et al. 2021) of drier-than-normal soil moisture conditions. These conditions were linked to the drought in the La Plata basin covering Uruguay, Bolivia, Paraguay, northeastern Argentina, and southern Brazil (Naumann et al. 2021). Southern regions in Argentina, e.g., Patagonia and surrounding areas, also experienced drier-than-normal soil moisture conditions. In northern South America, Venezuela, and Colombia experienced wetter-than-normal conditions throughout 2021, while in northeastern Brazil and northern Chile the positive anomalies were linked to heavy rain in the last three months of the year (sections 2d4, 7d).

Overall, Europe had wet soil moisture conditions, which were most intense in the western coastal and central-north areas and around the Black Sea region (contrasting with negative anomalies along the southern coast of the Black Sea and in the Middle East in April/May). The positive anomalies align with heavy rainfall and flooding throughout Europe during the summer (sections 2d5, 7f). Scandinavia and southern Spain were the only regions that recorded an overall drier-than-normal status for 2021.

The drought in the northern coastal regions of Africa, e.g., Morocco and Tunisia, were reflected in the widespread drier-than-normal soil moisture conditions. Western Africa and the Sahel started 2021 with above-average conditions, which later became drier-than-normal due to drought. Southern Chad and Sudan experienced wet conditions, caused by heavy rains during the summer. Eastern Africa had both positive anomalies (linked to widespread flooding in inland regions like South Sudan) and negative anomalies (regions experiencing droughts like Somalia and Kenya). Southern Africa had a clear split between below-average soil moisture conditions in Angola, Namibia, south Madagascar and southwest South Africa and above-average conditions in Botswana and northeast South Africa. This seems to align better with the precipitation extremes (section 2d5) and terrestrial water storage (section 2d8) than general precipitation anomalies

(section 2d4). In late 2021, drier-than-usual conditions were present in Madagascar and Tanzania, following wetter-than-usual conditions at the beginning of the year.

In Russia, Siberia and surrounding regions experienced low rainfall and high temperatures that continued below-average soil moisture conditions overall. These negative anomalies were widespread throughout much of central Asia, with countries like Kazakhstan, Kyrgyzstan, Turkmenistan, and Uzbekistan experiencing drought events. For Siberia, this was a continuation of 2020 conditions. India, Thailand, Mongolia, and large parts of China observed positive anomalies, caused by above-average precipitation (section 2d4). Northeastern China and southern India are particularly noteworthy, as they recorded the highest wet anomalies globally of 2021, linked to the second highest rainfall totals since 1961 in parts of China (Li et al. 2022) and highest recorded November rainfall since 1901 in southern India (IMD 2022).

The wetting trend in Australia continued in 2021, partly related to La Niña, with most regions recording average or above-average soil moisture levels. The most intense positive anomaly was detected over New South Wales, which coincides with the above-average rainfall in that region (section 2d4). New Zealand generally saw average soil moisture conditions.

The soil moisture anomalies (representing the top ~5 cm of the soil) used in this analysis were derived from the COMBINED product of ESA's Climate Change Initiative for Soil Moisture v06.2 (https://climate.esa.int/en/projects/soil-moisture/; Dorigo et al. 2017), a merged product based on multiple active (Wagner et al. 2013) and passive microwave (van der Schalie et al. 2017) sensors. Merging is done based on both the quality and the temporal and spatial availability of observations (Gruber et al. 2017, 2019).

10. MONITORING GLOBAL DROUGHT USING THE SELF-CALIBRATING PALMER DROUGHT SEVERITY INDEX—J. Barichivich, T. J. Osborn, I. Harris, G. van der Schrier, and P. D. Jones

The ongoing increase in global drought area, based on different severities of the self-calibrating Palmer Drought Severity Index (scPDSI), that began in mid-2019 (Barichivich et al. 2020) reached a new historical peak around August 2021 (Fig. 2.36), surpassing the previous high peak in October 2020 (Barichivich et al. 2021). Around 5.9% of the global land area experienced extreme drought conditions in September 2021, matching the earlier historical peak in October 1984. The extent of severe plus extreme drought conditions in 2021 peaked at 17% of the global land area in July and August, surpassing the earlier historical peak of this drought severity in December 2002 (16.6%). Similarly, moderate or worse drought conditions peaked in August at 32% of the global land area, surpassing the earlier historical peak in November 2002 (31.6%).

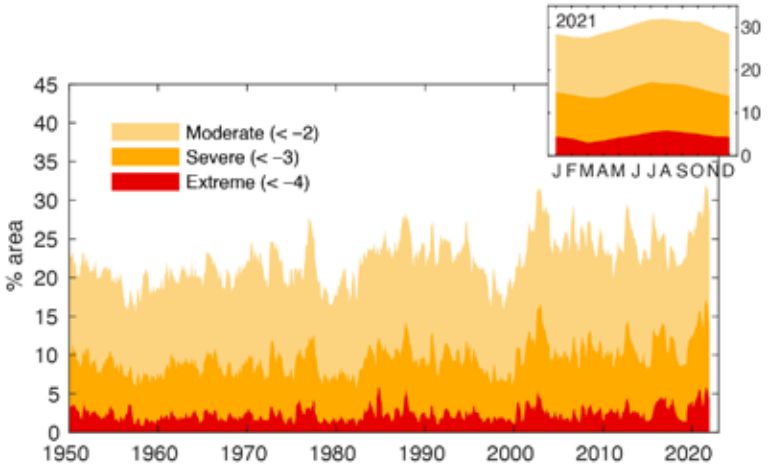

Fig. 2.36. Percentage of global land area (excluding ice sheets and deserts) with scPDSI levels of less than –2, –3, and –4, indicating moderate, severe, and extreme drought, respectively, for each month of 1950–2021.

The most extensive severe-to-extreme drought conditions in 2021 occurred across most of South America and western North America (Plate 2.1r), whereas the most extensive severe-to-extreme drought conditions in 2020 had been in Europe (Barichivich et al. 2021). Widespread drought in South America was mostly due to an intensification of previous drought (Fig. 2.37), leading to the expansion and intensification of earlier drought hotspots in central Chile and the Chaco region in northern Argentina (Barichivich et al. 2021). The ongoing protracted drought in central Chile reached its 12th consecutive year in 2021, becoming the longest drought in the historical record in the region. In

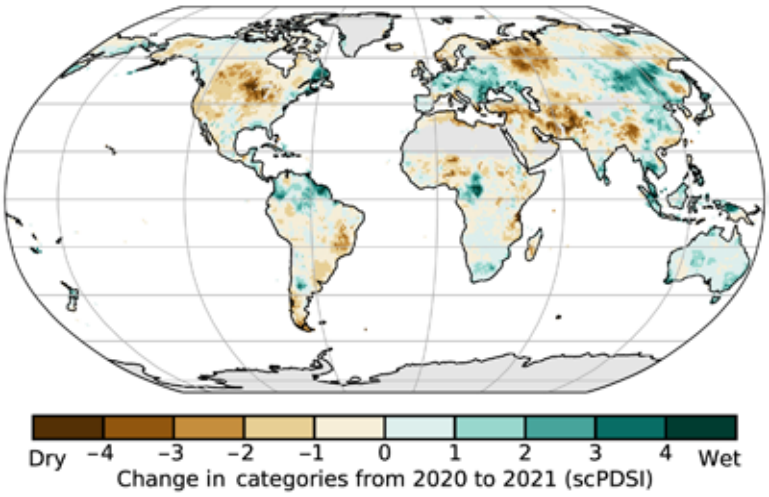

Fig. 2.37. Change in drought categories from 2020 to 2021 (mean scPDSI for 2021 minus mean scPDSI for 2020). Increases in drought severity are indicated by negative values (brown), decreases by positive values (blue). No calculation is made where a drought index is meaningless (gray areas: ice sheets or deserts with approximately zero mean precipitation).

North America, the intensification and expansion of drought through most of the western and formerly wetter central United States in 2021 (Fig. 2.37) weakened the east–west moisture contrast observed across the country since 2017 (Plate 2.1r). Under these persistent drought conditions, California saw another extreme season of wildfires (section 2h3), which was intensified by La Niña conditions.

Previous extensive severe-to-extreme drought across central Europe eased to moderate drought in 2021 (Fig. 2.37). Wet conditions in northern Europe from the British Isles to Scandinavia and western Russia continued through 2021 (Plate 2.1r). In northern Africa, previous drought conditions intensified along the Mediterranean coast. Most of tropical Africa saw a continuation of wet conditions from 2019 (Plate 2.1r), though changes in moisture anomalies in this region are uncertain due to the sparse coverage of meteorological station data. Persistent severe-to-extreme drought conditions in southern Africa since 2018 continued through 2021 but eased slightly compared to 2020 (Fig. 2.37).

In Australia, previous drought eased, but most of the country continued under drought conditions during 2021 (Plate 2.1r). In contrast, the Maritime Continent (Southeast Asia) experienced wet conditions, and previous drought in region eased, particularly across Vietnam. A large stretch along northeastern Siberia and the Far East region of Russia saw an intensification and expansion of severe drought along with extreme heat (Plate 2.1r), which led to unprecedented wildfires. Most of the Middle East from Turkey to Pakistan saw an intensification of drought to moderate-to-severe conditions.

Hydrological drought results from a period of abnormally low precipitation, sometimes exacerbated by a concurrent increase in evapotranspiration (ET). Its occurrence can be apparent in reduced river discharge, soil moisture, and/or groundwater storage, depending on season and duration of the event. Here, a simple estimate of drought called the self-calibrating Palmer Drought Severity Index (Wells et al. 2004; van der Schrier et al. 2013) is presented, using global precipitation and Penman-Monteith Potential ET from an early update of the CRU TS 4.06 dataset (Harris et al. 2020). Moisture categories are calibrated over the complete 1901–2021 period to ensure that "extreme" drought and pluvial (wet periods) relate to events that do not occur more frequently than in approximately 2% of the months. This calibration affects direct comparison with other hydrological cycle variables in Plate 2.1r that use a different baseline period.

This year's update is based on an extensively revised dataset that incorporates new estimates of some variables in CRU TS4.06 compared with CRU TS4.05 used in the report on 2020 (Barichivich et al. 2021). The revisions affect both precipitation (via an improved baseline climatology) and potential ET (all input variables are affected by the improved baseline climatology, and cloud cover is further modified by a new method for estimating it from diurnal temperature range). These revisions modify the scPDSI drought index values throughout, including during the mid-1980s period of extensive drought, which has a reduction in the extent of drought compared to that previously estimated.

11. LAND EVAPORATION—D. G. Miralles, A. Koppa, Q. Gou, D. Rains, P. Hulsman, H. E. Beck, and M. F. McCabe

In 2021, most regions experienced positive anomalies (more evaporation than normal), relative to the 30-year reference period (1991–2020), as illustrated in Plate 2.1s. Unusually high values were experienced in southeast Asia and India, eastern Australia, Amazonia, and the Congo rainforest. Some of these anomalies related to higher-than-normal radiation and temperatures (section 2b1). In Amazonia, the high evaporation also reflects above-average rainfall in 2021 (Espinoza et al. 2022; section 2d4); precipitation in rainforests can enhance evaporation via interception loss, i.e., the intense vaporization of water from wet vegetation canopies (van Dijk et al. 2015). In eastern Australia, positive evaporation anomalies mostly were in response to the exceptionally wet autumn in 2021, which caused floods during the month of March (Reid et al. 2021; section 2d4). On the other side of the spectrum, anomalously low evaporation was recorded in Angola and across the Horn of Africa, in the Mato Grosso and Caatinga regions in Brazil, in western North America, and in the Middle East. These negative anomalies in water-limited regions are mostly related to below-normal rainfall (Orimoloye et al. 2022; section 2d4). In the Horn of Africa, the negative evaporation anomalies relate to a multi-year drought (sections 2d10, 7e4).

The globally averaged land evaporation in 2021 was above the 1991–2020 mean, but slightly below the positive 1980–2021 trend (Fig. 2.38). This long-term trend of +0.76 mm yr^{-1} falls within the high-end of the values previously published in the literature (Y.-Q. Zhang et al. 2016; Brutsaert et al. 2017; Anabalón and Sharma 2017), although this value is still substantially lower than the latest estimates of +2.30 mm yr^{-1} based on gravimetric remote sensing for the period 2003–19 (Pascolini-Campbell et al. 2021). The overall positive global evaporation anomaly in 2021 resulted from mean positive anomalies in both hemispheres (Fig. 2.38), which persisted at most latitudes throughout the entire year (Fig. 2.39). The positive anomalies in Southern Hemisphere mean evaporation—that were also reflected in the global means—are a characteristic signature of La Niña conditions (Miralles et al. 2014; Martens et al. 2018), such as those that prevailed during 2020 and 2021 (see SOI in Fig. 2.38). This ENSO-induced variability in evaporation is superimposed upon the long-term trend, which is attributed to increasing global temperatures (Miralles et al. 2014) and terrestrial greening (Cheng et al. 2017).

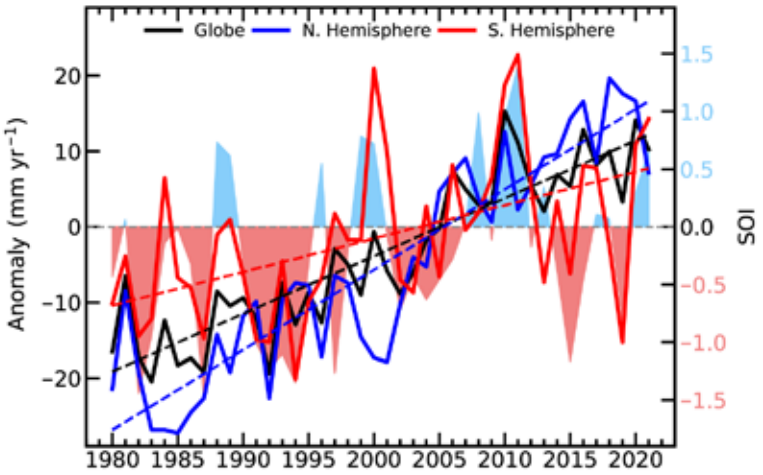

Fig. 2.38. Land evaporation anomaly (mm yr^{-1}; 1991–2020 base period) for the NH, SH, and the entire globe (blue, red, and black solid lines, respectively). Linear trends in evaporation (dashed lines) and the Southern Oscillation Index (SOI) from CRU (right axis, shaded area) are also shown. (Source: GLEAM.)

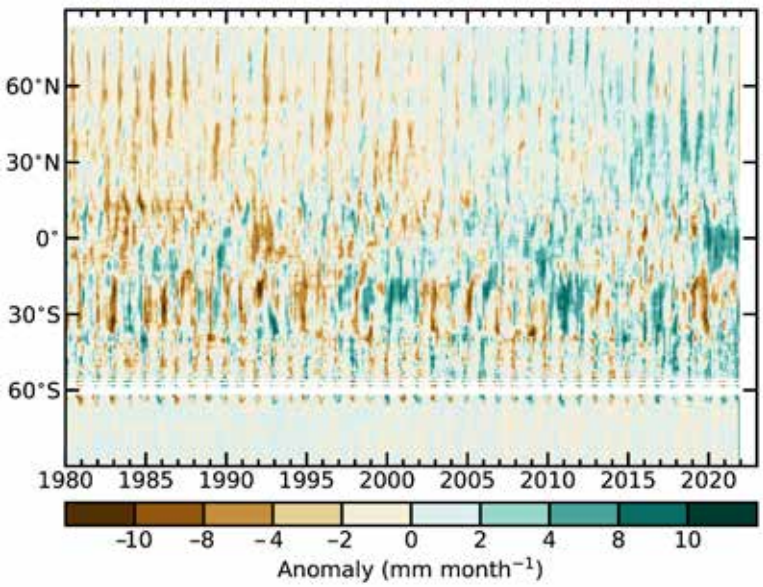

Fig. 2.39. Zonal mean terrestrial evaporation anomalies (mm $month^{-1}$; relative to 1991–2020 base period). (Source: GLEAM.)

The evaporation data that serve as the basis for these results come from version 3.6 of the Global Land Evaporation Amsterdam Model (GLEAM; Miralles et al. 2011). GLEAM v3.6 is based on microwave observations (of surface soil moisture, vegetation optical depth, and snow water equivalent), a precipitation dataset produced by blending gauge, satellite, and reanalysis sources (Beck et al. 2019), and a new bias-corrected, reanalysis-based product as atmospheric forcing (Beck et al. 2022). The accuracy of GLEAM v3 has been reported to be in the order of 0.7 mm day^{-1} (unbiased root mean square error), and its correlation against in situ eddy-covariance measurements is around 0.8 on average (Martens et al. 2017). While the ability to routinely monitor evaporation dynamics is critical for agriculture and water management, as well as to diagnose climate changes, global evaporation datasets (such as GLEAM v3.6) are still subject to model assumptions and uncertainties derived from parameterizations. In particular, the accuracy of the reported long-term trends is affected by the indirect representation of the influence of CO_2 and atmospheric aridity on stomatal conductance (Martens et al. 2017).

e. Atmospheric circulation

1. MEAN SEA LEVEL PRESSURE AND RELATED MODES OF VARIABILITY—B. Noll, D. Fereday, and N. Fedaeff

Global climate variability is influenced by the El Niño-Southern Oscillation (ENSO; indicated in the atmosphere by the Southern Oscillation Index [SOI]), as well as hemispheric-specific modes such as the Arctic Oscillation (AO), the North Atlantic Oscillation (NAO) and the Pacific/North America (PNA) pattern in the Northern Hemisphere (NH), and the Southern Annular Mode (SAM), also known as the Antarctic Oscillation (AAO), in the Southern Hemisphere (SH; see Kaplan 2011 for more details).

In 2021, La Niña conditions were present from January to May and then again from August through the end of the year, according to monthly Niño-3.4 SST anomalies (see also section 4b). The atmospheric response to La Niña was characterized by SOI values that were predominantly positive through the year. During July, a negative Indian Ocean dipole (IOD) event became established, in association with above-normal ocean temperatures in the tropical eastern Indian Ocean and cooler conditions relative to normal in the west (see section 4f). The development of an IOD event is correlated with ENSO by way of variations in the Walker Circulation (Behera et al. 2006). The overlying atmospheric pattern was dominated by the sinking branch of the Walker Circulation over the central and eastern Pacific and stronger-than-normal rising branch over Australia, the Maritime Continent, and the eastern Indian Ocean. These large-scale patterns influenced global atmospheric circulation patterns during the year.

In the NH, the PNA was on average negative in 2021, consistent with La Niña conditions (Yeh et al. 2018; Plate 2.1r). The principal large-scale circulation features occurred in the 2020/21 and 2021/22 winters. January and February 2021 saw a negative NAO, following a January sudden stratospheric warming (SSW; Figs. 2.40a,c). In SSW events, which occur in around 60% of boreal winters (Rao et al. 2019), the stratospheric polar vortex is disrupted by planetary-scale tropospheric waves. These waves may have been amplified in winter 2020/21 by reduced Arctic sea ice and a deepened Aleutian Low (Lu et al. 2021). In the weeks following SSW, the signal descends, often leading to the negative AO/NAO phase (Baldwin and Dunkerton 2001). The 2021 SSW followed this pattern (Figs. 2.40a,c), with the negative NAO in February possibly driven by the Madden-Julian Oscillation (MJO; Cassou 2008; Lockwood et al. 2022). Cold February conditions in northern Eurasia and eastern North America were a typical response to the negative AO/NAO.

By contrast, the winter 2021/22 stratospheric polar vortex was stronger than average (Fig. 2.40b). A strong vortex favors a positive NAO (Baldwin and Dunkerton 2001); although the December NAO was overall negative (Fig. 2.40d), the late-winter NAO was positive, consistent with the strong vortex. These contrasting winters (Figs. 2.40e,f) highlight some of the NAO drivers that vary interannually, reinforcing or counteracting each other (Scaife et al. 2014).

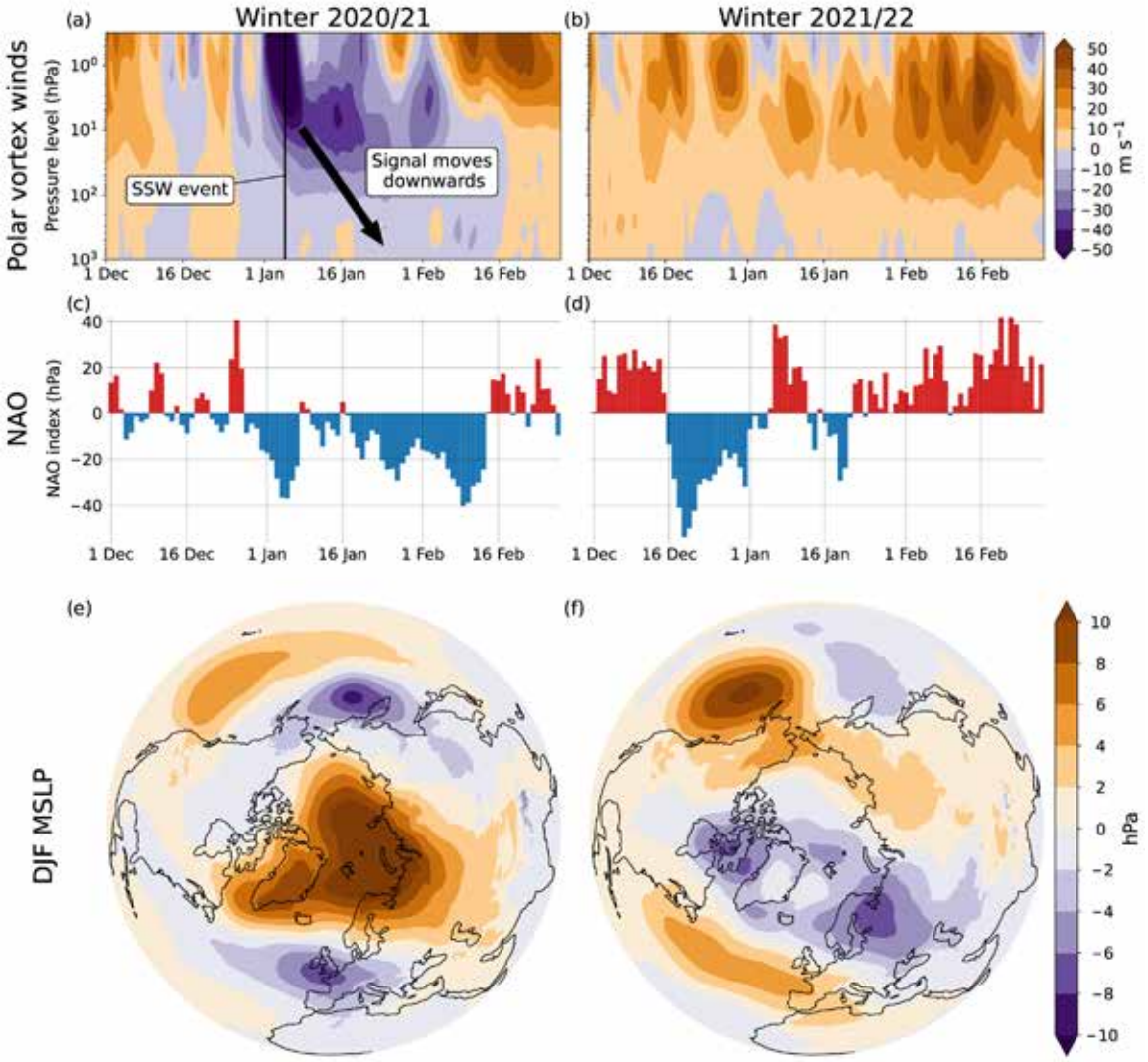

Fig. 2.40. Circulation differences between 2020/21 and 2021/22 boreal winters. (a),(b) Time–height cross section of zonal mean zonal wind anomalies (m s^{-1}) at 60°N (Met Office analysis). (c),(d) Daily North Atlantic Oscillation (NAO) index (Azores minus Iceland MSLP, hPa) anomaly, 1981–2010 base period (NCEP reanalysis). (e),(f) DJF mean MSLP anomaly (hPa), 1981–2010 base period (ERA5 reanalysis).

The SH featured a positive SAM during 73% of the year in 2021 (Fig. 2.41e). This was the fourth-highest percentage (and highest SAM index, section 2e3) since 1979. Accordingly, a broad area of higher-than-normal air pressure extended from east of New Zealand, across the South Pacific, and into southern Chile and Argentina (Figs. 2.41a–d). This was associated with New Zealand's warmest year on record, during which northerly quarter winds (315°W to 45°E) frequently affected the country, drawing down warmth from the tropics and contributing to a marine heatwave event in its coastal waters (NIWA 2021). Conversely, and as is consistent with the positive phase of the SAM, air pressure was lower than normal around much of Antarctica and the Southern Ocean (Figs. 2.41a–d). This was also linked to a stronger-than-normal stratospheric polar vortex above the South Pole, which contributed to very cold temperatures and the fifth-largest Antarctic sea ice extent for the month of August on record (NOAA 2021; see section 6e). Pressures were slightly lower than normal over Australia, as influenced by the combined effect of the IOD and La Niña teleconnection (Figs. 2.41a–d). 2021 was Australia's coolest year since 2012 and wettest since 2016, which resulted in a recharge of water storage following drought events from 2017 to 2019 (Bureau of Meteorology 2022; see also section 7h4).

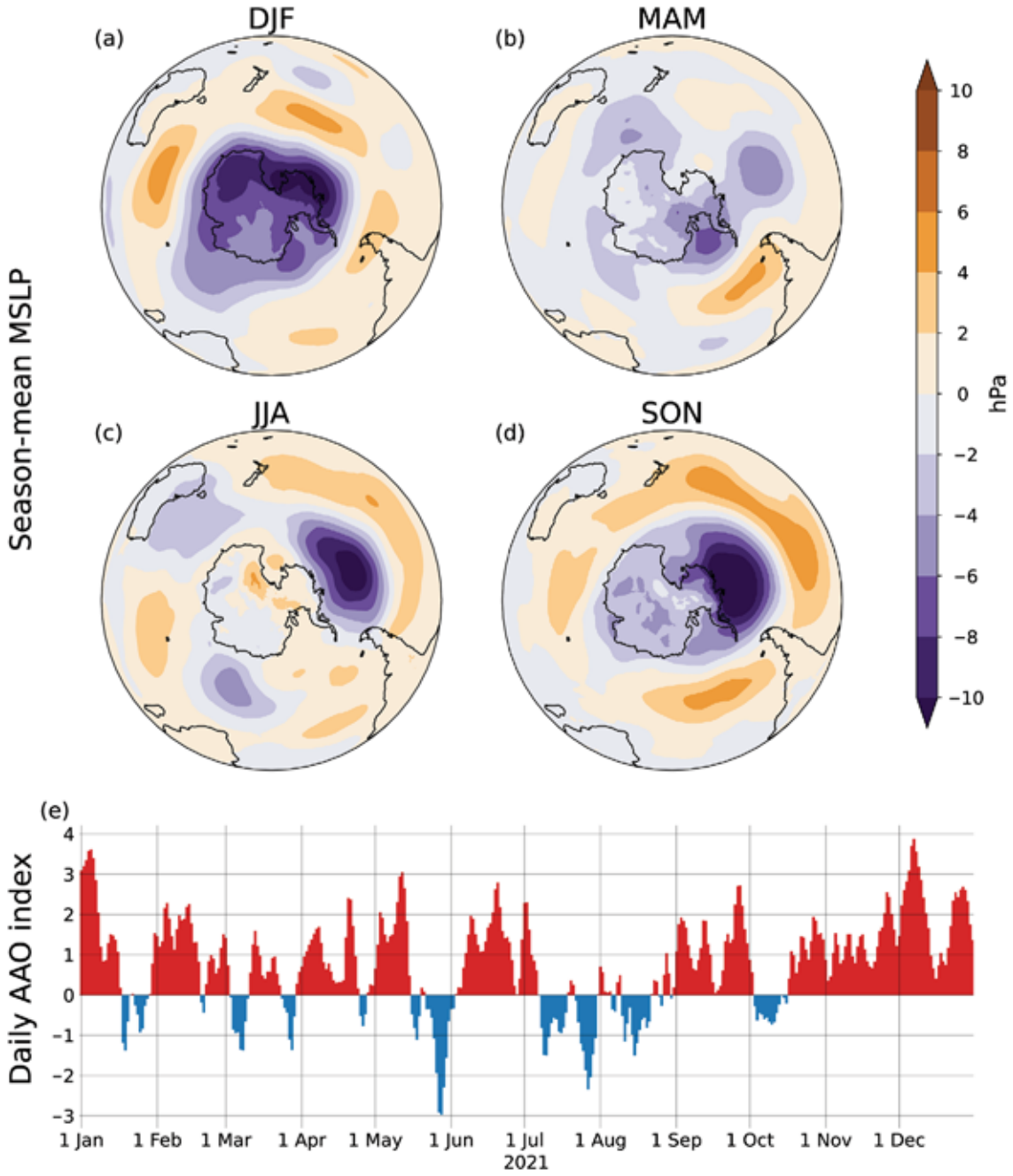

Fig. 2.41. Southern Hemisphere circulation in 2021. Seasonal mean MSLP anomalies (hPa) for (a) DJF 2020/21, (b) MAM 2021, (c) JJA 2021, and (d) SON 2021, 1981–2010 base period (ERA5 reanalysis). (e) Daily AAO index time series (NOAA CPC).

2. LAND AND OCEAN SURFACE WINDS—C. Azorin-Molina, R. J. H. Dunn, L. Ricciardulli, C. A. Mears, J. P. Nicolas, and T. R. McVicar

After about eight years of weak positive (near zero) anomalies in observed land surface winds (i.e., ~10 m above the ground), negative anomalies (with respect to the 1991–2020 climatology; Table 2.8) were recorded in the Northern Hemisphere (–0.028 m s^{-1}) in 2021, primarily in eastern North America (–0.063 m s^{-1}) and western Europe (–0.095 m s^{-1}). These exceptionally low winds, for example, in areas of the United Kingdom (Plate 2.1u), have not occurred in East Asia (+0.045 m s^{-1}), central Asia (+0.080 m s^{-1}), or South America (+0.080 m s^{-1}). Overall, the stilling (Roderick et al. 2007) observed before the 2010s (McVicar et al. 2012) ceased in the last decade, with a weak reversal or stabilization of surface winds globally (Zeng et al. 2019) and regionally (Minola et al. 2022; Fig. 2.42a). Two thresholds of wind intensities (i.e., > 3 m s^{-1} and > 10 m s^{-1}) show an opposite trend behavior with no trends (or even positive ones) for moderate winds (> 3 m s^{-1}; Fig. 2.42c) and moderate slowdowns for strong winds speeds (> 10 m s^{-1}; Fig. 2.42d), e.g., in South

Table 2.8. Northern Hemisphere (20°–70°N) and regional statistics for land surface wind speed (m s^{-1}) using the observational HadISD3 dataset for the period 1979–2021.

Region	Mean 1991–2020 (m s^{-1})	Anomaly 2021 (m s^{-1})	Trend 1979–2021 (m s^{-1} $decade^{-1}$) and 5th–95th percentile confidence range	Number of stations
Northern Hemisphere	3.309	−0.028	−0.059 (−0.073 to 0.044)	2886
North America	3.639	−0.063	−0.073 (−0.089 to 0.055)	853
Europe	3.652	−0.095	−0.052 (−0.073 to 0.034)	933
Central Asia	2.737	+0.080	−0.077 (−0.123 to 0.048)	304
East Asia	2.717	+0.045	−0.031 (−0.046 to 0.017)	534
South America	3.451	+0.080	+0.051 (−0.032 to 0.069)	101

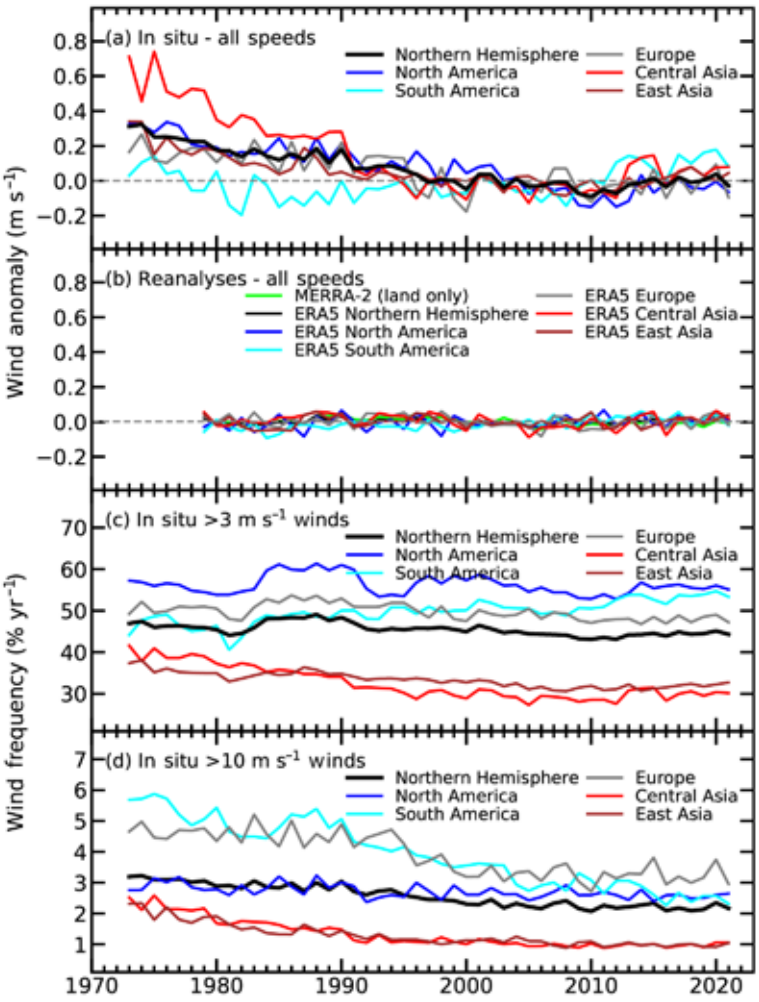

Fig. 2.42. Northern Hemisphere (20°–70°N) and regional annual time series of land surface wind speed anomaly (m s^{-1}; 1991–2020 base period) using (a) HadISD3 (1973–2021) observational dataset and (b) ERA5 (1979–2021) and MERRA-2 (1980–2021) reanalyses. HadISD3 occurrence frequencies (% yr^{-1}) for wind speeds (c) > 3 m s^{-1} and (d) > 10 m s^{-1}.

America (Azorin-Molina et al. 2021; Zhang et al. 2021).

This annual land surface wind report for 1979–2021 is based on 1) global in situ anemometer observations from the HadISD3 dataset (1973–2021; Dunn et al. 2012, 2016, 2019) and 2) two gridded reanalysis products: ERA5 (1979–2021; Hersbach et al. 2020) and MERRA-2 (1980–2021; Gelaro et al. 2017). Compared to in situ observations, the magnitudes of the anomalies from the reanalyses are smaller and do not reproduce their multidecadal variability (Fig. 2.42b; Torralba et al. 2017; Ramon et al. 2019; Wohland et al. 2019); observations are the basis for quantifying wind changes.

Over most land regions, the last 43 years (1979–2021) have seen a declining long-term trend (Northern Hemisphere: −0.059 m s^{-1} $decade^{-1}$; Table 2.8). This stilling has ceased or even reversed since the ~2010s, but winds are not yet back up to 1979 levels, so on average a long-term decline in global land wind speeds is still observed. South America, however, has experienced a positive trend (though with many fewer stations). Despite the lack of land-based observations in the Southern Hemisphere, both in situ and ERA5 data in Fig. 2.43 support this interhemispheric asymmetry of wind speed changes, also projected for the twenty-first century (Deng et al. 2022; Yu et al. 2022), such as a dominance of decreases across midlatitude regions of the Northern Hemisphere and weak increases in the Southern Hemisphere (e.g., parts of Antarctica and the Southern Ocean).

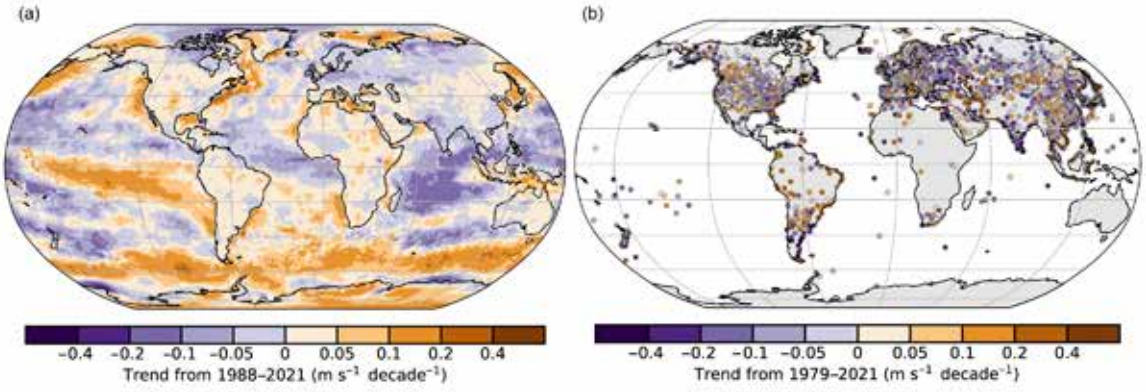

Fig. 2.43. Wind speed trends (m s^{-1} $decade^{-1}$) from (a) ERA5 reanalysis output over land/ice and Remote Sensing Systems (RSS) satellite radiometers (SSM/I, SSMIS, TMI, GMI, AMSR2, ASMR-E, and WindSat) over ocean (shaded areas) for the period 1988–2021 and (b) the observational HadISD3 dataset over land (circles) for the period 1979–2021.

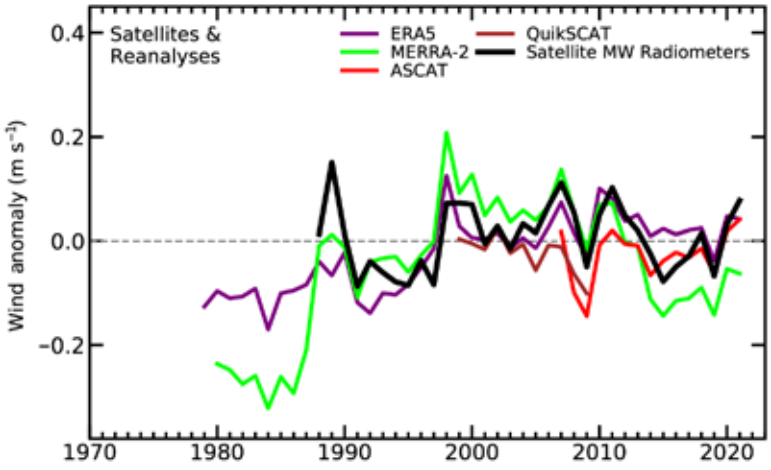

Fig. 2.44. Annual anomalies of global mean wind speed (m s^{-1}; 1991–2020 base period) over the ocean from satellite radiometers and scatterometers, MERRA-2, and ERA5.

The assessment of ocean surface winds for 1988–2021 was conducted using ERA5 reanalysis and satellite-based products including the Special Sensor Microwave/Imager (SSM/I), the Special Sensor Microwave Imager/Sounder (SSMIS), the Advanced Microwave Scanning Radiometer (AMSRE and AMSR2), TMI, GMI, WindSat, QuikSCAT, and ASCAT (Wentz 1997; Wentz et al. 2007, 2015; Ricciardulli and Wentz 2015; Ricciardulli and Manaster 2021). In 2021, positive anomalies were recorded by satellite radiometers (RSS: +0.078 m s^{-1}), slightly larger than satellite scatterometers (ASCAT: +0.041 m s^{-1}) and reanalysis (ERA5: +0.030 m s^{-1}) (Fig. 2.44). The most prominent positive anomalies were recorded over the Southern Ocean, specifically in the South Pacific (> +1.2 m s^{-1}) associated with a positive SAM phase, along with the equatorial Pacific Ocean, Gulf of Alaska, and Bering Sea (Plate 2.1u). This agrees with previous studies (e.g., Deng et al. 2022), which report a strengthening and shifting poleward of Southern Hemisphere westerlies. In contrast, large negative anomalies occurred in the North Atlantic, equatorial Atlantic, and Indian Oceans. Changes in ocean surface winds show a dominance of negative trends for 1988–2021, especially in the Indian and West Pacific Oceans (Fig. 2.43). Positive trends prevail in the Southern Ocean, the Pacific trade winds, the Bering Sea, and near the coastlines (e.g., North America; Young and Ribal 2019).

Studies investigating the trends and variability of surface winds demonstrated that the primary driver is exerted by internal decadal ocean–atmosphere oscillations (Zeng et al. 2019; Zhou et al. 2021), as modulated by changes in the temperature gradient (Zhang et al. 2021) induced by anthropogenic greenhouse gas forcings (Deng et al. 2021, 2022). Regionally and locally, land-use changes (Minola et al. 2022) and/or instrumentation issues (Azorin-Molina et al. 2018; Safaei Pirooz et al. 2020) have an impact on wind changes. Recent studies predict an interhemispheric asymmetry of future wind speed changes due to the reduction in Hadley, Ferrel, and Polar cells over the Northern Hemisphere and the strengthening of the Hadley cell over the Southern Hemisphere (Zha et al. 2021).

3. UPPER AIR WINDS—L. Haimberger, M. Mayer, and V. Schenzinger

The 2021 global mean wind speed anomaly at 850 hPa was about 0.1 m s^{-1} above the 1991–2020 climatology (Fig. 2.45a). The neutral or positive long-term wind trends at 850 hPa in the NH (40°–60°N) extratropics and in the global mean are now more consistent with surface winds (section 2e2), where the wind stilling reported in past annual reports has ceased or even reversed (section 2e2). As 2021 was the year with the highest Southern Annular Mode (SAM) index (average 0.8, estimated from NOAA monthly data) since 1979, we show the 70°–50°S average zonal wind time series in (Fig. 2.45b). The correlation coefficient between the AAO index and the 70°–50°S zonal mean 850-hPa wind speed on monthly timescales, calculated for 1979–2021, is 0.9. Thus, it is not surprising that the annual mean wind speed anomaly in this latitude belt was clearly positive in 2021, with maxima in autumn (not shown). Consistent with climate model predictions (Lee et al. 2019) there has been a notable increase in wind speed in this latitude belt, with highly significant trends 1991–2021 between 0.16 and 0.22 m s^{-1} $decade^{-1}$. Large positive zonal wind speed anomalies occur at 850 hPa over nearly all longitudes of the Southern Ocean (Plate 2.1v).

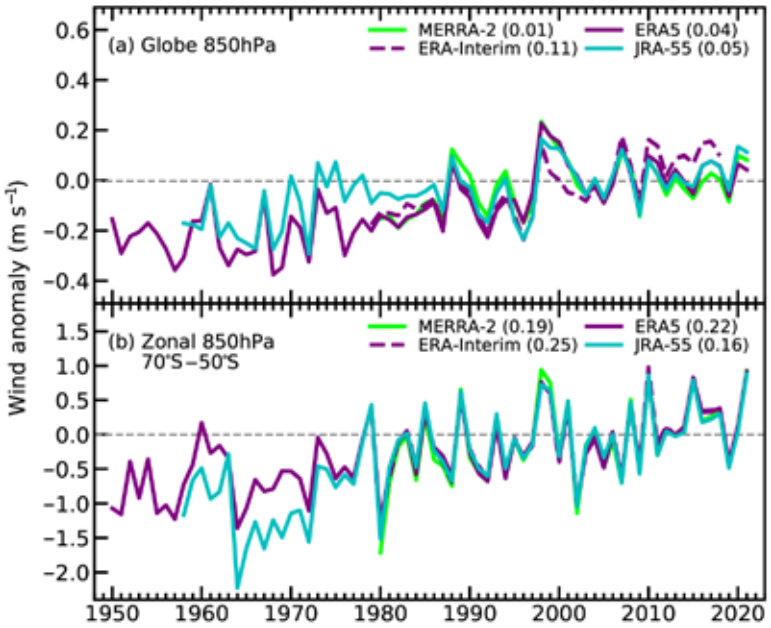

Fig. 2.45. Annual anomalies of (a) global mean, (b) 50°–70°S belt zonal mean wind speed (m s^{-1}; 1991–2020 base period) at 850 hPa from four reanalyses (ERA5 [Hersbach et al. 2020], ERA-Interim [Dee et al. 2011], MERRA-2 [Gelaro et al. 2017], and JRA-55 [Kobayashi et al. 2015]). The numbers in parentheses are linear trends in m s^{-1} $decade^{-1}$ for the period 1991–2020. ERA-Interim time series ends in 2019.

As in previous years, we consider large-scale anomalies in upper air winds through the velocity potential (χ) and divergent winds at 200 hPa. This diagnostic is particularly sensitive to changes in tropical convective activity and associated changes to the Walker Circulation. The most prominent seasonal anomalies of the velocity potential in 2021 were present during boreal autumn (SON), with negative χ anomalies centered over the Indo-Pacific Warm Pool and positive χ anomalies extending from the central tropical Pacific into the northern subtropical Atlantic. The negative anomaly is consistent with strengthened convective activity arising from increased SSTs in the eastern Indian Ocean (associated with weakly negative Indian Ocean dipole conditions during August–November; see section 4f) and in the western tropical Pacific (associated with moderate La Niña conditions; see sections 2e1, 4b). Moreover, a few weak Madden-Julian Oscillation (Madden and Julian 1971) events were observed over the Maritime Continent during SON 2021 (see section 4c), which contributed additionally to convective activity in that region. The positive χ anomalies over the eastern tropical Pacific as well as westerly anomalies of 200-hPa divergent wind in the western equatorial Pacific are consistent with below-average SSTs in this region (La Niña). Interestingly, the center of the positive χ anomaly, as well as the convergence of 200-hPa winds, extended well into the western subtropical Atlantic. Anomalies in the χ field have been used to link tropical cyclone activity with large-scale tropical climate anomalies (e.g., Wood et al. 2020; Bell and Chelliah 2006). However, despite the strong χ anomaly pattern, tropical cyclone activity during the 2021 season was close to climatology in all Northern Hemisphere basins in terms of accumulated cyclone energy (ACE; see section 4g); only named storms in the Atlantic basin were 50% above average.

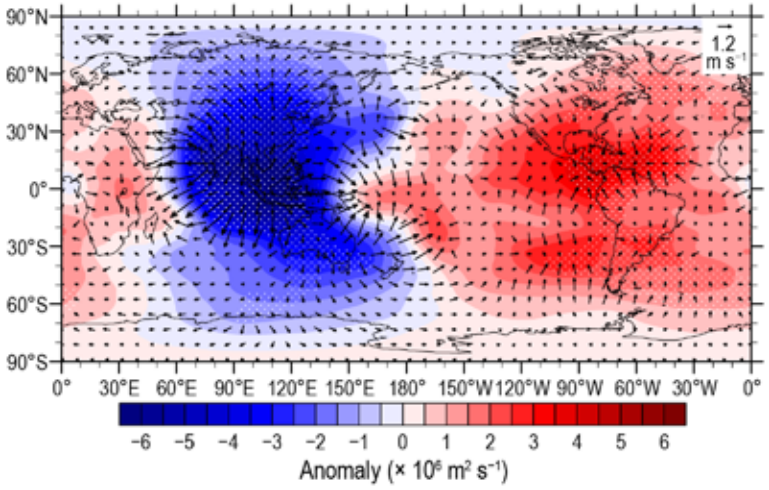

Fig. 2.46. Anomalous velocity potential (× 10^6 m^2 s^{-1}) and divergence winds (arrows, m s^{-1}) in SON 2021 from ERA5 (1991–2020 climatology) at 200 hPa. Stippling denotes anomalies exceeding 1.65σ of the temporal standard deviation of seasonally averaged velocity potential anomalies.

The availability of wind observations from the Aeolus instrument has been shown to constrain the uncertainties of notoriously difficult upper level divergence patterns and tropical weather forecast errors on short timescales (Rennie et al. 2021; Martin et al. 2021). Since those data will be used in future reanalyses (ERA5 does not yet assimilate Aeolus data), we looked at systematic impacts on seasonal means of winds and divergence to assess the potential for temporal discontinuities in these datasets. The root-mean square (rms) difference between velocity potentials from ECMWF assimilation experiments with/without Aeolus reaches only 2% of the rms value of the anomaly diagnostic in Fig. 2.46. Similar analysis of upper tropospheric zonal mean cross-equatorial velocity and divergence showed only negligible systematic differences, although on shorter time scales (sub-monthly) differences can become considerable. Overall these results suggest that Aeolus data are not expected to introduce major spurious shifts at their advent on seasonal and longer time scales, at least not in the quantities considered here.

After its latest disruption in 2020, the behavior of the quasi-biennial oscillation (QBO) in 2021 can be characterized as typical, comparable, for example, with 1958, 1981, 2009, and 2014. The westerly phase was at its strongest at 50 hPa in April, with a speed of 12.8 m s^{-1}. The following easterly phase, that has persisted above 15 hPa since April 2019, reached −36.8 m s^{-1} in October at the 20 hPa level, which is stronger than average, but not exceptional. This phase descended at a rate of about 0.61 km $month^{-1}$, which is close to the long term (60-year) average (−0.66 ± 0.75 km $month^{-1}$).

f. Earth radiation budget

1. EARTH RADIATION BUDGET AT TOP-OF-ATMOSPHERE—T. Wong, P. W. Stackhouse Jr., P. Sawaengphokhai, J. Garg, and N. G. Loeb

The top-of-atmosphere (TOA) Earth radiation budget (ERB) is defined as the difference between incoming total solar irradiance (TSI) and outgoing radiation from Earth, given by the sum of reflected shortwave (RSW) and outgoing longwave radiation (OLR). Regional imbalances in TOA ERB drive atmospheric and oceanic circulations.

An analysis of CERES TOA ERB measurements (Table 2.9) shows that the global annual mean OLR and RSW decreased by 0.65 W m^{-2} and 0.10 W m^{-2} in 2021, relative to 2020 (rounded to nearest 0.05 W m^{-2}). In contrast, the global annual mean TSI and net radiation increased by 0.05 W m^{-2} and 0.80 W m^{-2}, over the same period. Figure 2.47 shows regional annual mean maps of the difference between 2021 and 2020 in TOA OLR and TOA RSW. The largest reductions in OLR and increases in RSW are seen over the tropical western Pacific Ocean, Philippines, Indonesia, and New Guinea. Negative OLR and positive RSW differences also occur over the eastern Pacific Ocean, off the coast of Peru. The largest increases in OLR and decreases in RSW are observed in the tropical western Indian Ocean. These regional changes are associated with ENSO oscillation in the tropics as La Niña conditions persisted throughout much of 2021. Relative to the multiyear average from 2001 to 2020, the 2021 global annual mean TOA flux anomalies are +0.05, 0.0, −0.75, and +0.70 W m^{-2} for OLR, TSI, RSW, and total net flux (Table 2.9). These anomalies are within their respective 2-sigma interannual variability (Table 2.9) for this period.

Table 2.9. Global annual mean TOA radiative flux changes between 2020 and 2021, the 2021 global annual mean radiative flux anomalies relative to their corresponding 2001–20 mean climatological values, and the 2-sigma interannual variabilities of the 2001–20 global annual mean fluxes (all units in W m^{-2}) for the outgoing longwave radiation (OLR), total solar irradiance (TSI), reflected shortwave (RSW), absorbed solar radiation (ASR, determined from TSI-RSW) and total net fluxes. All flux values have been rounded to the nearest 0.05 W m^{-2} and only balance to that level of significance.

	One-Year Change (2021 minus 2020) (W m^{-2})	2021 Anomaly (Relative to Climatology) (W m^{-2})	Climatological Mean (2001–20) (W m^{-2})	Interannual Variability (2001–20) (W m^{-2})
OLR	–0.65	+0.05	240.25	±0.65
TSI	+0.05	0.00	340.00	±0.15
RSW	–0.10	–0.75	99.00	±0.95
ASR	+0.15	+0.75	241.00	±0.90
Net	**+0.80**	**+0.70**	**0.80**	**±0.80**

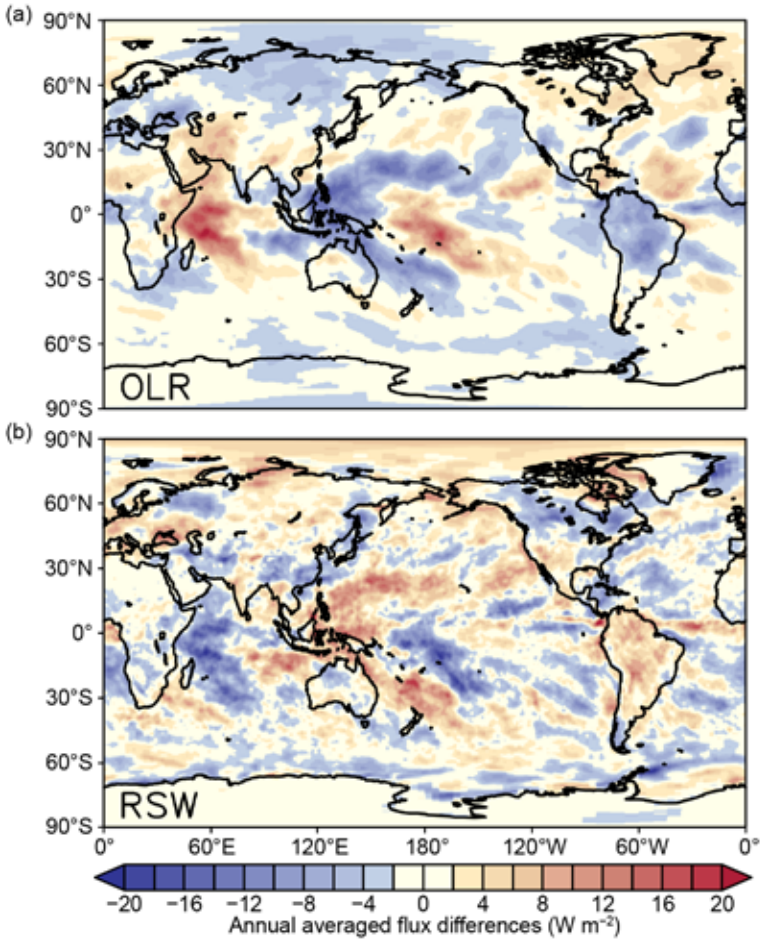

Fig. 2.47. Annual average TOA flux differences between 2021 and 2020 for (a) outgoing longwave radiation (OLR) and (b) reflected shortwave (RSW) radiation (W m^{-2}). The annual mean maps for 2021 were derived after adjusting Dec 2021 FLASHFlux v4A using the difference between EBAF and FF v4A in 2020.

Throughout 2021, the global monthly mean TOA OLR anomaly varied between positive and negative values (Fig. 2.48). OLR anomalies peaked at +0.7 W m^{-2} in February, but otherwise fluctuated between ±0.5 W m^{-2} the rest of the year. These results are consistent with NOAA HIRS (Lee and NOAA CDR Program 2011) and NASA AIRS (Susskind et al. 2012) OLR datasets (not shown). For the year as a whole, the 2021 global annual mean TOA OLR anomaly was +0.05 W m^{-2}. The global monthly mean TOA absorbed solar radiation (ASR, determined from TSI minus RSW) anomaly remained positive throughout 2021, peaking at +1.4 W m^{-2} in June. For the year as a whole, the 2021 global annual mean TOA ASR anomaly was +0.75 W m^{-2}. The global monthly mean TOA total net anomaly, which is calculated from ASR anomaly minus OLR anomaly, also stayed positive throughout 2021, topping out at +1.8 W m^{-2} in June. For the year as a whole, the 2021 global annual mean TOA total net anomaly was +0.70 W m^{-2}. The Earth energy imbalance (EEI) that had been observed prior to 2020 grew even larger during 2021, so that the doubling in observed EEI between 2005 and 2019 from both CERES and in situ observations (Loeb et al. 2021) continued to substantially increase, primarily because of an increase in ASR radiation. It should be noted that a 21-year trend is not necessarily indicative of a longer-term trend. At this timescale, internal variability in the climate system can offset or augment any forced, longer-term trend in net radiation.

The TSI data were obtained from the Total Irradiance Monitor aboard the Solar Radiation and Climate Experiment (SORCE) mission (Kopp and Lean 2011), the Royal Meteorological Institute

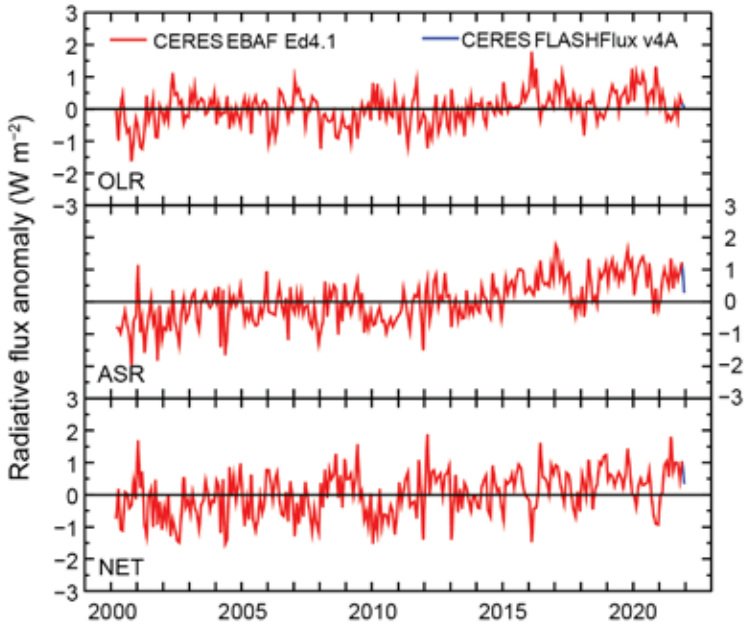

Fig. 2.48. Time series of global monthly mean deseasonalized anomalies (W m^{-2}) of TOA Earth radiation budget for outgoing longwave radiation (OLR; upper), absorbed solar radiation (ASR, determined from TSI-RSW; middle), and total net (TSI-RSW-OLR; lower) from Mar 2000 to Dec 2021. Anomalies are relative to their calendar month climatology (2001–20). Time series shows the CERES EBAF Ed4.1 1° data (Mar 2000–Nov 2021) in red and the CERES FLASHFlux version 4A data (Dec 2021) in blue; see text for merging procedure (Sources: https://ceres-tool.larc.nasa.gov/ord-tool/jsp/EBAF41Selection.jsp and https://ceres-tool.larc.nasa.gov/ord-tool/jsp/FLASH_TISASelection.jsp.)

of Belgium composite dataset (Dewitte et al. 2004), and the Total Solar and Spectral Irradiance Sensor-1 (TSIS-1, Coddington, 2017) mission, all renormalized to the SORCE Version 15. The TOA RSW and TOA OLR data, which are constructed with measurements from the CERES instruments (Wielicki et al. 1996, 1998) aboard *Terra* and *Aqua* spacecraft, are based on the CERES EBAF (Energy Balanced and Filled) Ed4.1 product (Loeb et al. 2009, 2012, 2018a) for March 2000–November 2021 and the CERES Fast Longwave and Shortwave Radiative Fluxes (FLASHFlux) version 4A product (Kratz et al. 2014) for December 2021. The FLASHFlux to EBAF data normalization procedure (Stackhouse et al. 2016) results in 2-sigma monthly uncertainties of ±0.30, ±0.04, ±0.18, and ±0.48 W m^{-2} for the OLR, TSI, RSW, and total net radiation, respectively.

2. MAUNA LOA APPARENT TRANSMISSION—J. A. Augustine, K. O. Lantz, H. Telg, J.-P. Vernier, and M. Todt

One of the longest records in the atmospheric sciences is the apparent atmospheric transmission at the Mauna Loa Observatory on Hawaii, which dates to 1958. Atmospheric transmission describes the fraction of solar radiation impinging at the top-of-atmosphere that is transmitted vertically to the surface. Because of its high altitude (3397 m a.s.l.), transmission at Mauna Loa is primarily affected by stratospheric aerosols, although tropospheric effects occur when dust from springtime storms in Asia pass over the island (Bodhaine et al. 1981). Since Mauna Loa is located near 20°N latitude, its transmission primarily reflects events in the Northern Hemisphere and is relatively uninfluenced by those in the Southern Hemisphere.

The updated time series of apparent transmission at Mauna Loa through 2021 is presented in Fig. 2.49. Recent trends show a gradual reduction in late 2017 and early 2018, caused by pyrocumulonimbus in Canada, and the June 2019 eruption of Raikoke in the Kuril Islands, ~800 km northeast of Japan. In 2020, transmission stabilized at a low level that was maintained by the eruption of Taal in the Philippines in January, remnants of Raikoke, and California wildfires (Augustine et al. 2020, 2021).

The inset of Fig. 2.49 shows the new data for 2021. The annual average of 0.925 is 0.009 lower than the background. The transmission held steady in early 2021 from the relatively low levels of

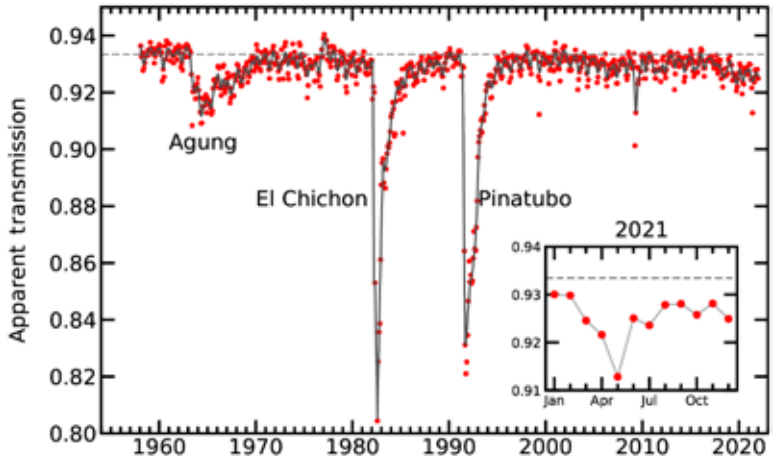

Fig. 2.49. Apparent transmission at Mauna Loa, Hawaii, from 1958 through 2021. Red dots are monthly averages of morning apparent transmission, the gray curve in the full time series plot is a LOWESS fit with a six-month smoother applied, and the horizontal dashed gray line is the average transmission for the clean period before the volcanic eruption of Mount Agung. Insert is an enlargement of the newest data for 2021.

the previous year. Significant aerosol activity began on 15 March with the largest sandstorm in the Gobi Desert since 2010, lofting dust up to 8 km (Gui et al. 2021). HYSPLIT trajectory analysis shows that dust plumes reached Mauna Loa in seven days. Volcanoes La Soufriere (Caribbean Island of St. Vincent) and Fukutoku-Okanoba (25 m below sea level, ~60 km south of Iwo Jima) erupted explosively during 9–12 April and 13 August, respectively. Fukutoku-Okanoba's plume extended only to the lower boundary of the stratosphere, and trajectory analysis revealed its plume never reached Mauna Loa.

La Soufriere erupted at least 20 times on four consecutive days. Its plume was observed as high as 20 km by MISR, well into the lower stratosphere (LS), and HYSPLIT trajectory analysis showed that it reached Mauna Loa one month later. CALIPSO detected a strong signal between 21 and 23 km in mid-August between the equator and 35°N. Lidar observations on Mauna Loa detected a large signal just above 21 km on 20 August, and SAGE tracked that same signal in the stratosphere through October. Balloon-borne aerosol concentration measurements in Kansas (United States) in August and later in France detected high aerosol concentrations at 20–21 km. Similar observations in Boulder, Colorado, show near-normal concentrations in the LS through mid-April, followed by elevated values between 15 and 19 km through the end of the year, albeit decreasing a bit in December. It also shows a small peak near 21 km in early October. Together, these observations strongly suggest that La Soufriere's plume circled the globe in the LS for the remainder of 2021.

Extensive pyro cumulonimbus activity occurred in the western United States and Canada in July and August. These events were associated with the drought and heat wave over the affected regions at that time (sections 2b4, Sidebar 7.1); however, CALIPSO and HYSPLIT analyses show the smoke plumes initially traveled northward and remained north of 30°N, well displaced from Mauna Loa.

Apparent transmission is calculated from the ratio of direct-normal pyrheliometer measurements at two solar elevations, following Ellis and Pueschel (1971). An average of three successive ratios, from morning pyrheliometer measurements made at 2, 3, 4, and 5 atmospheric pathlengths, is considered representative for the day. While any of these ratios are mathematically equivalent to a vertical transmission, variability at the longer pathlengths render the calculation an "apparent" transmission. Only morning data are used because upslope afternoon winds often carry sea level aerosols to the summit.

Sidebar 2.1: **Lightning**—M. FÜLLEKRUG, E. WILLIAMS, C. PRICE, S. GOODMAN, R. HOLZWORTH, K. VIRTS, AND D. BUECHLER

The World Meteorological Organization (WMO) recently declared lightning flashes to be an essential climate variable (ECV), based on a recommendation by the Task Team on Lightning Observation for Climate Applications (TT-LOCA) as part of the Atmospheric Observation Panel for Climate (AOPC) of the WMO and the Global Climate Observing System (GCOS; Aich et al. 2018; WMO 2019a). This endorsement reinforces the WMO Integrated Global Observing System (WIGOS) Vision 2040 (WMO 2019b) toward the operational observation of lightning by space agencies during the coming decades.

Lightning flashes are generated by thunderstorms, which develop when hot and humid air destabilizes the atmosphere and enables deep convection. As a result, the lightning ECV is grouped with other ECVs describing the atmosphere (Bojinski et al. 2014) which are closely related to thunderstorm development, such as the Earth radiation budget, upper-air temperature, water vapor, wind speed, and cloud properties (see sections 2f1, 2b1, 2b5, 2d2, 2e2, and 2d6). The lightning ECV is also related to ECVs that impact atmospheric composition, such as lightning NOx and cloud condensation nuclei (see sections 2g3 and 2g6).

Lightning is a natural hazard associated with the severe weather impacts of thunderstorms including high wind speeds with falling trees and branches, intense precipitation causing flooding, large hail affecting transport vehicles and crops, and cloud-to-ground lightning which can lead to casualties, ignite wildland fires, and cause significant damage to infrastructure, such as power lines (Cooper and Holle 2019; Holle 2016). Lightning has significant societal implications for public safety (Holle et al. 1999), power distribution (Piantini 2020), aviation (Ryley et al. 2020), and wildfires (Holzworth et al. 2021). Wildfires can increase convective instability for pyrocumulus to develop (Rudlosky et al. 2020; Liu et al. 2021; Augustine et al. 2021). Lightning is

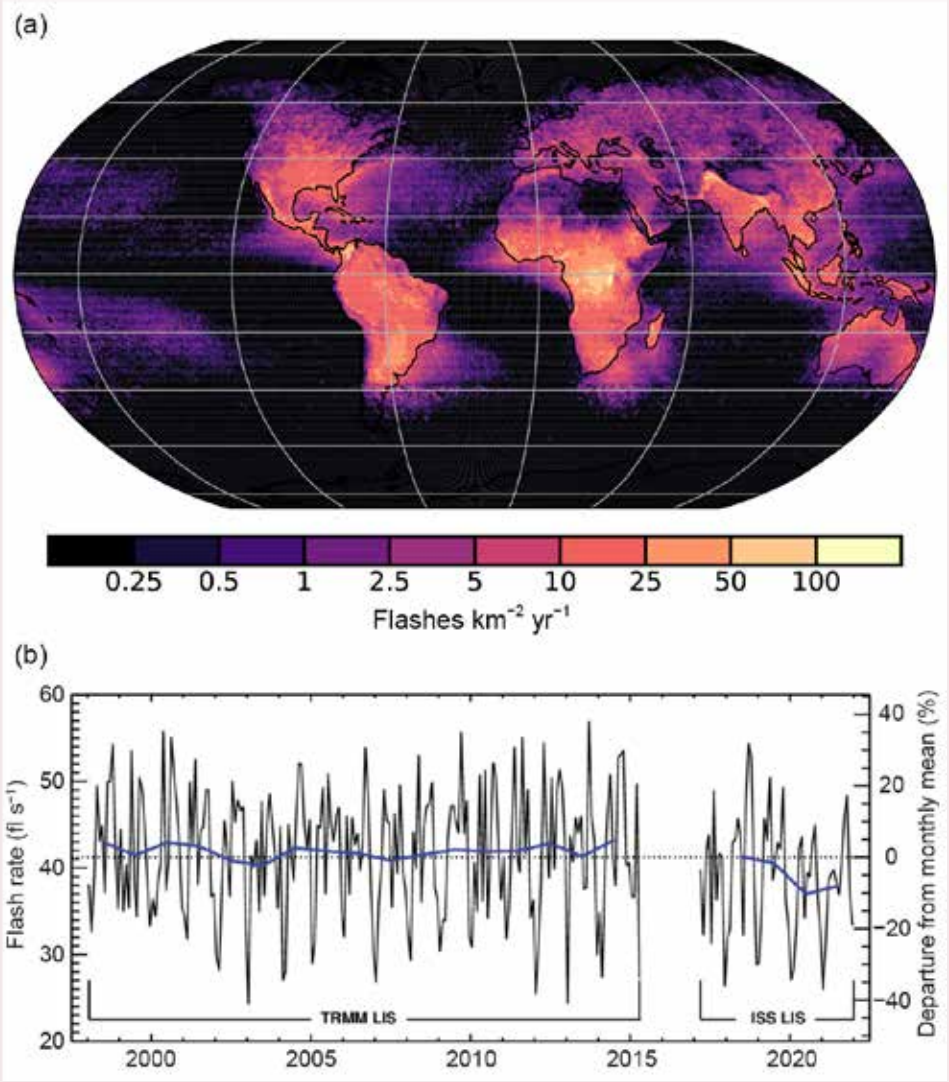

Fig. SB2.1. Lightning observations from space. (a) Global distribution of lightning flash rate density (fl km^{-2} yr^{-1}) for the period of record 1995–2021 from NASA's low earth orbit lightning imagers OTD (Optical Transient Detector, May 1995–Apr 2000), TRMM LIS (Lightning Imaging Sensor, Jan 1998–Dec 2014) and ISS LIS (Feb 2017–Dec 2021). Global lightning is dominant over the continental tropical belt. (b) Monthly (solid black) and annual (blue) mean lightning flash rates (fl s^{-1}) observed by the TRMM and ISS LIS instruments within the ±38° latitudinal coverage of the TRMM orbit. The black dotted line is the combined mean monthly global flash rate (41.2 fl s^{-1}). The mean monthly flash rate varies from ~24 to 57 fl s^{-1}. The seasonal variations are due to the annual cycle of lightning activity linked to the larger land area of the Northern Hemisphere. (Source: Courtesy of the NASA Lightning Imaging Sensor Science Team.)

closely linked to precipitation formation (Piepgrass et al. 1982; Petersen and Rutledge 1998), upper tropospheric water vapor concentrations (Price and Asfur 2006), and the ice providing for cirrus formation (Kent et al. 1995), allowing lightning to act as a proxy measure for some of these difficult-to-quantify meteorological parameters.

Lightning is currently monitored with lightning imagers on satellites (Christian et al. 2003; Blakeslee et al. 2020) and by commercial ground-based lightning detection networks based on radio wave detection (e.g., DiGangi et al. 2021; Said et al. 2010; Virts et al. 2013). The global climatology of lightning, based on satellite optical observations, is shown in Fig. SB2.1a (Christian et al. 2003; Goodman and Christian 1993; Blakeslee et al. 2020; Rudlosky and Virts 2020). The global lightning climatology follows solar insolation with a longitudinal migration that corresponds to a diurnal temperature variation (Price 1993) and a latitudinal migration that corresponds to an annual temperature variation (Christian et al. 2003; Williams 2020). The strong continental dominance of lightning has origins in both thermodynamics (Williams and Stanfield 2002a) and in aerosol-modulated cloud physics (Rosenfeld et al. 2008; Stolz et al. 2015). Their relative contributions are currently in debate, where the strong continental dominance of cloud condensation nuclei (CCN) is recognized (Williams et al. 2002b).

Satellite measurements and global lightning detection networks have not been operational long enough to detect substantial long-term changes in lightning activity (Fig. SB2.1b; Williams et al. 2019). Therefore, scientific studies use alternative methods over longer time scales to address climate questions. The thunder day is a WMO observation that has been carried out for more than a century in many countries (Brooks 1925) and represents a 24-hour day, for which thunder was heard at official national meteorological stations. Evidence has accrued that thunder days have been increasing over the last century, specifically at high latitudes (Kitagawa et al. 1989; Williams 2009; Pinto et al. 2013; Lavigne et al. 2019). Significant increases in thunderstorm activity over Africa since the 1990s have been detected using climate proxy data from reanalysis (Harel and Price 2020).

The declaration of the WMO elevates lightning flashes to a climate quantity due to its importance in climate change. It is generally agreed that lightning activity increases as the climate warms (Williams 1992, 1994; Price and Rind 1994; Romps et al. 2014), based on both considerations of the Clausius-Clapeyron relation and on the empirical evidence that CAPE increases with temperature in global climate models (Del Genio et al. 2007). The evidence for lightning increases in the Arctic (Holzworth et al. 2021), where the annually averaged Arctic near-surface air temperature increased by 3.1°C from 1971 to 2019, i.e., three times faster than the global average (AMAP 2021), which is consistent with a thermodynamic influence on lightning Fig. SB2.2. Global aerosols may decline as alternative energy sources and the reliance on fossil fuels are considered, as exemplified during the COVID-19 lockdown, such that the reduction of aerosols may diminish lightning via cloud microphysics (Stolz et al. 2015; Williams et al. 2002b). Lightning flashes also serve as a diagnostic for key manifestations of climate variability associated with deep convection. Examples include climate induced severe local convective storms accompanied by extraordinary lightning (Zipser et al. 2006; Holzworth et al. 2019; Virts and Goodman 2020; Peterson et al. 2022), the El Niño-Southern Oscillation (Goodman et al. 2000; Chronis et al. 2008; Satori et al. 2009; Williams et al. 2021), the Madden Julian Oscillation (Anyamba et al. 2000), planetary waves (Grandt 1992; Satori et al. 2009), and warming in the Arctic (Bieniek et al. 2020; Holzworth et al. 2021; Chen et al. 2021; Finney 2021).

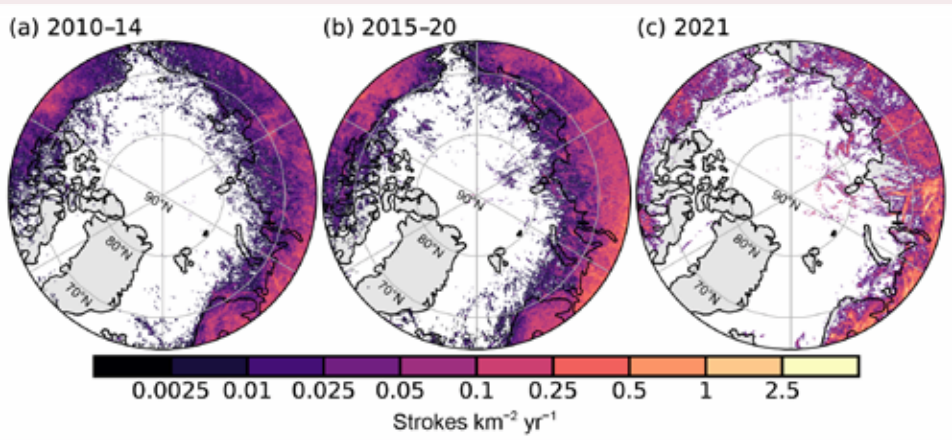

Fig. SB2.2. Arctic lightning densities (strokes km^{-2} yr^{-1}) recorded by the World Wide Lightning Location Network (WWLLN) and averaged over Jun–Aug during the years 2010–14, 2015–20, and 2021. The lightning flash densities increased during 2015–20 compared to 2010–14. In 2021, northern Europe and much of northern Russia continued to experience higher overall lightning densities. Eastern Russia and northern North America generally experienced less lightning than the 2015–20 period.

Lightning is a major source of NOx in the atmosphere (Gordillo-Vázquez et al. 2019; Schumann and Huntrieser 2007; Price et al. 1997), which contributes to climate change in a feedback loop (IPCC 2021). In particular, lightning NOx is a precursor to tropospheric ozone formation which is a greenhouse gas and also a designated ECV. The climate assessment of lightning needs to differentiate lightning occurrence frequencies against the effects of natural and man-made aerosol (Thornton et al. 2017; Wang et al. 2018; Williams 2020), which is also an ECV.

Lightning is becoming more important as a natural hazard, due to increasing vulnerability of critical infrastructures, such as electrical power grid and communications, and the growth in global population and associated lightning casualties, primarily in developing countries. Even if lightning activity remained constant in the future, its societal impact will increase dramatically. If lightning also increases with climate change, this impact may worsen.

g. Atmospheric composition

1. LONG-LIVED GREENHOUSE GASES—X. Lan, B. D. Hall, G. Dutton, J. Mühle, J. W. Elkins, and I. J. Vimont

Atmospheric burdens of many greenhouse gases, especially the long-lived greenhouse gases (LLGHGs) carbon dioxide (CO_2), methane (CH_4), and nitrous oxide (N_2O), have been increasing significantly since the industrial revolution, mainly as a result of human activity. The 2021 growth of atmospheric CH_4 reached another record high since systematic measurement started in 1983, while annual growth of CO_2 was the fifth highest since 1958 and N_2O was the third highest since 2001.

Carbon dioxide is the most important and prevalent anthropogenic GHG. In 2021, the annually averaged atmospheric CO_2 abundance at Mauna Loa Observatory (MLO) reached 416.5 ± 0.1 ppm (parts per million by moles in dry air; 1-σ uncertainties). Globally averaged CO_2, derived from remote marine boundary layer measurements, was 414.7 ± 0.1 ppm in 2021 (Fig. 2.50a; www.gml.noaa.gov/ccgg/trends). This is 49% above the atmospheric pre-industrial abundance of CO_2 of ~278 ppm, based on air extracted from ice in Greenland and Antarctica (Etheridge et al. 1996). Annual growth in global mean CO_2 has risen steadily from 0.6 ± 0.1 ppm yr^{-1} in the early 1960s to an average of 2.4 ppm yr^{-1} during the last decade, 2011–20 (Fig. 2.50a). The annual increase in global mean CO_2 in 2021 was 2.6 ± 0.1 ppm (Table 2.10), the fifth highest since the accurate measurements started in 1958.

The main driver of increasing atmospheric CO_2 is fossil fuel (FF) burning,

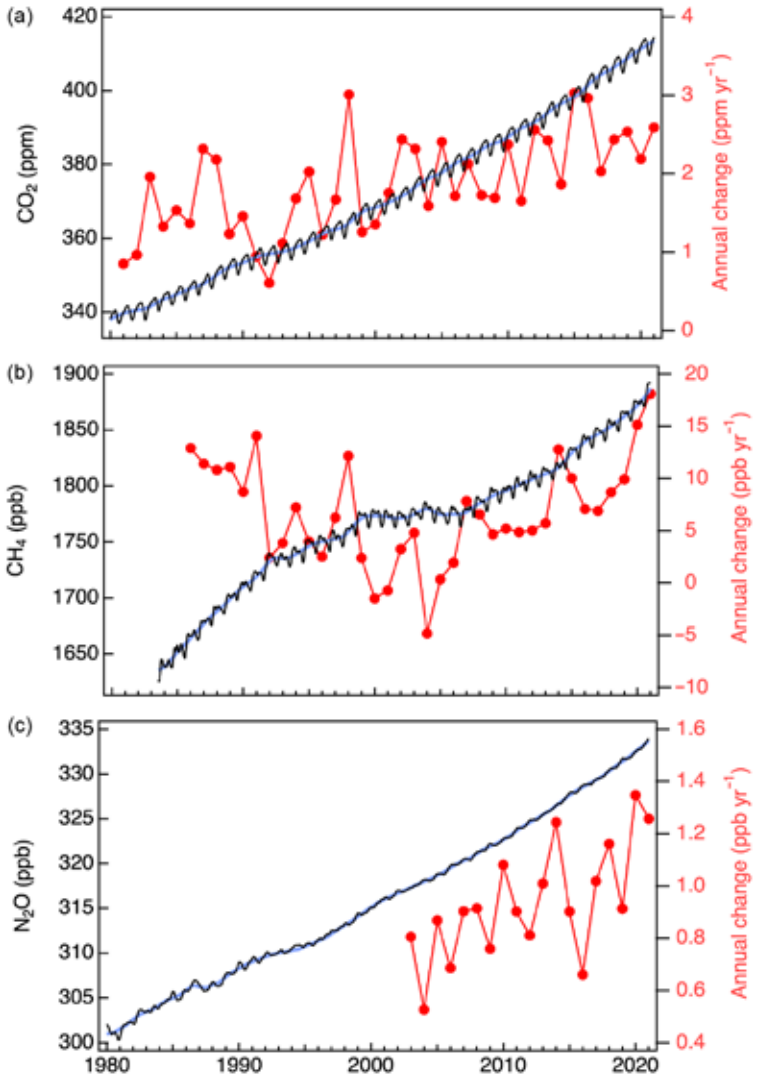

Fig. 2.50. Global mean dry-air surface mole fractions (approximately weekly data in black, left axis) and annual change (red, right axis) of (a) CO_2 (ppm), (b) CH_4 (ppb), and (c) N_2O (ppb) derived from the NOAA Global Greenhouse Gases Reference Network. Deseasonalized trend curves (see Dlugokencky et al. 1994b for methods) are shown in blue. N_2O data prior to 2001 are too sparse to allow robust estimates of annual growth rates.

Table 2.10. Summary table of long-lived greenhouse gases for 2021 (CO_2 mole fractions are in ppm, N_2O and CH_4 in ppb, and all others in ppt).

Industrial Designation or Common Name	Chemical Formula	AGGI	Radiative Efficiency (W m^{-2} ppb^{-1})[a]	Radiative Forcing (W m^{-2})	Mean surface mole fraction, 2021 (change from 2020)[b]	Lifetime (years)
Carbon Dioxide	CO_2	Y	1.37×10^{-5}	2.08	414.7 (2.3)	—
Methane	CH_4	Y	3.63×10^{-4}	0.52	1895.8 (16.7)	9.1
Nitrous Oxide	N_2O	Y	3.00×10^{-3}	0.20	334.2 (1.2)[c]	123
Chlorofluorocarbons						
CFC-11	CCl_3F	Y	0.26	0.059	222.2 (–1.8)[c]	52
CFC-12	CCl_2F_2	Y	0.32	0.161	493.9 (–3.2)[c]	102
CFC-113	CCl_2FCClF_2	Y	0.30	0.021	68.5 (–0.5)[c]	93
Hydrochlorofluorocarbons						
HCFC-22	$CHClF_2$	Y	0.21	0.052	248.9 (1.1)	11.9
HCFC-141b	CH_3CCl_2F	Y	0.16	0.004	24.6 (0.01)	9.4
HCFC-142b	CH_3CClF_2	Y	0.19	0.004	21.5 (–0.2)	18
Hydrofluorocarbons						
HFC-134a	CH_2FCF_3	Y	0.16	0.017	118.9 (5.8)	14
HFC-152a	CH_3CHF_2	Y	0.10	< 0.001	7.2 (0.2)	1.6
HFC-143a	CH_3CF_3	Y	0.16	0.004	26.5 (1.6)	51
HFC-125	CHF_2CF_3	Y	0.23	0.007	34.7 (3.4)	30
HFC-32	CH_2F_2	N	0.11	0.002	23.6 (3.1)	5.4
HFC-23	CHF_3	Y	0.18	0.006	34.9 (0.2)	228
HFC-365mfc	$CH_3CF_2CH_2C$	N	0.22	< 0.001	1.05 (0.03)	8.9
HFC-227ea	CF_3CHFCF_3	N	0.26	< 0.001	1.87 (0.17)	36
Chlorocarbons						
Methyl Chloroform	CH_3CCl_3	Y	0.07	< 0.001	1.2 (–0.2)	5.0
Carbon Tetrachloride	CCl_4	Y	0.17	0.013	76.2 (–1.1)[c]	32
Methyl Chloride	CH_3Cl	N	0.01	< 0.001	547.2 (–1.7)	0.9
Bromocarbons						
Methyl Bromide	CH_3Br	N	0.004	<< 0.001	6.61 (–0.06)	0.8
Halon 1211	$CBrClF_2$	Y	0.29	0.001	3.03 (–0.09)	16
Halon 1301	$CBrF_3$	Y	0.30	0.001	3.31 (0.01)	72
Halon 2402	$CBrF_2CBrF_2$	Y	0.31	< 0.001	0.396 (–0.03)	28
Fully fluorinated species						
Sulfur Hexafluoride	SF_6	Y	0.57	0.006	10.63 (0.35)	> 600
PFC-14	CF_4	N	0.09	0.005	87.4 (0.2)	~ 50 000
PFC-116	C_2F_6	N	0.25	0.001	5.03 (0.02)	~ 10 000
PFC-218	C_3F_8	N	0.28	< 0.001	0.721 (0.003)	~ 2600
PFC-318	c-C_4F_8	N	0.32	< 0.001	1.90 (0.01)	~ 3200

[a] Radiative efficiencies and lifetimes were taken from Appendix A in WMO (2018), except for SF_6 lifetime from Ray et al. (2017), CH_4 lifetime from Prather et al. (2012). For CO_2, numerous removal processes complicate the derivation of a global lifetime. AGGI = Annual Greenhouse Gas Index. For radiative forcing, see https://www.esrl.noaa.gov/gmd/aggi/aggi.html

[b] Mole fractions are global, annual surface means determined from NOAA Global Greenhouse Gas Reference Network marine boundary layer sites, except for PFC-14, PFC-116, PFC-218, PFC-318, and HFC-23, which were measured by AGAGE (Mühle et al. 2010; Miller et al. 2010). Changes indicated in brackets are the differences between the 2021 and 2020 means. These values differ from the growth rates reported in the main text and figures, which represent the net addition of a LLGHG to the atmosphere over the course of a year, calculated by differencing (approximately) the 1 Jan atmospheric abundances in successive years. All values are preliminary and subject to minor updates.

[c] Global mean estimates derived from multiple NOAA measurement programs ("Combined Dataset").

with emissions (including ~5% from cement production) increasing from 3.0 ± 0.2 Pg C yr^{-1} in the 1960s to 9.5 ± 0.5 Pg C yr^{-1} in the past decade (2011–20; Friedlingstein et al. 2021). About half of the overall FF emitted CO_2 since 1958 has remained in the atmosphere, while the rest has been stored by the ocean and the terrestrial biosphere. While emissions of CO_2 from FF combustion drive are increasing atmospheric burden, the interannual variability in the CO_2 growth rate is mostly driven by terrestrial biosphere exchange of CO_2, which is confirmed by measurements of its ^{13}C:^{12}C ratio (e.g., Keeling et al. 1985; Alden et al. 2010). Terrestrial biosphere flux variability is influenced by both temperature and moisture anomalies (Cox et al. 2013; Hu et al. 2019; Humphrey et al. 2018) often associated with ENSO.

For 2020, FF CO_2 emissions declined by 5.4%, relative to 2019, due to the COVID-19 pandemic (Friedlingstein et al. 2021). However, this reduction is not obvious in observed global atmospheric CO_2 signals, because it is a relatively small signal compared with the natural variability from terrestrial biosphere exchange. The estimated 5.4% reduction in global CO_2 emissions of 10 Pg C yr^{-1} would result in a ~0.24 ppm decrease in global CO_2 (given a conversion factor of 2.12 Pg C ppm^{-1}; Ballantyne et al. 2012), which is within the 1 std. dev. interannual variability of 0.4 ± 0.1 ppm yr^{-1} of CO_2 annual growth in 2010–19. Yet at least one analysis has detected regional impacts of COVID-19 on total column-CO_2 (Weir et al. 2021). Preliminary data for 2021 suggest a rebound in FF CO_2 emissions relative to 2020 of +4.9 ± 0.8% globally (Friedlingstein et al. 2021).

While a pulse of CO_2 will last in the atmosphere for thousands of years (Archer and Brovkin 2008), atmospheric CH_4 has a lifetime of about nine years, meaning that its atmospheric abundance (and radiative forcing) can be reduced much more quickly (United Nations Global Methane Assessment 2021). Global mean tropospheric CH_4 abundance increased to 1895.7 ± 0.6 ppb (parts per billion by moles in dry air) in 2021, a 162% increase compared to its pre-industrial level of 722 ± 15 ppb. Since the beginning of NOAA's systematic CH_4 measurements in 1983, global CH_4 abundance rose and then flattened prior to 2006 (Fig. 2.50b), which is consistent with an approach to steady state if there was no trend in its lifetime driven by CH_4 sinks (Dlugokencky et al. 2003). Atmospheric CH_4 growth restarted in 2007 and has significantly accelerated since 2014 (Fig. 2.50b). Preliminary measurement results show continued large growth in 2021, about 18.1 ± 0.4 ppb, following a similarly large increase seen in 2020 (15.1 ± 0.4 ppb).

Given the complexity of the CH_4 budget, the scientific community has not reached consensus on reasons for the magnitudes and long-term trends of many CH_4 sources. Fossil fuel exploitation is estimated to account for ~19% of total global CH_4 emissions since 2000 based on top-down approaches that use atmospheric CH_4 measurements and inverse models (Saunois et al. 2020). However, studies including radioactive (^{14}C:C) or stable (^{13}C:^{12}C) carbon isotope ratios of CH_4 suggest a much larger fraction of fossil emissions (~30% in 1984–2016; Lassey et al. 2007; Schwietzke et al. 2016; Lan et al. 2021). Measurements of ^{13}C:^{12}C in CH_4 also suggest that increased emissions from biogenic sources (e.g., wetlands and ruminant animals) are the dominant drivers for the post-2006 growth (Lan et al. 2021; Chang et al. 2019; Nisbet et al. 2019; Schaefer et al. 2016; Schwietzke et al. 2016).

It is an ongoing investigation to decipher the post-2019 CH_4 surge. A reduction in the global abundance of the hydroxyl radical (OH, the main sink for CH_4) may have contributed to the growth in 2020 due to the COVID-19 pandemic reduction in major OH precursors, NO_x and CO (Laughner et al. 2021). However, reduced OH abundance due to COVID-related pollution reductions is unlikely to contribute significantly to the continued rapid increase in 2021.

Nitrous oxide (N_2O) is an ozone-depleting LLGHG mainly emitted from natural and agricultural soils, animal manure, and the oceans (Ravishankara et al. 2009; Davidson 2009). Its atmospheric lifetime is about 123 years (Ko et al. 2013). Atmospheric N_2O has been increasing steadily throughout the industrial era, except for a brief period in the 1940s (MacFarling Meure et al. 2006; Thompson et al. 2019). The mean global atmospheric N_2O abundance in 2021 was 334.3 ± 0.1 ppb, a 24% increase over its preindustrial level of 270 ppb. The annual increase of 1.3 ± 0.1 ppb in 2021

(Fig. 2.50c) was higher than the average annual increase over 2011–20 (1.0 ± 0.2 ppb) and was the third highest growth since 2001. It is an ongoing investigation to understand the drivers for the large N_2O growth in 2021 and the record growth in 2020 (1.4 ± 0.1 ppb).

The increased burdens of LLGHGs are largely responsible for increasing global temperature (IPCC 2013). The impacts of these LLGHGs on global climate are estimated based on their abilities to change the global radiative energy balance. Compared with preindustrial times (1750), increasing atmospheric CO_2 abundance has increased radiative forcing by > 2.1 W m^{-2}. The increase in CH_4 has contributed to a 0.53 W m^{-2} increase in direct radiative forcing while the CH_4-related production of tropospheric O_3 and stratospheric H_2O has also contributed to ~0.30 W m^{-2} indirect radiative forcing (Myhre et al. 2014). While the atmospheric burdens of some greenhouse gases, such as chlorofluorocarbons, have declined in recent decades, the combined radiative forcing of CO_2, CH_4, and N_2O, in addition to other LLGHGs (all of which are halogenated compounds), has increased each year (Fig. 2.51). In 2021, the combined radiative forcing from all LLGHGs (Table 2.10) was 3.2 W m^{-2}, which is 3.6 times greater than in 1950, at the start of the "Great Acceleration." NOAA's Annual Greenhouse Gas Index (AGGI; Fig. 2.51) summarizes trends in the combined direct radiative forcing by all LLGHGs (Hofmann et al. 2006). This index represents the annual cumulative radiative forcing of LLGHGs relative to the Kyoto Protocol baseline year of 1990. The AGGI value of 1.49 in 2021 indicates an increase of 49% in radiative forcing of LLGHGs compared to 1990.

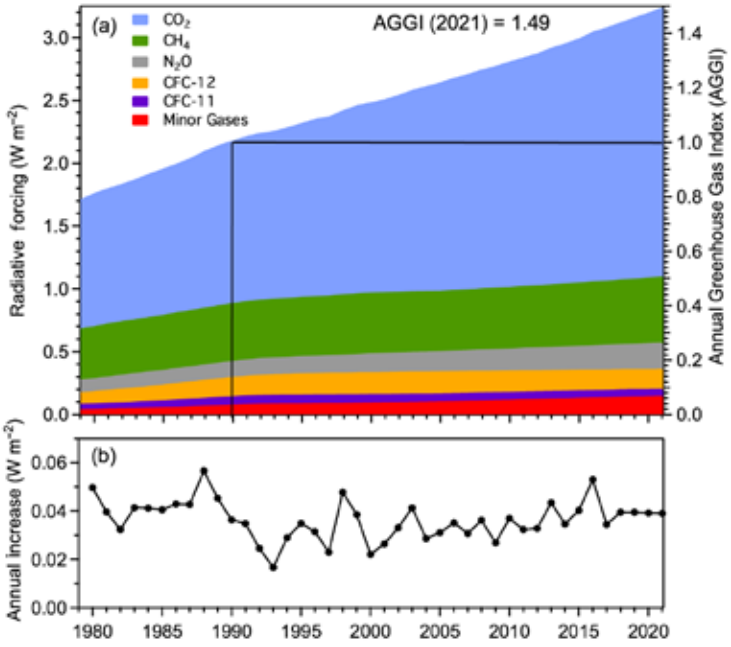

Fig. 2.51. (a) Direct radiative forcing (W m^{-2}) due to five major long-lived greenhouse gases (LLGHG) and 15 minor gases (left axis; see Table 2.10 for details of the 15 minor gases) and the associated values of the NOAA AGGI (right axis). The Annual Greenhouse Gas Index (AGGI) is defined to have a value of 1 in 1990. (b) Annual increase in direct radiative forcing (W m^{-2}).

2. OZONE-DEPLETING SUBSTANCES—I. J. Vimont, B. D. Hall, G. Dutton, S. A. Montzka, C. Siso, M. Crotwell, and M. Gentry

Halogenated trace gases affect the radiative energy balance of the atmosphere and climate through their direct absorption of infrared energy and through their ability to deplete stratospheric ozone (Karpechko and Maycock 2018). Halogenated compounds, such as chlorofluorocarbons (CFCs), hydrochlorofluorocarbons (HCFCs), hydrofluorocarbons (HFCs), chlorocarbons, and bromocarbons are controlled by the 1987 Montreal Protocol (https://www.unep.org/ozonaction/who-we-are/about-montreal-protocol) and its subsequent amendments.

The effect of these controls can be seen clearly in the overall decline in the atmospheric abundance of many of the controlled gases (Engel and Rigby 2018); however, even after production ceases, declines in atmospheric abundance vary by compound because these chemicals have different lifetimes, as well as different sizes of "banks" (i.e., reservoirs of produced, but not yet emitted chemicals). For example, by 2021, CFC-11 and CFC-12 had declined from their peak abundance by only around 17% and 9% despite a reported global phase-out by 2010, whereas methyl chloroform (phased out in 2015) had decreased by 99% (Fig. 2.52; Table 2.10). These differences are explained by 50-yr and 100-yr lifetimes for the CFCs versus 5 years for methyl chloroform, and the presence of substantial (and leaky) banks for the CFCs, but not for methyl chloroform.

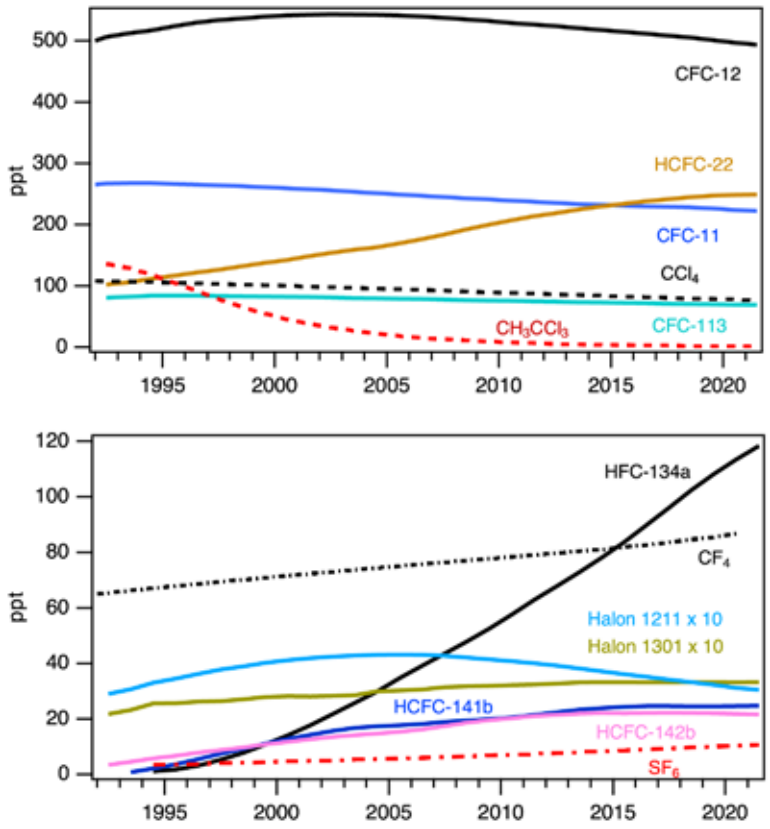

Fig. 2.52. Global mean abundances (mole fractions) at Earth's surface (parts per trillion = nmol mol^{-1} in dry air) for several halogenated gases, many of which also deplete stratospheric ozone. See Table 2.10 for the 2021 global mean mole fractions of these and other gases.

Long-term monitoring of the abundances of these species has proved to be important for ensuring the success of the Montreal Protocol. The decline of CFC-11 mole fractions in the atmosphere slowed down unexpectedly after 2012, which led to the discovery of renewed increases in global emissions through 2018 (Montzka et al. 2018; Rigby et al. 2019). Shortly after this discovery was announced in 2018, the mole fraction decline observed for CFC-11 accelerated to rates that were comparable to those measured before 2012. One possible, yet unverified, cause of the observed decline in CFC-11 global emissions is a decrease in unreported production of this chemical (Montzka et al. 2021).

HCFCs are another important set of ozone-depleting compounds controlled by the Montreal Protocol, and overall trends in recent years reflect reduced levels of production and consumption. A select number of HFCs, which are used as substitutes for ozone depleting substances (ODSs) in some applications, are scheduled for phase down by the Kigali Amendment to the Montreal Protocol, but these controls are only now coming into effect so have not substantially altered their mole fraction tendencies; some HFCs, such as HFC-134a, are steadily increasing in the atmosphere.

Equivalent effective stratospheric chlorine (EESC) is a measure of the reactive ozone-depleting halogen loading at a given time and place in the stratosphere, calculated from global mean surface mole fractions and consideration of mixing processes, time-dependent trace gas destruction in the stratosphere, and the relative ozone-destruction efficiency of bromine versus chlorine (Daniel et al. 1995; Montzka et al. 1996; Newman et al. 2007). Midlatitude EESC is calculated using a 3-year mean age-of-air, while Antarctic EESC is calculated with a 5.5-year mean age-of-air, as detailed in Newman et al. (2007). The abundance of reactive halogen in the midlatitude stratosphere is lower than in the Antarctic stratosphere, because air reaching the Antarctic has been in the stratosphere longer and has been transported to higher altitudes, which leads to more ODS destruction and release of reactive halogen (Montzka, Reimann et al. 2011). Most of the reactive

halogen in the atmosphere is due to CFCs, and they contribute strongly to EESC (Fig. 2.53) and still have high abundance in the atmosphere.

At the beginning of 2021, EESC in the midlatitudes was 1549 ppt, which represents a 20% decrease from its maximum value of 1936 ppt in 1997 (https://www.gml.noaa.gov/odgi; Fig. 2.53a). Antarctic EESC was 3659 ppt at the beginning of 2021, a 12% decrease from its maximum value of 4152 in 2001 and 2002 (https://www.gml.noaa.gov/odgi; Fig. 2.53b). To provide context for changes in the EESC, the Ozone Depleting Gas Index (ODGI) was developed. The ODGI is derived for both the midlatitude and Antarctic stratosphere by rescaling EESC values in these regions, where an ODGI of 100 represents the peak EESC value, and 0 represents the value of EESC at 1980 (Hoffmann and Montzka 2009; https://www.gml.noaa.gov/odgi). Ozone destruction had already begun by 1980, but a return of stratospheric halogen to levels last seen in 1980 would represent a major milestone for the Montreal Protocol. At the beginning of 2021, the Antarctic ODGI (ODGI-A) was 75.3 and midlatitude ODGI (ODGI-M) was 50.1. Reactive halogen abundance in the Antarctic stratosphere has declined 24.7% (100% minus 75.3%) of the way back to the 1980 benchmark value. In the midlatitudes, the decline is nearly half of that needed to reach the 1980 benchmark value. Currently, ODGI-A and ODGI-M are projected to reach 0 around 2076 and 2049, respectively (Carpenter et al. 2018; https://www.gml.noaa.gov/odgi).

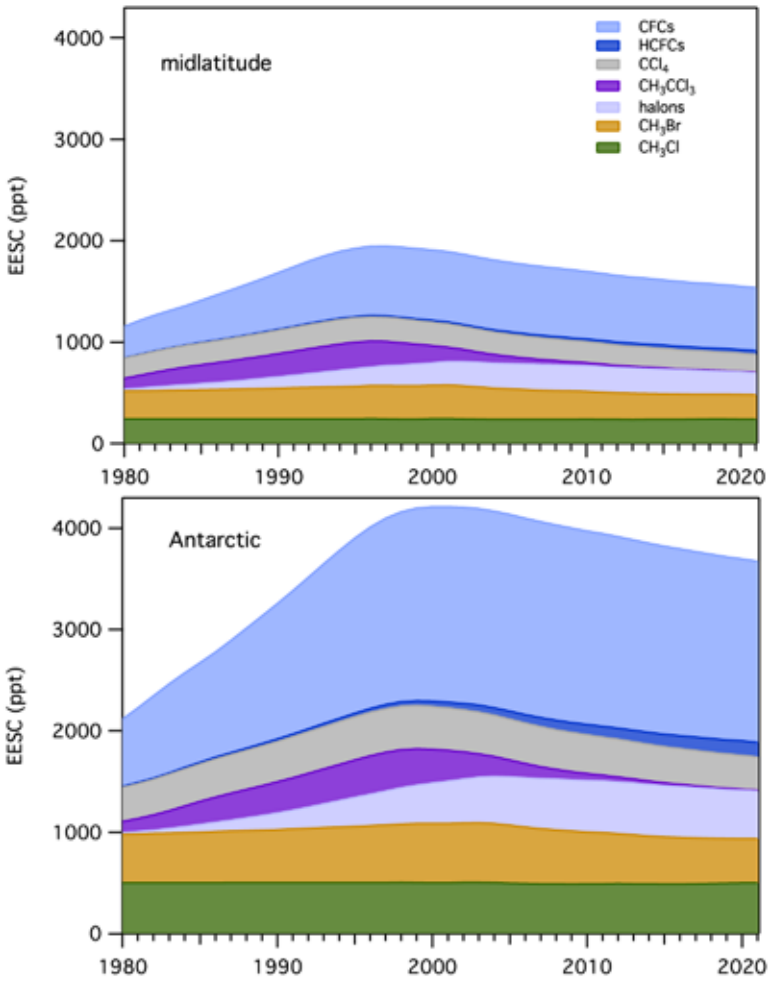

Fig. 2.53. Equivalent effective stratospheric chlorine (EESC, ppt) for the (a) midlatitude and (b) Antarctic stratosphere derived from surface measurements. The EESC values represent EESC on 1 Jan of each year.

3. AEROSOLS—S. Rémy, N. Bellouin, Z. Kipling, M. Ades, A. Benedetti, and O. Boucher

Aerosols represent a serious public health issue in many countries and hence are subject to monitoring and forecasting worldwide as part of air quality policies. Atmospheric aerosols also play an important role in the climate system, by scattering and absorbing radiation and by affecting the life cycle, optical properties and precipitation activity of clouds (IPCC 2021).

The Copernicus Atmosphere Monitoring Service (CAMS; http://atmosphere.copernicus.eu) runs a near-real time (NRT) global analysis of aerosols and trace gases. The CAMS project also produced a reanalysis of global aerosols and trace gases that covers the years 2003 to 2021: the CAMS reanalysis (Inness et al. 2019), by combining state of the art numerical modeling and aerosol remote sensing retrievals from MODIS (Levy et al. 2013) and the Advanced Along Track Scanning Radiometer (AATSR; Popp et al. 2016). Verification of aerosol optical depth (AOD) at 500 nm, against independent AERONET observations, shows that the CAMS reanalysis has a smaller bias and error than its predecessors: the CAMS interim reanalysis (Flemming et al. 2017) and the MACC reanalysis (Inness et al. 2013). This section uses data exclusively from the CAMS reanalysis.

AOD at 550 nm in 2021 (Fig. 2.54a) shows maxima over the polluted regions of India and China, as well as from dust over the Sahara and the Middle East. High values from seasonal or occasional extreme fires are seen over equatorial Africa and Siberia. The high values over Hawaii and close to Mexico City are a known artifact of the CAMS reanalysis related to volcanic outgassing. Figure 2.54b shows the time series of monthly and annual globally-averaged total AOD during 2003–21. Figure 2.54b shows strong seasonality, driven mainly by dust episodes between March and July in the Sahara, Middle East, and Taklimakan/Gobi deserts and seasonal biomass burning in Africa, South America, and Indonesia. Globally averaged AOD in 2021 was on average slightly higher than in 2020, by 0.6%, but with marked seasonal differences: the boreal summer months saw some of the highest values since 2003, but the winter months saw the lowest values since 2014/15. A series of exceptional fires in Siberia and North America contributed to the high values in July and August.

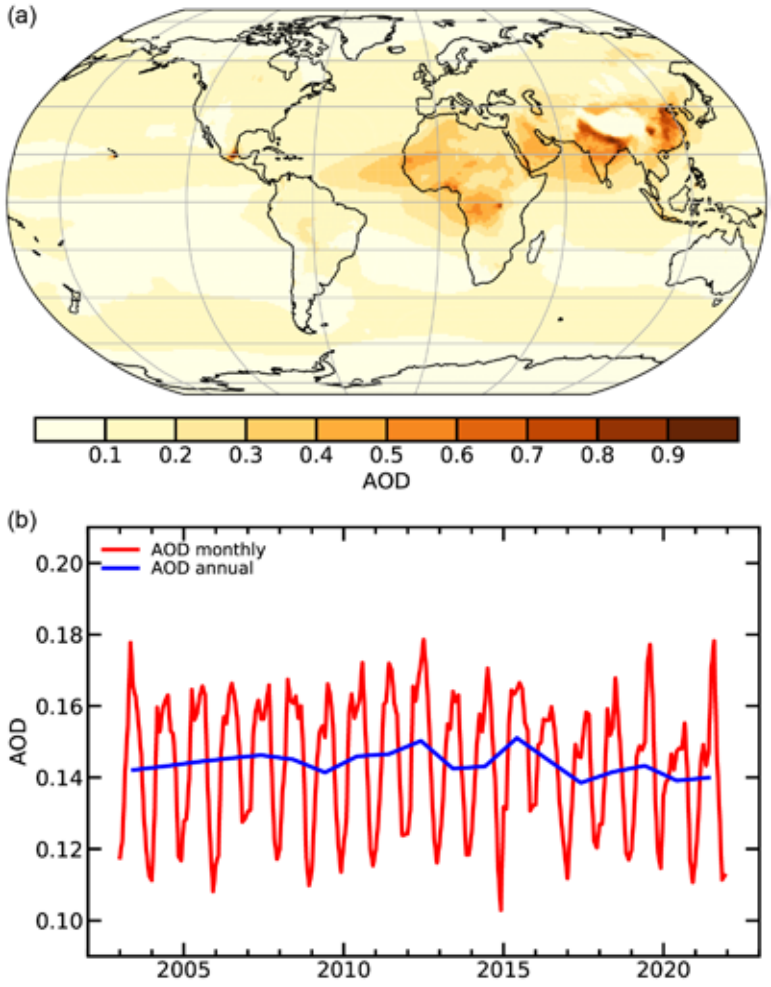

Fig. 2.54. (a) Global aerosol optical depth (AOD) at 550 nm in 2021. (b) Global average of total AOD at 550 nm averaged over monthly (red) and annual (blue) periods for 2003–21.

These exceptionally large biomass burning aerosol events caused the positive anomalies relative to the 2003–20 mean over Siberia and parts of North America in Plates 2.1u,v, while the positive anomalies over India and Iran were mostly caused by anthropogenic pollution events and are consistent with a positive AOD trend in these regions (see Figs. 2.55b,c). These fires also explain most of the extreme aerosol days shown in Plates 2.1u,v. Two large volcanic eruptions occurred in 2021. The Cumbre Vieja volcano (September) in the Canary Islands explains a positive anomaly there, while the Caribbean eruption of La Soufriere in Saint Vincent (April) injected a small amount of aerosols into the stratosphere. Dust storm activity was, in general, less than usual over most of the Sahara and Taklimakan, while the negative AOD anomalies over East Asia, Europe, and the Amazon basin can be explained by ongoing long-term decreasing trends of aerosol emissions and burden in these regions.

These trends are shown in Figs. 2.55b (2003–21) and 2.55c (2012–21). Between 2003 and 2021, there are significant negative AOD trends over most of the United States, Europe, East Asia, and the Amazon basin, the latter from reduced deforestation and associated burning activity. Positive trends are noted over Siberia, driven by biomass burning events, as well as over India and Iran, driven by an increase in anthropogenic emissions (Satheesh et al. 2017). Between 2012 and 2021, the picture is slightly different: there is no decreasing trend over the United States and the Amazon basin, indicating that most of the 2003–21 trend can be explained by changes between 2003 and 2012. Similarly, the 2012–21 negative trend over Europe is smaller than the 2003–21 trend, while it is the opposite over East Asia, which is consistent with the observed decrease of most anthropogenic emissions there since around 2012 (Li et al. 2017). A stronger positive trend between 2012 and 2021 is noted over most of Iran, while over the same period the positive trend over India is smaller than the 2003–21 trend.

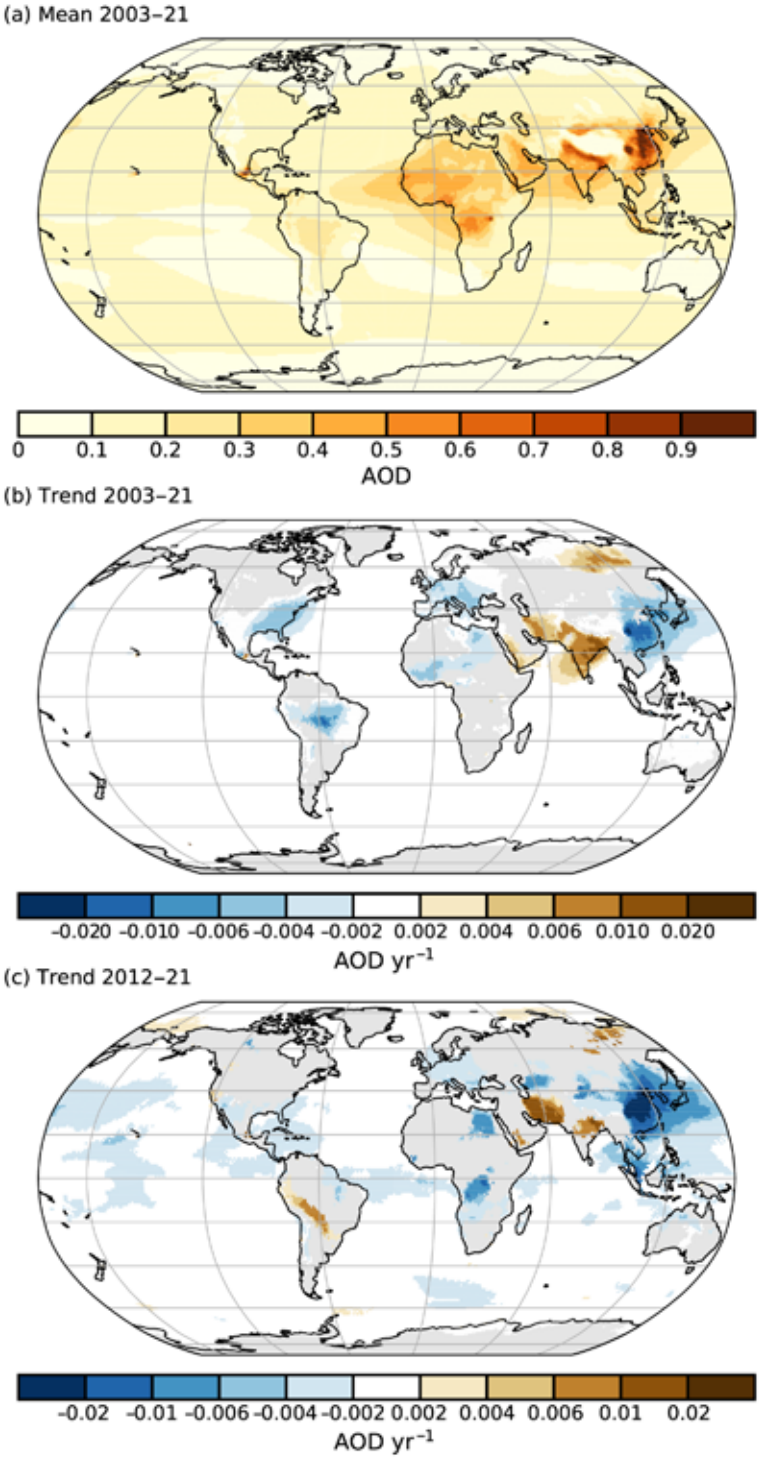

Fig. 2.55. (a) Total AOD at 550 nm averaged over the period 2003–21. Note the regional differences, with much greater total AOD values over parts of northern Africa, the Arabian Peninsula, southern Asia, and eastern China. Linear trends of total AOD (AOD unit yr^{-1}) for (b) 2003–21 and (c) 2012–21. Only trends that are statistically significant (95% confidence level) are shown. Regions with decreasing trends include the eastern United States, most of Europe, parts of Brazil and China, as well as the Korean Peninsula and Japan.

The AOD climatology between 2003 and 2021 (Fig. 2.55a) is close to the 2021 mean; it shows maxima over the highly populated regions of India and China, mainly caused by anthropogenic emissions, as well as over the Sahara, Middle East, and Taklimakan/Gobi from desert dust, and over central Africa, Indonesia, and the Amazon basin from fire emissions. The high values over Hawaii and close to Mexico City are a known artifact of the CAMS reanalysis related to volcanic outgassing.

Anthropogenic AOD and radiative forcing resulting from aerosol–radiation (RFari) and aerosol–cloud interactions (RFaci) are shown in Fig. 2.56 for 2021 and the period 2003–21. They are estimated using the methods described in Bellouin et al. (2020). The year 2021 was characterized by lower anthropogenic AOD and weak RFari and RFaci relative to the past 19 years. This decreasing trend is not yet statistically significant but is consistent with the decreasing trends in industrial and smoke aerosols seen in many regions, as mentioned above. The AOD anomalies for 2021 shown in Plate 2.1u exert a relatively weak top-of-atmosphere radiative forcing in part because they are mostly caused by aerosols that are fairly absorbing, which decreases their ability to scatter radiation back to space. These aerosols, however, still exert a sizeable radiative forcing at the surface.

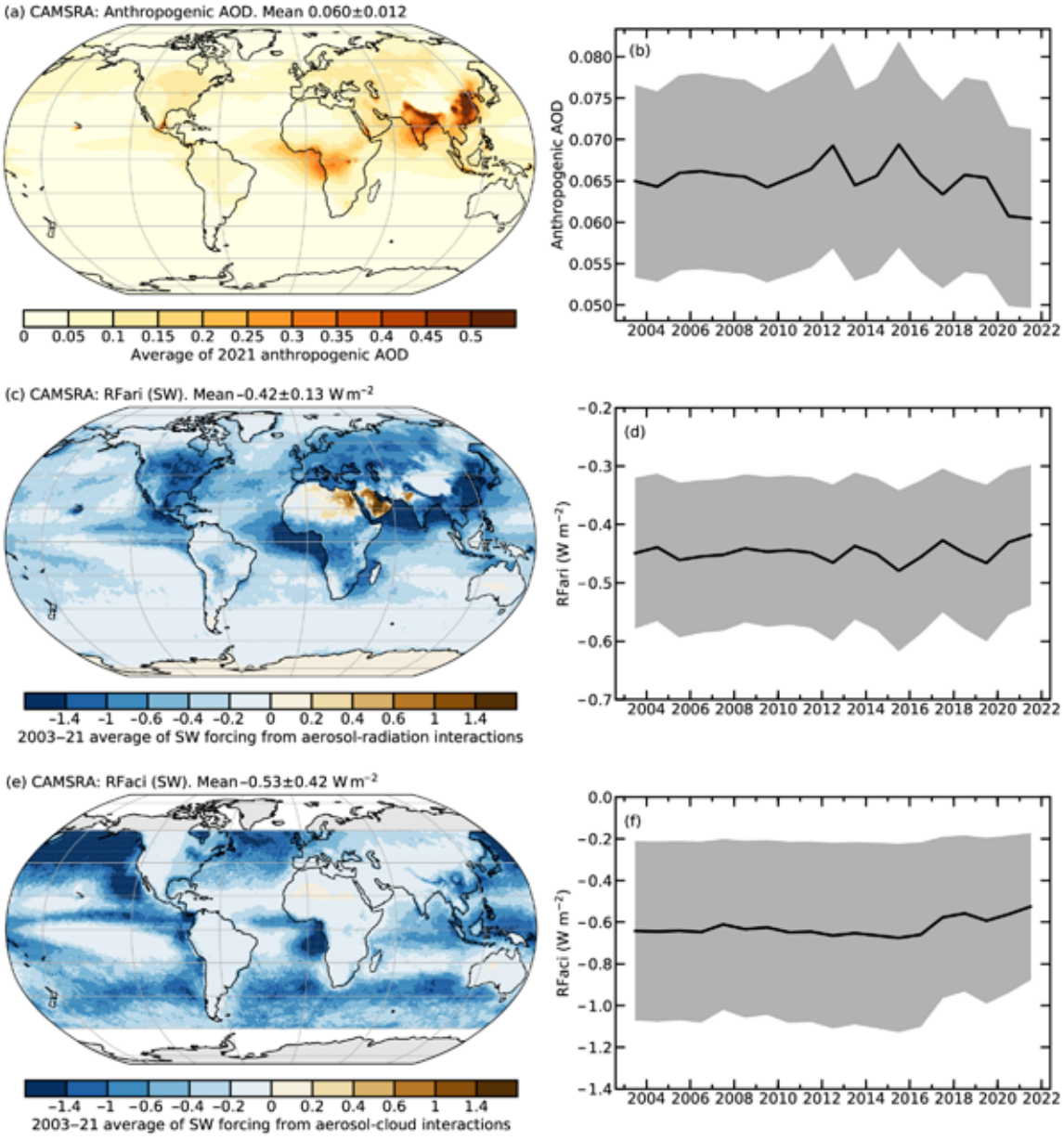

Fig. 2.56. CAMSRA (a) 2021 average of anthropogenic aerosol optical depth (AOD); (b) global annual average of anthropogenic AOD from 2003 to 2021. Radiative forcing (W m^{-2}) in the shortwave (SW) spectrum due to (c),(d) aerosol–radiation (RFari) and (e),(f) aerosol–cloud interactions (RFaci). The left column shows the average distribution for the period 2003–21. The right column shows a time series of global averages for the same period, with the 1-σ uncertainties of these estimates shown in gray.

4. STRATOSPHERIC OZONE—M. Weber, W. Steinbrecht, C. Arosio, R. van der A, S. M. Frith, J. Anderson, L. M. Ciasto, M. Coldewey-Egbers, S. Davis, D. Degenstein, V. E. Fioletov, L. Froidevaux, D. Hubert, D. Loyola, C. Roth, A. Rozanov, V. Sofieva, K. Tourpali, R. Wang, and J. D. Wild

Ninety percent of atmospheric ozone resides in the stratosphere with a maximum in the lower stratosphere. Stratospheric ozone protects Earth's biosphere from harmful ultraviolet (UV) radiation. Increases in anthropogenic ozone-depleting substances (ODS) thinned stratospheric ozone until the mid-1990s. The phase-out of ODS, mandated by the Montreal Protocol in the late 1980s (section 2g2), slowed stratospheric ozone loss, with some regions now showing a slow recovery. In addition, the rate and even the sign of long-term ozone changes depend on changes in chemical composition and stratospheric circulation caused by increasing concentrations of long-lived greenhouse gases (LLGHG) and varies by region and altitude. The clearest signs of ozone recovery related to ODS changes are evident in the upper stratosphere (WMO 2018).

The annual mean total ozone distribution in 2021 (Plate 2.1x) shows generally negative ozone global anomalies, except for two bands centered near 20° latitude on both sides of the equator, where ozone is higher by about 5 DU than the decadal mean (1998–2008). This pattern (low ozone in the inner tropics and high ozone in the outer tropics) is typical during the easterly wind shear phase of the quasi-biennial oscillation (QBO-east). During QBO-east, the meridional stratospheric circulation is generally stronger, resulting in enhanced ozone transport into the subtropical latitudes (Baldwin et al. 2001; Weber et al. 2011; Lawrence et al. 2020; Plate 2.1x). Negative total ozone anomalies in the Southern Hemisphere extratropics are possibly related to the combination of the unusually long-lasting Antarctic ozone hole of 2020, extending into 2021, and the large ozone hole in the second half of 2021. The westerly phase of the QBO in late autumn of 2020 likely resulted in weaker ozone transport and higher polar ozone deficits in the Northern Hemispheric winter of 2021.

Figure 2.57 shows the long-term evolution of annual total column ozone for different zonal bands (near-global, NH, tropics, and SH), and for polar caps in March (for the NH cap) and October (for the SH cap). These are the months when polar ozone losses are usually at their maximum after a cold stratospheric winter in the respective hemispheres, which occurs every year in the SH ("ozone hole") but is more sporadic in the NH (see sections 6h and 5j, respectively). Total ozone shows above-average total ozone levels in 2021 in the outer tropical/subtropical region (Plate 2.1x). At middle latitudes, total ozone is at the lower range of the values from the last two decades (Figs. 2.57b,e; Plate 2.1x). Total ozone was near the minimum annual mean values observed during the entire 43-year satellite observation period in the SH extratropics and above Antarctica in October (Figs. 2.57d,e; see section 6h).

ODS-related total ozone changes since 1996 are on the order of +0.5% decade^{-1} in the extratropics of both hemispheres, but opposing long-term changes in atmospheric dynamics contributed to near-zero overall trends in the NH extratropics from 2000 to present (Coldewey-Egbers et al. 2022; Weber et al. 2022). Mean total ozone levels during the period 2017–20 are still 4% and 5% below the 1964–1980 mean in the extratropics of the NH and SH extratropics, respectively (Figs. 2.57b,d; Weber et al. 2022).

Figure 2.58 shows ozone time series at two altitudes in the lower (50 hPa/22 km altitude) and upper stratosphere (2 hPa/42 km altitude). The ozone evolution at both levels is broadly consistent with the projected range from various models of the Phase 1 Chemistry Climate Model Initiative (CCMI) using current scenarios of ODS and GHG changes (thick gray line in Fig. 2.57a and shaded area in Fig. 2.58; SPARC/IO3C/GAW 2019).

In 2021 SH extratropical lower stratospheric ozone was close to the lowest values seen in the last decade but higher than in 2020. The lower values are related to the above-average sizes of the Antarctic ozone holes in 2020 and 2021 (see section 6h).

The earliest and clearest sign of ODS-related ozone recovery was detected in the upper stratosphere, where dynamic variability plays a lesser role (e.g., Newchurch et al. 2003; Godin-Beekmann

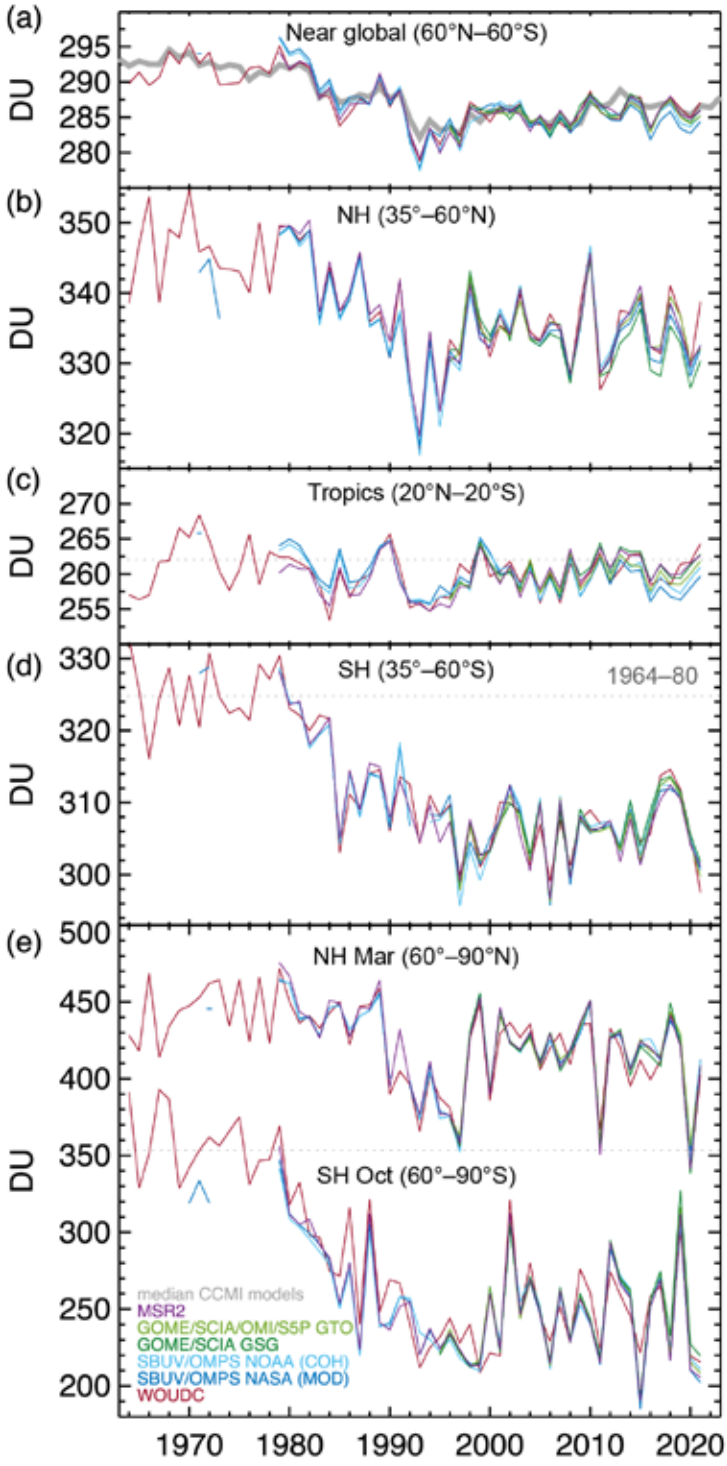

Fig. 2.57. Time series of annual mean total column ozone (DU) for (a) global (60°S–60°N), (b) NH (35°–60°N), (c) tropics (20°S–20°N), and (d) SH (35°–60°S); and (e) polar (60°–90°) total column ozone in Mar (NH) and Oct (SH), the months when polar ozone losses usually are largest. Data are from WOUDC (World Ozone and Ultraviolet Radiation Data Centre) ground-based measurements combining Brewer, Dobson, SAOZ (Système D'Analyse par Observations Zénithales), and filter spectrometer data (red: Fioletov et al. 2002, 2008); the BUV/SBUV/SBUV2/OMPS merged products from NASA (V8.7. dark blue, Frith et al. 2014, 2017), and NOAA (V8.8, light blue: J. D. Wild and L. M. Ciasto, person. comm. 2019); the GOME/SCIAMACHY/GOME-2 products GSG from University of Bremen (dark green, Weber et al. 2022), and GTO from ESA/DLR (light green, Coldewey-Egbers et al. 2015; Garane et al. 2018). MSR-2 (purple) assimilates nearly all ozone datasets after corrections based on the ground-based data (van der A et al. 2015). All datasets have been bias-corrected by subtracting averages for the reference period 1998–2008 and adding back the mean of these averages. The dotted gray lines in each panel show the average ozone level for 1964–80 calculated from the WOUDC data. The thick gray line (panel a) shows the median from chemistry-climate (CCMI)-1 ref C2 model runs (SPARC/IO3C/GAW 2019). Most of the observational data for 2021 are preliminary.

et al. 2022). Upper stratospheric ozone has shown an increase of about +2% decade^{-1} since the late 1990s (e.g., Steinbrecht et al. 2017; Arosio et al. 2019; Szelag et al. 2020; Sofieva et al. 2021; Godin-Beekmann et al. 2022). In general, ozone observations in the lower stratosphere suggest little change or even a continuing decline over the last two decades (Fig. 2.58; Ball et al. 2018, 2020; Chipperfield et al. 2018; Wargan et al. 2018; Godin-Beekmann et al. 2022).

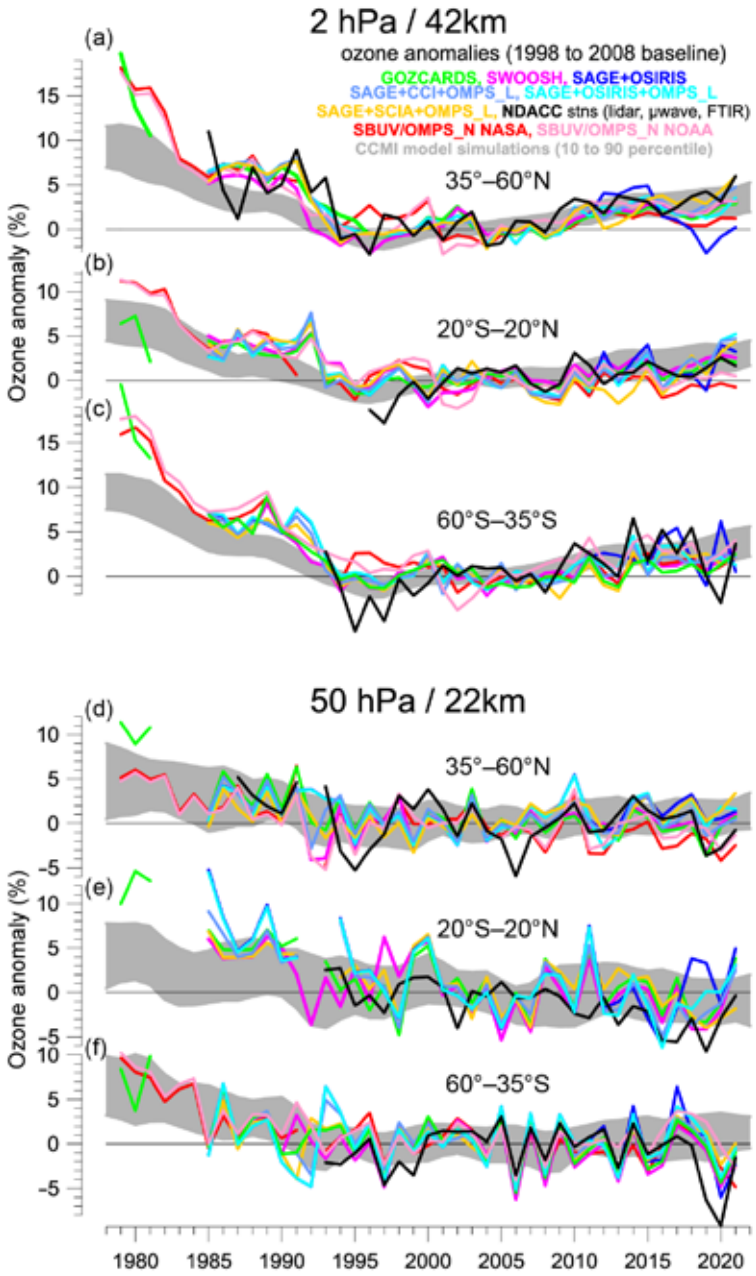

Fig. 2.58. Annual mean anomalies of ozone (%) in (a–c) the upper stratosphere near 42-km altitude or 2-hPa pressure and (d–f) in the lower stratosphere, near 22 km or 50 hPa for the NH (35°–60°N; a,d), tropics (20°S–20°N; b,e), and SH (35°–60°S; c,f), respectively. Anomalies are GOZCARDS referenced to the 1998–2008 baseline. Colored lines are long-term records obtained by merging different limb (SWOOSH, SAGE+OSIRIS, SAGE+CCI+OMPS-L, SAGE+SCIAMACHY+OMPS-L) or nadir-viewing (SBUV, OMPS-N) satellite instruments. The nadir-viewing instruments have much coarser altitude resolution than the limb-viewing instruments. This can cause differences in some years, especially at 50 hPa. The black line is from merging ground-based ozone records at seven NDACC stations employing differential absorption lidars and microwave radiometers. See Steinbrecht et al. (2017), WMO (2018), and Arosio et al. (2018) for details on the various datasets. Gray shaded area shows the range of chemistry–climate model simulations from CCMI-1 refC2 (SPARC/IO3C/GAW, 2019). Ozone data for 2021 are not yet complete for all instruments and are still preliminary.

5. STRATOSPHERIC WATER VAPOR—S. M. Davis, K. H. Rosenlof, D. F. Hurst, H. Vömel, and R. Stauffer

The amount of water vapor (WV) entering the stratosphere is controlled to a large degree by temperature variability in the tropical tropopause layer (TTL; ~14–19 km) and particularly at the cold-point tropopause (CPT), with more WV entering the stratosphere when CPT temperatures are higher. Variations in this so-called entry value of water vapor exerts a strong influence on overall stratospheric WV concentrations, as methane oxidation in the upper stratosphere and mesosphere represents the only other consistent source for WV in the stratosphere. Thus, processes that lead to variations in TTL and CPT temperatures on various timescales can affect stratospheric WV on a global scale.

For quantifying interannual changes in stratospheric WV, the *Aura* satellite's Microwave Limb Sounder (MLS) instrument provides a nearly continuous global (82°S–82°N) record of measurements dating back to August 2004. In 2021, de-seasonalized tropical (15°S–15°N) WV anomalies from *Aura* MLS were positive (wet) for all but one month of the year in the lowermost stratosphere at 82 hPa (~17 km; Fig. 2.59b). These WV anomalies ranged from −0.02 ppm (parts per million, i.e., μmol mol^{-1}) in June to +0.6 ppm in November, corresponding to deviations from the climatological monthly mean of −1% and +16%, respectively.

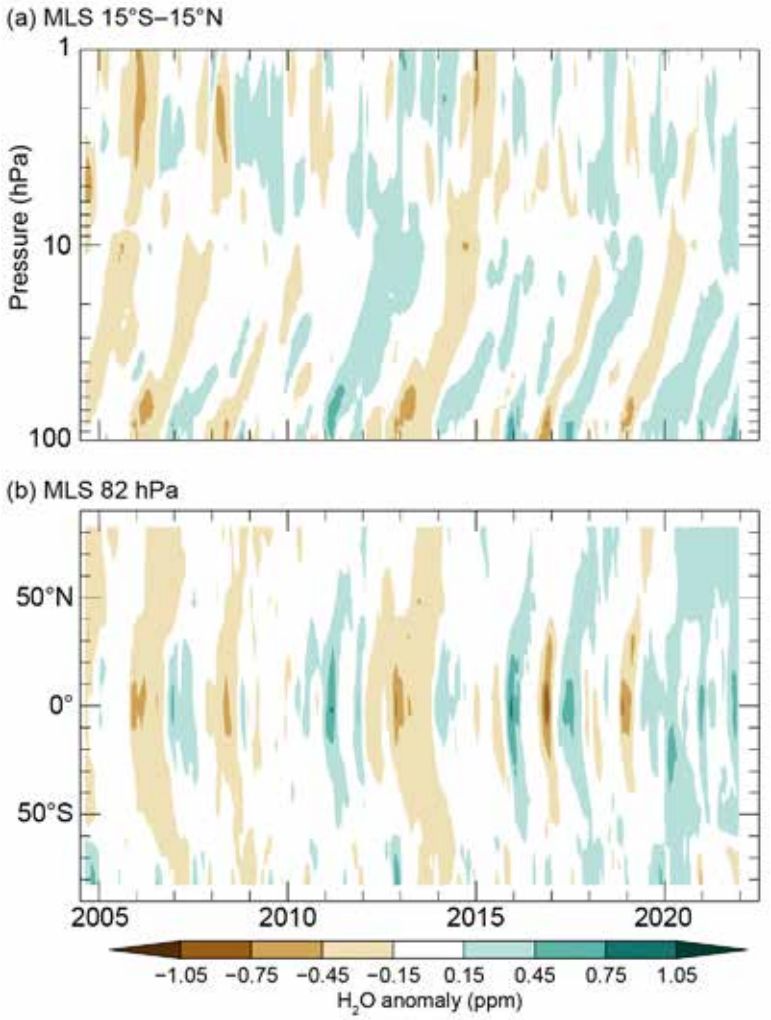

Fig. 2.59. (a) Time series of vertical profiles of tropical (15°S–15°N) lower stratospheric water vapor (WV) anomalies and (b) latitudinal distributions of WV anomalies (ppm) at 82 hPa. Both are based on version 5.0 *Aura* MLS data. Anomalies are differences from the mean 2004–20 WV mixing ratios for each month. (b) Propagation of tropical lower stratospheric WV anomalies (ppm) to higher latitudes in both hemispheres as well as the influences of dehydrated air masses from the Antarctic polar vortex as they are transported toward the SH midlatitudes at the end of each year. Tick marks denote the beginning of each year.

The tropical WV anomalies ascend in the so-called "tropical tape recorder" (i.e., the height–time plot of tropical-average WV showing the imprint of TTL temperatures on WV entering the stratosphere [Mote et al. 1996]) as illustrated in Fig. 2.59a, which shows a wet anomaly beginning around the middle of 2021 at 100 hPa and ascending for the duration of the year. At 100 hPa, the de-seasonalized tropical WV anomalies for August 2021 (+0.4 ppm, 8% above average) and September 2021 (+0.5 ppm, +11%) were the wettest over the MLS record for their respective months. In the following months, the strong positive anomalies were observed at the next highest MLS levels (82 hPa and 68 hPa) as the air ascended into the stratosphere as part of the mean meridional overturning circulation. The 82-hPa level had its wettest October on record (+0.4 ppm, +10%) in 2021, as did November (+0.4 ppm, +9%) and December (+0.4 ppm, +10%) at the 68 hPa level. The progression of these strong wet anomalies is illustrated further in Fig. 2.60, which shows maps of the anomalies as they propagate upward. In addition to propagating upwards, the 2021 tropical

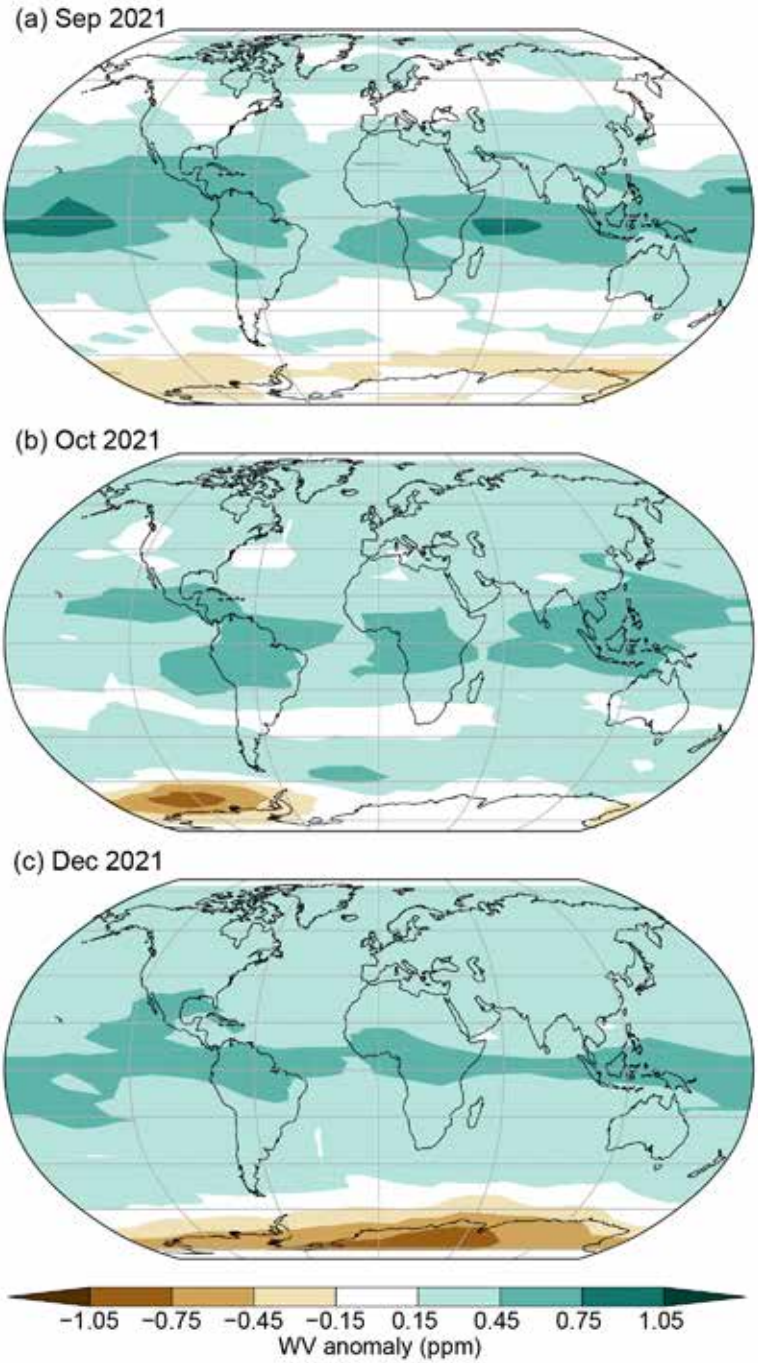

Fig. 2.60. Deseasonalized monthly lower stratospheric *Aura* Microwave Limb Sounder (MLS) version 5.0 anomalies (ppm; 2004–20 base period) at (a) 100 hPa in Sep 2021, (b) 82 hPa in Oct 2021, and (c) 68 hPa in Dec 2021.

WV anomaly exhibits a typical "U-shaped" behavior with time in the latitude–time plane at 82 hPa, as the anomalies propagate poleward in each hemisphere (Fig. 2.59b).

The behavior of lowermost stratospheric WV, observed by *Aura* MLS, is broadly consistent with balloon-borne frost point hygrometer soundings at five locations, as shown in Fig. 2.61. The newest version 5.0 of the MLS data, as well as the previous 4.2 version, are included in this figure to illustrate the reduction in drift relative to the frost point (FP) data in the newest version 5.0 data. Although the drift is not completely removed, the 2021 WV anomalies in v5.0 data are ~0.1 ppm less than in v4.2 for most sites. At the tropical stations, the WV anomalies are highly correlated with the tropical CPT temperature anomalies, as expected.

In 2021, the tropical CPT temperatures were anomalously high throughout the entire year, with an annual mean anomaly of +0.77K. It is well established that interannual variations in CPTs are correlated with interannual variability in climate phenomena such as the El Niño-Southern Oscillation (ENSO) and the quasi-biennial oscillation (QBO) in equatorial stratospheric winds (Dessler et al. 2014).

La Niña conditions were present for all months of 2021, except June and July (see section 4b). In boreal winter, La Niña is known to result in weaker tropical lower stratospheric upwelling, anomalously higher CPTs, and enhanced water vapor in the tropical lower stratosphere (e.g., Garfinkel

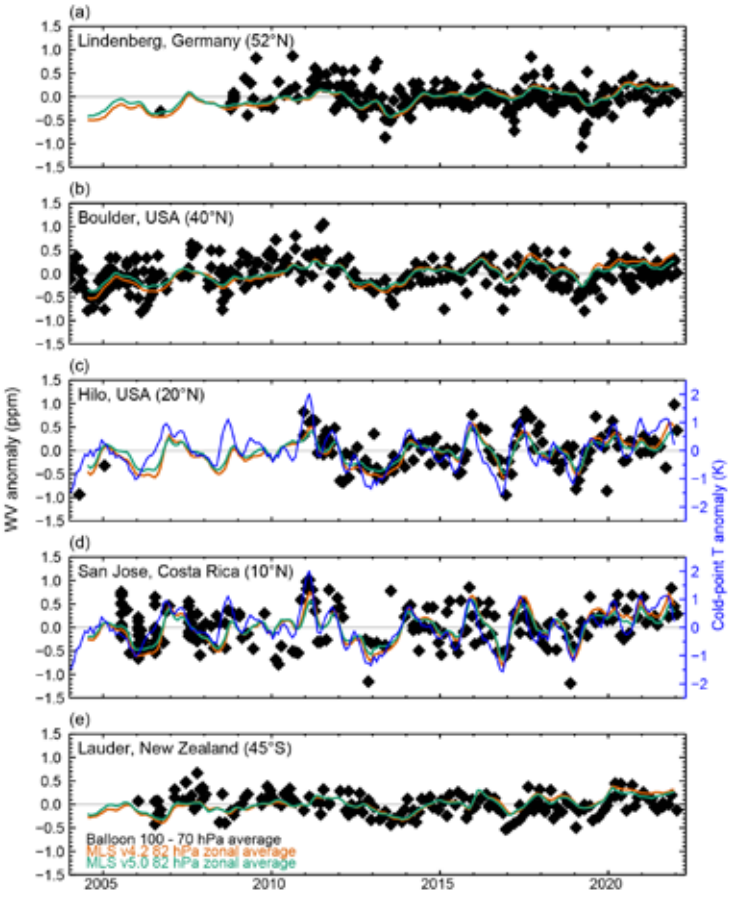

Fig. 2.61. Lower stratospheric water vapor (WV) anomalies (ppm) over five balloon-borne frost point (FP) hygrometer stations. (a–e) each shows the lower stratospheric anomalies of individual FP soundings (black) and of monthly zonal averages for versions 4.2 (orange) and 5.0 (green) of Microwave Limb Sounder (MLS) data at 82 hPa in the 5° latitude band containing the FP station (orange). The new MLS v5.0 data includes a correction for a drift contained in the earlier version 4.2 data (Hurst et al. 2016; Livesey et al. 2021), which were used in previous *State of the Climate* reports (e.g., Davis et al. 2021). High-resolution FP vertical profile data were averaged between 70 hPa and 100 hPa to emulate the MLS averaging kernel for 82 hPa. Each MLS monthly zonal mean was determined from 2000–3000 profiles. Anomalies for MLS and FP data are calculated relative to the 2004–20 period for sites except for Lindenberg (2009–21) and Hilo (2011–21). Tropical CPT anomalies based on the MERRA-2 reanalysis (d, blue curve), which are generally well correlated with the tropical lower stratospheric WV anomalies, are the driving force behind the variations in tropical WV during 2021.

et al. 2021). The positive anomalies in tropical lower stratospheric WV at the beginning of 2021 and again at the end of the year are consistent with the known behavior associated with La Niña.

Equatorial winds from the Singapore radiosonde wind data, which are a commonly used proxy for the QBO phase, were westerly at 50 hPa throughout 2021, until shifting to easterly in December. The QBO westerly phase is associated with anomalously weak tropical upwelling and anomalously high temperatures. Thus, although no formal attribution is attempted here, the combination of a La Niña phase and QBO westerlies likely contributed to the anomalously high CPTs and enhanced tropical lowermost stratospheric WV in 2021.

6. TROPOSPHERIC OZONE—O. R. Cooper, J. R. Ziemke, and K.-L. Chang,

Tropospheric ozone is a short-lived climate forcer that either originates naturally in the stratosphere or is produced in situ by photochemical reactions involving sunlight and precursor gases, such as nitrogen oxides (NO_x), non-methane volatile organic compounds, methane, and carbon monoxide (Archibald et al. 2020). Tropospheric ozone has a strong seasonal cycle that peaks in either spring or summer in response to the regional availability of sunlight, ozone precursors, and long-range transport (Cooper et al. 2014). Ozone precursors can originate naturally from wildfires, biogenic hydrocarbon emissions, lightning NO_x, and biogenic NO_x emissions from soils, and also from anthropogenic sources such as fossil fuel and biofuel combustion or crop burning. Tropospheric ozone also acts as a pollutant near the surface, impacting human health and vegetation (Fleming et al. 2018; Mills et al. 2018).

Long-term trends of tropospheric ozone were recently assessed by the IPCC (Gulev et al. 2021; Naik et al. 2021). An ensemble of chemistry-climate models indicates that the tropospheric ozone burden (TOB) has increased by 45% since 1850. The model-estimated present-day TOB of 347 ± 28 Tg agrees well with the observed value of 338 ± 6 Tg determined from satellite products and ozonesondes. An observation-based quantification of TOB is not possible prior to 1998 due to insufficient global coverage by satellites and ozonesondes (Gaudel et al. 2018). However, model estimates of a constant global increase of tropospheric ozone since the 1950s are consistent with the observed increase since the mid-1990s (Tarasick et al. 2019).

Combined *Aura* Ozone Monitoring Instrument (OMI) and Microwave Limb Sounder (MLS) satellite ozone measurements (OMI/MLS) indicate increasing TOB since the record began in 2004 (Ziemke et al. 2019). In 2021, broad regions of positive tropospheric column ozone (TCO) anomalies were found in the NH midlatitudes (~1.2 DU; 4%), with smaller anomalies of ~1 DU or less elsewhere (Plate 2.1y). Hemispheric and global TOB and their 95% confidence levels for 2021 were 159 ± 6 Tg (0°–60°N), 148 ± 8 Tg (0°–60°S), and 307 ± 10 Tg (60°S–60°N). Globally (60°S–60°N), the 2004–21 TOB increase was 1.48 ± 0.40 Tg yr^{-1}, or ~9% (Fig. 2.62). Spatially, the trends are overwhelmingly positive,

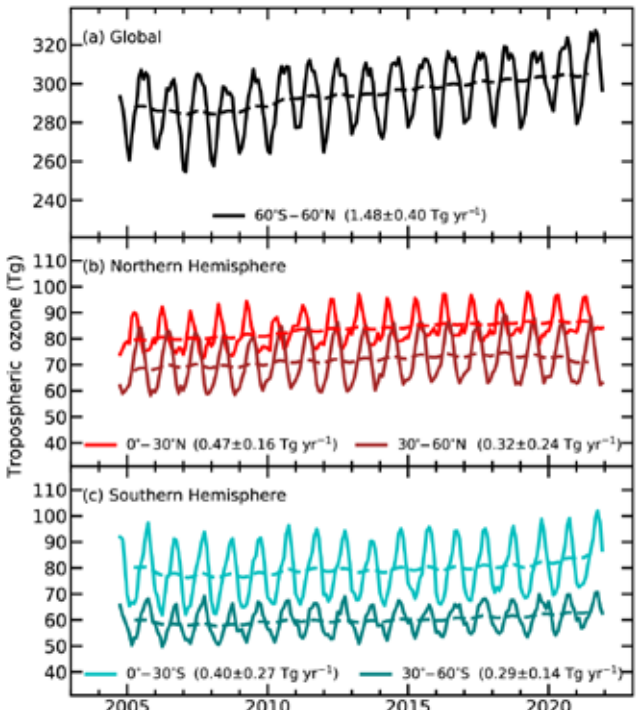

Fig. 2.62. Monthly averages (solid lines) and 12-month running means (dashed lines) of OMI/MLS tropospheric ozone burdens (Tg) from Oct 2004 through Dec 2021. (a) 60°S–60°N monthly averages with 12-month running mean, (b) monthly averages and running means for the NH tropics and midlatitudes, and (c) monthly averages and running means for the SH tropics and midlatitudes. Slopes of linear fits to the data are presented with their 95% confidence-level uncertainties. Vertical resolution of OMI/MLS monthly TCO is ~3 km about the tropopause with ~2 DU (7%) precision regionally; trend uncertainties are about 0.5 DU decade^{-1} (1.5% decade^{-1}).

reaching ~+3.2 DU decade^{-1} (~+1% yr^{-1}) east of China and Southeast Asia (Fig. 2.63), consistent with model simulations of increasing fossil fuel emissions from Southeast, East, and South Asia (Y. Zhang et al. 2016; Ziemke et al. 2019) and also consistent with ozone trends since the mid-1990s based on in situ observations in the boundary layer and free troposphere (Gaudel et al. 2020; Chang et al. 2022). Models indicate that ozone produced in these areas is transported northward and eastward in the free troposphere over the North Pacific Ocean (Zhang et al. 2020) as supported by the trend patterns in Fig. 2.63. Positive trends in the SH extra-tropics have been linked to a broadening of the Hadley circulation (Lu et al. 2018).

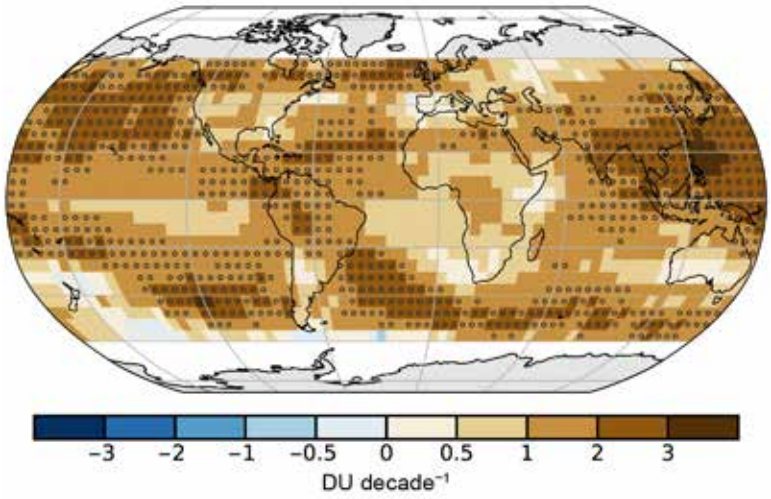

Fig. 2.63. Linear trends in OMI/MLS tropospheric column ozone (DU decade^{-1}) on a 5° × 5° grid from Oct 2004 through Dec 2021. Circles denote trends with *p*-values < 0.05. Trends were calculated using a multivariate linear regression model (e.g., Randel and Cobb 1994 and references therein) that included a seasonal cycle fit and the Niño 3.4 index as an ENSO proxy; trend uncertainties included autoregressive adjustment via Weatherhead et al. (1998).

At the surface, six baseline sites are available for quantifying multi-decadal ozone trends through the end of 2021 (Fig. 2.64; Table 2.11). At northern high latitudes, ozone increased at a rate of 0.57 ± 0.33 ppbv decade^{-1} since 1973 at Barrow Observatory, but decreased by 2.43 ± 0.97 ppbv decade^{-1} since 2000 at Summit, Greenland. At northern midlatitudes, ozone decreased by 0.96 ± 1.22 ppbv decade^{-1} since 1988 at Tudor Hill, Bermuda, but with large fluctuations. Mauna Loa Observatory, Hawaii, is located at the interface of the tropics and northern midlatitudes, allowing the ozone record to be split into mutually exclusive times series representing moist air (primarily a tropical origin) and dry air (primarily a midlatitude origin). Ozone in the MLO dry air (midlatitude) increased by 2.04 ± 0.41 ppbv decade^{-1} since 1974, while ozone in the MLO moist air (tropical) increased by 1.00 ± 0.38 ppbv decade^{-1}. In the southern high latitudes ozone at Arrival Heights, Antarctica has changed little since 1996. The trend at the South Pole, the most remote location on Earth, is +0.36 ± 0.37 ppbv decade^{-1} since 1975. While these data provide a range of trends at remote locations, they are too sparse to provide a global mean surface trend, and surface trends do not necessarily reflect trends in the free troposphere (Cooper et al. 2020).

Recent ozonesonde, lidar, and FTIR observations show a small ozone decrease in the NH mid- and lower troposphere (1–8 km) in 2020 in response to ozone precursor emissions reductions associated with the COVID-19 pandemic (Steinbrecht et al. 2021; Miyazaki et al. 2021). The decrease was strongest in the northern midlatitudes, with reductions of 5–6% above Europe and western North America (Chang et al. 2022). Future assessments will determine if this decrease was a temporary fluctuation or if it will have a long-term impact on the TOB trend.

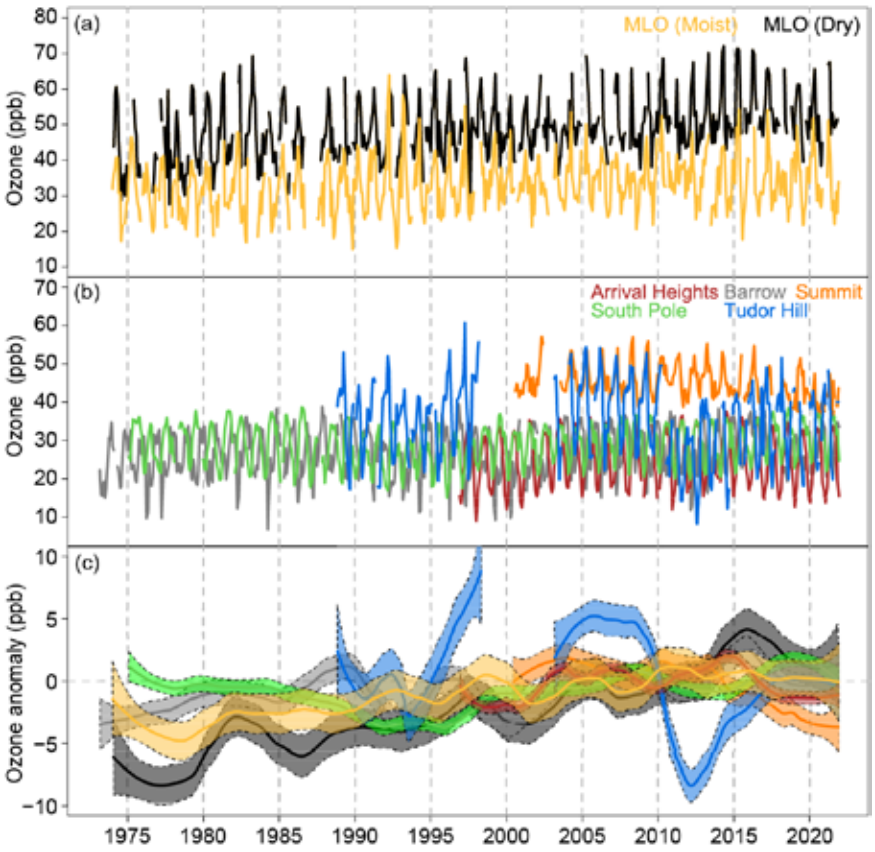

Fig. 2.64. (a) Nighttime monthly mean ozone values (ppb) at Mauna Loa (MLO), split into mutually exclusive times series, representing moist air (yellow, primarily a tropical origin) and dry air (black, primarily a midlatitude origin) based on observed relative humidity values (Gaudel et al. 2018). (b) Monthly mean surface ozone (ppb) at Barrow Observatory, Alaska (gray), Summit, Greenland (orange), Tudor Hill, Bermuda (blue), Arrival Heights, Antarctica (red), and South Pole (green). Monthly means are produced for months with at least 50% data availability, using observations from all 24 hours of the day. The locations of each site are listed in Table 2.11. (c) The same time series after conversion to monthly anomalies referenced to the monthly climatological values over 2000–20 and smoothed variability based on the LOWESS (locally weighted scatterplot smoothing) regression.

Table 2.11. Ozone trends at the six baseline monitoring sites shown in Fig. 2.64. Trends are estimated by the generalized least squares method, based on monthly anomalies referenced to the monthly climatological values over the period 2000–20 (Chang et al. 2021) and reported with 95% confidence intervals and *p*-values.

Site name Latitude, longitude, elevation (m)	Years with data	trend, ppbv decade^{-1}	*p*-value
Summit, Greenland 72.6°N, 38.5°W, 3238 m	2000–present	–2.43 ± 0.97	$p<0.01$
Barrow, Alaska 71.3°N, 156.6°W, 11 m	1973–present	0.57 ± 0.33	$p=0.00$
Tudor Hill, Bermuda 32.3°N, 64.9°W, 30 m	1988–98, 2003–present	–0.96 ± 1.22	$p=0.12$
Mauna Loa Observatory (MLO), Hawaii 19.5°N, 155.6°W, 3397 m	1973–present	2.04 ± 0.41 (dry air) 1.00 ± 0.38 (moist air)	$p<0.01$ $p<0.01$
Arrival Heights, Antarctica 77.8°S, 166.8°W, 50 m	1996–present	0.34 ± 0.59	$p=0.25$
South Pole, Antarctica 90.0°S, 59.0°E, 2840 m	1975–present	0.36 ± 0.37	$p=0.05$

7. CARBON MONOXIDE—J. Flemming and A. Inness

Carbon monoxide (CO) is emitted into the atmosphere by incomplete combustion from anthropogenic sources and from wildfires. The chemical production of CO in the atmosphere from formaldehyde as part of the oxidation chains of methane (CH_4), isoprene, and other volatile organic trace gases (Stein et al. 2014) is larger than these admissions. Oxidation of CO with the hydroxyl radical (OH) is the main loss process for CO. The greater abundance of OH in summer is a main driver for the typical CO seasonal cycle that peaks in boreal and austral winter. Carbon monoxide is an indirect short-lived climate forcer because it is an important precursor for tropospheric ozone (Szopa et al. 2021; section 2g6) and because it impacts OH, which controls the lifetime of CH_4.

Carbon monoxide concentrations doubled between the 1850s and the 2000s based on model studies (Griffiths et al. 2020). Based on a limited number of ice core samples, Northern Hemisphere (NH) CO levels were the highest (around 160 ppb) in the 1970s (Petrenko et al. 2013) but later declined by 30 ppb to 130 ppb by 2008. Surface CO concentrations have been measured as part of the global atmospheric watch (GAW) network using in situ sensors and flask observations in a routine way by NOAA's Global Monitoring Laboratory and other agencies since the 1990s (WMO 2021a). Tropospheric CO is observed, in situ, by the In-service Aircraft for a Global Observing System (IAGOS) aircraft observation program (Nédélec et al. 2015) and the Network for the Detection of Atmospheric Composition Change (NDACC; De Mazière et al. 2018) of ground-based remote sensing Fourier Transform Infrared Spectroscopy (FTIR) instruments, which provides atmospheric CO profiles. The advent of CO satellite sensors measuring CO in the early 2000s allowed more detailed monitoring of the global CO burden (Worden at al. 2013; Yin et al. 2015; Bucholz et al. 2021) in particular by assimilating these observations in atmospheric composition reanalyses (Flemming et al. 2017; Gaubert et al. 2017; Inness et al. 2019). The trend of the CO burdens and CO surface concentrations since the early 2000s varies spatially, but there is qualitative agreement between satellite-derived trends in CO burden and surface trends obtained from background in situ observations: the NH shows a decline of CO varying between 0.3% and 1.3% yr^{-1}, while SH values did not change significantly (Szopa et al. 2021).

Figure 2.65a shows a time series of the monthly global burden of CO from CAMS reanalysis for the period 2003–21. The total CO burden has reduced by 1.4 Tg yr^{-1} (based on a linear trend), and piecewise trends for the periods 2003–07, 2008–09, and 2009–21 are –3.1, –14.3, and 0.0 Tg yr^{-1} (Flemming and Inness 2018).

The spatial distribution of the annual CO anomalies, with respect to the period 2003–21, is shown in Plate 2.1z. Stronger-than-usual wildfire activity in northeastern Russia, starting in summer 2021 led to a widespread positive CO anomaly in mid- and higher latitudes of the NH, which was further increased by active wildfires in Canada and the western United States in August. This led to the highest monthly mean CO burdens in the Arctic region (60°–90°N) for the period covered by the CAMS reanalysis (Fig. 2.65b). Positive anomalies also occurred over India, caused by intensive agricultural waste burning in January and February. La Niña conditions in the tropical Pacific resulted in a pronounced negative CO anomaly over maritime Southeast Asia in the autumn period due to lower-than-normal biomass burning (Inness et al. 2015).

CAMS produced a retrospective analysis of CO, aerosols, and ozone for the period 2003–21 by assimilating satellite retrievals of atmospheric composition with the ECMWF model (Inness et al. 2019). The CAMS reanalysis-assimilated thermal infrared (TIR) total column CO retrievals (V6 from 2003 to 2016, near-real-time (NRT) V7 from January 2017 to June 2019, NRT V8 from July 2019 onward) from the MOPITT instrument (Deeter et al. 2014, 2017, 2019) globally, only excluding observations poleward of 65°N/S, using the ECWMF 4D-VAR data assimilation system. Anthropogenic emissions were taken from the MACCity inventory (Granier et al. 2011) that accounts for projected emission trends according to the IPCC Representative Concentration Pathway 8.5 scenario, but COVID-19 related emissions modifications were not applied. Biomass burning emissions (section 2h3) were taken from the Global Fire Assimilation System (v1.2; Kaiser et al. 2012) that is based on

MODIS fire radiative power retrievals (Giglio et al. 2016). A monthly mean climatology of biogenic emissions was taken from the MEGAN2.1 model following Sindelarova et al. (2014).

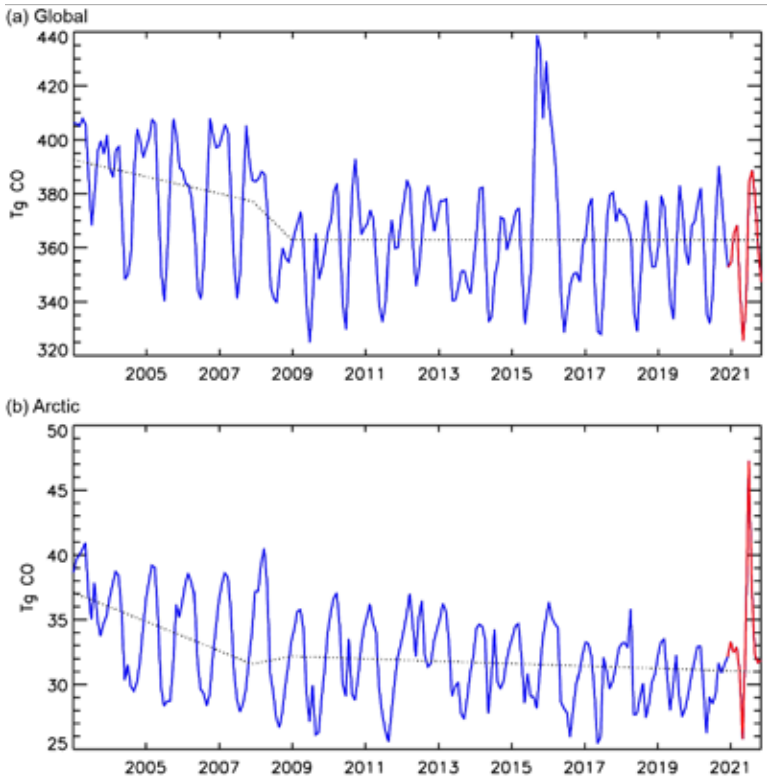

Fig. 2.65. Time series of the mean burden of CO for the (a) globe and (b) Arctic from the CAMS reanalysis and a piecewise linear trend for the periods 2003–07, 2008, and 2009–20.

h. Land surface properties

1. LAND SURFACE ALBEDO DYNAMICS—G. Duveiller and N. Gobron

The land surface was predominantly darker than normal during 2021 compared to the 2003–20 baseline in terms of visible broadband white-sky albedo and normal for near-infrared albedo (see Plates 2.1ac and 2.1ad, respectively). The patterns of surface albedo largely follow the dynamics of snow cover and vegetation dynamics, and 2021 was no exception. Several regions across the world had brighter surfaces due to above-average snow cover in either the beginning of the year (south/central United States, Spain, large parts of northern Europe), the end of the year (northwestern America and easternmost Russia, parts of the Tibetan plateau), or both (northeastern China). Lack of snow darkened the overall surface albedo in central North America and Quebec, Canada, in southeastern Europe, and in various parts of Russia (section 2c5). Where vegetation is greener (positive FAPAR anomalies; section 2h2), its contributions darken the surface overall by reducing the visible albedo, while near-infrared albedo rises slightly as denser vegetation scatters more light in this part of the spectrum. However, an exception to this case appeared in southern Africa where a decrease in near-infrared albedo occurred despite the increase in vegetation, possibly due to anomalously wet conditions. In contrast, the strong soil moisture deficit associated with the drought in the La Plata basin (section 2d10) resulted in an increase in visible albedo due to the drier conditions.

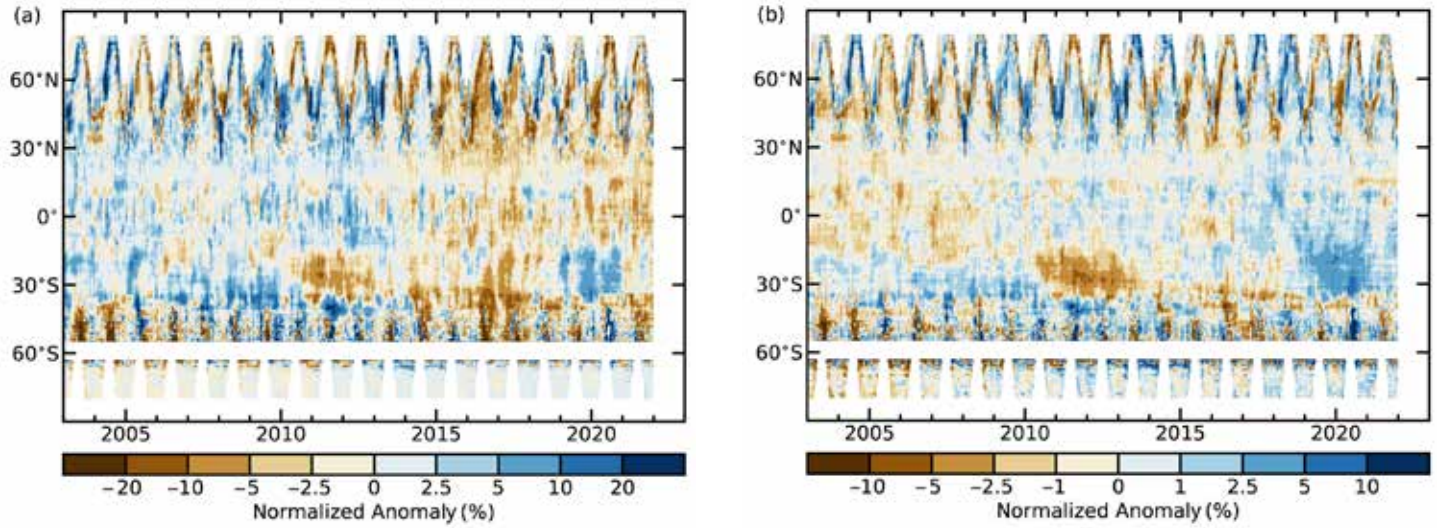

Fig. 2.66. Zonally averaged (a) white sky visible and (b) near-infrared albedo anomalies (%) for the period 2003–21 using a 2003–20 base period.

Surface albedo also largely follows the trends of decreasing snow cover observed in the past years (Figs. 2.66, 2.67). Also, as higher temperatures and CO_2 fertilization increase vegetation cover, the surface darkens considerably in terms of visible albedo and brightens slightly in terms of near-infrared albedo. The year 2021 seems to confirm that this general trend is also applicable to visible albedo anomalies in the Southern Hemisphere, when a return to negative values was observed after two years of positive values.

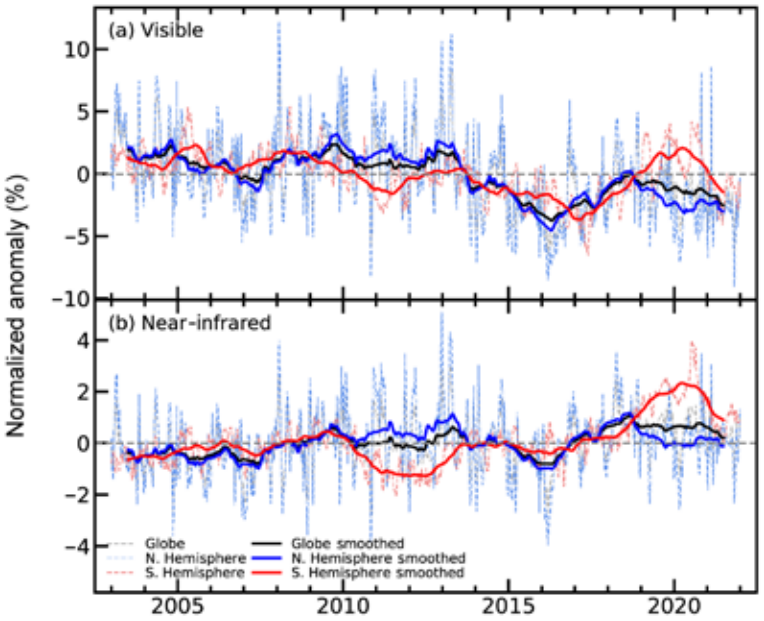

Fig. 2.67. Global (black lines), NH (blue), and SH (red) land surface (a) visible and (b) near-infrared albedo anomalies (%) for the period 2003–21 using a 2003–20 base period. Dotted lines denote each monthly period; solid lines indicate the 6-month running averaged mean.

This analysis is based on satellite records of visible and near-infrared white-sky albedo estimated from the Moderate Resolution Imaging Spectroradiometer (MODIS) instrument onboard the *Aqua* and *Terra* satellite platforms (Schaaf et al. 2002). White-sky albedo, also known as bihemispherical reflectance, is defined as the fraction of radiation that is reflected in the absence of a direct radiation component and when the diffuse radiation component is isotropic. Various studies have shown that these products well-represent ground properties, whether it is ice sheets (Stroeve et al. 2013) or vegetation (Cescatti et al. 2012). The baseline reference period is 2003–20, covering the extent of the MODIS record where data from both satellite platforms (*Terra* and *Aqua*) are available.

2. TERRESTRIAL VEGETATION DYNAMICS—N. Gobron

The fraction of absorbed photosynthetically active radiation (FAPAR) is used to track the overall land productivity associated with atmospheric CO_2 fixation. FAPAR anomalies in 2021 relative to the 1998–2020 mean show large surface variations, in terms of values and coverage, of vegetation productivity worldwide (Plate 2.1ae).

The greatest negative anomalies occurred over Central Asia, which had a record heatwave (see section 7g). The African continent also had strong negative anomalies in the east, over Somalia and Kenya, which were present during the entire year but strongest at the end of the year. To a lesser extent, the western coast from the Tropic of Capricorn to Nigeria also experienced numerous extreme events, with both droughts and floods that resulted in lower-than-average FAPAR. Negative anomalies were also present over far southern Africa and the southern half of Madagascar due to persistent drought inducing crop losses and other vegetation cover. The North American continent showed several negative hot-spots, including Montana, North Dakota, and Saskatchewan and along the Pacific coast, from California to Oregon, due to a series of wildfires that resulted from an exceptional heatwave and drought. Northeastern South America had low FAPAR in Guyana and Suriname. Small in extent but still significant, the Brazilian states of Rio Grande and Paraiba, Parque del Gran Chaco Kaa-Lya also had below-average FAPAR in 2021. Over Australia, Nullarbor Plain and a zone from Adelaide to Queensland, had low FAPAR. Over Alaska and northeastern Russia, with highest record temperatures during summer, there was below-average photosynthetic activity.

The most noticeable positive anomalies, most likely due to heavy rain linked to La Niña, took place in Botswana and northeastern Namibia, as well as eastern South Sudan. To a lesser extent, further positive anomalies in Africa were seen over the belt of humid savannas in the Sahel, from Liberia, Côte d'Ivoire, Ghana, Togo, and the south of Chad. These positive events were also enhanced by high precipitation totals over these regions (see section 2d4). In South America, positive anomalies occurred over regions such as northwestern Venezuela, the state of Marahnao (Brazil), and Argentina over La Mesopotamia and La Pampa. Southwestern Europe—comprised of Portugal, Spain, France, and around Moldova—had positive anomalies. A large part of northwestern Russia, mainly covered by tundra, also had positive anomalies. A large positive anomaly occurred over New South Wales and southern Queensland in Australia due to heavy precipitation in 2021, and another affected Malaysia.

Figure 2.68 shows the latitudinal anomalies average from 1998 to 2021 compared to the base period 1998–2020. In 2021, the positive behavior extended globally, with the exception of a few locations, highlighting the greenness of the terrestrial surfaces. The Southern Hemisphere (SH) was affected by strong negative anomalies, i.e., below −0.03, from 2002 to 2014, except in 2010–12, for which vegetation had recovered from severe and persistent droughts (Gobron and Belward 2011) and slightly negative anomalies in 2019/20. Fig. 2.69 shows the global and hemispherical anomalies, with more seasonal variability in the SH than in the Northern Hemisphere (NH). Global seasonal anomalies have been positive since 2013, following the NH trend. SH was generally positive but with monthly negative events during its summer period, e.g., 2015/16; 2018/19; 2019/20, and 2020/21. SH data reveal two positive extreme peaks in 2000 and 2017, while the lowest values occurred in 2008/09. The NH experienced fewer extreme negative events, e.g., values below −0.03, compared to the SH. In 2021, only positive FAPAR anomalies were recorded for both SH and NH averages.

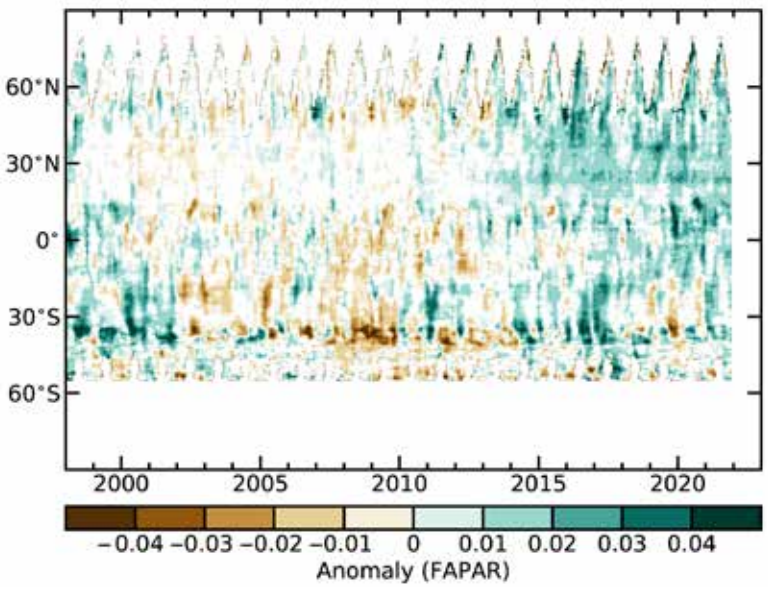

Fig. 2.68. Zonally averaged fraction of absorbed photosynthetically active radiation (FAPAR) anomalies for the period 1998–2021 (1998–2020 base period).

Earth observations are important for monitoring the terrestrial photosynthetic activity worldwide. They are used to infer FAPAR, an essential climate variable (as defined by GCOS [2016]). The 2021 study merged 24 years of global FAPAR monthly products based on three optical sensors from 1998 to 2021 (Gobron et al. 2010; Pinty et al. 2011; Gobron and Robustelli 2013). Uncertainties of each dataset were derived through various means, such as error propagation technique and comparisons against multiple proxies using ground measurements and radiative transfer simulations, that all provide an estimate of the uncertainties and biases. This long-term FAPAR dataset presents an estimated global average uncertainty close to 5%–10% when comparing to ground-based measurements.

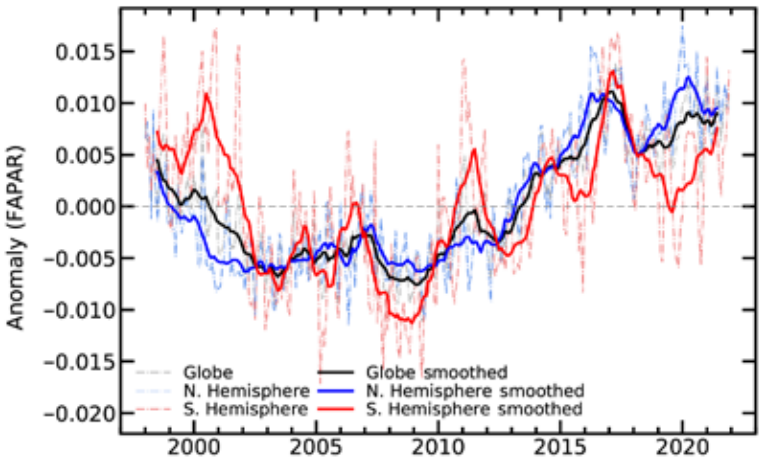

Fig. 2.69. Global (black/gray lines), Northern Hemisphere (blue), and Southern Hemisphere (red) fraction of absorbed photosynthetically active radiation (FAPAR) anomalies for the period 1998–2021 (1998–2020 base period). Dotted lines denote each monthly period; solid lines indicate the 6-month running averaged mean.

3. BIOMASS BURNING—

J. W. Kaiser and G. R. van der Werf

The year 2021 illustrated how two distinct trends that have emerged in global biomass burning over the last decade shaped current pyrogeography: a declining trend in many savanna regions related to agricultural expansion and an increasing trend in many forested regions where climate change has increased the flammability of the landscape. On one hand, 2021 was the fourth-lowest fire year in the Global Fire Assimilation System (GFAS) record (1837 Tg C; 11% below the 2003–20 average; Table 2.12; global map shown in Fig. 2.70), and fire activity in tropical Asia was the lowest since at least 2003. On the other hand, 2021 saw extreme regional fire activity in boreal North America and Siberia, as well as the western United States. After the extreme fires of 2019 and 2020 in the Arctic Circle and southeastern Australia, fire activity in these regions was again near and below average, respectively.

Table 2.12. Annual continental-scale biomass burning budgets in terms of carbon emission (Tg C yr^{-1}). (Source: GFASv1.4.)

Time Period		2003–20	2021	
Quantity Tg C yr^{-1}		Mean value (Range)	Value	Anomaly (%)
Global		2062 (1781–2421)	1837	–225 (–11%)
North America	30°–75°N 190°–330°E	85 (57–114)	114	+28 (+33%)
Central America	13°–30°N 90°–330°E	52 (38–72)	46	–6 (–12%)
South America	13°S–60°N 190°–330°E	368 (242–537)	316	–52 (–14%)
Europe and Mediterranean	30°–75°N 330°–60°E	42 (28–72)	34	–9 (–21%)
N. Hem. Africa	0°–30°N 330°–60°E	421 (308–494)	372	–49 (–12%)
S. Hem. Africa	0°–35°S 330°–60°E	477 (429–532)	476	–1 (0%)
Northern Asia	30°–75°N 60°–190°E	199 (116–436)	256	+57 (+29%)
South-East Asia	10°–30°N 60°–190°E	122 (86–162)	111	–11 (–9%)
Tropical Asia	10°S–10°N 60°–190°E	166 (37–475)	27	–139 (–83%)
Australia	10°–50°S 60°–190°E	129	86	–43 (–34%)
Arctic	67°–90°N 0°–360°E	8 (1–37)	7	–1 (–9%)
Western United States	30°–49°N 230°–260°E	19 (8–42)	37	+18 (+96%)

Global fire emissions are generally dominated by savanna burning. For example, African fire emissions account for roughly half of total fire carbon emissions, and fires here and in many other savanna regions have decreased over the past decade. This trend is partly driven by agricultural expansion into savanna ecosystems and associated fragmentation of the landscape (Andela et al. 2017). The trend continued in 2021, with Africa north of the equator observing emissions 12% below the 2003–20 average and the seven years with the lowest global fire activity in the GFAS record all occurring since 2013; however, emissions were close to average south of the equator in Africa and thus did not contribute to the trend. Fire activity in tropical Asia, including Indonesia, was the lowest on record (Fig. 2.71); fire activity in this region is strongly modulated by precipitation anomalies associated with the El Niño-Southern Oscillation. Environmental protection policies may also have contributed to the low fire activity.

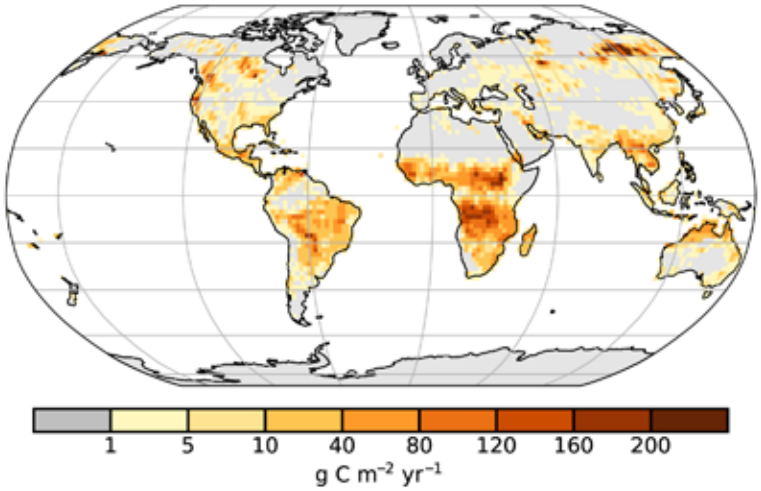

Fig 2.70. Global map of fire activity in 2021 in terms of carbon consumption (g C m^{-2} yr^{-1}). (Source: GFASv1.4.)

At higher latitudes, northern Asia and North America experienced particularly intense fire seasons in 2021, with anomalies of +29% and +33%, respectively. The continental-scale budgets are dominated by boreal fires. Nevertheless, the wildfires in the western United States were second only to those of 2020, consuming twice as much biomass as the long-term average (Fig. 2.71).

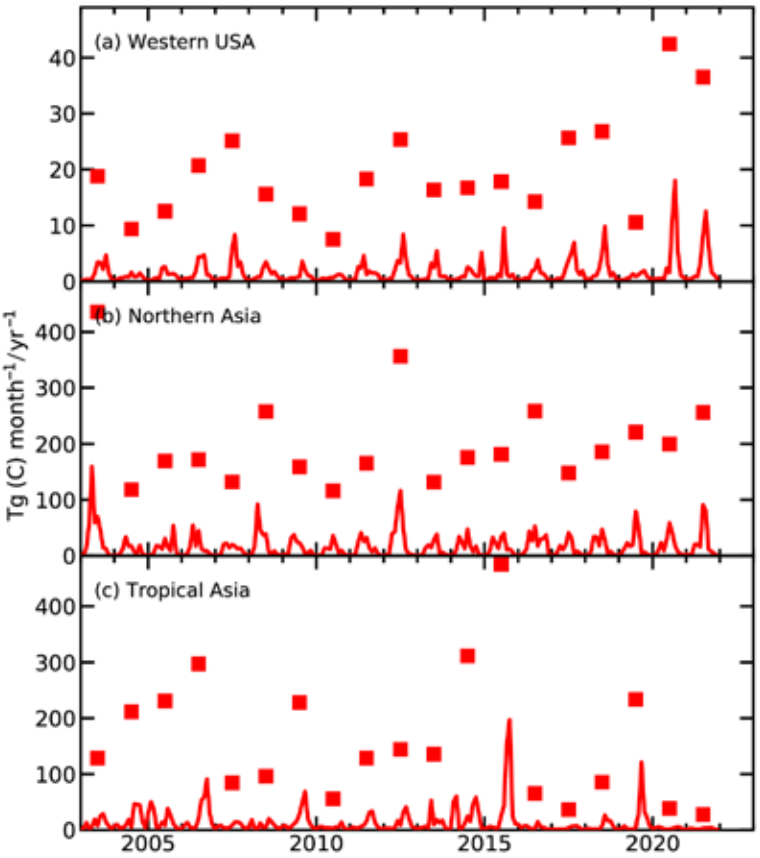

Fig. 2.71. Time series of annual (squares) and monthly (lines) regional fire activity, in terms of carbon consumption for (a) the western United States, (b) northern Asia, and (c) tropical Asia. (Source: GFASv1.4.)

GFAS produces global fire emission estimates in near real-time for the Copernicus Atmosphere Monitoring Service (CAMS; Kaiser et al. 2012). It is based on the MODIS Fire Radiative Power products (Giglio et al. 2016). Here, we use consistent reprocessing with input from MODIS Collection 6 for the entire period of 2003–21. The 14% bias, with respect to Collection 5, has been corrected and the satellite and observation time-specific bias correction factors from Hüser et al. (2018) have been applied for 17 August–2 September 2020 in order to compensate for the outage of observations from MODIS onboard the *Aqua* satellite. The time series in Plate 2.1ae also puts the GFAS time series, which begins in 2003, in the context of GFED4s, which is mostly based on burnt area observation and dates back to 1997 (van der Werf et al. 2017).

4. PHENOLOGY OF PRIMARY PRODUCERS—D. L. Hemming, O. Anneville, Y. Aono, J. Garforth, A. Menzel, J. O'Keefe, T. Park, A. D. Richardson, T. Rutishauser, T. H. Sparks, S. J. Thackeray, A. van Vliet, and Y. Yuan

During 2021, the phenology, of satellite-derived, PhenoCam-derived, terrestrial, and aquatic records, indicate a generally earlier start and longer growing season across the globe relative to the 2000–20 baseline, with the exception of extreme April temperature impacts in Europe. The satellite-derived (MODIS) normalized difference vegetation index (NDVI; Park et al. 2016) across Northern Hemisphere land (NH, > 30°N) revealed earlier mean start of season (SOS_M; –1.8 days) and later end of season (EOS_M, +4.2 days) relative to the baseline (SOS_M = day 135, 15 May and EOS_M = day 283, 10 October; Fig. 2.72). These differences were associated with higher spring (+0.24°C) and autumn (+0.54°C) temperatures from the MERRA-2 reanalysis (Gelaro et al. 2017) and resulted in a 6-day longer growing season in 2021. Regionally, SOS_M occurred earlier across western and

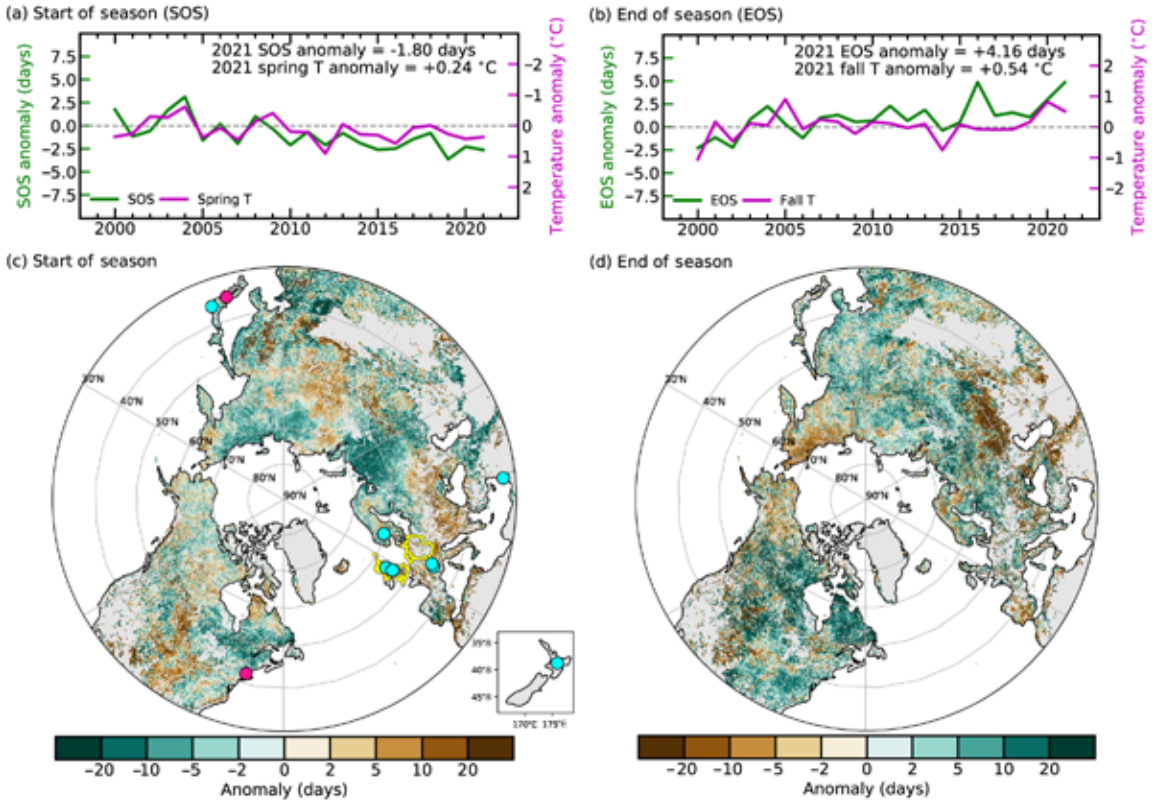

Fig. 2.72. (a) Time series of area-mean anomalies (days relative to 2000–20 baseline) in MODIS NDVI-based vegetation growing season onset (SOSM, green) and MERRA-2 spring (Mar–May, pink) temperature for Northern Hemisphere (> 30°N). (b) Same as (a) but for the end of growing season (EOSM, green) and autumn (Sep–Nov, pink) temperature. Note, temperature scale reversal for panel (a). (c),(d) Spatial pattern of (c) SOSM and (d) EOSM anomalies in 2021 with respect to the baseline. Highlights identify the location of sites shown in Figs. 2.73 and 2.74 and discussed in the text (Country mean phenology data: yellow; site PhenoCam and phenology observations: magenta; lake phytoplankton: blue).

northeastern Eurasia (EA), and northeastern North America (NA) and later across central EA and NA (Fig. 2.72c). A striking earlier SOS_M (–13 days) over western Russia (35°–75°E, 69°–57°N) was associated with an anomalous spring warm spell (+2.7°C). Most EA and NA regions showed a later EOS_M, whereas earlier EOS_M was observed in southwestern EA. The regions displaying early EOS_M were mostly temperate grass and shrublands, which experienced a drier summer and autumn seasons in 2021 (JRC 2021). Two decades of MODIS record show long-term trends of earlier SOS_M and later EOS_M (SOS_M: –1.74 ± 0.42 days decade^{-1}, $p < 0.001$; EOS_M: 1.93 ± 0.47 days decade^{-1}, $p < 0.001$).

PhenoCam data (Seyednasrollah et al. 2019) help link the coarse resolution of satellite-derived phenology with fine resolution visual observations on organisms and ecosystems (Richardson 2019). PhenoCam-derived estimates (2008–21) of SOS (SOS_{PC}) and EOS (EOS_{PC}) at Harvard Forest, a deciduous forest in Massachusetts (United States), were compared with ground observations of red oak (*Quercus rubra*; SOS_{RO} and EOS_{RO}; Richardson and O'Keefe 2009; O'Keefe 2021), and MODIS (SOS_M and EOS_M) for the associated pixel (Figs. 2.73a,b). SOS_{PC} and EOS_{PC} are strongly correlated with SOS_{RO} (r = 0.90) and EOS_{RO} (r = 0.83), and their timings were similar. Although SOS_{PC} and SOS_M were strongly correlated (r = 0.77), SOS_{PC} was later by 12 ± 3 days (Fig. 2.73b). The correlation between EOS_{PC} and EOS_M was weaker (r = 0.58), and EOS_{PC} was earlier by 47 ± 10 days (Fig. 2.73a). In 2021, SOS_{PC}, SOS_{RO}, and SOS_M were 8, 8, and 4 days earlier and EOS_{PC}, EOS_{RO}, and EOS_M were 13, 6, and 11 days later than in 2020 (Figs. 2.73a,b). EOS_{PC} was the latest in the PhenoCam series. All three Harvard Forest records showed a longer growing season in 2021 than 2020, with the PhenoCam showing the largest change where the earlier SOS_{PC} and later EOS_{PC} yielded a growing season that, at 178 days, was three weeks longer than 2020, and 11 days longer than the 2011–20 mean (167 days). First leaf (SOS_{PO}) and leaf falling/bare tree (EOS_{PO}) dates for pedunculate oak (*Quercus robur*) from Germany (D), the United Kingdom (UK), and the Netherlands (NL) are

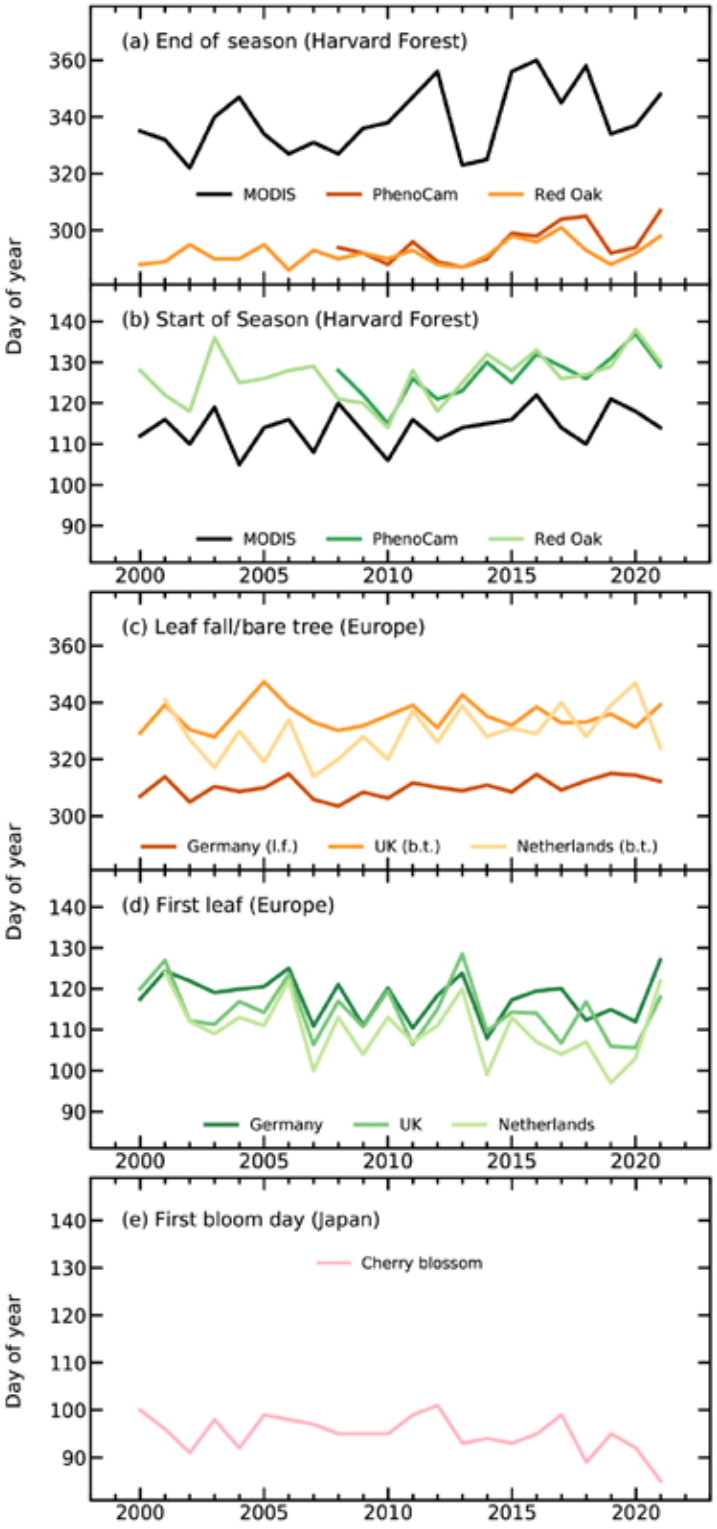

Fig. 2.73. Day of year of spring and autumn vegetation phenology indicators for (a),(b) Harvard Forest, Massachusetts, where (a) start and (b) end of season days are derived from MODIS remote sensing (black), PhenoCam observations and red oak (Quercus rubra) single-tree ground observations (green and orange); (c),(d) Germany, United Kingdom, and the Netherlands, where country-mean first leaf (green) and bare tree or leaf fall (orange) days are derived from ground observations of pedunculate oak (Quercus robur); and (e) Kyoto, Japan, showing first full bloom days for cherry blossom, Prunus jamasakura from ground observations (pink).

presented in Figs. 2.73c,d. The mean SOS_{PO} and EOS_{PO} for the 2000–20 baseline was 27 (D), 24 (UK), and 20 (NL) April, and 5, 30, and 26 November, respectively. Both events were strongly influenced by temperature; in general, it has been shown that SOS_{PO} advances by 4–6 days per °C increase in mean February–April temperature, and EOS_{PO} is delayed 2–4 days per °C increase in September–October temperature (Menzel et al. 2020). April 2021 temperatures were relatively cold in these countries, resulting in SOS_{PO} dates 10 (D), 3 (UK), and 13 (NL) days later than the baseline, while EOSPO dates were mixed; 6 days earlier in NL but 2 and 4 days later in D and UK. The net result was a shorter 2021 oak season in each country (see Kendon et al. 2022).

In Kyoto, Japan, full bloom dates (FBD) for a native cherry tree species, *Prunus jamasakura*, were acquired from historical documents (Aono and Kazui 2008) and updated with current observations. In 2021, the FBD was 26 March (day 85), which was 9.5 days earlier than the 2000–20 baseline mean and the earliest in the entire record, which began in AD 801, breaking the previous earliest date of 27 March in the year 1409.

Monitoring data on lake water concentrations of the photosynthetic pigment chlorophyll-*a* were available to estimate spring phytoplankton phenology in 1 SH and 10 NH lakes (Fig. 2.74). Seasonal timing was quantified for start of season (SOS_L *sensu* Park et al. 2016), day of maximum concentration (DOM_L), and center of gravity (COG_L; Edwards and Richardson 2004). Lake basins showed great interannual variation and mixed phenological behavior in 2021, relative to the 2000–20 baseline. 2021 SOS_L and COG_L were both earlier than the baseline interquartile range in 4 of the 11 lakes and 5 of the 11 for DOM_L. Earlier growth

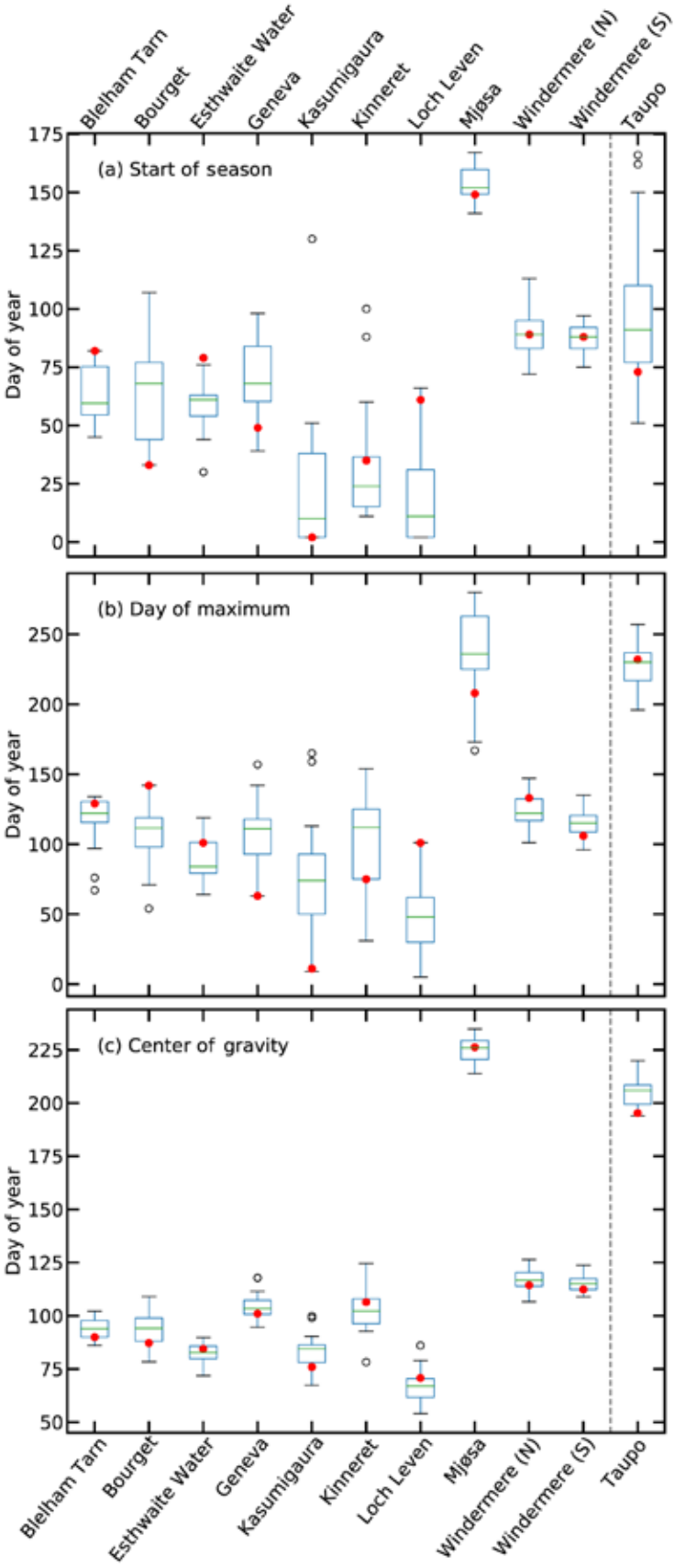

Fig. 2.74. Phenological metrics based on lake chlorophyll-*a* concentrations, as a proxy of phytoplankton biomass: (a) start of season, (b) day of maximum, and (c) center of gravity (a measure of the timing of the peak throughout the growing season). Boxplots show variation during the 2000–20 base period, and red dots show 2021 values. Dashed line identifies Northern Hemisphere (Blelham Tarn in United Kingdom [UK], Bourget in France, Esthwaite Water in UK, Geneva in France/Switzerland, Kasumigaura in Japan, Kinneret in Israel, Loch Leven in UK, Mjøsa in Norway, north and south basins of Windermere in UK) and Southern Hemisphere (Taupo in New Zealand) lakes.

typically occurs in deeper lakes where thermal stratification is an important trigger of spring phytoplankton growth (Sommer et al. 1986).

5. VEGETATION OPTICAL DEPTH—W. Dorigo, R. M. Zotta, R. van der Schalie, W. Preimesberger, L. Moesinger, and R. A. M. de Jeu

Vegetation optical depth (VOD) is a parameter describing the interaction of microwave radiance with vegetation. It is closely related to vegetation above-ground biomass (Mialon et al. 2020), leaf area index (Vreugdenhil et al. 2017), gross primary production (Teubner et al. 2019; Wild et al. 2022), and canopy water content (Konings et al. 2017). Thus, it is a valuable indicator of ecosystem health, agricultural drought, and crop status (Crocetti et al. 2020; Moesinger et al. 2022).

In 2021, VOD anomaly patterns largely resembled those of 2020 (Dorigo et al. 2021). Widespread patterns of negative VOD anomalies occurred in large parts of Russia, Central Asia, and Mongolia. For some of these predominantly rain-fed agricultural areas, below-average cereal production was reported by the UN Food and Agricultural Organization. Clear below-average VOD values were also detected in western Africa, Angola, and Namibia, the southwestern tip of Africa, Mozambique, and southern Madagascar, which were already observed in 2020 and persisted throughout 2021 (Plate 2.1ag). In Madagascar, ongoing droughts have reportedly led to crop failure, according to UN reports. Although some parts of Australia show lower-than-usual VOD, many areas, particularly in the east, shifted from a negative state in 2020 (Dorigo et al. 2021) to a positive one in 2021, as predominately wet conditions have prevailed following a major drought in 2017–19 (see section 7h4). The most evident region with above-average VOD was centered around Botswana and Namibia in southeastern Africa. Compared to 2020, VOD anomalies in this region became more positive and covered a larger area. Above-average rainfall amounts that are commonly associated with La Niña in this region (see section 7e) may have been responsible for this high VOD. Farther north, Uganda and South Sudan, in particular, had above-average VOD, likely related to heavy precipitation and flooding (see section 7e). Other areas of above-average VOD include parts of the Parana basin in South America, the Tigris floodplain in the Middle East, and the Indian subcontinent.

In the Southern Hemisphere, there was a clear connection between interannual variability in precipitation and vegetation activity and variations in ENSO and other climate modes (Fig. 2.75; Miralles et al. 2014; Martens et al. 2018). La Niña conditions prevailed in 2021, and several VOD anomalies coincided with rainfall anomaly patterns typically associated with this phase, including positive VOD anomalies in northeastern Brazil, southern Africa, the northern Sahel region, eastern Australia, and India. However, for VOD, the relationship with climate modes is generally less straightforward than for moisture supply, since VOD anomalies are also affected by drivers such as temperature, radiation, CO_2 fertilization, weather extremes, lagged effects, and land management (e.g., irrigation, fertilization, logging; Gonsamo et al. 2021; Reichstein et al. 2013).

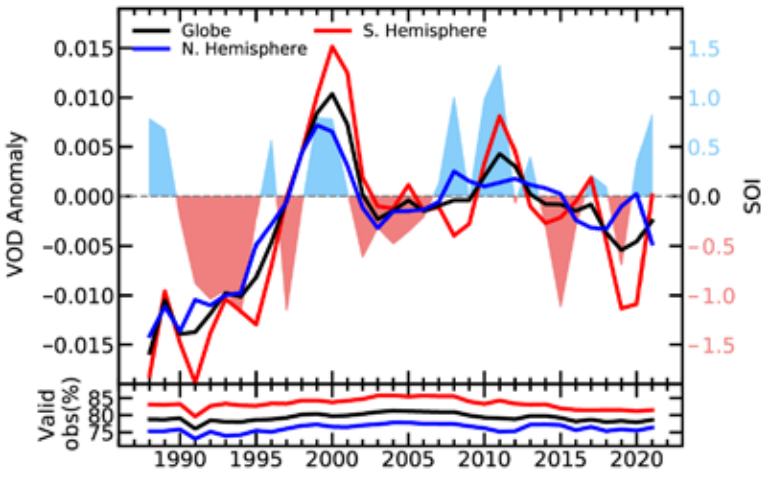

Fig. 2.75. Yearly Ku-band VOD anomalies computed from the 1991–2020 climatology and their agreement with the Southern Oscillation Index (SOI). SOI tracks the state of the El Niño Southern Oscillation, with values > 0.7 indicating La Niña and values < –0.7 indicating El Niño episodes (Source: VODCA, http://www.bom.gov.au/climate/enso/soi/.) The bottom plot shows the percentage of land pixels providing valid data for each year.

Several anomalies observed in 2021 are consistent with patterns of long-term change (Fig. 2.76). For instance,

the below-average vegetation activity in northern Mongolia and Brazil and Bolivia coincide with long-term negative trends related to land degradation and deforestation, respectively (Song et al. 2018). Above-average VOD in several regions can be linked to long-term trends in precipitation (Sahel; Dong and Sutton 2015), intensification of agricultural production (India, China), and reforestation (northeastern China; Song et al. 2018). To differentiate interannual variability from long-term change, one would need to detrend the data first (Moesinger et al. 2022). An alternative view is provided by the difference in VOD between the years 2021 and 2020 (Appendix Fig. A2.14), which reveals, for example, that although Kenya in 2021 had above-average vegetation activity, it was below that of 2020.

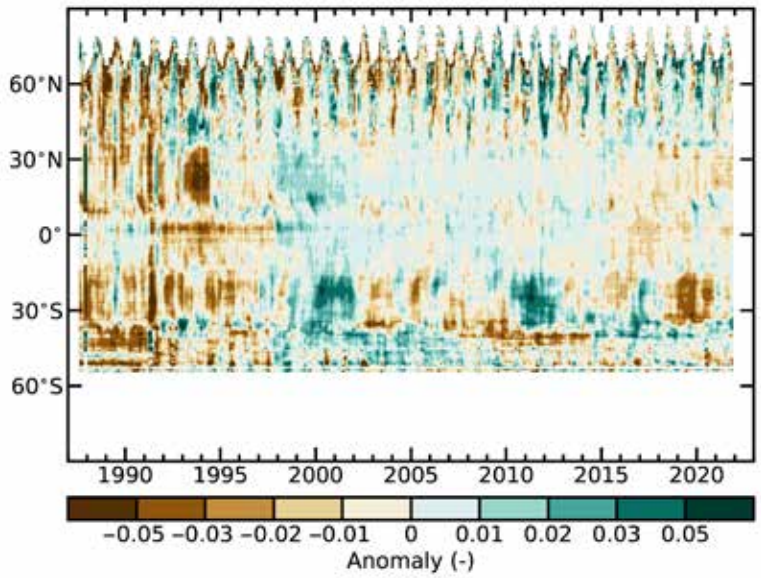

Fig. 2.76. Time–latitude diagram of VOD anomalies (1991–2020 base period). Data are masked where no retrieval is possible or where the quality is not assured and flagged due to frozen soil, radio frequency interference, etc. (Source: VODCA.)

The VOD anomalies were computed from the VOD Climate Archive (VODCA; Moesinger et al. 2020). VODCA blends VOD observations retrieved with the Land Parameter Retrieval Model (Meesters et al. 2005; van der Schalie et al. 2017) from several space-borne radiometers, including SSM/I, TRMM, Windsat, AMSR-E, and AMSR2, into a harmonized long-term dataset. VODCA contains individual datasets for Ku-band (covering the period 1987–2021), X-band (1997–2021), and C-band (2002–21) at 0.25° spatial and daily temporal resolutions. Here, we used the VODCA Ku-band dataset, the longest available record, to compute anomalies from the long-term (1991–2020) climatology. Despite its theoretically higher sensitivity to the upper canopy, intra and interannual dynamics of Ku-band observations strongly agree with those of X-band and C-band (Moesinger et al. 2022). VOD cannot be retrieved over frozen or snow-covered areas for which they are masked in winter (Appendix Fig. A2.13).

Acknowledgments

2.a.1 Introduction

Freya Aldred, Robert Dunn, and Kate Willett were supported by the Met Office Hadley Centre Climate Programme funded by BEIS. We thank John Kennedy, David Parker, and Katrina McNeill for their detailed comments when developing this chapter. We thank the BAMS Editor and the seven anonymous reviewers whose detailed comments improved the contents and presentation of this chapter. We also thank Atsushi Goto and Fumi Sezaki (JMA), Julien Nicolas (ECMWF), and Mike Bosilovich (NASA) for their help in providing the reanalysis data used in this chapter.

2.b.2 Lake Surface Temperature

Lake surface water temperatures from satellite data have been generated within the GloboLakes project funded by the UK National Environment Research Council (NE/J023345/2), with extensions funded by the EU Copernicus Climate Change Service (C3S) programme.

Part of the in situ measurements used to validate the LSWT dataset have been kindly shared by Eugene Silow (Irkutsk State University, Russia), Merja Pulkkanen (SYKE, Helsinki, Finland), Antii Raike (SYKE, Helsinki, Finland), Eric Leibensperger (Department of Physics and Astronomy, Ithaca College, Ithaca, U.S.A.), Alo Laas (Estonian University of Life Sciences, Tartu, Estonia), Michela Rogora (CNR Institute for Water Research, Italy), Martin Dokulil (Austria), Shin-ichiro Matsuzaki (National Institute for Environmental Studies, Japan), Claudia Giardino (CNR IREA, Italy), Curtis DeGasperi (King County Water and Land Resources Division, Department of Natural Resources and Parks, Seattle, Washington), Martin Schmid (Eawag, Switzerland), Don Pierson (Uppsala University, Sweden).

2.b.3 Night Marine Air Temperatures

R. Junod was supported by the U.S. Department of Energy (DE-SC0019296).

2.b.4 Land and Marine temperature extremes

Robert Dunn was supported by the Met Office Hadley Centre Climate Programme funded by BEIS.

2.b.5 Lower Tropospheric Temperature

Work performed by Stephen Po-Chedley at Lawrence Livermore National Laboratory (LLNL) was supported by the Regional and Global Model Analysis Program of the Office of Science at the Department of Energy and performed under the auspices of the DOE under Contract DE-AC52-07NA27344.

2.c.1 Permafrost and ALT

The Swiss Permafrost Monitoring Network PERMOS is financially supported by MeteoSwiss in the framework of GCOS Switzerland, the Federal Office for the Environment, and the Swiss Academy of Sciences, and acknowledges the important contribution of its partner institutions and principal investigators. The French Network PermaFRANCE is financially supported by the Observatoire des Sciences de l'Univers Grenoble and the French Research Infrastructure OZCAR. The research on James Ross Island is supported by Czech Antarctic Research Programme and Czech Science Foundation project (22-28659M).

2.c.2 Rock Glacier Velocity

Rock glacier monitoring at Hinteres Langtalkar and Dösen rock glaciers (AT) is supported by the Hohe Tauern National Park Carinthia through its long-term permafrost monitoring program.

Laurichard (FR) survey is supported by CryobsClim "long-term Observation and Experimentation System for Environmental Research" (SOERE/All'envi-OZCAR Research Infrastructure) and the PermaFrance observatory "monitoring the mountain permafrost in the French Alps" as well as French National Research Agency in the framework of the *Investissements d'Avenir* programs: Risk@UGA (ANR-15-IDEX-02) and LabEx OSUG@2020 (ANR10 LABX56).

The Ecrins National Park helps field surveys since the early 2000s.

The Swiss Permafrost Monitoring Network PERMOS is financially supported by MeteoSwiss in the framework of GCOS Switzerland, the Federal Office for the Environment, and the Swiss Academy of Sciences. PERMOS acknowledges the important contribution of the partner institutions and principal investigators.

The time series for Central Asian rock glaciers was compiled with the ESA Permafrost_CCI project (4000123681/18/I-NB).

The time series for the Dry Andes was supported by the Centro de Estudios Avanzados en Zonas Áridas (CEAZA) and the Leading House for the Latin American Region (University of St. Gallen), grant number MOB1829.

2.c.4 Lake Ice Cover

We thank Alexander Mills, Huaxia Yao, Lars Rudstam, Mr. Miyasaka, Ichiro Matsuzaki, Greg Sass, Don Pierson, the Minnesota Department of Natural Resources, North Temperate Lakes Long-Term Ecological Research Network, and citizen scientist contributors from the Community Lake Ice Collaboration for providing ice phenology records for their local lakes each winter.

Funding was provided by Natural Sciences Engineering and Research Council Discovery Grant to S. Sharma.

T. Nõges was supported by the Estonian Environment Agency and Estonian Research Council project PRG709.

2.c.5 NH Snow Cover

This work is funded in part by NOAA's Climate Data Record (CDR) Program at the National Centers for Environmental Information.

2.d.1 Surface Humidity

Kate Willett was supported by the Met Office Hadley Centre Climate Programme funded by BEIS and Defra. Adrian Simmons and David Lavers were supported by the Copernicus Climate Change Service implemented by ECMWF on behalf of the European Commission.

2.d.5 Land Based Precipitation Extremes

Stephen Blenkinsop is supported by the UK Natural Environment Research Council (NERC) funded FUTURE-STORMS project, grant no. NE/R01079X/1.

2.d.6 Cloudiness

Thank you to the following for providing data for this analysis:
Larry Di Girolamo – University of Illinois at Urbana-Champaign, Illinois
Guangyu Zhao – University of Illinois at Urbana-Champaign, Illinois
Sunny Sun-Mack – Science Systems and Applications, Inc., Hampton, Virginia
Martin Stengel – Deutscher Wetterdienst, Offenbach, Germany

2.d.7 Runoff and River Discharge

This work (research) was supported by the National Research Foundation of Korea (NRF) grant Funded by the Korea Government (MSIT) (2021H1D3A2A03097768) and the Japan Society for the Promotion of Science KAKENHI (21H05002) for this contribution.

2.d.8 Groundwater and Terrestrial Water Storage

M. Rodell and D. Wiese were supported by NASA's GRACE-FO Science Team.

They also thank the German Space Operations Center of the German Aerospace Center (DLR) for providing nearly 100% of the raw telemetry data of the twin GRACE satellites.

2.d.9 Soil Moisture

This work was supported by the ESA Climate Change Initiative Soil Moisture project.

2.d.10 Drought

Tim Osborn received funding from UK NERC (NE/S015582/1).

Ian Harris received funding from UK National Centre for Atmospheric Science (NCAS).

The research presented in the drought section was carried out on the High Performance Computing Cluster supported by the Research and Specialist Computing Support service at the University of East Anglia.

2.d.11 Land Evaporation

D. G. Miralles acknowledges support from the European Research Council (ERC) under grant agreement no. 715254 (DRY–2–DRY).

M. F. McCabe is supported by the King Abdullah University of Science and Technology.

2.e.1 Mean Sea Level Pressure and Related Modes of Variability

David Fereday was supported by the Met Office Hadley Centre Climate Programme funded by BEIS.

2.e.2 Surface Winds

C. Azorin-Molina was supported by CSIC-UV-GVA and funded by RTI2018-095749-A-I00, AICO/2021/023, Leonardo-FBBVA and the CSIC Interdisciplinary Thematic Platform PTI-CLIMA. R. J. H. Dunn was supported by the Met Office Hadley Centre Climate Programme funded by BEIS. L. Ricciardulli was supported by NASA Ocean Vector Wind Science Team grant 80HQTR19C0003.

2.e.3 Upper Air Winds

We thank Martin Weissmann and Anne Martin (both University of Vienna) for their support in estimating the impact of Aeolus data on global analyses in the Tropics and Michael Rennie (ECMWF) for provision of data.

Sidebar 2.1 Lightning

The work of M. Füllekrug was sponsored by the Royal Society (UK) grant NMG/R1/180252 and the Natural Environment Research Council (UK) under grants NE/L012669/1 and NE/H024921/1.

E. Williams is supported for studies on global circuit response to climate change from the Physical and Dynamic Meteorology Program at the National Science Foundation on grant no. 6942679.

C. Price was supported in his lightning research by the Israel Science Foundation (ISF) grant 2701/17 and the Ministry of Energy grant no. 220-17-002.

S. Goodman was supported by NASA Grant 80NSSC21K0923 and NASA Contract 80GSFC20C044.

K. Virts is supported in part by the GOES-R Series Science, Demonstration, and Cal/Val Program at Marshall Space Flight Center.

D. Buechler is supported by the NASA MSFC/UAH Cooperative Agreement NNM11AA01A.

The authors wish to thank Peter Thorne at Maynooth University in Ireland and at the European Centre for Medium Range Weather Forecast (ECMWF) for suggesting and initiating this work and for recommending that lightning be made an essential climate variable.

The data used to generate Fig. SB2.1 are available from the NASA Global Hydrometeorology Resource Center DAAC, Huntsville, Alabama.

The data used to generate Fig. SB.2.2 are provided by WWLLN to GHRC as part of GLM cal/val activities.

2.f.1 Earth Radiation Budget

This research has been supported by the NASA CERES project.

The NASA Langley Atmospheric Sciences Data Center processed the instantaneous Single Scanner Footprint (SSF) data used as input to EBAF Ed4.1 and processes the FLASHFlux TISA version 4A.

2.g.4 Stratospheric Ozone

Carlo Arosio, Melanie Coldewey-Egbers, Daan Hubert, Diego Loyola, Viktoria Sofieva, Alexei Rozanov, and Mark Weber are grateful to ESA's Climate Change Initiative Ozone (CCI+) project and to the EU Copernicus Climate Change Service, 312b Lot4 Ozone project for supporting the generation and extension of the GTO-ECV total ozone and SAGE-CCI-OMPS data records.

Stacey M. Frith is supported by the NASA Long Term Measurement of Ozone program WBS 479717.

Lucien Froidevaux's contribution, with the assistance of Ryan Fuller, was performed at the Jet Propulsion Laboratory, California Institute of Technology, under contract with NASA.

Daan Hubert acknowledges the partial support by the EU/ERC Horizon 2020 project GAIA-CLIM.

2.h.1 Albedo

The authors thank Mirko Marioni for his technical support and NASA's Land Processes Distributed Active Archive Center (LP DAAC) for providing access to the remote sensing data.

2.h.2 Terrestrial Vegetation Dynamics

The author thanks Mirko Marioni for his technical support and the providers of the remote sensing dataset needed to perform this research, i.e., the SeaWiFS Project (Code 970.2) and the Goddard Earth Sciences Data and Information Services Center/Distributed Active Archive Center (Code 902) at the Goddard Space Flight Center, Greenbelt, Maryland .

MERIS products were processed at the Grid On Demand facility of European Space Agency (ESA/ESRIN) using JRC software code.

The standard Two-stream Inversion Package (JRC-TIP) datasets were produced on JRC Big Data Analytics Platform (BDAP).

2.h.4 Phenology

Debbie Hemming acknowledges support from the Met Office Hadley Centre Climate Programme funded by BEIS and the Met Office Climate Service on Food, Farming and Natural Environment funded by Defra, and thanks all co-authors for their interesting and helpful contributions and Robert Dunn for his expertise finalizing the figures for this section.

Taejin Park acknowledges support from the NASA Earth Science Directorate (grants NNX16AO34H and 80NSSC18K0173-CMS).

Andrew Richardson acknowledges support from the National Science Foundation through the Macrosystems Biology (award 1702697) and LTER (award 1832210) programs.

John O'Keefe also acknowledges support from the National Science Foundation through the LTER (award 1832210) program.

Nature's Calendar (Woodland Trust) in the UK thanks all its volunteer recorders and support from players of People's Postcode Lottery.

De Natuurkalender (Nature's Calendar) program in the Netherlands thanks all the volunteers and school children in the GLOBE program for their many observations.

Annette Menzel and Ye Yuan acknowledge support from the Bavarian State Ministry of Science and the Arts in the context of the Bavarian Climate Research Network (BayKlif) (BAYSICS project - Bavarian Citizen Science Portal for Climate Research and Science Communication).

Orlane Anneville acknowledges support from INRAE.

Stephen Thackeray thanks Werner Eckert, Heidrun Feuchtmayr, Shin-Ichiro Matsuzaki, Linda May, Ryuichiro Shinohara, Jan-Erik Thrane, Piet Verburg, Tamar Zohary, and all field and lab workers associated with the provision of the lake chlorophyll-a data.

We acknowledge funding from Vassdragsforbundet for Mjøsa med tilløpselver (https://www.vassdragsforbundet.no/om-oss/) and Natural Environment Research Council award number NE/R016429/1 as part of the UK-SCAPE programme delivering National Capability.

Data for Lakes Geneva and Bourget were contributed by The Observatory on LAkes (OLA), © SOERE OLA-IS, AnaEE-France, INRAE of Thonon-les-Bains, CIPEL, CISALB.

2.h.5 Vegetation Optical Depth

W. Dorigo, R.M. Zotta, and L. Moesinger, acknowledge the TU Wien Wissenschaftspreis 2015, a personal grant awarded to W. Dorigo.

We also acknowledge support from the ESA Climate Change Initiative Soil Moisture project.

Appendix 1: Chapter 2 – Acronyms

AAO	Antarctic Oscillation
AATSR	Advanced Along Track Scanning Radiometer
ALEXI	Atmosphere–Land Exchange Inverse
ALT	active layer thickness
AMSRE-E	Advanced Microwave Scanning Radiometer
AO	Arctic Oscillation
AOD	aerosol optical depth
ATSR	Along Track Scanning Radiometer
AVHRR	Advanced Very High Resolution Radiometer
BDC	Brewer-Dobson circulation
BRW	Barrow Atmospheric Baseline Observatory
C3S	Copernicus Climate Change Service
CALIOP	Cloud-Aerosol Lidar with Orthogonal Polarization
CAMS	Copernicus Atmosphere Monitoring Service
CAMSRA	Copernicus Atmosphere Monitoring Service Reanalysis
CCMI	Chemistry Climate Model Initiative
CEI	Climate Extremes Index
CERES	Clouds and the Earth's Radiant Energy System
CFC	chlorofluorocarbon
CH_4	methane
Cl	chlorine
CO	carbon monoxide
CO_2	carbon dioxide
CPT	cold-point tropopause
CRU TS	Climatic Research Unit gridded Time Series
DDM	drainage direction map
DU	Dobson unit
EA	Eurasia
ECV	essential climate variable
EESC	equivalent effective stratospheric chlorine
EESC-A	equivalent effective stratospheric chlorine-Antarctic
EESC-M	equivalent effective stratospheric chlorine-Midlatitude
ENSO	El Niño–Southern Oscillation
EOFs	empirical orthogonal functions
EOS	end of season
ERB	Earth's radiation budget
ESA CCI SM	European Space Agency's Climate Change Initiative for Soil Moisture
ET	evapotranspiration
ETCCDI	WMO Expert Team in Climate Change Detection and Indices
FAPAR	Fraction of Absorbed Photosynthetically Active Radiation
FF	fossil fuel
GCOS	Global Climate Observing System
GFAS	Global Fire Assimilation System
GFED	Global Fire Emissions Database
GGGRN	NOAA's Global Greenhouse Gas Reference Network
GHCN	Global Historical Climatology Network

GHCNDEX	Global Historical Climatology Network-Daily database
GIN-P	Global Terrestrial Network for Permafrost
GLEAM	Global Land Evaporation Amsterdam Model
GMST	global mean surface temperature
GNSS	Global Navigation Satellite System
GPCC	Global Precipitation Climatology Centre
GPCP	Global Precipitation Climatology Project
GPS-RO	Global Positioning System-Radio Occultation
GRACE	Gravity Recovery and Climate Experiment
GRACE-FO	Gravity Recovery and Climate Experiment - Follow On
GTN-P	Global Terrestrial Network for Permafrost
HFCF	hydrochlorofluorocarbon
HFC	hydrofluorocarbon
HIRS	High Resolution Infra Red Radiation Sounder
HWF	heat wave frequency
HWM	heat wave magnitude
IOD	Indian Ocean dipole
IPA	International Permafrost Association
ITCZ	Intertropical Convergence Zone
LLGHG	long-lived greenhouse gases
LSA-SAF	Land Surface Analysis Satellite Applications Facility
LSWT	lake surface water temperature
LTT	lower tropospheric temperature
LWL	lake water level
MACC	Monitoring Atmospheric Composition and Climate
MAT	marine air temperature
MBL	marine boundary layer
MHW	marine heatwave
MLO	Mauna Loa, Hawaii
MLS	Microwave Limb Sounder
MODIS	Moderate Resolution Imaging Spectroradiometer
MOPITT	Measurement of Pollution in the Troposphere
MSU/AMSU	Microwave Sounding Unit/Advanced Microwave Sounding Unit
N_2O	nitrous oxide
NA	North America
NAO	North Atlantic Oscillation
NDVI	normalized difference vegetation index
NH	Northern Hemisphere
NMAT	night marine air temperature
O_3	ozone
ODGI	Ozone Depleting Gas Index
ODGI-A	Ozone Depleting Gas Index-Antarctic
ODGI-M	Ozone Depleting Gas Index-Midlatitude
ODS	ozone-depleting substances
OH	hydroxyl radical
OLR	outgoing longwave radiation
OMI	Ozone Monitoring Instrument
PDO	Pacific Decadal Oscillation
PSC	polar stratospheric cloud
QBO	quasi-biennial oscillation

QTP	Qinghai-Tibetan Plateau
RFaci	radiative forcing resulting from aerosol–cloud interactions
RFari	radiative forcing resulting from aerosol–radiation
RGK	rock glacier kinematics
RH	relative humidity
RO	radio occultation
RSW	reflected shortwave
SAM	Southern Annular Mode
SAR	Synthetic Aperture Radar
SCE	snow cover extent
scPDSI	self-calibrating Palmer Drought Severity Index
SH	Southern Hemisphere
SLSTR	Sea and Land Surface Temperature Radiometer
SOI	Southern Oscillation Index
SORCE	Solar Radiation and Climate Experiment
SOS	start of season
SPO	South Pole Observatory
SSM/I	Special Sensor Microwave/Imager
SSMIS	Special Sensor Microwave Imager/Sounder
SST	sea surface temperature
SSU	Stratospheric Sounding Unit
SW	shortwave
TCWV	total column water vapor
TIR	thermal infrared
TLS	lower stratospheric temperature
TOA	top of the atmosphere
TSI	total solar irradiance
TSIS-1	Total Solar and Spectral Irradiance Sensor-1
TTL	tropical tropopause layer
TTT	tropical tropospheric temperature
TWS	terrestrial water storage
UTH	upper tropospheric (relative) humidity
UV	ultraviolet
VOC	volatile organic compound
VOD	vegetation optical depth
VODCA	vegetation optical depth Climate Archive
WGMS	World Glacier Monitoring Service
WMO	World Meteorological Organization
WV	water vapor

Appendix 2: Supplemental Material

2.b.1 Surface Temperature

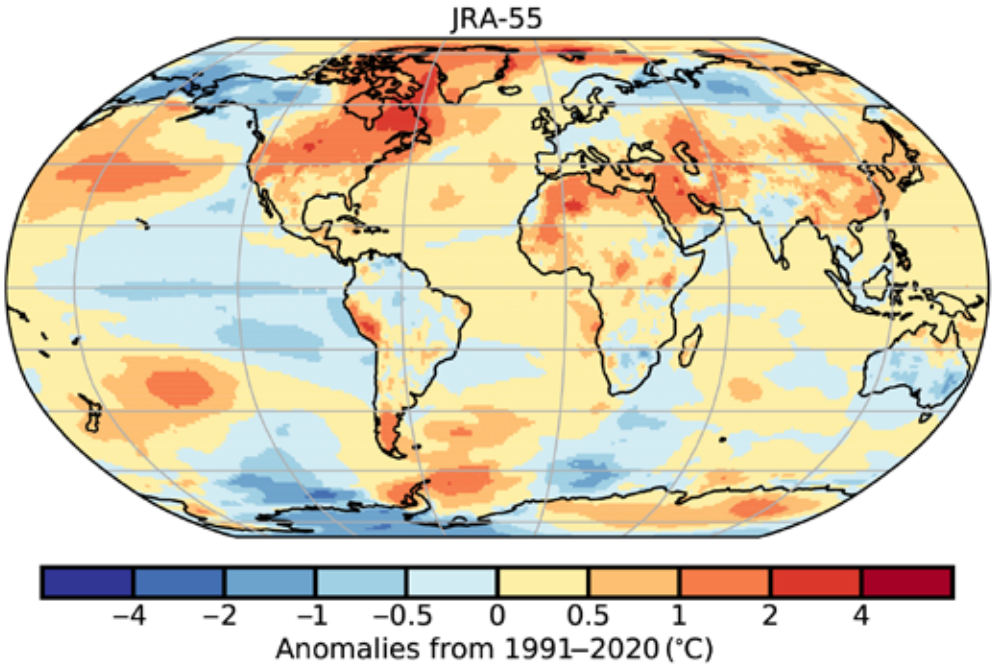

Fig. A2.1. JRA-55 2-m surface temperature anomalies (°C; 1991–2020 base period).

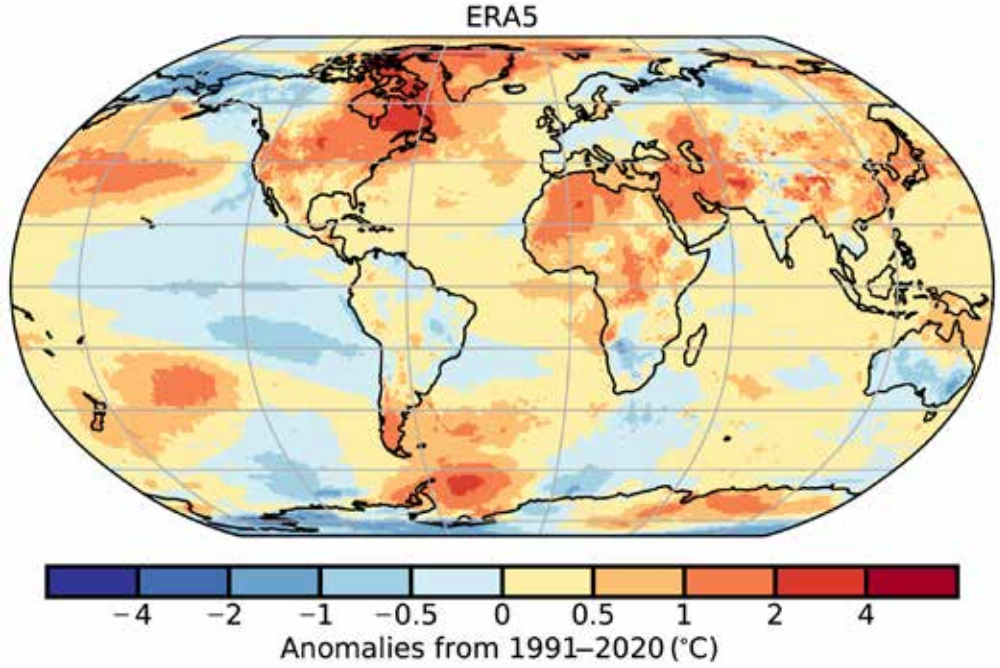

Fig. A2.2. ERA5 2-m surface temperature anomalies (°C; 1991–2020 base period).

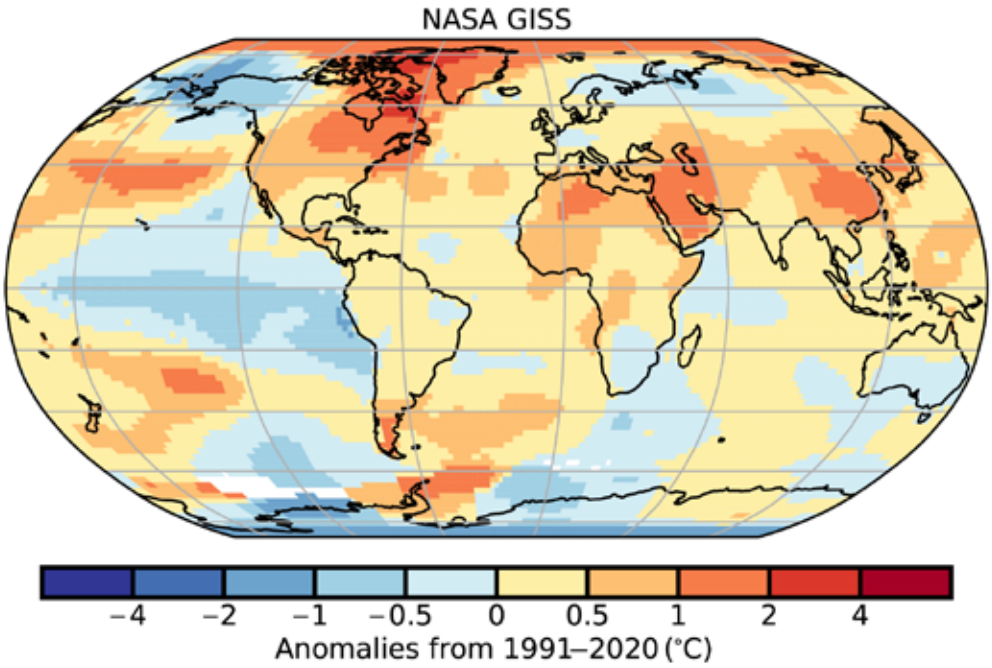

Fig. A2.3. NASA surface temperature anomalies (°C; 1991–2020 base period).

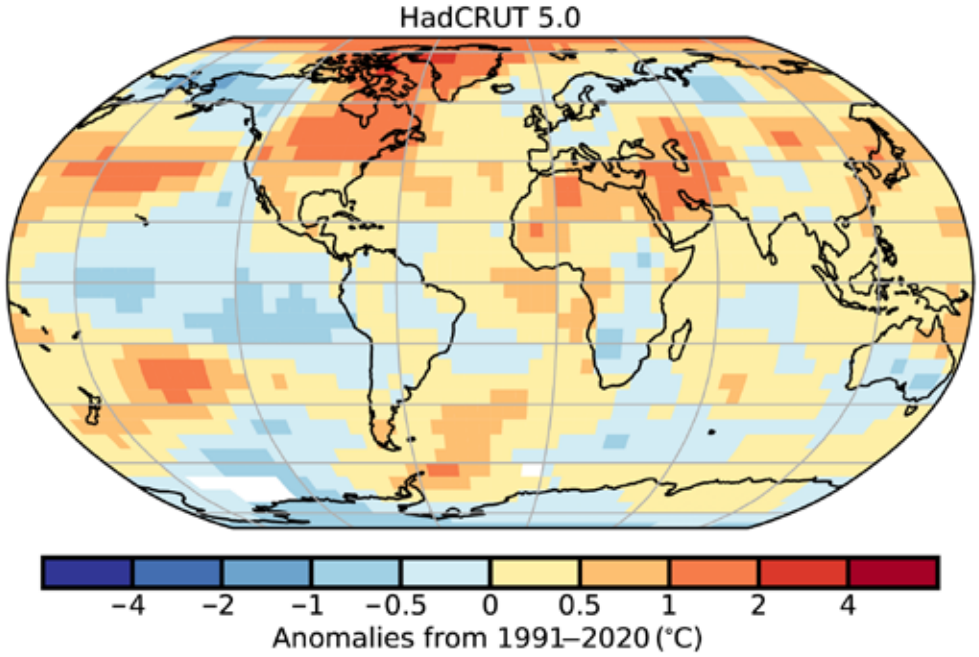

Fig. A2.4. HadCRUT5 surface temperature anomalies (°C; 1991–2020 base period).

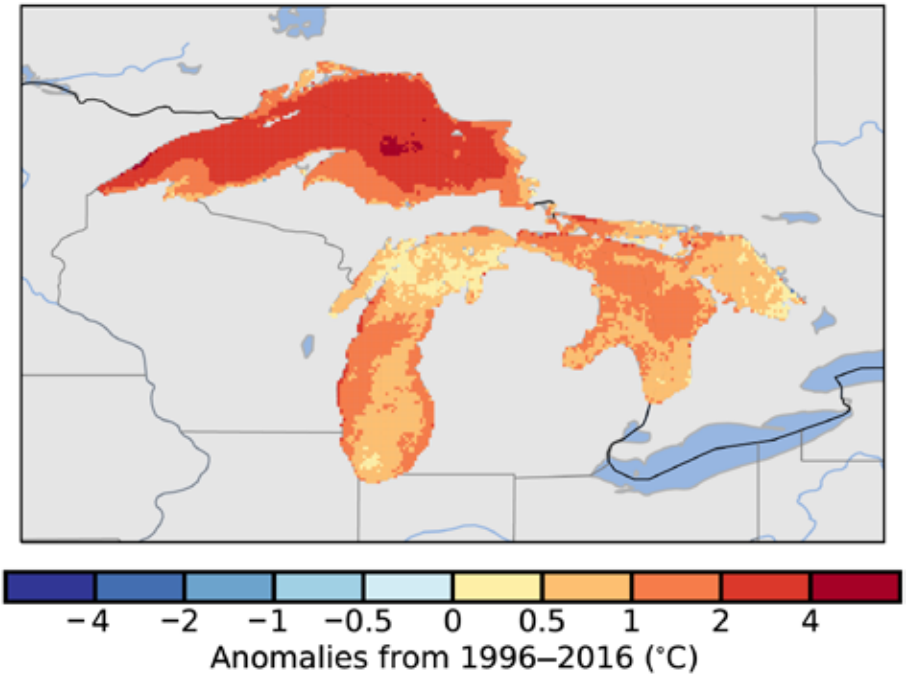

Fig. A2.5. Spatial distribution of the 2021 LSWT anomalies (°C) for Lake Superior, Huron, and Michigan in North America (1996–2016 base period).

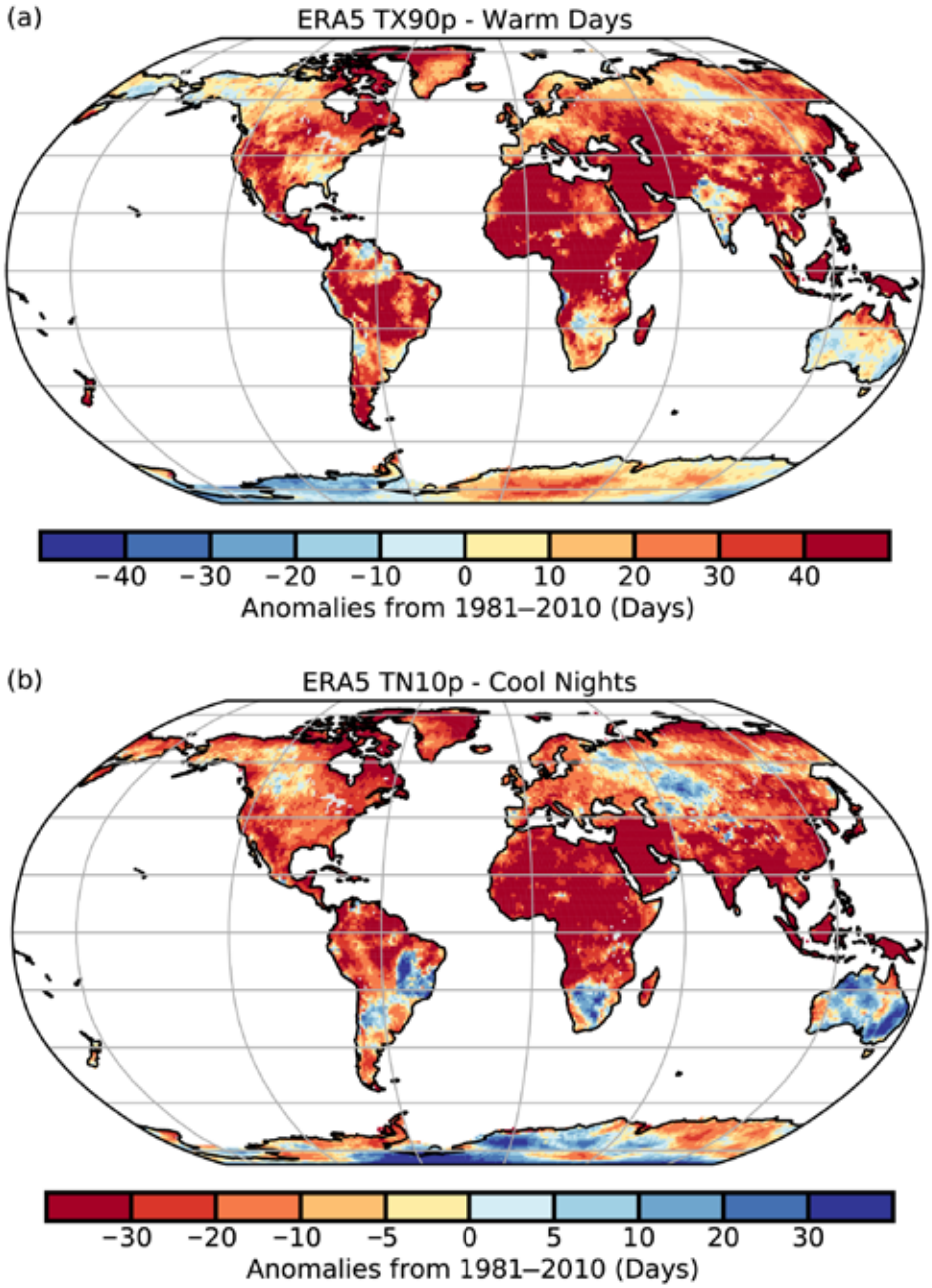

Fig. A2.6. Anomalies of (a) TX90p and (b) TN10p from ERA5 (1981–2010 base period).

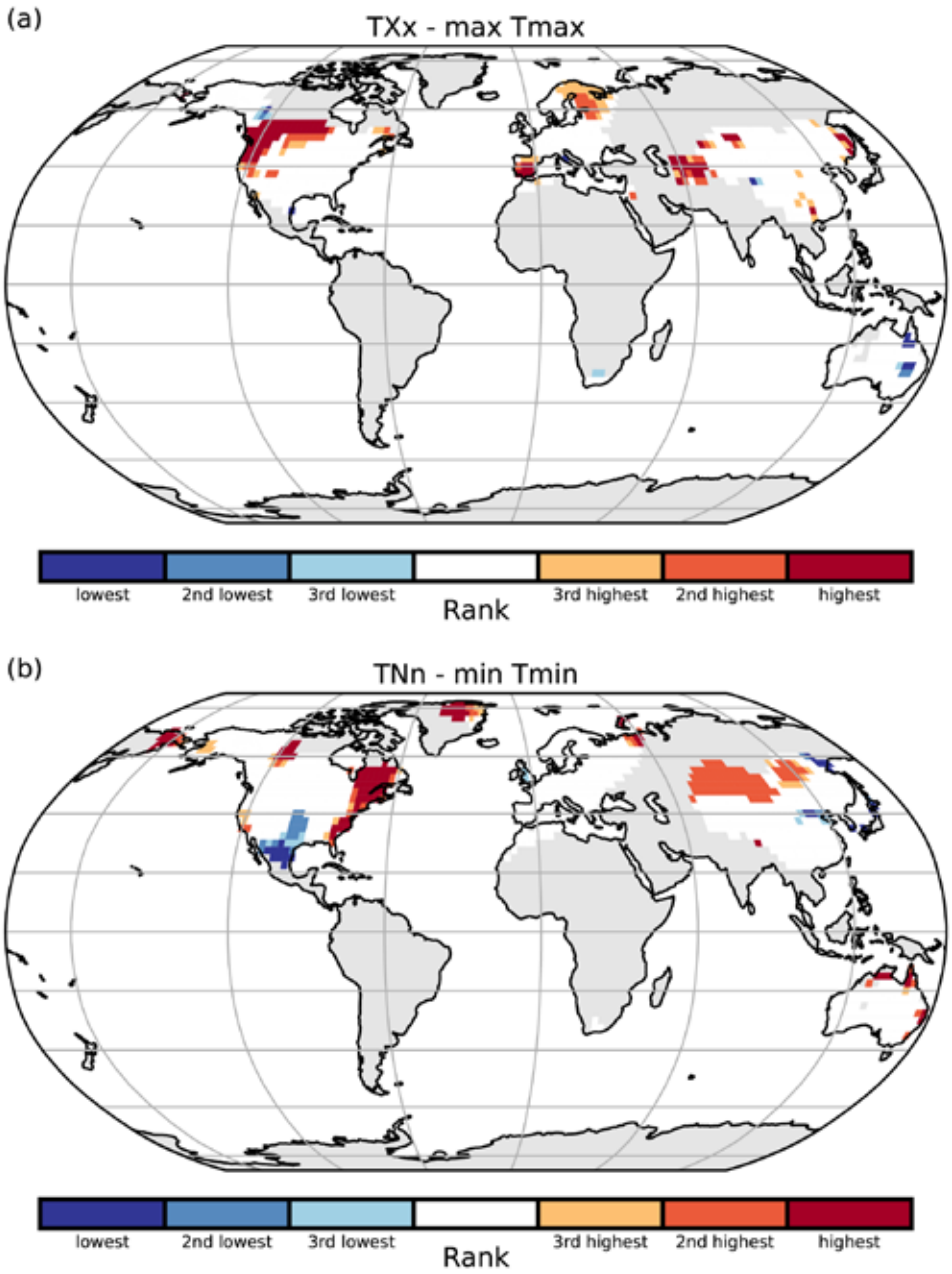

Fig. A2.7. Rank plots highlighting locations where the highest maximum temperature (TXx) and lowest minimum temperature (TNn) in 2021 were among the highest or lowest three on record.

Appendix Table 2.1. Selected extreme temperatures in 2021 relevant to the events discussed in the text. Additional records are presented in the WMO State of the Global Climate in 2021 (WMO 2022).

Location	Country	Date	Value	Notes
Clot del Tuc de la Llança	Spain	6 Jan	–34.1	National minimum record, coldest since station records began in 1956
Houston	Texas, USA	16 Feb	–11	Coldest since 1989
Dallas	Texas, USA	16 Feb	–18.9	Coldest since 1930
Strasbourg	France	31 Mar	26.3	March maximum record
Rheinau-Memprechtshofen	Germany	31 Mar	27.2	National March maximum record
Orléans	France	6 Apr	–5.4	April minimum record
Chalon-sur-Saône	France	7 Apr	–5.4	April minimum record
Orange	France	8 Apr	–3.2	April minimum record
Nova vas na Blokah	Slovenia	7 Apr	–20.6	April minimum record
Moscow	Russia	23 Jun	34.8	June maximum record
Yerevan	Armenia	24 Jun	41.1	June maximum record
Baku	Azerbaijan	26 Jun	40.5	June maximum record
Lytton	British Columbia, Canada	29 Jun	49.6	National record (by 4.6°C)
Utsjoki- Kevo	Lapland, Finland	5 Jul	33.6	Highest maximum since 1914
Death Valley	California, USA	9 Jul	54.4	Equal to hottest maximum temperature since at least 1930s.
Esashi	Iwate Prefecture, Japan	19 Jul	37.3	Equal to station record
Cizre	Turkey	20 Jul	49.1	National maximum record
Tbilisi	Georgia	20 Jul	40.6	National maximum record
Castlederg	Northern Ireland	21 Jul	31.3	Maximum record
Rafha	Saudi Arabia	24 Jul	50.6	—
Dammam	Saudi Arabia	31 Jul	50.4	Equal maximum record (set 2020)
Kairouan	Tunisia	2 Aug	50.3	National maximum record
Syracuse	Italy	11 Aug	48.8	Provisional European maximum record
Montoro	Cordoba, Spain	14 Aug	47.4	National maximum record
Makrakomi Ftiotida	Greece	2 Aug	46.3	National maximum record

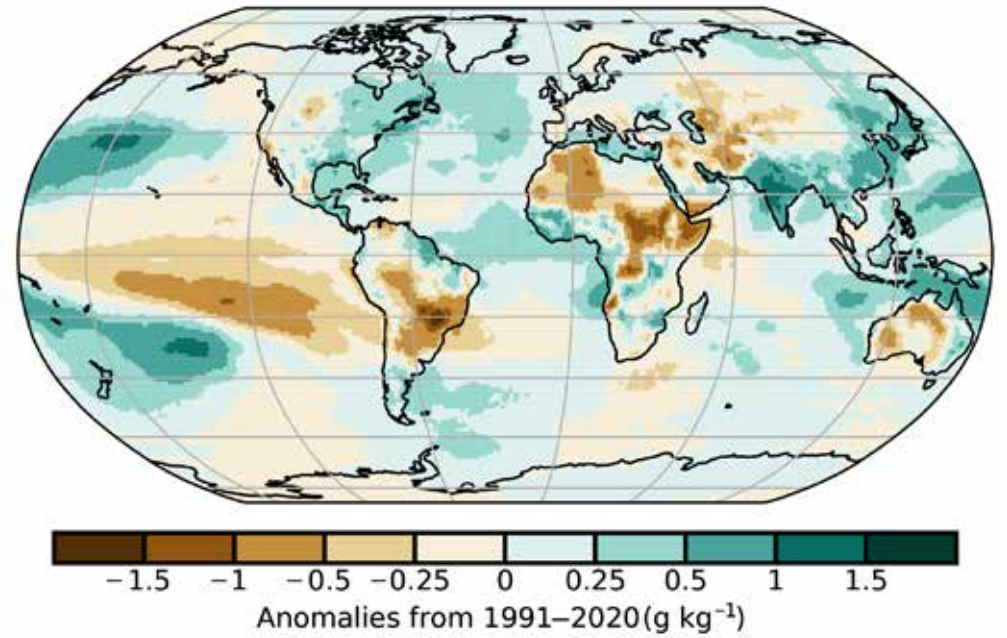

Fig. A2.8. ERA5 surface specific humidity annual average anomalies (g kg^{-1}) for 2021 (1991–2020 base period).

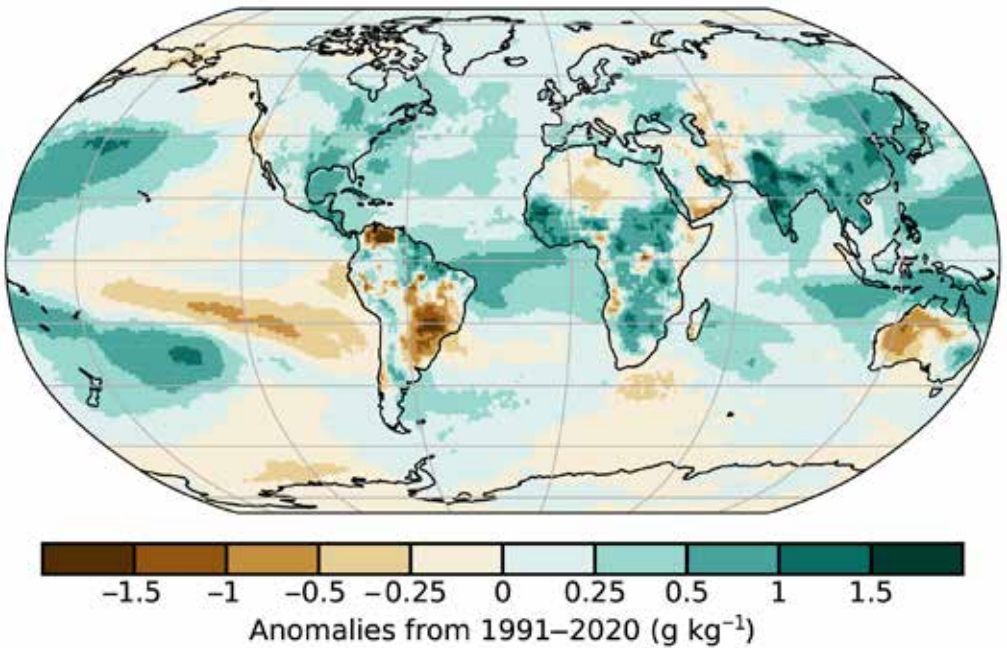

Fig. A2.9. MERRA2 surface specific humidity annual average anomalies (g kg^{-1}) for 2021 (1991–2020 base period).

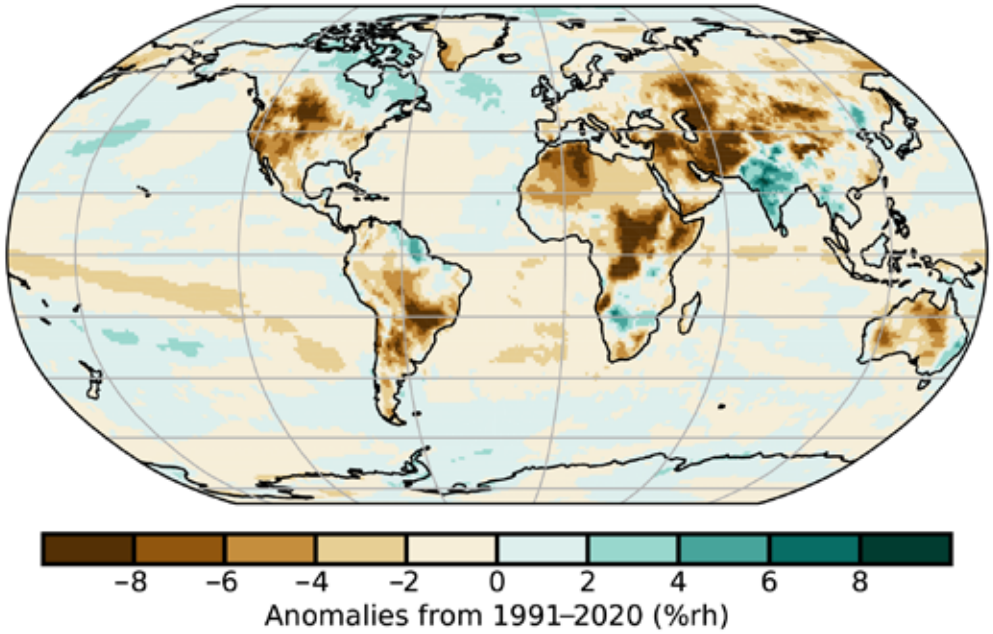

Fig. A2.10. ERA5 surface relative humidity annual average anomalies (%rh) for 2021 (1991–2020 base period).

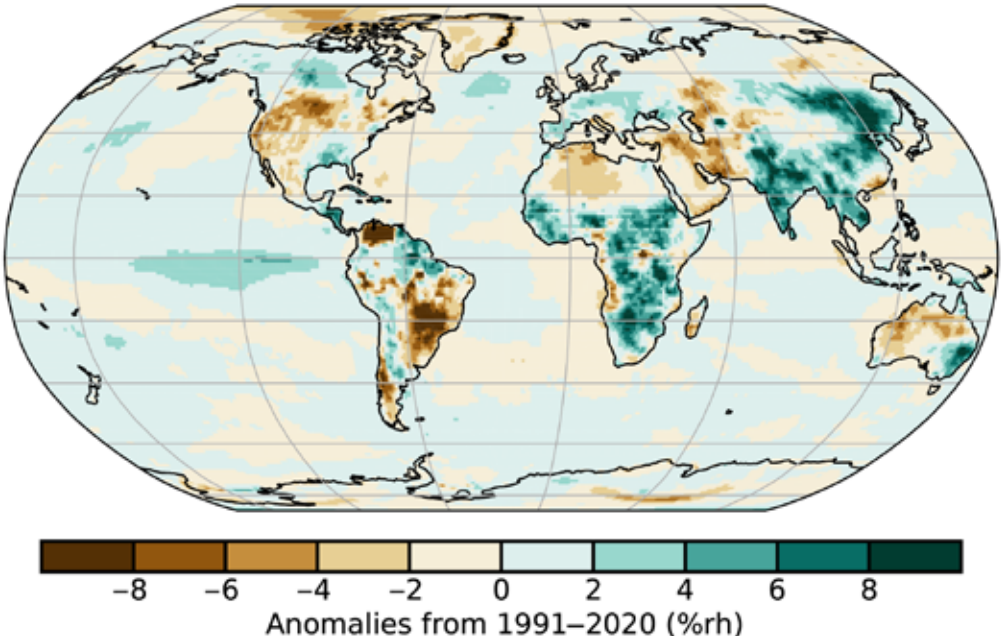

Fig. A2.11. MERRA2 surface relative humidity annual average anomalies (%rh) for 2021 (1991–2020 base period).

Appendix Table 2.2. Selected extreme precipitation events in 2021. The value column shows the recorded amount and accumulation period. Events are listed in the order referred to in the text. Events noted as records are for the location listed unless otherwise stated.

Location	Country	Date	Value	Notes
Paso Robles Airport, California	United States	25 Oct	39 mm (24-h)	Record 24-h total for October
Abbotsford	Canada	14 Nov	100.4 mm (24-h)	Record 24-h total
New York City	United States	1 Sep	80 mm (1-h)	Hurricane Ida set record 1-h total, breaking record of 49 mm set by Henri earlier in the month
Newark, New Jersey	United States	1 Sep	213.6 mm (24-h)	Record 24-h total
Wipperfurth-Gardenau	Germany	14–15 Jul	162.4 mm (24-h)	Record 24-h total
Gävle	Sweden	17–18 Aug	161.6 mm (24-h)	Record 24-h total
Kindee Bridge, New South Wales	Australia	20 Mar	283.4 mm (24-h)	Record 24-h total for March
Samuel Hill Aero, Queensland	Australia	10 Nov	340.8 mm (24-h)	Record 24-h total for November (> 3 times previous record)
Newbicup, Western Australia	Australia	12 Apr	74.0 mm (24-h)	Record 24-h total for April
Zhengzhou, Henan Province	China	20 Jul	201.9 mm (1-h)	Typhoon In-fa. 1-h total reported as national record for mainland China
Taiyuan, Shanxi Province	China	2–7 Oct	185.5 mm (12-h)	Regional record 12-h total for October
Beira	Mozambique	23 Jan	250 mm (24-h)	Close to regional monthly average rainfall

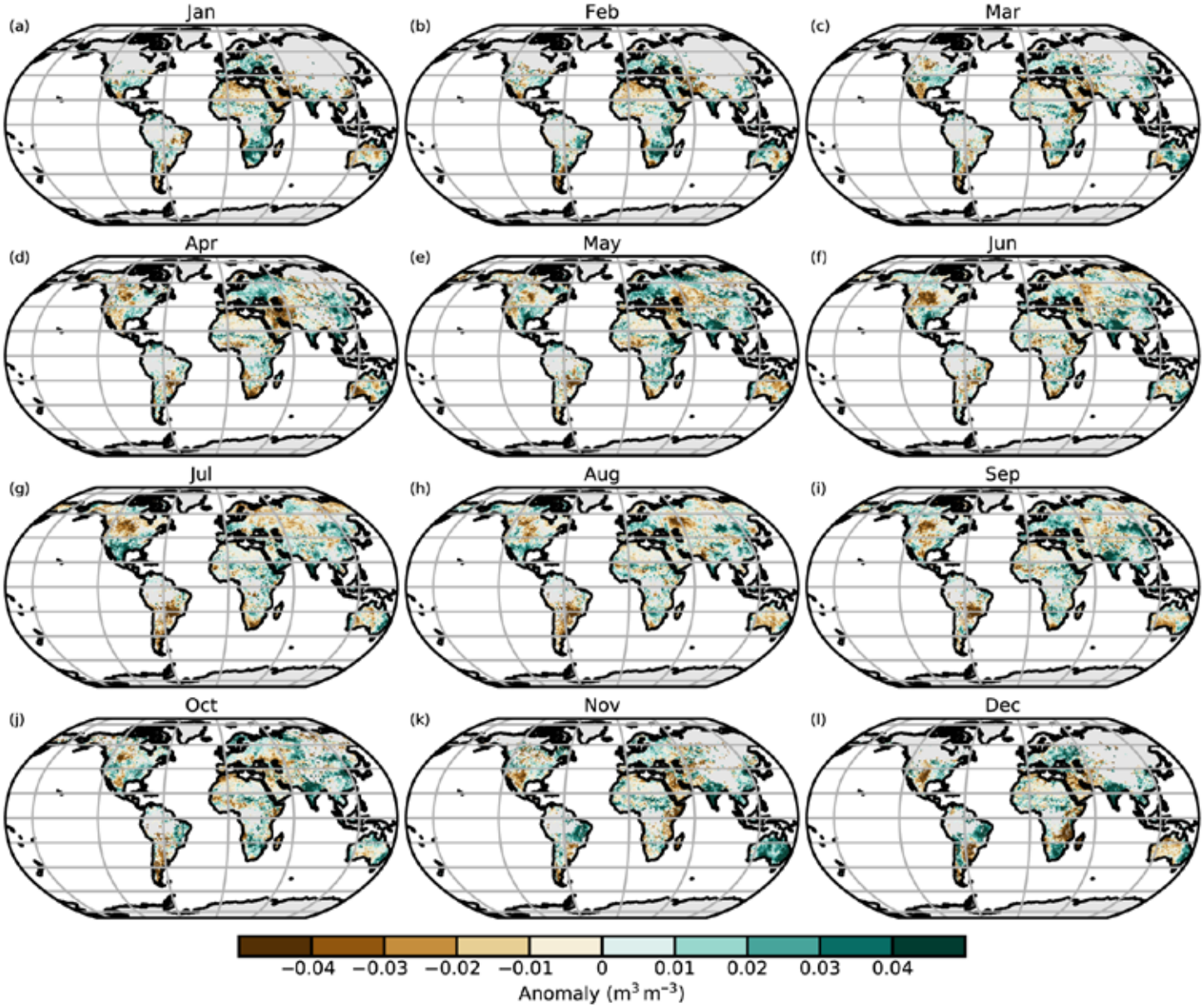

Fig. A2.12. ESA CCI soil moisture monthly average soil moisture anomalies ($m^3\ m^{-3}$) for 2021 (1991–2020 base period). Data are masked where no retrieval is possible or where the quality is not assured and flagged due to dense vegetation, frozen soil, radio frequency interference, etc.

2.h.5 Vegetation Optical Depth

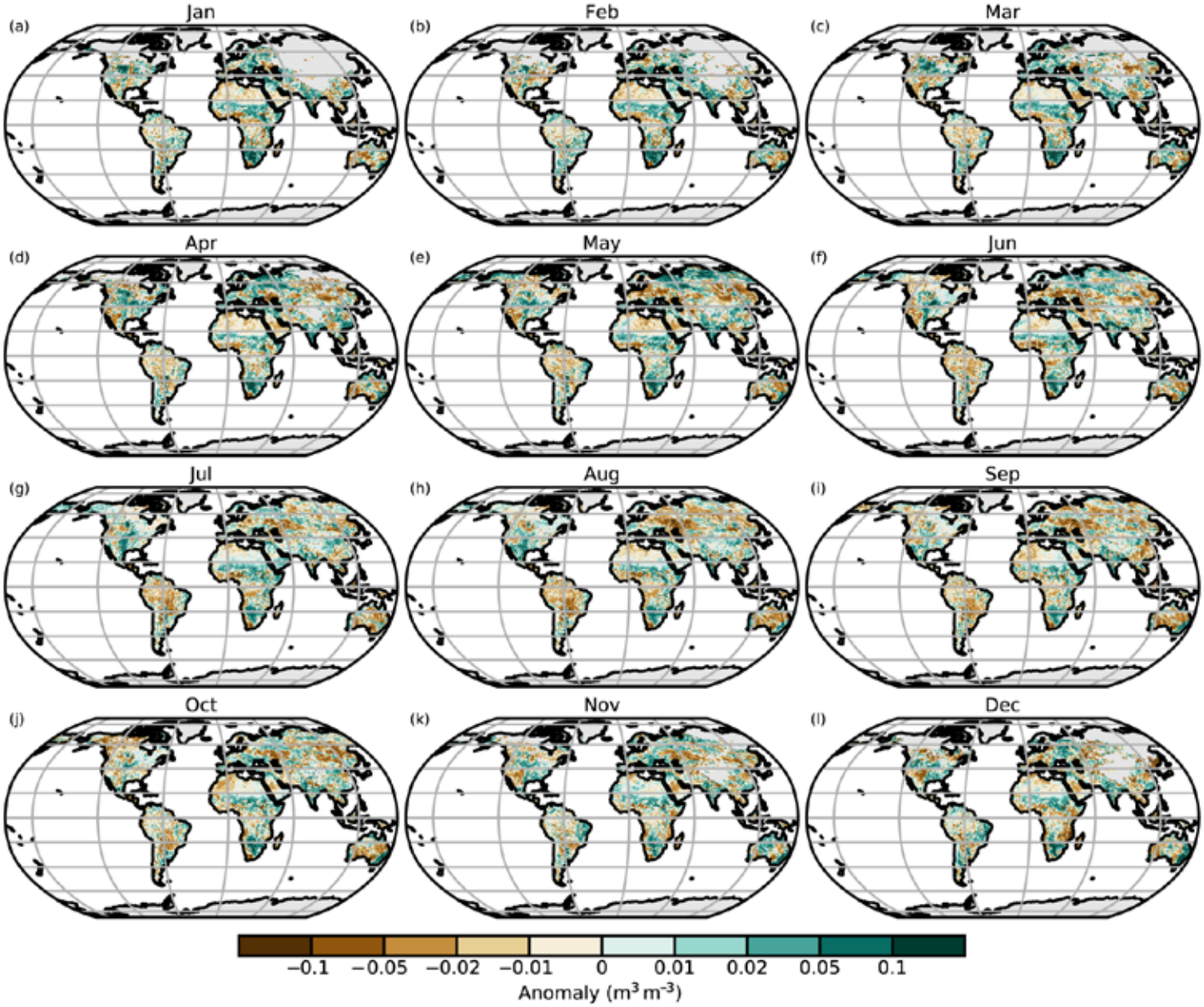

Fig. A2.13. (a–l) VODCA monthly Ku-band VOD anomalies ($m^3\ m^{-3}$) for 2021 (1991–2020 base period).

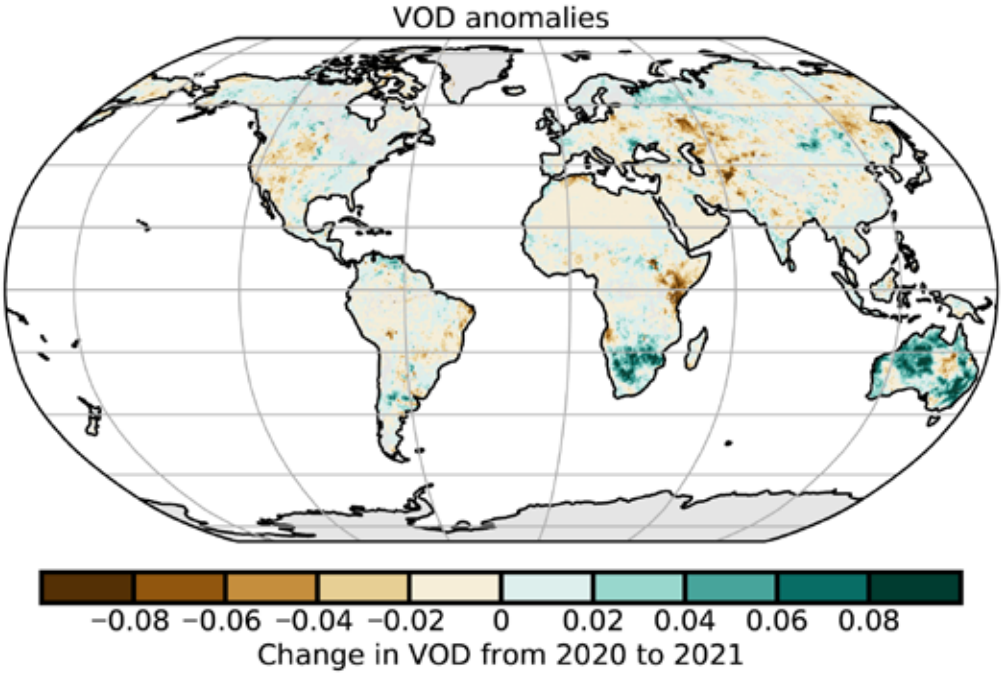

Fig. A2.14. Difference in average Ku-band VOD between the years 2021 and 2020. Brown/green colors indicate areas where VOD in 2021 was lower/higher than in 2020. (Source: VODCA.)

References

Adler, R., and Coauthors, 2018: The global Precipitation Climatology Project (GPCP) monthly analysis (new version 2.3) and a review of 2017 global precipitation. *Atmosphere*, **9**, 138, https://doi.org/10.3390/atmos9040138.

Aich, V., R. Holzworth, S. Goodman, Y. Kuleshov, C. Price, and E. Williams, 2018: Lightning: A new essential climate variable. *Eos*, **99**, https://doi.org/10.1029/2018EO104583.

Alden, C. B., J. B. Miller, and J. W. C. White, 2010: Can bottom-up ocean CO_2 fluxes be reconciled with atmospheric ^{13}C observations? *Tellus*, **62B**, 369–388, https://doi.org/10.1111/j.1600-0889.2010.00481.x.

Anabalón, A., and A. Sharma, 2017: On the divergence of potential and actual evapotranspiration trends: An assessment across alternate global datasets. *Earth's Future*, **5**, 905–917, https://doi.org/10.1002/2016EF000499.

Andela, N., and Coauthors, 2017: A human-driven decline in global burned area. *Science*, **356**, 1356–1362, https://doi.org/10.1126/science.aal4108.

Anyamba, E., E. Williams, J. Süsskind, A. Fraser-Smith, and M. Füllekrug, 2000: The manisfestation of the Madden–Julian oscillation in global deep convection and in the Schumann resonance intensity. *J. Atmos. Sci.*, **57**, 1029–1044, https://doi.org/10.1175/1520-0469(2000)057<1029:TMOTMJ>2.0.CO;2.

Aono, Y., and K. Kazui, 2008: Phenological data series of cherry tree flowering in Kyoto, Japan, and its application to reconstruction of springtime temperatures since the 9th century. *Int. J. Climatol.*, **28**, 905–914, https://doi.org/10.1002/joc.1594.

Archer, D., and V. Brovkin, 2008: The millennial atmospheric lifetime of anthropogenic CO2. *Climatic Change*, **90**, 283–297, https://doi.org/10.1007/s10584-008-9413-1.

Archibald, A. T., and Coauthors, 2020: Tropospheric Ozone Assessment Report: A critical review of changes in the tropospheric ozone burden and budget from 1850 to 2100. *Elem. Sci. Anthropocene*, **8**, 034, https://doi.org/10.1525/elementa.2020.034.

AMAP, 2021: Arctic Climate Change Update 2021: Key trends and impacts: Summary for Policy-makers. Arctic Monitoring and Assessment Programme, 16 pp., www.amap.no/documents/doc/arctic-climate-change-update-2021-key-trends-and-impacts.-summary-for-policy-makers/3508.

Arguez, A., and Coauthors, 2020: Should we expect each year in the next decade (2019–28) to be ranked among the top 10 warmest years globally? *Bull. Amer. Meteor. Soc.*, **101**, E655–E663, https://doi.org/10.1175/BAMS-D-19-0215.1.

Arosio, C., A. Rozanov, E. Malinina, K.-U. Eichmann, T. von Clarmann, and J. P. Burrows, 2018: Retrieval of ozone profiles from OMPS limb scattering observations. *Atmos. Meas. Tech.*, **11**, 2135–2149, https://doi.org/10.5194/amt-11-2135-2018.

——, ——, ——, M. Weber, and J. P. Burrows, 2019: Merging of ozone profiles from SCIAMACHY, OMPS and SAGE II observations to study stratospheric ozone changes. *Atmos. Meas. Tech.*, **12**, 2423–2444, https://doi.org/10.5194/amt-12-2423-2019.

Augustine, J. A., K. O. Lantz, J.-P. Vernier, and H. Telg, 2020: Mauna Loa clear-sky "apparent" solar transmission [in "State of the Climate in 2019"]. *Bull. Amer. Meteor. Soc.*, **101** (8), S61–S62, https://doi.org/10.1175/BAMS-D-20-0104.1.

——, ——, and ——, 2021: Mauna Loa apparent transmission [in "State of the Climate in 2020"]. *Bull. Amer. Meteor. Soc.*, **102** (8), S82–S83, https://doi.org/10.1175/BAMS-D-21-0098.1.

Azorin-Molina, C., J. Asin, T. R. McVicar, L. Minola, J. I. Lopez-Moreno, S. M. Vicente-Serrano, and D. Chen, 2018: Evaluating anemometer drift: A statistical approach to correct biases in wind speed measurement. *Atmos. Res.*, **203**, 175–188, https://doi.org/10.1016/j.atmosres.2017.12.010.

——, and Coauthors, 2021: A decline of observed daily peak wind gusts with distinct seasonality in Australia, 1941–2016. *J. Climate*, **34**, 3103–3127, https://doi.org/10.1175/JCLI-D-20-0590.1.

Baldwin, M. P., and T. J. Dunkerton, 2001: Stratospheric harbingers of anomalous weather regimes. *Science*, **294**, 581–584, https://doi.org/10.1126/science.1063315.

——, and Coauthors, 2001: The quasi-biennial oscillation. *Rev. Geophys.*, **39**, 179–229, https://doi.org/10.1029/1999RG000073.

Ball, W. T., and Coauthors, 2018: Evidence for a continuous decline in lower stratospheric ozone offsetting ozone layer recovery. *Atmos. Chem. Phys.*, **18**, 1379–1394, https://doi.org/10.5194/acp-18-1379-2018.

——, G. Chiodo, M. Abalos, J. Alsing, and A. Stenke, 2020: Inconsistencies between chemistry–climate models and observed lower stratospheric ozone trends since 1998. *Atmos. Chem. Phys.*, **20**, 9737–9752, https://doi.org/10.5194/acp-20-9737-2020.

Ballantyne, A. P., C. B. Alden, J. B. Miller, P. P. Tans, and J. W. C. White, 2012: Increase in observed net carbon dioxide uptake by land and oceans during the past 50 years. *Nature*, **488**, 70–72, https://doi.org/10.1038/nature11299.

Barichivich, J., T. J. Osborn, I. Harris, G. van der Schrier, and P. D. Jones, 2020: Monitoring global drought using the self-calibrating Palmer Drought Severity Index [in "State of the Climate in 2019"]. *Bull. Amer. Meteor. Soc.*, **101** (8), S59–S60, https://doi.org/10.1175/BAMS-D-20-0104.1.

——, ——, ——, ——, and ——, 2021: Monitoring global drought using the self-calibrating Palmer Drought Severity Index [in "State of the Climate in 2020"]. *Bull. Amer. Meteor. Soc.*, **102** (8), S68–S70, https://doi.org/10.1175/BAMS-D-21-0098.1.

Beck, H. E., and Coauthors, 2019: MSWEP V2 global 3-hourly 0.1° precipitation: Methodology and quantitative assessment. *Bull. Amer. Meteor. Soc.*, **100**, 473–500, https://doi.org/10.1175/BAMS-D-17-0138.1.

——, A. I. J. M. van Dijk, P. R. Larraondo, T. R. McVicar, M. Pan, E. Dutra, and D. G. Miralles. 2022: MSWX: Global 3-hourly 0.1° bias-corrected meteorological data including near real-time updates and forecast ensembles. *Bull. Amer. Meteor. Soc.*, 103, E710–E732, https://doi.org/10.1175/BAMS-D-21-0145.1.

Becker, A., P. Finger, A. Meyer-Christoffer, B. Rudolf, K. Schamm, U. Schneider, and M. Ziese, 2013: A description of the global land-surface precipitation data products of the Global Precipitation Climatology Centre with sample applications including centennial (trend) analysis from 1901–present. *Earth Syst. Sci. Data*, **5**, 71–99, https://doi.org/10.5194/essd-5-71-2013.

Behera, S. K., J. J. Luo, S. Masson, S. A. Rao, H. Sakuma, and T. Yamagata, 2006: A CGCM study on the interaction between IOD and ENSO. *J. Climate*, **19**, 1688–1705, https://doi.org/10.1175/JCLI3797.1.

Bell, B., and Coauthors, 2021: The ERA5 global reanalysis: Preliminary extension to 1950. *Quart. J. Roy. Meteor. Soc.*, **147**, 4186–4227, https://doi.org/10.1002/qj.4174.

Bell, G. D., and M. Chelliah, 2006: Leading tropical modes associated with interannual and multidecadal fluctuations in North Atlantic hurricane activity. *J. Climate*, **19**, 590–612, https://doi.org/10.1175/JCLI3659.1.

Bellouin, N., and Coauthors, 2020: Radiative forcing of climate change from the Copernicus reanalysis of atmospheric composition. *Earth Syst. Sci. Data*, **12**, 1649–1677, https://doi.org/10.5194/essd-12-1649-2020.

Bieniek, P., and Coauthors, 2020: Lightning variability in dynamically downscaled simulations of Alaska's present and future summer climate. *J. Appl. Meteor. Climatol.*, **59**, 1139–1152, https://doi.org/10.1175/JAMC-D-19-0209.1.

Biskaborn, B. K., and Coauthors, 2019: Permafrost is warming at a global scale. *Nat. Commun.*, **10**, 264, https://doi.org/10.1038/s41467-018-08240-4.

Blakeslee, R., and Coauthors, 2020: Three years of the Lightning Imaging Sensor onboard the International Space Station: Expanded global coverage and enhanced applications. *J. Geophys. Res. Atmos.*, **125**, e2020JD032918, https://doi.org/10.1029/2020JD032918.

Bock, O., 2020: Global GNSS Integrated Water Vapour data, 1994-2020. AERIS, accessed 20 February 2022, https://doi.org/10.25326/68.

Bodhaine, B. A., B. G. Mendonca, J. M. Harris, and J. M. Miller, 1981: Seasonal variations in aerosols and atmospheric transmission at Mauna Loa Observatory. *J. Geophys. Res.*, **86**, 7395–7398, https://doi.org/10.1029/JC086iC08p07395.

Bojinski, S., M. Verstraete, T. Peterson, C. Richter, A. Simmons, and M. Zemp, 2014: The concept of essential climate variables in support of climate research, applications, and policy. *Bull. Amer. Meteor. Soc.*, **95**, 1431–1443, https://doi.org/10.1175/BAMS-D-13-00047.1.

Brohan, P., J. J. Kennedy, I. Harris, S. F. B. Tett, and P. D. Jones, 2006: Uncertainty estimates in regional and global observed temperature changes: A new data set from 1850. *J. Geophys. Res.*, **111**, D12106, https://doi.org/10.1029/2005JD006548.

Brooks, C., 1925: *The Distribution of Thunderstorms over the Globe*. Geophysical Memoirs, No. 24, H. M. Stationery Office, 164 pp.

Brown, J. R., and Coauthors, 2020: South Pacific Convergence Zone dynamics, variability and impacts in a changing climate. *Nat. Rev. Earth Environ.*, **1**, 530–543, https://doi.org/10.1038/s43017-020-0078-2.

Brutsaert, W., 2017: Global land surface evaporation trend during the past half century: Corroboration by Clausius-Clapeyron scaling. *Adv. Water Resour.*, **106**, 3–5, https://doi.org/10.1016/j.advwatres.2016.08.014.

Buchholz, R. R., and Coauthors, 2021: Air pollution trends measured from Terra: CO and AOD over industrial, fire-prone, and 22 background regions. *Remote Sens. Environ.*, **256**, 112275, https://doi.org/10.1016/j.rse.2020.112275.

Bureau of Meteorology, 2021a: New South Wales in March 2021: A very wet and cool month with extensive flooding. Accessed 9 February 2022, www.bom.gov.au/climate/current/month/nsw/archive/202103.summary.shtml.

——, 2021b: New South Wales in November 2021: Wettest on record. Accessed 9 February 2022, www.bom.gov.au/climate/current/month/nsw/archive/202111.summary.shtml.

——, 2021c: Queensland in November 2021: Seventh-wettest November; wettest since 2010. Accessed 9 February 2022, www.bom.gov.au/climate/current/month/qld/archive/202111.summary.shtml.

——, 2021d: Western Australia in April 2021: Wet in the west; warm in the south. Accessed 9 February 2022, www.bom.gov.au/climate/current/month/wa/archive/202104.summary.shtml.

——, 2022: Annual climate statement 2021: 2021 coolest year in nearly a decade and wettest since 2016. 1 June 2022, https://media.bom.gov.au/releases/919/2021-coolest-year-in-nearly-a-decade-and-wettest-since-2016/.

Carpenter, L. J., and J. S. Daniel, 2018: Scenarios and information for policy makers. Scientific Assessment of Ozone Depletion: 2018, Global Ozone Research and Monitoring Project Rep. 58, 6.1–6.69, https://ozone.unep.org/sites/default/files/2019-05/SAP-2018-Assessment-report.pdf.

Carrea, L., O. Embury, and C. J. Merchant, 2015: Datasets related to in-land water for limnology and remote sensing applications: Distance-to-land, distance-to-water, water-body identifier and lake-centre co-ordinates. *Geosci. Data J.*, **2**, 83–97, https://doi.org/10.1002/gdj3.32.

——, and Coauthors, 2019: Lake surface temperature [in "State of the Climate in 2018"]. *Bull. Amer. Meteor. Soc.*, **100** (9), S13–S14, https://doi.org/10.1175/2019BAMSStateoftheClimate.1.

——, and Coauthors, 2020: Lake surface temperature [in "State of the Climate in 2019"]. *Bull. Amer. Meteor. Soc.*, **101** (8), S26–S28, https://doi.org/10.1175/BAMS-D-20-0104.1.

——, C. Merchant, B. Calmettes, and J.-F. Cretaux, 2021: Lake surface temperature [in "State of the Climate in 2020"]. *Bull. Amer. Meteor. Soc.*, **102** (8), S28–S31, https://doi.org/10.1175/BAMS-D-21-0098.1.

Cassou, C., 2008: Intraseasonal interaction between the Madden-Julian Oscillation and the North Atlantic Oscillation. *Nature*, **455**, 523–527, https://doi.org/10.1038/nature07286.

Cescatti, A., and Coauthors, 2012: Intercomparison of MODIS albedo retrievals and in situ measurements across the global FLUXNET network. *Remote Sens. Environ.*, **121**, 323–334, https://doi.org/10.1016/j.rse.2012.02.019.

Chang, J., S. Peng, P. Ciais, M. Saunois, S. R. Dangal, M. Herrero, P. Havlík, H. Tian, and P. Bousquet, 2019: Revisiting enteric methane emissions from domestic ruminants and their $\delta^{13}C_{CH4}$ source signature. *Nat. Comms.*, **10** (1), 1–14, https://doi.org/10.1038/s41467-019-11066-3.

Chang, K.-L., M. G. Schultz, X. Lan, A. McClure-Begley, I. Petropavlovskikh, X. Xu, and J. R. Ziemke, 2021: Trend detection of atmospheric time series: Incorporating appropriate uncertainty estimates and handling extreme events. *Elem. Sci. Anthropocene*, **9**, 00035, https://doi.org/10.1525/elementa.2021.00035.

——, and Coauthors, 2022: Impact of the COVID-19 economic downturn on tropospheric ozone trends: An uncertainty weighted data synthesis for quantifying regional anomalies above western North America and Europe, *AGU Adv.*, **3**, e2021AV000542, https://doi.org/10.1029/2021AV000542.

Chen, Y., D. Romps, J. Seeley, S. Veraverbeke, W. Riley, Z. Mekonnen, and J. Randerson, 2021: Future increases in Arctic lightning and fire risk for permafrost carbon. *Nat. Climate Change*, **11**, 404–410, https://doi.org/10.1038/s41558-021-01011-y.

Cheng, L., and Coauthors, 2017: Recent increases in terrestrial carbon uptake at little cost to the water cycle. *Nat. Commun.*, **8**, 110, https://doi.org/10.1038/s41467-017-00114-5.

Chipperfield, M. P., and Coauthors, 2018: On the cause of recent variations in lower stratospheric ozone. *Geophys. Res. Lett.*, **45**, 5718–5726, https://doi.org/10.1029/2018GL078071.

Christian, H., and Coauthors, 2003: Global frequency and distribution of lightning as observed from space by the optical transient detector. *J. Geophys. Res.*, **108**, 4005, https://doi.org/10.1029/2002JD002347.

Christiansen, H. H., G. L. Gilbert, U. Neumann, N. Demidov, M. Guglielmin, K. Isaksen, M. Osuch, and J. Boike, 2021: Ground ice content, drilling methods and equipment and permafrost dynamics in Svalbard 2016–2019 (PermaSval). SESS Report 2020, M. Moreno-Ibáñez et al., Eds., Svalbard Integrated Arctic Earth Observing System, 259–275, https://sios-svalbard.org/SESS_Issue3.

Christy, J. R., R. W. Spencer, W. D. Braswell, and R. Junod, 2018: Examination of space-based bulk atmospheric temperatures for climate research. *Yaogan Xuebao*, **39**, 3580–3607, https://doi.org/10.1080/01431161.2018.1444293.

Chronis, T., S. Goodman, D. Cecil, D. Buechler, F. Robertson, J. Pittman, and R. Blakeslee, 2008: Global lightning activity from the ENSO perspective. *Geophys. Res. Lett.*, **35**, L19804, https://doi.org/10.1029/2008GL034321.

Chung, E.-S., B. Soden, and V. O. John, 2013: Intercalibrating microwave satellite observations for monitoring long-term variations in upper- and midtropospheric water vapor. *J. Atmos. Oceanic Technol.*, **30**, 2303–2319, https://doi.org/10.1175/JTECH-D-13-00001.1.

——, B. J. Soden, X. Huang, L. Shi, and V. O. John, 2016: An assessment of the consistency between satellite measurements of upper tropospheric water vapor. *J. Geophys. Res.*, **121**, 2874–2887, https://doi.org/10.1002/2015JD024496.

Cicoira, A., J. Beutel, J. Faillettaz, and A. Vieli, 2019: Water controls the seasonal rhythm of rock glacier flow. *Earth Planet. Sci. Lett.*, **528**, 115844, https://doi.org/10.1016/j.epsl.2019.115844.

Coddington, O. M., 2017: TSIS Algorithm Theoretical Basis Document. Laboratory for Atmospheres and Space Physcis (LASP) Document 151430 RevA, 108 pp., https://docserver.gesdisc.eosdis.nasa.gov/public/project/TSIS/TSIS_Algorithm_Theoretical_Basis_Document_151430RevA.pdf.

Coldewey-Egbers, M., and Coauthors, 2015: The GOME-type Total Ozone Essential Climate Variable (GTO-ECV) data record from the ESA Climate Change Initiative. *Atmos. Meas. Tech.*, **8**, 3923–3940, https://doi.org/10.5194/amt-8-3923-2015.

——, D. G. Loyola, C. Lerot, and M. Van Roozendael, 2022: Global, regional and seasonal analysis of total ozone trends derived from the 1995–2020 GTO-ECV climate data record. *Atmos. Chem. Phys.*, **22**, 6861–6878, https://doi.org/10.5194/acp-22-6861-2022.

Colman, R., and B. J. Soden, 2021: Water vapor and lapse rate feedbacks in the climate system. *Rev. Mod. Phys.*, **93**, 045002, https://doi.org/10.1103/RevModPhys.93.045002.

Cooper, M., and R. Holle, 2019: *Reducing Lightning Injuries Worldwide.* Springer, 233 pp., https://doi.org/10.1007/978-3-319-77563-0.

Cooper, O. R., and Coauthors, 2014: Global distribution and trends of tropospheric ozone: An observation-based review. *Elem. Sci. Anthropocene*, **2**, 000029, http://doi.org/10.12952/journal.elementa.000029.

——, and Coauthors, 2020: Multi-decadal surface ozone trends at globally distributed remote locations. *Elem. Sci. Anthropocene*, **8**, 23, https://doi.org/10.1525/elementa.420.

Cornes, R. C., E. C. Kent, D. I. Berry, and J. J. Kennedy, 2020: CLASSnmat: A global night marine air temperature data set, 1880–2019. *Geosci. Data J.*, **7**, 170–184, https://doi.org/10.1002/gdj3.100.

——, D. I. Berry, R. Junod, E. C. Kent, and N. A. Rayner, 2021: Night marine air temperature [in "State of the Climate in 2020"]. *Bull. Amer. Meteor. Soc.*, **102** (8), S39–S41, https://doi.org/10.1175/BAMS-D-21-0098.1.

Cox, P. M., D. Pearson, B. B. Booth, P. Friedlingstein, C. Huntingford, C. D. Jones, and C. M. Luke, 2013: Sensitivity of tropical carbon to climate change constrained by carbon dioxide variability. *Nature*, **494**, 341–344, https://doi.org/10.1038/nature11882.

Crocetti, L., and Coauthors, 2020: Earth Observation for agricultural drought monitoring in the Pannonian Basin (southeastern Europe): Current state and future directions. *Reg. Environ. Change*, **20**, 123, https://doi.org/10.1007/s10113-020-01710-w.

Cusicanqui, D., A. Rabatel, C. Vincent, X. Bodin, E. Thibert, and B. Francou, 2021: Interpretation of volume and flux changes of the Laurichard Rock Glacier between 1952 and 2019, French Alps. *J. Geophys. Res. Earth Surface*, 126, e2021JF006161, https://doi.org/10.1029/2021JF006161.

Daniel, J. S., S. Solomon, and D. L. Albritton, 1995: On the evaluation of halocarbon radiative forcing and global warming potentials. *J. Geophys. Res.*, **100**, 1271–1285, https://doi.org/10.1029/94JD02516.

Davidson, E. A., 2009: The contribution of manure and fertilizer nitrogen to atmospheric nitrous oxide since 1860. *Nat. Geosci.*, **2**, 659–662, https://doi.org/10.1038/ngeo608.

Davis, S. M., K. H. Rosenlof, D. F. Hurst, and H. Vömel, 2021: Stratospheric water vapor [in "State of the Climate in 2020"]. *Bull. Amer. Meteor. Soc.*, **102** (8), S95–S98, https://doi.org/10.1175/BAMS-D-21-0098.1.

Dee, D. P., and Coauthors, 2011: The ERA-Interim reanalysis: Configuration and performance of the data assimilation system. *Quart. J. Roy. Meteor. Soc.*, **137**, 553–597, https://doi.org/10.1002/qj.828.

Deeter, M. N., and Coauthors, 2014: The MOPITT Version 6 product: Algorithm enhancements and validation. *Atmos. Meas. Tech.*, **7**, 3623–3632, https://doi.org/10.5194/amt-7-3623-2014.

——, D. P. Edwards, G. L. Francis, J. C. Gille, S. Martínez-Alonso, H. M. Worden, and C. Sweeney, 2017: A climate-scale satellite record for carbon monoxide: the MOPITT Version 7 product. *Atmos. Meas. Tech.*, **10**, 2533–2555, https://doi.org/10.5194/amt-10-2533-2017.

——, and Coauthors, 2019: Radiance-based retrieval bias mitigation for the MOPITT instrument: The version 8 product. *Atmos. Meas. Tech.*, **12**, 4561–4580, https://doi.org/10.5194/amt-12-4561-2019.

Del Genio, A., M. Yao, and J. Jonas, 2007: Will moist convection be stronger in a warmer climate? *Geophys. Res. Lett.*, **34**, L16703, https://doi.org/10.1029/2007GL030525.

Delaloye, R., and Coauthors, 2008: Recent interannual variations of rock glacier creep in the European Alps. *Proc. of the 9th Int. Conf. on Permafrost*, Fairbanks, AK, University of Alaska Fairbanks, 343–348.

——, C. Lambiel, and I. Gärtner-Roer, 2010: Overview of rock glacier kinematics research in the Swiss Alps. *Geogr. Helv.*, **65**, 135–145, https://doi.org/10.5194/gh-65-135-2010.

De Mazière, M., and Coauthors, 2018: The Network for the Detection of Atmospheric Composition Change (NDACC): History, status and perspectives. *Atmos. Chem. Phys.*, **18**, 4935–4964, https://doi.org/10.5194/acp-18-4935-2018.

Deng, K., C. Azorin-Molina, L. Minola, G. Zhang, and D. Chen, 2021: Global near-surface wind speed changes over the last decades revealed by reanalyses and CMIP6 model simulations. *J. Climate*, **34**, 2219–2234, https://doi.org/10.1175/JCLI-D-20-0310.1.

——, ——, S. Yang, C. Hu, G. Zhang, L. Minola, and D. Chen, 2022: Changes of Southern Hemisphere westerlies in the future warming climate. *Atmos. Res.*, **270**, 106040, https://doi.org/10.1016/j.atmosres.2022.106040.

Dessler, A. E., M. R. Schoeberl, T. Wang, S. M. Davis, K. H. Rosenlof, and J. P. Vernier, 2014: Variations of stratospheric water vapor over the past three decades. *J. Geophys. Res. Atmos.*, **119**, 12 588–12 598, https://doi.org/10.1002/2014JD021712.

Dewitte, S., D. Crommelynck, and A. Joukof, 2004: Total solar irradiance observations from DIARAD/VIRGO. *J. Geophys. Res.*, **109**, A02102, https://doi.org/10.1029/2002JA009694.

Di Girolamo, L., A. Menzies, G. Zhao, K. Mueller, C. Moroney, and D. J. Diner, 2010: Multi-angle imaging SpectroRadiometer level 3 cloud fraction by altitude algorithm theoretical basis document. JPL Publ., D-62358, 23 pp., https://eospso.nasa.gov/sites/default/files/atbd/MISR_CFBA_ATBD.pdf.

DiGangi, E. A., M. Stock, and J. Lapierre, 2022: Thunder hours: How old methods offer new insights into thunderstorm climatology. *Bull. Amer. Meteor. Soc.*, **103**, E548–E569, https://doi.org/10.1175/BAMS-D-20-0198.1.

Dlugokencky, E. J., L. P. Steele, P. M. Lang, and K. A. Masarie, 1994: The growth rate and distribution of atmospheric methane. *J. Geophys. Res. Atmos.*, **99**(D8), 17 021–17 043, https://doi.org/10.1029/94JD01245.

——, S. Houweling, L. Bruhwiler, K. A. Masarie, P. M. Lang, J. B. Miller, and P. P. Tans, 2003: Atmospheric methane levels off: Temporary pause or a new steady-state? *Geophys. Res. Lett.*, **30**, 1992, https://doi.org/10.1029/2003GL018126.

Döll, P., and B. Lehner, 2002: Validation of a new global 30-min drainage direction map. *J. Hydrol.*, **258**, 214–231, https://doi.org/10.1016/S0022-1694(01)00565-0.

Donat, M., L. Alexander, H. Yang, I. Durre, R. Vose, and J. Caesar, 2013: Global land based datasets for monitoring climatic extremes. *Bull. Amer. Meteor. Soc.*, **94**, 997–1006, https://doi.org/10.1175/BAMS-D-12-00109.1.

Dong, B., and R. Sutton, 2015: Dominant role of greenhouse-gas forcing in the recovery of Sahel rainfall. *Nat. Climate Change*, **5**, 757–760, https://doi.org/10.1038/nclimate2664.

Dorigo, W. A., and Coauthors, 2017: ESA CCI Soil Moisture for improved Earth system understanding: State-of-the art and future directions. *Remote Sens. Environ.*, **203**, 185–215, https://doi.org/10.1016/j.rse.2017.07.001.

——, L. Moesinger, R. van der Schalie, R. M. Zotta, T. Scanlon, and R. A. M. de Jeu, 2021: Long-term monitoring of vegetation state through passive microwave satellites [in "State of the Climate in 2020"]. *Bull. Amer. Meteor. Soc.*, **102** (8), S110–S112, https://doi.org/10.1175/BAMS-D-21-0098.1.

Dunn, R. J. H., 2019: HadISD version 3: Monthly updates. Hadley Centre Technical Note 103, 10 pp., www.metoffice.gov.uk/research/library-and-archive/publications/science/climate-science-technical-notes.

——, and C. P. Morice, 2022: On the effect of reference periods on trends in percentile-based extreme temperature indices. *Environ. Res. Lett.*, **17**, 034026, https://doi.org/10.1088/1748-9326/ac52c8.

——, K. M. Willett, P. W. Thorne, E. V. Woolley, I. Durre, A. Dai, D. E. Parker, and R. S. Vose, 2012: HadISD: A quality-controlled global synoptic report database for selected variables at long-term stations from 1973–2011. *Climate Past*, **8**, 1649–1679, https://doi.org/10.5194/cp-8-1649-2012.

——, K. M. Willett, D. E. Parker, and L. Mitchell, 2016: Expanding HadISD: Quality-controlled, sub-daily station data from 1931. *Geosci. Instrum. Methods Data Syst.*, **5**, 473–491, https://doi.org/10.5194/gi-5-473-2016.

——, and Coauthors, 2020: Development of an updated global land in-situ-based dataset of temperature and precipitation extremes: HadEX3. *J. Geophys. Res. Atmos.*, **125**, e2019JD032263, https://doi.org/10.1029/2019JD032263.

Dussaillant, I., and Coauthors, 2019: Two decades of glacier mass loss along the Andes. *Nat. Geosci.*, **12**, 802–808, https://doi.org/10.1038/s41561-019-0432-5.

Edwards, M., and A. Richardson, 2004: Impact of climate change on marine pelagic phenology and trophic mismatch. *Nature*, **430**, 881–884, https://doi.org/10.1038/nature02808.

Ellis, H. T., and R. F. Pueschel, 1971: Solar radiation: Absence of air pollution trends at Mauna Loa. *Science*, **172**, 845–846, https://doi.org/10.1126/science.172.3985.845.

Else, H., 2021: Climate change implicated in Germany's deadly floods. *Nature*, https://doi.org/10.1038/d41586-021-02330-y.

Engel, A., and M. Rigby, 2018: Update on ozone-depleting substances (ODSs) and other gases of interest to the Montreal protocol. Scientific Assessment of Ozone Depletion: 2018, Global Ozone Research and Monitoring Project Rep. 58, 1.1–1.66, https://ozone.unep.org/sites/default/files/2019-05/SAP-2018-Assessment-report.pdf.

Eriksen, H. Ø., L. Rouyet, T. R. Lauknes, I. Berthling, K. Isaksen, H. Hindberg, Y. Larsen, and G. D. Corner, 2018: Recent acceleration of a rock glacier complex, Ádjet, Norway, documented by 62 years of remote sensing observations. *Geophys. Res. Lett.*, **45**, 8314–8323, https://doi.org/10.1029/2018GL077605.

Espinoza, J.-C., J. A. Marengo, J. Schongart, and J. C. Jimenez, 2022: The new historical flood of 2021 in the Amazon River compared to major floods of the 21st century: Atmospheric features in the context of the intensification of floods. *Wea. Climate Extremes*, **35**, 100406, https://doi.org/10.1016/j.wace.2021.100406.

Estilow, T. W., A. H. Young, and D. A. Robinson, 2015: A long-term Northern Hemisphere snow cover extent data record for climate studies and monitoring. *Earth Syst. Sci. Data*, **7**, 137–142, https://doi.org/10.5194/essd-7-137-2015.

Etheridge, D. M., L. P. Steele, R. L. Langenfelds, R. J. Francey, J. M. Barnola, and V. I. Morgan, 1996: Natural and anthropogenic changes in atmospheric CO_2 over the last 1000 years from air in Antarctic ice and firn. *J. Geophys. Res.*, **101**, 4115–4128, https://doi.org/10.1029/95JD03410.

Etzelmüller, B., and Coauthors, 2020: Twenty years of European mountain permafrost dynamics – The PACE legacy. *Environ. Res. Lett.*, **15**, 104070, https://doi.org/10.1088/1748-9326/abae9d.

Finney, D., 2021: Lightning threatens permafrost. *Nat. Climate Change*, **11**, 379–380, https://doi.org/10.1038/s41558-021-01016-7.

Fioletov, V. E., G. E. Bodeker, A. J. Miller, R. D. McPeters, and R. Stolarski, 2002: Global and zonal total ozone variations estimated from ground-based and satellite measurements: 1964–2000. *J. Geophys. Res.*, **107**, 4647, https://doi.org/10.1029/2001JD001350.

——, and Coauthors, 2008: The performance of the ground-based total ozone network assessed using satellite data. *J. Geophys. Res.*, **113**, D14313, https://doi.org/10.1029/2008JD009809.

Fleming, Z. L., and Coauthors, 2018: Tropospheric Ozone Assessment Report: Present-day ozone distribution and trends relevant to human health. *Elem. Sci. Anthropocene*, **6**, 12, https://doi.org/10.1525/elementa.273.

Flemming, J., and A. Inness, 2018: Carbon monoxide [in "State of the Climate in 2017"]. *Bull. Amer. Meteor. Soc.*, **99** (8), S59–S61, https://doi.org/10.1175/2018BAMSStateoftheClimate.1.

——, and Coauthors, 2017: The CAMS interim reanalysis of carbon monoxide, ozone and aerosol for 2003–2015. *Atmos. Chem. Phys.*, **17**, 1945–1983, https://doi.org/10.5194/acp-17-1945-2017.

Frauenfelder, R., W. Haeberli, and M. Hoelzle, 2003: Rock glacier occurrence and related terrain parameters in a study area of the Eastern Swiss Alps. *Permafrost: Proceedings of the 8th International Conference on Permafrost*, M. Phillips, S. M. Springman, and L. U. Arenson, Eds., A. A. Balkema, 253–258.

Free, M., D. J. Seidel, J. K. Angel, J. Lanzante, I. Durre, and T. C. Peterson, 2005: Radiosonde Atmospheric Temperature Products for Assessing Climate (RATPAC): A new dataset of large-area anomaly time series. *J. Geophys. Res.*, **110**, D22101, https://doi.org/10.1029/2005JD006169.

Friedlingstein, P., and Coauthors, 2022: Global carbon budget 2021. *Earth Syst. Sci. Data*, **14**, 1917–2005, https://doi.org/10.5194/essd-14-1917-2022.

Frith, S. M., N. A. Kramarova, R. S. Stolarski, R. D. McPeters, P. K. Bhartia, and G. J. Labow, 2014: Recent changes in total column ozone based on the SBUV Version 8.6 Merged Ozone Data Set. *J. Geophys. Res. Atmos.*, **119**, 9735–9751, https://doi.org/10.1002/2014JD021889.

——, R. S. Stolarski, N. A. Kramarova, and R. D. McPeters, 2017: Estimating uncertainties in the SBUV Version 8.6 merged profile ozone data set. *Atmos. Chem. Phys.*, **17**, 14695–14707, https://doi.org/10.5194/acp-17-14695-2017.

Garane, K., and Coauthors, 2018: Quality assessment of the Ozone_cci Climate Research Data Package (release 2017): 1. Ground-based validation of total ozone column data products. *Atmos. Meas. Tech.*, **11**, 1385–1402, https://doi.org/10.5194/amt-11-1385-2018.

Garcia, H. E., and Coauthors 2019: World Ocean Atlas 2018: Product documentation. NOAA, 20 pp., www.ncei.noaa.gov/sites/default/files/2020-04/woa18documentation.pdf.

Garfinkel, C. I., and Coauthors, 2021: Influence of the El Niño–Southern Oscillation on entry stratospheric water vapor in coupled chemistry–ocean CCMI and CMIP6 models. *Atmos. Chem. Phys.*, **21**, 3725–3740, https://doi.org/10.5194/acp-21-3725-2021.

Gaubert, B., and Coauthors, 2017: Chemical feedback from decreasing carbon monoxide emissions. *Geophys. Res. Lett.*, **44**, 9985–9995, https://doi.org/10.1002/2017GL074987.

Gaudel, A., and Coauthors, 2018: Tropospheric Ozone Assessment Report: Present-day distribution and trends of tropospheric ozone relevant to climate and global atmospheric chemistry model evaluation. *Elem. Sci. Anthropocene*, 6, 39, https://doi.org/10.1525/elementa.291.

——, and Coauthors, 2020: Aircraft observations since the 1990s reveal increases of tropospheric ozone at multiple locations across the Northern Hemisphere. *Sci. Adv.*, **6**, eaba8272, https://doi.org/10.1126/sciadv.aba8272.

GCOS, 2016: The Global Observing System for Climate: Implementation needs. Tech. Rep. GCOS-200, World Meteorological Organization, 315 pp., https://library.wmo.int/doc_num.php?explnum_id=3417.

Gelaro, R., and Coauthors, 2017: The Modern-Era Retrospective Analysis for Research and Applications, version 2 (MERRA-2). *J. Climate*, **30**, 5419–5454, https://doi.org/10.1175/JCLI-D-16-0758.1.

Getirana, A., S. Kumar, M. Girotto, and M. Rodell, 2017: Rivers and floodplains as key components of global terrestrial water storage variability. *Geophys. Res. Lett.*, **44**, 10359–10368, https://doi.org/10.1002/2017GL074684.

Giglio, L., W. Schroeder, and C. O. Justice, 2016: The Collection 6 MODIS active fire detection algorithm and fire products. *Remote Sens. Environ.*, **178**, 31–41, https://doi.org/10.1016/j.rse.2016.02.054.

GISTEMP Team, 2022: GISS Surface Temperature Analysis (GISTEMP v4). NASA Goddard Institute for Space Studies, accessed 15 February 2022, https://data.giss.nasa.gov/gistemp/.

Gobron, N., and A. S. Belward, 2011: Fraction of Absorbed Photosynthetically Active Radiation (FAPAR) [in "State of the Climate in 2010"]. *Bull. Amer. Meteor. Soc.*, **92** (6), S72, https://doi.org/10.1175/1520-0477-92.6.S1.

——, and M. Robustelli, 2013: Monitoring the state of the global terrestrial surfaces. *Proc. 2013 ESA Living Planet Symp.*, Edinburgh, United Kingdom, European Space Agency, JRC84937, https://publications.jrc.ec.europa.eu/repository/handle/JRC84937.

——, A. S. Belward, B. Pinty, and W. Knorr, 2010: Monitoring biosphere vegetation 1998-2009. *Geophys. Res. Lett.*, **37**, L15402, https://doi.org/10.1029/2010GL043870.

Godin-Beekmann, S., and Coauthors, 2022: Updated trends of the stratospheric ozone vertical distribution in the 60°S–60°N latitude range based on the LOTUS regression model *Atmos. Chem. Phys.*, https://doi.org/10.5194/acp-2022-137, in press.

Gonsamo, A., and Coauthors, 2021: Greening drylands despite warming consistent with carbon dioxide fertilization effect. *Global Change Biol.*, **27** (14), 3336–3349, https://doi.org/10.1111/gcb.15658.

Goodman, S. J., and H. Christian, 1993: Global observations of lightning. *Atlas of Satellite Observations Related to Global Change*, R. Gurney, J. Foster, and C. Parkinson, Eds., Cambridge University Press, 191–222.

——, D. E. Buechler, K. Knupp, K. Driscoll, and E. W. McCaul, 2000: The 1997–98 El Nino event and related wintertime lightning variations in the southeastern United States. *Geophys. Res. Lett.*, **27**, 541–544, https://doi.org/10.1029/1999GL010808.

Gordillo-Vázquez, F. J., F. J. Pérez-Invernón, H. Huntrieser, and A. K. Smith, 2019: Comparison of six lightning parameterizations in CAM5 and the impact on global atmospheric chemistry. *Earth Space Sci.*, **6**, 2317–2346, https://doi.org/10.1029/2019EA000873.

Grandt, C., 1992: Thunderstorm monitoring in South Africa and Europe by means of very low frequency sferics. *J. Geophys. Res.*, **97**, 18215–18226, https://doi.org/10.1029/92JD01623.

Granier, C., and Coauthors, 2011: Evolution of anthropogenic and biomass burning emissions of air pollutants at global and regional scales during the 1980–2010 period. *Climatic Change*, **109**, 163–190, https://doi.org/10.1007/s10584-011-0154-1.

Grant, L., and Coauthors, 2021: Attribution of global lake systems change to anthropogenic forcing. *Nat. Geosci.*, **14**, 849–854, https://doi.org/10.1038/s41561-021-00833-x.

Griffiths, P. T., and Coauthors, 2021: Tropospheric ozone in CMIP6 simulations. *Atmos. Chem. Phys.*, 21, 4187–4218, https://doi.org/10.5194/acp-21-4187-2021.

Gruber, A., W. A. Dorigo, W. Crow, and W. Wagner, 2017: Triple collocation-based merging of satellite soil moisture retrievals. I*EEE Trans. Geosci. Remote Sens.*, **55**, 6780–6792, https://doi.org/10.1109/TGRS.2017.2734070.

——, T. Scanlon, R. van der Schalie, W. Wagner, and W. Dorigo, 2019: Evolution of the ESA CCI Soil Moisture climate data records and their underlying merging methodology. *Earth Syst. Sci. Data*, **11**, 717–739, https://doi.org/10.5194/essd-11-717-2019.

Gui, K., and Coauthors, 2022: Record-breaking dust loading during two mega dust storm events over northern China in March 2021: aerosol optical and radiative properties and meteorological drivers. *Atmos. Chem. Phys.*, 22, 7905–7932, https://doi.org/10.5194/acp-22-7905-2022.

Gulev, S. K., and Coauthors, 2021: Changing state of the climate system. *Climate Change 2021: The Physical Science Basis*, V. Masson-Delmotte et al., Eds., Cambridge University Press, 287–422, https://doi.org/10.1017/9781009157896.004.

Haberkorn, A., R. Kenner, J. Noetzli, and M. Phillips, 2021: Changes in ground temperature and dynamics in mountain permafrost in the Swiss Alps. *Front. Earth Sci.*, **9**, 626686, https://doi.org/10.3389/feart.2021.626686.

Haimberger, L., C. Tavolato, and S. Sperka, 2012: Homogenization of the global radiosonde temperature dataset through combined comparison with reanalysis background series and neighboring stations. *J. Climate*, **25**, 8108–8131, https://doi.org/10.1175/JCLI-D-11-00668.1.

Hansen, J., R. Ruedy, M. Sato, and K. Lo, 2010: Global surface temperature change. *Rev. Geophys.*, **48**, RG4004, https://doi.org/10.1029/2010RG000345.

Harel, M., and C. Price, 2020: Thunder trends over Africa. *J. Climate*, **33**, 2741–2755, https://doi.org/10.1175/JCLI-D-18-0781.1.

Harris, I., T. J. Osborn, P. D. Jones, and D. H. Lister, 2020: Version 4 of the CRU TS monthly high-resolution gridded multivariate climate dataset. *Sci. Data*, **7**, 109, https://doi.org/10.1038/s41597-020-0453-3.

Heidinger, A. K., M. J. Foster, A. Walther, and X. Zhao, 2013: The Pathfinder Atmospheres–Extended AVHRR Climate Dataset. *Bull. Amer. Meteor. Soc.*, **95**, 909–922, https://doi.org/10.1175/BAMS-D-12-00246.1.

Hersbach, H., and Coauthors, 2020: The ERA5 global reanalysis. *Quart. J. Roy. Meteor. Soc.*, **146**, 1999–2049, https://doi.org/10.1002/qj.3803.

Ho, S.-P., X. Zhou, Y.-H. Kuo, D. Hunt, and J.-H. Wang, 2010a: Global evaluation of radiosonde water vapor systematic biases using GPS radio occultation from COSMIC and ECMWF analysis. *Remote Sens.*, **2**, 1320–1330, https://doi.org/10.3390/rs2051320.

——, Y.-H. Kuo, W. Schreiner, and X. Zhou, 2010b: Using SI-traceable global positioning system radio occultation measurements for climate monitoring [in "State of the Climate in 2009"]. *Bull. Amer. Meteor. Soc.*, **91** (7), S36–S37, https://doi.org/10.1175/BAMS-91-7-StateoftheClimate.

——, and Coauthors, 2020a: The COSMIC/FORMOSAT-3 radio occultation mission after 12 years: Accomplishments, remaining challenges, and potential impacts of COSMIC-2. *Bull. Amer. Meteor. Soc.*, **101**, E1107–E1136, https://doi.org/10.1175/BAMS-D-18-0290.1.

——, and Coauthors, 2020b: Initial assessment of the COSMIC-2/FORMOSAT-7 neutral atmosphere data quality in NESDIS/STAR using in situ and satellite data. *Remote Sens.*, **12**, 4099, https://doi.org/10.3390/rs12244099

Hobday, A. J., and Coauthors, 2016: A hierarchical approach to defining marine heatwaves. *Prog. Oceanogr.*, **141**, 227–238, https://doi.org/10.1016/j.pocean.2015.12.014.

——, and Coauthors, 2018: Categorizing and naming marine heatwaves. *Oceanography*, **31**, 162–173, https://doi.org/10.5670/oceanog.2018.205.

Hock, R., and Coauthors, 2019: High mountain areas. *IPCC Special Report on the Ocean and Cryosphere in a Changing Climate*, H.-O. Pörtner, Eds., IPCC, 131–202, www.ipcc.ch/srocc/.

Hofmann, D. J., and S. A. Montzka, 2009: Recovery of the Ozone Layer: The Ozone Depleting Gas Index. *Eos, Trans. Amer. Geophys. Union*, **90**, 1–2, https://doi.org/10.1029/2009EO010001.

——, J. H. Butler, E. J. Dlugokencky, J. W. Elkins, K. Masarie, S. A. Montzka, and P. Tans, 2006: The role of carbon dioxide in climate forcing from 1979 to 2004: Introduction of the annual greenhouse gas index. *Tellus*, **58B**, 614–619, https://doi.org/10.1111/j.1600-0889.2006.00201.x.

Holle, R., 2016: A recent summary of national-scale lightning fatality studies. *Wea. Climate Soc.*, **8**, 35–42, https://doi.org/10.1175/WCAS-D-15-0032.1.

——, R. Lopez, and C. Zimmermann, 1999: Updated recommendations for lightning safety–1998. *Bull. Amer. Meteor. Soc.*, **80**, 2035–2041, https://doi.org/10.1175/1520-0477(1999)080<2035:URFLS>2.0.CO;2.

Holzworth, R. H., M. P. McCarthy, J. B. Brundell, A. R. Jacobson, and C. J. Rodger, 2019: Global distribution of superbolts. *J. Geophys. Res. Atmos.*, **124**, 9996–10 005, https://doi.org/10.1029/2019JD030975.

——, J. B. Brundell, M. P. McCarthy, A. R. Jacobson, C. J. Rodger, and T. S. Anderson, 2021: Lightning in the Arctic. *Geophys. Res. Lett.*, **48**, e2020GL091366, https://doi.org/10.1029/2020GL091366.

Hrbáček, F., and Coauthors, 2021: Active layer monitoring in Antarctica: An overview of results from 2006 to 2015. *Polar Geogr.*, **44**, 217–231, https://doi.org/10.1080/1088937X.2017.1420105.

Hu, L., and Coauthors, 2019: Enhanced North American carbon uptake associated with El Niño. *Sci. Adv.*, **5**, eaaw0076, https://doi.org/10.1126/sciadv.aaw0076.

Huang, B., C. Liu, V. Banzon, E. Freeman, G. Graham, B. Hankins, T. Smith, and H.-M. Zhang. 2021: Improvements of the Daily Optimum Interpolation Sea Surface Temperature (DOISST) version 2.1. *J. Climate*, **34**, 2923–2939, https://doi.org/10.1175/JCLI-D-20-0166.1.

Huang, C.-Y., W.-H. Teng, S.-P. Ho, and Y. H. Kuo, 2013: Global variation of COSMIC precipitable water over land: Comparisons with ground-based GPS measurements and NCEP reanalyses. *Geophys. Res. Lett.*, **40**, 5327–5331, https://doi.org/10.1002/grl.50885.

Hugonnet, R., and Coauthors, 2021: Accelerated global glacier mass loss in the early twenty-first century. *Nature*, **592**, 726–731, https://doi.org/10.1038/s41586-021-03436-z.

Humphrey, V., J. Zscheischler, P. Ciais, L. Gudmundsson, S. Sitch, and S. I. Seneviratne, 2018: Sensitivity of atmospheric CO_2 growth rate to observed changes in terrestrial water storage. *Nature*, **560**, 628–631, https://doi.org/10.1038/s41586-018-0424-4.

Hurst, D. F., and Coauthors, 2016: Recent divergences in stratospheric water vapor measurements by frost point hygrometers and the Aura Microwave Limb Sounder. *Atmos. Meas. Tech.*, **9**, 4447–4457, https://doi.org/10.5194/amt-9-4447-2016.

Hüser, I., B. Gehrke, and J. W. Kaiser, 2018: Methodology to correct biases in individual satellite FRP products. CAMS Rep. CAMS44-2016SC3-D44.3.3.1-2018-20187, ECMWF, Reading, United Kingdom. 20 pp.

IMD, 2022: Statement on Climate of India during 2021. Climate Research and Services, India Meteorological Department, Ministry of Earth Sciences, Government of India, 9 pp., https://mausam.imd.gov.in/Forecast/marquee_data/Annual%20Statement%20on%20Climate%20of%20India%202021%20in%20English.pdf.

Ingram, W., 2010: A very simple model for the water vapour feedback on climate change. *Quart. J. Roy. Meteor. Soc.*, **136**, 30–40, https://doi.org/10.1002/qj.546.

Inness, A., and Coauthors, 2013: The MACC reanalysis: An 8-year data set of atmospheric composition. *Atmos. Chem. Phys.*, **13**, 4073–4109, https://doi.org/10.5194/acp-13-4073-2013.

——, A. Benedetti, J. Flemming, V. Huijnen, J. W. Kaiser, M. Parrington, and S. Remy, 2015: The ENSO signal in atmospheric composition fields: Emission-driven versus dynamically induced changes. *Atmos. Chem. Phys.*, **15**, 9083–9097, https://doi.org/10.5194/acp-15-9083-2015.

——, and Coauthors, 2019: The CAMS reanalysis of atmospheric composition. *Atmos. Chem. Phys.*, **19**, 3515–3556, https://doi.org/10.5194/acp-19-3515-2019.

IPCC, 2013: *Climate Change 2013: The Physical Science Basis*. Cambridge University Press, 1535 pp., https://doi.org/10.1017/CBO9781107415324.

——, 2021: Summary for policymakers. *Climate Change 2021: The Physical Science Basis*. V. Masson-Delmotte et al., Eds., Cambridge University Press, 3–32, https://doi.org/10.1017/9781009157896.001.

John, V. O., G. Holl, R. P. Allan, S. A. Buehler, D. E. Parker, and B. J. Soden, 2011: Clear-sky biases in satellite infra-red estimates of upper tropospheric humidity and its trends. *J. Geophys. Res.*, **116**, D14108, https://doi.org/10.1029/2010JD015355.

Joint Research Centre, 2021: Drought in southern Urals and Turan Depression October 2021. GDO Analytical Rep., 21 pp., https://edo.jrc.ec.europa.eu/documents/news/GDODroughtNews202110_Southern_Urals_and_Turan_Depression.pdf.

Junghänel, T. and Coauthors, 2021: Hydro-klimatologische Einordnung der Stark- und Dauerniederschläge in Teilen Deutschland sim Zusammenhang mit dem Tiefdruckgebiet "Bernd" vom 12. bis 19. Juli 2021 (in German). DWD, 16 pp., www.dwd.de/DE/leistungen/besondereereignisse/niederschlag/20210721_bericht_starkniederschlaege_tief_bernd.pdf?__blob=publicationFile&v=10.

Junod, R. A., and J. R. Christy, 2020: A new compilation of globally gridded nighttime marine air temperatures: The UAHNMATv1 dataset. *Int. J. Climatol.*, **40**, 2609–2623, https://doi.org/10.1002/joc.6354.

Kääb, A., R. Frauenfelder, and I. Roer, 2007: On the response of rockglacier creep to surface temperature increase. *Global Planet. Change*, **56**, 172–187, https://doi.org/10.1016/j.gloplacha.2006.07.005.

——, T. Strozzi, T. Bolch, R. Caduff, H. Trefall, M. Stoffel, and A. Kokarev, 2021: Inventory and changes of rock glacier creep speeds in Ile Alatau and Kungöy Ala-Too, northern Tien Shan, since the 1950s. *Cryosphere*, **15**, 927–949, https://doi.org/10.5194/tc-15-927-2021.

Kaiser, J. W., and Coauthors, 2012: Biomass burning emissions estimated with a global fire assimilation system based on observed fire radiative power. *Biogeosciences*, **9**, 527–554, https://doi.org/10.5194/bg-9-527-2012.

Kaplan, A., 2011: Patterns and indices of climate variability [in "State of the Climate in 2010"]. *Bull. Amer. Meteor. Soc.*, **92** (6), S20–S25, https://doi.org/10.1175/1520-0477-92.6.S1.

Karlsson, K.-G., and Coauthors, 2017: CLARA-A2: The second edition of the CM SAF cloud and radiation data record from 34 years of global AVHRR data. *Atmos. Chem. Phys.*, **17**, 5809–5828, https://doi.org/10.5194/ACP-17-5809-2017.

——, and Coauthors, 2020: CLARA-A2.1: CM SAF CLoud, Albedo and Surface RAdiation Dataset from AVHRR Data - Edition 2.1. Satellite Application Facility on Climate Monitoring, accessed 23 February 2022, https://doi.org/10.5676/EUM_SAF_CM/CLARA_AVHRR/V002_01.

——, and Coauthors, 2021: ICDR AVHRR - Based on CLARA-A2 Methods. Satellite Application Facility on Climate Monitoring, accessed 23 February 2022, https://wui.cmsaf.eu/safira/action/viewICDRDetails?acronym=CLARA_AVHRR_V002_ICDR.

Karpechko, A. Y., and A. C. Maycock, 2018: Stratospheric ozone changes and climate. Scientific Assessment of Ozone Depletion: 2018, Global Ozone Research and Monitoring Project Rep. 58, 5.1–5.50, https://ozone.unep.org/sites/default/files/2019-05/SAP-2018-Assessment-report.pdf.

Keeling, C. D., and R. Revelle, 1985: Effects of El-Nino Southern Oscillation on the atmospheric content of carbon-dioxide. *Meteoritics*, **20**, 437–450.

Kellerer-Pirklbauer, A., and V. Kaufmann, 2012: About the relationship between rock glacier velocity and climate parameters in central Austria. *Aust. J. Earth Sci.*, **105** (2), 94–112.

——, and Coauthors, 2018: Interannual variability of rock glacier flow velocities in the European Alps. *5th European Conf. on Permafrost*, Chamonix, France. Laboratoire EDYTEM, 615–616, https://hal.archives-ouvertes.fr/hal-01816115/.

Kendon, M., M. McCarthy, S. Jevrejeva, A. Matthews, T. Sparks, and J. Garforth, 2022: State of the UK Climate 2021. *Int. J. Climatol.*, **42** (S1), 1–80, https://doi.org/10.1002/joc.7787.

Kennedy, J. J., N. A. Rayner, C. P. Atkinson, and R. E. Killick, 2019: An ensemble data set of sea surface temperature change from 1850: The Met Office Hadley Centre HadSST.4.0.0.0 data set. *J. Geophys. Res. Atmos.*, **124**, 7719–7763, https://doi.org/10.1029/2018JD029867.

Kent, G. S., E. R. Williams, P. Wang, M. P. McCormick, and K. M. Skeens, 1995: Surface temperature-related variations in tropical cirrus clouds as measured by SAGE II. *J. Climate*, **8**, 2577–2594, https://doi.org/10.1175/1520-0442(1995)008%3C2577:STRVIT%3E2.0.CO;2.

Kim, H., 2020: River discharge and runoff [in "State of the Climate in 2019"]. *Bull. Amer. Meteor.*, **101** (8), S53–S55, https://doi.org/10.1175/BAMS-D-20-0104.1.

——, and D. Tokuda, 2021: River discharge and runoff [in "State of the Climate in 2020"]. *Bull. Amer. Meteor. Soc.*, **102** (8), S63–S65, https://doi.org/10.1175/BAMS-D-21-0098.1.

——, P. J.-F. Yeh, T. Oki, and S. Kanae, 2009: Role of rivers in the seasonal variations of terrestrial water storage over global basins. *Geophys. Res. Lett.*, **36**, L17402, https://doi.org/10.1029/2009GL039006.

Kitagawa, N., 1989: Long-term variations in thunder-day frequencies in Japan. *J. Geophys. Res.*, **94**, 13 183–13 189, https://doi.org/10.1029/JD094iD11p13183.

Klein Tank, A. M. G., and Coauthors, 2002: Daily dataset of 20th-century surface air temperature and precipitation series for the European Climate Assessment. *Int. J. Climatol.*, **22**, 1441–1453, https://doi.org/10.1002/joc.773.

Ko, M. K., P. A. Newman, S. Reimann, and S. E. Strahan, 2013: Recommended values for steady-state atmospheric lifetimes and their uncertainties. Lifetimes of Stratospheric Ozone-Depleting Substances, Their Replacements, and Related Species, M. K. W. Ko et al., Eds., SPARC Rep. 6, WCRP-15-2013, 6-1–6-21, www.sparc-climate.org/publications/sparc-reports/sparc-report-no-6/.

Kobayashi, S., and Coauthors, 2015: The JRA-55 Reanalysis: General specifications and basic characteristics. *J. Meteor. Soc. Japan*, **93**, 5–48, https://doi.org/10.2151/jmsj.2015-001.

Konings, A. G., Y. Yu, L. Xu, Y. Yang, D. S. Schimel, and S. S. Saatchi, 2017: Active microwave observations of diurnal and seasonal variations of canopy water content across the humid African tropical forests. *Geophys. Res. Lett.*, **44**, 2290–2299, https://doi.org/10.1002/2016GL072388.

Kopp, G., and J. L. Lean, 2011: A new, lower value of total solar irradiance: evidence and climate significance. *Geophys. Res. Lett.*, **38**, L01706, https://doi.org/10.1029/2010GL045777.

Kratz, D. P., P. W. Stackhouse Jr., S. K. Gupta, A. C. Wilber, P. Sawaengphokhai, and G. R. McGarragh, 2014: The Fast Longwave and Shortwave Flux (FLASHFlux) data product: Single scanner footprint fluxes. *J. Appl. Meteor. Climatol.*, **53**, 1059–1079, https://doi.org/10.1175/JAMC-D-13-061.1.

Lan, X., and Coauthors, 2021: Improved constraints on global methane emissions and sinks using $\delta^{13}C$-CH_4. *Global Biogeochem. Cycles*, **35**, e2021GB007000, https://doi.org/10.1029/2021GB007000.

Landerer, F. W., and Coauthors, 2020: Extending the global mass change data record: GRACE Follow-On instrument and science data performance. *Geophys. Res. Lett.*, **47**, e2020GL088306, https://doi.org/10.1029/2020GL088306.

Lassey, K. R., D. M. Etheridge, D. C. Lowe, A. M. Smith, and D. F. Ferretti, 2007: Centennial evolution of the atmospheric methane budget: What do the carbon isotopes tell us? *Atmos. Chem. Phys.*, **7**, 2119–2139, https://doi.org/10.5194/acp-7-2119-2007.

Laughner, J. L., and Coauthors, 2021: Societal shifts due to COVID-19 reveal large-scale complexities and feedbacks between atmospheric chemistry and climate change. *Proc. Natl. Acad. Sci. USA*, **118**, e2109481118, https://doi.org/10.1073/pnas.2109481118.

Lavigne, T., C. Liu, and N. Liu, 2019: How does the trend in thunder days relate to the variation of lightning flash density? *J. Geophys. Res. Atmos.*, **124**, 4955–4974, https://doi.org/10.1029/2018JD029920.

Lawrence, Z. D., J. Perlwitz, A. H. Butler, G. L. Manney, P. A. Newman, S. H. Lee, and E. R. Nash, 2020: The remarkably strong arctic stratospheric polar vortex of winter 2020: Links to record-breaking arctic oscillation and ozone loss. *J. Geophys. Res. Atmos.*, **125**, e2020JD033271, https://doi.org/10.1029/2020JD033271.

Lee, D. Y., M. R. Petersen, and W. Lin, 2019: The southern annular mode and southern ocean surface westerly winds in E3SM. *Earth Space Sci.*, **6**, 2624–2643, https://doi.org/10.1029/2019EA000663.

Lee, H.-T., and NOAA CDR Program, 2011: NOAA Climate Data Record (CDR) of Monthly Outgoing Longwave Radiation (OLR), version 2.2-1. Subset: March 2000–December 2021, NOAA National Climatic Data Center, accessed 6 January 2022, https://doi.org/10.7289/V5222RQP.

Lee, S. H., 2021: The January 2021 sudden stratospheric warming. *Weather*, **76**, 135–136, https://doi.org/10.1002/wea.3966.

Lenssen, N. J. L., G. A. Schmidt, J. E. Hansen, M. J. Menne, A. Persin, R. Ruedy, and D. Zyss, 2019: Improvements in the GISTEMP uncertainty model. *J. Geophys. Res. Atmos.*, **124**, 6307–6326, https://doi.org/10.1029/2018JD029522.

Levy, R. C., S. Mattoo, L. A. Munchak, L. A. Rember, A. M. Sayer, F. Patadia, and N. C. Hsu, 2013: The Collection 6 MODIS aerosol products over land and ocean. *Atmos. Meas. Tech.*, **6**, 2989–3034, https://doi.org/10.5194/amt-6-2989-2013.

Li, M., and Coauthors, 2017: Anthropogenic emission inventories in China: A review. *Nat. Sci. Rev.*, **4**, 834–866, https://doi.org/10.1093/nsr/nwx150.

Li, W., S. Zhao, Y. Chen, L. Wang, W. Hou, Y. Jiang, X. Zou, and S. Shi, 2022: State of China's climate in 2021. *Atmos. Ocean. Sci. Lett.*, **15**, 100211, https://doi.org/10.1016/j.aosl.2022.100211.

Lieb, G. K., and A. Kellerer-Pirklbauer, 2021: Sammelbericht über die Gletschermessungen des Österreichischen Alpenvereins im Jahr 2020. Letzter Bericht: Bergauf 2/2020, Jg. 75 (145), S. 6–15, www.alpenverein.at/portal_wAssets/docs/service/presse/2021/gletscherbericht/Alpenverein_Bergauf-2-21_Gletscherbericht.pdf.

Liu, Y., and Coauthors, 2021: Lightning enhancement in moist convection with smoke-laden air advected from Australian wildfires. *Geophys. Res. Lett.*, **48**, e2020GL092355, https://doi.org/10.1029/2020GL092355.

Livesey, N. J., and Coauthors, 2021: Investigation and amelioration of long-term instrumental drifts in water vapor and nitrous oxide measurements from the Aura Microwave Limb Sounder (MLS) and their implications for studies of variability and trends. *Atmos. Chem. Phys.*, **21**, 15 409–15 430, https://doi.org/10.5194/acp-21-15409-2021.

Lockwood, J. and Coauthors, 2022: Predictability of winter 2020/21: Influence of a mid-winter sudden stratospheric warming. *Atmos. Sci. Lett.*, in press, https://doi.org/10.1002/ASL.1126.

Loeb, N. G., B. A. Wielicki, D. R. Doelling, G. L. Smith, D. F. Keyes, S. Kato, N. Manalo-Smith, and T. Wong, 2009: Toward optimal closure of the Earth's top-of-atmosphere radiation budget. *J. Climate*, **22**, 748–766, https://doi.org/10.1175/2008JCLI2637.1.

——, S. Kato, W. Su, T. Wong, F. Rose, D. R. Doelling, and J. Norris, 2012: Advances in understanding top-of-atmosphere radiation variability from satellite observations. *Surv. Geophys.*, **33**, 359–385, https://doi.org/10.1007/s10712-012-9175-1.

——, and Coauthors, 2018a: Clouds and the Earth's Radiant Energy System (CERES) Energy Balanced and Filled (EBAF) top-of-atmosphere (TOA) Edition-4.0 data product. *J. Climate*, **31**, 895–918, https://doi.org/10.1175/JCLI-D-17-0208.1.

——, T. J. Thorsen, J. R. Norris, H. Wang, and W. Su, 2018b: Changes in Earth's energy budget during and after the "pause" in global warming: An observational perspective. *Climate*, **6**, 62, https://doi.org/10.3390/cli6030062.

——, G. C. Johnson, T. J. Thorsen, J. M. Lyman, F. G. Rose, and S. Kato, 2021: Satellite and ocean data reveal marked increase in Earth's heating rate. *Geophys. Res. Lett.*, **48**, e2021GL093047, https://doi.org/10.1029/2021GL093047.

Lu, Q., J. Rao, Z. Liang, D. Guo, J. Luo, S. Liu, C. Wang, and T. Wang, 2021: The sudden stratospheric warming in January 2021. *Environ. Res. Lett.*, **16**, 084029, https://doi.org/10.1088/1748-9326/ac12f4.

Lu, X., and Coauthors, 2019: Surface and tropospheric ozone trends in the Southern Hemisphere since 1990: Possible linkages to poleward expansion of the Hadley circulation. *Sci. Bull.*, **64**, 400–409, https://doi.org/10.1016/j.scib.2018.12.021.

MacCallum, S. N., and C. J. Merchant, 2012: Surface water temperature observations of large lakes by optimal estimation. *Can. J. Rem. Sens.*, **38**, 25–45, https://doi.org/10.5589/m12-010.

MacFarling Meure, C., D. Etheridge, C. Trudinger, P. Steele, R. Langenfelds, T. van Ommen, A. Smith, and J. Elkins, 2006: Law Dome CO_2, CH_4 and N_2O ice core records extended to 2000 years BP. *Geophys. Res. Lett.*, **33**, L14810, https://doi.org/10.1029/2006GL026152.

Madden, R. A., and P. R. Julian, 1971: Detection of a 40–50 day oscillation in the zonal wind in the tropical Pacific. *J. Atmos. Sci.*, **28**, 702–708, https://doi.org/10.1175/1520-0469(1971)028<0702:DOADOI>2.0.CO;2.

Magnin, F., P. Deline, L. Ravanel, J. Noetzli, and P. Pogliotti, 2015: Thermal characteristics of permafrost in the steep alpine rock walls of the Aiguille du Midi (Mont Blanc Massif, 3842 m asl). *Cryosphere*, **9**, 109–121, https://doi.org/10.5194/tc-9-109-2015.

Magnusson, L., A. Simmons, S. Harrigan, and F. Pappenberger, 2021: Extreme rain in Germany and Belgium in July 2021. *ECMWF Newsletter*, No. 169, ECMWF, Reading, United Kingdom, www.ecmwf.int/en/newsletter/169/news/extreme-rain-germany-and-belgium-july-2021.

Martens, B., and Coauthors, 2017: GLEAM v3: Satellite-based land evaporation and root-zone soil moisture. *Geosci. Model Dev.*, **10**, 1903–1925, https://doi.org/10.5194/gmd-10-1903-2017.

——, W. Waegeman, W. A. Dorigo, N. E. C. Verhoest, and D. G. Miralles, 2018: Terrestrial evaporation response to modes of climate variability. *npj Climate Atmos. Sci.*, **1**, 43, https://doi.org/10.1038/s41612-018-0053-5.

Martin, A., M. Weissmann, O. Reitebuch, M. Rennie, A. Geiß, and A. Cress, 2021: Validation of Aeolus winds using radiosonde observations and numerical weather prediction model equivalents. *Atmos. Meas. Tech.*, **14**, 2167–2183, https://doi.org/10.5194/amt-14-2167-2021.

McVicar, T. R., and Coauthors, 2012: Global review and synthesis of trends in observed terrestrial near-surface wind speeds: Implications for evaporation. *J. Hydrol.*, **416–417**, 182–205, https://doi.org/10.1016/j.jhydrol.2011.10.024.

Mears, C. A., and F. J. Wentz, 2016: Sensitivity of satellite-derived tropospheric temperature trends to the diurnal cycle adjustment. *J. Climate*, **29**, 3629–3646, https://doi.org/10.1175/JCLI-D-15-0744.1.

——, D. K. Smith, L. Ricciardulli, J. Wang, H. Huelsing, and F. J. Wentz, 2018: Construction and uncertainty estimation of a satellite-derived total precipitable water data record over the world's oceans. *Earth Space Sci.*, **5**, 197–210, https://doi.org/10.1002/2018EA000363.

Meesters, A. G. C. A., R. A. M. De Jeu, and M. Owe, 2005: Analytical derivation of the vegetation optical depth from the microwave polarization difference index. *IEEE Trans. Geosci. Remote Sens.*, **2**, 121–123, https://doi.org/10.1109/LGRS.2005.843983.

Meng, L., J. Liu, D. W. Tarasick, W. J. Randel, A. K. Steiner, H. Wilhelmsen, L. Wang, and L. Haimberger, 2021: Continuous rise of the tropopause in the Northern Hemisphere over 1980–2020. *Sci. Adv.*, **7**, eabi8065, https://doi.org/10.1126/sciadv.abi8065.

Menne, M. J., I. Durre, R. S. Vose, B. E. Gleason, and T. G. Houston, 2012: An overview of the Global Historical Climatology Network-Daily database. *J. Atmos. Oceanic Technol.*, **29**, 897–910, https://doi.org/10.1175/JTECH-D-11-00103.1.

Menzel, A., Y. Yuan, M. Matiu, T. H. Sparks, H. Scheifinger, R. Gehrig, and N. Estrella, 2020: Climate change fingerprints in recent European plant phenology. *Global Change Biol.*, **26**, 2599–2612, https://doi.org/10.1111/gcb.15000.

MeteoSwiss, 2022: Klimabulletin Jahr 2021. MeteoSwiss, 13 pp., www.meteoschweiz.admin.ch/home/service-und-publikationen/publikationen.subpage.html/de/data/publications/2022/1/klimabulletin-jahr-2021.html.

Mialon, A., N. Rodriguez-Fernandez, M. Santoro, S. Saatchi, S. Mermoz, E. Bousquet, and Y. Kerr, 2020: Evaluation of the sensitivity of SMOS L-VOD to forest above-ground biomass at global scale. *Remote Sens.*, **12**, 1450, https://doi.org/10.3390/rs12091450.

Miller, B. R., and Coauthors, 2010: HFC-23 (CHF_3) emission trend response to HCFC-22 ($CHClF_2$) production and recent HFC-23 emission abatement measures. *Atmos. Chem. Phys.*, 10, 7875–7890, https://doi.org/10.5194/acp-10-7875-2010.

Mills, G., and Coauthors, 2018: Tropospheric Ozone Assessment Report: Present-day tropospheric ozone distribution and trends relevant to vegetation. *Elem. Sci. Anthropocene*, **6**, 47, https://doi.org/10.1525/elementa.302.

Minnis, P., and Coauthors, 2008: Cloud detection in nonpolar regions for CERES using TRMM VIRS and Terra and Aqua MODIS data. *IEEE Trans. Geosci. Remote Sens.*, **46**, 3857–3884, https://doi.org/10.1109/TGRS.2008.2001351.

Minola, L., H. Reese, H. W. Lai, C. Azorin-Molina, J. A. Guijarro, S. W. Son, and D. Chen, 2022: Wind stilling-reversal across Sweden: The impact of land-use and large-scale atmospheric circulation changes. *Int. J. Climatol.*, 42, 1049–1071, https://doi.org/10.1002/joc.7289.

Miralles, D. G., T. R. H. Holmes, R. A. M. De Jeu, J. H. Gash, A. G. C. A. Meesters, and A. J. Dolman, 2011: Global land-surface evaporation estimated from satellite-based observations. *Hydrol. Earth Syst. Sci.*, **15**, 453–469, https://doi.org/10.5194/hess-15-453-2011.

——, and Coauthors, 2014: El Niño–La Niña cycle and recent trends in continental evaporation. *Nat. Climate Change*, **4**, 122–126, https://doi.org/10.1038/nclimate2068.

Miyazaki, K., K. Bowman, T. Sekiya, M. Takigawa, J. L. Neu, K. Sudo, G. Osterman, and H. Eskes, 2021: Global tropospheric ozone responses to reduced NOx emissions linked to the COVID-19 worldwide lockdowns. *Sci. Adv.*, **7**, eabf7460, https://doi.org/10.1126/sciadv.abf7460.

Moesinger, L., W. Dorigo, R. de Jeu, R. van der Schalie, T. Scanlon, I. Teubner, and M. Forkel, 2020: The global long-term microwave Vegetation Optical Depth Climate Archive (VODCA). *Earth Syst. Sci. Data*, **12**, 177–196, https://doi.org/10.5194/essd-12-177-2020.

——, R.-M. Zotta, R. van der Schalie, T. Scanlon, R. de Jeu, and W. Dorigo, 2022: Monitoring vegetation condition using microwave remote sensing: The Standardized Vegetation Optical Depth Index SVODI. *Biogeosci. Discuss.*, https://doi.org/10.5194/bg-2021-360.

Mollaret, C., C. Hilbich, C. Pellet, A. Flores-Orozco, R. Delaloye, and C. Hauck, 2019: Mountain permafrost degradation documented through a network of permanent electrical resistivity tomography sites. *Cryosphere*, **13**, 2557–2578, https://doi.org/10.5194/tc-13-2557-2019.

Montzka, S. A., J. H. Butlerrichard, C. Myers T. M. Thompson, T. H. Swanson, A. D. Clarke, L. T. Lock, and J. W. Elkins, 1996: Decline in the tropospheric abundance of halogen from halocarbons: Implications for stratospheric ozone depletion. *Science*, **272**, 1318–1322, https://doi.org/10.1126/science.272.5266.1318.

——, and Coauthors, 2011: Ozone-depleting substances (ODSs) and related chemicals. Scientific Assessment of Ozone Depletion: 2010, Global Ozone Research and Monitoring Project Rep.. 52, World Meteorological Organization, Ch. 1, https://tsapps.nist.gov/publication/get_pdf.cfm?pub_id=909747.

——, and Coauthors, 2018: An unexpected and persistent increase in global emissions of ozone-depleting CFC-11. *Nature*, **557**, 413–417, https://doi.org/10.1038/s41586-018-0106-2.

——, and Coauthors, 2021: A decline in global CFC-11 emissions during 2018–2019. *Nature*, **590**, 428–432, https://doi.org/10.1038/s41586-021-03260-5.

Morice, C. P., and Coauthors, 2021: An updated assessment of near-surface temperature change from 1850: The HadCRUT5 data set. *J. Geophys. Res. Atmos.*, **126**, e2019JD032361, https://doi.org/10.1029/2019JD032361.

Mote, P. W., and Coauthors, 1996: An atmospheric tape recorder: The imprint of tropical tropopause temperatures on stratospheric water vapor. *J. Geophys. Res. Atmos.*, **101**(D2), 3989–4006, https://doi.org/10.1029/95JD03422.

Mühle, J., and Coauthors, 2010: Perfluorocarbons in the global atmosphere: tetrafluoromethane, hexafluoroethane, and octafluoropropane. *Atmos. Chem. Phys.*, **10**, 5145–5164, https://doi.org/10.5194/acp-10-5145-2010.

Myhre, G., and Coauthors, 2013: Anthropogenic and natural radiative forcing. *Climate Change 2013: The Physical Science Basis*, T. F. Stocker et al., Eds., Cambridge University Press, 659–740.

Naumann, G., and Coauthors, 2021: The 2019–2021 extreme drought episode in La Plata Basin. EUR 30833 EN, Publications Office of the European Union, 44 pp., https://doi.org/10.2760/773.

Nédélec, P., and Coauthors, 2015: Instrumentation on commercial aircraft for monitoring the atmospheric composition on a global scale: the IAGOS system, technical overview of ozone and carbon monoxide measurements. *Tellus*, **67B**, 27791, https://doi.org/10.3402/tellusb.v67.27791.

Newchurch, M. J., E. S. Yang, D. M. Cunnold, G. C. Reinsel, J. M. Zawodny, and J. M. Russell III, 2003: Evidence for slowdown in stratospheric ozone loss: First stage of ozone recovery. *J. Geophys. Res.*, **108**, 4507, https://doi.org/10.1029/2003JD003471.

Newman, P. A., J. S. Daniel, D. W. Waugh, and E. R. Nash, 2007: A new formulation of equivalent effective stratospheric chlorine (EESC). *Atmos. Chem. Phys.*, **7**, 4537–4552, https://doi.org/10.5194/acp-7-4537-2007.

Nisbet, E. G., and Coauthors, 2019. Very strong atmospheric methane growth in the 4 years 2014–2017: Implications for the Paris Agreement. *Global Biogeochem. Cycles*, **33** (3), 318–342, https://doi.org/10.1029/2018GB006009.

NIWA, 2022: New Zealand's warmest year on record. 11 January, NIWA, https://niwa.co.nz/climate/summaries/annual-climate-summary-2021.

NOAA, 2021a: October 2021 was the sixth warmest on record for US. 8 November, accessed 9 February 22, www.noaa.gov/news/october-2021-was-sixth-warmest-on-record-for-us#:~:text=The%20U.S.%20precipitation%20total%20for,Louisiana%20saw%20its%20fourth%20wettest.

——, 2021b: National climate report - August 2021. Accessed 14 February 2022, www.ncdc.noaa.gov/sotc/national/202108.

——, 2021c: Global climate report - April 2021. Accessed 14 February 2022, www.ncdc.noaa.gov/sotc/global/202104.

——, 2021d: Assessing the global climate in August 2021. 14 September, www.ncei.noaa.gov/news/global-climate-202108.

——, 2022a: U.S. Climate Extremes Index (CEI): Definition. Accessed 20 June 2022, www.ncdc.noaa.gov/extremes/cei/definition.

——, 2022b: U.S. Climate Extremes Index (CEI): Graph. Accessed 7 February 2022, www.ncdc.noaa.gov/extremes/cei/graph/us/01-12/4.

——, 2022c: State of the Climate: Monthly global climate report for annual 2021. Accessed 9 February 2022, www.ncei.noaa.gov/access/monitoring/monthly-report/global/202113.

——, 2022d: Assessing the global climate in 2021. 13 January, www.ncei.noaa.gov/news/global-climate-202112.

——, 2022e: State of the Climate: Monthly national climate report for annual 2021. Accessed 9 February 2022, www.ncdc.noaa.gov/sotc/national/202113.

Noetzli, J., and Coauthors, 2018: Permafrost thermal state [in "State of the Climate in 2017"]. *Bull. Amer. Meteor. Soc.*, **99** (8), S20–S22, https://doi.org/10.1175/2018BAMSStateoftheClimate.1.

——, H. H. Christiansen, K. Isaksen, S. Smith, L. Zhao, and D. A. Streletskiy, 2021a: Permafrost thermal state [in "State of the Climate in 2019"]. *Bull. Amer. Meteor. Soc.*, 101 (8), S34–S36, https://doi.org/10.1175/BAMS-D-20-0104.1.

——, and Coauthors, 2021b: Best practice for measuring permafrost temperature in boreholes based on the experience in the Swiss Alps. *Front. Earth Sci.*, **9**, 607875, https://doi.org/10.3389/feart.2021.607875.

O'Keefe, J., 2021: Phenology of woody species at Harvard Forest since 1990 ver 32. Environmental Data Initiative, accessed 10 February 2022, https://doi.org/10.6073/pasta/6b0a6e266e06ab52148af3e5cd942159.

O'Reilly, C. M., and Coauthors, 2015: Rapid and highly variable warming of lake surface waters around the globe. *Geophys. Res. Lett.*, **42**, 10773–10781, https://doi.org/10.1002/2015GL066235.

Orimoloye, I. R., J. A. Belle, Y. M. Orimoloye, A. O. Olusola, and O. O. Ololade, 2022: Drought: A common environmental disaster. *Atmosphere*, **13**, 111, https://doi.org/10.3390/atmos13010111.

Osborn, T. J., P. D. Jones, D. H. Lister, C. P. Morice, I. R. Simpson, J. P. Winn, E. Hogan, and I. C. Harris, 2021: Land surface air temperature variations across the globe updated to 2019: The CRUTEM5 dataset. *J. Geophys. Res. Atmos.*, **126**, e2019JD032352, https://doi.org/10.1029/2019JD032352

Park, T., and Coauthors, 2016: Changes in growing season duration and productivity of northern vegetation inferred from long-term remote sensing data. *Environ. Res. Lett.*, **11**, 084001, https://doi.org/10.1088/1748-9326/11/8/084001.

Pascolini-Campbell, M., J. T. Reager, H. A. Chandanpurkar, and M. A. Rodell, 2021: 10 per cent increase in global land evapotranspiration from 2003 to 2019. *Nature*, **593**, 543–547, https://doi.org/10.1038/s41586-021-03503-5.

Pellet, C., X. Bodin, R. Delaloye, V. Kaufmann, J. Noetzli, E. Thibert, and A. Kellerer-Pirklbauer, 2021: Rock glacier kinematics [in "State of the Climate in 2020"]. *Bull. Amer. Meteor. Soc.*, **102** (8), S44–S45, https://doi.org/10.1175/BAMS-D-21-0098.1.

Pelto, M., P. Panday, T. Matthews, J. Maurer, and L. B. Perry, 2021: Observations of winter ablation on glaciers in the Mount Everest region in 2020–2021. *Remote Sens.*, **13**, 2692, https://doi.org/10.3390/rs13142692.

——, M. Dryak, J. Pelto, T. Matthews, and L. B. Perry, 2022: Contribution of glacier runoff during heat waves in the Nooksack River basin USA. *Water*, **14**, 1145, https://doi.org/10.3390/w14071145.

PERMOS, 2019: Permafrost in Switzerland 2014/2015 to 2017/2018. Glaciological Report Permafrost No. 16–19, J. Noetzli, C. Pellet, and B. Staub, Eds., Cryospheric Commission of the Swiss Academy of Sciences, 104 pp., https://doi.org/10.13093/permos-rep-2019-16-19.

——, 2022. Swiss Permafrost Bulletin 2021. J. Noetzli and C. Pellet, Eds., Swiss Permafrost Monitoring Network, 22 pp., https://doi.org/10.13093/permos-bull-2022.

Petersen, W. A., and S. A. Rutledge, 1998: On the relationship between cloud-to-ground lightning and convective rainfall. *J. Geophys. Res.*, **103**, 14 025–14 040, https://doi.org/10.1029/97JD02064.

Peterson, M. J., and Coauthors, 2022: New WMO certified megaflash lightning extremes for flash distance and duration recorded from space. *Bull. Amer. Meteor. Soc.*, 103, 257–261, https://doi.org/10.1175/BAMS-D-21-0254.1.

Petrenko, V., and Coauthors, 2013: A 60 yr record of atmospheric carbon monoxide reconstructed from Greenland firn air. *Atmos. Chem. Phys.*, **13**, 7567–7585, https://doi.org/10.5194/acp-13-7567-2013.

Philip, S. Y., and Coauthors, 2021: Rapid attribution analysis of the extraordinary heatwave on the Pacific Coast of the US and Canada June 2021. *Earth Syst. Dyn. Discuss.*, https://doi.org/10.5194/esd-2021-90.

Piepgrass, M., E. Krider, and C. Moore, 1982: Lightning and surface rainfall during Florida thunderstorms. *J. Geophys. Res.*, **87**, 11 193–11 201, https://doi.org/10.1029/JC087iC13p11193.

Pinto, O., Jr., K. P. Naccarato, and I. R. C. A. Pinto, 2013: Thunderstorm incidence in southeastern Brazil estimated from different data sources. *Ann. Geophys.*, **31**, 1213–1219, https://doi.org/10.5194/angeo-31-1213-2013.

Pinty, B., and Coauthors, 2011: Exploiting the MODIS albedos with the Two-stream Inversion Package (JRC-TIP): 2. Fractions of transmitted and absorbed fluxes in the vegetation and soil layers. *J. Geophys. Res.*, **116**, D09106, https://doi.org/10.1029/2010JD015373.

Pisoft, P., and Coauthors, 2021: Stratospheric contraction caused by increasing greenhouse gases. *Environ. Res. Lett.*, **16**, 064038, https://doi.org/10.1088/1748-9326/abfe2b.

Platnick, S., 2022: Cloud Issues (06_L2). NASA Atmosphere Discipline Team Imager Products, accessed 14 February 2022, https://atmosphere-imager.gsfc.nasa.gov/issues/cloud.

——, and Coauthors, 2015: MODIS Atmosphere L3 Monthly Product. NASA MODIS Adaptive Processing System, Goddard Space Flight Center, accessed 11 February 2022, https://doi.org/10.5067/MODIS/MYD08_M3.061.

Po-Chedley, S., T. J. Thorsen, and Q. Fu, 2015: Removing diurnal cycle contamination in satellite-derived tropospheric temperatures: Understanding tropical tropospheric trend discrepancies. *J. Climate*, **28**, 2274–2290, https://doi.org/10.1175/JCLI-D-13-00767.1.

——, J. R. Christy, L. Haimberger, and C. A. Mears, 2021: Tropospheric temperature [in "State of the Climate in 2020"]. *Bull. Amer. Meteor. Soc.*, **102** (8), S34–S37, https://doi.org/10.1175/BAMS-D-21-0098.1.

Pogliotti, P., M. Guglielmin, E. Cremonese, U. M. di Cella, G. Filippa, C. Pellet, and C. Hauck, 2015: Warming permafrost and active layer variability at Cime Bianche, Western European Alps. *Cryosphere*, **9**, 647–661, https://doi.org/10.5194/tc-9-647-2015.

Popp, T., and Coauthors, 2016: Development, production and evaluation of aerosol climate data records from European satellite observations (Aerosol_cci). *Remote Sens.*, **8**, 421, https://doi.org/10.3390/rs8050421.

Potocki, M., and Coauthors, 2022: Mt. Everest's highest glacier is a sentinel for accelerating ice loss. *npj Climate Atmos. Sci.*, **5**, 7, https://doi.org/10.1038/s41612-022-00230-0.

Prather, M. J., C. D. Holmes, and J. Hsu, 2012: Reactive greenhouse gas scenarios: Systematic exploration of uncertainties and the role of atmospheric chemistry. *Geophys. Res. Lett.*, 39, L09803, https://doi.org/10.1029/2012GL051440.

Price, C., 1993: Global surface temperature and the atmospheric electric circuit. *Geophys. Res. Lett.*, **20**, 1363–1366, https://doi.org/10.1029/93GL01774.

——, and D. Rind, 1993: What determines the cloud-to-ground lightning fraction in thunderstorms. *Geophys. Res. Lett.*, **20**, 463–466, https://doi.org/10.1029/93GL00226.

——, and M. Asfur, 2006: Can lightning observations be used as an indicator of upper-tropospheric water vapor variability? *Bull. Amer. Meteor. Soc.*, **87**, 291–298, https://doi.org/10.1175/BAMS-87-3-291.

——, J. Penner, and M. Prather, 1997: NO_x from lightning: 1. Global distribution based on lightning physics. *J. Geophys. Res.*, **102**, 5929–5941, https://doi.org/10.1029/96JD03504.

Ramon, J., L. Lledó, V. Torralba, A. Soret, and F. J. Doblas-Reyes, 2019: What global reanalysis best represents near-surface winds? *Quart. J. Roy. Meteor. Soc.*, **145**, 3236–3251, https://doi.org/10.1002/qj.3616.

Randel, W. J., and J. B. Cobb, 1994: Coherent variations of monthly mean total ozone and lower stratospheric temperature. *J. Geophys. Res.*, **99**, 5433–5447, https://doi.org/10.1029/93JD03454.

Rao, J., C. I. Garfinkel, H. Chen, and I. P. White, 2019: The 2019 New Year stratospheric sudden warming and its real-time predictions in multiple S2S models. *J. Geophys. Res. Atmos.*, **124**, 11 155–112174, https://doi.org/10.1029/2019JD030826.

Ravishankara, A. R., J. S. Daniel, and R. W. Portmann, 2009: Nitrous oxide (N_2O): The dominant ozone-depleting substance emitted in the 21st century. *Science*, **326**, 123–125, https://doi.org/10.1126/science.1176985.

Ray, E. A., F. L. Moore, J. W. Elkins, K. H. Rosenlof, J. C. Laube, T. Röckmann, D. R. Marsh, and A. E. Andrews, 2017: Quantification of the SF6 lifetime based on mesospheric loss measured in the stratospheric polar vortex. *J. Geophys. Res. Atmos.*, **122**, 4626– 4638, https://doi.org/10.1002/2016JD026198.

Reichstein, M., and Coauthors, 2013: Climate extremes and the carbon cycle. *Nature*, **500**, 287–295, https://doi.org/10.1038/nature12350.

Reid, K. J., T. A. O'Brien, A. D. King, and T. P. Lane, 2021: Extreme water vapor transport during the march 2021 Sydney floods in the context of climate projections. *Geophys. Res. Lett.*, **48**, e2021GL095335, https://doi.org/10.1029/2021GL095335.

Rennie, M. P., L. Isaksen, F. Weiler, J. de Kloe, T. Kanitz, and O. Reitebuch, 2021: The impact of Aeolus wind retrievals on ECMWF global weather forecasts. *Quart. J. Roy. Meteor. Soc.*, **147**, 3555–3586, https://doi.org/10.1002/qj.4142.

RGIK, 2021: Towards standard guidelines for inventorying rock glaciers: Baseline concepts (version 4.2.1). IPA Action Group Rock glacier inventories and kinematics, 13 pp., https://bigweb.unifr.ch/Science/Geosciences/Geomorphology/Pub/Website/IPA/Guidelines/V4/210801_Baseline_Concepts_Inventorying_Rock_Glaciers_V4.2.1.pdf.

——, 2022: Rock Glacier Velocity as an associated parameter of ECV Permafrost: Baseline concepts (version 3.1). IPA Action Group Rock glacier inventories and kinematics, 12 pp., https://bigweb.unifr.ch/Science/Geosciences/Geomorphology/Pub/Website/IPA/RGV/RockGlacierVelocity_V3.1.pdf.

Ricciardulli, L., and F. J. Wentz, 2015: A scatterometer geophysical model function for climate-quality winds: QuikSCAT Ku-2011. *J. Atmos. Oceanic Technol.*, **32**, 1829–1846, https://doi.org/10.1175/JTECH-D-15-0008.1.

——, and A. Manaster, 2021: Intercalibration of ASCAT scatterometer winds from MetOp-A, -B, and -C, for a stable climate data record. *Remote Sens.*, **13**, 3678, https://doi.org/10.3390/rs13183678.

Richardson, A. D., 2019: Tracking seasonal rhythms of plants in diverse ecosystems with digital camera imagery. *New Phytol.*, **222**, 1742–1750, https://doi.org/10.1111/nph.15591.

——, and J. O'Keefe, 2009: Phenological differences between understory and overstory. *Phenology of Ecosystem Processes*, A. Noormets, Eds., Springer, 87–117, https://doi.org/10.1007/978-1-4419-0026-5_4.

Rieger, L. A., W. J. Randel, A. E. Bourassa, and S. Solomon, 2021: Stratospheric temperature and ozone anomalies associated with the 2020 Australian New Year fires. *Geophys. Res. Lett.*, **48**, e2021GL095898, https://doi.org/10.1029/2021GL095898.

Rigby, M., and Coauthors, 2019: Increase in CFC-11 emissions from eastern China based on atmospheric observations. *Nature*, **569**, 546–550, https://doi.org/10.1038/s41586-019-1193-4.

Rodell, M., J. S. Famiglietti, D. N. Wiese, J. T. Reager, H. K. Beaudoing, and M.-H. Lo, 2018: Emerging trends in global freshwater availability. *Nature*, **557**, 651–659, https://doi.org/10.1038/s41586-018-0123-1.

Roderick, M. L., L. D. Rotstayn, G. D. Farquhar, and M. T. Hobbins, 2007: On the attribution of changing pan evaporation. *Geophys. Res. Lett.*, **34**, L17403, https://doi.org/10.1029/2007GL031166.

Rohde, R. A., and Z. Hausfather, 2020: The Berkeley Earth land/ocean temperature record. *Earth Syst. Sci. Data*, **12**, 3469–3479, https://doi.org/10.5194/essd-12-3469-2020.

Romps, D. M., J. T. Seeley, D. Vollaro, and J. Molinari, 2014: Projected increase in lightning strikes in the United States due to global warming. *Science*, **346**, 851–854, https://doi.org/10.1126/science.1259100.

Rosenfeld, D., U. Lohmann, G. B. Raga, C. D. O'Dowd, M. Kulmata, A. Reissell, and M. O. Andreae, 2008: Flood or drought: How do aerosols affect precipitation? *Science*, **321**, 1309–1313, https://doi.org/10.1126/science.1160606.

Rudlosky, S., and K. Virts, 2021: Dual geostationary lightning mapper observations. *Mon. Wea. Rev.*, **149**, 979–998, https://doi.org/10.1175/MWR-D-20-0242.1.

——, S. Goodman, K. Calhoun, C. Schultz, A. Back, B. Kuligowski, S. Stevenson, and C. Gravelle, 2020: Geostationary Lightning Mapper value assessment. NOAA Tech. Rep. NESDIS 153, 46 pp., https://doi.org/10.25923/2616-3v73.

Ryley, T., S. Baumeister, and L. Coulter, 2020: Climate change influences on aviation: A literature review. *Transp. Policy*, **92**, 55–64, https://doi.org/10.1016/j.tranpol.2020.04.010.

Safaei Pirooz, A. A., R. G. Flay, L. Minola, C. Azorin-Molina, and D. Chen, 2020: Effects of sensor response and moving average filter duration on maximum wind gust measurements. *J. Wind Eng. Ind. Aerodyn.*, **206**, 104354, https://doi.org/10.1016/j.jweia.2020.104354.

Said, R. K., U. S. Inan, and K. L. Cummins, 2010: Long-range lightning geolocation using a VLF radio atmospheric waveform bank. *J. Geophys. Res.*, **115**, D23108, https://doi.org/10.1029/2010JD013863.

Sánchez-Lugo, A., C. Morice, J. P. Nicolas, and A. Argüez, 2021: Global surface temperature [in "State of the Climate in 2020"]. *Bull. Amer. Meteor. Soc.*, **102** (8), S26–S28, https://doi.org/10.1175/BAMS-D-21-0098.1.

Santer, B. D., and Coauthors, 2008: Consistency of modelled and observed temperature trends in the tropical troposphere. *Int. J. Climatol.*, **28**, 1703–1722, https://doi.org/10.1002/joc.1756.

——, and Coauthors, 2021: Using climate model simulations to constrain observations. *J. Climate*, **34**, 6281–6301, https://doi.org/10.1175/JCLI-D-20-0768.1.

Satheesh, S. K., S. Suresh Babu, B. Padmakumari, G. Pandithurai, and V. K. Soni, 2017: Variability of atmospheric aerosols over India. *Observed Climate Variability and Change over the Indian Region*, M. N. Rajeevan and S. Nayak, Eds., Springer, 221–248, https://doi.org/10.1007/978-981-10-2531-0_13.

Sátori, G., V. Mushtak, and E. Williams, 2009: Schumann resonance signatures of global lightning activity. *Lightning: Principles, Instruments and Applications: Review of Modern Lightning Research*, H.-D Betz, U. Schumann, and P. Laroche, Eds., Springer, 347–386, https://doi.org/10.1007/978-1-4020-9079-0_16.

Saunois, M., and Coauthors, 2020: The global methane budget 2000–2017. *Earth Syst. Sci. Data*, **12**, 1561–1623, https://doi.org/10.5194/essd-12-1561-2020.

Scaife, A. A., and Coauthors, 2014: Skilful long range prediction of European and North American winters. *Geophys. Res. Lett.*, **41**, 2514–2519, https://doi.org/10.1002/2014GL059637.

Schaaf, C. B., and Coauthors, 2002: First operational BRDF, albedo nadir reflectance products from MODIS. *Remote Sens. Environ.*, **83**, 135–148, https://doi.org/10.1016/S0034-4257(02)00091-3.

Schaefer, H., and Coauthors, 2016; A 21st-century shift from fossil-fuel to biogenic methane emissions indicated by 13CH4. *Science*, **352** (6281), 80–84, https://doi/10.1126/science.aad2705.

Schamm, K., M. Ziese, A. Becker, P. Finger, A. Meyer-Christoffer, B. Rudolf, and U. Schneider, 2013: GPCC First Guess Daily Product at 1.0°: Near Real-Time First Guess Daily Land-Surface Precipitation from Rain-Gauges Based on SYNOP Data. Global Precipitation Climatology Centre, accessed 18 January 2021, https://doi.org/10.5676/DWD_GPCC/FG_D_100.

Schneider, U., A. Becker, P. Finger, R. Elke, and M. Ziese, 2020: GPCC Monitoring Product: Near Real-Time Monthly Land-Surface Precipitation from Rain-Gauges based on SYNOP and CLIMAT Data, Global Precipitation Climatology Centre Global Precipitation Climatology Centre, accessed 7 February 2022, https://doi.org/10.5676/DWD_GPCC/MP_M_V2020_100.

Schumann, U., and H. Huntrieser, 2007: The global lightning-induced nitrogen oxides source. *Atmos. Chem. Phys.*, **7**, 3823–3907, https://doi.org/10.5194/acp-7-3823-2007.

Schwietzke, S., and Coauthors, 2016: Upward revision of global fossil fuel methane emissions based on isotope database. *Nature*, **538**, 88–91, https://doi.org/10.1038/nature19797.

Seneviratne, S. I., T. Corti, E. L. Davin, M. Hirschi, E. B. Jaeger, I. Lehner, B. Orlowsky, and A. J. Teuling, 2010: Investigating soil moisture–climate interactions in a changing climate: A review. *Earth-Sci. Rev.*, **99**, 125–161, https://doi.org/10.1016/j.earscirev.2010.02.004.

Seyednasrollah, B., A. M. Young, K. Hufkens, T. Milliman, M. A. Friedl, S. Frolking, and A. D. Richardson, 2019: Tracking vegetation phenology across diverse biomes using Version 2.0 of the PhenoCam Dataset. *Sci. Data*, **6**, 261, https://doi.org/10.1038/s41597-019-0270-8.

Sharma, S., and R. I. Woolway, 2021: Lake ice [in "State of the Climate in 2020"]. *Bull. Amer. Meteor. Soc.*, **102** (8), S48–S51, https://doi.org/10.1175/BAMS-D-21-0098.1.

——, and Coauthors, 2021: Loss of ice cover, shifting phenology, and more extreme events in Northern Hemisphere lakes. *J. Geophys. Res. Biogeosci.*, **126**, e2021JG006348, https://doi.org/10.1029/2021JG006348.

Shi, L., and J. J. Bates, 2011: Three decades of intersatellite-calibrated high-resolution infrared radiation sounder upper tropospheric water vapor. *J. Geophys. Res.*, **116**, D04108, https://doi.org/10.1029/2010JD014847.

Simmons, A. J., P. Berrisford, D. P. Dee, H. Hersbach, S. Hirahara, and J. N. Thepaut, 2017: A reassessment of temperature variations and trends from global reanalyses and monthly surface climatological datasets. *Quart. J. Roy. Meteor. Soc.*, **143**, 101–119, https://doi.org/10.1002/qj.2949.

——, and Coauthors, 2021: Low frequency variability and trends in surface air temperature and humidity from ERA5 and other datasets. ECMWF Tech. Memo. 881, 97 pp., https://doi.org/10.21957/ly5vbtbfd.

Sindelarova, K., and Coauthors, 2014: Global data set of biogenic VOC emissions calculated by the MEGAN model over the last 30 years. *Atmos. Chem. Phys.*, **14**, 9317–9341, https://doi.org/10.5194/acp-14-9317-2014.

SMHI, 2021: August 2021 - Rainy month with torrential rain over Gävle. 15 November, accessed 9 February 2022, www.smhi.se/klimat/klimatet-da-och-nu/manadens-vader-och-vatten-sverige/manadens-vader-i-sverige/augusti-2021-meteorologi-1.173428#:~:text=Augustiv%C3%A4dret%20blev%20en%20skarp%20kontrast,kraftigt%20regn%20och%20lokala%20%C3%B6versv%C3%A4mningar.

Smith, S. L., H. B. O'Neill, K. Isaksen, J. Noetzli, and V. E. Romanovsky, 2022: The changing thermal state of permafrost. *Nat. Rev. Earth Environ.*, **3**, 10–23, https://doi.org/10.1038/s43017-021-00240-1.

Sofieva, V. F., and Coauthors, 2021: Measurement report: regional trends of stratospheric ozone evaluated using the MErged GRIdded Dataset of Ozone Profiles (MEGRIDOP). *Atmos. Chem. Phys.*, **21**, 6707–6720, https://doi.org/10.5194/acp-21-6707-2021.

Sommer, U., Z. M. Gliwicz, W. Lampert, and A. Duncan, 1986: The PEG-model of seasonal succession of planktonic events in fresh waters. *Arch. Hydrobiol.*, **106** (4), 433–471.

Song, X.-P., M. C. Hansen, S. V. Stehman, P. V. Potapov, A. Tyukavina, E. F. Vermote, and J. R. Townshend, 2018: Global land change from 1982 to 2016. *Nature*, **560**, 639–643, https://doi.org/10.1038/s41586-018-0411-9.

SPARC/IO3C/GAW, 2019: SPARC/IO3C/GAW report on long-term ozone trends and uncertainties in the stratosphere. I. Petropavlovskikh et al., Eds., SPARC Rep. 9, WCRP-17/2018, GAW Rep. 241, 99 pp., https://doi.org/10.17874/f899e57a20b.

Spencer, R. W., J. R. Christy, and W. D. Braswell, 2017: UAH Version 6 global satellite temperature products: Methodology and results. *Asia-Pac. J. Atmos. Sci.*, **53**, 121–130, https://doi.org/10.1007/s13143-017-0010-y.

Stackhouse, P. W., T. Wong, D. P. Kratz, P. Sawaengphokhai, A. C. Wiber, S. K. Gupta, and N. G. Loeb, 2016: Earth radiation budget at top-of-atmosphere [in "State of the Climate in 2015"]. *Bull. Amer. Meteor. Soc.*, **97** (8), S41–S43, https://doi.org/10.1175/2016BAMSStateoftheClimate.1.

Staub, B., C. Lambiel, and R. Delaloye, 2016: Rock glacier creep as a thermally-driven phenomenon: A decade of inter-annual observation from the Swiss Alps. XI Int. Conf. on Permafrost, Potsdam, Germany, Alfred Wegener Institute Helmholtz Center for Polar and Marine Research, 96–97, https://doi.org/10.2312/GFZ.LIS.2016.001.

Stein, O., M. G. Schultz, I. Bouarar, H. Clark, V. Huijnen, A. Gaudel, M. George, and C. Clerbaux, 2014: On the wintertime low bias of Northern Hemisphere carbon monoxide found in global model simulations. *Atmos. Chem. Phys.*, **14**, 9295–9316, https://doi.org/10.5194/acp-14-9295-2014.

Steinbrecht, W., and Coauthors, 2017: An update on ozone profile trends for the period 2000 to 2016. *Atmos. Chem. Phys.*, **17**, 10675–10690, https://doi.org/10.5194/acp-17-10675-2017.

——, and Coauthors, 2021: COVID-19 crisis reduces free tropospheric ozone across the Northern Hemisphere. *Geophys. Res. Lett.*, **48**, e2020GL091987, https://doi.org/10.1029/2020GL091987.

Steiner, A. K., and Coauthors, 2020: Observed temperature changes in the troposphere and stratosphere from 1979 to 2018. *J. Climate*, **33**, 8165–8194, https://doi.org/10.1175/JCLI-D-19-0998.1.

Stocker, M., F. Ladstädter, and A. K. Steiner, 2021: Observing the climate impact of large wildfires on stratospheric temperature. *Sci. Rep.*, **11**, 22994, https://doi.org/10.1038/s41598-021-02335-7.

Stolz, D., S. Rutledge, and J. Pierce, 2015: Simultaneous influences of thermodynamics and aerosols on deep convection and lightning in the tropics. *J. Geophys. Res. Atmos.*, **120**, 6207–6231, https://doi.org/10.1002/2014JD023033.

Streletskiy, D., J. Noetzli, S. L. Smith, G. Vieira, P. Schoeneich, F. Hrbacek, and A. M. Irrgang, 2021: Strategy and Implementation Plan 2021–2024 for the Global Terrestrial Network for Permafrost (GTN-P). International Permafrost Association, 44 pp., https://doi.org/10.5281/ZENODO.6075468.

Stroeve, J., J. E. Box, Z. Wang, C. Schaaf, and A. Barrett, 2013: Re-evaluation of MODIS MCD43 Greenland albedo accuracy and trends. *Remote Sens. Environ.*, **138**, 199–214, https://doi.org/10.1016/j.rse.2013.07.023.

Susskind, J., G. Molnar, L. Iredell, and N. G. Loeb, 2012: Interannual variability of outgoing longwave radiation as observed by AIRS and CERES. *J. Geophys. Res.*, **117**, D23107, https://doi.org/10.1029/2012JD017997.

Szeląg, M. E., V. F. Sofieva, D. Degenstein, C. Roth, S. Davis, and L. Froidevaux, 2020: Seasonal stratospheric ozone trends over 2000–2018 derived from several merged data sets. *Atmos. Chem. Phys.*, **20**, 7035–7047, https://doi.org/10.5194/acp-20-7035-2020.

Szopa, S., and Coauthors, 2021: Short-lived climate forcers. *Climate Change 2021: The Physical Science Basis*, V. Masson-Delmotte et al., Eds., Cambridge University Press, 817–922, https://doi.org/10.1017/9781009157896.008.

Tapley, B. D., S. Bettadpur, J. C. Ries, P. F. Thompson, and M. M. Watkins, 2004: GRACE measurements of mass variability in the Earth system. *Science*, **305**, 503–505, https://doi.org/10.1126/science.1099192.

Tarasick, D. W., and Coauthors, 2019: Tropospheric Ozone Assessment Report: Tropospheric ozone from 1877 to 2016, observed levels, trends and uncertainties. *Elem. Sci. Anthropocene*, **7**, 39, https://doi.org/10.1525/elementa.376.

Teng, W.-H., C.-Y. Huang, S.-P. Ho, Y.-H. Kuo, and X.-J. Zhou, 2013: Characteristics of global precipitable water in ENSO events revealed by COSMIC measurements. *J. Geophys. Res. Atmos.*, **118**, 8411–8425, https://doi.org/10.1002/jgrd.50371.

Teubner, I. E., and Coauthors, 2019: A carbon sink-driven approach to estimate gross primary production from microwave satellite observations. *Remote Sens. Environ.*, **229**, 100–113, https://doi.org/10.1016/j.rse.2019.04.022.

Thompson, R. L., and Coauthors, 2019: Acceleration of global N_2O emissions seenfrom two decades of atmospheric inversion. *Nat. Climate Change*, **9**, 993–998, https://doi.org/10.1038/s41558-019-0613-7.

Thornton, J. A., K. S. Virts, R. H. Holzworth, and T. P. Mitchell, 2017: Lightning enhancement over major oceanic shipping lanes. *Geophys. Res. Lett.*, **44**, 9102–9111, https://doi.org/10.1002/2017GL074982.

Torralba, V., F. J. Doblas-Reyes, and N. Gonzalez-Reviriegol, 2017: Uncertainty in recent near-surface wind speed trends: A global reanalysis intercomparison. *Environ. Res. Lett.*, **12**, 114019, https://doi.org/10.1088/1748-9326/aa8a58.

Trepte, Q. Z., P. Minnis, C. R. Trepte, S. Sun-Mack, and R. Brown, 2010: Improved cloud detection in CERES Edition 3 algorithm and comparison with the CALIPSO Vertical Feature Mask. *13th Conf. on Atmospheric Radiation and Cloud Physics*, Portland, OR, Amer. Meteor. Soc., JP1.32, https://ams.confex.com/ams/13CldPhy13AtRad/webprogram/Paper171785.html.

UN Environment Programme, 2021: Global Methane Assessment: Benefits and Costs of Mitigating Methane Emissions. United Nations Environment Programme and Climate and Clean Air Coalition Rep., 172 pp., www.unep.org/resources/report/global-methane-assessment-benefits-and-costs-mitigating-methane-emissions.

van der A, R. J., M. A. F. Allaart, and H. J. Eskes, 2015: Extended and refined multi sensor reanalysis of total ozone for the period 1970–2012. *Atmos. Meas. Tech.*, **8**, 3021–3035,, https://doi.org/10.5194/amt-8-3021-2015.

van der Schalie, R., and Coauthors, 2017: The merging of radiative transfer-based surface soil moisture data from SMOS and AMSR-E. *Remote Sens. Environ.*, **189**, 180–193, https://doi.org/10.1016/j.rse.2016.11.026.

——, and Coauthors, 2021: Soil moisture [in "State of the Climate in 2020"]. *Bull. Amer. Meteor. Soc.*, **102** (8), S67–S68, https://doi.org/10.1175/BAMS-D-21-0098.1.

van der Schrier, G., J. Barichivich, K. R. Briffa, and P. D. Jones, 2013: A scPDSI-based global dataset of dry and wet spells for 1901-2009. *J. Geophys. Res. Atmos.*, **118**, 4025–4048, https://doi.org/10.1002/jgrd.50355.

van der Werf, G. R., and Coauthors, 2017: Global fire emissions estimates during 1997–2016. *Earth Syst. Sci. Data*, **9**, 697–720, https://doi.org/10.5194/essd-9-697-2017.

van Dijk, A. I. J. M., and Coauthors, 2015: Rainfall interception and the coupled surface water and energy balance. *Agric. For. Meteor.*, **214–215**, 402–415, https://doi.org/10.1016/j.agrformet.2015.09.006.

Virts, K. S., and S. J. Goodman, 2020: Prolific lightning and thunderstorm Initiation over the lake Victoria basin in East Africa. *Mon. Wea. Rev.*, **148**, 1971–1985, https://doi.org/10.1175/MWR-D-19-0260.1.

——, J. M. Wallace, M. L. Hutchins, and R. H. Holzworth, 2013: Highlights of a new ground-based, hourly global lightning climatology. *Bull. Amer. Meteor. Soc.*, 94, 1381–1391, https://doi.org/10.1175/BAMS-D-12-00082.1.

Vivero, S., X. Bodin, D. Farías-Barahona, S. MacDonell, N. Schaffer, B. A. Robson, and C. Lambiel, 2021: Combination of aerial, satellite, and UAV photogrammetry for quantifying rock glacier kinematics in the Dry Andes of Chile (30°S) since the 1950s. *Front. Remote Sens.*, **2**, 784015, https://doi.org/10.3389/frsen.2021.784015.

Vreugdenhil, M., S. Hahn, T. Melzer, B. Bauer-Marschallinger, C. Reimer, W. Dorigo, and W. Wagner, 2017: Assessing vegetation dynamics over mainland Australia with Metop ASCAT. *IEEE J. Sel. Top. Appl. Earth Obs. Remote Sens.*, **10**, 2240–2248, https://doi.org/10.1109/JSTARS.2016.2618838.

Wagner, W., and Coauthors, 2013: The ASCAT Soil Moisture Product: A review of its specifications, validation results, and emerging applications. *Meteor. Z.*, **22**, 5–33, https://doi.org/10.1127/0941-2948/2013/0399.

Wang, Q., Z. Li, J. Guo, C. Zhao, and M. Cribb, 2018: The climate impact of aerosols on the lightning flash rate: Is it detectable from long-term measurements? *Atmos. Chem. Phys.*, **18**, 12 797–12 816, https://doi.org/10.5194/acp-18-12797-2018.

Wang, X., and Coauthors, 2021: High-resolution mapping of ice cover changes in over 33,000 lakes across the North Temperate Zone. *Geophys. Res. Lett.*, **48**, e2021GL095614, https://doi.org/10.1029/2021GL095614.

Wargan, K., C. Orbe, S. Pawson, J. R. Ziemke, L. D. Oman, M. A. Olsen, L. Coy, and K. E. Knowland, 2018: Recent decline in extratropical lower stratospheric ozone attributed to circulation changes. *Geophys. Res. Lett.*, **45**, 5166–5176, https://doi.org/10.1029/2018GL077406.

Weatherhead, E. C., and Coauthors, 1998: Factors affecting the detection of trends: Statistical considerations and applications to environmental data. *J. Geophys. Res.*, **103**, 17 149–17 161, https://doi.org/10.1029/98JD00995.

Weber, M., S. Dikty, J. P. Burrows, H. Garny, M. Dameris, A. Kubin, J. Abalichin, and U. Langematz, 2011: The Brewer-Dobson circulation and total ozone from seasonal to decadal time scales. *Atmos. Chem. Phys.*, **11**, 11 221–11 235, https://doi.org/10.5194/acp-11-11221-2011.

Weber, M., and Coauthors, 2022: Global total ozone recovery trends attributed to ozone-depleting substance (ODS) changes derived from five merged ozone datasets. *Atmos. Chem. Phys.*, 22, 6843–6859, https://doi.org/10.5194/acp-22-6843-2022.

Weir, B., and Coauthors, 2021: Regional impacts of COVID-19 on carbon dioxide detected worldwide from space. *Sci. Adv.*, **7**, eabf9415, https://doi.org/10.1126/sciadv.abf9415.

Wells, N., S. Goddard, and M. J. Hayes, 2004: A self-calibrating palmer drought severity index. *J. Climate*, **17**, 2335–2351, https://doi.org/10.1175/1520-0442(2004)017<2335:ASPDSI>2.0.CO;2.

Wentz, F. J., 1997: A well calibrated ocean algorithm for Special Sensor Microwave/Imager. *J. Geophys. Res.*, **102**, 8703–8718, https://doi.org/10.1029/96JC01751.

——, 2015: A 17-year climate record of environmental parameters derived from the Tropical Rainfall Measuring Mission (TRMM) microwave imager. *J. Climate*, **28**, 6882–6902, https://doi.org/10.1175/JCLI-D-15-0155.1.

——, L. Ricciardulli, K. Hilburn, and C. Mears, 2007: How much more rain will global warming bring? *Science*, **317**, 233–235, https://doi.org/10.1126/science.1140746.

WGMS, 2021: Global Glacier Change Bulletin No. 4 (2018-2019). M. Zemp et al., Eds., ISC(WDS)/IUGG(IACS)/UNEP/UNESCO/WMO, World Glacier Monitoring Service, 278 pp., https://wgms.ch/downloads/WGMS_GGCB_04.pdf.

Wielicki, B. A., B. R. Barkstrom, E. F. Harrison, R. B. Lee III, G. L. Smith, and J. E. Cooper, 1996: Clouds and the Earth's Radiant Energy System (CERES): An Earth observing system experiment. *Bull. Amer. Meteor. Soc.*, **77**, 853–868, https://doi.org/10.1175/1520-0477(1996)077<0853:CATERE>2.0.CO;2.

——, and Coauthors, 1998: Clouds and the Earth's Radiant Energy System (CERES): Algorithm overview. *IEEE Trans. Geosci. Remote Sens.*, **36**, 1127–1141, https://doi.org/10.1109/36.701020.

Wiese, D. N., F. W. Landerer, and M. M. Watkins, 2016: Quantifying and reducing leakage errors in the JPL RL05M GRACE mascon solution. *Water Resour. Res.*, **52**, 7490–7502, https://doi.org/10.1002/2016WR019344.

Wild, B., I. Teubner, L. Moesinger, R. Zotta, M. Forkel, R. van der Schalie, S. Sitch, and W. Dorigo, 2022: VODCA2GPP – A new global, long-term (1988–2020) gross primary production dataset from microwave remote sensing. *Earth Syst. Sci. Data*, **14**, 1063–1085, https://doi.org/10.5194/essd-14-1063-2022.

Willett, K. M., C. N. Williams Jr., R. J. H. Dunn, P. W. Thorne, S. Bell, M. de Podesta, P. D. Jones, and D. E. Parker, 2013: HadISDH: An updated land surface specific humidity product for climate monitoring. *Climate Past*, **9**, 657–677, https://doi.org/10.5194/cp-9-657-2013.

——, R. J. H. Dunn, P. W. Thorne, S. Bell, M. de Podesta, D. E. Parker, P. D. Jones, and C. N. Williams Jr., 2014: HadISDH land surface multi-variable humidity and temperature record for climate monitoring. *Climate Past*, **10**, 1983–2006, https://doi.org/10.5194/cp-10-1983-2014.

——, ——, J. Kennedy, and D. Berry, 2020: Development of the HadISDH marine humidity climate monitoring dataset. *Earth Syst. Sci. Data*, **12**, 2853–2880, https://doi.org/10.5194/essd-12-2853-2020.

Williams, E. R., 1992: The Schumann resonance: A global tropical thermometer, *Science*, **256**, 1184–1187, https://doi.org/10.1126/science.256.5060.1184.

——, 1994: Global circuit response to seasonal variations in global surface air temperature. *Mon. Wea. Rev.*, **122**, 1917–1929, https://doi.org/10.1175/1520-0493(1994)122%3C1917:GCRTSV%3E2.0.CO;2.

——, 2009: The global electrical circuit: A review. *Atmos. Res.*, **91**, 140–152, https://doi.org/10.1016/j.atmosres.2008.05.018.

——, 2020: Lightning and climate change. Fundamentals and Modelling, Vol. 1, *Lightning Interaction with Power Systems*, A. Piantini, Ed., CRC Press, 1–46, https://doi.org/10.1049/PBPO172F_ch1.

——, and S. Stanfield, 2002: The physical origin of the land-ocean contrast in lightning activity. *C. R. Phys.*, **3**, 1277–1292, https://doi.org/10.1016/S1631-0705(02)01407-X.

——, and Coauthors, 2002: Contrasting convective regimes over the Amazon: Implications for cloud electrification. *J. Geophys. Res.*, **107**, 8082, https://doi.org/10.1029/2001JD000380.

——, A. Guha, R. Boldi, H. Christian, and D. Buechler, 2019: Global lightning activity and the hiatus in global warming. *J. Atmos. Sol.-Terr. Phys.*, **189**, 27–34, https://doi.org/10.1016/j.jastp.2019.03.011.

——, and Coauthors, 2021: Evolution of global lightning in the transition from cold to warm phase preceding two super El Niño events. *J. Geophys. Res. Atmos.*, **126**, e2020JD033526, https://doi.org/10.1029/2020JD033526.

WMO, 2018: Scientific assessment of ozone depletion, 2018. Global Ozone Research and Monitoring Project Rep. 58, 588 pp., https://csl.noaa.gov/assessments/ozone/2018.

——, 2019a: Lightning for climate. GCOS-227, 56 pp., https://library.wmo.int/doc_num.php?explnum_id=6262.

——, 2019b: Vision for the WMO Integrated Global Observing System in 2040. WMO-1243, 38 pp., https://library.wmo.int/doc_num.php?explnum_id=10278.

——, 2021a: GAW data: Volume IV-Greenhouse and related gases. WMO WDCGG Data Summary, WDCGG 45, 97 pp. https://gaw.kishou.go.jp/static/publications/summary/sum45/sum45.pdf.

——, 2021b: Provisional report on the state of the global climate 2021. Provisional Rep., 47 pp., accessed 9 February 2022, https://reliefweb.int/sites/reliefweb.int/files/resources/WMO%20Provisional%20Report%20on%20the%20State%20of%20the%20Global%20Climate%202021.pdf.

——, 2022: State of the Global Climate 2021. WMO-1290, 54 pp., https://library.wmo.int/doc_num.php?explnum_id=11178.

Wohland, J., N.-E. Omrani, D. Witthaut, and N.-S. Keenlyside, 2019: Inconsistent wind speed trends in current twentieth century reanalyses. *J. Geophys. Res. Atmos.*, **124**, 1931–1940, https://doi.org/10.1029/2018JD030083.

Wood, K. M., P. J. Klotzbach, J. M. Collins, L.-P. Caron, R. E. Truchelut, and C. J. Schreck, 2020: Factors affecting the 2019 Atlantic hurricane season and the role of the Indian Ocean Dipole. *Geophys. Res. Lett.*, **47**, e2020GL087781, https://doi.org/10.1029/2020GL087781.

Woolway, R. I., and C. J. Merchant, 2018: Intralake heterogeneity of thermal responses to climate change: A study of large Northern Hemisphere lakes. *J. Geophys. Res. Atmos.*, **123**, 3087–3098, https://doi.org/10.1002/2017JD027661.

——, and Coauthors, 2017: Lake surface temperature [in "State of the Climate in 2016"]. *Bull. Amer. Meteor. Soc.*, **98** (8), S13–S14, https://doi.org/10.1175/2017BAMSStateoftheClimate.1.

——, and Coauthors, 2018: Lake surface temperature [in "State of the Climate in 2017"]. *Bull. Amer. Meteor. Soc.*, **99** (8), S13–S15, https://doi.org/10.1175/2018BAMSStateoftheClimate.1.

Worden, H. M., and Coauthors, 2013: Decadal record of satellite carbon monoxide observations. *Atmos. Chem. Phys.*, **13**, 837–850, https://doi.org/10.5194/acp-13-837-2013.

Yamazaki, D., S. Kanae, H. Kim, and T. Oki, 2011: A physically based description of floodplain inundation dynamics in a global river routing model. *Water Resour. Res.*, **47**, W04501, https://doi.org/10.1029/2010WR009726.

Yeh, S.-W., and Coauthors, 2018: ENSO atmospheric teleconnections and their response to greenhouse gas forcing. *Rev. Geophys.*, **56**, 185– 206, https://doi.org/10.1002/2017RG000568

Yin, Y., F. Chevallier, P. Ciais, G. Broquet, A. Fortems-Cheiney, I. Pison, and M. Saunois, 2015: Decadal trends in global CO emissions as seen by MOPITT. *Atmos. Chem. Phys.*, **15**, 13 433–13 451, https://doi.org/10.5194/acp-15-13433-2015.

Yosef, Y., E. Aguilar, and P. Alpert, 2021: Is it possible to fit extreme climate change indices together seamlessly in the era of accelerated warming? *Int. J. Climatol.*, **41** (S1), E952–E963, https://doi.org/10.1002/joc.6740.

Young, I., and A. Ribal, 2019: Multiplatform evaluation of global trends in wind speed and wave height. *Science*, **364**, 548–552, https://doi.org/10.1126/science.aav9527.

Yu, B., X. Zhang, G. Li, and W. Yu, 2022: Interhemispheric asymmetry of climate change projections of boreal winter surface winds in CanESM5 large ensemble simulations. *Climatic Change*, **170**, 23, https://doi.org/10.1007/s10584-022-03313-2.

Yu, P., and Coauthors, 2021: Persistent stratospheric warming due to 2019–2020 Australian wildfire smoke. *Geophys. Res. Lett.*, **48**, e2021GL092609, https://doi.org/10.1029/2021GL092609.

Yulaeva, E., and J. M. Wallace, 1994: The signature of ENSO in global temperature and precipitation fields derived from the microwave sounding unit. *J. Climate*, **7**, 1719–1736, https://doi.org/10.1175/1520-0442(1994)007<1719:TSOEIG>2.0.CO;2.

Zeng, Z., and Coauthors, 2019: A reversal in global terrestrial stilling and its implications for wind energy production. *Nat. Climate Change*, **9**, 979–985, https://doi.org/10.1038/s41558-019-0622-6.

Zha, J., and Coauthors, 2021: Projected changes in global terrestrial near-surface wind speed in 1.5° C–4.0° C global warming levels. *Environ. Res. Lett.*, **16**, 114016, https://doi.org/10.1088/1748-9326/ac2fdd.

Zhang, G., and Coauthors, 2021: Uneven warming likely contributed to declining near-surface wind speeds in northern China between 1961 and 2016. *J. Geophys. Res. Atmos.*, **126**, e2020JD033637, https://doi.org/10.1029/2020JD033637.

Zhang, H.-M., and Coauthors, 2019: Updated temperature data give a sharper view of climate trends. *Eos*, **100**, https://doi.org/10.1029/2019EO128229.

Zhang, X., L. Alexander, G. C. Hegerl, P. Jones, A. Klein Tank, T. C. Peterson, B. Trewin, and F. W. Zwiers, 2011: Indices for monitoring changes in extremes based on daily temperature and precipitation data. *Wiley Interdiscip. Rev.: Climate Change*, **2**, 851–870, https://doi.org/10.1002/wcc.147.

Zhang, Y., J. M. Wallace, and D. S. Battisti, 1997: ENSO-like interdecadal variability: 1900-93. *J. Climate*, **10**, 1004–1020, https://doi.org/10.1175/1520-0442(1997)010<1004:ELIV>2.0.CO;2.

Zhang, Y.-Q., and Coauthors, 2016: Multi-decadal trends in global terrestrial evapotranspiration and its components. *Sci. Rep.*, **5**, 19124, https://doi.org/10.1038/srep19124.

Zhang, Y., O. R. Cooper, A. Gaudel, A. M. Thompson, P. Nédélec, S.-Y. Ogino, and J. J. West, 2016: Tropospheric ozone change from 1980 to 2010 dominated by equatorward redistribution of emissions. *Nat. Geosci.*, **9**, 875–879, https://doi.org/10.1038/ngeo2827.

——, and Coauthors, 2021: Contributions of world regions to the global tropospheric ozone burden change from 1980 to 2010. *Geophys. Res. Lett.*, **48**, e2020GL089184, https://doi.org/10.1029/2020GL089184.

Zhao, L., and Coauthors, 2020: Changing climate and the permafrost environment on the Qinghai–Tibet (Xizang) Plateau. *Permafrost Periglacial Processes*, **31**, 396–405, https://doi.org/10.1002/ppp.2056.

——, and Coauthors, 2021: A synthesis dataset of permafrost thermal state for the Qinghai–Tibet (Xizang) Plateau, China. *Earth Syst. Sci. Data*, **13**, 4207–4218, https://doi.org/10.5194/essd-13-4207-2021.

Zhou, L., and Coauthors, 2021: A continuous decline of global seasonal wind speed range over land since 1980. *J. Climate*, **34**, 9443–9461, https://doi.org/10.1175/JCLI-D-21-0112.1.

Ziemke, J. R., and Coauthors, 2019: Trends in global tropospheric ozone inferred from a composite record of TOMS/OMI/MLS/OMPS satellite measurements and the MERRA-2 GMI simulation. *Atmos. Chem. Phys.*, **19**, 3257–3269, https://doi.org/10.5194/acp-19-3257-2019.

Zipser, E. J., D. J. Cecil, C. Liu, S. W. Nesbitt, and D. P. Yorty, 2006: Where are the most intense thunderstorms on Earth? *Bull. Amer. Meteor. Soc.*, **87**, 1057–1072, https://doi.org/10.1175/BAMS-87-8-1057.

Zou, C.-Z., and W. Wang, 2011: Intersatellite calibration of AMSU-A observations for weather and climate applications. *J. Geophys. Res.*, **116**, D23113, https://doi.org/10.1029/2011JD016205.

——, H. Xu, X. Hao, and Q. Fu, 2021: Post-millennium atmospheric temperature trends observed from satellites in stable orbits. *Geophys. Res. Lett.*, **48**, e2021GL093291, https://doi.org/10.1029/2021GL093291.

STATE OF THE CLIMATE IN 2021

GLOBAL OCEANS

G. C. Johnson and R. Lumpkin, Eds.

Special Online Supplement to the *Bulletin of the American Meteorological Society*, Vol. 103, No. 8, August 2022

https://doi.org/10.1175/ BAMS-D-22-0072.1

Corresponding author: Rick Lumpkin / rick.lumpkin@noaa.gov

STATE OF THE CLIMATE IN 2021
Global Oceans

Editors

Jessica Blunden
Tim Boyer

Chapter Editors

Freya Aldred
Peter Bissolli
Kyle R. Clenn
Howard J. Diamond
Matthew L. Druckenmiller
Robert J. H. Dunn
Catherine Ganter
Nadine Gobron
Gregory C. Johnson
Rick Lumpkin
Ademe Mekonnen
John B. Miller
Twila A. Moon
Marilyn N. Raphael
Ahira Sánchez-Lugo
Carl J. Schreck III
Sharon Stammerjohn
Richard L. Thoman
Kate M. Willett
Zhiwei Zhu

Technical Editor

Laura Ohlmann

BAMS Special Editor for Climate

Michael A. Alexander

American Meteorological Society

Cover credit:
"Ocean-Ice-Atmosphere"

Original artwork by Gregory C. Johnson–chapter co-editor. Livestock marker and pencil on oil paper painted from a reference photo by Derek Oyen.

Global Oceans is a chapter from the *State of the Climate in 2021* annual report. This chapter is available from https://doi.org/10.1175/ BAMS-D-22-0072.1. Compiled by NOAA's National Centers for Environmental Information, *State of the Climate in 2021* is based on contributions from scientists from around the world. It provides a detailed update on global climate indicators, notable weather events, and other data collected by environmental monitoring stations and instruments located on land, water, ice, and in space. The full report is available from: https://doi.org/10.1175/2022BAMSStateoftheClimate.1.

How to cite this document:

Citing the complete report:
Blunden, J. and T. Boyer, Eds., 2022: State of the Climate in 2021. *Bull. Amer. Meteor. Soc.*, **103** (8), Si–S465, https://doi.org/10.1175/2022BAMSStateoftheClimate.1.

Citing this chapter:
Johnson, G. C. and R. L. Lumpkin, Eds., 2022: Global Oceans [in "State of the Climate in 2021"]. *Bull. Amer. Meteor. Soc.*, **103** (8), S143–S191, https://doi.org/10.1175/ BAMS-D-22-0072.1.

Citing a section (example):
Franz, B. A., I. Cetinić, M. Gao, D. A. Siegel, and T. K. Westberry, 2022: Global ocean phytoplankton [in "State of the Climate in 2021"]. *Bull. Amer. Meteor. Soc.*, **103** (8), S180–S183, https://doi.org/10.1175/ BAMS-D-22-0072.1.

Editor and Author Affiliations (alphabetical by name)

Boyer, Tim, NOAA/NESDIS National Centers for Environmental Information, Silver Spring, Maryland
Bringas, Francis, NOAA/OAR Atlantic Oceanographic and Meteorological Laboratory, Miami, Florida
Cetinić, Ivona, NASA Goddard Space Flight Center, Greenbelt, Maryland, and Morgan State University, Baltimore, Maryland
Chambers, Don P., College of Marine Science, University of South Florida, St. Petersburg, Florida
Cheng, Lijing, International Center for Climate and Environment Sciences, Institute of Atmospheric Physics, Chinese Academy of Sciences, Beijing, China
Dong, Shenfu, NOAA/OAR Atlantic Oceanographic and Meteorological Laboratory, Miami, Florida
Feely, Richard A., NOAA/OAR Pacific Marine Environmental Laboratory, Seattle, Washington
Fox-Kemper, Baylor, Department of Earth, Environmental, and Planetary Sciences, Brown University, Providence, Rhode Island
Frajka-Williams, Eleanor, National Oceanography Centre, United Kingdom
Franz, Bryan A., NASA Goddard Space Flight Center, Greenbelt, Maryland
Fu, Yao, School of Earth and Atmospheric Sciences, Georgia Institute of Technology, Atlanta, Georgia
Gao, Meng, NASA Goddard Space Flight Center, Greenbelt, Maryland, and Science Systems and Application Inc., Lanham, Maryland
Garg, Jay, Science Systems and Applications, Inc., Hampton, Virginia
Gilson, John, Scripps Institution of Oceanography, University of California San Diego, La Jolla, California
Goni, Gustavo, NOAA/OAR Atlantic Oceanographic and Meteorological Laboratory, Miami, Florida
Hamlington, Benjamin D., Jet Propulsion Laboratory, California Institute of Technology, Pasadena, California
Hewitt, Helene T., Met Office Hadley Centre, Exeter, United Kingdom
Hobbs, William R., Australian Antarctic Program Partnership, Institute for Marine and Antarctic Studies, and Australian Research Council Centre of Excellence for Climate Extremes, University of Tasmania, Hobart, Tasmania
Hu, Zeng-Zhen, NOAA/NWS NCEP Climate Prediction Center, College Park, Maryland
Huang, Boyin, NOAA/NESDIS National Centers for Environmental Information, Asheville, North Carolina
Jevrejeva, Svetlana, National Oceanography Centre, Liverpool, United Kingdom
Johns, William E., Rosenstiel School of Marine and Atmospheric Science, University of Miami, Miami, Florida
Johnson, Gregory C., NOAA/OAR Pacific Marine Environmental Laboratory, Seattle, Washington
Katsunari, Sato, Japan Meteorological Agency, Tokyo, Japan
Kennedy, John J., Met Office Hadley Centre, Exeter, United Kingdom
Kersalé, Marion, Cooperative Institute for Marine and Atmospheric Studies, University of Miami, and NOAA/OAR Atlantic Oceanographic and Meteorological Laboratory, Miami, Florida; currently at Direction Générale de l'Armement, Ingénierie des projets, Paris, France
Killick, Rachel E., Met Office Hadley Centre, Exeter, United Kingdom
Leuliette, Eric, NOAA/NWS NCWCP Laboratory for Satellite Altimetry, College Park, Maryland
Locarnini, Ricardo, NOAA/NESDIS National Centers for Environmental Information, Silver Spring, Maryland
Lozier, M. Susan, School of Earth and Atmospheric Sciences, Georgia Institute of Technology, Atlanta, Georgia
Lumpkin, Rick, NOAA/OAR Atlantic Oceanographic and Meteorological Laboratory, Miami, Florida
Lyman, John M., Cooperative Institute for Marine and Atmospheric Research, University of Hawaii, Honolulu, Hawaii, and NOAA/OAR Pacific Marine Environmental Laboratory, Seattle, Washington
Merrifield, Mark A., Scripps Institution of Oceanography, University of California San Diego, La Jolla, California
Mishonov, Alexey, Earth System Science Interdisciplinary Center/Cooperative Institute for Satellite Earth System Studies Maryland, University of Maryland, College Park, Maryland, and NOAA/NESDIS National Centers for Environmental Information, Silver Spring, Maryland
Mitchum, Gary T., College of Marine Science, University of South Florida, St. Petersburg, Florida
Moat, Ben I., National Oceanography Centre, United Kingdom
Nerem, R. Steven, Colorado Center for Astrodynamics Research, Cooperative Institute for Research in Environmental Sciences, University of Colorado Boulder, Boulder, Colorado
Notz, Dirk, Center for Earth System Research and Sustainability (CEN), Universität Hamburg and Max Planck Institute for Meteorology, Hamburg, Germany
Perez, Renellys C., NOAA/OAR Atlantic Oceanographic and Meteorological Laboratory, Miami, Florida
Purkey, Sarah G., Scripps Institution of Oceanography, University of California San Diego, La Jolla, California
Rayner, Darren, National Oceanography Centre, Southampton, United Kingdom
Reagan, James, NOAA/NESDIS National Centers for Environmental Information, Silver Spring, Maryland
Schmid, Claudia, NOAA/OAR Atlantic Oceanographic and Meteorological Laboratory, Miami, Florida
Siegel, David A., University of California–Santa Barbara, Santa Barbara, California
Smeed, David A., National Oceanography Centre, United Kingdom
Stackhouse, Paul W., NASA Langley Research Center, Hampton, Virginia
Sweet, William, NOAA/NOS Center for Operational Oceanographic Products and Services, Silver Spring, Maryland
Thompson, Philip R., Cooperative Institute for Marine and Atmospheric Research, University of Hawaii, Honolulu, Hawaii
Volkov, Denis L., Cooperative Institute for Marine and Atmospheric Studies, University of Miami, and NOAA/OAR Atlantic Oceanographic and Meteorological Laboratory, Miami, Florida
Wanninkhof, Rik, NOAA/OAR Atlantic Oceanographic and Meteorological Laboratory, Miami, Florida
Weller, Robert A., Woods Hole Oceanographic Institution, Woods Hole, Massachusetts
Wen, Caihong, NOAA/NWS NCEP Climate Prediction Center, College Park, Maryland
Westberry, Toby K., Oregon State University, Corvallis, Oregon
Widlansky, Matthew J., Cooperative Institute for Marine and Atmospheric Research, University of Hawaii, Honolulu, Hawaii
Willis, Josh K., Jet Propulsion Laboratory, California Institute of Technology, Pasadena, California
Yu, Lisan, Woods Hole Oceanographic Institution, Woods Hole, Massachusetts
Zhang, Huai-Min, NOAA/NESDIS National Centers for Environmental Information, Asheville, North Carolina

Editorial and Production Team

Allen, Jessicca, Graphics Support, Cooperative Institute for Satellite Earth System Studies, North Carolina State University, Asheville, North Carolina

Hammer, Gregory, Content Team Lead, Communications and Outreach, NOAA/NESDIS National Centers for Environmental Information, Asheville, North Carolina

Love-Brotak, S. Elizabeth, Lead Graphics Production, NOAA/NESDIS National Centers for Environmental Information, Asheville, North Carolina

Misch, Deborah J., Graphics Support, Innovative Consulting and Management Services, LLC, NOAA/NESDIS National Centers for Environmental Information, Asheville, North Carolina

Ohlmann, Laura, Technical Editor, Innovative Consulting and Management Services, LLC, NOAA/NESDIS National Centers for Environmental Information, Asheville, North Carolina

Riddle, Deborah B., Graphics Support, NOAA/NESDIS National Centers for Environmental Information, Asheville, North Carolina

Veasey, Sara W., Visual Communications Team Lead, Communications and Outreach, NOAA/NESDIS National Centers for Environmental Information, Asheville, North Carolina

3. Table of Contents

*Please refer to Chapter 8 (Relevant datasets and sources) for a list of all climate variables and datasets used in this chapter for analyses, along with their websites for more information and access to the data.

3. GLOBAL OCEANS

G. C. Johnson and R. Lumpkin, Eds.

a. Overview—G. C. Johnson and R. Lumpkin

Patterns of variability in ocean properties are often closely related to large-scale climate pattern indices, and 2021 is no exception. The year 2021 started and ended with La Niña conditions, charmingly dubbed a "double-dip" La Niña. Hence, stronger-than-normal easterly trade winds in the tropical south Pacific drove westward surface current anomalies in the equatorial Pacific; reduced sea surface temperature (SST) and upper ocean heat content in the eastern tropical Pacific; increased sea level, upper ocean heat content, and salinity in the western tropical Pacific; resulted in a rim of anomalously high chlorophyll-*a* (Chl*a*) on the poleward and westward edges of the anomalously cold SST wedge in the eastern equatorial Pacific; and increased precipitation over the Maritime Continent.

The Pacific decadal oscillation remained strongly in a negative phase in 2021, with negative SST and upper ocean heat content anomalies around the eastern and equatorial edges of the North Pacific and positive anomalies in the center associated with low Chl*a* anomalies. The South Pacific exhibited similar patterns. Fresh anomalies in the northeastern Pacific shifted towards the west coast of North America.

The Indian Ocean dipole (IOD) was weakly negative in 2021, with small positive SST anomalies in the east and nearly-average anomalies in the west. Nonetheless, upper ocean heat content was anomalously high in the west and lower in the east, with anomalously high freshwater flux and low sea surface salinities (SSS) in the east, and the opposite pattern in the west, as might be expected during a negative phase of that climate index.

In the Atlantic, the only substantial cold anomaly in SST and upper ocean heat content persisted east of Greenland in 2021, where SSS was also low, all despite the weak winds and strong surface heat flux anomalies into the ocean expected during a negative phase of the North Atlantic Oscillation. These anomalies held throughout much of 2021. An Atlantic and Benguela Niño were both evident, with above-average SST anomalies in the eastern equatorial Atlantic and the west coast of southern Africa. Over much of the rest of the Atlantic, SSTs, upper ocean heat content, and sea level anomalies were above average.

Anthropogenic climate change involves long-term trends, as this year's chapter sidebars emphasize. The sidebars relate some of the latest IPCC ocean-related assessments (including carbon, the section on which is taking a hiatus from our report this year). This chapter estimates that SST increased at a rate of 0.16–0.19°C decade^{-1} from 2000 to 2021, 0–2000-m ocean heat content warmed by 0.57–0.73 W m^{-2} (applied over Earth's surface area) from 1993 to 2021, and global mean sea level increased at a rate of 3.4 ± 0.4 mm yr^{-1} from 1993 to 2021. Global mean SST, which is more subject to interannual variations than ocean heat content and sea level, with values typically reduced during La Niña, was ~0.1°C lower in 2021 than in 2020. However, from 2020 to 2021, annual average ocean heat content from 0 to 2000 dbar increased at a rate of ~0.95 W m^{-2}, and global sea level increased by ~4.9 mm. Both were the highest on record in 2021, and with year-on-year increases substantially exceeding their trend rates of recent decades. A haiku form summary follows:

Ocean climate change,
varies with La Niña, yet,
warming trends are clear.

b. Sea surface temperatures—B. Huang, Z.-Z. Hu, J. J. Kennedy, and H.-M. Zhang

Sea surface temperature (SST) changes and their uncertainties are assessed over the global oceans including seas and large lakes in 2021 using three updated SST products: the Extended Reconstruction Sea-Surface Temperature (ERSSTv5; Huang et al. 2017, 2020), U.K. Met Office Hadley Centre SST (HadSST.4.0.1.0; Kennedy et al. 2019), and Daily Optimum Interpolation SST (DOISST v2.1; Huang et al. 2021a). SST anomalies (SSTAs) are calculated relative to their 1991–2020 baseline period climatologies. The magnitudes of SSTAs are compared against SST standard deviations (std. dev.) for 1991–2020.

Over the global oceans, ERSSTv5 analysis shows that average SSTA decreased from +0.41° ± 0.02°C in 2019 and +0.39° ± 0.01°C in 2020, to +0.29° ± 0.01°C in 2021, due to continued La Niña conditions in the tropical Pacific (detailed later in this section). Here, the uncertainty is estimated by a Student's t-test using a 500-member ensemble based on ERSSTv5 with randomly drawn parameter values within reasonable ranges in the SST reconstructions (Huang et al. 2015, 2020).

Annually averaged SSTAs in 2021 (Fig. 3.1a) have a pattern typical of La Niña in the Pacific: SSTAs were between +0.2°C and +1.0°C in the western North Pacific and western South Pacific and between −0.2°C and −0.5°C in the tropical Pacific east of 165°E, and the eastern South Pacific south of 45°S. SSTAs were between +0.2°C and +1.0°C in most of the North Atlantic and between +0.2°C and +0.5°C in the tropical and South Atlantic. SSTAs were weak (within ±0.2°C) in the Indian Ocean and the coastal Arctic.

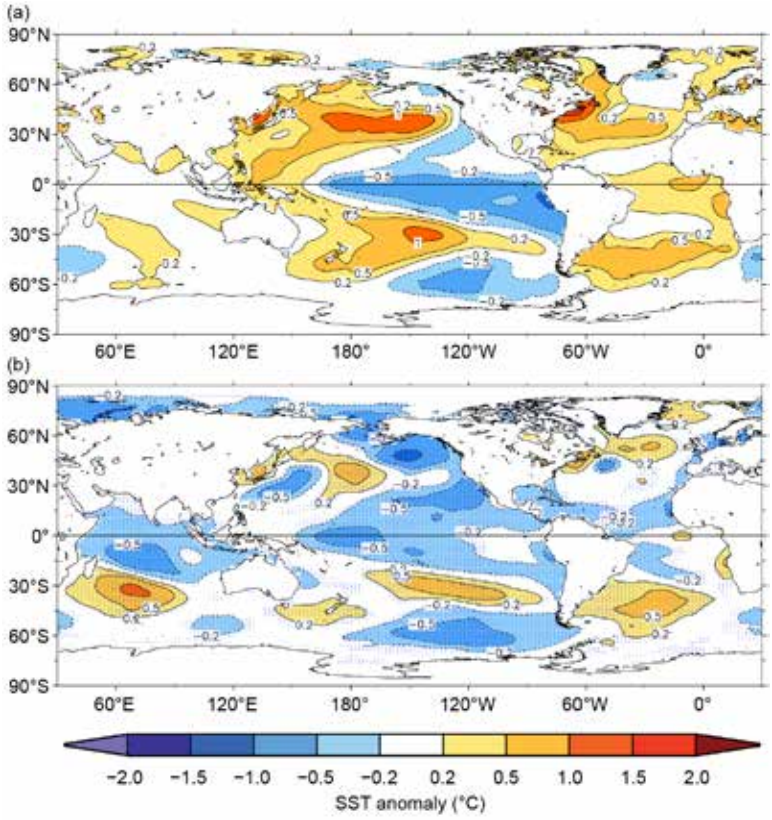

Fig. 3.1. (a) Annually-averaged SSTAs in 2021 and (b) difference of annually-averaged SSTAs between 2021 and 2020. Values (°C) are relative to 1991–2020 climatology and the SSTA difference is significant at 95% confidence in stippled areas.

Averaged SSTs in 2021 compared with 2020 values (Fig. 3.1b) decreased in most of the global oceans by −0.2°C to −0.5°C, except for localized increases in the southern Indian Ocean near 30°S, the central North Pacific near 35°N and 180°, the central South Pacific near 30°S, the South Atlantic near 45°S, and the North Atlantic north of 45°N.

Cooling in the tropical Pacific (Fig. 3.1b) is associated with the evolution of a sustained La Niña, which weakened from November 2020 to May 2021, then reformed in July 2021, and strengthened through the end of the year (Li et al. 2022). The negative SSTAs along the west coast of North America and large positive SSTAs in the central and western North Pacific (Fig. 3.1a) are consistent with the negative phase of the Pacific decadal oscillation (PDO; Mantua and Hare 2002). The PDO index became more negative between 2020 and 2021. The Indian Ocean dipole (IOD) index (Saji et al. 1999), which is correlated with the east–west SSTA gradient in the Indian Ocean, was weakly

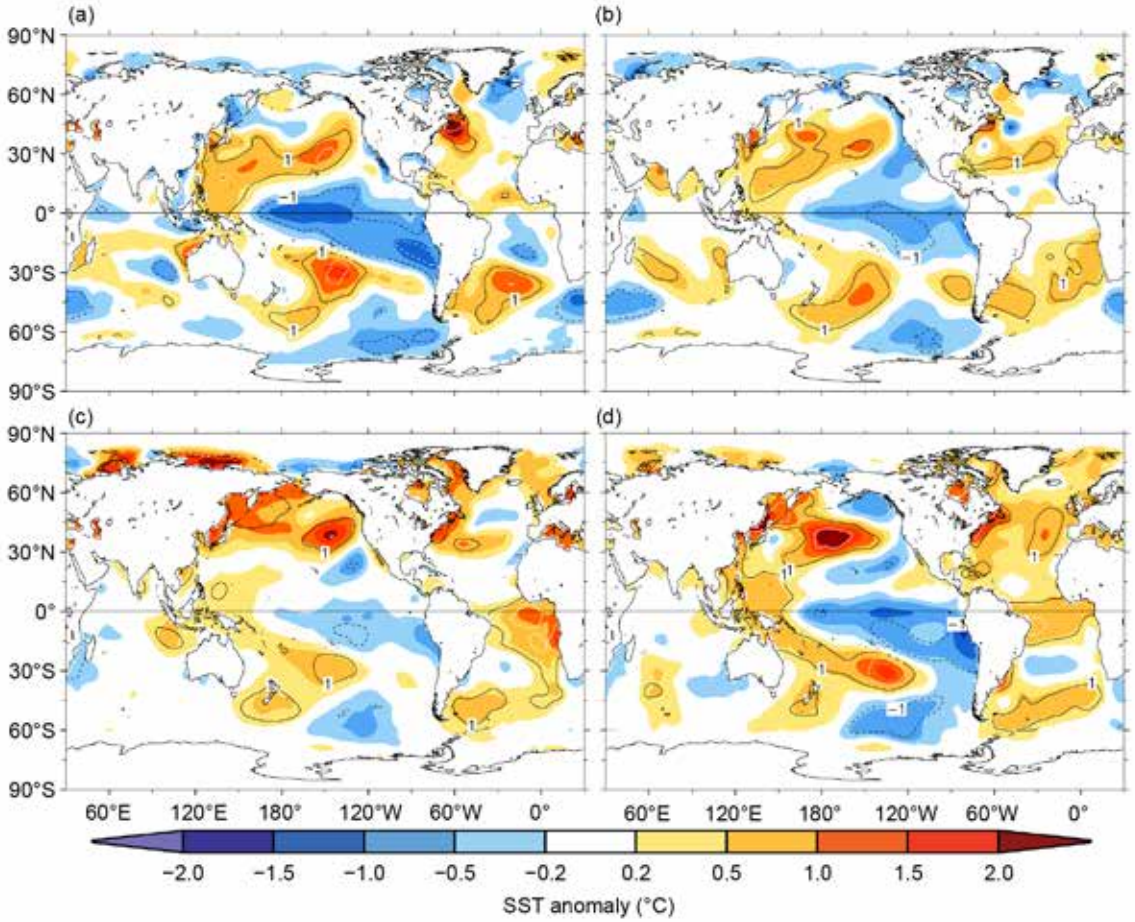

Fig. 3.2. Seasonally-averaged SSTAs of ERSSTv5 (°C, shading) for (a) Dec 2020–Feb 2021, (b) Mar–May 2021, (c) Jun–Aug 2021, and (d) Sep–Nov 2021. Normalized seasonal mean SSTAs relative to seasonal mean standard deviations over 1991–2020 are indicated by contours of –2 (dashed white), –1 (dashed black), 1 (solid black), and 2 (solid white).

negative, but near-neutral (within ±0.5°C) in 2021. The Atlantic Niño index (ATL3; Zebiak 1993), which was associated with the evolution of an Atlantic Niño represented by the positive SSTA in the central-eastern tropical Atlantic in JJA and SON (Figs. 3.2c,d). There was also a substantial positive SSTA off the west coast of southern Africa in JJA, indicating a substantial Benguela Niño (Fig. 3.2c). The overall pattern of SSTAs in the four seasons of 2021 (Fig. 3.2) is similarly reflective of the sustained La Niña and close to that of annually-averaged SSTA in Fig. 3.1. The negative SSTAs in the central-eastern tropical Pacific were strong (–1.0°C to –1.5°C; 1 to 2 std. dev. below average) in DJF and SON, but weaker in JJA. The positive SSTAs in the North and South Pacific were strong (+1.0°C to +1.5°C; 1 to 2 std. dev. above average) in DJF and SON but weaker in JJA. These seasonal SST patterns are directly associated with the weakening La Niña in the first half of 2021 and the emerging second year La Niña in the latter half of 2021, a typical double-dip La Niña event (Okumura and Deser 2010; Hu et al. 2014).

The large positive SSTAs resulted in a series of marine heatwaves in the past few years (Oliver et al. 2017; Perkins-Kirkpatrick et al. 2019; Babcock et al. 2019; Huang et al. 2021b). In 2021, marine heatwaves were observed in the North Pacific in JJA, the regions of the Maritime Continent in JJA and SON, the western boundary of the North Atlantic in JJA, and the Arctic coast of Eurasia in JJA (see section 2b4 for more information on global marine heatwaves).

Long-term warming of global ocean SSTs since the 1950s is clear. The averaged SST reached its record high in 2016 (SSTA of +0.44°C; Figs. 3.3a,b) and decreased slightly after 2016. The averaged SSTAs were +0.39°C in 2020 and +0.29°C in 2021. The linear trend of globally annually-averaged ERSSTv5 SSTAs is 0.10° ± 0.01°C decade^{-1} over 1950–2021 (Table 3.1). The warming remained largest in the tropical Indian Ocean (Fig. 3.3e; 0.14° ± 0.02°C decade^{-1}) and smallest in the North Pacific

(Fig. 3.3d; 0.09° ± 0.04°C decade^{-1}). In contrast, the warming trend was high in the North Pacific (0.36° ± 0.13°C) and low in the tropical Pacific (0.14° ± 0.16°C) in the more recent period (2000–21).

Variations of SSTAs in the North Atlantic (Fig. 3.3f) are evident at interannual and interdecadal time scales and in long-term trends (Li et al. 2020). The interdecadal component is mainly

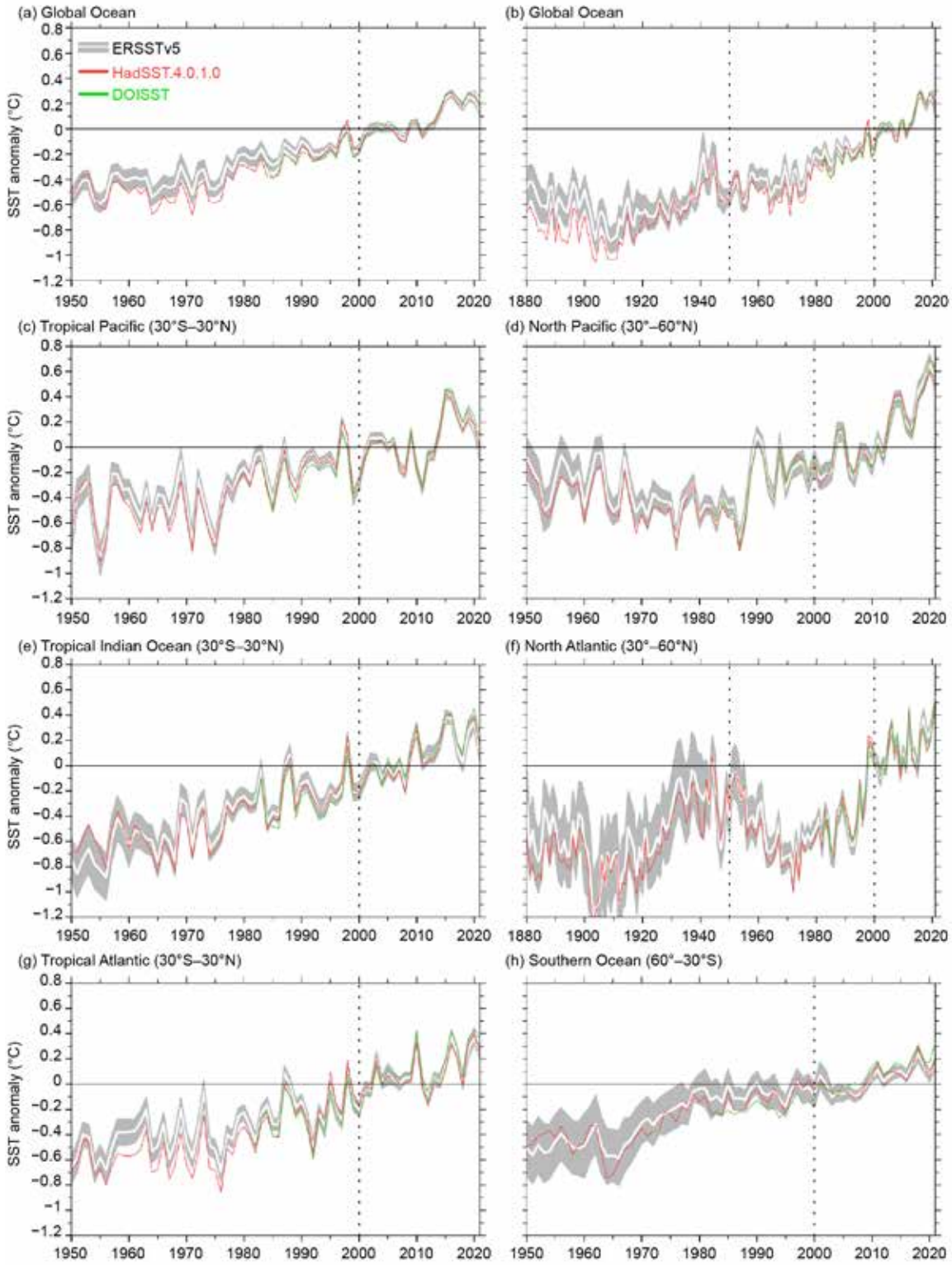

Fig. 3.3. Annually-averaged SSTAs (°C) of ERSSTv5 (solid white) and 2 std. dev. (gray shading) of ERSSTv5, SSTAs of HadSST.4.0.1.0 (solid red), and SSTAs of DOISST v2.1 (solid green) for 1950–2021 except for (b,f). (a) Global, (b) global for 1880–2021, (c) tropical Pacific, (d) North Pacific, (e) tropical Indian, (f) North Atlantic for 1880–2021, (g) tropical Atlantic, and (h) Southern Oceans. The 2 std. dev. envelope was derived from a 500-member ensemble analysis based on ERSSTv5 (Huang et al. 2020) and centered to SSTAs of ERSSTv5. The years 2000 and 1950 in (b) and (f) are indicated by vertical black dotted lines.

Table 3.1. Linear trends (°C decade^{-1}) of annually and regionally averaged SSTAs from ERSSTv5, HadSST4.0.1.0, and DOISST v2.1. Uncertainties at 95% confidence level are estimated accounting for the effective degrees of freedom estimated using lag-1 autocorrelations of annually-averaged SST time series.

Product	Region	2000–2021 (°C decade^{-1})	1950–2021 (°C decade^{-1})
HadSST.4.0.1.0	Global	0.175 ± 0.067	0.117 ± 0.018
DOISST v2.1	Global	0.190 ± 0.057	N/A
ERSSTv5	Global	0.158 ± 0.065	0.102 ± 0.013
ERSSTv5	Tropical Pacific (30°S–30°N)	0.141 ± 0.163	0.099 ± 0.026
ERSSTv5	North Pacific (30°–60°N)	0.364 ± 0.127	0.086 ± 0.040
ERSSTv5	Tropical Indian Ocean (30°S–30°N)	0.184 ± 0.083	0.141 ± 0.017
ERSSTv5	North Atlantic (30°–60°N)	0.158 ± 0.088	0.115 ± 0.046
ERSSTv5	Tropical Atlantic (30°S–30°N)	0.151 ± 0.084	0.112 ± 0.020
ERSSTv5	Southern Ocean (30°–60°S)	0.117 ± 0.053	0.098 ± 0.015

associated with the Atlantic Multidecadal Variability (AMV; Schlesinger and Ramankutty 1994). The AMV may have in turn resulted from some internal and external factors such as aerosol emissions and variations in the strength of the Atlantic meridional overturning circulation (Wang and Yang 2017; Zhang et al. 2019). In the North Atlantic, there were warm periods in the AMV from the 1930s to the 1950s and from the late 1990s to the 2010s, and cold periods before the 1930s and from the 1960s to the early 1990s (Li et al. 2020). In the North Pacific (Fig. 3.3d), SSTAs decreased from the 1960s to the late 1980s, followed by an increase from the later 1980s to the 2010s.

ERSSTv5 SSTAs were compared with those from HadSST.4.0.1.0 and DOISST v2.1. All datasets were annually averaged and interpolated to a 2° × 2° grid for comparison purposes. Departures of DOISST v2.1 and HadSST.4.0.1.0 annual anomalies from those of ERSSTv5 are largely within ±2 std. dev. (gray shading in Fig. 3.3) except in the 1960s–1970s and before the 1910s. The ±2 std. dev. envelope was derived from a 500-member ensemble analysis based on ERSSTv5 (Huang et al. 2020) and centered on SSTAs of ERSSTv5. In the 2000s–2010s, SSTAs were slightly higher in DOISST v2.1 than in ERSSTv5 in the southern, tropical Atlantic, tropical Indian, and tropical Pacific Oceans. As a result, SST trends were slightly higher in DOISST v2.1 over 2000–21 than in ERSSTv5. Previous studies (Huang et al. 2015; Kent et al. 2017) have indicated that these SSTA differences are mostly attributable to the differences in bias corrections applied to ship observations in those products and represent structural uncertainty among different SST products (Kennedy 2013).

c. Ocean heat content—G. C. Johnson, J. M. Lyman, T. Boyer, L. Cheng, J. Gilson, S. Katsunari, R. E. Killick, R. Locarnini, A. Mishonov, S. G. Purkey, and J. Reagan

Owing to increases in greenhouse gases in the atmosphere, the oceans have been warming for decades, storing about 91% of the energy gained by Earth's climate system from 1971 to 2018 (IPCC 2021). Ocean thermal expansion from warming accounted for about 50% of the increase in global average sea level during this same period (IPCC 2021). This warming, while surface intensified, has also been observed from 4000 to 6000-m depth in the coldest, densest bottom waters that sink from the surface to the abyss around Antarctica (Purkey and Johnson 2010). Regional climate patterns such as ENSO effect changes in ocean heating through air–sea heat flux and wind-driven thermocline depth variations. The overall warming trend has become increasingly widespread with time (Johnson and Lyman 2020). This trend has increased the frequency and intensity of marine heat waves (Laufkötter et al. 2020), at least relative to a fixed historical base period. Additionally, warmer upper ocean waters can drive stronger hurricanes (Goni et al. 2009). Ocean warming has also been shown to increase melting rates of ice sheet outlet glaciers around Greenland (Castro de la Guardia et al. 2015) and Antarctica (Schmidtko et al. 2014).

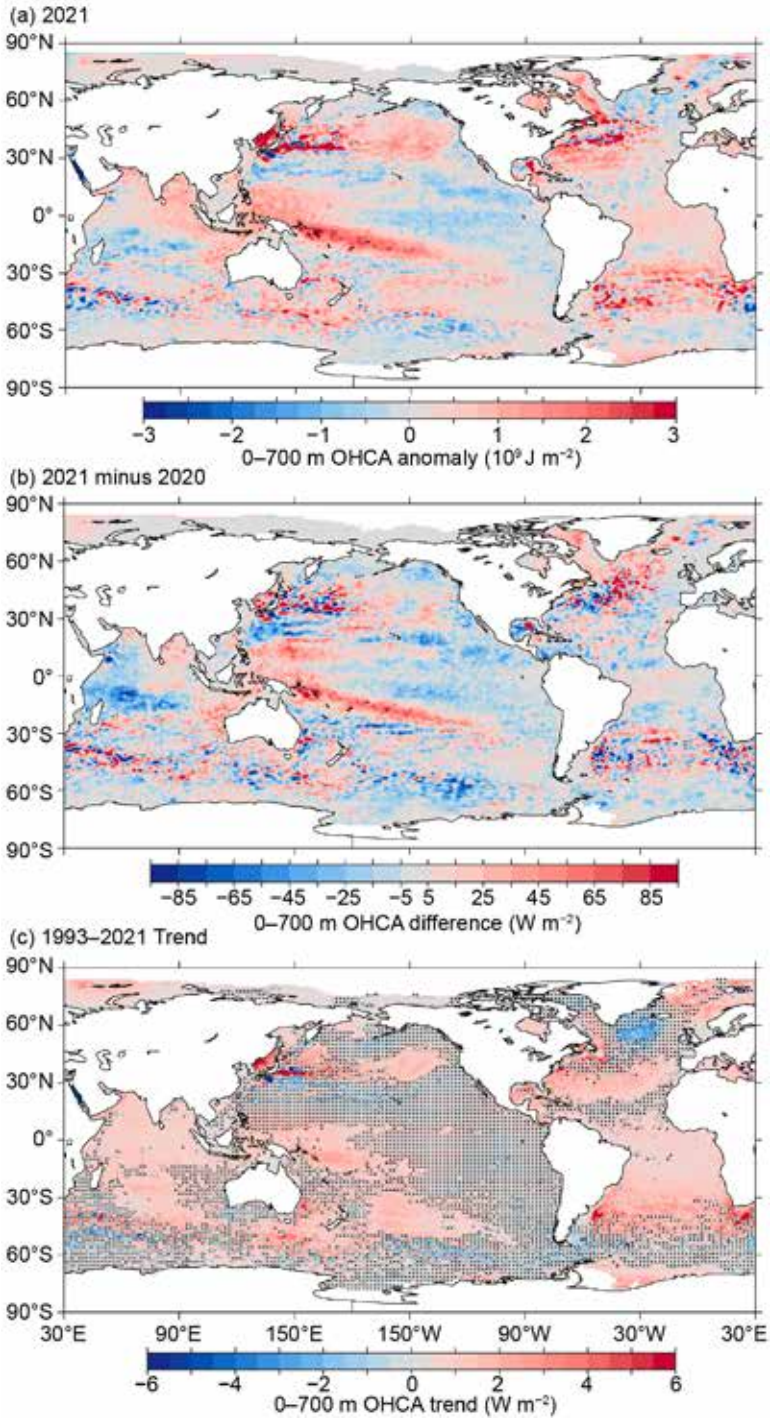

Fig. 3.4. (a) Combined satellite altimeter and in situ ocean temperature data estimate of upper (0–700 m) OHCA (× 10^9 J m^{-2}) for 2021 analyzed following Willis et al. (2004) but using an Argo monthly climatology and displayed relative to a 1993–2021 baseline. (b) 2021 minus 2020 combined estimates of OHCA expressed as a local surface heat flux equivalent (W m^{-2}). For (a) and (b) comparisons, note that 95 W m^{-2} applied over one year results in a 3 × 10^9 J m^{-2} change of OHCA. (c) Linear trend from 1993–2021 of the combined estimates of upper (0–700 m) annual OHCA (W m^{-2}). Areas with statistically insignificant trends are stippled.

Maps of annual (Fig. 3.4) upper (0–700 m) ocean heat content anomaly (OHCA) relative to a 1993–2021 baseline mean are generated from a combination of in situ ocean temperature data and satellite altimetry data following Willis et al. (2004), but using Argo (Riser et al. 2016) data downloaded from an Argo Global Data Assembly Centre in January 2022. Near-global average seasonal temperature anomalies (Fig. 3.5) versus pressure from Argo data (Roemmich and Gilson 2009, updated) since 2004 and in situ global estimates of OHCA (Fig. 3.6) for three pressure layers (0–700 m, 700–2000 m, and 2000–6000 m) from five different research groups are also discussed.

La Niña conditions existed from August 2020 through May 2021, and then again from August 2021 through at least December 2021 (see section 4b). Thus, the 2021 minus 2020 difference of 0–700-m OHCA (Fig. 3.4b) in the tropical Pacific is much like that for 2020 minus 2019 (Johnson et al. 2021), showing a continued increase in the western tropical Pacific and a continued decrease in the central to eastern equatorial Pacific. This pattern exists because anomalously strong easterly trade winds (see Fig. 3.13a) associated with La Niña drive anomalous westward surface currents on the equator (see Figs. 3.18 and 3.19b–d) linked to a shoaling of the equatorial thermocline in the central and eastern equatorial Pacific and a deepening of the western tropical Pacific warm pool, which also shifts warm anomalies from 0–100 dbar down to 100–400 dbar in the global average (Fig. 3.5a). As a result of these prolonged La Niña conditions, the 2021 upper ocean heat content anomalies (Fig. 3.4a) in the equatorial Pacific are negative in the east and positive in the west, with a remarkable warm band extending east-southeastward from about 5°S, 150°E to 25°S, 120°W. Outside of the tropics, higher 2021 minus 2020 differences exist in the centers of the North and South Pacific basins, with some lower values in the eastern portions of the basins consistent with a continued intensified negative phase of

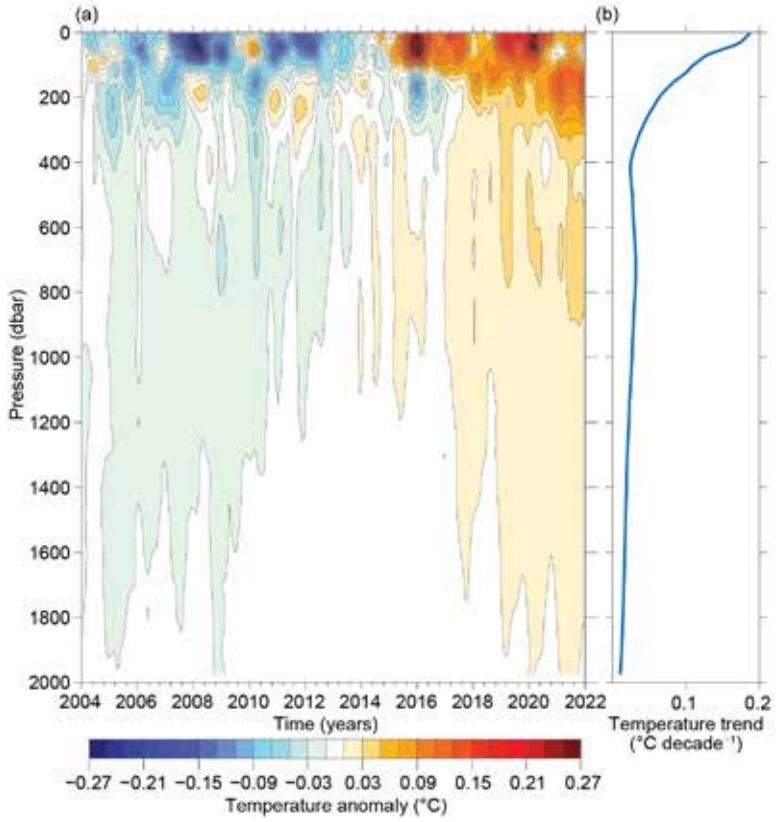

Fig. 3.5. (a) Near-global (65°S–80°N, excluding continental shelves, the Indonesian seas, and the Sea of Okhostk) average monthly ocean temperature anomalies (°C; updated from Roemmich and Gilson [2009]) relative to record-length average monthly values, smoothed with a 5-month Hanning filter and contoured at odd 0.02°C intervals (see color bar) vs. pressure and time. (b) Linear trend of temperature anomalies over time for the length of the record in (a) plotted vs. pressure in °C decade^{-1} (blue line).

the Pacific decadal oscillation index in 2021 (section 3b). The center of the Pacific sector of the Southern Ocean cooled from 2020 to 2021. The Kuroshio extension was anomalously warm in 2021, consistent with a northward shift of that current (see Fig. 3.18), as was the center of the North Pacific basin.

In the Indian Ocean, the 2021 minus 2020 difference of 0–700-m OHCA (Fig. 3.4b) exhibits decreases from about 15°N to 15°S in the western third of the basin, extending into the central third in a band from about 5°S to 15°S. Much of the rest of the basin warmed in 2021 relative to 2020. These changes were consistent with a weakly negative phase of the Indian Ocean dipole index for much of 2021. Upper OHCA values for 2021 were above the 1993–2021 mean in much of the Indian Ocean (Fig. 3.4a), but a band of values below the mean was evident in the western two-thirds of the basin from about 5°S to 15°S.

The 2021 minus 2020 differences of 0–700-m OHCA (Fig. 3.4b) in the Atlantic Ocean are positive in the Labrador Sea, the Irminger Sea, much of the Greenland Sea, and much of the North Atlantic Current. The equatorial Atlantic region also exhibited a warming, but weaker than the northern warming over this time period. The Caribbean Sea and Gulf of Mexico exhibited mostly cooling, except in the region of the Loop Current in the Gulf, which warmed substantially. In 2021, much of the Atlantic Ocean exhibited upper OHCA above the 1993–2021 average (Fig. 3.4a) with the main exception being cooler-than-average conditions southeast of Greenland and in the center of the Greenland-Iceland-Norwegian Seas. The western North Atlantic and southern portions of the subtropical South Atlantic warm anomalies were especially large in 2021.

As expected, the large-scale statistically significant (Fig. 3.4c) regional patterns in the 1993–2021 local linear trends of upper OHCA were quite similar to those from 1993–2020 (Johnson et al. 2021) and earlier reports. Warming trends that were statistically significantly greater than zero occupy 49% of the global ocean surface area, including much of the Indian Ocean and South Atlantic Ocean, the subtropical North Atlantic, the center of the North Pacific, and the western South Pacific. The western boundary current extensions all exhibited strong warming trends, which may be attributed to their intensification and poleward shift under greenhouse gas warming (Wu et al. 2012; Yang et al. 2016). Statistically significant cooling trends occupied only 3% of the ocean area, with the most prominent region being southeast of Greenland in the North Atlantic, linked to a decrease in the Atlantic meridional overturning circulation (AMOC; Dima and Lohmann 2010; Caesar et al. 2018) as well as aerosol-shortwave-cloud feedbacks (Josey et al. 2018). In general, the longer the period over which these trends are estimated, the more of the ocean surface area warms and the less of it cools at statistically significant rates (Johnson and Lyman 2020).

Near-global average seasonal temperature anomalies (Fig. 3.5a) from the start of 2004 through the end of 2021 exhibit a clear surface-intensified, record-length warming trend (Fig. 3.5b) that approaches +0.2°C decade^{-1} at the surface, matching well with SST trends from 2001 to 2021 (section 3b). This trend generally decreases with increasing pressure (depth), but is positive from the surface to the 2000-dbar target maximum sampling pressure of Core Argo. The reduction of warm anomalies during 2020 and 2021 in the upper 100 dbar, with increases in warming from 100 to 400 dbar, is consistent with the presence of La Niña conditions in 2020 and 2021. The opposite pattern is evident during El Niño years (e.g., 2009/10, 2015/16, and 2018/19).

As noted in previous reports, the analysis is extended back in time from the Argo period to 1993 and expanded to examine greater depths, using sparser, more heterogeneous historical data collected mostly from ships (e.g., Abraham et al. 2013). The different estimates of annual globally integrated 0–700-m OHCA (Fig. 3.6a) all reveal a large increase since 1993, with all of the five analyses reporting 2021 as a record high. All five of the globally integrated 700–2000-m OCHA annual analyses (Fig. 3.6b) also report 2021 as a record high, and the long-term warming trend in this layer is also clear. The water column from 0–700 m and 700–2000 m gained 10.2 (±1.6) and 5.1 (±1.1) ZJ, respectively (means and standard deviations given) from 2020 to 2021. Causes of differences among estimates are discussed in Johnson et al. (2015).

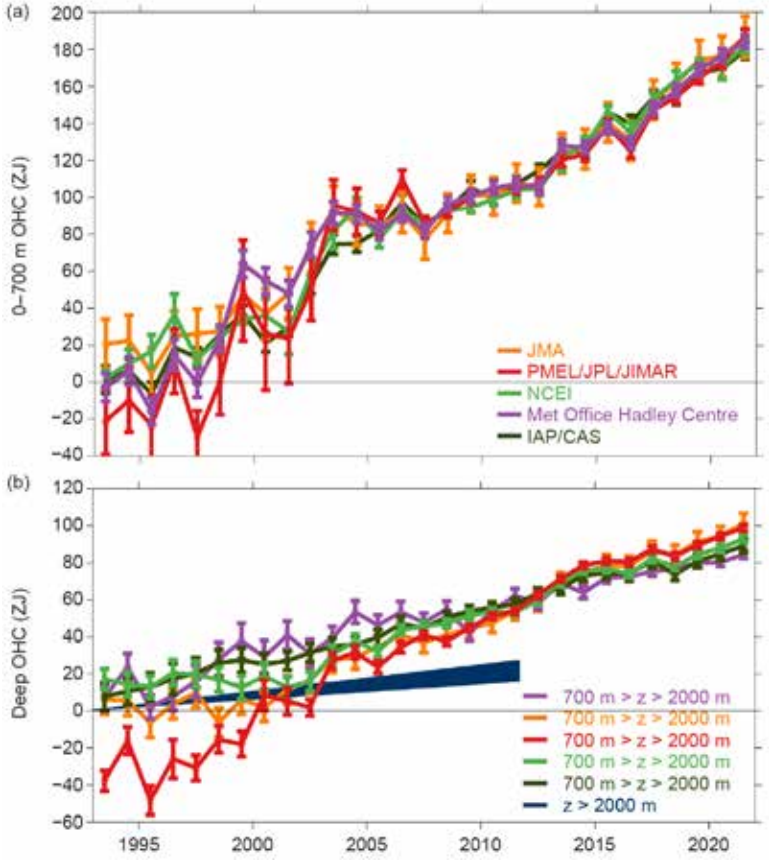

Fig. 3.6. (a) Annual average global integrals of in situ estimates of upper (0–700 m) OHCA (ZJ; 1 ZJ = 10^{21} J) for 1993–2021 with standard errors of the mean. The MRI/JMA estimate is an update of Ishii et al. (2017). The PMEL/JPL/JIMAR estimate is an update and refinement of Lyman and Johnson (2014). The Met Office Hadley Centre estimate is computed from gridded monthly temperature anomalies (relative to 1950–2019) following Palmer et al. (2007) and Good et al. (2013). Both the PMEL and Met Office estimates use Cheng et al. (2014) XBT corrections and Gouretski and Cheng (2020) MBT corrections. The NCEI estimate follows Levitus et al. (2012). The IAP/CAP estimate is reported in Cheng et al. (2021). See Johnson et al. (2014) for details on uncertainties, methods, and datasets. For comparison, all estimates have been individually offset (vertically on the plot), first to their individual 2005–21 means (the best sampled time period), and then to their collective 1993 mean. (b) Annual average global integrals of in situ estimates of intermediate (700–2000 m) OHCA for 1993–2021 with standard errors of the mean, and a long-term trend with one standard error uncertainty shown from September 1992 to January 2012 for deep and abyssal (z > 2000 m) OHCA following Purkey and Johnson (2010) but updated using all repeat hydrographic section data available from https://cchdo.ucsd.edu/ as of Jan 2022

The estimated linear rates of heat gain for each of the five global integral estimates of 0–700-m OHCA from 1993 through 2021 (Fig. 3.6a) range from 0.37 (±0.05) to 0.44 (±0.12) W m^{-2} applied over the surface area of Earth (Table 3.2), rather than the surface area of the ocean, the better to compare to top-of-the-atmosphere energy imbalance (e.g., Loeb et al. 2021). These results are not much different from those in previous reports, although with an increasing record length, trend uncertainties tend to decrease and differences among analyses tend to grow smaller. Linear trends from the 700–2000-m layer over the same time period range from 0.17 (±0.03) to 0.29 (±0.03) W m^{-2}.

Table 3.2. Trends of ocean heat content increase (in W m^{-2} applied over the 5.1 × 10^{14} m^2 surface area of Earth) from six different research groups over three depth ranges (see Fig. 3.6 for details). For the 0–700-m and 700–2000-m depth ranges, estimates cover 1993–2021, with 5%–95% uncertainties based on the residuals taking their temporal correlation into account when estimating degrees of freedom (Von Storch and Zwiers 1999). The 2000–6000-m depth range estimate, an update of Purkey and Johnson (2010), uses data from 1981 to 2021, having a global average start and end date of September 1992 to January 2012, again with 5%–95% uncertainty.

	Global ocean heat content trends (W m^{-2}) for three depth ranges		
Research Group	0–700 m	700–2000 m	2000–6000 m
MRI/JMA	0.37 ± 0.05	0.24 ± 0.04	
PMEL/JPL/JIMAR	0.44 ± 0.12	0.29 ± 0.03	
NCEI	0.39 ± 0.05	0.19 ± 0.05	
Met Office Hadley Centre	0.40 ± 0.08	0.17 ± 0.03	
IAP/CAS	0.41 ± 0.04	0.18 ± 0.01	
Purkey and Johnson			0.07 ± 0.03

Trends in the 0–700-m layer all agree within their 5%–95% confidence intervals. However, as noted in previous reports, the trends in the 700–2000-m layer, which is quite sparsely sampled prior to the start of the Argo era (circa 2005), do not all overlap within uncertainties. Different methods for dealing with under-sampled regions likely cause this disagreement. Using repeat hydrographic section data collected from 1981 to 2021 to update the estimate of Purkey and Johnson (2010) for 2000–6000 m, the linear trend is 0.07 (±0.03) W m^{-2} from September 1992 to January 2012 (these dates are global average times of first and last sampling of the sections). Summing the three layers (despite their slightly different time periods as given above), the full-depth ocean heat gain rate ranges from 0.64 to 0.80 W m^{-2} applied to Earth's entire surface.

d. Salinity—G. C. Johnson, J. Reagan, J. M. Lyman, T. Boyer, C. Schmid, and R. Locarnini

1) INTRODUCTION

Salinity is the mass of dissolved salts per unit mass of sea water, and a nearly conservative tracer. Climatological mean salinity values fall below 28.0 or above 37.4 g kg^{-1} for only 1% of the ocean surface area each. Temperature and salinity are used in tandem to identify water masses and assess water mass mixing throughout the global ocean. Surface mixed layer salinity is modified through evaporation, precipitation, advection, mixing, entrainment, river runoff, and ice freezing or melting (Ren et al. 2011; Yu et al. 2011). Large-scale salinity patterns generally reflect large-scale evaporation and precipitation patterns (Wüst 1936), with precipitation-dominated regions (e.g., the ITCZ) exhibiting low values and evaporation-dominated regions (e.g., subtropics) exhibiting high values. Roughly 86% of global evaporation and 78% of global precipitation occurs over the ocean (Baumgartner and Reichel 1975; Schmitt 1995). Changes in salinity have been used to estimate changes in the hydrological cycle (e.g., Durack et al. 2012; Skliris et al. 2014, 2016).

Seawater density is a function of temperature, salinity, and pressure. Thus, any changes to salinity distributions potentially impact a water parcel's ability to sink. Relatively cold, salty, dense waters that sink at high latitudes comprise the lower limb of the global thermohaline circulation (Gordon 1986; Broecker 1991). Numerical model experiments have shown that the Atlantic meridional overturning circulation (section 3h) generally weakens in response to surface freshening (e.g., Stouffer et al. 2006; Smith and Gregory 2009). It is therefore critical that surface and subsurface salinity changes are monitored since they can act as a proxy for changes in the hydrological cycle and can impact the global ocean circulation.

To investigate interannual changes of subsurface salinity, all available salinity profile data are quality controlled following Boyer et al. (2018) and then used to derive 1° monthly mean gridded salinity anomalies relative to a long-term monthly mean for years 1955–2017 (World Ocean Atlas 2018, WOA18; Zweng et al. 2018) at standard depths from the surface to 2000 m (Boyer et al. 2018). In recent years, the largest source of salinity profiles is the profiling floats of the Argo program (Riser et al. 2016). These data are a mix of real-time (preliminary) and delayed-mode (scientific quality controlled) observations. Hence, the estimates presented here may be subject to instrument biases such as a positive salinity drift identified in a subset of Argo CTDs, and will change after all data are subjected to scientific quality control. The SSS analysis relies on Argo data downloaded in January 2022, with annual anomaly maps relative to a seasonal climatology generated following Johnson and Lyman (2012), as well as monthly maps of bulk (as opposed to skin) SSS data from the Blended Analysis of Surface Salinity (BASS; Xie et al. 2014). BASS blends in situ SSS data with data from the *Aquarius* (Le Vine et al. 2014; mission ended in June 2015), Soil Moisture and Ocean Salinity (SMOS; Font et al. 2013), and the Soil Moisture Active Passive (SMAP; Fore et al. 2016) satellite missions. Despite the larger uncertainties of satellite data relative to Argo data, their higher spatial and temporal sampling allows higher spatial and temporal resolution maps than are possible using in situ data alone at present. All salinity values used in this section are reported as observed, on the dimensionless Practical Salinity Scale-78 (PSS-78; Fofonoff and Lewis 1979).

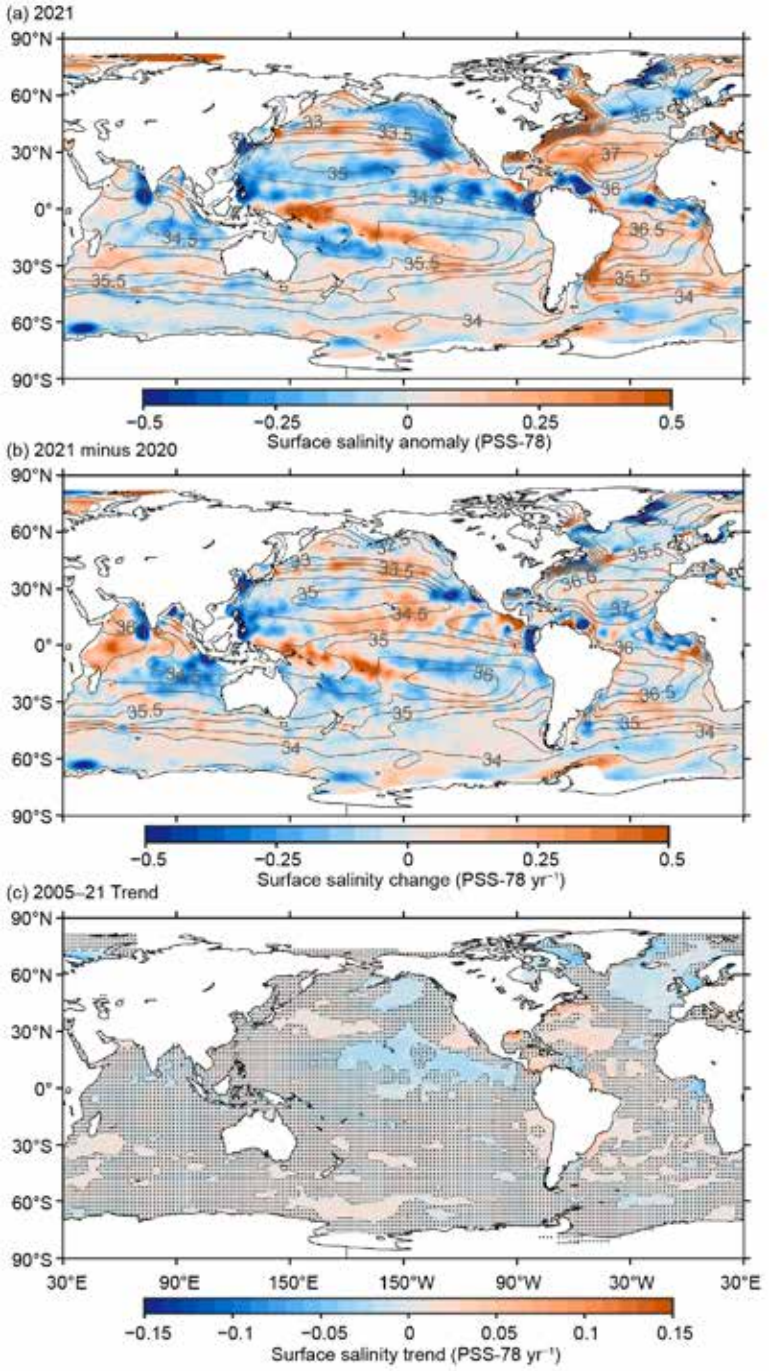

Fig. 3.7. (a) Map of the 2021 annual surface salinity anomaly (colors, PSS-78) with respect to monthly climatological 1955–2012 salinity fields from WOA13v2 (yearly average, gray contours at 0.5 intervals, PSS-78). (b) Difference of 2021 and 2020 surface salinity maps (colors, PSS-78 yr^{-1}). White ocean areas are too data-poor (retaining < 80% of a large-scale signal) to map. (c) Map of local linear trends estimated from annual surface salinity anomalies for 2005–21 (colors, PSS-78 yr^{-1}). Areas with statistically insignificant trends at 5%–95% confidence are stippled. All maps are made using Argo data.

2) SEA SURFACE SALINITY—

G. C. Johnson and J. M. Lyman

As noted in previous reports, since salinity has no direct feedback to the atmosphere, large-scale SSS anomalies can be quite persistent. (In contrast, SST anomalies are often damped by air–sea heat exchange.) For instance, the large fresh SSS anomaly in 2021 in the northeastern Pacific (Fig. 3.7a) began around 2016 in the central North Pacific (near 40°N between Hawaii and the Aleutian

Islands), shifting slowly eastward and then southward over time (see previous *State of the Climate* reports), in the same direction as the prevailing currents. This upper ocean fresh anomaly increased density stratification, a condition conducive to prolonging and amplifying a marine heatwave in the region that started in 2019 (Scannell et al. 2020), and persisted through much of 2021 (see Figs. 3.2, 3.4a). Elsewhere in the Pacific Ocean, the 2021 fresh SSS anomalies (Fig. 3.7a) observed over much of the ITCZ and SPCZ (South Pacific Convergence Zone) and extending north of Hawaii in the central Pacific began around 2015 (see previous *State of the Climate* reports) but were generally somewhat reduced from previous years in 2021. In contrast, the salty anomalies along and just south of the equator in the western and central Pacific, respectively, strengthened in 2021 (Figs. 3.7a,b), again owing to the westward migration of the eastern edge of the fresh pool with the persistence of La Niña in much of 2021 (section 4b), linked to the anomalous westward currents across the equator in 2021 (Fig. 3.18a) as well as westward shifts in precipitation in the region (Fig. 3.12d).

There was mostly freshening of SSS from 2020 to 2021 in the tropical Atlantic ITCZ, salinification over much of the South Atlantic, and freshening in much of the Labrador Sea and off the east coast of Greenland (Fig. 3.7b). In the Atlantic in 2021, as in many previous years, the relatively fresh regions (the subpolar North Atlantic, subantarctic South Atlantic, under the ITCZ, and off northern Brazil and Venezuela) were fresher than climatology, and the relatively saltier regions (the subtropics) were saltier than climatology (Fig. 3.7a). In 2021 conditions were anomalously salty offshore of the east coast of North America from the Gulf of Mexico to Labrador as well as offshore of much of the South American east coast.

Freshening in the southeastern tropical Indian Ocean and salinification in much of the north and west from 2020 to 2021 (Fig. 3.7b) is consistent with a weak negative Indian Ocean dipole index for much of 2021, with increased precipitation in the southeast and reduced precipitation to the north and west (see Fig. 3.12). A pronounced freshening west of India from 2020 to 2021 left that region fresher than climatology in 2021 (Fig. 3.7a).

As discussed in previous reports, in a warming climate the atmosphere can hold more water, leading to expectations of more evaporation in regions where evaporation is dominant over

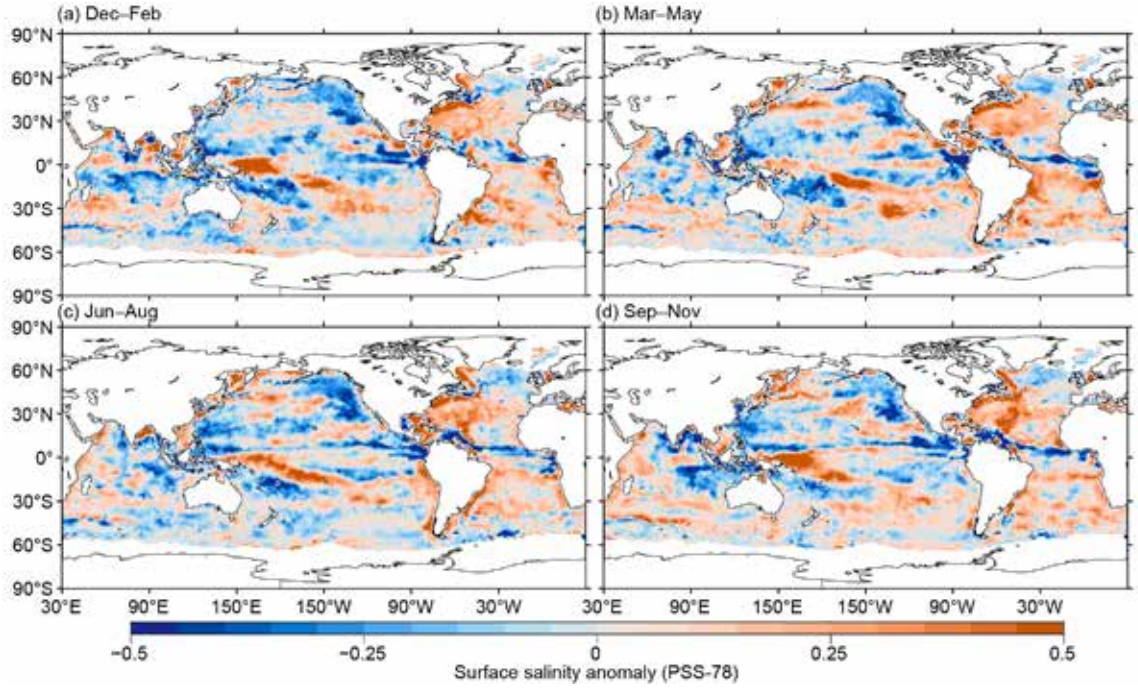

Fig. 3.8. Seasonal maps of SSS anomalies (colors) from monthly blended maps of satellite and in situ salinity data (BASS; Xie et al. 2014) relative to monthly climatological 1955–2012 salinity fields from WOA13v2 for (a) Dec 2020–Feb 2021, (b) Mar–May 2021, (c) Jun–Aug 2021, and (d) Sep–Nov 2021. Areas with maximum monthly errors exceeding 10 PSS-78 are left white.

precipitation and more precipitation where precipitation exceeds evaporation (Held and Soden 2006; Durack and Wijffels 2010). In the ocean this translates roughly to "Salty gets saltier and fresh gets fresher." This pattern has been evident in *State of the Climate* reports going back as far as 2006, the first year of the salinity section. In 2021 this pattern held (Fig. 3.7a), with salty SSS anomalies in most of the subtropical salinity maxima and fresh SSS anomalies in the eastern subpolar North Pacific and North Atlantic, as well as the ITCZs of the Pacific and Atlantic. The 2005–21 SSS trends (Fig. 3.7c) reflect this pattern to some extent as well, with statistically significant (unstippled areas) freshening trends evident in the eastern subpolar North Pacific and North Atlantic, the Pacific ITCZ, and the Gulf of Guinea, as well as statistically significant salty trends in parts of the subtropics in all basins.

In 2021, the seasonal BASS (Xie et al. 2014) SSS anomalies (Fig. 3.8) show the seasonal progressions of many of the features in the annual anomaly map using Argo data alone (Fig. 3.7a), and with higher spatial resolution, albeit with somewhat less accuracy. Iceberg A-68A drifted from the Weddell Sea northward and approached South Georgia Island in late 2020 and had broken up and nearly completely melted by April 2021. It left behind a fresh SSS anomaly near South Georgia Island (54°S, 37°W) in December 2020–February 2021 that drifted slowly eastward during 2021 and was still visible, although diminished somewhat, in September–November 2021 (Fig. 3.8).

3) SUBSURFACE SALINITY—J. Reagan, T. Boyer, C. Schmid, and R. Locarnini

For the second straight year, all monthly basin-averaged salinity anomalies for 0–1000-m depth in the Atlantic were positive in 2021 (Fig. 3.9a). Salinity anomalies > 0.01 reached from 300 to 500 m during 2012–16, but have increased with depth since, reaching 800 m in 2021. Larger salinity

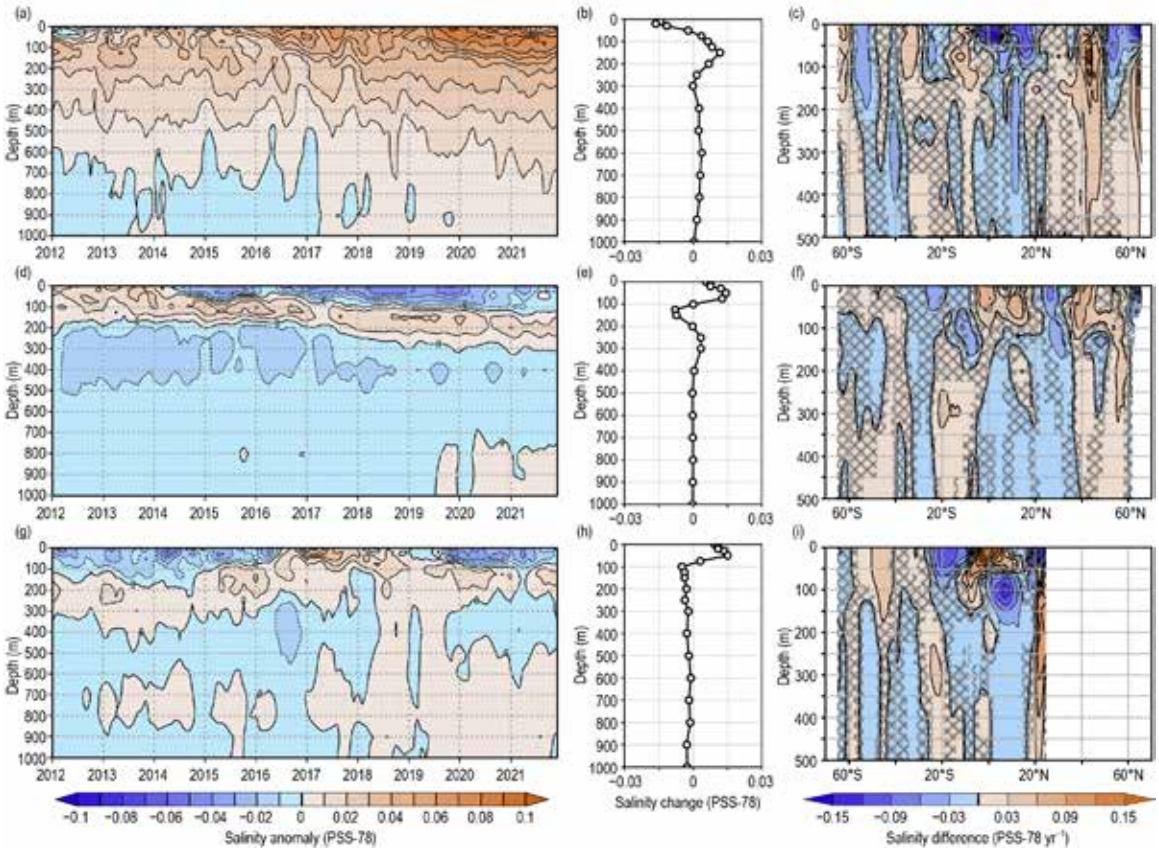

Fig. 3.9. Average monthly salinity anomalies from 0–1000 m for 2012–21 for the (a) Atlantic, (d) Pacific, and (g) Indian Oceans. Change in salinity from 2020 to 2021 for the (b) Atlantic, (e) Pacific, and (h) Indian Oceans. Change in the 0–500 m zonal-average salinity from 2020 to 2021 in the (c) Atlantic, (f) Pacific, and (i) Indian Oceans with areas of statistically insignificant change, defined as < ±1 std. dev. and calculated from all year-to-year changes between 2005 and 2021, stippled in dark gray. Data were smoothed using a 3-month running mean. Anomalies are relative to the long-term (1955–2017) WOA18 monthly salinity climatology (Zweng et al. 2018).

anomalies have followed suit and have also deepened since 2017. This increase is reflected in the 2020 to 2021 Atlantic salinity changes (Fig. 3.9b), with the Atlantic increasing in salinity from 75 to 1000 m. The maximum increase of ~0.013 at 150 m coincides with an increase in zonally-averaged salinity between 2020 and 2021 at 43°N and 65°N (Fig. 3.9c). In contrast to what was seen between 2019 and 2020 (Reagan et al. 2021), the upper 50 m of the Atlantic freshened by ~−0.015 (Fig. 3.9b) from 2020 to 2021, which is largely a result of freshening just north of the equator and north of 50°N (Fig. 3.9c).

The basin-averaged monthly salinity anomalies from 0–1000 m in the Pacific (Fig. 3.9d) have followed a similar pattern since 2015 (see Reagan et al. 2020, 2021). The changes from 2020 to 2021 (Fig. 3.9e) are largely similar to the changes from 2019 to 2020 (Reagan et al. 2021), with increasing salinity in the upper 100 m (max of ~0.015 at 50 m) and freshening from 100 to 200 m (max of ~−0.0075 at 125 m). The near-surface salinification is visible in the 2020 to 2021 zonally-averaged Pacific salinity change (Fig. 3.9f), with increases (> 0.03) confined to the upper 100 m between 5°S and 20°N and between 35°N and 43°N with the tropical region's salinification likely due to a precipitation decrease (Fig. 3.12) associated with transitioning from a neutral (early 2020) to a La Niña phase (late 2020 into 2021) in the Pacific. The freshening from 100 to 200 m (Fig. 3.9e) is primarily associated with the subsurface freshening < ~−0.03 at 10°S and 30°N (Fig. 3.9f).

The 2021 0–1000-m Indian basin-average monthly salinity anomalies look similar to those in 2020 (Fig. 3.9g; Reagan et al. 2021). However, unlike the 2019 to 2020 freshening that took place in the upper 100 m (see Fig. 3.9h in Reagan et al. 2021), there was salinification from 2020 to 2021 in this layer (Fig. 3.9h), which appears to be related to the strong (> 0.06) near-surface equatorial salinification (Figs. 3.7b and 3.9i). On the other hand, for depths 100 to 1000 m, there was very weak (> −0.005) freshening (Fig. 3.9h) from 2020 to 2021.

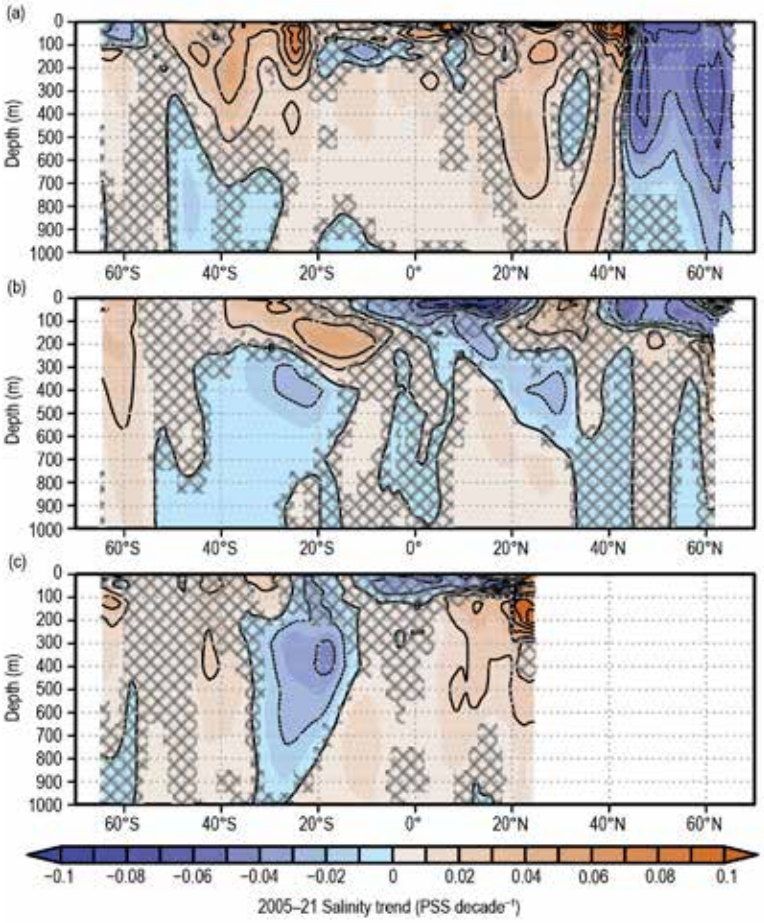

Fig. 3.10. The linear trend of zonally-averaged salinity from 2005 to 2021 over the upper 1000 m for the (a) Atlantic, (b) Pacific, and (c) Indian Oceans. The salinity trend is per decade and computed using least squares regression. Areas that are stippled in dark gray are not significant at the 95% confidence interval. SST differences are significant at 95% level in stippled areas.

Zonally-averaged 2005–21 salinity trends, with 95% confidence intervals, reveal that salinification trends dominate much of the Atlantic south of 45°N (Fig. 3.10a). There is a broad area of salinification (> 0.02 decade^{-1}) from ~50°S to 20°S, extending from the surface to 500 m at 38°S. There are pockets of strong near-surface salinification trends (> 0.08 decade^{-1}) at 7°N, 27°N, and 40°N, with the latter two locations having salinification trends extending down to 750 and 1000 m, respectively. Despite basin-wide salinification trends from 2005 to 2020 (see Fig. 3.10a in Reagan et al. 2021), which are driven by both large-scale and intense small-scale salinification trends between 50°S and 45°N, a freshening trend from 0 to 1000 m in the subpolar North Atlantic between 45°N and 65°N from 2005 to 2021 is observed (Fig. 3.10a). This subpolar North Atlantic freshening may increase stratification and decrease density (Gelderloos et al.

2012), which may affect overflow waters and the deep western boundary current, thus decreasing the Atlantic meridional overturning circulation.

The positive and negative zonally-averaged salinity trends are more randomly distributed in the Pacific than the Atlantic (Fig. 3.10b). Salinification trends (> 0.02 decade^{-1}) are primarily found in the South Pacific centered at 60°S to a depth of 550 m, and at the surface at 30°S extending downward and equatorward to ~300 m at 10°S. Near-surface freshening trends (< −0.06 decade^{-1}) are found between the equator and 20°N, as well as between 45°N and 60°N.

Finally, the Indian Ocean's zonally-averaged salinity trends from 2005 to 2021 primarily involve the subsurface. The only region that experienced a freshening trend is between 200 and 900 m, centered at 18°S and 350 m. Salinification trends dominate much of the subsurface centered at ~65°S, 40°S, and 22°N, with the latter exhibiting trends greater than 0.10 decade^{-1} at 200 m (Fig. 3.10c).

e. Global ocean heat, freshwater, and momentum fluxes—L. Yu, P. W. Stackhouse, J. Garg, C. Wen, and R. A. Weller

The ocean and the atmosphere communicate physically via interfacial exchanges of heat, freshwater, and momentum. Most of the shortwave radiation (SW) absorbed by the ocean's surface is returned to the atmosphere by three processes: longwave radiation (LW), turbulent heat loss by evaporation (latent heat flux, or LH), and by conduction (sensible heat flux, or SH). The residual heat is stored in the warming ocean and transported by the ocean's circulation, forced primarily by the momentum transferred to the ocean by wind stress. Evaporation connects heat and moisture transfers; and the latter, together with precipitation and continental runoff, determines the local surface freshwater flux. Identifying changes in air–sea fluxes is essential to deciphering observed changes in ocean circulation and its transport of heat and salt from the tropics to the poles.

Here we examine air–sea heat fluxes, freshwater fluxes, and wind stress in 2021 and their relationships with ocean surface variables. Anomalies for 2021 are relative to a 2001–15 climatology, which spans from the first full year available, 2001, to 2015, just before the strong El Niño that followed. The net surface heat flux, Q_{net}, is the sum of four terms: SW+LW+LH+SH. The net surface freshwater flux into the ocean (neglecting riverine and glacial fluxes from land) is precipitation (P) minus evaporation (E), or the $P - E$ flux. Wind stress is computed from satellite wind retrievals using the bulk parameterization COARE version 3.5 (Fairall et al. 2003). The production of the global maps of Q_{net}, $P - E$, and wind stress (Figs. 3.11–3.13) and the long-term perspective of the change of the forcing functions (Fig. 3.14) is made possible by integrating multi-group efforts. Ocean surface LH, SH, E and wind stress values are from the Objectively Analyzed air–sea Fluxes (OAFlux) project (Yu and Weller 2007). Surface SW and LW radiative fluxes are from the Clouds and the Earth's Radiant Energy Systems (CERES) Fast Longwave And Shortwave Radiative Fluxes (FLASHFlux) version 4A product (Stackhouse et al. 2006). Global P is derived from the Global Precipitation Climatology Project (GPCP) version 2.3 products (Adler et al. 2018). The CERES Energy Balanced and Filled (EBAF) surface SW and LW version 4.1 products (Loeb et al. 2018; Kato et al. 2018) are used in the time series analysis.

1) SURFACE HEAT FLUXES

The 2021 Q_{net} anomaly pattern (Fig. 3.11a) has predominant positive anomalies (anomalously downward heat input; a warming effect on the ocean) in the equatorial and South Pacific and Indian Oceans. In the North Pacific, positive anomalies occurred along the Kuroshio extension near 35°N, perhaps associated with a northward shift in that current (Fig. 3.18a), resulting in less heat flux out of the ocean (positive anomalous fluxes into the ocean) in the region where the current vacated. In the North Atlantic, positive anomalies occurred at two locations: the Gulf of Mexico and the Sargasso Sea (10°–30°N), and the subpolar gyre including the Labrador and the Irminger Seas (40°–65°N). Negative Q_{net} anomalies (anomalously upward heat release; a cooling

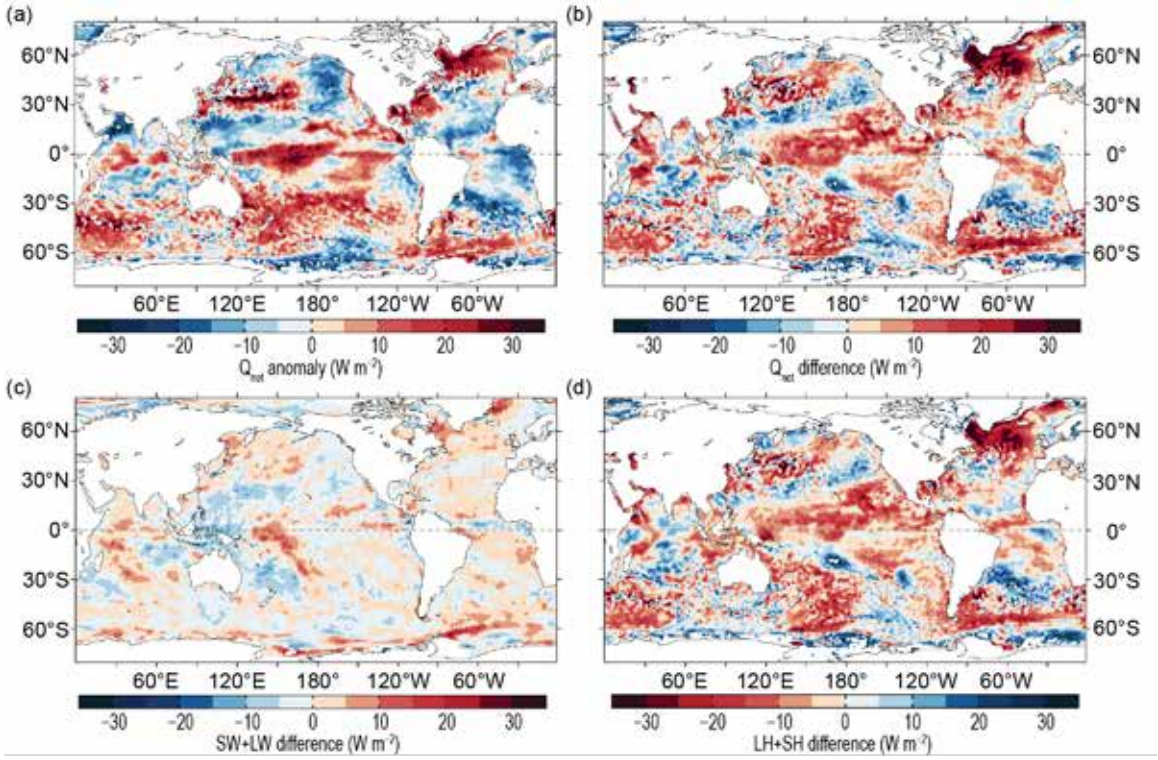

Fig. 3.11. (a) Surface heat flux (Q_{net}) anomalies (W m^{-2}) for 2021 relative to a 2001–15 climatology. Positive values denote ocean heat gain. 2021 minus 2020 difference for (b) Q_{net} and (c) surface radiation (SW+LW), and (d) turbulent heat fluxes (LH+SH), respectively. Positive differences denote more ocean heat gain in 2021 than in 2020, consistent with the reversal of the color scheme in (d). LH+SH are from OAFlux, and SW+LW is the NASA FLASHFlux version 4A.

effect on the ocean) dominated the tropical Atlantic from 30°S to 30°N, and also the subtropical (5°–20°N) and eastern (30°–60°N) North Pacific. The magnitude of maximum positive and negative anomalies exceeded 20 W m^{-2} in some localized bands.

The 2021 minus 2020 Q_{net} differences (Fig. 3.11b) have a spatial structure similar to the 2021 anomalies (Fig. 3.11a) in the extratropical region but different in the tropical ocean. There are more positive Q_{net} 2021 minus 2020 differences in the tropical basins, which are attributable to the reduced LH+SH differences (negative in reddish colors). Here, increased LH+SH (positive anomalies) have a cooling effect (blue colors) on the ocean and conversely, reduced LH+SH (negative anomalies) have a warming effect (red colors). In regions where winds are moderate and less variable, LH+SH heat release generally decreases with decreasing SST and increases with increasing SST. During this double-dip La Niña, LH+SH weakened accordingly associated with negative SSTA in the central and eastern tropical Pacific, resulting in an increase of Q_{net} input to the ocean. In general, SW+LW 2021 minus 2020 differences (Fig. 3.11c) are comparably weaker than LH+SH differences, with maximum magnitude around 10 W m^{-2}. However, SW+LW and LH+SH differences have similar spatial structures over most of the global ocean.

Outside of the tropical ocean, the LH+SH anomalies are most pronounced in the subpolar North Atlantic (40°–65°N), including the Labrador and Irminger Seas, with magnitude reduced by more than 25 W m^{-2}. The subdued turbulent heat release was associated with marked weakening of surface winds (Fig. 3.13b) and surface warming (see Fig. 3.1b) in the region.

2) SURFACE FRESHWATER FLUXES

The spatial structure of the 2021 $P - E$ anomaly field (Fig. 3.12a) has an interesting correlation with the 2021 SSTA pattern (Fig. 3.1a). In the Pacific, the SSTA horseshoe pattern is shaped by a strong negative Pacific decadal oscillation (PDO) phase and a double-dip La Niña, with positive SSTA in the western Pacific and negative SSTA in the central and eastern Pacific. $P - E$ had positive anomalies (green colors in Fig. 3.12; a freshening effect on the ocean surface) in regions

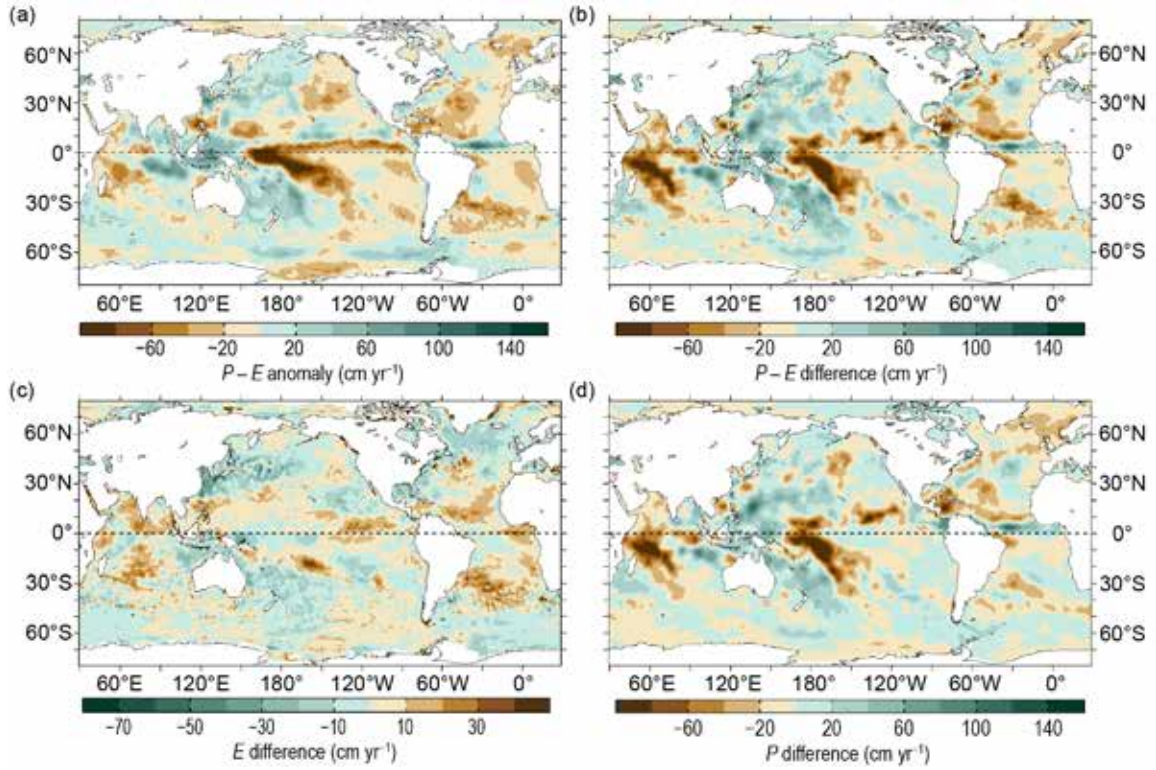

Fig. 3.12. (a) Surface freshwater (*P* – *E*) flux anomalies (cm yr^{-1}) for 2021 relative to a 1988–2015 climatology. 2021 minus 2020 differences for (b) *P* – *E*, (c) evaporation (*E*), and (d) precipitation (*P*). Green colors denote anomalous ocean moisture gain, and browns denote loss, consistent with the reversal of the color scheme in (c). *P* is the GPCP version 2.3rB1 product, and *E* is from OAFlux.

of positive SSTA and negative anomalies (brown colors in Fig. 3.12; a salinification effect on the ocean surface) in regions of negative SSTA. The reduced net freshwater input (> 60 cm yr^{-1}) in the central and eastern equatorial Pacific was caused by the westward retreat of tropical rainfall during La Niña.

The relationship between *P* – *E* and SSTA in the Atlantic Ocean, however, differs from that in the Pacific. The Atlantic Ocean was abnormally warm in 2021 across almost all latitudes except for a limited cool region in the Irminger Sea near 60°N. The positive SSTA pattern corresponds with negative (dry) *P* – *E* anomalies, excluding the equatorial band. The drying condition was caused primarily by the reduction in *P*, leading to a net freshwater deficit of about 20 cm yr^{-1}.

The 2021 minus 2020 *P* – *E* difference pattern (Fig. 3.12b) is similar to the 2021 *P* – *E* anomaly pattern (Fig. 3.12a), with the tropical Indian Ocean being the only region where the differences are substantially larger than anomalies. Bands of reduced *P* – *E* differences (negative anomalies with magnitude greater than 60 cm yr^{-1}) dominated the equatorial and western tropical Indian Ocean. These changes were induced primarily by *P* (Fig. 3.12d) and secondarily by *E* (Fig. 3.12c). These *P* – *E* differences coincided with the bands of increased SW+LW differences (Fig. 3.11c), indicating that SW+LW increased in areas of reduced rainfall when the region was subject to a negative Indian Ocean dipole (IOD) index with predominant negative SSTA.

3) WIND STRESS

The 2021 wind stress anomaly pattern (Fig. 3.13a) is dominated by wind changes at mid- to high latitudes. In the Southern Hemisphere, the westerlies strengthened substantially over the Antarctic Circumpolar Current (ACC) region between 50° and 60°S, featuring positive anomalies across the entire belt with varying magnitudes. The center of the maximum enhancement occurred in the Pacific sector (from the dateline to 80°E), with the anomalies reaching up to 0.05 N m^{-2}, whereas anomalies in the Atlantic and Indian Ocean sectors were 0.03 N m^{-2}. In the North Pacific and North Atlantic Oceans, the midlatitude westerlies became weaker, with negative wind

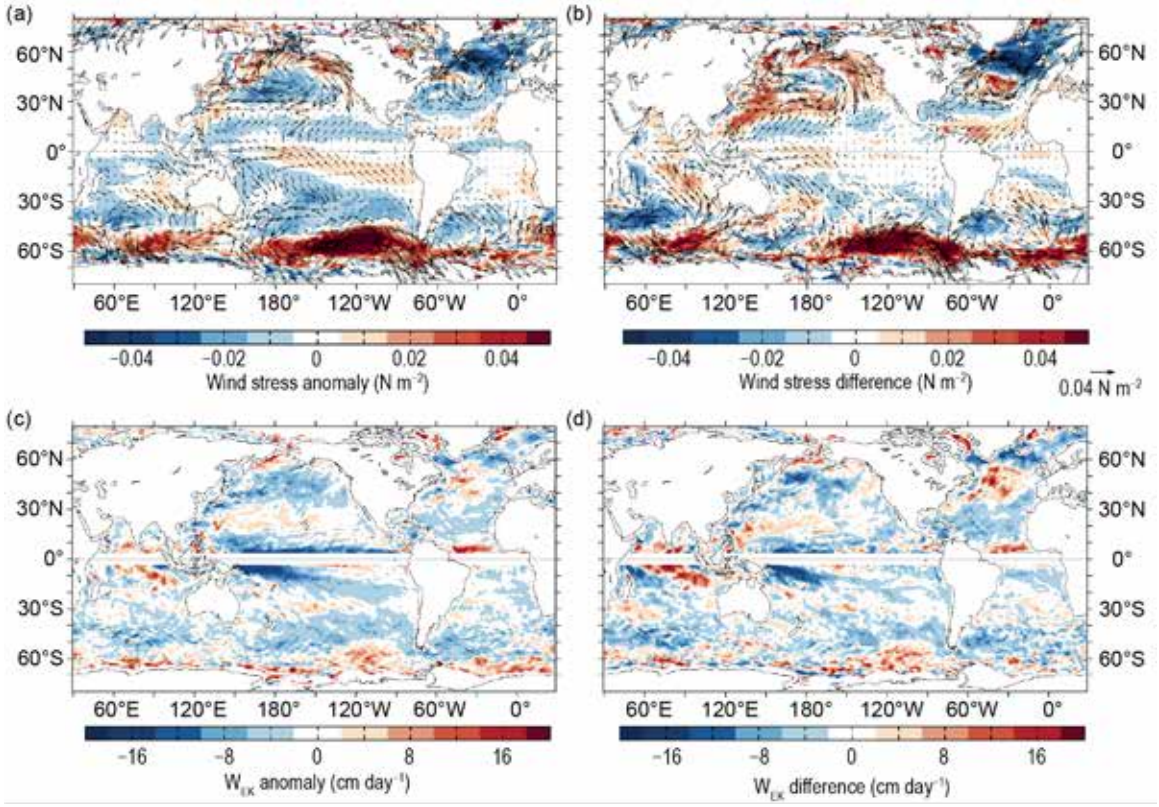

Fig. 3.13. (a) Wind stress magnitude (colors) and vector anomalies (N m^{-2}) for 2021 relative to a 1988–2015 climatology, (b) 2021 minus 2020 differences in wind stress, (c) Ekman vertical velocity (W_{EK}; cm day^{-1}) anomalies for 2021 relative to a 1988–2015 climatology, and (d) 2021 minus 2020 differences in W_{EK}. In (c) and (d), positive values denote upwelling tendency, and negative downwelling tendency. Winds are computed from the OAFlux.

anomalies predominating in the mid- to high latitudes (30°–70°N). The westerlies in the North Pacific weakened in the central basin and strengthened in the peripheral areas. By comparison, the westerlies in the North Atlantic weakened considerably around a slightly strengthened core near 50°N, and the reduction in wind magnitude was particularly pronounced in the northern North Atlantic between 50° and 65°N, with anomalies exceeding −0.05 N m^{-2}. Wind changes in the tropical oceans were small, where northeasterlies decreased slightly and southeasterlies increased slightly in the Pacific. The extratropical wind stress anomaly pattern in 2021 is further amplified in the 2021 minus 2020 wind stress difference map (Fig. 3.13b), most evidently in the North Atlantic and over the southern ACC. The westerlies in the North Pacific were mostly stronger than those in 2020, though weaker than those in 2020 in the center of the basin.

Spatial variations of winds cause divergence and convergence of the Ekman transport, leading to a vertical velocity, termed Ekman pumping (downwelling; directed downward) and suction (upwelling; directed upward) velocity, W_{EK}, at the base of the Ekman layer. $W_{EK} = 1/p\Delta\times(\tau/f)$, where p is the density and f the Coriolis force. The 2021 W_{EK} anomaly pattern (Fig. 3.13c) shows marked downwelling (negative) anomalies in the off-equatorial Pacific and marked upwelling (positive) anomalies in the off-equatorial Indian Ocean with magnitudes exceeding 16 cm yr^{-1} in both regions. These anomalies represent an enhancement of the regional mean conditions. On the other hand, the upwelling (positive) anomalies north of the equatorial Atlantic were a reduction of the typical downwelling condition. Outside of the equatorial zones, W_{EK} anomalies of substantial magnitude are observed at higher latitudes. The strengthened westerlies over the ACC induced larger upwelling (positive) anomalies, further amplifying the typical upper Ekman suction. The weakened westerlies in the North Atlantic produced downwelling anomalies to the north and upwelling anomalies to the south, which weakened the mean conditions. The 2021 W_{EK} 2021 minus 2020 difference pattern (Fig. 3.13d) suggests that there was an enhanced mean upwelling in the southeastern equatorial Indian Ocean during this weakly negative IOD index year,

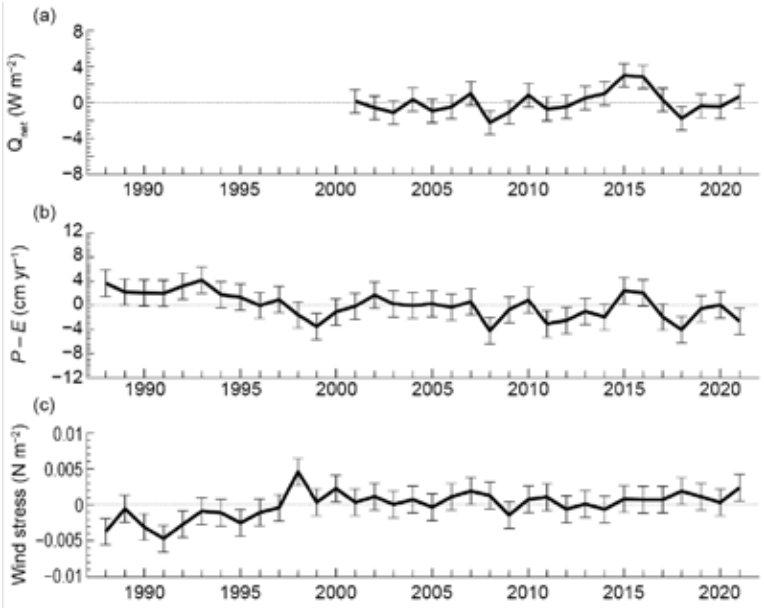

Fig. 3.14. Annual mean time series of global averages of (a) net surface heat flux (Q_{net}; W m^{-2}) from the combination of CERES EBAF4.1 SW+LW and OAFlux LH+SH. The 2021 Q_{net} estimate is based on FLASHFlux and OAFlux. Qnet anomalies are relative to the 2001–15 climatology, and positive anomalies denote increased net downward heat flux into the ocean that has a warming effect on the ocean surface. (b) Net freshwater flux ($P - E$; cm yr^{-1}) from the combination of GPCP P and OAFlux E. P $P - E$ and anomalies are relative to a 1988–2015 climatology, and positive anomalies denote increased freshwater flux into the ocean that causes sea surface freshening. (c) Wind stress magnitude (N m^{-2}) from OAFlux. Wind stress anomalies are relative to a 1988–2015 climatology, and positive anomalies denote increased wind stress magnitude over the ocean. Error bars denote one standard deviation of annual mean variability.

an enhanced mean downwelling in the western equatorial Pacific during the double-dip La Niña, and a weakened mean downwelling in the equatorial Atlantic when a strong Atlantic Niño prevailed.

4) LONG-TERM PERSPECTIVE

Multi-decade annual mean time series of Q_{net}, $P - E$, and wind stress averaged over the global ice-free oceans (Figs. 3.14a–c) provide a long-term perspective on the 2021 ocean surface forcing functions. The Q_{net} time series commenced in 2001, when CERES EBAF4.1 surface radiation products became available. The $P - E$ and wind stress time series both start in 1988 when modern flux data records can be assembled with the availability of Special Sensor Microwave/Imager (SSM/I) satellite retrievals.

Q_{net} was less variable between 2001 and 2007 but had large interannual fluctuations thereafter. The total downward heat flux into the global ocean increased by about 3 W m^{-2} during 2011–16, when the tropical Pacific underwent a strong La Niña event in 2011 and a strong El Niño event in 2016. This period of increased oceanic heat gain coincided with an increase of the global mean SST by about 0.35°C (see Fig. 3.3). Q_{net} went down during the 2017–18 La Niña and has slowly built up since then. The 2021 Q_{net} was up slightly from the 2020 Q_{net}. The $P - E$ time series shows similar interannual variability to that of the Q_{net} time series, and the 2021 level was down slightly from the 2020 level. The data record of wind stress is largely flat in the recent two decades after a regime shift around 1999. The 2021 winds were up slightly from the 2020 level. The error bars in the time series represent one standard deviation of year-to-year variability.

Sidebar 3.1: **Ocean, cryosphere, and sea level change in the IPCC AR6**—B. FOX-KEMPER, H. T. HEWITT, AND D. NOTZ

The Sixth Assessment Report (AR6) of the United Nations Intergovernmental Panel on Climate Change (IPCC) was approved and released in 2022. We were authors of the "Ocean, Cryosphere, and Sea Level Change" chapter (Fox-Kemper et al. 2021a). The AR6 differs from past reports in format: previous topics are recombined into global chapters, process chapters (including ours), regional chapters, and an interactive atlas. The AR6 cycle also includes two special reports with significant oceanic content (IPCC 2018, 2019).

The AR6 covers observations and projections of key climate metrics, including two new ones: upper ocean stratification and mixed layer depth (Figs. SB 3.1b,c). These metrics link climate change with ocean ecosystem impacts (IPCC 2019) and air–sea transfer biases. Rapid progress in analyzing these metrics is

reflected by the AR6 assessment of a 4.9 ± 1.5% increase in 0–200 m stratification from 1970 to 2018, roughly double the rate reported by IPCC (2019).

New and continuing monitoring—by tide gauges, Argo, satellites, moorings, and glacier and ice sheet inventories—lengthened and improved on observations in previous reports. Notably, loss of ice mass from the ice sheets in Greenland and the Antarctic over the period 1992–2020 accounts for more than 20 mm of global sea level rise. The combined ice mass loss during 2010–19 quadruples the loss over 1992–99, contributing alongside increased thermosteric expansion to a rate of sea level rise over 2006–18 more than double the 1901–2018 rate.

New model intercomparison projects (MIPs; Eyring et al. 2016), including the latest CMIP6 ensemble of traditional climate models, but also eddy-permitting ocean models, process MIPs, and emulators of these MIPs (e.g., Edwards et al. 2021) build upon past approaches but allow for more revealing projections in AR6, including anthropogenic attribution of regional and extreme events. High-resolution models often improve SST, ocean overturning circulation, ocean heat content change, and sea ice cover considerably over coarser resolution models.

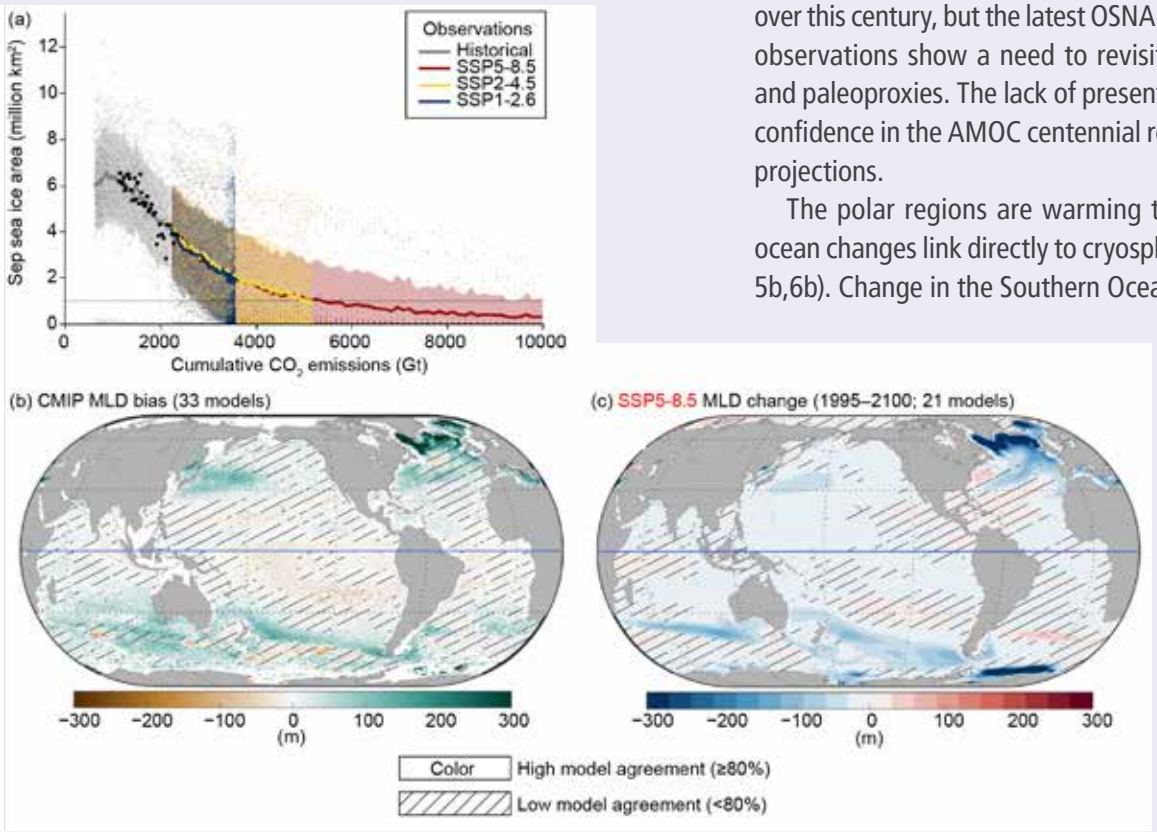

Fig. SB3.1. New scaling and metrics from the IPCC (Fox-Kemper et al. 2021). (a) Arctic September sea ice area (million km^2) as a function of cumulative CO_2 emissions from observations and projections (SSPs). (b) CMIP6 33-model winter (Dec–Feb) mixed layer depth ensemble mean bias vs. an Argo climatology (m; Holte et al. 2017). (c) CMIP6 22-model ensemble mean winter (Dec–Feb) mixed layer depth change (m) from 1995 to 2100 following the SSP5-8.5 scenario.

Over all assessed time windows, the oceans retain over 90% of the anthropogenic warming in Earth's energy budget, over 30% of the anthropogenic carbon in Earth's carbon budget, and over 40% of anthropogenic sea level rise can be attributed to thermosteric expansion (Canadell et al. 2021; Forster et al. 2021; Fox-Kemper et al. 2021a). CMIP6 models tended toward higher climate sensitivity than CMIP5 models, highlighting the need to use observations to constrain the assessment (Sherwood et al. 2020) and motivating a new AR6 method for assessing temperature, energy, and sea level budgets (Forster et al. 2021; Fox-Kemper et al. 2021a). Using consistent emulators in the energy and sea level assessments proved possible and transparent (Palmer et al. 2018; Smith et al. 2021; Fox-Kemper et al. 2021b). Measured changes in contributing processes in the observed sea level and energy budgets consistently sum to agree with observed total rise and warming. The oceanic carbon and energy uptake are understood through shared processes and circulations (Canadell et al. 2021, IPCC Cross-Chapter Box 5.3), such as the Atlantic meridional overturning circulation (AMOC, section 3h), Southern Ocean overturning, and water mass transformations. Both low-resolution and high-resolution models consistently project steady decline in AMOC strength over this century, but the latest OSNAP data and selected earlier observations show a need to revisit AMOC in these models and paleoproxies. The lack of present agreement lowered AR6 confidence in the AMOC centennial reconstructions and model projections.

The polar regions are warming the fastest and there the ocean changes link directly to cryospheric change (see sections 5b,6b). Change in the Southern Ocean and adjacent shelves is intimately linked to the future of the Antarctic ice sheet, oceanic and atmospheric drivers of ice melt, and thus sea level rise uncertainty. Even high-resolution models do not capture important coastal, submesoscale, and sub-ice shelf processes. Overall oceanic Antarctic change has not emerged as clearly as Arctic change, but regional Antarctic changes are increasingly apparent in observations

and high-resolution models. Arctic September sea ice loss is noted in AR6 to be a near-linear function of warming level rather than related to a possible tipping point (Fig. SB3.1a).

The observed rate of sea level rise (section 3f) continues to increase, assessed in the AR6 as 3.69 [3.21–4.17] mm yr^{-1} over 2006 to 2018, compared to 1.73 [1.28–2.17] mm yr^{-1} from 1901 to 2018. Overall, projected sea level rise ranges in AR6 are consistent with past reports (IPCC 2013, 2019), although emulators of ice sheet model comparisons (ISMIP6 and LARMIP-2) and ocean thermosteric expansion allow a greater and more transparent exploration of the impacts of ice sheet instabilities, and scenario and model uncertainties on the ranges. For example, considering only processes projectable with medium confidence, global mean sea level (GMSL) will likely rise by 2100 between 0.38 [0.28–0.55] m in the low-emission SSP1-1.9 scenario and 0.77 [0.63–1.02] m in the high-emission SSP5-8.5 from 1995–2014 levels. By contrast, an AR6 low-likelihood, high-impact storyline building upon emulators of models including ice sheet instabilities and structured expert judgment has roughly double the upper limit of the likely range of sea level increase. The potential contribution of processes that cannot be ruled out are quantified in AR6 even while still clouded by deep uncertainty.

Building on the IPCC (2018) warming level approach, we also sketched outcomes as a function of future potential warming. Under 1.5–2°C global warming, a practically sea ice-free Arctic Ocean is expected in September at least in some years as is the loss of up to half of today's glacier mass and top 3 m of permafrost volume. In the long term, committed GMSL rise over 2000 years is projected to be 2–6 m with 2°C of peak warming. By contrast, warming between 3° and 5°C causes the Arctic Ocean to be sea ice-free for several months in most years, irreversible loss of the West Antarctic Ice Sheet and most of the Greenland Ice Sheet, complete loss of nearly all alpine glaciers, and committed GMSL rise over 2000 years of 4–22 m will likely occur after this level of peak warming.

In summary, the most recent IPCC report (IPCC 2021) highlights yet again the vulnerability and fragility of the world's ocean and cryosphere. Our increasing skill in projecting oceanic and cryospheric changes and attributing them to anthropogenic climate change foretells millennia of consequences for the oceans and cryosphere.

f. Sea level variability and change—P. R. Thompson, M. J. Widlansky, E. Leuliette, D. P. Chambers, W. Sweet, B. D. Hamlington, S. Jevrejeva, M. A. Merrifield, G. T. Mitchum, and R. S. Nerem

Annual average global mean sea level (GMSL) from satellite altimetry (1993–present) reached a new high during 2021, rising to 97.0 mm above 1993 (Fig. 3.15a). This marks the 10th consecutive year (and 26th out of the last 28) that GMSL increased relative to the previous year, reflecting an ongoing multi-decadal trend of 3.4 ± 0.4 mm yr^{-1} in GMSL during the satellite altimetry era (Fig. 3.15a). A quadratic fit with corrections for the eruption of Mount Pinatubo (Fasullo et al. 2016) and ENSO effects (Hamlington et al. 2020) yields a climate-driven trend of 3.0 ± 0.4 mm yr^{-1} and acceleration of 0.081 ± 0.025 mm yr^{-2} (updated from Nerem et al. 2018).

Independent observing systems measure the contributions to GMSL rise from increasing ocean mass, primarily due to melting of glaciers and ice sheets (see sections 5e, 6d, 6e), and decreasing ocean density, primarily due to ocean warming (section 3c). Data from Argo profiling floats analyzed by Scripps Institution of Oceanography (SIO; Roemmich and Gilson 2009) show a global mean steric (i.e., density-related) sea level trend of 1.4 ± 0.2 mm yr^{-1} during 2005–21 (Fig. 3.15a). Global ocean mass (excluding regions within 300 km of land), produced by the NASA Jet Propulsion Laboratory (JPL) using mass concentration anomalies from the Gravity Recovery and Climate Experiment (GRACE) and GRACE Follow-On (GRACE-FO) missions, show a global mean ocean mass trend of 2.2 ± 0.4 mm yr^{-1} during 2005–21 (Fig. 3.15a). The sum of these trend contributions agrees within uncertainties with the GMSL trend of 3.9 ± 0.4 mm yr^{-1} measured by satellite altimetry since 2005 (Leuliette and Willis 2011; Chambers et al. 2017). Consistency among trends from these independent observing systems is a significant achievement and increases confidence in estimates of Earth's energy imbalance (e.g., Hakuba et al. 2021; Marti et al. 2022).

Annually averaged GMSL from satellite altimetry increased 4.9 mm from 2020 to 2021, exceeding the sum of year-over-year increases in global mean steric sea level from Argo, 1.0 mm,

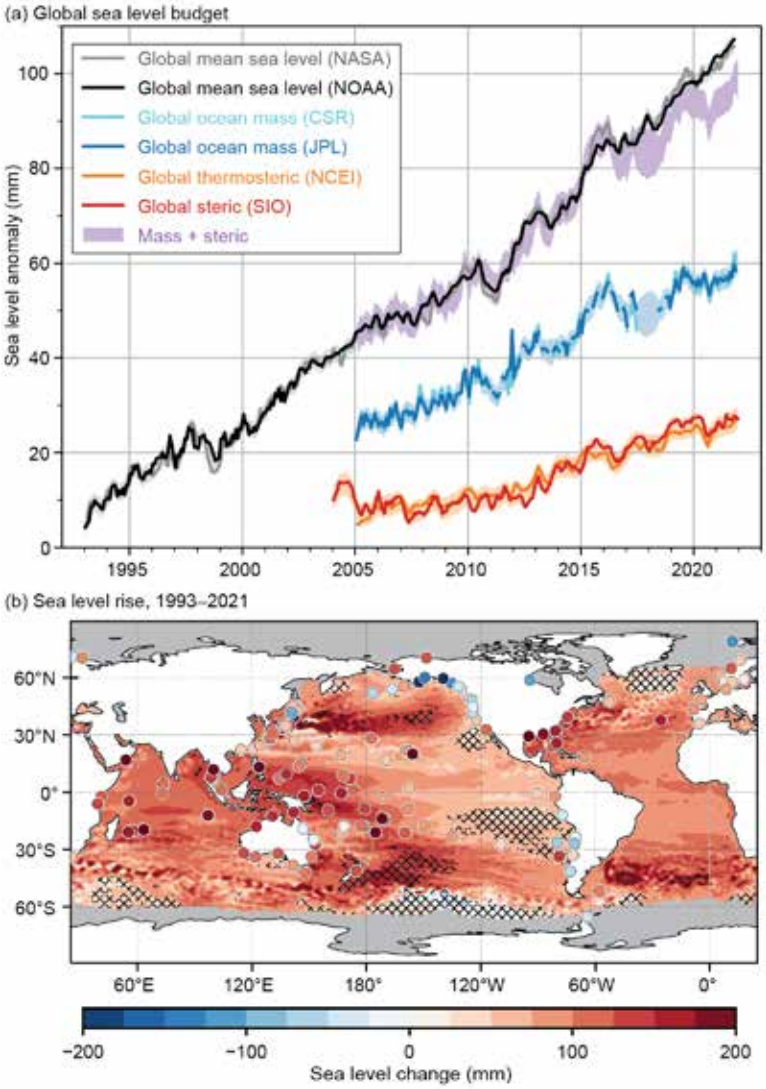

Fig. 3.15. (a) Monthly averaged GMSL (mm) observed by satellite altimeters (1993–2021) from the NOAA Laboratory for Satellite Altimetry (black) and NASA Sea Level Change Program (gray). Monthly global ocean mass (2005–21) from GRACE and GRACE-FO calculated from mascons produced by NASA JPL (blue) and University of Texas Center for Space Research (CSR, cyan). Mascons fewer than 300 km from land were excluded in both ocean mass time series. Monthly global mean steric sea level (2004–21) from SIO Argo data (red). Monthly global mean thermosteric sea level from NCEI Argo and hydrographic data (orange). Monthly global ocean mass plus steric (purple). Shading around all data sources represents a 95% confidence range based on Gaussian process regressions onto each pair of time series. (b) Total local sea level change during 1993–2021 as measured by satellite altimetry (contours) and tide gauges (circles). Hatching indicates local changes that differ from the change in GMSL by more than one standard deviation.

and global mean ocean mass from GRACE-FO, 1.2 mm. The discrepancy is a continuation of misclosure in the sea level budget since 2016 (Fig. 3.15a; Chen et al. 2020), and its cause is an area of active research. Misclosure in the sea level budget is unlikely to be predominantly due to errors in estimating the global mass component of the budget (Hakuba et al. 2021). However, uncertainties in estimating changes in global ocean mass (e.g., leakage near land, geocenter, and glacial isostatic adjustment) warrant investigation (Chen et al. 2020). Likewise, error sources in the altimeter measurements, such as the wet tropospheric correction, may contribute but are unlikely to completely account for the discrepancy (Barnoud et al. 2021). Drift in Argo salinity measurements, the cause of which is still being investigated (Roemmich et al. 2019) can artificially suppress increasing global mean steric sea level, but quality control procedures applied in the SIO data product used here mitigate the impact of salinity drift (Barnoud et al. 2021). The SIO time series of steric sea level also compares favorably with a time series of global mean thermosteric sea level from the NOAA National Centers for Environmental Information (NCEI; Fig. 3.15a). Undersampling of the ocean by Argo, especially around the Malay Archipelago between Asia and Australia (von Schuckmann et al. 2014), could also lead to underestimates of global mean steric rise.

Spatial structure in sea level changes over the 29-year altimeter record (Fig. 3.15b) is due to a combination of natural fluctuations in coupled modes of atmosphere–ocean variability (Han et al. 2017) and the oceanic response to anthropogenic radiative forcing (Fasullo and Nerem 2018). It is difficult to disentangle these contributions to regional differences in long-term sea level change (Hamlington et al. 2019), but as the altimetry record grows in length, the impact of natural fluctuations on regional sea level trends decreases. At present, only a small fraction of the global ocean has experienced sea level trends that differ from the global mean trend by more than one standard deviation (hatched areas, Fig. 3.15b). Reduced sea level trends in the tropical eastern Pacific reflect the impact of multidecadal variability in the strength of Pacific trade winds (e.g.,

Merrifield 2011), while enhanced sea level change in the high latitude South Pacific can be attributed to regional warming (Llovel and Terray 2016; Volkov et al. 2017). Sea level change relative to land (i.e., the quantity measured by tide gauges; circles, Fig. 3.15b) is most relevant for societal impacts and can differ substantially from satellite-derived changes in tectonically active regions (e.g., Japan) and areas strongly affected by glacial isostatic adjustment (e.g., Alaska; Fig. 3.15b).

Due to long-term trends in GMSL (Fig. 3.15), annual sea level anomalies during 2021 were positive nearly everywhere (Fig. 3.16a). In the global tropics, the highest sea level anomalies were in the western Pacific and the eastern Indian Ocean (10–15 cm above the climatological average), whereas the lowest anomalies were in the northeastern Pacific and parts of the south-central Indian Ocean (0–5 cm below average). Sea level anomalies were positive across most of the subtropics, although the amounts varied regionally. The 2021 annual mean anomalies exceeded 15 cm in parts of the midlatitudes, such as in the extension regions of the Kuroshio and Gulf Stream Currents.

The double-dip La Niña events that developed during summer 2020 and again in August 2021 (see section 4b) explain the mostly consistent sea level pattern during both years, at least in the equatorial central Pacific (Fig. 3.16b). Year-to-year sea level increases exceeding 10 cm occurred in the tropical western Pacific, as well as in the eastern Indian Ocean, which were mostly continuing positive changes from the prior two years. In the South Pacific Convergence Zone (SPCZ) region (Brown et al. 2020), the 2021 sea levels were also 10–15 cm higher compared to 2020. The largest regions of decreasing sea levels during 2021 compared to 2020 were in the tropical western Indian Ocean as well as in the western, central, and eastern tropical North Pacific basin. Around Hawaii, the 10 cm decrease in sea level (2021 minus 2020) nearly cancelled the prior year-over-year increase. In the Atlantic Ocean, the 2021 minus 2020 sea level difference was mostly positive, although typically less than 5 cm in magnitude. Larger changes during 2021 occurred in the Gulf of Mexico (associated with the Loop Current) and in the regions most affected by mesoscale oceanic eddies (generally poleward of ±30° latitude). Overall, these sea level changes from 2020 to 2021 (Fig. 3.16b) are representative of the underlying OHCA changes in these locations (Fig. 3.4b).

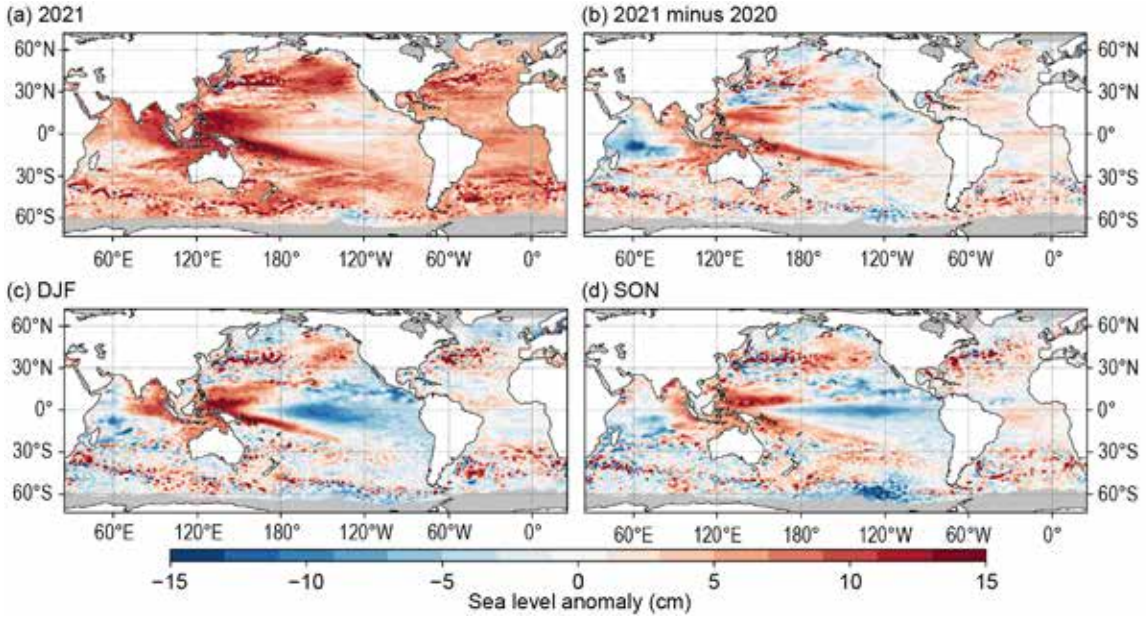

Fig. 3.16. (a) Annual average sea level anomaly during 2021 relative to average sea level at each location during 1993–2021. (b) Average 2021 minus 2020 sea level anomaly. (c) Average sea level anomaly during DJF 2021 relative to the 1993–2020 average. (d) Same as (c), but for SON. Units are given in cm. GMSL was subtracted from panels (c),(d) to emphasize regional, non-secular change. Altimetry data were obtained from the gridded, multi-mission product maintained by the Copernicus Marine and Environment Monitoring Service (CMEMS).

The double-dip La Niña (see section 4b) during 2021, and the respective continuation of below-average sea levels in the eastern half and above-normal value in the western half of the equatorial Pacific, limited the amount of intra-seasonal changes evident in the comparison of December–February (DJF) and September–November (SON) anomalies (Figs. 3.16c,d). In the Indian Ocean, the sea level pattern was also mostly similar at the beginning and end of 2021 (i.e., sea level anomalies increasing from west to east). Some of the highest regional sea level anomalies during 2021 occurred in Bay of Bengal, where satellite-observed seasonal anomalies were more than 15 cm above average during both DJF and SON. In the northwestern Atlantic Ocean, seasonal sea level anomalies were overall higher during SON compared to the beginning of the year, especially near the U.S. mid-Atlantic coast.

Ongoing trends, year-to-year variability, and seasonal changes in sea level impact coastal communities by increasing the magnitude and frequency of positive sea level extremes that contribute to flooding and erosion. Minor impacts tend to emerge when local water levels exceed the 99th percentile of daily sea level maxima (Sweet et al. 2014). Using 1993–2021 as the analysis epoch (consistent with the altimetry baseline), daily sea level maxima that exceed the 99th percentile—hereafter extreme sea level events—occurred more frequently in recent years compared to previous decades. Across 114 tide-gauge locations with sufficient data volume and quality for analysis, the median number of extreme sea level events per year and location increased from one during 1993–97 to four during 2017–21 (not shown). The 90th percentile of events per year and location increased from six during 1993–97 to 15 during 2017–21 (not shown).

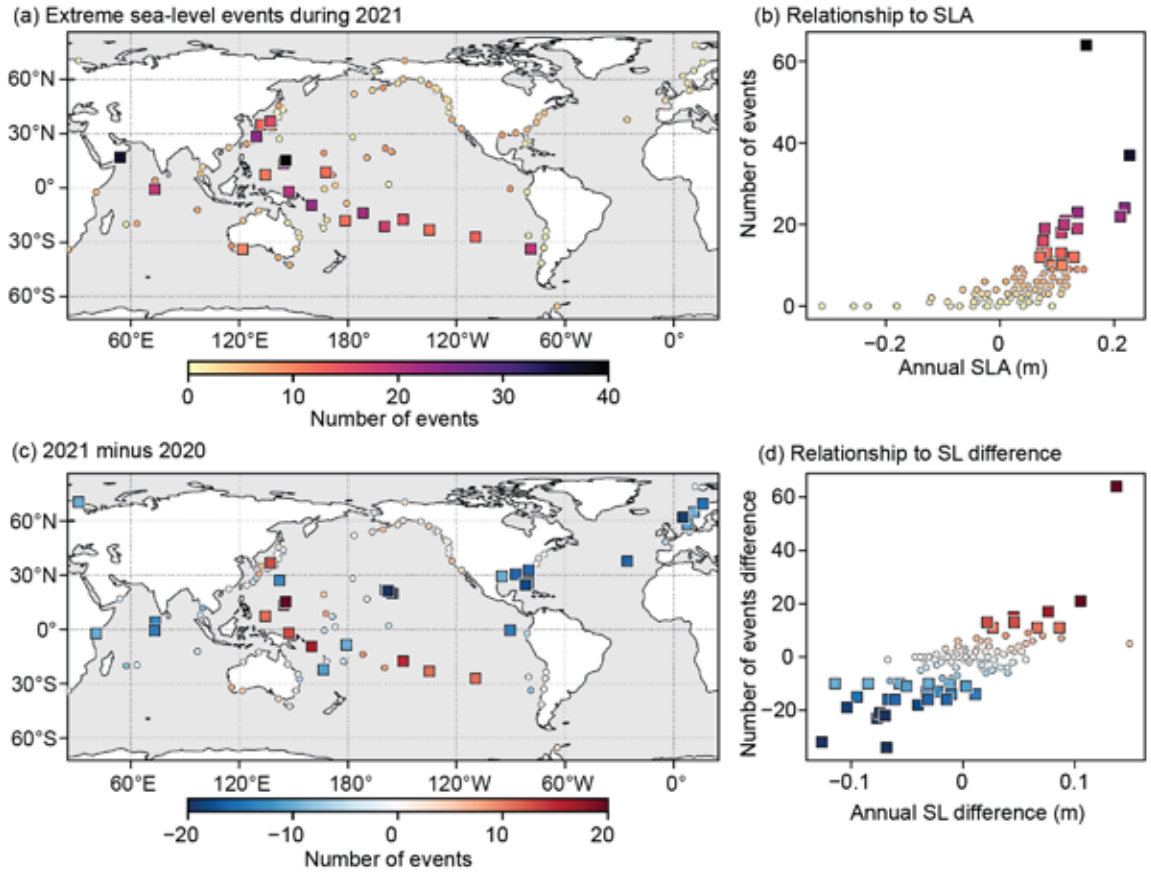

Fig. 3.17. (a) Number of extreme sea level events from tide gauges during 2021. (b) Counts in (a) as a function of annual sea level anomaly during 2021. Square markers in (a) and (b) highlight locations with more than 10 extreme events. (c) Change in number of extreme sea level events from 2020 to 2021. (d) Counts in (c) as a function of the change in annual sea level from 2020 to 2021. Square markers in (c) and (d) highlight locations where the magnitudes of changes in counts of extreme events were greater than 10. Counts of extreme sea level events were calculated from hourly tide gauge observations obtained from the University of Hawaii Sea Level Center Fast Delivery database. Only records with at least 80% completeness during 1993–2021 and 80% completeness during both 2020 and 2021, individually, were analyzed.

Twenty of the 114 locations experienced more than 10 extreme sea level events during 2021, which were especially concentrated in the tropical western Pacific and in a diagonal region of the South Pacific near the SPCZ (Fig. 3.17a) where annual sea level anomalies were largest (Figs. 3.16a, 3.17b). Many of these locations experienced increases of more than 10 extreme events per year from 2020 to 2021 (Fig. 3.17c), reflecting year-over-year increases in annual mean sea level (Figs. 3.16b, 3.17d). Twenty-four locations experienced at least 10 fewer extreme events per year in 2021 compared to 2020, which were concentrated in the western Indian Ocean, Hawaiian Islands, U.S. Gulf of Mexico and southeast Atlantic coasts, and northern Europe (Fig. 3.17c). In each of these regions, the annual mean sea level during 2021 was either mostly unchanged or lower compared to the prior year (Figs. 3.16b, 3.17d). Along the U.S. mid-Atlantic and New England coasts, the annual numbers of extreme events were similar during 2020 and 2021 (Fig. 3.17c), although most of the 2021 extremes occurred during SON when the regional sea level anomaly was 5–15 cm higher than earlier in the year (Figs. 3.16c,d). Of the 114 locations analyzed, Saipan experienced the greatest number (64) of extreme events during 2021 due—at least in part—to an annual mean sea level anomaly greater than 15 cm. Other locations experienced larger sea level anomalies but far fewer events, because it is the magnitude of the annual sea level anomaly relative to the typical range of hourly variability (including tides, synoptic variations, etc.) that most closely relates to the frequency of extreme events. In Saipan, 15 cm is more than 65% of the local standard deviation in hourly water levels—the highest percentage of locations analyzed.

g. Surface currents—R. Lumpkin, F. Bringas, and G. Goni

This section describes variations of ocean surface currents, transports, and associated features, such as rings, inferred from surface currents. Surface currents are obtained from in situ (a global array of drogued drifters and regional mooring arrays) and satellite (altimetry and wind stress) observations. Transports are derived from a combination of sea surface height anomaly (from altimetry) and climatological hydrography. See Lumpkin et al. (2011) for details of these calculations. Zonal surface current anomalies are calculated with respect to a 1993–2020 climatology and are discussed below for individual ocean basins.

1) PACIFIC OCEAN

In 2021, zonal geostrophic currents in the equatorial Pacific exhibited annual mean westward current anomalies of 6–8 cm s^{-1} from 150°E–100°W (Fig. 3.18a), 1°S–3.5°N, associated with the 2021 double-dip La Niña (see section 4b). In the same longitude range, westward

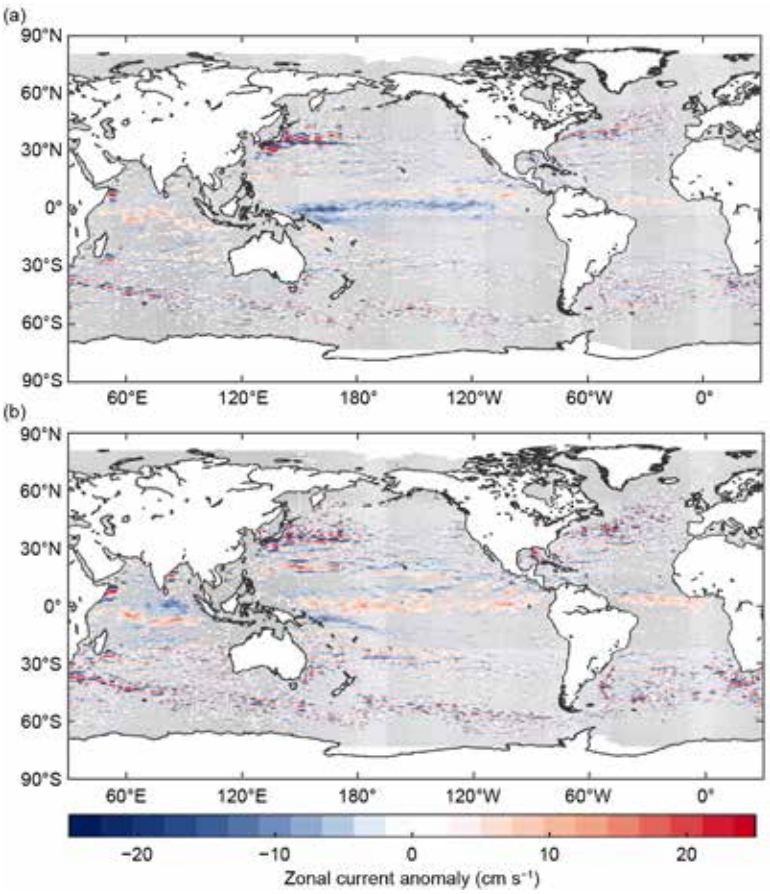

Fig. 3.18. Annually-averaged geostrophic zonal current anomalies (cm s^{-1}; positive is eastward, negative is westward) for (a) 2021 and (b) 2021 minus 2020 derived from a synthesis of drifters, altimetry, and winds. Gray stippling indicates where values are not significantly different from zero.

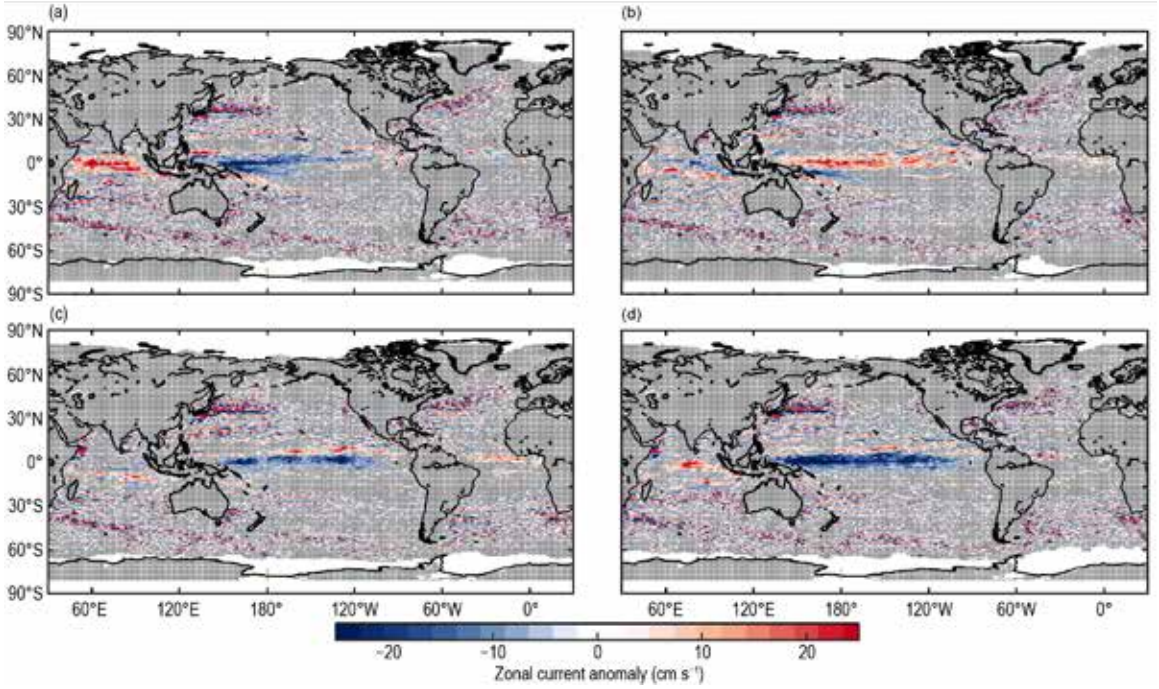

Fig. 3.19. Seasonally-averaged zonal geostrophic current anomalies with respect to seasonal climatology, for (a) Dec 2020–Feb 2021, (b) Mar–May 2021, (c) Jun–Aug 2021, and (d) Sep–Nov 2021. Gray stippling indicates where values are not significantly different from zero.

anomalies of 4–5 cm s^{-1} at 4°–6°S indicated a strengthened South Equatorial Current (SEC). The 2018–20 northward shift of the North Equatorial Countercurrent (NECC) was not observed in 2021. Because westward anomalies were larger through most of 2020, 2021 minus 2020 differences (Fig. 3.18b) show weak eastward equatorial anomalies.

Westward anomalies exceeding 20 cm s^{-1} were present in the western equatorial (1°S–1°N, 150°E–170°W) Pacific in December–February (Fig. 3.19a); in this longitude band, westward currents were anomalously strong from 7°S to 3°N. In March–May, eastward anomalies of 10–20 cm s^{-1} developed across the basin at 3°S to 2°N, leading the transition from La Niña to ENSO-neutral SST anomalies the following season (see section 4b). The equatorial anomalies reversed again in June–August, exceeding 10 cm s^{-1} westward from 1°S to 3°N across the basin with zonally-averaged maxima of 14 cm s^{-1} on the equator and at 2°N, again leading the development of La Niña SST anomalies the following season. North of this pattern, eastward anomalies of 5–8 cm s^{-1} were associated with an accelerated NECC during June–August. Both anomaly patterns persisted in September–November, with the westward equatorial anomalies strengthening to 20–25 cm s^{-1} at 0.5°S–1.5°N.

In the northwest Pacific, zonal current anomalies of ±20 cm s^{-1} bracketing 35.5°N (Fig. 3.18a) indicated a 2021 northward shift of up to 2° latitude of the Kuroshio extension, consistent with anomalously warm ocean heat content anomalies north of the climatological path of the Kuroshio (Fig. 3.4a) and perhaps associated with heat flux anomalies in the region (Fig. 3.11a).

2) INDIAN OCEAN

Annually averaged zonal currents in the Indian Ocean were close to their 1993–2020 climatological averages, with weak (2–4 cm s^{-1}) eastward anomalies from 8°S to the equator across most of the basin (Fig. 3.18a). Because eastward anomalies in this latitude range were significantly stronger (10–20 cm s^{-1}) in 2020, 2021 minus 2020 differences (Fig. 3.18b) exhibit negative anomalies of ~15 cm s^{-1} across the basin. During December–February (Fig. 3.19a), eastward anomalies of 10–20 cm s^{-1} were present across the basin from 2° to 6°S; these were replaced by westward

anomalies of 3–7 cm s^{-1} in March–May (Fig. 3.19b) that disappeared by June–August (Fig. 3.19c). Eastward anomalies of 10–20 cm s^{-1} developed in the central basin at 70°–85°E, 4.5°S–0.5°N in September–November (Fig. 3.19d), with peak values of 20 cm s^{-1} at 1°S reflecting an acceleration of the seasonal eastward Southwest Monsoon Current.

3) ATLANTIC OCEAN

Annual mean zonal currents in the tropical Atlantic Ocean in 2021 exhibited weak (4–5 cm s^{-1}) eastward anomalies from 3° to 4.5°N, indicating a southward shift of the NECC and the interface between it and the northern core of the South Equatorial Current (nSEC; see Lumpkin and Garzoli 2005) to its south. The core strength of the westward nSEC and other branches of the SEC were close to their climatological averages. Weak eastward anomalies were present in December–February and March–May, strengthened in June–August to a maximum of 10 cm s^{-1} at 3°N with anomalies > 5 cm s^{-1} at 1°–4.5°N, and weakened to near-zero values in September–November (Fig. 3.19).

Variability of key Atlantic Ocean currents is continuously monitored in near-real-time by leveraging relationships between in situ and satellite altimetry observations (https://www.aoml.noaa.gov/phod/indexes/index.php). In the South Atlantic, the number of rings shed by the Agulhas Current remained similar to the average number of shedding events in a given year during the 1993–2021 record. The annual transport of the Agulhas Current, an indicator of Indian-Atlantic Ocean interbasin water exchange, was slightly below the average by –1.5 Sv in a cross section at ~28°E and between 34° and 40°S and has remained within 1 std. dev. of the long-term average of 50.9 ± 3.2 Sv. In the southwestern Atlantic, the location of the Brazil-Malvinas Confluence has demonstrated a southward trend since 1993 at decadal time scales (cf. Lumpkin and Garzoli 2011; Goni et al. 2011), and was displaced to the south with respect to its 1993–2021 mean location for the fifth consecutive year. This southward trend is important since the location of the confluence indicates where waters of subtropical origin are entrained into a subpolar region. A northward shift of the confluence observed in 2016 (Fig. 3.20) appears to have been transient. During 2021, the confluence was on average 0.9 degrees of latitude south of its 1993–2020 mean location (37.8 ± 1.1)°S, a –0.5° shift compared to the previous year, and over 2 degrees of latitude south of its average location in the early 1990s (Fig. 3.20). This shift may be related to anomalously warm upper ocean heat content at this location driving a southward migration of the westerlies (see Figs. 3.4a, 3.13a). In the North Atlantic, the North Brazil Current (NBC) and associated rings serve as interhemispheric conduits for water masses and heat from the South Atlantic into the North Atlantic (Goni and Johns 2003). Some of their waters enter the Caribbean Sea while carrying low salinity Amazon River waters (Ffield 2007), which are known for creating barrier layers that can magnify hurricane intensification (e.g., Balaguru et al. 2012; Domingues et al. 2015). As in previous years, this current transport continues to show negative anomalies, possibly associated with fresh surface salinity anomalies in the NBC retroflection region (Fig. 3.7), while the number of rings do not show a departure from their mean values. Farther to the north, the Yucatan Current and Florida Current exhibited negative anomalies of –0.3 Sv and –0.5 Sv, respectively, with the transport in the Yucatan Current approximately 1 Sv below its long-term average during 2021 and relative low variability

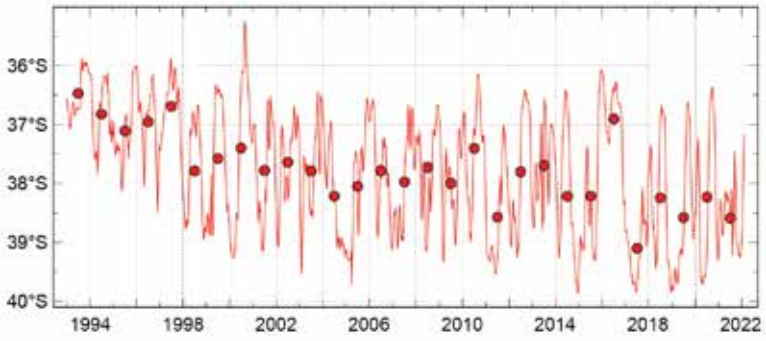

Fig. 3.20. Time series of the latitude of separation of the Brazil Current (BC) front from the continental shelf, defined as the intersection between the 1000 m bathymetry contour and the contour where the 10°C isotherm is 200 m deep. The red line is a 28-day running mean, red circles are annual mean values. The mean latitude of separation between 1993 and 2022 is (37.8 ± 1.1)°S. (Source: www.aoml.noaa.gov/phod/altimetry/cvar/mal/BM_ts.php)

during the last three years, with values within 1 std. dev. of its 27.5 ± 1.0 Sv average since 1993. This slight reduction in the 2021 Florida Current transport with respect to the period 1993–2020 is not significantly different from transport changes derived from cable measurements reported in the next section, for the period 1982–2021. The continuous lower-than-usual Florida Current transport is closely tied to higher coastal sea level and "sunny day" flooding events along the U.S. southeast coast (Ezer and Atkinson 2014; Domingues et al. 2016; Volkov et al. 2020). Further studies addressing the North Brazil Current to Florida Current connection may help develop early warnings for such flooding events.

h. Meridional overturning circulation and heat transport in the Atlantic Ocean—D. L. Volkov, S. Dong, J. Willis, W. Hobbs, W. Johns, D. A. Smeed, B. I. Moat, Y. Fu, S. Lozier, M. Kersalé, R. C. Perez, D. Rayner, E. Frajka-Williams, and G. Goni

The meridional overturning circulation (MOC) affects meridional large-scale transports of heat and freshwater that impact global and regional climate and weather patterns, sea level, and ecosystems. Several observational arrays exist across the Atlantic Ocean to monitor changes in the Atlantic MOC (AMOC) and meridional heat transport (AMHT; Frajka-Williams et al. 2019). Since the previous *State of the Climate in 2020* report (Volkov et al. 2021), the AMOC and AMHT estimates based on moored arrays (Fig. 3.21a) have been extended to March 2020 for the RAPID-MOCHA-WBTS array at 26.5°N and to May 2018 for the OSNAP array between 53° and 60°N (Frajka-Williams et al. 2021; Li et al. 2021a,b). No updates are presently available for the AMOC at 34.5°S, but the AMHT estimates at the SAMBA array based on direct observations have been published for the first time (Kersalé et al. 2021). In this report, we review updated AMOC/AMHT estimates from the moored arrays and present blended estimates based on combinations of satellite altimetry and in situ hydrographic data.

The subpolar North Atlantic is a key region for deep water formation, hence it plays an important role in the AMOC. A collaborative international effort to measure the AMOC here led to the establishment of the OSNAP array in 2014 (Lozier et al. 2017), which consists of two segments: OSNAP-West between Labrador and Greenland and OSNAP-East between Greenland and Scotland (Fig. 3.21a). The latest published AMOC/AMHT estimates span the first four years of observations (Li et al. 2021a,b; Fig. 3.21b), which will soon be extended to a nearly six-year record using the recently recovered data. Over the period from August 2014 to May 2018, the AMOC across the OSNAP array had a time-mean of 16.6 ± 0.7 Sv (1 Sv = 10^6 m^3 s^{-1}; the uncertainty is the standard error of the mean; Li et al. 2021a). The 30-day averages of the AMOC at the OSNAP array exhibit variability ranging from 8.2 to 24.5 Sv, with a standard deviation of 3.5 Sv. The OSNAP observations have revealed that the eastern subpolar basin (OSNAP-East) dominates the mean and variability of the AMOC across the entire subpolar North Atlantic. The OSNAP-East mean (16.8 ± 0.6 Sv) is more than six times greater than the OSNAP-West mean (2.6 ± 0.3 Sv). The AMOC across the entire OSNAP array is less than the sum across OSNAP-West and OSNAP-East because of cancellations between northward and southward transports (Lozier et al. 2019). The AMHT in 2014–18 had a time-mean of 0.50 ± 0.05 PW (1 PW = 10^{15} W), and was correlated at 0.8 with the AMOC (Fig. 3.21b). The remaining variance is attributed to the subpolar gyre circulation. Winter convection during 2014–18 in the interior subpolar basins had minimal impact on density changes in the deep western boundary currents (Li et al. 2021a). Contrary to previous modeling studies, no discernible relationship between western boundary changes and subpolar overturning variability has been found.

The longest-maintained trans-basin AMOC/AMHT observing array along approximately 26.5°N (RAPID-MOCHA-WBTS; Fig. 3.21a) has been updated through the spring of 2020 (Frajka-Williams et al. 2021; Fig. 3.21c). The mean AMOC and AMHT at 26.5°N for 2004–20 were 16.9 ± 0.7 Sv and 1.19 ± 0.06 PW, respectively. The mean AMOC and AMHT in 2019–20 were 15.4 ± 0.5 Sv and

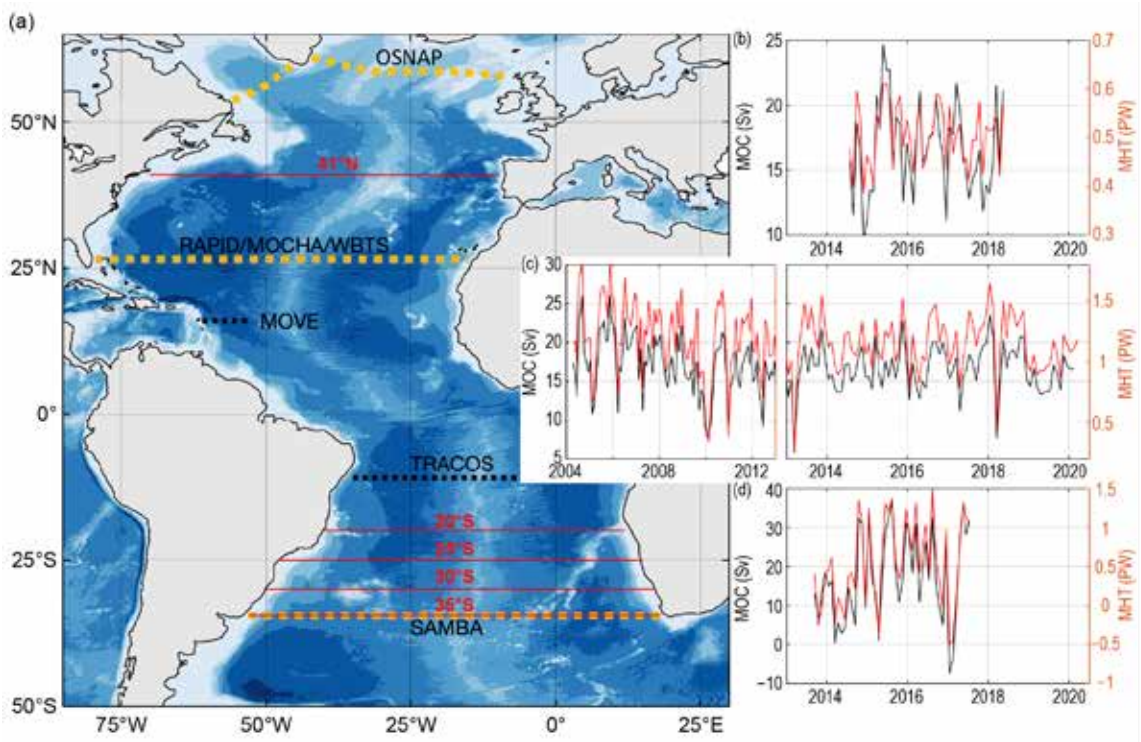

Fig. 3.21. (a) The Atlantic meridional overturning circulation (AMOC) observing system: moored arrays (dashed black and orange lines) and sections across which the AMOC is estimated by combining in situ measurements (Argo, XBT, bottom pressure) with satellite altimetry data (red lines). The moored arrays that have been updated since the *State of the Climate in 2020* report (orange dashed lines) include: OSNAP (Overturning in the Subpolar North Atlantic Program) in the subpolar North Atlantic, RAPID-MOCHA-WBTS (Rapid Climate Change/MOC and Heatflux Array/Western Boundary Time Series) at 26.5°N, and SAMBA (South Atlantic MOC Basin-wide Array) at 34.5°S. The arrays that have not yet been updated (black dashed lines) include: MOVE (Meridional Overturning Variability Experiment) at 16°N and TRACOS (Tropical Atlantic Circulation Overturning) at 11°S. (b) Monthly time series of the AMOC northward volume transport (black) and AMHT (red) across the OSNAP array. (c) Monthly time series of the AMOC northward volume transport (black) and AMHT (red) across the RAPID/MOCHA/WBTS array (the plot is split in two panels to zoom in on the time interval common for all arrays). (d) Monthly time series of the AMOC northward volume transport (black) and AMHT (red) across the SAMBA. Units for the AMOC/AMHT are Sv/PW.

1.03 ± 0.04 PW, lower than the 2004–20 mean values. The strongest AMOC/AMHT was observed during the first four years of observations. From April 2008 to March 2012, the AMOC was 2.7 Sv weaker on average than during the first four years of observations (Smeed et al. 2014), and it remained weaker thereafter (Smeed et al. 2018). By combining estimates of the RAPID-MOCHA-WBTS and OSNAP arrays, a time-mean heat divergence of 0.68 ± 0.14 PW during the 2014–18 period has been determined in the extratropical North Atlantic between the two arrays (Li et al. 2021b).

Interannual and longer variability of the AMOC/AMHT at 26.5°N is dominated by changes in the upper-ocean geostrophic flows between the Bahamas and Canary Islands (McCarthy et al. 2012). However, the Florida Current volume transport, which is measured by a submarine cable between Florida and the Bahamas and is part of the AMOC estimate at 26.5°N, has exhibited an intensification of its interannual variability since around 2014 (Dong et al. 2022; Volkov et al. 2020). In 2021, the Florida Current volume transport was 30.8 ± 0.5 Sv, which is slightly below its long-term (1982–2021) mean value of 31.8 ± 0.1 Sv, but not significantly different from the 2020 mean value of 31.2 ± 0.6 Sv.

A new method for combining satellite sea level observations with historical hydrographic measurements (CTD and Argo) and PIES data has been developed and used to derive the AMHT at 34.5°S (Kersalé et al. 2021; red curve in Fig. 3.21d). The average AMHT during 2013–17 was 0.5 ± 0.2 PW, with a peak-to-peak range of 4.6 PW and a daily standard deviation of 0.8 PW. The daily AMHT and AMOC at 34.5°S exhibit a strong positive correlation with the northward transport in the AMOC upper cell (r=0.96; black curve in Fig. 3.21d) and a modest negative correlation

with the southward volume transport in the AMOC abyssal cell (r= −0.52). The AMHT estimate seasonal cycle has a prevailing semi-annual period and a maximum equatorward heat transport in July–September and December–January. The four-year record (2013–17) reveals a weak positive AMHT trend of 0.14 ± 0.18 PW yr^{-1}, not statistically different from zero.

Combination of satellite altimetry and in situ hydrography data provides information on the state of the AMOC/AMHT in 2021. Updated AMOC/AMHT estimates at 41°N (Fig.3.22a), based on satellite altimetry and Argo measurements (Willis 2010; Hobbs and Willis 2012), are about 20% and 25% below their average values in 2021, respectively. The reduction in the AMOC was largely due to a weaker-than-normal upper ocean northward geostrophic transport. The reduction in the

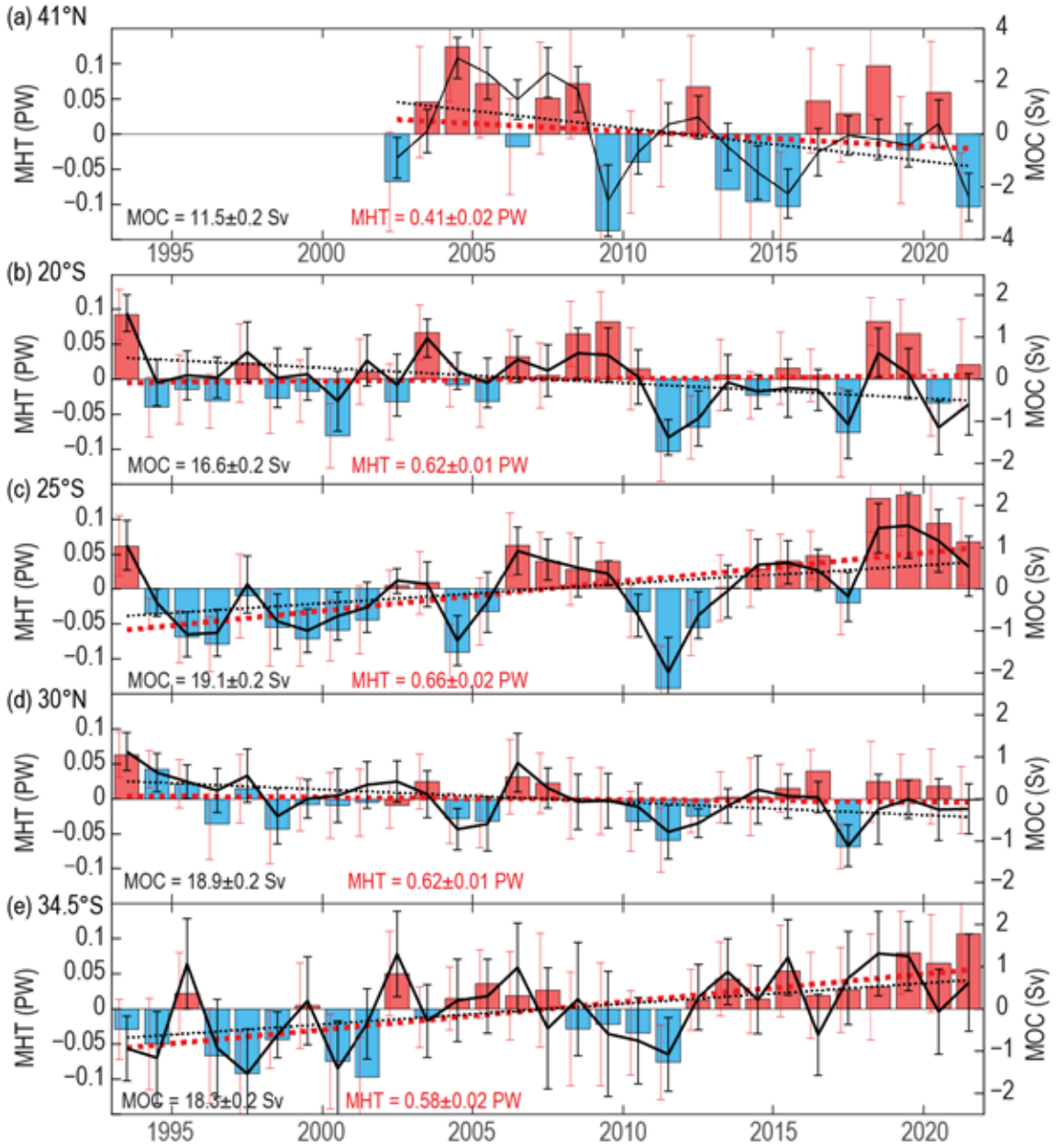

Fig. 3.22. The AMHT (colored bars) and the AMOC (black curves) anomalies obtained by combining satellite altimetry and in situ data at (a) 41°N, (b) 20°S, (c) 25°S, (d) 30°S, and (e) 34.5°S. The vertical error bars show standard errors (red) for the AMHT and (black) for the AMOC. The anomalies are computed with respect to the time-mean values shown in the plots. Linear trends (dashed red lines) for the AMHT are equal to: −0.002 ± 0.010 PW yr^{-1} at 41°N, 0.000 ± 0.003 PW yr^{-1} at 20°S, 0.004 ± 0.003 PW yr^{-1} at 25°S, 0.000 ± 0.002 PW yr^{-1} at 30°S, and 0.004 ± 0.002 PW yr^{-1} at 34.5°S. Linear trends (dashed black lines) for the AMOC are equal to: −0.13 ± 0.14 Sv yr^{-1} at 41°N, −0.04 ± 0.03 Sv yr^{-1} at 20°S, 0.05 ± 0.04 Sv yr^{-1} at 25°S, −0.03 ± 0.02 Sv yr^{-1} at 30°S, and 0.05 ± 0.04 Sv yr^{-1} at 34.5°S. The estimates at 41°N are based on satellite altimetry and Argo data (Willis 2010; Hobbs and Willis 2012), and the estimates at 20°S, 25°S, 30°S, and 34.5°S are based on satellite altimetry and the Global Temperature and Salinity Profile Program data (Dong et al. 2021).

AMHT, however, was due to a southward anomaly in Ekman transport, while the upper ocean geostrophic temperature transport had a positive anomaly. The geostrophic temperature transport anomaly was due to the upper 1000-m temperature. As evidenced by Argo data (not shown), this temperature in 2021 was higher than the 2002–21 average temperature. Therefore, even though there was less upper-ocean northward transport, there was greater net heat transport. It should be noted that these estimates for 2021 are still preliminary and may change after satellite altimetry and Argo data undergo additional validation, quality control, and improvements. Similar to the estimates at 26.5°N (Fig. 3.21c), the AMOC/AMHT at 41°N in 2009–21 were 10–20% lower than they were in 2004–08 without any indication of a rebound. While the AMOC and AMHT trends for 2002–21 are negative at 41°N (−0.13 ± 0.14 Sv yr^{-1} and −0.002 ± 0.009 PW yr^{-1}, respectively), they are not statistically significantly different from zero.

The AMOC/AMHT estimates at 20°S, 25°S, 30°S, and 34.5°S (Figs. 3.22b–e; updated from Dong et al. 2021) based on satellite altimetry and the Global Temperature and Salinity Profile Program (GTSPP; Sun et al. 2010) data were not significantly different from those in 2020. Meaningful positive AMHT trends exist at 25°S (0.004 ± 0.002 PW yr^{-1}) and 34.5°S (0.004 ± 0.003 PW yr^{-1}), while trends at 20°S and 30°S are statistically insignificant. The negative AMOC trends at 20°S and 30°S, and the positive AMOC trends at 25°S and 35°S, are all statistically significant. This result suggests that there is a long-term heat divergence between 30° and 25°S and heat convergence between 34.5° and 30°S and between 25° and 20°S. There is a possible northward propagation of the MHT anomalies in the South Atlantic. For example, mainly positive anomalies in 2003–07, negative anomalies in 2008–12, and positive anomalies 2013–21 at 34.5°S are observed at the lower latitudes about one year later.

In summary, AMOC and AMHT estimates based on moored and blended data continue to show highly variable transports across the Atlantic Ocean. While some of the long-term trends are found to be marginally significant, given the limited observational record, it is not yet possible to conclude that the AMOC is changing in response to climate change. It remains important to reconcile the AMOC and AMHT estimates based on the different methodologies used to compute them. This will help to improve the methodologies and reduce uncertainties in the estimates of oceanic transports. Sustained observations are necessary for detecting and understanding climate-relevant changes in the AMOC.

Sidebar 3.2: **IPCC AR6 assessment of the role of the oceans in the carbon cycle**—R. A. FEELY AND R. WANNINKHOF

The global ocean plays a major role in the global carbon cycle by absorbing a substantial fraction of the excess carbon dioxide (CO_2) that humans release into the atmosphere. As a result of humankind's collective input of CO_2 into the atmosphere, referred to as "anthropogenic CO_2" (C_{anth}) emissions, global average atmospheric CO_2 concentrations have risen from pre-industrial levels of about 278 parts per million (ppm) to ~415 ppm in 2021. The recent IPCC Working Group I contribution to the Sixth Assessment Report provides a comprehensive understanding of the drivers that affect how the carbon cycle in the ocean is changing and the role of human influence (IPCC 2021). Evidence from both global ocean biogeochemical models (GOBMs) and observations provide a "high confidence" that the ocean sink increased from 1.0 ± 0.3 PgC yr^{-1} in 1960–69 to 2.5 ± 0.3 PgC yr^{-1} in 2010–19, with the total cumulative uptake accounting for approximately 23% of the total anthropogenic CO_2 emissions over the entire period (Friedlingstein et al. 2020, 2022). The multi-decadal trends in the ocean carbon air–sea flux show an increase in the ocean sink with a "hiatus" in the 1990s (Fig. SB3.2). The hiatus appears to be associated with either decadal changes in Southern Ocean mixing and circulation processes (Le Quéré et al. 2007; Canadell et al. 2021), external forcing (McKinley et al. 2020), or a combination thereof. Over the last six decades the land and ocean C_{anth} sinks have been roughly consistent with the atmospheric CO_2 increase on decadal scales such that the fraction of anthropogenic CO_2 emissions that has been retained in the atmosphere has remained roughly constant at about 44% over the years.

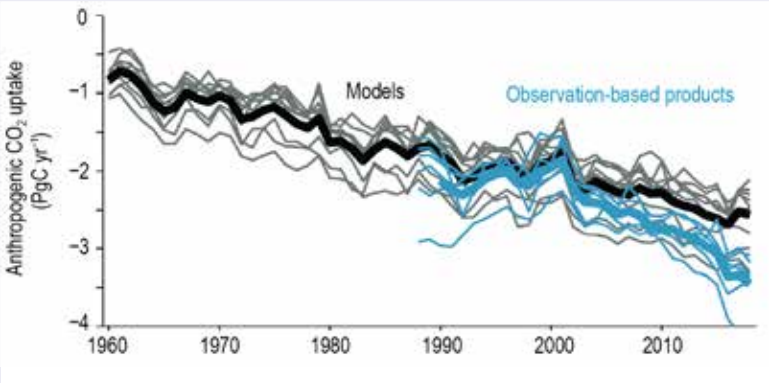

Fig. SB3.2. Comparison of trends for oceanic anthropogenic CO_2 uptake (PgC yr^{-1}) from GOBMs (1960–2018) and observations (1987–2018). The hiatus of the increasing oceanic sink in the 1990s appears to be related to decadal changes in the Southern Ocean (after Canadell et al. 2021).

The uptake of the excess CO_2 by the oceans involves a twofold process in which CO_2 is exchanged across the air–sea interface followed by mixing and transport in the ocean interior where it is stored in deep water masses via mixing and circulation processes on time scales of decades to centuries (DeVries et al. 2017, 2019; Gruber et al. 2019). Both GOBMs and observations indicate that uptake and CO_2 storage mainly occur in the oceanic midlatitude regions, where the mixing and ventilation of subtropical and subpolar surface water contribute to the formation and transport of Mode, Intermediate, and Deep waters that carry the anthropogenic CO_2 into the ocean interior. In contrast, outgassing of CO_2 mostly occurs in areas with upwelling such as eastern boundaries, the equatorial Pacific, and divergence zones in the Southern Ocean. The cumulative amount of anthropogenic CO_2 stored in the ocean interior since the start of the industrial revolution (≈1750) has been estimated to be approximately 170 ± 20 PgC through 2019 (Friedlingstein et al. 2020, 2022). It is anticipated that the ocean sink will continue to increase with increasing anthropogenic emission, but substantial changes to the multi-decadal trends in the ocean sinks are anticipated once these emissions are curtailed.

Different regions have been observed to impact interannual and decadal changes of the CO_2 flux variability in the global oceans. The high latitude (≈>45°) regions, mostly in the Southern Ocean, have the largest influence over the decadal-scale variations due to changes in wind forcing and circulation processes. For example, in the Pacific sector of the Southern Ocean, the rate of anthropogenic CO_2 storage increased from 8.8 ± 1.1 PgC $decade^{-1}$ during 1995–2005 to 11.7 ± 1.1 PgC $decade^{-1}$ during 2005–15 (Carter et al. 2017, 2019). On the other hand, the impact of ENSO in the tropical oceans has caused this portion of the oceans to have the largest influence over the interannual variability (Ishii et al. 2020).

Both observations and models suggest that increases in the seasonal amplitude of surface ocean pCO_2 due to uptake of anthropogenic CO_2 correspond to reductions in the buffering capacity of seawater. This decrease in buffer capacity is starting to have a large-scale impact on the carbonate chemistry of seawater (Fassbender et al. 2018; Landschützer et al. 2018; Jiang et al. 2019). Moreover, model results (Rodgers et al. 2020) suggest that re-emergence of previously stored anthropogenic CO_2 is changing the buffering capacity of the ocean mixed layer and consequently increasing the potential for reducing the ocean sink of C_{anth} over time.

Extensive carbonate chemistry and pH measurements throughout the global ocean have revealed that acidification of the surface ocean has resulted in an overall decline in the rate of pH change in the range of −0.017 to −0.027 $decade^{-1}$ over the last four decades. These rates are consistent with the increase in atmospheric CO_2 and amount to approximately a 4% increase in surface ocean hydrogen ion concentration per decade. The rate of pH decline is slowest in the western Pacific Warm Pool and subtropics (−0.010 to −0.019 $decade^{-1}$) and higher in the upwelling region of the tropical Pacific (−0.022 to −0.026). In the polar and subpolar regions rates of pH decline are more variable (−0.003 to −0.026); however, highly resolved long time series data are sparser there. These changes to the carbonate system result in a declining saturation state from −0.07 to −0.12 $decade^{-1}$ for the biogenic calcium carbonate mineral aragonite, which makes up the skeletal material of many calcifying organisms of economic importance. Within the ocean interior, changes in circulation and metabolic activity have also caused enhanced acidification in the deeper waters of the South Atlantic and North Pacific (Ríos et al. 2015; Sasano et al. 2015). These changes in the acidification of the ocean interior have resulted in a shoaling of the aragonite saturation horizon, where $\Omega_{ar} = 1.0$, ranging from 1–2 m yr^{-1} in the North Pacific (Feely et al. 2012) to as much as 10–15 m yr^{-1} in the Irminger and Iceland Seas (Olafsson et al. 2009; Perez et al. 2018).

i. Global ocean phytoplankton—B. A. Franz, I. Cetinić, M. Gao, D. A. Siegel, and T. K. Westberry

Marine phytoplankton contribute roughly 50% of global net primary production, generating much of the oxygen we breathe and serving the energy needs of oceanic ecosystems, while also providing a critical pathway for carbon sequestration to the deep oceans. The diversity, abundance, and distribution of phytoplankton are controlled by numerous biotic (zooplankton grazing and viruses) and abiotic factors, with the latter including nutrient and light availability that, in turn, are highly dependent on physical properties and processes such as ocean temperature and circulation (e.g., Behrenfeld et al. 2006). Spaceborne radiometers such as SeaWiFS (McClain 2004) and MODIS (Esaias et al. 1998) provide a synoptic view of spatial and temporal changes in phytoplankton, either through measurements of near-surface concentrations of the phytoplankton pigment chlorophyll-*a* (Chl*a*; mg m^{-3}) or phytoplankton carbon (C_{phy}; mg m^{-3}). Measurements of Chl*a* contain information pertaining to both biomass and phytoplankton physiology, while C_{phy} is a direct measurement of phytoplankton biomass. C_{phy} and Chl*a* often covary, but departures from this covariance can indicate changes in the physiological or compositional characteristics of phytoplankton communities (Dierssen 2010; Geider et al. 1997; Siegel et al. 2013; Westberry et al. 2016).

In this report, we evaluate the global distribution of phytoplankton over the one-year period from October 2020 through September 2021 (the analysis year) using remotely sensed Chl*a* and C_{phy} measurements from the continuous 24-year record that combines observations of SeaWiFS (1997–2010) and MODIS on Aqua (MODIS-A, 2002–present). The MODIS-A daytime SST (°C) is also assessed over a consistent time period to provide context on the physical state of the oceans. The Chl*a* product was derived using the Ocean Color Index algorithm of Hu et al. (2012), while C_{phy} was derived from the particle backscattering coefficient, b_{bp}, at 443 nm (Generalized Inherent Optical Properties algorithm; Werdell et al. 2013) and a linear relationship between b_{bp} and C_{phy} as described in Graff et al. (2015). In merging the time series of SeaWiFS and MODIS-A, differences between the sensors were assessed over the overlapping period from 2003 through 2008, and a small bias correction (± 1.8e-3 mg m^{-3} in Chl*a*, ± 4.1e-5 m^{-1} in b_{bp}) was estimated and applied per instrument per variable to ensure continuity.

Variations in the two phytoplankton distribution metrics were evaluated by subtracting monthly climatological means for MODIS-A (October 2002–September 2020) from their monthly mean values of MODIS-A Chl*a* and C_{phy} in the analysis year. These monthly anomalies were then averaged to produce the global Chl*a* and C_{phy} annual mean anomaly maps (Figs. 3.23a,b). Similar calculations were performed on MODIS-A SST data to produce an equivalent SST annual mean anomaly for the same time period (Fig. 3.23c). The permanently stratified ocean (PSO), used for the analysis depicted in Figs. 3.24 and 3.25, is defined as the region, spanning the tropical and subtropical oceans, where annual average SST is greater than 15°C and surface mixed layers are typically low in nutrients and shallower than the nutricline (black lines near 40°N and 40°S in Fig. 3.23; Behrenfeld et al. 2006).

The Chl*a* anomaly distribution for this year (Fig. 3.23a) is characterized by strongly elevated Chla concentrations in a boomerang pattern centered on the western equatorial Pacific, with values exceeding 40% of the climatological mean. This band of elevated chlorophyll sits along the edge of the anomalously low SST waters in the equatorial Pacific (Fig. 3.23c), indicative of the prevailing La Niña conditions during 2021 (see section 4b). In contrast, large regions of anomalously low Chl*a* concentrations (–20%) are observed over much of the North and South Pacific and the southern reaches of the Atlantic, extending to the boundaries of the PSO and beyond. These regions are generally characterized by anomalously warm SST, elevated 0.6° to 0.8°C (Fig. 3.23c). Within the PSO, such positive SST anomalies typically correspond to a shallower surface mixed layer (Deser et al. 2010), which increases effective light exposure of the phytoplankton within that layer and leads to a physiological response of decreased cellular chlorophyll concentration (Behrenfeld et al. 2015). PSO regions are typically nutrient-depleted, leading to further decoupling

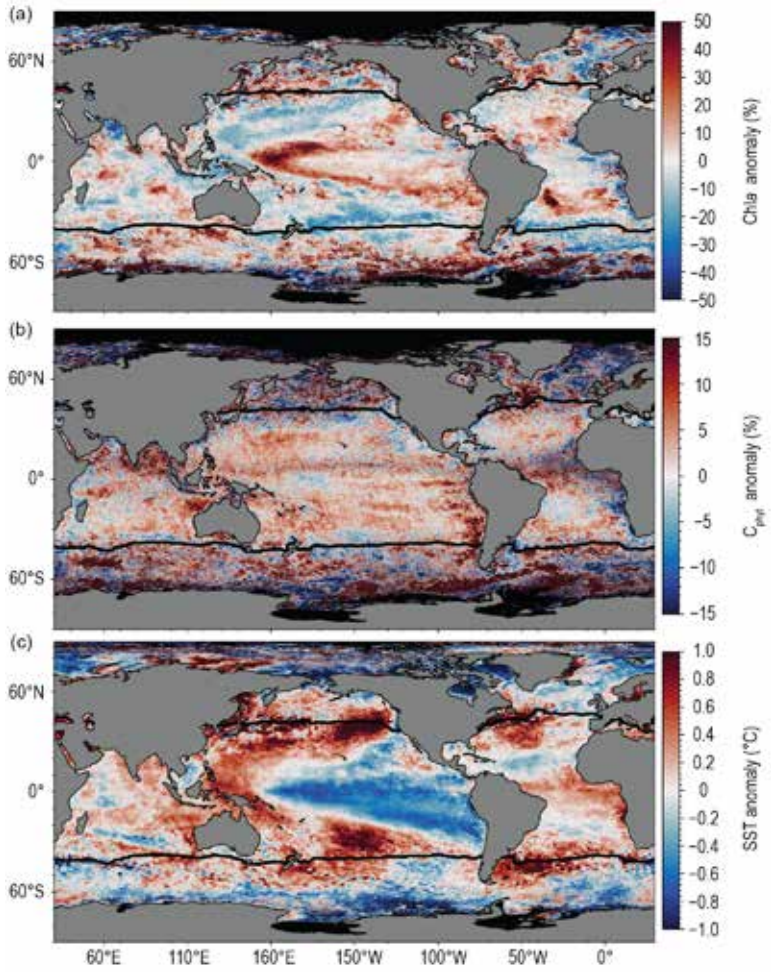

Fig. 3.23. Spatial distribution of average monthly (a) MODIS-A Chl*a* anomalies (%), (b) MODIS-A C_{phy} anomalies (%), and (c) MODIS-A SST anomalies (°C) for Oct 2020–Sep 2021, where monthly differences were derived relative to the MODIS-A 18-year climatological record (Oct 2002–Sep 2020). Chl*a* and C_{phy} are stated as % difference from climatology, while SST is shown as an absolute difference. Also shown in each panel is the location of the mean 15°C SST isotherm (black lines) delineating the permanently stratified ocean (PSO). Differences in the SST anomalies here versus in Fig. 3.1 are owing to differences in climatological periods, smoothing, and data sources.

of Chl*a* and C_{phy} anomalies in these warmer, stratified waters, as a result of further decreased cellular chlorophyll-to-carbon ratios (Westberry et al. 2016). Outside of the PSO, phytoplankton anomalies (Figs. 3.23a,b) showed greater spatial variability, including some large patches of highly elevated (> 50% in Chl*a*) phytoplankton biomass anomalies in the Southern Ocean, especially in the Pacific sector, as well as in the Labrador Sea (> 15 % in C_{phy}). In these higher-latitude, well-mixed waters, Chl*a* and C_{phy} anomalies generally covary, consistent with previous studies (e.g., Franz et al. 2021). The greater spatial variability typically observed poleward of the PSO is expected due to the episodic and intense nature of phytoplankton blooms in these regions, but the relatively poor spatial and temporal sampling at high latitudes due to clouds and low-light conditions also contributes to higher noise in the ocean color signal, thus limiting confidence in the interpretation of interannual changes.

Seasonal changes in phytoplankton biomass in the PSO typically display two annual peaks (Figs. 3.24a,b), reflecting vernal increases in biomass in the Northern (Figs. 3.24c,d) and Southern (Figs. 3.24 g,h) Hemispheres. Peaks in monthly climatological C_{phy} tend to lag peaks in Chl*a* by roughly two to three months, reflecting a reduction in phytoplankton chlorophyll-to-carbon ratios as the seasonal bloom progresses (e.g., Westberry et al. 2016). In 2021, the Northern Hemisphere Chl*a* peak occurred in March–April, followed by C_{phy} maximum in June (Fig. 3.24d), while the Southern Hemisphere peaks for Chl*a* and C_{phy} occurred in September–October and December,

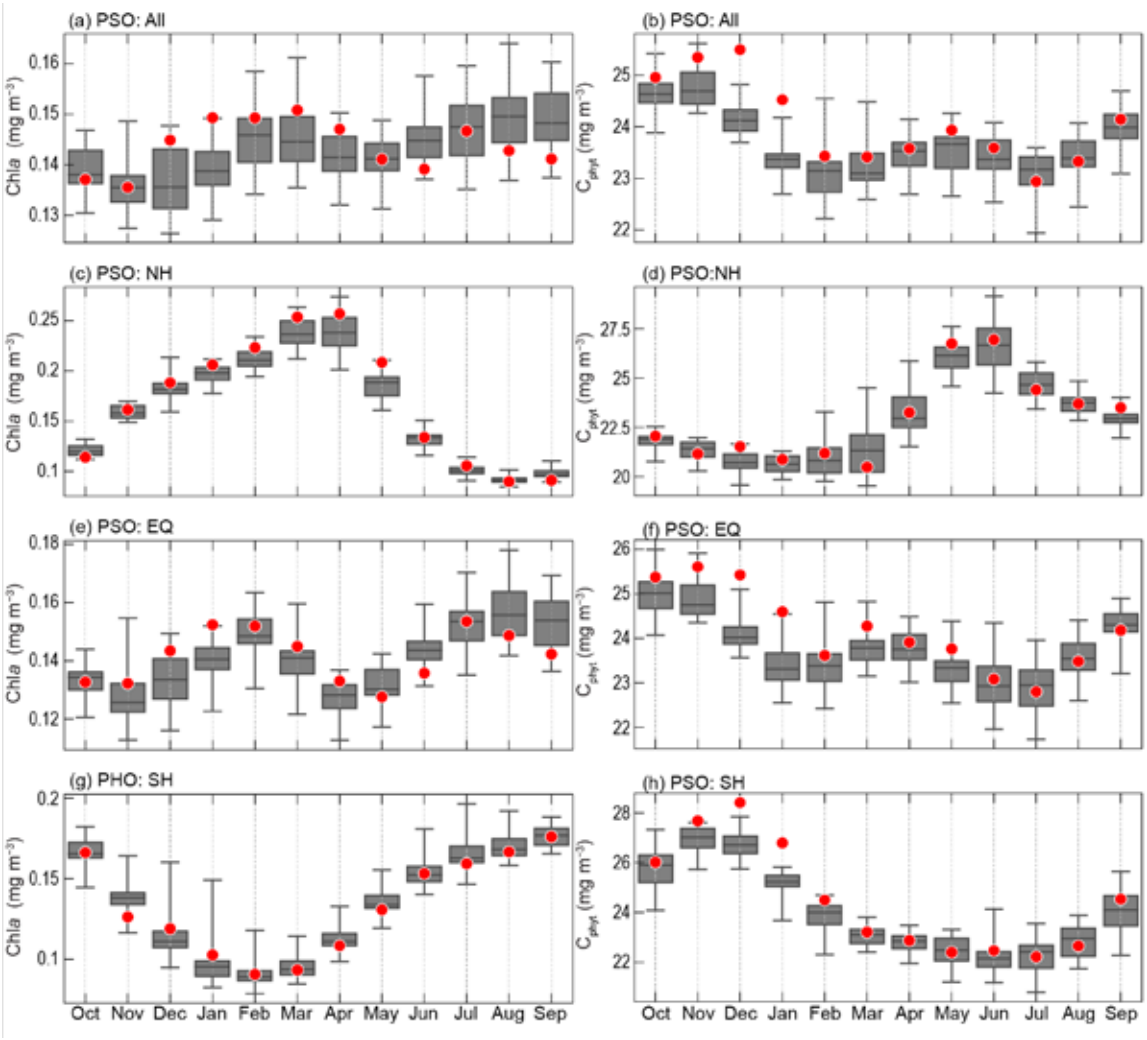

Fig. 3.24. Distribution of Oct 2020–Sep 2021 monthly means (red circles) for (a) MODIS-A Chl*a* and (b) MODIS-A C_{phy} for the permanently stratified ocean (PSO) region (see Fig. 3.23), superimposed on the climatological values as derived from the combined time series of SeaWiFS and MODIS-A over the 23-year period of 1998–2020. Gray boxes show the interquartile range of the climatology, with a black line for the median value and whiskers extending to minimum and maximum values. Subsequent panels show latitudinally segregated subsets of the PSO for the Northern Hemisphere (north of the tropics), NH (c),(d), tropical ±23.5° latitude subregion, EQ (e),(f), and Southern Hemisphere (south of the tropics), SH (g),(h). Units for (a), (c), (e), and (g) are Chl*a* (mg m^{-3}) and (b), (d), (f), and (h) are C_{phy} (mg m^{-3}).

respectively (Figs. 3.24g,h). Generally, monthly mean values of Chl*a* and C_{phy} fell within the range of climatological norms in both hemispheres, with the exception of anomalously high C_{phy} concentrations in the equatorial and Southern Hemisphere regions of the PSO, December to January. In 2021 the largest peak in Chl*a* for the global PSO (February–March) is driven by the vernal increase in the Northern Hemisphere and increased Chl*a* in the equatorial region. In contrast, the dominant peak in global PSO is typically associated with the trend in the Southern Hemisphere, which is the case for C_{phy} this year, but not for Chl*a*.

Over the 24-year time series of spatially averaged monthly mean Chl*a* within the PSO (Fig. 3.25a), concentrations vary by ±15% (±0.02 mg m^{-3}) around a long-term average of 0.142 mg m^{-3} (Fig. 3.25a). This variability includes significant seasonal cycles in Chl*a* distributions and responses to climatic events, as has been observed previously (e.g., Behrenfeld et al. 2006; Franz et al. 2021). C_{phy} over the same 24-year period varies by ±8% (±2 mg m^{-3}) around an average of 23.7 mg m^{-3} (Fig. 3.25c). Seasonal cycles in C_{phy} are more clearly defined than those of Chl*a*, consistent with the assertion that C_{phy} better represents variability of phytoplankton biomass, independent of the confounding influence of physiology.

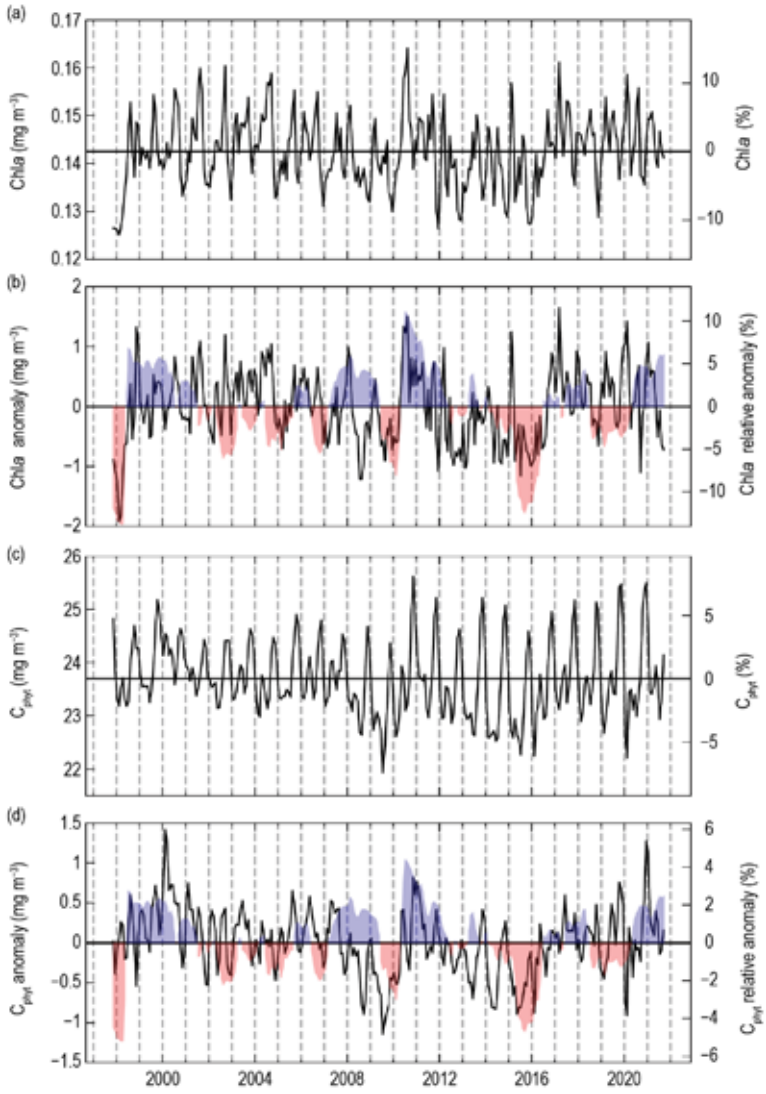

Fig. 3.25. 24-year, multi-mission record of Chl*a* (mg m^{-3}) and C_{phy} (mg m^{-3}) averaged over the PSO. (a) Monthly Chla, with the horizontal line indicating the multi-mission mean Chl*a* concentration for the entire PSO region. (b) Monthly Chl*a* anomalies after subtraction of the 23-year multi-mission climatological mean (Fig. 3.24a). Shaded blue and red colors show the Multivariate ENSO Index, inverted and scaled to match the range of the Chl*a* and C_{phy} anomalies, where blue indicates La Niña conditions and red indicate El Niño conditions.

Chl*a* monthly anomalies within the PSO (Fig. 3.25b) vary by as much as 10% (±0.015 mg m^{-3}) over the multi-mission time series, with the largest deviations generally associated with ENSO events (Pearson correlation coefficient, r = −0.37), as demonstrated by the correspondence of Chl*a* anomaly variations with the Multivariate ENSO Index (MEI; Wolter and Timlin 1998; presented in the inverse to illustrate the covariation). Over the analysis year, monthly Chl*a* anomalies within the PSO varied by ±7%, rising to a peak in January before falling to a minimum at the end of the analysis period. C_{phy} anomalies, which are slightly less correlated with MEI (r = −0.34) due to the inherent lag between environmental change and growth, also peaked in December–January at ~5% or 1.2 mg m^{-3}, reaching one of the highest positive values in our 24-year record (second only to the C_{phy} peak during the La Niña event of 2000). C_{phy} anomalies declined over the remainder of the year, but generally remained positive.

Through the continuous observation of ocean color, we are able to track variability in the global distribution of phytoplankton that drive biogeochemical processes, govern the role of the oceans in the global carbon cycle, and through their productivity exert a controlling influence on marine ecosystems, food webs, and fisheries. Subtle changes in Chl*a* and C_{phy} allow us to distinguish climate driven variability in phytoplankton biomass from changes in physiology and community response. Future satellite missions, such as the upcoming hyperspectral Plankton, Aerosol, Cloud, ocean Ecosystem (PACE) mission, should enable a more precise identification of phytoplankton absorption features (Werdell et al. 2019) and separation of those features from non-algal optical contributions (e.g., Pahlevan et al. 2021; Siegel et al. 2005), and thereby facilitate the assessment of changes in phytoplankton species or community composition (e.g., Kramer et al. 2022; Lange et al. 2020) that will further advance our ability to disentangle the impacts of climate forcing on global phytoplankton communities.

Acknowledgments

- Sandra Bigley provided invaluable editorial support for Chapter 3. Internal reviewers, external reviews, and report editors all provided comments that helped to improve the chapter.
- Argo data used in the chapter were collected and made freely available by the International Argo Program and the national programs that contribute to it. (https://argo.ucsd.edu, https://www.ocean-ops.org). The Argo Program is part of the Global Ocean Observing System. Many authors of the chapter are supported by NOAA Research, the NOAA Global Ocean Monitoring and Observing Program, or the NOAA Ocean Acidification Program.
- L. Cheng is supported by National Natural Science Foundation of China (42076202) and Strategic Priority Research Program of the Chinese Academy of Sciences (XDB42040402).
- R. E. Killick is supported by the Met Office Hadley Centre Climate Programme funded by BEIS and Defra. PMEL contribution numbers 5214, 5215, 5216, 5217, and 5247.

Appendix 1: Chapter 3 – Acronyms

ACC	Antarctic Circumpolar Current
AMOC	Atlantic meridional overturning circulation
AMHT	Atlantic meridional heat transport
BASS	Blended Analysis of Surface Salinity
C_{anth}	anthropogenic CO_2
CERES	Clouds and the Earth's Radiant Energy System
Chl*a*	chlorophyll-*a*
CO_2	carbon dioxide
COARE	Coupled Ocean-Atmosphere Response Experiment
C_{phy}	phytoplankton carbon
DJF	December–February
DOISST	Daily Optimum Interpolation SST version 2.1
E	evaporation
E–*P*	evaporation minus precipitation
EBAF	Energy Balanced and Filled
ENSO	El Niño–Southern Oscillation
ERSSTv5	Extended Reconstruction Sea Surface Temperature version 5
FC	Florida Current
FLASHFlux	Fast Longwave And Shortwave Radiative Fluxes
GMSL	global mean sea level
GPCP	Global Precipitation Climatology Project
GRACE	Gravity Recovery and Climate Experiment
GRACE-FO	Gravity Recovery and Climate Experiment Follow-On
HadSST	Hadley Centre SST
IO	Indian Ocean
IOD	Indian Ocean dipole
ITCZ	Intertropical Convergence Zone
JJA	June–August
LH	latent heat
LW	longwave
MAM	March–May
MEI	Multivariate ENSO Index
MHW	marine heat wave
MOC	meridional overturning circulation
MODIS	Moderate Resolution Imaging Spectroradiometer
MODIS-A	MODIS on *Aqua*
NAC	North Atlantic Current
NECC	North Equatorial Countercurrent
NH	Northern Hemisphere
NPG	North Pacific Gyre
NPP	net primary production
OAFlux	Objectively Analyzed air-sea Fluxes
OHCA	ocean heat content anomaly
OSNAP	Overturning in the Subpolar North Atlantic Program

P	precipitation
PACE	Plankton, Aerosol, Cloud, ocean Ecosystem
P–*E*	precipitation minus evaporation
ppm	parts per million
PSO	permanently stratified ocean
RAPID/MOCHA/WBTS	Rapid Climate Change/MOC and Heatflux Array/Western Boundary Time Series
SAMBA	South Atlantic MOC Basin-wide Array
SEC	South Equatorial Current
SH	sensible heat flux
SH	Southern Hemisphere
SMAP	Soil Moisture Active Passive
SMOS	Soil Moisture and Ocean Salinity
SOCAT	Surface Ocean CO_2 Atlas
SON	September–November
SPCZ	South Pacific Convergence Zone
SSM/I	Special Sensor Microwave/Imager
SSS	sea surface salinity
SST	sea surface temperature
SSTA	sea surface temperature anomaly
std. dev.	standard deviation
SW	shortwave
TRACOS	Tropical Atlantic Circulation and Overturning at 11°S
XBT	eXpendable BathyThermograph

References

Abraham, J. P., and Coauthors, 2013: A review of global ocean temperature observations: Implications for ocean heat content estimates and climate change. *Rev. Geophys.*, **51**, 450–483, https://doi.org/10.1002/rog.20022.

Adler, R. F., and Coauthors, 2018: The Global Precipitation Climatology Project (GPCP) monthly analysis (new version 2.3) and a review of 2017 global precipitation. *Atmosphere*, **9**, 138, https://doi.org/10.3390/atmos9040138.

Babcock, R. C., and Coauthors, 2019: Severe continental-scale impacts of climate change are happening now: Extreme climate events impact marine habitat forming communities along 45% of Australia's coast. *Front. Mar. Sci.*, **6**, 411, https://doi.org/10.3389/fmars.2019.00411

Balaguru, K., P. Chang, R. Saravanan, L. R. Leung, Z. Xu, M. Li, and J. S. Hsieh, 2012: Ocean barrier layers' effect on tropical cyclone intensification. *Proc. Natl. Acad. Sci. USA*, **109**, 142343–142347, https://doi.org/10.1073/pnas.1201364109.

Barnoud, A., and Coauthors, 2021: Contributions of altimetry and Argo to nonclosure of the global mean sea level budget since 2016. *Geophys. Res. Lett.*, **48**, e2021GL092824, https://doi.org/10.1029/2021GL092824.

Baumgartner, A., and E. Reichel, 1975: *The World Water Balance*, Elsevier, 179 pp.

Behrenfeld, M. J., and Coauthors, 2006: Climate-driven trends in contemporary ocean productivity. *Nature*, **444**, 752–755, https://doi.org/10.1038/nature05317.

——, and Coauthors, 2015: Revaluating ocean warming impacts on global phytoplankton. *Nat. Climate Change*, **6**, 323–330, https://doi.org/10.1038/nclimate2838.

Boyer, T. P., and Coauthors, 2018: *World Ocean Database 2018*. A.V. Mishonov, Ed., NOAA Atlas NESDIS 87, 207 pp.

Broecker, W. S., 1991: The Great Ocean Conveyor. *Oceanography*, **4**, 79–89, https://doi.org/10.5670/oceanog.1991.07.

Brown, J. R., and Coauthors, 2020: South Pacific convergence zone dynamics, variability and impacts in a changing climate. *Nat. Rev. Earth Environ.*, **1**, 530–543, https://doi.org/10.1038/s43017-020-0078-2.

Caesar, L., S. Rahmstorf, A. Robinson, G. Feulner, and V. Saba, 2018: Observed fingerprint of a weakening Atlantic Ocean overturning circulation. *Nature*, **556**, 191–196, https://doi.org/10.1038/s41586-018-0006-5.

Canadell, J. G., and Coauthors, 2021: Global carbon and other biogeochemical cycles and feedbacks. *Climate Change 2021: The Physical Science Basis*, V. Masson-Delmotte et al., Eds., Cambridge University Press, 673–816, https://doi.org/10.1017/9781009157896.007.

Carter, B. R., and Coauthors, 2017: Two decades of Pacific anthropogenic carbon storage and ocean acidification along Global 4 Ocean Ship-based Hydrographic Investigations Program sections P16 and P02. *Global Biogeochem. Cycles*, **31**, 306–327, https://doi.org/10.1002/2016GB005485.

——, and Coauthors, 2019: Pacific anthropogenic carbon between 1991 and 2017. Global Biogeochem. Cycles, 33, 102597–102617, https://doi.org/10.1029/2018GB006154.

Castro de la Guardia, L., X. Hu, and P. G. Myers, 2015: Potential positive feedback between Greenland Ice Sheet melt and Baffin Bay heat content on the west Greenland shelf. *Geophys. Res. Lett.*, **42**, 4922–4930, https://doi.org/10.1002/2015GL064626.

Chambers, D. P., A. Cazenave, N. Champollion, H. Dieng, W. Llovel, R. Forsberg, K. von Schuckmann, and Y. Wada, 2017: Evaluation of the global mean sea level budget between 1993 and 2014. *Surv. Geophys.*, **38**, 309–327, https://doi.org/10.1007/s10712-016-9381-3.

Chen, J., B. Tapley, C. Wilson, A. Cazenave, K. W. Seo, and J. S. Kim, 2020: Global ocean mass change from GRACE and GRACE follow-on and altimeter and Argo measurements. *Geophys. Res. Lett.*, **47**, e2020GL090656, https://doi.org/10.1029/2020GL090656.

Cheng, L., J. Zhu, R. Cowley, T. Boyer, and S. Wijffels, 2014: Time, probe type, and temperature variable bias corrections to historical expendable bathythermograph observations. *J. Atmos. Oceanic Technol.*, **31**, 1793–1825, https://doi.org/10.1175/JTECH-D-13-00197.1.

——, and Coauthors, 2020: Record-setting ocean warmth continued in 2019. *Adv. Atmos. Sci.*, **37**, 137–142, https://doi.org/10.1007/s00376-020-9283-7.

Deser, C., M. A. Alexander, S. P. Xie, and A. S. Phillips, 2010: Sea surface temperature variability: Patterns and mechanisms. *Annu. Rev. Mar. Sci.*, **2**, 115–143, https://doi.org/10.1146/annurev-marine-120408-151453.

DeVries, T., M. Holzer, and F. Primeau, 2017: Recent increase in oceanic carbon uptake driven by weaker upper-ocean overturning. *Nature*, **542**, 215–218, https://doi.org/10.1038/nature21068.

——, and Coauthors, 2019: Decadal trends in the ocean carbon sink. *Proc. Natl. Acad. Sci. USA*, **116**, 112646–112651, https://doi.org/10.1073/pnas.1900371116.

Dierssen, H. M., 2010: Perspectives on empirical approaches for ocean color remote sensing of chlorophyll in a changing climate. *Proc. Natl. Acad. Sci. USA*, **107**, 172073–172078, https://doi.org/10.1073/pnas.0913800107.

Dima, M., and G. Lohmann, 2010: Evidence for two distinct modes of large-scale ocean circulation changes over the last century. *J. Climate*, **23**, 5–16, https://doi.org/10.1175/2009JCLI2867.1.

Domingues, R., and Coauthors, 2015: Upper ocean response to Hurricane Gonzalo (2014): Salinity effects revealed by sustained and targeted observations from underwater gliders. *Geophys. Res. Lett.*, **42**, 7131–7138, https://doi.org/10.1002/2015GL065378.

——, M. Baringer, and G. Goni, 2016: Remote sources for year-to-year changes in the seasonality of the Florida Current transport. *J. Geophys. Res. Oceans*, **121**, 7547–7559, https://doi.org/10.1002/2016JC012070.

Dong, S., G. Goni, R. Domingues, F. Bringas, M. Goes, J. Christophersen, and M. Baringer, 2021: Synergy of in-situ and satellite ocean observations in determining meridional heat transport in the Atlantic Ocean. *J. Geophys. Res. Oceans*, **126**, e2020JC017073, https://doi.org/10.1029/2020JC017073.

——, D. L. Volkov, G. Goni, K. Pujiana, F. Tagklis, and M. Baringer, 2022: Remote impact of the equatorial Pacific on Florida Current transport. *Geophys. Res. Lett.*, **49**, e2021GL096944, https://doi.org/10.1029/2021GL096944.

Durack, P. J., and S. E. Wijffels, 2010: Fifty-year trends in global ocean salinities and their relationship to broad-scale warming. *J. Climate*, **23**, 4342–4362, https://doi.org/10.1175/2010JCLI3377.1.

——, ——, and R. J. Matear, 2012: Ocean salinities reveal strong global water cycle intensification during 1950 to 2000. *Science*, **336**, 455–458, https://doi.org/10.1126/science.1212222.

Edwards, T. L., and Coauthors, 2021: Projected land ice contributions to twenty-first-century sea level rise. *Nature*, **593**, 74–82, https://doi.org/10.1038/s41586-021-03302-y.

Esaias, W. E., and Coauthors, 1998: An overview of MODIS capabilities for ocean science observations. *IEEE Trans. Geosci. Remote Sens.*, **36**, 1250–1265, https://doi.org/10.1109/36.701076.

Eyring, V., S. Bony, G. A. Meehl, C. A. Senior, B. Stevens, R. J. Stouffer, and K. E. Taylor, 2016: Overview of the Coupled Model Intercomparison Project Phase 6 (CMIP6) experimental design and organization. *Geosci. Model Dev.*, **9**, 1937–1958, https://doi.org/10.5194/gmd-9-1937-2016.

Ezer, T., and L. P. Atkinson, 2014: Accelerated flooding along the U.S. East Coast: On the impact of sea-level rise, tides, storms, the Gulf Stream, and the North Atlantic Oscillations. *Earth's Future*, **2**, 362–382, https://doi.org/10.1002/2014EF000252.

Fairall, C. W., E. F. Bradley, J. E. Hare, A. A. Grachev, and J. B. Edson, 2003: Bulk parameterization of air–sea fluxes: Updates and verification for the COARE algorithm. *J. Climate*, **16**, 571–591, https://doi.org/10.1175/1520-0442(2003)016<0571:BPOASF>2.0.CO;2.

Fassbender, A. J., K. B. Rodgers, H. I. Palevsky, and C. L. Sabine, 2018: Seasonal asymmetry in the evolution of surface ocean pCO_2 and pH thermodynamic drivers and the influence on sea-air CO_2 flux. *Global Biogeochem. Cycles*, **32**, 1476–1497, https://doi.org/10.1029/2017GB005855.

Fasullo, J. T., and R. S. Nerem, 2018: Altimeter-era emergence of the patterns of forced sea-level rise in climate models and implications for the future. *Proc. Natl. Acad. Sci. USA*, **115**, 122944–122949, https://doi.org/10.1073/pnas.1813233115.

——, ——, and B. Hamlington, 2016: Is the detection of accelerated sea level rise imminent? *Sci. Rep.*, **6**, 31245, https://doi.org/10.1038/srep31245.

Feely, R. A., and Coauthors, 2012: Decadal changes in the aragonite and calcite saturation state of the Pacific Ocean. Global Biogeochem. Cycles, 26, 2011GB004157, https://doi.org/10.1029/2011GB004157.

Ffield, A., 2007: Amazon and Orinoco River plumes and NBC rings: Bystanders or participants in hurricane events? *J. Climate*, **20**, 316–333, https://doi.org/10.1175/JCLI3985.1.

Fofonoff, N. P., and E. L. Lewis, 1979: A practical salinity scale. *J. Oceanogr. Soc. Japan*, **35**, 63–64, https://doi.org/10.1007/BF02108283.

Font, J., and Coauthors, 2013: SMOS first data analysis for sea surface salinity determination. *Int. J. Remote Sens.*, **34**, 3654–3670, https://doi.org/10.1080/01431161.2012.716541.

Fore, A. G., S. H. Yueh, W. Q. Tang, B. W. Stiles, and A. K. Hayashi, 2016: Combined active/passive retrievals of ocean vector wind and sea surface salinity with SMAP. *IEEE Trans. Geosci. Remote Sens.*, **54**, 7396–7404, https://doi.org/10.1109/TGRS.2016.2601486.

Forster, P., and Coauthors, 2021: The Earth's energy budget, climate feedbacks, and climate sensitivity. *Climate Change 2021: The Physical Science Basis*, V. Masson-Delmotte et al., Eds., Cambridge University Press, 923–1054, https://doi.org/10.1017/9781009157896.009.

Fox-Kemper, B., and Coauthors, 2021a: Ocean, cryosphere and sea level change. *Climate Change 2021: The Physical Science Basis*, V. Masson-Delmotte et al. Eds., Cambridge University Press, 1211–1362, https://doi.org/10.1017/9781009157896.011.

——, and Coauthors, 2021b: Ocean, cryosphere and sea level change supplementary material. *Climate Change 2021: The Physical Science Basis*, V. Masson-Delmotte et al. Eds., Cambridge University Press, https://www.ipcc.ch/report/ar6/wg1/, in press.

Frajka-Williams, E., and Coauthors, 2019: Atlantic meridional overturning circulation: Observed transports and variability. *Front. Mar. Sci.*, **6**, 260, https://doi.org/10.3389/fmars.2019.00260.

——, B. I. Moat, D. A. Smeed, D. Rayner, W. E. Johns, M. O. Baringer, D. Volkov, and J. Collins, 2021: Atlantic meridional overturning circulation observed by the RAPID-MOCHA-WBTS (RAPID-Meridional Overturning Circulation and Heatflux Array-Western Boundary Time Series) array at 26N from 2004 to 2020 (v2020.1). British Oceanographic Data Centre, Natural Environment Research Council, accessed 2 December 2021, https://doi.org/10.5285/cc1e34b3-3385-662b-e053-6c86abc03444.

Franz, B. A., I. Cetinic, J. P. Scott, D. A. Siegel, and T. K. Westberry, 2021: Global ocean phytoplankton [in "State of the Climate in 2020"]. *Bull. Amer. Meteor. Soc.*, **102** (8), S179–S193, https://doi.org/10.1175/BAMS-D-21-0083.1.

Friedlingstein, P., and Coauthors, 2020: Global carbon budget 2020. *Earth Syst. Sci. Data*, **12**, 3269–3340, https://doi.org/10.5194/essd-12-3269-2020.

——, and Coauthors, 2022: Global carbon budget 2021. *Earth Syst. Sci. Data*, **14**, 1917–2005, https://doi.org/10.5194/essd-14-1917-2022.

Geider, R. J., H. L. MacIntyre, and T. M. Kana, 1997: Dynamic model of phytoplankton growth and acclimation: Responses of the balanced growth rate and the chlorophyll *a*:carbon ratio to light, nutrient limitation and temperature. *Mar. Ecol. Prog. Ser.*, **148**, 187–200, https://doi.org/10.3354/meps148187.

Gelderloos, R., F. Straneo, and C. A. Katsman, 2012: Mechanisms behind the temporary shutdown of deep convection in the Labrador Sea: Lessons from the great salinity anomaly years 1968–71. *J. Climate*, **25**, 6743–6755, https://doi.org/10.1175/JCLI-D-11-00549.1.

Goni, G. J., and W. E. Johns, 2003: Synoptic study of warm rings in the North Brazil Current retroflection region using satellite altimetry. *Interhemispheric Water Exchange in the Atlantic Ocean*, G. J. Goni, and P. Malanotte-Rizzoli, Eds., Elsevier Oceanography Series, Vol. 68, Elsevier, 335–356, https://doi.org/10.1016/S0422-9894(03)80153-8.

——, and Coauthors, 2009: Applications of satellite-derived ocean measurements to tropical cyclone intensity forecasting. *Oceanography*, **22**, 190–197, https://doi.org/10.5670/oceanog.2009.78.

——, F. Bringas, and P. N. Di Nezio, 2011: Observed low frequency variability of the Brazil Current front. *J. Geophys. Res.*, **116**, C10037, https://doi.org/10.1029/2011JC007198.

Good, S. A., M. J. Martin, and N. A. Rayner, 2013: EN4: Quality controlled ocean temperature and salinity profiles and monthly objective analyses with uncertainty estimates. *J. Geophys. Res. Atmos.*, **118**, 6704–6716, https://doi.org/10.1002/2013JC009067.

Gordon, A. L., 1986: Interocean exchange of thermocline water. *J. Geophys. Res.*, **91**, 5037–5046, https://doi.org/10.1029/JC091iC04p05037.

Gouretski, V., and L. Cheng, 2020: Correction for systematic errors in the global dataset of temperature profiles from mechanical bathythermographs. *J. Atmos. Oceanic Technol.*, **37**, 841–855, https://doi.org/10.1175/JTECH-D-19-0205.1.

Graff, J. R., and Coauthors, 2015: Analytical phytoplankton carbon measurements spanning diverse ecosystems. *Deep-Sea Res. I*, **102**, 16–25, https://doi.org/10.1016/j.dsr.2015.04.006.

Gruber, N., and Coauthors, 2019: The oceanic sink for anthropogenic CO_2 from 1994 to 2007. *Science*, **363**, 1193–1199, https://doi.org/10.1126/science.aau5153.

Hakuba, M. Z., T. Frederikse, and F. W. Landerer, 2021: Earth's energy imbalance from the ocean perspective (2005–2019). *Geophys. Res. Lett.*, **48**, e2021GL093624, https://doi.org/10.1029/2021GL093624.

Hamlington, B. D., J. T. Fasullo, R. S. Nerem, K. Kim, and F. W. Landerer, 2019: Uncovering the pattern of forced sea level rise in the satellite altimeter record. *Geophys. Res. Lett.*, **46**, 4844–4853, https://doi.org/10.1029/2018GL081386.

——, C. G. Piecuch, J. T. Reager, H. Chandanpurkar, T. Frederikse, R. S. Nerem, J. T. Fasullo, and S.-H. Cheon, 2020: Origin of interannual variability in global mean sea level. *Proc. Natl. Acad. Sci. USA*, **117**, 132983–132990, https://doi.org/10.1073/pnas.1922190117.

Han, W., G. A. Meehl, D. Stammer, A. Hu, B. Hamlington, J. Kenigson, H. Palanisamy, and P. Thompson, 2017: Spatial patterns of sea level variability associated with natural internal climate modes. *Surv. Geophys.*, **38**, 217–250, https://doi.org/10.1007/s10712-016-9386-y.

Held, I. M., and B. J. Soden, 2006: Robust responses of the hydrological cycle to global warming. J. Climate, 19, 5686–5699, https://doi.org/10.1175/JCLI3990.1

Hobbs, W. R., and J. K. Willis, 2012: Midlatitude North Atlantic heat transport: A time series based on satellite and drifter data. J. Geophys. Res., 117, C01008, https://doi.org/10.1029/2011JC007039.

Holte, J., L. D. Talley, J. Gilson, and D. Roemmich, 2017: An Argo mixed layer climatology and database. *Geophys. Res. Lett.*, **44**, 5618–5626, https://doi.org/10.1002/2017GL073426.

Hu, C., Z. Lee, and B. A. Franz, 2012: Chlorophyll a algorithms for oligotrophic oceans: A novel approach based on three-band reflectance difference. *J. Geophys. Res.*, **117**, C01011, https://doi.org/10.1029/2011JC007395.

Hu, Z.-Z., A. Kumar, Y. Xue, and B. Jha, 2014: Why were some La Niñas followed by another La Niña? *Climate Dyn.*, **42**, 1029–1042, https://doi.org/10.1007/s00382-013-1917-3.

Huang, B., and Coauthors, 2015: Extended Reconstructed Sea Surface Temperature version 4 (ERSST.v4), Part I. Upgrades and intercomparisons. *J. Climate*, **28**, 911–930, https://doi.org/10.1175/JCLI-D-14-00006.1.

——, and Coauthors, 2017: Extended Reconstructed Sea Surface Temperature version 5 (ERSSTv5), upgrades, validations, and intercomparisons. *J. Climate*, **30**, 8179–8205, https://doi.org/10.1175/JCLI-D-16-0836.1.

——, and Coauthors, 2020: Uncertainty estimates for sea surface temperature and land surface air temperature in NOAAGlobalTemp version 5. *J. Climate*, **33**, 1351–1379, https://doi.org/10.1175/JCLI-D-19-0395.1.

——, C. Liu, V. Banzon, E. Freeman, G. Graham, B. Hankins, T. Smith, and H.-M. Zhang, 2021a: Improvements of the daily optimum interpolation sea surface temperature (DOISST) version 2.1. *J. Climate*, **34**, 2923–2939, https://doi.org/10.1175/JCLI-D-20-0166.1.

——, Z. Wang, X. Yin, A. Arguez, G. Graham, C. Liu, T. Smith, H.-M. Zhang, 2021b: Prolonged marine heatwaves in the Arctic: 1982–2020. *Geophys. Res. Lett.*, **48**, e2021GL095590, https://doi.org/10.1029/2021GL095590.

IPCC, 2013: *Climate Change 2013: The Physical Science Basis*. T. F. Stocker et al., Eds., Cambridge University Press, 1535 pp.

——, 2018: *Global Warming of 1.5°C*. V. Masson-Delmotte et al., Eds., IPCC, 616 pp., https://www.ipcc.ch/sr15/.

——, 2019: *IPCC Special Report on the Ocean and Cryosphere in a Changing Climate*, H.-O. Pörtner et al. Eds., IPCC, 755 pp., https://www.ipcc.ch/srocc/.

——, 2021: *Climate Change 2021: The Physical Science Basis*. V. Masson-Delmotte et al., Eds., Cambridge University Press, 3949 pp., https://doi.org/10.1017/9781009157896.

Ishii, M., Y. Fukuda, S. Hirahara, S. Yasui, T. Suzuki, and K. Sato, 2017: Accuracy of global upper ocean heat content estimation expected from present observational datasets. *SOLA*, **13**, 163–167, https://doi.org/10.2151/sola.2017-030.

——, and Coauthors, 2020: Ocean acidification from below in the tropical Pacific. Global Biogeochem. Cycles, 34, e2019GB006368, https://doi.org/10.1029/2019GB006368.

Jiang, L.-Q., B. R. Carter, R. A. Feely, S. K. Lauvset, and A. Olsen, 2019: Surface ocean pH and buffer capacity: Past, present and future. *Sci. Rep.*, **9**, 18624, https://doi.org/10.1038/s41598-019-55039-4.

Johnson, G. C., and J. M. Lyman, 2012: Sea surface salinity [in "State of the Climate in 2011"]. Bull. Amer. Meteor. Soc., 93 (7), S68–S69, https://doi.org/10.1175/2012BAMSStateoftheClimate.1.

——, and ——, 2020: Warming trends increasingly dominate Global Ocean. *Nat. Climate Change*, **10**, 757–761, https://doi.org/10.1038/s41558-020-0822-0.

——, ——, J. K. Willis, T. Boyer, J. Antonov, S. A. Good, C. M. Domingues, and N. Bindoff, 2014: Ocean heat content [in "State of the Climate in 2013"]. *Bull. Amer. Meteor. Soc.*, **95** (7), S54–S57, https://doi.org/10.1175/2014BAMSStateoftheClimate.1.

——, and Coauthors, 2015: Ocean heat content [in "State of the Climate in 2014"]. Bull. Amer. Meteor. Soc., 96 (7), S64–S66, https://doi.org/10.1175/2015BAMSStateoftheClimate.1.

——, and Coauthors, 2021: Ocean heat content [in "State of the Climate in 2020"]. *Bull. Amer. Meteor. Soc.*, **102** (8), S156–S159, https://doi.org/10.1175/BAMS-D-21-0083.1.

Josey, S. A., and Coauthors, 2018: The recent Atlantic cold anomaly: Causes, consequences, and related phenomena. *Annu. Rev. Mar. Sci.*, **10**, 475–501, https://doi.org/10.1146/annurev-marine-121916-063102.

Kato, S., and Coauthors, 2018: Surface irradiances of edition 4.0 clouds and the Earth's Radiant Energy System (CERES) energy balanced and filled (EBAF) data product. J. Climate, 31, 4501–4527, https://doi.org/10.1175/JCLI-D-17-0523.1.

Kennedy, J. J., 2013: A review of uncertainty in in situ measurements and data sets of sea-surface temperature. *Rev. Geophys.*, **51**, 1–32, https://doi.org/10.1002/2013RG000434.

——, N. A. Rayner, C. P. Atkinson, and R. E. Killick, 2019: An ensemble data set of sea surface temperature change from 1850: The Met Office Hadley Centre HadSST.4.0.0.0 data set. *J. Geophys. Res. Atmos.*, **124**, 7719–7763, https://doi.org/10.1029/2018JD029867.

Kent, E. C., and Coauthors, 2017: A call for new approaches to quantifying biases in observations of sea surface temperature. *Bull. Amer. Meteor. Soc.*, **98**, 1601–1616, https://doi.org/10.1175/BAMS-D-15-00251.1.

Kersalé, M., and Coauthors, 2021: Multi-year estimates of daily heat transport by the Atlantic meridional overturning circulation at 34.5°S. J. Geophys. Res. Oceans, 126, e2020JC016947, https://doi.org/10.1029/2020JC016947.

Kramer, S. J., D. A. Siegel, S. Maritorena, and D. Catlett, 2022: Modeling surface ocean phytoplankton pigments from hyperspectral remote sensing reflectance on global scales. *Remote Sens. Environ.*, **270**, 112879, https://doi.org/10.1016/j.rse.2021.112879.

Landschützer, P., N. Gruber, D. C. E. Bakker, I. Stemmler, and K. D. Six, 2018: Strengthening seasonal marine CO_2 variations due to increasing atmospheric CO_2. *Nat. Climate Change*, **8**, 146–150, https://doi.org/10.1038/s41558-017-0057-x.

Lange, P. K., and Coauthors, 2020: Radiometric approach for the detection of picophytoplankton assemblages across oceanic fronts. *Opt. Express*, **28**, 252682–252705, https://doi.org/10.1364/OE.398127.

Laufkötter, C., J. Zscheischler, and T. L. Frölicher, 2020: High-impact marine heatwaves attributable to human-induced global warming. *Science*, **369**, 1621–1625, https://doi.org/10.1126/science.aba0690.

Le Quéré, C., and Coauthors, 2007: Saturation of the Southern Ocean CO_2 sink due to recent climate change. *Science*, **316**, 1735–1738, https://doi.org/10.1126/science.1136188.

Leuliette, E. W., and J. K. Willis, 2011: Balancing the sea level budget. *Oceanography*, **24**, 122–129, https://doi.org/10.5670/oceanog.2011.32.

Le Vine, D. M., E. P. Dinnat, G. S. E. Lagerloef, P. de Matthaeis, S. Abraham, C. Utku, and H. Kao, 2014: Aquarius: Status and recent results. *Radio Sci.*, **49**, 709–720, https://doi.org/10.1002/2014RS005505.

Levitus, S., and Coauthors, 2012: World ocean heat content and thermosteric sea level change (0–2000 m), 1955–2010. *Geophys. Res. Lett.*, **39**, L10603, https://doi.org/10.1029/2012GL051106.

Li, F., and Coauthors, 2021a: Subpolar North Atlantic western boundary density anomalies and the meridional overturning circulation. *Nat. Commun.*, **12**, 3002, https://doi.org/10.1038/s41467-021-23350-2.

——, and Coauthors, 2021b: Observation-based estimates of heat and freshwater exchanges from the subtropical North Atlantic to the Arctic. *Prog. Oceanogr.*, **197**, 102640, https://doi.org/10.1016/j.pocean.2021.102640.

Li, X., Z.-Z. Hu, and B. Huang, 2020: Subannual to interannual variabilities of SST in the North Atlantic Ocean. *J. Climate*, **33**, 5547–5564, https://doi.org/10.1175/JCLI-D-19-0556.1.

——, ——, Y.-H. Tseng, Y. Liu, and P. Liang, 2022: A historical perspective of the La Niña event in 2020/21. *J. Geophys. Res. Atmos.*, 127, e2021JD035546, https://doi.org/10.1029/2021JD035546.

Llovel, W., and L. Terray, 2016: Observed southern upper-ocean warming over 2005–2014 and associated mechanisms. *Environ. Res. Lett.*, **11**, 124023, https://doi.org/10.1088/1748-9326/11/12/124023.

Loeb, N. G., and Coauthors, 2018: Clouds and the Earth's Radiant Energy System (CERES) Energy Balanced and Filled (EBAF) Top-of-Atmosphere (TOA) edition-4.0 data product. *J. Climate*, **31**, 895–918, https://doi.org/10.1175/JCLI-D-17-0208.1.

——, G. C. Johnson, T. J. Thorsen, J. M. Lyman, F. G. Rose, and S. Kato, 2021: Satellite and ocean data reveal marked increase in Earth's heating rate. *Geophys. Res. Lett.*, **48**, e2021GL093047, https://doi.org/10.1029/2021GL093047.

Lozier, M. S., and Coauthors, 2017: Overturning in the subpolar North Atlantic program: A new international ocean observing system. *Bull. Amer. Meteor. Soc.*, **98**, 737–752, https://doi.org/10.1175/BAMS-D-16-0057.1.

——, and Coauthors, 2019: A sea change in our view of overturning in the subpolar North Atlantic. *Science*, **363**, 516–521, https://doi.org/10.1126/science.aau6592.

Lumpkin, R., and S. L. Garzoli, 2005: Near-surface circulation in the tropical Atlantic Ocean. *Deep-Sea Res. I*, **52**, 495–518, https://doi.org/10.1016/j.dsr.2004.09.001.

——, and ——, 2011: Interannual to decadal changes in the western South Atlantic's surface circulation. *J. Geophys. Res.*, **116**, C01014, https://doi.org/10.1029/2010JC006285.

——, G. Goni, and K. Dohan, 2012: Surface currents [in "State of the Climate in 2011"]. Bull. Amer. Meteor. Soc., 93 (7), S75–S78, https://doi.org/10.1175/2012BAMSStateoftheClimate.1.

Lyman, J. M., and G. C. Johnson, 2014: Estimating global ocean heat content changes in the upper 1800 m since 1950 and the influence of climatology choice. *J. Climate*, **27**, 1946–1958, https://doi.org/10.1175/JCLI-D-12-00752.1.

Mantua, N. J., and S. R. Hare, 2002: The Pacific decadal oscillation. *J. Oceanogr.*, **58**, 35–44, https://doi.org/10.1023/A:1015820616384.

Marti, F., and Coauthors, 2022: Monitoring the ocean heat content change and the Earth energy imbalance from space altimetry and space gravimetry. *Earth Syst. Sci. Data*, **14**, 229–249, https://doi.org/10.5194/essd-14-229-2022.

McCarthy, G., and Coauthors, 2012: Observed interannual variability of the Atlantic Meridional Overturning Circulation at 26.5°N. *Geophys. Res. Lett.*, **39**, L19609, https://doi.org/10.1029/2012GL052933.

McClain, C. R., C. R. McClain, G. C. Feldman, and S. B. Hooker, 2004: An overview of the SeaWiFS Project and strategies for producing a climate research quality global ocean bio-optical time series. *Deep-Sea Res. II*, **51**, 5–42, https://doi.org/10.1016/j.dsr2.2003.11.001.

McKinley, G. A., A. R. Fay, Y. A. Eddebbar, L. Gloege, and N. S. Lovenduski, 2020: External forcing explains recent decadal variability of the ocean carbon sink. AGU Adv., 1, e2019AV000149, https://doi.org/10.1029/2019AV000149.

Merrifield, M., 2011: A shift in western tropical Pacific sea level trends during the 1990s. *J. Climate*, **24**, 4126–4138, https://doi.org/10.1175/2011JCLI3932.1.

Nerem, R. S., B. D. Beckley, J. T. Fasullo, B. D. Hamlington, D. Masters, and G. T. Mitchum, 2018: Climate-change-driven accelerated sea-level rise detected in the altimeter era. *Proc. Natl. Acad. Sci. USA*, **115**, 2022–2025, https://doi.org/10.1073/pnas.1717312115.

Okumura, Y. M., and C. Deser, 2010: Asymmetry in the duration of El Niño and La Niña. *J. Climate*, **23**, 5826–5843, https://doi.org/10.1175/2010JCLI3592.1.

Olafsson, J., S. R. Olafsdottir, A. Benoit-Cattin, M. Danielsen, T. S. Arnarson, and T. Takahashi, 2009: Rate of Iceland Sea acidification from time series measurements. *Biogeosciences*, **6**, 2661–2668, https://doi.org/10.5194/bg-6-2661-2009.

Oliver, E. C., J. A. Benthuysen, N. L. Bindoff, A. J. Hobday, N. J. Holbrook, C. N. Mundy, and S. E. Perkins-Kirkpatrick, 2017: The unprecedented 2015/16 Tasman Sea marine heatwave. *Nat. Commun.*, **8**, 16101, https://doi.org/10.1038/ncomms16101.

Pahlevan, N., B. Smith, C. Binding, D. Gurlin, L. Li, M. Bresciani, and C. Giardino, 2021: Hyperspectral retrievals of phytoplankton absorption and chlorophyll-a in inland and nearshore coastal waters. *Remote Sens. Environ.*, **253**, 112200, https://doi.org/10.1016/j.rse.2020.112200.

Palmer, M. D., K. Haines, S. F. B. Tett, and T. J. Ansell, 2007: Isolating the signal of ocean global warming. *Geophys. Res. Lett.*, **34**, L23610, https://doi.org/10.1029/2007GL031712.

——, G. R. Harris, and J. M. Gregory, 2018: Extending CMIP5 projections of global mean temperature change and sea level rise due to thermal expansion using a physically-based emulator. *Environ. Res. Lett.*, **13**, 084003, https://doi.org/10.1088/1748-9326/aad2e4.

Perez, F. F., and Coauthors, 2018: Meridional overturning circulation conveys fast acidification to the deep Atlantic Ocean. *Nature*, **554**, 515–518, https://doi.org/10.1038/nature25493.

Perkins-Kirkpatrick, S. E., A. D. King, E. A. Cougnon, N. J. Holbrook, M. R. Grose, E. C. J. Oliver, S. C. Lewis, and F. Pourasghar, 2019: The role of natural variability and anthropogenic climate change in the 2017/18 Tasman Sea marine heatwave. *Bull. Amer. Meteor. Soc.*, **100**, S105–S110, https://doi.org/10.1175/BAMS-D-18-0116.1.

Purkey, S. G., and G. C. Johnson, 2010: Warming of global abyssal and deep Southern Ocean waters between the 1990s and 2000s: Contributions to global heat and sea level rise budgets. *J. Climate*, **23**, 6336–6351, https://doi.org/10.1175/2010JCLI3682.1.

Reagan, J., T. Boyer, C. Schmid, and R. Locarnini, 2020: Subsurface salinity [in "State of the Climate in 2019"]. *Bull. Amer. Meteor. Soc.*, **101** (8), S144–S148, https://doi.org/10.1175/2020BAMSStateoftheClimate.1.

——, ——, ——, and ——, 2021: Subsurface salinity [in "State of the Climate in 2020"]. *Bull. Amer. Meteor. Soc.*, **102** (8), S162–S164, https://doi.org/10.1175/BAMS-D-21-0083.1.

Ren, L., K. Speer, and E. P. Chassignet, 2011: The mixed layer salinity budget and sea ice in the Southern Ocean. *J. Geophys. Res.*, **116**, C08031, https://doi.org/10.1029/2010JC006634.

Ríos, A. F., and Coauthors, 2015: Decadal acidification in the water masses of the Atlantic Ocean. *Proc. Natl. Acad. Sci. USA*, **112**, 9950–9955, https://doi.org/10.1073/pnas.1504613112.

Riser, S. C., and Coauthors, 2016: Fifteen years of ocean observations with the global Argo array. *Nat. Climate Change*, **6**, 145–153, https://doi.org/10.1038/nclimate2872.

Rodgers, K. B., and Coauthors, 2020: Reemergence of anthropogenic carbon into the ocean's mixed layer strongly amplifies transient climate sensitivity. *Geophys. Res. Lett.*, **47**, e2020GL089275, https://doi.org/10.1029/2020GL089275.

Roemmich, D., and J. Gilson, 2009: The 2004–2008 mean and annual cycle of temperature, salinity, and steric height in the global ocean from the Argo Program. *Prog. Oceanogr.*, **82**, 81–100, https://doi.org/10.1016/j.pocean.2009.03.004.

——, and Coauthors, 2019: On the future of Argo: A global, full-depth, multi-disciplinary array. *Front. Mar. Sci.*, **6**, 439, https://doi.org/10.3389/fmars.2019.00439.

Saji, N. H., B. N. Goswami, P. N. Vinayachandran, and T. Yamagata, 1999: A dipole mode in the tropical Indian Ocean. *Nature*, **401**, 360–363, https://doi.org/10.1038/43854.

Sasano, D., Y. Takatani, N. Kosugi, T. Nakano, T. Midorikawa, and M. Ishii, 2015: Multidecadal trends of oxygen and their controlling factors in the western North Pacific. *Global Biogeochem. Cycles*, **29**, 935–956, https://doi.org/10.1002/2014GB005065.

Scannell, H. A., G. C. Johnson, L. Thompson, J. M. Lyman, and S. C. Riser, 2020: Subsurface evolution and persistence of marine heatwaves in the Northeast Pacific. *Geophys. Res. Lett.*, **47**, e2020GL090548, https://doi.org/10.1029/2020GL090548.

Schlesinger, M. E., and N. Ramankutty, 1994: An oscillation in the global climate system of period 65–70 years. *Nature*, **367**, 723–726, https://doi.org/10.1038/367723a0.

Schmidtko, S., K. J. Heywood, A. F. Thompson, and S. Aoki, 2014: Multidecadal warming of Antarctic waters. *Science*, **346**, 1227–1231, https://doi.org/10.1126/science.1256117.

Schmitt, R. W., 1995: The ocean component of the global water cycle. *Rev. Geophys.*, **33**, 1395–1409, https://doi.org/10.1029/95RG00184.

Sherwood, S. C., and Coauthors, 2020: An assessment of Earth's climate sensitivity using multiple lines of evidence. Rev. Geophys., 58, e2019RG000678, https://doi.org/10.1029/2019RG000678.

Siegel, D. A., S. Maritorena, N. B. Nelson, M. J. Behrenfeld, and C. R. McClain, 2005: Colored dissolved organic matter and its influence on the satellite-based characterization of the ocean biosphere. *Geophys. Res. Lett.*, **32**, L20605, https://doi.org/10.1029/2005GL024310.

——, and Coauthors, 2013: Regional to global assessments of phytoplankton dynamics from the SeaWiFS mission. *Remote Sens. Environ.*, **135**, 77–91, https://doi.org/10.1016/j.rse.2013.03.025.

Skliris, N., R. Marsh, S. A. Josey, S. A. Good, C. Liu, and R. P. Allan, 2014: Salinity changes in the World Ocean since 1950 in relation to changing surface freshwater flux. *Climate Dyn.*, **43**, 709–736, https://doi.org/10.1007/s00382-014-2131-7.

——, J. D. Zika, G. Nurser, S. A. Josey, and R. Marsh, 2016: Global water cycle amplifying at less than the Clausius-Clapeyron rate. *Sci. Rep.*, **6**, 38752, https://doi.org/10.1038/srep38752.

Smeed, D. A., and Coauthors, 2014: Observed decline of the Atlantic meridional overturning circulation 2004–2012. *Ocean Sci.*, **10**, 29–38, https://doi.org/10.5194/os-10-29-2014.

——, and Coauthors, 2018: The North Atlantic Ocean is in a state of reduced overturning. *Geophys. Res. Lett.*, **45**, 1527–1533, https://doi.org/10.1002/2017GL076350.

Smith, C., Z. R. J. Nicholls, K. Armour, W. Collins, P. Forster, M. Meinshausen, M. D. Palmer, and M. Watanabe, 2021: The Earth's energy budget, climate feedbacks, and climate sensitivity supplementary material. *Climate Change 2021: The Physical Science Basis*, V. Masson-Delmotte et al., Eds., Cambridge University Press, https://www.ipcc.ch/report/ar6/wg1/, in press.

Smith, R. S., and J. M. Gregory, 2009: A study of the sensitivity of ocean overturning circulation and climate to freshwater input in different regions of the North Atlantic. *Geophys. Res. Lett.*, **36**, L15701, https://doi.org/10.1029/2009GL038607.

Stackhouse, P. W., D. P. Kratz, G. R. McGarragh, S. K. Gupta, and E. B. Geier, 2006: Fast Longwave and Shortwave Flux (FLASHFlux) products from CERES and MODIS measurements. *12th Conf. on Atmospheric Radiation*, Amer. Meteor. Soc., Madison, WI, P1.10, https://ams.confex.com/ams/Madison2006/techprogram/paper_113479.htm.

Stouffer, R. J., and Coauthors, 2006: Investigating the causes of the response of the thermohaline circulation to past and future climate changes. *J. Climate*, **19**, 1365–1387, https://doi.org/10.1175/JCLI3689.1.

Sun, C., and Coauthors, 2010: The data management system for the global temperature and salinity profile programme. *Proc. OceanObs'09: Sustained Ocean Observations and Information for Society*, Vol. 2, J. Hall, D. E. Harrison, and D. Stammer, Eds., ESA Publ.WPP-306, https://doi.org/10.5270/OceanObs09.cwp.86.

Sweet, W.V., J. Park, J. J. Marra, C. Zervas, and S. Gill, 2014: Sea level rise and nuisance flood frequency changes around the United States. NOAA Tech. Rep. NOS CO-OPS 073, 58 pp., https://tidesandcurrents.noaa.gov/publications/NOAA_Technical_Report_NOS_COOPS_073.pdf.

Volkov, D. L., S.-K. Lee, F. W. Landerer, and R. Lumpkin, 2017: Decade-long deep-ocean warming detected in the subtropical South Pacific. *Geophys. Res. Lett.*, **44**, 927–936, https://doi.org/10.1002/2016GL071661.

——, R. Domingues, C. S. Meinen, R. Garcia, M. Baringer, G. Goni, and R. H. Smith, 2020: Inferring Florida current volume transport from satellite altimetry. J. Geophys. Res. Oceans, 125, e2020JC016763, https://doi.org/10.1029/2020JC016763.

——, and Coauthors, 2021: Meridional overturning circulation and heat transport in the Atlantic Ocean [in "State of the Climate in 2020"]. *Bull. Amer. Meteor. Soc.*, **102** (8), S176–S179, https://doi.org/10.1175/BAMS-D-21-0083.1.

von Schuckmann, K., J.-B. Sallée, D. Chambers, P.-Y. Le Traon, C. Cabanes, F. Gaillard, S. Speich, and M. Hamon, 2014: Consistency of the current global ocean observing systems from an Argo perspective. *Ocean Sci.*, **10**, 547–557, https://doi.org/10.5194/os-10-547-2014.

Von Storch, H., and F. W. Zwiers, 1999: *Statistical Analysis in Climate Research*. Cambridge University Press, 484 pp..

Wang, J., and B. Yang, 2017: Internal and external forcing of multidecadal Atlantic climate variability over the past 1,200 years. *Nat. Geosci.*, **10**, 512–517, https://doi.org/10.1038/ngeo2962.

Werdell, P. J., and Coauthors, 2013: Generalized ocean color inversion model for retrieving marine inherent optical properties. *Appl. Opt.*, **52**, 2019–2037, https://doi.org/10.1364/AO.52.002019.

——, and Coauthors, 2019: The Plankton, Aerosol, Cloud, Ocean Ecosystem mission: Status, science, advances. *Bull. Amer. Meteor. Soc.*, **100**, 1775–1794, https://doi.org/10.1175/BAMS-D-18-0056.1.

Westberry, T. K., and Coauthors, 2016: Annual cycles of phytoplankton biomass in the subarctic Atlantic and Pacific Ocean. *Global Biogeochem. Cycles*, **30**, 175–190, https://doi.org/10.1002/2015GB005276.

Willis, J. K., 2010: Can in situ floats and satellite altimeters detect long-term changes in Atlantic Ocean overturning? *Geophys. Res. Lett.*, **37**, L06602, https://doi.org/10.1029/2010GL042372.

——, D. Roemmich, and B. Cornuelle, 2004: Interannual variability in upper ocean heat content, temperature, and thermosteric expansion on global scales. *J. Geophys. Res.*, **109**, C12036, https://doi.org/10.1029/2003JC002260.

Wolter, K., and M. S. Timlin, 1998: Measuring the strength of ENSO events: How does 1997/98 rank? *Weather*, **53**, 315–324, https://doi.org/10.1002/j.1477-8696.1998.tb06408.x.

Wu, L. X., and Coauthors, 2012: Enhanced warming over the global subtropical western boundary currents. *Nat. Climate Change*, **2**, 161–166, https://doi.org/10.1038/nclimate1353.

Wüst, G., 1936: Oberflächensalzgehalt, Verdunstung und Niederschlag auf dem Weltmeere. *Länderkundliche Forschung: Festschrift zur Vollendung des sechzigsten Lebensjahres Norbert Krebs*, J. Engelhorns Nachfahren, 347–359.

Xie, P., and Coauthors, 2014: An in situ-satellite blended analysis of global sea surface salinity. *J. Geophys. Res. Oceans*, **119**, 6140–6160, https://doi.org/10.1002/2014JC010046.

Yang, H., G. Lohmann, W. Wei, M. Dima, M. Ionita, and J. Liu, 2016: Intensification and poleward shift of subtropical western boundary currents in a warming climate. *J. Geophys. Res. Oceans*, **121**, 4928–4945, https://doi.org/10.1002/2015JC011513.

Yu, L., 2011: A global relationship between the ocean water cycle and near-surface salinity. *J. Geophys. Res.*, **116**, C10025, https://doi.org/10.1029/2010JC006937.

——, and R. A. Weller, 2007: Objectively analyzed air–sea heat fluxes for the global ice-free oceans (1981–2005). *Bull. Amer. Meteor. Soc.*, **88**, 527–540, https://doi.org/10.1175/BAMS-88-4-527.

Zebiak, S. E., 1993: Air-sea interaction in the equatorial Atlantic region. *J. Climate*, **6**, 1567–1568, https://doi.org/10.1175/1520-0442(1993)006<1567:AIITEA>2.0.CO;2.

Zhang, R., and Coauthors, 2019: A review of the role of the Atlantic meridional overturning circulation in Atlantic multidecadal variability and associated climate impacts. *Rev. Geophys.*, **57**, 316–375, https://doi.org/10.1029/2019RG000644.

Zweng, M. M., and Coauthors, 2018: *Salinity. Vol. 2, World Ocean Atlas 2018*, NOAA Atlas NESDIS 82, 50 pp., https://data.nodc.noaa.gov/woa/WOA18/DOC/woa18_vol2.pdf.

STATE OF THE CLIMATE IN 2021

THE TROPICS

H. J. Diamond and C. J. Schreck, Eds.

Special Online Supplement to the *Bulletin of the American Meteorological Society*, Vol.103, No. 8, August 2022

https://doi.org/10.1175/BAMS-D-22-0069.1.

Corresponding author: Howard J. Diamond / howard.diamond@noaa.gov

STATE OF THE CLIMATE IN 2021
The Tropics

Editors
Jessica Blunden
Tim Boyer

Chapter Editors

Freya Aldred
Peter Bissolli
Kyle R. Clem
Howard J. Diamond
Matthew L. Druckenmiller
Robert J. H. Dunn
Catherine Ganter
Nadine Gobron
Gregory C. Johnson
Rick Lumpkin
Ademe Mekonnen
John B. Miller
Twila A. Moon
Marilyn N. Raphael
Ahira Sánchez-Lugo
Carl J. Schreck III
Richard L. Thoman
Kate M. Willett
Zhiwei Zhu

Technical Editor

Laura Ohlmann

BAMS Special Editor for Climate

Michael A. Alexander

American Meteorological Society

Cover credit:
Hurricane Ida hits near the Louisiana and Mississippi border on August 29, 2021 bringing high winds, flooding and a dangerous storm surge as seen. © Warren Faidley, Getty

The Tropics is one chapter from the *State of the Climate in 2021* annual report and is available from https://doi.org/10.1175/BAMS-D-22-0069.1. Compiled by NOAA's National Centers for Environmental Information, *State of the Climate in 2021* is based on contributions from scientists from around the world. It provides a detailed update on global climate indicators, notable weather events, and other data collected by environmental monitoring stations and instruments located on land, water, ice, and in space. The full report is available from https://doi.org/10.1175/2022BAMSStateoftheClimate.1.

How to cite this document:

Citing the complete report:
Blunden, J. and T. Boyer, Eds., 2022: State of the Climate in 2021. *Bull. Amer. Meteor. Soc.,* **103** (8), Si–S465, https://doi.org/10.1175/2022BAMSStateoftheClimate.1.

Citing this chapter:
Diamond, H.J. and C. J. Schreck, Eds., 2022: The Tropics [in "State of the Climate in 2021"]. *Bull. Amer. Meteor. Soc.,* **103** (8), S193–S256, https://doi.org/10.1175/BAMS-D-22-0069.1.

Citing a section (example):
Halpert, M. S., M. L'Heureux, A. Kumar, E. Becker, and Z.-Z. Hu, 2022: ENSO and the tropical Pacific [in "State of the Climate in 2021"]. *Bull. Amer. Meteor. Soc.,* **103** (8), S199–S203, https://doi.org/10.1175/BAMS-D-22-0069.1.

Editor and Author Affiliations (alphabetical by name)

Allgood, Adam, NOAA/NWS Climate Prediction Center, College Park, Maryland
Becker, Emily J., University of Miami Rosenstiel School of Marine and Atmospheric Science, Miami, Florida
Blake, Eric S., NOAA/NWS National Hurricane Center, Miami, Florida
Bringas, Francis G., NOAA/OAR/AOML Physical Oceanography Division, Miami, Florida
Camargo, Suzana J., Lamont-Doherty Earth Observatory, Columbia University, Palisades, New York
Chen, Lin, Institute for Climate and Application Research (ICAR)/KLME/ILCEC/CIC-FEMD, Nanjing University of Information Science and Technology, Nanjing, China
Coelho, Caio A. S., CPTEC/INPE Center for Weather Forecasts and Climate Studies, National Institute for Space Research, Cachoeira Paulista, Brazil
Diamond, Howard J., NOAA/OAR Air Resources Laboratory, College Park, Maryland
Fauchereau, Nicolas, National Institute of Water and Atmospheric Research, Ltd., Auckland, New Zealand
Goldenberg, Stanley B., NOAA/OAR/AOML Hurricane Research Division, Miami, Florida
Goni, Gustavo, NOAA/OAR/AOML Physical Oceanography Division, Miami, Florida
Halpert, Michael S., NOAA/NWS Climate Prediction Center, College Park, Maryland
He, Qiong, Earth System Modeling Center, Nanjing University of Information Science and Technology, Nanjing, China
Hu, Zeng-Zhen, NOAA/NWS Climate Prediction Center, College Park, Maryland
Klotzbach, Philip J., Department of Atmospheric Science, Colorado State University, Fort Collins, Colorado
Knaff, John A., NOAA/NESDIS Center for Satellite Applications and Research, Fort Collins, Colorado
Kumar, Arun, NOAA/NWS Climate Prediction Center, College Park, Maryland
Landsea, Chris W., NOAA/NWS National Hurricane Center, Miami, Florida
L'Heureux, Michelle, NOAA/NWS Climate Prediction Center, College Park, Maryland
Lin, I.-I., National Taiwan University, Taipei, Taiwan
Lorrey, Andrew M., National Institute of Water and Atmospheric Research, Ltd., Auckland, New Zealand
Luo, Jing-Jia, Institute for Climate and Application Research (ICAR)/KLME/ILCEC/CIC-FEMD, Nanjing University of Information Science and Technology, Nanjing, China
Magee, Andrew D., Centre for Water, Climate and Land, School of Environmental and Life Sciences, University of Newcastle, Callaghan, NSW, Australia
Pasch, Richard J., NOAA/NWS National Hurricane Center, Miami, Florida
Pezza, Alexandre B., Greater Wellington Regional Council, Wellington, New Zealand
Rosencrans, Matthew, NOAA/NWS Climate Prediction Center, College Park, Maryland
Schreck III, Carl J., North Carolina State University, North Carolina Institute for Climate Studies, Cooperative Institute for Satellite Earth System Studies, Asheville, North Carolina
Trewin, Blair C., Australian Bureau of Meteorology, Melbourne, Victoria, Australia
Truchelut, Ryan E., WeatherTiger LLC, Tallahassee, Florida
Wang, Bin, SOEST, Department of Meteorology and IPRC, University of Hawaii, Honolulu, Hawaii
Wang, Hui, NOAA/NWS Climate Prediction Center, College Park, Maryland
Wood, Kimberly M., Department of Geosciences, Mississippi State University, Mississippi State, Mississippi
Woolley, John-Mark, National Institute of Water and Atmospheric Research, Ltd., Auckland, New Zealand

Editorial and Production Team

Allen, Jessicca, Graphics Support, Cooperative Institute for Satellite Earth System Studies, North Carolina State University, Asheville, North Carolina
Hammer, Gregory, Content Team Lead, Communications and Outreach, NOAA/NESDIS National Centers for Environmental Information, Asheville, North Carolina
Love-Brotak, S. Elizabeth, Lead Graphics Production, NOAA/NESDIS National Centers for Environmental Information, Asheville, North Carolina
Misch, Deborah J., Graphics Support, Innovative Consulting and Management Services, LLC, NOAA/NESDIS National Centers for Environmental Information, Asheville, North Carolina
Ohlmann, Laura, Technical Editor, Innovative Consulting and Management Services, LLC, NOAA/NESDIS National Centers for Environmental Information, Asheville, North Carolina
Riddle, Deborah B., Graphics Support, NOAA/NESDIS National Centers for Environmental Information, Asheville, North Carolina
Veasey, Sara W., Visual Communications Team Lead, Communications and Outreach, NOAA/NESDIS National Centers for Environmental Information, Asheville, North Carolina

4. Table of Contents

*Please refer to Chapter 8 (Relevant datasets and sources) for a list of all climate variables and datasets used in this chapter for analyses, along with their websites for more information and access to the data.

4. THE TROPICS

H. J. Diamond and C. J. Schreck, Eds.

a. Overview—H. J. Diamond and C. J. Schreck

The tropics in 2021, in terms of the El Niño-Southern Oscillation (ENSO), featured La Niña episodes at both the beginning and end of the year. The year started with the continuation of a moderate strength La Niña (peak Oceanic Niño Index [ONI] value between –1.0° and –1.4°C is considered to be moderate strength) that had begun during July–September 2020 and ended during April–June 2021. The ONI then reflected a brief period of ENSO-neutral conditions May–July through June–August 2021, with the index increasing to –0.4°C, just greater than the minimum La Niña threshold of –0.5°C. Moderate La Niña conditions continued through the end of the year.

For the global tropics, NOAA GlobalTemp (Zhang et al. 2019) indicates the combined average land and ocean surface temperature (measured 20°S–20°N) was +0.07°C above the 1991–2020 average, tying with 1987 as the 12th-warmest year for the tropics since records began in 1880. While 2021 marked the coolest year since 2013, the five warmest years have all occurred since 2015. Data from the Global Precipitation Climatology Project indicate a mean annual total precipitation value of 1402.5 mm across the 20°S–20°N latitude band over land. This is just 0.5 mm below the 1991–2020 average and in the middle of all years (23rd wettest) for the 1979–2021 period of record.

Globally, 97 named tropical cyclones (TCs; maximum sustained winds ≥ 34 kt; or ≥ 17 m s^{-1}) were observed during the 2021 Northern Hemisphere season (January–December 2021) and the 2020/21 Southern Hemisphere season (July–June 2020/21; see Table 4.2), as documented in IBTrACSv4 (Knapp et al. 2010). Overall, this number was well above the 1991–2020 global average of 87 TCs but well below the 102 TCs reported during the 2020 season (Diamond and Schreck 2021) and the record 104 named storms in 1992. The 21 named storms in the North Atlantic during 2021 were the third most on record behind the 30 named storms from 2020 and the 28 in 2005. The 2021 season marked the second consecutive season, and third season overall, during which the designated list of 21 storm names was exhausted. For the North Atlantic, the seven hurricanes that occurred during 2021 were much less the 14 hurricanes in 2020. The four major hurricanes were also fewer than the seven observed in 2020.

Globally, Accumulated Cyclone Energy (ACE; Bell et al. 2000) was 13% higher in 2021 than in 2020, but still 18% below normal. The eastern North Pacific, western North Pacific, and Australian region each observed ACE in the bottom tercile of their 1991–2020 climatologies. The North Atlantic was more active than normal with 149% of the 1951–2020 median ACE.[1] This value is the 13th highest since 1970 and is above NOAA's threshold of 130% of the median ACE for an above-normal season. There have now been a record six consecutive above-normal seasons, which far surpasses the previous record of three set in 2003–05 and equaled in 2010–12. The western North Pacific observed four super typhoons in 2021 (Surigae, Chanthu, Mindulle, and Rai) that achieved Category 5 on the Saffir–Simpson Hurricane Wind Scale (SSHWS; https://www.nhc.noaa.gov/aboutsshws.php), but the overall ACE was still 30% below the 1991–2020 average. In total, there were seven Category 5 tropical cyclones across the globe—four in the western North Pacific and one each in the South Indian Ocean.

[1] Given the long-term North Atlantic hurricane record, we continue to use the 1951–2020 timeframe here to assist with year-to-year comparisons with past versions of The Tropics chapter.

b. ENSO and the tropical Pacific—M. S. Halpert, M. L'Heureux, A. Kumar, E. Becker, and Z.-Z. Hu

The El Niño-Southern Oscillation (ENSO) is a coupled ocean–atmosphere climate phenomenon centered across the tropical Pacific Ocean, with its opposite phases called El Niño and La Niña. For historical purposes, NOAA's Climate Prediction Center (CPC) classifies and assesses the strength and duration of El Niño and La Niña events using the Oceanic Niño Index (ONI, shown for mid-2020 through 2021 in Fig. 4.1). The ONI is the 3-month (seasonal) running average of sea surface temperature (SST) anomalies in the Niño-3.4 region (5°S–5°N, 170°–120°W), currently calculated as the departure from the 1991–2020 base period mean.[2] El Niño (the warm phase) is classified when the ONI is at or greater than +0.5°C for at least five consecutive, overlapping seasons, while La Niña (the cool phase) is classified when the ONI is at or less than −0.5°C for at least five consecutive, overlapping seasons.

The time series of the ONI (Fig. 4.1) shows that 2021 featured La Niña episodes at both the beginning and the end of the year. The year started with the continuation of a moderate strength La Niña (peak ONI value between −1.0° and −1.4°C is considered to be moderate strength) that began during July–September 2020 and ended during April–June 2021. The ONI then reflected a brief period of ENSO-neutral conditions May–July through June–August (JJA) 2021, with the index increasing to −0.4°C, just above the minimum La Niña threshold of −0.5°C. Starting in July–September (JAS) 2021, La Niña thresholds were again met, with ONI values decreasing through October–December (OND) 2021. In OND, the ONI reached −1.0°C, indicating that the second consecutive boreal winter (2021/22) would feature at least a moderate strength episode, albeit weaker than the previous winter (2020/21).

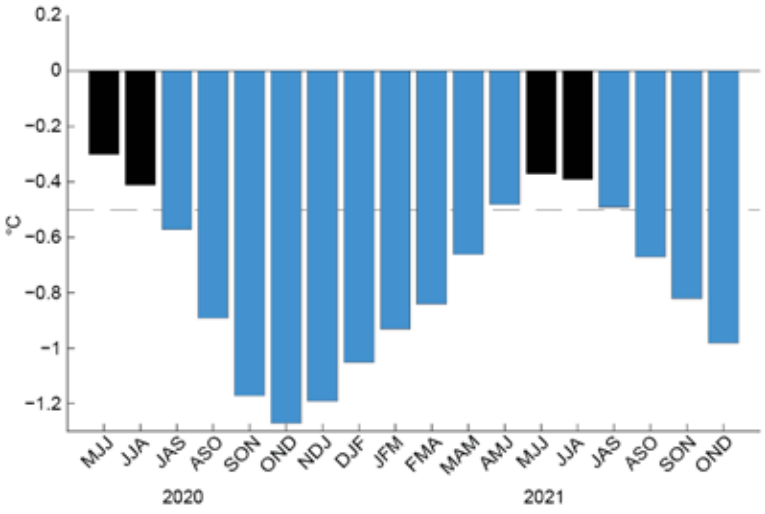

Fig. 4.1. Time series of the Oceanic Niño Index (ONI; °C) from mid-2020 through 2021. Overlapping 3-month seasons are labeled on the x-axis, with initials indicating the first letter of each month in the season. Blue bars indicate negative values below −0.5°C (dashed line). ONI values are derived from the ERSSTv5 dataset and are based on departures from the 1991–2020 period monthly means (Huang et al. 2017).

1) OCEANIC CONDITIONS

Figure 4.2 displays the mean SST (left column) and SST anomalies (right column) during December–February (DJF) 2020/21 through September–November (SON) 2021. SST anomalies on the equator during DJF (Fig. 4.2b) were less than −1.0°C in the central Pacific between 160°E and 140°W. Associated with this cooling, the western Pacific warm pool contracted westward, with the 30°C isotherm only extending to about 160°E (Fig. 4.2b). The east-central and eastern equatorial Pacific SSTs were also below average during DJF, but less so than SST anomalies in the central Pacific, remaining between −1.0°C and −0.5°C. Conversely, SSTs were above average in the western equatorial Pacific and portions of the western subtropical Pacific of both hemispheres. The resulting horseshoe-shaped anomaly pattern is typical of La Niña.

During MAM, La Niña weakened (ONI of −0.6°C) as the central Pacific returned to near-average and the largest SST departures shifted into the eastern part of the Pacific (Fig. 4.2c). By JJA (Fig. 4.2e), the entire tropical Pacific returned to average with NOAA's CPC officially declaring the

[2] The ONI is an index measuring a climate phenomenon, ENSO, and for that reason, the base period is updated every five years with a rolling 30-year climatology. SSTs in the Niño-3.4 region have a positive trend going back to 1950 or earlier, and the rolling climatology is partially used to remove those SST trends and focus on the state of ENSO.

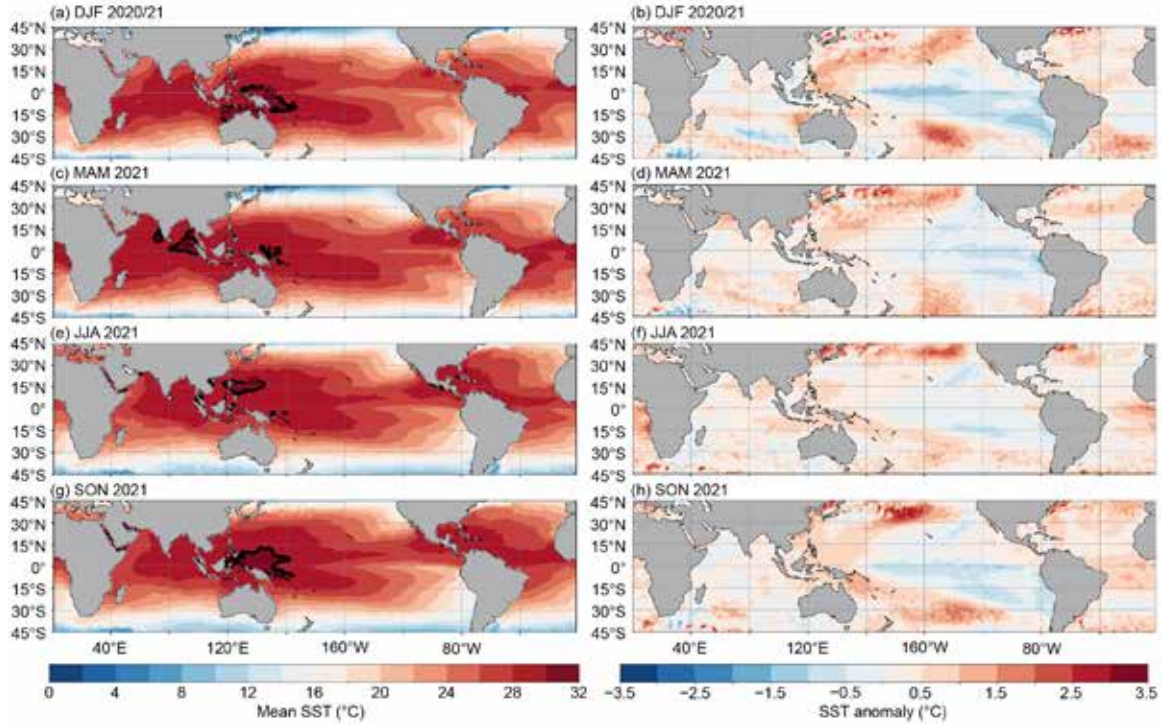

Fig. 4.2. Mean SST (left) and SST anomaly (right) for (a, b) DJF 2020/21, (c, d) MAM 2021, (e, f) JJA 2021, and (g, h) SON 2021. The bold contour for total SST is located at 30°C. Anomalies are departures from the 1991–2020 seasonal adjusted OISST climatology (Huang et al. 2020).

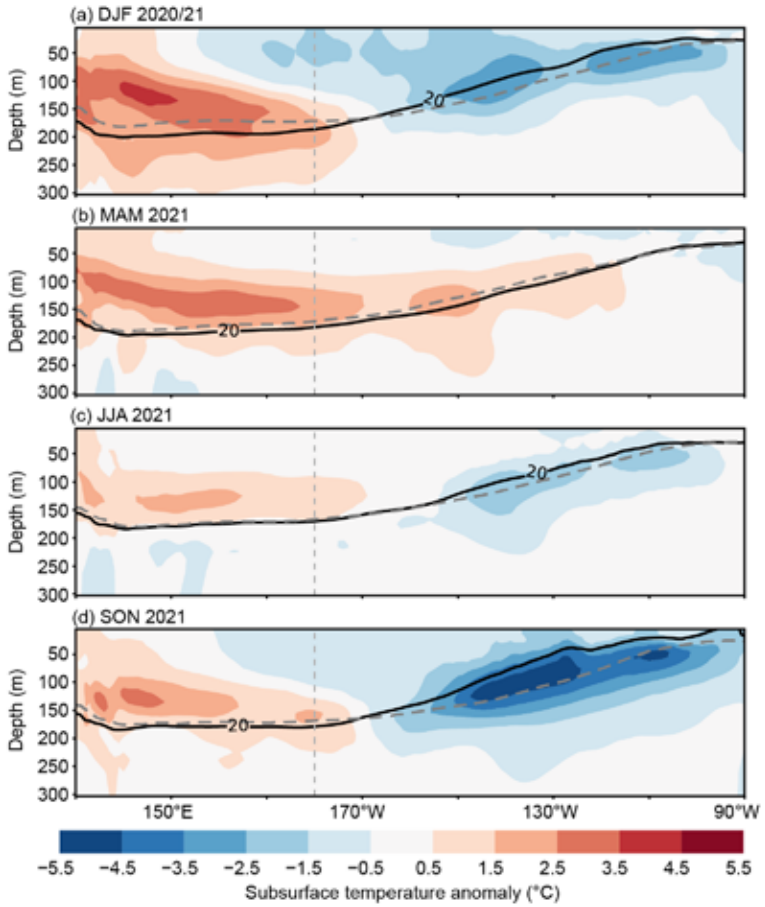

end of La Niña in May. After a brief period of ENSO-neutral conditions, the tropical Pacific again cooled, with SST anomalies generally between –0.5°C and –1.0°C observed during SON (Fig. 4.2g), and NOAA's CPC declaring La Niña had returned in October. The equatorial cold tongue strengthened and expanded westward in association with the renewed development of La Niña (Fig. 4.2h).

Consistent with the above evolution, the subsurface temperature anomaly structure varied considerably during the year (Fig. 4.3). Subsurface temperatures during DJF 2020/21 were below average in the central and eastern equatorial Pacific Ocean and above average in the western and central Pacific, mostly at ocean depths of 100–200 m (Fig. 4.3a). This overall anomaly pattern is typical of La Niña with

Fig. 4.3. Equatorial depth–longitude section of Pacific Ocean temperature anomalies (°C) averaged between 5°S and 5°N during (a) DJF 2020/21, (b) MAM 2021, (c) JJA 2021, and (d) SON 2021. The 20°C isotherm (thick solid line) approximates the center of the oceanic thermocline. The gray dashed line shows the climatology of the 20°C isotherm based on 1991–2020. The data are derived from a reanalysis system that assimilates oceanic observations into an oceanic general circulation model (Behringer 2007). Anomalies are departures from the 1991–2020 period monthly means.

the thermocline shallower than average in the eastern Pacific and deeper than normal in the western Pacific.

During MAM 2021, subsurface temperatures returned to near-average in the eastern half of the equatorial Pacific, and the area of above-average temperatures expanded eastward into the central and east-central Pacific (Fig. 4.3b). This evolution reflected the transition to ENSO-neutral conditions that began in AMJ, partly in association with the downwelling phase of an equatorial oceanic Kelvin wave (see section 4c). During JJA 2021, below average subsurface temperatures returned to the east-central and eastern Pacific (Fig. 4.3c). By SON, the subsurface temperature pattern again reflected an increased east–west thermocline gradient more reminiscent of conditions seen during DJF 2020/21, heralding the return of La Niña (Fig. 4.3d).

2) ATMOSPHERIC CIRCULATION

Although SSTs and sub-surface temperatures in the equatorial Pacific returned to near-average during the boreal summer, many aspects of the tropical atmospheric circulation at least weakly retained their La Niña characteristics. As a result, the low-level 850-hPa trade or easterly winds in the western and central equatorial Pacific (west of 150°W) were generally enhanced throughout the year (Fig. 4.4). Additionally, westerly wind anomalies generally prevailed at 200 hPa throughout the year across the central equatorial Pacific, as did a cyclonic circulation couplet straddling the equator in the central Pacific of the subtropics of both hemispheres, particularly during DJF and MAM (Fig. 4.5). These conditions were associated with below-average precipitation (positive OLR anomalies, brown shading in Fig. 4.6) in the western and central Pacific during all seasons. Collectively, they reflected well-known La Niña-related features, such as an enhanced equatorial Walker circulation and a suppressed Hadley circulation over the central Pacific.

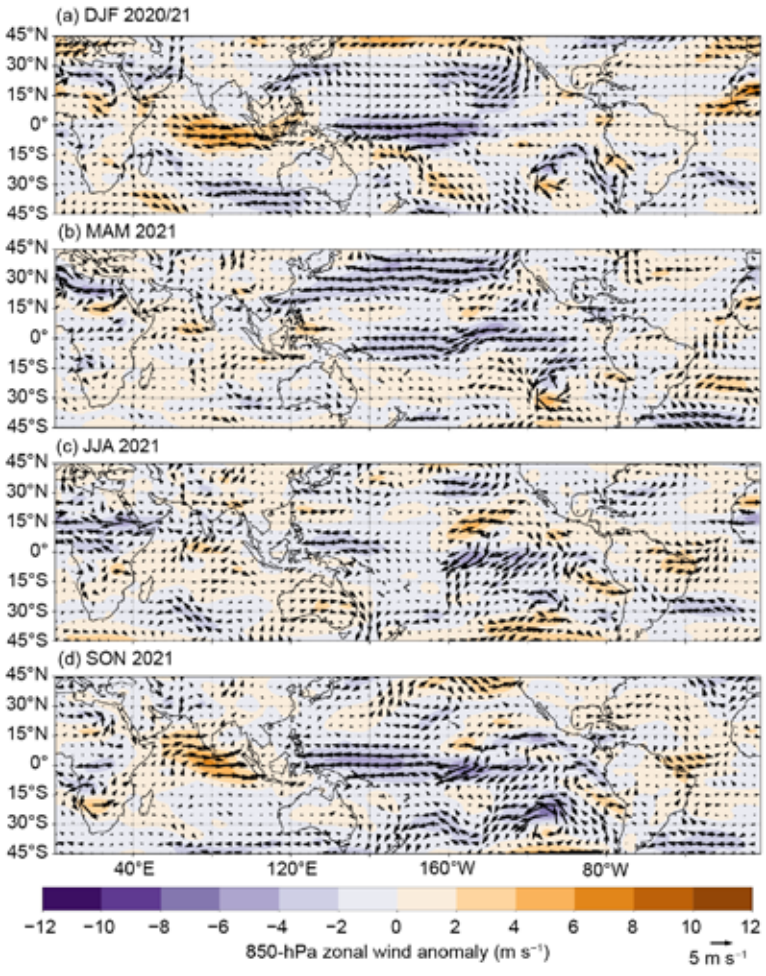

Fig. 4.4. Anomalous 850-hPa wind vectors (arrows) and zonal wind speed (m s^{-1}) during (a) DJF 2020/21, (b) MAM 2021, (c) JJA 2021, and (d) SON 2021. The reference wind vector (m s^{-1}) is located on the bottom left. Anomalies are departures from the 1991–2020 period monthly means. Data are from the NCEP/NCAR Reanalysis (Kalnay et al. 1996).

While the large-scale tropical atmospheric circulation was mainly consistent with La Niña throughout the year, there were some notable circulation differences among the seasons. The pattern of enhanced convection over Indonesia (green shading) and suppressed convection over the west-central equatorial Pacific was strongest as mature La Niña conditions developed during DJF (Fig. 4.6a) and again during SON when La Niña redeveloped and strengthened (Fig. 4.6d). The region of suppressed convection near the date line was weakest during the middle of the year (Figs. 4.6b,c), while the enhanced convection near Indonesia weakened in MAM (Fig. 4.6b), before strengthening again in JJA (Fig. 4.6c) and especially during SON (Fig. 4.6d).

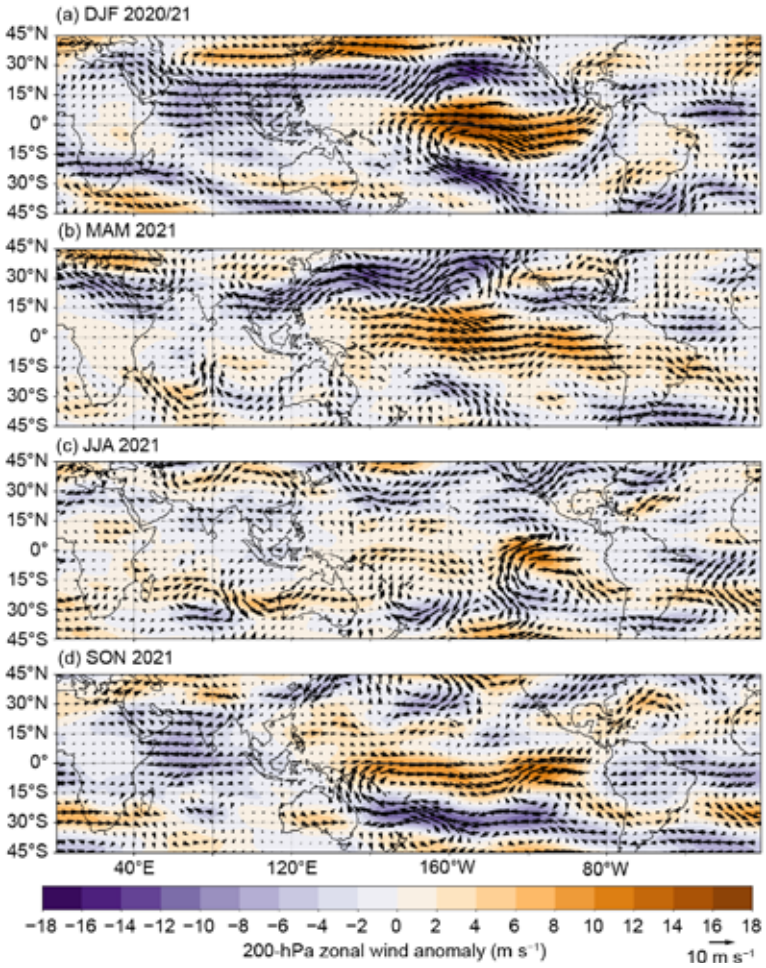

Fig. 4.5. Anomalous 200-hPa wind vectors (arrows) and zonal wind speed (m s^{-1}) during (a) DJF 2020/21, (b) MAM 2021, (c) JJA 2021, and (d) SON 2021. The reference wind vector (m s^{-1}) is located on the bottom right. Anomalies are departures from the 1991–2020 period monthly means. Data are from the NCEP/NCAR Reanalysis (Kalnay et al. 1996).

Consistent with the declining strength of the convective anomalies through the middle of the year, the anomalous 850-hPa equatorial easterlies and anomalous 200-hPa equatorial westerlies over the tropical Pacific were also strongest during DJF (Figs. 4.4a, 4.5a) and SON (Figs. 4.4d, 4.5d). This pattern of winds also persisted during MAM (Figs. 4.4b, 4.5b), before weakening during JJA (Figs. 4.4c, 4.5c). The anomalous cyclonic circulation anomalies in the subtropics of both hemispheres, located just to the east of suppressed convection, were prominent during DJF and MAM. These anomalies were weaker and located farther east during JJA, and then only in the Southern Hemisphere during SON, also farther west, closer to the date line.

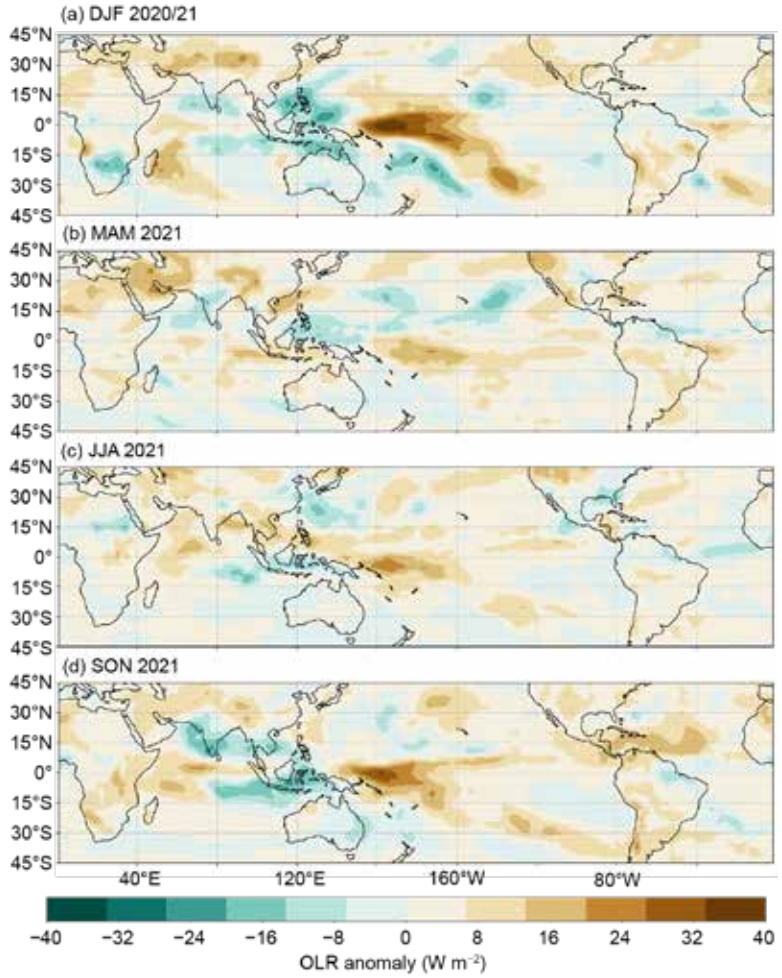

Fig. 4.6. Outgoing longwave radiation (OLR) anomalies (shaded, W m^{-2}), during (a) DJF 2020/21, (b) MAM 2021, (c) JJA 2021, and (d) SON 2021. Anomalies are departures from the 1991–2020 period monthly means. Data are from the NCEP/NCAR Reanalysis (Kalnay et al. 1996).

3) GLOBAL PRECIPITATION LINKS

During DJF 2020/21 (Appendix Fig. 4.1a), precipitation patterns typically associated with La Niña (Ropelewski and Halpert 1989) were observed over many parts of the world. These included below-average precipitation over the tropical central Pacific Ocean, much of the southern tier of the contiguous United States, and southeastern South America. With the development of La Niña during the latter part of the year, many of these impacts also became re-established (Appendix Fig. 4.1b). Impacts during both DJF and SON also included above-average precipitation over northern and eastern Australia, northern South America, Indonesia, the Philippines, and Southeast Asia. During SON (Appendix Fig. 4.1b), above-average precipitation was also observed over India, indicating an enhanced end to their monsoon season.

c. Tropical intraseasonal activity—A. Allgood and C. J. Schreck

Tropical intraseasonal activity is primarily modulated by several different modes of coherent atmospheric variability, most notably the Madden-Julian oscillation (MJO; Madden and Julian 1971, 1972, 1994; Zhang 2005). The MJO is characterized by eastward propagating envelopes of large-scale enhanced and suppressed convection that typically circumnavigate the globe in a 30–60-day period. MJO-related convective anomalies are similar in spatial extent to those generated by the atmospheric response to ENSO, but the latter signal does not propagate around the world. Other impactful modes of variability include convectively coupled waves, such as atmospheric Kelvin waves and westward propagating equatorial Rossby waves (Wheeler and

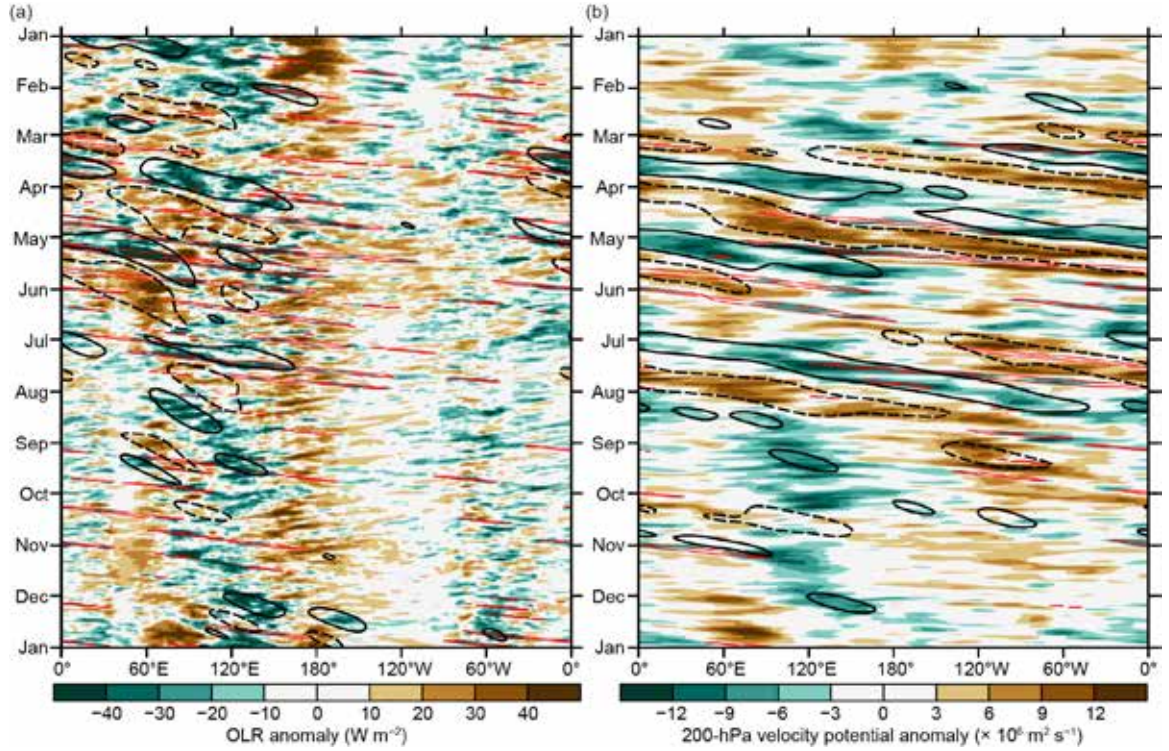

Fig. 4.7. Time–longitude section with (a) OLR anomalies (W m^{-2}; Schreck et al. 2018) and (b) 200-hPa velocity potential anomalies (× 10^6 m^2 s^{-1}) from the CFSR (Saha et al. 2014). Both variables are averaged 10°S–10°N. Time increases downward on this graph, beginning with Jan 2021 at the top and ending with Jan 2022 at the bottom. Negative anomalies indicate enhanced convection, and positive anomalies indicate suppressed convection. Contours identify anomalies filtered for the MJO (black) and atmospheric Kelvin waves (red, negative only). Contours are drawn at ±12 W m^{-2} and ±4 × 10^6 m^2 s^{-1} with the enhanced (suppressed) convective phase of these phenomena indicated by solid (dashed, MJO only) contours. Anomalies are departures from the 1991–2020 base period daily means.

Kiladis 1999; Kiladis et al. 2009). These waves are typically shorter and propagate faster than the MJO. Therefore, the MJO typically generates the strongest extratropical responses (Knutson and Weickmann 1987; Kiladis and Weickmann 1992; Mo and Kousky 1993; Kousky and Kayano 1994; Kayano and Kousky 1999; Cassou 2008; Lin et al. 2009; Riddle et al. 2012; Schreck et al. 2013; Baxter et al. 2014), and plays a role in modulating both monsoonal activity (Krishnamurti and Subrahmanyam 1982; Lau and Waliser 2012) and tropical cyclone activity (Mo 2000; Frank and Roundy 2006; Camargo et al. 2009; Schreck et al. 2012; Diamond and Renwick 2015).

MJO activity can exhibit sustained periods of robust activity, as well as periods of weak or indiscernible activity (Matthews 2008). This activity can be diagnosed through time–longitude analyses of various atmospheric fields, including anomalous outgoing longwave radiation (OLR, Fig. 4.7a) and 200-hPa velocity potential. OLR can be used as a proxy for convective anomalies due to the strong connection between OLR and high cloud cover. Velocity potential identifies the large-scale divergent circulations. MJO activity appears on these diagrams as coherent anomaly couplets that propagate eastward from the upper left towards the lower right. Computerized filtering on these analyses identifies this MJO activity, with enhanced convective activity represented by solid black contours and suppressed activity represented by dashed black contours. Another diagnostic tool frequently used to identify MJO activity is the Wheeler-Hendon (2004) Real-time Multivariate MJO (RMM) index. In RMM plots, robust atmospheric anomalies on a spatial scale resembling the MJO appear as a signal outside of the unit circle, and eastward propagation is represented by counterclockwise looping of the index about the origin (Fig. 4.8).

MJO activity was weak during early 2021, which is fairly typical when La Niña conditions are present. La Niña produces destructive interference with the MJO's enhanced convective envelope over the equatorial Pacific and the suppressed envelope over the Maritime Continent

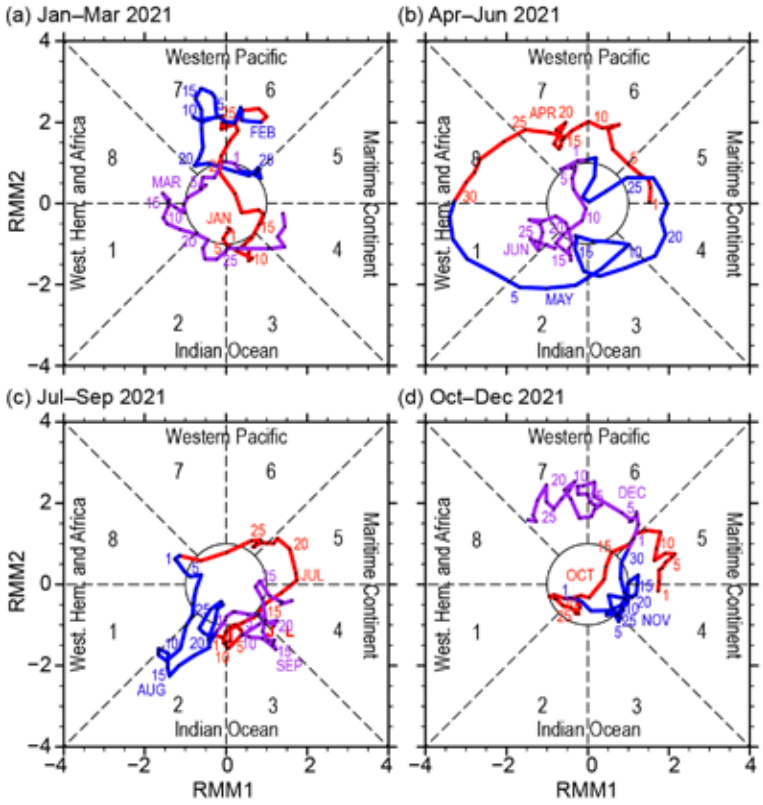

Fig. 4.8. Wheeler and Hendon (2004) Real-time Multivariate MJO (RMM) index for (a) Jan–Mar, (b) Apr–Jun, (c) Jul–Sep, and (d) Oct–Dec 2021. Each point represents the MJO amplitude and location on a given day, and the connecting lines illustrate its propagation. Amplitude is indicated by distance from the origin, with points inside the circle representing weak or no MJO activity. The eight phases around the origin identify the region experiencing enhanced convection, and counter-clockwise movement is consistent with eastward propagation.

(Hendon et al. 1999; Zhang and Gottschalck 2002; Zhang 2005). SST anomalies were below average across the equatorial Pacific during the first few months of 2021 (see Fig. 4.2). A sustained period of MJO activity began in March, lasting through mid-May (Figs. 4.7, 4.8). The enhanced convective phase of the MJO crossed the Pacific during April, weakening the enhanced trade wind regime (Fig. 4.9a) and coincided with the weakening of La Niña conditions observed at that time. After circumnavigating the globe and returning to the Indian Ocean during early May, the MJO weakened over the Pacific by the end of the month, with higher frequency modes such as Kelvin waves becoming the dominant features during June (Fig. 4.7b, red contours).

A second period of MJO activity initiated in July, with the enhanced phase crossing the Western Hemisphere and returning to the Indian Ocean during August. This intraseasonal activity very possibly contributed to the beginning of a hyperactive period of tropical cyclone development over the Atlantic basin during the second half of August and September (see section 4g2).

During October, MJO activity became less discernible as low frequency climate anomalies associated with the redevelopment of La Niña conditions became increasingly dominant and destructively interfered with the MJO enhanced convective envelope over the Pacific during the latter half of October. The atmospheric response to the increased negative SST anomalies across the equatorial Pacific was evident as stationary envelopes of anomalous ascent (negative OLR and 200-hPa velocity potential anomalies) centered near 120°E and descent (positive OLR and 200-hPa velocity potential anomalies) near or east of the date line (Fig. 4.7). Developing La Niña conditions remained the dominant driver of anomalous tropical convection in November. However, a third period of MJO activity initiated in December, with the enhanced phase propagating to the Pacific, generating a fairly substantial low-level westerly wind burst over the West Pacific. This westerly wind burst generated a downwelling oceanic Kelvin wave in the Pacific (Fig. 4.9b).

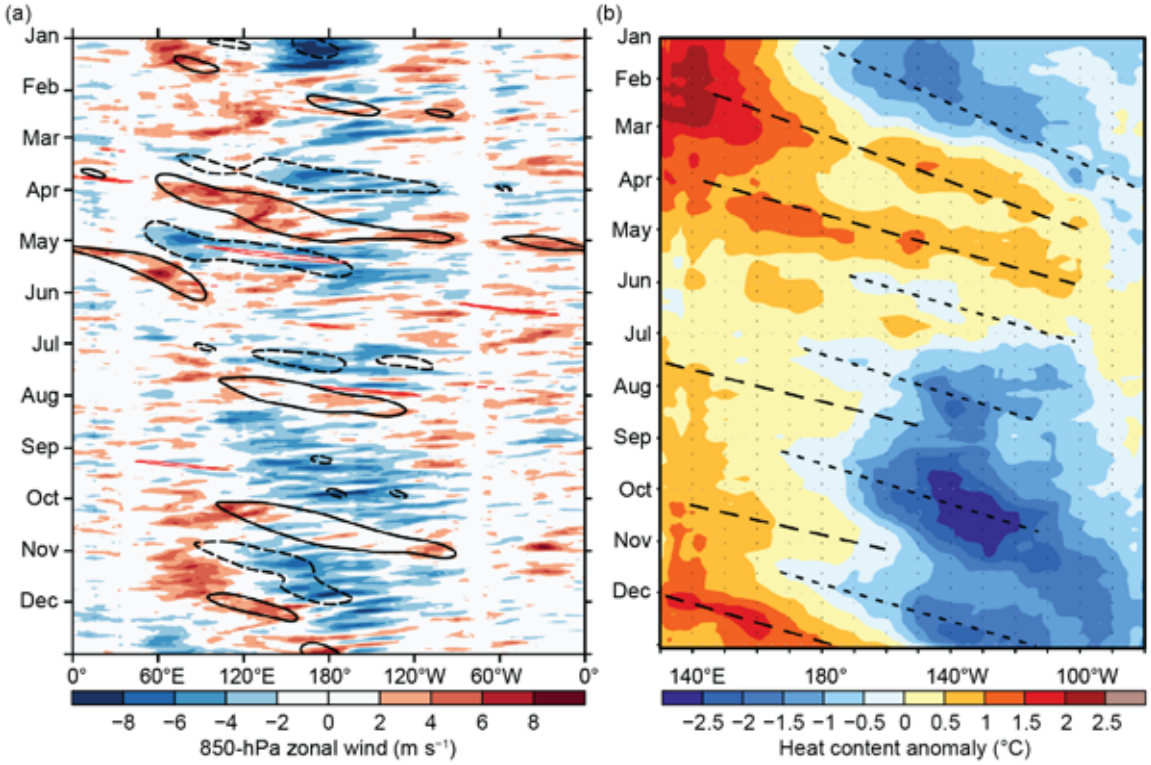

Fig. 4.9. (a) Time–longitude section for 2021 of anomalous 850-hPa zonal wind (m s^{-1}) averaged between 10°N and 10°S. Contours identify anomalies filtered for the MJO. (b) Time–longitude section for 2021 of anomalous equatorial Pacific Ocean heat content (°C), calculated as the mean temperature anomaly between 0 and 300-m depth. Yellow/red (blue) shading indicates above- (below-) average heat content. Relative warming (dashed lines) and cooling (dotted lines) due to downwelling and upwelling equatorial oceanic Kelvin waves are indicated. Anomalies are departures from the 1991–2020 base period pentad means. Data in (b) are derived from an analysis system that assimilates oceanic observations into an oceanic general circulation model (Behringer et al. 1998).

d. Intertropical convergence zones

1) PACIFIC—N. Fauchereau

Tropical Pacific rainfall patterns are dominated by two convergence zones: the Intertropical Convergence Zone (ITCZ; Schneider et al. 2014) north of the equator, and the South Pacific Convergence Zone (SPCZ; Vincent 1994). Figure 4.10 summarizes the behavior for both convergence zones during 2021 using rainfall from NOAA's Climate Prediction Center (CPC) Merged Analysis of Precipitation (CMAP) dataset (Xie and Arkin 1997). Rainfall transects over 30°S to 20°N are presented for each quarter of the year, averaged across successive 30-degree longitude bands, starting in the western Pacific at 150°E–180°. The 2021 seasonal variation is compared against the longer-term 1991–2020 climatology.

Early in the year, the tropical Pacific was still in a La Niña state, albeit weakened compared to the peak reached in October 2020 (section 4b). The maximum negative SST anomalies were also shifted slightly towards the central Pacific, compared to earlier during the development of the event. The transects for January–March (Fig. 4.10a) for the western and central Pacific (150°E to 150°W, especially 150°E to the date line) show that the SPCZ mean signature was shifted south and west of its climatological position, while rainfall rates within the ITCZ were reduced compared to climatology. This signature is consistent with typical anomalies recorded in the Southern Hemisphere summer during La Niña.

La Niña conditions eased as the year progressed and officially ended in May 2021, marking a return to ENSO-neutral state, although weak negative SST anomalies persisted in the central and eastern tropical Pacific. These anomalies re-intensified starting in October, reaching –2°C towards the end of the year off the coast of South America, in a typical 'canonical' ENSO pattern. Accordingly, rainfall anomalies, especially in the western Pacific (Fig. 4.10d), responded in

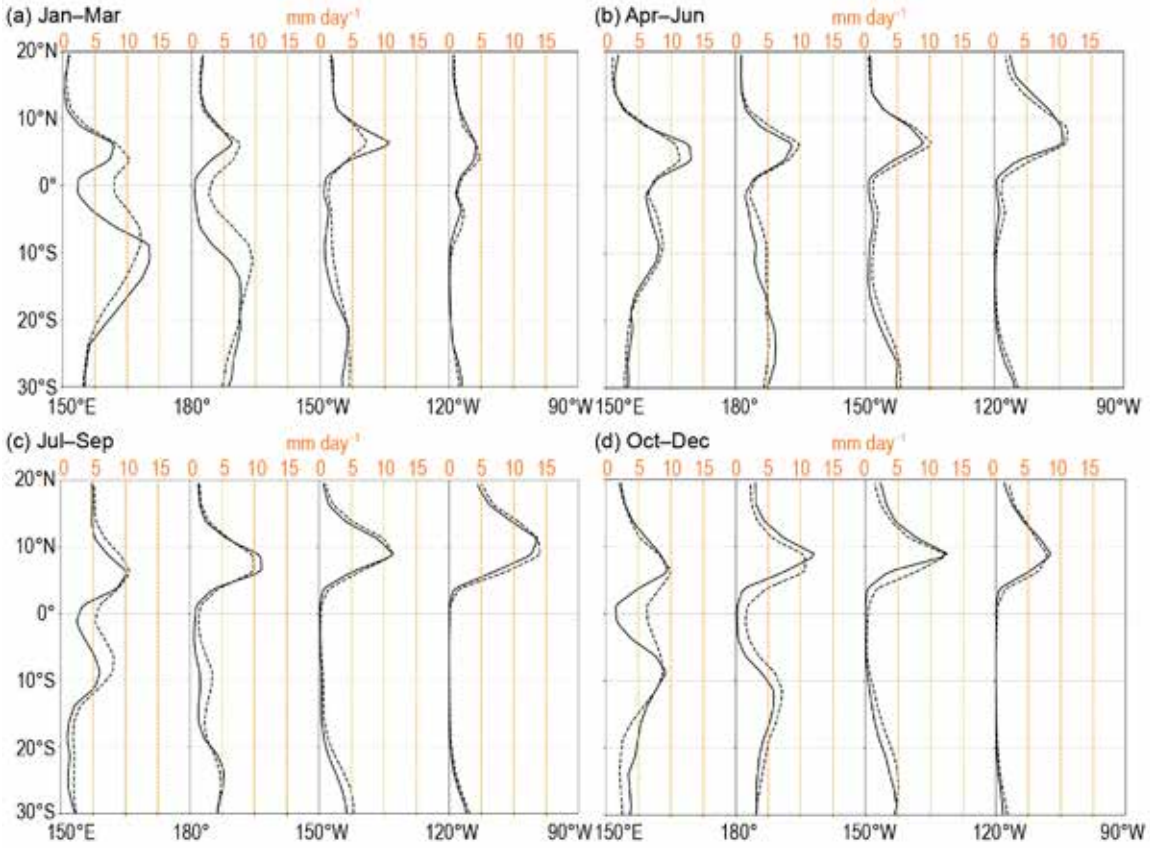

Fig. 4.10. Rainfall rate (mm day^{-1}) from CMAP for (a) Jan–Mar, (b) Apr–Jun, (c) Jul–Sep, and (d) Oct–Dec 2021. The separate panels for each quarter show the 2021 rainfall cross-section between 30°S and 20°N (solid line) and the 1991–2020 climatology (dotted line), separately for four 30° sectors from 150°E–180° to 120°–90°W.

a pattern broadly similar to the one present during the first quarter of the year, with decreased rainfall rates in the equatorial band. Rainfall rates were higher than climatology south of ~10°S.

The most consistent, large, and spatially coherent rainfall anomalies were recorded in the first months of 2021. When averaged over January–March 2021, for example (Fig. 4.11), a large area of below-normal rainfall extended from just north of the Solomon Islands southeast towards French Polynesia, while above-normal precipitation was recorded from Vanuatu to southeast of Fiji, corresponding to a clear southwestward shift in the mean position of the SPCZ. Meanwhile, the ITCZ was suppressed in the western Pacific (Fig. 4.10a) and slightly intensified in the central-eastern Pacific and is consistent with the climatologies as depicted in Figs. 4.10a and 4.11.

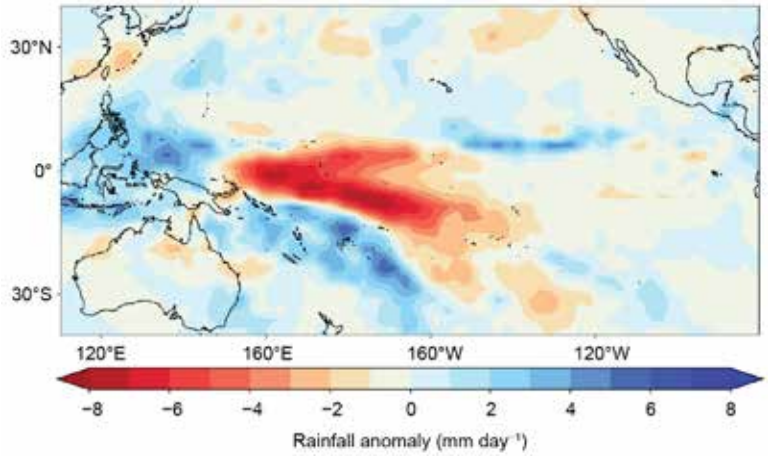

Fig. 4.11. Rainfall anomalies (mm day^{-1}) from CMAP for Jan–Mar 2021. The anomalies are calculated with respect to the 1991–2020 climatology.

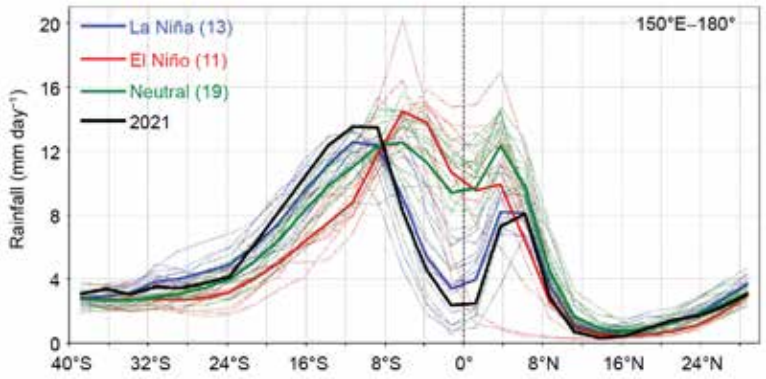

Fig. 4.12. CMAP rainfall rate (mm day^{-1}) for the Jan–Mar quarter, for each year from 1979 to 2021, averaged over the longitude sector 150°E–180°. The cross-sections are color-coded according to NOAA's ONI (with a threshold of ± 0.5°C), except 2021 which is shown in black. Dotted lines are individual years, and solid lines are the average over all years in each ENSO phase. The inset legend indicates how many years went into each composite.

Figure 4.12 shows a more detailed comparison of the western Pacific (150°E–180°) CMAP rainfall transect during January–March 2021, corresponding to the period where La Niña conditions were clearly established, relative to all other years in this dataset. It shows a clear La Niña signal, with the mean anomalies during these three months (black line) closely following the average of La Niña seasons (blue line).

2) ATLANTIC—A. B. Pezza and C. A. S. Coelho

The Atlantic ITCZ is a well-organized convective band that oscillates between approximately 5°–12°N during July–November and 5°S–5°N during January–May (Waliser and Gautier 1993; Nobre and Shukla 1996). Equatorial atmospheric Kelvin waves can modulate ITCZ intraseasonal variability (Guo et al. 2014). ENSO and the Southern Annular Mode (SAM) can also influence the ITCZ on interannual time scales (Münnich and Neelin 2005). The SAM, also known as the Antarctic Oscillation (AAO), describes the north–south movement of the westerly wind belt that circles Antarctica. A negative SAM event reflects an expansion of the westerly wind belt towards the equator, with more abundant precipitation at midlatitudes in general (Ding et al. 2012; Liu et al. 2021; Moreno et al. 2018).

As in 2020, a highlight of the year was a strongly positive SAM pattern (see section 2e), with vigorous low-pressure anomalies around Antarctica and a weaker South Atlantic subtropical anticyclone (Fig. 4.13a). A La Niña pattern and near-neutral equatorial Atlantic Ocean (Fig. 4.13b) temperatures dominated most of the year. Albeit mostly neutral for the yearly average, the Atlantic SST anomalies north of the equator were slightly above normal at the start of 2021, with

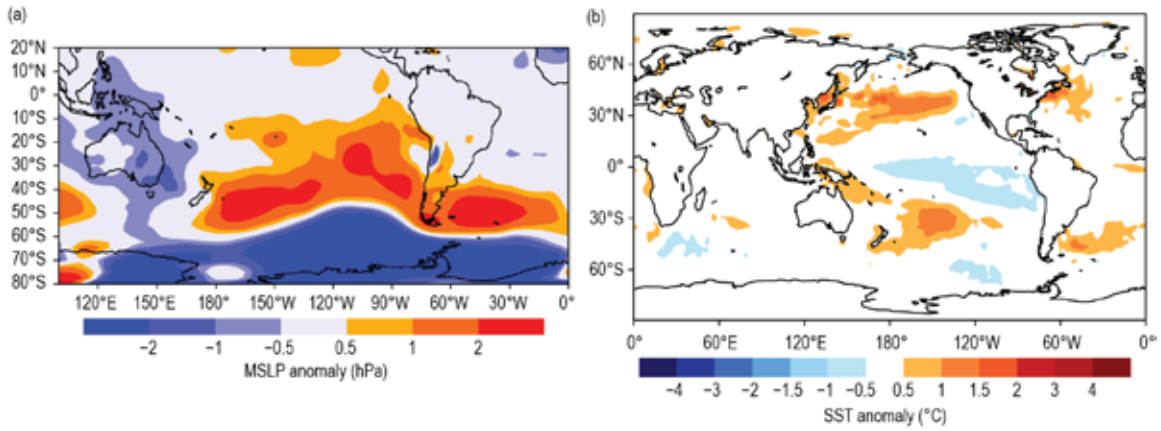

Fig. 4.13. Observed (a) South American and Southern Hemisphere high latitude MSLP anomalies (hPa) and (b) global SST anomalies (°C) for Jan–Dec 2021. MSLP anomalies are calculated with respect to a 1991–2020 climatology derived from the NCEP/NCAR Reanalysis (Kalnay et al. 1996).

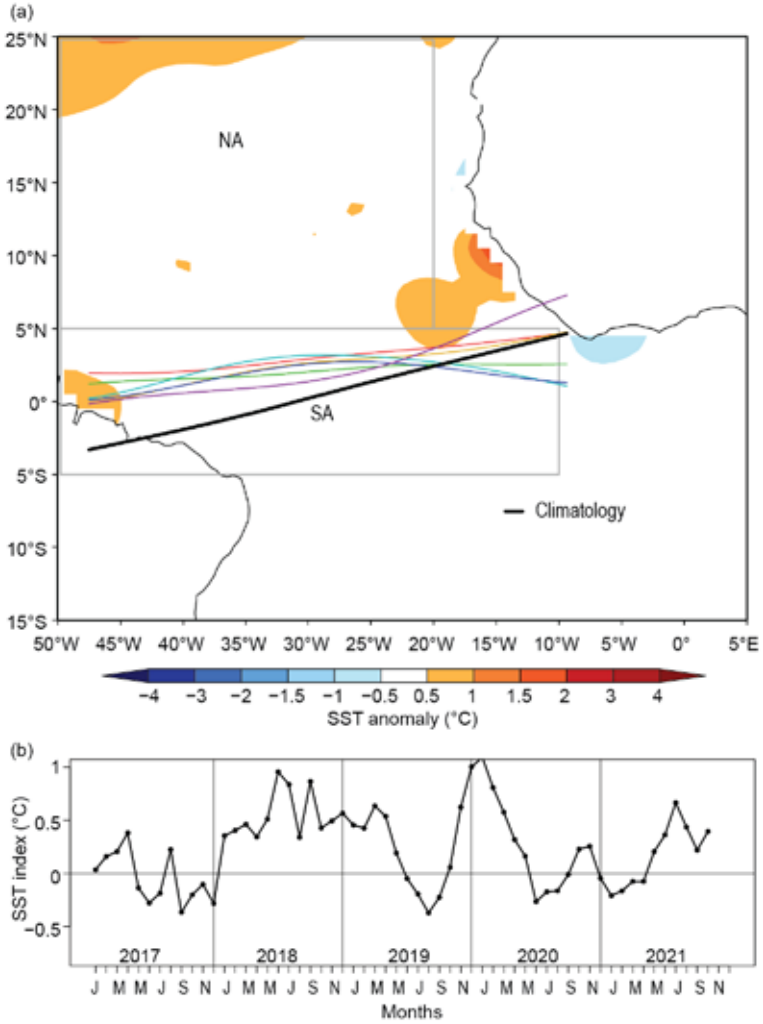

Fig. 4.14. (a) Atlantic ITCZ position inferred from OLR (Liebmann and Smith 1996) during Mar 2021. The colored thin lines indicate the approximate position for the six pentads of the month. The black thick line indicates the Atlantic ITCZ climatological position for Mar. The SST anomalies (°C) for Mar 2021 calculated, with respect to the 1982–2020 climatology, are shaded. The two boxes indicate the areas used for the calculation of the Atlantic index in (b), which shows the monthly OISST (Smith et al. 2008) anomaly time series averaged over the South Atlantic sector (SA region, 5°S–5°N, 10°–50°W) minus the SST anomaly time series averaged over the North Atlantic sector (NA region, 5°–25°N, 20°–50°W) for the period 2017–21, forming the Atlantic index. The positive phase of the index indicates favorable conditions for enhanced Atlantic ITCZ activity south of the equator.

the warm band moving southward in the second half of the year. As expected, the ITCZ and the Atlantic Index (see Fig. 4.14 for definition) followed suit, staying over the area of positive SST anomalies, with associated low-level wind convergence north of the equator at the start of the year (Fig. 4.14a), before shifting south from around May onward (Fig. 4.14b). A large portion of inland Brazil experienced severe precipitation deficits, especially during the first half of the year when the ITCZ stayed north of its climatological position, during the negative phase of the index (Fig. 4.14b). Compared to 2020 (Pezza and Coelho 2021), less anomalous activity in the equatorial Atlantic in 2021 coincided with a greater dominance of the positive SAM pattern encircling the Southern Hemisphere (Fig. 4.13a), with strong pressure anomalies concentrated over mid and high latitudes. Liu et al. (2021) found that the SAM modulates the Walker circulation, which may have contributed to the southern shift of the Atlantic ITCZ.

e. Global monsoon summary—B. Wang and Q. He

Globally, monsoon activity is the dominant mode of annual precipitation and circulation variability and one of the defining features of Earth's climate system. Here, we summarize the global and regional monsoon precipitation anomalies in the 2021 monsoon year, which includes the Southern Hemisphere (SH) summer (November 2020–April 2021) and Northern Hemisphere (NH) summer (May 2021–October 2021) monsoons. Figure 4.15 presents the monsoon domain (red lines) defined by rainfall characteristics (rainy summer versus dry winter; Wang 1994) rather than the traditional definition by winds (Ramage 1971). Two criteria define the monsoon domain: (1) the annual precipitation range (hemispheric summer minus hemispheric winter) exceeds 300 mm and (2) the hemispheric summer precipitation is > 55% of the total annual precipitation amount, where summer here means May–September for the NH and November–March for the SH (Wang and Ding 2008). The NH monsoon includes five regional monsoons: Northern Africa, India, East Asia, the western North Pacific, and North America. The SH monsoon consists of three monsoons: southern Africa, Australia, and South America.

Regional precipitation and circulation indices are used to measure the regional monsoon intensity. The precipitation indices represent the anomalous precipitation rate averaged over the blue rectangular box regions shown in Fig. 4.15. Note that the precipitation averaged in each blue box represents the precipitation averaged over the entire corresponding regional monsoon domain value (r >0.90; Yim et al. 2014). The definitions of the circulation indices for each monsoon region are provided in Table 4.1. They are modified from indices originally depicted by Yim et al. (2014). All circulation indices are defined by the meridional shear of the zonal winds at 850 hPa (or 700 hPa in highland southern Africa), which measures the intensity (relative vorticity) of the monsoon troughs except for the northern African and East Asian monsoons. The northern African monsoon circulation index is defined by the westerly monsoon strength, reflecting the north–south thermal contrast between the South and North Atlantic. The East Asian summer monsoon (EASM) circulation index is determined by the meridional wind strength, reflecting

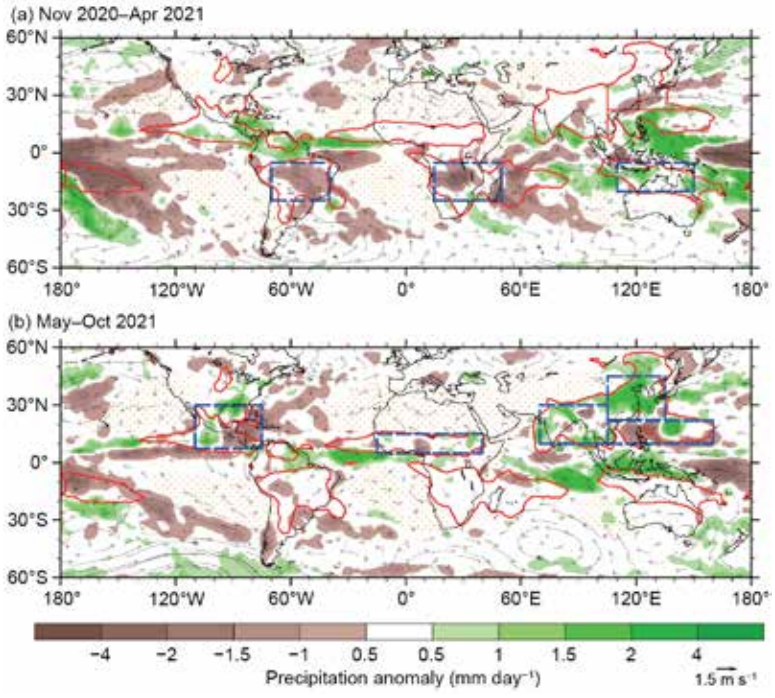

Fig. 4.15. Seasonal mean precipitation anomalies (mm day^{-1}) and 850-hPa wind anomalies (m s^{-1}) for (a) the SH summer monsoon season: Nov 2020–Apr 2021 and (b) the NH summer monsoon season: May–Oct 2021. Climatological mean was made for 1991–2020. Red lines outline the monsoon precipitation domain defined in the text. The dotted area represents the dry region where the local summer precipitation rate is below 1 mm day^{-1}. Rainfall data were taken from the Global Precipitation Climatology Project (GPCP; Huffman et al. 2009).

Table 4.1. Definition of the regional summer monsoon circulation indices and their correlation coefficients (*r*) with the corresponding regional summer monsoon precipitation indices for 1979/80–2020/21. The precipitation indices are defined by the areal mean precipitation over the blue box regions shown in Fig. 4.15. The correlation coefficients were computed using monthly time series (168 summer months; Jun–Sep in NH [1980–2021] and Dec–Mar in SH [1979/80–2020/21]). Bolded numbers represent significance at the 99% confidence level. (Adapted from Yim et al. 2014.)

Regional monsoon	Definition of the circulation index	*r*
Indian (ISM)	U850 (5°–15°N, 40°–80°E) minus U850 (25°–35°N, 70°–90°E)	**0.72**
Western North Pacific (WNPSM)	U850 (5°–15°N, 100°–130°E) minus U850 (20°–35°N, 110°–140°E)	**0.87**
East Asian (EASM)	V850 (20°–35°N, 120°–140°E) plus V850 (10°–25°N, 105°–115°E)	**0.74**
North American (NASM)	U850 (5°–15°N, 130°–100°W) minus U850 (20°–30°N, 110°–80°W)	**0.85**
Northern African (NAFSM)	U850 (0°–10°N, 40°W–10°E)	**0.70**
South American (SASM)	U850 (20°–5°S, 70°–40°W) minus U850 (35°–20°S, 70°–40°W)	**0.82**
Southern African (SAFSM)	U700 (10°S–0°S, 0°–30°E) minus U700 (25°–10°S, 40°–70°E)	**0.46**
Australian (AUSSM)	U850 (15°S–0°, 90°–130°E) minus U850 (30°–20°S, 100°–140°E)	**0.88**

the east–west thermal contrast between the Asian continent and the western North Pacific. The precipitation and circulation indices are well correlated for most regional monsoons, with correlation coefficients ranging from 0.70 to 0.88, except for the southern African monsoon (Table 4.1). Thus, the precipitation and circulation indices generally provide consistent measurements of the strength of each regional monsoon system.

ENSO dominates year-to-year variation of the monsoons (Ropelewski and Halpern 1987). La Niña conditions prevailed during the 2020/21 SH summer from November 2020 to April 2021. During the 2021 NH summer monsoon season, La Niña weakened to ENSO-neutral conditions in June–July (although eastern and central Pacific SSTs were still below average), La Niña re-emerged in August and rapidly cooled in September (section 4b).

During the 2020/21 SH summer, the La Niña-driven anomalous Walker circulation caused suppressed rainfall over the central-western Pacific and increased rainfall over the Maritime Continent. Precipitation in the Australian monsoon region was above normal (Fig. 4.15a). However, precipitation was significantly reduced over the South American and southern African monsoon regions. The Indian Ocean rainfall anomalies were also driven by the negative phase of the Indian Ocean dipole (Saji et al. 1999; section 4f). Figure 4.16 shows areal-averaged monsoon intensities. The Australian summer monsoon precipitation was 0.5 standard deviations (std. dev.) above normal, and the corresponding circulation intensity was 1 std. dev. above average (Fig. 4.16g). The South American monsoon region measured precipitation that was 2 std. dev. below normal, yet the related circulation's strength was less than 0.5 std. dev. below normal (Fig. 4.16h). The southern African summer monsoon precipitation was 2 std. dev. below normal, but the circulation intensity was 1 std. dev. above average (Fig. 4.16f). Overall, the South American and southern African monsoons responded uncharacteristically to the 2020/21 La Niña, although the reasons why are unclear.

During the 2021 NH summer monsoon season (May–October), precipitation over the Maritime Continent was significantly above normal, while there was a noticeable reduction of precipitation in the equatorial western Pacific and near the northern Philippines (Fig. 4.15b).

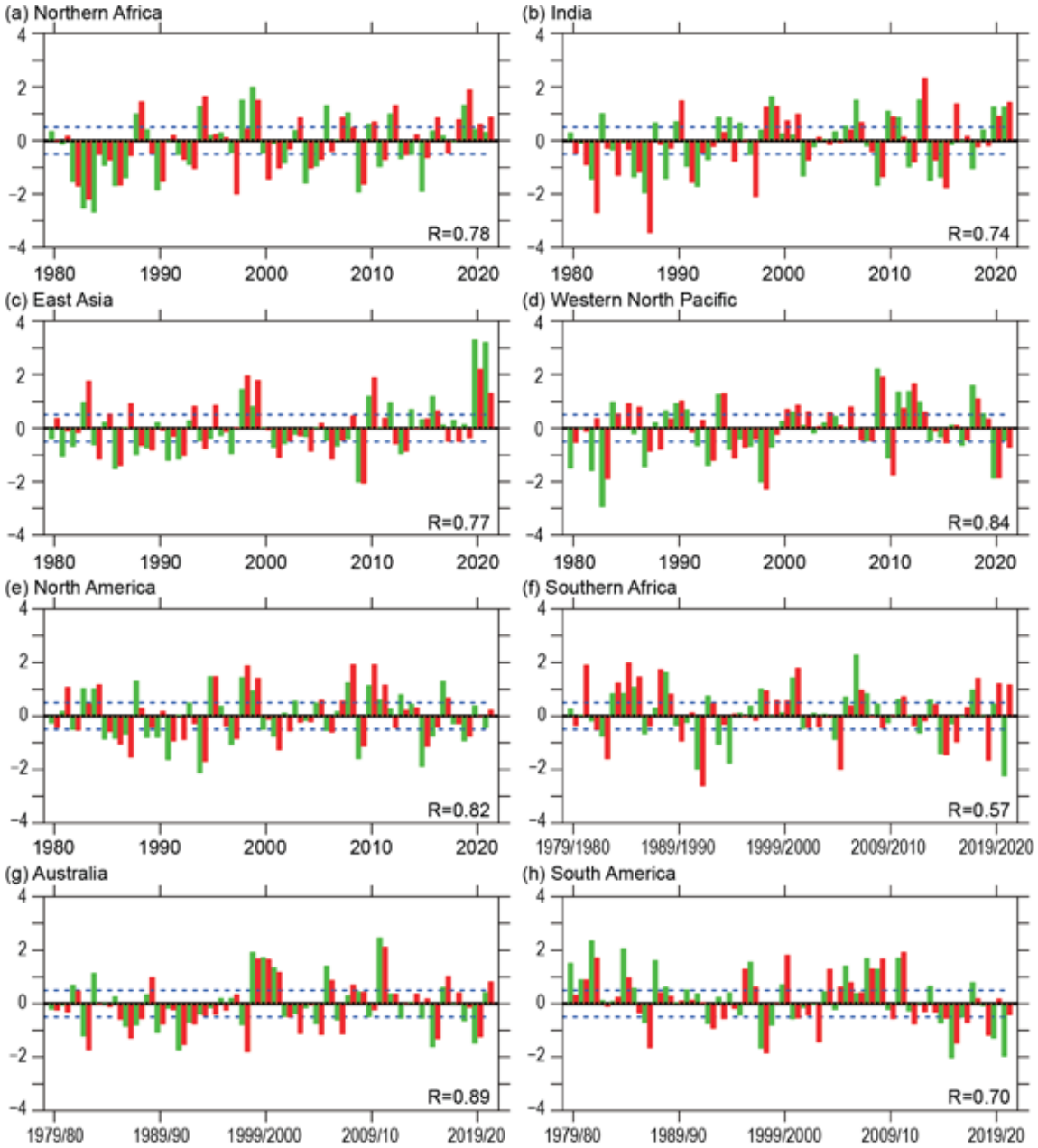

Fig. 4.16. (a–h) Temporal variations of summer monsoon precipitation and low-level circulation indices for eight regional monsoons. Green and red bars show the summer mean precipitation and circulation indices, respectively. All indices were normalized by their corresponding standard deviation with respect to the mean during 1991–2020 (ordinate). Numbers shown in the bottom right of each panel denote the correlation coefficient (R) between the seasonal mean precipitation and circulation indices (sample size: 42). Dashed lines indicate ±0.5 std. dev. The summer monsoon seasons are May–Oct for the NH and Nov–Apr for the SH. (Data source: GPCP for precipitation and ERA5 [Hersbach et al. 2020] for circulation.)

These characteristics resemble a typical precipitation anomaly pattern during a La Niña. While there is a general increase in NH monsoon precipitation, there are notable regional differences. The EASM showed record high precipitation and enhanced southerly monsoon in consecutive seasons in 2020 and 2021, with 2020 a bit greater (Fig. 4.16c). The EASM precipitation anomaly was nearly 3 std. dev. above average, and the corresponding southerly monsoon intensity was 1.2 std. dev. above normal (Fig. 4.16c). The Indian summer monsoon precipitation and circulation indices were both more than 1 std. dev. above normal (Fig. 4.16b). Precipitation over the northern African monsoon region was slightly above average (Fig. 4.16a). The North American monsoon showed average precipitation and circulation intensity due to a dipole pattern in the area (Fig. 4.16e). The western North Pacific oceanic monsoon precipitation, generally out of phase with the EASM, was 0.5 std. dev. below normal (Fig. 4.16d).

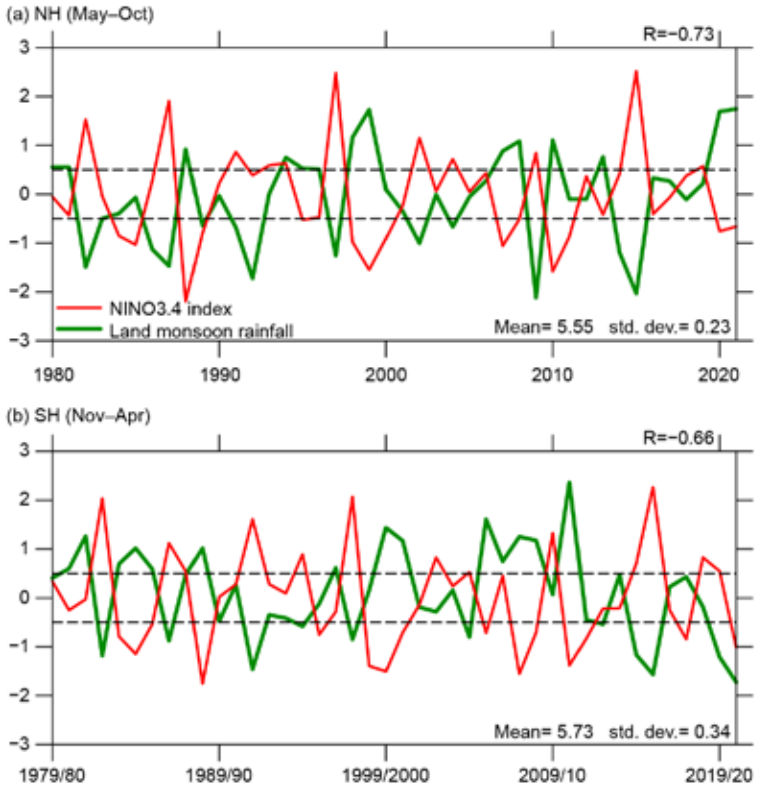

Fig. 4.17. (a) NH summer (May–Oct) land monsoon precipitation anomaly (green) normalized by its standard deviation. The climatological mean NH summer land monsoon precipitation during 1991–2020 (mean) and standard deviation (std. dev.) are shown in the lower right panel (mm day^{-1}). Numbers shown in each panel's top right denote the correlation coefficient (R) between the seasonal mean precipitation anomaly and the simultaneous Niño 3.4 index (red). Dashed lines indicate ±0.5 std. dev. (b) As in (a) except for the SH summer (Nov–Apr). Note that the land monsoon precipitation excludes the monsoon rainfall over the oceanic monsoon domain. (Data source: GPCP for precipitation, HadISST and ERSSTv5 for SST.)

Monsoon rainfall over land has more important socio-economic impacts than oceanic monsoon rainfall. Therefore, we specifically examine land monsoon rainfall (LMR). The NH and SH LMR indices were computed by the average precipitation over the corresponding land areas within the monsoon domain. The LMR on a global scale is strongly influenced by ENSO (Wang et al. 2012). Figure 4.17 shows that both the NH and SH land summer monsoon precipitation are anti-correlated with the simultaneous Niño-3.4 index. This is especially the case for NH land monsoon rainfall which has a simultaneous correlation of –0.73 from 1980 to 2021. Of note, the total amount of 2021 NH land monsoon precipitation was a record high over the past four decades, with the average daily rainfall almost 2 std. dev. higher than normal. Furthermore, the NH land monsoon rainfall was high in both 2020 and 2021 (Fig. 4.17a). This is primarily attributed to nearly consecutive annual record-high East Asian monsoon precipitation that exceeded 3 std. dev. (Fig. 4.16c). The summer precipitation total in northern China was the second highest in the last 40 years just behind 2020 (see section 7g3 for more details).

f. Indian Ocean dipole—L. Chen and J.-J. Luo

The Indian Ocean dipole (IOD), referring to the anomalous SST gradient between the eastern and western equatorial Indian Ocean (IO), is a major interannual mode in the tropical Indian Ocean. It can stem from tropical ENSO forcing and/or local air–sea interaction processes (Saji et al. 1999; Luo et al. 2010, 2012). In general, the IOD starts to develop in boreal summer, peaks in boreal autumn, and decays rapidly in early boreal winter. A positive IOD (pIOD) event usually features cold SST anomalies in the eastern IO and weak warm SST anomalies in the western IO, and vice versa for a negative event. The IOD exhibits nonlinearity, e.g., the magnitude of a

pIOD event is generally stronger than that of a negative IOD (nIOD) event, due to the asymmetric ocean–atmosphere coupling between the two phases of the IOD phenomenon (Luo et al. 2007; Hong et al. 2008).

A nIOD event occurred in the latter half of 2021 (Figs. 4.18, 4.19), marking the first negative event since 2016. The IOD index reached −0.55°C in October–November 2021 (Fig. 4.18b), with significant positive SST anomalies in the eastern pole and small negative SST anomalies in the western pole (Fig. 4.18a). For comparison, the two strongest nIOD events on record in 1998 and 2016 reached −0.97°C and −0.95°C, respectively (Luo 2017).

The nIOD development in 2021 was mainly due to the rapid increase of SST anomalies over the eastern pole of the IOD (hereafter IODE) during January–July 2021 (Fig. 4.18a). Following a neutral IOD in boreal autumn 2020 (Chen and Luo 2021), below-average SSTs and precipitation occurred across the entire equatorial IO during the boreal winter 2020, from the western pole of the IOD (IODW) to the IODE, as seen in Figs. 4.19a and 4.20a. The SST anomalies averaged over IODE were −0.7°C in January 2021 but quickly increased to +0.6°C in July 2021 (Fig. 4.18a). The development of the nIOD-related SST anomalies during the first half of the year is mainly attributed to anomalous westerly winds over the entire equatorial IO region during December 2020–February 2021 (Fig. 4.19a) and anomalous westerly winds over the western equatorial IO region during March–May (Fig. 4.19b).

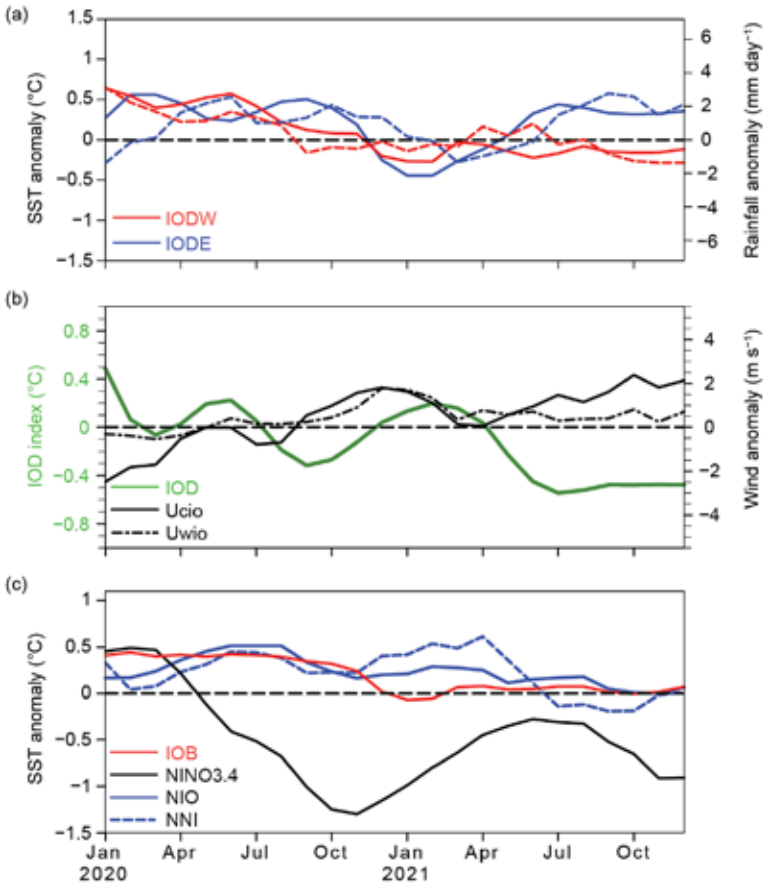

Fig. 4.18. (a) 3-monthly running mean SST anomalies (°C; solid lines) and precipitation (mm day^{-1}; dashed lines) in the eastern pole (IODE; 10°S–0°, 90°–110°E; blue lines) and the western pole (IODW; 10°S–10°N, 50°–70°E; red lines) of the IOD. (b) As in (a), but for the IOD index (measured by the SST difference between IODW and IODE, green line) and surface zonal wind anomaly (m s^{-1}) in the central equatorial IO (Ucio; 5°S–5°N, 70°–90°E; solid black line) and western equatorial IO (Uwio; 5°S–5°N, 50°–70°E; dashed black line). (c) As in (a), but for SST anomalies in the Niño 3.4 region (5°S–5°N, 170°–120°W; black line), the tropical IO (IOB; 20°S–10°N, 40°–120°E; red line), the northern IO (NIO; 5°–20°N, 60°–120°W; solid blue line), and the region off western Australia (22°–28°S, 108°–117°E; dashed blue line). Anomalies are relative to the 1991–2020 base period. (Sources: NOAA OISST [Reynolds et al. 2002]; monthly GPCP precipitation analysis [https://psl.noaa.gov/data/gridded/data.gpcp.html]; and JRA-55 atmospheric reanalysis [Ebita et al. 2011].)

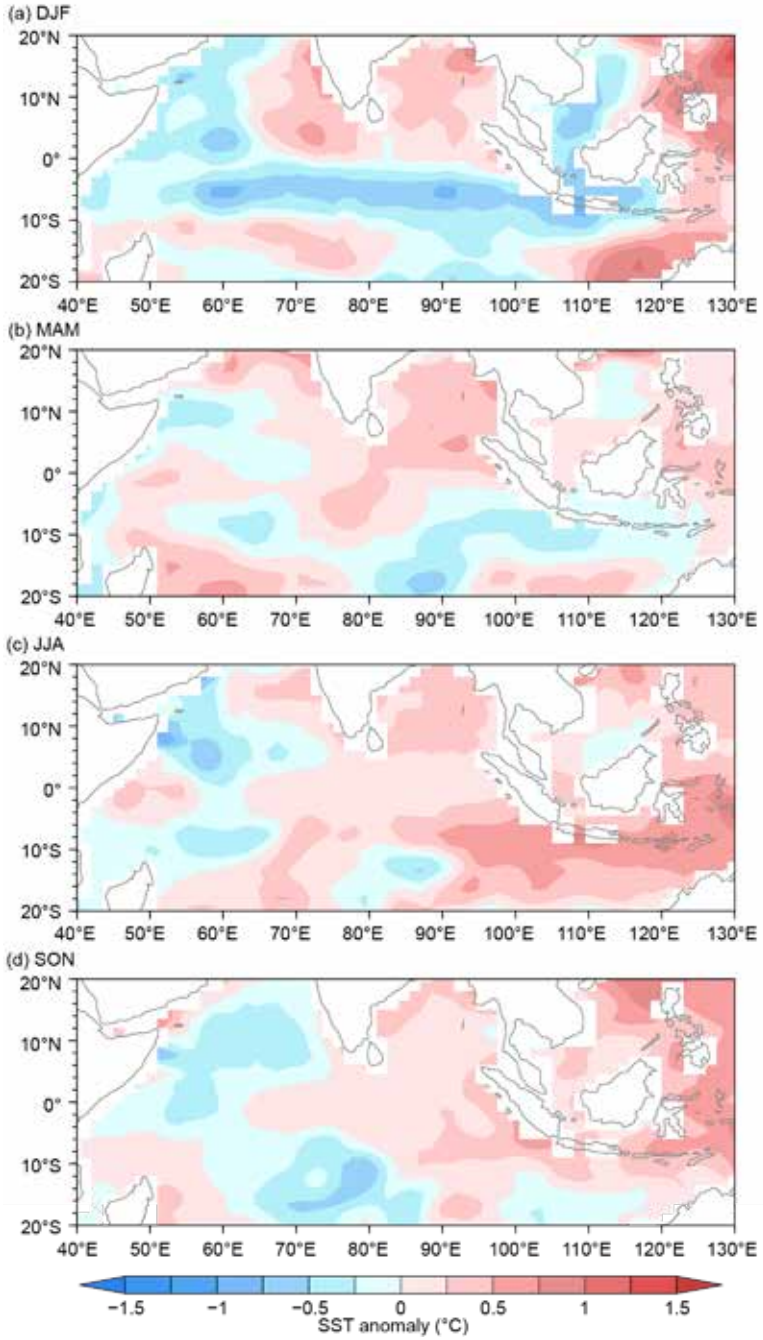

Fig. 4.19. SST anomalies (°C, colored scale) during (a) Dec 2020–Feb 2021, (b) Mar–May 2021, (c) Jun–Aug 2021, and (d) Sep–Nov 2021. Anomalies were calculated relative to the 1991–2020 climatology. (Sources: NOAA OISST [Reynolds et al. 2002].)

The westerly wind anomalies over the equatorial IO region during December 2020–February 2021 were consistent with a Rossby–Kelvin wave response (Matsuno 1966; Gill 1980) to two positive precipitation belts located on both sides of the equator in the IO (Fig. 4.20e). The convection in the northern IO (NIO; including the eastern Arabian Sea and the Bay of Bengal) was due to the above-average SST anomalies in that region (Figs. 4.19a, 4.20a). The anomalous warmth in the southern tropical IO region (5°–20°S, 78°–108°E) was largely attributed to the warm Ningaloo Niño event (a phenomenon featured by above-average SST off the coast of western Australia; Feng et al. 2013), as previous studies (e.g., Zheng et al. 2020) have indicated that the above-average precipitation tends to occur in the northwestern regions of the above-average SST anomalies associated with the Ningaloo Niño.

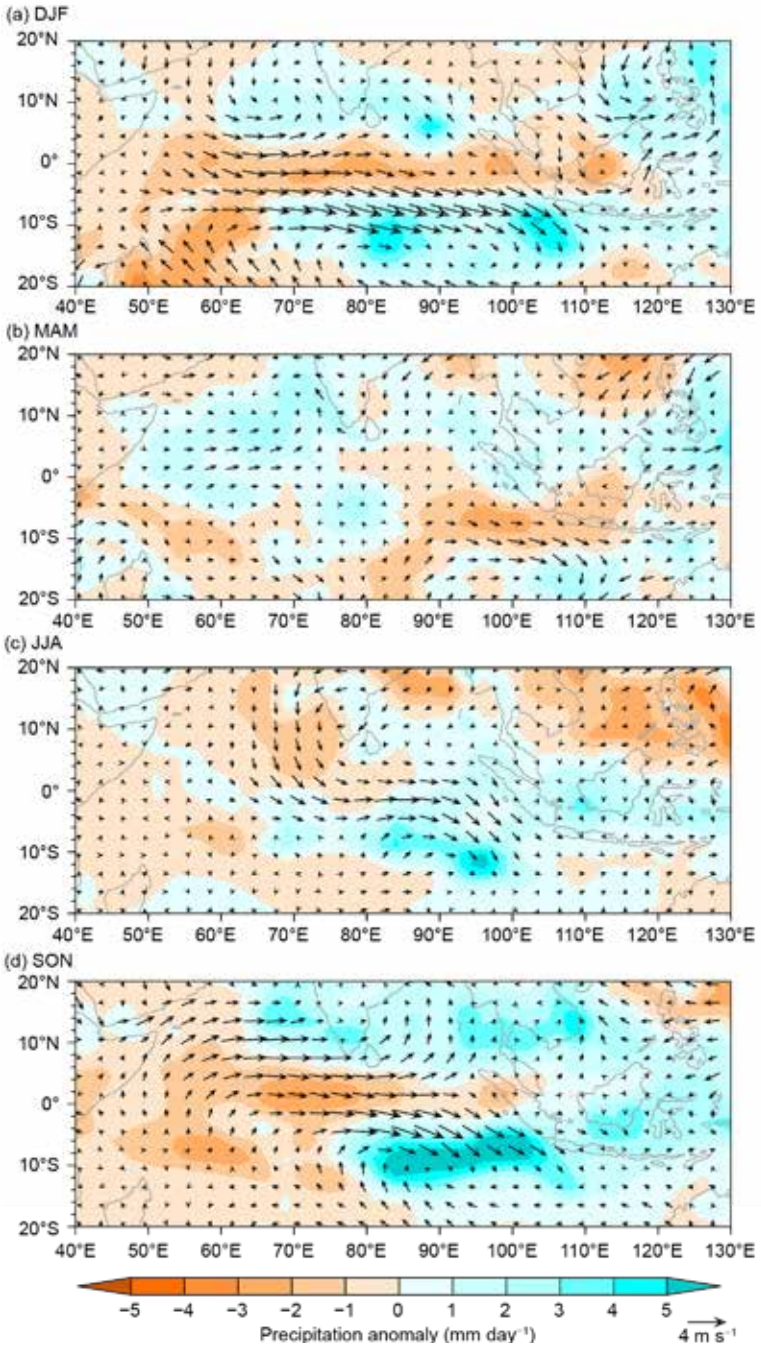

Fig. 4.20. Precipitation (mm day^{-1}) and surface wind (m s^{-1}) anomalies relative to 1991–2020 during (a) Dec 2020–Feb 2021, (b) Mar–May 2021, (c) Jun–Aug 2021, and (d) Sep–Nov 2021. (Sources: monthly GPCP precipitation analysis [https://psl.noaa.gov/data/gridded/data.gpcp.html] and JRA-55 atmospheric reanalysis [Ebita et al. 2011].)

During March–May 2021, the anomalous westerly wind was confined over the western equatorial IO region, arising from above-average precipitation and corresponding above-average SST over the northeastern Arabian Sea (Figs. 4.19b, 4.20b). To summarize, the aforementioned two convective centers induced by the above-average SST over the NIO and the western Australian coast (hereafter subtropical IO regions) contributed to the westerly wind anomalies over the whole IO equator during December 2020–February 2021, and the northern convection continued to trigger westerly wind anomalies over the western equatorial IO during March–May 2021. As a result, the continuous warm Kelvin wave propagated eastward along the IO equator, causing warm SSTs in the IODE during the first half of 2021.

During boreal summer and autumn 2021, the nIOD event continued due to air–sea coupling over the tropical IO. As seen in Figs. 4.19c,d and Figs. 4.20c,d, positive (negative) SST anomalies

in IODE (IODW) are accompanied by positive (negative) precipitation anomalies, along with pronounced westerly wind anomalies over the central equatorial IO. Meanwhile, ENSO-neutral conditions were present in boreal summer 2021 before La Niña re-emerged in boreal autumn (Fig. 4.18c). The rapid growth of the nIOD in the first half of 2021 was largely due to the above-average SSTs and the concurring above-average precipitation over the subtropical IO regions. Additionally, considering the entire IO, only a marginal IO basin-wide warming appeared throughout 2021, despite the multidecadal basin-wide warming over the tropical IO SST (Luo et al. 2012), while a strong IO basin-wide warming persisted throughout 2020 (Chen and Luo 2021).

In summary, a moderate nIOD event occurred in 2021, with the IOD index reaching −0.55°C during boreal autumn. The development of this event was mainly due to the rapid increase of SSTs over the IODE during the first half of 2021, from −0.7°C below average in January to +0.6°C above average in July. It is suggested that the convection induced by the above-average SSTs over the subtropical IO regions caused the westerly wind anomalies over the equatorial IO regions, which led to the positive SST anomalies over IODE. The nIOD event continued due to air–sea interactions during boreal summer and autumn.

g. Tropical cyclones

1) OVERVIEW—H. J. Diamond and C. J. Schreck

The IBTrACS dataset comprises historical tropical cyclone (TC) best-track data from numerous sources around the globe, including all of the World Meteorological Organization (WMO) Regional Specialized Meteorological Centers (RSMCs; Knapp et al. 2010). This dataset represents the most complete compilation of global TC data. From these data, 1991–2020 climatological values of TC activity for each basin using statistics from both the WMO RSMCs and the Joint Typhoon Warning Center (JTWC) are calculated following Schreck et al. (2014). These values are referenced in each subsection. Tallying the global TC numbers is challenging and involves more than simply adding up basin totals, because some storms cross TC basin boundaries, some TC basins overlap, and multiple agencies track and categorize TCs. The Northern Hemisphere (NH) basins are typically measured from January to December while Southern Hemisphere (SH) basins are typically measured from July to June. Global values here are the sum of the Northern Hemisphere for 2021 and the Southern Hemisphere for 2020/21.

Based on preliminary data from NOAA's National Hurricane Center and the JTWC as archived in IBTrACS (Fig. 4.21), the combined 2021 season had 97 named storms (sustained wind speeds ≥ 34 kt or 17 m s^{-1}), which is five fewer than last season (2020; Diamond and Schreck 2020). The 2021 season count had the eighth most named storms on record and is well above the 1991–2020 average of 87. However, there were just 38 hurricanes/typhoons/cyclones (HTCs; sustained wind speeds ≥ 64 kt or 33 m s^{-1}; average 48), and only 17 of those reached major HTC status (sustained wind speeds ≥ 96 kt or 49 m s^{-1}; average 26). Both of these numbers are at least tied for the third fewest on record since 1980. The Accumulated Cyclone Energy (ACE) for the season was 649×10^4 kt^2, which is 10% higher than last year (Diamond and Schreck 2019) but still 17% below the climatological mean.

In sections 4g2–4g8, 2020/21 (SH) and 2021 (NH) seasonal TC activity is described and compared to the historical record for each of the seven WMO-defined TC basins. For simplicity, all counts are broken down by the U.S. Saffir-Simpson Hurricane Wind Scale (SSHWS).[3] The overall picture of global TCs during 2021 is shown in Fig. 4.21, and counts by category are documented in Table 4.2. Similar to 2020, the North Atlantic played an out-sized role in global tropical cyclone activity in 2021. The 21 named storms were the third most on record, behind 2020 (30) and 2005 (28). The seven hurricanes were near normal, the four major hurricanes were above normal, and

[3] SSHWS is based on 1-minute averaged winds, and the categories are defined at: https://www.weather.gov/mfl/saffirsimpson; the Australian category scale is based on 10-minute averaged winds, and those categories are defined at http://www.bom.gov.au/cyclone/tropical-cyclone-knowledge-centre/understanding/tc-info/

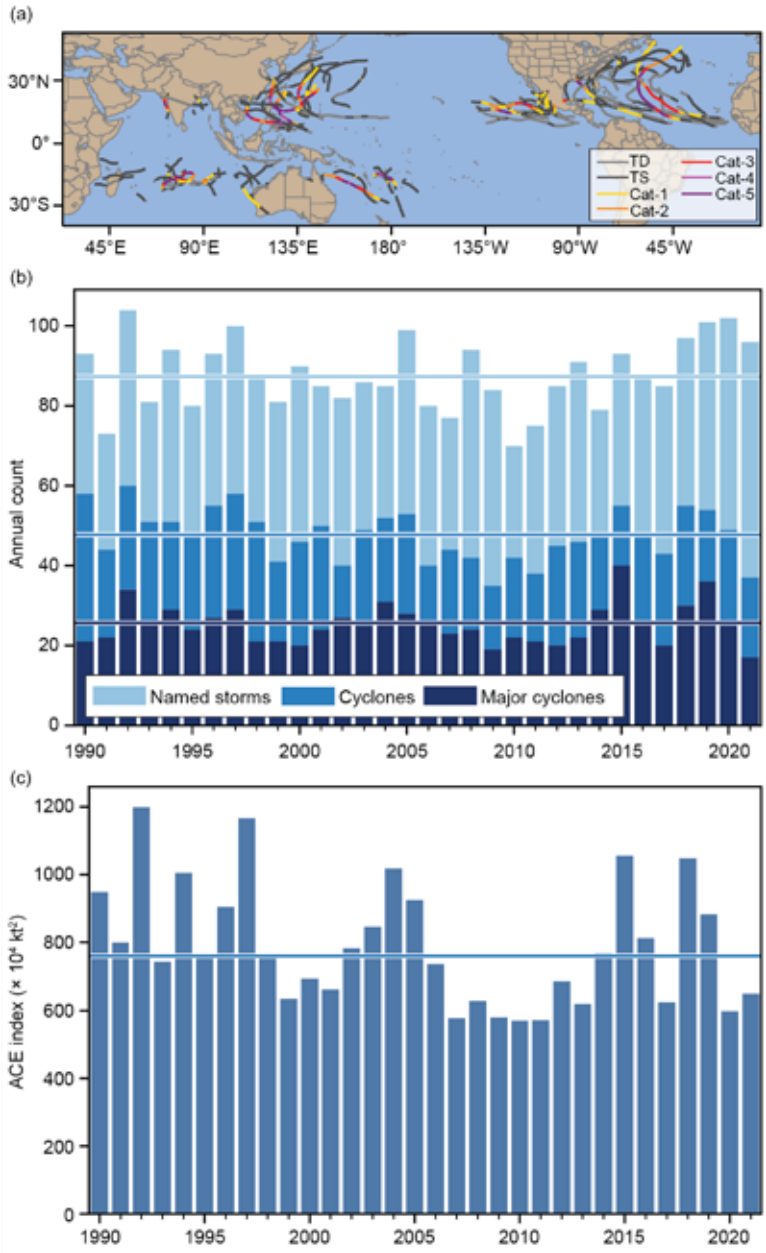

Fig. 4.21. Annual global TC statistics for the period 1990–2021. (a) storm tracks for 2021, (b) number of named storms, cyclones, and major cyclones, and (c) ACE (× 10^4 kt^2). The 1991–2020 means (horizontal lines) are included in both (b) and (c).

the ACE was 149% of the 1951–2020 median. The eastern North Pacific had more named storms than normal, but the ACE was below normal. The western North Pacific was quieter than normal by most metrics, but it produced four SSHWS Category 5 strength (sustained wind speeds ≥ 137 kt or 70.5 m s^{-1}) typhoons. The North Indian Ocean had near-normal activity. Each of the Southern Hemisphere basins had above-normal numbers of named storms. However, the ACE was below normal for Australia and near-normal for the South Indian Ocean and the Southwest Pacific.

Globally, seven storms reached SSHWS Category 5 strength, which is four more than last year (Diamond and Schreck 2021) and also more than the 1991–2020 mean of 5.3. Four of those storms occurred in the western North Pacific (Surigae, Chanthu, Mindulle, and Rai), and there was one in each of the three Southern Hemisphere basins: Faraji in the South Indian Ocean, Niran near Australia, and Yasa in the Southwest Pacific. Yasa caused major damage to Fiji in December 2020. Super Typhoon Rai was the third costliest typhoon in the history of the Philippines, causing about $1 billion (U.S. dollars) in damages and more than 400 deaths. While not reaching Category 5 status, Hurricane Ida was the most impactful storm in the Atlantic. At $75 billion (U.S. dollars) in damage, Ida was the costliest U.S. disaster of 2021 and the fifth most expensive hurricane on

record (since 1980). Ida's destruction was unique in that its damage was concentrated in two distinct regions. It made landfall as a powerful Category 4 storm in Louisiana, causing heavy damage to the Gulf Coast. As Ida's remnants moved northward, it merged with a frontal system to produce severe weather and flash flooding in the mid-Atlantic states and Northeast, with especially significant impacts in areas of Pennsylvania, New Jersey, and New York. Sidebar 4.1 provides more details on Ida's meteorological history and records.

Table 4.2. Global counts of TC activity by basin for 2021. "+" denotes top tercile; "++" is top 10%; "–" is bottom tercile; "––" is bottom 10% (all relative to 1991–2020). (Note that some inconsistencies between Table 4.2 and the text of the various basin write-ups in section 4g exist and are unavoidable, as tallying global TC numbers is challenging and involves more than simply adding up basin totals, because some storms cross TC basin boundaries, some TC basins overlap, and multiple agencies are involved in tracking and categorizing TCs.)

Basin	TCs	HTCs	Major HTCs	SS Cat 5	ACE ($\times 10^4$ kt^2)
North Atlantic	21 ++	7	4 +	0	146
Eastern Pacific	19 +	8	2 –	0	94 –
Western Pacific	23 –	10 ––	5 –	4 +	209 –
North Indian	5	3 +	1 +	0	21
South Indian	12 +	5	2 –	1 ++	100
Australia	12 +	3 –	2	1 ++	44 –
Southwest Pacific	9 +	4	2	1 ++	41
Global Totals	**97 +**	**38 ––**	**17 ––**	**7 +**	**656 –**

2) ATLANTIC BASIN—M. Rosencrans, E. S. Blake, C. W. Landsea, H. Wang, S. B. Goldenberg, and R. J. Pasch

(i) 2021 Seasonal activity

The 2021 Atlantic hurricane season produced 21 named storms, of which 7 became hurricanes and 4 of those became major hurricanes (Fig. 4.22b). The HURDAT2 (Landsea and Franklin 2013) 1991–2020 seasonal averages (included in IBTrACS) are 14.4 named storms, 7.2 hurricanes, and 3.2 major hurricanes. The 21 named storms during 2021 were the third most on record, trailing the 30 named storms in 2020 and 28 in 2005. Eight of the 21 named storms during 2021 were short-lived (≤ 2 days). There has been a large increase (approximately five per year) in detection of these "shorties" since 2000 (Landsea et al. 2010; Klotzbach et al. 2022). These increased counts primarily reflect new observational capabilities such as scatterometers, Advanced Microwave Sounding Units, and the Advanced Dvorak Technique, and have no association with any known climate variability (Villarini et al. 2011).

The 2021 seasonal Accumulated Cyclone Energy (ACE) value was 149.2% of the 1951–2020 median (which is 96.7×10^4 kt^2; Fig. 4.22c). This value was the 13th highest since 1970 and above NOAA's threshold for an above-normal season (126.1×10^4 kt^2, or 130% of median). There have now been a record six consecutive above-normal seasons, extending the current record of five. Since the current Atlantic high-activity era began in 1995 (Goldenberg et al. 2001; Bell et al. 2019, 2020), there have been 17 above-normal seasons, with 10 of those considered extremely active (ACE ≥ 165% of median, also referred to as hyperactive). By comparison, the preceding 24-year low-activity era of 1971–94 had only two above-normal seasons with none extremely active.

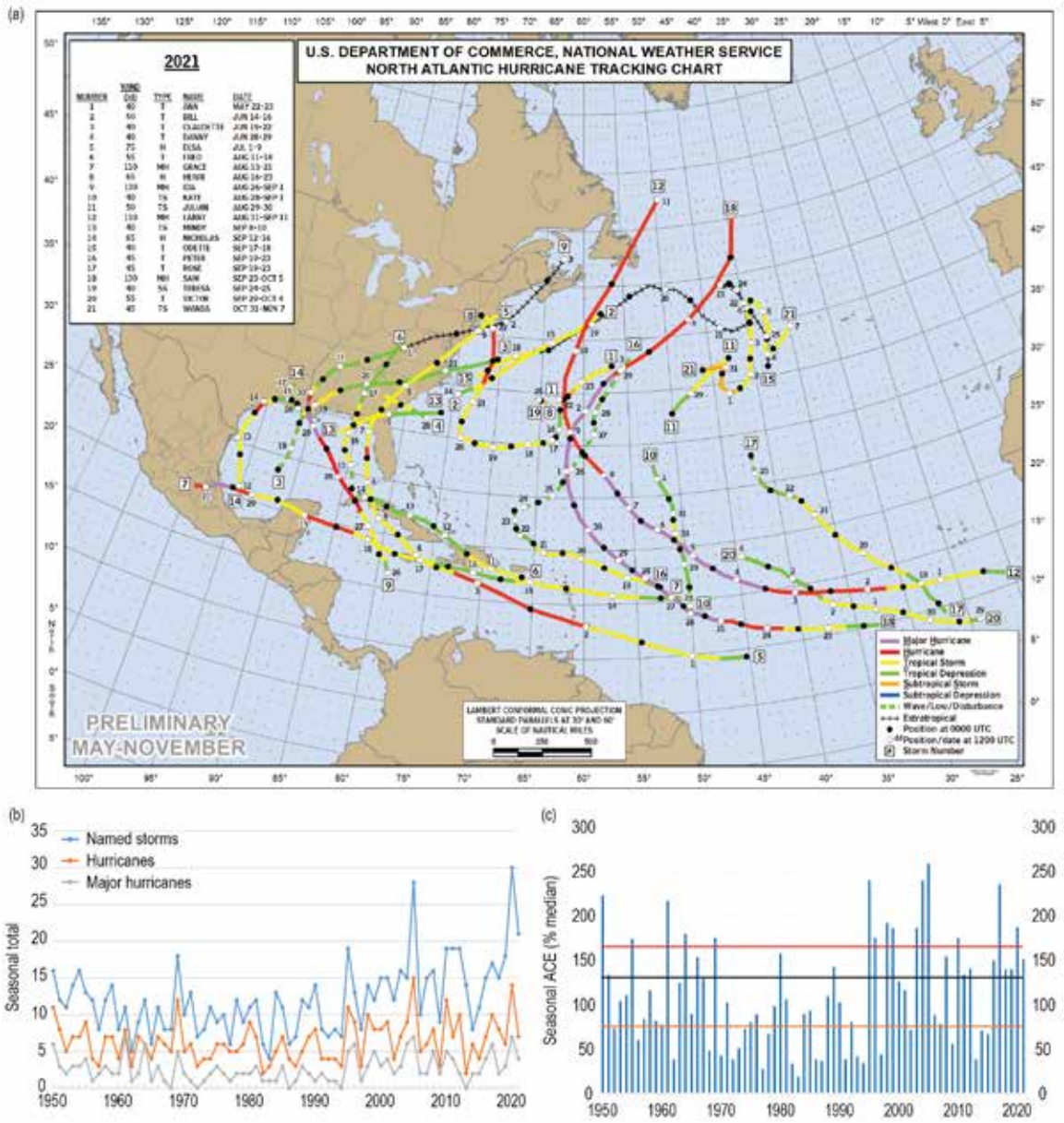

Fig. 4.22. (a) 2021 Atlantic basin storm tracks. Seasonal Atlantic hurricane activity during 1950–2021 for (b) numbers of named storms (blue), hurricanes (orange), and major hurricanes (gray) and (c) the Accumulated Cyclone Energy (ACE) index expressed as percent of the 1951–2020 median value. ACE is calculated by summing the squares of the 6-hourly maximum sustained surface wind speed (kt) for all periods while the storm is at least tropical storm strength. The black (orange) line represents NOAA's limit for an above-normal (below-normal) season and the red line is the threshold for an extremely- (aka hyper-) active season, (http://www.cpc.ncep.noaa.gov/products/outlooks/ background_information.shtml). Note that there is a low bias in activity from the 1950s to the early 1970s due to the lack of satellite imagery and technique (Dvorak) to interpret tropical cyclone intensity for systems over the open ocean. (Source: HURDAT2 [Landsea and Franklin 2013].)

(ii) Storm formation times, regions, and landfalls

Tropical cyclone (TC) activity occurred throughout most of the 2021 hurricane season (Fig. 4.23b), with a TC present every month in the official season as well as in May. Activity ramped up relatively quickly, with Elsa becoming the earliest developing fifth named Atlantic storm on record when it formed on 1 July. Of the first five named storms in the 2021 Atlantic hurricane season, four were classified as a "shortie", lasting two days or fewer. On average, 1–2 named storms form per year during May–July.

August–October (ASO), typically the most active part of the hurricane season, featured 16 named storms during 2021 compared with the 1991–2020 average of 11.1, and at least one TC was present at all times from mid-August through early October. Six of these 16 storms became hurricanes (the

seventh hurricane of the season, Elsa, formed in July), and four of those became major hurricanes. Most of these ASO storms (9 of 16) formed in the main development region (MDR), which is also typical of an above-normal season. The MDR spans the tropical Atlantic Ocean and Caribbean Sea between 9.5°N and 21.5°N (Goldenberg and Shapiro 1996; Goldenberg et al. 2001; Bell and Chelliah 2006; Bell et al. 2017, 2018, 2019). After a highly active late August and most of September, Atlantic TC activity dropped precipitously, with only one named storm developing after 29 September. Tropical Storm Wanda was first named as a subtropical storm on 31 October, gaining tropical characteristics in early November, ending a nearly month-long quiet period.

Historically, above-normal seasons result from a sharp increase in the number, intensity, and duration of storms that develop in the MDR. For the entire 2021 season, 10 of the 21 named storms formed in the MDR (Fig. 4.23a) and accounted for five of the season's seven hurricanes and all of the season's four major hurricanes. The associated MDR-related ACE value was 129% of the basin-wide median. By comparison, named storms forming in the Gulf of Mexico only contributed 5% of the basin-wide median in 2021, and storms from the extratropics contributed 15%. This MDR-related ACE value is lower than the 1991–2020 MDR average for above-normal seasons of 140% of the median. These values are roughly five times higher than the MDR average of 20% of the median for below-normal seasons (defined by NOAA as having a total basin-wide ACE less than 73×10^4 kt^2).

The actual storm tracks during 2021 (Fig. 4.22a) showed two main regions of activity. One area was oriented from west-southwest to east-northeast across the extratropics, where eight named storms formed. The MDR was also active, but in the middle of these active areas there was a quiet area in the extreme southwest Atlantic including the east coast of Florida and the Bahamas.

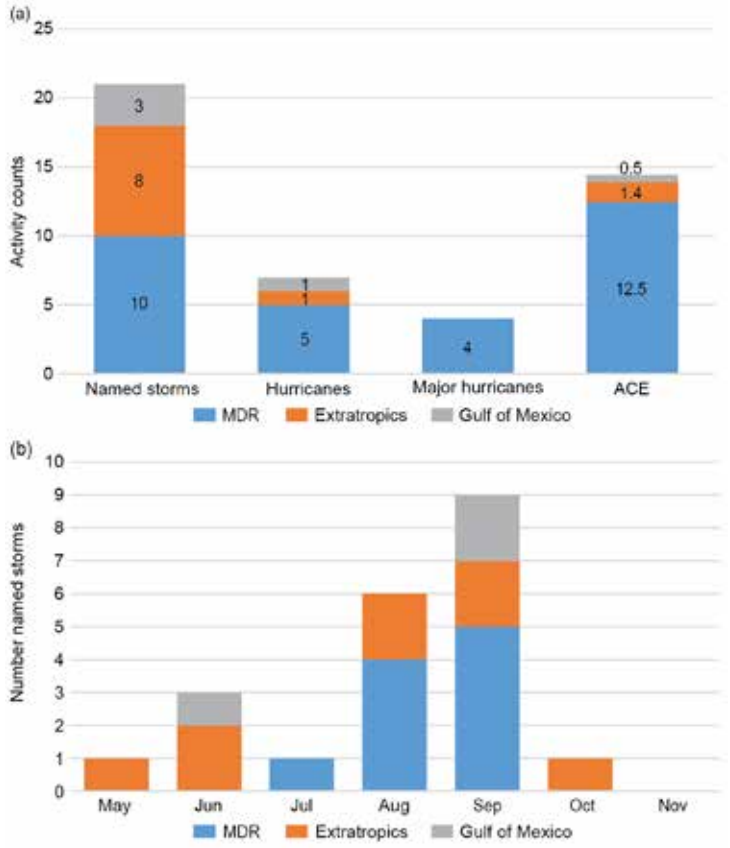

Fig. 4.23. Atlantic TC activity in 2021. (a) Total seasonal storm counts for the three storm classifications and for ACE shown for each region the storm was first named. (b) Named storm counts shown for the month and region the storm was first named. ACE reflects the entire storm ACE and is attributed to the region in which the storm was first named. Regions in (a) and (b) are indicated by the color bar below panel (b). The Atlantic MDR spans 20°–87.5°W and 9.5°–21.5°N. The "extratropics" includes all regions except for the MDR and Gulf of Mexico. (Source: HURDAT2 [Landsea and Franklin 2013].)

Several of the MDR formations have long tracks to the west-northwest. The season also featured eight storms making landfall in the continental United States, with others impacting the Caribbean, Mexico, Central America, Newfoundland, and Bermuda.

Several notable individual storms formed during the 2021 hurricane season. Hurricane Sam was a major hurricane for 7.75 days, contributing ~38% of the total seasonal ACE. Fortunately, Sam's track remained out to sea with minimal impacts. In terms of damage, Hurricane Ida was the largest disaster for the United States in 2021, causing $75 billion (U.S. dollars). Preliminary estimates indicate Ida had winds of 130 kt as it made landfall in Louisiana, which would be tied for the fifth-strongest hurricane to make landfall in the United States since more reliable records began around 1900. In addition to significant damage along the Gulf Coast, Ida also interacted with a cold front to produce torrential rain and flooding across the mid-Atlantic and Northeast. More information on Hurricane Ida is detailed in Sidebar 4.1. Hurricane Henri also brought significant rains to the Northeast just a week earlier, establishing some localized daily records but no large regional records, and causing an estimated $700 million (U.S. dollars) in damage. Hurricane Grace spread damage across the Caribbean and into Mexico, causing an estimated $300 million (U.S. dollars) in damage. Tropical Storms Elsa and Fred and Hurricane Nicholas were storms that each caused more than $1 billion (U.S. dollars) in damage (see section 7b2).

(iii) Sea surface temperatures

Four main sea surface temperature (SST) signals were present during ASO 2021 (Fig. 4.24). First, SSTs were above average throughout the MDR (Fig. 4.24a), and the area-averaged SST anomaly was +0.35°C (Fig. 4.24b). The largest anomalies in the MDR were observed throughout the Caribbean Sea and ranged from just above 0°C to +0.5°C.

Second, the area-averaged SST anomaly in the MDR was higher (by +0.17°C) than that of the remainder of the global tropics (Fig. 4.24c). This signal typifies the warm phase of the Atlantic multi-decadal oscillation (AMO; Enfield and Mestas-Nuñez 1999; Bell and Chelliah 2006) and is a ubiquitous characteristic of Atlantic high-activity eras, such as 1950–70 and 1995–present (Goldenberg et al. 2001; Vecchi and Soden 2007; Bell et al. 2018).

The third SST signal during ASO 2021 reflected above-average temperatures across most of the North Atlantic Ocean. Outside of the MDR, the largest anomalies (exceeding +1°C) occupied the western, and portions of the central, North Atlantic (Fig. 4.24a), areas where numerous tropical storms and hurricanes tracked. The area-averaged SST anomaly in the western North Atlantic (red box, Fig. 4.24a) was +0.79°C and reflected a continuation of exceptional warmth that began in 2014 (Fig. 4.24d).

The fourth SST signal during ASO 2021 was the development of La Niña in the equatorial Pacific (section 4b). As discussed below, La Niña contributed to the enhanced hurricane activity during August and September.

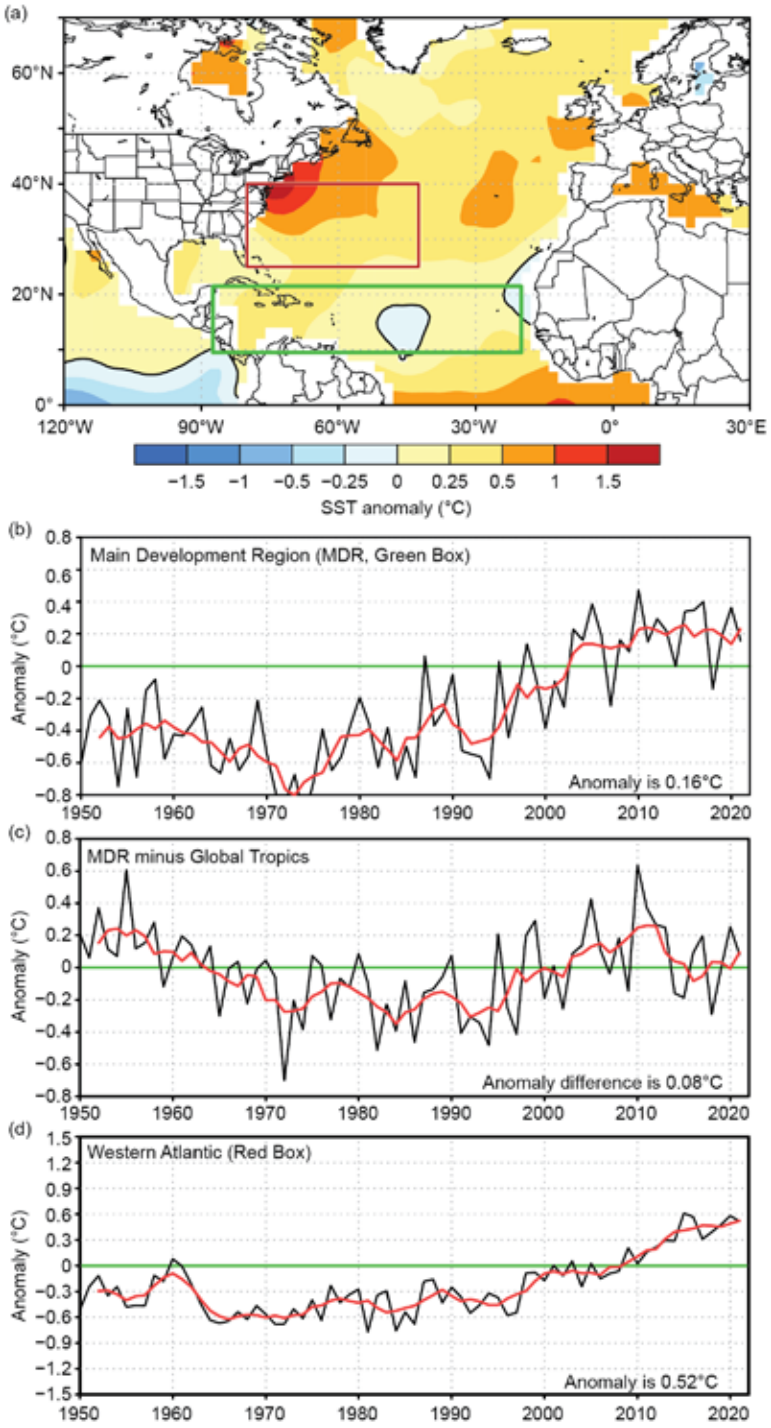

Fig. 4.24. (a) Aug–Oct 2021 SST anomalies (°C). (b–d) Time series of Aug–Oct area-averaged SST anomalies (black) and 5-pt running mean of the time series (red); (b) In the MDR (green box in (a) spanning 20°–87.5°W and 9.5°–21.5°N); (c) difference between the MDR and the global tropics (20°S–20°N); and (d) in the western North Atlantic (red box in (a) spanning 42.5°–80°W and 25°–40°N). Anomalies are departures from the 1991–2020 period means. (Source: ERSST-v5 [Huang et al. 2017].)

(iv) Atmospheric conditions

Climatologically, the ASO peak in Atlantic hurricane activity largely reflects the July–September (JAS) peak in the West African monsoon as noted in section 4e. The inter-related circulation features of an enhanced monsoon act to further increase hurricane activity, while those with an anomalously weak monsoon act to suppress it (Gray 1990; Hastenrath 1990; Landsea et al. 1992; Bell and Chelliah 2006; Bell et al. 2018, 2020). The association on multi-decadal time scales between the West African monsoon and Atlantic hurricane activity largely exists because of a common relationship to multi-decadal modes of variability (Bell and Chelliah 2006).

The West African monsoon was enhanced during JAS 2021, as indicated by negative outgoing longwave radiation (OLR) anomalies across the African Sahel (red box, Fig. 4.25a). Total OLR values in this region averaged 239 W m^{-2} (Fig. 4.25b), with values less than 240 W m^{-2}, indicating deep tropical convection. Consistent with these conditions, the larger-scale divergent circulation at 200-hPa featured an extensive area of anomalous divergence and a core of negative velocity

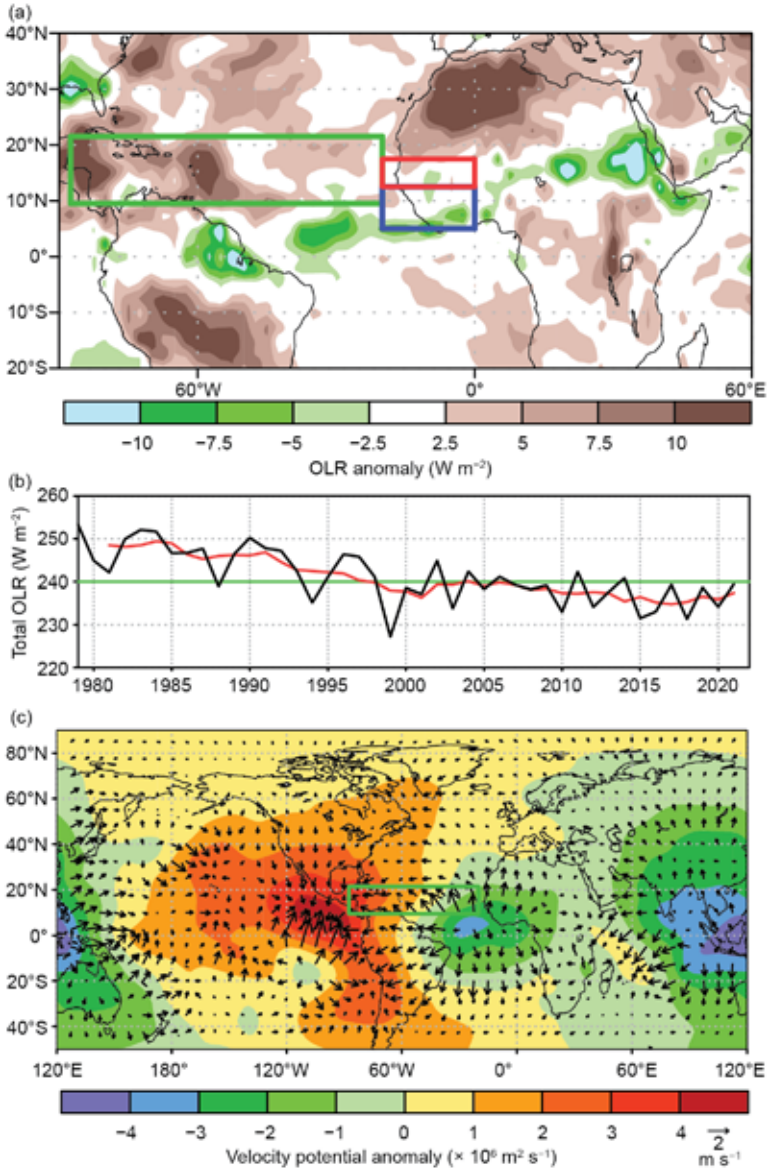

Fig. 4.25. (a) Jul–Sep 2021 anomalous OLR (W m^{-2}), with negative (positive) values indicating enhanced (suppressed) convection. (b) Time series of Jul–Sep total OLR (black) and 5-pt running mean of the time series (red) averaged over the African Sahel region (red box in (a, c) spanning 20°W–0° and 12.5°–17.5°N). (c) Aug–Oct 2021 anomalous 200-hPa velocity potential (× 10^6 m^2 s^{-1}) and divergent wind vectors (m s^{-1}). In (a), contours show total OLR values of 220 W m^{-2} and 240 W m^{-2}. In (a, c), the green box denotes the Atlantic MDR. Anomalies are departures from the 1991–2020 means. (Sources: NCEP/NCAR Reanalysis [Kalnay et al. 1996] for velocity potential and wind, and Liebmann and Smith [1996] for OLR.)

potential anomalies across subtropical northern Africa extending into the eastern Atlantic (Fig. 4.25c). The OLR time series shows that an enhanced monsoon has largely prevailed throughout the current Atlantic high-activity era and warm AMO of 1995–present (Fig. 4.25b). By contrast, a much weaker monsoon with OLR values well above 240 W m^{-2} in the Sahel region was typical of the low-activity and cool AMO period from 1971 to 1994. During ASO 2021, core atmospheric conditions within the MDR reflected a combination of the enhanced West African monsoon, La Niña, and midlatitude influences.

At 200-hPa, the enhanced monsoon amplified subtropical ridges (indicated by anticyclonic streamfunction anomalies) across Africa in both hemispheres (Fig. 4.26a). La Niña impacts in that field (Bell and Chelliah 2006) included cyclonic streamfunction anomalies in both hemispheres of the western and central subtropical Pacific. Farther north, a large anticyclonic anomaly was evident over eastern Canada. Troughing extended from northern Mexico, across Florida, and into the central extratropical Atlantic near 40°N. The streamfunction pattern over the western and central subtropical Pacific aligns with the La Niña response identified in Bell and Chelliah (2006), while the cyclonic streamfunction anomalies over northern Mexico, across Florida, and into the extratropical Pacific are dissimilar to that identified response pattern, pointing to some other source of variability having influence over those regions. The 1000-hPa anomalous height and wind field (Fig. 4.26c) showed just how strong some of the midlatitude circulations were and even shows evidence of flow deep into the tropics. Sea level pressure was also below normal over the central and eastern MDR, which would typically correspond to decreased wind shear and more convection, but vertical wind shear was near normal for the season, and OLR indicates slightly above-normal convection.

The West African monsoon was enhanced and showed direct influences on the circulation pattern during ASO 2021. An aspect of the enhanced West African monsoon system during ASO 2021 was an upward extension of the westerly wind anomalies over the eastern half of the MDR to at least 700-hPa (Fig. 4.26d), which is the approximate level of the African Easterly Jet (AEJ). This anomaly pattern contributed to a deep layer of anomalous cyclonic relative vorticity (i.e., increased horizontal cyclonic shear) along the equatorward flank of the AEJ. These conditions are known to favor increased TC activity by helping African easterly waves to be better maintained

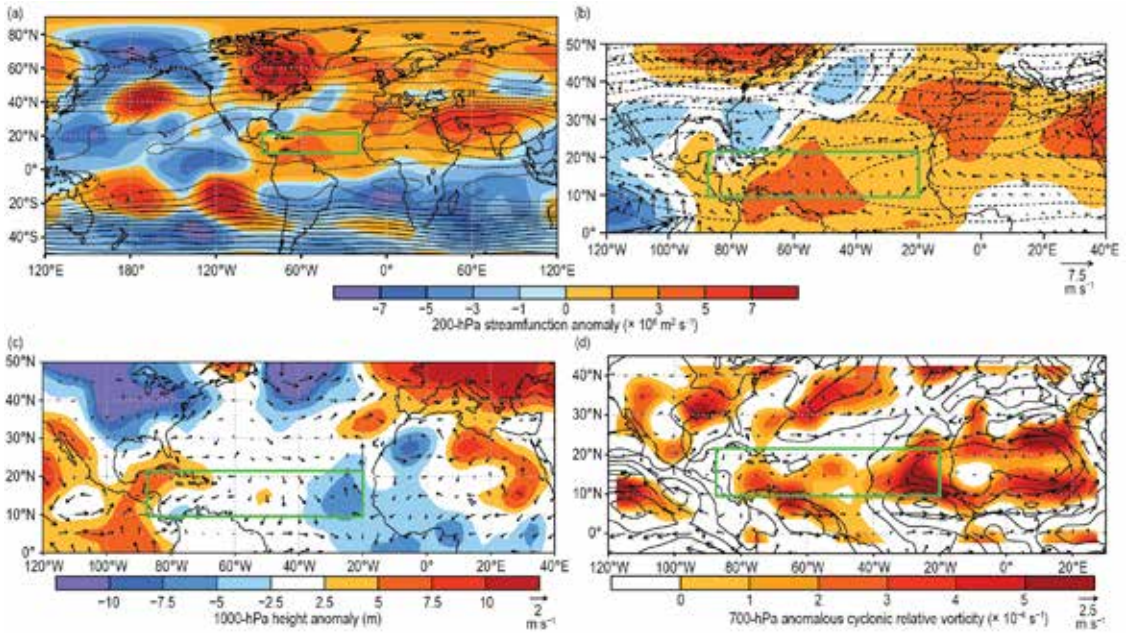

Fig. 4.26. Aug–Oct 2021: (a) 200-hPa streamfunction (contours, interval is 5 × 10^6 m^2 s^{-1}) and anomalies (shaded), with anomalous vector winds (m s^{-1}) also shown in (b); (c) anomalous 1000-hPa heights (shaded, m) and vector winds; and (d) anomalous 700-hPa cyclonic relative vorticity (shaded, × 10^6 m^2 s^{-1}) and vector winds. Green box denotes the MDR. Anomalies are departures from the 1991–2020 means. (Source: NCEP/NCAR Reanalysis [Kalnay et al. 1996].)

and by providing an inherent cyclonic rotation to their embedded convective cells (Bell et al. 2020; Landsea et al. 1998).

The anomalous low-level circulation also reflected an extensive flow of deep tropical moisture into the southern half of the central and eastern MDR. This moisture not only helps feed the monsoon, but also favors increased Atlantic hurricane activity. This situation contrasts with the drier and cooler air that normally accompanies enhanced northeasterly trade winds when the monsoon is weak.

The ASO 2021 200–850-hPa vertical wind shear was about average for much of the MDR and slightly higher than average for the western MDR/Caribbean (Fig. 4.27a). The area-averaged magnitude of the vertical wind shear for the entire MDR was 9.4 m s^{-1} (Fig. 4.27b) and for the Gulf of Mexico was 10.4 m s^{-1} (Fig. 4.27c). Both of these values are above the upper threshold of 8 m s^{-1} considered conducive to hurricane formation on monthly time scales (Bell et al. 2017), so the above-normal overall activity is even more remarkable. The sharp peak and busy month of September, in which nine named storms developed (Fig. 4.23b), was coincident with a period of anomalously low vertical wind shear in the MDR (Fig. 4.27d). The abrupt end to the season, with only one storm developing after 29 September, coincided with a period of anomalously strong wind shear across the Gulf of Mexico, Caribbean, MDR, and the extratropical Atlantic.

The MJO (Madden and Julian 1971), as discussed in section 4c, was generally stationary and inactive during September and October. Nonetheless, variations in the large-scale tropical convection may have played a role in the quiescent October. From September to October, the main convective activity shifted from the Indian Ocean to the Maritime Continent, as assessed via a combination of the multivariate MJO index of Wheeler and Hendon (2004; Fig. 4.8d) and Climate Prediction Center's weekly MJO analysis. For a typical MJO, this circulation results in increased shear over and decreased convection in the tropical Atlantic (Mo 2000), both of which decrease

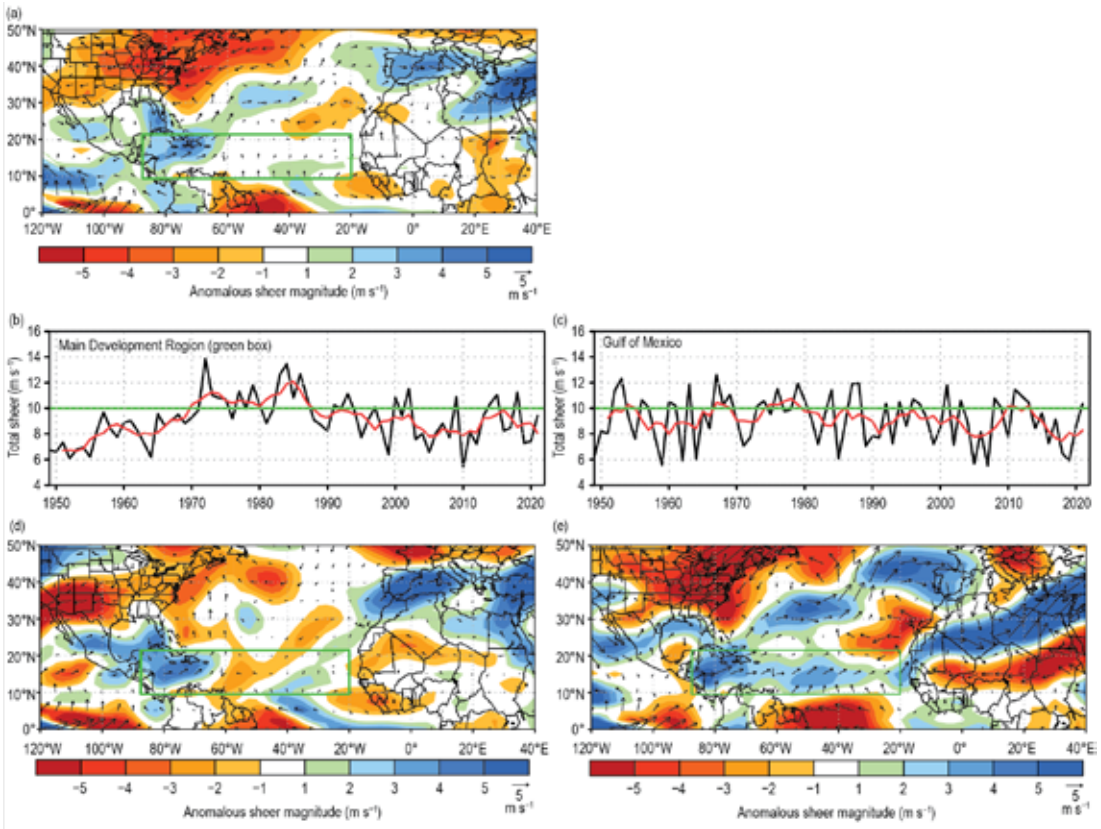

Fig. 4.27. Aug–Oct (ASO) magnitude of the 200–850-hPa vertical wind shear (m s^{-1}): (a) 2021 anomalous magnitude and vector. (b, c) Time series of ASO vertical wind shear magnitude (black) and 5-pt running mean of the time series (red) averaged over (b) the MDR (spanning 87.5°–20°W and 9.5°–21.5°N), and (c) the western Gulf of Mexico (spanning 80°–97.5°W and 21.5°–30°N). (d) Same as (a), but for Sep 2021. (e) Same as (d), but for Oct 2021. Anomalies are departures from the 1991–2020 means. (Source: NCEP/NCAR Reanalysis [Kalnay et al. 1996].)

tropical cyclone formations. Even if this were not a typical MJO, the shift in the variations of the tropical circulation may have contributed to the lack of activity in October.

The above conditions typified the many active seasons seen during the current Atlantic high-activity era. However, as with other years, interannual signals were also in play during 2021. One of those was La Niña, which favors enhanced activity as in other recent La Niña events (2010, 2016, and 2020). However, the La Niña impact may have been reduced by other interannual signals like the strong ridge over eastern Canada (Figs. 4.26a,c) with troughing over the central extratropical Atlantic and over the Gulf of Mexico. The ridge/trough combinations likely contributed to increased wind shear, especially late in the season, which may have capped activity, despite the presence of many features of the high-activity era (above-normal SST, enhanced West African Monsoon, and early season activity).

Sidebar 4.1: **Hurricane Ida: A landfalling Louisiana major hurricane for the record books**—P. KLOTZBACH AND R. TRUCHELUT

The 2021 Atlantic hurricane season was the sixth consecutive above-average season based on NOAA's definition, with 21 named storms, seven hurricanes, and four major hurricanes. Eight named storms and two hurricanes made landfall in the continental United States, with Hurricane Ida by far the most significant landfalling Atlantic tropical cyclone of the year. Ida struck near Port Fourchon, Louisiana, with maximum 1-minute sustained winds of 130 kt (67 m s^{-1}) on 29 August. Wind and surge caused tremendous destruction in south-central and southeastern Louisiana, with the New Orleans metropolitan area also experiencing significant wind damage. Ida's remnants interacted with a frontal system to cause significant flash flooding across the coastal plain of the northeastern United States, including Pennsylvania, New Jersey, New York, and Connecticut. The National Hurricane Center's best track report on Hurricane Ida (Beven et al. 2022) estimated that Ida caused ~$75 billion (U.S. dollars) in damage.

Here, we discuss the meteorological history of Ida and highlight some of the records that Ida set. Historical landfall records from 1851 to present are taken from the National Hurricane Center/Atlantic Oceanographic and Meteorological Laboratory archive (http://www.aoml.noaa.gov/hrd/hurdat/All_U.S._Hurricanes.html). Ida's observed values are taken from the Atlantic hurricane database (HURDAT2; Landsea and Franklin 2013) that is based on Beven et al. (2022).

Ida developed from a high-amplitude easterly wave, becoming a tropical depression at 1200 UTC on 26 August in the west-central Caribbean and intensifying into a tropical storm by 1800 UTC. Over the following 24 hours, Ida rapidly intensified from 35 kt (18 m s^{-1}) to 70 kt (36 m s^{-1}), while tracking northwestward in a light shear and warm water environment in the western Caribbean. Ida made two landfalls in Cuba as a Category 1 hurricane on 27 August, the first on the Isle of Youth and the second on Pinar Del Rio. Disruption of Ida's circulation due to land interaction and dry air entrainment temporarily arrested Ida from strengthening, and it remained a Category 1 hurricane through 28 August.

As Ida continued northwest, vertical wind shear relaxed as the hurricane tracked over a warm eddy in the east-central Gulf of Mexico, causing rapid intensification. Between 1200 UTC on 28 August and 1200 UTC on 29 August, Ida's maximum sustained winds increased by 60 kt (31 m s^{-1}), from 70 kt (36 m s^{-1}) to 130 kt (67 m s^{-1}). This 60-kt intensification in 24 hours slightly exceeded Hurricane Laura (2020)'s rate of 55 kt (28 m s^{-1}) in 24 hours in the Gulf of Mexico. Laura also made landfall over Louisiana as a 130 kt (67 m s^{-1}) hurricane in late August. During this same time period, Ida's minimum central pressure fell 57 hPa (from 986 hPa to 929 hPa). At the peak of its intensification, Ida's pressure per aircraft reconnaissance fell by ~11 hPa in one hour between 1000 UTC and 1100 UTC on 29 August. Ida maintained a 130-kt intensity until initial landfall near Port Fourchon, Louisiana at ~1655 UTC on 29 August (Fig. SB4.1).

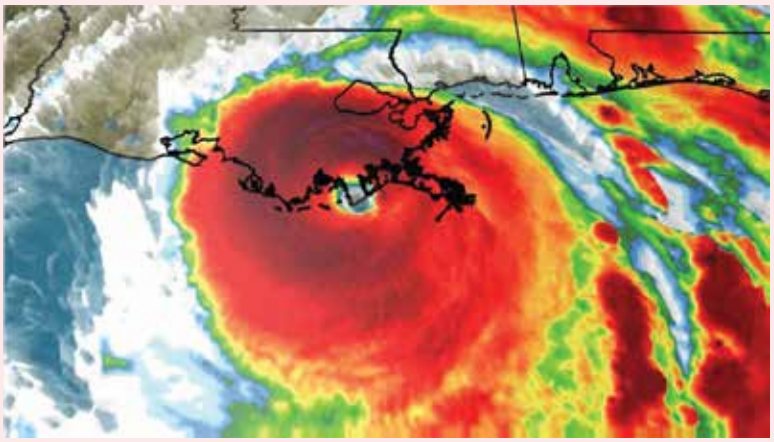

Fig. SB4.1. Infrared satellite image of Hurricane Ida at the time of its landfall at ~1655 UTC on 29 Aug 2021. Image courtesy of NOAA.

Following landfall, Ida only slowly weakened. Ida maintained Category 3+ hurricane intensity for at least five hours and Category 1+ hurricane intensity for at least 11 hours following initial landfall. This is likely due to a combination of factors, including a slow forward motion that kept part of Ida's circulation over water for most of 29 August and elevated soil moisture due to heavy antecedent rainfall over southern Louisiana. The system weakened to a tropical storm by mid-day on 30 August as it accelerated northeast over Mississippi, and it became a tropical depression on 31 August.

Ida was officially declared post-tropical while located over West Virginia on 1 September. However, as a post-tropical cyclone, Ida interacted with a frontal zone and produced copious rainfall (Fig. SB4.2), several violent tornadoes, and devastating flash flooding across the northern mid-Atlantic and southern New England. Flooding was particularly severe in and around the New York City metropolitan area, where widespread rainfall totals of 150–250 mm were recorded, including a 1-hour accumulation of 80 mm in New York's Central Park between ~0100 and 0200 UTC on 2 September. The estimated return period for 12-hour rainfall totals as observed from post-tropical Ida from the northern suburbs of Philadelphia northeast into coastal Connecticut is generally 100 to 200 years, with locally higher return periods. The final advisory on post-tropical Ida was issued on 2 September.

Hurricane Ida caused tremendous damage in southern Louisiana, with loss estimates in Louisiana of ~$55 billion (U.S. dollars), according to Beven et al. (2022). Flash flooding in the mid-Atlantic states was responsible for an additional ~$205 million in damage. Ida caused 55 direct and 32 indirect fatalities in the United States, and its precursor disturbance also caused significant flooding in Venezuela, which led to 20 fatalities. Storm surge exceeding three meters was reported to the east of where Ida made landfall. Ida's strong winds also led to extensive power outages, with over one million residents in Louisiana reported without electricity at one point.

Ida's 130 kt (67 m s^{-1}) intensity at landfall ties the Last Island Hurricane (1856) and Hurricane Laura (2020) for the strongest maximum sustained winds for a Louisiana landfalling hurricane on record. These sustained winds also equaled the fifth strongest on record for the continental United States. Ida's landfall pressure of 931 hPa was the second lowest for a Louisiana hurricane on record, trailing only Katrina (920 hPa), which struck on the same date 16 years prior to Ida. Laura and Ida are also the first two 130+ kt hurricanes on record to make landfall in the continental United States in consecutive years. The continental United States has now experienced three 130+ kt hurricane landfalls in the past four years: Michael (2018), Laura (2020), and Ida (2021). This equals the three 130+ kt hurricane landfalls recorded in the previous 82 years, 1936–2017: Camille (1969), Andrew (1992), and Charley (2004).

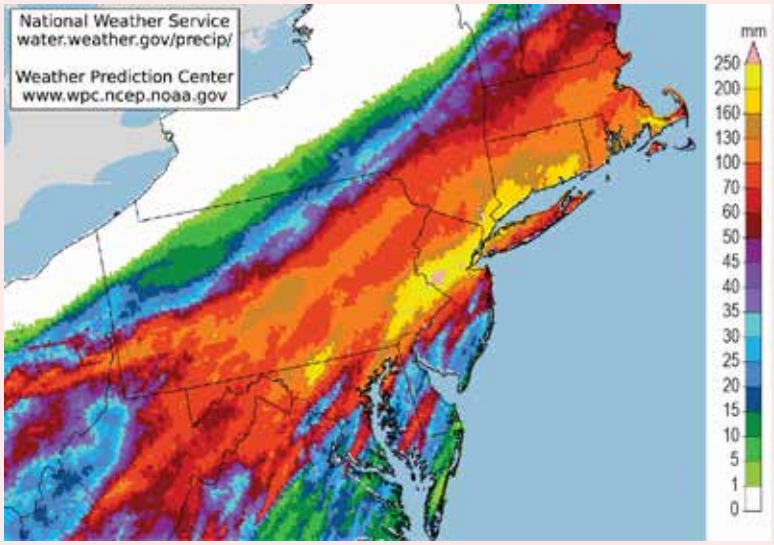

Fig. SB4.2. 48-h radar-estimated rainfall (mm) across the mid-Atlantic states and southern New England ending at 1200 UTC on 2 Sept 2021. Image courtesy of Gregory Carbin, NOAA/Weather Prediction Center.

3) EASTERN NORTH PACIFIC AND CENTRAL NORTH PACIFIC BASINS—K. M. Wood and C. J. Schreck

(i) Seasonal activity

Storm counts in this section are combined from the two agencies responsible for issuing advisories and warnings in the eastern North Pacific (ENP) basin: NOAA's National Hurricane Center in Miami, Florida (for the region from the Pacific coast of North America to 140°W), and NOAA's Central Pacific Hurricane Center in Honolulu, Hawaii (for the region between 140°W and the date line, the central North Pacific [CNP]).

A total of 19 named storms formed in the combined ENP/CNP basin (Fig. 4.28a), 8 of which became hurricanes and 2 became major hurricanes. This activity is above normal for named storms, near normal for hurricanes, and below normal for major hurricanes compared with the 1991–2020 averages of 16.9 named storms, 8.8 hurricanes, and 4.6 major hurricanes. All but one named storm occurred between the official hurricane season start date of 15 May and end date of 30 November. The first TC of the season, Tropical Storm Andres, developed on 9 May. The final named storm, Tropical Storm Sandra, weakened to a tropical depression (TD) on 8 November and dissipated the next day. No named storms were active within the CNP, which is well below the 1991–2020 average of 3.4 for the CNP.

The 2021 seasonal ACE index was 94.0 × 10^4 kt^2, or 71% of the 1991–2020 mean of 132.8 × 10^4 kt^2 (Fig. 4.28b; Bell et al. 2000), continuing the streak of below-normal activity that has persisted since 2019 (Fig. 4.28b; Wood and Schreck 2020, 2021). Much of this season's TC activity, including

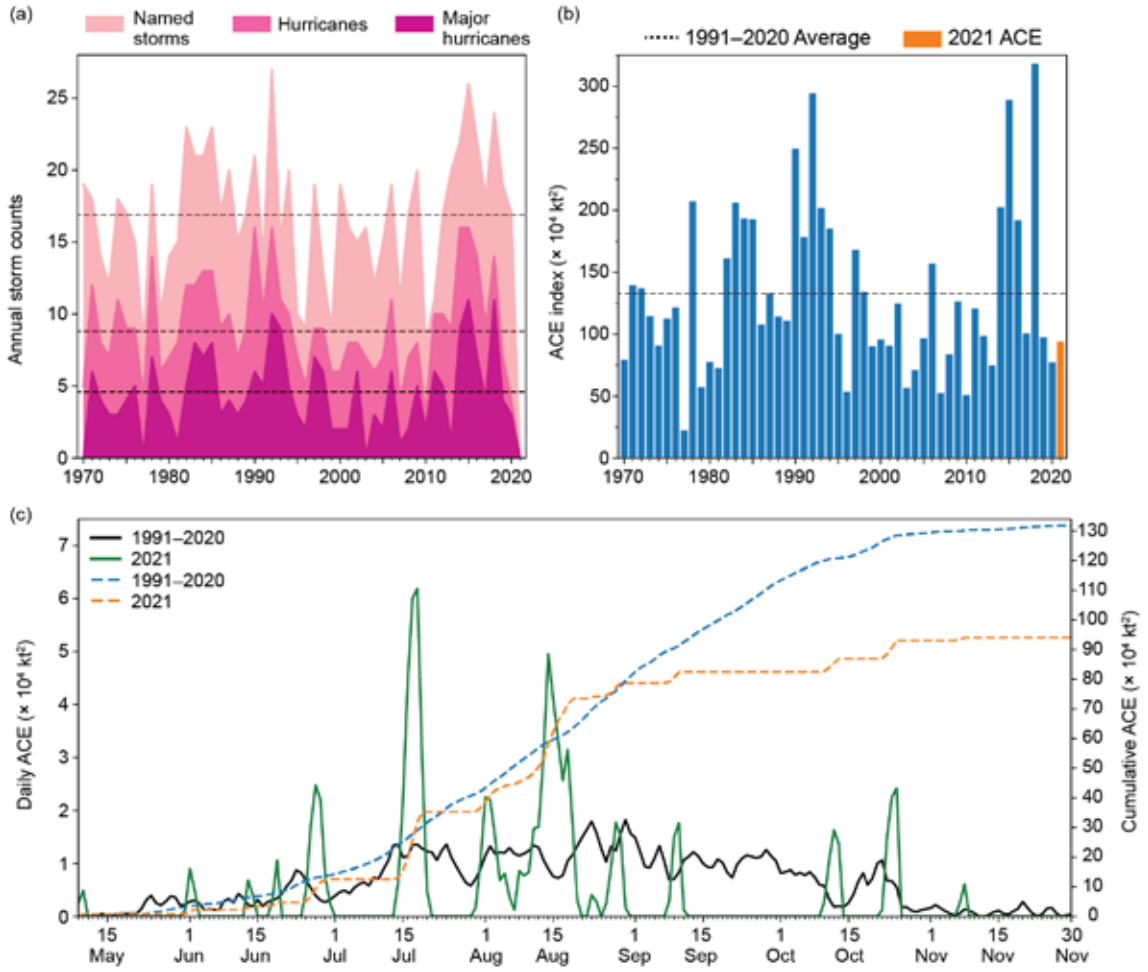

Fig. 4.28. (a) Annual ENP/CNP storm counts by category during the period 1970–2021, with the 1991–2020 average by category denoted by each dashed line. (b) Annual ACE (× 10^4 kt^2) during 1970–2021, with 2021 highlighted in orange and the 1991–2020 average denoted by the dashed line. (c) Daily ACE during 1991–2020 (solid black) and during 2021 (solid green); accumulated daily ACE during 1991–2020 (dashed blue) and during 2021 (dashed orange).

three hurricanes and both major hurricanes, was confined to July and August, in which 71% of the total ACE occurred. One hurricane (Olaf) formed in September and two (Pamela and Rick) in October (Fig. 4.28c).

The two 2021 ENP TCs that peaked as at least Category 4 hurricanes (115 kt; 59 m s^{-1}) on the Saffir-Simpson Hurricane Wind Scale contributed just over half of the season's total ACE. Hurricane Felicia (14–20 July; Cangialosi 2021a) rapidly intensified (≥ 30 kt or 15.4 m s^{-1} in 24 hours) prior to reaching its peak intensity of 125 kt (64 m s^{-1}) and eventually rapidly weakened while over the open ocean (≤ –30 kt or –15.4 m s^{-1} in 24 hours; Wood and Ritchie 2015). Hurricane Linda (10–19 August; Reinhart 2021) also rapidly intensified prior to peaking as a 115-kt major hurricane, followed by a weakening and re-intensification period that ultimately resulted in rapid weakening prior to dissipation. Both Felicia and Linda exhibited a peak 24-hour intensification of 35 kt (18 m s^{-1}). Though neither TC maintained its peak intensity for more than 12 hours, Felicia remained at major hurricane strength for 66 hours and Linda for 48 hours, their longevity contributed to these two TCs becoming the highest ACE producers of the season.

(ii) Environmental influences

Negative sea surface temperature (SST) anomalies marked much of the equatorial eastern Pacific during the 2021 ENP hurricane season alongside easterly 850-hPa wind anomalies (Fig. 4.29), likely associated with the La Niña event established in August, following the 2020 La Niña (NOAA 2020, 2021). Notably, season-averaged SSTs were near or above normal where most TCs formed and tracked (Fig. 4.29a). Most TC activity was confined to the eastern part of the basin, where OLR anomalies were near or below normal and co-located with near- or below-normal vertical wind shear (Figs. 4.29b,c). However, few TCs tracked through the below-normal shear that occurred near 140°W. Unlike recent ENP seasons, 2021 was marked by enhanced 850-hPa westerly flow near Central America, which may have contributed to the clustering of activity in the eastern part of the basin by enhancing the available low-level cyclonic vorticity (Fig. 4.29d).

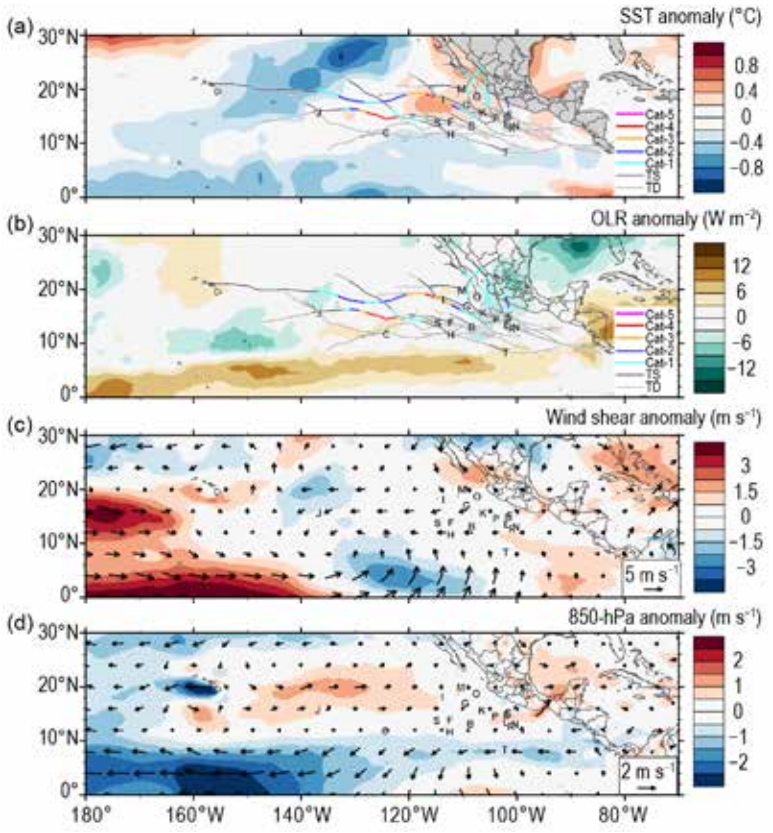

Fig. 4.29. 15 May–30 Nov 2021 anomaly maps of (a) SST (°C; Banzon and Reynolds 2013), (b) OLR (W m^{-2}; Schreck et al. 2018), (c) 200–850-hPa vertical wind shear (m s^{-1}) vector (arrows) and scalar (shading) anomalies, and (d) 850-hPa wind (m s^{-1}, arrows) and zonal wind (shading) anomalies. Anomalies are relative to the annual cycle from 1991–2020. Letters denote where each TC reached tropical storm intensity. Wind data are obtained from CFSR (Saha et al. 2014).

Tropical cyclone activity in the ENP, especially cyclogenesis, can be affected by the MJO as well as convectively-coupled Kelvin waves (e.g., Maloney and Hartmann 2001; Aiyyer and Molinari 2008; Schreck and Molinari 2011; Ventrice et al. 2012a,b; Schreck 2015, 2016). A relatively robust MJO signal occurred in late July into early August, coinciding with the formation of four TCs in the eastern part of the basin: Hilda, Ignacio, Kevin, and Linda (Fig. 4.30; see Kiladis et al. 2005, 2009 for methodology). In addition, the passage of a Kelvin wave coincided with the development of Hilda and Ignacio. Other Kelvin waves likely contributed

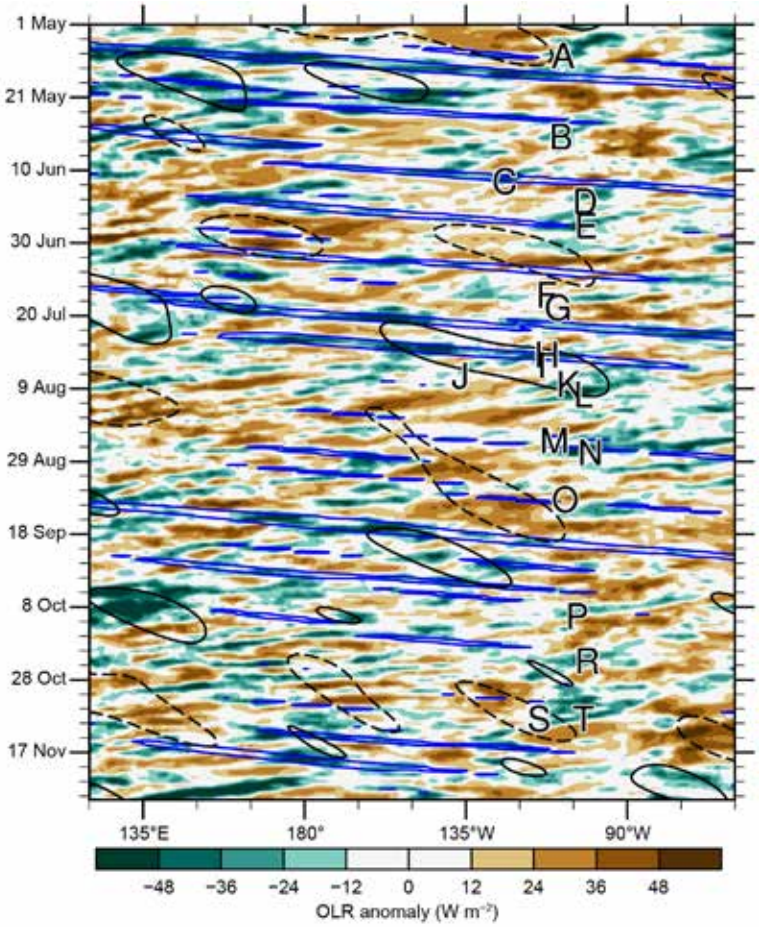

Fig. 4.30. Longitude–time Hovmöller diagram of 5°–15°N average OLR (W m^{-2}; Schreck et al. 2018). Unfiltered anomalies, from a daily 1991–2020 climatology are shaded. Negative anomalies (green) indicate enhanced convection. Anomalies filtered for Kelvin waves are contoured in blue at –10 W m^{-2} and MJO-filtered anomalies in black at ±10 W m^{-2} (dashed for positive, solid for negative). Letters denote the longitude and time when each TC reached tropical storm intensity.

to the formation of Carlos and Enrique. Finally, easterly wave activity can be inferred from Fig. 4.30 as westward-moving negative (green) anomalies; such waves were active during most of the ENP genesis events.

(iii) Impacts

Five ENP TCs made landfall on the west coast of Mexico in 2021: Tropical Storm Dolores, and Hurricanes Nora, Olaf, Pamela, and Rick. In addition, Hurricane Enrique dissipated just offshore of Baja California in the southern Gulf of California. The earlier-noted cluster of TC activity in the eastern part of the basin likely contributed to an enhanced risk of landfall relative to climatology; on average, 1.8 ENP TCs make landfall in Mexico each year (Raga et al. 2013).

Tropical Storm Dolores (18–20 June) caused three deaths from lightning, produced significant flooding in multiple Mexican states, and is estimated to have caused $50 million (U.S. dollars) in economic losses (Papin 2022). Hurricane Nora (26–30 August; https://www.nhc.noaa.gov/data/tcr/EP142021_Nora.pdf), moved parallel to the Mexican coast for an extended period of time before finally moving inland, likely causing at least $125 million (U.S. dollars) in damage in Mexico and three deaths (Aon 2021a,b). Hurricane Olaf (7–11 September) led to one direct fatality from a mudslide, caused over 190,000 customers to lose power, and resulted in an estimated $10 million (U.S. dollars) in damage (Latto 2022). No direct deaths were attributed to Hurricane Pamela (10–13 October), but two people died in Texas due to flooding induced by its remnants. The storm also caused widespread flooding and moderate wind damage in Mexico (Cangialosi 2021b). Hurricane Rick (22–25 October) caused one direct fatality, damaged over 1200 houses, and likely caused tens of millions of dollars in economic losses (Berg 2022). Though Hurricane Enrique (25–30 June) did not make landfall, its heavy rains caused freshwater flooding, river flooding, and landslides in northwest Mexico, with a peak rainfall estimate of 542 mm at Lazaro Cardenas, resulting in damage and power outages. Two direct deaths were attributed to high surf and rip currents (Latto 2021).

4) WESTERN NORTH PACIFIC BASIN—S. J. Camargo

(i) Overview

The 2021 TC season in the western North Pacific was below normal by most measures of TC activity. The data used here are primarily from JTWC best-track data for 1945–2020 and preliminary operational data for 2021. All statistics are based on the 1991–2020 climatological period unless otherwise noted.

According to the JTWC a total of 23 TCs (bottom quartile ≤ 23) reached tropical storm intensity in 2021. From these, 10 reached typhoon intensity (bottom quartile ≤ 13), with 4 reaching super typhoon status (≥ 130 kt, median = 5). There were also 6 tropical depressions (median 4.5). Only 44% of the tropical storms intensified into typhoons (bottom quartile ≤ 56%), while 40% of the typhoons reached super typhoon intensity (median = 29%). Figure 4.31a shows the number of storms in each category for the period 1945–2021.

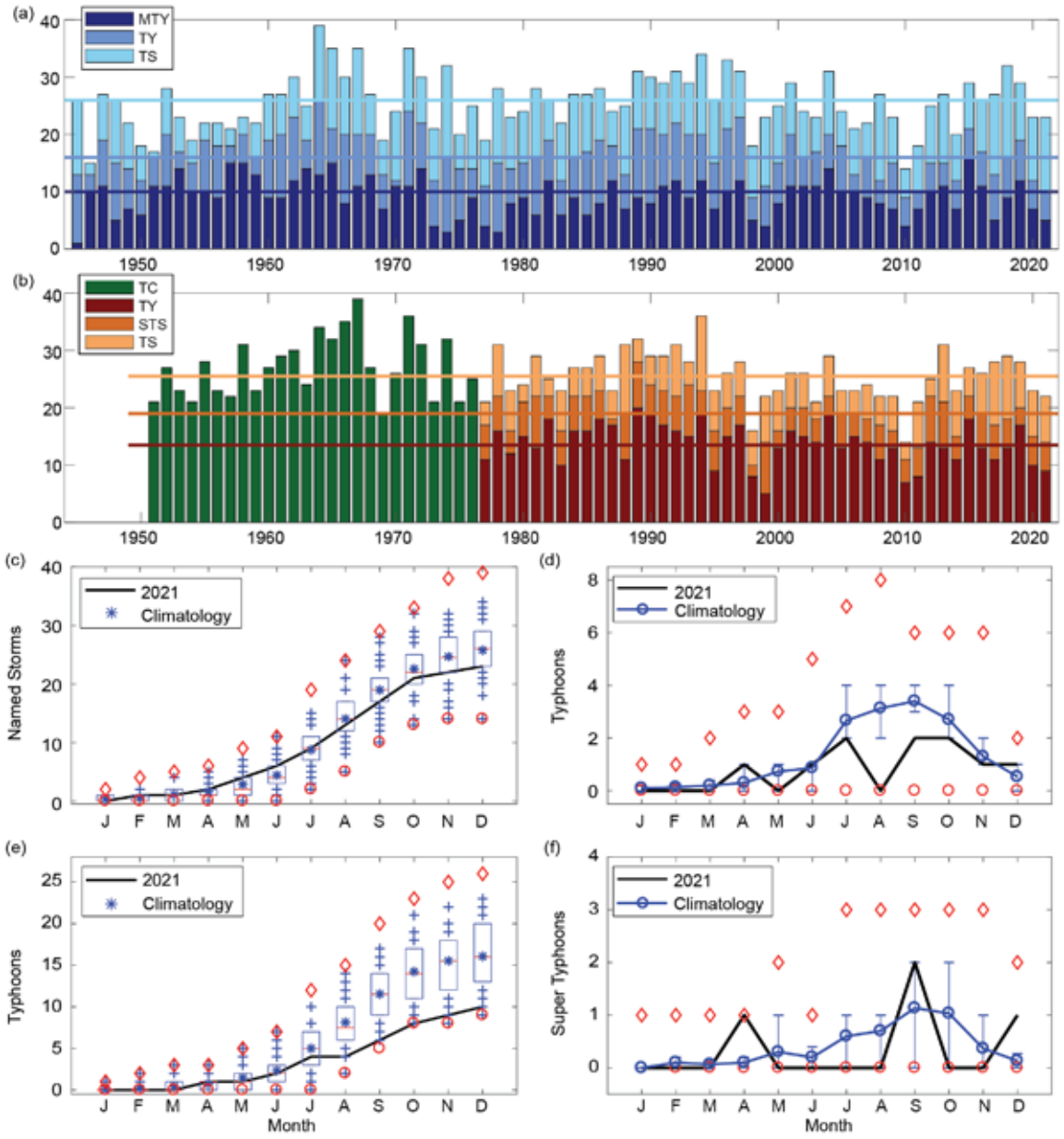

Fig. 4.31. (a) Number of tropical storms (TSs), typhoons (TYs), and major typhoons (MTY ≥ 96 kt) per year in the western North Pacific (WNP) for the period 1945–2021 based on JTWC data. (b) Number of tropical cyclones (TCs; all storms that reach TS intensity or higher) from 1951 to 1976; number of TSs, severe tropical storms (STSs), and TYs from 1977 to 2021 based on JMA data. (c) Cumulative number of tropical cyclones with TS intensity or higher (named storms) per month in the WNP in 2021 (black line) and climatology (1991–2020) as box plots (interquartile range: box; median: red line; mean: blue asterisk; values in the top or bottom quartile: blue crosses; high (low) records in the 1945–2021 period: red diamonds (circles). (e) As in (c) but for the number of typhoons. (d) and (f) show the number of typhoons and super typhoons (≥ 130 kt) per month in 2021 (black line) and the climatological mean (blue line); the red diamonds and circles denote the maximum and minimum monthly historical records and the blue error bars show the climatological interquartile range for each month (in the case of no error bars, the upper and/or lower percentiles coincide with the median). (Sources: 1945–2020 Joint Typhoon Warning Center [JTWC] best-track dataset, 2021 JTWC preliminary operational track data for [a], [c], [d], [e], and [f]. 1951–2021 Regional Specialized Meteorological Center-Tokyo, Japan Meteorological Agency [JMA] best-track dataset for [b].)

The JMA total for 2021 was 22 TCs (bottom quartile ≤ 23). As is typically the case, there were differences between the JTWC and JMA counts.[4] Storm Three (03W) was considered a tropical storm by JTWC, but was not included among the JMA 2021 storms. Namtheun was considered a typhoon by JTWC, but not by JMA (severe tropical storm). Of the 22 JMA TCs, 9 were tropical storms (top quartile ≥ 8), 5 were severe tropical storms (median = 5), and 9 were typhoons (bottom quartile ≤ 11). Only 41% of the storms reached typhoon intensity (bottom quartile ≤ 48%). The number of all TCs (1951–76) and tropical storms, severe tropical storms and typhoons (1977–2021) according to the JMA are shown in Fig. 4.31b. The Philippine Atmospheric, Geophysical and Astronomical Services Administration (PAGASA) named 15 TCs that entered its area of responsibility, including Storm 03W, named Crising locally by PAGASA, and tropical depression Nando (8–16 October), which was not named by JMA or JTWC.

(ii) Seasonal activity

The 2021 season started with the occurrence of only one storm in the period January–March (median = 0): Tropical Storm Dujuan (local name Auring), which affected the Philippines in February. Super Typhoon Suriage was active in April, only the ninth year in the historical record with a super typhoon in April (top quartile > 0), followed by Tropical Storms 03W and Choi-wan in May (top quartile ≥ 2). June had two storms (top quartile ≥ 2): Tropical Storm Koguma (top quartile ≥ 1) and Typhoon Champi (top quartile ≥ 1). The early typhoon season (January–June) had a total of 6 TCs (median = 6), with 4 tropical storms (top quartile ≥ 3) and 2 typhoons (median = 2), including 1 super typhoon (top quartile ≥ 1), as shown in Figs. 4.31c–f.

July had 5 TCs (median = 4), 2 tropical depressions (07W and 08W), 1 tropical storm (Nepartak; median = 1), and 2 typhoons (In-fa and Cempaka; bottom quartile ≤ 2). There were also 5 TCs in August (median = 6), 1 tropical depression (12W), and 4 tropical storms (Lupit, Mirinae, Nida, and Omais; top quartile ≥ 3), but none intensified to typhoon strength. The lack of typhoons active in August is a rather unusual occurrence (bottom quartile ≤ 2; see Figs. 4.31d,e) and previously only occurred in three other years in the historical record (1976, 1977, and 2014).

September also had 5 TCs (bottom quartile ≤ 5), 1 tropical depression (17W), 2 tropical storms (Conson and Dianmu; top quartile ≥ 2), and 2 typhoons (Chanthu and Mindulle; bottom quartile ≤ 3), both reaching super typhoon intensity (top quartile ≥ 2). While the number of typhoons in September was below normal, the number of super typhoons was above normal (Figs. 4.31d,f). October also had 5 TCs (top quartile ≥ 5): 1 tropical depression (26W), 2 tropical storms (Lionrock and Kompasu; top quartile ≥ 1), and 2 typhoons (Namtheun and Malou; median = 2.5). The peak season (July–October) had a total of 21 TCs (median = 20) and 9 tropical storms (top quartile ≥ 8). The number of TCs and tropical storms is in the near-normal range, but only 7 typhoons (bottom quartile ≤ 9) with just 2 reaching super typhoon intensity (bottom quartile ≤ 2) occurred during the peak season (Figs. 4.31c,e).

Typhoon Nyatoh formed in November, the only storm active in that month (TC and typhoon bottom quartiles ≤ 1). The season closed with 2 TCs in December (top quartile ≥ 2): the devastating Super Typhoon Rai (typhoons: top quartile ≥ 1; super typhoons: top quartile > 0) followed by Tropical Depression 29W. Super typhoons in December are uncommon. Since 1980, when the data quality became more reliable, super typhoons have only developed in four other Decembers (1997, 2001, 2002, and 2016), with the remaining other seven occurrences happening in the 1950s and 1960s. The total number of TCs in the late season (November and December) was 3 (bottom quartile ≤ 3), including 2 typhoons (top quartile ≥ 2) and 1 super typhoon (top quartile ≥ 1). The low number of typhoons and super typhoons during the peak season was mainly responsible for the season being characterized as below normal, even with the relatively high level of activity in December.

[4] It is well known that there are systematic differences between the JMA and the JTWC and the datasets, which have been extensively documented in the literature (e.g., Knapp et al. 2013; Schreck et al. 2014).

The total seasonal ACE in 2021 (Fig. 4.32a) was in the bottom quartile of the climatological distribution, the 16th lowest in the historical record. The ACE value was in the bottom quartile of the climatological distribution in January, March, August, October, and November (Fig. 4.32b). January and March both had zero ACE, while the latter three months were respectively the third, seventh, and fourth lowest ACE values in the historical record for those months. In contrast, in February, April, and December, the ACE values were in the top quartile of the climatological distribution, reaching the 10th, 4th, and 13th highest ACE values in the historical record for those months. While the ACE climatological values are typically low in January and March (climatologically: 0.3% and 0.9% of the season total), August and October are in the peak typhoon season and have high climatological ACE values, typically contributing a combined 40% of seasonal ACE; therefore, the combined low ACE value in those months (only 14%) was a major factor in the low total ACE value. Low ACE values are typical of La Niña in the western North Pacific (Camargo and Sobel 2005), which was present most of the year (section 4b). During La Niña events the mean typhoon genesis is displaced to the northwest, leading to shorter tracks and weaker typhoons and, subsequently, to lower ACE values.

The ACE for four storms in 2021 were in the top quartile of the climatological ACE for individual storms: Typhoon Rai and Super Typhoons Surigae, Chanthu, and Mindulle. The ACE for Surigae was in the 99th percentile. Together these four storms contributed to 65% of the total seasonal ACE (21%, 19%, 14%, and 11% respectively).

The mean genesis location in 2021 was 15.3°N and 133.3°E, northwest of the climatological mean of 13.3°N, 140.5°E. The mean track position in 2021 was 18.9°N, 132.1°E, similarly northwest of the climatology mean of 17.8°N, 135.9°E (standard deviations of 1.6° latitude and 5.2° longitude). There is a well-known connection between genesis and track shifts in the WNP basin and El Niño/La Niña (Chia and Ropelewski 2002; Camargo and Sobel 2005; Camargo et al. 2007a) to the southeast/northwest. The 2021 first position conditions are typical of La Niña seasons (genesis mean La Niña: 15.1°N, 136.5°E).

There were 88.25 days in 2021 with active tropical storms and typhoons (bottom quartile ≤ 86). From these active days, 36.75 had typhoons (bottom quartile ≤ 42.7), 18.5 days had major (including super) typhoons (SSHWS categories 3–5; bottom quartile ≤ 15.75). The percentage of active days with typhoons and major typhoons was 28% (bottom quartile ≤ 27%) and 14% (median = 15%), respectively. The median lifetime for TCs reaching tropical storm intensity was 5.5 days (bottom quartile ≤ 7 days) and for those reaching typhoon intensity was 7.5 days (bottom quartile ≤ 7.75 days).

The longest-lived storm in 2021 was Typhoon In-fa (14 days), followed by Tropical Storm Omais (13.75 days) and Super

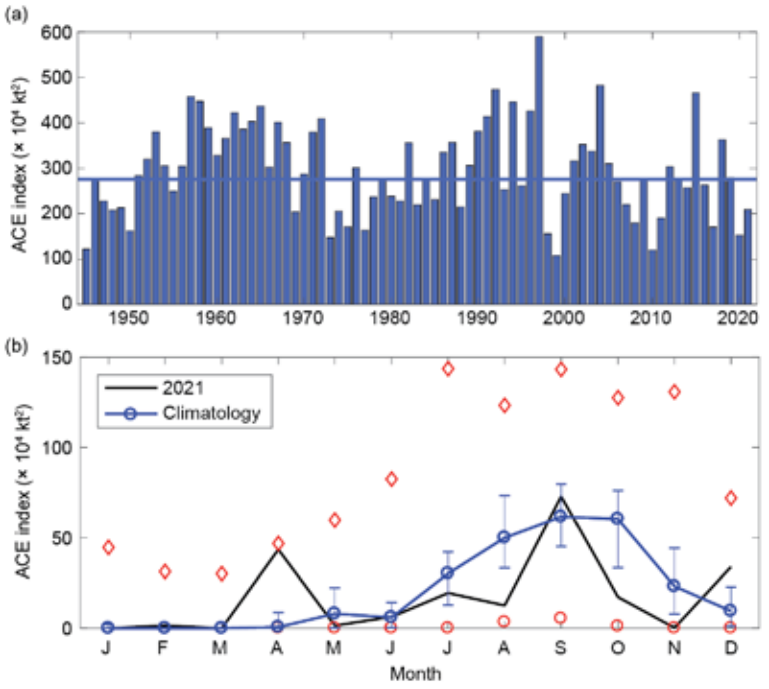

Fig. 4.32. (a) Accumulated Cyclone Energy (ACE, × 10^4 kt^2) per year in the western North Pacific for the period 1945–2021. The solid blue line indicates the median for the climatology (1991–2020). (b) ACE per month in 2021 (black line) and the median during 1991–2020 (blue line), the blue error bars indicate the climatological interquartile range. In case of no error bars, the upper and/or lower percentiles coincide with the median. The red diamonds and circles denote the maximum and minimum values per month during the 1945–2020 period. (Source: 1945–2020 Joint Typhoon Warning Center [JTWC] best-track dataset, 2021 JTWC preliminary operational track data.)

Typhoons Surigae (12.25 days) and Chanthu (12 days), with all four storms in the top quartile of the distribution (≥ 10 days). From the 23 TCs, only 8 had lifetimes above the median (7.25 days). Short-lived storms are another characteristic of La Niña in the western North Pacific (Camargo and Sobel 2005; Camargo et al. 2007a). The maximum number of TCs active simultaneously in 2021 was four and occurred on 5 August (Tropical Depression 12W and Tropical Storms Lupit, Mirinae, and Nida). The historical record is six active TCs in the basin (14–15 August 1996).

(iii) Environmental conditions

Figure 4.33 shows the tracks and environmental conditions associated with the 2021 typhoon season. The La Niña event that started in 2020 returned to cool neutral ENSO conditions during the summer of 2021, but returned to La Niña conditions in August 2021 and strengthened through the end of the year to moderate conditions. The SST anomaly pattern during the peak typhoon season (JASO) was dominated by the standard eastern Pacific La Niña pattern, which includes above-normal SSTs in the western North Pacific near the Asian continent (Fig. 4.33a). The potential intensity (Emanuel 1988; Fig. 4.33b) had weak negative anomalies in the eastern part of the basin and positive anomalies closer to the Asian continent. With the exception of two bands of 600-hPa relative humidity anomalies (Fig. 4.33c) in the equatorial region (positive to the west, negative to the east), the mid-level relative humidity was close to climatological conditions.

The genesis potential index (GPI; Fig. 4.33d; Emanuel and Nolan 2004; Camargo et al. 2007b) is an empirical nonlinear index that describes regions of enhanced probability of TC formation,

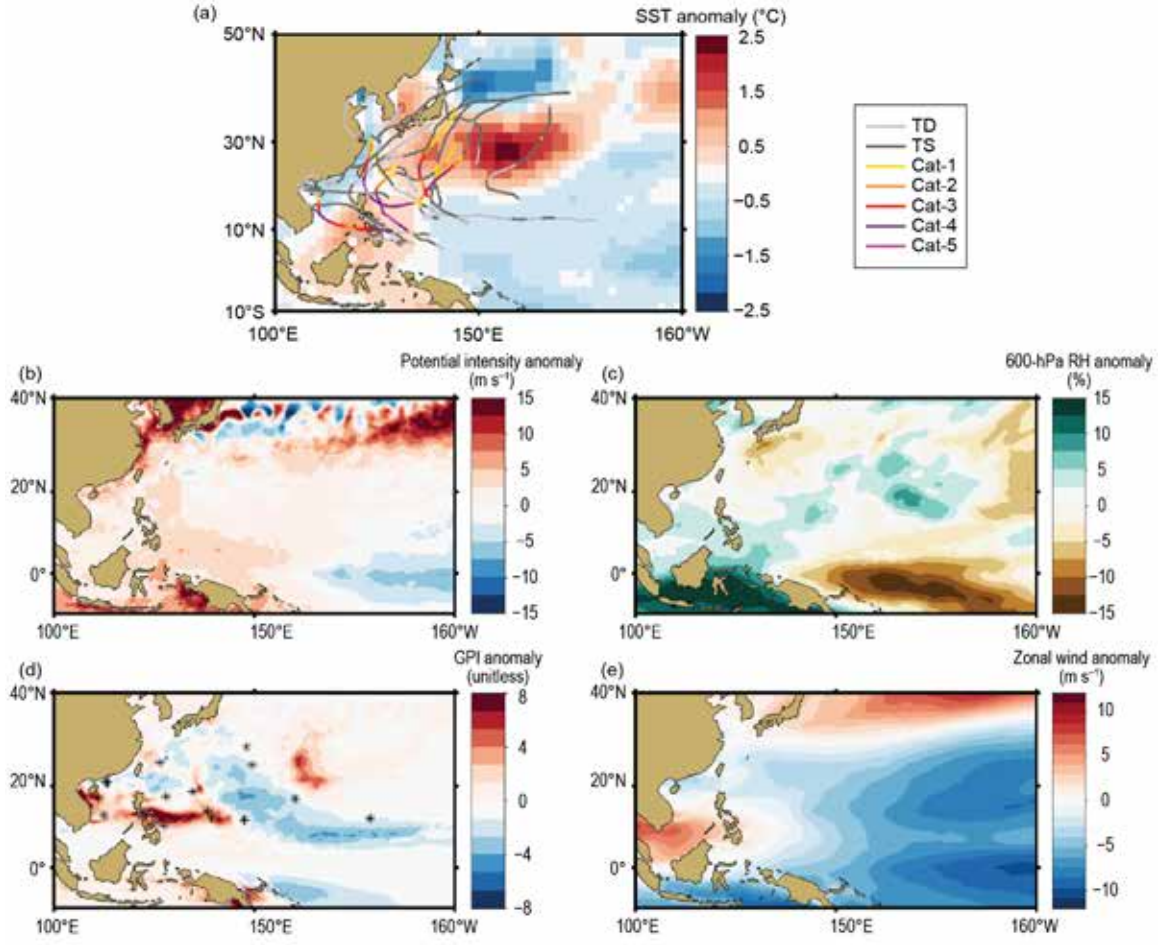

Fig. 4.33. Jul–Oct (JASO) 2021: (a) SST anomalies (°C) and the tracks of all 2021 storms with colors denoting their intensity, (b) potential intensity anomalies (m s^{-1}), (c) 600-hPa relative humidity anomalies (%), (d) genesis potential index (GPI) anomalies and first position of storms from JASO 2021 marked with an asterisk, and (e) zonal winds at 850-hPa (m s^{-1}). All anomalies are relative to their 1991–2020 climatologies. (Sources: SST: ERSSTv5 [Huang et al. 2017]; other environmental fields: ECMWF ERA5 reanalysis [Hersbach et al. 2020], tracks and first position: JTWC preliminary operational track data.)

based on four environmental fields: potential intensity, mid-level relative humidity, vertical wind shear, and low-level relative vorticity. In JASO 2021 was characterized by one region of positive anomalies, in the South China Sea and the Philippines, and a larger negative region to the east. The first position of the storms forming during those months is also shown in Fig. 4.33d (black asterisks), with TCs that formed located outside of the negative GPI anomaly region. The extent of the monsoon trough, defined by the 850-hPa zonal winds (Fig. 4.33e), was restricted from the South China Sea to the Philippines, as is typical in La Niña events, which would be reflected in the vorticity field of GPI. Tropical cyclone activity south of 30°N was restricted to the area close to the Philippines. The below-normal SST conditions and potential intensity in most of the basin, as well as the short extension of the monsoon trough, help explain the below-normal activity in the basin in 2021.

(iv) Tropical cyclone impacts

Including tropical depressions, 19 storms made landfall in 2021 (median = 17.5, 1961–2020 climatology). Landfall here is defined when the storm track is over land and the previous location was over the ocean. In order to include landfall over small islands, tracks were interpolated from 6-hour to 15-minute intervals, and a high-resolution land mask was used. In the case of multiple landfalls, we considered the landfall with the highest intensity for each storm. Eleven storms made landfall as tropical depressions (top quartile > 5), 5 as tropical storms (bottom quartile < 8), and 2 as typhoons (bottom quartile < 3): Cempaka and Super Typhoon Rai.

Rai (named Odette by PAGASA) caused the most severe and widespread damage, making nine landfalls in different locations in the southern Philippines, including as a Category 5 typhoon. More than 400 people were killed, and it was the third costliest typhoon in the Philippines history, causing $1 billion (U.S. dollars) in economic losses and damage (Aon 2022). The impacts were mainly caused by widespread flooding, which damaged or destroyed over a million houses and affected crops. The extent of the damage led the provinces of Cebu and Bohol to be placed into a state of calamity. The United Nations estimated that 13 million people were affected by the typhoon, which led to an international effort to assist the country.

5) NORTH INDIAN OCEAN BASIN—A. D. Magee and C. J. Schreck

(i) Seasonal activity

The North Indian Ocean (NIO) TC season typically occurs between April and December, with two peaks of activity: May–June and October–December, due to the presence of the monsoon trough over tropical waters of the NIO during these periods. Tropical cyclone genesis typically occurs in the Arabian Sea and the Bay of Bengal between 8°N and 15°N. The Bay of Bengal, on average, experiences four times more TCs than the Arabian Sea (Dube et al. 1997).

The 2021 NIO TC season had five named storms, three of which became cyclones, including one major cyclone (Extremely Severe Cyclonic Storm Tauktae). These numbers were all near the IBTrACS–JTWC 1991–2020 climatology of 5.5 named storms, 2.2 cyclones, and 1.1 major cyclones (Fig. 4.34).

While the number of storms was near-normal, the 2021 seasonal ACE index (January–December 2021) of 16.3×10^4 kt^2 was almost one-third less than the 1991–2020 mean of 24.7×10^4 kt^2 and over five times less than the record ACE of 93.0×10^4 kt^2 recorded in 2019. Indian Ocean dipole (IOD) conditions, as measured by the Dipole Mode Index, were positive during March and April and negative between May and July 2021 (section 4f). Environmental conditions during May were characterized by cooler SSTs in the western Arabian Sea and warmer SSTs in the Bay of Bengal (Fig. 4.35a). There was also a large area of enhanced convection in the Arabian Sea, present near the areas of cyclogenesis around Extremely Severe Super Cyclonic Storm Tauktae (Fig. 4.35b). Neutral/negative wind shear anomalies (Fig. 4.35c) were also present around the areas of cyclogenesis for both Extremely Severe Super Cyclonic Storm Tauktae and Very Severe Cyclonic Storm Yaas.

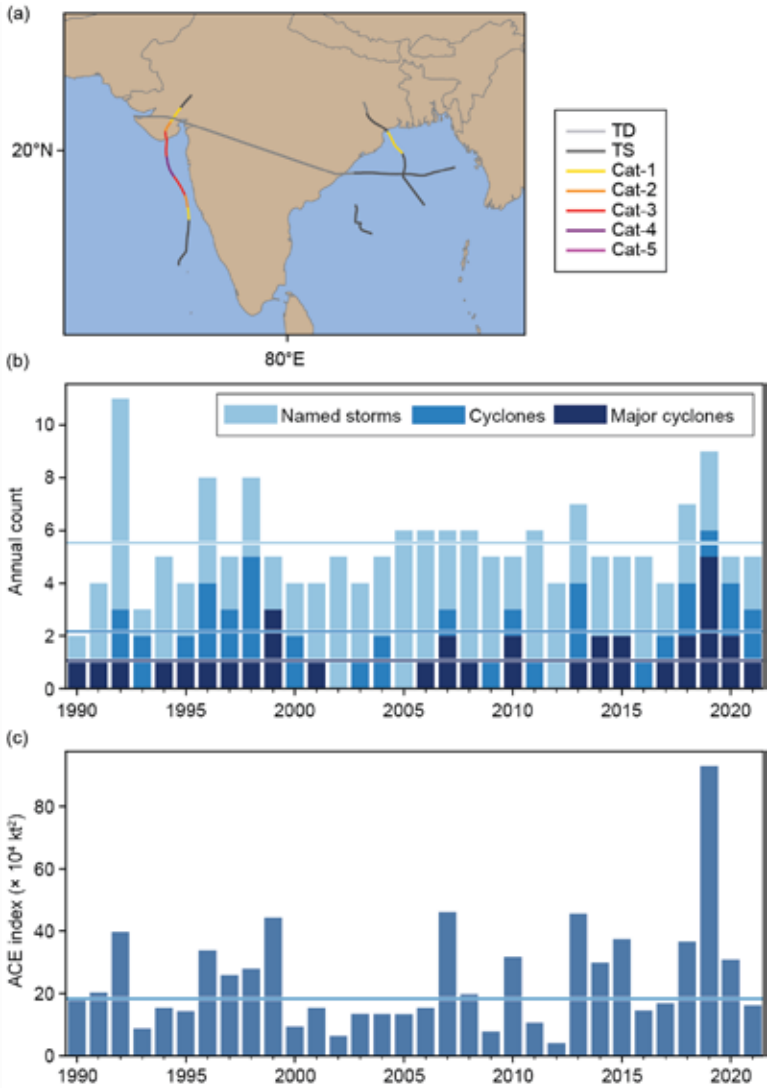

Fig. 4.34. Annual TC statistics for the NIO for 1990–2021: (a) storm tracks for 2021, (b) number of named storms, cyclones, and major cyclones, and (c) ACE (× 10^4 kt^2). Horizontal lines, representing the 1991–2020 climatology are included in both (b) and (c).

(ii) Individual tropical cyclones and impacts

Extremely Severe Super Cyclonic Storm Tauktae was the first cyclone of the 2021 season to form in the NIO basin. Initially forming from a depression off the Indian coast of Kerala in the Arabian Sea on 14 May, the low tracked towards the east and began to strengthen while tracking towards the north. On 15 May, Tauktae reached severe cyclonic storm status and continued to track parallel to the coastline of Kerala, Karnataka, Goa, and Maharashtra, eventually reaching peak intensity with maximum 1-minute sustained winds of 119 kt (61 m s^{-1}) and a minimum central pressure of 935 hPa on 17 May, equivalent to a SSHWS Category 4 system. Shortly after, Cyclone Tauktae underwent an eyewall replacement cycle resulting in a temporary reduction in intensity before it re-intensified and made landfall on the Gujarat coastline. In total, 174 deaths were reported, with a further 80 people reported missing. A number of fishing vessels and fishermen were lost at sea due to the substantial storm surge associated with this event. Cyclone Tauktae brought heavy rainfall and flash flooding across Gujarat, causing significant damage to infrastructure and agriculture. In Vijapadi, a village near to where Tauktae made landfall, most houses were destroyed by the cyclone. Wave heights in excess of four meters were reported off the coast of Gujarat. Impacts were also reported in neighboring Pakistan, where strong winds resulted in a number of roof and wall collapse incidents.

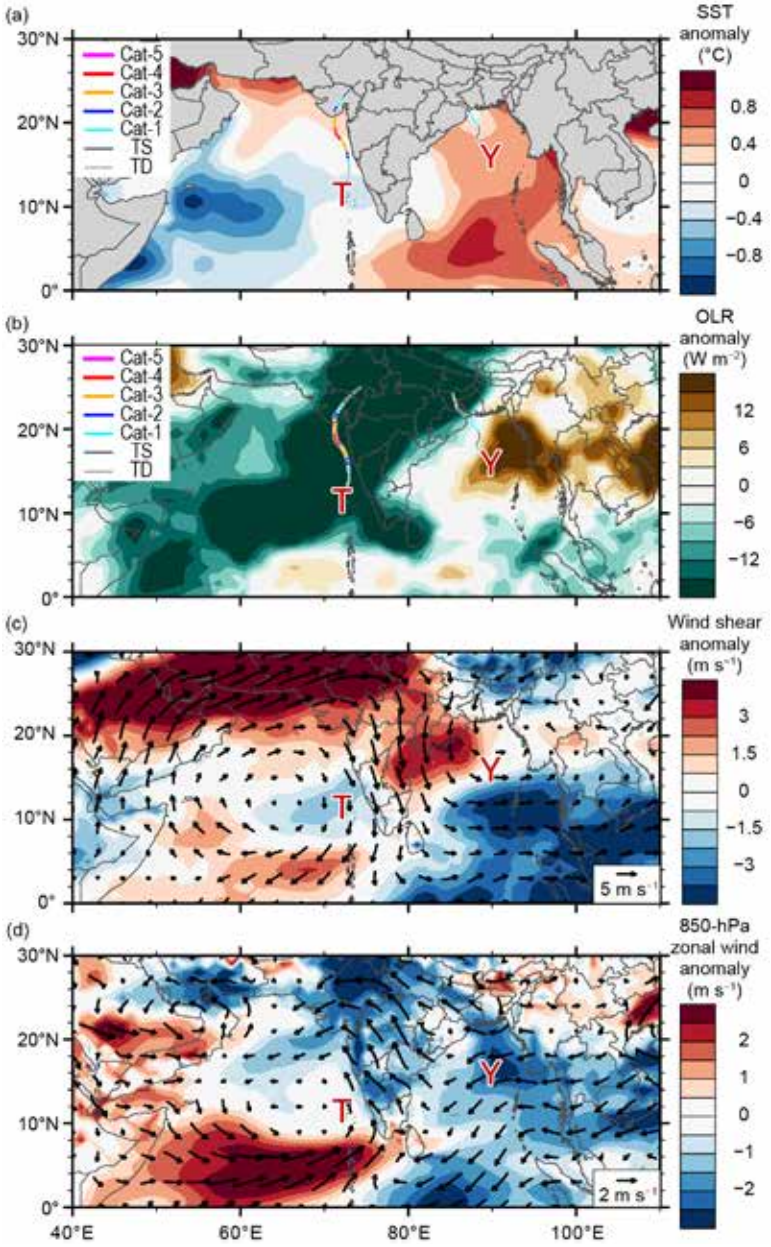

Fig. 4.35. May 2021 NIO anomaly maps of (a) SST (°C; Banzon and Reynolds, 2013), (b) OLR (W m^{-2}; Schreck et al. 2018); (c) 200–850-hPa vertical wind shear (m s^{-1}) vector (arrows) and scalar anomalies (shading), and (d) 850-hPa winds (m s^{-1}, arrows) and zonal wind anomalies (shading). Anomalies are relative to the annual cycle from 1991–2020. Letter symbols denote where each NIO TC attained its initial tropical storm intensity. (Source: Wind data from CFSR [Saha et al. 2014].)

Very Severe Cyclonic Storm Yaas formed from a low-pressure system in the Bay of Bengal. Favorable environmental conditions and anomalously high SSTs promoted intensification, and the system tracked in a northwesterly direction towards the coastline of northern Odisha. Yaas achieved its peak intensity with maximum sustained winds of 64 kt (33 m s^{-1}) and a minimum central pressure of 974 hPa on 25 May as it made landfall on the northern Odisha coastline of India. Impacts associated with Cyclone Yaas resulted in 20 fatalities and widespread destruction across India, Bangladesh, and Nepal. Over 1000 villages in West Bengal were submerged by floodwaters, and strong winds uprooted trees and snapped palm trees along the coast. Widespread and prolonged rainfall also resulted in flooding of farmland in West Bengal and Odisha. Storm surge generated by Cyclone Yaas impacted low-lying coastal communities in Bangladesh, resulting in the inundation of several villages. The Sundarbans were also inundated with seawater.

Cyclones Gulab and Shaheen were related tropical cyclones that occurred consecutively and in quick succession. Cyclone Gulab, the third named cyclone of the 2021 NIO TC season, formed

from a low-pressure system over the Bay of Bengal. Favorable SSTs and wind shear, along with an active pulse of the MJO (section 4c), assisted with the organization of Gulab, which followed a westerly trajectory towards northern Andhra Pradesh, India. Cyclone Gulab made landfall on 26 September, with maximum sustained winds of 39 kt (20 m s^{-1}) and a minimum central pressure of 983 hPa. Gulab continued to track over the Indian subcontinent and began to decay, eventually weakening to an area of low pressure near west Vidarbha. In the Arabian Sea, favorable environmental conditions, including SSTs up to 31°C, enabled the regeneration of the system, named Cyclone Shaheen, which continued to track towards the west.

On 3 October, Cyclone Shaheen achieved peak intensity with maximum sustained winds of 70 kt (36 m s^{-1}) and a minimum central pressure of 975 hPa, a Category 1 TC on the SSHWS. Shortly after, Cyclone Shaheen made landfall over the northern coast of Oman. In Oman alone, 14 people were killed, and many locations recorded a year's worth of rain in less than 24 hours, causing coastal and inland flooding. This flooding forced many people to seek shelter from the rising water on their roofs. Dams reportedly overflowed, and intense and prolonged rainfall resulted in numerous landslides across Oman. Widespread power outages were reported across the country. Impacts were also reported in Iran, the United Arab Emirates, and Yemen. The trajectory of Cyclones Gulab and Shaheen, from the Bay of Bengal, across the Indian subcontinent, and across the Arabian Sea into the Gulf of Oman, is a relatively infrequent occurrence. This track path has only been observed twice previously (1981 and 1959).

6) SOUTH INDIAN OCEAN BASIN—A. D. Magee and C. J. Schreck

(i) Seasonal activity

The South Indian Ocean TC basin extends south of the equator and from the African coastline to 90°E. While the SIO TC season extends year-round, from July to June, most TC activity typically occurs between November and April when the Intertropical Convergence Zone is located in the SH. The 2020/21 season includes TCs that occurred from July 2020 to June 2021. Landfalling TCs typically impact Madagascar, Mozambique, and the Mascarene Islands, including Mauritius and La Réunion; however, impacts can be felt in other locations within the region. Above-average storm activity was observed in the SIO basin with 12 named storms, compared to the IBTrACS-JTWC 1991–2020 mean of 10.5 (Fig. 4.36). The 5 cyclones were near-average (6.1), while the 2 major cyclones were below average (3.5). January 2021 was a particularly active month with three named cyclones (Danilo, Joshua, and Eloise) occurring within the basin.

The 2020/21 seasonal ACE index was 99.8×10^4 kt^2, which is near the 1991–2020 climatology of 94.4×10^4 kt^2. Cyclone-favorable conditions, including anomalously high SSTs (Fig. 4.37a), large areas of enhanced convection (< –12 W m^{-2}; Fig. 4.37b) in the eastern part of the basin (Fig. 4.37a), anomalously weak wind shear (Fig. 4.37c), and low-level westerly anomalies (Fig. 4.37d) were present in the main development region east of 70°E.

(ii) Noteworthy TCs and impacts

Severe Tropical Storm Chalane was the first storm of the season to make landfall, and did so across Madagascar and then Mozambique. Favorable environmental conditions enabled the cyclone to intensify while the system tracked in a westerly direction towards Madagascar. On approach to Madagascar, Chalane encountered strong wind shear, resulting in a temporary deterioration of the system prior to its landfall on 26 December in Mahavelona, Madagascar. The storm tracked towards the southwest over Madagascar as a surface trough and entered the Mozambique Channel on 28 December. Chalane intensified and gained severe tropical storm status with maximum sustained winds of 60 kt (31 m s^{-1}) and a minimum central pressure of 990 hPa—a tropical storm event on the SSHWS. On 30 December, Chalane made landfall near Beira, Mozambique, with flooding due to prolonged rainfall claiming seven lives. In Madagascar,

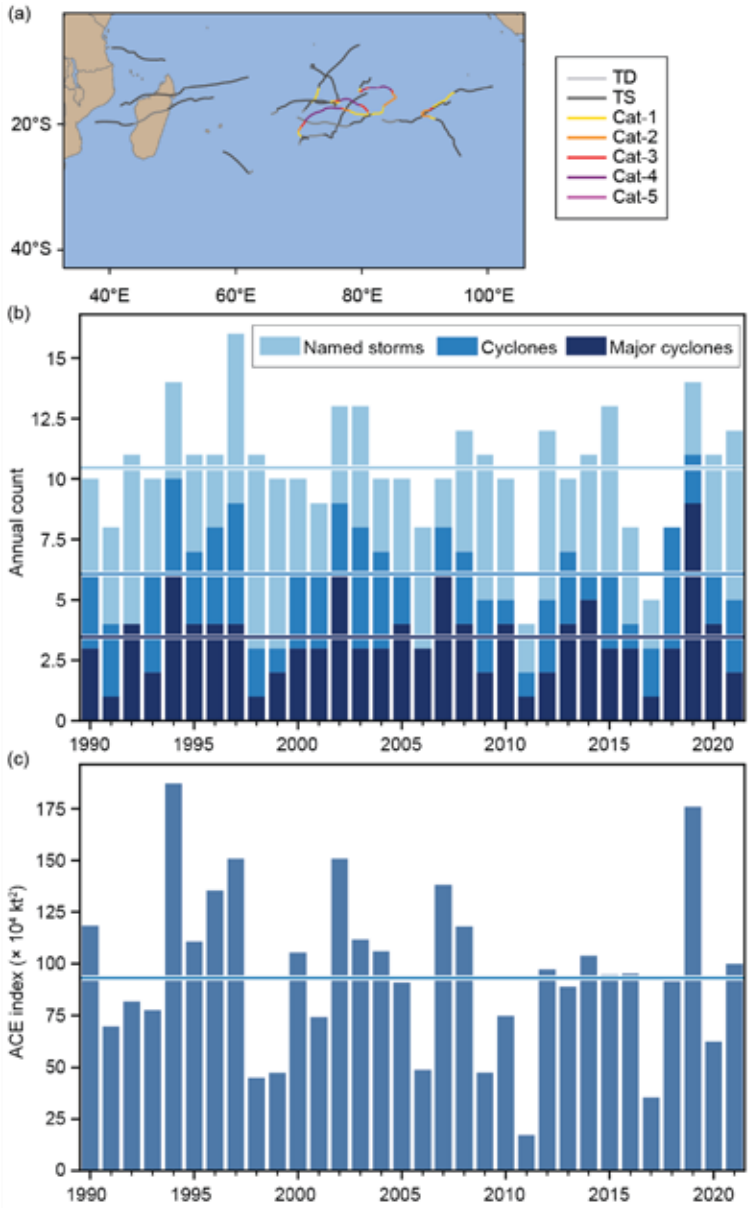

Fig. 4.36. Annual TC statistics for the SIO for 1990–2021: (a) storm tracks for 2021, (b) number of named storms, cyclones, and major cyclones, and (c) ACE (× 10^4 kt^2). Horizontal lines, representing the 1991–2020 climatology, are included in both (b) and (c). Note that the preliminary data for Tropical Cyclone Guambe were corrupted. It has been included in the counts, but it is missing from the track maps.

351 mm of rainfall was recorded in a 24-hour period at Toamasina. Impacts were also reported in Zimbabwe and Namibia.

Severe Tropical Storm Eloise, the third of three storms to form in January 2021, developed from an area of disturbed weather across the central South Indian Ocean. Eloise tracked to the southwest toward Madagascar and continued to intensify, reaching a peak intensity of 51 kt (26 m s^{-1}) and minimum central pressure of 994 hPa on 18 January, equivalent to a tropical storm event on the SSHWS. Eloise made landfall in Antalaha, Madagascar, on 19 January, and similar to Severe Tropical Storm Chalane, re-emerged into the Mozambique Channel after weakening upon landfall and tracking towards the southwest. Eloise made landfall north of Beira, Mozambique, and caused extreme flooding and unusually wet conditions in the weeks before Eloise made landfall. Eloise resulted in 27 confirmed fatalities across Madagascar, Mozambique, Zimbabwe, South Africa, and Eswatini.

Very Intense Tropical Cyclone Faraji, the only Category 5 (SSHWS) event to occur in the basin during the 2020/21 SIO TC season, developed from a well-defined surface circulation on 4 February

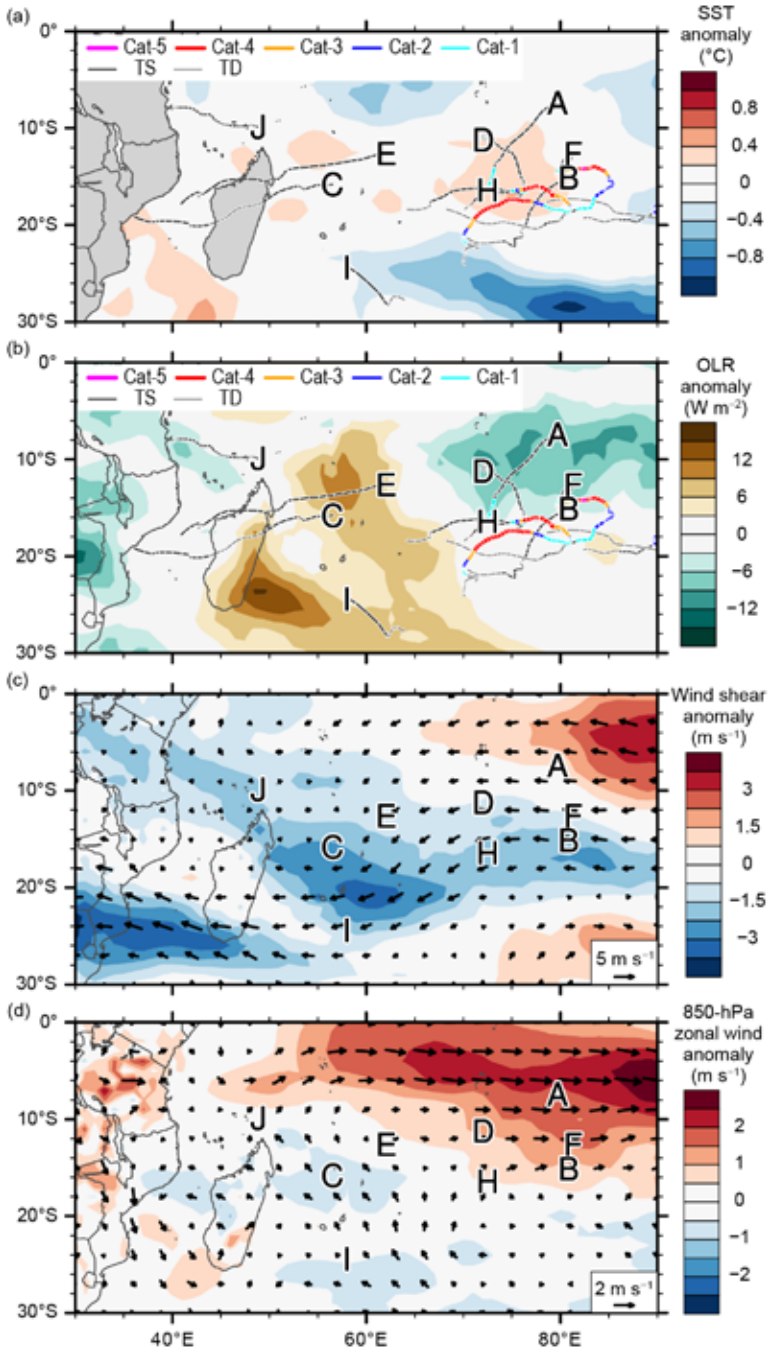

Fig. 4.37. Nov 2020–Apr 2021 SIO anomaly maps of (a) SST (°C; Banzon and Reynolds 2013), (b) OLR (W m^{-2}; Schreck et al. 2018); (c) 200–850-hPa vertical wind shear (m s^{-1}) vector (arrows) and scalar anomalies (shading), and (d) 850-hPa winds (m s^{-1}, arrows) and zonal wind anomalies (shading). Anomalies are relative to the annual cycle from 1991 to 2020. Letter symbols denote where each SIO TC attained its initial tropical storm intensity. (Source: Wind data from CFSR [Saha et al. 2014].)

near the Chagos Archipelago. After tracking towards the south, Faraji rapidly intensified to a Category 4 system before weakening slightly, caused by cooler SSTs due to upwelling. As Faraji tracked towards the east, favorable environmental conditions enabled intensification to reach a peak intensity of 138 kt (71 m s^{-1}) and a minimum central pressure of 920 hPa on 8 February (a Category 5 system on the SSHWS). Faraji subsequently weakened as it turned towards the south and then tracked towards the west, where it decayed. Faraji did not make landfall and no significant damage was reported.

Tropical Cyclone Guambe, the third tropical cyclone of 2021 to make landfall across Mozambique, initially developed as a disturbance in the Mozambique Channel. Guambe made landfall near Inhambane close to where Severe Tropical Storm Eloise had made landfall weeks earlier.

After moving inland and delivering prolonged and intense rainfall, the system tracked towards the northeast and re-entered the Mozambique Channel, where the system then tracked towards the south. The system continued to intensify and reached a peak intensity of 54 kt (28 m s^{-1}) and a minimum central pressure of 980 hPa on 22 February, equivalent to a tropical storm on the SSHWS. No fatalities were reported, but damage was reported in Madagascar, Mozambique, South Africa, and Eswatini.

Moderate Tropical Storm Iman initially formed from a weak tropical disturbance in the Mozambique Channel. Iman continued to organize and strengthen as a tropical depression where it made landfall on the west coast of Madagascar on 5 March. The system emerged into the South Indian Ocean and continued to track towards the southeast as it strengthened to achieve tropical storm intensity on the SSHWS, with maximum intensity of 45 kt (23 m s^{-1}) and a minimum central pressure of 991 hPa on 7 March. Although Iman did not make landfall on La Reunion, intense thunderstorms associated with the system did impact the island. Intense rainfall, wind, and lightning resulted in widespread loss of power on La Reunion and flooding in Saint-Denis.

The last named storm of the season, Severe Tropical Storm Jobo, formed from a zone of disturbed weather to the east of the Chagos Archipelago. The system tracked towards the west and reached a maximum intensity of 55 kt (28 m s^{-1}) and a minimum central pressure of 995 hPa on 21 April (equivalent to a tropical storm on the SSHWS), as the system passed approximately 200 km to the north of Madagascar. Jobo continued to track towards the northwest, and the system was downgraded to a remnant low before making landfall on the coast of Tanzania. Extreme wind associated with Jobo resulted in damage to some of the outer islands of the Seychelles, and 22 deaths were reported across the Seychelles, northern Madagascar, and Tanzania.

7) AUSTRALIAN BASIN—B. C. Trewin

(i) Seasonal activity

The 2020/21 TC season was close to normal for the broader Australian basin (areas south of the equator and between 90°E and 160°E,[5] which includes Australian, Papua New Guinea, and Indonesian areas of responsibility). The 1991–2020 IBTrACS seasonal averages for the basin are 10.2 named storms, 5.0 TCs, and 2.5 major TCs, which compares with the 2020/21 counts of 12, 3, and 2, respectively (Fig. 4.38; Table 4.2), but four of the 2020/21 storms were too weak to be classified as named storms by the Australian Bureau of Meteorology. Weak-to-moderate La Niña conditions were present during the 2020/21 season, which are historically associated with increased TC occurrence in the Australian region.

There were four named TCs in the western sector[6] of the broader Australian region during 2020/21, none in the northern sector, and four in the eastern sector. Two systems made landfall in Australia as TCs: one in Western Australia and one in the Gulf of Carpentaria.

(ii) Landfalling and other significant TCs

The most significant tropical cyclone in the region in 2020/21, in terms of impact, was Seroja. Seroja's precursor low formed near the southwestern end of the island of Timor on 3 April. The precursor low brought extremely heavy rain, with Kupang, in western Timor, receiving 551 mm total during 1–4 April, including 460 mm on the 3rd and 4th alone.

After having been nearly stationary for two days, the low reached cyclone intensity on 5 April. It commenced moving west to southwest, parallel to and several hundred kilometers to the northwest of the Western Australian coast, continuing on that track for several days to reach

[5] The Australian Bureau of Meteorology's warning area overlaps both the southern Indian Ocean and southwest Pacific.

[6] The western sector covers areas between 90°E and 125°E. The eastern sector covers areas east of the eastern Australian coast to 160°E, as well as the eastern half of the Gulf of Carpentaria. The northern sector covers areas from 125°E east to the western half of the Gulf of Carpentaria. The western sector incorporates the Indonesian area of responsibility, while the Papua New Guinea area of responsibility is incorporated in the eastern sector.

21°S, 108°E on 10 April. Its turn towards the southeast, which had been delayed by a Fujiwara interaction (rare in the Australian region; https://glossary.ametsoc.org/wiki/Fujiwhara_effect) with Cyclone Odette, started at this point, as it accelerated towards the Western Australia coast over the following 36 hours. The storm intensified as it reached the coast, reaching severe Category 3 intensity and making landfall at about 28°S, just south of Kalbarri, at about 1200 UTC on 11 April, at near peak intensity (central pressure 971 hPa, maximum 10-minute sustained winds 65 kt [33 m s^{-1}]). A gust of 92 kt (47 m s^{-1}) was reported at Meanarra Tower, near Kalbarri. Seroja continued to move on a southeastern track inland and was downgraded to a tropical low near Merredin on 12 April. No severe cyclone had made landfall so far south since 1956. Cyclone Alby (1978) had major impacts on southwest Western Australia but did not make landfall.

At least 226 deaths were attributed to Seroja, almost all due to flooding and landslides from the precursor low. Indonesia reported 181 deaths, mostly in East Nusa Tenggara province on the islands of Flores and Timor, with 44 reported in Timor-Leste. One death occurred in Australia in storms associated with the Seroja-Odette circulation. According to Reliefweb (UN Office from Coordination of Humanitarian Affairs), this was the largest known loss of life from a tropical cyclone in the basin for more than 40 years, since the Flores cyclone in 1973 resulted in 1653 deaths (http://www.bom.gov.au/cyclone/nt/Unnamed_Flores_Sea.shtml). In Australia, there was severe wind damage near the landfall point, with an estimated 70% of the buildings in the towns of Kalbarri and Northampton significantly damaged or destroyed. Building codes in this area are less stringent than in areas farther north, which are more frequently affected by tropical cyclones.

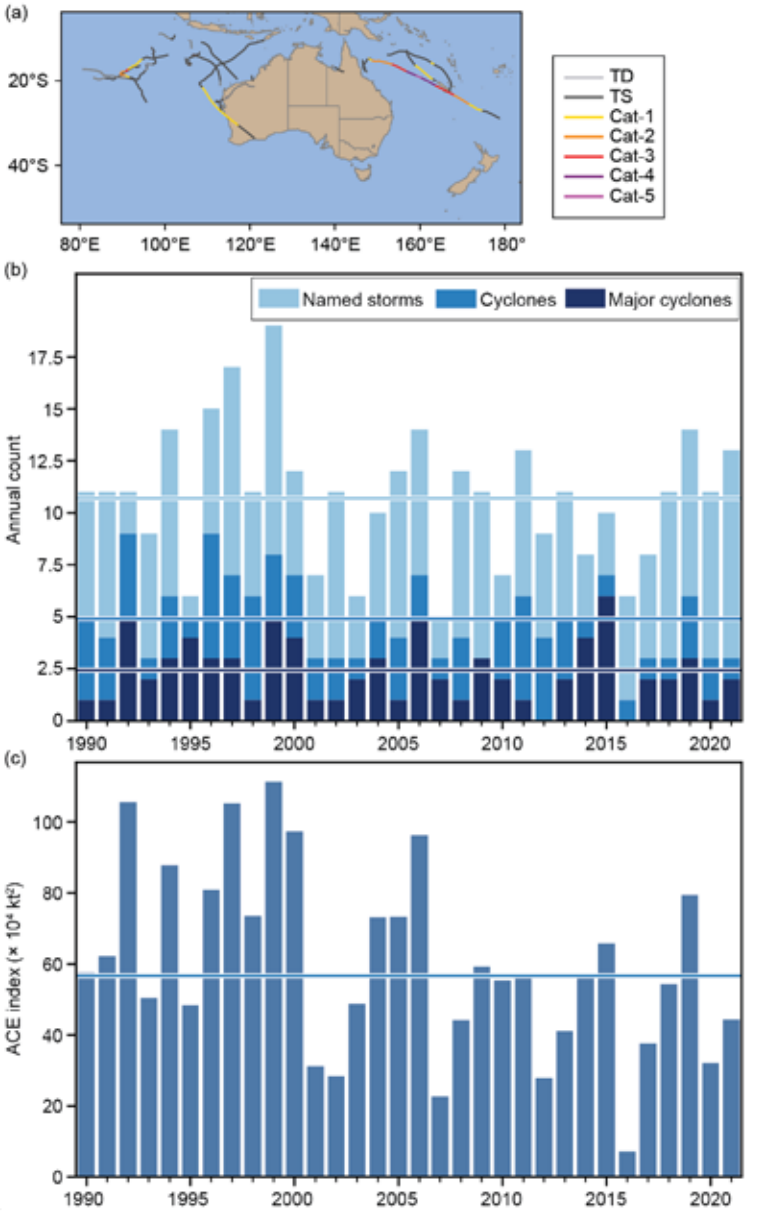

Fig. 4.38. Annual TC statistics for the Australian basin for 1990–2021: (a) storm tracks for 2021, (b) number of named storms, cyclones, and major cyclones, and (c) ACE (× 10^4 kt^2). The 1991–2020 means (horizontal lines) are included in both (b) and (c). Classifications are based on the SSHWS.

The most intense cyclone of the season in the region was Cyclone Niran, which formed off the coast of Queensland, reaching cyclone intensity on 2 March, before moving east and intensifying. The storm reached Category 5 intensity on 5 March near 19°S, 159°E, just before leaving the Australian region, with maximum sustained winds of 110 kt (56.6 m s^{-1}). The most significant impacts of Niran in Australia were from strong winds and heavy rain associated with its precursor low on 1–2 March. There were significant losses to crops, particularly bananas, in the Innisfail area. Niran went on to have substantial impacts in New Caledonia after leaving the Australian region (section 4g8).

Along with Seroja and Niran, the third severe cyclone of the season in the region was Marian, a long-lived system (26 February to 6 March), which remained well off the west coast of Australia and affected no land areas. Marian's peak intensity (maximum sustained winds 85 kt (43.7 m s^{-1}) was reached near 19°S, 90°E on 2 March.

Eastern Australia's only landfall of the season was Cyclone Imogen, a short-lived cyclone which made landfall as a Category 1 system on 3 January near Karumba on the east coast of the Gulf of Carpentaria, with maximum sustained winds of 45 kt (23.2 m s^{-1}). Imogen's major impacts resulted from heavy rain and flooding, although there was also some tree damage. Normanton received 262.6 mm of rain in the 24 hours to 0900 local time on 4 January, its heaviest 24-hour total since 1958, while Sweers Island received 222 mm on the 4th and 450 mm over the three days 2–4 January.

8) SOUTHWEST PACIFIC BASIN—A. D. Magee, A. M. Lorrey, H. J. Diamond, and J.-M. Woolley

(i) Seasonal activity

The 2020/21 Southwest Pacific TC season officially commenced in November 2020 and ended in April 2021. Best track data for 2020/21 were gathered from the Fiji Meteorological Service, Australian Bureau of Meteorology, and New Zealand MetService, Ltd. The Southwest Pacific basin (defined by Diamond et al. [2012] as 135°E–120°W) had nine TCs (based on the Australian TC Intensity Scale unless noted otherwise), including two severe (or major) TCs (based on the Australian TC intensity scale). Figure 4.39 shows the TC activity based on the basin spanning the area 160°E–120°W to avoid overlaps with the Australian basin that could result in double counting of storms; however, it is important to use the climatological definition of the Southwest Pacific basin (Diamond et al. 2012) instead of the more traditional political boundary.

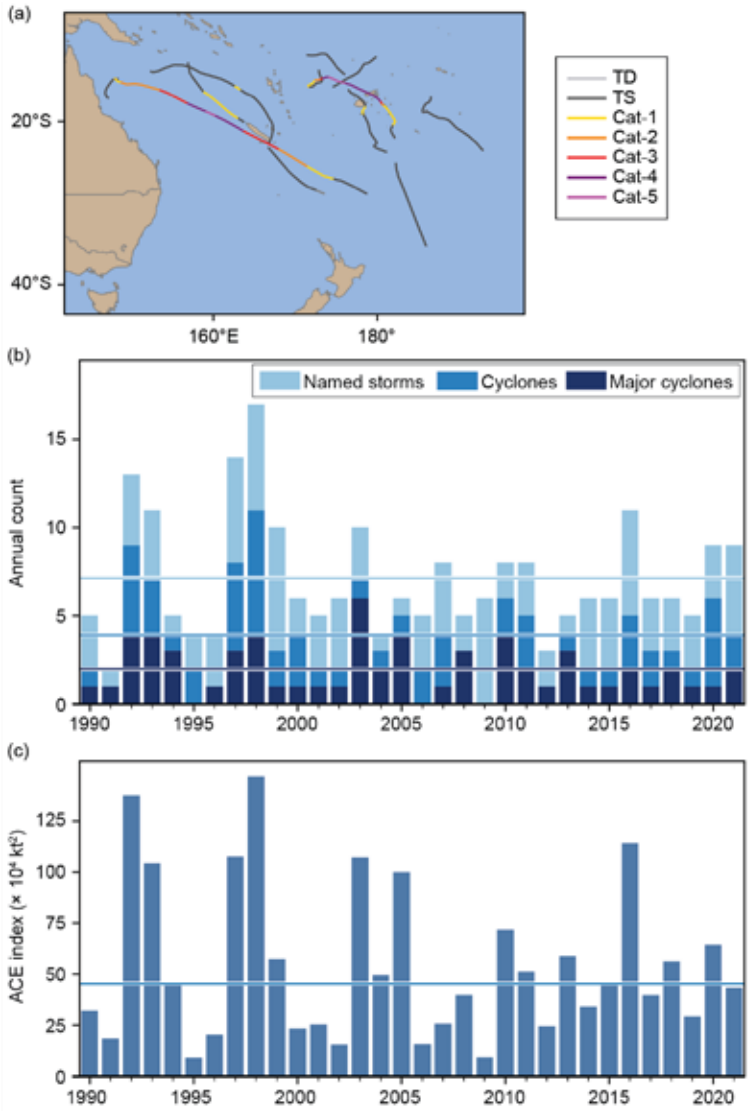

Fig. 4.39. Annual TC statistics for the Southwest Pacific for 1990–2021: (a) storm tracks for 2021, (b) number of named storms, cyclones, and major cyclones, and (c) ACE (× 10^4 kt^2). The 1991–2020 means (horizontal lines) are included in both (b) and (c). Classifications are based on the SSHWS.

The South Pacific Enhanced Archive of Tropical Cyclones (SPEArTC; Diamond et al. 2012) indicates a 1991–2020 seasonal average of 9.8 named TCs, including 4.3 severe (or major) TCs. Therefore, the 2020/21 TC season had near-normal activity with 8 named (and one unnamed) tropical cyclones, of which 3 were severe (Category 3 or above), as per Magee et al. (2022).

(ii) Storm tracks, landfalls, and impacts

Severe Tropical Cyclone Yasa was the first tropical cyclone and severe tropical cyclone of the 2020/21 Southwest Pacific tropical cyclone season. Developing from an area of low pressure north of Port Vila, Vanuatu, Yasa intensified to Category 1 status on 13 December 2020. Cyclone Yasa

underwent rapid intensification and after a slow loop northwest of Fiji, eventually tracked southeast towards Fiji, achieving Category 5 intensity on 16 December with peak 10-minute sustained winds of 125 kt (64 m s^{-1}) and a minimum central pressure of 917 hPa. Severe Tropical Cyclone Yasa made landfall over Vanua Levu, Fiji, and resulted in considerable widespread damage. Four lives were lost due to strong winds and flooding associated with the event. Since the beginning of reliable records, Yasa was the earliest Category 5 tropical cyclone (on both the Australian scale and SSHWS) in the basin.

Tropical Cyclone Zazu initially formed as a tropical disturbance approximately 500 km to the northeast of Niue. Favorable conditions promoted intensification and on 15 December, Cyclone Zazu achieved Category 2 status with peak 10-minute sustained winds of 50 kt (26 m s^{-1}) and a minimum central pressure of 980 hPa. Heavy surf associated with Zazu damaged a wharf on Niue, and strong winds caused minor damage in Tonga.

Tropical Cyclone Imogen originated from a tropical low that formed in the Gulf of Carpentaria under favorable conditions, including SSTs up to 31°C, which promoted intensification. On 3 January, Imogen was named and achieved Category 1 status, eventually achieving peak 10-minute sustained winds of 45 kt (23 m s^{-1}) and a minimum central pressure of 990 hPa. Cyclone Imogen was the first tropical cyclone of the 2020/21 Australian region TC season (section 4g7).

Tropical Cyclone Kimi formed from a weak tropical low to the northeast of Cooktown on 17 January. Kimi continued to track to the south and was expected to make landfall; however, a notable increase in wind shear caused the system to loop and quickly dissipate on 19 January. This short-lived and relatively compact system achieved Category 2 status with peak 10-minute sustained winds of 55 kt (28 m s^{-1}) and minimum central pressure of 987 hPa. Cyclone Kimi caused Townsville Airport to temporarily cease operations (between 18 and 19 January) and resulted in considerable rainfall and flash flooding with 24-hour accumulated rainfall of 158 mm at Innisfail.

Severe Tropical Cyclone Ana developed from a tropical disturbance that formed approximately 200 km to the northeast of Port Vila, Vanuatu. Initially tracking to the east and then southeast, Ana gradually intensified and achieved Category 1 intensity on 29 January, approximately 350 km to the northwest of Nadi, Fiji. Tracking towards the southeast, Cyclone Ana passed through the northern Yasawa Islands, where it continued to intensify, making landfall near Rakiraki, Fiji, on 31 January. Near Kadavu Island, Severe Tropical Cyclone Ana achieved Category 3 intensity with peak 10-minute sustained winds of 65 kt (33 m s^{-1}) and minimum central pressure of 970 hPa. Ana rapidly weakened to a subtropical low on 1 February and continued to track towards the southeast. On approach to Fiji, Severe Tropical Cyclone Ana caused significant flooding in Nadi and Rakiraki, and considerable damage was reported in Suva after landfall. Five people were reported missing with one confirmed fatality. This event prompted a humanitarian aid response as the region was still recovering from Severe Tropical Cyclone Yasa, a Category 5 event, one month prior.

Tropical Cyclone Bina developed from an east-northeastward tracking TD that initially developed approximately 700 km northeast of Port Vila. Favorable environmental conditions promoted intensification to a Category 1 tropical cyclone on 31 January with peak 10-minute sustained winds of 45 kt (23 m s^{-1}) and a minimum central pressure of 991 hPa. Bina tracked in a southeasterly direction towards Vanua Levu, Fiji, where it was downgraded to a TD on 1 February. Although the event made landfall over Vanua Levu as a TD, it did so within 24 hours of Severe Tropical Cyclone Ana, prolonging the gale force winds and rainfall.

Tropical Cyclone Lucas originated from a tropical low formed from a monsoon trough in the Gulf of Carpentaria. Tracking towards the east over the Cape York Peninsula and then towards the southwest, Lucas eventually intensified to a Category 2 system, achieving peak 10-minute sustained winds of 60 kt (31 m s^{-1}) and a minimum central pressure of 975 hPa. Cyclone Lucas made landfall on New Caledonia on 2 February and resulted in damage to power infrastructure and power outages across the Loyalty Islands, as well as contamination of drinking water supplies.

Severe Tropical Cyclone Niran, the third severe TC and second Category 5 TC for the season, initially formed off the coast of northern Queensland and was named on 1 March (see section 4g7) while tracking towards the southwest. Niran intensified to a Category 5 system on 5 March on approach to New Caledonia, achieving peak 10-minute sustained winds of 110 kt (57 m s^{-1}) and a minimum central pressure of 931 hPa. Unfavorable wind shear weakened the system to a Category 3 event before it passed close to the southern coastline of New Caledonia.

h. Tropical cyclone heat potential—F. Bringas, G. J. Goni, I-I Lin, and J. A. Knaff

Tropical cyclone heat potential (TCHP; e.g., Goni et al. 2009, 2017) is an indicator of the available heat stored in the upper ocean that can potentially induce tropical cyclone (TC) intensification and regulate ocean–atmosphere enthalpy fluxes and TC-induced sea surface temperature (SST) cooling (e.g., Lin et al. 2013). TCHP is calculated as the integrated heat content between the sea surface and the 26°C isotherm (D26), which is generally taken to be the minimum temperature required for TC genesis and intensification (Leipper and Volgenau 1972; Dare and McBride 2011).

Provided that atmospheric conditions are favorable, TC intensification, including rapid intensification, has been associated with areas in the ocean that have TCHP values above 50 kJ cm^{-2} (e.g., Shay et al. 2000; Mainelli et al. 2008; Lin et al. 2014; 2021; Knaff et al. 2018, 2020). High SSTs prior to TC formation usually lead to less SST cooling during the lifetime of the TC, and hence higher enthalpy fluxes from the ocean into the storm, favoring intensification (e.g., Lin et al. 2013). Similarly, upper ocean salinity is another condition of relevance for TC intensification because fresh water-induced barrier layers may also modulate the upper ocean mixing and cooling during a TC, and hence the air–sea fluxes (e.g., Balaguru 2012; Domingues et al. 2015). Upper ocean thermal conditions observed during 2021 are presented here in terms of two parameters: (1) TCHP anomaly values with respect to their long-term mean (1993–2020) and (2) TCHP anomaly values compared to conditions observed in 2020. TCHP anomalies during 2021 (Fig. 4.40) are computed for June–November in the Northern Hemisphere and November 2020–April 2021 in the Southern Hemisphere. In Fig. 4.40, the seven regions where TCs are known to form, travel, and intensify are highlighted. In all of these regions, TCHP values exhibit large temporal and spatial variability due to mesoscale features, trends, and short- to long-term modes of variability, such as the North Atlantic Oscillation (NAO), El Niño-Southern Oscillation (ENSO), and the Pacific Decadal Oscillation (PDO). The differences in TCHP anomalies between 2020 and 2021 are also computed for the primary months of TC activity in each hemisphere (Fig. 4.41).

During the 2021 season, TCHP exhibited above-average values across most basins (Fig. 4.40). TCHP anomalies above 30 kJ cm^{-2} were observed in areas within several regions, including the North Indian Ocean, southeast Indian Ocean, western Pacific Ocean, and the Gulf of Mexico. These positive anomalies may be indicative of favorable oceanic conditions during 2021 for TC development and intensification. Compared to 2020, TCHP anomalies in 2021 were higher in the southeast Indian Ocean, southwest Pacific, and part of the Gulf of Mexico basin, while the anomalies were lower in the rest of the basins (Fig. 4.41). In particular, TCHP anomalies during 2021 were lower than those in 2020 and below the long-term average in the eastern North Pacific basin, linked to the negative phase of ENSO (La Niña) that re-emerged in August 2021.

In the Southern Hemisphere, TCHP during 2021 was mostly above the long-term average, with values of more than 30 kJ cm^{-2} in the southeast Indian Ocean and ~10 kJ cm^{-2} in the southwest Indian Ocean (Fig. 4.40). TCHP was more than 20 kJ cm^{-2} higher than 2020 values in the southeast Indian Ocean and southwest Pacific, while they were 20 kJ cm^{-2} lower in areas of the southwest Indian Ocean (Fig. 4.41). The 2020/21 cyclone season in the southwest Indian Ocean was above average and produced seven TCs of Category 1 or above intensity, including Very Intense TC Faraji (Category 5; section 4g6). Ocean conditions with high TCHP anomalies in the southeast Indian Ocean and southwest Pacific around Australia translated, however, to a below-average but deadly season with five TCs, including Severe TC Seroja and Category 5 Niran (section 4g8), the most

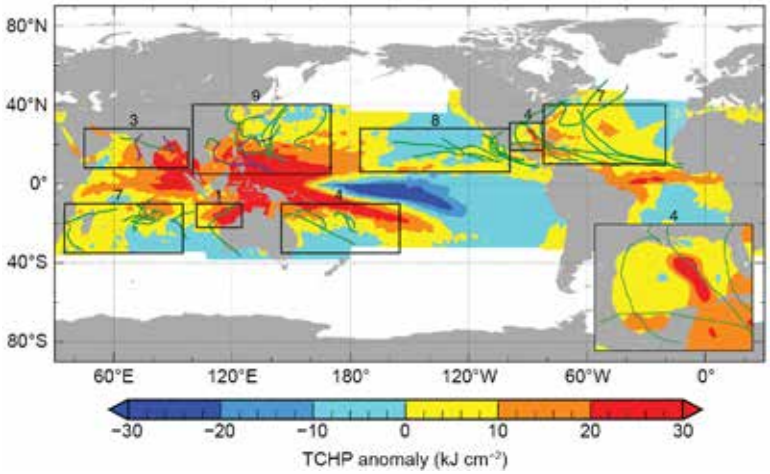

Fig. 4.40. Global anomalies of TCHP (kJ cm^{-2}) during 2021 computed as described in the text. The boxes indicate the seven regions where TCs occur: from left to right, southwest Indian, North Indian, northwest Pacific, southeast Indian, South Pacific, East Pacific, and North Atlantic (shown as Gulf of Mexico and tropical Atlantic separately). The green lines indicate the trajectories of all tropical cyclones reaching at least Category 1 (1-min average wind ≥ 64 kt, 34 m s^{-1}) and above during Nov 2020–Apr 2021 in the Southern Hemisphere and Jun–Nov 2021 in the Northern Hemisphere. The purple lines indicate the trajectories of tropical cyclones Category 1 or stronger in the Northern Hemisphere that occurred outside the Jun–Nov 2021 period. The numbers above each box correspond to the number of Category 1 and stronger cyclones that travel within each box. The Gulf of Mexico conditions are shown in the inset in the lower right corner.

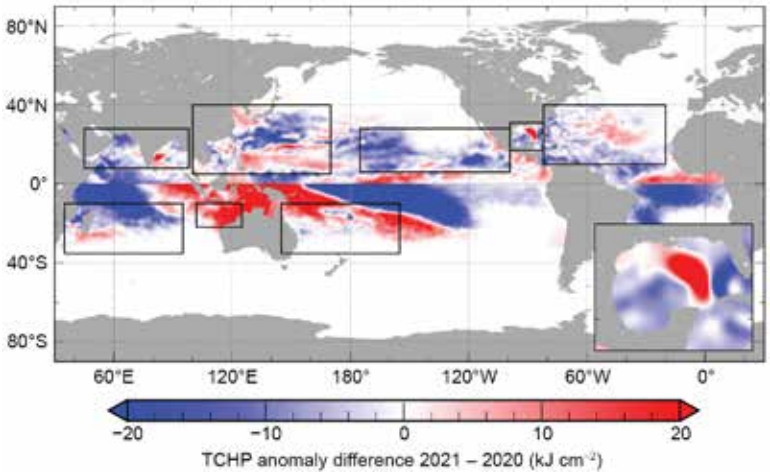

Fig. 4.41. TCHP anomaly difference (kJ cm^{-2}) between the 2021 and 2020 tropical cyclone seasons (Jun–Nov in the Northern Hemisphere and Nov–Apr in the Southern Hemisphere). The Gulf of Mexico conditions are shown in the inset in the lower right corner.

intense storm of the region for this season. Anomalously high values of TCHP in the Coral Sea were partially responsible for Niran's slow, but steady, development just off the coast of Queensland while being nearly stationary and noticeably affected by vertical wind shear on 2–3 March, followed by its rapid intensification that commenced once the storm began to move on 4 March.

The North Indian Ocean was characterized by above-average TCHP during 2021, with anomalies in excess of 30 kJ cm^{-2} in the Bay of Bengal (Fig. 4.40); however, these values were lower than those observed the previous year (Fig. 4.41). Three Category 1 or stronger TCs occurred in the region (Fig. 4.40), two of which occurred in May and are shown in Fig. 4.40 as purple lines. The most intense TC in this basin during 2021 was Extremely Severe TC Tauktae in May (section 4g5), with peak intensity of 3-minute sustained wind speed of 100 kt (51 m s^{-1}) and minimum pressure of 950 hPa. TCHP values exceeding 140 kJ cm^{-2} over the southeast Arabian Sea were cited as a contributing environmental factor, noting values were lower but exceeding 50 kJ cm^{-2} along the storm track (IMD 2021).

Upper ocean thermal conditions are largely modulated by the state of ENSO in the North Pacific (e.g., Lin et al. 2014, 2020; Zheng et al. 2015). During 2021, La Niña was observed from August to the end of the year. This is similar to 2020, in which a stronger La Niña (compared to 2021) was observed during August 2020 to May 2021. As is typical during a La Niña year, TCHP was above average in the western North Pacific (Lin et al. 2014, 2020), with anomalies well above 30 kJ cm^{-2} closer to the equator and average anomalies of ~20 kJ cm^{-2} throughout the region compared to the long-term average (Fig. 4.40). Compared to 2020, TCHP in the western North Pacific displayed both negative and positive anomalies, possibly associated with the difference in the La Niña characteristics of these two years. TCHP anomalies were slightly negative compared to average in the eastern North Pacific and moderately negative compared to 2020 (Fig. 4.41). Category 5 Super Typhoon Surigae was the most intense storm both in the western North Pacific and globally in 2021. Interestingly, it occurred

in April (i.e., boreal spring) and not summer and is therefore shown in Fig. 4.40 as a purple track line. TCHP observations show that Surigae intensified to 165 kts (85 m s^{-1}) peak intensity over a region of high TCHP of ~120–140 kJ cm^{-2}, ~30 kJ cm^{-2} higher than the long-term mean for April. Another notable western North Pacific Category 5 TC was Super Typhoon Chanthu, which intensified to its peak intensity of 155 kts (80 m s^{-1}) in September, when traveling over the Kuroshio warm current region south of Taiwan, where high TCHP values of ~130 kJ cm^{-2} were observed.

In the North Atlantic basin, upper ocean thermal conditions during the 2021 hurricane season were characterized by TCHP values moderately above the long-term average, with anomalies between +10 and +20 kJ cm^{-2} (Fig. 4.40) but as much as 10 kJ cm^{-2} lower than the previous year in the regions where most TCs form and intensify in this basin (Fig. 4.41). An exception was the area associated with the location of the northern extension of the Loop Current in the Gulf of Mexico, where TCHP anomalies were more than 30 kJ cm^{-2} higher than the long-term average and more than 20 kJ cm^{-2} higher than the values of 2020. Consistent with the higher-than-average TCHP anomalies, 2021 was the third most active Atlantic hurricane season on record with 21 named storms, including seven hurricanes at Category 1 or above intensity.

During 2021, Hurricanes Grace and Ida reached their peak intensities, corresponding to Category 3 and 4 storms, respectively. The genesis of Hurricane Grace started off Cabo Verde on 10 August. The system continued to organize and became a named tropical storm on 14 August, reaching Category 1 when traveling in the Caribbean Sea. After the storm moved offshore from the Yucatan Peninsula into the southwest region of the Gulf of Mexico, Grace underwent rapid intensification on 23 August from Category 1 to Category 3 in a 15-hour period while moving over an area with SST > 28°C and TCHP > 60 kJ cm^{-2}, above the 50-kJ cm^{-2} threshold required to support Atlantic hurricane intensification (Mainelli et al. 2008). Hurricane Ida, the second most intense Atlantic storm in 2021, reached Category 1 when traveling on 26–27 August over an area in the Caribbean Sea with favorable ocean conditions, including TCHP values of more than 120 kJ cm^{-2} and extensive areas of low salinity surface layers associated with the Amazon and Orinoco riverine plumes, observed by underwater gliders deployed in the region (https://www.aoml.noaa.gov/hurricane-glider-project). Low-surface salinity areas create barrier layer conditions that reduce upper-ocean turbulent mixing and maintain high enthalpy fluxes from the ocean into the hurricane, therefore contributing to TC organization and intensification (e.g., Balaguru et al. 2015; Domingues et al. 2015). After traveling over the western portion of Cuba and entering the Gulf of Mexico, Ida moved over a region of increasingly favorable ocean conditions over the main location of the northern extension of the Loop Current, the same area where the largest TCHP anomalies in the North Atlantic and Gulf of Mexico basins occurred (Fig. 4.40). These favorable conditions contributed to Ida's intensification, including rapid intensification reaching Category 4 on 29 August with peak intensity of 1-minute sustained wind speeds of 130 kt (67 m s^{-1}) and a minimum central barometric pressure of 929 hPa, after traveling over a warm region with TCHP > 140 kJ cm^{-2} associated with a strong anticyclonic eddy that was shed by the Loop Current.

In summary, favorable upper-ocean thermal conditions were observed in all seven basins during the 2021 season, except in the eastern North Pacific, where conditions were average to slightly below average compared to the long-term mean. Additionally, TCHP anomaly values during 2021 exhibited similar to lower values in most regions compared to the previous year in most basins.

Acknowledgments

Our thanks go out to Gregory Carbin, Alex Lamers, and David Novak, of NOAA's Weather Prediction Center for assisting us with re-constructing a key precipitation graphic in Sidebar 4.1 on the Hurricane Ida story.

Appendix 1: Chapter 4 – Acronyms

ACE	Accumulated Cyclone Energy
AEJ	African Easterly Jet
AMO	Atlantic multi-decadal oscillation
ASO	August–October
CNP	central North Pacific
CPC	Climate Prediction Center
DJF	December–February
EASM	East Asian summer monsoon
ENP	eastern North Pacific
ENSO	El Niño–Southern Oscillation
GPCP	Global Precipitation Climatology Project
GPI	genesis potential index
HTCs	hurricanes/typhoons/cyclones
IBTrACS	International Best Track Archive for Climate Stewardship
IO	Indian Ocean
IOB	Indian Ocean basin
IOD	Indian Ocean dipole
ITCZ	Intertropical Convergence Zone
JAS	July–September
JASO	July–October
JJA	June–August
JMA	Japan Meteorological Agency
JTWC	Joint Typhoon Warning Center
MAM	March–May
MDR	main development region
MJO	Madden-Julian oscillation
NAF	northern Africa
NH	Northern Hemisphere
NIO	North Indian Ocean
nIOD	Negative Indian Ocean dipole
OLR	outgoing longwave radiation
OND	October–December
ONI	Oceanic Niño Index
PAGASA	Philippine Atmospheric, Geophysical and Astronomical Services Administration
RMM	Real-time Multivariate
RSMCs	Regional Specialized Meteorological Centers

SAM	Southern Annular Mode
SH	Southern Hemisphere
SON	September–November
SPCZ	South Pacific Convergence Zone
SPEArTC	South Pacific Enhanced Archive of Tropical Cyclones
SSHWS	Saffir-Simpson Hurricane Wind Scale
SST	sea surface temperature
std. dev.	standard deviation
TC	tropical cyclone
TCHP	tropical cyclone heat potential
TD	tropical depression
WMO	World Meteorological Organization
WNP	western North Pacific

Appendix 2: Supplemental Material

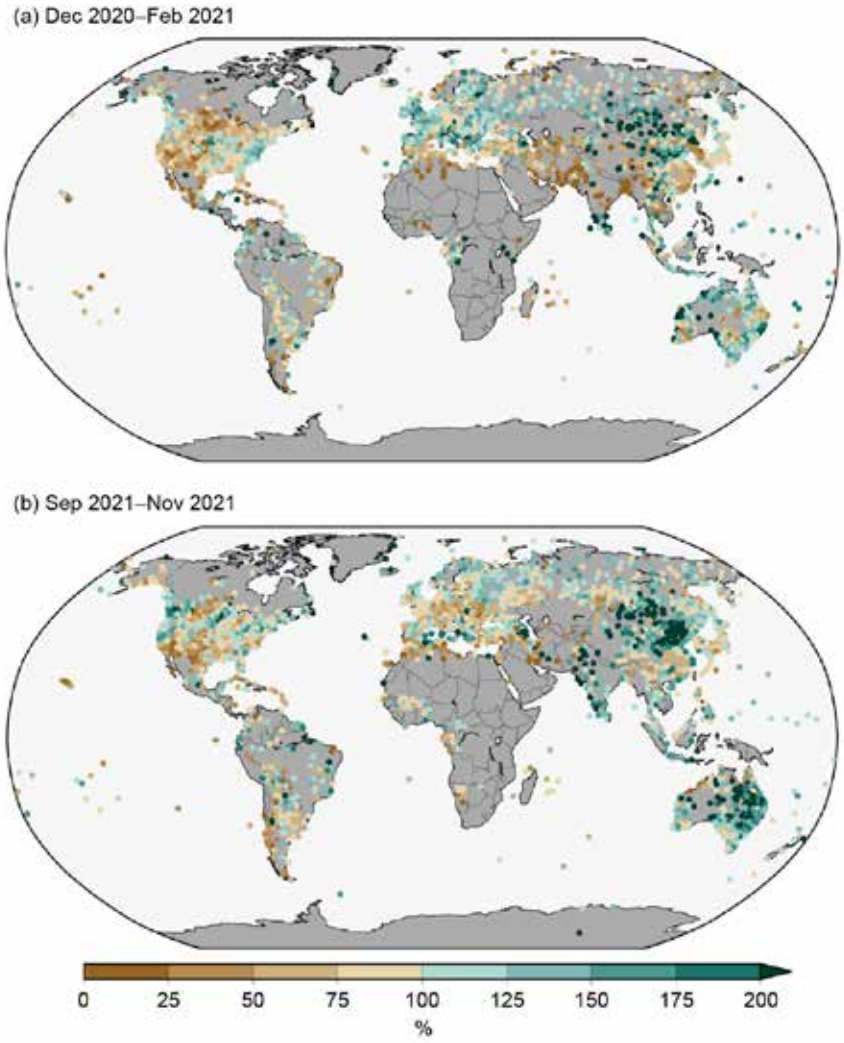

Fig. A4.1. Land-only percent of normal precipitation during (a) DJF 2020/21 and (b) SON 2021 (relative to a 1961–1990 base period). [Figure provided by NOAA NCEI and data are from GHCN-M version 4beta (Menne et al. 2017).]

References

Aiyyer, A., and J. Molinari, 2008: MJO and tropical cyclogenesis in the Gulf of Mexico and eastern Pacific: Case study and idealized numerical modeling. *J. Atmos. Sci.*, **65**, 2691–2704, https://doi.org/10.1175/2007JAS2348.1.

Aon, 2021a: Global Catastrophe Recap, August 2021, 19 pp, http://thoughtleadership.aon.com/Documents/20210009_analytics-if-august-global-recap.pdf.

——, 2021b: Global Catastrophe Recap, September 2021, 22 pp, http://thoughtleadership.aon.com/Documents/20210012-analytics-if-september-global-recap.pdf.

——, 2022: Global Catastrophe Recap, December 2021, 23 pp, https://www.aon.com/reinsurance/getmedia/e5d555d8-ade5-4fc4-b4b2-24ddad4bfb3d/20220124-analytics-if-december-global-recap.pdf.aspx.

Balaguru, K., P. Chang, R. Saravanan, L. R. Leung, Z. Xu, M. Li, and J. S. Hsieh, 2012: Ocean barrier layers' effect on tropical cyclone intensification. *Proc. Natl. Acad. Sci. USA*, **109**, 142343–142347, https://doi.org/10.1073/pnas.1201364109.

Banzon, V. F., and R. W. Reynolds, 2013: Use of WindSat to extend a microwave-based daily optimum interpolation sea surface temperature time series. *J. Climate*, **26**, 2557–2562, https://doi.org/10.1175/JCLI-D-12-00628.1.

Baxter, S., S. Weaver, J. Gottschalck, and Y. Xue, 2014: Pentad evolution of wintertime impacts of the Madden–Julian oscillation over the contiguous United States. *J. Climate*, **27**, 7356–7367, https://doi.org/10.1175/JCLI-D-14-00105.1.

Behringer, D. W., 2007: The Global Ocean Data Assimilation System (GODAS) at NCEP. *11th Symp. on Integrated Observing and Assimilation Systems for Atmosphere, Oceans, and Land Surface*, San Antonio, TX, Amer. Meteor. Soc., 3.3, http://ams.confex.com/ams/87ANNUAL/techprogram/paper_119541.htm.

——, M. Ji, and A. Leetmaa, 1998: An improved coupled model for ENSO prediction and implications for ocean initialization. Part I: The ocean data assimilation system. *Mon. Wea. Rev.*, **126**, 1013–1021, https://doi.org/10.1175/1520-0493(1998)126<1013:AICMFE>2.0.CO;2.

Bell, G. D., and M. Chelliah, 2006: Leading tropical modes associated with interannual and multi-decadal fluctuations in North Atlantic hurricane activity. *J. Climate*, **19**, 590–612, https://doi.org/10.1175/JCLI3659.1.

——, and Coauthors, 2000: The 1999 North Atlantic Hurricane season [in "Climate Assessment for 1999"]. *Bull. Amer. Meteor. Soc.*, **81** (6), S19–S22, https://doi.org/10.1175/1520-0477(2000)81[s1:CAF]2.0.CO;2.

——, E. S. Blake, C. W. Landsea, C. Wang, J. Schemm, T. Kimberlain, R. J. Pasch, and S. B. Goldenberg, 2017: Atlantic basin [in "State of the Climate in 2016"]. *Bull. Amer. Meteor. Soc.*, **98** (8), S108–S112, https://doi.org/10.1175/2017BAMSStateoftheClimate.1.

——, ——, ——, S. B. Goldenberg, and R. J. Pasch, 2018: Atlantic basin [in "State of the Climate in 2017"]. *Bull. Amer. Meteor. Soc.*, **99** (8), S114–S118, https://doi.org/10.1175/2018BAMSStateoftheClimate.1.

——, ——, ——, H. Wang, S. B. Goldenberg, and R. J. Pasch 2019: Atlantic basin [in "State of the Climate in 2018"]. *Bull. Amer. Meteor. Soc.*, **100** (9), S113–S119, https://doi.org/10.1175/2019BAMSStateoftheClimate.1.

——, E. S. Blake, C. W. Landsea, M. Rosencrans, H. Wang, S. B. Goldenberg, and R. J. Pasch, 2020: Atlantic basin [in "State of the Climate in 2019"]. *Bull. Amer. Meteor. Soc.*, **101** (7), S204–S212, https://doi.org/10.1175/BAMS-D-20-0077.1.

Berg, R., 2022: Hurricane Rick (EP172021). National Hurricane Center Tropical Cyclone Rep., 21 pp., https://www.nhc.noaa.gov/data/tcr/EP172021_Rick.pdf.

Beven, J., A. Hagen, and R. Berg, 2022: Hurricane Ida (AL092021). National Hurricane Center Tropical Cyclone Rep., 163 pp., https://www.nhc.noaa.gov/data/tcr/AL092021_Ida.pdf.

Camargo, S. J., and A. H. Sobel, 2005: Western North Pacific tropical cyclone intensity and ENSO. *J. Climate*, **18**, 2996–3006, https://doi.org/10.1175/JCLI3457.1.

——, A. W. Robertson, S. J. Gaffney, P. Smyth, and M. Ghil, 2007a: Cluster analysis of typhoon tracks: Part II: Large-scale circulation and ENSO. *J. Climate*, **20**, 3654–3676, https://doi.org/10.1175/JCLI4203.1.

——, K. A. Emanuel, and A. H. Sobel, 2007b: Use of a genesis potential index to diagnose ENSO effects on tropical cyclone genesis. *J. Climate*, **20**, 4819–4834, https://doi.org/10.1175/JCLI4282.1.

——, M. C. Wheeler, and A. H. Sobel, 2009: Diagnosis of the MJO modulation of tropical cyclogenesis using an empirical index. *J. Atmos. Sci.*, **66**, 3061–3074, https://doi.org/10.1175/2009JAS3101.1.

Cangialosi, J. P., 2021a: Hurricane Felicia (EP062021). National Hurricane Center Tropical Cyclone Rep., 15 pp., https://www.nhc.noaa.gov/data/tcr/EP062021_Felicia.pdf.

——, 2021b: Hurricane Pamela (EP162021). National Hurricane Center Tropical Cyclone Rep., 17 pp., https://www.nhc.noaa.gov/data/tcr/EP162021_Pamela.pdf.

Cassou, C., 2008: Intraseasonal interaction between the Madden–Julian Oscillation and the North Atlantic Oscillation. *Nature*, **455**, 523–527, https://doi.org/10.1038/nature07286.

Chia, H. H., and C. F. Ropelewski, 2002: The interannual variability in the genesis location of tropical cyclones in the northwest Pacific. *J. Climate*, **15**, 2934–2944, https://doi.org/10.1175/1520-0442(2002)015<2934:TIVITG>2.0.CO;2.

Chen, L., and J.-J. Luo, 2021: Indian Ocean dipole [in "State of the Climate in 2020"]. *Bull. Amer. Meteor. Soc.*, **103** (8), S21–S25, https://doi.org/10.1175/BAMS-D-21-00090.1.

Dare, R. A., and J. L. McBride, 2011: Sea surface temperature response to tropical cyclones. *Mon. Wea. Rev.*, **139**, 3798–3808, https://doi.org/10.1175/MWR-D-10-05019.1.

Diamond, H. J., and J. A. Renwick, 2015: The climatological relationship between tropical cyclones in the southwest Pacific and the Madden–Julian Oscillation. *Int. J. Climatol.*, **35**, 676–686, https://doi.org/10.1002/joc.4012.

——, and C. J. Schreck III , Eds., 2019: The tropics [in "State of the Climate in 2018"]. *Bull. Amer. Meteor. Soc.*, **100** (9), S101–S140, https://doi.org/10.1175/2019BAMSStateoftheClimate.1.

——, and ——, Eds, 2020: The tropics [in "State of the Climate in 2019"]. *Bull. Amer. Meteor. Soc.*, **100** (8), S185–S238, https://doi.org/10.1175/BAMS-D-20-0077.1.

——, and ——, Eds., 2021: The tropics [in "State of the Climate in 2020"]. *Bull. Amer. Meteor. Soc.*, **102** (8), S199–S262, https://doi.org/10.1175/BAMS-D-21-0080.1.

——, A. M. Lorrey, K. R. Knapp, and D. H. Levinson, 2012: Development of an enhanced tropical cyclone tracks database for the southwest Pacific from 1840 to 2011. *Int. J. Climatol.*, **32**, 2240–2250, https://doi.org/10.1002/joc.2412.

Ding, Q., E. J. Steig, D. S. Battisti, and J. M. Wallace, 2012: Influence of the tropics on the southern annular mode. *J. Climate*, **25**, 6330–6348, https://doi.org/10.1175/JCLI-D-11-00523.1.

Domingues, R., and Coauthors, 2015: Upper ocean response to Hurricane Gonzalo (2014): Salinity effects revealed by targeted and sustained underwater glider observations. *Geophys. Res. Lett.*, **42**, 7131–7138, https://doi.org/10.1002/2015GL065378.

Dube, S. K., D. Rao, P. C. Sinha, T. S. Murty, and N. Bahuluyan, 1997: Storm surge in the Bay of Bengal and Arabian Sea: The problem and its prediction. *Mausam*, **48**, 283–304, https://doi.org/10.54302/mausam.v48i2.4012.

Ebita, A., and Coauthors, 2011: The Japanese 55-year Reanalysis "JRA-55": An interim report. *SOLA*, **7**, 149–152, https://doi.org/10.2151/sola.2011-038.

Emanuel, K. A., 1988: The maximum intensity of hurricanes. *J. Atmos. Sci.*, **45**, 1143–1155, https://doi.org/10.1175/1520-0469(1988)045<1143:TMIOH>2.0.CO;2.

——, and D. S. Nolan, 2004: Tropical cyclone activity and the global climate system. *26th Conf. on Hurricanes and Tropical Meteorology*, Miami, FL, Amer. Meteor. Soc., 10A.2, https://ams.confex.com/ams/26HURR/techprogram/paper_75463.htm.

Enfield, D. B., and A. M. Mestas-Nuñez, 1999: Multiscale variabilities in global sea surface temperatures and their relationships with tropospheric climate patterns. *J. Climate*, **12**, 2719–2733, https://doi.org/10.1175/1520-0442(1999)012<2719:MVIGSS>2.0.CO;2.

Feng, M., M. J. McPhaden, S. Xie, and J. Hafner, 2013: La Niña forces unprecedented Leeuwin Current warming in 2011. *Sci. Rep.*, **3**, 1277. https://doi.org/10.1038/srep01277.

Frank, W. M., and P. E. Roundy, 2006: The role of tropical waves in tropical cyclogenesis. *Mon. Wea. Rev.*, **134**, 2397–2417, https://doi.org/10.1175/MWR3204.1.

Gill, A. E., 1980: Some simple solutions for heat-induced tropical circulation. *Quart. J. Roy. Meteor. Soc.*, **106**, 447–462, https://doi.org/10.1002/qj.49710644905.

Goldenberg, S. B., and L. J. Shapiro, 1996: Physical mechanisms for the association of El Niño and West African rainfall with Atlantic major hurricane activity. *J. Climate*, **9**, 1169–1187, https://doi.org/10.1175/1520-0442(1996)009<1169:PMFTAO>2.0.CO;2.

——, C. W. Landsea, A. M. Mestas-Nuñez, and W. M. Gray, 2001: The recent increase in Atlantic hurricane activity: Causes and implications. *Science*, **293**, 474–479, https://doi.org/10.1126/science.1060040.

Goni, G. J., and Coauthors, 2009: Applications of satellite-derived ocean measurements to tropical cyclone intensity forecasting. *Oceanography*, **22**, 190–197, https://doi.org/10.5670/oceanog.2009.78.

——, and Coauthors, 2017: Autonomous and Lagrangian ocean observations for Atlantic tropical cyclone studies and forecasts. *Oceanography*, **30**, 92–103, https://doi.org/10.5670/oceanog.2017.227.

Gray, W. M., 1990: Strong association between West African rainfall and U.S. landfall of intense hurricanes. *Science*, **249**, 1251–1256, https://doi.org/10.1126/science.249.4974.1251.

Guo, Y., X. Jiang, and D. E. Waliser, 2014: Modulation of the convectively coupled Kelvin waves over South America and the tropical Atlantic Ocean in association with the Madden–Julian Oscillation. *J. Atmos. Sci.*, **71**, 1371–1388, https://doi.org/10.1175/JAS-D-13-0215.1.

Hastenrath, S., 1990: Decadal-scale changes of the circulation in the tropical Atlantic sector associated with Sahel drought. *Int. J. Climatol.*, **10**, 459–472, https://doi.org/10.1002/joc.3370100504.

Hendon, H., C. Zhang, and J. Glick, 1999: Interannual variation of the Madden–Julian oscillation during austral summer. *J. Climate*, **12**, 2538–2550, https://doi.org/10.1175/1520-0442(1999)012<2538:IVOTMJ>2.0.CO;2.

Hersbach, H., and Coauthors, 2020: The ERA5 global reanalysis. *Quart. J. Roy. Meteor. Soc.*, **146**, 1999–2049, https://doi.org/10.1002/qj.3803.

Hong, C.-C., T. Li, and J.-J. Luo, 2008: Asymmetry of the Indian Ocean Dipole. Part II: Model diagnosis. *J. Climate*, **21**, 4849–4858.

Huang, B., and Coauthors, 2017: Extended Reconstructed Sea Surface Temperature, version 5 (ERSSTv5): Upgrades, validations, and intercomparisons. *J. Climate*, **30**, 8179–8205, https://doi.org/10.1175/JCLI-D-16-0836.1.

Huang, B., C. Liu, V. Banzon, E. Freeman, G. Graham, B. Hankins, T. Smith, and H.-M. Zhang, 2020: Improvements of the Daily Optimum Interpolation Sea Surface Temperature (DOISST) version 2.1. *J. Climate*, **34**, 2923–2939, https://doi.org/10.1175/JCLI-D-20-0166.1.

Huffman, G. J., R. F. Adler, D. T. Bolvin, and G. Gu, 2009: Improving the global precipitation record: GPCP version 2.1. *Geophys. Res. Lett.*, **36**, L17808, https://doi.org/10.1029/2009GL040000.

IMD, 2021: Extremely Severe Cyclonic Storm TAUKTAE over the Arabian Sea (14th–19th May, 2021): A report. India Meteorological Department, 64 pp., https://rsmcnewdelhi.imd.gov.in/uploads/report/26/26_e0cc1a_Preliminary%20Report%20on%20ESCS%20TAUKTAE-19july.pdf.

Kalnay, E., and Coauthors, 1996: The NCEP/NCAR 40-Year Reanalysis Project. *Bull. Amer. Meteor. Soc.*, **77**, 437–471, https://doi.org/10.1175/1520-0477(1996)077<0437:TNYRP>2.0.CO;2.

Kayano, M., and V. Kousky, 1999: Intraseasonal (30–60 day) variability in the global tropics: Principal modes and their evolution. *Tellus*, **51**, 373–386, https://doi.org/10.3402/tellusa.v51i3.13459.

Kiladis, G. N., and K. M. Weickmann, 1992: Circulation anomalies associated with tropical convection during northern winter. *Mon. Wea. Rev.*, **120**, 1900–1923, https://doi.org/10.1175/1520-0493(1992)120<1900:CAAWTC>2.0.CO;2.

——, K. H. Straub, and P. T. Haertel, 2005: Zonal and vertical structure of the Madden–Julian oscillation. *J. Atmos. Sci.*, **62**, 2790–2809, https://doi.org/10.1175/JAS3520.1.

——, M. C. Wheeler, P. T. Haertel, K. H. Straub, and P. E. Roundy, 2009: Convectively coupled equatorial waves. *Rev. Geophys.*, **47**, RG2003, https://doi.org/10.1029/2008RG000266.

Klotzbach, P. J., K. M. Wood, C. J. Schreck III, S. G. Bowen, C. M. Patricola, and M. M. Bell, 2022: Trends in global tropical cyclone activity: 1990–2021. *Geophys. Res. Lett.*, **49**, e2021GL095774, https://doi.org/10.1029/2021GL095774.

Knaff, J. A., C. R. Sampson, and K. D. Musgrave, 2018: An operational rapid intensification prediction aid for the western North Pacific. *Wea. Forecasting*, **33**, 799–811, https://doi.org/10.1175/WAF-D-18-0012.1.

Knapp, K. R., M. C. Kruk, D. H. Levinson, H. J. Diamond, and C. J. Neumann, 2010: The International Best Track Archive for Climate Stewardship (IBTrACS): Unifying tropical cyclone data. *Bull. Amer. Meteor. Soc.*, **91**, 363–376, https://doi.org/10.1175/2009BAMS2755.1.

——, J. A. Knaff, C. R. Sampson, G. M. Riggio, and A. D. Schnapp, 2013: A pressure-based analysis of the historical western North Pacific tropical cyclone intensity record. *Mon. Wea. Rev.*, **141**, 2611–2631, https://doi.org/10.1175/MWR-D-12-00323.1.

Knutson, T. R., and K. M. Weickmann, 1987: 30–60 day atmospheric oscillations: Composite life cycles of convection and circulation anomalies. *Mon. Wea. Rev.*, **115**, 1407–1436, https://doi.org/10.1175/1520-0493(1987)115<1407:DAOCLC>2.0.CO;2.

Kousky, V. E., and M. T. Kayano, 1994: Principal modes of outgoing longwave radiation and 250-mb circulation for the South American sector. *J. Climate*, **7**, 1131–1143, https://doi.org/10.1175/1520-0442(1994)007<1131:PMOOLR>2.0.CO;2.

Krishnamurti, T. N., and D. Subrahmanyam, 1982: The 30–50 day mode at 850 mb during MONEX. *J. Atmos. Sci.*, **39**, 2088–2095, https://doi.org/10.1175/1520-0469(1982)039<2088:TDMAMD>2.0.CO;2.

Landsea, C. W., and J. L. Franklin, 2013: Atlantic hurricane database uncertainty and presentation of a new database format. *Mon. Wea. Rev.*, **141**, 3576–3592, https://doi.org/10.1175/MWR-D-12-00254.1.

——, W. M. Gray, P. W. Mielke, and K. J. Berry, 1992: Long-term variations of western Sahelian monsoon rainfall and intense U.S. landfalling hurricanes. *J. Climate*, **5**, 1528–1534, https://doi.org/10.1175/1520-0442(1992)005<1528:LTVOWS>2.0.CO;2.

——, G. D. Bell, W. M. Gray, and S. B. Goldenberg, 1998: The extremely active 1995 Atlantic hurricane season: Environmental conditions and verification of seasonal forecasts. *Mon. Wea. Rev.*, **126**, 1174–1193, https://doi.org/10.1175/1520-0493(1998)126<1174:TEAAHS>2.0.CO;2.

——, G. A. Vecchi, L. Bengtsson, and T. R. Knutson, 2010: Impact of duration thresholds on Atlantic tropical cyclone counts. *J. Climate*, **23**, 2508–2519, https://doi.org/10.1175/2009JCLI3034.1.

Latto, A., 2021: Hurricane Enrique (EP052021). National Hurricane Center Tropical Cyclone Rep., 20 pp., https://www.nhc.noaa.gov/data/tcr/EP052021_Enrique.pdf.

——, 2022: Hurricane Olaf (EP152021). National Hurricane Center Tropical Cyclone Rep., 21 pp., https://www.nhc.noaa.gov/data/tcr/EP152021_Olaf.pdf.

Lau, W. K.-M., and D. E. Waliser, 2012: *Intraseasonal Variability in the Atmosphere-Ocean Climate System*. Springer, 642 pp.

Leipper, D. F., and D. Volgenau, 1972: Hurricane heat potential of the Gulf of Mexico. *J. Phys. Oceanogr.*, **2**, 218–224, https://doi.org/10.1175/1520-0485(1972)002<0218:HHPOTG>2.0.CO;2.

Liebmann, B., and C. A. Smith, 1996: Description of a complete (interpolated) outgoing longwave radiation dataset. *Bull. Amer. Meteor. Soc.*, **77**, 1275–1277, https://doi.org/10.1175/1520-0477-77.6.1274.

Lin, I. I., and Coauthors, 2013: An ocean coupling potential intensity index for tropical cyclones. *Geophys. Res. Lett.*, **40**, 1878–1882, https://doi.org/10.1002/grl.50091.

Lin, H., G. Brunet, and J. Derome, 2009: An observed connection between the North Atlantic oscillation and the Madden–Julian oscillation. *J. Climate*, **22**, 364–380, https://doi.org/10.1175/2008JCLI2515.1.

——, I.-F. Pun, and C.-C. Lien, 2014: "Category-6" Supertyphoon Haiyan in global warming hiatus: Contribution from subsurface ocean warming. *Geophys. Res. Lett.*, **41**, 8547–8553, https://doi.org/10.1002/2014GL061281.

——, and Coauthors, 2020: ENSO and tropical cyclones. *El Niño Southern Oscillation in a Changing Climate, Geophys. Monogr.*, Vol. 253, Amer. Geophys. Union, 377–408, https://doi.org/10.1002/9781119548164.ch17.

Liu, T., J. Li, C. Sun, T. Lian, and Y. Zhang, 2021: Impact of the April–May SAM on central Pacific Ocean sea temperature over the following three seasons. *Climate Dyn.*, **57**, 775–786, https://doi.org/10.1007/s00382-021-05738-4.

Luo, J.-J., 2017: Indian Ocean dipole [in "State of the Climate in 2016"]. *Bull. Amer. Meteor. Soc.*, **98** (8), S126–S128, https://doi.org/10.1175/2017BAMSStateoftheClimate.1.

——, S. Masson, S. Behera, and T. Yamagata, 2007: Experimental forecasts of the Indian Ocean Dipole using a coupled OAGCM. *J. Climate*, **20**, 2178–2190, https://doi.org/10.1175/JCLI4132.1.

——, R. Zhang, S. K. Behera, Y. Masumoto, F.-F. Jin, R. Lukas, and T. Yamagata, 2010: Interaction between El Niño and extreme Indian Ocean dipole. *J. Climate*, **23**, 726–742, https://doi.org/10.1175/2009JCLI3104.1.

——, W. Sasaki, and Y. Masumoto, 2012: Indian Ocean warming modulates Pacific climate change. *Proc. Natl. Acad. Sci. USA*, **109**, 18 701–18 706, https://doi.org/10.1073/pnas.1210239109.

Madden, R., and P. Julian, 1971: Detection of a 40–50 day oscillation in the zonal wind in the tropical Pacific. *J. Atmos. Sci.*, **28**, 702–708, https://doi.org/10.1175/1520-0469(1971)028<0702:DOADOI>2.0.CO;2.

——, and ——, 1972: Description of global-scale circulation cells in the tropics with a 40–50 day period. *J. Atmos. Sci.*, **29**, 1109–1123, https://doi.org/10.1175/1520-0469(1972)029<1109:DOGSCC>2.0.CO;2.

——, and ——, 1994: Observations of the 40–50-day tropical oscillation: A review. *Mon. Wea. Rev.*, **122**, 814–837, https://doi.org/10.1175/1520-0493(1994)122<0814:OOTDTO>2.0.CO;2.

Magee, A. D., A. S. Kiem, and A. M. Lorrey, 2022: Insights into the usefulness of a new extreme weather guidance tool: The Long-Range Tropical Cyclone Outlook for the Southwest Pacific (TCO-SP). *Bull. Amer. Meteor. Soc.*, **103**, E1220–E1233, https://doi.org/10.1175/BAMS-D-21-0108.1.

Mainelli, M., M. DeMaria, L. Shay, and G. Goni, 2008: Application of oceanic heat content estimation to operational forecasting of recent Atlantic category 5 hurricanes. *Wea. Forecasting*, **23**, 3–16, https://doi.org/10.1175/2007WAF2006111.1.

Maloney, E. D., and D. L. Hartmann, 2001: The Madden–Julian Oscillation, barotropic dynamics, and North Pacific tropical cyclone formation. Part I: Observations. *J. Atmos. Sci.*, **58**, 2545–2558, https://doi.org/10.1175/1520-0469(2001)058<2545:TMJOBD>2.0.CO;2.

Matsuno, T., 1966: Quasi-geostrophic motions in the equatorial area. *J. Meteor. Soc. Japan*, **44**, 25–43, https://doi.org/10.2151/jmsj1965.44.1_25.

Matthews, A. J., 2008: Primary and successive events in the Madden–Julian Oscillation. *Quart. J. Roy. Meteor. Soc.*, **134**, 439–453, https://doi.org/10.1002/qj.224.

Mo, K. C., 2000: The association between intraseasonal oscillations and tropical storms in the Atlantic Basin. *Mon. Wea. Rev.*, **128**, 4097–4107, https://doi.org/10.1175/1520-0493(2000)129<4097:TABIOA>2.0.CO;2.

——, and V. E. Kousky, 1993: Further analysis of the relationship between circulation anomaly patterns and tropical convection. *J. Geophys. Res.*, **98**, 5103–5113, https://doi.org/10.1029/92JD02952.

Moreno, P. I., and Coauthors, 2018: Onset and evolution of southern annular mode-like changes at centennial timescale. *Sci. Rep.*, **8**, 3458, https://doi.org/10.1038/s41598-018-21836-6.

Münnich, M., and J. D. Neelin, 2005: Seasonal influence of ENSO on the Atlantic ITCZ and equatorial South America. *Geophys. Res. Lett.*, **32**, L21709, https://doi.org/10.1029/2005GL023900.

NOAA, 2020: El Niño/Southern Oscillation (ENSO) diagnostic discussion. NOAA/NWS, 10 September, https://www.cpc.ncep.noaa.gov/products/analysis_monitoring/enso_disc_sep2020/ensodisc.shtml.

——, 2021: El Niño/Southern Oscillation (ENSO) diagnostic discussion. NOAA/NWS, 12 August, https://www.cpc.ncep.noaa.gov/products/analysis_monitoring/enso_disc_aug2021/ensodisc.shtml.

Nobre, P., and J. Shukla, 1996: Variations of sea surface temperature, wind stress and rainfall over the tropical Atlantic and South America. *J. Climate*, **9**, 2464–2479, https://doi.org/10.1175/1520-0442(1996)009<2464:VOSSTW>2.0.CO;2.

Papin, P. P., 2022: Tropical Storm Dolores (EP042021). National Hurricane Center Tropical Cyclone Rep., 20 pp., https://www.nhc.noaa.gov/data/tcr/EP042021_Dolores.pdf.

Pezza, A. B., and A. S. Coelho, 2021: Atlantic [in "State of the Climate in 2020"]. *Bull. Amer. Meteor. Soc.*, **102** (9), S215–S216, https://doi.org/10.1175/BAMS-D-21-0080.1.

Raga, G. B., B. Bracamontes-Ceballos, L. Farfán, and R. Romero-Centeno, 2013: Landfalling tropical cyclones on the Pacific coast of Mexico: 1850–2010. *Atmósfera*, **26**, 209–220, https://doi.org/10.1016/S0187-6236(13)71072-5.

Ramage, C. S., 1971: *Monsoon Meteorology*. Academic Press, 296 pp.

Reinhart, B. J., D. Wroe, and S. Houston, 2021: Hurricane Linda (EP122021). National Hurricane Center Tropical Cyclone Rep.,19 pp., https://www.nhc.noaa.gov/data/tcr/EP122021_Linda.pdf.

Reynolds, R. W., N. A. Rayner, T. M. Smith, D. C. Stokes, and W. Wang, 2002: An improved in situ and satellite SST analysis for climate. *J. Climate*, **15**, 1609–1625, https://doi.org/10.1175/1520-0442(2002)015<1609:AIISAS>2.0.CO;2.

Riddle, E., M. Stoner, N. Johnson, M. L'Heureux, D. Collins, and S. Feldstein, 2013: The impact of the MJO on clusters of wintertime circulation anomalies over the North American region. *Climate Dyn.*, 40, 1749–1766, https://doi.org/10.1007/s00382-012-1493-y.

Ropelewski, C. F., and M. S. Halpert, 1987: Global and regional scale precipitation patterns associated with the El Niño–Southern Oscillation. *Mon. Wea. Rev.*, **115**, 1606–1626, https://doi.org/10.1175/1520-0493(1987)115<1606:GARSPP>2.0.CO;2.

——, and ——, 1989: Precipitation patterns associated with the high index phase of the Southern Oscillation. *J. Climate*, **2**, 268–284, https://doi.org/10.1175/1520-0442(1989)002<0268:PPAWTH>2.0.CO;2.

Saha, S., and Coauthors, 2014: The NCEP Climate Forecast System version 2. *J. Climate*, **27**, 2185–2208, https://doi.org/10.1175/JCLI-D-12-00823.1.

Saji, N. H., B. N. Goswami, P. N. Vinayachandran, and T. Yamagata, 1999: A dipole mode in the tropical Indian ocean. *Nature*, **401**, 360–363, https://doi.org/10.1038/43854.

Schneider, T., T. Bischoff, and G. H. Haug, 2014: Migrations and dynamics of the intertropical convergence zone. *Nature*, **513**, 45–53, https://doi.org/10.1038/nature13636.

Schreck, C. J., 2015: Kelvin waves and tropical cyclogenesis: A global survey. *Mon. Wea. Rev.*, **143**, 3996–4011, https://doi.org/10.1175/MWR-D-15-0111.1.

——, 2016: Convectively coupled Kelvin waves and tropical cyclogenesis in a semi-Lagrangian framework. *Mon. Wea. Rev.*, **144**, 4131–4139, https://doi.org/10.1175/MWR-D-16-0237.1.

——, and J. Molinari, 2011: Tropical cyclogenesis associated with Kelvin waves and the Madden–Julian oscillation. *Mon. Wea. Rev.*, **139**, 2723–2734, https://doi.org/10.1175/MWR-D-10-05060.1.

——, ——, and A. Aiyyer, 2012: A global view of equatorial waves and tropical cyclogenesis. *Mon. Wea. Rev.*, **140**, 774–788, https://doi.org/10.1175/MWR-D-11-00110.1.

——, J. M. Cordeira, and D. Margolin, 2013: Which MJO events affect North American temperatures? *Mon. Wea. Rev.*, **141**, 3840–3850, https://doi.org/10.1175/MWR-D-13-00118.1.

——, K. R. Knapp, and J. P. Kossin, 2014: The impact of best track discrepancies on global tropical cyclone climatologies using IBTrACS. *Mon. Wea. Rev.*, **142**, 3881–3899, https://doi.org/10.1175/MWR-D-14-00021.1.

——, H.-T. Lee, and K. R. Knapp, 2018: HIRS outgoing longwave radiation—Daily climate data record: Application toward identifying tropical subseasonal variability. *Remote Sens.*, **10**, 1325, https://doi.org/10.3390/rs10091325.

Shay, L. K., G. J. Goni, and P. G. Black, 2000: Effects of a warm oceanic feature on Hurricane Opal. *Mon. Wea. Rev.*, **128**, 1366–1383, https://doi.org/10.1175/1520-0493(2000)128<1366:EOAWOF>2.0.CO;2.

Smith, T. M., R. W. Reynolds, T. C. Peterson, and J. Lawrimore, 2008: Improvements to NOAA's historical merged land–ocean surface temperature analysis (1880–2006). *J. Climate*, **21**, 2283–2296, https://doi.org/10.1175/2007JCLI2100.1.

Vecchi, G. A., and B. J. Soden, 2007: Effect of remote sea surface temperature change on tropical cyclone potential intensity. *Nature*, **450**, 1066–1071, https://doi.org/10.1038/nature06423.

Ventrice, M. J., C. D. Thorncroft, and M. A. Janiga, 2012a: Atlantic tropical cyclogenesis: A three-way interaction between an African easterly wave, diurnally varying convection, and a convectively coupled atmospheric Kelvin wave. *Mon. Wea. Rev.*, **140**, 1108–1124, https://doi.org/10.1175/MWR-D-11-00122.1.

Ventrice, M. J., C. D. Thorncroft, and C. J. Schreck, 2012b: Impacts of convectively coupled Kelvin waves on environmental conditions for Atlantic tropical cyclogenesis. *Mon. Wea. Rev.*, **140**, 2198–2214, https://doi.org/10.1175/MWR-D-11-00305.1.

Villarini, G., G. A. Vecchi, T. R. Knutson, and J. A. Smith, 2011: Is the recorded increase in short duration North Atlantic tropical storms spurious? *J. Geophys. Res.*, **116**, D10114, https://doi.org/10.1029/2010JD015493.

Vincent, D. G., 1994: The South Pacific Convergence Zone (SPCZ): A review. *Mon. Wea. Rev.*, **122**, 1949–1970, https://doi.org/10.1175/1520-0493(1994)122<1949:TSPCZA>2.0.CO;2.

Waliser, D. E., and C. Gautier, 1993: A satellite-derived climatology of the ITCZ. *J. Climate*, **6**, 2162–2174, https://doi.org/10.1175/1520-0442(1993)006<2162:ASDCOT>2.0.CO;2.

Wang, B., 1994: Climatic regimes of tropical convection and rainfall. *J. Climate*, **7**, 1109–1118, https://doi.org/10.1175/1520-0442(1994)007<1109:CROTCA>2.0.CO;2.

——, and Q. Ding, 2008: Global monsoon: Dominant mode of annual variation in the tropics. *Dyn. Atmos. Ocean*, **44**, 165–183, https://doi.org/10.1016/j.dynatmoce.2007.05.002.

——, J. Liu, H. J. Kim, P. J. Webster, and S. Y. Yim, 2012: Recent change of the global monsoon precipitation (1979–2008). *Climate Dyn.*, **39**, 1123–1135, https://doi.org/10.1007/s00382-011-1266-z.

Wheeler, M. C., and G. N. Kiladis, 1999: Convectively coupled equatorial waves: Analysis of clouds and temperature in the wavenumber-frequency domain. *J. Atmos. Sci.*, **56**, 374–399, https://doi.org/10.1175/1520-0469(1999)056<0374:CCEWAO>2.0.CO;2.

——, and H. H. Hendon, 2004: An all-season real-time multivariate MJO index: Development of an index for monitoring and prediction. *Mon. Wea. Rev.*, **132**, 1917–1932, https://doi.org/10.1175/1520-0493(2004)132<1917:AARMMI>2.0.CO;2.

Wood, K. M., and E. A. Ritchie, 2015: A definition for rapid weakening in the North Atlantic and eastern North Pacific. *Geophys. Res. Lett.*, **42**, 10 091–10 097, https://doi.org/10.1002/2015GL066697.

——, and C. J. Schreck, 2020: Eastern North Pacific and Central North Pacific basins [in "State of the Climate in 2019"]. *Bull. Amer. Meteor. Soc.*, **101** (8), S212–S214, https://doi.org/10.1175/BAMS-D-20-0077.1.

——, and ——, 2021: Eastern North Pacific and Central North Pacific basins [in "State of the Climate in 2020"]. *Bull. Amer. Meteor. Soc.*, **102** (8), S233–S236, https://doi.org/10.1175/BAMS-D-21-0080.1.

Xie, P., and P. A. Arkin, 1997: Global precipitation: A 17-year monthly analysis based on gauge observations, satellite estimates, and numerical model outputs. *Bull. Amer. Meteor. Soc.*, **78**, 2539–2558, https://doi.org/10.1175/1520-0477(1997)078<2539:GPAYMA>2.0.CO;2.

Yim, S. Y., B. Wang, J. Liu, and Z. W. Wu, 2014: A comparison of regional monsoon variability using monsoon indices. *Climate Dyn.*, **43**, 1423–1437, https://doi.org/10.1007/s00382-013-1956-9.

Zhang, C., 2005: Madden–Julian oscillation. *Rev. Geophys.*, **43**, RG2003, https://doi.org/10.1029/2004RG000158.

——, and J. Gottschalck, 2002: SST anomalies of ENSO and the Madden–Julian oscillation in the equatorial Pacific. *J. Climate*, **15**, 2429–2445, https://doi.org/10.1175/1520-0442(2002)015<2429:SAOEAT>2.0.CO;2.

Zhang, H.-M., and Coauthors, 2019: Updated temperature data give a sharper view of climate trends. *Eos*, **100**, https://doi.org/10.1029/2019EO128229.

Zheng, T., T. Feng, K. Xu, and X. Cheng, 2020: Precipitation and the associated moist static energy budget off Western Australia in conjunction with Ningaloo Niño. *Front. Earth Sci.*, **8**, https://doi.org/10.3389/feart.2020.597915

Zheng, Z.-W., I.-I. Lin, B. Wang, H.-C. Huang, and C.-H. Chen, 2015: A long neglected damper in the El Nino–typhoon relationship: A 'Gaia-like' process. *Sci. Rep.*, **5**, 11103, https://doi.org/10.1038/srep11103.

STATE OF THE CLIMATE IN 2021

THE ARCTIC

R. Thoman, M. L. Druckenmiller, and T. Moon, Eds.

Special Online Supplement to the *Bulletin of the American Meteorological Society*, Vol. 103, No. 8, August 2022

https://doi.org/10.1175/BAMS-D-22-0082.1.

Corresponding author: Richard Thoman / rthoman@alaska.edu

STATE OF THE CLIMATE IN 2021

The Arctic

Editors

Jessica Blunden
Tim Boyer

Chapter Editors

Freya Aldred
Peter Bissolli
Kyle R. Clem
Howard J. Diamond
Matthew L. Druckenmiller
Robert J. H. Dunn
Catherine Ganter
Nadine Gobron
Gregory C. Johnson
Rick Lumpkin
Ademe Mekonnen
John B. Miller
Twila A. Moon
Marilyn N. Raphael
Ahira Sánchez-Lugo
Carl J. Schreck III
Richard L. Thoman
Kate M. Willett
Zhiwei Zhu

Technical Editor

Laura Ohlmann

BAMS Special Editor for Climate

Michael A. Alexander

American Meteorological Society

Cover credit:
Cover image courtesy of Gay Sheffield. The mountain at Cape Prince of Wales in the background with sea ice breaking up. Sky is cloudy and tinted orange from smoke from wildfires in Chukotka, Russia.

The Arctic is one chapter from the *State of the Climate in 2021* annual report and is available from https://doi.org/10.1175/BAMS-D-22-0082.1. Compiled by NOAA's National Centers for Environmental Information, *State of the Climate in 2021* is based on contributions from scientists from around the world. It provides a detailed update on global climate indicators, notable weather events, and other data collected by environmental monitoring stations and instruments located on land, water, ice, and in space.
The full report is available from https://doi.org/10.1175/2022BAMSStateoftheClimate.1.

How to cite this document:

Citing the complete report:
Blunden, J. and T. Boyer, Eds., 2022: "State of the Climate in 2021". *Bull. Amer. Meteor. Soc.*, **103** (8), Si–S465, https://doi.org/10.1175/2022BAMSStateoftheClimate.1.

Citing this chapter:
Thoman, R., M. L. Druckenmiller, and T. Moon, Eds., 2022: "State of the Climate in 2021"]. *Bull. Amer. Meteor. Soc.*, **103** (8), S257–S306, https://doi.org/10.1175/BAMS-D-22-0082.1.

Citing a section (example):
Meier, W. N., D. Perovich, S. Farrell, C. Haas, S. Hendricks, A. Petty, M. Webster, D. Divine, S. Gerland, L. Kaleschke, R. Ricker, A. Steer, X. Tian-Kunze, M. Tschudi, and K. Wood, 2022: Sea ice [in "State of the Climate in 2021"]. *Bull. Amer. Meteor. Soc.*, **103** (8), S270–S273, https://doi.org/10.1175/BAMS-D-22-0082.1.

Editor and Author Affiliations (alphabetical by name)

Andreassen, L. M., Section for Glaciers, Snow and Ice, Norwegian Water Resources and Energy Directorate, Oslo, Norway
Baker, E., United States Geological Survey, Alaska Science Center, Anchorage, Alaska
Ballinger, Thomas J., International Arctic Research Center, University of Alaska Fairbanks, Fairbanks, Alaska
Berner, Logan T., School of Informatics, Computing, and Cyber Systems, Northern Arizona University, Flagstaff, Arizona
Bernhard, Germar H., Biospherical Instruments Inc., San Diego, California, United States
Bhatt, Uma S., Geophysical Institute, University of Alaska Fairbanks, Fairbanks, Alaska
Bjerke, Jarle W., Norwegian Institute for Nature Research, FRAM and High North Research Centre for Climate and the Environment, Tromsø, Norway
Boisvert, L.N., NASA Goddard Space Flight Center, Greenbelt, Marylamd
Box, Jason E., Geological Survey of Denmark and Greenland, Copenhagen, Denmark
Brettschneider, B., National Weather Service Alaska Region, NOAA, Anchorage, Alaska
Burgess, D., Geological Survey of Canada, Ottawa, Ontario, Canada
Butler, Amy H., NOAA Chemical Sciences Laboratory, Boulder, Colorado
Cappelen, John, Danish Meteorological Institute, Copenhagen, Denmark
Christiansen, Hanne H., Geology Department, University Centre in Svalbard, The University Center in Svalbard, Longyearbyen, Norway
Decharme, B., Centre National de Recherches Météorologiques, Toulouse, France
Derksen, C., Climate Research Division, Environment and Climate Change Canada, Downsview, Ontario, Canada
Divine, Dmitry, Norwegian Polar Institute, Fram Centre, Tromsø, Norway
Drozdov, D. S., Earth Cryosphere Institute, and Tyumen State University, Tyumen, Russia
Druckenmiller, Matthew L., National Snow and Ice Data Center, Cooperative Institute for Research in Environmental Sciences, University of Colorado, Boulder, Colorado
Elias Chereque, A., Department of Physics, University of Toronto, Toronto, Canada
Epstein, Howard E., Department of Environmental Sciences, University of Virginia, Charlottesville, Virginia
Farrell, Sinead L., Department of Geographical Sciences, University of Maryland, College Park, Maryland
Fausto, Robert S., Geological Survey of Denmark and Greenland, Copenhagen, Denmark
Fettweis, Xavier, SPHERES research unit, University of Liège, Liège, Belgium
Fioletov, Vitali E., Environment and Climate Change Canada, Toronto, Ontario, Canada
Forbes, Bruce C., Arctic Centre, University of Lapland, Rovaniemi, Finland
Frost, Gerald V., ABR, Inc. Environmental Research & Services, Fairbanks, Alaska
Gerland, Sebastian, Norwegian Polar Institute, Fram Centre, Tromsø, Norway
Goetz, Scott J., School of Informatics, Computing, and Cyber Systems, Northern Arizona University, Flagstaff, Arizona
Grooß, Jens-Uwe, Forschungszentrum Jülich, Jülich, Germany
Haas, Christian, Alfred Wegener Institute, Helmholtz Centre for Polar and Marine Research, Bremerhaven, Germany
Hanna, Edward, School of Geography and Lincoln Centre for Water and Planetary Health, University of Lincoln, Lincoln, United Kingdom
Hanssen-Bauer, Inger, Norwegian Meteorological Institute, Blindern, Oslo, Norway
Heijmans, M. M. P. D., Department of Environmental Sciences, Wageningen University & Research, Wageningen, Netherlands
Hendricks, Stefan, Alfred Wegener Institute, Helmholtz Centre for Polar and Marine Research, Bremerhaven, Germany
Ialongo, Iolanda, Finnish Meteorological Institute, Helsinki, Finland
Isaksen, K., Norwegian Meteorlogical Institute, Blindern, Oslo, Norway
Jensen, C. D., Danish Meteorological Survey, Copenhagen, Denmark
Johnsen, Bjørn, Norwegian Radiation and Nuclear Safety, Østerås, Norway
Kaleschke, L., Alfred Wegener Institute, Helmholtz Centre for Polar and Marine Research, Bremerhaven, Germany
Kholodov, A. L., Earth Cryosphere Institute, Tyumen Science Center, Tyumen, Russia
Kim, Seong-Joong, Korea Polar Research Institute, Incheon, Republic of Korea
Kohler, J., Norwegian Polar Institute, Tromsø, Norway
Korsgaard, Niels J., Geological Survey of Denmark and Greenland, Copenhagen, Denmark
Labe, Zachary, Colorado State University, Fort Collins, Colorado, United States
Lakkala, Kaisa, Finnish Meteorological Institute, Sodankylä, Finland
Lara, Mark J., Department of Plant Biology, University of Illinois at Urbana-Champaign, Urbana, Illinois
Lee, Simon H., Department of Applied Physics and Applied Mathematics, Columbia University, New York, New York
Loomis, Bryant, NASA Goddard Space Flight Center, Greenbelt, Maryland
Luks, B., Institute of Geophysics, Polish Academy of Sciences, Warsaw, Poland
Luojus, K., Arctic Research Centre, Finnish Meteorological Institute, Helsinki, Finland
Macander, Matthew J., ABR, Inc., Environmental Research & Services, Fairbanks, Alaska
Magnússon, R. Í, Department of Environmental Sciences, Wageningen University & Research, Wageningen, Netherlands
Malkova, G. V., Earth Cryosphere Institute, Tyumen Science Center, Tyumen, Russia
Mankoff, Kenneth D., Geological Survey of Denmark and Greenland, Copenhagen, Denmark
Manney, Gloria L., NorthWest Research Associates, Socorro, New Mexico
Meier, Walter N., National Snow and Ice Data Center, Cooperative Institute for Research in Environment Sciences at the University of Colorado, Boulder, Colorado
Moon, Twila A., National Snow and Ice Data Center, Cooperative Institute for Research in Environmental Sciences, University of Colorado, Boulder, Colorado
Mote, Thomas, Department of Geography, University of Georgia, Athens, Georgia
Mudryk, Lawrence, Climate Research Division, Environment and Climate Change Canada, Downsview, Ontario, Canada
Müller, Rolf, Forschungszentrum Jülich, Jülich, Germany
Nyland, K. E., Department of Geography, George Washington University, Washington, D.C.
Overland, James E., NOAA/OAR Pacific Marine Environmental Laboratory, Seattle, Washington
Pálsson, F., Institute of Earth Sciences, University of Iceland, Reykjavík, Iceland
Park, T., NASA Ames Research Center, Mountain View, California, and Bay Area Environmental Research Institute, Moffett Field, California
Parker, C. L., NASA Goddard Space Flight Center, Greenbelt, MD; Earth System Science Interdisciplinary Center, University of Maryland, College Park, Maryland
Perovich, Don, Thayer School of Engineering, Dartmouth College, Hanover, New Hampshire
Petty, Alek, NASA Goddard Space Flight Center, Greenbelt, Maryland
Phoenix, Gareth K., Department of Animal and Plant Sciences, University of Sheffield, Sheffield, United Kingdom
Pinzon, J. E., NASA Goddard Space Flight Center, Greenbelt, Maryland

Editor and Author Affiliations (alphabetical by name)

Ricker, Robert, Alfred Wegener Institute, Helmholtz Centre for Polar and Marine Research, Bremerhaven, Germany
Romanovsky, Vladimir E., Geophysical Institute, University of Alaska Fairbanks, Fairbanks, Alaska; Earth Cryosphere Institute, Tyumen Science Center, Tyumen, Russia
Serbin, S. P., Environmental and Climate Sciences Department, Brookhaven National Laboratory, Upton, New York
Sheffield, G., University of Alaska Fairbanks, Marine Advisory Program, Alaska Sea Grant, Nome, Alaska
Shiklomanov, Nikolai I., Department of Geography, George Washington University, Washington, D.C.
Smith, Sharon L., Geological Survey of Canada, Natural Resources Canada, Ottawa, Ontario, Canada
Stafford, K.M., Oregon State University, Marine Mammal Institute, Newport, Oregon
Steer, A., Norwegian Polar Institute, Fram Centre, Tromsø, Norway
Streletskiy, Dimitri A., Department of Geography, George Washington University, Washington, D.C.
Svendby, Tove, NILU-Norwegian Institute for Air Research, Kjeller, Norway
Tedesco, Marco, Lamont Doherty Earth Observatory, Columbia University, Palisades, New York, and NASA Goddard Institute of Space Studies, New York, New York
Thoman, Richard L., International Arctic Research Center, University of Alaska Fairbanks, Fairbanks, Alaska
Thomson, L., Queen's University, Kingston, Ontario, Canada
Thorsteinsson, T., Icelandic Meteorological Office, Reykjavík, Iceland
Tian-Kunze, X., Alfred Wegener Institute, Helmholtz Centre for Polar and Marine Research, Bremerhaven, Germany
Timmermans, Mary-Louise, Yale University, New Haven, Connecticut
Tømmervik, Hans, Norwegian Institute for Nature Research, FRAM and High North Research Centre for Climate and the Environment, Tromsø, Norway
Tschudi, Mark, Aerospace Engineering Sciences, University of Colorado, Boulder, Colorado
Tucker, C. J., Environmental and Climate Sciences Department, Brookhaven National Laboratory, Upton, New York
Walker, Donald A., Institute of Arctic Biology, University of Alaska Fairbanks, Alaska
Walsh, John E., International Arctic Research Center, University of Alaska Fairbanks, Fairbanks, Alaska
Wang, Muyin, NOAA/OAR Pacific Marine Environmental Laboratory, and Cooperative Institute for Climate, Ocean, and Ecosystem Studies, University of Washington, Seattle, Washington
Webster, Melinda, Geophysical Institute, University of Alaska Fairbanks, Fairbanks, Alaska; University of Alaska, Fairbanks, Alaska
Wehrlé, A., Institute of Geography, University of Zurich, Zurich, Switzerland
Winton, Øyvind, Geological Survey of Denmark and Greenland, Copenhagen, Denmark
Wolken, G., Alaska Division of Geological & Geophysical Surveys, Fairbanks, Alaska
Wood, K., NOAA, Pacific Marine Environmental Laboratory, Seattle, Washington
Wouters, B., Institute for Marine and Atmospheric Research, Utrecht University, Utrecht, Netherlands
Yang, D., Environmental and Climate Sciences Department, Brookhaven National Laboratory, Upton, New York; Department of Ecology and Evolution, Stony Brook University, Stony Brook, New York

Editorial and Production Team

Allen, Jessicca, Graphics Support, Cooperative Institute for Satellite Earth System Studies, North Carolina State University, Asheville, North Carolina
Hammer, Gregory, Content Team Lead, Communications and Outreach, NOAA/NESDIS National Centers for Environmental Information, Asheville, North Carolina
Love-Brotak, S. Elizabeth, Lead Graphics Production, NOAA/NESDIS National Centers for Environmental Information, Asheville, North Carolina
Misch, Deborah J., Graphics Support, Innovative Consulting and Management Services, LLC, NOAA/NESDIS National Centers for Environmental Information, Asheville, North Carolina
Ohlmann, Laura, Technical Editor, Innovative Consulting and Management Services, LLC, NOAA/NESDIS National Centers for Environmental Information, Asheville, North Carolina
Riddle, Deborah B., Graphics Support, NOAA/NESDIS National Centers for Environmental Information, Asheville, North Carolina
Veasey, Sara W., Visual Communications Team Lead, Communications and Outreach, NOAA/NESDIS National Centers for Environmental Information, Asheville, North Carolina

5. Table of Contents

*Please refer to Chapter 8 (Relevant datasets and sources) for a list of all climate variables and datasets used in this chapter for analyses, along with their websites for more information and access to the data.

5. THE ARCTIC

R. Thoman, M. L. Druckenmiller, and T. Moon, Eds.

a. Overview—R. Thoman, M. L. Druckenmiller, and T. Moon

Disruptive environmental change in the Arctic continued in 2021. While few indicators were at record levels, the ongoing trends provide a stark illustration of an Arctic that is a very different place than the Arctic of the twentieth century. Air and ocean temperatures in the Arctic are intimately linked with sea ice and are directly connected to the biological productivity of the region. Terrestrial snow cover, or the lack thereof, plays an important role in modulating air temperatures and the hydrologic cycle. During the winter, lower latitude drivers such as the El Niño-Southern Oscillation, the Madden-Julian Oscillation, and the evolution of the stratospheric polar vortex affect regional conditions and sub-seasonal variability. These processes add to the complexity of annually assessing the state of the Arctic, despite numerous examples of observed broadscale directional change across the region.

For the Arctic (poleward of 60°N) as a whole, 2021 was the coolest year since 2013. Yet, 2021 was still the 13th-warmest year on record (since 1900), highlighting the dominance of the strong warming trend in recent decades. Within the Arctic, both the European (0°–90°E) and Asian (90°E–180°) sectors each experienced spring (April–June) temperatures among their highest 10% among all springs, while the Greenland-Iceland region experienced mean temperatures in the highest 10th percentile during all seasons, except spring. Collectively, these contributed substantially to the annual temperature anomaly for the entire Arctic. Spring and summer air temperatures are linked to the strong increase in tundra vegetation productivity that emerged in the late 1990s, a phenomenon known as "the greening of the Arctic." The overall trend in circumpolar "greening" is strongly positive but recent years have seen the emergence of increased regional variability, such as strong greening on the Alaska North Slope, but "browning" in parts of northeast Asia. In 2021, the circumpolar greening index was the second highest since observations commenced in 2000, just 2.7% lower than in 2020.

Evidence for increasing Arctic precipitation (liquid and frozen) comes from the intensifying hydrologic cycle and long-term trend of increasing river discharge (Holmes et al. 2021), but has not been previously been reported in the *State of the Climate* reports. Today, advances in reanalysis now allow for regionally reliable year-round precipitation estimates (Barrett et al. 2020; Wang et al. 2019). In 2021, total precipitation was modestly higher than the 1991–2020 climatology, but on average consisted of a considerably lower percentage of snowfall, relative to the 30-year average. Timing of the seasonal transition of the predominant phase of precipitation, the terrestrial snow cover establishment in autumn and melt in spring, has profound effects on air temperatures. Similarly, the snowpack mass at the end of the accumulation season drives ecosystem and hydrologic responses during and beyond the melt season. Snow accumulation during the 2020/21 winter was near-normal across the Eurasian Arctic and above normal across the North American Arctic. Despite the absence of a significant negative trend in snow mass, spring snow extent has been persistently below normal for the last 15 years due to earlier snow melt.

The seasonal maximum sea ice extent for the Arctic is typically reached in March. In 2021, the March extent was the ninth lowest since 1979. Spring melt was rapid in the Laptev Sea, resulting in record low ice extent for May and June in this region, and the East Greenland Sea was nearly ice-free during much of the summer. This early loss of sea ice contributed to August 2021 mean

SSTs that were 1° to 3.5°C above the 1982–2010 average in the Kara, Laptev, and East Greenland Seas. In contrast, cloudy and cool weather, combined with more unusually high concentrations of multi-year ice for recent years in the Chukchi and Beaufort Seas, resulted in the 12th-lowest September mean extent in the 43-year record. Also, northern Barents Sea, Baffin Bay, and Chukchi Sea were marked by anomalously low SSTs in August 2021, up to 1°C lower than the 1982–2010 mean. Yet, near the end of the melt season in September 2021, the amount of multiyear ice remaining in the Arctic was still the second lowest on record, indicating the Arctic's sustained transition to a younger, thinner ice cover. Changes in sea ice seasonality and warming ocean ecosystems allow for expanded Arctic maritime activity, increasing pollution in the region. This takes the form of conventional "trash" and potentially toxic materials, and of increased ocean noise levels, with potential impacts to marine species, especially marine mammals for whom underwater sounds can disrupt communication that is critical to their normal activities.

Mass changes on the Greenland Ice Sheet and other Arctic glaciers and ice caps that make up the Arctic year-round terrestrial cryosphere are quite sensitive to summer temperatures. Although Greenland Ice Sheet mass loss in the 2020/21 season was about half of the 2000–21 average, the ice sheet has now lost mass every year since 1998. Extreme events during summer 2021 included a widespread melt event on 14 August, the latest on record, which produced for the first time on record (since 1989) rain at Summit Station (3216 m a.s.l.). Outside of Greenland, observations of monitored Arctic glaciers and ice caps from 2020 and 2021 show regional and inter-annual variations in mass change, with a continuing trend of significant ice loss throughout the Arctic, especially in Alaska and Arctic Canada.

Permafrost refers to ground materials that remain at or below 0°C for at least two consecutive years and underlies extensive regions of the high-latitude landscape. Permafrost temperatures continue to increase across the Arctic. Greater increases in permafrost temperature are generally observed in colder permafrost at higher latitudes, where the largest increase in air temperature has been observed. Permafrost temperatures in 2021 were generally higher than those observed in 2020 and the highest on record at many monitoring sites. However, some recent, slight cooling occurred at a few sites as well.

During the polar night, the very cold stratospheric polar vortex facilitates ozone depletion through chemical reactions that are inactive at temperatures higher than –78°C, while strong anomalies in stratospheric temperatures and winds can descend to the lower stratosphere where they persist for many weeks, affecting both the stratospheric ozone layer and the jet stream. Early stratospheric polar vortex formation in November 2020, which was conducive to ozone depletion, was cut short by a major Sudden Stratospheric Warming event in January 2021. Another result was that the average Arctic total ozone columns (ozone amounts integrated from Earth's surface to the top of the atmosphere) in March 2021 were close to normal, and spring UV index values were generally within two standard deviations of the 2005–20 mean.

(This chapter includes a focus on glaciers and ice caps outside Greenland, section 5f, which alternates yearly with a section on Arctic river discharge, as the scales of regular observation for both of these climate components are best suited for reporting every two years.)

b. Surface air temperature—T. J. Ballinger, J. E. Overland, R. Thoman, M. Wang, M. A. Webster, L. N. Boisvert, C. L. Parker, U. S. Bhatt, B. Brettschneider, E. Hanna, I. Hanssen-Bauer, S.-J. Kim, and J. E. Walsh

1) ARCTIC TERRESTRIAL SURFACE AIR TEMPERATURES: A HISTORICAL REVIEW

Increased air temperatures are a fundamental indicator of Arctic change (Box et al. 2019). Warming has been linked with changing frequency, intensity, and duration of high-latitude atmospheric extremes that impact snow and ice melt (Walsh et al. 2020). The 2021 annual surface air temperature (SAT) anomaly for terrestrial areas within 60°–90°N was 0.4°C above the 1991–2020 mean, marking the eighth consecutive year that Arctic land temperatures have exceeded the 30-year

average (Fig. 5.1). With respect to the 1900–2021 historical period, 2021 ranked as the 13th-warmest year on record but coolest since 2013. The Arctic experienced its fourth-warmest spring (April–June), which contributed substantially to the annual temperature anomaly. Within the Arctic, both the European (0°–90°E) and Asian (90°–180°E) sectors' temperatures exceeded the 90th percentile during spring (Ballinger et al. 2021). Air temperatures throughout other seasons were above normal, but not extreme for most Arctic areas. The Greenland-Iceland region (60°W–0°) was the exception, with warming above the 90th percentile during winter (January–March), summer (July–September), and autumn (October–December; Ballinger et al. 2021). As discussed below in subsection 2, much of this region's seasonal warming was confined to marine and coastal areas. Despite the warm pattern, the region's air temperatures remained broadly subfreezing in winter and autumn, coincident with ~50% less Greenland Ice Sheet mass loss in 2020/21 than the 2000–21 mean (section 5e). The year 2021 was marked by near-normal temperatures over the central Arctic with large deviations over the subarctic continents in response to jet stream variability. In the following section, we characterize seasonal air temperature anomalies in further detail.

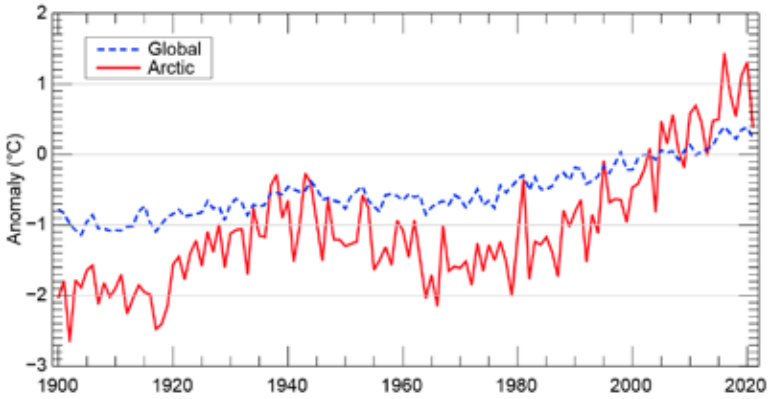

Fig. 5.1. Annual mean SAT anomalies (°C) for weather stations located on Arctic lands, 60°–90°N (red line), and globally (blue line) from 1900 to 2021. The temperature anomalies are shown with respect to their 1991–2020 mean. It is worth noting that the 1991–2020 mean was > 0.6°C higher than the 1981–2010 mean. (Source: CRUTEM5 SAT data are obtained from the Climate Research Unit [University of East Anglia] and Met Office.)

2) SUMMARY OF 2021 SEASONAL AIR TEMPERATURES

Air temperature anomalies, relative to the 1991–2020 mean, are discussed for 2021 by season and presented in Fig. 5.2. Seasonal temperature anomalies at the 925-hPa level are described to emphasize large-scale spatial patterns rather than local-scale variability.

In winter 2021, a distinct temperature gradient was found between the higher-than-average Atlantic side of the Arctic Ocean, including areas stretching northward from the eastern Canadian Arctic and Hudson Bay, and lower-than-average Eurasia and northwest North America. Air temperatures around the central Arctic Ocean extending south into northern Greenland and Svalbard were 2–4°C higher than normal. Western Greenland and adjacent Baffin Bay, Davis Strait, and Labrador Sea saw temperature anomalies of +2° to +3°C that increased westward to a +5° to +6°C maximum over northern Quebec and Newfoundland. Cold anomalies extended southward from Arctic coastal zones to northern Russia, Chukotka, Alaska, and the Yukon and Northwest Territories (Fig. 5.2a). Two upper-level low geopotential height centers over north-central Siberia and the Canadian Archipelago were concurrent with this swath of below-normal temperatures (Fig. 5.3a).

Spring was characterized by above-normal temperatures extending from the Arctic Ocean margins southward into adjacent lands (Fig. 5.2b), associated with a low over the central Arctic and primarily zonal (west-to-east) flow over these areas (Fig. 5.3b). For example, air temperatures over northern Eurasian coastal areas and adjacent Arctic waters were 2–4°C higher than the 1991–2020 average. Baffin Bay and the Labrador Sea were also higher than normal. The Eurasian spring temperature anomalies were linked to low regional snow cover (section 5g) and early sea ice melt in the Laptev Sea (section 5d). Several Arctic weather stations reported record air temperatures during spring 2021, including 39.9°C observed at Fort Smith, Northwest Territories, Canada, on 30 June, which set the maximum surface temperature record in the province (Henson and Masters 2021).

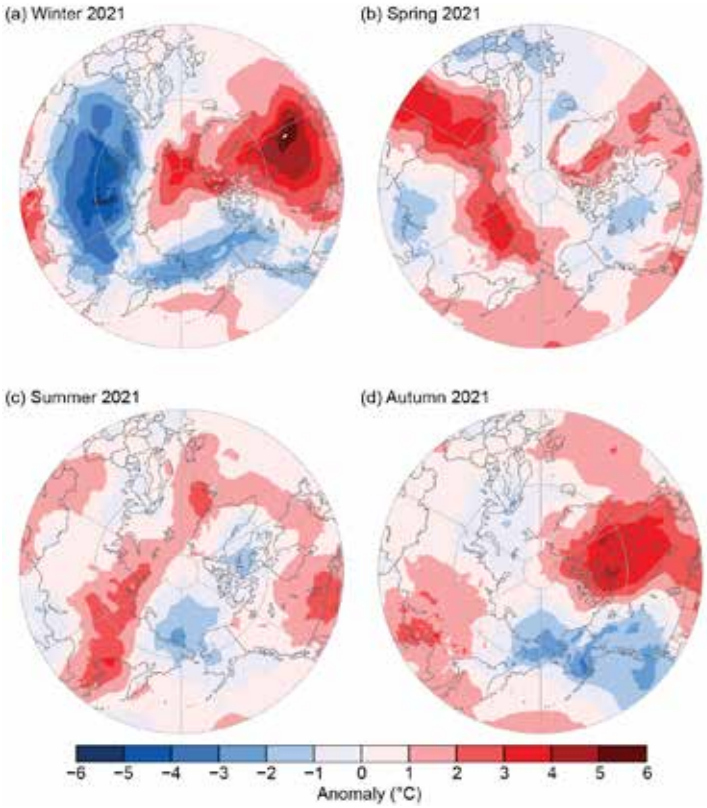

Fig. 5.2. Near-surface (925 hPa) seasonal air temperature anomalies (°C) in 2021 for (a) winter, (b) spring, (c) summer, and (d) autumn. Anomalies are shown relative to their 1991–2020 means. (Source: ERA5 reanalysis air temperature data are obtained from the Copernicus Climate Change Service.)

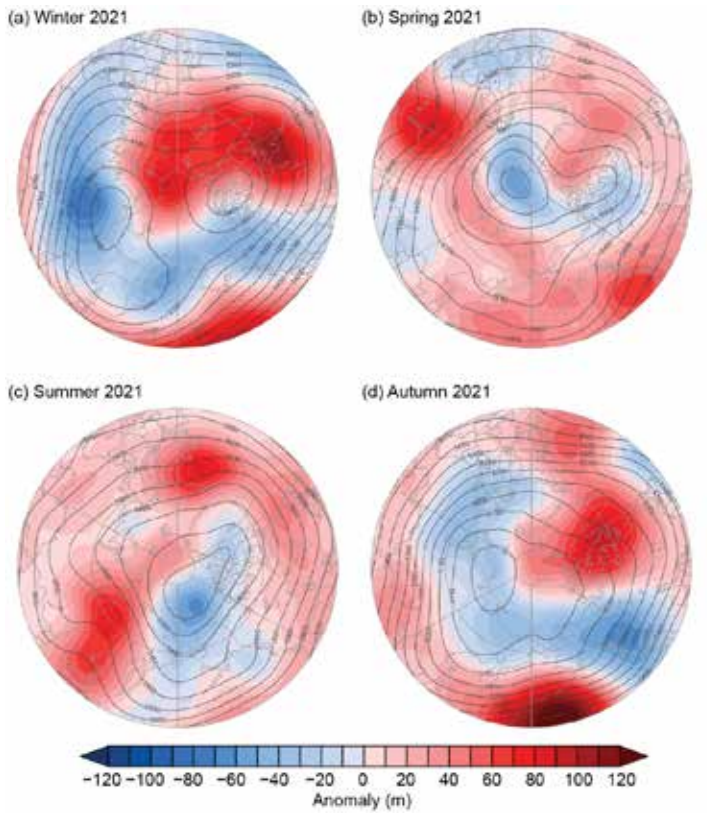

Fig. 5.3. Seasonal atmospheric circulation patterns in 2021 for (a) winter, (b) spring, (c) summer, and (d) autumn. The contours (shading) represent 500-hPa geopotential height values (anomalies relative to the 1991–2020 seasonal means, m). Upper-level winds tend to circulate clockwise around higher geopotential height values. (Source: ERA5 reanalysis geopotential height data are obtained from the Copernicus Climate Change Service.)

Notably warm summer air temperature anomalies were found over northern Iceland and the southern Greenland Sea (+2° to +3°C) and extended from the northern Sea of Okhotsk (+2° to +4°C) into northeastern Siberia (Fig. 5.2c). The corresponding 500-hPa flow was similar to spring, though the low center moved into the Pacific Arctic sector (Fig. 5.3c). Following on from recent warm, fire-prone summers, above-normal Siberian air temperatures coincided with an extreme fire season during 2021 (York et al. 2020; Ponomarev et al. 2022). In contrast, 1–2°C below-normal temperatures occurred over portions of the Beaufort, Chukchi, and East Siberian Seas.

Exceptional summer warmth over the Greenland-Iceland region was primarily found over marine, coastal, and low-elevation areas of the Greenland Ice Sheet (Fig. 5.2c). These seasonal anomalies were punctuated by anomalous air temperature events that occurred in late July and mid-August, producing widespread Greenland Ice Sheet melt. The latter event coincided with remarkably late and extensive ice sheet melt and the first rain event at Summit Station, Greenland's highest elevation area, since it was established in 1989 (section 5e).

Autumn air temperature anomalies of 2–4°C above average were found from western Greenland to eastern Canada (Fig. 5.2d), concurrent with a jet stream trough over Hudson Bay that funneled warm air into these areas from lower latitudes (Fig. 5.3d). Upstream regions of the Pacific Arctic, including Chukotka, Alaska, and south-central Yukon and Northwest Territories, experienced temperatures 1–3°C below normal due to a relatively zonal jet stream that prevented incursions of warm air masses (Fig. 5.3d).

3) ARCTIC PRECIPITATION IN 2021: A RESPONSE TO WARMING

Increased precipitation and greater probabilities of rain at the expense of snow are impacts of a warming Arctic (Łupikasza and Cielecka-Nowak 2020; McCrystall et al. 2021). Using ERA5, these characteristics manifested in 2021 as modestly higher total precipitation but, on average, consisted of considerably less snowfall relative to the 1991–2020 climatology (Fig. 5.4). Winter, summer, and autumn were characterized by anomalously low snowfall (blue shading) and high rainfall (red shading; Figs. 5.4e,g,h,i,k,l), while spring had markedly more snowfall (Fig. 5.4f) and total precipitation (Fig. 5.4b). Canada broke a new spring record, receiving 19% more total precipitation than normal. Alaska and the Pacific Arctic sector (60°–90°N, 150°E–120°W) had the second-highest spring snowfall amounts since 1979, totaling 19 mm and 14 mm water equivalent, respectively. Anomalously low precipitation fell on Russia during spring, but of that precipitation more than 90% fell as rain rather than snow (Figs. 5.4b,f,j), aligned with persistent warm air temperatures (Fig. 5.2b).

Summer warmth during 2021 (Fig. 5.2c) also contributed to diminished Arctic snowfall (Fig. 5.4g). Overall, there was 7% less snowfall than average with the largest anomalies occurring in Alaska (–16 mm) and the Pacific Arctic sector (–11 mm). Similarly, Greenland saw more precipitation (+23 mm) and more rainfall (+22 mm) than any year during 1991–2020, including the Summit Station rain event (section 5e). During autumn, snowfall amounts were 3% below average for the Arctic with the Alaska and Pacific Arctic sectors receiving the least snowfall (23–24% below normal). Alaska received 13% more rainfall than the 1991–2020 autumn average, tied to a late December rain-on-snow event.

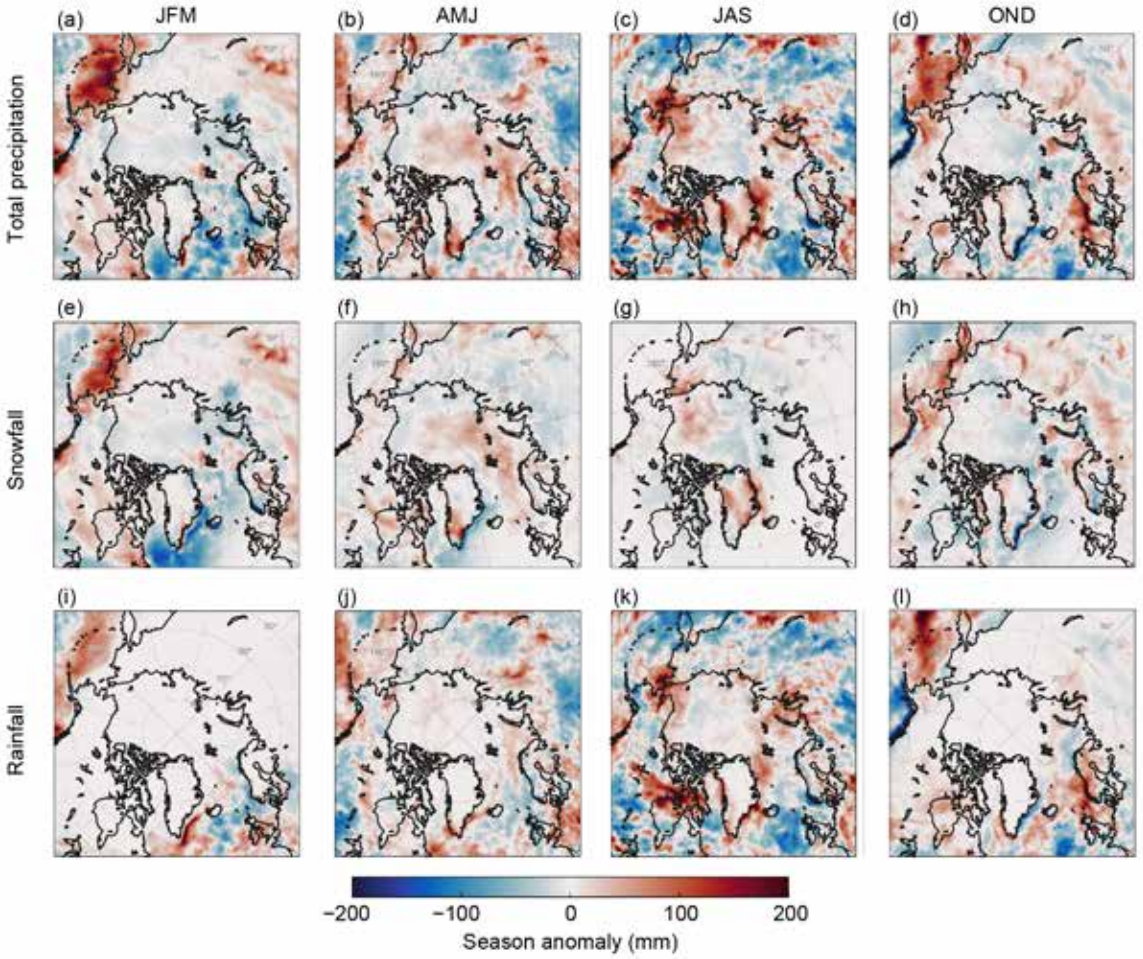

Fig. 5.4. The 2021 season anomalies (mm) in (a–d) total precipitation, (e–h) snowfall, and (i–l) rainfall for the winter (JFM, panels a,e,i), spring (AMJ, panels b,f,j), summer (JAS, panels c,g,k), and autumn (OND, panels d,h,l) relative to the 1991–2020 climatology. Rainfall is inferred from the difference between total precipitation and snowfall. (Source: ERA5 total precipitation and snowfall data are obtained from the Copernicus Climate Change Service.)

c. Sea surface temperature—M.-L. Timmermans and Z. Labe

Arctic Ocean sea surface temperatures (SSTs) in the summer (June–August) are driven by the amount of incoming solar radiation absorbed by the sea surface and by the flow of warm waters into the Arctic from the North Atlantic and North Pacific Oceans. Solar warming of the Arctic Ocean surface is influenced by the distribution of sea ice (with greater warming occurring in ice-free regions), cloud cover, and upper-ocean stratification. Discharge of relatively warm Arctic river waters can provide an additional source of heat to the surface of marginal seas.

Arctic SST is an essential indicator of the role of the ice–albedo feedback mechanism in any given summer sea ice melt season. As the area of sea ice cover decreases, more incoming solar radiation is absorbed by the ocean and, in turn, the warmer ocean melts more sea ice. In addition, higher SSTs are associated with delayed autumn freeze-up and increased ocean heat storage throughout the year. In another positive (amplifying) feedback related to global warming, higher SSTs can be associated with reduced ocean uptake of carbon dioxide from the atmosphere. Marine ecosystems are also influenced by SSTs, which affect the timing and development of production cycles, as well as available habitat.

The SST data presented here are a blend of in situ and satellite measurements from August 1982 to August 2021, taken from the monthly mean NOAA Optimum Interpolation (OI) SST Version 2 product (OISSTv2; Reynolds et al. 2002, 2007). In the Arctic Ocean overall, the OISSTv2 product has been found to exhibit a cold bias (i.e., underestimate SST) of up to 0.5°C compared to in situ measurements (Stroh et al. 2015). The OISSTv2 product uses a simplified linear relationship with

sea ice concentration to infer SST under sea ice (Reynolds et al. 2007), which means SSTs may be too low by up to 0.2°C where there is sea ice cover. The potential cool bias under sea ice can be reflected in trends and variability in the vicinity of the ice edge. We focus on August mean SSTs, which provide the most appropriate representation of Arctic Ocean summer SSTs because they are not affected by the cooling and subsequent sea ice growth that typically takes place in the latter half of September. Note that the SST reference period is August 1982–2010 because the satellite SST record begins in December 1981.

August 2021 mean SSTs ranged from 6° to 10°C in the southeast Chukchi and Barents Seas to around 0° to 3°C in the East Siberian, Kara and Laptev Seas, Baffin Bay, and in the ice-free waters east of Greenland (Fig. 5.5a). August 2021 mean SSTs were notably high (around 1–3.5°C higher than the 1982–2010 August mean) in the Kara and Laptev Seas (Fig. 5.5b). This is consistent with early-season sea ice retreat in these regions (section 5d), and anomalously warm spring (April–June) 2021 air temperatures over northern Eurasia (section 5b). SSTs in the waters east of Greenland were also higher than the 1982–2010 August mean by around 1–3°C. It is notable that in the same region, summer 2021 surface air temperatures were about 2–5°C higher than the climatological mean (section 5b).

The northern Barents Sea, Baffin Bay, and the Chukchi Sea experienced anomalously cool SSTs in August 2021, around 0.5° to 1°C below the 1982–2010 mean (Fig. 5.5b). Surface air temperatures in summer (June–August) were below average in the Beaufort and Chukchi Sea regions, and conditions were cloudy, limiting solar fluxes to the surface ocean. Lower SSTs are also consistent with greater sea ice extents (closer to normal) in the Chukchi and Beaufort Sea regions compared to recent past years, related to wind-driven transport of thick multiyear ice into the region in early 2021 (section 5d).

There is significant variability from year to year in the particular regions that exhibit anomalously low or high SSTs. The strong interannual variability in spatial patterns are evident in the differences between August 2021 and August 2020 SSTs (Fig. 5.5c). August 2021 SSTs were around 0.5°C (and up to 2°C) cooler than

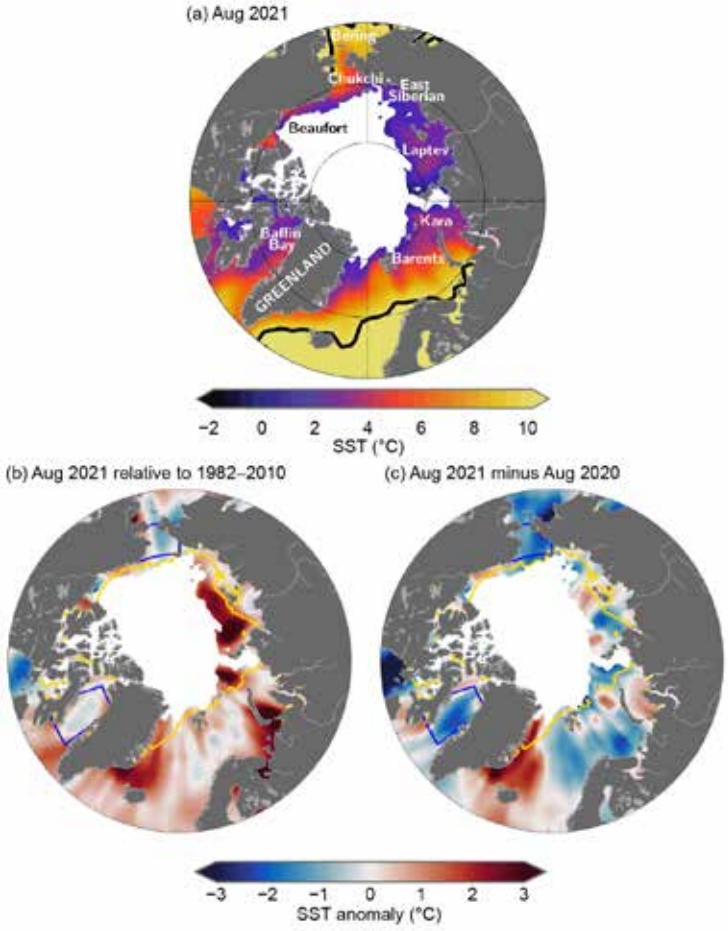

Fig. 5.5. (a) Mean sea surface temperature (SST; °C) in Aug 2021. Black contours indicate the 10°C SST isotherm. (b) SST anomalies (°C) in Aug 2021 relative to the Aug 1982–2010 mean. (c) Difference between Aug 2021 SSTs and Aug 2020 SSTs (negative values indicate where 2021 was cooler). White shading in all panels is the Aug 2021 mean sea ice extent. The yellow lines in (b) and (c) indicate the median ice edge for Aug 1982–2010. The two regions marked by blue boxes in (b) and (c) indicate regions of Baffin Bay and the Chukchi Sea and relate to data presented in Figs. 5.6c,d. (Data sources: SST data are the NOAA OISSTv2 provided by the NOAA/OAR/ESRL PSD, Boulder, Colorado, https://psl.noaa.gov/data/gridded/data.noaa.oisst.v2.html [accessed 8 Feb 2022; Reynolds et al. 2007]; sea ice concentration data are the NOAA/NSIDC Climate Data Record of Passive Microwave Sea Ice Concentration, Version 4 (https://nsidc.org/data/g02202) and Near-Real-Time NOAA/NSIDC Climate Data Record of Passive Microwave Sea Ice Concentration, Version 2 (https://nsidc.org/data/g10016) [Peng et al. 2013; Meier et al. 2021a,b], where a threshold of 15% concentration is used to calculate extent.)

in August 2020 over a significant portion of the ice-free regions, with some exceptions, including (up to 3°C) higher SSTs off of east Greenland (Fig. 5.5c).

Mean August SST warming trends from 1982 to 2021 persist over much of the Arctic Ocean, with statistically significant (at the 95% confidence interval) linear warming trends shown in Fig. 5.6a. Mean August SSTs for the entire Arctic (the Arctic Ocean and marginal seas north of 67°N) exhibit a linear warming trend of +0.03 ± 0.01°C yr^{-1} (Fig. 5.6b). Even while anomalously low SSTs in Baffin Bay and the Chukchi Sea were prominent in the August 2021 SST field (Figs. 5.5b, 5.6c,d), SSTs in both of these regions show long-term warming. Baffin Bay August SSTs exhibit a linear warming trend over 1982–2021 of +0.05 ± 0.01°C yr^{-1} (Fig. 5.6c). Similarly, Chukchi Sea August mean SSTs are warming with a linear trend of +0.06 ± 0.03°C yr^{-1} (Fig. 5.6d). The cooling trend (~−0.06°C yr^{-1}) in mean August SSTs in the north-central Barents Sea region remains a notable exception (Timmermans et al. 2020), although the cooling trend is not observed for most other months, nor for other parts of the Barents Sea (Lind et al. 2018; Smedsrud et al. 2022). Further, in this region Barents Sea waters contact cooler, fresher Arctic waters, and shifts in this boundary complicate interpretation of trends (see Barton et al. 2018).

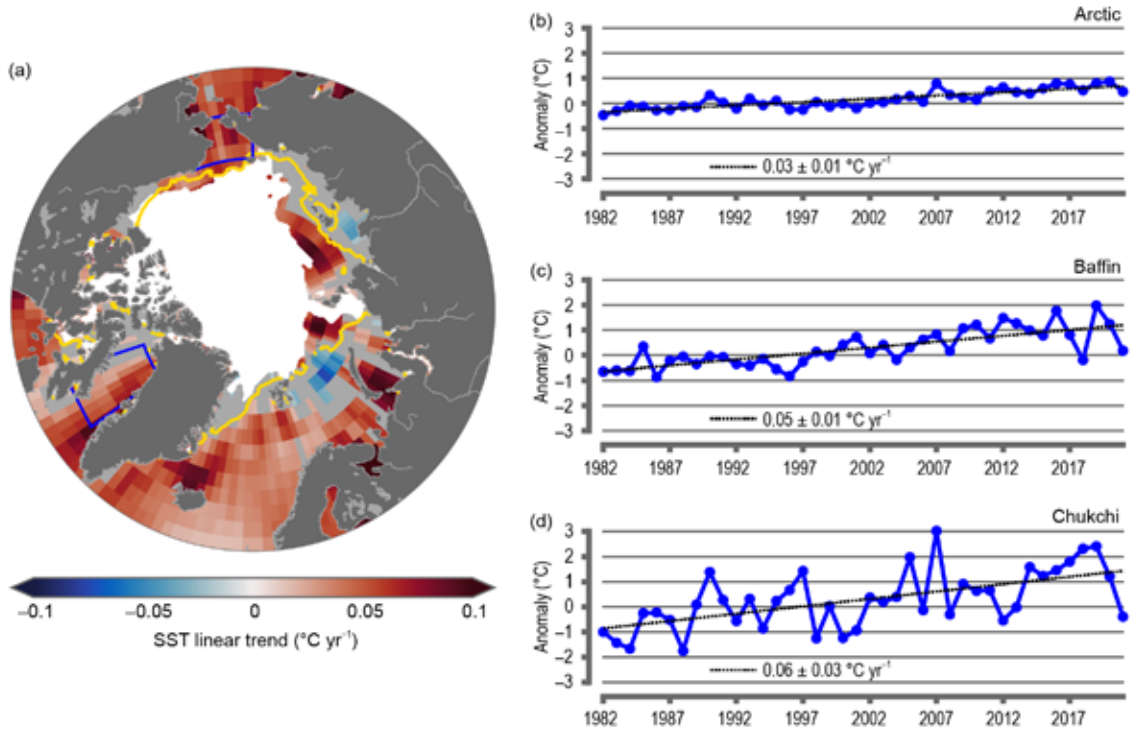

Fig. 5.6. (a) Linear SST trend (°C yr^{-1}) for Aug of each year from 1982 to 2021. The trend is only shown for values that are statistically significant at the 95% confidence interval; the region is shaded gray otherwise. White shading is the Aug 2021 mean sea ice extent, and the yellow line indicates the median ice edge for Aug 1982–2010. (b,c,d) Area-averaged SST anomalies (°C) for Aug of each year (1982–2021) relative to the 1982–2010 Aug mean for (b) the entire Arctic Ocean north of 67°N, (c) Baffin Bay, and (d) Chukchi Sea regions shown by blue boxes in (a). The dotted lines show the linear SST anomaly trends over the period shown and trends in °C yr^{-1} (with 95% confidence intervals) are indicated on the plots. (Data sources: see Fig. 5.5 caption.) (Source: Data are from NSIDC and University of Colorado [Tschudi et al. 2019, 2020]).

d. Sea ice—W. N. Meier, D. Perovich, S. Farrell, C. Haas, S. Hendricks, A. Petty, M. Webster, D. Divine, S. Gerland, L. Kaleschke, R. Ricker, A. Steer, X. Tian-Kunze, M. Tschudi, and K. Wood

Arctic sea ice is the frozen interface between the ocean and atmosphere in the North, limiting ocean–atmosphere exchanges of energy and moisture and playing a critical role in Arctic ecosystems and Earth's climate. Sea ice also plays a key role in Arctic human activities, including

Indigenous hunting and transportation, marine navigation, and national security responsibilities. Overall, 2021 continued to demonstrate the profound changes underway in the Arctic sea ice system.

1) SEA ICE EXTENT

Arctic sea ice began 2021 recovering from record or near-record low coverage and a notably late freeze-up in autumn 2020. By January 2021, sea ice extent (defined as the total area covered by at least 15% ice concentration) was lower than the 1981–2010 average in the Bering and Barents Seas, but near-average elsewhere. Extent values are from the NSIDC Sea Ice Index (Fetterer et al. 2017), one of several extent products (Lavergne et al. 2019; Ivanova et al. 2014) derived from satellite-borne passive microwave sensors operating since 1979. Persistent high pressure in the Siberian Arctic sector during January–February resulted in divergence of ice from the Siberian coast and strong advection of thicker, multiyear ice into the Beaufort and Chukchi Seas.

By March, the month with the greatest ice cover, the total sea ice extent of 14.64 $\times 10^6$ km^2 was 0.79 $\times 10^6$ km^2 (5.1%) lower than the 1981–2010 average and the ninth-lowest March extent in the 43-year record. The low sea ice extent in March 2021 was less extreme than during 2015–19, but continued the statistically significant downward trend of –2.6 % per decade over the 1979–2021 record (Fig. 5.7a). On a regional basis, March 2021 was characterized by below-average extent in the Bering Sea, Baffin Bay, and the Gulf of St. Lawrence and near-normal extent elsewhere (Fig. 5.7b).

After March, the seasonal retreat of ice began. The multiyear ice in the Beaufort and Chukchi Seas that developed earlier in winter delayed the retreat of sea ice on the North American side of the Arctic. On the Siberian side, strong pressure gradients facilitated early melt onset and local sea ice retreat in spring, leading to a record low extent in the Laptev Sea during May and June.

During summer 2021, the atmospheric circulation (marked by general low pressure over the Arctic Ocean; section 5b), along with the thicker ice in the Beaufort and Chukchi Seas, slowed the decline in ice extent. The summer circulation limited sea ice export through Fram Strait, resulting in the unusual occurrence of a nearly ice-free East Greenland Sea during much of the summer.

Sea ice extent in September 2021 was characterized by below-average coverage in the Siberian and East Greenland Seas

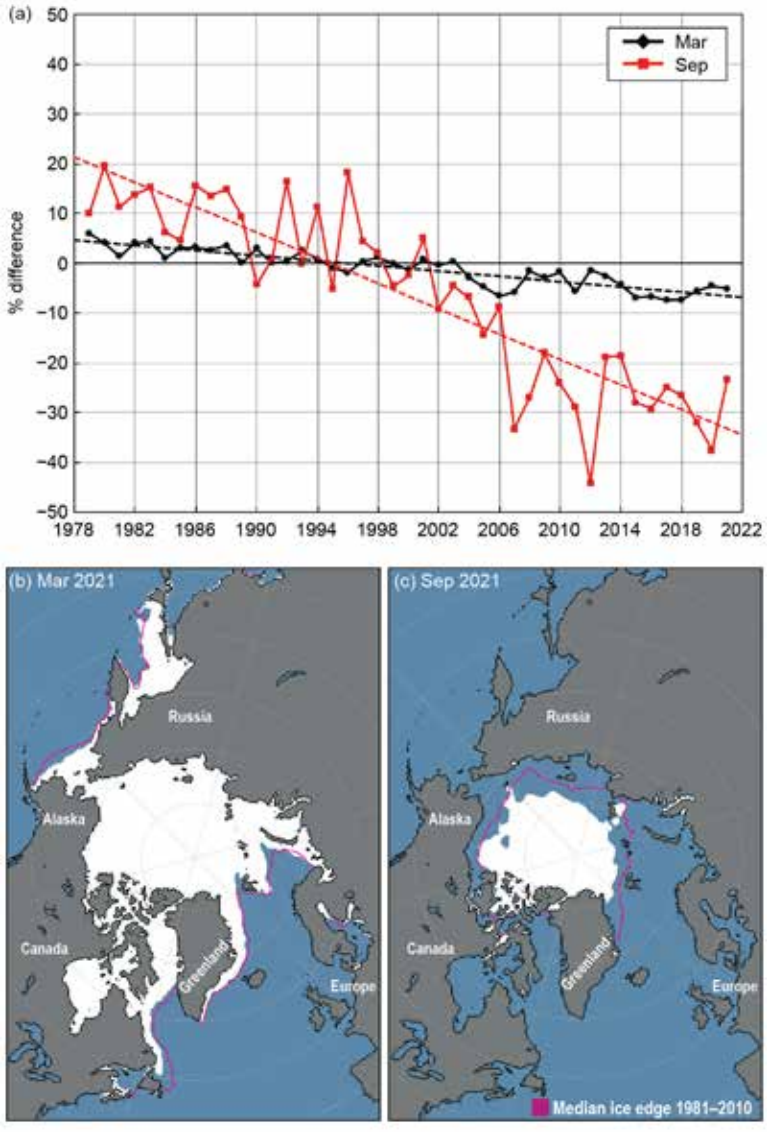

Fig. 5.7. (a) Monthly sea ice extent anomalies (solid lines) and linear trend lines (dashed lines) for Mar (black) and Sep (red) from 1979 to 2021. The anomalies are relative to the 1981–2010 average for each month. (b) Mar 2021 and (c) Sep 2021 monthly average sea ice extent; the median extent for 1981–2010 is shown by the magenta contour.

and closer-to-normal coverage in the Beaufort and Chukchi Seas (Fig. 5.7c). Arctic-wide, the slower summer decline resulted in a September 2021 total sea ice extent of 4.92×10^6 km^2, which was 1.49×10^6 km^2 (23.2%) lower than the 1981–2010 average and the 12th-lowest September extent on record. The September trend from 1979 through 2021 is –12.7% decade^{-1} and like all other months, is statistically significant. The 15 lowest September extents in the satellite record have all occurred in the last 15 years (2007–21).

2) SEA ICE AGE, THICKNESS, AND VOLUME

Sea ice age is a rough proxy for thickness as multiyear ice (ice that survives at least one summer melt season) grows thicker over successive winters. Sea ice age is presented here (Fig. 5.8) for the period 1985–2021, based on Tschudi et al. (2019a,b). One week before the 2021 annual minimum extent, when the age values of the remaining sea ice are incremented by one year, the amount of multiyear ice remaining in the Arctic was the second lowest on record (above only 2012). The September multiyear ice extent declined by 70.7%, from 4.40×10^6 km^2 in 1985 to 1.29×10^6 km^2 in 2021 (Fig. 5.8). Over the same period, the oldest ice (> 4 years old) declined by 94.1%, from 2.36×10^6 km^2 to 0.14×10^6 km^2. In the 37 years since ice-age records began in 1985, the Arctic has changed from a region dominated by multiyear sea ice to one where first-year sea ice prevails. A younger ice cover implies a thinner, less voluminous ice pack and one that is more fragile and vulnerable.

Sea ice drifts with wind and ocean currents, while growing and melting thermodynamically. Ice convergence leads to dynamic thickening, while ice divergence creates leads and, in winter, new ice. Sea ice thickness is an important indicator of overall ice conditions because it provides a record of the cumulative effect of dynamic and thermodynamic processes. The ESA CryoSat-2/SMOS satellites have provided a record of seasonal (October to April) ice thickness and volume (Ricker et al. 2017) since the 2010/11 winter. Since 2018, the NASA ICESat-2 satellite has also provided thickness estimates (Petty et al. 2020, 2021). Some differences between these two products are seen for April 2021 (the month of maximum annual thickness), with ICESat-2 indicating thicker ice along the Canadian Archipelago and Alaskan coast (Fig. 5.9a), while CryoSat-2/SMOS shows thicker ice in the eastern Arctic (Fig. 5.9b). However, the overall spatial patterns are similar. Compared to the 2011–20 April average, the 2021 CryoSat-2/SMOS product shows thinner ice along the northern Canadian Archipelago and Greenland coasts, the East Greenland and Barents Seas, and somewhat thicker-than-average ice in the Laptev Sea and along the Alaskan coast (Fig. 5.9c). On average, the 2020/21 winter sea ice was the thinnest in the CryoSat-2/SMOS record.

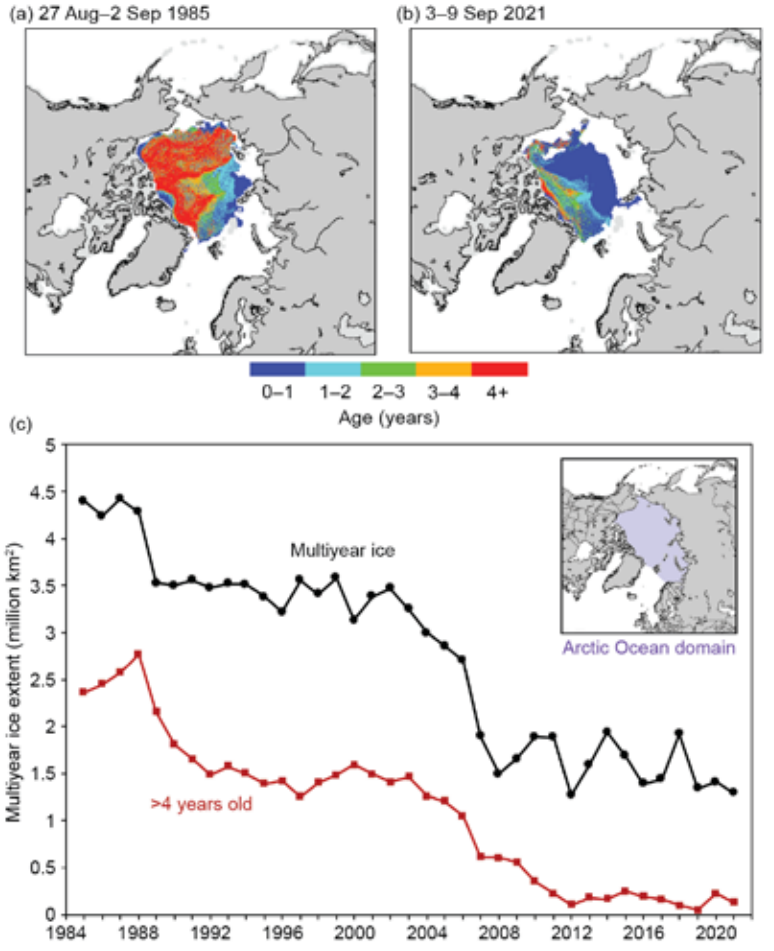

Fig. 5.8. Sea ice age coverage map for the week before minimum total extent (when age values are incremented to one year older) in (a) 1985 and (b) 2021; (c) extent of multiyear ice (black) and ice > 4 years old (red) within the Arctic Ocean (inset) for the week of the minimum total extent.

Sea ice thickness is integrated with ice concentration to provide winter volume estimates for 2010–21. The seasonal timeseries (Fig. 5.10) indicates below-average ice volume throughout the 2020/21 winter, with record low conditions spanning October to mid-November. Volume growth typically slows by early March as spring warming begins. In 2021, the volume experienced near-zero growth for much of March and decreased slightly thereafter. Ice volume in April 2021 was the lowest in the 2010–21 April record. While the rate of decline in September sea ice extent over the 2010–21 period has slowed compared to previous decades, Arctic sea ice volume continues to rapidly shrink.

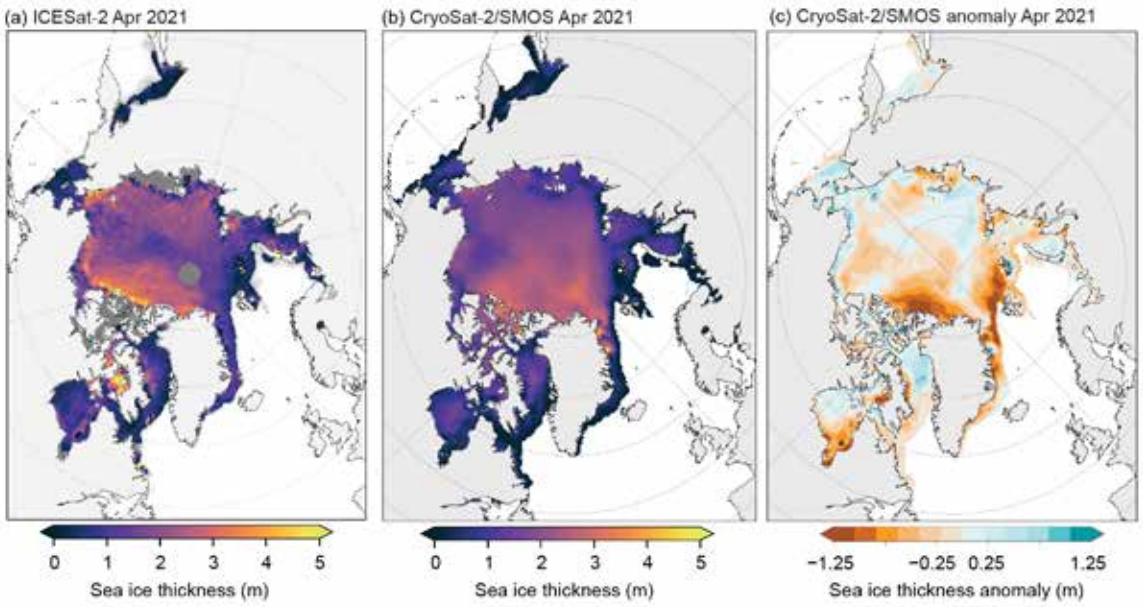

Fig. 5.9. (a) ICESat-2 (dark gray areas have no data) and (b) CryoSat-2/SMOS sea ice thickness (m) for Apr 2021; (c) CryoSat-2/SMOS thickness anomaly (m) for Apr 2021 (relative to the 2010–20 average). Note that ICESat-2 thickness estimates outside the Arctic Ocean domain (see the Fig. 5.8c inset) are not as reliable due to uncertainties in snow cover.

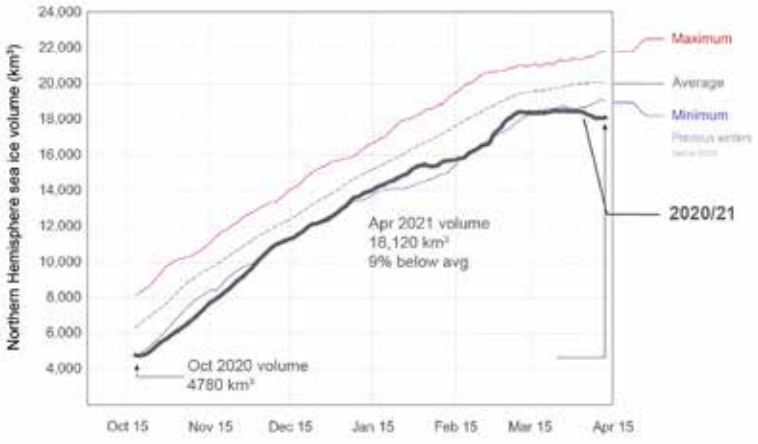

Fig. 5.10. CryoSat-2/SMOS Northern Hemisphere sea ice volume from 15 Oct to 15 Apr for the 2020/21 season. The maximum (red line), minimum (blue line), and average (dashed gray line) volume over the 11-year (2010–20) record are also provided.

SIDEBAR 5.1: IN TRANSITION: MARITIME POLLUTION AND THE BERING STRAIT REGION—G. SHEFFIELD AND K.M. STAFFORD

The Bering Strait region is a narrow transboundary waterway between eastern Chukotka (Russia) and western Alaska (United States) and is the only marine corridor from the Pacific to the Arctic Ocean. The maritime ecosystem of the northern Bering Sea/Bering Strait region is distinct from the southern Bering Sea, separated by a thermal barrier created and maintained by the once stable seasonal sea ice. The remote coastal communities of this region are ethnically diverse and reliant on the non-commercial acquisition of marine resources for their nutritional, cultural, and economic well-being (Fig. SB5.1).

The ongoing reduction in the quality, extent, and duration of sea ice in the Bering Strait region is rapidly transforming the environment and reorganizing marine ecosystems (Stevenson and Lauth 2019; Eisner et al. 2020; Thoman et al. 2020). More economic opportunities are resulting in an increase in the size, duration, and diversity of industrial ship traffic transiting and/or utilizing the region (Humpert 2021; Smith 2021; USCMTS 2019). Unprecedented numbers of multi-national ships are chasing southern Bering Sea fisheries that are advancing northwards and/or utilizing the Strait as a transportation corridor. Impacts of increased industrial ship traffic include increases and/or changes in marine debris and ambient noise.

Fig. SB5.1. Seal and walrus meat, harvested for subsistence purposes, drying on a wooden rack for preservation and later consumption by community members on Little Diomede Island, Alaska. Big Diomede Island, Chukotka, Russian Federation is in the background. Photo credit: G. Sheffield.

Marine Debris

During summer 2020, the Bering Strait region of Alaska experienced a novel foreign marine debris event. Through mid-November, individuals from 14 Alaskan coastal communities discovered and documented over 350 individual items ashore, most with Russian, Korean, and/or other Asian lettering or branding (Sheffield et al. 2021). This number was considered a minimum, with qualitative reports of mostly uncounted debris extending "for miles." Reporting communities included locations in Norton Sound, Bering Strait, and the Chukchi Sea region. Additional reports of debris ashore were received from the U.S. Coast Guard.

The novelty of this event was not due to foreign debris of commercial fishing equipment, but rather the widespread everyday garbage, including plastics, food items, and hazardous materials (Fig. SB5.2). Most plastic items were un-weathered, indicating they had entered the water recently. April 2020 was the most recent date of manufacturing noted on any item. Hazardous materials included cans and other containers that had and/or still contained insecticides, toilet cleaners, drain clog remover, lubricating oils, butane gas, and spray paints.

Regional residents, tribal leadership, and coastal communities provided awareness of the event, documented, reported, conducted clean-up activities, and investigated the source of debris on a voluntary basis using personal resources, little to no training, and limited response capacity (Sheffield et al. 2021). The foreign debris event negatively affected regional peoples' sense of security regarding the health of the transitioning northern Bering Sea marine ecosystem (Stevenson and Lauth 2019; Eisner et al. 2020; Spies et al. 2020) and the level of future risks and impacts from the forecasted and observed increase of industrial ship traffic in the Bering Strait region (USCMTS 2019; Humpert 2021).

Without regular and relevant collaborative transboundary communications between the United States and the Russian Federation and enforcement of existing international marine pollution rules (IMO 2021), the Bering Strait region can expect similar or higher levels of marine garbage in the future as industrial ship traffic increases.

Ambient Noise

In the ocean, the combination of naturally occurring sounds from wind, waves, and marine animals contribute to ambient noise. Unique to the polar regions are the sounds contributed by sea ice and icebergs, which generate noise via ice

Fig. SB5.2. Items from 2020 foreign marine debris event: (a) plastics scattered along the shoreline; photo credit: L. Apatiki, (b) shampoo bottle; photo credit: T. Pelowook, (c) miscellaneous aerosol cans of butane, paint, and lubricating oil, foods, and bottles of bathroom cleaners, water bottles, etc; photo credit: G. Sheffield, (d) 1L carton of milk; photo credit: A. Ahmasuk, (e) deck boot; photo credit: G. Sheffield, (f) longline anchor buoy from a Vladivostok-based fishing company with the Pacific cod permit attached; photo credit: R. Tokeinna.

formation and deformation, pressure ridging, and cracking, but also decrease noise due to the lack of wind-driven waves in ice-covered waters. The sounds from storms and from novel marine animals that have moved into the ice-free regions of the Arctic are changing underwater ambient noise profiles, but are also giving us insight into natural atmospheric and biologic changes that are occurring. While marine debris and oil spills provide visual evidence of pollution, underwater sound can also be considered a form of pollution. 'Sound' becomes 'noise' when it may negatively impact the health or behavior of marine animals and is driven by increased shipping, including cargo and fishing vessels (Rolland et al. 2013). Underwater noise is created from the rotation of ships' propellers; this noise is relatively continuous and low-frequency (under 1000 Hz). Noise is also created by icebreakers breaking through sea ice. Ship noise overlaps in frequency with the sounds produced and received by Arctic marine mammals. Signals in the same frequency band are more likely to interfere with animals' ability to hear and respond to important sounds (Blackwell and Thode 2021; Tervo et al. 2021). Increases in overall noise levels increase stress hormones in individual animals and may have long-term impacts on their ability to navigate, communicate, feed, and reproduce.

The most persistent anthropogenic noise source in the Bering Strait region is industrial ship traffic, most of which sails the Northern Sea Route (NSR) across waters north of Russia from the Pacific to the Atlantic (CHNL 2022). Most large ships traverse the NSR during July to October when sea ice coverage is minimal. However, in January 2021, at least four liquid natural gas tankers sailed the NSR without icebreaker support. Because large volumes of industrial maritime traffic in the Arctic are a relatively new phenomenon, Arctic marine wildlife may have a lower tolerance for, and react more strongly to, noise from these ships (PAME 2019).

Summary

With continued sea ice reduction and ecosystem-wide shifts expected, increased industrial ship traffic in/among the Bering Strait region will continue to elevate existing regional food security, public health, wildlife health, and conservation concerns. Potential risks to marine wildlife from marine debris include entanglements, exposure to hazardous chemicals, and ingestion of plastics and/or hazardous materials and chemicals. Potential risks to marine wildlife, from increasing ambient noise, include deflection from important feeding areas, changes in timing of movements, and a reduced ability to communicate opportunities or risks. Without enforcement of existing international pollution laws and/or mitigation efforts regarding emerging impacts from multi-national industrial ship traffic, the Arctic and the Bering Strait region can expect increasing amounts and types of marine debris and noise pollution.

For more details on the 2020 marine debris event in Bering Strait the changing Arctic marine soundscape, please see the 2021 Arctic Report Card (Sheffield et al. 2021; Stafford 2021).

:

e. Greenland ice sheet—T. A. Moon, K. D. Mankoff, R. S. Fausto, X. Fettweis, M. Tedesco, A. Wehrlé, B. D. Loomis, T. L. Mote, C. D. Jensen, N. Korsgaard, J. E. Box, J. Cappelen, and Ø. A. Winton

The Greenland Ice Sheet has lost mass every year since 1998, with negative impacts of ice loss experienced globally. The ice sheet contains enough ice to generate ~7.4 m of eustatic sea level rise (rise caused by ocean mass changes only; Morlighem et al. 2017). With multiple methods available for measuring Greenland Ice Sheet mass balance, we compare 1 September 2020 through 31 August 2021 mass change values derived from satellite gravimetry using Gravity Recovery and Climate Experiment Follow On (GRACE-FO) measurements (–125 ± 35 Gt) and an input-output (I/O) method (–165 ± 89 Gt; see Fig. 5.11 for details on methods and references). GRACE-FO values include Greenland glaciers and ice caps not directly connected to the main ice sheet, while I/O values do not, introducing a likely bias of ~15–20% (Bolch et al. 2013; though acknowledging potentially higher bias values) and lowering the agreement between methods. The change in GRACE-FO mass balance reported here as compared to Moon et al. (2021) is due to the availability of additional 2021 data to improve the calculation. Across the two methods, the estimated range in mass loss represents ~0.3–0.5 mm of global mean sea level rise in 2020/21 (excluding ongoing thermal expansion [IPCC 2021]). Using the satellite gravimetry time series, the 2020/21 ice loss was ~138 Gt less than the 2002–21 average of –263 ± 15 Gt yr^{-1}.

This year of moderate twenty-first century ice loss includes substantial variations in ice sheet surface conditions, particularly over the summer melt season. The ice sheet balance year (1 September–31 August) captures the annual cycle of snow accumulation (gain) and ice/snow ablation (loss), using seasonal breaks at September–November (autumn), December–February (winter), March–May (spring), and June–August (summer). Except for an above-average melt event on 27 April, the ice sheet daily melt extent as estimated by satellites remained low until 26 May and through mid-summer remained mostly within the 1981–2010 10th to 90th percentiles (Fig. 5.12). In situ observations are provided via 15 mostly terrestrial Danish Meteorological Institute (DMI) weather stations and eight on-ice automatic weather station transects from the Programme for Monitoring of the Greenland Ice Sheet (PROMICE) at the Geological Survey of Greenland and Denmark (GEUS; Fausto et al. 2021). PROMICE stations recorded surface air temperatures within ± 1 std. dev. of monthly means for June and July. Late July and August, however, included three extreme melt episodes (Fig. 5.12b). The first, on 19 July, had melt across 702,000 km^2 (~43%) of the ice sheet surface. A second melt episode on 28 July extended across 54% of the ice sheet surface, and a third melt episode concentrated on 14 August had extended across 53% of the ice sheet surface and reached the highest ice sheet elevations at the National Science Foundation's (NSF) Summit Station (3216 m a.s.l.).

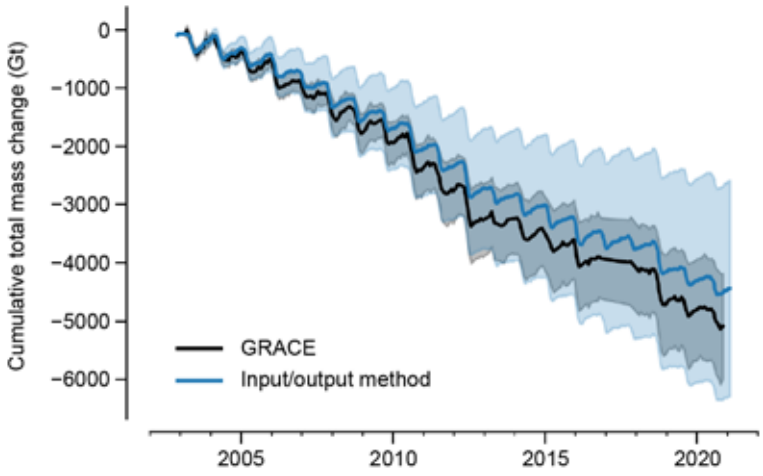

Fig. 5.11. Comparison of results using GRACE and GRACE-FO (black; includes peripheral glaciers and ice caps) and the input/output method (I/O; blue; does not include peripheral glaciers and ice caps) for total mass balance. Shading for I/O method represents the systematic or bias (not random) uncertainty (e.g., uncertain ice thickness), and shading for GRACE also includes monthly noise estimates. These uncertainties accumulate. GRACE (2002–17) and GRACE–FO (2018–present) satellite data and technical notes are hosted at https://podaac-tools.jpl.nasa.gov/drive/files/allData. GRACE and GRACE-FO data are corrected for glacial isostatic adjustment (Peltier et al. 2018). The I/O method is the mean of MAR, RACMO, and HIRHAM/HARMONIE regional climate models minus discharge from Mankoff et al. (2020, data: https://doi.org/10.22008/promice/data/ice_discharge/d/v02).

The mid-summer rapid rise in ice loss is reflected in ice ablation measurements taken at some PROMICE stations

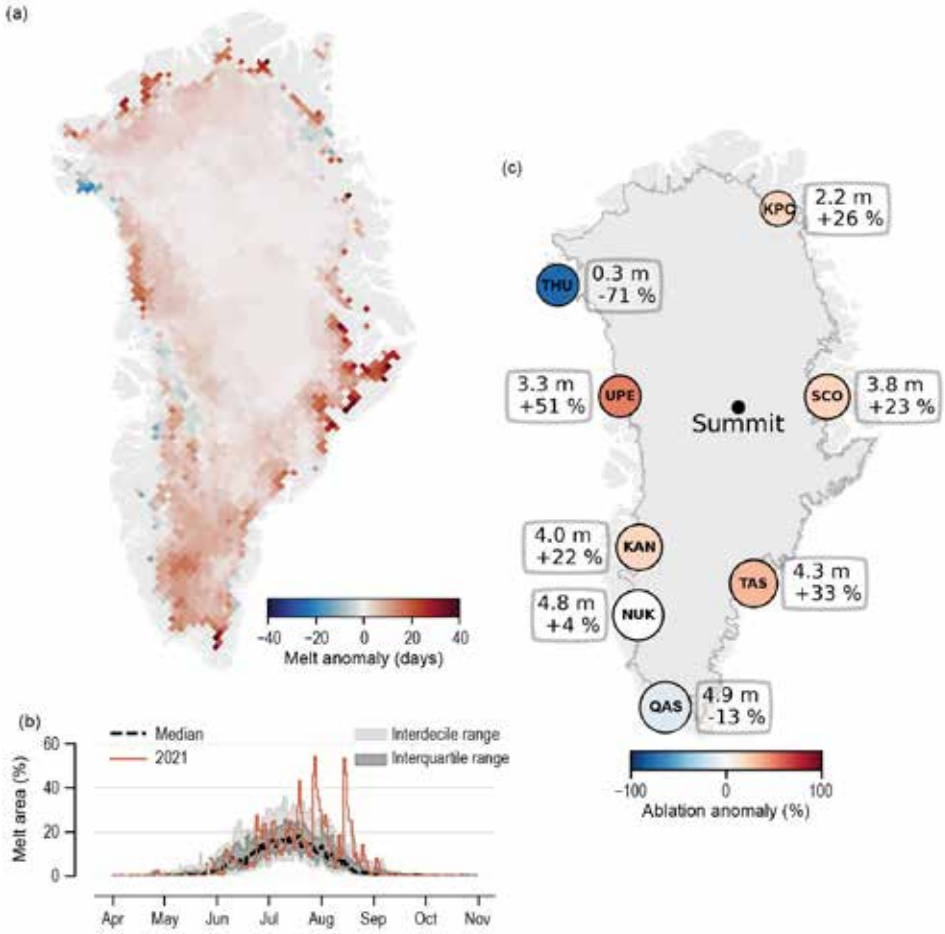

Fig. 5.12. (a) 2021 melt anomaly (in number of melting days) with respect to a 1981–2010 reference period. (b) Surface melt extent as a percentage of the ice sheet area during 2021 (solid red). Surface melt duration and extent measurements are derived from daily Special Sensor Microwave Imager/Sounder (SSMIS) 37 GHz, horizontally polarized passive microwave radiometer satellite data (Mote 2007). (c) Net ablation (represents ice loss) in 2021 measured by PROMICE weather transects and referenced to a 1981–2010 standard period. Circle size is scaled to the ablation in m of ice equivalent and color-scaled with anomaly value. White circles indicate anomaly values not exceeding methodological and measurement uncertainty. Stations are: Thule (THU), Upernavik (UPE), Kangerlussuaq (KAN), Nuuk (NUK), Qassimuit (QAS), Tasiliiq (TAS), Scorebysund (SCO), and Kronprins Christians Land (KPC). NSF Summit Station is also marked.

(following Van As et al. 2016), which show significantly above-average ablation along the central western and eastern Greenland coasts (Fig. 5.12c).

The stark contrast between ice sheet conditions in early and late summer is also reflected in measurements of ice sheet broadband albedo (relative amount of energy reflected by the surface in all wavelength bands) and bare glacial ice exposure (Fig. 5.13). A low albedo (dark) ice sheet surface absorbs sunlight and can enhance ice melt, while a high albedo (bright) surface can reflect sunlight and reduce melt potential. Snow can create a high albedo surface while a dark surface can result from exposure of bare glacial ice, snow grain growth, organic and inorganic surface materials (e.g., microbes or black carbon), etc.

An above-average July albedo was offset by a below-average August albedo, creating an overall average June–August albedo (Fig. 5.13b). Regionally, brighter-than-normal southwest conditions and darker-than-normal northern conditions are evident (Fig. 5.13a). The regionally-opposing anomalies obscure a temporal shift that is clearer in the bare ice area variation (Fig. 5.13c), which reached extremely large area values that rivaled 2019, an extreme ice loss year. August 2021 had the latest peak in bare ice area during the past five years (2017–21). The local ablation (Fig. 5.12b) and albedo anomalies (Fig. 5.13a) may not intuitively align due to factors such as summer snowfall, surface atmospheric conditions, and extreme melt events (e.g., Box et al. 2022).

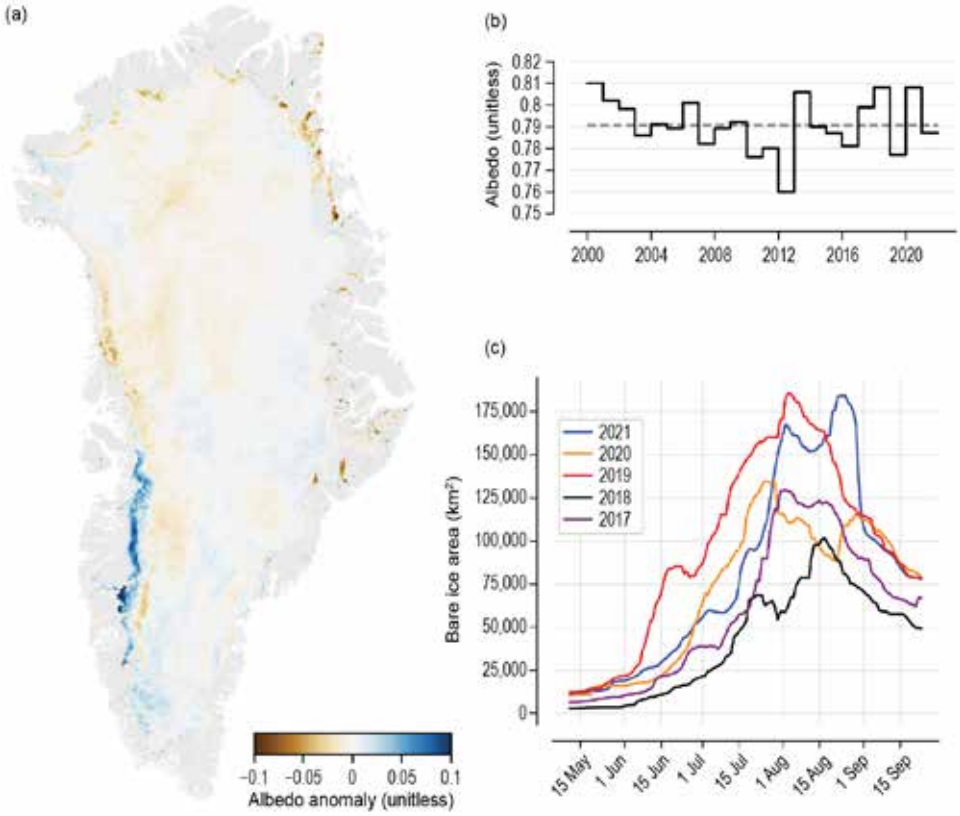

Fig. 5.13. (a) Albedo anomaly for summer 2021, relative to a 2000–09 reference period. NASA MODIS satellite data provide multi-decadal albedo monitoring (Box et al. 2017). (b) Time series for average Greenland Ice Sheet summer albedo from MODIS. (c) Bare ice area (km^2) from the Sentinel-3 SICE product (Kokhanovsky et al. 2020; Wehrlé et al. 2021).

Along with ice loss via melt, the Greenland Ice Sheet also loses mass via breaking off of solid ice, hereafter 'discharge', into the ocean at the ice sheet–ocean boundaries (Fig. 5.14), though mass loss variability is dominated by surface mass gain/loss, not solid ice discharge (Mankoff et al. 2020). The 2010–19 solid ice discharge averaged ~−487 ± 46 Gt yr^{-1}, and the 1981–2010 average is ~−444 ± 47 Gt yr^{-1}. Solid ice discharge for January–December 2021 was −496 ± 48 Gt, with the southeast remaining the largest contributor (Fig. 5.14a).

If solid ice discharge is more rapid than replacement from ice flow, the glacier front retreats and glacier area is lost. For 2020/21, net glacier surface area loss due to retreat was −18.9 km^2 for 47 major and representative Greenland tidewater glaciers (Fig. 5.14b,c), substantially lower than the mean annual area loss of −103.3 km^2 for these glaciers since 2002 (Andersen et al. 2019).

Despite moderate ice loss for 2020/21, the year brought unprecedented conditions to the ice sheet. Based on the 1978–present satellite record, the anomalous melt event centered on 14 August was the latest on record that affected more than half of the ice sheet (> 815,000 km^2). Further, 2021 is only the second year on record (the other is 2012) with more than one melt event on this scale. Year 2021 was also the first time that rainfall was reported at NSF's Summit Station (operations began in 1989), though surface melting without rainfall was observed at Summit in 1995, 2012, and 2019. The exceptional August rainfall was associated with an atmospheric river (a concentrated poleward flow of heat and moisture). This rain episode increased snow and ice melt and lowered surface albedo between 0.4 and 0.1, contributing to anomalously high late meltwater production in 2021. According to the MARv3.12 model forced by fifth ECMWF Reanalysis (ERA5; Hersbach et al. 2020) data, the amount of rainfall across the ice sheet (75 Gt yr^{-1}) in 2021 was the highest since at least 1950, with an anomaly of +103% with respect to the 1991–2020 baseline. The model-derived meltwater runoff (−445 Gt yr^{-1}) was 20% larger in 2021 than the baseline, with 2021 producing the fifth-highest surface melt after 2012, 2019, 2010, and 2016. Along with the

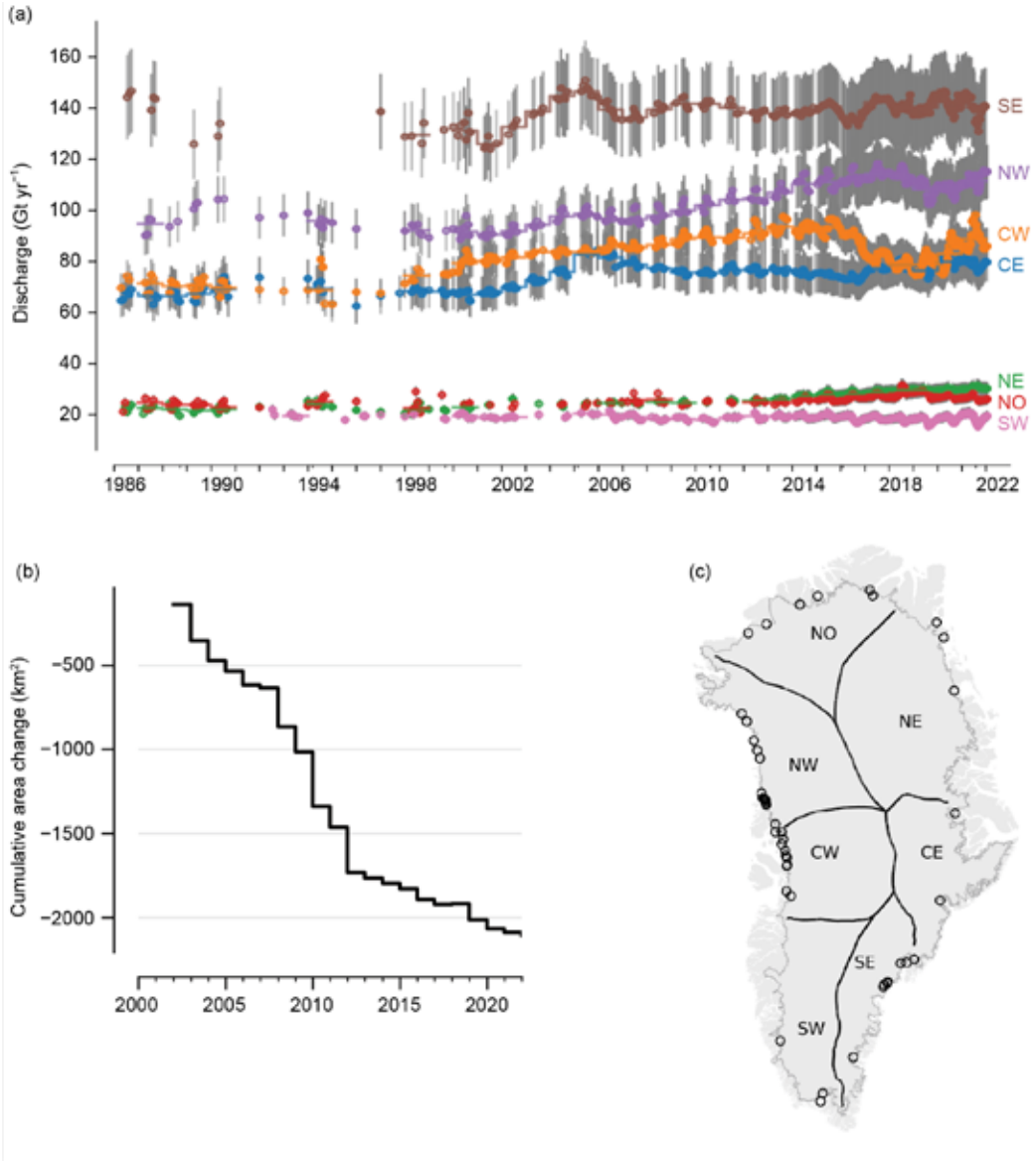

Fig. 5.14. (a) Solid ice discharge (Gt yr^{-1}; gray bars show ±10% uncertainty range). PROMICE combines ice thickness estimates with ice velocity measurements based on Sentinel-1 satellite data to create a high temporal resolution solid ice discharge product (representing ice loss) integrated over Greenland (following Mankoff et al. 2020). (b) Cumulative total area change at 47 major Greenland tidewater glaciers. (c) Regions for solid ice discharge (a): north (NO), northeast (NE), central east (CE), southeast (SE), southwest (SW), central west (CW), and northwest (NW) and sampled glaciers for (b) indicated with open circles.

exceptional summer rainfall (73 Gt yr^{-1}, representing an anomaly of +120%), 10% larger snowfall accumulation than average (711 Gt yr^{-1}) counterbalanced the excess of melt to give a total surface mass balance close to the 1991–2020 average.

f. Glaciers and ice caps outside Greenland—D. Burgess, G. Wolken, B. Wouters, L. M. Andreassen, J. Kohler, F. Pálsson, E. Baker, B. Luks, L. Thomson, and T. Thorsteinsson

The Arctic hosts 63% of the world's mountain glaciers and ice caps by area outside of the ice sheets of Greenland and Antarctica (RGI Consortium 2017; Fig. 5.15). While their potential longer-term contribution to sea level rise is small compared to the ice sheets, they are sensitive to changes in climate and have been a large contributor to recent sea level rise in response to continued atmospheric warming (Ciracì et al. 2020; Hugonnet et al. 2021; Millan et al. 2017; Wouters et al. 2019). Recent increases in global temperature, amplified at high northern latitudes (section 5b, Fig. 5.1), have accelerated melt rates of Arctic glaciers and ice caps three-fold since the mid-1990s

(Zemp et al. 2019). Observations of monitored Arctic glaciers and ice caps from 2020 and 2021 show regional and inter-annual variations in mass change, with a continuing trend of significant ice loss throughout the Arctic, especially in Alaska and Arctic Canada.

Glaciers and ice caps gain mass through surface accumulation (snow, rime, freezing rain) and lose mass by surface melt and runoff, and by iceberg calving where they terminate in oceans or lakes. The total mass balance is thus defined as the difference between annual accumulation and annual mass losses (by iceberg calving plus runoff; Ostrem and Brugman 1991). Of the 27 Arctic glaciers currently monitored, only Kongsvegen, Hansbreen, and Devon Ice Cap (NW) lose mass by iceberg calving, which is not accounted for in this study (World Glacier Monitoring Service [https://wgms.ch/] 2021). For all glaciers discussed, we report the climatic mass balance (B_{clim}, the difference between annual accumulation and annual runoff), which is a measure of annual thickness change (millimeters water equivalent, mm w.e.) averaged across the entire glacier or ice cap basin.

We report B_{clim} for the 2020/21 mass balance year (September 2020 to August 2021) for the 20 monitored Arctic glaciers for which mass balance data were available. These glaciers are located in Arctic Canada (three), Svalbard (three), Alaska (three), Iceland (nine), and Norway (two). Because some of these data are still provisional, we provide added context to recent changes in pan-Arctic glacier mass balance by also reporting on the 24 glaciers measured in the previous mass balance year of 2019/20 (World Glacier Monitoring Service [https://wgms.ch/] 2021; Kjøllmoen et al. 2021). These glaciers are located in Alaska (three), Arctic Canada (four), Iceland (nine), Svalbard (three), Norway (two), and Sweden (three; Fig. 5.15). Cumulative measurements of B_{clim} record regional variations in thinning which range from ~–14 m w.e. across glaciers in Arctic Canada (1959–2021) to ~–35 m w.e. for glaciers in Alaska (1953–2021), with an overall average of ~–24 m w.e. for all regions combined (Fig. 5.16).

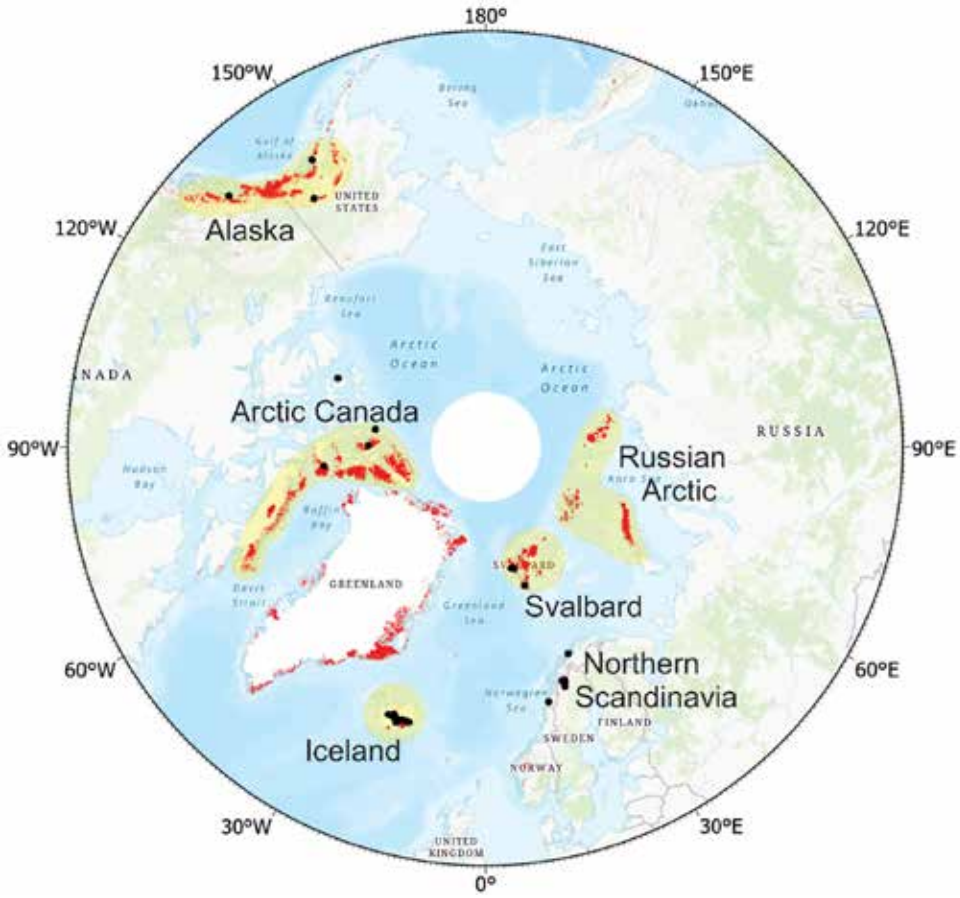

Fig. 5.15. Arctic glaciers and ice caps (red), including ice caps in Greenland that are separate from the ice sheet. Yellow shading shows the GRACE- and GRACE-FO-derived mass anomaly domains, used to estimate changes in regional annual glacier mass balance for heavily glacierized Arctic regions. Black dots indicate long-term Arctic glacier monitoring sites.

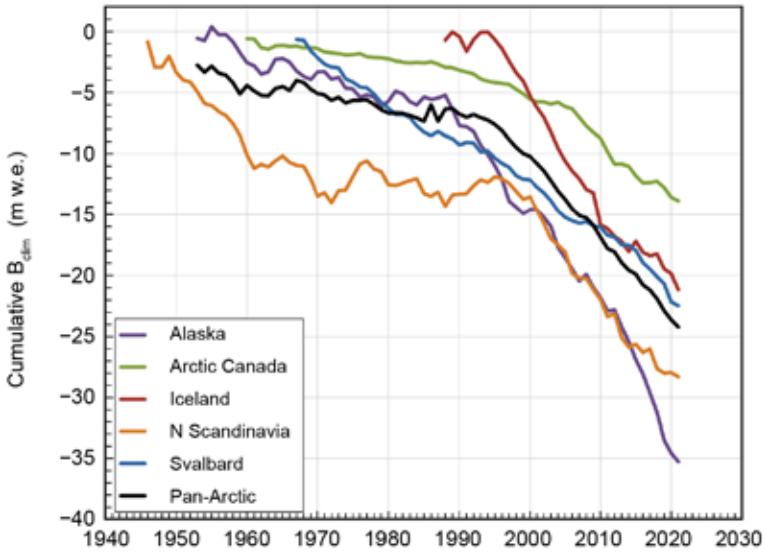

Fig. 5.16. Cumulative B_{clim} in meters of water equivalent (m w.e.) for monitored glaciers in five regions of the Arctic and for the Arctic as a whole (pan-Arctic). Regional climatic mass balances are derived as arithmetic means for all monitored glaciers within each region for each year, and these means are summed over the period of record. Due to homogenization and calibration of mass balance datasets from Norwegian glaciers (Andreassen et al. 2016), post-1970 cumulative thickness change values for North Scandinavia are more negative than reported previously in Wolken et al. (2020). (Source: Data are from the World Glacier Monitoring Service [WGMS 2021: https://wgms.ch/].)

Average B_{clim} of –735 mm w.e. across pan-Arctic glaciers and ice caps in the mass balance year 2019/20 represented the 14th most negative balance since 1960. Regionally, the greatest thinning occurred over Svalbard, where record negative values of B_{clim} were recorded for Midtre Lovénbreen (–1590 mm w.e.), Austre Brøggerbreen (–1740 mm w.e.), and Kongsvegen (–1140 mm w.e.). Negative B_{clim} of –795 mm w.e. averaged across monitored glaciers and ice caps in the Canadian Arctic Archipelago was consistent with post-2005 melting which has been about four times greater than the 1960–2004 average (Sharp et al. 2011). Thinning by ~1 m across Alaskan glaciers in 2019/20 mass balance year corresponded to a moderately negative B_{clim} anomaly (–446 mm w.e.) relative to the 1981–2010 mean.

Surface mass balance and overall state-of-health of Arctic glaciers and ice caps is closely linked with summer warmth (Box et al. 2019). Strongly negative values of B_{clim} for glaciers and ice caps across Svalbard in the 2019/20 balance year were associated with summer (June–August, JJA) atmospheric temperature (925 hPa; NCEP/NCAR) anomalies 2.5° to 3°C above the 1981–2010 mean (Ballinger et al. 2020). Similarly, near-record high melting across glaciers and ice caps in the Canadian Arctic coincided with positive temperature anomalies (+1.5° to +2°C; NCEP/NCAR) recorded for summer 2020 (Ballinger et al. 2020). Radiosonde temperature data (JJA, 850 hPa) collected by the Government of Canada in 2020 registered the first and second highest JJA (850 hPa) positive anomalies on record at Resolute Bay and Eureka, Nunavut, weather stations, respectively (Fig. 5.17). In the 2019/20 balance year, a strong positive B_{clim} anomaly for Engabreen in northern Scandinavia (522 mm w.e. higher than the 1981–2010 average) coincided with the fifth-highest winter accumulation on record (WGMS 2021).

Average surface mass balance of pan-Arctic glaciers and ice caps in 2020/21 was overall less negative (by 132 mm w.e.) than in the 2019/20 balance year (Fig. 5.17b). Strongly negative balances, however, prevailed across Icelandic glaciers for which an average B_{clim} of –1278 mm w.e. represented the third most negative mass balance across this region since measurements began in 1986. Enhanced glacier melt over northern Iceland, relative to southern Iceland, was associated with summer (July–September) temperatures in excess of 3°C above the 1981–2010 average (section 5b).

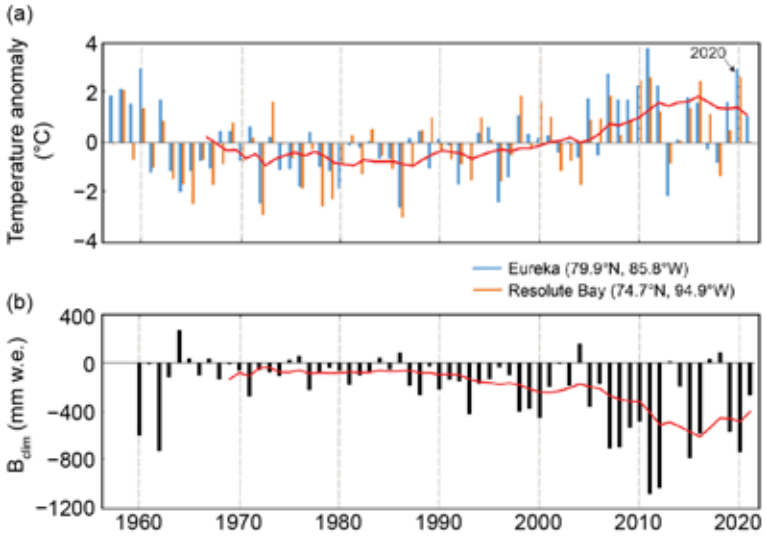

Fig. 5.17. (a) Annual temperature anomalies (°C) derived from the Integrated Global Radiosonde Archive (Imke et al. 2016) and (b) average climatic mass balance (B_{clim}; mm w.e.) for monitored glaciers in the Canadian High Arctic. Solid red lines indicate decadal averages. Summer temperature anomalies (JJA 850 hPa) and B_{clim} are strongly correlated with Pearson correlation coefficients of −0.8 and −0.97 for annual and decadal correlations, respectively, over approximately six decades for which overlapping measurements are available. Near-record high temperature anomalies in 2020 correspond to the fifth most negative B_{clim} measured since 1960.

Glaciers and ice caps at high northern latitudes have been increasingly important contributors to global sea level rise since the early 1990s (Box et al. 2018). Gravity anomalies measured from the combined GRACE (2002–16) and GRACE-FO (2018–21) satellite missions indicate that pan-Arctic glaciers and ice caps have consistently lost mass since 2002 at an average rate of –174 ± 24 Gt yr^{-1} (Fig. 5.18), or ~66% of the annual mass loss from the Greenland Ice Sheet (including Greenland peripheral glaciers and ice caps) over the same period (section 5e). Uncertainties in the GRACE measurements were estimated at two standard deviations and include corrections for glacial isostatic adjustment and terrestrial hydrology as per Wouters et al. (2019). An increase in the rate of annual mass loss over the 19-year period (2002–21), relative to the previously reported

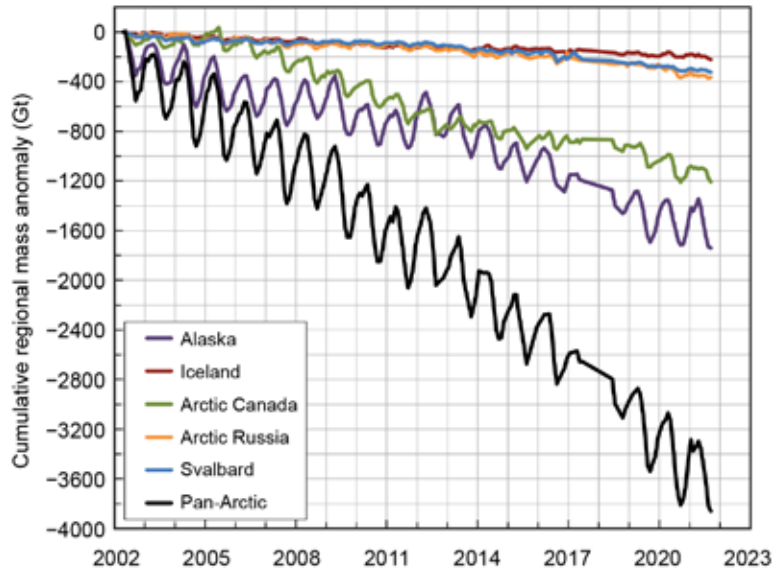

Fig. 5.18. Cumulative changes in regional total stored water (Gt) for 2002–21 derived from GRACE (https://www.nasa.gov/mission_pages/Grace/index.html) and GRACE-FO (https://gracefo.jpl.nasa.gov/) satellite gravimetry for the five regions shown in Fig. 5.15 and for the total of these five regions (i.e., pan-Arctic). Linear interpolation is applied through a measurement gap between the GRACE and GRACE-FO missions from Jul 2017 to May 2018.

annual average of –165 ± 26 Gt yr^{-1} (Wolken et al. 2020) for 2002–16, was driven largely by extreme mass losses of –432 ± 28 Gt in the 2018/19 balance year. Sustained losses in 2019/20 (–272 ± 30 Gt) were influenced primarily by Arctic Canada (44%) and the Russian Arctic (27%) where glaciers and ice caps lost mass about five times faster than the 2002–21 average. For the 2020/21 balance year, near-zero change in glacier mass was measured across both the Alaska (–24 ± 46 Gt) and Arctic Canada (+3 ± 23 Gt) regions. Total loss of –752 ± 52 Gt from pan-Arctic glaciers and ice caps between September 2018 and August 2021 contributed 2.05 ± 0.14 mm to global sea level rise, or 0.69 ± 0.05 mm yr^{-1} over this 3-year period.

g. Terrestrial snow cover—L. Mudryk, A. Elias Chereque, C. Derksen, K. Luojus, and B. Decharme

Many components of the Arctic land surface are directly influenced by snow cover from autumn through spring, including the surface energy budget and ground thermal regime, with implications on the carbon cycle, permafrost, and terrestrial and freshwater ecosystems (Brown et al. 2017; Meredith et al. 2019 and references therein). Even following the snow cover season, the influence of spring snow melt timing persists through impacts on river discharge timing and magnitude, surface water, soil moisture, vegetation phenology, and fire risk (Meredith et al. 2019).

Historical snow cover extent (SCE) anomalies during spring are shown separately for the North American and Eurasian terrestrial sectors of the Arctic in Fig. 5.19 relative to the 1981–2010 baseline (data from the NOAA snow chart climate data record; Robinson et al. 2012). In 2021, Eurasian Arctic SCE anomalies were strongly negative during both May (fifth lowest in the record since 1967) and June (third lowest). North American Arctic SCE anomalies in 2021 were also below average (14th and 16th lowest, respectively).

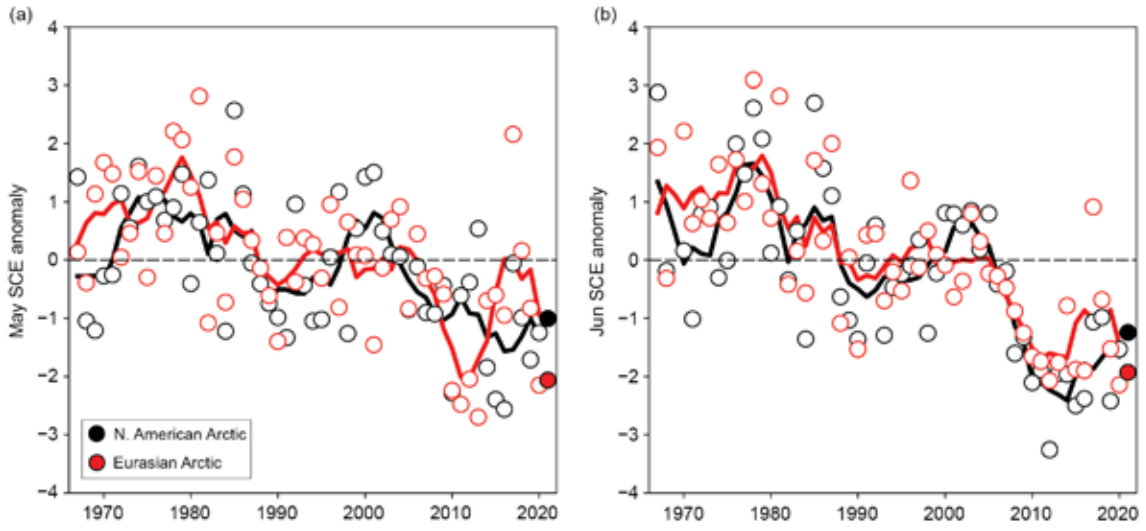

Fig. 5.19. Monthly snow cover extent (SCE) anomalies for Arctic terrestrial land areas (> 60°N) for (a) May and (b) Jun from 1967 to 2021. Anomalies are relative to the average for 1981–2010 and standardized (each observation differenced from the mean and divided by the standard deviation, and thus unitless). Solid black and red lines depict 5-yr running means for North America and Eurasia, respectively. Filled circles are used to highlight 2021 anomalies. (Source: Robinson et al. 2012.)

Snow cover duration (SCD) anomalies (1999–2021 baseline) across the Arctic region for the 2020/21 snow season are shown in Figs. 5.20a,b as percent differences relative to the climatological number of snow-free days (data from the NOAA daily Interactive Multisensor Snow and Ice Mapping System snow cover product; U.S. National Ice Center 2008). Anomalies in the total number of days with snow cover were computed separately for each half of the snow season: August 2020 to January 2021, referred to as "onset period," and February to July 2021, referred to as "melt period." Onset anomalies indicate snow cover during autumn 2020 began later than normal over much of Eurasia, particularly in eastern Siberia, as well as over much of Alaska and the western

Canadian Arctic (Fig. 5.20a). Spring 2021 (Fig. 5.20b) had early snow melt and hence shorter snow cover duration over almost the entire Arctic. In particular, across broad expanses of Eurasia the duration of the spring snow-free period was 30–50% longer than normal. The early Eurasian melt in 2021 was driven by persistent, above-average temperatures during April–June (section 5b).

Snow water equivalent (SWE; equivalent mass where the snowpack is converted to water) characterizes the amount of snow at a location as well as the contribution of that snow to the hydrological cycle once it melts. March–June SWE fields were obtained from four daily-frequency gridded products over the 1981–2021 period: (1) the European Space Agency Snow CCI SWE version1 product derived through a combination of satellite passive microwave brightness temperatures

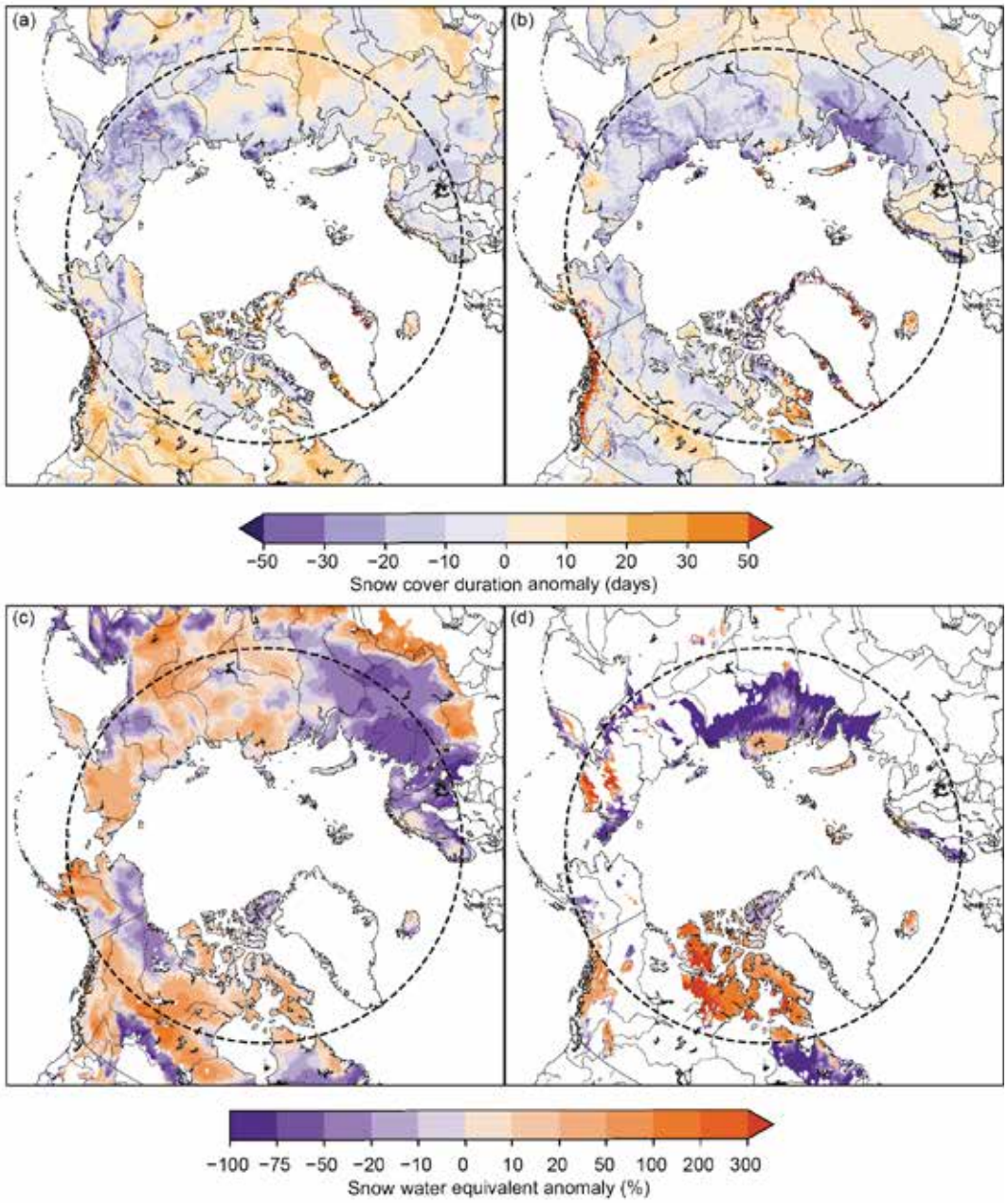

Fig. 5.20. Snow cover duration (SCD) anomalies (% difference relative to climatological number of snow-free days for the 1999–2021 baseline) for the 2020/21 snow year: (a) snow onset period (Aug 2020–Jan 2021) and (b) snow melt period (Feb 2021–Jul 2021). Purple (orange) indicates fewer (more) days with snow cover relative to the 1999–2021 mean. Snow water equivalent (SWE) anomalies (% difference from the 1981–2010 baseline) in 2021 for (c) Apr and (d) Jun. Purple (orange) indicates less (more) snow than average. Latitude 60°N marked by gray dashed circle; land north of this defines the Arctic terrestrial area considered in this study. (Sources: (a,b) U.S. National Ice Center (2008); (c,d) four SWE products from Snow CCI [Luojus et al. 2020], MERRA2 [GMAO 2015]; ERA5 [Muñoz Sabater 2019], Crocus [Brun et al. 2013].)

and climate station snow depth observations (Luojus et al. 2020); (2) the Modern-Era Retrospective Analysis for Research and Applications version 2 (MERRA-2, GMAO 2015) daily SWE fields; (3) SWE output from the ERA5-Land analysis (Muñoz Sabater 2019); and (4) the physical snowpack model Crocus (Brun et al. 2013) driven by ERA5 meteorological forcings. Reduced availability of climate station snow depth measurements limits the accuracy of the Snow CCI SWE product during May and June, hence it is only used during March and April. An approach using gridded products is required because in situ observations are too sparse to be representative of hemispheric snow conditions, especially in the Arctic.

For April, the SWE fields from each product are aggregated across Arctic land regions (> 60°N) for both North American and Eurasian sectors and standardized relative to the 1981–2010 baseline to produce standardized April snow mass anomalies. The ensemble mean anomalies and the range of estimates among the products are presented in Fig. 5.21. April is chosen because it is the approximate seasonal snow mass peak for the terrestrial pan-Arctic region, reflecting total snowfall accumulations since the preceding autumn before increasing temperatures during May and June lead to melt. The 2021 anomalies highlighted in Fig. 5.20 indicate above-normal total snow accumulation during the 2020/21 snow season in the North American Arctic and slightly below-average accumulation over the Eurasian Arctic. Figure 5.20c illustrates the SWE spatial distribution during both April and June, presented as percent differences of the ensemble-mean field relative to the 1981–2010 baseline. While snow accumulation across Eurasia was near-normal through March (not shown), the high spring temperatures (mentioned above) began to drive SWE reductions across western Eurasia by April (also see April–June temperature anomaly pattern in section 5b). Eastern Eurasian SWE was still above normal in April as seen in Fig 5.20 but decreased to below normal by May (not shown; also see April–June temperature anomaly pattern in section 5b). In contrast to Eurasia, SWE across North America generally remained above normal through June, particularly in the Canadian Arctic Archipelago (Fig. 5.20d). However, even where SWE was seasonally above average, complete snow melt tended to occur slightly earlier than usual over most of the region. This combination of increased snow accumulation (expressed as April SWE in Fig. 5.20c) but early snow melt (expressed by shorter snow cover duration in Fig. 5.20b) is consistent with the expected changes to Arctic snow cover in a warmer Arctic (Meredith et al. 2019) and also reflected in earlier and larger peak river discharge as observed over Eurasia during spring 2020 (Holmes et al. 2021).

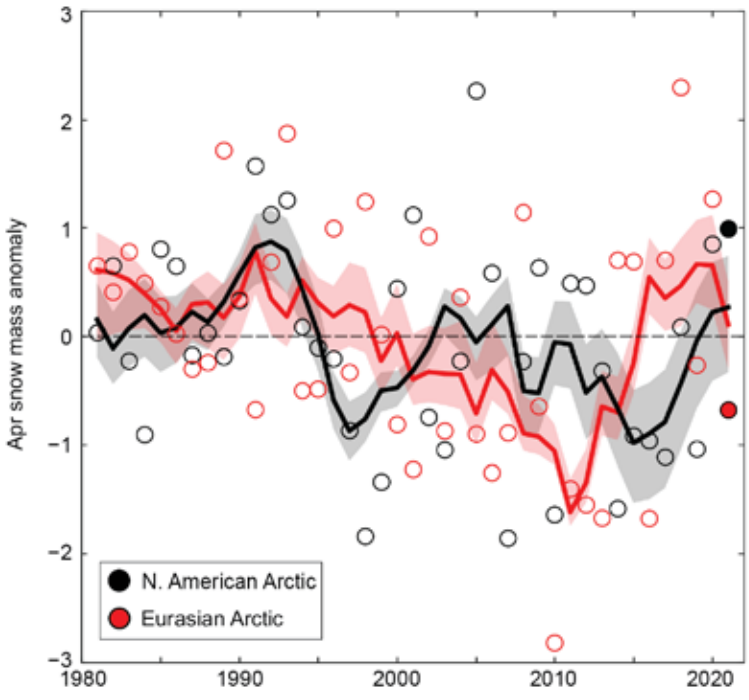

Fig. 5.21. Mean April snow mass anomalies for Arctic terrestrial areas calculated for North American (black) and Eurasian (red) sectors of the Arctic for 1981–2021. Anomalies are relative to the average for 1981–2010 and standardized (each observation differenced from the mean and divided by the standard deviation, and thus unitless). Filled circles are used to highlight 2021 anomalies. Solid black and red lines depict 5-yr running means for North America and Eurasia, respectively, and the spread among the running means for individual datasets is shown in shading. (Sources: four SWE products from Snow CCI [Luojus et al. 2020], MERRA2 [GMAO 2015]; ERA5 [Muñoz Sabater 2019], and Crocus [Brun et al. 2013].)

In summary, snow accumulation during the 2020/21 winter was near-normal across the Eurasian Arctic and above normal across the North American Arctic. Despite no significant negative trend in

snow mass (Fig. 5.21), spring snow extent has been persistently below normal for the last 15 years (Fig. 5.19), reflecting earlier snow melt. Since 2006, North American June SCE has been below the long-term average every year, while Eurasian June SCE has been below the long-term average for all but one year.

h. Permafrost—S. L. Smith, V. E. Romanovsky, K. Isaksen, K. E. Nyland, A. L. Kholodov, N. I. Shiklomanov, D. A. Streletskiy, D. S. Drozdov, G. V. Malkova, and H. H. Christiansen

Permafrost refers to earth materials (e.g., bedrock, mineral soil, organic matter) that remain at or below 0°C for at least two consecutive years and underlies extensive regions of the high-latitude landscape (Brown et al. 1997). Overlying the permafrost is the active layer, which thaws and refreezes annually. Permafrost, especially where it contains large volumes of ice, can play a critical role in the stability of Arctic landscapes. Warming of permafrost, active layer thickening, and ground ice melt cause changes in surface topography, hydrology, and landscape stability, with implications for Arctic infrastructure and ecosystem integrity and human lifestyles (Romanovsky et al. 2017; Bjella 2019; Wolken et al. 2021). Changes in permafrost conditions can also affect the rate of carbon dioxide and methane release to the atmosphere, with the potential to accelerate global warming (Schuur 2020).

Permafrost conditions respond to shifts in the surface energy balance through a combination of interrelated changes in ground temperature and active layer thickness (ALT). Ground temperatures fluctuate seasonally near the surface, while below the depth of seasonal temperature variation, ground temperature reflects longer-term changes in climate. Long-term changes in permafrost temperatures are driven by changes in air temperature (Romanovsky et al. 2017); however, permafrost temperature trends also show local variability due to other important influences such as snow cover, vegetation characteristics, and soil moisture. Monitoring sites across the Arctic (Fig. 5.22) have been recording ground temperature in the upper 30 m for up to five decades, providing critical data on changes in permafrost stability. Observed changes in ALT are more reflective of shorter-term (year-to-year) fluctuations in climate and are especially sensitive to changes in summer air temperature and precipitation.

Data collection was affected less by COVID-19 related travel restrictions in 2021 compared to 2020. However, for some sites there has been data loss for 2020 and 2021 (Figs. 5.23, 5.24).

1) PERMAFROST TEMPERATURES

Permafrost temperatures continue to increase across the Arctic. Greater increases in permafrost temperature are generally observed in colder permafrost at higher latitudes (Smith et al. 2021, 2022), where the largest increases in air temperature were observed (Figs. 5.22, 5.23). Although permafrost temperatures in 2021 were higher than those observed in 2020 and the highest on record at many sites, recent cooling occurred at some sites (Fig. 5.23, Table 5.1). In northern Alaska for example, permafrost temperatures in 2021 were up to 0.2°C lower than in 2020 at some sites while at others, such as Utqiaġvik (Barrow), permafrost temperatures continue to increase (Fig. 5.23a). Observed permafrost cooling was a result of decreasing mean annual air temperatures (e.g., at Deadhorse station air temperatures were 2.5°C lower in 2020 and 2021 compared to 2018 and 2019). Lower permafrost temperatures were also observed in northwestern Canada in the northern Mackenzie region (NC–01). In the Alaskan interior, the 2021 permafrost temperature was higher at all sites except for Old Man, where the temperature was slightly lower in 2021 than in 2020 (Fig. 5.23b). In the Nordic high-Arctic cold permafrost of Svalbard, each year since 2005 has been warmer than the previous one until 2019/20 (Smith et al. 2021). Although permafrost temperatures decreased in 2021 (Fig. 5.23d), these values were the third highest in the longest record dating back to 1998 (Janssonhaugen).

Throughout the Arctic, the response of permafrost with temperatures close to 0°C (i.e., warm permafrost sites at temperatures > –2°C) is slower (generally < 0.3°C decade^{-1}) than

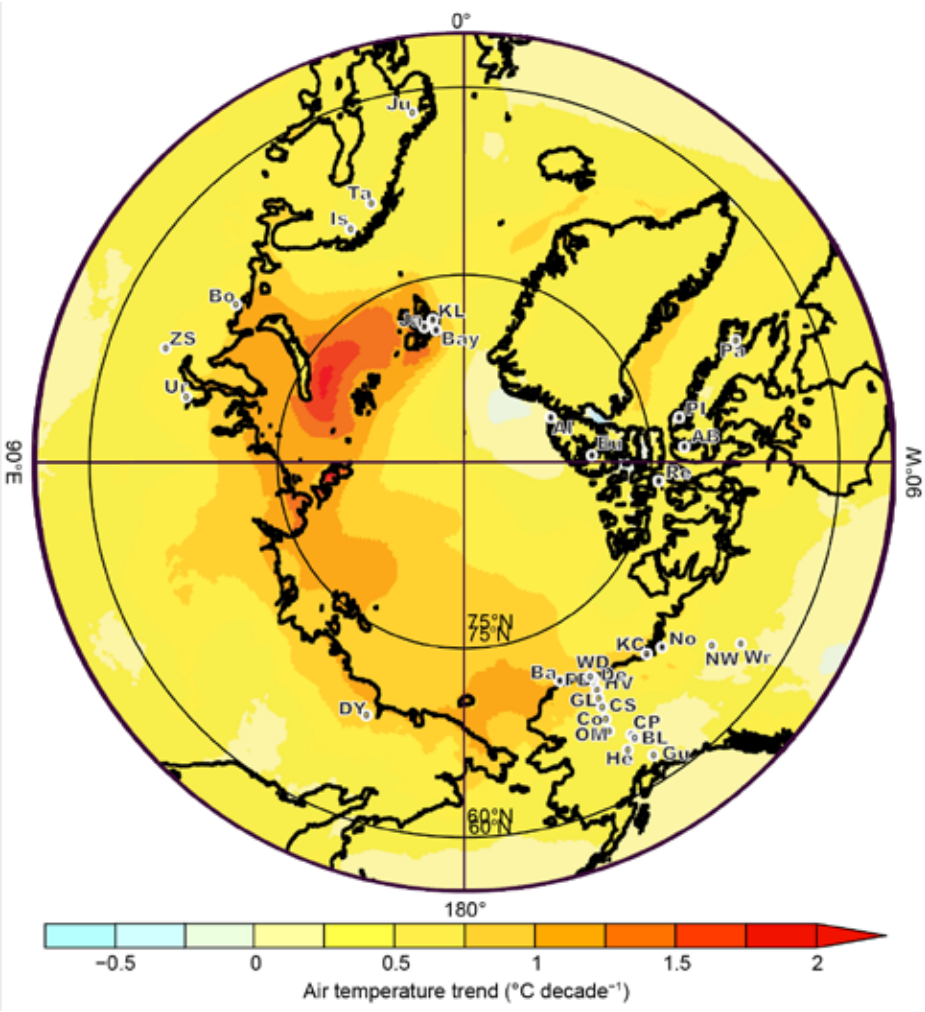

Fig. 5.22. Locations of the permafrost temperature monitoring sites (for which data are shown in Fig. 5.23), superimposed on average surface air temperature trend (°C decade^{-1}) during 1981–2020 from the ERA5-reanalysis (Hersbach et al. 2020). Reanalysis data provided by the COPERNICUS climate data store (https://cds.climate.copernicus.eu). See Table 5.1 for site names. Information about these sites is available at http://gtnpdatabase.org/, http://permafrost.gi.alaska.edu/sites_map, https://www2.gwu.edu/~calm/.

colder permafrost sites due to latent heat effects related to melting ground ice. At cold continuous permafrost sites in the Beaufort-Chukchi region, permafrost temperatures have increased by 0.33–0.76°C decade^{-1} (Fig. 5.23a; Table 5.1). In the eastern and high Canadian Arctic, similar increases (0.4–0.7°C decade^{-1}) have been observed (Fig. 5.23c; Table 5.1). Permafrost on Svalbard at the Janssonhaugen and Kapp Linne sites (Table 5.1), has warmed by 0.7°C decade^{-1} since 2000.

Although rates of warming were lower in warm permafrost, temperatures in these locations generally increased. In the discontinuous permafrost regions of Scandinavia (Juvvasshøe and Iskoras), warming reported by Etzelmüller et al. (2020) is continuing, with 2021 permafrost temperatures being the highest measured (Fig. 5.23d). Similar rates of warming were found for warm permafrost in Russia (e.g., Bolvansky #56; Malkova et al. 2022) and northwestern North America (Figs. 5.23b,d).

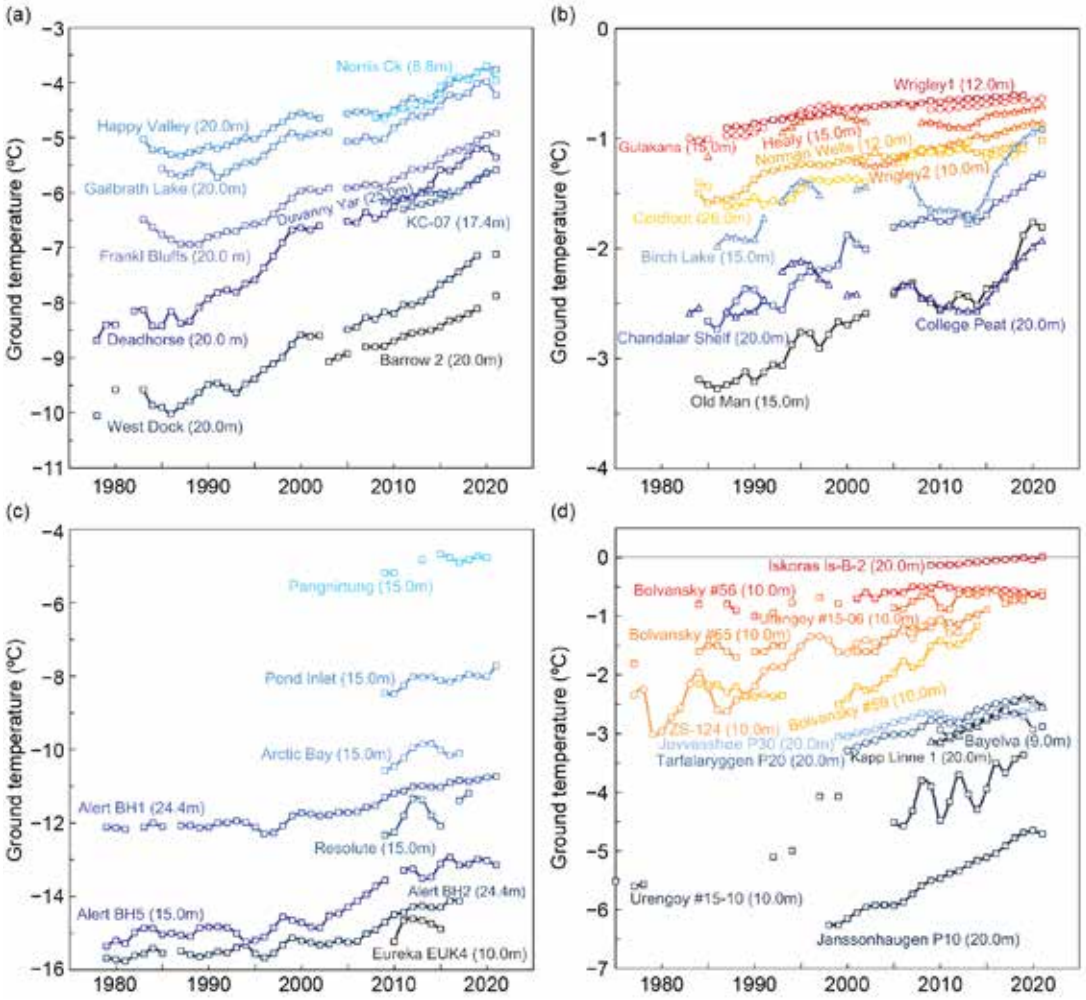

Fig. 5.23. Time series of mean annual ground temperature (°C) at depths of 9–26 m below the surface at selected measurement sites that fall roughly into Adaptation Actions for a Changing Arctic Project priority regions (see Romanovsky et al. 2017): (a) cold continuous permafrost of northwestern North America and northeastern East Siberia (Beaufort–Chukchi region); (b) discontinuous permafrost in Alaska and northwestern Canada; (c) cold continuous permafrost of eastern and High Arctic Canada (Baffin Davis Strait); (d) continuous to discontinuous permafrost in Scandinavia, Svalbard, and Russia/Siberia (Barents region). Temperatures are measured at or near the depth of zero annual amplitude where the seasonal variations of ground temperature are less than 0.1°C. Note differences in y-axis value range. Borehole locations are shown in Fig. 5.22. (Sources: Data are updated from Christiansen et al. 2010; Smith et al. 2021; Boike et al. 2018; and Etzelmüller et al. 2020.)

Table 5.1. Rate of change in mean annual ground temperature (°C decade^{-1}) for permafrost monitoring sites shown in Fig. 5.22. For sites where measurements began prior to 2000, the rate of change for the entire available record and the period after 2000 are provided. The periods of record are shown in parenthesis below the rates of change. The names of the stations with record high temperatures in 2021 are shown in red. * denotes sites not reporting in 2021.

Subregions	Sites	Entire Record	Since 2000
Beaufort-Chukchi Region			
North of East Siberia	Duvany Yar (DY)*	NA	+0.44 (2009–20)
Alaskan Arctic plain	West Dock (WD), Deadhorse (De), Franklin Bluffs (FB), Barrow (Ba)	+0.40 to +0.76 (1978–2021)	+0.47 to +0.67 (2000–21)
Northern foothills of the Brooks Range, Alaska	Happy Valley (HV), Galbraith Lake (GL)	+0.33 to +0.36 (1983–2021)	+0.36 to +0.47 (2000–21)
Northern Mackenzie Valley	Norris Ck (No), KC-07(KC)	NA	+0.7 (2008–21)
Discontinuous Permafrost Alaska and Northwestern Canada			
Southern foothills of the Brooks Range, Alaska	Coldfoot (Co), Chandalar Shelf (CS), Old Man (OM)	+0.12 to +0.36 (1983–2021)	+0.21 to +0.4 (2000–21)
Interior Alaska	College Peat (CP), Birch Lake (BL), Gulkana (Gu), Healy (He)	+0.09 to +0.30 (1983–2021)	+0.04 to +0.26 (2000–21)
Central Mackenzie Valley	Norman Wells (NW), Wrigley (Wr)	Up to +0.1 (1984–2021)	<+0.1 to +0.2 (2000–21)
Baffin Davis Strait Region			
Baffin Island	Pangnirtung (Pa)*, Pond Inlet (PI)	NA	+0.4 (2009–21)
High Canadian Arctic	Resolute (Re)*	NA	+0.7 (2009–18)
High Canadian Arctic	Alert (Al) @15m Alert (Al) @24m	+0.6 +0.4 (1979–2021)	+0.9 +0.6 (2000–21)
Barents Region			
North of West Siberia	Urengoy 15-06 and 15-08 (Ur)*	+0.20 to +0.48 (1974–2021)	+0.08 to +0.81 (2005–21)
Russian European North	Bolvansky 56, and 65 (Bo)	+0.09 to +0.27 (1984–2021)	+0.02 to +0.51 (2001–21)
Svalbard	Janssonhaugen (Ja), Bayelva (Bay), Kapp Linne 1 (KL)	+0.7 (1998–2021)	+0.5 to +0.7 (2000–21)
Northern Scandinavia	Tarfalarggen (Ta)*, Iskoras Is-B-2 (Is)	NA	+0.1 to +0.5 (2000–21)
Southern Norway	Juvvasshøe (Ju)	+0.2 (1999–2021)	+0.2 (2000–21)

2) ACTIVE LAYER THICKNESS

Three common methods for monitoring active layer thickness (ALT) are: direct measurement with mechanical probing, interpolation of the maximum seasonal depth of the 0°C isotherm from borehole temperatures, or thaw tube records. The majority of sites comprising trends shown in Fig. 5.24 are based on mechanical probing to determine the top of permafrost (Shiklomanov et al. 2012).

Distinct positive trends in ALT are evident since 1996 for the interior of Alaska, Greenland, Svalbard, the Russian European North, and West Siberia (Fig. 5.24), but trends are less apparent for the Alaskan North Slope, Canada, and East Siberia (Smith et al. 2022). Sites in interior Alaska and Greenland experienced ALTs in 2021 well above the 2003 to 2012 mean, similar to the preceding three years. Positive anomalies in 2021 were also reported for the Russian European North and West and East Siberia (Kaverin et al. 2021). The interior of Alaska and the Russian European North are experiencing the greatest rates of ALT increase over the 25-year observation period at 0.015 and 0.013 m yr^{-1}, respectively. The reduced ALT reported in 2021 for sites in Svalbard and East Siberia, for example, could be due to short-term cooling, as significant thickening trends have been reported for these regions (Strand et al. 2021; Abramov et al. 2021).

Average ALT in 2021 for the North Slope of Alaska and Chukotka were within 0.01 m of the 2003 to 2012 mean values. Thaw-induced consolidation (subsidence), which is common in ice-rich permafrost, is not accounted for in manual probing measurements, and these data alone may underestimate ALT (Nyland et al. 2021). Correcting manual probing data for ground surface displacement can therefore allow better detection of climate trends.

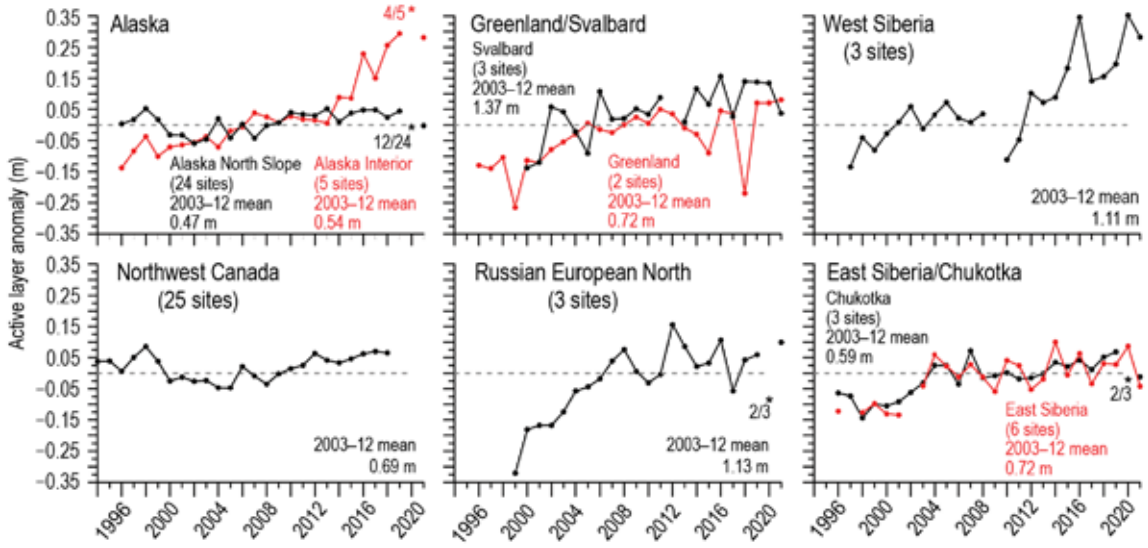

Fig. 5.24. Long-term active layer thickness anomalies in six different Arctic regions as observed by the Circumpolar Active Layer Monitoring (CALM) program. The data are shown as annual anomalies (m) relative to the mean value for the reference period 2003–12. Positive and negative anomaly values indicate the active layer is thicker or thinner than the 10-yr mean values, respectively. The number of sites varies by region (numbers provided on figure) because only sites with > 20 years of continuous thaw depth observations from the end of the thaw season were included. Asterisks on the figure represent 2020 and 2021 data, as observations from fewer sites (number provided beside asterisks) were possible due to pandemic-related restrictions. Note that there are no ALT data for northwestern Canada after 2018 due to travel restrictions (measurements are made by thaw tubes and observations represent maximum thaw depths from the previous year). Site-specific data and metadata are available at www2.gwu.edu/~calm/.

i. Tundra greenness—G. V. Frost, M. J. Macander, U. S. Bhatt, L. T. Berner, J. W. Bjerke, H. E. Epstein, B. C. Forbes, S. J. Goetz, M. M. P. D. Heijmans, M. J. Lara, R. Í Magnússon, T. Park, G. K. Phoenix, J. E. Pinzon, S. P. Serbin, H. Tømmervik, C. J. Tucker, D. A. Walker, and D. Yang

Earth's northernmost continental landmasses and island archipelagos are home to the Arctic tundra biome, a 5.1 million km^2 region characterized by low-growing, treeless vegetation adapted to short, cool summers (CAVM Team 2003). The Arctic tundra biome has become a "hotspot" of global environmental change because vegetation and underlying permafrost soils are strongly influenced by ongoing climatic warming and sea ice loss on the nearby Arctic Ocean (Bhatt et al. 2021; sections 5b,d). In the late 1990s, a strong increase in the productivity of tundra vegetation began to emerge in global satellite observations, a phenomenon known as "the greening of the Arctic." Arctic greening is dynamically linked with Earth's changing climate, permafrost, seasonal snow, and sea ice cover, and has motivated multi-disciplinary scientific efforts to understand its causes and consequences (Myers-Smith et al. 2020).

Tundra greenness has been monitored from space for 40 years using the Normalized Difference Vegetation Index (NDVI), a spectral metric that is strongly correlated with the biomass of aboveground vegetation (Raynolds et al. 2012). Here, we analyze tundra greenness trends using two spaceborne datasets. The first satellite record of tundra greenness began in 1982 using the Advanced Very High Resolution Radiometer (AVHRR), a sensor that continues to operate onboard polar-orbiting satellites. Tundra greenness has also been independently monitored since 2000 by the Moderate Resolution Imaging Spectroradiometer (MODIS), a separate satellite-based sensor with improved calibration and 500-m spatial resolution. For AVHRR, we analyze the Global Inventory Modeling and Mapping Studies 3g V1.2 dataset (GIMMS-3g+) that is produced using daily observations at approximately 8-km spatial resolution (Pinzon and Tucker 2014). For MODIS, we analyze daily Nadir Bidirectional Reflectance Distribution Function Adjusted Reflectance data at 500-m spatial resolution (MCD43A4, version 6; Schaaf 2021). All data were masked to include only ice-free land within the extent of the Circumpolar Arctic Vegetation Map (CAVM Team 2003; as shown in Figs. 5.25 and 5.27). We summarize the AVHRR and MODIS records for annual maximum NDVI (MaxNDVI), representing the annual peak greenness which is achieved in midsummer.

Both AVHRR and MODIS records indicate that MaxNDVI increased across most of the Arctic tundra biome since 1982 and 2000, respectively (Figs. 5.25a,b). Several Arctic regions display particularly strong trends in both records. In North America, increases have been strongest in

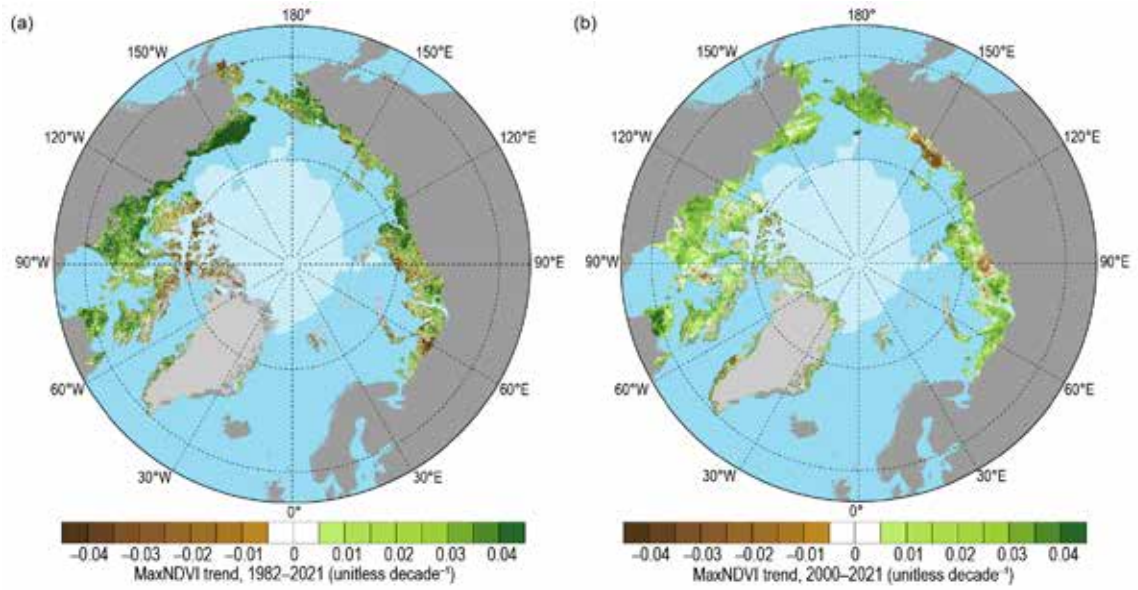

Fig. 5.25. Magnitude of the MaxNDVI trend calculated as the change decade^{-1} via ordinary least squares regression for (a) 1982–2021 based on the AVHRR GIMMS 3-g+ dataset and (b) 2000–21 based on the MODIS MCD43A4 dataset. The 2021 minimum sea ice extent is indicated by light shading in each panel.

northern Alaska and mainland Canada, while flat or negative trends are evident in parts of the Canadian Arctic Archipelago and southwestern Alaska. In Eurasia, strong greening has occurred in Chukotka, but MaxNDVI declines are evident in the East Siberian Sea sector and parts of the Taymyr Peninsula. AVHRR and MODIS have recorded divergent trends in northwestern Siberia and the European Arctic, potentially due to the different observational periods of the two records.

In 2021, circumpolar mean MaxNDVI declined from the record high values set the previous year for both datasets. AVHRR-observed MaxNDVI declined 8.3% from 2020; nonetheless, the 2021 value still exceeded the 1991–2010 mean value and represented the 15th highest value recorded in the full 40-year record (Fig. 5.26). The 2021 decline in MaxNDVI from 2020 was less pronounced for MODIS (2.7%); the 2021 value was the second highest value in the 22-year record for that sensor, and circumpolar values have now exceeded the 2000–20 mean for the last 11 growing seasons. Circumpolar MaxNDVI time series for the two sensors show virtually identical trends for the period of overlap (2000–20), although the AVHRR record displays higher variability (i.e., "noise"), particularly over the last 10 years of the record. This is likely due in part to AVHRR's lower spatial resolution and less advanced calibration compared to MODIS.

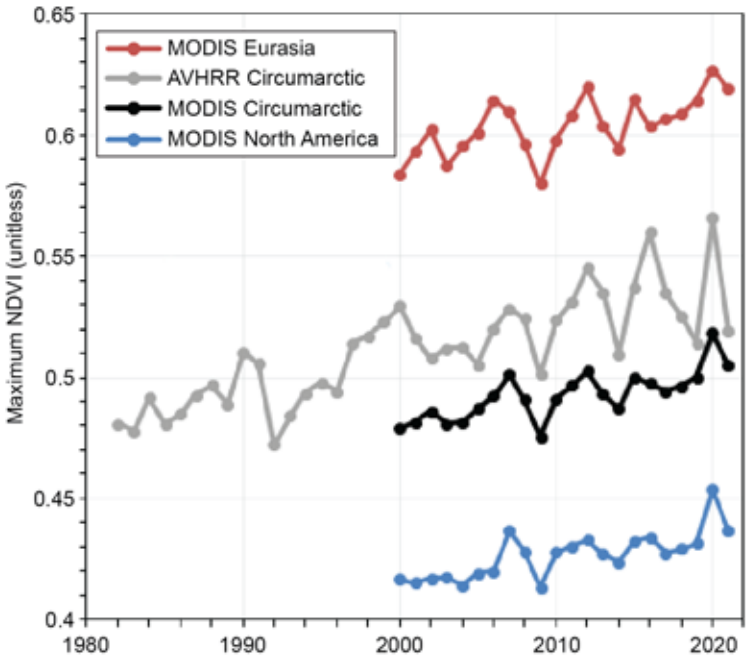

Fig. 5.26. Time series of MaxNDVI from the MODIS MCD43A4 (2000–21) dataset for the Eurasian Arctic (red), North American Arctic (blue), and the circumpolar Arctic (black), and from the long-term AVHRR GIMMS-3g+ dataset (1982–2021) for the circumpolar Arctic (gray).

Regional contrasts in greenness highlight the dynamic linkages between tundra ecosystems and the local characteristics of sea ice, permafrost, seasonal snow, soil composition and moisture, disturbance regimes, wildlife, and human activities (Campbell et al. 2021; Heijmans et al. 2022; Seider et al. 2022). For example, in 2021, several regional MaxNDVI anomalies suggest potential relationships to surface air temperature and sea ice extent (Fig. 5.27). Strong positive and negative MaxNDVI anomalies were evident in the Taymyr Peninsula and the Canadian Arctic Archipelago, respectively, coincident with unusually warm and cool growing season temperatures in the two regions (section 5b).

What biological and physical mechanisms underlie satellite observations of Arctic greening, and what types of change might be apparent to a field observer? Persistent increases in the abundance and height of Arctic shrubs have been widely documented across the Arctic, with wide-ranging impacts to tundra biomass, biodiversity, surface energy balance, permafrost temperatures, biogeochemical cycling, and wildlife (Kropp et al. 2021; Way and Lapalme 2021; Mekonnen et al. 2021; Tape et al. 2021). Circumpolar greening also signals changes to the timing of phenological events and the duration of the Arctic growing season (Parmentier et al. 2021; Karlsen et al. 2021; see section 2h4), with implications for seasonal movements and life-history events of migratory animals such as caribou and reindeer (Severson et al. 2021).

Although spaceborne observations provide unequivocal evidence of Arctic greening, substantial regional variability exists, and some parts of the Arctic exhibit little or no long-term trend (Berner et al. 2020; Huemmrich et al. 2021). Some regions, most notably the East Siberian Sea sector, exhibit declining tundra productivity, which is thought to be related to surface subsidence

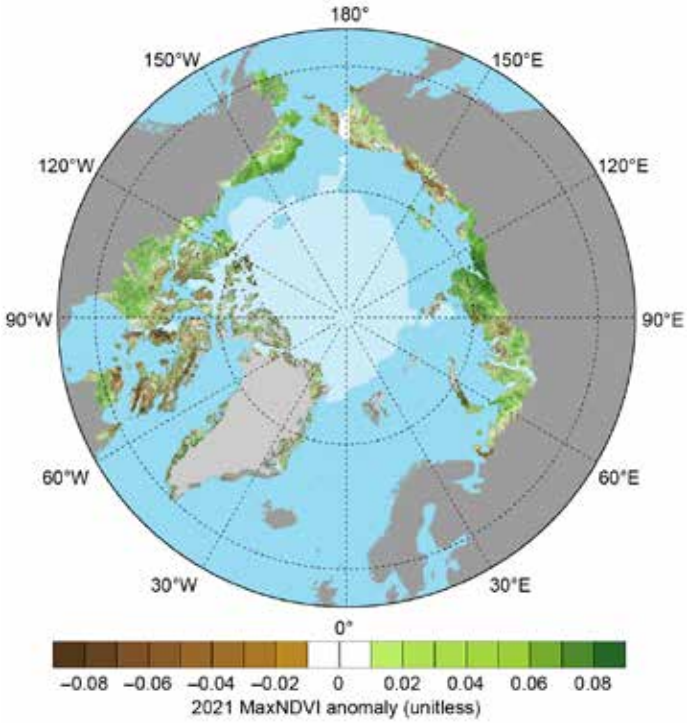

Fig. 5.27. Circumpolar MaxNDVI anomalies for the 2021 growing season relative to mean values (2000–20) from the MODIS MCD43A4 dataset. The 2021 minimum sea ice extent is indicated by light shading.

and increased surface water resulting from thaw of ice-rich permafrost (van Huissteden et al. 2021; Veremeeva et al. 2021; section 5h). Wildfire, extreme weather events, herbivory, and other ecological disturbances introduce additional complexity in Arctic greenness trends (Gaglioti et al. 2021; Magnússon 2021; Veselkin 2021; Talucci et al. 2022). While warming is likely to continue to drive Arctic greening, extreme events and other causes of regional or localized NDVI decline are also increasing in frequency (Christensen et al. 2021), highlighting the emergence of increased variability as a component of Arctic climate change.

j. Ozone and UV radiation—G. H. Bernhard, V. E. Fioletov, J.-U. Grooß, I. Ialongo, B. Johnsen, K. Lakkala, G. L. Manney, R. Müller, and T. Svendby

Past emissions of man-made chlorine-containing substances, such as chlorofluorocarbons (CFCs), have caused substantial chemical depletion of stratospheric ozone (WMO 2018). The resulting ozone loss led to increases of ultraviolet (UV) radiation at Earth's surface with adverse effects on human health and the environment (Barnes et al. 2019; EEAP 2019). The chemical destruction of polar ozone occurs within a cold stratospheric cyclone known as the polar vortex, which forms over the North Pole every winter (WMO 2018). The polar vortex between November 2020 and April 2021 was weakened by a Sudden Stratospheric Warming (SSW; see Sidebar 5.2) event in early January 2021 that decreased depletion of stratospheric ozone in the Northern Hemisphere until at least April. A similar SSW event occurred in January 2013. The progressions of chemical ozone loss in the winters of 2012/13 and 2020/21 are therefore compared below.

1) OZONE

Chemical processes that drive ozone depletion in the polar stratosphere are initiated at temperatures below about 195 K (–78°C) at altitudes of approximately 15 to 25 km. These low temperatures lead to the formation of polar stratospheric clouds (PSCs), which act as a catalyst to transform inactive forms of chlorine-containing substances into active, ozone-destroying chlorine species such as chlorine monoxide (ClO).

Temperatures were low enough for PSC formation by mid-November 2020 as observed by the Aura Microwave Limb Sounder (MLS, 2005–present; Waters et al. 2006). Activation of chlorine started in late November 2020, and ClO concentrations at ~16 km altitude between 20 December 2020 and 10 January 2021 were exceeded only by those in 2012/13 in the MLS data record (Fig. 5.28a). If cold conditions had persisted beyond December 2020, this could have led to large Arctic ozone depletion in spring 2021, like that observed in spring 2020 (Manney et al. 2020). Instead, similar to the behavior in 2012/13 (Manney et al. 2015a), an unusually early major SSW on 5 January 2021 warmed the lower stratosphere above temperatures at which active chlorine can be maintained. ClO concentrations subsequently declined to near-zero between 10 and 25 January as ClO was converted back to inactive forms of chlorine.

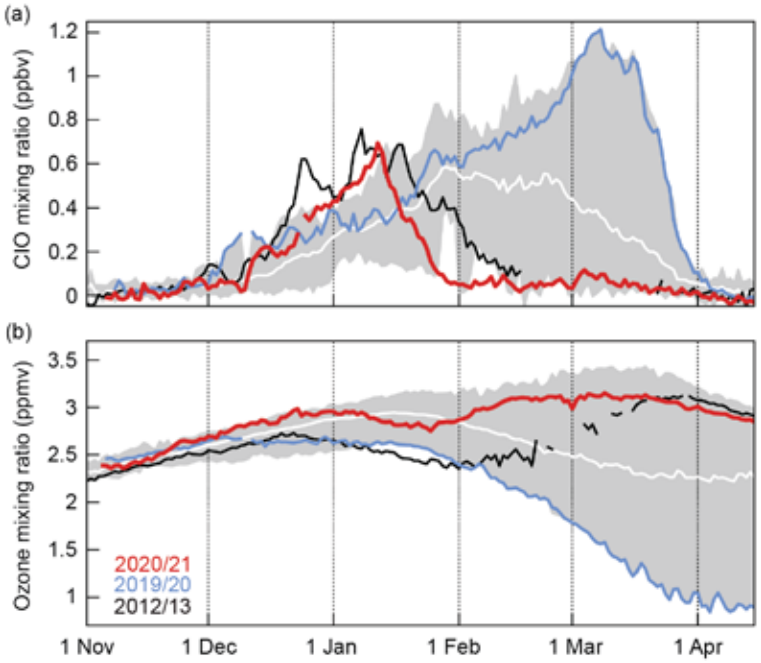

Fig. 5.28. Average (a) daytime ClO (expressed as ClO mixing ratio in ppbv) and (b) ozone concentrations (ozone mixing ratio in ppmv) measured by Aura MLS at an altitude of ~16 km for the area bounded by the Arctic stratospheric polar vortex. Data from 2012/13 (black), 2019/20 (blue), and 2020/21 (red) are compared with the average (solid white) and minimum/maximum range (gray shading) from 2004/05 to 2019/20, excluding 2012/13. Gaps in the 2012/13 record are periods where the polar vortex was not well defined (Manney et al. 2015a).

In both winters of 2012/13 and 2020/21, chemical ozone destruction involving ClO started in late December and continued through January, as evidenced by the decline in ozone mixing ratios (Fig. 5.28b). The rapid drop in ClO halted further chemical ozone loss in late January in both years, and ozone mixing ratios rebounded to be among the highest in the MLS record by mid-March. The faster rebound in 2021 compared to 2013 can be explained by the differences in the polar vortex structure between the two years and may also be related to differences in planetary wave activity (see Sidebar 5.2), which affects ozone transport from low to polar latitudes. The high ozone concentrations at ~16 km between mid-February and April 2021 were exceeded only by those in 2013 (Manney et al. 2015a), 2015 (Manney et al. 2015b), and 2019.

The evolution of ozone in 2020/21 is in stark contrast to that in 2019/20, when the lowest ozone values in the MLS record resulted from an exceptionally strong, cold, and persistent stratospheric polar vortex (e.g., Lawrence et al. 2020; Manney et al. 2020).

The early termination of chemical ozone loss in the lower stratosphere during winter/spring 2020/21 led to average Arctic total ozone columns (TOC; i.e., ozone amounts integrated from Earth's surface to the top of the atmosphere) between January and July. Figure 5.29 illustrates the variation in TOC between 1979 and 2021 for March by showing the minimum of the daily mean TOC within an area that encloses the polar vortex and is surrounded by the 63°N contour of "equivalent latitude" (Butchart and Remsberg 1986). March was selected because this has historically been the month with the largest potential for chemical ozone depletion in the Arctic (WMO 2018). In March 2021, the minimum Arctic daily TOC was 374 Dobson units (DU), which was identical to the average TOC since the start of satellite observations in 1979 and 2% (8 DU) above the average of 365 DU for the period of measurements (2005–present) by MLS and the Ozone Monitoring Instrument (OMI).

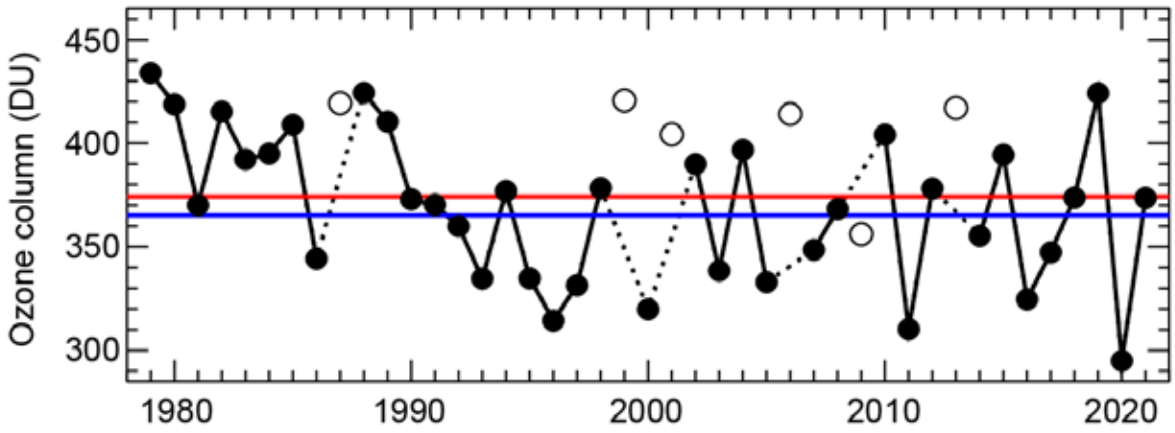

Fig. 5.29. Minimum of the daily average total ozone column (Dobson units, DU) for Mar poleward of 63°N equivalent latitude (Butchart and Remsberg 1986). Open circles represent years in which the polar vortex was not well-defined in Mar, resulting in relatively high values owing to mixing with lower latitude air masses and a lack of significant chemical ozone depletion. Red and blue lines indicate the average total ozone column for 1979–2020 and 2005–20, respectively. Ozone data for 1979–2019 are based on the combined NIWA-BS total column ozone database version 3.5.1 (Bodeker et al. 2021). Ozone data for 2020/21 are from the OMI. The graph is adapted from Müller et al. (2008) and WMO (2018), and updated using ERA5 reanalysis data (Hersbach et al. 2020) for determining equivalent latitude.

2) ULTRAVIOLET RADIATION

Ultraviolet radiation is quantified with the UV index (UVI), which measures the ability of UV radiation to cause erythema (sunburn) in human skin (WHO 2002). In addition to its dependence on TOC, the UVI depends on the sun angle, clouds, aerosols, and surface albedo (Weatherhead et al. 2005). In the Arctic, the UVI scale ranges from 0 to about 7; UVI values north of 80°N remain below 3. For comparison, the summertime UVI at midlatitudes may reach 12 ([Bernhard at al. 2022]).

Figures 5.30c,d quantify spatial differences in monthly average noontime UVIs from past (2005–20) averages based on measurements by OMI. UVI differences in March 2021 (Fig. 5.30c) varied by up to ± 58% but remained within 2 std. dev. of past observations, with few exceptions. The larger variability compared to TOC (Fig. 5.30a) can be explained by the added effect from clouds. UVIs in April 2021 (Fig. 5.30d) were elevated beyond 2 std. dev. north of Alaska (consistent with the low TOCs for this region; Fig. 5.30b), a small band east of Greenland, and a small region in Northwest Russia. Since TOCs for these regions were close to average, the elevated UVI was likely caused by unusually clear skies. While UVI anomalies assessed with satellite (OMI) data provide complete spatial coverage, they can sometimes indicate spurious anomalies of up to 59% (Bernhard et al. 2015), for example when the surface albedo (reflectivity) assumed in the retrieval algorithm (Tanskanen et al. 2003) deviates from the actual albedo. UVI anomalies for 2021 derived from OMI data generally agree with ground-based measurements at 10 Arctic and sub-Arctic sites (indicated in Figs. 5.30c,d) within ± 11%. The only exception is Eureka in April where measurements at the ground indicate a 14% larger anomaly than OMI data, likely due to the uncertainty in the OMI albedo climatology.

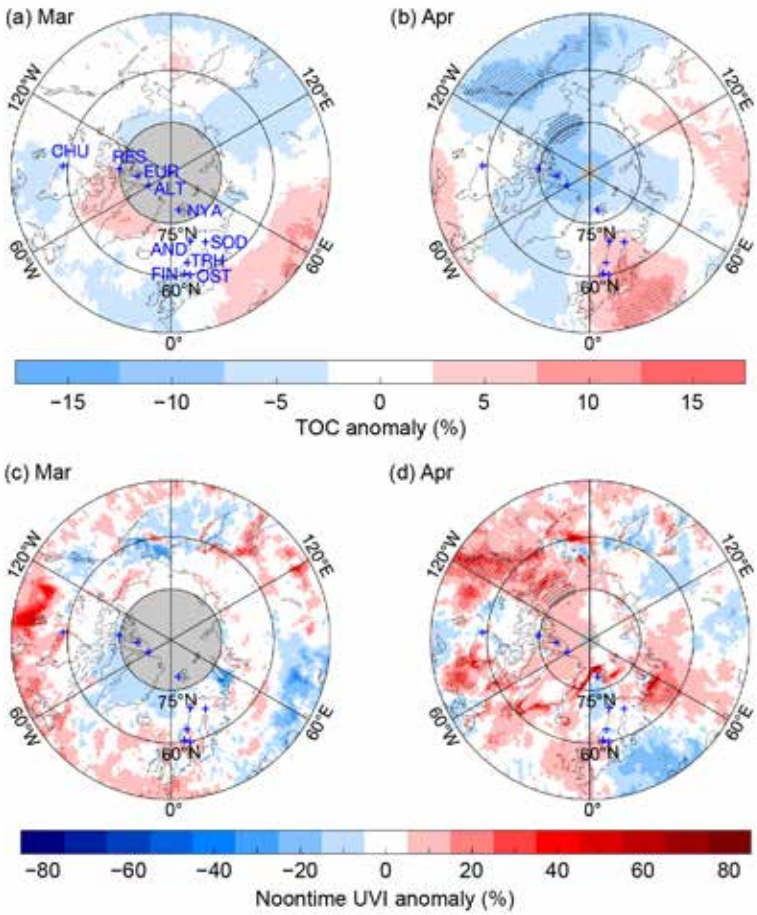

Fig. 5.30. Monthly mean anomaly maps of (a,b) TOC (%) and (c,d) noontime UVI (%) for Mar and Apr 2021 relative to 2005–20 means. Stippling indicates pixels where anomalies exceed 2 std. dev. Gray-shaded areas centered at the North Pole indicate latitudes where no OMI data are available because of polar darkness. Locations of ground stations are indicated by blue crosses in every map, with labels added to the first map. Maps are based on the OMTO3 Level 3 total ozone product (Bhartia and Wellemeyer 2002). Site abbreviations are ALT: Alert (83°N); EUR: Eureka (80°N); NYA: Ny-Ålesund (79°N); RES: Resolute (75°N); AND: Andøya (69°N); SOD: Sodankylä (67°N); TRH: Trondheim (63°N); FIN: Finse (61°N); OST: Østerås (60°N); and CHU: Churchill (59°N).

SIDEBAR 5.2: THE 2021 ARCTIC SUDDEN STRATOSPHERIC WARMING—A. H. BUTLER AND S. H. LEE

A major Sudden Stratospheric Warming (SSW) occurred in the Arctic on 5 January 2021 (Lee 2021). During an SSW, the climatological westerly winds of the wintertime polar stratosphere—the stratospheric polar vortex—decelerate and temperatures in the polar stratosphere rapidly increase (Baldwin et al. 2021). Large perturbations in stratospheric temperatures and winds can descend to the lower stratosphere where they persist for many weeks, affecting both the stratospheric ozone layer (section 5j), as well as the likelihood of cold Arctic air outbreaks and other weather extremes (Domeisen and Butler 2020). This sidebar describes the January 2021 SSW and its influence on stratospheric ozone and weather in the weeks that followed.

Cause and evolution of the event

Tropospheric and stratospheric winds are strongly coupled via interactions between the mean wind flow and planetary-scale atmospheric waves, which are generated primarily by land–sea contrasts, topography, and convective heating. Disturbances to the stratospheric polar vortex in the form of SSWs arise when these large-scale waves either amplify vertically from the troposphere into the stratosphere or when waves are created within the stratosphere from resonance (Baldwin et al. 2021).

In late December 2020, persistent tropospheric weather patterns led to the amplification of planetary-scale atmospheric

waves into the stratosphere. In particular, a low pressure system over the North Pacific and a high pressure system over the North Atlantic and Eurasia formed a "wavenumber-1" type pattern (i.e., one trough and one ridge around a latitude circle) that then amplified into the stratosphere. A wavenumber-2 pattern (i.e., two troughs and two ridges around a latitude circle) also contributed during the onset of the event (Lu et al. 2021).

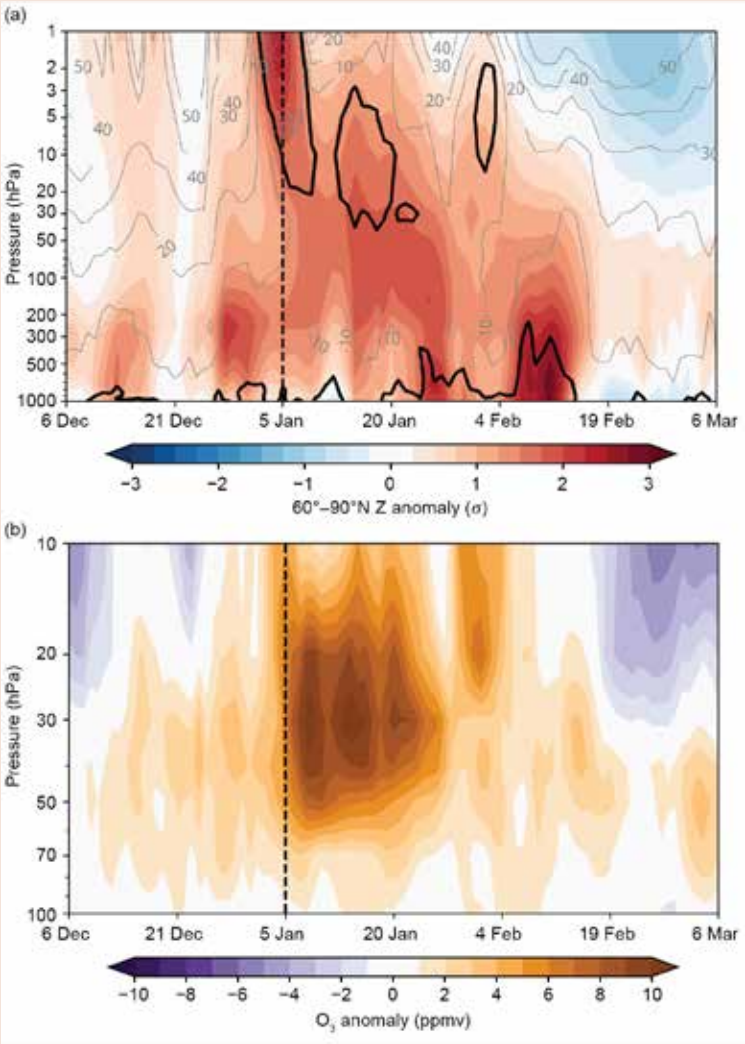

Fig. SB5.3. The vertical coupling for 30 days before to 60 days after the 5 January 2021 SSW, shown as pressure–time cross-sections of daily-mean (a) 60°–90°N geopotential height anomalies (std. dev.; shading) and 60°N zonal-mean zonal winds (m s^{-1}; gray contours, with the zero wind line in black) from the ERA5 reanalysis, and (b) 65°–90°N ozone anomalies (ppmv) from the MERRA2 reanalysis. All anomalies are created with respect to the daily climate over 1991–2020. The geopotential height anomalies are additionally normalized at each pressure level by the standard deviation of all days in the 90-day window shown during 1991–2020. The dashed black vertical line indicates the date of the SSW.

From a peak wind speed near 44 m s^{-1} on 24 December 2020, the 10 hPa (~30 km) 60°N zonal-mean zonal winds rapidly decelerated over the next 12 days until they reversed direction on 5 January 2021, which defines the central date of the SSW (Fig. SB5.3a). During this same time, average temperatures at 10 hPa within the polar cap (latitudes ≥ 60°N) increased by about 30°C (Lee 2021).

Influence on stratospheric ozone

There can be significant changes to atmospheric composition over the Arctic when the polar vortex becomes disturbed during an SSW (de la Camara et al. 2018). The barrier that the polar vortex creates in the stratosphere between ozone-poor polar air and ozone-rich mid-latitude air is degraded by rapid mixing. Additionally, the large-scale waves that drive the SSW also accelerate the stratospheric overturning circulation, transporting more ozone from the tropical to the polar stratosphere.

These changes were evident during the 2021 SSW, with anomalously high ozone in the mid-to-lower stratosphere as the zonal-mean winds reversed direction on 5 January (Fig. SB5.3b). While the recovery of the polar vortex winds in February led to anomalously low ozone in the mid-stratosphere, anomalously high ozone persisted in the lower stratosphere through March. Given the lack of solar insolation at the pole in January when the SSW occurred, concurrent changes in ozone likely had minimal effects on UV radiation at the surface or feedbacks on the circulation (section 5j).

Influence on weather patterns and their predictability

The 2021 SSW showed a downward influence on the polar atmospheric circulation from the upper stratosphere to the surface for six weeks after the event (as is typical of most SSWs), with anomalously high geopotential heights (Fig. SB5.3a) and sea level pressure over the Arctic, and anomalously low sea level pressure over the North Atlantic (Figs. SB 5.4b,d). This pattern is a signature of the downward influence of the stratosphere and represents the negative phase of the North Atlantic Oscillation (NAO). The January NAO was at its lowest value since 2010 (Lee 2021). During the 6-week period following the SSW, surface temperatures were anomalously high over Greenland and the Canadian Arctic and anomalously low over Europe, northern Asia, and the United States, with a cold air outbreak first occurring over Europe and northern Asia during January and then over North America in the first two weeks of February (section 5b).

This SSW, like most other SSWs (Domeisen et al. 2020), was not well predicted by sub-seasonal to seasonal forecast systems more than two weeks in advance (Rao et al. 2021). However, only those forecast members that predicted a reversal of the polar vortex winds were able to predict the persistent cold anomalies over Eurasia following the event (Rao et al. 2021). Recent research (Kretschmer et al. 2018) suggests that the location of the polar vortex as the SSW evolves may be linked to where the most significant weather extremes occur. The SSW in 2021 provided at least anecdotal evidence for these effects. The coldest temperature anomalies first occurred over Eurasia in mid-January (Fig. SB5.4b), as the vortex became elongated and shifted towards that region (Fig. SB5.4a; Wright et al. 2021; Zhang et al. 2022). During this time, most of the United States was anomalously warm. As the vortex began to elongate towards Canada in early February (Fig. SB5.4c; Cohen et al. 2021), an extreme cold air outbreak occurred over the central United States (Fig. SB5.4d), leading to massive power outages, damage to infrastructure, loss of life, and economic losses estimated at $130 billion (U.S. dollars) in Texas alone (Busby et al. 2021; see section 7b2). Nonetheless, though the SSW increased the likelihood of cold-air outbreaks in the subsequent weeks (Huang et al. 2021), model experiments suggest limited direct influence of the SSW itself on the central United States cold-air outbreak (Davis et al. 2022; Zhang et al. 2022.)

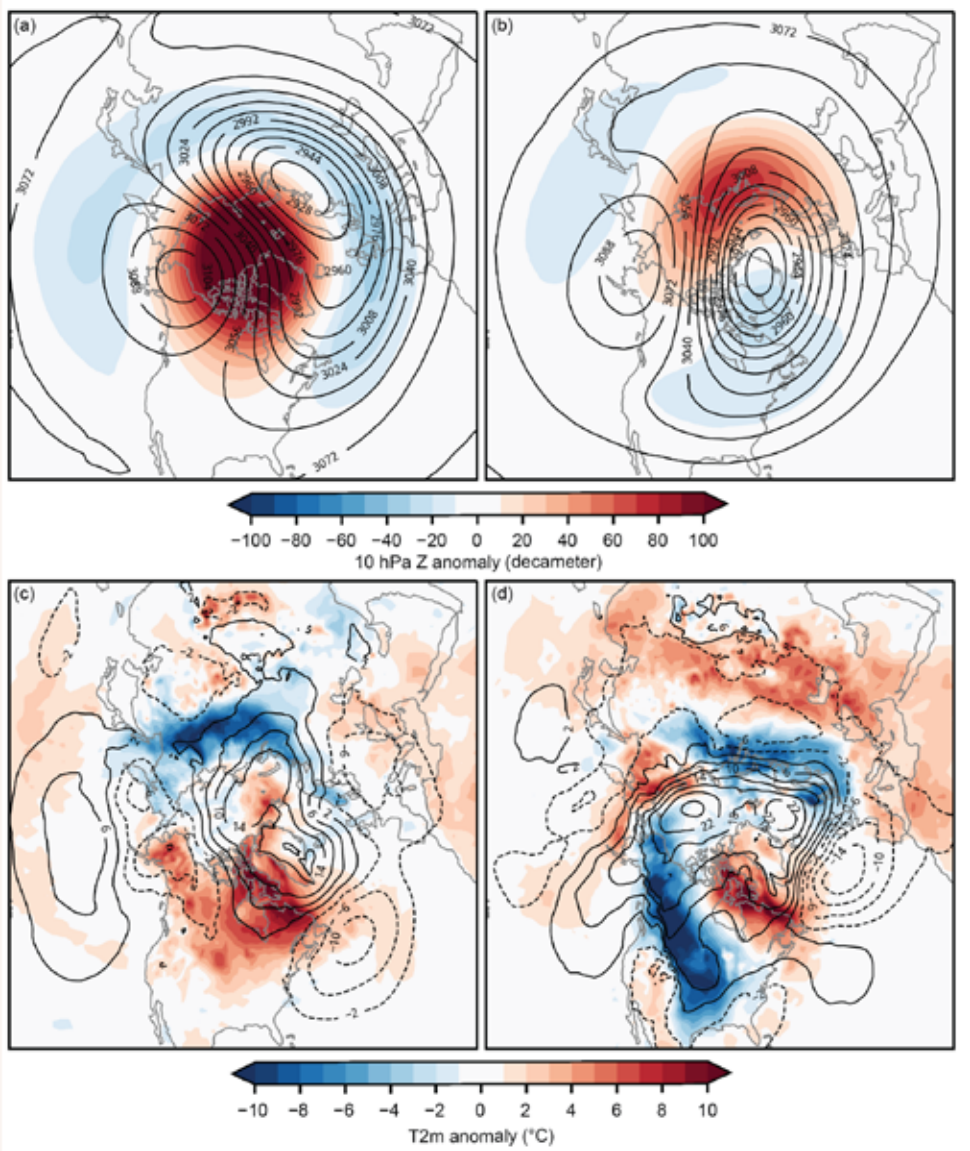

Fig. SB5.4. Stratospheric evolution and associated surface impacts of the January 2021 SSW, according to ERA5 reanalysis. Two periods following the SSW are shown, (a,b) 5–30 January and (c,d) 1–16 February. (a,c) shows the 10-hPa geopotential heights (dam; contours) and anomalies (dam; shading), while (b,d) shows the sea level pressure anomalies (hPa; contours) and near-surface (2m) temperature anomalies (°C; shading).

Acknowledgments

The editors wish to thank the six anonymous reviewers and the general editors for providing reviews of the full chapter. Their careful readthrough and thoughtful input improved each of the sections and led to better coherency between the sections.

a (Overview)

Matthew Druckenmiller and Twila Moon appreciate support from NOAA's Arctic Research Office. Rick Thoman appreciates support from NOAA's Climate Program Office.

e (Greenland ice sheet)

Data from the Programme for Monitoring of the Greenland Ice Sheet (PROMICE) were provided by the Geological Survey of Denmark and Greenland (GEUS) at http://www.promice.dk.

Twila Moon was supported by the University of Colorado Boulder Cooperative Institute for Research in Environmental Sciences. Marco Tedesco was supported by National Science Foundation ANS #1713072, National Science Foundation PLR-1603331, NASA MAP #80NSSC17K0351, NASA #NNX17AH04G, and the Heising-Simons foundation.

Thomas Mote was supported by National Science Foundation #1900324. Sentinel-3 SICE data processing via PolarView.org is made possible by the European Space Agency (ESA) Network of Resources. Summit Station is owned and operated by the National Science Foundation Office of Polar Programs with permission from the Government of Greenland. Data from land-based weather stations in Greenland were provided by the Danish Meteorological Institute, and Summit Station data provided by NOAA GEOSummit.

j (Ozone and UV radiation)

Germar Bernhard and coauthors acknowledge the support of Biospherical Instruments, San Diego; the Research Council of Norway through its Centres of Excellence funding scheme, project number 223268/F50; the Academy of Finland for supporting UV measurements through the FARPOCC, SAARA, and CHAMPS (grant no. 329225) projects; the European Space Agency for supporting the DACES project; the Norwegian Environment Agency for funding UV measurements at Andøya and Ny-Ålesund; and the European Union for supporting e-shape. The authors also would like to thank Bodeker Scientific, funded by the New Zealand Deep South National Science Challenge, for providing the combined NIWA-BS total column ozone database; the Microwave Limb Sounder team at NASA's Jet Propulsion Laboratory for data-processing and analysis support; the European Centre for medium-range weather forecasts for providing reanalysis data; and Juha M. Karhu, Tomi Karppinen, and Markku Ahponen from the Finnish Meteorological Institute for operating the Brewer UV spectroradiometer at Sodankylä.

Appendix 1: Chapter 5 – Acronyms

ALT	active layer thickness
AMJ	April, May, June
AMSR2	Advanced Microwave Scanning Radiometer
AO	Arctic Oscillation
AON	Arctic Observing Network
ARC	Arctic Report Card
AVHRR	Advanced Very High Resolution Radiometer
AWS	Automated Weather Station
B_{clim}	climatic mass balance
CALM	Circumpolar Active Layer Monitoring program
CCI	Climate Change Initiative
CRUTEM	Climatic Research Unit Temperature
DMI	Danish Meteorological Institute
DMSP	Defense Meteorological Satellite Program
DU	Dobson unit
EASE-	Grid Equal Area Scalable Earth Grid
ECMWF	European Centre for Medium-range Weather Forecasts
ERA	ECMWF Reanalysis
ESA	European Space Agency
GEUS	Geological Survey of Denmark and Greenland
GIMMS-3g+	Global Inventory Modeling and Mapping Studies 3g V1.2 dataset
GRACE	Gravity Recovery and Climate Experiment
ICESat-2	Ice, Cloud, and land Elevation 2 laser altimeter
IMS	Interactive Multisensor Snow and Ice Mapping System snow cover product
JAS	July, August, September
JFM	January, February, March
JJA	June, July, August
MaxNDVI	Maximum Normalized Difference Vegetation Index
MERRA-2	Modern-Era Retrospective Analysis for Research and Applications version 2 product
MLS	Microwave Limb Sounder
MODIS	Moderate Resolution Imaging Spectroradiometer
NCEP	National Center for Environmental Prediction
NCAR	National Center for Atmospheric Research
NDVI	Normalized Difference Vegetation Index
NSIDC	National Snow and Ice Data Center
OISSTv2	Optimum Interpolation (OI) SST Version 2 product
OMI	Ozone Monitoring Instrument
OND	October, November, December
PM	Passive Microwave
PROMICE	Program for the Monitoring of the Greenland Ice Sheet
PSC	polar stratospheric clouds

SAT	surface air temperature
SCD	snow cover duration
SCE	snow cover extent
SMB	surface mass balance
SLP	sea level pressure
SMOS	Soil Moisture and Ocean Salinity mission
SSMIS	Special Sensor Microwave Imager/Sounder
SSTs	sea surface temperature
SSW	Sudden Stratospheric Warming
SWE	snow water equivalent
TOC	Total Ozone Columns
UV	Ultraviolet
UVI	Ultraviolet Index
VIIRS	Visible Infrared Imaging Radiometer Suite
VIR	Visible and Infrared

References

Abramov, A., and Coauthors, 2021: Two decades of active layer thickness monitoring in northeastern Asia. *Polar Geogr.*, **44**, 186–202, https://doi.org/10.1080/1088937X.2019.1648581.

Andersen, J. K., and Coauthors, 2019: Update of annual calving front lines for 47 marine terminating outlet glaciers in Greenland (1999–2018). *Geol. Surv. Denmark Greenl. Bull.*, **43**, e2019430202, https://doi.org/10.34194/GEUSB-201943-02-02.

Andreassen, L. M., H. Elvehøy, B. Kjøllmoen, and R. V. Engeset, 2016: Reanalysis of long-term series of glaciological and geodetic mass balance for 10 Norwegian glaciers. *Cryosphere*, **10**, 535–552, https://doi.org/10.5194/tc-10-535-2016.

Baldwin, M. P., and Coauthors, 2021: Sudden stratospheric warmings. *Rev. Geophys.*, **59**, e2020RG000708, https://doi.org/10.1029/2020RG000708.

Ballinger, T. J., and Coauthors, 2020: Surface air temperature. *Arctic Report Card 2020*, R. L. Thoman, J. Richter-Menge, and M. L. Druckenmiller, Eds., NOAA, 7 pp., https://doi.org/10.25923/gcw8-2z06.

——, and Coauthors, 2021: Surface air temperature. *Arctic Report Card 2021*, T. A. Moon, M. L. Druckenmiller, and R. L. Thoman, Eds., NOAA, 8–14, https://doi.org/10.25923/53xd-9k68.

Barnes, P. W., and Coauthors, 2019: Ozone depletion, ultraviolet radiation, climate change and prospects for a sustainable future. *Nat. Sustainability*, **2**, 569–579, https://doi.org/10.1038/s41893-019-0314-2.

Barrett, A. P., J. C. Stroeve, and M. Serreze, 2020: Arctic Ocean precipitation from atmospheric reanalyses and comparisons with North Pole drifting station records. *J. Geophys. Res. Oceans*, **125**, e2019JC015415, https://doi.org/10.1029/2019JC015415.

Barton, B. I., Y. D. Lenn, and C. Lique, 2018: Observed Atlantification of the Barents Sea causes the Polar Front to limit the expansion of winter sea ice. *J. Phys. Oceanogr.*, **48**, 1849–1866, https://doi.org/10.1175/JPO-D-18-0003.1.

Berner, L. T., and Coauthors, 2020: Summer warming explains widespread but not uniform greening in the Arctic tundra biome. *Nat. Commun.*, **11**, 4621, https://doi.org/10.1038/s41467-020-18479-5.

Bernhard, G., and Coauthors, 2015: Comparison of OMI UV observations with ground-based measurements at high northern latitudes. *Atmos. Chem. Phys.*, **15**, 7391–7412, https://doi.org/10.5194/acp-15-7391-2015.

——, R. L. McKenzie, K. Lantz, and S. Stierle, 2022: Updated analysis of data from Palmer Station, Antarctica (64° S), and San Diego, California (32° N), confirms large effect of the Antarctic ozone hole on UV radiation. *Photochem. Photobiol. Sci.*, **21**, 373–384, https://doi.org/10.1007/s43630-022-00178-3.

Bhartia, P. K., and C. W. Wellemeyer, 2002: TOMS-V8 total O3 algorithm. OMI Algorithm Theoretical Basis Document Volume II, NASA Goddard Space Flight Center Tech. Doc. ATBD-OMI-02, 15–31, https://eospso.gsfc.nasa.gov/sites/default/files/atbd/ATBD-OMI-02.pdf.

Bhatt, U. S., and Coauthors, 2021: Climate drivers of Arctic tundra variability and change using an indicators framework. *Environ. Res. Lett.*, **16**, 055019, https://doi.org/10.1088/1748-9326/abe676.

Bjella, K., 2019: Warming and thawing permafrost and impacts on infrastructure [in "State of the Climate in 2018"]. *Bull. Amer. Meteor. Soc.*, **100** (9), S157–S159, 10.1175/2019BAMSStateoftheClimate.1.

Blackwell, S., and A. Thode, 2021: Effects of noise. *The Bowhead Whale: Balaena mysticetus: Biology and Human Interactions*, J. C. George and J. G. M. Thewissen, Eds., Academic Press, 565–576, https://doi.org/10.1016/B978-0-12-818969-6.00035-2.

Bodeker, G. E., and S. Kremser, 2021: Indicators of Antarctic ozone depletion: 1979 to 2019. *Atmos. Chem. Phys.*, **21**, 5289–5300, https://doi.org/10.5194/acp-21-5289-2021.

Boike, J., and Coauthors, 2018: A 20-year record (1998–2017) of permafrost, active layer, and meteorological conditions at a High Arctic permafrost research site (Bayelva, Spitsbergen). *Earth Syst. Sci. Data*, **10**, 355–390, https://doi.org/10.5194/essd-10-355-2018.

Bolch, T., L. S. Sørensen, S. B. Simonsen, N. Mölg, H. Machguth, P. Rastner, and F. Paul, 2013: Mass loss of Greenland's glaciers and ice caps 2003–2008 revealed from ICESat laser altimetry data. *Geophys. Res. Lett.*, **40**, 875–881, https://doi.org/10.1002/grl.50270.

Box, J. E., D. van As, and K. Steffen, 2017: Greenland, Canadian and Icelandic land ice albedo grids (2000–2016). *Geol. Surv. Denmark Greenl. Bull.*, **38**, 53–56, https://doi.org/10.34194/geusb.v38.4414.

——, W. Colgan, B. Wouters, D. Burgess, S. O'Neel, L. Thomson, and S. Mernild, 2018: Global sea-level contribution from Arctic land ice: 1971–2017. *Environ. Res. Lett.*, **13**, 125012, https://doi.org/10.1088/1748-9326/aaf2ed.

——, and Coauthors, 2019: Key indicators of Arctic climate change: 1971–2017. *Environ. Res. Lett.*, **14**, 045010, https://doi.org/10.1088/1748-9326/aafc1b.

——, A. Wehrlé, D. van As, R. S. Fausto, K. K. Kjeldsen, A. Dachauer, A. P. Ahlstrøm, and G. Picard, 2022: Greenland ice sheet rainfall, heat and albedo feedback impacts from the mid-August 2021 atmospheric river. *Geophys. Res. Lett.*, **49**, e2021GL097356, https://doi.org/10.1029/2021GL097356.

Brown, J., O. J. Ferrians Jr., J. A. Heginbottom, and E. S. Melnikov, 1997: Circum-Arctic map of permafrost and ground-ice conditions. U.S. Geological Survey Circum-Pacific Map CP-45, 1:10,000,000, https://doi.org/10.3133/cp45.

Brown, R., D. Vikhamar Schuler, O. Bulygina, C. Derksen, K. Luojus, L. Mudryk, L. Wang, and D. Yang, 2017: Arctic terrestrial snow cover. *Snow, Water, Ice and Permafrost in the Arctic (SWIPA) 2017*, Arctic Monitoring and Assessment Programme, 25–64.

Brun, E., V. Vionnet, A. Boone, B. Decharme, Y. Peings, R. Valette, F. Karbou, and S. Morin, 2013: Simulation of Northern Eurasian local snow depth, mass, and density using a detailed snowpack model and meteorological reanalyses. *J. Hydrometeor.*, **14**, 203–219, https://doi.org/10.1175/JHM-D-12-012.1.

Busby, J. W., and Coauthors, 2021: Cascading risks: Understanding the 2021 winter blackout in Texas. *Energy Res. Soc. Sci.*, **77**, 102106, https://doi.org/10.1016/j.erss.2021.102106.

Butchart, N., and E. E. Remsberg, 1986: The area of the stratospheric polar vortex as a diagnostic for tracer transport on an isentropic surface. *J. Atmos. Sci.*, **43**, 1319–1339, https://doi.org/10.1175/1520-0469(1986)043<1319:TAOTSP>2.0.CO;2.

Campbell, T. K. F., T. C. Lantz, R. H. Fraser, and D. Hogan, 2021: High Arctic vegetation change mediated by hydrological conditions. *Ecosystems*, **24**, 106–121, https://doi.org/10.1007/s10021-020-00506-7.

CAVM Team, 2003: Circumpolar arctic vegetation map (1:7,500,000 scale). Conservation of Arctic Flora and Fauna (CAFF) Map No. 1, U.S. Fish and Wildlife Service, https://www.geobotany.uaf.edu/cavm/.

CHNL, 2022: Statistics page. Center for High North Logistics, Nord University, https://arctic-lio.com/category/statistics/.

Christensen, T. R., and Coauthors, 2021: Multiple ecosystem effects of extreme weather events in the Arctic. *Ecosystems*, **24** 122–136, https://doi.org/10.1007/s10021-020-00507-6.

Christiansen, H., and Coauthors, 2010: The thermal state of permafrost in the Nordic area during the International Polar Year 2007–2009. *Permafrost Periglacial Processes*, **21**, 156–181, https://doi.org/10.1002/ppp.687.

Ciracì, E., I. Velicogna, and S. Swenson, 2020: Continuity of the mass loss of the world's glaciers and ice caps from the GRACE and GRACE Follow-On missions. *Geophys. Res. Lett.*, **47**, e2019GL086926, https://doi.org/10.1029/2019GL086926.

Cohen, J., L. Agel, M. Barlow, C. Garfinkel, and I. White, 2021: Linking Arctic variability and change with extreme winter weather in the United States. *Science*, **373**, 1116–1121, https://doi.org/10.1126/science.abi9167.

Davis, N. A., J. H. Richter, A. A. Glanville, J. Edwards, and E. LaJoie, 2022: Limited surface impacts of the January 2021 sudden stratospheric warming. *Nat. Commun.*, **13**, 1136, https://doi.org/10.1038/s41467-022-28836-1.

de la Cámara, A., M. Abalos, P. Hitchcock, N. Calvo, and R. R. Garcia, 2018: Response of Arctic ozone to sudden stratospheric warmings. *Atmos. Chem. Phys.*, **18**, 16 499–16 513, https://doi.org/10.5194/acp-18-16499-2018.

Domeisen, D. I. V., and A. H. Butler, 2020: Stratospheric drivers of extreme events at the Earth's surface. *Commun. Earth Environ*., **1**, 59, https://doi.org/10.1038/s43247-020-00060-z.

——, and Coauthors, 2020: The role of the stratosphere in subseasonal to seasonal prediction: 1. Predictability of the stratosphere. *J. Geophys. Res. Atmos.*, **125**, e2019JD030920, https://doi.org/10.1029/2019JD030920.

Durre, I., X. Yin, R. S. Vose, S. Applequist, and J. Arnfield, 2016: Integrated Global Radiosonde Archive (IGRA), Version 2. Subset: IGRA 2 Monthly-Mean Files. NOAA National Centers for Environmental Information, accessed January 2022, https://doi.org/10.7289/V5X63K0Q.

EEAP, 2019: Environmental Effects and Interactions of Stratospheric Ozone Depletion, UV Radiation, and Climate Change. 2018 Assessment Report. Environmental Effects Assessment Panel, United Nations Environment Programme, 390 pp. https://ozone.unep.org/sites/default/files/2019-04/EEAP_assessment-report-2018%20%282%29.pdf.

Eisner, L. B., Y. I. Zuenko, E. O. Basyuk, L. L. Britt, J. T. Duffy-Anderson, S. Kotwicki, C. Ladd, and W. Cheng, 2020: Environmental impacts on walleye pollock (*Gadus chalcogrammus*) distribution across the Bering Sea shelf. *Deep-Sea Res. II*, **181–182**, 104881, https://doi.org/10.1016/j.dsr2.2020.104881.

Etzelmüller, B., and Coauthors, 2020: Twenty years of European mountain permafrost dynamics—The PACE legacy. *Environ. Res. Lett.*, **15**, 104070, https://doi.org/10.1088/1748-9326/abae9d.

Fausto, R. S., and Coauthors, 2021: Programme for Monitoring of the Greenland Ice Sheet (PROMICE) automatic weather station data. *Earth Syst. Sci. Data*, **13**, 3819–3845, https://doi.org/10.5194/essd-13-3819-2021.

Fetterer, F., K. Knowles, W. N. Meier, M. Savoie, and A. K. Windnagel, 2017: Sea Ice Index, version 3. National Snow and Ice Data Center, accessed 27 August 2021, https://doi.org/10.7265/N5K072F8.

Gaglioti, B. V., and Coauthors, 2021: Tussocks enduring or shrubs greening: Alternate responses to changing fire regimes in the Noatak River Valley, Alaska. *J. Geophys. Res. Biogeosci.*, **126**, e2020JG006009, https://doi.org/10.1029/2020JG006009.

GMAO, 2015: MERRA-2tavg1_2d_lnd_Nx:2d, 1-Hourly, Time-Averaged, Single-Level, Assimilation, Land Surface Diagnostics V5.12.4. Goddard Earth Sciences Data and Information Services Center, accessed 11 August 2021, https://doi.org/10.5067/RKPHT8KC1Y1T.

Heijmans, M. M. P. D., and Coauthors, 2022: Tundra vegetation change and impacts on permafrost. *Nat. Rev. Earth Environ.*, **3**, 68–84, https://doi.org/10.1038/s43017-021-00233-0.

Henson, B., and J. Masters, 2021: Western Canada burns and deaths mount after world's most extreme heat wave in modern history. Yale Climate Connections, https://yaleclimateconnections.org/2021/07/western-canada-burns-and-deaths-mount-after-worlds-most-extreme-heat-wave-in-modern-history/.

Hersbach, H., and Coauthors, 2020: The ERA5 global reanalysis. *Quart. J. Roy. Meteor. Soc.*, **146**, 1999–2049, https://doi.org/10.1002/qj.3803.

Holmes, R. M., A. I. Shiklomanov, A. Suslova, M. Tretiakov, J. W. McClelland, L. Scott, R. G. M. Spencer, and S. E. Tank, 2021: River discharge. *Arctic Report Card 2021*, T. A. Moon, M. L. Druckenmiller, and R. L. Thoman, Eds., NOAA, 78–84, https://doi.org/10.25923/zevf-ar65.

Huang, J., P. Hitchcock, A. C. Maycock, C. M. McKenna, and W. Tian, 2021: Northern Hemisphere cold air outbreaks are more likely to be severe during weak polar vortex conditions. *Commun. Earth Environ.*, **2**, 147, https://doi.org/10.1038/s43247-021-00215-6.

Huemmrich, K. F., S. Vargas Zesati, P. Campbell, and C. Tweedie, 2021: Canopy reflectance models illustrate varying NDVI responses to change in high latitude ecosystems. *Ecol. Appl.*, **31**, e02435, .

Hugonnet, R., and Coauthors, 2021: Accelerated global glacier mass loss in the early twenty-first century. *Nature*, **592**, 726–731, https://doi.org/10.1038/s41586-021-03436-z.

Humpert, M., 2021: Winter transits along the Northern Sea Route open up a new frontier in Arctic shipping. Arctic Today, 25 January, https://www.arctictoday.com/winter-transits-along-the-northern-sea-route-open-up-a-new-frontier-in-arctic-shipping/.

IMO, 2021: Prevention of pollution by garbage from ships. International Maritime Organization, accessed 7 June 2022, https://www.imo.org/en/OurWork/Environment/Pages/Garbage-Default.aspx.

IPCC, 2021: *Climate Change 2021: The Physical Science Basis*. V. Masson-Delmotte et al., Eds., Cambridge University Press, 3949 pp., https://doi.org/10.1017/9781009157896.

Ivanova, N., O. M. Johannessen, L. T. Pedersen, and R. T. Tonboe, 2014: Retrieval of Arctic sea ice parameters by satellite passive microwave sensors: A comparison of eleven sea ice concentration algorithms. *IEEE Trans. Geosci. Remote Sens.*, **52**, 7233–7246, https://doi.org/10.1109/TGRS.2014.2310136.

Karlsen, S. R., L. Stendardi, H. Tømmervik, L. Nilsen, I. Arntzen, and E. J. Cooper, 2021: Time-series of cloud-free Sentinel-2 NDVI data used in mapping the onset of growth of central Spitsbergen, Svalbard. *Remote Sens.*, **13**, 3031, https://doi.org/10.3390/rs13153031.

Kaverin, D., and Coauthors, 2021: Long-term active layer monitoring at CALM sites in the Russian European North. *Polar Geogr.*, **44**, 203–216, https://doi.org/10.1080/1088937X.2021.1981476.

Kjøllmoen, B., L. Andreassen, H. Elvehøy, and K. Melvold, 2021: Glaciological investigations in Norway 2021. NVE Rep. 33/2021, 92 pp., https://publikasjoner.nve.no/rapport/2021/rapport2021_31.pdf.

Kokhanovsky, A., J. E. Box, B. Vandecrux, K. D. Mankoff, M. Lamare, A. Smirnov, and M. Kern, 2020: The determination of snow albedo from satellite measurements using fast atmospheric correction technique. *Remote Sens.*, **12**, 234, https://doi.org/10.3390/rs12020234.

Kretschmer, M., J. Cohen, V. Matthias, J. Runge, and D. Coumou, 2018: The different stratospheric influence on cold-extremes in Eurasia and North America. *npj Climate Atmos. Sci.*, **1**, 44, https://doi.org/10.1038/s41612-018-0054-4.

Kropp, H., and Coauthors, 2021: Shallow soils are warmer under trees and tall shrubs across Arctic and Boreal ecosystems. *Environ. Res. Lett.*, **16**, 015001, https://doi.org/10.1088/1748-9326/abc994.

Lavergne, T., and Coauthors, 2019: Version 2 of the EUMETSAT OSI SAF and ESA CCI sea-ice concentration climate data records. *Cryosphere*, **13**, 49–78, https://doi.org/10.5194/tc-13-49-2019.

Lawrence, Z. D., J. Perlwitz, A. H. Butler, G. L. Manney, P. A. Newman, S. H. Lee, and E. R. Nash, 2020: The remarkably strong Arctic stratospheric polar vortex of winter 2020: Links to record-breaking Arctic oscillation and ozone loss. *J. Geophys Res. Atmos*, **125**, e2020JD033271, https://doi.org/10.1029/2020JD033271.

Lee, S. H., 2021: The January 2021 sudden stratospheric warming. *Weather*, **76**, 135–136, https://doi.org/10.1002/wea.3966.

Lind, S., R. B. Ingvaldsen, and T. Furevik, 2018: Arctic warming hotspot in the northern Barents Sea linked to declining sea ice import. *Nat. Climate Change*, **8**, 634–639, https://doi.org/10.1038/s41558-018-0205-y.

Lu, Q., J. Rao, Z. Liang, D. Guo, J. Luo, S. Liu, C. Wang, and T. Wang, 2021: The sudden stratospheric warming in January 2021. *Environ. Res. Lett.*, **16**, 084029, https://doi.org/10.1088/1748-9326/ac12f4.

Luojus, K., and Coauthors, 2020: ESA Snow Climate Change Initiative (Snow_cci): Snow Water Equivalent (SWE) level 3C daily global climate research data package (CRDP) (1979 – 2018), version 1.0. Centre for Environmental Data Analysis, accessed 19 July 2021, https://doi.org/10.5285/fa20aaa2060e40cabf5fedce7a9716d0.

Łupikasza, E. B., and K. Cielecka-Nowak, 2020: Changing probabilities of days with snow and rain in the Atlantic sector of the Arctic under the current warming trend. *J. Climate*, **33**, 2509–2532, https://doi.org/10.1175/JCLI-D-19-0384.1.

Magnússon, R. Í., 2021: Shrub decline and expansion of wetland vegetation revealed by very high resolution land cover change detection in the Siberian lowland tundra. *Sci. Total Environ.*, **782**, 146877, https://doi.org/10.1016/j.scitotenv.2021.146877.

Malkova, G., and Coauthors, 2022: Spatial and temporal variability of permafrost in the western part of the Russian Arctic. *Energies*, **15**, 2311, https://doi.org/10.3390/en15072311.

Mankoff, K. D., A. Solgaard, W. Colgan, A. P. Ahlstrøm, S. A. Khan, and R. S. Fausto, 2020: Greenland Ice Sheet solid ice discharge from 1986 through March 2020. *Earth Syst. Sci. Data*, **12**, 1367–1383, https://doi.org/10.5194/essd-12-1367-2020.

Manney, G. L., Z. D. Lawrence, M. L. Santee, N. J. Livesey, A. Lambert, and M. C. Pitts, 2015a: Polar processing in a split vortex: Arctic ozone loss in early winter 2012/2013. *Atmos. Chem. Phys.*, **15**, 5381–5403, https://doi.org/10.5194/acp-15-5381-2015.

——, and Coauthors, 2015b: A minor sudden stratospheric warming with a major impact: Transport and polar processing in the 2014/2015 Arctic winter. *Geophys. Res. Lett.*, **42**, 7808–7816, https://doi.org/10.1002/2015GL065864.

——, and Coauthors, 2020: Record-low Arctic stratospheric ozone in 2020: MLS observations of chemical processes and comparisons with previous extreme winters. *Geophys. Res. Lett.*, **47**, e2020GL089063, https://doi.org/10.1029/2020GL089063.

McCrystall, M. R., J. Stroeve, M. Serreze, B. C. Forbes, and J. A. Screen, 2021: New climate models reveal faster and larger increases in Arctic precipitation than previously projected. *Nat. Commun.*, **12**, 6765, https://doi.org/10.1038/s41467-021-27031-y.

Meier, W. N., F. Fetterer, A. K. Windnagel, and J. S. Stewart, 2021a: NOAA/NSIDC climate data record of passive microwave sea ice concentration, version 4. Subset: 1982–2021, National Snow and Ice Data Center, accessed 11 February 2022, https://doi.org/10.7265/efmz-2t65.

——, ——, ——, and ——, 2021b: Near-real-time NOAA/NSIDC climate data record of passive microwave sea ice concentration, version 2. Subset: 1982–2021, accessed 11 February 2022, https://doi.org/10.7265/tgam-yv28.

Mekonnen, Z. A., and Coauthors, 2021: Arctic tundra shrubification: A review of mechanisms and impacts on ecosystem carbon balance. *Environ. Res. Lett.*, **16**, 053001, https://doi.org/10.1088/1748-9326/abf28b.

Meredith, M., and Coauthors, 2019: Polar regions. *IPCC Special Report on the Ocean and Cryosphere in a Changing Climate*, H.-O. Pörtner et al., Eds., Cambridge University Press, 203–320, https://www.ipcc.ch/srocc/.

Millan, R., J. Mouginot, and E. Rignot, 2017: Mass budget of the glaciers and ice caps of the Queen Elizabeth Islands, Canada from 1991-2015. *Environ. Res. Lett.*, **12**, 024016, .

Moon, T. A., and Coauthors, 2021: Greenland Ice Sheet. *Arctic Report Card 2021*, T. A. Moon, M. L. Druckenmiller, and R. L. Thoman, Eds., NOAA, 23–31, https://doi.org/10.25923/546g-ms61.

Morlighem, M., and Coauthors, 2017: BedMachine v3: Complete bed topography and ocean bathymetry mapping of Greenland from multibeam echo sounding combined with mass conservation. *Geophys. Res. Lett.*, **44**, 11 051–11 061, https://doi.org/10.1002/2017GL074954.

Mote, T., 2007: Greenland surface melt trends 1973–2007: Evidence of a large increase in 2007. *Geophys. Res. Lett.*, **34**, L22507, https://doi.org/10.1029/2007GL031976.

Müller, R., J.-U. Grooß, C. Lemmen, D. Heinze, M. Dameris, and G. Bodeker, 2008: Simple measures of ozone depletion in the polar stratosphere. *Atmos. Chem. Phys.*, **8**, 251–264, https://doi.org/10.5194/acp-8-251-2008.

Muñoz Sabater, J., 2019: ERA5-Land hourly data from 1981 to present. Copernicus Climate Change Service (C3S) Climate Data Store (CDS), accessed 11 August 2021, https://doi.org/10.24381/cds.e2161bac.

Myers-Smith, I. H., and Coauthors, 2020: Complexity revealed in the greening of the Arctic. *Nat. Climate Change*, **10**, 106–117, https://doi.org/10.1038/s41558-019-0688-1.

Nyland, K. E., N. I. Shiklomanov, D. A. Streletskiy, F. E. Nelson, A. E. Klene, and A. L. Kholodov, 2021: Long-term Circumpolar Active Layer Monitoring (CALM) program observations in northern Alaskan tundra. *Polar Geogr.*, **44**, 167–185, https://doi.org/10.1080/1088937X.2021.1988000.

PAME, 2019: Underwater noise in the Arctic: A state of knowledge report. Protection of the Arctic Marine Environment Secretariat, 58 pp., https://www.pame.is/projects/arctic-marine-shipping/underwater-noise-in-the-arctic.

Parmentier, F.-J. W., L. Nilsen, H. Tømmervik, and E. J. Cooper, 2021: A distributed time-lapse camera network to track vegetation phenology with high temporal detail and at varying scales. *Earth Syst. Sci. Data*, **13**, 3593–3606, https://doi.org/10.5194/essd-13-3593-2021.

Peltier, W. R., D. F. Argus, and R. Drummond, 2018: Comment on "An assessment of the ICE-6G_C (VM5a) glacial isostatic adjustment model" by Purcell et al. *J. Geophys. Res. Solid Earth*, **123**, 2019–2028, https://doi.org/10.1002/2016JB013844.

Peng, G., W. N. Meier, D. J. Scott, and M. H. Savoie, 2013: A long-term and reproducible passive microwave sea ice concentration data record for climate studies and monitoring. *Earth Syst. Sci. Data*, **5**, 311–318, https://doi.org/10.5194/essd-5-311-2013.

Petty, A. A., N. T. Kurtz, R. Kwok, T. Markus, and T. A. Neumann, 2020: Winter Arctic sea ice thickness from ICESat-2 freeboards. *J. Geophys. Res.*, **125**, e2019JC015764, https://doi.org/10.1029/2019JC015764.

——, ——, ——, ——, and ——, 2021: ICESat-2 L4 monthly gridded sea ice thickness, version 1. National Snow and Ice Data Center Distributed Active Archive Center, accessed 9 September 2021, https://doi.org/10.5067/CV6JEXEE31HF.

Pinzon, J., and C. Tucker, 2014: A non-stationary 1981–2012 AVHRR NDVI3g time series. *Remote Sens.*, **6**, 6929–6960, https://doi.org/10.3390/rs6086929.

Ponomarev, E., A. Zabrodin, and T. Ponomareva, 2022: Classification of fire damage to boreal forests of Siberia in 2021 based on the dNBR index. *Fire*, **5**, 19, https://doi.org/10.3390/fire5010019.

Rao, J., C. I. Garfinkel, T. Wu, Y. Lu, Q. Lu, and Z. Liang, 2021: The January 2021 sudden stratospheric warming and its prediction in subseasonal to seasonal models. *J. Geophys. Res. Atmos.*, **126**, e2021JD035057, https://doi.org/10.1029/2021JD035057.

Raynolds, M. K., D. A. Walker, H. E. Epstein, J. E. Pinzon, and C. J. Tucker, 2012: A new estimate of tundra-biome phytomass from trans-Arctic field data and AVHRR NDVI. *Remote Sens. Lett.*, **3**, 403–411, https://doi.org/10.1080/01431161.2011.609188.

Reynolds, R. W., N. A. Rayner, T. M. Smith, D. C. Stokes, and W. Wang, 2002: An improved in situ and satellite SST analysis for climate. *J. Climate*, **15**, 1609–1625, https://doi.org/10.1175/1520-0442(2002)015<1609:AIISAS>2.0.CO;2.

——, T. M. Smith, C. Liu, D. B. Chelton, K. S. Casey, and M. G. Schlax, 2007: Daily high-resolution-blended analyses for sea surface temperature. *J. Climate*, **20**, 5473–5496, https://doi.org/10.1175/2007JCLI1824.1.

Ricker, R., S. Hendricks, L. Kaleschke, X. Tian-Kunze, J. King, and C. Haas, 2017: A weekly Arctic sea-ice thickness data record from merged CryoSat-2 and SMOS satellite data. *Cryosphere*, **11**, 1607–1623, https://doi.org/10.5194/tc-11-1607-2017.

RGI Consortium, 2017: Randolph glacier inventory—A dataset of global glacier outlines, version 6. National Snow and Ice Data Center, https://doi.org/10.7265/4m1f-gd79

Robinson, D. A., T. W. Estilow, and NOAA CDR Program, 2012: NOAA Climate Data Record (CDR) of Northern Hemisphere (NH) Snow Cover Extent (SCE), version 1 [r01]. NOAA National Centers for Environmental Information, https://doi.org/10.7289/V5N014G9.

Rolland, R. M., S. E. Parks, K. E. Hunt, M. Castellote, P. J. Corkeron, D. P. Nowacek, S. K. Wasser, and S. D. Kraus, 2012: Evidence that ship noise increases stress in right whales. *Proc. Roy. Soc.*, **B279**, 2363–2368, https://doi.org/10.1098/rspb.2011.2429.

Romanovsky, V., and Coauthors, 2017: Changing permafrost and its impacts. Snow, Water, Ice and Permafrost in the Arctic (SWIPA) 2017, Arctic, Monitoring and Assessment Programme, 65–102, https://www.amap.no/documents/doc/snow-water-ice-and-permafrost-in-the-arctic-swipa-2017/1610.

Schaaf, C. B., 2021: MCD43A4 v006 MODIS/Terra+Aqua Nadir BRDF-Adjusted Reflectance (NBAR) Daily L3 Global 500 m SIN Grid, accessed 1 September 2021, https://doi.org/10.5067/MODIS/MCD43A4.006.

Schuur, E. A. G., 2020: Permafrost carbon [in "State of the Climate in 2019"]. *Bull. Amer. Meteor. Soc.*, **101** (8), S270–S271, https://doi.org/10.1175/BAMS-D-20-0086.1.

Seider, J. H., T. C. Lantz, T. Hermosilla, M. A. Wulder, and J. A. Wang, 2022: Biophysical determinants of shifting tundra vegetation productivity in the Beaufort Delta region of Canada. *Ecosystems*, https://doi.org/10.1007/s10021-021-00725-6, in press.

Severson, J. P., H. E. Johnson, S. M. Arthur, W. B. Leacock, and M. J. Suitor, 2021: Spring phenology drives range shifts in a migratory Arctic ungulate with key implications for the future. *Global Change Biol.*, **27**, 4546–4563, https://doi.org/10.1111/gcb.15682.

Sharp, M., D. Burgess, J. Cogley, M. Ecclestone, C. Labine, and G. Wolken, 2011: Extreme melt on Canada's Arctic ice caps in the 21st century. *Geophys. Res. Lett.*, **38**, L11501, https://doi.org/10.1029/2011GL047381.

Sheffield, G., A. Ahmasuk, F. Ivanoff, A. Noongwook, and J. Koonooka, 2021: 2020 foreign marine debris event–Bering Strait. *Arctic Report Card 2021*, T. A. Moon, M. L. Druckenmiller, and R. L. Thoman, Eds., NOAA, 85–92, https://doi.org/10.25923/jwag-eg41.

Shiklomanov, N. I., D. A. Streletskiy, and F. E. Nelson, 2012: Northern Hemisphere component of the global Circumpolar Active Layer Monitoring (CALM) program. *Proc. 10th Int. Conf. on Permafrost*, Vol. 1, Salekhard, Russia, Tyumen Oil and Gas University, 377–382.

Smedsrud, L. H., and Coauthors, 2022: Nordic Seas heat loss, Atlantic inflow, and Arctic sea ice cover over the last century. *Rev. Geophys.*, **60**, e2020RG000725, https://doi.org/10.1029/2020RG000725.

Smith, R. B., 2021: Russian tanker passes through Bering Strait in the midst of winter. *The Nome Nugget*, 15 January, http://www.nomenugget.com/news/russian-tanker-passes-through-bering-strait-midst-winter.

Smith, S. L., and Coauthors, 2021: Permafrost [in "State of the Climate in 2020"]. *Bull. Amer. Meteor. Soc.*, **102** (8), S293–S297, https://doi.org/10.1175/BAMS-D-21-0086.1.

——, H. B. O'Neill, K. Isaksen, J. Noetzli, and V. E. Romanvsky, 2022: The changing thermal state of permafrost. *Nat. Rev. Earth Environ.*, **3**, 10–23, https://doi.org/10.1038/s43017-021-00240-1.

Spies, I., K. M. Gruenthal, D. P. Drinan, A. B. Hollowed, D. E. Stevenson, C. M. Tarpey, and L. Hauser, 2020: Genetic evidence of a northward range expansion in the eastern Bering Sea stock of Pacific cod. *Evol. Appl.*, **13**, 362–375, https://doi.org/10.1111/eva.12874.

Stafford, K. M., 2021: The changing Arctic marine soundscape. *Arctic Report Card 2021*, T.A. Moon, M. L. Druckenmiller, and R. L. Thoman, Eds., NOAA, 102–108, https://doi.org/10.25923/jagc-4a84.

Stevenson, D. E., and R. R. Lauth, 2019: Bottom trawl surveys in the northern Bering Sea indicate recent shifts in the distribution of marine species. *Polar Biol.*, **42**, 407–421, https://doi.org/10.1007/s00300-018-2431-1.

Strand, S. M., H. H. Christiansen, M. Johansson, J. Akerman, and O. Humlum, 2021: Active layer thickening and controls on interannual variability in the Nordic Arctic compared to the circum-Arctic. *Permafrost Periglacial Processes*, **32**, 47–58, https://doi.org/10.1002/ppp.2088.

Stroh, J. N., G. Panteleev, S. Kirillov, M. Makhotin, and N. Shakhova, 2015: Sea-surface temperature and salinity product comparison against external in situ data in the Arctic Ocean. *J. Geophys. Res. Oceans*, **120**, 7223–7236, https://doi.org/10.1002/2015JC011005.

Talucci, A. C., M. M. Loranty, and H. D. Alexander, 2022: Siberian taiga and tundra fire regimes from 2001–2020. *Environ. Res. Lett.*, **17**, 025001, https://doi.org/10.1088/1748-9326/ac3f07.

Tanskanen, A., A. Arola, and J. Kujanpää, 2003: Use of the moving time-window technique to determine surface albedo from the TOMS reflectivity data. *Proc. SPIE*, **4896**, 239–250, https://doi.org/10.1117/12.483407.

Tape, K. D., J. A. Clark, B. M. Jones, H. C. Wheeler, P. Marsh, and F. Rosell, 2021. Beaver engineering: Tracking a new disturbance in the Arctic. *Arctic Report Card 2021*, T. A. Moon, M. L. Druckenmiller, and R. L. Thoman, Eds., NOAA, 66–71, https://doi.org/10.25923/0jtd-vv85.

Tervo, O., S. Blackwell, S. Ditlevsen, A. Conrad, A. Samson, E. Garde, R. Hansen, and M. P. Heide-Jørgensen, 2021: Narwhals react to ship noise and airgun pulses embedded in background noise. *Biol. Lett.*, **17**, 20210220, https://doi.org/10.1098/rsbl.2021.0220.

Thoman, R., and Coauthors, 2020: The record low Bering Sea ice extent in 2018: Content, impacts, and an assessment of the role of anthropogenic climate change. *Bull. Amer. Meteor. Soc.*, **101**, S53–S58, https://doi.org/10.1175/BAMS-D-19-0175.1.

Timmermans, M.-L., Z. M. Labe, and C. Ladd, 2020: Sea surface temperature [in "State of the Climate in 2019"]. *Bull. Amer. Meteor. Soc.*, **101** (8), S249–S251, https://doi.org/10.1175/BAMS-D-20-0086.1.

Tschudi, M., W. N. Meier, J. S. Stewart, C. Fowler, and J. Maslanik, 2019a: EASE-Grid Sea Ice Age, version 4. Subset: March 1984–2020, National Snow and Ice Data Center Distributed Active Archive Center, accessed 1 September 2021, https://doi.org/10.5067/UTAV7490FEPB.

——, ——, and ——, 2019b: Quicklook Arctic Weekly EASE-Grid Sea Ice Age, version 1. Subset: March 2021, National Snow and Ice Data Center Distributed Active Archive Center, accessed 1 September 2021, https://doi.org/10.5067/2XXGZY3DUGNQ.

——, ——, and ——, 2020: An enhancement to sea ice motion and age products at the National Snow and Ice Data Center (NSIDC). *Cryosphere*, **14**, 1519–1536, https://doi.org/10.5194/tc-14-1519-2020.

USCMTS, 2019: A ten-year projection of maritime activity in the U.S. Arctic region, 2020–2030. U.S. Committee on the Marine Transportation System, 153 pp., https://www.cmts.gov/downloads/CMTS_2019_Arctic_Vessel_Projection_Report.pdf.

U.S. National Ice Center, 2008: IMS Daily Northern Hemisphere Snow and Ice Analysis at 1 km, 4 km, and 24 km resolutions, version 1. National Snow and Ice Data Center, accessed 11 August 2021, https://doi.org/10.7265/N52R3PMC.

van As, D., R. S. Fausto, J. Cappelen, R. S. van de Wal, R. J. Braithwaite, and H. Machguth, 2016: Placing Greenland ice sheet ablation measurements in a multi-decadal context. *Geol. Surv. Denmark Greenl. Bull.*, **35**, 71–74, https://doi.org/10.34194/geusb.v35.4942.

van Huissteden, J., K. Teshebaeva, Y. Cheung, R. Í. Magnússon, H. Noorbergen, S. V. Karsanaev, T. C. Maximov, and A. J. Dolman, 2021: Geomorphology and InSAR-tracked surface displacements in an ice-rich Yedoma landscape. *Front. Earth Sci.*, **9**, 680565, https://doi.org/10.3389/feart.2021.680565.

Veremeeva, A., I. Nitze, F. Günther, G. Grosse, and E. Rivkina, 2021: Geomorphological and climatic drivers of thermokarst lake area increase trend (1999–2018) in the Kolyma Lowland Yedoma region, north-eastern Siberia. *Remote Sens.*, **13**, 178, https://doi.org/10.3390/rs13020178.

Veselkin, D. V., L. M. Morozova, and A. M. Gorbunova, 2021: Decrease of NDVI values in the southern tundra of Yamal in 2001–2018 correlates with the size of domesticated reindeer population. *Sovrem. Probl. Distantsionnogo Zondirovaniya Zemli Kosmosa*, **18**, 143–155, https://doi.org/10.21046/2070-7401-2021-18-2-143-155.

Walsh, J. E., T. J. Ballinger, E. S. Euskirchen, E. Hanna, J. Mård, J. E. Overland, H. Tangen, and T. Vihma, 2020: Extreme weather and climate events in northern areas: A review. *Earth-Sci. Rev.*, **209**, 103324, https://doi.org/10.1016/j.earscirev.2020.103324.

Wang, C., R. M. Graham, K. Wang, S. Gerland, and M. A. Granskog, 2019: Comparison of ERA5 and ERA-Interim near-surface air temperature, snowfall and precipitation over Arctic sea ice: effects on sea ice thermodynamics and evolution. *Cryosphere*, **13**, 1661–1679, https://doi.org/10.5194/tc-13-1661-2019.

Waters, J. W., and Coauthors, 2006: The Earth Observing System Microwave Limb Sounder (EOS MLS) on the Aura satellite. *IEEE Trans. Geosci. Remote Sens.*, **44**, 1075–1092, https://doi.org/10.1109/TGRS.2006.873771.

Way, R. G., and C. M. Lapalme, 2021: Does tall vegetation warm or cool the ground surface? Constraining the ground thermal impacts of upright vegetation in northern environments. *Environ. Res. Lett.*, **16**, 054077, https://doi.org/10.1088/1748-9326/abef31.

Weatherhead, B., A. Tanskanen, and A. Stevermer, 2005: Ozone and ultraviolet radiation. *Arctic Climate Impact Assessment*, Cambridge University Press, 151–182, www.amap.no/documents/download/1086/inline.

Wehrlé, A., J. E. Box, A. M. Anesio, and R. S. Fausto, 2021: Greenland bare-ice albedo from PROMICE automatic weather station measurements and Sentinel-3 satellite observations. *Geol. Surv. Denmark Greenl. Bull.*, **47**, https://doi.org/10.34194/geusb.v47.5284.

WGMS, 2021: Fluctuations of Glaciers Database. World Glacier Monitoring Service, accessed 7 May 2021, https://doi.org/10.5904/wgms-fog-2021-05.

WHO, 2002: Global Solar UV Index: A Practical Guide. WHO/SDE/OEH/02.2, 28 pp., https://apps.who.int/iris/handle/10665/42459.

——, 2018: Scientific Assessment of Ozone Depletion: 2018. Global Ozone Research and Monitoring Project Rep. 58, World Meteorological Organization, 588 pp., https://csl.noaa.gov/assessments/ozone/2018/.

Wolken, G. J., B. Wouters, M. Sharp, L. M. Andreassen, D. Burgess, J. Kohler, and B. Luks, 2020: Glaciers and ice caps outside Greenland. *Arctic Report Card 2020*, R. L. Thoman, J. Richter-Menge, and M. L. Druckenmiller, Eds., NOAA, 8 pp., https://doi.org/10.25923/nwqq-8736.

——, and Coauthors, 2021: Glacier and permafrost hazards. *Arctic Report Card 2021*, T. A. Moon, M. L. Druckenmiller, and R. L. Thoman, Eds., NOAA, 93–101, https://doi.org/10.25923/v40r-0956.

Wouters, B., A. Gardner, and G. Moholdt, 2019: Global glacier mass loss during the GRACE satellite mission (2002–2016). Front. *Earth Sci.*, **7**, https://doi.org/10.3389/feart.2019.00096.

Wright, C. J., R. J. Hall, T. P. Banyard, N. P. Hindley, I. Krisch, D. M. Mitchell, and W. J. M. Seviour, 2021: Dynamical and surface impacts of the January 2021 sudden stratospheric warming in novel Aeolus wind observations, MLS and ERA5. *Wea. Climate Dyn.*, **2**, 1283–1301, https://doi.org/10.5194/wcd-2-1283-2021.

York, A., U. S. Bhatt, E. Gargulinski, Z. Grabinski, P. Jain, A. Soja, R. L. Thoman, and R. Ziel, 2020: Wildland fire in the high northern latitudes. *Arctic Report Card 2020*, R. L. Thoman, J. Richter-Menge, and M. L. Druckenmiller, Eds., NOAA, 11 pp., https://doi.org/10.25923/2gef-3964.

Zemp, M., and Coauthors, 2019: Global glacier mass changes and their contributions to sea-level rise from 1961 to 2016. *Nature*, **568**, 382–386, https://doi.org/10.1038/s41586-019-1071-0.

Zhang, M., X.-Y. Yang, and Y. Huang, 2022: Impacts of sudden stratospheric warming on extreme cold events in early 2021: An ensemble-based sensitivity analysis. *Geophys. Res. Lett.*, **49**, e2021GL096840, https://doi.org/10.1029/2021GL096840.

STATE OF THE CLIMATE IN 2021

ANTARCTICA AND THE SOUTHERN OCEAN

K. R. Clem and M. N. Raphael, Eds.

Special Online Supplement to the *Bulletin of the American Meteorological Society*, Vol. 103, No. 8, August 2022

https://doi.org/10.1175/BAMS-D-22-0078.1

Corresponding author: Kyle R. Clem / kyle.clem@vuw.ac.nz

STATE OF THE CLIMATE IN 2021

Antarctica and the Southern Ocean

Editors

Jessica Blunden
Tim Boyer

Chapter Editors

Freya Aldred
Peter Bissolli
Kyle R. Clem
Howard J. Diamond
Matthew L. Druckenmiller
Robert J. H. Dunn
Catherine Ganter
Nadine Gobron
Gregory C. Johnson
Rick Lumpkin
Ademe Mekonnen
John B. Miller
Twila A. Moon
Marilyn N. Raphael
Ahira Sánchez-Lugo
Carl J. Schreck III
Richard L. Thoman
Kate M. Willett
Zhiwei Zhu

Technical Editor

Laura Ohlmann

BAMS Special Editor for Climate

Michael A. Alexander

American Meteorological Society

Cover credit:
Photograph taken at the South Pole in 2021 by Jeffrey Keller, USAP/PAE, Preventative Manitenance Foreman, Colorado Springs, Colorado.

Antarctica and the Southern Ocean is one chapter from the *State of the Climate in 2021* annual report and is available from https://doi.org/10.1175/BAMS-D-22-0078.1. Compiled by NOAA's National Centers for Environmental Information, *State of the Climate in 2021* is based on contributions from scientists from around the world. It provides a detailed update on global climate indicators, notable weather events, and other data collected by environmental monitoring stations and instruments located on land, water, ice, and in space. The full report is available from 10.1175/2022BAMSStateoftheClimate.1.

How to cite this document:

Citing the complete report:
Blunden, J. and T. Boyer, Eds., 2022: "State of the Climate in 2021". *Bull. Amer. Meteor. Soc.,* **103** (8), Si–S465, https://doi.org/10.1175/2022BAMSStateoftheClimate.1

Citing this chapter:
Clem, K. R. and M. N. Raphael, Eds., 2022: Antarctica and the Southern Ocean [in "State of the Climate in 2021"]. *Bull. Amer. Meteor. Soc.*, **103** (8), S307–S340, https://doi.org/10.1175/BAMS-D-22-0078.1.

Citing a section (example):
Reid, P., S. Stammerjohn, R. A. Massom, S. Barreira, T. Scambos, and J. L. Lieser, 2022: Sea ice extent, concentration, and seasonality [in "State of the Climate in 2021"]. *Bull. Amer. Meteor. Soc.*, **103** (8), S325–S329, https://doi.org/10.1175/BAMS-D-21-0078.1.

Editor and Author Affiliations (alphabetical by name)

Adusumilli, Susheel, Scripps Institution of Oceanography, University of California San Diego, La Jolla, California

Baiman, Rebecca, Department of Atmospheric and Oceanic Sciences, University of Colorado Boulder, Boulder, Colorado

Banwell, Alison F., Earth Science and Observation Center, CIRES, University of Colorado, Boulder, Colorado

Barreira, Sandra, Argentine Naval Hydrographic Service, Buenos Aires, Argentina

Beadling, Rebecca L., NOAA, Geophysical Fluid Dynamics Laboratory, Princeton University Atmospheric and Oceanic Sciences Program, Princeton, New Jersey and University Corporation for Atmospheric Research, Boulder, Colorado

Clem, Kyle R., School of Geography, Environment and Earth Sciences, Victoria University of Wellington, Wellington, New Zealand

Colwell, Steve, British Antarctic Survey, Cambridge, United Kingdom

Coy, Lawrence, Science Systems and Applications, Inc., Lanham, Maryland, and NASA Goddard Space Flight Center, Greenbelt, Maryland

Datta, Rajashree T., Department of Atmospheric and Oceanic Sciences, University of Colorado Boulder, Boulder, Colorado

De Laat, Jos, Royal Netherlands Meteorological Institute (KNMI), DeBilt, Netherlands

Dunmire, Devon, Department of Atmospheric and Oceanic Sciences, University of Colorado Boulder, Boulder, Colorado

Fogt, Ryan L., Department of Geography, Ohio University, Athens, Ohio

Freeman, Natalie M., Department of Atmospheric and Oceanic Sciences, University of Colorado Boulder, Boulder, Colorodo

Fricker, Helen Amanda, Scripps Institution of Oceanography, University of California San Diego, La Jolla, California

Gardner, Alex S., Jet Propulsion Laboratory, California Institute of Technology, Pasadena, California

Johnson, Bryan, NOAA/OAR Earth System Research Laboratory, Global Monitoring Division, and University of Colorado Boulder, Boulder, Colorado

Keller, Linda M., Department of Atmospheric and Oceanic Sciences, University of Wisconsin-Madison, Madison, Wisconsin

Kramarova, Natalya A., NASA Goddard Space Flight Center, Greenbelt, Maryland

Lazzara, Matthew A., Department of Physical Sciences, School of Arts and Sciences, Madison Area Technical College, and Space Science and Engineering Center, University of Wisconsin-Madison, Madison, Wisconsin

Lieser, Jan L., Australian Bureau of Meteorology and Institute for Marine and Antarctic Studies (IMAS), University of Tasmania, Hobart, Tasmania, Australia

MacFerrin, Michael, Earth Science and Observation Center, CIRES, University of Colorado, Boulder, Colorado

MacGilchrist, Graeme A., NOAA, Geophysical Fluid Dynamics Laboratory, and Princeton University Atmospheric and Oceanic Sciences Program, Princeton, New Jersey

MacLennan, Michelle L., Department of Atmospheric and Oceanic Sciences, University of Colorado Boulder, Boulder, Colorado

Massom, Robert A., Australian Antarctic Division, Australian Antarctic Program Partnership (AAPP) and Australian Centre for Excellence in Antarctic Science (ACEAS), Hobart, Tasmania, Australia

Mazloff, Matthew R., Scripps Institution of Oceanography, University of California, San Diego, La Jolla, California

Mote, Thomas L., Department of Geography, University of Georgia

Nash, Eric R., Science Systems and Applications, Inc., Lanham, Maryland, and NASA Goddard Space Flight Center, Greenbelt, Maryland

Newman, Paul A., NASA Goddard Space Flight Center, Greenbelt, Maryland

Norton, Taylor, Department of Atmospheric and Oceanic Sciences, University of Wisconsin-Madison, Madison, Wisconsin

Petropavlovskikh, Irina, NOAA/OAR Earth System Research Laboratory, Global Monitoring Division, and University of Colorado Boulder, Boulder, Colorado

Pitts, Michael, NASA Langley Research Center, Hampton, Virginia

Raphael, Marilyn N., Department of Geography, University of California-Los Angeles, Los Angeles, California

Reid, Phillip, Australian Bureau of Meteorology and Australian Antarctic Program Partnership (AAPP), Hobart, Tasmania, Australia

Santee, Michelle L., NASA Jet Propulsion Laboratory, Pasadena, California

Scambos, Ted A., Earth Science and Observation Center, CIRES, University of Colorado, Boulder, Colorado

Shi, Jia-Rui, Woods Hole Oceanographic Institution, Woods Hole, Massachusetts

Stammerjohn, Sharon, Institute of Arctic and Alpine Research, University of Colorado, Boulder, Colorado

Strahan, Susan E., University of Maryland Baltimore County, Baltimore, Maryland, and NASA Goddard Space Flight Center, Greenbelt, Maryland

Thompson, Andrew F., Environmental Science and Engineering, California Institute of Technology, Pasadena, California

Wille, Jonathan D., Institut des Géosciences de l'Environnement, CNRS/UGA, Saint Martin d'Hères, France

Wilson, Earle, Environmental Science and Engineering, California Institute of Technology, Pasadena, California

Editorial and Production Team

Allen, Jessicca, Graphics Support, Cooperative Institute for Satellite Earth System Studies, North Carolina State University, Asheville, North Carolina

Hammer, Gregory, Content Team Lead, Communications and Outreach, NOAA/NESDIS National Centers for Environmental Information, Asheville, North Carolina

Love-Brotak, S. Elizabeth, Lead Graphics Production, NOAA/NESDIS National Centers for Environmental Information, Asheville, North Carolina

Misch, Deborah J., Graphics Support, Innovative Consulting and Management Services, LLC, NOAA/NESDIS National Centers for Environmental Information, Asheville, North Carolina

Ohlmann, Laura, Technical Editor, Innovative Consulting and Management Services, LLC, NOAA/NESDIS National Centers for Environmental Information, Asheville, North Carolina

Riddle, Deborah B., Graphics Support, NOAA/NESDIS National Centers for Environmental Information, Asheville, North Carolina

Veasey, Sara W., Visual Communications Team Lead, Communications and Outreach, NOAA/NESDIS National Centers for Environmental Information, Asheville, North Carolina

6. Table of Contents

*Please refer to Chapter 8 (Relevant datasets and sources) for a list of all climate variables and datasets used in this chapter for analyses, along with their websites for more information and access to the data.

6. ANTARCTICA AND THE SOUTHERN OCEAN

K. R. Clem and M. N. Raphael, Eds..

a. Overview—K. R. Clem and M. N. Raphael

Antarctica and the Southern Ocean were dominated by below-average pressure and stronger than average circumpolar westerly winds through much of 2021, resulting in many new low-pressure records set across the continent. The low pressure that gripped the polar cap extended vertically through the troposphere and stratosphere and was accompanied by a persistently strong and stable polar vortex. This helped deliver the coldest winter on record to the South Pole (see Sidebar 6.1) and also helped maintain one of the longest-lived ozone holes on record (second only to the 2020 ozone hole), which did not close until 23 December. Despite the long duration of the ozone hole, its size and the minimum ozone concentrations did not reach exceptional levels, and its slow growth rate in 2021 is consistent with ongoing recovery trends.

Embedded within the low pressure over the polar cap were several strong regional cyclonic circulations that produced marked anomalies in all aspects of the coupled climate system. In particular, the Amundsen Sea Low was stronger than normal through most of the year. This brought persistent warm northerly winds to the Antarctic Peninsula (AP) and the surrounding Bellingshausen and western Weddell Seas regions (see Fig. 6.1 for map). Esperanza and Marambio stations on the northeastern Peninsula experienced their warmest (tied) and second warmest years on record, respectively; sea ice concentration and extent in the Bellingshausen and western Weddell Seas remained well below average through most of the year. The annual surface mass balance (accumulated precipitation minus sublimation/surface meltwater runoff) was over 25% higher than average on the Peninsula, while surface melt was also above average, particularly across the Larsen C and remnant Larsen B ice shelves, where there were more than 30 days above the average number of surface melt days during the 2020/21 melt season. Meanwhile, strong storms and turbulent conditions brought near-record high ocean mixed layer depth and salinity across the southeast South Pacific, which contributed to the second highest chlorophyll concentration and phytoplankton growth on record for this region in January 2021.

Strong, regional, cyclonic anomalies were also seen near Dronning Maud Land (~30°W–30°E) and Wilkes Land (~90°–120°E). These helped trigger and guide a higher-than-normal number of landfalling atmospheric rivers into these regions, particularly during October in Wilkes Land and December in Dronning Maud Land. This resulted in an annual surface mass balance that was over 50% above average in both regions for 2021.

Despite the higher-than-normal surface mass gains in several regions, Antarctica as a whole continued to lose mass in 2021. A net mass loss of 50 Gt occurred from December 2020 to December 2021 (~0.14 mm of global sea level rise), almost all of which came from the coastal margins of West Antarctica where there was also a continued decrease in surface elevation. However, the mass loss in 2021 was far less than the average rate of annual mass loss of 140 Gt yr^{-1} since 2003, suggesting a major positive contribution of surface processes to seasonal mass and height changes. Despite such large regional surface mass gains, the loss of ice from the West Antarctic Ice Sheet (WAIS) continued to overwhelm gains from surface accumulation, and Antarctica continued its ongoing contribution to global sea level rise in 2021.

Antarctic sea ice anomalies exhibited dramatic seasonal variability, similar to that seen in recent years. The year began with below-average overall sea ice extent in January and February,

before abruptly switching to above average in late February; the above-average conditions persisted until September, reaching near-record high daily extents in August. Following an anomalously early daily maximum extent on 30 August, sea ice then retreated rapidly from September to December, with sea ice area plummeting to record low daily values in parts of October and December. A new monthly mean record-low sea ice area was set in December 2021.

More details on Antarctica's climate and cryosphere, the Southern Ocean, and the ozone hole for 2021 are presented in this chapter. In most cases, where data are available, 2021 anomalies are based on the 1991–2020 climatological average. Otherwise, the climatological period is provided within each section. The geographical locations of place names mentioned throughout the Chapter are provided in Fig. 6.1.

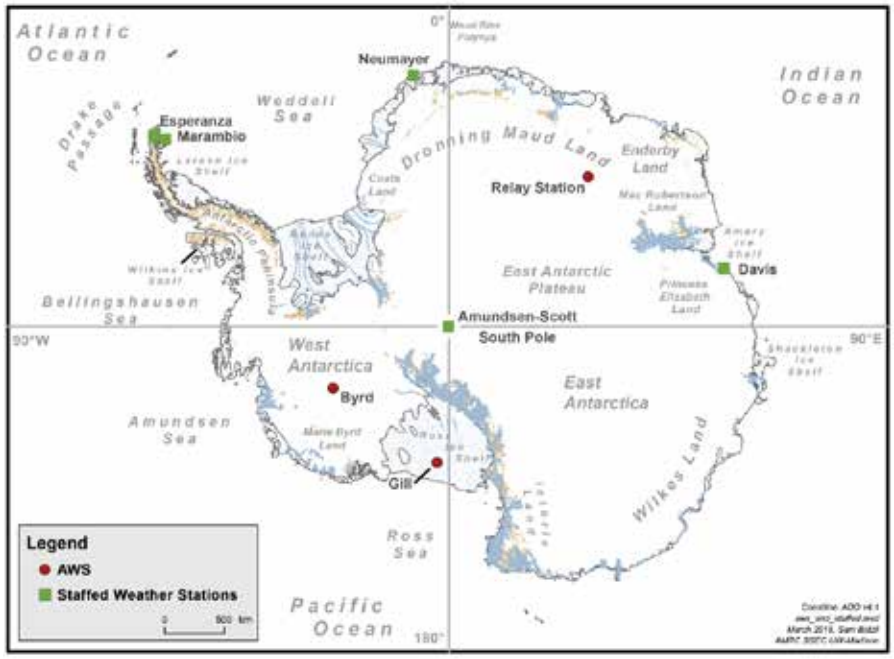

Fig. 6.1. Map of the automated (AWS) and staffed weather stations and regions discussed in this chapter. Light brown areas are rock exposures on the Antarctic continent; blue stippling indicates ice shelf areas, but in areas of heavy crevassing on both the ice shelves and the ice sheet, the surface is shown in solid gray-blue on the map. A few selected flow line features and shear margins are shown as blue lines.

b. Atmospheric circulation and surface observations—K. R. Clem, S. Barreira, R. L. Fogt, S. Colwell, L. M. Keller, M. A. Lazzara, and T. Norton

Much of continental Antarctica experienced below-average surface pressure during 2021, which was accompanied by predominantly positive phases of the Southern Annular Mode (SAM; the leading mode of extratropical Southern Hemisphere atmospheric circulation; the positive phase reflects above-average pressure in the middle latitudes and below-average pressure over Antarctica). Many negative pressure records were set across the continent throughout the year, with the strongest negative pressure anomalies occurring during December in the Antarctic Peninsula, West Antarctica, and the Ross Ice Shelf region; no positive pressure records were set in Antarctica during 2021. Surface pressure was also well below average in the Amundsen and Bellingshausen Seas for most of the year, reflecting an anomalously deep Amundsen Sea Low, which is consistent with the South Pacific atmospheric circulation response to the La Niña conditions that persisted through much of 2021 (Turner et al. 2013; see section 4b). The atmospheric circulation anomalies produced anomalously warm conditions across the Antarctic Peninsula for most of the year, with Esperanza tying 2016 for its warmest year on record and Marambio recording its second-warmest year on record behind 2016 (both located on the northeast Peninsula). Parts of the interior, especially the South Pole region into Dronning Maud Land, experienced the coldest winter on record (see Sidebar 6.1 for details), while conversely the remainder of East Antarctica experienced a slightly warmer-than-average year (around 1°C above average) due to localized warm advection from a persistent regional cyclonic anomaly near the Amery Ice Shelf. Above the surface, geopotential height and temperature over the polar cap were generally below average in the upper troposphere and stratosphere throughout the year, especially during the early and late

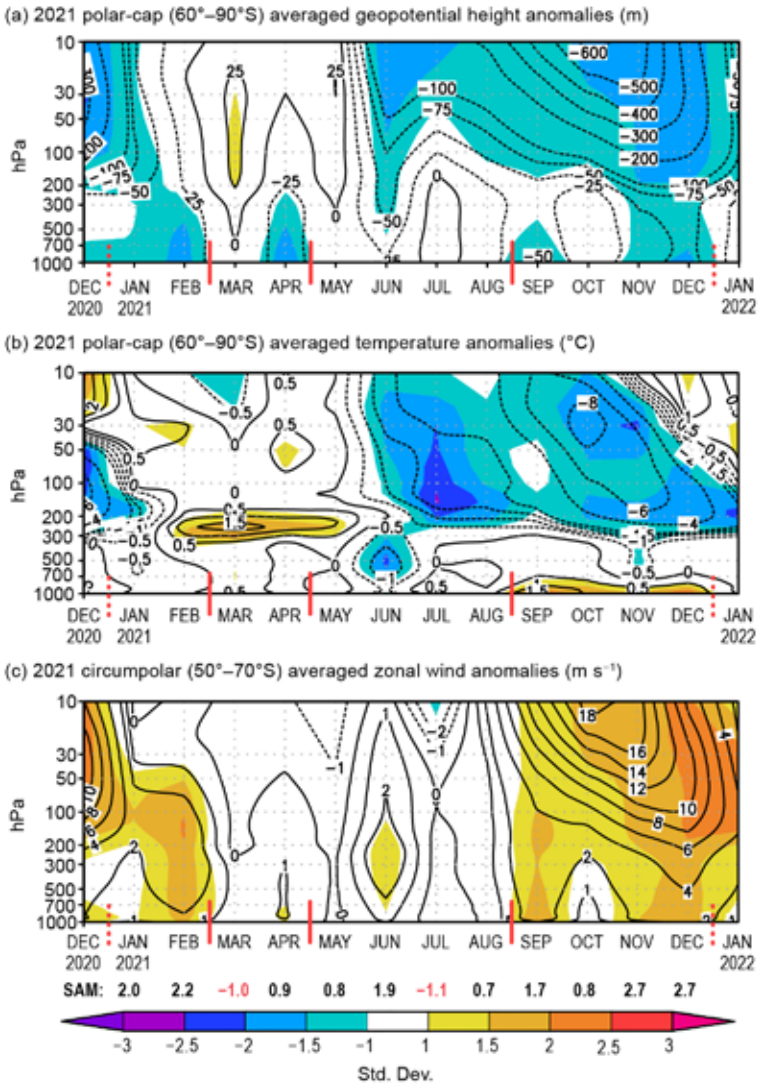

Fig. 6.2. Area-averaged (weighted by cosine of latitude) monthly anomalies over the southern polar region in 2021 relative to 1991–2020: (a) polar cap (60°–90°S) averaged geopotential height anomalies (contour interval is 25 m up to ±100 m and 100 m after ±100 m); (b) polar cap (60°–90°S) averaged temperature anomalies (contour interval is 0.5°C up to ±2°C and 2°C after ±2°C); (c) circumpolar (50°–70°S) averaged zonal wind anomalies (contour interval is 2 m s^{-1} with an additional contour at ±1 m s^{-1}). Shading depicts standard deviation of monthly anomalies from the 1991–2020 climatological average as indicated by the color bar at bottom. Red vertical bars indicate the four climate periods used for compositing in Fig. 6.3; the dashed lines near Dec 2020 and Dec 2021 indicate circulation anomalies wrapping around the calendar year. Values from the Marshall (2003) SAM index are shown below (c) in black (positive values) and red (negative values). (Source: ERA5 reanalysis.)

quarters, associated with the anomalously large and deep spring ozone holes in 2020 and 2021, respectively (Kramarova et al. 2021; see section 6h for more details). This resulted in near- or stronger-than-average circumpolar westerly winds for all of 2021.

The Antarctic atmospheric circulation anomalies were examined using the European Centre for Medium-Range Weather Forecasts fifth generation atmospheric reanalysis (ERA5). Figure 6.2 shows the monthly geopotential height (Fig. 6.2a) and temperature (Fig. 6.2b) anomalies averaged over the polar cap (60°–90°S) and the monthly circumpolar zonal wind anomalies (Fig. 6.2c) averaged over 50°–70°S. The anomalies (contoured) and the standard deviations (shaded) are relative to the 1991–2020 climatology. To highlight the main surface climate anomalies, the year was split into four periods based on relative persistence of climate anomalies: January–February, March–April, May–August, and September–December. The surface pressure and temperature anomalies (contours) and standard deviations (shaded) are averaged for each group relative to their 1991–2020 climatology (Fig. 6.3). Monthly temperature and pressure anomalies are also shown for select Antarctic staffed (Marambio, Neumayer, Davis) and automated (Relay Station AWS, Byrd AWS, Gill AWS) weather stations located throughout the continent (Fig. 6.4).

From January to February, strong negative geopotential height (Fig. 6.2a) and surface pressure (Fig. 6.3a) anomalies and below-average temperatures (Fig. 6.3b) dominated Antarctica. The negative pressure anomalies were accompanied by a ring of positive pressure anomalies across the middle latitudes, resulting in anomalously strong circumpolar westerlies through the troposphere and lower stratosphere (2–3 m s^{-1}, 1–2 std. dev. above average; Fig. 6.2c), reaching a peak in February. Neumayer station observed its coldest January on record, at −6.2°C (2.1°C below average; Fig. 6.4b), and just to the east, Novolazarevskaya station (not shown) observed its coldest February on record. While negative pressure anomalies occurred over the entire continent, they were strongest over West Antarctica where pressure was more than 10 hPa (3 std. dev.) below average (Fig. 6.3a); in this region, Byrd AWS and Gill AWS (on the Ross Ice Shelf) both observed their lowest mean February pressure on record, (10–11 hPa

below average; Figs. 6.4e,f), while on the plateau, Relay Station AWS also observed its lowest February pressure on record (6.7 hPa below average).

The negative pressure anomalies and cold temperatures over the continent relaxed during March–April (Figs. 6.3c,d), and a strong cyclonic anomaly developed across the Weddell Sea region. This brought marked surface warming across Dronning Maud Land and to parts of the plateau, which peaked during March when temperatures were 4–6°C (> 3 std. dev.) above average (not shown). Neumayer (Fig. 6.4b), Novolazarevskaya (not shown), and Relay Station AWS (Fig. 6.4d) all observed their warmest March on record. Neumayer also observed its lowest mean April pressure on record (Fig. 6.4b). In contrast, negative temperature anomalies were observed across Marie Byrd Land and the Ross Ice Shelf during March–April (Fig. 6.3d).

From May to August, surface pressure across the continent remained relatively stable and close to average, and a zonal wave-3 pattern developed over the Southern Ocean (Fig. 6.3e). The most noteworthy monthly feature occurred in June when negative surface pressure and geopotential height anomalies over the polar cap developed through the upper troposphere and lower stratosphere (Fig. 6.2a), coinciding with a strengthening of the circumpolar westerlies (Fig. 6.2c) and strong negative surface temperature anomalies near the pole (Fig. 6.3f). The South Pole recorded a June temperature of –63.9°C that was 5.8°C below average (see Sidebar 6.1) which equaled 1984 for its second coldest June temperature on record. No monthly temperature or pressure records were set over this period, but temperatures were 3–4°C (1–2 std. dev.) below average, stretching from the South Pole toward Dronning Maud Land, where Neumayer observed its coldest austral winter (June–August) on record (not shown), and the South Pole observed its coldest extended winter season (April–September, Sidebar 6.1) on record.

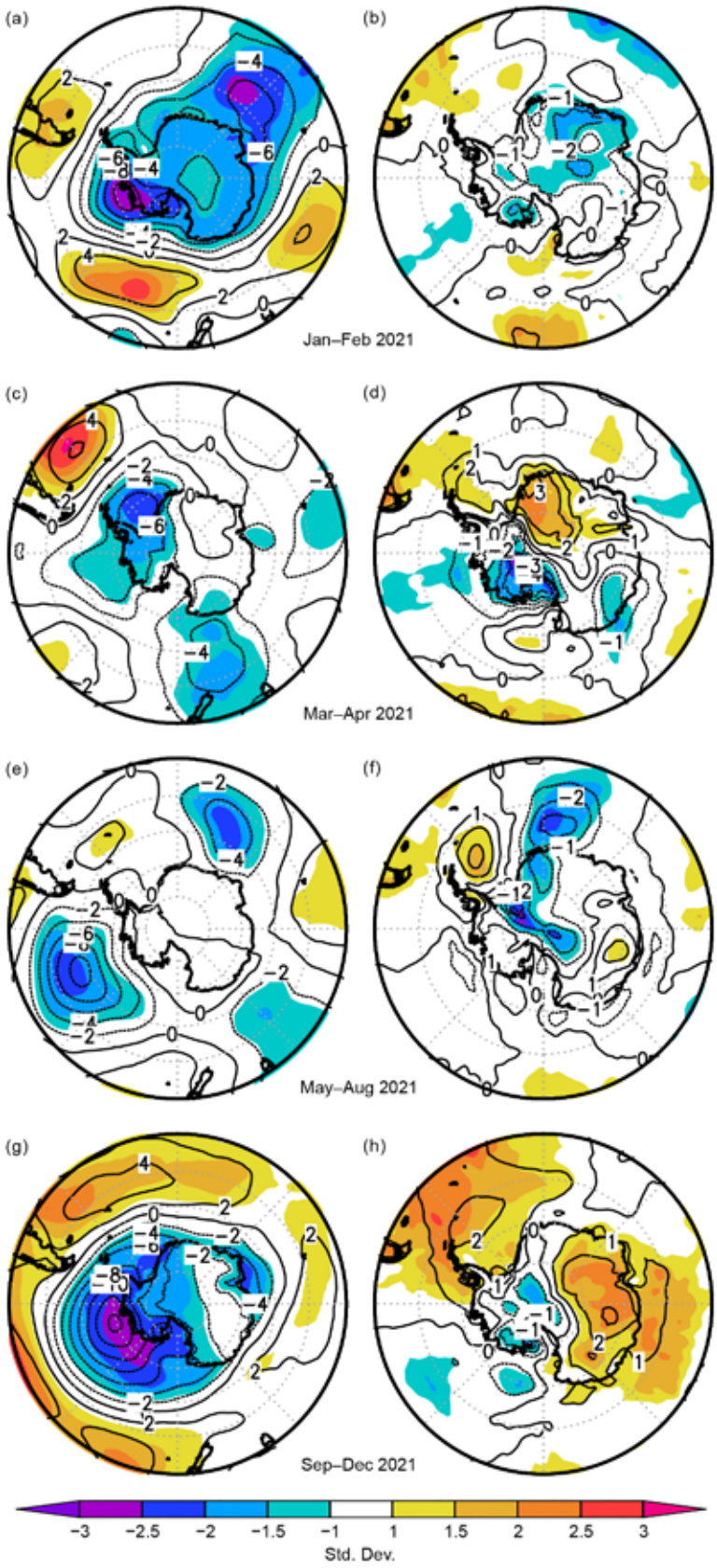

Fig. 6.3. (left) Surface pressure and (right) 2-m temperature anomalies relative to 1991–2020 for (a,b) Jan–Feb 2021; (c,d) Mar–Apr 2021; (e,f) May–Aug 2021; (g,h) Sep–Dec 2021. Contour interval is 2 hPa for surface pressure anomalies and 1°C for 2-m temperature anomalies. Shading shows the standard deviation of the anomalies. (Source: ERA5 reanalysis.)

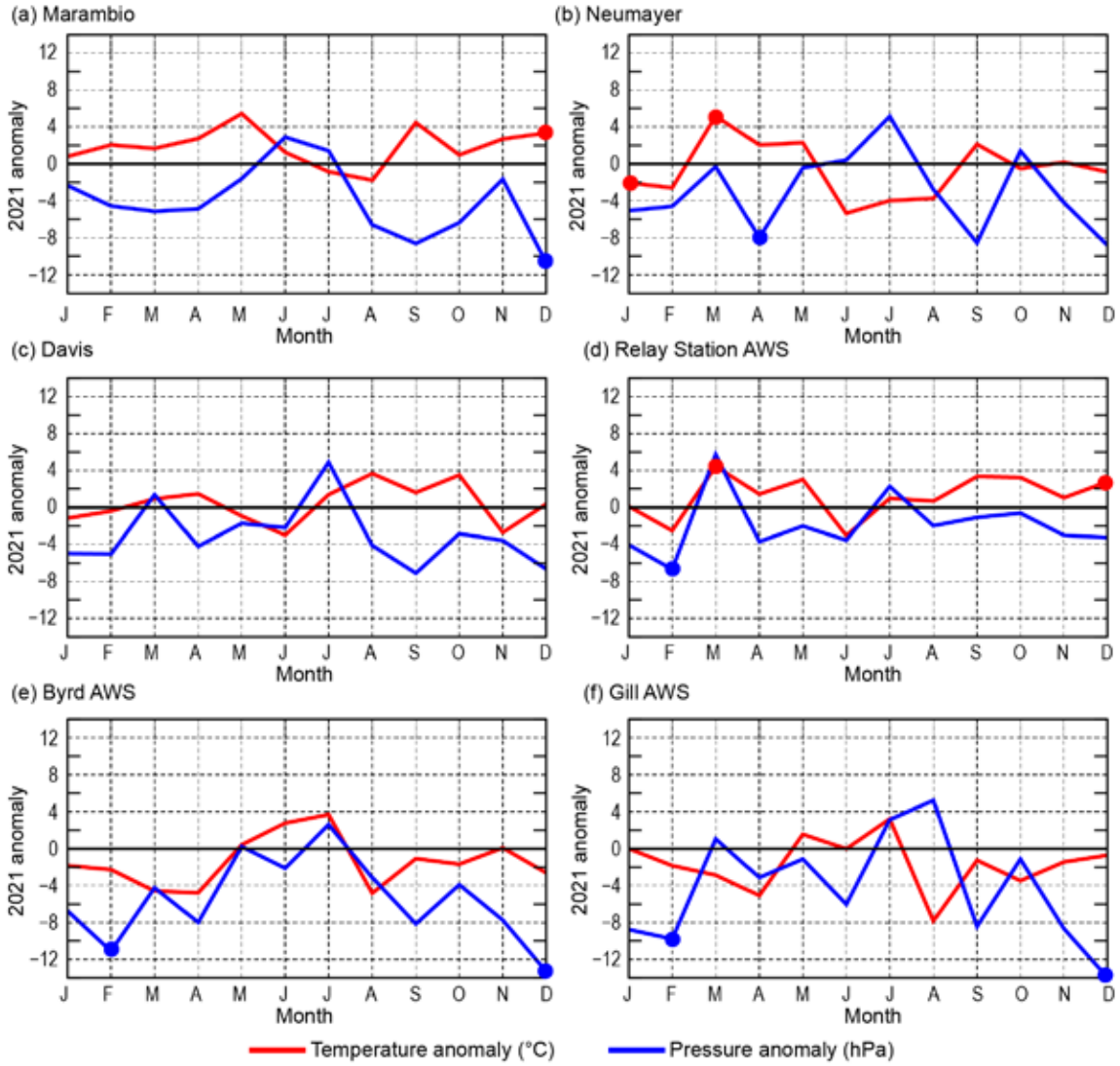

Fig. 6.4. Monthly Antarctic climate anomalies during 2021 at six representative stations (three staffed [a–c], and three automatic [d–f]). Anomalies for temperature (°C) are shown in red and MSLP/surface pressure (hPa) are shown in blue, with filled circles denoting monthly-mean records set for each station in 2021. All anomalies are based on differences from the monthly 1991–2020 averages. Observational data used to calculate records start in 1970 for Marambio, 1981 for Neumayer, 1957 for Davis, 1980 for Byrd AWS, 1995 for Relay Station AWS, and 1985 for Gill AWS.

Surface pressure was below average again in most regions from September to December, especially across West Antarctica and over the Amundsen Sea (Fig. 6.3g). Negative pressure anomalies along coastal West Antarctica of –12 to –14 hPa (> 2.5 std. dev.) were associated with warm air advection across the Antarctic Peninsula and Weddell Sea region and temperatures were 1–2°C (> 2 std. dev.) above average (Fig. 6.3h). Austral spring (September–November) was especially warm on the Peninsula, with Faraday, Rothera, Bellingshausen, and Esperanza all experiencing one of their three warmest springs on record (not shown). Meanwhile, in early spring East Antarctica also experienced temperatures that were 2–3°C (2 std. dev.) above average over this period on the plateau (Fig. 6.3h) and 3–4°C above average at the coast near Davis (Fig. 6.4c). Strong negative pressure anomalies were observed over the continent in November and December, with Marambio, Byrd AWS, and Gill AWS all setting new low-pressure records in December, while Marambio and Relay AWS both tied for their warmest Decembers on record. These large Antarctic climate anomalies in late 2021 were likely a result of the downward propagation of negative geopotential height anomalies from the stratosphere to the lower troposphere (Fig. 6.2a) via dynamical and diabatic forcing (Song and Robinson 2004; Thompson et al. 2006) from the anomalously deep ozone hole and associated stratospheric anomalies in 2021 (section 6h).

Sidebar 6.1: A record cold winter at the South Pole in 2021—T. NORTON, L. KELLER, K. R. CLEM, M. LAZZARA, T. SCAMBOS, AND S. BARREIRA.

The Amundsen-Scott South Pole station had its lowest austral winter average temperature in 2021, at –61.0°C (April–September, AMJJAS; blue line in Fig. SB6.1a) since records began in 1957. During these months when the South Pole is in continuous darkness, there were 153 days (out of 183) where the daily average temperature was –50°C or below, second only to the polar night period in 2012. Meteorological winter (June–August, JJA) was the second coldest on record (behind 2004), with June and August each having 28 days at or below –50°C. The annual mean temperature for the 2021 calendar year tied for third coldest on record at –50.5°C (red line in Fig. SB6.1a), 1.3°C below average.

Generally, a stable polar vortex creates prime conditions for extensive cold periods by minimizing the intrusions of warm air into the continental (ice sheet) interior. Clear sky conditions augment the tendency towards low temperatures by increasing radiative cooling, and low wind speeds reduce mixing of boundary layer air, resulting in a strong surface inversion (Neff et al. 2018; Keller et al. 2022). Under strong inversion conditions, the mean wind direction at the South Pole is grid east/northeast (40°–80°; Neff et al. 2018; Keller et al. 2022), as air drains off the East Antarctic Plateau. All of these factors were in play in 2021, resulting in a polar night that was substantially colder than average, although records were not set in any of the individual months. Further, the below-average annual mean temperature in 2021 did not substantially reduce the overall warming trend over the last 30+ years at the South Pole (Clem et al. 2020). The annual mean temperature trend from 1989 to the record warm year in 2018 is 0.61 ± 0.34°C decade^{-1} ($p < 0.01$, solid black line in Fig. SB6.1a), and it remains positive (although smaller) and significant when the trend is extended to 2021 at 0.47 ± 0.32°C decade^{-1} ($p < 0.01$; dashed black line in Fig. SB6.1a).

The persistent cold from April to September 2021 was a result of multiple compounding factors. Although the Amundsen Sea Low (ASL) was anomalously strong during AMJJAS, shown by the large negative geopotential height anomalies (contours) in Fig. SB6.1b, the center of the cyclonic anomaly in 2021 was located in the southernmost South Pacific near 60°S, north of its winter average position of ~70°S (Hosking et al. 2013) and away from the continent. This limited the advection of warmer, maritime air to the Antarctic Peninsula and West Antarctic coastline. By comparison, the anomalous cyclonic circulation in 2018 extended eastward and poleward into the Weddell Sea and across West Antarctica, driving warm air inland. In addition, a large cyclonic anomaly dominated winter conditions in Dronning Maud Land in 2021 compared to a strong anticyclone in 2018. This extended onto the East Antarctic Plateau, producing anomalous easterly flow off the high Polar Plateau clockwise towards the Weddell Sea, suppressing the intrusion of warm air masses off the Weddell Sea, unlike what occurred in 2018.

Comparing the 2021 synoptic conditions (blue lines in Figs. SB6.1c–f) with those of 2018 (red lines), the South Pole's anomalous warm conditions in 2018 peaked during May–August (Fig. SB6.1c), coinciding with a higher-than-average number of cloudy days (Fig. SB6.1d), which would reduce radiative cooling. In 2021, July and August had significantly clearer sky conditions, which in conjunction with the cold air flow off the plateau (Fig. SB6.1b), would further amplify the cold conditions. Satellite composite imagery (https://doi.org/10.48567/hevb-j127) confirmed the persistent clear skies over the South Pole and the limited maritime air mass intrusions through the winter. Cloud movement patterns indicated that continental air was trapped over the interior for extended periods, with little low-latitude air intrusion. The monthly average vector wind directions observed at the South Pole between June and September were between 50° and 80° (grid northeast/east; not shown), which were 10°–30° east of average (Fig. SB6.1e), consistent with cold air advection from the higher plateau. This contrasts with the anomalous westerly wind directions in 2018 that are more consistent with onshore flow from the Weddell Sea. Monthly average vector wind speeds were also anomalously low, particularly in the last three quarters of the year (Fig. SB6.1f). In comparison, 2018 saw above-average wind speeds, particularly during May and June when the largest positive temperature anomalies occurred. The combination of colder, easterly flow from the plateau, radiational cooling, and reduced mixing due to anomalously low wind speeds all contributed to the comparatively cold 2021 winter (Keller et al. 2022).

From this analysis, it is evident that small changes in local conditions can result in large temperature anomalies at the South Pole, which could help to explain why interannual variability in temperature at the South Pole is substantial (Clem et al. 2020). While there is uncertainty in the precise role of each mechanism given the unique atmospheric environment at the South Pole during the winter, regional and local wind direction, wind speed, and cloud cover all appear to be important and contribute to the large interannual variability, especially when contrasting the conditions with 2018.

While the difference in mean winter temperature between 2021 and recent years is dramatic, the underlying conditions that

favor warming at the South Pole may still be at play (Clem et al. 2020; Stammerjohn and Scambos 2020) and the significant long-term warming trend remains. However, the 2021 winter underscores the high degree of interannual variability seen in the southern continent and surrounding ocean, a quality that is reflected in sea ice conditions, accumulation patterns, and oceanic characteristics.

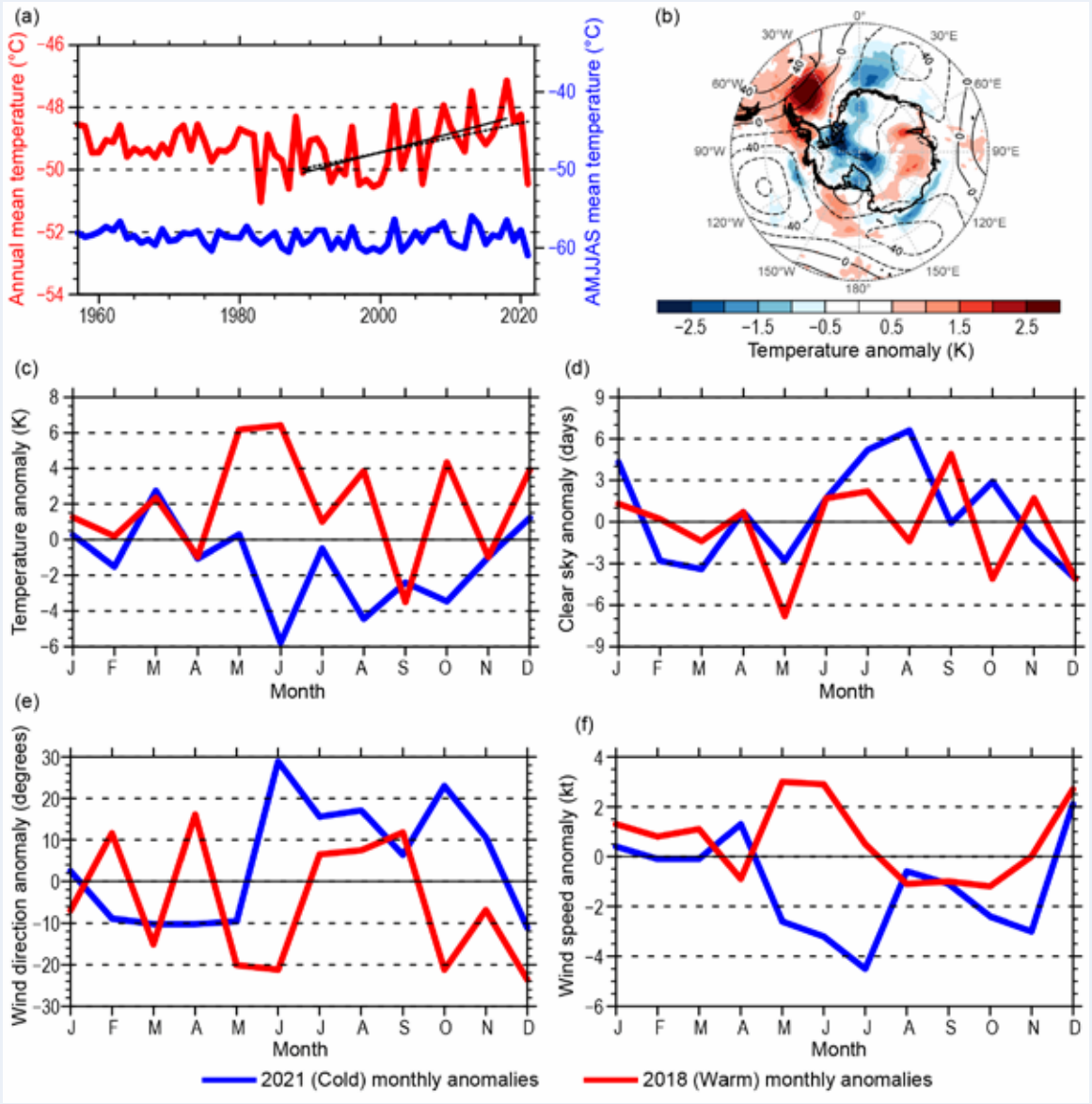

Fig. SB6.1. (a) Observed annual mean (red line) and Apr–Sep, AMJJAS, mean (blue line) South Pole temperature during the period 1957–2021. Also shown are the linear trend lines for 1989–2018 (solid black line) and 1989–2021 (dashed black line). (b) The 2021 AMJJAS 500-hPa geopotential height (m) and 2-m temperature (K) anomalies relative to the 1991–2020 climatology. (Source: ERA5.) (c)–(f) The observed 2021 (blue lines) and 2018 (red lines) monthly anomalies in (c) temperature, (d) number of clear sky days, (e) wind direction, and (f) wind speed at the South Pole relative to the 1991–2020 monthly climatologies.

c. Ice sheet surface mass balance—R. T. Datta, D. Dunmire, B. Baiman, M. Maclennan, and J. Wille

Surface mass balance (SMB) is the net effect of all processes that add to (precipitation) or take away (sublimation/runoff) mass from the surface of the ice sheet. Because the Antarctic Ice Sheet (AIS) is characterized by a cold climate, only in peak summer are atmospheric temperatures high enough to produce widespread surface melt or liquid precipitation anywhere on the grounded ice sheet (section 6d). Any meltwater that is produced refreezes locally in the firn (dense recrystallized snow left over from previous seasons), implying that meltwater runoff is generally negligible

on the AIS. On the other hand, sublimation is a significant contributor to AIS SMB (Agosta et al. 2019; Lenaerts and Van Den Broeke 2012; Mottram et al. 2020), especially in summer and in the windy escarpment zones of the ice sheet, where blowing snow occurs frequently (> 50%, Palm et al. 2018). The dominant contributor of AIS SMB, with an approximate magnitude of ~2300 Gt yr^{-1} (from reanalysis) over the grounded AIS, is solid precipitation (snowfall). In both absolute terms and as a driver of interannual variability, precipitation is strongly affected by sporadic extreme events, often in the form of atmospheric rivers (ARs; Turner et al. 2019; Wille et al. 2021). Future SMB trends indicate a divergence in SMB behavior as temperatures increase, with ice shelves being strongly affected by melt while the grounded ice sheet receives enhanced precipitation (Kittel et al. 2021).

Atmospheric reanalysis products are useful tools to analyze AIS SMB and its two dominant contributors, snowfall and sublimation, in near-real time. Here we use MERRA-2 (0.5° × 0.625° horizontal resolution; Gelaro et al. 2017) and ERA5 (0.25° × 0.25° horizontal resolution) to analyze the 2021 AIS SMB, its spatial and seasonal characteristics, and compare it to its climatological (1991–2020) record. Based on recent work comparing reanalysis products with in situ observations on Antarctica, MERRA-2 and ERA5 stood out as best-performing; however, important biases remain, including an overestimation of near-surface temperatures over the AIS interior during winter (Gossart et al. 2019; Medley and Thomas 2019; Wang et al. 2016).

The climatological AIS SMB from MERRA-2 and ERA5 is 2155 ± 128 Gt yr^{-1} and 1977 ± 103 Gt yr^{-1}, respectively. While the AIS SMB from ERA5 is significantly ($p < 0.05$) drier than MERRA-2, both reanalyses have comparable interannual variations during the climatological period and neither suggest a significant long-term trend in SMB (not shown). The 2021 AIS SMB was 2277 Gt according to MERRA-2, which falls within 1 standard deviation (std. dev.) of the climatological mean, and 2118 Gt according to ERA5, which is more than 1 std. dev. above the climatological mean for that dataset. Since both reanalyses produce similar spatial results, we use MERRA-2 hereafter to focus on spatial characteristics of the 2021 SMB. As described by various studies, AIS SMB (also in 2021, Fig. 6.5a) is relatively high (> 500 mm water equivalent) in the coastal areas of the ice sheet and decreases sharply from the coast upward and poleward on the ice sheet, with SMB values < 50 mm water equivalent (w.e.) in the high-elevation interior of the East Antarctic Ice Sheet.

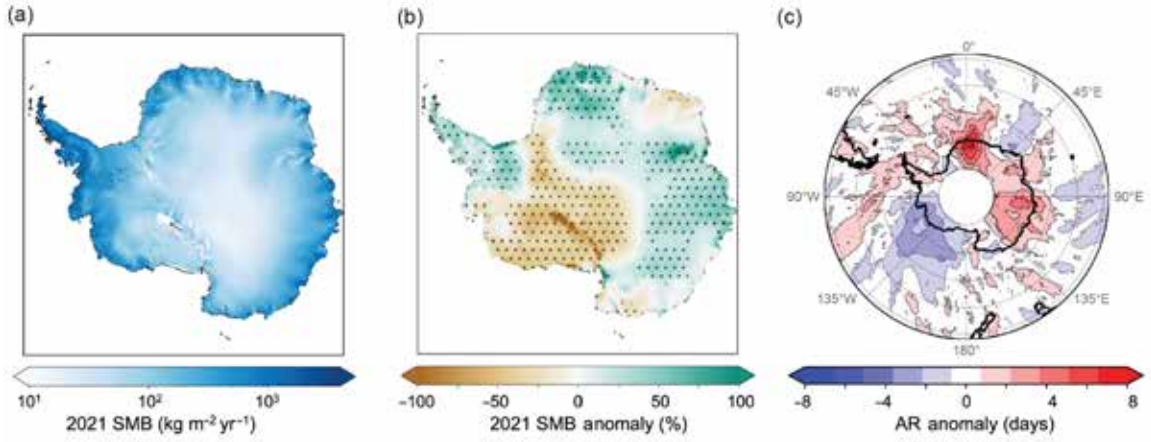

Fig. 6.5. (a) 2021 SMB in (kg m^{-2} yr^{-1}). (b) 2021 SMB anomaly(%) relative to 1991–2020 mean. 2021 SMB anomaly is greater than the 1991–2020 standard deviation in the stippled areas. (c) 2021 atmospheric river (AR) occurrence anomaly in number of days relative to the 1991–2020 mean.

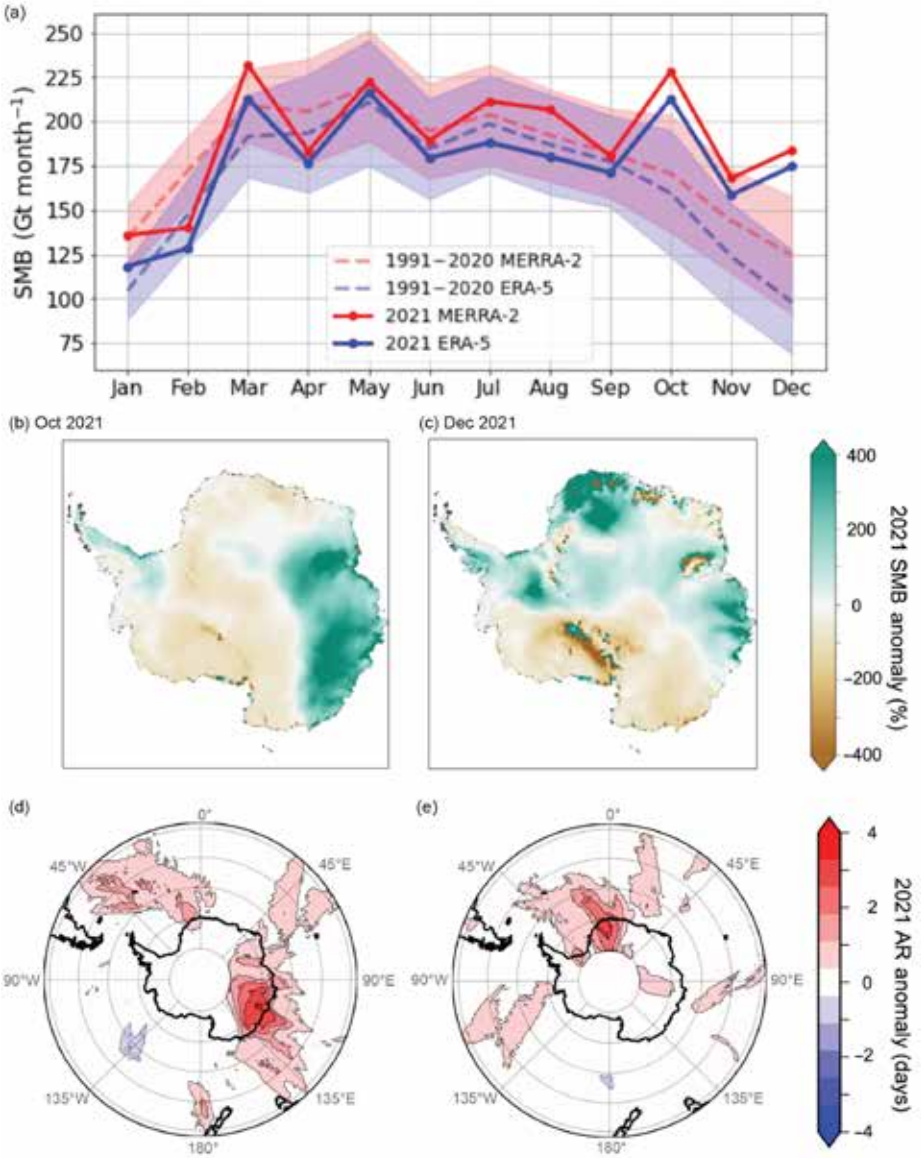

Fig. 6.6. (a) Seasonal cycle of (grounded) Antarctic Ice Sheet integrated surface mass balance in Gt yr^{-1}, according to MERRA-2 (red) and ERA5 (blue), with 2021 values shown in solid lines, 1991–2020 mean shown in the dashed lines with shading indicating one standard deviation. MERRA-2 SMB anomaly for the month relative to the 1991–2020 mean for (b) Oct 2021 and (c) Dec 2021. Anomalous number of days when an atmospheric river (AR) was detected for the month compared to the 1991–2020 mean for (d) Oct 2021 and (e) Dec 2021.

SMB anomalies in 2021 from MERRA-2 indicate substantial spatial variability relative to the climatology (Fig. 6.5b). In particular, SMB was significantly lower than climatology (< 50% of the climatological mean) over Marie Byrd Land (135°W longitude), suggesting that low SMB in this region will supplement the dynamic mass loss again in 2021, which has been ongoing in the region (section 6e). Conversely, 2021 SMB was exceptionally above average in western Dronning Maud Land and Wilkes Land (> 150% of the climatological mean) and slightly higher over the Antarctic Peninsula (> 125% of the climatological mean). The SMB anomalies in these regions are mirrored by AR anomalies over the year (Figs. 6.5c, 6.6d,e), calculated using the algorithm originally presented by Wille et al. (2021) calculated from the 98th percentile of meridional integrated vapor transport over the time series, shown here in anomalous numbers of days where ARs occurred. These results emphasize the importance of high-impact AR occurrences to total SMB and in controlling regional interannual snowfall variability.

Throughout the year, the climatological AIS SMB varies considerably (Fig. 6.6), with a minimum in summer (120–140 Gt month^{-1}) and a maximum in autumn and spring (220–240 Gt month^{-1}). In 2021, the seasonal cycle for SMB diverged substantially from climatology in October and December, concurrent

with anomalously low pressure and above-average temperatures over the continent (section 6b). In these months, SMB values exceeded the monthly climatological mean by 1 std. dev. for MERRA-2 (shown in red shading) as well as in ERA5 (shown in blue shading). SMB anomaly maps indicate that these months in 2021 were characterized by strong anomalies in Wilkes Land (October, Fig. 6.6b) and in Dronning Maud Land (December, Fig. 6.6c), driven by frequent AR activity over these regions (Figs. 6.6d,e, respectively). These periods were also characterized by positive SMB anomalies over the eastern AP (October, Fig. 6.6b) and over the western AP (December, Fig. 6.6c), despite a lack of anomalous AR activity in the region.

d. Ice sheet seasonal melt extent and duration—M. MacFerrin, T. Mote, A. Banwell, and T. Scambos

Surface melt on the Antarctic Ice Sheet (AIS) occurs primarily on the coastal margins, especially on the Antarctic Peninsula and Antarctica's ice shelves. It is generally not a significant component of Antarctica's net surface mass balance because few areas have significant runoff of meltwater. However, surface melt has a large effect on the density of underlying glacial firn and can induce calving and/or glacier acceleration through hydrofracture (Scambos et al. 2003; Banwell et. al. 2013) and is important to monitor for ice sheet and ice shelf stability. The austral melt season is defined here as 1 October through 30 April. Although small brief melt events can be measured along Antarctica's northern coastal margins during austral winter, the vast majority of surface melt happens during these seven months, with the most melt being typically in December and January (Johnson et al. 2021). Here we focus on the 2020/21 melt season ending 30 April 2021. The 2021/22 austral melt season will be discussed in next year's report.

Daily surface melt is mapped using satellite passive-microwave brightness temperatures. The source data are distributed as daily composited polar stereographic brightness temperatures by the National Snow and Ice Data Center (products NSIDC-0001; Meier et al. 2019 and NSIDC-0007; Gloersen 2006) spanning 1979 through present-day. Daily passive microwave brightness temperatures using the 37-GHz horizontal polarization as well as the 37- and 19-GHz vertical polarization channels are acquired by the SMMR, SSM/I, and SSMIS sensors aboard the NOAA Nimbus-7 and DMSP F8, F11, F13, F17, and F18 satellites. Melt is determined by 37-GHz horizontally polarized brightness temperatures that exceed a dynamically established threshold each season from a simple microwave emission model that would be expected in the presence of liquid water in near-surface layers of ice and snowpack. The method used here was first developed to track Greenland's ice sheet surface melting on a daily basis (Mote and Anderson 1995; Mote 2007; Mote et al. 2014). Melt days are mapped both as sums over the melt season and as anomalies with respect to the mean annual melt day totals from the 1990–2020 baseline melt period (Figs. 6.7a,b). Large seasonal fluctuations in passive microwave emissions from some areas of dry polar firn in Antarctica can create false positive melt indications in an unmodified version of the Greenland algorithm. This was mitigated by filtering areas that only marginally exceed the melt threshold (< 10K) in the 37 GHz horizontal polarization in regions with a negative 18/19-GHz minus 37-GHz frequency gradient in the vertical polarization (MacFerrin et al. 2021). An ice extent mask of 25-km grid cells for the AIS was developed from the Quantarctica v3.0 Detailed Basemap dataset (Norwegian Polar Institute 2018). All 25-km cells that contain ≥ 50% land-ice or ice-shelf are included. We divide the AIS into seven melt extent and climate regions by clustering glaciological drainage basins (based on Shepherd et al. 2012; Fig. 6.8).

The 2020/21 austral melt season began early, with a spatially and temporally extensive melt event on the Antarctic Peninsula in the last days of October into early November (Fig. 6.7c). On the Peninsula, over the northern Larsen C and Larsen B remnant ice shelves in the 2020/21 season, there were approximately 30 more melt days than during the 1990–2020 reference period (Figs. 6.7a, 6.8b). The mid-peninsula regions, including the George VI Ice Shelf and the Wilkins Ice Shelf, had near-average to below-average melt seasons in duration and extent, particularly in comparison to the exceptional melt season that occurred on these ice shelves during the 2019/20 austral melt season (Banwell et al. 2021; MacFerrin et al. 2021). By contrast, the southern area

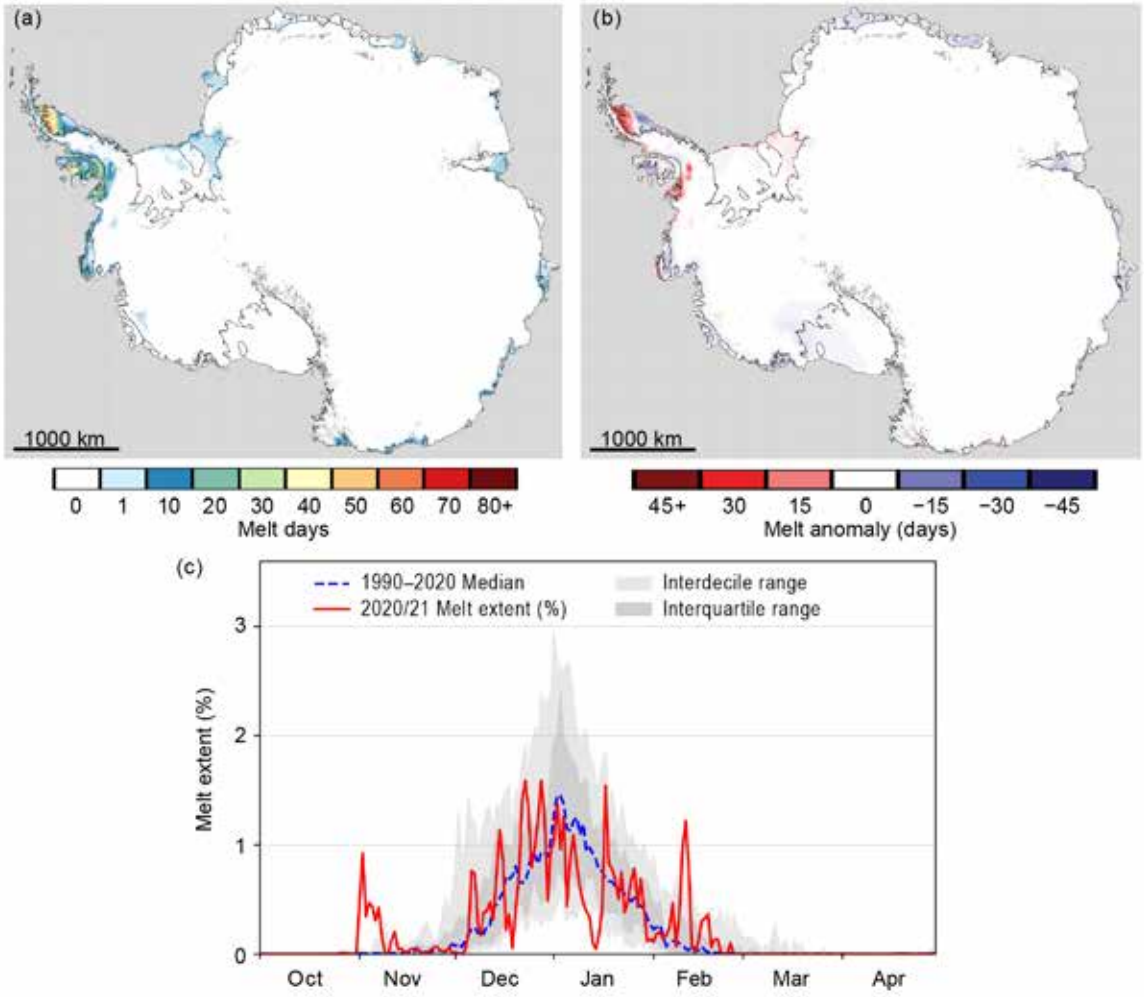

Fig. 6.7. Surface melt across the Antarctic Ice Sheet as detected from passive-microwave satellites. (a) Map of the sum of melt days from 1 Oct 2020 to 30 Apr 2021. (b) Map of the sum of melt days relative to the 1990–2020 baseline average. (c) Daily melt extent (dotted blue line) with interquartile (dark gray) and inter-decile (light gray) ranges from the 1990–2020 baseline period.

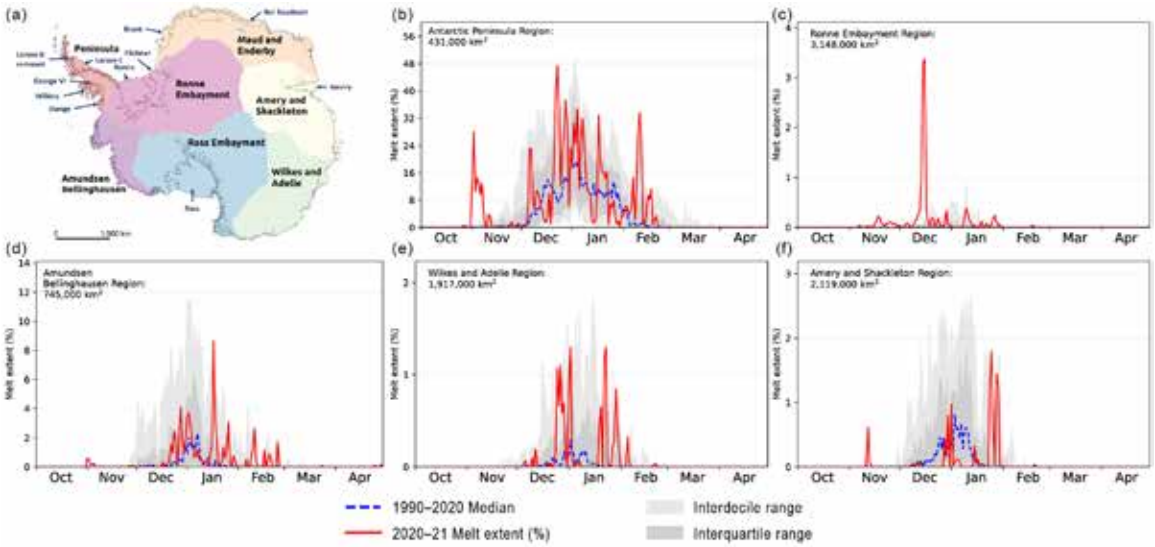

Fig. 6.8. Daily melt extents across regions of Antarctica. (a) Map of major regions of Antarctica used in regional analyses. Regional daily melt extents from (b) the Antarctic Peninsula, (c) Ronne Embayment, (d) Amundsen Bellingshausen, (e) Wilkes and Adelie, and (f) Amery and Shackleton.

of the Peninsula had an above-average number of melt days, notably in the area of the Stange Ice Shelf. Elsewhere, it is the absence of melt that is most notable: the Amery Ice Shelf (Fig. 6.8f) had 5 to 10 days of below-average melt days with only two notable melt events occurring in late January; the Roi Baudoin Ice Shelf had about 10 melt days below average overall; and on the northeastern Ross Ice Shelf, essentially zero surface melt was recorded for the season. Total melt for the season over the continent was moderately above average (Fig. 6.7a). The Peninsula, Ronne Embayment, Wilkes and Adelie, and Amundsen-Bellingshausen regions showed above-average melt indices, while the Maud and Enderby, Amery and Shackleton, and Ross Embayment regions displayed below-average melt.

On the Filchner and Brunt ice shelves, a brief but extensive melt event occurred in mid-December that reached far to the south, covering the entire length of the Filchner shelf on the eastern edge of the Ronne Ice Shelf (Figs. 6.7a, 6.8c). High atmospheric pressure in Queen Maud Land and a large low-pressure area stretching across the Ronne Ice Shelf drove strong winds from the north, bringing warm conditions all along Coats Land and as far south as the South Pole (section 6b). The South Pole remained well below freezing, but temperatures were still above average during this period. Such anomalous incursions of warm air in this region are consistent with changes in atmospheric circulation that have favored relative warm air incursions in the Ronne Embayment region deep into the continent (Stammerjohn and Scambos 2020; Clem et al. 2019, 2020), with relatively decreasing amounts of melt occurring on the Peninsula compared to the early 2000s (Barrand et al. 2013; Olivia et al. 2017). It remains unclear if this change in circulation patterns is part of a long-term trend or natural variability (Turner et al. 2016).

e. Ice sheet mass balance—S. Adusumilli, H. A. Fricker, and A. S. Gardner

The Antarctic Ice Sheet (AIS) gains mass from accumulation (snowfall minus sublimation) at the surface and primarily loses mass at the margins through its floating extensions, called ice shelves. Mass loss can occur due to the episodic calving of icebergs at ice shelf fronts, which occurs at multi-annual to multi-decadal time scales, or through continuous ocean-driven basal melting under ice shelves (Rignot et al. 2013; Depoorter et al. 2013; Adusumilli et al. 2020). For any given time period, the net mass balance between competing mass gains and losses depends on interactions between the ice, ocean, and atmosphere (e.g., Smith et al. 2020a). Over the past two decades, the ice sheet has experienced net mass loss of grounded ice (e.g., The IMBIE Team 2018), which is in part due to net mass loss of its floating ice shelves (e.g., Paolo et al. 2015) and a corresponding reduction in their "buttressing" effect that otherwise slows the flow of grounded ice into the ocean (e.g., Gudmundsson et al. 2019). Mass loss over the ice sheet has sometimes occurred rapidly in the past (e.g., during the collapse of Larsen B Ice Shelf; Scambos et al. 2004), stressing the need for continuous monitoring through satellite observations.

Since 2018, data from the ICESat-2 mission have been used to show elevation changes in the ice sheet at higher spatial and temporal resolution compared to earlier observations and have provided important information on the processes occurring at these scales. Several studies published during 2020–22 have used ICESat-2 data to provide new observations of the ice sheet, advancing our understanding of surface melt and drainage (Warner et al. 2021); supraglacial lake volumes (Fair et al. 2020; Fricker et al. 2020; Datta et al. 2021); the movement of subglacial water below the ice sheet (Neckel et al. 2021; Siegfried and Fricker 2021); dynamics at grounding zones zones (Li et al. 2022); biases between radar- and laser-derived estimates of height (Aublanc et al. 2021); the ongoing weakening of Thwaites Eastern Ice Shelf (Alley et al. 2021; Wild et al. 2022); the calving of the large tabular icebergs (Walker et al. 2021); and the calving of small icebergs through buoyancy-driven flexure at the ice shelf front (Becker et al. 2021).

At the time of writing, there were no published estimates of total Antarctic mass or height change for 2021. Therefore, we derive estimates of height changes over the ice sheet from NASA's ICESat-2 laser altimeter for the latest annual data available: November 2020 to November 2021. We used the

ATLAS/ICESat-2 ATL06 L3A Land Ice Height, Version 5 data product (Smith et al. 2020b), which provides precise estimates of height along repeated ground tracks. We derived along-track height changes between Cycle 9 (October–December 2020) and Cycle 13 (October–December 2021) from these data (Fig. 6.9a). We smoothed the final height change map using a Gaussian filter with a 30-km diameter. The conversion of height changes to mass changes requires a firn density model (e.g., Ligtenberg et al. 2011), which is not yet available for this period. We do not derive results for the ice shelves for 2021.

We also show annual mass anomalies derived from NASA's satellite gravimeter (GRACE-FO; Fig. 6.9b). We used data from the JPL GRACE and GRACE-FO Ocean, Ice, and Hydrology Equivalent Water Height Coastal Resolution Improvement (CRI) Filtered Release 06 Version 02 mascon data that solve for mass anomalies on 300-km diameter spherical caps (Wiese et al. 2022). We calculated gravity-derived mass anomalies for the same November 2020 to November 2021 period as used for ICESat-2, with the same 3-month averaging. To determine ice sheet mass anomalies, we identified all mascons containing more than 10,000 km^2 of land, according to the provided Coastline Resolution Improvement (CRI) land mask. We interpolated the area-averaged rates of change using bilinear interpolation according to the location of the geometric center of the land area contained within the mascon. We then masked all non-land areas using the Bedmachine ice mask (Morlighem et al. 2020).

The maps of annual changes in ice sheet height from ICESat-2 (Fig. 6.9a) and mass from GRACE-FO (Fig. 6.9b) show ongoing losses of ice in the Amundsen Sea sector of West Antarctica, the same region where losses have been observed over the previous decade (Smith et al. 2020a). There was a net mass loss over the ice sheet between December 2020 and December 2021 of 50 Gt (not shown), much lower than the average annual mass loss of 140 Gt yr^{-1} between December 2003 and December 2021. This lower-than-average mass loss was likely due to surface mass gains across the Antarctic Peninsula, Dronning Maud Land, and Wilkes Land associated with an above-average number of landfalling atmospheric rivers in those regions (section 6c), which partially offset (but did not fully compensate for) the large mass losses in West Antarctica.

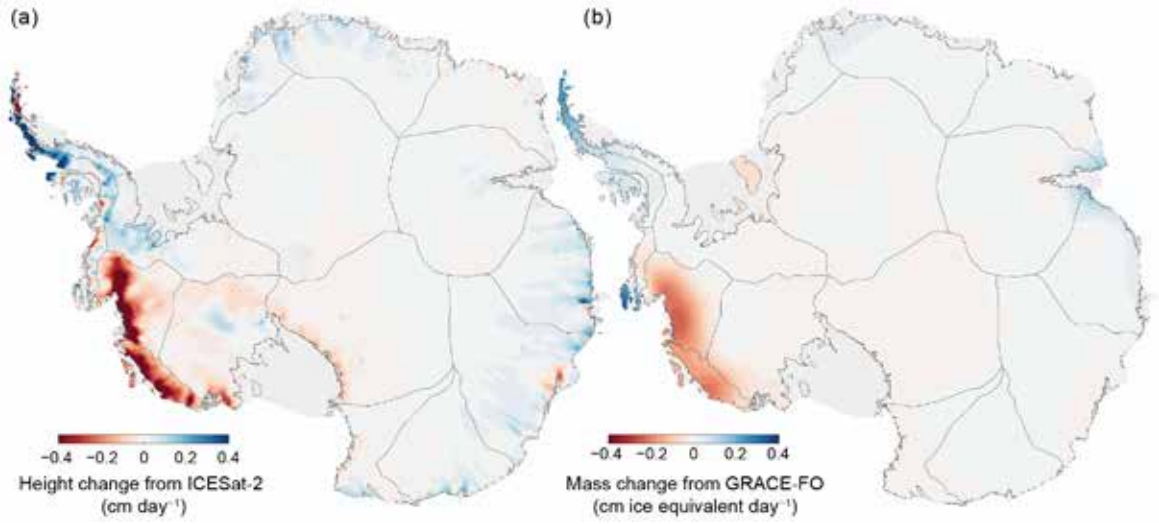

Fig. 6.9. Maps of (a) height change (cm day^{-1}) from ICESat-2 and (b) ice equivalent mass change (cm ice equivalent day^{-1}) from GRACE-FO for the period Nov 2020 to Nov 2021.

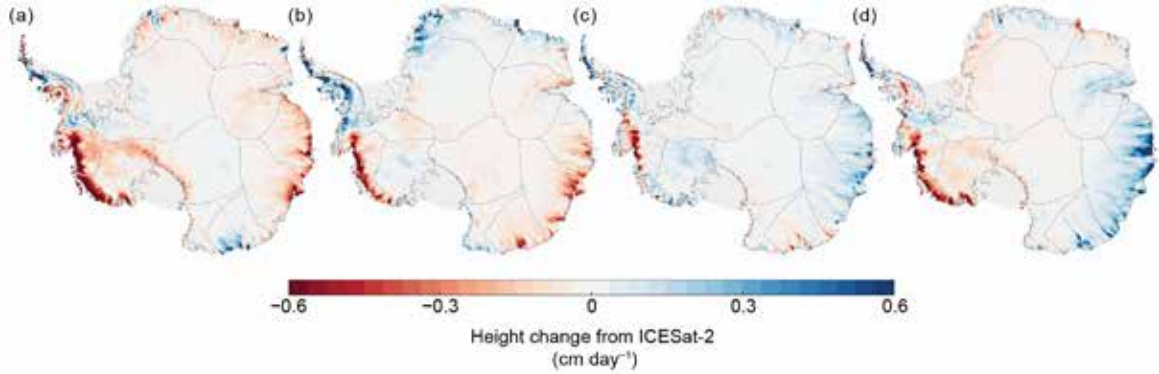

Fig. 6.10. Maps of height change (cm day^{-1}) from ICESat-2 for (a) Nov 2020–Feb 2021, (b) Feb–May 2021, (c) May–Aug 2021, and (d) Aug–Nov 2021. Dates represent the central month of each 3-month ICESat-2 data acquisition cycle.

To examine seasonal variability, we also derived height changes from ICESat-2 at 3-month intervals between November 2020 and November 2021 period using the technique described above for deriving the annual height change map (Fig. 6.10). Although data from the GRACE-FO mission were available at monthly intervals during this period, a small seasonal bias in the AIS mass change signal has been noticed in the GRACE-FO data, which is due to the accelerometer transplant calibration (the accelerometer on one spacecraft is currently not used due to noise; Harvey et al. 2022). This bias is related to the orbital beta-angle, and thus affects the seasonal variations only. The mission's Science Data System has developed an updated accelerometer calibration that removes this seasonal bias in the next data release (planned for boreal spring 2022; F. Landerer, person. comm.). Therefore, we only include annual estimates of ice sheet mass loss from GRACE-FO in this report. Many of the spatial patterns of increases in height across Antarctica correspond well with patterns of positive surface mass balance anomalies reported in 2020 (see Fig. 6.5b). For example, large increases in height over Wilkes Land, East Antarctica, during August–November (Fig. 6.10d) coincided with increases in the frequency of landfalling atmospheric rivers (Adusumilli et al. 2021) during this period (see Fig. 6.6d). This further suggests a major contribution of surface processes in driving seasonal height and mass changes. Meanwhile, decreases in height continued to dominate coastal West Antarctica for all of 2021.

f. Sea ice extent, concentration, and seasonality—P. Reid, S. Stammerjohn, R. A. Massom, S. Barreira, T. Scambos, and J. L. Lieser

During 2021, and following on from 2020, net Antarctic sea ice coverage continued to exhibit strong variability (Fig. 6.11a), with distinct regional and seasonal contributions (Fig. 6.11b). The year began with below-average overall sea ice extent (SIE) in January through February (Fig. 6.11a), compared to the 1991–2020 average, but abruptly switched to above average in late February where it remained almost continuously until early September. Sea ice then retreated at rates faster than average, with net SIE at ~1.5×10^6 km^2 below average in late December. Annual daily minimum SIE occurred on 22 February (2.68×10^6 km^2), which was slightly below average, while the annual daily maximum (18.79×10^6 km^2) was slightly above average but very early (30 August)—the second earliest daily maximum on record. Sea ice area (SIA), which is the product of SIE and concentration, followed a similar overall pattern to SIE but attained near record-high levels in late August (second highest on record), before plummeting to record-low daily values during parts of October and December. A new monthly-mean low SIA (5.45×10^6 km^2) was recorded for December. In terms of regional contributions, the western Weddell, Bellingshausen, and Ross Seas sectors generally experienced smaller-than-average SIE through much of 2021, whereas the Amundsen Sea sector recorded larger-than-average SIE through the year.

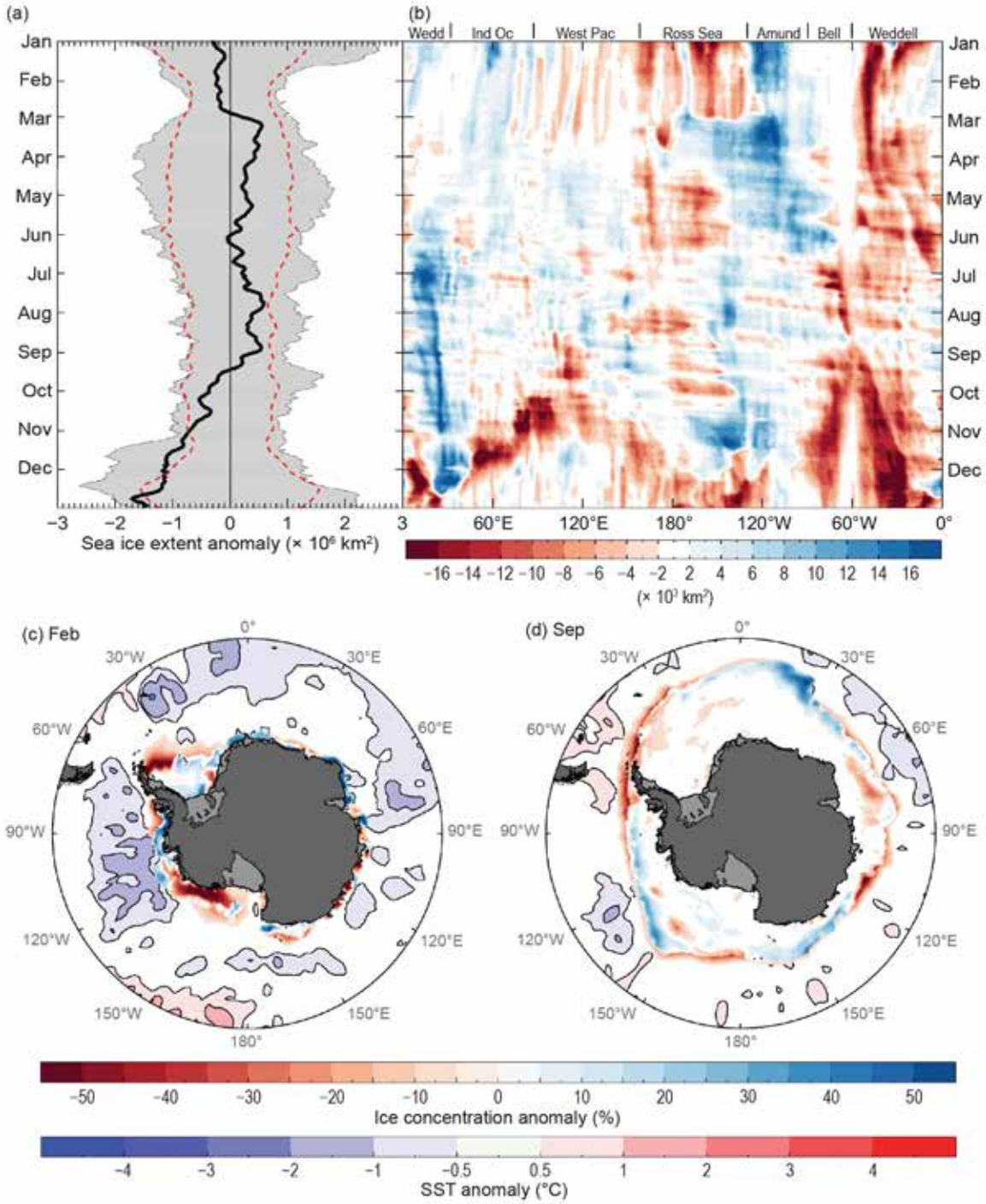

Fig. 6.11. (a) Time series of net daily SIE anomaly (× 10^6 km^2) for 2021 (solid black line) based on 1991–2020 climatology. The gray shading represents the historical (1979–2020) daily SIE anomaly. (b) Hovmöller (time–longitude) representation of daily SIE anomaly (× 10^3 km^2 per degree of longitude) for 2021. Maps of sea ice concentration anomaly (%) and SST anomaly (°C; Reynolds et al. 2002; Smith et al. 2008) for (c) Feb 2021 and (d) Sep 2021. Sea ice concentration is based on satellite passive-microwave ice concentration data (Cavalieri et al. 1996, updated annually, for climatology; Maslanik and Stroeve 1999), for the 2021 sea ice concentration. See Fig. 6.1 for relevant place names.

The low values of SIE and area during the early and then latter months of 2021 continue the recent trend towards decreased Antarctic sea ice coverage. Since 2015, 8 of the 12 calendar months have registered record low net Antarctic SIE (Parkinson and DiGirolamo 2021), but there are distinct regional and seasonal components to these events (Parkinson 2019; Stammerjohn and Maksym 2017). Overall, net Antarctic SIE has displayed substantial variability over the last decade, with record high values during 2012–14 (Reid and Massom 2015), followed by several years of low and record low values (Parkinson 2019; Reid et al. 2021). Through much of 2021, atmospheric anomalies were strong and distinct (section 6b), particularly the depth of the Amundsen Sea Low (ASL) from September onwards. However, given the pattern of generally sustained low sea ice coverage since 2016, it is quite probable that there are ocean influences predisposing the sea ice to early retreat (section 6g; Kusahara et al. 2018; Meehl et al. 2019). Below, we discuss four sequential phases of spatio-temporal progressions of Antarctic sea ice in 2021 based on the patterns and changes shown in Figs. 6.11a,b. These four sea ice phases (January–February, March–April, May–August, and September–December) reflect similar patterns in the atmospheric pressure and wind fields (section 6b) and sea surface temperatures (SSTs).

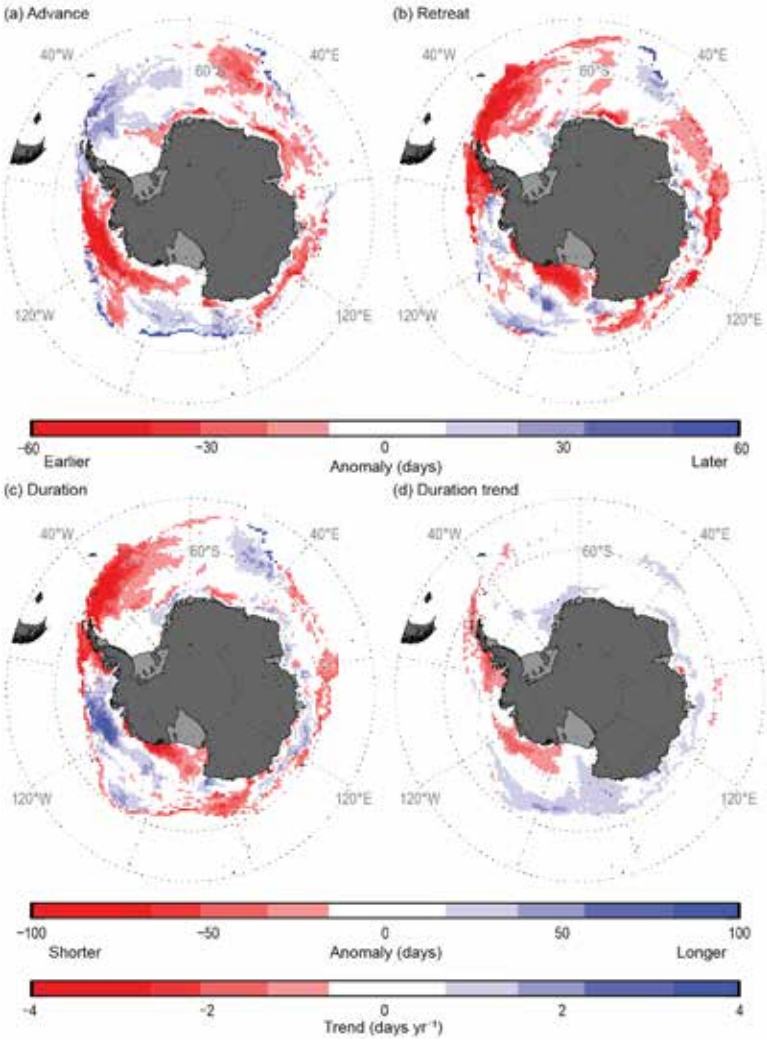

Fig. 6.12. Maps of seasonal sea ice anomalies (days) in 2021 during (a) autumn ice-edge advance, (b) spring ice-edge retreat, (c) winter ice season duration; together with (d) winter ice season duration trend (days yr^{-1}; Stammerjohn et al. 2008). The seasonal anomalies (a–c) are computed against the 1991/92 to 2020/21 climatology; the trend (d) is computed over 1979/80 to 2020/21. (Source: GSFC Bootstrap v3.1 daily data [Comiso 2017] through 31 May 2021, augmented with NASA Team NRTSI daily data [Meier et al. 2021] through 15 Feb 2022.)

As a continuation of the 2020/21 sea ice retreat process, regional patterns of sea ice coverage in January–February 2021 closely followed those of late 2020 (Reid et al. 2021). The regions of persistent high SIE and slower-than-normal seasonal retreat in the Indian Ocean off Dronning Maud Land (~0°–70°E) and in the Amundsen Sea (Fig. 6.11b, and reflected by an earlier advance in Fig. 6.12a) were consistent with below-average SSTs in those regions (Fig. 6.11c; section 6g). These cooler, icier regions were possibly due to the influence of two dominant atmospheric low-pressure anomalies (> 2.5 std. dev. below normal) at ~100°W and 40°E that contributed to the northward advection of cooler air and sea ice. Elsewhere, however, extensive faster-than-average sea ice retreat occurred across much of East Antarctica, the Ross Sea (~70°E–120°W), and the western Weddell Sea (~0°–60°W; Figs. 6.11b,c), leading to a net overall negative SIE anomaly (Fig. 6.11a).

During March, an abrupt change from a negative to a strongly positive anomaly in regional SIE took place in the eastern Ross Sea (Fig. 6.11b) in response to an eastward shift of a well-developed ASL (section 6b). This strong low-pressure anomaly and coincident below-normal SSTs (section

6g) led to rapid sea ice advance in the eastern Ross Sea and across the Amundsen Sea during March–April (Figs. 6.11b, 6.12a). At the same time, an extensive zone of anomalously persistent ice coverage at ~40°–70°E coincided with the southward incursion of a negative SST anomaly associated with a high-pressure anomaly centered on ~25°E. Elsewhere, a relatively slow autumn sea ice advance (Fig. 6.12a) led to negative SIE anomalies across the western Antarctic Peninsula through the Weddell Sea, and also in the western Ross Sea and southwest Pacific Ocean (Fig. 6.11b). In April, circum-Antarctic sea ice was strongly influenced by the development of a zonal wave-3 atmospheric pattern with low-pressure centers at ~40°E, 160°E, and 90°W (see Fig. 6.3e). At this time, the appearance of a predominantly positive SIE anomaly across much of East Antarctica (~0°–130°E) coincided with an increase in cyclonic activity there, and the positive anomaly in the far eastern Ross Sea and Amundsen Sea sector persisted as well. In contrast, SIE remained below average across the western Peninsula and western Weddell Sea and in the Ross Sea region.

During May–July, sea ice conditions were strongly affected by the redevelopment of a deep ASL (a typical La Niña response due to Rossby-wave activity; Yuan 2004) in concert with the persistent, but spatially variable, circumpolar atmospheric zonal wave-3 pattern (section 6b). As part of this pattern, the appearance in May of a deep low-pressure system off Enderby Land (centered on ~45°E) provided strong equatorward air flow that led to enhanced late-autumn sea ice advance (Fig. 6.12a) and a regional positive SIE anomaly that persisted in the eastern limb of the Weddell Gyre through mid-December (Fig. 6.11b). Sea ice advance was also earlier than average across much of East Antarctica west of ~150°E, with persistence of a zonally-extensive positive SIE anomaly from May through July (Fig. 6.11b), likely a result of stronger-than-normal westerly winds due to the combination of low-pressure systems to the south of the sea ice edge and a high-pressure ridge to the north (section 6b). SIE also remained larger than normal in the Amundsen Sea region, but smaller-than-average in the Bellingshausen, western Weddell, and Ross Seas (Fig. 6.11b). This regional pattern of circum-Antarctic anomalies in SIE remained through August, after which there was a development of a more zonally consistent pattern of circumpolar lows (see Fig. 6.3g).

The period of September–December was characterized by an abrupt downturn in overall net SIE around Antarctica (Fig. 6.11a) as a result of zonally-extensive negative SIE anomalies in the Indian and West Pacific Oceans, Bellingshausen through western Weddell Seas, and latterly the Ross Sea (Figs. 6.11b,d). This pattern of anomalously early sea ice retreat (in all sectors apart from the outer eastern Weddell Sea, outer eastern Ross Sea, and portions of the Bellingshausen-Amundsen sector between 80°W and 120°W; Fig. 6.12b) was strongly influenced by a re-emergence and deepening of the ASL in September, which persisted to the end of the year (section 6b). Prevailing warm northerly winds in the eastern part of the ASL particularly impacted the western Peninsula region and western Weddell Sea (~0°–90°W), where SIE was 1–3 std. dev. below the mean from September to the end of the year. Due to the prevalence of cold southerly winds in the western flank of the ASL in the Amundsen and eastern Ross Seas (~90°–150°W), SIE remained predominantly larger than normal until December, at which time it started to retreat rapidly. The exception was the northern Amundsen Sea, where SIE remained above average through to the end of the year (Fig. 6.11b). The continuation of a strong negative SIE anomaly and rapid sea ice retreat in the West Pacific sector in October (Figs. 6.11b, 6.12b) coincided with the development of a major high-pressure anomaly centered offshore at ~170°E. For much of East Antarctica and from September onwards, sea ice retreated rapidly (Fig. 6.12b) and at times regional (~50°–100°E) SIE was 3–4 std. dev. below average. By the end of the year, only the eastern Amundsen Sea and small embayments across East Antarctica showed larger-than-average SIE (not shown).

Large regional anomalies in seasonal advance and retreat combine to produce a distinct pattern of ice season duration anomalies (Fig. 6.12c), with the western Antarctic Peninsula and much of the outer Weddell and inner Ross seas experiencing a much shorter ice season duration by more than 50 days. The shorter ice season along the western Antarctic Peninsula and eastern

Ross Sea are consistent with their long-term trends, in contrast to the ice season anomalies in the Bellingshausen-Amundsen region between 80°W and 120°W and the western Ross Sea, both of which were opposite to their long-term trends (Figs. 6.12 c,d).

g. Southern Ocean—R. L. Beadling, N. M. Freeman, G. A. MacGilchrist, M. Mazloff, J.-R. Shi, A. F. Thompson, and E. Wilson

The Southern Ocean (SO) moderates the climate system as a vast, but variable, sink for anthropogenic heat (Frölicher et al. 2015; Shi et al. 2018) and carbon dioxide (CO_2, Frölicher et al. 2015). Additionally, nutrients upwelled in the subpolar SO and advected northward fertilize three quarters of global ocean biological productivity (Sarmiento et al. 2004). Motivated by their imprint on the climate system through their role in the SO heat and carbon budget, we present 2021 anomalies of SO sea surface temperature (SST), mixed layer (ML) properties, ocean heat content (OHC), and surface chlorophyll concentration. The state of the SO in 2021 was characterized by zonally-asymmetric SST anomalies, near-record positive anomalies in ML salinity (MLS) and ML depth (MLD) in portions of the SO, a continued increase in ocean heat content (OHC), accelerated upper ocean zonal flow, and near-record summer chlorophyll concentrations.

1) SEA SURFACE TEMPERATURE AND MIXED LAYER PROPERTIES

Southern Ocean SST and ML properties in 2021 are analyzed with respect to the 2004–20 period. Monthly SST data are from the NOAA Optimum Interpolation (OISST) V2 product (Reynolds et al. 2002), while ML properties are from the Argo-based Roemmich-Gilson dataset (Roemmich and Gilson 2009; RG09). We focus on 40°–65°S since this region encapsulates variations around the Antarctic Circumpolar Current (ACC). Following the de Boyer Montegut et al. (2004) threshold method, MLD is defined as the depth at which potential density changes by the threshold value of 0.03 kg m^{-3} relative to the 10-m surface reference value.

In 2021, SO SST anomalies exhibited a distinct zonal asymmetry, with anomalies largely compensating in the zonal mean (Figs. 6.13a,b). Anomalous cooling spanned the central Atlantic to central Indian Oceans and across the eastern Pacific, while anomalous warming was prominent across the western portions of the Pacific and Atlantic. These anomaly patterns are consistent with the Southern Annular Mode (SAM) being in a strongly positive state for much of 2021 (section 6b; Sallée et al. 2010). Zonal-mean MLS approached record highs (~0.02 g kg^{-1}) toward the end of 2021, with large anomalies in the South Atlantic (Figs. 6.13c,d). This may be viewed as a resumption of the higher-than-normal MLS that persisted from 2015 to 2020. Possible factors contributing to the high MLS include the reduction in Antarctic SIE (section 6f), a poleward shift of precipitation away from midlatitudes associated with a more southerly storm track during the positive SAM phase, and a stronger South Atlantic subtropical gyre. A stronger gyre implies increased transport of saline sub-tropical waters to the region. Sea surface height (SSH) maps from Archiving, Validation, and Interpretation of Satellites Oceanographic Data (AVISO; www.aviso.altimetry.fr/duacs/) support a continued (Qu et al. 2019) spin-up of this gyre, with 2021 mean SSH magnitudes ~2 cm greater in the center of the gyre relative to the 1993–2020 climatology (Southern Hemisphere spatially-averaged trend was first removed; not shown here). Distinguishing between these plausible mechanisms would require a thorough salinity budget analysis. Deep winter MLDs (anomalies > 100 m) were found across the southeastern Pacific in 2021 (Fig. 6.13e,f), comparable to the record MLD anomalies that occurred in 2010. Similar to 2010, 2021 was dominated by a positive SAM, which favors deeper winter mixed layers in the southeastern Pacific (Fogt et al. 2011; Sallée et al. 2010) increasing local ocean ventilation and creating conditions conducive to enhanced mode water formation in the region (MacGilchrist et al. 2021; Morrison et al. 2022).

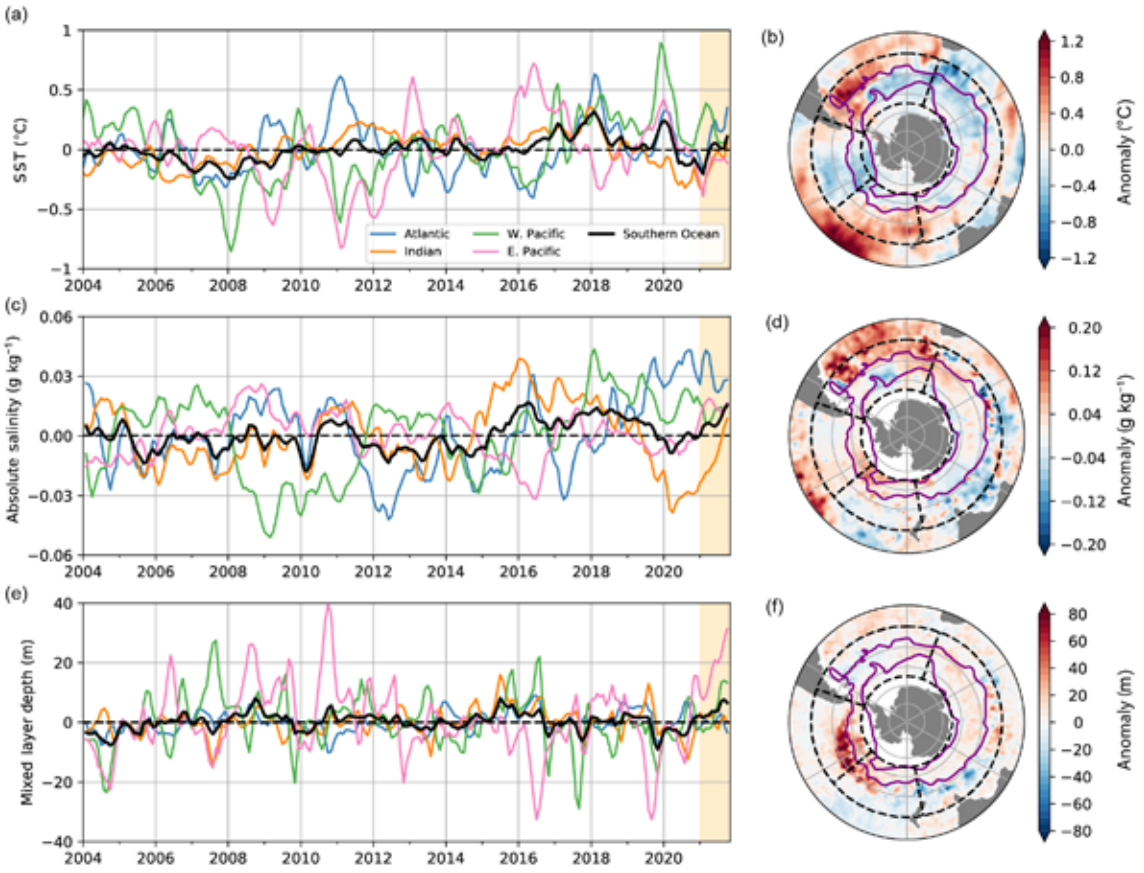

Fig. 6.13. Monthly averaged (a,b) sea surface temperature (SST; °C), (c,d) mixed layer absolute salinity (g kg^{-1}), and (e,f) mixed layer depth anomalies (m) for the SO. Left column: anomaly time series. Right column: corresponding annual mean anomaly maps for 2021, where purple contours outline the subantarctic and southern ACC Fronts as defined by Orsi et al. (1995). Regions highlighted in the anomaly time series correspond to the regional boundaries (SO, Atlantic, Indian, West Pacific, and East Pacific) defined by the dashed lines in the anomaly maps spanning 40°–65°S. Anomalies are computed relative to the 2004–20 monthly climatology and smoothed using a 3-month moving average. 2021 is highlighted with yellow shading on each time series (a,c,e).

2) OCEAN HEAT CONTENT AND ZONAL FLOW

We use monthly gridded temperature data from RG09 to evaluate 0 to 2000-m SO (south of 30°S) OHC and subsurface potential temperature anomalies relative to the 2005–20 climatological seasonal cycle. In 2021, the SO annual mean upper 2000-m OHC anomaly was +28.9 ZJ (10^{21} J) (Fig. 6.14a), increasing by ~2.5 ZJ compared to 2020. South of 40°S, the OHC anomaly was +19.8 ZJ, increasing by 0.1 ZJ compared to 2020. These increases in OHC relative to 2020 are smaller than the interannual variability (5.0 ZJ south of 30°S; 2.3 ZJ south of 40°S) estimated from the std. dev. of the detrended annual OHC during 2005–21. The long-term positive trend in OHC reflects continued multi-decadal subsurface warming in the SO and is consistent with the 2021 global OHC increase (Cheng et al. 2022). Most of the enhanced OHC occurred north of the ACC, with pronounced positive anomalies in the South Atlantic and southwest Pacific around western boundary currents (Fig. 6.14b). The coherence between the strong positive Atlantic OHC and MLS anomalies is consistent with a spin-up of the South Atlantic gyre. The 2021 OHC anomalies were negligible within and south of the ACC where the upwelling of cool deep waters to the upper ocean mitigates the anthropogenic warming signal. This spatial asymmetry in SO OHC anomalies resulted in a north–south gradient in subsurface potential temperature anomalies (Fig. 6.14c), with maximum warming peaking around 46°–50°S below 100 m. Consistent with the enhanced meridional temperature gradient, the baroclinic component of SO eastward flow

in 2021 accelerated within 48°–58°S (Shi et al. 2020, 2021). Weak negative anomalies (~0.1°C) in subsurface temperature were found at depths of about 100 m south of 55°S, which may be related to an anomalous northward Ekman transport of sea ice (Haumann et al. 2020) associated with the positive SAM phase in 2021.

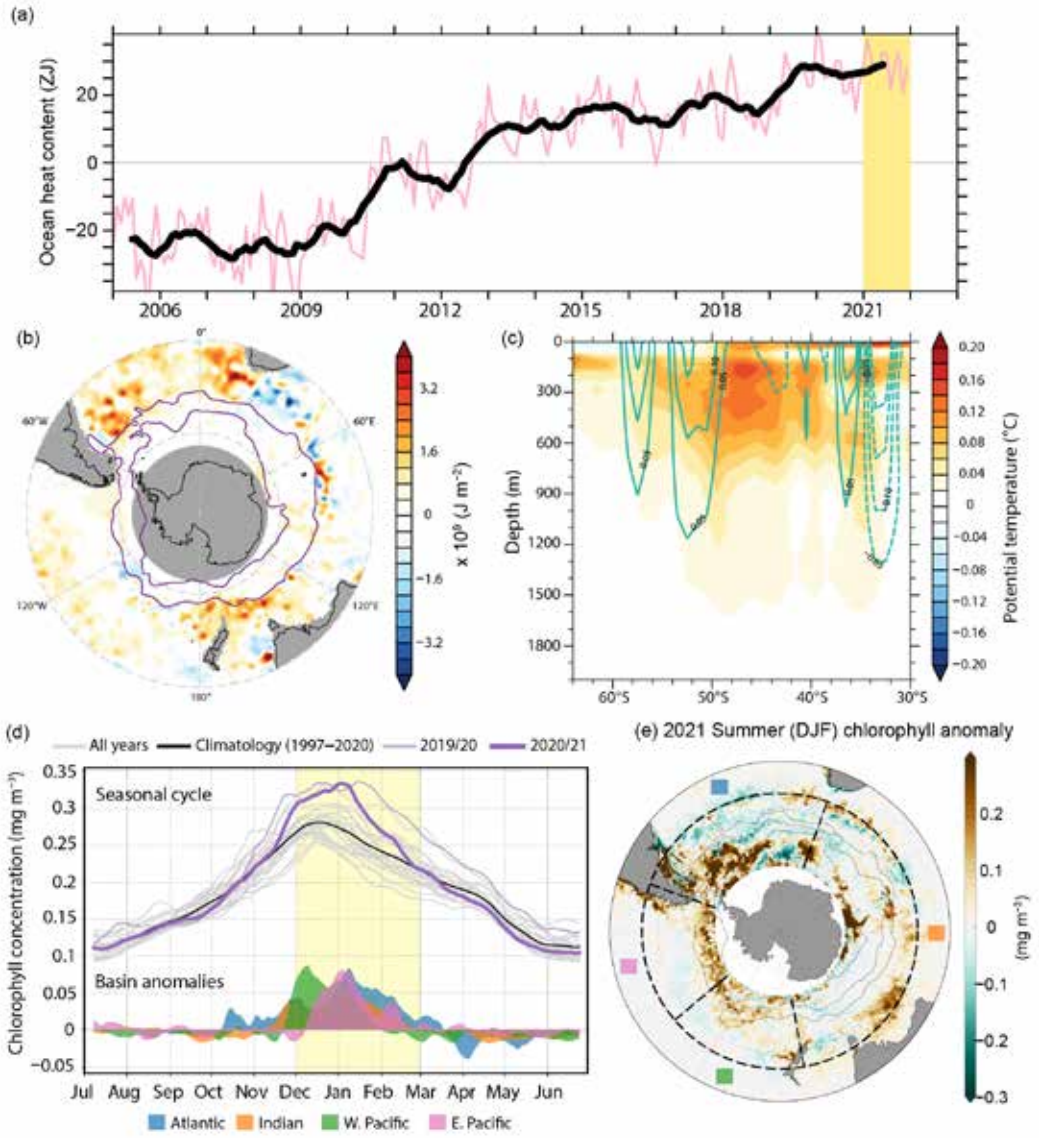

Fig. 6.14. (a,b) 2021 anomalies of upper 2000-m OHC relative to 2005–20 Argo climatology. (a) Time series of monthly mean OHC anomaly (ZJ or 10^{21} J) relative to 2005–20 Argo climatology south of 30°S (pink curve) with 12-month running mean plotted on top (black curve) and 2021 highlighted in yellow shading. (b) Map of 2021 OHC anomalies (10^9 J m^{-2}) relative to climatology (2005–20) with the mean position of the subantarctic and southern ACC Fronts from Orsi et al. (1995) contoured in purple. (c) SO Zonal mean 2021 potential temperature anomalies (°C) with the 2021 zonal geostrophic velocity anomalies contoured in green. Solid contours represent eastward anomalies and dashed are westward anomalies. (d, top section) Seasonal cycle of the area-weighted (40°–65°S), daily (arithmetic) mean chlorophyll concentration (mg m^{-3}): all historical years (1997–2020), the climatological mean (1997–2020), and the most recent 2019/20 and 2020/21 growing seasons. A 14-day rolling average filter was applied to the daily GlobColour product, a spatially and temporally interpolated ("cloud-free") multi-satellite merged product (https://doi.org/10.48670/moi-00100). Missing days were linearly interpolated; for weighted-averaging purposes, grid locations that are not resolved via satellite, particularly in data-sparse winter, are set to zero. (d, bottom section) Chlorophyll anomalies (mg m^{-3}) in 2020/21 contributed by each ocean basin, where the anomaly is computed relative to the climatology of that basin, delineated as in Fig. 6.13. The x-axis in (d) is centered on the austral summer months of Dec, Jan, and Feb (DJF), highlighted with vertical yellow shading. (e) Map of 2020/21 DJF chlorophyll anomalies (30°–65°S), computed relative to the 1997–2020 DJF climatology, using the monthly version of the GlobColour product. Overlain are zonal and meridional (dashed) outlines of the subdivided ocean basins (d, 40°–65°S) and, from north to south, the subantarctic, polar, and southern ACC fronts (solid gray contours; Orsi et al. 1995).

3) SURFACE CHLOROPHYLL

Chlorophyll concentration in the open (ice free) ocean is examined using the GlobColour merged ocean color product (L4 daily and monthly at 4 km; September 1997–June 2021; Fanton d'Andon et al. 2009; Maritorena et al. 2010), with 2021 anomalies computed relative to the 1997–2020 climatology. SO phytoplankton abundance (indicated by surface chlorophyll concentration) exhibited anomalous seasonal variability during the 2020/21 growing season (July 2020–June 2021; Figs. 6.14d,e). The pronounced 2020/21 austral summer (DJF) peak joins the 2019/20 season as the two highest chlorophyll summers observed in the GlobColour record (Fig. 6.14d). The 2020/21 growing season began at near-normal winter–spring chlorophyll levels, followed by anomalously rapid summer growth beginning in mid-November, reaching a maximum in early January (> 0.3 mg m^{-3}), the largest in the GlobColour record (Fig. 6.14d). Following the summer peak, chlorophyll concentration quickly declined to anomalously low levels in most regions by mid-March, remaining consistently below climatological values throughout the autumn–winter transition (Fig. 6.14d).

Phytoplankton in the Atlantic, Indian, and west Pacific sectors accounted for most of the rapid growth from mid-November (Fig. 6.14d), after which, anomalously high chlorophyll was maintained through DJF by strong, positive anomalies across all sectors (Figs. 6.14d,e). Across the SO, the strongest positive anomalies were found south of the Subantarctic Front, most notably in the Pacific and Atlantic basins (Fig. 6.14e). The deep Amundsen Sea Low and strong positive SAM (section 6b) created conditions conducive to the upwelling of nutrients in support of an invigoration of the spring bloom. In the Atlantic, most of the basin-wide chlorophyll increase was concentrated east of Drake Passage near the Scotia Arc (Fig.6.14e).

h. 2021 Antarctic ozone hole—N. A. Kramarova, P. A. Newman, E. R. Nash, S. E. Strahan, B. Johnson, M. Pitts, M. L. Santee, I. Petropavlovskikh, L. Coy, and J. De Laat

The 2021 Antarctic ozone hole was the 13th largest in 42 years of satellite observations since 1979, with an area of 23.34×10^6 km^2 (the average area for 7 September–13 October) and a minimum daily total ozone column of 92 DU. The 2021 polar stratospheric vortex was stable with consistently cold temperatures that created favorable conditions for ozone depletion. The meteorological conditions and seasonal development of the ozone hole in 2021 were similar to those in 2020. Weaker-than-usual amplitudes of planetary scale Rossby waves in the September–October period helped maintain a strong vortex and led to below-average Antarctic ozone columns in late austral spring and early summer.

Antarctic lower stratospheric temperatures were consistently near- or below average during austral winter and spring 2021 (Fig. 6.15a). Cold air facilitated formation of polar stratospheric clouds (PSCs; Fig. 6.15b), whose spatial volume was near-average in July–August and above average in September. PSC particles provide surfaces for heterogeneous chemical reactions that release active chlorine (Cl_2) for ozone depletion as sunlight returns to polar latitudes in August–September. Concentrations of ClO (Fig. 6.15c) were near- or below average until mid-September and above average in early October, similar to those in 2020. *Aura* Microwave Limb Sounder (MLS) observations showed that the 2021 vortex-averaged ozone concentration (Fig. 6.15d) on the 440-K isentropic surface (~60 hPa) was substantially above the average. However, the change in ozone concentration between the first week of July and the first week of October indicated that seasonal ozone losses were about 2.22 ppmv, which is comparable to the losses in two other cold years: 2.18 ppmv in 2020 and 2.24 ppmv in 2006. The Antarctic ozone hole area, defined by the region with total ozone columns below 220 DU, reached its peak at 24.8×10^6 km^2 on 7 October (Fig. 6.15e). The weaker-than-average amplitudes of planetary scale Rossby waves through austral spring (which propagate from the upper troposphere into the stratosphere, depositing momentum and warming the Antarctic stratosphere) produced colder temperatures inside the vortex and inhibited mixing across the vortex edge, allowing the ozone hole area to remain well above the average until it disappeared on 23 December. This was one of the longest-lasting ozone holes on

record, second only to 2020 (Kramarova et al. 2021). In 2006 (orange line in Fig. 6.15e), the area of the ozone hole grew faster in August–September partly because the level of ozone depleting substances was ~3.7 ppbv, which is 0.4 ppbv higher than today (NASA 2022). Below-average temperatures in 2006 resulted in the largest ozone hole on record. The slower growth rate of the 2021 ozone hole is consistent with other indications of recovery, such as the delayed onset of the hole's appearance and its decreasing size in September, all attributable to decreasing levels of ozone depleting substances (Stone et al. 2021).

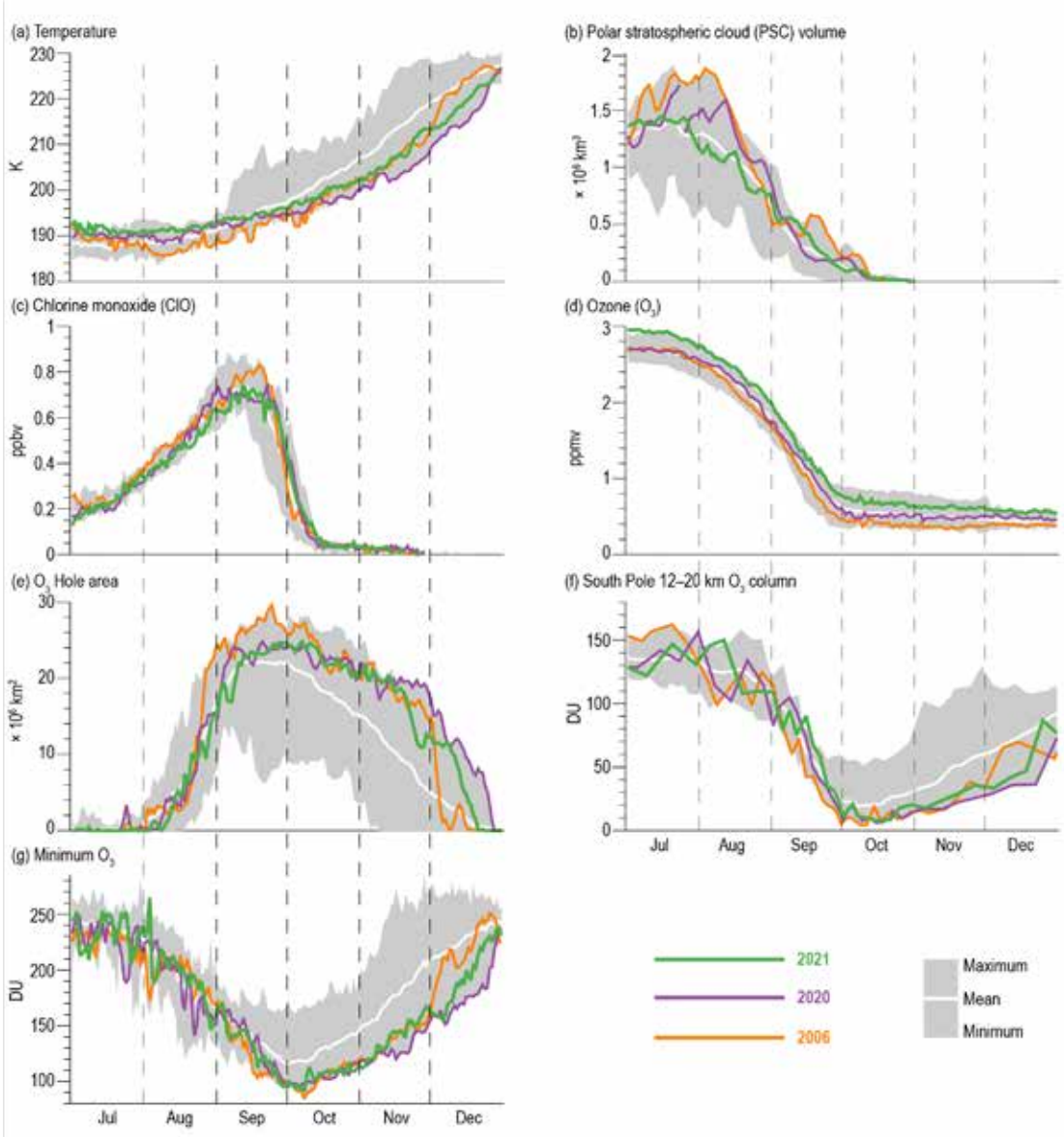

Fig. 6.15. Antarctic values of (a) vortex-averaged MERRA-2 temperature (K), (b) CALIPSO PSC volume (× 10^6 km^3) updated from Pitts et al. (2018), (c,d) vortex-averaged ClO (ppbv) and O_3 (ppmv) measured by Aura MLS (updated from Manney et al. 2011), (e) OMI/OMPS Antarctic ozone hole area (× 10^6 km^2, area with ozone total column less than 220 DU), (f) lower stratospheric ozone columns (DU, 12–20 km) based on sonde measurements at South Pole, and (g) minimum total ozone columns (DU) over 60°–90°S from OMI/OMPS. MERRA-2 temperature and MLS averages are made inside the polar vortex on the 440-K potential temperature surface (~19 km or 60 hPa). Gray shading shows the range of daily Antarctic values for 2005 (for all but (b), which starts in 2006) through 2020. The white curve indicates the 2005–20 long-term mean.

Sonde observations at South Pole station indicated that the lower stratospheric column between 12 and 20 km was near-average in July–September (Fig. 6.15f) but was below average from October through December. The lowest 12–20-km column measured was 7.6 DU on 15 October, about two weeks later than in most years. The minimum total column ozone over the Antarctic (60°–90°S) were detected on 7 and 8 October at 92 DU, and minimum total ozone columns were also consistently below the average from mid-September to December. This seasonal behavior is similar to that in 2006 and 2020 (orange and purple lines in Fig. 6.15, respectively)—the two prior years with similarly weak wave activity and cold temperatures that resulted in persistently large holes and low ozone columns in October–December. The ClO concentration and PSC volumes dropped to near zero by mid-October (Figs. 6.15b,c), marking the termination of seasonal ozone depletion (Fig. 6.15d), but the stable vortex in 2021 kept ozone columns below average for the rest of the year by preventing meridional mixing of ozone-rich air from the midlatitude stratosphere into polar latitudes.

September is the key time period for Antarctic ozone depletion (e.g., Strahan et al. 2019). As the sunlight returns to polar latitudes, catalytic ozone destruction is initiated by reactions with active chlorine and bromine species produced on PSC surfaces during polar night. Colder September temperatures increase PSC surface area, leading to greater ozone depletion and a larger hole area. Figure 6.16a shows the interannual variability in the September vortex temperature with the

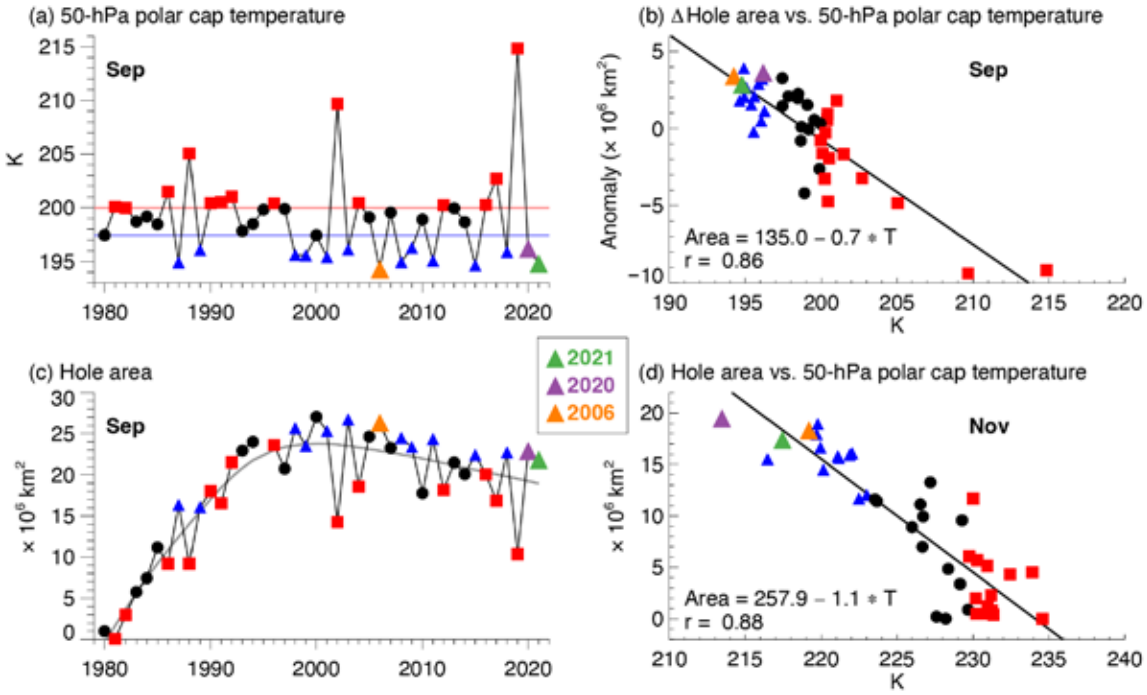

Fig. 6.16. (a) MERRA-2 50-hPa Sep temperature (K) averaged over 60°–90°S, (b) inter-annual anomalies of the ozone hole area (× 10^6 km^2) in Sep (see text) vs. 50-hPa temperature (K), (c) Sep average Antarctic ozone hole area (× 10^6 km^2), and (d) Nov ozone hole areas (× 10^6 km^2) vs. 50-hPa Nov temperature (K). Years with temperatures in the lowest (highest) third are shown as blue triangles (red squares), and three cold years 2006, 2020, and 2021 are highlighted in orange, purple, and green, respectively. The horizontal blue and red lines in (a) indicate 33% and 66% percentiles. The gray curve in (c) shows a quadratic fit of EESC with a 5.2 year mean age (Newman et al. 2007) to the Sep hole areas. Ozone data for 1979–92 are from Total Ozone Mapping Spectrometer (TOMS) Nimbus-7, 1993–94 are from TOMS Meteor-3, 1996–2004 are from EPTOMS, 2005–15 are from *Aura* Ozone Monitoring Instrument (OMI), and 2015–21 are from Suomi National Polar-orbiting Partnership (SNPP) Ozone Mapping and Profiler Suite (OMPS). There were no satellite total ozone observations for 1995. The black lines in (b) and (d) show the linear fit, with a correlation of 0.86 and 0.88 (statistically significant at > 99.9% confidence level) for Sep and Nov, respectively.

coldest one-third of years shown in blue. The September ozone hole area also depends on levels of active chlorine (Fig. 6.16c). The effective equivalent stratospheric chlorine (EESC) represents an estimated concentration of human-produced and natural chlorine and bromine compounds in the stratosphere (Newman et al. 2007). EESC concentration reached its maximum level in the early 2000s and declined thereafter because of the implementation of the Montreal Protocol and its amendments. EESC levels were 13% lower in 2021 compared to the maximum. The impact of the slow rate of EESC decline on the ozone hole area is only observable on decadal or longer timescales, while the interannual variations are modulated by lower stratospheric temperatures: the ozone hole is larger in colder years and smaller in warmer years (Fig. 6.16c). To isolate the temperature effect, we fit a quadratic function of EESC with a 5.2 year mean age (shown as gray line in Fig. 6.16c) to the observed ozone hole areas, then determined the relationship between temperature and the deviation of the observed area from the fitted area (Fig. 6.16b). The September area anomalies are highly correlated with September temperatures ($r = 0.86$, Fig. 6.16b). Thus, the above-average area in September 2021 was largely the result of below-average temperatures.

Ozone depletion ceased by mid-October (Fig. 6.15d) because the ClO concentration and PSC volume dropped to near zero (Figs. 6.15b,c). Therefore, the ozone hole area in November fully depended on cold meteorological conditions that allowed the ozone-depleted air mass to persist over Antarctica. Figure 6.16d demonstrates a strong linear dependence between the area of the November ozone hole and lower stratospheric temperatures in November ($r = 0.88$).

While the 2021 Antarctic ozone hole was larger than average, it was smaller than ozone holes in the late 1990s and 2000s when the levels of ozone depleting substances were near their maximum. The weak amplitudes of planetary scale waves throughout spring 2021 slowed the winter-to-summer transition, resulting in one of the longest-lived ozone holes in the observational record. These results demonstrate that the changes in the Antarctic ozone hole area are consistent with our understanding of ozone depletion, and that ozone recovery due to the implementation of the Montreal Protocol has emerged despite large interannual fluctuations in stratospheric dynamics.

Acknowledgements

- N. M. Freeman was supported by the NASA Ocean Vector Winds Science Team (NASA award 80NSSC19K0059).
- R. L. Fogt acknowledges support from the National Science Foundation grant OPP-1744998.
- M. A. Lazzara, L. M. Keller, and T. Norton were supported in part by the National Science Foundation Grant OPP-1924730.
- K. R. Clem acknowledges support from the Royal Society of New Zealand Marsden Fund grant MFP-VUW2010.
- J. D. Wille acknowledges support from the Agence Nationale de la Recherche projects ANR-20-CE01-0013 (ARCA).
- R. T. Datta acknowledges support from the National Science Foundation, Award No. 1952199
- E. Wilson acknowledges support from Caltech's Terrestrial Hazard Observations and Reporting (THOR) Center.
- A. F. Thompson acknowledges support from NASA Jet Propulsion Laboratory's Internal Research and Development program, Earth 2050.
- G. A. MacGilchrist and M. Mazloff acknowledge support from NSF's Southern Ocean Carbon and Climate Observations and Modeling (SOCCOM) Project under NSF Award PLR-1425989, with additional support from NOAA and NASA. Logistical support for SOCCOM in the Antarctic was provided by the U.S. NSF through the U.S. Antarctic Program.
- Work at the Jet Propulsion Laboratory, California Institute of Technology, was done under contract with the National Aeronautics and Space Administration (NASA). Support was also provided by the NASA Modeling and Analysis Program. We are indebted to the many NOAA Corps Officers and GML technical personnel who spend the winters at South Pole Station to obtain the ongoing balloon and ground-based data sets. We also acknowledge the logistics support in Antarctica provided by the National Science Foundation Office of Polar Programs.
- Section 6h: © 2022. All rights reserved.
- P. Reid and J. Lieser were supported through the Australian Bureau of Meteorology, and R. Massom by the Australian Antarctic Division. The work of P. Reid and R. Massom also contributes to the Australian Government's Australian Antarctic Partnership Program (AAPP). For R. Massom, this work was also supported by the Australian Research Council Special Research Initiative the Australian Centre for Excellence in Antarctic Science (Project Number SR200100008).
- S. Stammerjohn was supported under NSF PLR 1440435; she also thanks the Institute of Arctic and Alpine Research and the National Snow and Ice Data Center, both at the University of Colorado Boulder, for institutional and data support.
- S. Barreira was supported by the Argentine Naval Hydrographic Service.
- T. Scambos was supported under NASA grants NNX14AM54G and 80NSSC21K0750, the Arctic Sea Ice News and Analysis project and NSF ANT 1738992, and the NSF-NERC International Thwaites Glacier Collaboration TARSAN project.

Appendix 1: Chapter 6 – Acronyms

ACC	Antarctic Circumpolar Current
AIS	Antarctic ice sheet
AP	Antarctic Peninsula
AR	atmospheric river
ASL	Amundsen Sea Low
AWS	automated weather stations
CL_2	chlorine
ClO	chlorine monoxide
CO_2	carbon dioxide
EESC	effective equivalent stratospheric chlorine
ENSO	El Niño–Southern Oscillation
ML	mixed layer
MLD	mixed layer depth
MLS	Microwave Limb Sounder
MSLP	mean sea level pressure
NSIDC	National Snow and Ice Data Center
OMI	ozone monitoring instrument
PSC	polar stratospheric cloud
SAM	Southern Annular Mode
SIE	sea ice extent
SMB	surface mass balance
SNPP OMPS	Suomi National Polar-orbiting Partnership/Ozone Mapping and Profiler
SO	Southern Ocean
SOCCOM	Southern Ocean Carbon and Climate Observations and Modeling
std. dev.	standard deviation
w.e.	water equivalent
WAIS	West Antarctic ice sheet

References

Adusumilli, S., H. A. Fricker, B. Medley, L. Padman, and M. R. Siegfried, 2020: Interannual variations in meltwater input to the Southern Ocean from Antarctic ice shelves. *Nat. Geosci.*, **13**, 616–620, https://doi.org/10.1038/s41561-020-0616-z.

——, A. M. Fish, H. A. Fricker, and B. Medley, 2021: Atmospheric river precipitation contributed to rapid increases in surface height of the west Antarctic ice sheet in 2019. *Geophys. Res. Lett.*, 48, e2020GL091076, https://doi.org/10.1029/2020GL091076.

Agosta, C., and Coauthors, 2019: Estimation of the Antarctic surface mass balance using the regional climate model MAR (1979–2015) and identification of dominant processes. *Cryosphere*, **13**, 281–296, https://doi.org/10.5194/tc-13-281-2019.

Alley, K. E., and Coauthors, 2021: Two decades of dynamic change and progressive destabilization on the Thwaites Eastern Ice Shelf. *Cryosphere*, **15**, 5187–5203, https://doi.org/10.5194/tc-15-5187-2021.

Aublanc, J., P. Thibaut, A. Guillot, F. Boy, and N. Picot, 2021: Ice sheet topography from a new CryoSat-2 SARIn processing chain, and assessment by comparison to ICESat-2 over Antarctica. *Remote Sens.*, **13**, 4508, https://doi.org/10.3390/rs13224508.

Banwell, A. F., D. R. MacAyeal, and O. V. Sergienko, 2013: Breakup of the Larsen B ice shelf triggered by chain reaction drainage of supraglacial lakes. *Geophys. Res. Lett.*, **40**, 5872–5876, https://doi.org/10.1002/2013GL057694.

——, R. T. Datta, R. L. Dell, M. Moussavi, L. Brucker, G. Picard, C. A. Shuman, and L. A. Stevens, 2021: The 32-year record-high surface melt in 2019/2020 on the northern George VI Ice Shelf, Antarctic Peninsula. *Cryosphere*, **15**, 909–925, https://doi.org/10.5194/tc-15-909-2021.

Barrand, N. E., D. G. Vaughan, N. Steiner, M. Tedesco, P. Kuipers Munneke, M. R. Van den Broeke, and J. S. Hosking, 2013: Trends in Antarctic Peninsula surface melting conditions from observations and regional climate modeling. *J. Geophys. Res. Earth Surf.*, **118**, 315–330, https://doi.org/10.1029/2012JF002559.

Becker, M. K., S. L. Howard, H. A. Fricker, L. Padman, C. Mosbeux, and M. R. Siegfried, 2021: Buoyancy-driven flexure at the front of Ross Ice Shelf, Antarctica, observed with ICESat-2 laser altimetry. *Geophys. Res. Lett.*, **48**, e2020GL091207, https://doi.org/10.1029/2020GL091207.

Cavalieri, D. J., C. L. Parkinson, P. Gloersen, and H. J. Zwally, 1996: Sea ice concentrations from Nimbus-7 SMMR and DMSP SSM/I-SSMIS passive microwave data, version 1. NASA National Snow and Ice Data Center Distributed Active Archive Center, accessed 4 January 2022, https://doi.org/10.5067/8GQ8LZQVL0VL.

Cheng, L., and Coauthors, 2022: Another record: Ocean warming continues through 2021 despite La Niña conditions. *Adv. Atmos. Sci.*, **39**, 373–385, https://doi.org/10.1007/s00376-022-1461-3.

Clem, K. R., B. R. Lintner, A. J. Broccoli, and J. R. Miller, 2019: Role of the South Pacific convergence zone in West Antarctic decadal climate variability. *Geophys. Res. Lett.*, **46**, 6900–6909, https://doi.org/10.1029/2019GL082108.

——, R. L. Fogt, J. Turner, B. R. Lintner, G. J. Marshall, J. R. Miller, and J. A. Renwick, 2020: Record warming at the South Pole during the past three decades. *Nat. Climate Change*, **10**, 762–770, https://doi.org/10.1038/s41558-020-0815-z.

Comiso, J. C., 2017: Bootstrap sea ice concentrations from Nimbus-7 SMMR and DMSP SSM/I-SSMIS, version 3. NASA National Snow and Ice Data Center Distributed Active Archive Center, accessed 4 January 2022, https://doi.org/10.5067/7Q8HCCWS4I0R

Datta, R. T., and B. Wouters, 2021: Supraglacial lake bathymetry automatically derived from ICESat-2 constraining lake depth estimates from multi-source satellite imagery. *Cryosphere*, **15**, 5115–5132, https://doi.org/10.5194/tc-15-5115-2021.

de Boyer Montegut, C., G. Madec, A. S. Fischer, A. Lazar, and D. Iudicone, 2004: Mixed layer depth over the global ocean: An examination of profile data and a profile-based climatology. *J. Geophys. Res.*, **109**, C12003, https://doi.org/10.1029/2004JC002378.</jrn>

Depoorter, M. A., J. L. Bamber, J. A. Griggs, J. T. Lenaerts, S. R. Ligtenberg, M. R. van den Broeke, and G. Moholdt, 2013: Calving fluxes and basal melt rates of Antarctic ice shelves. *Nature*, **502**, 89–92, https://doi.org/10.1038/nature12567.</jrn>

Fair, Z., M. Flanner, K. M. Brunt, H. A. Fricker, and A. Gardner, 2020: Using ICESat-2 and operation icebridge altimetry for supraglacial lake depth retrievals. *Cryosphere*, **14**, 4253–4263, https://doi.org/10.5194/tc-14-4253-2020.

Fanton d'Andon, O., and Coauthors, 2009: GlobColour – The European Service for Ocean Colour. *2009 IEEE Int. Geoscience and Remote Sensing Symp.*, Cape Town, South Africa, IEEE.

Fogt, R. L., Ed., 2011: Antarctica [in "State of the Climate in 2010"]. *Bull. Amer. Meteor. Soc.*, **92** (6), S161–S171, https://doi.org/10.1175/1520-0477-92.6.S1.

Fricker, H. A., and Coauthors, 2021: ICESat-2 meltwater depth estimates: Application to surface melt on Amery ice shelf, East Antarctica. *Geophys. Res. Lett.*, 48, e2020GL090550, https://doi.org/10.1029/2020GL090550.

Frölicher, T. L., J. L. Sarmiento, D. J. Paynter, J. P. Dunne, J. P. Krasting, and M. Winton, 2015: Dominance of the Southern Ocean in anthropogenic carbon and heat uptake in CMIP5 models. *J. Climate*, **28**, 862–886, https://doi.org/10.1175/JCLI-D-14-00117.1.

Gelaro, R., and Coauthors, 2017: The Modern-Era Retrospective Analysis for Research and Applications, version 2 (MERRA-2). *J. Climate*, **30**, 5419–5454, https://doi.org/10.1175/JCLI-D-16-0758.1.

Gloersen, P., 2006: Nimbus-7 SMMR polar gridded radiances and sea ice concentrations, version 1. Subset: 37 & 19 GHz, h-polarization, 25 km grid, Oct 1979–April 1987. NASA National Snow and Ice Data Center Distributed Active Archive Center, accessed 5 May 2020, https://doi.org/10.5067/QOZIVYV-3V9JP.

Gossart, A., S. Helsen, J. T. M. Lenaerts, S. Vanden Broucke, N. P. M. van Lipzig, and N. Souverijns, 2019: An evaluation of surface climatology in state-of-the-art reanalyses over the Antarctic ice sheet. *J. Climate*, **32**, 6899–6915, https://doi.org/10.1175/JCLI-D-19-0030.1.

Gudmundsson, G. H., F. S. Paolo, S. Adusumilli, and H. A. Fricker, 2019: Instantaneous Antarctic ice sheet mass loss driven by thinning ice shelves. *Geophys. Res. Lett.*, **46**, 132903–132909, https://doi.org/10.1029/2019GL085027.

Harvey, N., C. M. McCullough, and H. Save, 2022: Modeling GRACE-FO accelerometer data for the version 04 release. *Adv. Space Res.*, **69**, 1393–1407, https://doi.org/10.1016/j.asr.2021.10.056.

Haumann, F. A., N. Gruber, and M. Münnich, 2020: Sea-ice induced Southern Ocean subsurface warming and surface cooling in a warming climate. *AGU Adv.*, **1**, e2019AV000132, https://doi.org/10.1029/2019AV000132.

Hersbach, H., and Coauthors, 2020: The ERA5 global reanalysis. *Quart. J. Roy. Meteor. Soc.*, **146**, 1999–2049, https://doi.org/10.1002/qj.3803.

Hosking, J. S., A. Orr, G. J. Marshall, J. Turner, and T. Phillips, 2013: The influence of the Amundsen–Bellingshausen Seas low on the climate of West Antarctica and its representation in coupled climate model simulations. *J. Climate*, **26**, 6633–6648, https://doi.org/10.1175/JCLI-D-12-00813.1.

Johnson, A., R. Hock, and M. Fahnestock, 2021: Spatial variability and regional trends of Antarctic ice shelf surface melt duration over 1979–2020 derived from passive microwave data. *J. Glaciol.*, 68, 533–546, https://doi.org/10.1017/jog.2021.11.

Keller, L. M., K. J. Maloney, M. A. Lazzara, D. E. Mikolajczyk, and S. Di Battista, 2022: An investigation of extreme cold events at the South Pole. *J. Climate*, **35**, 1761–1772, https://doi.org/10.1175/JCLI-D-21-0404.1.

Kittel, C., and Coauthors, 2021: Diverging future surface mass balance between the Antarctic ice shelves and grounded ice sheet. *Cryosphere*, **15**, 1215–1236, https://doi.org/10.5194/tc-15-1215-2021.

Kramarova, N., and Coauthors, 2021: 2020 Antarctic ozone hole [in "State of the Climate in 2020"]. *Bull. Amer. Meteor. Soc.*, **102** (8), S345–S349, https://doi.org/10.1175/BAMS-D-21-0081.1.

Kusahara, K., P. Reid, G. D. Williams, R. Massom, and H. Hasumi, 2018: An ocean-sea ice model study of the unprecedented Antarctic sea ice minimum in 2016. *Environ. Res. Lett.*, **13**, 084020, https://doi.org/10.1088/1748-9326/aad624.

Lenaerts, J. T. M., and M. R. Van Den Broeke, 2012: Modeling drifting snow in Antarctica with a regional climate model: 2. Results. *J. Geophys. Res.*, **117**, D05109, https://doi.org/10.1029/2010JD015419.

Li, T., G. Dawson, S. Chuter, and J. Bamber, 2021: A high-resolution Antarctic grounding zone product from ICESat-2 laser altimetry. *Earth Syst. Sci. Data*, **14**, 535–557, https://doi.org/10.5194/essd-14-535-2022.

Ligtenberg, S. R. M., M. M. Helsen, and M. R. Van den Broeke, 2011: An improved semi-empirical model for the densification of Antarctic firn. *Cryosphere*, **5**, 809–819, https://doi.org/10.5194/tc-5-809-2011.

MacFerrin, M., T. Mote, H. Wang, L. Liu, L. Montgomery, and T. Scambos, 2021: Ice sheet seasonal melt extent and duration [in "State of the Climate in 2020"]. *Bull. Amer. Meteor. Soc.*, **102** (8), S331–S334, https://doi.org/10.1175/BAMS-D-21-0081.1.

MacGilchrist, G. A., H. L. Johnson, C. Lique, and D. P. Marshall, 2021: Demons in the North Atlantic: Variability of deep ocean ventilation. *Geophys. Res. Lett.*, **48**, e2020GL092340, https://doi.org/10.1029/2020GL092340.</unknown>

Manney, and Coauthors, 2011: Unprecedented Arctic ozone loss in 2011. *Nature*, **478**, 469–475, https://doi.org/10.1038/nature10556.

Maritorena, S., O. H. Fanton d'Andon, A. Mangin, and D. A. Siegel, 2010: Merged satellite ocean color data products using a bio-optical model: Characteristics, benefits, and issues. *Remote Sens. Environ.*, **114**, 1791–1804, https://doi.org/10.1016/j.rse.2010.04.002.

Marshall, G. J., 2003: Trends in the southern annular mode from observations and reanalyses. *J. Climate*, **16**, 4134–4143, https://doi.org/10.1175/1520-0442(2003)016<4134:TITSAM>2.0.CO;2.

Maslanik, J., and J. Stroeve, 1999: Near-real-time DMSP SSM/I-SSMIS daily polar gridded sea ice concentrations. National Snow and Ice Data Center, accessed 28 March 2022, https://doi.org/10.5067/U8C09DWVX9LM.

Medley, B., and E. R. Thomas, 2019: Increased snowfall over the Antarctic Ice Sheet mitigated twentieth-century sea-level rise. *Nat. Climate Change*, **9**, 34–39, https://doi.org/10.1038/s41558-018-0356-x.

Meehl, G. A., and Coauthors, 2019: Sustained ocean changes contributed to sudden Antarctic sea ice retreat in late 2016. *Nat. Commun.*, **10**, 14, https://doi.org/10.1038/s41467-018-07865-9.

Meier, W. N., H. Wilcox, M. A. Hardman, and J. S. Stewart, 2019: DMSP SSM/I-SSMIS daily polar gridded brightness temperatures, version 5. Subset: 37 & 19 GHz, h-polarization, 25 km grid, Oct 1987–April 2020. NASA National Snow and Ice Data Center Distributed Active Archive Center, accessed 11 February 2021, https://doi.org/10.5067/QU2UYQ6T0B3P.

——, J. S. Stewart, H. Wilcox, M. A. Hardman, and D. J. Scott, 2021: Near-real-time DMSP SSMIS daily polar gridded sea ice concentrations, version 2 [6/1/2021 to 3/27/2022]. NASA National Snow and Ice Data Center Distributed Active Archive Center, accessed 28 March 2022, https://doi.org/10.5067/YTTHO2FJQ97K.

Morlighem, M., and Coauthors, 2020: Deep glacial troughs and stabilizing ridges unveiled beneath the margins of the Antarctic ice sheet. *Nat. Geosci.*, **13**, 132–137, https://doi.org/10.1038/s41561-019-0510-8.

Morrison, A. K., D. W. Waugh, A. McC. Hogg, D. C. Jones, and R. P. Abernathey, 2022: Ventilation of the Southern Ocean pycnocline. *Annu. Rev. Mar. Sci.*, **14**, 405–430, https://doi.org/10.1146/annurev-marine-010419-011012.

Mote, T. L., 2007: Greenland surface melt trends 1973–2007: Evidence of a large increase in 2007. *Geophys. Res. Lett.*, **34**, L22507, https://doi.org/10.1029/2007GL031976.

——, 2014: MEaSUREs Greenland surface melt daily 25km EASE-Grid 2.0, version 1. NASA National Snow and Ice Data Center Distributed Active Archive Center, accessed 30 August 2021, https://doi.org/10.5067/MEASURES/CRYOSPHERE/nsidc-0533.001.

——, and M. R. Anderson, 1995: Variations in snowpack melt on the Greenland ice sheet based on passive microwave measurements. *J. Glaciol.*, **41**, 51–60, https://doi.org/10.1017/S0022143000017755.

Mottram, R., and Coauthors, 2020: What is the surface mass balance of Antarctica? An intercomparison of regional climate model estimates. *Cryosphere*, 15, 3751–3784, https://doi.org/10.5194/tc-15-3751-2021.

NASA, 2022: What is EESC? NASA OzoneWatch, accessed 10 February 2022, https://ozonewatch.gsfc.nasa.gov/facts/eesc_SH.html.

Neckel, N., S. Franke, V. Helm, R. Drews, and D. Jansen, 2021: Evidence of cascading subglacial water flow at Jutulstraumen Glacier (Antarctica) derived From Sentinel-1 and ICESat-2 measurements. *Geophys. Res. Lett.*, **48**, e2021GL094472, https://doi.org/10.1029/2021GL094472.

Neff, W. D., J. Crawford, M. Buhr, J. Nicovich, G. Chen, and D. Davis, 2018: The meteorology and chemistry of high nitrogen oxide concentrations in the stable boundary layer at the south pole. *Atmos. Chem. Phys.*, **18**, 3755–3778, https://doi.org/10.5194/acp-18-3755-2018.

Newman, P. A., J. S. Daniel, D. W. Waugh, and E. R. Nash, 2007: A new formulation of equivalent effective stratospheric chlorine (EESC). *Atmos. Chem. Phys.*, **7**, 4537–4552, https://doi.org/10.5194/acp-7-4537-2007.

Norwegian Polar Institute, 2018: Quantarctica v3.0, detailed basemap. https://www.npolar.no/quantarctica/.

Oliva, M., F. Navarro, F. Hrbáček, A. Hernandéz, D. Nývlt, P. Pereira, J. Ruiz-Fernandéz, and R. Trigo, 2017: Recent regional climate cooling on the Antarctic Peninsula and associated impacts on the cryosphere. *Sci. Total Environ.*, **580**, 210–223, https://doi.org/10.1016/j.scitotenv.2016.12.030.

Orsi, A. H., T. Whitworth III, and W. D. Nowlin Jr., 1995: On the meridional extent and fronts of the Antarctic Circumpolar Current. *Deep-Sea Res. I*, **42**, 641–673, https://doi.org/10.1016/0967-0637(95)00021-W.

Palm, S. P., V. Kayetha, and Y. Yang, 2018: Toward a satellite-derived climatology of blowing snow Over Antarctica. *J. Geophys. Res. Atmos.*, **123**, 102301–102313, https://doi.org/10.1029/2018JD028632.

Paolo, F. S., H. A. Fricker, and L. Padman, 2015: Volume loss from Antarctic ice shelves is accelerating. *Science*, **348**, 327–331, https://doi.org/10.1126/science.aaa0940.

Parkinson, C. L., 2019: A 40-y record reveals gradual Antarctic sea ice increases followed by decreases at rates far exceeding the rates seen in the Arctic. *Proc. Natl. Acad. Sci. USA*, **116**, 142414–142423, https://doi.org/10.1073/pnas.1906556116.

——, and N. E. DiGirolamo, 2021: Sea ice extents continue to set new records: Arctic, Antarctic, and global results. *Remote Sens. Environ.*, **267**, 112753, https://doi.org/10.1016/j.rse.2021.112753.

Pitts, M. C., L. R. Poole, and R. Gonzalez, 2018: Polar stratospheric cloud climatology based on CALIPSO spaceborne lidar measurements from 2006 to 2017. *Atmos. Chem. Phys.*, **18**, 10881–10913, https://doi.org/10.5194/acp-18-10881-2018.

Qu, T., I. Fukumori, and R. A. Fine, 2019: Spin-up of the southern hemisphere super gyre. *J. Geophys. Res. Oceans*, **124**, 154–170, https://doi.org/10.1029/2018JC014391.

Reid, P. A., and R. A. Massom, 2015: Successive Antarctic sea ice extent records during 2012, 2013 & 2014 [in "State of the Climate in 2014"]. *Bull. Amer. Meteor. Soc.*, **96** (7), S163–S164, https://doi.org/10.1175/2015BAMSStateoftheClimate.1.

——, S. Stammerjohn, R. A. Massom, S. Barreira, T. Scambos, and J. Lieser, 2021: Sea ice extent, concentration, and seasonality [in "State of the Climate in 2020"]. *Bull. Amer. Meteor. Soc.*, **102** (8), S336–S338, https://doi.org/10.1175/BAMS-D-21-0081.1.

Reynolds, R. W., N. A. Rayner, T. M. Smith, D. C. Stokes, and W. Wang, 2002: An improved in situ and satellite SST analysis for climate. *J. Climate*, **15**, 1609–1625, https://doi.org/10.1175/1520-0442(2002)015<1609:AIISAS>2.0.CO;2.

Rignot, E., S. Jacobs, J. Mouginot, and B. Scheuchl, 2013: Ice-shelf melting around Antarctica. *Science*, **341**, 266–270, https://doi.org/10.1126/science.1235798.

Roemmich, D., and J. Gilson, 2009: The 2004–2008 mean and annual cycle of temperature, salinity, and steric height in the global ocean from the Argo Program. *Prog. Oceanogr.*, **82**, 81–100, https://doi.org/10.1016/j.pocean.2009.03.004.

Sallée, J. B., K. G. Speer, and S. R. Rintoul, 2010: Zonally asymmetric response of the Southern Ocean mixed-layer depth to the southern annular mode. *Nat. Geosci.*, **3**, 273–279, https://doi.org/10.1038/ngeo812.

Sarmiento, J. L., N. Gruber, M. A. Brzezinski, and J. P. Dunne, 2004: High-latitude controls of thermocline nutrients and low latitude biological productivity. *Nature*, **427**, 56–60, https://doi.org/10.1038/nature02127.

Scambos, T., C. Hulbe, and M. Fahnestock, 2003: Climate-induced ice shelf disintegration in the Antarctic Peninsula. *Antarctic Peninsula Climate Variability: Historical and Paleoenvironmental Perspectives*, E. Domack et al., Eds., Antarctic Research Series, Vol. 79, Amer. Geophys. Union, 79–92, https://doi.org/10.1029/AR079p0079.

——, J. A. Bohlander, C. A. Shuman, and P. Skvarca, 2004: Glacier acceleration and thinning after ice shelf collapse in the Larsen B embayment, Antarctica. *Geophys. Res. Lett.*, **31**, L18402, https://doi.org/10.1029/2004GL020670.

Shepherd, A., and Coauthors, 2012: A reconciled estimate of ice-sheet mass balance. Science, 338, 1183–1189, https://doi.org/10.1126/science.1228102.

Shi, J.-R., S.-P. Xie, and L. D. Talley, 2018: Evolving relative importance of the Southern Ocean and North Atlantic in anthropogenic ocean heat uptake. *J. Climate*, **31**, 7459–7479, https://doi.org/10.1175/JCLI-D-18-0170.1.

——, L. D. Talley, S.-P. Xie, W. Liu, and S. T. Gille, 2020: Effects of buoyancy and wind forcing on Southern Ocean climate change. *J. Climate*, **33**, 10 003–10 020, https://doi.org/10.1175/JCLI-D-19-0877.1.

——, ——, ——, Q. Peng, and W. Liu, 2021: Ocean warming and accelerating Southern Ocean zonal flow. *Nat. Climate Change*, **11**, 1090–1097, https://doi.org/10.1038/s41558-021-01212-5.

Siegfried, M. R., and H. A. Fricker, 2021: Illuminating active subglacial lake processes with ICESat-2 laser altimetry. *Geophys. Res. Lett.*, **48**, e2020GL091089, https://doi.org/10.1029/2020GL091089.

Smith, B., and Coauthors, 2020a: Pervasive ice sheet mass loss reflects competing ocean and atmosphere processes. *Science*, **368**, 1239–1242, https://doi.org/10.1126/science.aaz5845.

——, and Coauthors, 2020b: ATLAS/ICESat-2 L3A land ice height, version 5. NASA National Snow and Ice Data Center Distributed Active Archive Center, accessed 25 January 2022, https://doi.org/10.5067/ATLAS/ATL06.005.

Smith, T. M., R. W. Reynolds, T. C. Peterson, and J. Lawrimore, 2008: Improvements to NOAA's historical merged land–ocean surface temperature analysis (1880–2006). *J. Climate*, **21**, 2283–2296, https://doi.org/10.1175/2007JCLI2100.1.

Song, Y., and W. A. Robinson, 2004: Dynamical mechanisms for stratospheric influences on the troposphere. *J. Atmos. Sci.*, **61**, 1711–1725, https://doi.org/10.1175/1520-0469(2004)061<1711:DMFSIO>2.0.CO;2.

Stammerjohn, S., and T. Maksym, 2017: Gaining (and losing) Antarctic sea ice: Variability, trends and mechanisms. *Sea Ice*, D. N. Thomas, Ed., Wiley, 261–289, https://doi.org/10.1002/9781118778371.ch10.

——, and T. A. Scambos, 2020: Warming reaches the South Pole. *Nat. Climate Change*, **10**, 710–711, https://doi.org/10.1038/s41558-020-0827-8.

——, D. G. Martinson, R. C. Smith, X. Yuan, and D. Rind, 2008: Trends in Antarctic annual sea ice retreat and advance and their relation to El Niño–Southern Oscillation and southern annular mode variability. *J. Geophys. Res.*, **113**, C03S90, https://doi.org/10.1029/2007JC004269.

Stone, K. A., S. Solomon, D. E. Kinnison, and M. J. Mills, 2021: On recent large Antarctic ozone holes and ozone recovery metrics. *Geophys. Res. Lett.*, **48**, e2021GL095232, https://doi.org/10.1029/2021GL095232.

Strahan, S. E., A. R. Douglass, and M. R. Damon, 2019: Why do Antarctic ozone recovery trends vary? *J. Geophys. Res. Atmos.*, **124**, 8837–8850, https://doi.org/10.1029/2019JD030996.

The IMBIE Team, 2018: Mass balance of the Antarctic Ice Sheet from 1992 to 2017. *Nature*, **558**, 219–222, https://doi.org/10.1038/s41586-018-0179-y.

Thompson, D. W. J., J. C. Furtado, and T. G. Shepherd, 2006: On the tropospheric response to anomalous stratospheric wave drag and radiative heating. *J. Atmos. Sci.*, **63**, 2616–2629, https://doi.org/10.1175/JAS3771.1.

Turner, J., T. Phillips, J. S. Hosking, G. J. Marshall, and A. Orr, 2013: The Amundsen Sea low. *Int. J. Climatol.*, **33**, 1818–1829, https://doi.org/10.1002/joc.3558.

——, and Coauthors, 2016: Absence of 21st century warming on Antarctic Peninsula consistent with natural variability. *Nature*, **535**, 411–415, https://doi.org/10.1038/nature18645.

——, and Coauthors, 2019: The dominant role of extreme precipitation events in Antarctic snowfall variability. *Geophys. Res. Lett.*, **46**, 3502–3511, https://doi.org/10.1029/2018GL081517.

Walker, C. C., M. K. Becker, and H. A. Fricker, 2021: A high resolution, three-dimensional view of the D-28 calving event from Amery ice shelf with ICESat-2 and satellite imagery. *Geophys. Res. Lett.*, **48**, e2020GL091200, https://doi.org/10.1029/2020GL091200.

Wang, Y., and Coauthors, 2016: A comparison of Antarctic Ice Sheet surface mass balance from atmospheric climate models and in situ observations. *J. Climate*, **29**, 5317–5337, https://doi.org/10.1175/JCLI-D-15-0642.1.

Warner, R. C., H. A. Fricker, S. Adusumilli, P. Arndt, J. Kingslake, and J. J. Spergel, 2021: Rapid formation of an ice doline on Amery Ice Shelf, East Antarctica. *Geophys. Res. Lett.*, **48**, https://doi.org/10.1029/2020GL091095.

Wiese, D. N., D.-N. Yuan, C. Boening, F. W. Landerer, and M. M. Watkins, 2022: JPL GRACE and GRACE-FO Mascon Ocean, Ice, and Hydrology Equivalent Water Height Coastal Resolution Improvement (CRI) Filtered Release 06 Version 02. PO.DAAC, accessed 25 January 2022, https://doi.org/10.5067/TEMSC-3JC62.

Wild, C. T., K. E. Alley, A. Muto, M. Truffer, T. A. Scambos, and E. C. Pettit, 2022: Weakening of the pinning point buttressing Thwaites Glacier, West Antarctica. *Cryosphere*, **16**, 397–417, https://doi.org/10.5194/tc-16-397-2022.

Wille, J. D., and Coauthors, 2021: Antarctic Atmospheric river climatology and precipitation impacts. *J. Geophys. Res. Atmos.*, **126**, e2020JD033788, https://doi.org/10.1029/2020JD033788.

Yuan, X., 2004: ENSO-related impacts on Antarctic sea ice: A synthesis of phenomenon and mechanisms. *Antarct. Sci.*, **16**, 415–425, https://doi.org/10.1017/S0954102004002238.

STATE OF THE CLIMATE IN 2021

REGIONAL CLIMATES

P. Bissolli, C. Ganter, A. Mekonnen, A. Sánchez-Lugo, and Z. Zhu, Eds.

Special Online Supplement to the *Bulletin of the American Meteorological Society*, Vol. 103, No. 8, August 2022

10.1175/2022BAMSStateoftheClimate.1
Corresponding authors:
North America: Ahira Sánchez-Lugo / Ahira.Sanchez-Lugo@noaa.gov.
Central America and the Caribbean: Ahira Sánchez-Lugo / Ahira.Sanchez-Lugo@noaa.gov
South America: Ahira Sánchez-Lugo / Ahira.Sanchez-Lugo@noaa.gov
Africa: Ademe Mekonnen / amekonne@ncat.edu
Europe: Peter Bissolli / Peter.Bissolli@dwd.de
Asia: Zhiwei Zhu / zwz@nuist.edu.cn
Oceania: Catherine Ganter / Catherine.Ganter@bom.gov.au

STATE OF THE CLIMATE IN 2021
Regional Climates

Editors

Jessica Blunden
Tim Boyer

Chapter Editors

Freya Aldred
Peter Bissolli
Kyle R. Clem
Howard J. Diamond
Matthew L. Druckenmiller
Robert J. H. Dunn
Catherine Ganter
Nadine Gobron
Gregory C. Johnson
Rick Lumpkin
Ademe Mekonnen
John B. Miller
Twila A. Moon
Marilyn N. Raphael
Ahira Sánchez-Lugo
Carl J. Schreck III
Richard L. Thoman
Kate M. Willett
Zhiwei Zhu

Technical Editor

Laura Ohlmann

BAMS Special Editor for Climate

Michael A. Alexander

American Meteorological Society

Cover credit:
Flames and smoke from wildfires above the Fraser River Valley near Lytton, British Columbia, Canada, on 2 July 2021. Photographer: James MacDonald/Bloomberg ©2021 Bloomberg Finance LP - Getty

Regional Climates is one chapter from the *State of the Climate in 2021* annual report. Compiled by NOAA's National Centers for Environmental Information, *State of the Climate in 2021* is based on contributions from scientists from around the world. It provides a detailed update on global climate indicators, notable weather events, and other data collected by environmental monitoring stations and instruments located on land, water, ice, and in space. The full report is available from 10.1175/2022BAMSStateoftheClimate.1.

How to cite this document:

Citing the complete report:
Blunden, J. and T. Boyer, Eds., 2022: "State of the Climate in 2021". *Bull. Amer. Meteor. Soc.,* **103** (8), Si–S465, https://doi.org/10.1175/2022BAMSStateoftheClimate.1.

Citing this chapter:
Bissolli, P., C. Ganter, A. Mekonnen, A. Sánchez-Lugo, and Z. Zhu, Eds. 2022: Regional Climates [in "State of the Climate in 2021"]. *Bull. Amer. Meteor. Soc.*, **103** (8), S341–S453, https://doi.org/10.1175/2022BAMSStateoftheClimate_Chapter7.1.

Citing a section (example):
Koren, G., 2022: Major floods in the Amazon basin [in "State of the Climate in 2021"]. Bull. Amer. Meteor. Soc., **103** (8), S369–S370, https://doi.org/10.1175/2022BAMSStateoftheClimate_Chapter7.1.

Editor and Author Affiliations (alphabetical by name)

Abida, A., Agence Nationale de l'Aviation Civile et de la Météorologie, Union des Comores

Agyakwah, W., Climate Prediction Center, National Centers for Environmental Prediction, NOAA, College Park, Maryland

Aldeco, Laura S., Servicio Meteorológico Nacional, Buenos Aires, Argentina

Alfaro, Eric J., Center for Geophysical Research and School of Physics, University of Costa Rica, San José, Costa Rica

Allen, Teddy, Caribbean Institute for Meteorology and Hydrology, Bridgetown, Barbados

Alves, Lincoln M., Centro Nacional de Monitoramento e Alertas de Desastres Naturais CEMADEN, São Paulo, Brazil

Amador, Jorge A., Center for Geophysical Research and School of Physics, University of Costa Rica, San José, Costa Rica

Andrade, B., Seychelles Meteorological Authority, Mahe, Seychelles

Asgarzadeh, P., National Center for Climate and Drought Crisis Management, Islamic Republic of Iranian Meteorological Organization, Iran

Avalos, Grinia, Servicio Nacional de Meteorología e Hidrología del Perú, Lima, Perú

Baez, Julian, Universidad Católica Nuestra Señora de la Asunción, Asunción, Paraguay

Bardin, M. Yu., Yu. A. Izrael Institute of Global Climate and Ecology; Institute of Geography, Russian Academy of Sciences, Russia

Bekele, E., Climate Prediction Center, National Centers for Environmental Prediction, NOAA, College Park, Maryland

Bertalanic, Renato, Slovenian Environment Agency, Slovenia

Bissolli, Peter, Deutscher Wetterdienst, WMO RA VI Regional Climate Centre Network, Offenbach, Germany

Bochníček, Oliver, Slovak Hydrometeorological Institute, Slovakia

Bukunt, Brandon, NOAA/NWS Weather Forecast Office, Guam

Calderón, Blanca, Center for Geophysical Research, University of Costa Rica, San José, Costa Rica

Campbell, Jayaka D., Department of Physics, The University of the West Indies, Jamaica

Chandler, Elise, Bureau of Meteorology, Melbourne, Victoria, Australia

Charlton, Candice S, Department of Physics, The University of the West Indies, Jamaica

Cheng, Vincent Y. S., Environment and Climate Change Canada, Toronto, Ontario, Canada

Clarke, Leonardo A., Department of Physics, The University of the West Indies, Jamaica

Correa, Kris, Servicio Nacional de Meteorología e Hidrología del Perú, Lima, Perú

Cortés Salazar, Catalina R., Dirección de Meteorológica de Chile, Santiago de Chile, Chile

Costa, Felipe, Centro Internacional para la Investigación del Fenómeno de El Niño (CIIFEN), Guayaquil, Ecuador

Crhová, Lenka, Czech Hydrometeorologival Institute, Czechia

Cunha, Ana Paula, Centro Nacional de Monitoramento e Alertas de Desastres Naturais CEMADEN, São Paulo, Brazil

Demircan, Mesut, Turkish State Meteorological Service, Ankara, Türkiye

Dhurmea, K. R., Mauritius Meteorological Service, Vacoas, Mauritius

Domínguez, Diana A., Servicio Meteorológico Nacional, Buenos Aires, Argentina

Dulamsuren, Dashkhuu, Institute of Meteorology, Hydrology and Environment, National Agency for Meteorology, Ulaanbaatar, Mongolia

ElKharrim, M., Direction de la Météorologie Nationale Maroc, Rabat, Morocco

Espinoza, Jhan-Carlo, Université Grenoble Alpes, Institut des Géosciences de l'Environnement, IRD, CNRS, Grenoble INP, Grenoble, France

Fazl-Kezemi, A., National Center for Climate and Drought Crisis Management, Islamic Republic of Iranian Meteorological Organization, Iran

Fedaeff, Nava, National Institute of Water and Atmospheric Research, Ltd. (NIWA), Auckland, New Zealand

Fenimore, Chris, NOAA/NESDIS National Centers for Environmental Information, Asheville, North Carolina

Fuhrman, Steven, NOAA/NWS National Centers for Environmental Prediction, Climate Prediction Center, College Park, Maryland

Ganter, Catherine, Bureau of Meteorology, Melbourne, Victoria, Australia

Gleason, Karin, NOAA/NESDIS National Centers for Environmental Information, Asheville, North Carolina

Guard, Charles "Chip" P., Tropical Weather Sciences, Sinajana, Guam

Hagos, Samson, Pacific Northwest National Lab, Department of Energy, Washington

Hanafusa, Mizuki, Tokyo Climate Center, Japan Meteorological Agency, Japan

Heim, Jr., Richard R., NOAA/NESDIS National Centers for Environmental Information, Asheville, North Carolina

Kennedy, John, Met Office Hadley Centre, Exeter, United Kingdom

Hellström, Sverker, Swedish Meteorological and Hydrological Institute, Sweden

Hidalgo, Hugo G., Center for Geophysical Research and School of Physics, University of Costa Rica, San José, Costa Rica

Ijampy, I. A., Nigerian Meteorological Agency, Abuja, Nigeria

Im, Gyo Soon, Climate Change Monitoring Division, Korea Meteorological Administration, South Korea

Jumaux, G., Météo France, Direction Interrégionale pour l'Océan Indien, Réunion

Kabidi, K., Direction de la Météorologie Nationale Maroc, Rabat, Morocco

Kerr, Kenneth, Trinidad and Tobago Meteorological Service, Trinidad

Khalatyan, Yelena, Hydrometeorology and Monitoring Center, Armenia

Khan, Valentina, Hydrometcenter of Russia, WMO North EurAsia Climate Center, Moscow, Russia

Khiem, Mai Van, Viet Nam National Center of Hydro-Meteorology Forecasting, Viet Nam Meteorology Hydrology Administration, Viet Nam

Koch, Tobias, Soil and Water Ecosystems (SWEco), Faculty of Geography, University of Marburg, Marburg, Germany

Koren, Gerbrand, Copernicus Institute of Sustainable Development, Utrecht University, the Netherlands

Korshunova, Natalia N., All-Russian Research Institute of Hydrometeorological Information, World Data Center, Obninsk, Russia

Kruger, A. C., Climate Service, South African Weather Service, Pretoria, South Africa

Lakatos, Mónika, Climatology Unit, Hungarian Meteorological Service, Budapest, Hungary

Mamen, Jostein, Climate Division, Norwegian Meteorological Institute, Oslo, Norway

Lam, Hoang Phuc, Viet Nam National Center of Hydro–Meteorology Forecasting, Viet Nam Meteorology Hydrology Administration, Viet Nam

Lander, Mark A., University of Guam, Mangilao, Guam

Lavado-Casimiro, Waldo, Servicio Nacional de Meteorología e Hidrología del Perú, Lima, Perú

Lee, Tsz-Cheung, Hong Kong Observatory, Hong Kong, China

Leung, Kinson H. Y., Environment and Climate Change Canada, Toronto, Ontario, Canada

Liu, Xuefeng, Nanjing University of Information Science and Technology, Nanjing, China

Lu, Rui, Nanjing University of Information Science and Technology, Nanjing, China

Marengo, José A., Centro Nacional de Monitoramento e Alertas de Desastres Naturais CEMADEN, São Paulo, Brazil

Editor and Author Affiliations (alphabetical by name)

Marjan, Mohammadi, National Center for Climate and Drought Crisis Management, Islamic Republic of Iranian Meteorological Organization, Iran
Martínez, Ana E., National Meteorological Service of Mexico, Mexico City, Mexico
McBride, Charlotte, Climate Service, South African Weather Service, Pretoria, South Africa
Mekonnen, Ademe, Department of Physics, North Carolina A & T University, Greensboro, North Carolina
Mietus, Mirek, Instytut Meteorologii i Gospodarki Wodnej PIB, Poland
Misevicius, Noelia, Instituto Uruguayo de Meteorología, Montevideo, Uruguay
Moise, Aurel, Centre for Climate Research Singapore, Meteorological Service Singapore, Singapore
Molina-Carpio, Jorge, Universidad Mayor de San Andrés, La Paz, Bolivia
Mora, Natali, Center for Geophysical Research, University of Costa Rica, San José, Costa Rica
Mostafa, Awatif E., Department of Seasonal Forecast and Climate Research, Cairo Numerical Weather Prediction, Egyptian Meteorological Authority, Cairo, Egypt
Ndiaye, O., Senegalese Meteorological Service, Dakar, Senegal
Nieto, Juan J., Centro Internacional para la Investigación del Fenómeno de El Niño (CIIFEN), Guayaquil, Ecuador
Olafsdottir, Kristin, Icelandic Meteorological Service, Iceland
Pascual Ramírez, Reynaldo, National Meteorological Service of Mexico, Mexico City, Mexico
Phillips, David, Environment and Climate Change Canada, Toronto, Ontario, Canada
Porat, Amos, Israel Meteorological Service, Israel
Rodriguez Guisado, Esteban, Agencia Estatal de Meteorología, Madrid, Spain
Rajeevan, Madhavan, Earth System Science Organization, Ministry of Earth Sciences, New Delhi, India
Ramos, Andrea M., Instituto Nacional de Meteorologia, Brasilia, Brazil
Recalde Coronel, Cristina, NOAA/NWS National Centers for Environmental Prediction, Climate Prediction Center, College Park, Maryland
Reyes Kohler, Alejandra J., Dirección de Meteorológica de Chile, Santiago de Chile, Chile
Robjhon, M., Climate Prediction Center, National Centers for Environmental Prediction, NOAA, College Park, Maryland
Ronchail, Josyane, Laboratoire LOCEAN-IPSL, Paris, France
Salinas, Roberto, Dirección de Meteorología e Hidrología / Dirección Nacional de Aeronáutica Civil, Asunción, Paraguay
Sánchez-Lugo, Ahira, NOAA/NESDIS National Centers for Environmental Information, Asheville, North Carolina
Sato, Hirotaka, Tokyo Climate Center, Japan Meteorological Agency, Japan
Sato, Hitoshi, Tokyo Climate Center, Japan Meteorological Agency, Japan
Sayouri, Amal, Direction de la Météorologie Nationale Maroc, Rabat, Morocco
Sensoy, Serhat, Turkish State Meteorological Service, Ankara, Türkiye
Setiawan, Amsari Mudzakir, Division for Climate Variability Analysis, BMKG, Indonesia
Sima, F., Division of Meteorology, Department of Water Resources, Banjul, The Gambia.
Smith, Adam, NOAA/NESDIS National Centers for Environmental Information, Asheville, North Carolina
Sorel, Matthieu, Météo France, Toulouse, France
Spillane, Sandra, Met Éireann, Dublin, Ireland
Spence, Jacqueline M., Meteorological Service, Jamaica, Kingston, Jamaica
Sreejith, O. P., India Meteorological Department, Pune, India
Srivastava, A. K., India Meteorological Department, Pune, India
Stephenson, Tannecia S., Department of Physics, The University of the West Indies, Jamaica
Takahashi, Kiyotoshi, Tokyo Climate Center, Japan Meteorological Agency, Japan
Taylor, Michael A., Department of Physics, The University of the West Indies, Jamaica
Thiaw, Wassila M., NOAA/NWS National Centers for Environmental Prediction, Climate Prediction Center, College Park, Maryland
Tobin, Skie, Bureau of Meteorology, Melbourne, Victoria, Australia
Trescilo, Lidia, State Hydrometeorological Service, Moldova
Trotman, Adrian R., Caribbean Institute for Meteorology and Hydrology, Bridgetown, Barbados
Van Meerbeeck, Cedric J., Caribbean Institute for Meteorology and Hydrology, Bridgetown, Barbados
Vazifeh, A., National Center for Climate and Drought Crisis Management, Islamic Republic of Iranian Meteorological Organization, Iran
Wakamatsu, Shunya, Tokyo Climate Center, Japan Meteorological Agency, Japan
Zaheer, M. F., Afghanistan Famine Early Warning System Network, Afghanistan
Zeng, F., Pacific Northwest National Lab, Department of Energy, Washington
Zhang, Peiqun, National Climate Centre, China Meteorological Administration, Beijing, China
Zhu, Zhiwei, Nanjing University of Information Science and Technology, Nanjing, China

Editorial and Production Team

Allen, Jessicca, Graphics Support, Cooperative Institute for Satellite Earth System Studies, North Carolina State University, Asheville, North Carolina
Hammer, Gregory, Content Team Lead, Communications and Outreach, NOAA/NESDIS National Centers for Environmental Information, Asheville, North Carolina
Love-Brotak, S. Elizabeth, Lead Graphics Production, NOAA/NESDIS National Centers for Environmental Information, Asheville, North Carolina
Misch, Deborah J., Graphics Support, Innovative Consulting and Management Services, LLC, NOAA/NESDIS National Centers for Environmental Information, Asheville, North Carolina
Ohlmann, Laura, Technical Editor, Innovative Consulting and Management Services, LLC, NOAA/NESDIS National Centers for Environmental Information, Asheville, North Carolina
Riddle, Deborah B., Graphics Support, NOAA/NESDIS National Centers for Environmental Information, Asheville, North Carolina
Veasey, Sara W., Visual Communications Team Lead, Communications and Outreach, NOAA/NESDIS National Centers for Environmental Information, Asheville, North Carolina

7. Table of Contents

7. Table of Contents

*Please refer to Chapter 8 (Relevant datasets and sources) for a list of all climate variables and datasets used in this chapter for analyses, along with their websites for more information and access to the data.

7. REGIONAL CLIMATES

P. Bissolli, C. Ganter, A. Mekonnen, A. Sánchez-Lugo, and Z. Zhu, Eds.

a. Overview

This chapter provides summaries of the 2021 temperature and precipitation conditions across seven broad regions: North America, Central America and the Caribbean, South America, Africa, Europe and the Middle East, Asia, and Oceania. In most cases, summaries of notable weather events are also included. Local scientists provided the annual summary for their respective regions and, unless otherwise noted, the source of the data used is typically the agency affiliated with the authors. The base period used for these analyses in many countries is now 1991–2020, as new 30-year climate normals are being utilized (see Chapter 1 for details). However, please note that on occasion different nations, even within the same section, may use unique periods to define their normal and many countries still use the 1981–2010 base period. Section introductions typically define the prevailing practices for that section, and exceptions will be noted within the text. In a similar way, many contributing authors use languages other than English as their primary professional language. To minimize additional loss of fidelity through re-interpretation after translation, editors have been conservative and careful to preserve the voice of the author. In some cases, this may result in abrupt transitions in style from section to section.

b. North America—A. Sánchez-Lugo, Ed.

1) CANADA—K. H. Y. Leung, V. Y. S. Cheng, and D. Phillips

In Canada, 2021 was characterized by above-average winter and spring temperatures in most of southern Canada and northeastern Nunavut and by below-average winter and spring temperatures in most of the Yukon and Northwest Territories. The country also experienced above-average summer temperatures in most of western and southern Canada and below-average summer temperatures in central northern Canada. The national average temperature for autumn 2021 was the highest in the 74-year record (1948–2021).

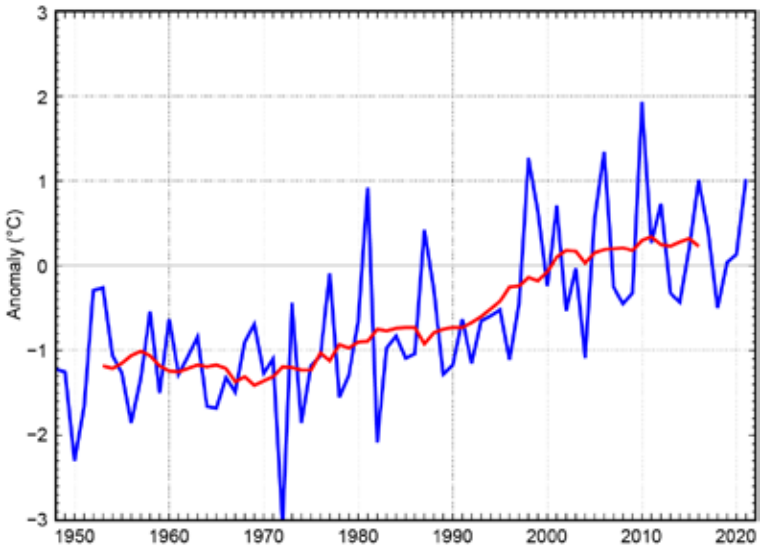

Fig. 7.1. Annual average temperature anomalies (°C; 1991–2020 base period) in Canada for the period 1948–2021. Red line is the 11-year running mean. (Source: Environment and Climate Change Canada.)

(i) Temperature

The annual average temperature for Canada in 2021 was 1.0°C above the 1991–2020 baseline average, and the fourth-warmest year in the 74-year record (Fig. 7.1). The warmest year on record was 2010 at 1.9°C above average. Over the past 74 years (1948–2021), the national annual average temperature has exhibited a linear warming trend of +1.9°C, and three of the 10 warmest years occurred during the last decade. Annual anomalies for 2021 above +2.5°C were recorded in the northernmost parts of Canada, and anomalies

above +0.5°C were recorded in eastern Canada. Annual anomalies below −0.5°C were observed in an area centered over the southern Yukon and extending into the western Northwest Territories and northern British Columbia (Fig. 7.2). In 2021, eight provinces/territories reported an annual average temperature that was among their 10 highest on record: Newfoundland and Labrador, New Brunswick, and Quebec (second highest); Ontario and Nunavut (third highest); Nova Scotia and Prince Edward Island (fourth); and Manitoba (10th).

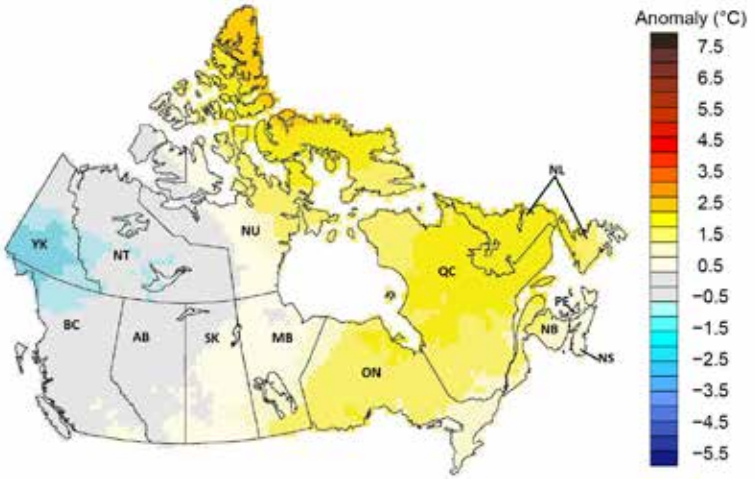

Fig. 7.2. Annual average temperature anomalies (°C; 1991–2020 base period) in Canada for 2021. (Source: Environment and Climate Change Canada.)

Seasonally, the national average temperature for the winter season (December 2020–February 2021) was 2.1°C above the 1991–2020 average, making it the fourth highest on record. The national average temperature for the winter season has increased by 3.5°C over the past 74 years. Winter anomalies of +3.0°C were recorded over eastern Quebec, eastern Nunavut, and most of the Atlantic provinces. As a result, the provinces of Nova Scotia and Prince Edward Island experienced their warmest winters on record. New Brunswick, Newfoundland and Labrador, and Quebec each experienced their second-warmest winter, while Nunavut experienced its third warmest. Below-average temperatures were observed in most of the Northwest Territories and in northern parts of the Yukon. Moreover, the month of February was among the 10 coldest on record for the Yukon, Alberta, and Saskatchewan. Some areas within those regions experienced a monthly temperature more than 5°C below average.

During spring (March–May), above-average temperatures were observed from interior British Columbia eastward to eastern and northeastern Canada, with departures above 2.0°C observed in northern Nunavut and parts of central Quebec. Below-average temperatures were recorded over northwestern Canada, with temperatures 2.0°C below average in central Yukon and eastern Northwest Territories. The national average temperature for spring 2021 was 0.6°C above average and the 14th highest in the 74-year record. Quebec and Newfoundland and Labrador both observed their seventh-warmest spring on record. The national average spring temperature has increased by 1.6°C over the past 74 years.

The national average temperature for summer (June–August) was 0.5°C above average, the fifth highest in the 74-year record. The central region of Nunavut and northern Quebec experienced summer temperatures that were 1.0°C below average. Southwestern Canada experienced summer anomalies above 1.5°C, with British Columbia having its warmest summer on record. Other provinces with temperatures among their 10 highest include Alberta and Saskatchewan (second highest); New Brunswick and Prince Edward Island (fifth highest); Newfoundland and Labrador, Nova Scotia and Yukon (sixth); Ontario (seventh); and Manitoba (ninth). The national average summer temperature has increased by 1.5°C over the past 74 years.

The national average temperature for autumn (September–November) was 2.2°C above average, the highest in the 74-year record. Most of Canada experienced temperatures at least 1.5°C above average, with Manitoba, parts of northwestern Ontario, and most of Nunavut, experiencing temperatures 2.5°C, 3.5°C, and 4.0°C above average, respectively. Only a small region between British Columbia and Yukon experienced temperatures below average. Quebec, New Brunswick, and Nunavut all experienced their highest autumn temperatures in the 74-year record. The national

average autumn temperature has increased by 1.8°C over the past 74 years. The temperature records presented above were based on adjusted and homogenized Canadian climate data.

(ii) Precipitation

Over the past decade, precipitation monitoring technology has evolved and Environment and Climate Change Canada (ECCC) and its partners implemented a transition from manual observations to the use of automatic precipitation gauges. Extensive data integration is required to link the current precipitation observations to the long-term historical manual observations. The update and reporting of historical adjusted precipitation trends and variations will be on temporary hiatus pending an extensive data reconciliation, and will be resumed thereafter. ECCC remains committed to providing credible climate data to inform adaptation decision making, while ensuring the necessary data reconciliation occurs as monitoring technology evolves.

(iii) Notable events and impacts

The record-breaking weather records in this section are based on non-homogenized station data. During the first two weeks of February, temperatures were 20°C below normal in Alberta and Saskatchewan, but 20°C above normal in southern Baffin Island. February temperatures from −35°C to −50°C were reported in parts of the Arctic and Prairies, resulting in the issuance of many extreme cold warnings. These extreme low temperatures broke minimum temperature records that dated back more than 50 years. The all-time daily minimum temperature for Edmonton International Airport reached −43.8°C, which is close to the all-time minimum of −43.9°C set in 1994 for the station.

A widespread and long-lasting dry period across western Canada from June to August 2021 was the worst on record. The southern regions between British Columbia and northwestern Ontario faced one of their driest summers in the 74-year record, with many places recording less than half of their normal rainfall in the growing season. Victoria Airport had its driest spring in 80 years. From 16 June to 6 August, Vancouver Airport recorded 53 consecutive days without a measurable rainfall event (0.2 mm or more)—the longest interval without rainfall in 35 years.

British Columbia was impacted by a historic seven atmospheric river-fueled storms in November 2021. Some of these large, wet systems featured unseasonably high temperatures (around 15°C) that were sufficient to melt snow at mid-elevations. The duration of some of these atmospheric river events ranged from two to three days instead of the usual 24 hours. According to station data, rainfall totals associated with the mid-November atmospheric river were 200–300 mm in 2.5 days, which was well above the climatological average for the entire month of November. During this storm, over 40 daily rainfall records were broken. Station data also show that rainfall totals along the south coast of British Columbia, during the last week of November, ranged from 100 mm to 350 mm, which turned valuable farm fields into wetlands. These November rain-flood storms resulted in the evacuation of almost 15,000 people from their homes and led to at least four fatalities. By the end of the month, autumn 2021 was the wettest on record for at least 10 sites across the south coast of British Columbia.

Sidebar 7.1: "Hell on Earth"—D. PHILLIPS

In the final week of June and first week of July 2021, a high-pressure ridge—an atmospheric juggernaut with incredible strength, height, scope, and persistence—built over western North America, sprawling from California to the Arctic Circle. Several factors conspired to strengthen the massive ridge and generate record blistering heat. The general circulation took a far-north arching route into northwestern Canada locking in the ridge (dome) in a slow-moving wavy pattern called an Omega Block. Clouds vanished under the dome, giving the sun an unobstructed line of sight, further warming the surface directly. As the atmospheric pressure increased under the dome, the descending air became denser and grew hotter. The air was made even hotter by the drought-stricken landscape. An exceptionally dry spring across the West led to a scarcity of soil moisture. Less soil moisture meant less solar energy being used to evaporate water, thus cooling, and instead directly heating the air and baking the ground. Timing was also crucial. The development of the ridge at the beginning of the Northern Hemisphere's summer solstice coincided with the year's highest sun angle and longest amount of daylight, further augmenting the sun's ability to heat the surface. Other dynamic factors significant in warming the air to record highs included the development of a thermal trough or "heat low" over California's Mojave Desert that spread to the California coast.

The widespread hot spell was particularly impactful as it occurred five to six weeks earlier than the typical warmest time of the year. Heat waves generally tend to be more dangerous when they occur early in the summer, before people have had time to fully acclimatize. Daytime highs were 15° to 25°C above normal with little reprieve at night as the temperature did not fall much below 20°C (Fig. SB7.1). The inferno-like heat shattered over 1000 daily maximum/minimum temperature records over 11 days, across all four Canadian western provinces and three northern territories, with over 100 records between 40° and 50°C. Lytton, a village 260 km northeast of Vancouver in British Columbia's Fraser Canyon, set a new Canadian record high temperature of 49.6°C on 28 June, nearly 24°C above normal. Two days earlier, on 26 June, Lytton first broke the previous national record of 45°C that had stood for 84 years in Saskatchewan. The new record fell again on 27 June, and again on 28 June (Fig. SB7.2). The next day, raging wildfires incinerated 90% of the village. The fire resulted in two deaths and the displacement of all 1200 residents. Lytton experienced a temperature higher than any location in the United States outside the Desert Southwest and higher than any temperature ever observed in Europe or South America. Indeed, it was the most extreme high temperature observed anywhere in the world above 45° latitude. Six other locations also observed a maximum temperature that exceeded the previous high Canadian heat record set in 1937.

At the peak of the heat wave on 28 June, Victoria (the capital city of British Columbia), with one of the most moderate climates in Canada, recorded a maximum temperature of 40°C, an all-time record for Victoria and a staggering 21°C above average. Kamloops (city in British Columbia) reported six days with maximum temperatures surpassing 40°C, significant because the city had never before observed 40°C in June. Among the thousands of temperature records broken across the Northwest was 39.9°C on 30 June in Fort Smith, Northwest Territories, the highest temperature ever recorded north of latitude 60°.

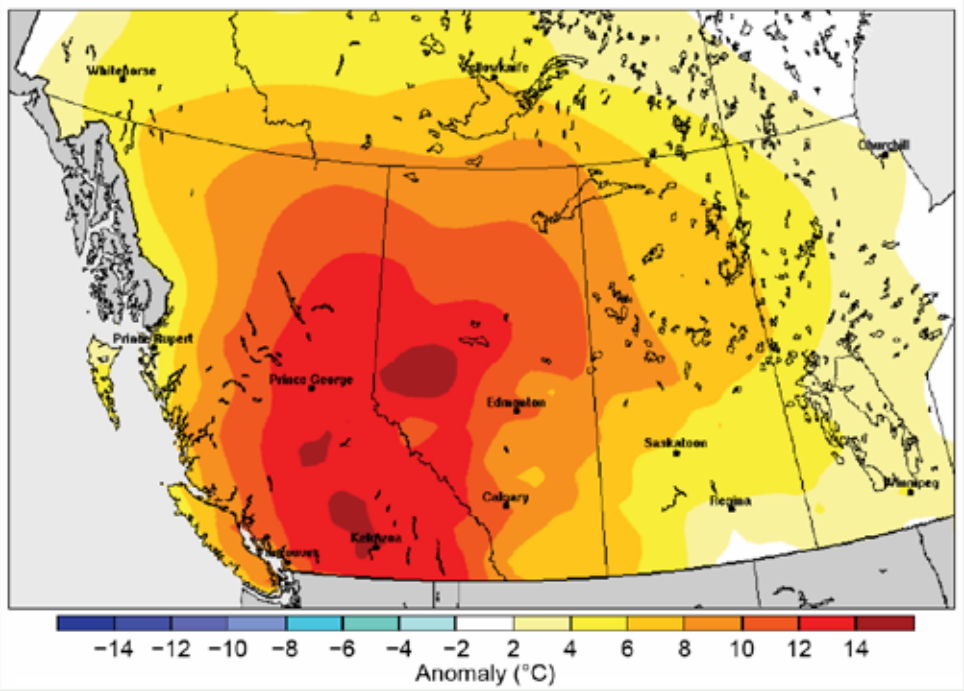

Fig. SB7.1. Surface air temperature departure (°C; 1981–2010 base period) for the period 28–30 June 2021. (Credit: National Laboratory, Central Region, Meteorological Service of Canada.)

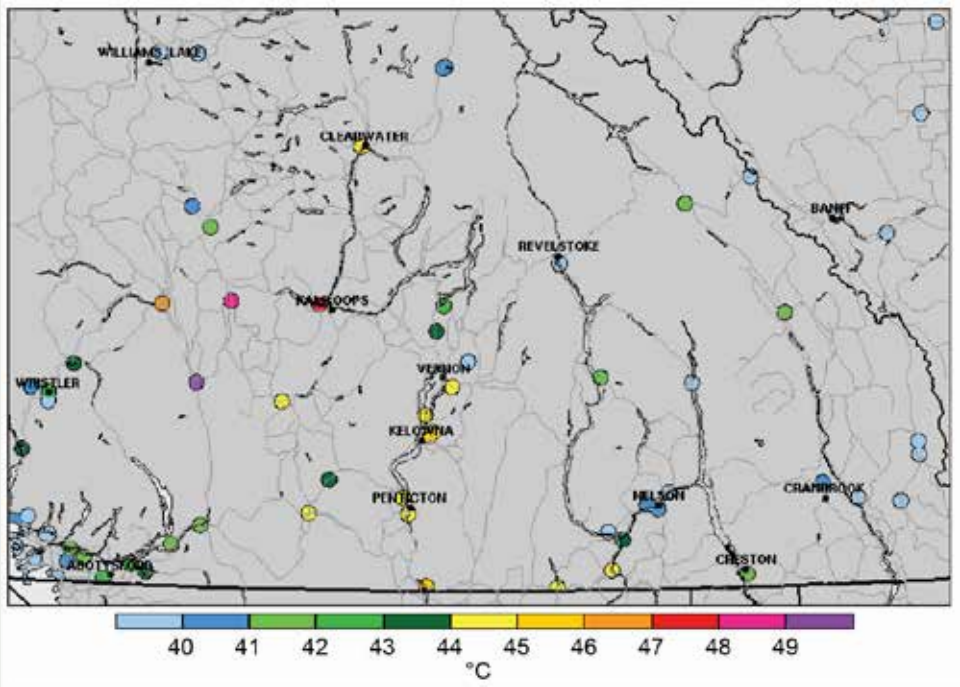

Fig. SB7.2. Highest daily maximum surface air temperature during the period of 23 June–4 July 2021. (Credit: National Laboratory, Central Region, Meteorological Service of Canada.)

The unbearable heat left millions of people overheated in western Canada. Power grids failed, asphalt melted, highways buckled, salmon cooked in hot river waters, and fruit baked on vines and trees. City workers turned on portable spray parks, added heavy misters, and converted hockey rinks into cooling centers. In Vancouver, Canada's third largest city, only 28% of households have any type of air conditioning, well below the national urban average of 60%. Officials kept shopping malls and theaters open longer to give residents additional air-conditioned comfort. Hospitals canceled outdoor COVID-19 testing and vaccination clinics or moved them indoors. Because it was almost impossible to safely go outside, people moved mattresses into basements—the coolest area of a home—to escape the heat, while others checked into air-conditioned hotels with their pets. Restaurants and bars closed after kitchen temperatures rose to potentially deadly levels. Some companies cut operating hours or suspended business, and outdoor workers opted to start before dawn and finish work at noon.

The hottest week in Canadian history was also one of the deadliest. Across Vancouver and Victoria, the historic heat wave was a contributing factor in the premature deaths of almost 600 people, with more than half occurring during 28–29 June. Alberta reported 185 heat-related fatalities. Two-thirds of the heatstroke victims were age 60 or older with underlying health conditions, socially isolated, or living alone in their homes. Emergency calls created a backlog for police and paramedic services. More than 650,000 farm animals perished. Poultry producers sprayed barn walls with cool water, but thousands of chickens were roasted alive. Dairy cows gave less milk, and raspberry crops withered on the stems. Countless wild animals and birds also perished in the record heat. The late June heat dome coincided with the lowest tides in years and some of the longest days. As a result, along the Pacific coast, a billion intertidal and marine organisms died, including mussels, clams, and fish, leaving shorelines with a foul odor for days.

2) UNITED STATES—K. Gleason, C. Fenimore, R. R. Heim Jr., and A. Smith

The annual average temperature for the contiguous United States (CONUS) in 2021 was 12.5°C, which was 0.7°C above the 1991–2020 average, the fourth highest in the 127-year record (Fig. 7.3a). Much of the northern Plains experienced temperature anomalies at least 1°C or more above average (Fig. 7.4a). Based on a linear regression of data from 1895 to 2021, the annual CONUS temperature over the 127-year record is increasing at an average rate of 0.09°C decade–1 (0.27°C decade^{-1} since 1970). Average precipitation totaled 774 mm, which is 97% of the 1991–2020 average (Fig. 7.3b). Although below average for 2021, the annual precipitation total has been increasing at an average rate of 5 mm decade^{-1} (4 mm decade^{-1} since 1970). The average annual temperature across Alaska in 2021 was 0.9°C below average. The annual temperature for Alaska over the 97-year record is increasing at an average rate of 0.17°C decade^{-1} (0.44°C decade^{-1} since 1970).

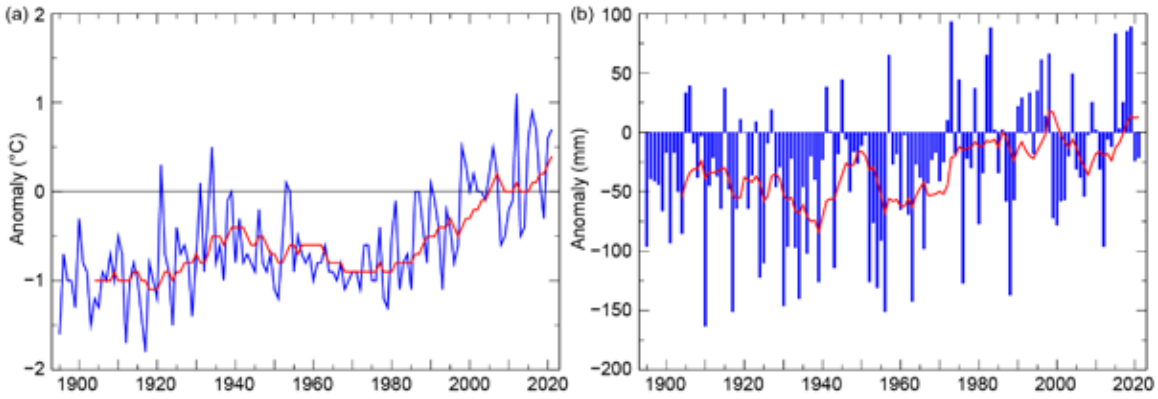

Fig. 7.3. Annual (a) mean temperature anomalies (°C) and (b) precipitation anomalies (mm) for the CONUS during 1895–2021 (1991–2020 base period). Red line is the lagged 10-year running mean. (Source: NOAA/NCEI.)

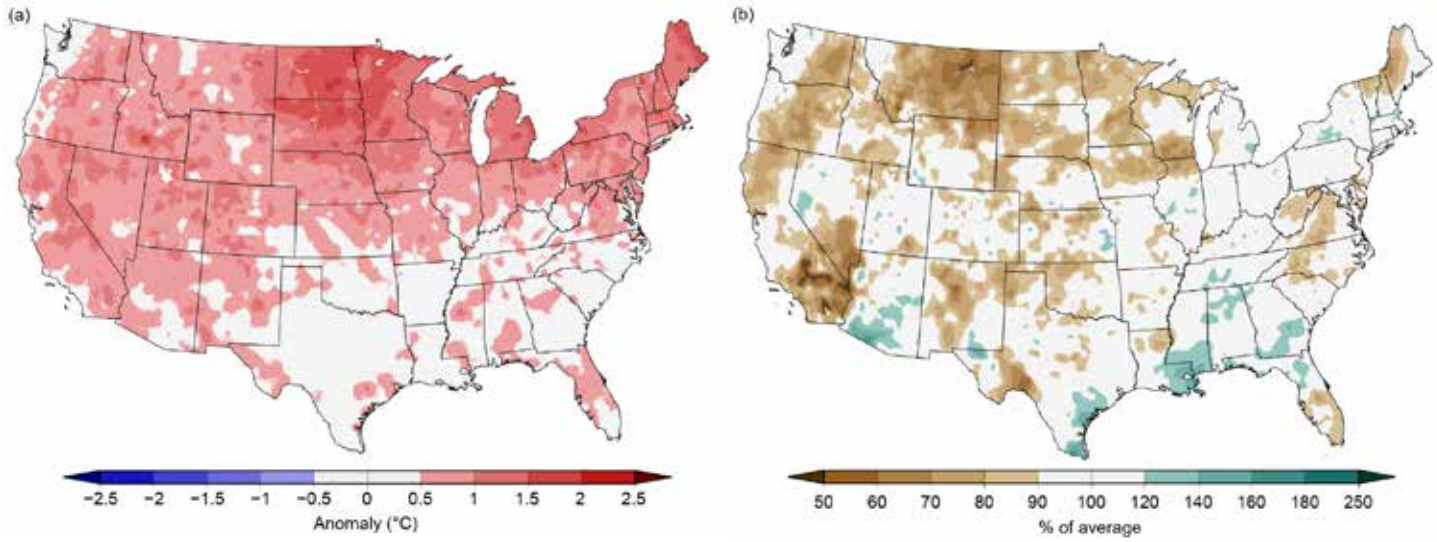

Fig. 7.4. Annual (a) average temperature anomalies (°C) and (b) total precipitation (% of average) in the CONUS for 2021 (1991–2020 base period). (Source: NOAA/NCEI.)

(i) Temperature

The winter (December–February) 2020/21 CONUS temperature was –0.2°C below average and was influenced by some of the coldest air to reach the central United States in more than 30 years, during a cold-air outbreak in February. Six states (Nebraska, Iowa, Kansas, Missouri, Oklahoma, and Arkansas) had their 10th coldest, or colder, February in the 1895–2021 record; the extreme cold, combined with icy conditions, caused widespread power outages across much of the South,

especially in Texas. Above-average warmth was present across portions of the West and from the northern Plains to the Northeast.

The CONUS spring (March–May) temperature was 0.2°C above average, with the highest anomalies occurring across parts of the Great Lakes. The summer (June–August) CONUS temperature was 0.9°C above average and virtually tied with 1936 as the warmest summer on record. California, Idaho, Nevada, Oregon, and Utah each observed their warmest summer on record.

The autumn (September–November) CONUS temperature was 1.2°C above average and was third highest on record. Temperatures were above average from the Southwest to the Great Lakes and into the Northeast, with the highest departures from average occurring across parts of the Plains. Colorado, Montana, and Wyoming each had their second-warmest autumn on record. The year ended with record warmth in the central and southern Plains and Mid- to Lower Mississippi Valley; 10 states in this region reported their warmest December, and an additional 21 states from the Rockies to the East Coast observed one of their five warmest Decembers on record. This widespread warmth resulted in the warmest December on record nationally, with a CONUS temperature anomaly of +3.7°C.

(ii) Precipitation

The weather across the contiguous United States in 2021 was driven by a pair of ridges that waxed and waned throughout the year. One ridge dominated across the North Pacific and extended over the western United States. The second ridge was situated across eastern Canada and the Northeast. This pattern brought warm, dry air to much of the West throughout the year, while an active storm track impacted the weather from the central Gulf Coast to the Great Lakes and into portions of the Northeast. In the East, Massachusetts had its ninth-wettest year on record while in the West, Montana had its ninth-driest year in 2021 (Fig. 7.4b).

Winter precipitation across the CONUS was 88% of average and ranked in the driest third of the historical record. Regionally, precipitation was above average along portions of the East Coast while dry conditions dominated much of the West, northern Plains, Great Lakes, and the South. Precipitation totals across North Dakota were third lowest on record for the season. Spring precipitation was 91% of average overall, but was above average from the central Plains to the Gulf Coast. Louisiana had its third-wettest spring on record. Precipitation was below average across much of the West, northern Plains, Great Lakes, and East Coast, resulting in the second-driest spring for Washington, Oregon, and Idaho.

Summer precipitation was 110% of average across the CONUS and ranked eighth wettest in the historical record. Above-average precipitation was observed along the southern Tier, from the Great Lakes to the Northeast, and in the summer monsoon region of the Southwest. Mississippi experienced its wettest summer on record. It was drier than average across much of the West, central Plains to Upper Mississippi Valley, and northern New England.

The autumn CONUS precipitation total was 93% of average. Drier-than-average conditions were present across parts of the northern Rockies, Southwest, South, western Great Lakes, and Mid Atlantic, while precipitation was above average across portions of the West, northern Plains, eastern Great Lakes, and Northeast.

The CONUS drought coverage remained significant and steady throughout much of 2021 with a minimum extent of 43.4% occurring on 25 May and maximum coverage of 55.5% on 7 December. Drought conditions remained intact across much of the West and northern Plains throughout the year. Excessive spring–summer dryness, coupled with record June–July (JJ) heat, rapidly intensified drought in the Pacific Northwest, and drought emerged in portions of the Lower Mississippi Valley and the Carolinas near the end of the year. Moderate (D1) to exceptional (D4) drought peaked at 94.6% of the western United States on 7 December; this is the largest drought coverage for this region in the 22-year U.S. Drought Monitor (USDM) history. Extreme (D3) and exceptional drought—the two worst categories—covered about 26.8% of the CONUS on 17 August

and marked the largest extent of D3 and D4 drought in USDM history. Moderate to exceptional drought extent grew rapidly in Hawaii during the summer months, peaking at 59% in July, and was most intense in November and early December, with extreme and exceptional drought covering nearly 11% of the islands.

(iii) Notable events and impacts

There were 20 weather and climate events across the United States during 2021 with losses each exceeding $1 billion U.S. dollars: eight severe weather events, four tropical cyclones (TC), three tornado outbreaks, two flooding events, one drought/heat wave, one winter storm/cold wave, and one wildfire event (Fig. 7.5). This was the second-highest number of events on record, with a total loss estimate of $145 billion U.S. dollars—the third highest cost on record. Hurricane Ida alone caused $75 billion U.S. dollars in damage and ranked among the five most costly U.S. hurricanes on record (since 1980; see section 4g2 and Sidebar 4.1 for more details on Ida). The total cost estimate of U.S. billion-dollar disasters over the last five years (2017–21) is in excess of $742 billion (U.S. dollars; NOAA 2022; www.ncei.noaa.gov/access/billions/).

One of these events was a cold wave during 10–19 February that produced temperature departures well below normal from Nebraska to Texas. The prolonged Arctic air caused widespread power outages in Texas, as well as other southern states, with multiple days of sustained below-freezing temperatures. At the peak of the outage, nearly 10 million people were without power. Additional impacts were frozen water pipes, which burst upon thawing, causing water damage to buildings. These extreme conditions caused or contributed to the deaths of more than 210 people in Texas alone. There were also snow and ice impacts across numerous states including Oklahoma, Arkansas, Missouri, Illinois, Kentucky, Tennessee, Louisiana, Mississippi, Colorado, Oregon, and Washington. This event is now the costliest U.S. winter storm event on record, at $24.5 billion U.S. dollars, more than doubling the inflation-adjusted cost of the 'Storm of the Century' that occurred in March 1993 (Smith 2022).

A historic heat wave developed across the Pacific Northwest from late-June into early-July, shattering numerous all-time high temperature records across the region. This prolonged heat dome was maximized over the states of Oregon and Washington and extended well into Canada (Sidebar 7.1). Hundreds of direct and indirect heat-related fatalities were reported across Oregon and Washington.

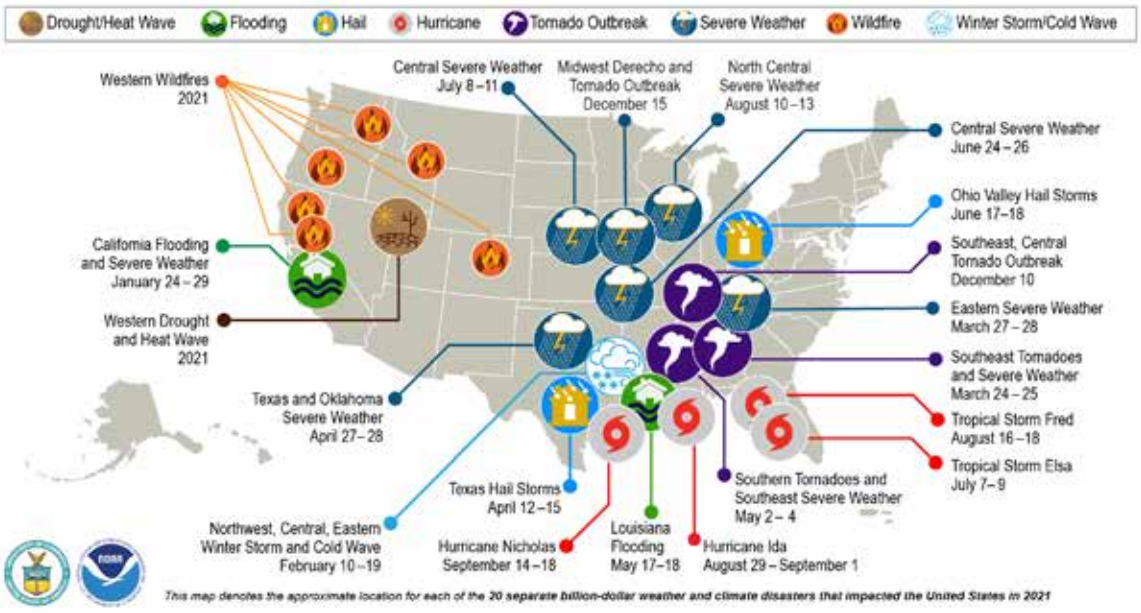

Fig. 7.5. Map depicting date, approximate location, and type of the 20 weather and climate disasters in the United States in 2021, with losses for each exceeding $1 billion (U.S. dollars). (Source: NOAA/NCEI.)

Preliminary reports indicate that there were 1376 tornadoes across the CONUS during 2021, above the 1991–2010 annual average of 1251 tornadoes. A tornado event on 10–11 December in the Mid-Mississippi River Valley spawned two EF-4 (on the Enhanced Fujita Scale) tornadoes, including the longest-track December tornado on record (nearly 266 km across Tennessee and Kentucky) and the deadliest December outbreak on record with at least 90 fatalities reported. Another significant outbreak occurred on 15 December and produced 94 tornadoes from Nebraska to Wisconsin—the most tornadoes confirmed on any day during 2021.

3) MEXICO—R. Pascual Ramírez and A. E. Martínez

The year 2021 was Mexico's fourth-warmest year on record and marked the nation's 11th consecutive year with above-normal temperatures. The 2021 annual precipitation was slightly above normal for the nation; however, precipitation varied across the region, with several regions across the southwest experiencing above-normal conditions, while northern states had below-normal annual precipitation.

(i) Temperature

The 2021 national mean temperature was 0.8°C above the 1991–2020 average (Fig. 7.6a) and the fourth highest on record. Only the years of 2017, 2019, and 2020 were warmer. Every month in 2021, with the exception of January, was warmer than average. December 2021 was Mexico's warmest December on record. While no state reported their warmest year on record in 2021, 12 states (of 32) observed an annual average temperature that ranked among their five highest.

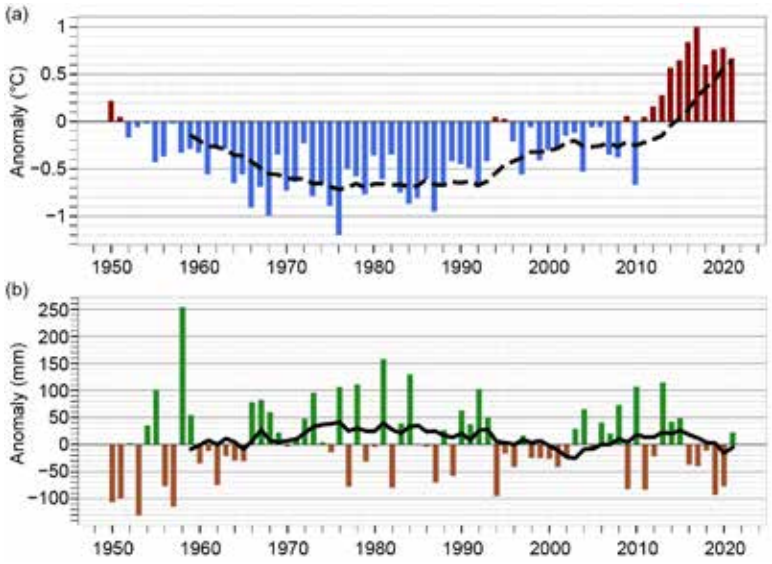

Fig. 7.6. Annual (a) temperature (°C) and (b) precipitation (mm) anomalies for Mexico for the period 1950–2021 (1991–2020 base period). Black solid lines represent a 10-year running mean. (Source: National Meteorological Service of Mexico.)

Regionally, above-normal annual temperatures were observed across the north-central region, along the Pacific coast, and over the Yucatan Peninsula, with the largest positive anomalies (> +2°C) in Coahuila in northern Mexico. Only small regions in the south and along the Sierra Madre Occidental had below-normal annual temperatures, while near-normal temperatures were present across the northwest and parts of states along the Gulf of Mexico (Fig. 7.7a).

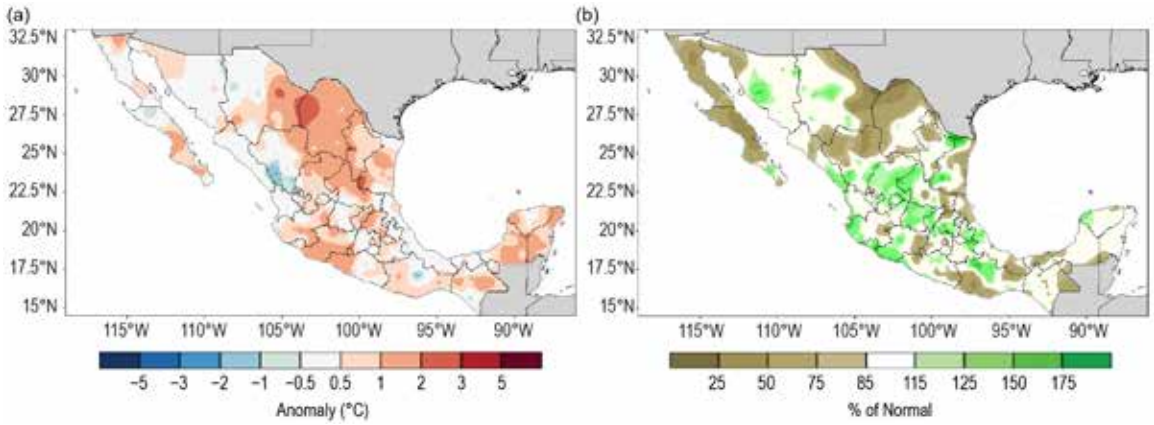

Fig. 7.7. 2021 annual mean (a) temperature (°C) and (b) precipitation (% of average) anomalies over Mexico (1991–2020 base period). (Source: National Meteorological Service of Mexico.)

(ii) Precipitation

Precipitation in 2021 varied across the country (Fig. 7.7b). Below-normal annual precipitation was observed across parts of northern and northwestern Mexico, while above-normal conditions were present across central Mexico. Averaged as a whole, Mexico had its wettest year since 2015 with 769.5 mm, which is 103.7% of normal. On a state basis, Colima, located in southwestern Mexico, had its wettest year on record, while five other states in the same region (Morelos, Aguascalientes, Jalisco, Nayarit, and Sinaloa) had an annual precipitation total that ranked among their 10 highest on record. Meanwhile, several states (San Luis Potosí, Tabasco, and Baja California) reported annual rainfall totals that ranked among their nine driest years on record. This year marked the second consecutive year with below-average rainfall across the northern states.

The hurricane season typically provides a considerable amount of precipitation for Mexico; however, despite an active 2021 hurricane season in the Atlantic, only two tropical cyclones (Grace and Nicholas) in this basin were close to or made landfall in Mexico from the Caribbean or Gulf of Mexico coast (1991–2020 average is 2.7), and thus brought significant localized precipitation. In the Pacific basin, five hurricanes (Enrique, Nora, Olaf, Pamela, and Rick) and one tropical storm (Dolores) brought significant rainfall to the west coast of the country, promoting an above-average rainfall pattern (Fig. 7.7b).

Climatologically, September is Mexico's rainiest month, typically contributing the largest amount of precipitation to the country; however, in 2021, August was the rainiest month, mainly due to Hurricanes Nora and Grace, which brought significant precipitation over the Pacific coast and into eastern Mexico. September had below-normal precipitation, mainly due to the lack of cyclonic activity during the month. Climatologically, March is the driest month of the year with an average of 13.1 mm, just 1.8% of annual precipitation; however, in 2021, February was Mexico's driest month with only 7.9 mm or 1% of the annual precipitation for 2021.

(iii) Notable events and impacts

During the first few months of 2021, the effects of winter storms were felt mainly in northern Mexico. The interaction of a frontal system and a winter storm on 14–15 February brought snowfall to the states of Sonora, Chihuahua, and Coahuila. Snowfall and colder-than-normal conditions caused power outages and blackouts in Chihuahua, Coahuila, Nuevo Leon, and Tamaulipas. The lowest temperatures (–7°C to –14°C) were recorded between 15 and 20 February in northeastern Mexico. This event was part of a cold wave that also affected eastern Canada and the southeastern United States.

During the first half of the year, severe to extreme drought, and in some cases, exceptional drought conditions dominated some areas of northwest Mexico, according to Mexico's Drought Monitor. Over 7330 fires were reported during 2021, with 7161 of them occurring in the first six months; a wet second half of the year helped alleviate the fire activity. Overall, 2021 had the third-highest surface area burned, behind 2011 and 2017, according to data since 2011.

c. Central America and the Caribbean— A. Sánchez-Lugo, Ed.

1) CENTRAL AMERICA—J. A. Amador, H. G. Hidalgo, E. J. Alfaro, B. Calderón, and N. Mora

For this region, nine stations from five countries were analyzed (see Fig. 7.8 for data and station list). The station distribution is representative of the relevant seasonal and intraseasonal regimes of precipitation (Amador 1998; Magaña et al. 1999; Amador et al. 2016a,b), wind (Amador 2008), and temperature (Hidalgo et al. 2019) on the Caribbean and Pacific slopes of Central America (CA). Precipitation and temperature records for the stations analyzed and regional winds were provided either by CA National Weather Services (CA-NWS), NOAA, or the University of Costa Rica. Anomalies are reported using a 1991–2020 base period and were calculated from CA-NWS data. The methodologies used for all variables can be found in Amador et al. (2011).

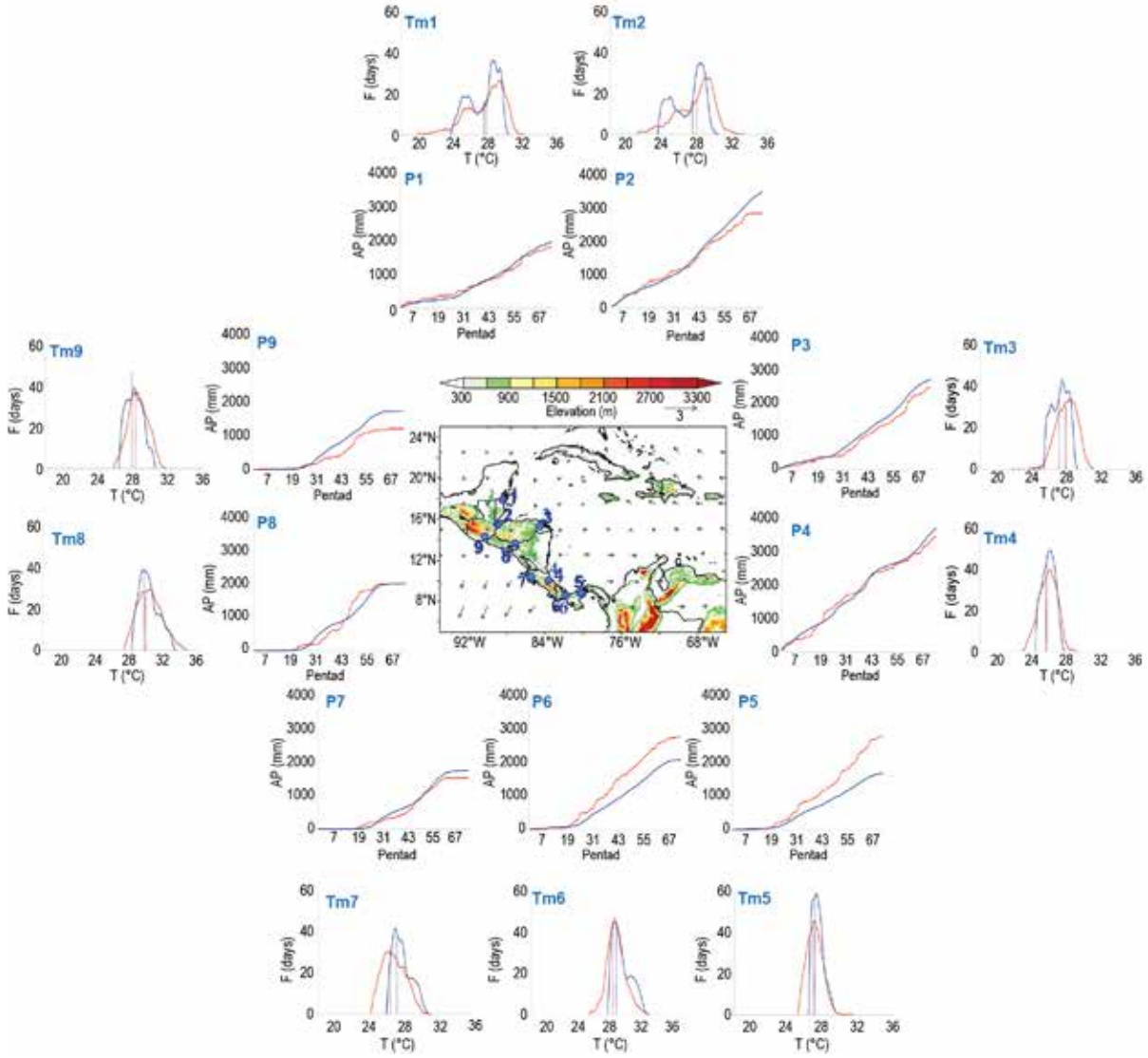

Fig. 7.8. Mean surface temperature (Tm; °C) frequency (F; days) and accumulated pentad precipitation (P; mm) time series are presented for nine stations (blue dots) in Central America: (1) Philip Goldson International Airport, Belize; (2) Puerto Barrios, Guatemala; (3) Puerto Lempira, Honduras; (4) Puerto Limón, Costa Rica; (5) Tocumen International Airport, Panamá; (6) David, Panamá; (7) Liberia, Costa Rica; (8) Choluteca, Honduras; and (9) Puerto San José, Guatemala. The blue solid line represents the 1991–2020 average values and the red solid line shows 2021 values. Vertical dashed lines show the mean temperature for 2021 (red) and the 1991–2020 period (blue). Vectors indicate July wind anomalies at 925 hPa (1991–2020 base period). Shading depicts regional elevation (m). (Sources: NOAA/NCEI and CA-NWS.)

(i) Temperature

The mean temperature (Tm, °C) pentad frequency distributions in 2021, as well as the climatology, for all stations analyzed are shown in Fig. 7.8. Most stations across Central America had near- to above-normal annual temperatures. Only the stations of David, Panamá (Tm6), Tocumen International Airport, Panamá (Tm5), and Liberia, Costa Rica (Tm7), had significant below-normal annual temperature anomalies: −0.6°C, −0.2°C and −0.9°C, respectively. Philip Goldson International Airport, Belize (Tm1), Puerto Limón, Costa Rica (Tm4), and Choluteca, Honduras (Tm8), had near-normal annual temperatures. Meanwhile, Puerto Barrios, Guatemala (Tm2), San Jose, Guatemala (Tm9), and Lempira, Honduras (Tm3), had above-normal annual temperature anomalies, ranging between +0.4°C and +0.8°C. The two northernmost stations, Philip Goldson International Airport, Belize (Tm1), and Puerto Barrios, Guatemala (Tm2), exhibited a bimodal temperature distribution over the course of the seasonal cycle during 1991–2020. An explanation of that distribution is beyond the scope of this report, but it is suggestive of a different climate when compared with the previous base period 1981–2010, as in last year´s climate report. The two-peak

distribution in Tm is also visible in both stations in 2021, a feature observed for the first time at those stations in 2017 (Amador et al. 2018). A comparison between the climatology and the 2021 pentad distributions show that five of the nine stations presented different distributions, except Limón (Tm4), Tocumen (Tm5), Choluteca (Tm8), and San Jose (Tm9), indicating that the Tm for around half the stations was distributed significantly differently from the climatology in 2021.

(ii) Precipitation

The accumulated pentad precipitation (P, mm) time series for the nine stations in Central America are presented in Fig. 7.8. Most stations had a drier-than-normal year, with the exceptions of Tocumen International Airport (P5) and David (P6), both located in Panama, which had wetter-than-normal conditions throughout most of the year. Choluteca, Honduras, had a near-normal annual precipitation total (P8). Belize (P1), Puerto Barrios (P2), Limon (P4), David (P6), Liberia (P7), Choluteca (P8), and San Jose (P9) showed different 2021 distributions from that of the base period, while the remainder of the stations showed no significant differences from climatology. San Jose (P9) was drier-than-normal for the year, while the rest of the stations showed no significant change in the annual average. Note that Liberia (P7) and San José (P9) had a relatively prolonged mid-summer drought-like period (Magaña et al. 1999), a regional precipitation characteristic that was also observed, but to a lesser extent, in Choluteca (P8).

Despite 2021 being a prevailing La Niña year (see section 4b), low-level circulation anomalies in the westernmost Caribbean Sea and Pacific regions showed opposite signs (positive and negative deviations, respectively) from the 1991–2020 average winds related to the trade system during July (vectors in Fig. 7.8). This wind pattern that has been associated with the precipitation distribution during boreal summer did not follow the normal behavior (Amador 2008). During a typical La Niña event, below-normal winds dominate both basins, implying below-normal precipitation along the Caribbean slopes as in Puerto Barrios, Puerto Lempira, and Limón, and above-normal precipitation on the Pacific slopes, a feature not observed in Liberia and San José. This is the second consecutive year with an anomalously active hurricane season in both basins, which may be responsible for those anomalies.

(iii) Notable events and impacts

Tropical cyclone activity during 2021 was considered near-normal in the Caribbean basin, where there were four named systems: Hurricane Elsa (2–5 July), Tropical Storm Fred (11–13 August), Hurricane Grace (15–19 August), and Hurricane Ida (26–27 August). The strongest storm in the basin was Hurricane Elsa (Category 1), and no storms made landfall in Central America. In 2021, no systems formed in the eastern tropical Pacific that impacted Central America. During the rainy season, 59 fatalities were reported due to hydro-meteorological events and 19 deaths by lightning strikes.

2) CARIBBEAN—T. S. Stephenson, M. A. Taylor, A. R. Trotman, C. Charlton, T. Allen, L. A. Clarke, J. M. Spence, J. D. Campbell, K. Kerr, and C. J. Van Meerbeeck

The year 2021 was generally characterized by above-normal mean temperatures and below-normal rainfall. The annual average temperature was 0.34°C above the 1991–2020 average, marking the fifth-warmest year since the start of the record in 1891 (Fig. 7.9a). Every year since 2014 (except 2018) ranks among the 10 warmest years on record. The annual temperatures since 1891 have been increasing at an average rate of 0.11°C decade^{-1} (0.22°C decade^{-1} since 1970). Positive anomalies were highest over the northwestern Caribbean (Jamaica, Cuba, and the Bahamas) and over Trinidad, Barbados, and the Windward Islands (Fig. 7.10a). The San Juan Metro Area in Puerto Rico observed its ninth warmest year (0.4°C above average) since its records commenced in 1899. The average annual rainfall anomaly for the Caribbean was −0.27 mm day^{-1}, marking the 18th-driest year since the record began in 1921 (Figure 7.9b). Annual rainfall total is decreasing at

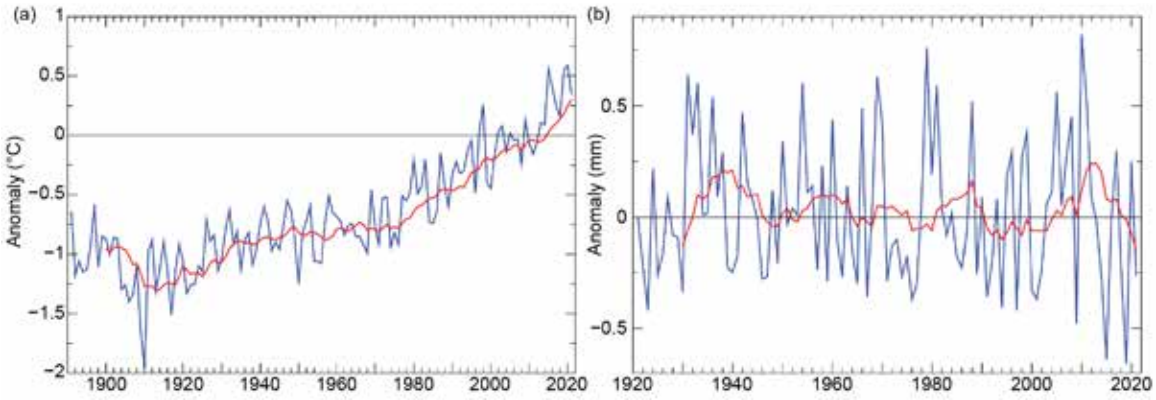

Fig. 7.9. Annual average (a) 2-m temperature anomalies (°C) and (b) rainfall anomalies (mm day^{-1}) for the Caribbean (9°–27°N, 58°–90°W) for the periods 1891–2021 and 1921–2021, respectively, relative to the 1991–2020 average. The red line is the 10-year running mean. (Sources: NCDC v3 and GPCC v2020 from the KNMI Climate Explorer.)

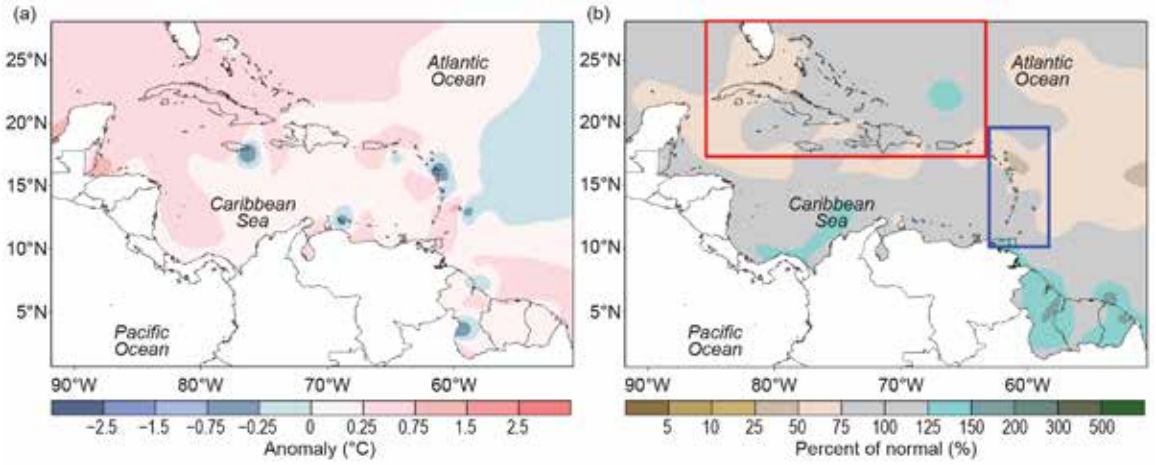

Fig. 7.10. Annual (a) mean temperature anomalies (°C) and (b) total precipitation anomalies (% of normal) relative to 1991–2020. (Source: Caribbean Climate Outlook Forum [CariCOF] and the Caribbean Institute for Meteorology and Hydrology.)

a rate of approximately –1.9 mm decade^{-1} (–1.1 mm decade^{-1} since 1970), even as strong multi-year and year-to-year variations are observed.

(i) Temperature

The December–February temperatures were above normal over much of the region, with negative anomalies in the northwest. The season's 2m-average temperature anomaly was 0.32°C above normal and was the fifth highest since records began in 1881 (Fig. 7.9a); this follows 2020, which was the warmest December–February period on record (0.59°C above normal). Each year since 2014 ranks among the 10 highest December–February average temperatures. Crown Point, Tobago, recorded its highest mean maximum temperature (0.7°C above average) and mean temperature (also 0.7°C above average) for the December–February period since its record began in 1973.

During spring (March–May) and summer (June–August), the region-wide temperature anomalies changed to positive over the north (Cuba, The Bahamas, Jamaica, and Haiti) and negative over the south. In summer, above-normal temperatures occurred over eastern Cuba, eastern Jamaica, and the northern Bahamas. The below-average temperatures in the south were interspersed with some above-normal temperatures over the eastern Caribbean. Anomalies for March–May were 0.18°C above average, while June–August temperatures were 0.11°C above normal. Positive anomalies covered most of the region in September–November.

(ii) Precipitation

In 2021, below-normal rainfall was observed over most of the Caribbean (Fig. 7.10b). Exceptionally dry conditions were observed in Martinique, Antigua, southeastern Dominican Republic, eastern Jamaica, western Cuba, and the northern Bahamas. Four stations recorded their driest year in the last 51 years: VC Bird Airport, Antigua (47% of normal); La Derisade, Guadeloupe (47% of normal); La Trinité, Martinique (50%); and Le Vauclin, Martinique (52%). Henry Rohlsen Airport, St. Croix, recorded its driest year since the start of its record in 1964 (60% of normal). Cyril King Airport, St. Thomas had its sixth driest year in its 50-year record (70% of normal).

The region generally experienced below-normal rainfall for December–February. In spring, some locations observed normal to above-normal rainfall, likely due to La Niña conditions that facilitate wetter conditions in the southeastern Caribbean during the dry season of November–April (Taylor et al. 2002). Very dry conditions were recorded for Antigua, parts of the Bahamas, northern Cuba, and eastern Guadeloupe while very wet conditions were observed for Grenada and Trinidad. Cabrera in the Dominican Republic recorded its lowest rainfall (40% of normal) for December–February since 1971. In March–May, Caroni, Trinidad, recorded its highest spring rainfall total (279% of normal) since 1971. The expansion of normal to above-normal rainfall conditions was notable in the northern Caribbean during summer when the El Niño-Southern Oscillation (ENSO) was neutral (see section 4b for details). Piarco, Trinidad, recorded its second highest summer rainfall (891.1 mm) since 1998. Overall, the annual rainfall at Piarco was 124% of normal and was the fourth wettest year since 1946. Below-normal rainfall returned over the region in September–November. Tobago experienced its driest November (23% of normal) since 1969.

(iii) Notable events and impacts

Hurricane Elsa impacted St. Lucia, Barbados, St. Vincent and the Grenadines, Haiti, and Jamaica during 2–6 July. In St. Lucia, strong winds damaged buildings and telecommunications along with water infrastructure. Agriculture and fisheries were also impacted. Elsa was the first hurricane to impact Barbados in 66 years, since Hurricane Janet. Impacts to Barbados, Haiti, and Jamaica included power outages, displaced roofs, fallen trees, flooding, and damage to agriculture.

Trinidad was impacted by two tropical waves and the Intertropical Convergence Zone, which produced intense rainfall and thunderstorm activity primarily during 17–20 August. The adverse weather resulted in overflowing riverbanks, impassable roads, and wide-scale flooding. Other significant rain events were recorded on 8, 12, 14, and 15 August, which together yielded the seventh-wettest August (386.8 mm, 151% of average) in the 76-year record.

Hurricane Grace impacted Haiti on 16–17 August, causing flooding in more than 600 houses. Grace also impacted Jamaica on 17–18 August as a tropical storm, causing silt and debris to impact several communities and about 200 roads. Initial damage estimates were $1.1 million (U.S. dollars). Jamaica and Cuba were impacted by Tropical Storm Ida on 26–28 August. Impacts included flooding, landslides and fallen trees affecting roads and infrastructure.

Sidebar 7.2: **Rainfall extremes across Central America**—S. Fuhrman, C. Recalde, and W. M. Thiaw

In Guatemala, flooding and landslides affected many departments at various times in 2021. During mid-January, floods were reported in the municipalities of Las Cruces, Sayaxché, and San Luis in Guatemala's Petén Department. Severe weather during 21–24 May affected more than 10,000 people in the departments of Baja Verapaz, Izabal, Petén, Quetzaltenango, San Marcos, Santa Rosa, Suchitepéquez, and Sololá. Flash floods, landslides, coastal flooding, and high winds all contributed to damage of more than 200 homes. In mid-June, flash floods caused three fatalities when the Quibá River overflowed in Sololá and severely damaged 30 homes. Heavy downpours during the week of 25 July triggered flooding and landslides, resulting in many people affected in the departments of Alta Verapaz, Izabal, and Zacapa. According to Crisis24, a global risk management organization, as of 26 July, more than 632,000 people were affected by the floods; eight people died, and at least 5600 people were evacuated. The eruption of the Pacaya Volcano near Guatemala City on 4 August sent steam and gas plumes into the atmosphere as high as 1 km above the summit and drifted as far as 3 km in multiple directions during 5–10 August, according to the Smithsonian/US Geological Survey Weekly Volcanic Activity Report, and exacerbated the disaster in this region. Heavy rains also caused problems in Guatemala in mid-September, when floods and landslides were reported in areas of San Marcos, Sololá, Guatemala, and Santa Rosa. The floods destroyed two bridges in Tajumulco, San Marcos, and other roads in San Antonio Palopó, San Lucas Tolimán, and Santa Catarina Palopó municipalities in Sololá and also damaged over 70 homes in Barberena, Santa Rosa. Landslides damaged four roads and at least four homes in various areas. In December, despite general drying conditions, localized heavy rain caused flash floods in some parts of Guatemala that included Izabal Department during the week of 16–22 December. Floods were also reported in the Petén department within the municipalities of Dolores and Sayaxché during the final week of the month.

Early in the year, the northern Honduran coast was plagued by flooding during the weekend of 16–17 January. Rainfall in excess of 100 mm led to rising rivers, including Lancetilla, Ruth García, and Highland Creek, in Atlántida and Tela Departments. During the summer, heavy rainfall from 22 to 29 July caused destructive and deadly flooding in Costa Rica and Panama. Several rivers in Costa Rica overflowed their banks. According to Costa Rica's emergency management department, Comisión Nacional de Emergencias, over 2700 incidents, including floods, landslides, and road collapses, were reported in 36 of the country's 82 cantons, along with at least two fatalities. In Panama, rivers, including the Sixaola and its tributaries, also overflowed their banks. Twenty people had to be rescued, and over 5000 homes were damaged, according to news sources. Five landslides were also reported. Panama also reported heavy rains on 21 November, which triggered flash floods in Las Cuevas de Bayano, located 50 km east of Panama City. According to Panama's Sistema Nacional de Protección, there were at least two fatalities and 13 injuries.

Dry conditions were also observed during 2021 across different countries in Central America. Rainfall deficits in the region were observed since May; in Nicaragua and Honduras, deficits of more than 100 mm degraded vegetation health and impacted Primera season (April–June) cropping activities. Low Standardized Precipitation Index (SPI) values for the 2-month period May–June indicate a significant moisture deficit in these areas (Fig. SB7.3). Following already dry conditions in September, very low monthly rainfall in October caused abnormal dryness to rapidly expand through the area and drought conditions emerged.

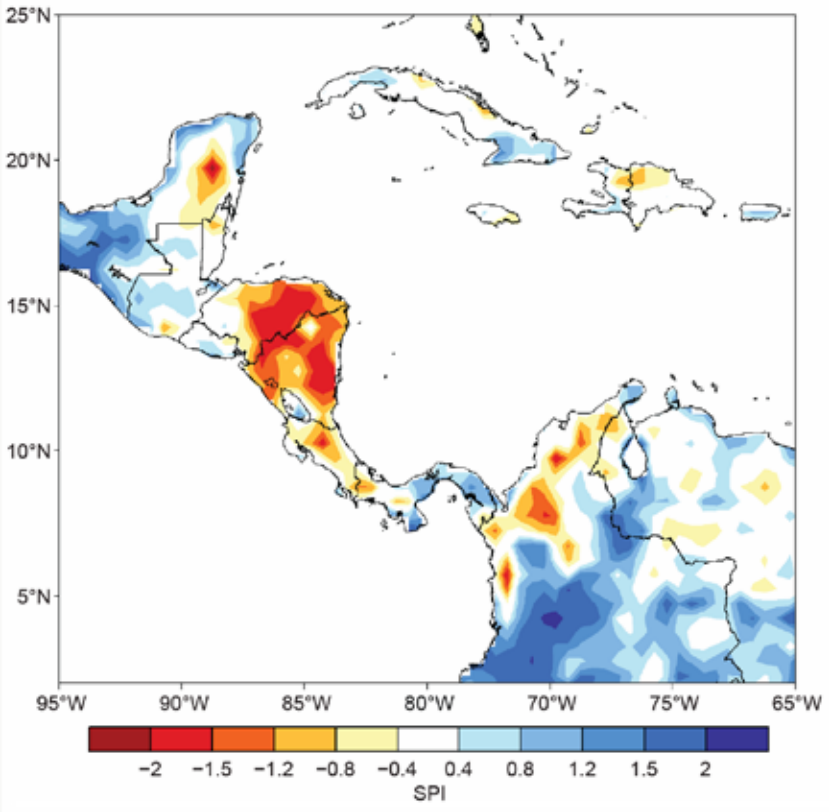

Fig. SB7.3. Standardized Precipitation Index (SPI) for May–June 2021 (1999–2020 base period). (Source: CMORPH, NCEP.)

Rainfall deficits during the September–October period increased substantially through Honduras, Nicaragua, Guatemala, and Belize. Deficits widely exceeded 100 mm and locally were more than 300 mm. Moisture deficits combined with periods of heat negatively impacted growing conditions. In December, wildfires were of particular concern. The onset of the dry season after a largely failed Postrera rainfall season (August–December) created ground conditions that were highly favorable for fire activity. Many fires were reported throughout 10 departments in Guatemala. Over 39 hectares were consumed, according to the country's government. Maps of 'hot spots' registered by MODIS-VIRS satellite-based infrared sensor show that fire activity was not only observed in Guatemala over the course of December, but also across other Central American countries with abnormally dry ground conditions, including El Salvador, Honduras, northern Belize, and northern Nicaragua.

d. South America—A. Sánchez-Lugo, Ed.

La Niña was present in the tropical Pacific Ocean throughout much of 2021, strengthening southerly winds, which were present in the Pacific coastal region of northern South America throughout the year. Additionally, the positive pressure pattern, as measured by the Southern Oscillation Index (SOI), which had high values (+20) at the start of the year, helped keep the Intertropical Convergence Zone (ITCZ) farther north than normal during the first three months of the year. Between April and June, the SOI returned to near-normal values; however, by June it again reached thresholds characteristic of a La Niña event and remained throughout most of the year, which added to the strengthening of the trade winds and the negative sea surface temperature anomalies (SSTA) in the southeast Pacific, decreasing the convective activity of the ITCZ.

Meanwhile, via meridional winds from the north, humidity from the Caribbean entered the region, advancing through northeastern South America and contributing to increased rainfall in some countries, as well as in part of the Andean region. This led to the development of some extreme events across the region.

1) NORTHERN SOUTH AMERICA—J. Nieto and F. Costa

The northern South America region includes Colombia, Ecuador, French Guiana, Guyana, Suriname, and Venezuela.

(i) Temperature

The 2021 mean temperature for northern South America was 0.30°C above normal and the sixth-highest on record. Venezuela had the highest annual national temperature anomaly for the region at +0.45°C, while Ecuador had the lowest at +0.03°C. The highest temperature anomaly observed throughout the year was recorded in November in the Caribbean region of Colombia with a temperature departure of +4.70°C, while the lowest was observed at Margarita Island in Venezuela, which had an anomaly of –3.74°C in September.

Minimum annual temperatures for 2021 were below normal across much of central and northern regions of Venezuela (up to –0.75°C) and across much of Ecuador, predominantly in the south (up to –1°C). Above-normal minimum annual temperatures were observed in French Guiana, Suriname, and the southern half of Guyana (up to +1°C; Fig. 7.11a), as well as in southern Venezuela and southern and Caribbean regions of Colombia. The below-normal minimum temperature anomalies in Ecuador during the year may be associated with the influence of the La Niña in the tropical Pacific Ocean throughout most of the year.

The 2021 maximum annual temperatures were near- to above normal across the region, with the highest temperature departures in Venezuela, especially in the northern region (up to +1.5°C).

Mean annual temperatures were slightly above normal across much of Venezuela, French Guiana, Suriname, and Guyana (+0.50°C). Above-normal temperatures were also observed in the Caribbean (up to +0.75°C), east-central region of Colombia, and eastern Ecuador (+0.50°C; Fig. 7.11b).

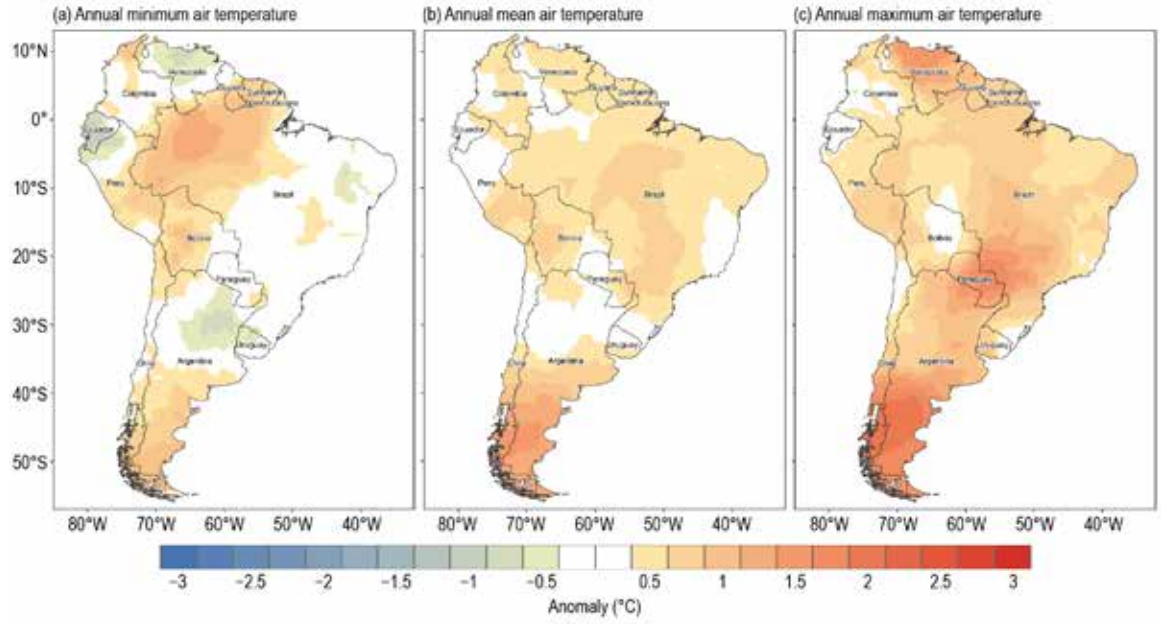

Fig. 7.11. The 2021 (a) annual minimum, (b) mean, and (c) maximum temperature anomalies (°C; 1981–2010 base period). (Source: Data from NMHSs of Argentina, Bolivia, Brazil, Chile, Colombia, Ecuador, Paraguay, Peru, Uruguay, and Venezuela; processed by CIIFEN.)

(ii) Precipitation

In 2021, northern South America had predominantly near- to above-normal precipitation. Below-normal precipitation was only observed in a small area in central Colombia and the Colombian Caribbean region (up to −40%) and in a small area along the central coast of Ecuador (–20%). Above-normal precipitation was observed across much of French Guiana, Suriname, and Guyana (up to +30%), in southeastern Venezuela (up to +30%), most of the Pacific and east-central region of Colombia (up to +50%), in the northern Andes (up to +30%), and northern and southern parts of Ecuador (up to +50%; Fig. 7.12). The average precipitation total for the region was 3.9% above normal.

(iii) Notable events and impacts

During 2021, the most notable hydrometeorological events across northern South America were related to intense rainfall. In Guayaquil, in the southern coastal region of Ecuador, the first accumulated rain of 2021 was 41% above average for January. Thunderstorms brought moderate to heavy rainfall to the region, prompting floods that damaged many vehicles.

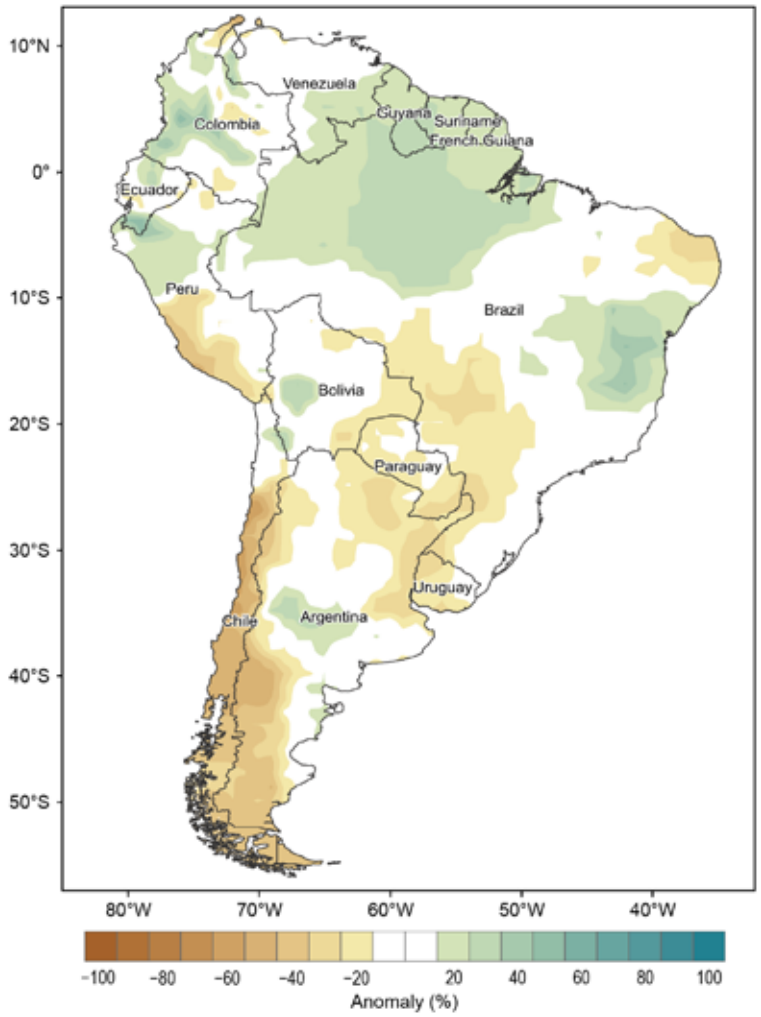

Fig. 7.12. The 2021 annual precipitation anomalies (%; 1981–2010 base period). (Source: Data from NMHSs of Argentina, Bolivia, Brazil, Chile, Colombia, Ecuador, Paraguay, Peru, Uruguay, and Venezuela; processed by CIIFEN.)

Torrential rain fell across Suriname during April, causing floods across the nation's 10 districts. Roads were flooded in several locations, making these areas inaccessible. The flood situation worsened between the Nickerie River and Wageningen when the dam located in this region broke. Gas stations, supermarkets, and houses were flooded with water up to one meter, and in some regions access to electricity was limited. Heavy rains were also recorded in May, causing floods to last for weeks in regions and isolating some communities.

Also, in May, intense rainfall caused rivers to overflow in the city of Cuenca, in the southern Andean region of Ecuador, causing widespread damage. The Tarqui River observed its worst flood in the last 11 years. Sixty homes were affected, as well as pastures and pedestrian bridges, and water system pipes were damaged. In July, heavy rains were also observed in the provinces of Pastaza, Napo, and Tungurahua in the central and southern highlands and in the Amazon region of Ecuador. Some regions of the Amazon, which typically receive close to 300 mm of precipitation during July, observed 77 mm of rain during one 24-hour period.

During 24 May to 10 June, heavy rain fell across Guyana, with precipitation totals reaching 510 mm in some regions. The intense rainfall resulted in the overflow of rivers and triggered severe floods across Region Nine in southern Guyana, affecting over 15,000 people. The floods wreaked havoc across the region, damaging roads, infrastructure, and about 16,000 hectares of crops. About 30,000 families were affected by the floods.

On 12 July in the city of Guayana, in Venezuela, there was a 3-hour episode of intense rains with strong winds, which caused widespread damage to the region. More than 60 trees collapsed, there was an extended interruption of electricity, internet, and water services, as well as collapsed roofs and damage to other infrastructure.

In August, intense rain events were again recorded in some regions of Venezuela, including the Mérida region, where floods and landslides killed 20 people and led the government to declare a state of emergency in this and other states. During this event, close to 55,000 people were affected throughout the country.

Colombia's department of Putumayo, bordering Ecuador, had intense rains during July that affected more than 10,000 families in 12 municipalities, including Mocoa, Putumayo's capital. This rain event destroyed crops, domestic animals disappeared, primary and secondary roads were blocked, municipalities were left without aqueduct service, bridges were obstructed, and areas were isolated. Overall, total rainfall for the month in Putumayo was 40% above normal.

According to the National Unit for Disaster Risk Management between 15 September and 27 October, there were 72 floods, 15 flash floods, 61 landslides, 45 gales, 27 storms, 8 hailstorms, and thunderstorms in 27 of the 32 departments of Colombia. At the beginning of November, intense rainfall occurred in the department of Nariño and triggered a landslide in Mallama, where at least 12 people died and another 10 were injured. Overall, Mallama received November precipitation 60% above its average.

2) CENTRAL SOUTH AMERICA—J. A. Marengo, J. C. Espinoza, L. M. Alves, J. Ronchail, A. P Cunha, A. M. Ramos, J. Molina-Carpio, K. Correa, G. Avalos, W. Lavado-Casimiro, J. Baez, and R. Salinas

This region includes Brazil, Peru, Paraguay, and Bolivia.

(i) Temperature

The 2021 mean temperature for central South America was 0.4°C above normal, resulting in its seventh-warmest year since records began in 1961 (Fig. 7.13). The year was characterized with near- to above-normal mean temperatures across the region. Parts of central and southern Brazil had the largest mean annual temperature departures, ranging between 0.5° and 1.0°C above normal (Fig. 7.11b). During the year, the highest monthly mean temperature departures (2–5°C above normal) occurred during August–September across the region east of the Andes (15°–25°S). Below-normal minimum annual temperatures were observed across much of Peru and a small

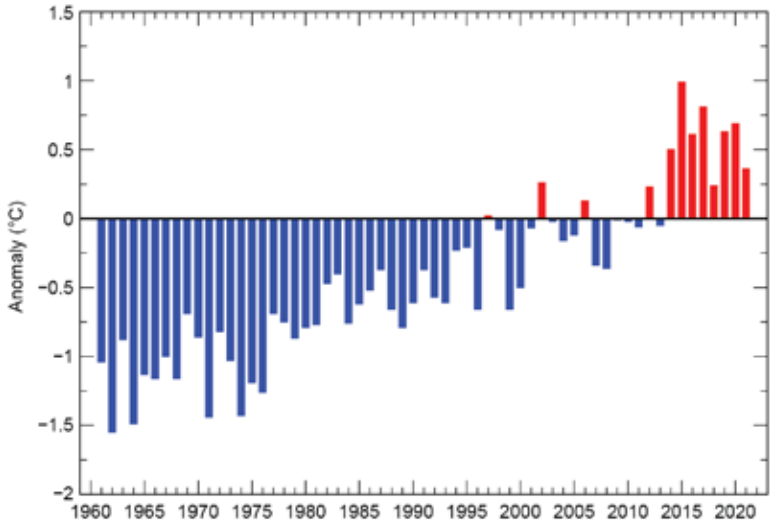

Fig. 7.13. Time series of mean annual regional air temperature anomalies (°C; 1991–2020 base period) for the period 1961–2021 for central South America (Brazil, Bolivia, Paraguay, and Peru). (Source: NOAA/NCEP GHCN CAMS data.)

area in northeastern Brazil, while the rest of the region had near- to above-normal minimum annual temperatures (Fig. 7.11a). Maximum annual temperatures were above-normal across the region (Fig. 7.11c).

Several significant heat waves were also observed across the region. Of note, temperatures were above 30°C in the Peruvian Amazon during 13–15 April, reaching an all-time historical maximum record of 34.2°C in the city of Jelacio, San Martin State. Conversely, between the end of June and the first week of July, two powerful cold spells impacted the region (see *Notable events and impacts* section).

(ii) Precipitation

Above-normal annual precipitation was observed across much of northern Brazil and across parts of northwestern Peru, eastern Brazil, and western Bolivia (Fig 7.12). Below-normal annual precipitation was present across parts of southwestern Peru, northeastern and western Brazil, eastern Bolivia, and across Paraguay.

During January–October, precipitation was below normal across most of the region, including the coast of Peru, the southern Amazon, and southeast Brazil, and from August to October in the Bolivian Andes. Rainfall was above normal during December 2020–May 2021 in the northern Amazonia (north of 5°S) and, by 1 June, the Rio Negro at Manaus reached its highest water level in 102 years of record, resulting in significant floods (see *Notable events and impacts* section).

(iii) Notable events and impacts

Several significant weather and climate extreme events occurred across central South America in 2021 (see Fig. 7.14).

After several months of above-normal rainfall, the water level of the Rio Negro in Manaus (central Brazilian Amazon) was above 29.00 m (the emergency threshold) by early June 2021 and remained above that threshold for a total of 91 days. It reached a record high level of 30.02 m on 16 June, surpassing the previous record of 29.97 m set in June 2012. The overflow of the river caused damaging floods that surpassed the "once-in-a-century" Amazon flood in 2012 (Espinoza et al. 2021; see Sidebar 7.3 for more information). Over 800 houses, educational centers, bridges, and road sections were reported damaged. By the end of June, according to IDAM (2021), the flood in the Brazilian Amazonia generated economic losses of $40 million (U.S. dollars) for the rural sector and affected more than 450,000 people.

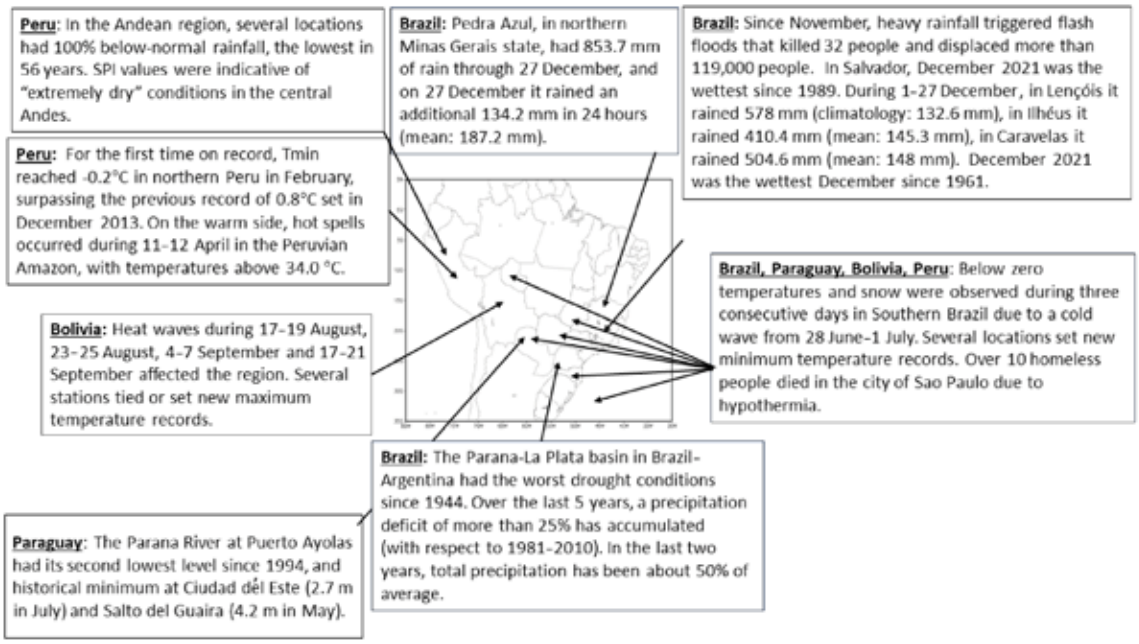

Fig. 7.14. Extreme and notable events across central South America in 2021. (Sources of information: Peru: SENAMHI; Bolivia: SENAMHI, Paraguay: DMH; Brazil: INMET, CEMADEN, Climatempo, INPE; International: UN OCHA, Web Relief, UNDRR). The historic flood in Amazonia is discussed Sidebar 7.3.

A multi-year drought affected central-southern Brazil (Minas Gerais, São Paulo, Paraná, Mato Grosso do Sul) and parts of Paraguay and Bolivia throughout the year. Due to its prolonged duration and severity, the drought impacted many socio-economic and ecological systems, increased risk of wildfires, decreased river transport, reduced hydroelectric energy production, and impacted crops and livestock in these highly agricultural regions. By May 2021, more than half of the municipalities in Upper Parana had about 40% of their crops damaged by the drought (Naumann et al. 2021). The government declared a water crisis in September, as reservoirs in southeastern and central-western Brazil were operating at 23%, the lowest level in 20 years, and these regions were at high risk of water and energy shortages and rising water and electricity prices.

Drought spanned the Paraguayan Chaco, Brazilian Pantanal, and southeastern, central, and southern Brazil, and the southwestern Bolivian Amazon during the austral summer and autumn, as shown by the IDI (Cunha et al. 2019; Figs. 7.15a–d. The Paraguay River shrank to its lowest levels in half a century, resulting in potable water accessibility issues and limited river traffic, March–May soil moisture deficits, delayed planting operations and wheat germination, and brake on cereal production in Paraguay. Parts of the Chiquitania dry forest region in Bolivia were also affected by drought and warm weather in August–October, favoring fires that had burned 3.4 million hectares by 15 October (Rodriguez and Ibarnegaray 2021), about 94% in the Santa Cruz and Beni provinces.

The effects of the 2020–21 drought in the Paraná basin on ecosystems were particularly severe in the Pantanal, one of the largest wetlands in the Americas (Libonati et al. 2021; Marengo et al. 2021). Authorities were concerned about the cumulative effects of fires in 2020 and 2021, and the area affected by fire in the Brazilian Pantanal at the end of September 2021 (1,089,975 ha) was well above the historical average of 616,125 ha. However, differently from 2020, when fires reached the northern part of Pantanal, the most critical region affected in 2021 was the southern part.

In November and December 2021, rainfall was more than 300% above normal in northeastern Brazil, triggering the worst flash floods in recent decades in the states of Bahia and Minas Gerais. On 7 December, storms caused by instabilities associated with a subtropical cyclone over the Atlantic Ocean affected several cities in the southern part of Bahia, which impacted about 220,000

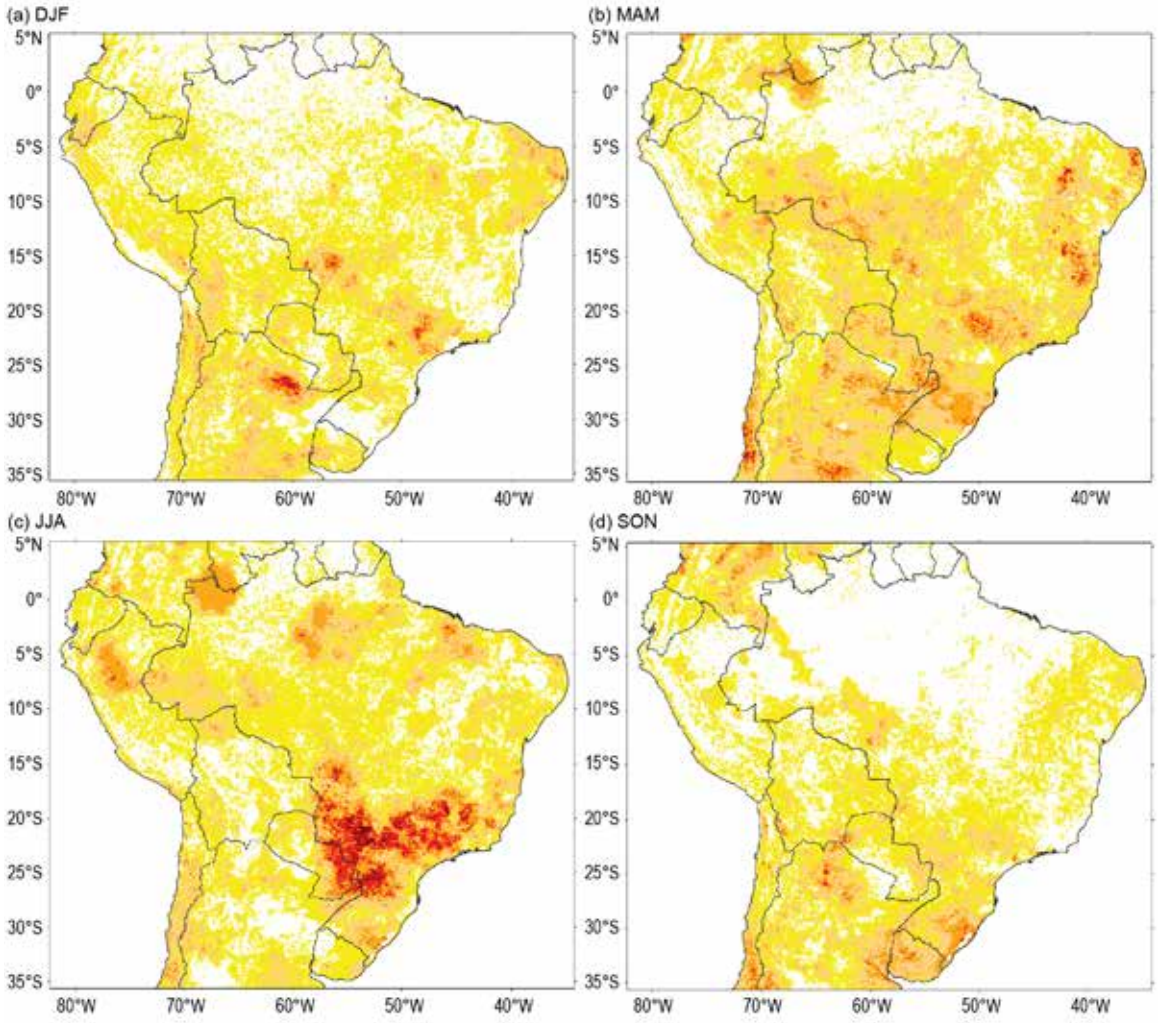

Fig. 7.15. Integrated Drought Index (IDI) maps for central South America during (a) DJF 2020/21, (b) MAM 2021, (c) JJA 2021, and (d) SON 2021. (Source: CEMADEN.)

people and caused 12 fatalities and over 260 injuries. In the same region, flooding on 23 December destroyed and damaged houses, schools, hospitals, and other infrastructure, affecting over 810,000 people and caused over 30 fatalities and 500 injuries. According to INMET and CEMADEN, the rain total for December 2021 was almost 400–500 mm above normal. Daily values surpassed 150 mm and accumulated values in some locations reached 500 mm during 23–27 December, and up to 800 mm during the month of December (climatology between 150–200 mm).

Three significant cold waves affected central South America during 20 June, 26 June–2 July, and 27 July–1 August, where some locations reported minimum temperatures that were 11–29°C below average and set new minimum temperature records. Of note, the Campo Belo station in the National Park Itaiaia, in the highlands of the state of Rio de Janeiro, recorded a minimum temperature of –14.8°C (climatology: 14.4°C) on 1 July, and, if verified, could be the lowest minimum temperature on record. Thirteen fatalities were attributed to these cold waves, and frost affected coffee, vegetables, fruit, and wine production in southern and southeastern Brazil, reducing the production by 30% and contributing to increased prices of food and commodities. The cold waves also affected western Amazonia, where minimum temperatures were 8–11°C below average. Some locations across Paraguay observed close to freezing temperatures, and several locations across eastern Bolivia set new record low minimum temperatures. Frost was recorded for the first time on record in some areas (FAN 2021).

Sidebar 7.3: **Major floods in the Amazon**—G. Koren

The Amazon forest has experienced several extreme events in the last decade, including large-scale floods and droughts. In 2021, with La Niña conditions present most of the year, the Amazon experienced higher-than-normal precipitation, leading to anomalously high river discharge and floods in downstream regions. Here, a quantification of the severity and extent of these anomalies are reported, including an assessment of the societal impacts of these extreme events, which coincided with the ongoing COVID pandemic.

Earlier major floods occurred in 2009, following extreme rainfall that progressed from the western to eastern part of the Amazon during the first months of that year (Filizola et al. 2014). A few years later, in 2012, record-high water levels were reached in the Manaus Port, as a result of excess atmospheric moisture supply in the preceding months, focused mostly on the western part of the Amazon basin (Satyamurty et al. 2013). There were also major floods in 2014, but these were located primarily in the southwestern region of the Amazon basin (Espinoza et al. 2014).

Precipitation anomalies

An overview of precipitation estimated by CHIRPS (Funk et al. 2015) over the Amazon forest and surrounding regions is presented in Fig. SB7.4. The map shows the accumulated precipitation anomalies over the first four months of 2021. These anomalies were calculated with respect to the 1991–2020 baseline, which includes the aforementioned wet years, but also

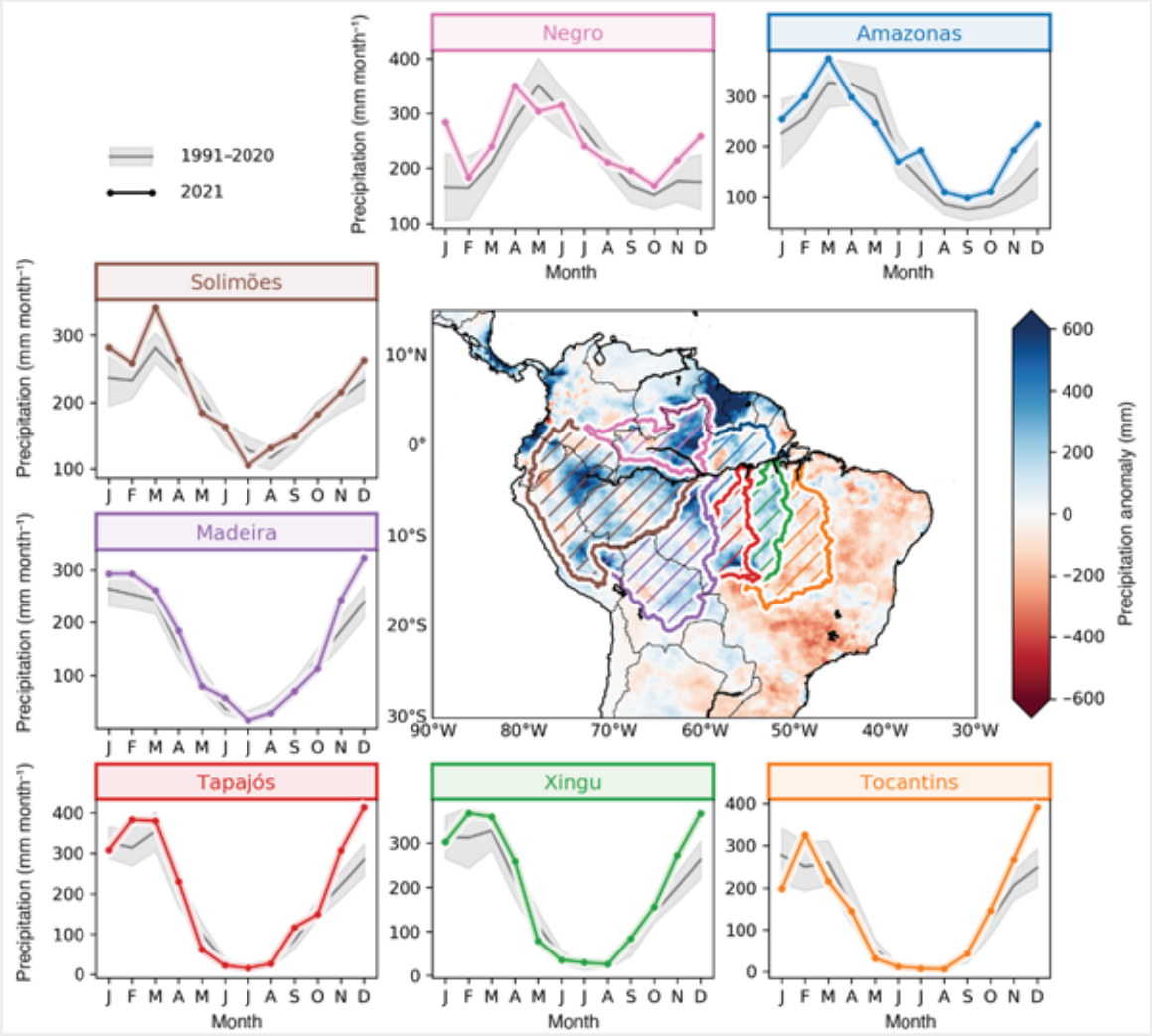

Fig. SB7.4. Precipitation (mm month^{-1}) over the Amazon forest and surrounding areas. The map shows the accumulated precipitation anomalies over Jan–Apr 2021, relative to the baseline 1991–2020. The time series plots show the mean precipitation (gray line) and its standard deviation (gray shading) with the 2021 precipitation averaged over the Tocantins basin (orange) and sub-basins of the Amazon (other colors). The location of these (sub-)basins follows the HydroBASIN definition (Lehner and Grill 2013) and is illustrated by the corresponding color in the map. (Source: CHIRPS [Funk et al. 2015].)

the dry years 2010 (Lewis et al. 2011) and 2015–16 (Koren et al. 2018). Across the Amazon basin, above-average precipitation anomalies were dominant, and are linked to strengthening of the Walker circulation (Espinoza et al. 2022). High rainfall totals are also apparent north of the Brazilian Amazon, in Guyana and Suriname, whereas drier-than-usual conditions were found to the east of the Amazon, in the Caatinga and Cerrado regions.

The temporal variation of precipitation averaged over the Tocantins basin and several sub-basins of the Amazon basin was calculated using the HydroBASIN definitions from Lerner and Grill (2013) and is included in Fig. SB7.4. The climatologies (gray lines and shading) reveal a substantial difference between the dry season minima for the northwestern sub-basins (e.g., always exceeding 100 mm month^{-1} for the Negro sub-basin), whereas precipitation over the Xingu sub-basin remained for a period of roughly five months below the 100 mm month^{-1} threshold. Focusing on the 2021 precipitation (colored lines), it is clear that both the start and end of the year 2021 were anomalously wet, whereas the drier period in the middle of the year was not exceptional. There is also a spatial dependency in the anomalies: the western sub-basins (e.g., Solimões) experienced high anomalies in the early part of 2021, whereas for the southeastern (sub-)basins (e.g., Xingu, Tocantins), the wet anomalies at the end of 2021 are most pronounced.

River discharge and floods

The anomalous rainfall in 2021 resulted in extreme discharge in the Amazon basin. Discharge measurements from the Óbidos station, which is situated along the Amazon River and drains an area of approximately 4.7 million km2 (van Schaik et al. 2018), show positive anomalies throughout the year, even exceeding 2-σ standard deviation (Fig. SB7.5). To verify that this is not simply resulting from the intensification of the hydrological cycle in the Amazon (Barichivich et al. 2018), the effect of removing the long-term linear trend is also included.

Figure. SB7.5 also contains a map of discharge anomalies from the GloFAS-ERA5 reanalysis product v3.1 (Harrigan et al. 2020) integrated over the period March–June (the integration period was delayed by two months relative to the map in Fig. SB7.4, as the discharge peaks for Óbidos were delayed by roughly two months relative to the peaks in rainfall). Spatial patterns in the discharge anomalies resemble the precipitation anomalies in Fig. SB7.4, with positive anomalies in the Amazon basin and the Guyanas, whereas the Cerrado and Caatinga areas to the southeast of the Amazon show negative anomalies.

Impacts

The floods during May and June affected several villages and cities around the Amazon River, including the Amazonas state capital Manaus. The town Anamã with its ~13,000 inhabitants, which is situated alongside the Amazon river in the Solimões region, was completely flooded. Unfortunately, the floods coincided with high infection rates of COVID-19 in this region, complicating evacuations and other means to manage the flood impact.

Several months later, at the end of 2021, regions outside the Amazon forest also experienced heavy rainfall, culminating in major floods in the northeastern state of Bahia. Two dams in the region collapsed, leading to major floods that resulted in severe damage and casualties in the city of Itabuna with its ~200,000 inhabitants. The impacts of these extreme events extend into 2022.

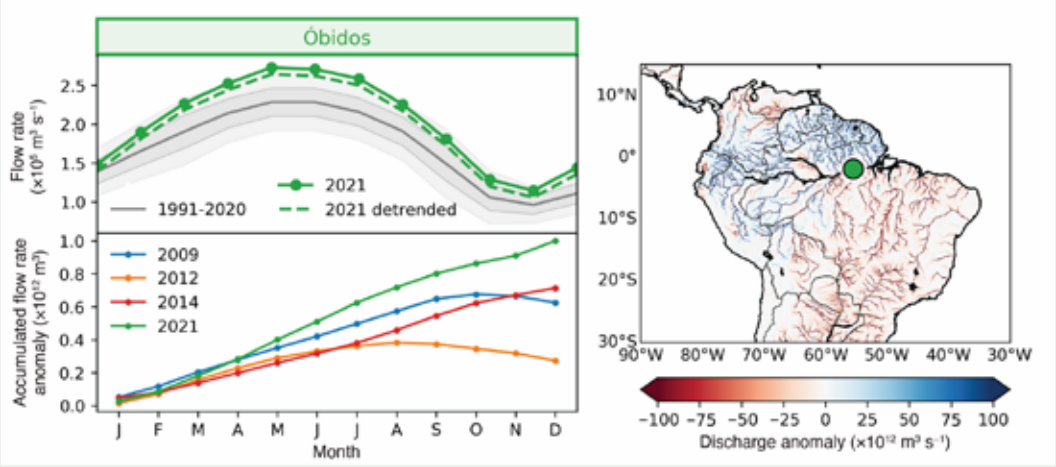

Fig. SB7.5. River discharge (m^3 s^{-1}) from in situ observations. The time series plot (top panel) shows the mean climatology (gray solid line) and the 1 std. dev. (dark gray shading) and 2 std. dev. (light gray shading) areas are indicated, alongside the discharge for 2021 (green line) for the Óbidos station. The bottom panel shows the accumulation of the discharge anomaly over time for four recent wet years (2009, 2012, 2014, and 2021). The map shows GloFAS discharge anomalies for Mar–Jun 2021, and the location of the Óbidos station is indicated (green circle). (Source: National Water Agency of Brazil (ANA 2021) and the GloFAS-ERA5 reanalysis product v3.1 [Harrigan et al. 2020].)

1) SOUTHERN SOUTH AMERICA—L. S. Aldeco, C. R. Cortés Salazar, D. A. Domínguez, N. Misevicius, and A. J. Reyes Kohler

This region includes Argentina, Chile, and Uruguay.

(i) Temperature

Above-normal temperatures were observed across most parts of southern South America (SSA) during 2021 (Fig. 7.11b). The highest temperature departures were observed south of 35°S. Below-normal temperatures were limited to northern parts of Uruguay and Chile and across parts of central and northern Argentina. The national mean temperature anomalies for Argentina, Chile, and Uruguay were +0.52°C, +0.51°C and +0.1°C, respectively (Fig. 7.16). These anomalies placed 2021 as the fifth-warmest year on record for Argentina and Chile and the 13th-warmest year on record for Uruguay, all in the 1961–2021 period. Near- to below-normal annual minimum temperatures during 2021 were observed across northern parts of Argentina and Uruguay, while above-average conditions were present across much of southern Argentina and northern and southern Chile (Fig. 7.11a). Annual maximum temperatures were above normal across the region (Fig. 7.11c).

Summer (December–February) 2020/21 had near-normal temperatures, on average, in most parts of the region. Some parts of northern and western Argentina, northern Uruguay, and central and northern Chile recorded below-normal temperatures. Above-normal temperatures were recorded in western Patagonia, Argentina, and Chile. Heat waves affected Uruguay, Chile, and central and northern Patagonia in Argentina, leading to several locations setting new historical maximum temperature records in Patagonia of Chile and Argentina: Cipolletti (Argentina) recorded a maximum temperature of 43.8°C on 22 January, its highest value since 1961, and Puerto Williams (Chile) recorded 26.1°C on 27 February, its highest since 1968.

During austral autumn (March–May) temperatures were near-normal in most parts of the region and higher temperatures were recorded at central and southern Argentina.

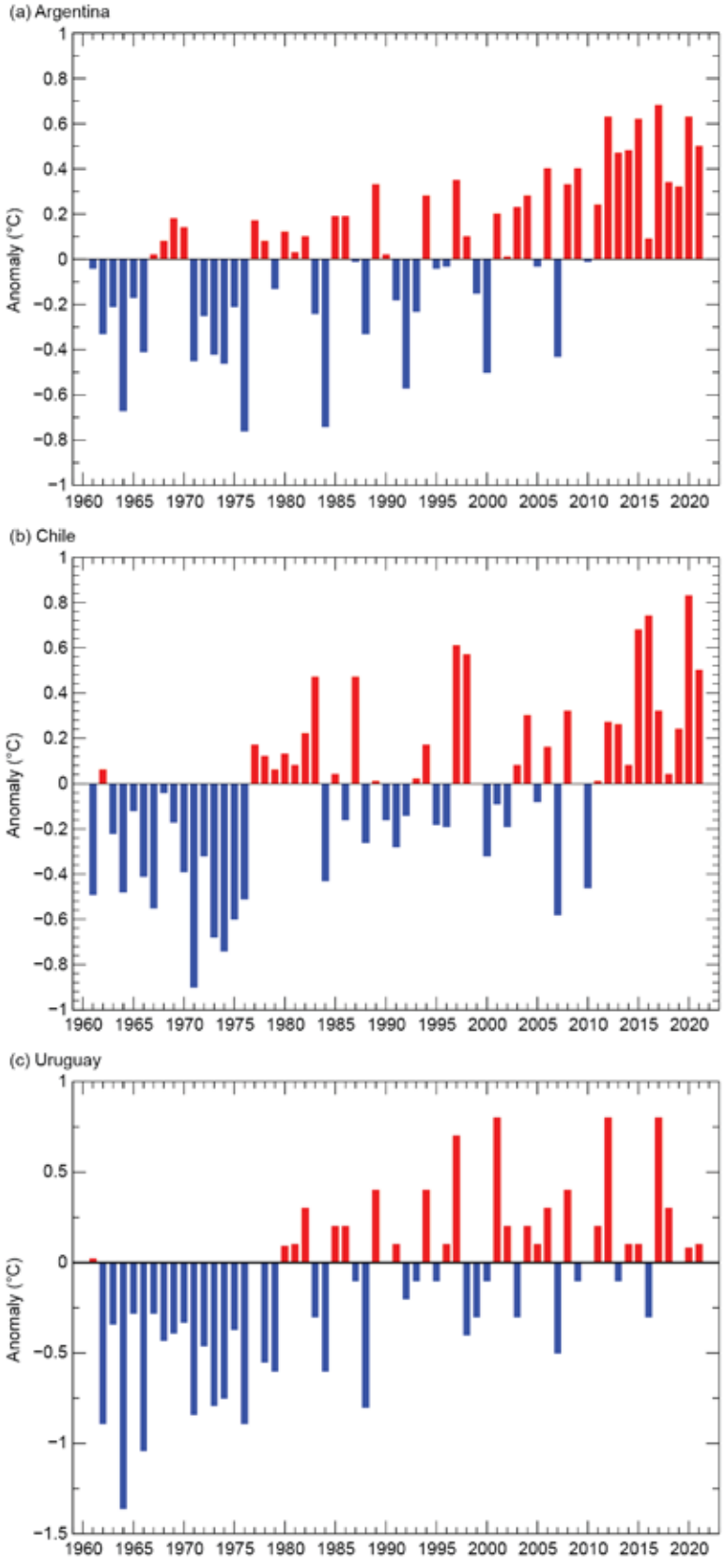

Fig. 7.16. National annual temperature anomalies (°C) for (a) Argentina, (b) Chile, and (c) Uruguay for the period 1961 to 2021.

March temperatures were above average during the first half of the month in northwestern Patagonia in Argentina, leading to the warmest March for the city of Bariloche since 1961. Some locations across Uruguay had their highest mean temperature for April since 1981 (Carrasco, Prado, Colonia, and Mercedes).

Winter (June–August) was warmer than normal in the southern regions of Chile and Argentina. Most of Chile, Uruguay, and northern Argentina had below- to near-normal temperatures. Cold air outbreaks occurred in Uruguay and central and northern Argentina during the last two weeks of June. In Argentina, new minimum and maximum temperature records were set. Of note, Villa María del Río Seco recorded its lowest minimum temperature (–9°C on 30 June) and Laboulaye its lowest maximum temperature (5.8°C on 16 June), both since 1961. Colonia and Salto in Uruguay recorded maximum temperatures of 9.8°C and 7.2°C, respectively, on 28 June. By the end of July, another cold irruption favored colder temperatures in the northern regions of Argentina and Uruguay, and a new record for minimum temperature in Argentina was set in Presidencia Roque Saénz Peña with –7.4°C on 29 July, its lowest since 1961.

Spring (September–November) was characterized by a period of high temperatures that were recorded during the last week of October. This warm period affected central and southern parts of Argentina and Uruguay, resulting in 22 stations in Argentina setting new daily maximum temperature records for October. In Uruguay, several records were set for the highest mean, maximum, and minimum temperature for the season at several stations since records began in 1981.

(ii) Precipitation

Most of southern SSA had below-average annual rainfall during 2021 (Fig. 7.12). The most affected region was south-central Chile and northeastern Argentina. Within that area, the annual rainfall was 30–60% below average. Since 2010, south-central Chile has been under a rainfall deficit period that has been called the "Mega Drought", and 2021 added to this period. The city of Santiago de Chile recorded its fifth driest year since 1914, and Junín in Argentina had its driest year since 1961. Also, from La Araucanía region to the Lakes region in Chile, 2021 was the driest year since 1961 with a deficit of –42%. Meanwhile, local regions in central and northwest Argentina had above-average annual rainfall, with the highest anomalies ranging between 20–40% above normal.

During austral summer 2020/21, La Niña conditions were present, and most of the SSA region had below-normal rainfall. Typically, La Niña favors less precipitation than normal in Uruguay and central and northeast Argentina, especially during spring and summer, while northern Chile tends to have above-normal precipitation during summer. During summer 2020/21, above-normal rainfall was recorded in eastern Uruguay, northeastern and central-western Argentina, and central Chile, mainly due to sub-seasonal variability that favored some precipitation events. In Argentina, rainfall was about double its normal in San Rafael, and other stations, including Dolores, Puerto Deseado, and Iguazú, recorded rainfall between 50–75% above normal. Dolores recorded its highest daily rainfall since 1961 (276 mm on 5 January). In Chile, Curicó recorded 59.6 mm on 30 January—its highest daily and monthly precipitation for January since 1950.

During austral autumn, frontal activity favored above-normal rainfall in central and northwestern Argentina, Chile, and Uruguay. During this season, Marcos Juárez and General Pico, in central Argentina, recorded rainfall 97% and 85% above normal, respectively. In Chile, Juan Fernandez station recorded 121 mm on 19 April—its second highest daily rainfall since 1963. In Uruguay, the highest daily rainfall of the year was recorded in Treinta y Tres Orientales with 230 mm on 10 April. Nevertheless, drier conditions continued affecting Uruguay, central and southern Chile, and southern and northeastern Argentina, reinforcing drought. In northeastern Argentina, the Iguazú station recorded precipitation that was 71% below its normal.

Typically, during spring, La Niña favors below-normal precipitation in central and southern Chile. Winter and spring 2021 had below-normal precipitation over most parts of SSA. La Niña was present at the time, and the most affected regions with precipitation deficits were south-central

Chile and central, western, and northern Argentina. Some stations in Argentina reported rainfall totals that were 80%–90% below normal for winter. Argentina had its fourth-driest October since 1961. Above-normal rainfall was only recorded in localized parts of northern Argentina and southeastern Uruguay.

(iii) Notable events and impacts

Argentina, parts of Uruguay, and Chile were under severe drought conditions during 2021 (Fig. 7.17). Drought was extreme or exceptional across parts of the region, according to the Drought Monitor. In addition, these conditions, combined with high temperatures, favored the development of fires and bushfires in different parts of central, southwestern, and northern Argentina during the summer. The city of El Bolsón, western Patagonia, was one of the most affected regions, with great damages and human loss during February and March.

Polar air irruptions led not only to below-normal temperatures in most of the SSA region, but also to unusual snow events in central Argentina during June and in Uruguay during July. Of note, the city of Pilar, Argentina recorded a snow event for the first time for the month of June.

During austral autumn and spring, some convective precipitation events affected central and northern Argentina and Uruguay, leading to flooding in some regions and forcing the evacuation of residents. Santiago del Estero city (Argentina) recorded 108.6 mm on 3 March, San Rafael recorded 81 mm on 20 April, and Marcos Juárez recorded 225 mm on 8 April. All set a new record for their highest daily value since 1961. The heavy rain prompted floods in San Rafael and Marcos Juárez.

During the last week in October strong wind events affected parts of the Argentinian Patagonia, with major damage reported in Comodoro, Rivadavia, and Esquel Cities. Gusts of more than 150 km h^{-1} were recorded during that period.

Fig. 7.17. Extreme and notable events in southern South America during 2021 (Argentina, Chile, and Uruguay).

e. Africa—A. Mekonnen, Ed.

This 2021 report for Africa is based on observational records from meteorological and hydrological services across the region, rainfall from the Global Precipitation Climatology Project (GPCP), and reanalysis products from the National Centers for Environmental Prediction/National Center for Atmospheric Research (NCEP/NCAR). Notable events in 2021 across the continent were compiled based on reports and information from government agencies, regional and international organizations, and research/Early Warning organizations. The climatological base period is 1991–2020. Terms "normal" and "average" are interchangeably used to refer to as the 1991–2020 climatology.

In 2021, temperatures over much of Africa were above normal. Annual temperatures ranging from 1.5° to 2°C above normal were observed over most of Algeria, Sudan, southern South Sudan, and adjoining southwest Ethiopia and northern Uganda, while areas across the boundaries of Niger-Nigeria-Chad had below normal temperatures (Fig. 7.18). Below-normal temperatures were also evident over most of South Africa, Botswana, and southern Namibia.

The mean annual rainfall over much of the continent was within normal ranges (±0.5 mm day^{-1} around normal). However, rainfall over most of southern Nigeria, southwest Ethiopia, Uganda, southeastern Kenya, most of Zambia, Malawi, northeastern areas of Democratic Republic of Congo, and eastern Angola was below normal (Fig. 7.19).

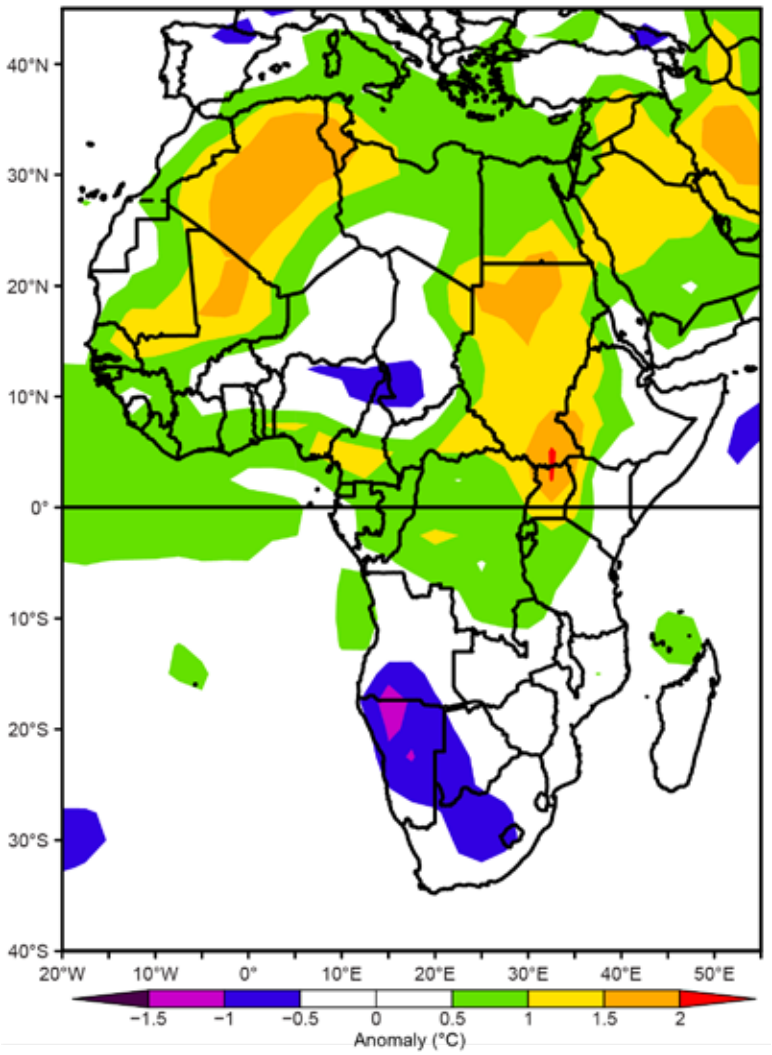

Fig. 7.18. The 2021 annual temperature anomalies for Africa (°C; base period 1991–2020). (Source: NCEP/NCAR.)

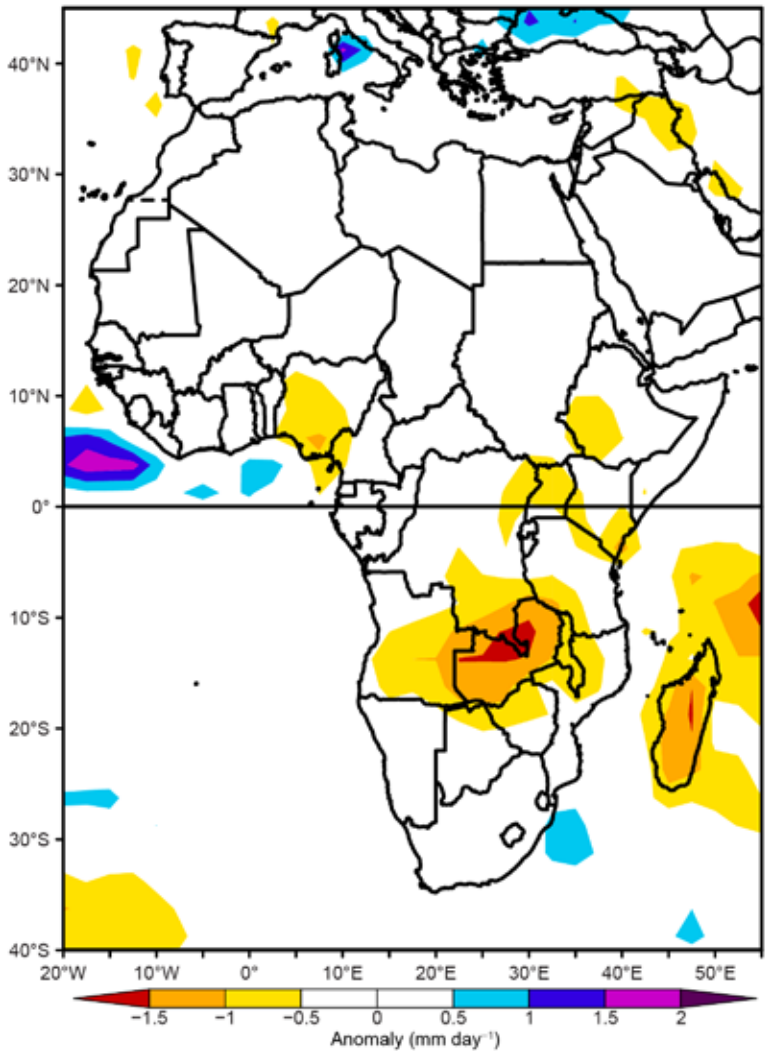

Fig. 7.19. The 2021 annual rainfall anomalies for Africa (mm day^{-1}; base period 1991–2020). (Source: NCEP/NCAR.)

Extreme weather events and high climate variabilities were also reported from several countries. Cold snaps, heat waves, and forest fires that affected extensive areas were reported from Morocco and Algeria. Record maximum temperatures, heavy rains resulting in extreme flooding and river overflows, and windstorms were observed in Central and West Africa. Heavy downpours over the Blue Nile catchment that affected downstream countries were reported from the Horn of Africa. In contrast, annual rainfall in equatorial East Africa was much below normal. Extremely heavy rainfall was reported in parts of southern Africa. An active tropical cyclone season was observed over the southwest Indian Ocean. The details of these and other extreme events are compiled by region below.

1) NORTH AFRICA—K. Kabidi, A. Sayouri, M. ElKharrim, and A. E. Mostafa

North Africa comprises Mauritania, Morocco, Algeria, Tunisia, Libya, and Egypt. Much of this region is characterized by arid and semi-arid climate, while northern parts exhibit Mediterranean climates. Precipitation over the region is highly variable both in space and time. Rainfall over western North Africa is generally of short duration but at times intense. Overall, station records from Morocco show below-average (19% below normal) rainfall during 2021. Egyptian stations reported below-average rainfall in the south, while above-average rainfall was reported in the north. The 2021 mean temperatures over the region were above average.

(i) Temperature

The winter (DJF; December 2020–February 2021) mean temperature over the region was above average. Morocco observed temperatures about 0.4°C above normal (Fig. 7.20a); however, in January, temperatures of 0.9°C below normal were reported from mountain regions of the country, while February temperatures were 1–3°C above normal over eastern parts. Most Algerian and Tunisian meteorological stations reported temperatures up to 3°C above normal in February. Winter temperatures over much of Egypt were 1–2°C above average.

Spring (March–May) temperatures were above average (+0.5°C) over Morocco, Mauritania, and much of Egypt. Most of Algeria and Tunisia were about 1–2°C above normal (Fig. 7.20b). In March, near-normal temperatures were reported from Algeria, Tunisia, and northern Libya. In May, mean maximum temperatures ranging from 1.5° to 2°C above normal were observed over northern and Saharan regions and 3°C above normal was reported over central regions in Morocco. During April and May, temperatures were about 2–4°C above normal over central Algeria, southern Tunisia, and western Libya.

Summer (June–August) temperatures were 0.6°C above normal over the region. Northern and northeastern Algeria and Tunisia exhibited temperatures 2° to > 3°C above normal (Fig. 7.20c). Summer temperatures more than 1°C above normal were also observed in Mauritania, Libya, and parts of Egypt. In July, temperatures exceeding 40°C were reported from several areas of Morocco (> 60% of stations reported heat waves). Generally, maximum temperatures of 1.1°C above normal were observed over Morocco, with anomalies of +1.5° to +3°C in central and southern regions of Morocco and parts of Egypt. A new record of 49.6°C was reported from Sidi-Slimane station in Morocco on 10 July. A maximum temperature of 48°C was reported at El-Wadi Al-Gadid station in Egypt on 12 June and again on 3 July. Anomalies of +4°C were reported from central Algeria and southern Tunisia in June and +2.5°C during July in Algeria, Tunisia, and Libya. In August, temperature anomalies reached +3.5°C in northeast Algeria and Tunisia. Tunisia had its hottest summer on record since 1950.

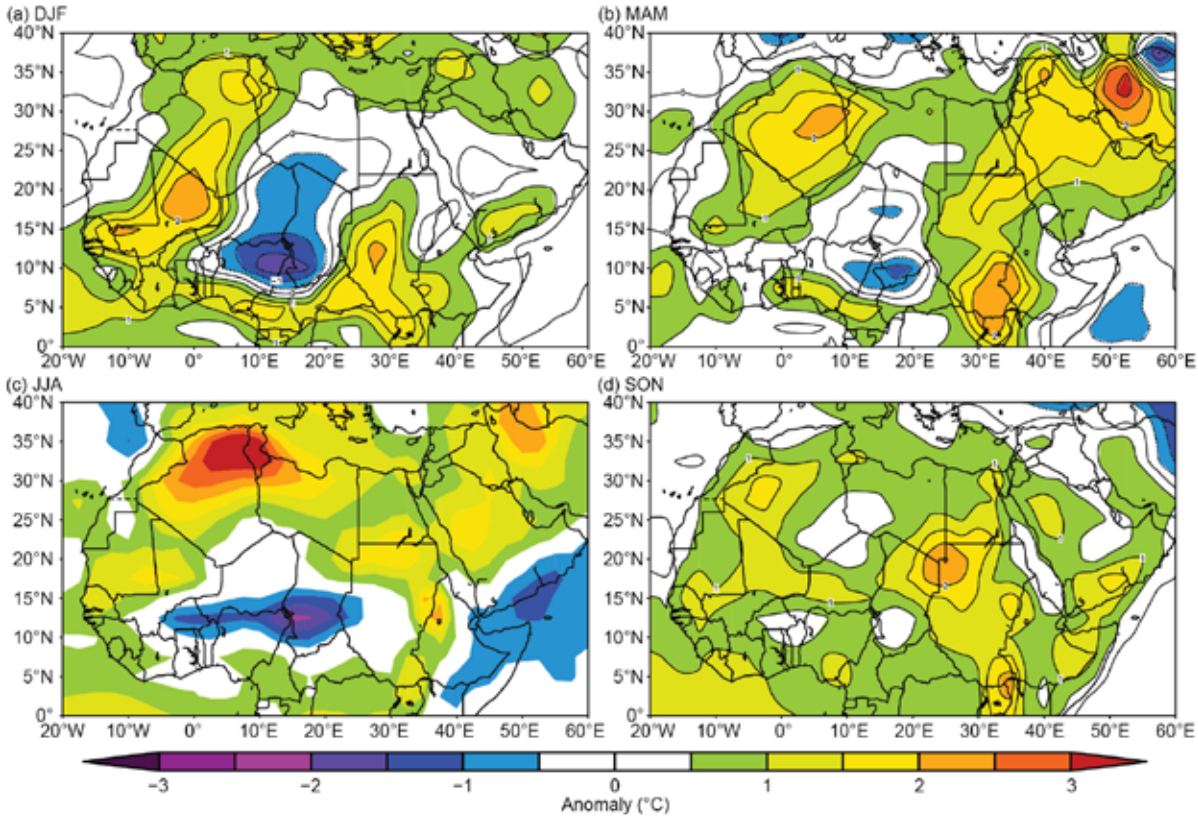

Fig. 7.20. North Africa seasonally averaged mean temperature anomalies (°C; 1991–2020 base period) for (a) DJF 2020/21, (b) MAM 2021, (c) JJA 2021, and (d) SON 2021. (Source: NOAA/NCEP.)

During autumn (September–November), temperature anomalies of about +1° to +2°C were observed over southern Algeria, northeastern Mauritania, southern Egypt, and southeastern Libya (Fig. 7.20d). Autumn temperatures were near normal to slightly above normal over much of Morocco. However, average minimum temperature anomalies of more than –1.4°C (range of –0.5° to –2.7°C) were reported across all Moroccan stations. In September, temperatures were above normal in central Algeria, and in October near-normal temperatures were reported in Algeria, Tunisia, and Libya. November temperatures were 2–3.5°C below normal in Libya. Additionally, a minimum temperature of –1°C was reported on 1 November at Saint Catherine in Egypt.

(ii) Precipitation

Winter precipitation was near-normal over most of central and southern Morocco and southern Algeria, Egypt, and Libya (Fig. 7.21a). Precipitation ranging from 50% to 126% above average was reported during January over northern Morocco. Reports also indicate more than 100% of normal precipitation over southern Morocco.

Spring rains were below to near-normal over much of the region (Fig. 7.21b). Seasonal precipitation totals were 55% below normal over Morocco; however, in March, heavy rainfall (47% to 349% above normal) was observed. Spring rains were below to near-normal in Algeria, Tunisia, and Libya. The summer season was mostly dry over North Africa.

Autumn rains were below normal over most parts of the region (Fig. 7.21c); however, above-normal precipitation was reported from northern Algeria in November. The seasonal deficit reached 49% in Morocco and about 36% in Tunisia.

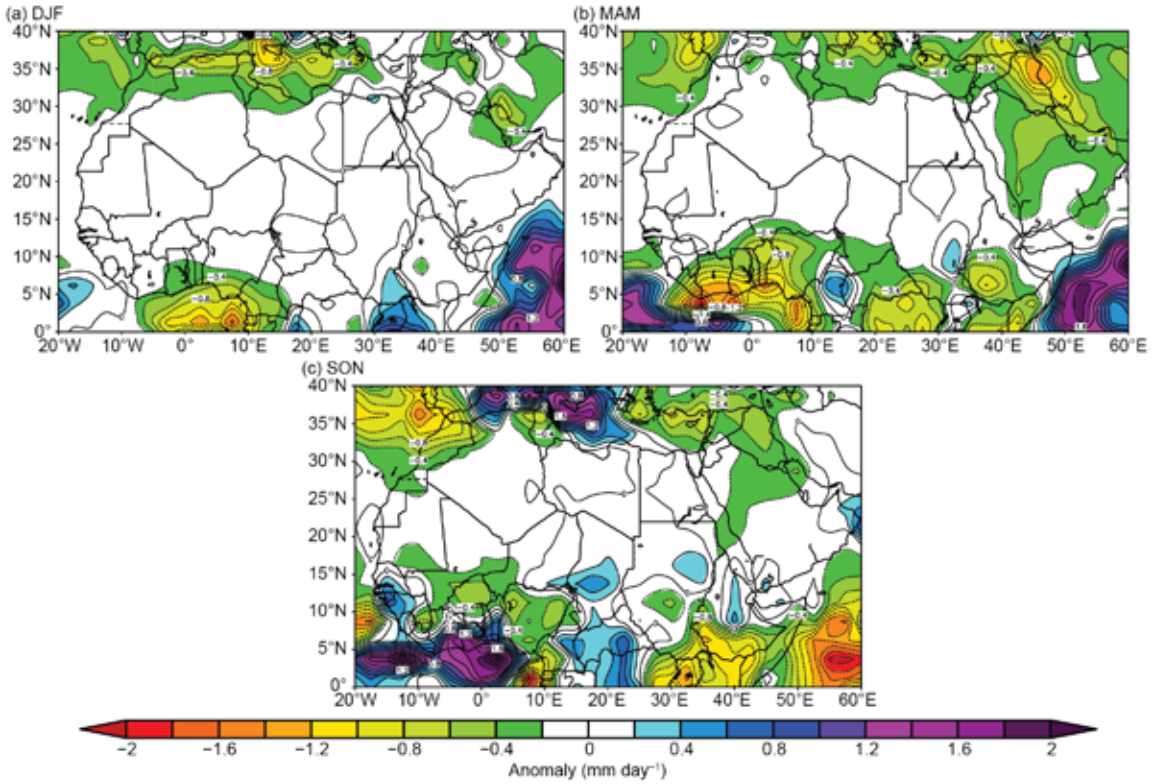

Fig. 7.21. North Africa seasonally averaged rainfall anomalies (mm day–1; 1991–2020 base period) for (a) DJF 2020/21, (b) MAM 2021, and (c) SON 2021. (Source: GPCP NOAA/NCEP.).

(iii) Notable events and impacts

Severe storms, heat and cold waves, strong winds exceeding 140 km h^{-1} in the Saharan region and 100 km h^{-1} in the extreme north region, and forest fires were all reported in Morocco and Algeria in 2021. Additional information is given below.

Meteorological and hydrological services of Morocco reported heat waves during February, July, October, and December. Similar heat waves were reported from Algeria in July, August, and September. Additionally, 285 forest fires that affected 2782 hectares were reported between January and September in northern Morocco and Algeria. The fires damaged more than 89,000 hectares and caused at least 90 deaths.

In January and March, Morocco experienced several storm events that led to flooding. Flash floods caused by convective precipitation occurred in March in extreme northern areas of Morocco, where extensive property damage was reported. Heavy rains affected northwestern Algeria during March, October, and November, causing 11 fatalities in total and significant property damage. Heavy rainfall also occurred in northwestern Tunisia during September and October, causing three deaths and extensive property damage.

2) WEST AFRICA—W. M. Thiaw, W. Agyakwah, S. Hagos, F. Zeng, I. A. Ijampy, F. Sima, and O. Ndiaye

West Africa extends from the Guinea coast to about 20°N and from the eastern Atlantic coast to Niger. Climatologically, it consists of two distinct but inherently linked sub-regions: (1) The Sahel to the north from about 12° to 17°N, spanning countries from Senegal and The Gambia in the west to Niger in the east and (2) the Gulf of Guinea region to the south from about 4° to 10°N encompassing the Guineas to the west along the east Atlantic coast and Nigeria and Cameroon to the east. The rain season over the Sahel runs from June to September and its interannual variability is controlled by the adjacent (Atlantic Ocean) and remote (central and eastern Pacific and the Indian Ocean) sea surface temperatures, including variabilities of the middle tropospheric easterly jet, Saharan heat low, and north–south movement of the deep convective zone.

(i) Temperature

The highest mean annual temperatures, between 28° and 30°C, were observed across the western and central Sahel, encompassing eastern, southern Mauritania, and central Mali (Fig. 7.22a). Mean annual temperatures were between 22° and 28°C in the eastern and southern Sahel and the Gulf of Guinea Region (GGR), with the lowest temperatures of 22–24°C registered over western GGR. Mean annual temperatures were above normal over the western region and along

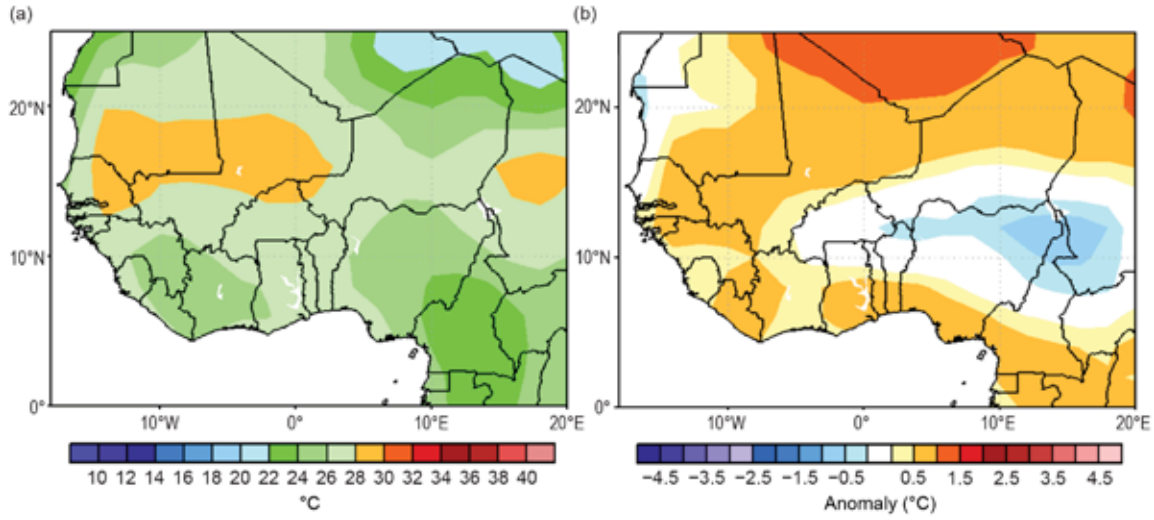

Fig. 7.22. Annual (a) mean temperature and (b) mean temperature anomaly (°C; base period 1991–2020) for West Africa. (Source: NOAA/NCEP.)

the Guinean coast, with departures from the mean of about +0.5° to +1°C (Fig. 7.22b), placing 2021 among the 3% of warmest years in this area. Temperatures were 0.5° to 1°C below the mean over northern Nigeria. Annual maximum temperatures (Tmax) exceeded 36°C in central Mali (1° to 1.5°C above the mean) and ranged between 34° and 36°C across most areas from eastern Senegal to Niger. These were average values in the western Sahel but 1° to 2°C below the mean in the area encompassing Burkina Faso to northern Nigeria. Tmax was 28–32°C (1.5–2.5°C above the mean) over the southern Nigeria. The highest Tmax values were observed during March–May season, averaging 40° to 46°C across the Sahel from eastern Senegal to Niger, with peak values extending from southeastern Mali and northwestern Burkina Faso to southern Niger. These were 1–1.5°C above the mean in this sector, but 1–2°C below the mean in the western Sahel. Annual minimum temperatures (Tmin) exceeded 24°C along the Sahel and Guinea coasts, about 1.5–2.5°C above the mean and ranking in the 90th percentile in the western Sahel.

(ii) Precipitation

Annual rainfall ranged between 1000 and 2000 mm over the Gulf of Guinea region with areas of maximum rainfall over 2000 mm along the western Guinea coast over Sierra Leone and western Liberia (Fig. 7.23a). Rainfall decreased northward from 2000 mm in the Guinean Highlands to 300 mm at about 15°N in the Sahel. The climatologically dry areas of the northern Sahel near 20°N registered rainfall between 50 and 300 mm. Overall, annual rainfall was average over much of the Sahel and the Gulf of Guinea region, except for areas in western Mali, which observed cumulative totals between 1000 and 1500 mm (only 50 to 100 mm above the mean), and along the Guinean coast from Liberia to Ghana, where totals ranged between 1250 and 1500 mm (also 50 to 150 mm above the mean). Rainfall was below average over Nigeria with the largest deficits at least 200 mm below the mean in the central and southeastern areas.

In the Sahel, rainfall totals during the period July–September account for much of the annual cumulative rainfall. Totals ranged from 100 mm at about 20°N to 500 mm at 15°N, between 500 mm and 1000 mm in the central areas (12°–15°N), to over 1200 mm in the areas of maximum precipitation, including the western Guinean coast (Fig.7.23b). These corresponded to above-average rainfall in the western Sahel with moisture surpluses between 20 and 100 mm in Senegal and western Mali. Above-average rainfall was also observed during the 2019 and 2020 seasons in the Sahel. However, rainfall was off to a slow start in the western Sahel in June and July 2021, with deficits more than 100 mm below the mean in southeastern Senegal and western Mali. Mali quickly recovered in July with surpluses more than 50 mm above the mean in some locations,

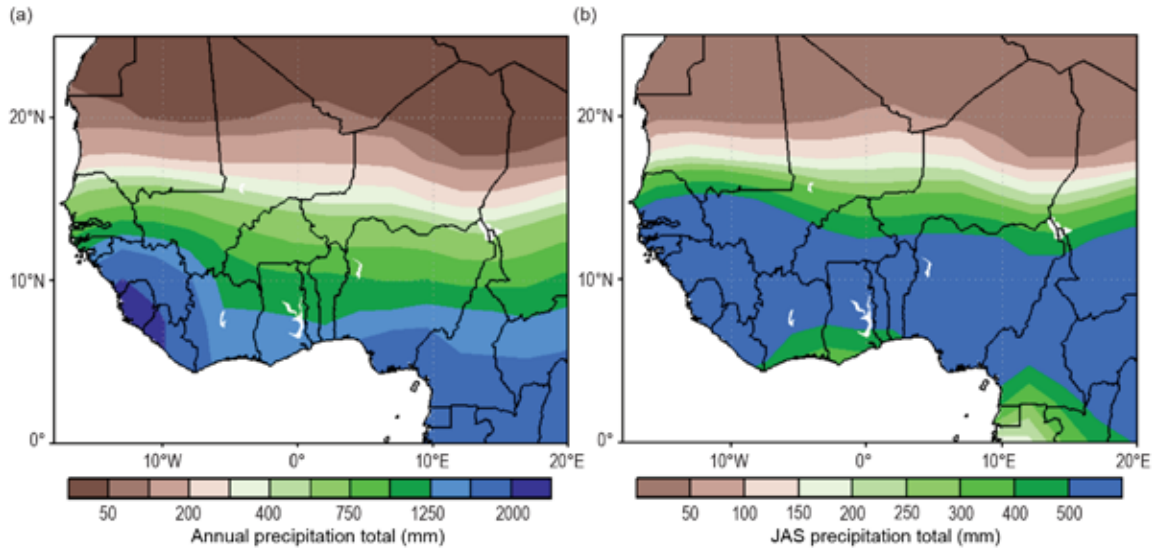

Fig. 7.23. Annual (a) rainfall total (mm) and (b) July–September rainfall total (mm) for West Africa. (Source: NOAA/NCEP.)

while deficits about 50 mm below the mean persisted over Senegal. Heavy downpours in August of about 300 mm (100 mm above the mean and ranking in the 90th percentile) in Senegal contributed to the overall wetter-than-normal rainfall season in this western sub-region of the Sahel. The rainfall period over West Africa runs from June to September. Figure 7.24 shows the June–September (JJAS) rainfall anomaly over the region. Consistent with the warm SST conditions over the Gulf of Guinea, the precipitation was mainly concentrated along the coastal regions with interior West Africa being comparatively dry. Below-normal rainfall over much of Nigeria and western Cameroon was observed.

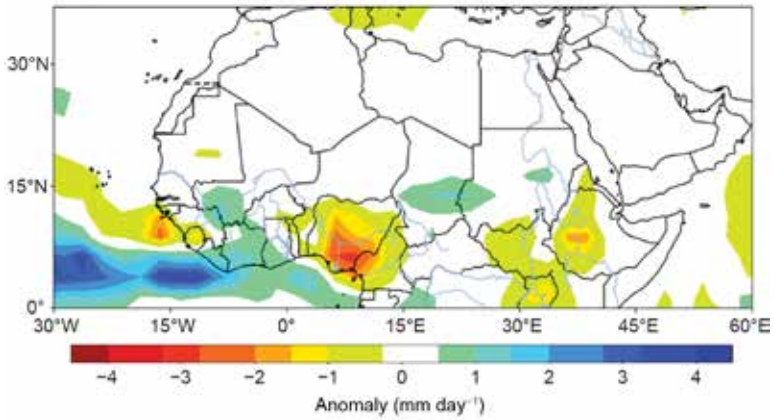

Fig. 7.24. Rainfall anomalies for June–September (mm day–1; base period 1991–2020) for West Africa. (Source: GPCP via NOAA/NCEP.)

Along the Guinean coast, much of the annual rains fall during the spring during April–June and in the autumn during September–November following the seasonal north–south displacement of the area of maximum convergence in West Africa. However, in the area extending from Sierra Leone to Ghana, the July–September rains surpassed 700 mm (100–150 mm above the mean). The performance of the seasonal rainfall in the GGR during April–June was poor as totals ranged between 300 and 500 mm, except for southeastern Nigeria which received amounts in excess of 500 mm. Rainfall deficits across the area encompassing southwestern Nigeria to Sierra Leone exceeded 100 mm below the mean, with the highest deficits reported in May, which was among the 3% of driest months in the recent 30-year period. The months of September and November brought rainfall surpluses more than 100 mm above the mean along the coast from Ghana to Sierra Leone in September and in southern Nigeria in November.

(iii) Notable events and impacts

Reports show September 2021 was the warmest September on record for the region, while July and August were the seventh and third warmest for their respective months. In Nigeria, before the start of the rainy season, the average maximum daily temperature surpassed 40°C on more than 50 days at several stations (Dutse, Maiduguri, Nguru, Potiskum, Sokoto, Yola, Zaria stations), according to the Nigerian Meteorological Agency.

Most of the extreme precipitation and associated costly flooding events occurred near the end of the rainy season. In Douala, Cameroon, extreme flooding affected several neighborhoods after 186 mm of rain fell over 24 hours during 11–12 August. Hundreds of homes were flooded. Later that month, Ouémé River overflow in southern Benin led to severe flooding in the town of Zagnanado, according to local media. Similarly, in Niger, 60 people were reported to have died either from drowning in flood water or from collapsing buildings, according to the nation's Civil Protection Authorities. In northeastern Ghana, five people died while attempting to cross a swollen river and due to lightning strikes. During 30–31 August, heavy rains in Guinea led to five fatalities, and

the resulting flood affected about 70,000 people in total, according to Guinea Red Cross Society. According to Nigeria's Emergency Management Agency, flooding due to heavy rains that fell on 12 September in Abuja and surrounding areas led to four fatalities.

In Chad, the UN Office for the Coordination of Humanitarian Affairs (OCHA) reported that flooding affected nearly 247,000 people across 400 villages. Fifteen people lost their lives, 17 were reported missing, and a total of 329 people were injured over the rainy season. In early October, the meteorological agency of Côte d'Ivoire reported that 105 mm of rain fell in Yopougon and 106 mm in Attécoubé in a 12-hour period.

Flood events were recorded in many parts of Nigeria between June and November. The resultant floods from heavy rainfall destroyed homes, valuable properties, farms, roads, and bridges. As a result, thousands of people were displaced and several lives were lost. These events also contributed to the spread of vector borne diseases and exacerbated the cholera outbreak in many states of the country. Kano was one of the most affected states, with a rainfall total of 98.8 mm on 24 July following a torrential downpour that lasted several hours. This led to 19 fatalities in the Doguwa Local Government Area after a vehicle was washed away in a flood. During the same period, several homes were submerged and property damage was estimated at over 100 million naira ($240,000 U.S. dollars), according to Kano State Emergency Management Agency (SEMA).

In July, The Gambia experienced a windstorm surge that affected almost 17,000 people in more than 100 communities across all seven regions, causing internal displacement and homelessness. More than 100 people were severely injured as a result of fallen walls and trees. 10 deaths were confirmed as a result of collapsed buildings. According to the Meteorological Department, on 7 July, winds reached 85 km h–1 and was the highest wind speed recorded in the last five years. 12 people died and more than 109,000 people were affected.

3) CENTRAL AFRICA—W. M. Thiaw and W. Agyakwa

Central Africa features a unique climate system marked by a strong annual cycle as it spans a wide area of Africa across both the Northern and Southern Hemispheres (SH). It extends from the southern tip of the Democratic Republic of Congo (DRC) northward into the central areas of Chad. Longitudinally, the region extends from about 5°E to ~35°E. Given the overlap with areas in West Africa and East Africa, this analysis focuses strictly on the sub-region encompassing Cameroon, Chad, Central Africa Republic (CAR), DRC, Congo, Gabon, Equatorial Guinea, and Sao Tome & Principe.

(i) Temperature

The mean annual temperature was between 22° and 28°C across much of the region, except for the western and southern ends of DRC, where it was 22–24°C. Temperatures were 0.5–1°C above the mean across the region, except for southwestern Chad and northern Cameroon, where they were 1°C below the mean. Much of DRC westward to Gabon and southern Cameroon reported annual temperatures above the 90th percentile (Fig. 7.25a). The months of September through December had the highest anomalies in mean temperature, reaching 28°C in western DRC, and overall exceeding the 95th percentile across much of the region. Below-normal temperature anomalies in excess of –3°C prevailed over northern Cameroon and southwestern Chad in February, making this month the coldest in the 30-year base period.

Annual maximum temperatures were around 30–34°C, above the 95th percentile across much of the region (Fig. 7.25b). Though Tmax reached or exceeded 40°C in southern Chad and northern Cameroon, the temperatures were 2°C below the mean and in the 3% lowest temperatures in the base period, with the period April–August accounting for much of the low Tmax values. Southern DRC reported record-breaking Tmax exceeding 38°C, with the highest elevated values of more than 5°C above the mean in July through September; with the warmest August in the 30-year period. Annual minimum temperature (Tmin) was above normal in the northern areas

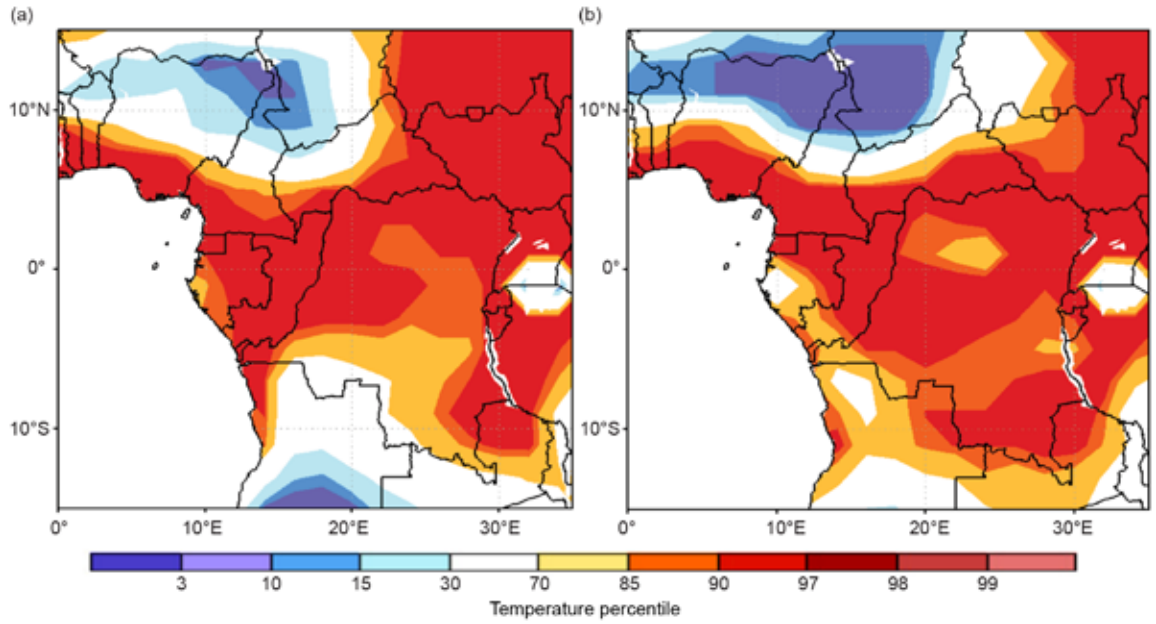

Fig. 7.25. Annual (a) average temperature percentile rank and (b) maximum temperature percentile rank for Central Africa. (Source: NOAA/NCEP.)

of the region with the highest positive anomalies (about 2°C above the mean) observed during January–March and November–December.

(ii) Precipitation

As stated earlier, the climate of Central Africa (CA) exhibits seasonality at both the north and south ends of the region. The rainfall pattern is closely related to the north–south movement of the maximum deep convective zone and wind flow pattern. Rainfall is unimodal in the northern areas of the region and marked with dry conditions during the NH autumn through spring and a return of the rains in the summer. The southern areas of the region are dry during the NH summer and wet during autumn through early spring seasons. The central areas of the region around the equator receive rainfall year-round. The area of maximum annual rainfall is located along coastal Cameroon with annual totals exceeding 2000 mm. On average, rainfall amounts range between 1200 mm over the southern tip of DRC and the southern areas of CAR and Cameroon to 2000 mm across much of DRC, Congo, Gabon, and southern Cameroon (Fig. 7.26a). Annual rainfall totals are generally less over southern Chad with a steep north–south gradient indicated by about 200 mm in the central areas of Chad to about 1000 mm in the southern tip.

During 2021, an area of maximum annual rainfall over east central DRC, with totals exceeding 2000 mm (Fig. 7.26a). A rain band in the 2000 mm covering most of the northern half of DRC narrowed and extended to the west to cover the area from central Congo to coastal Cameroon. Annual rains totaled 500 mm in the southern tip of DRC, with a northward gradient reaching 1750 mm in the southern areas bordering Angola and in the east. A similar pattern is observed in the northern areas of CA, with lower rainfall totals about 500 mm in central Chad increasing southward to northern DRC. Rainfall was above average over the western half of DRC, Congo, and southern CAR, with surpluses ranging between 50 and 150 mm (Fig. 7.26b) and totals ranking in the 85th percentile. Western Cameroon and southeastern DRC observed rainfall deficits of 200 mm below the mean, ranking in the 10th and 3rd percentiles, respectively.

Examination of the evolution of rainfall throughout the year suggested deficits reaching 100 mm below the mean (15th percentile) in February in the area encompassing Congo northward to Cameroon. Rainfall was significantly below average over the southern tip of DRC during January–March as totals averaged less than 300 mm, bringing rainfall deficits to more 150 mm (3rd

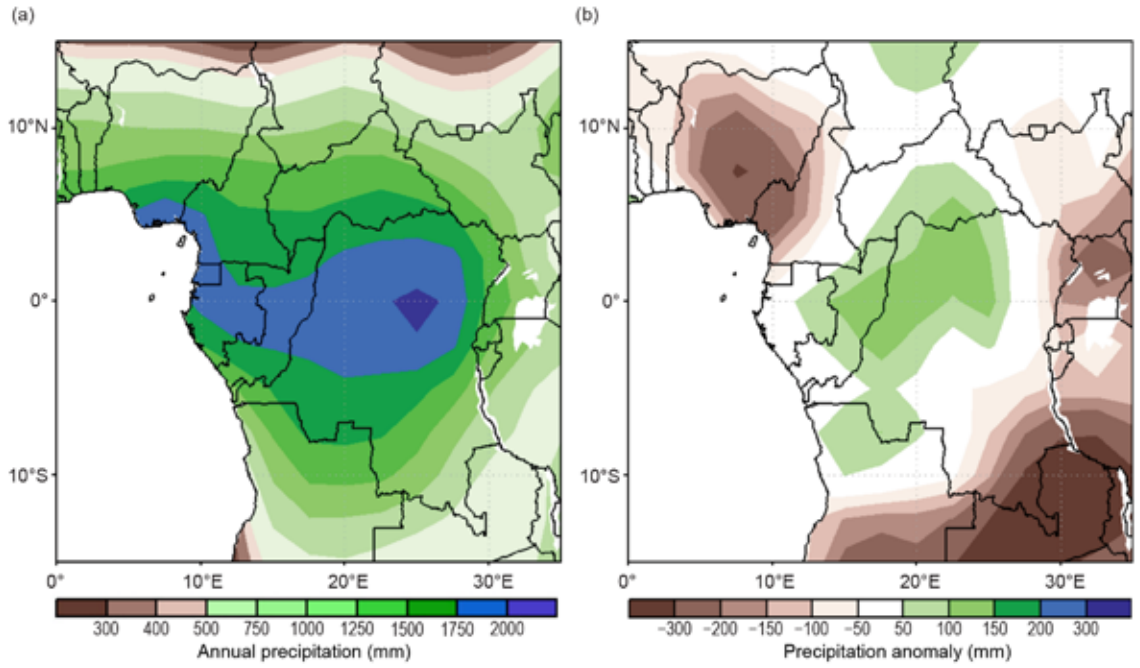

Fig. 7.26. Annual (a) total rainfall and (b) rainfall anomaly (mm; base period 1991–2020) for Central Africa. (Source: GPCP via NOAA/NCEP.)

percentile), indicative of extremely dry conditions. Rainfall was much above average in the western two-thirds of DRC during August–October, with departures from the mean exceeding 150 mm; much of the surplus was due to heavy downpours in October, with excess rains more than 300 mm (above the 95th percentile). A similar pattern with rainfall surpluses about 100 mm above the mean was observed in December.

(iii) Notable events and impacts

Heavy rainfall in Bangui (CAR) during 19–23 July flooded several districts in the city, affecting more than 70 families and 300 people. Stagnant water and mud remained for days in some areas, increasing risk of waterborne diseases, according to the International Organization for Migration (IOM). About two weeks following the floods, torrential rain fell over Bangui on 7 August, damaging or destroying more than 400 households in over a dozen districts and affecting 4000 people who needed shelter, according to the International Federation of Red Cross (IFRC).

Heavy rains triggered flash flooding in Bukavu in DRC on 19 August, causing widespread damage, while the neighboring province of North Kivu was pounded by heavy rain on 20 August, causing the Nyakariba River to overflow its banks in Rutshuru Territory. Flood water, debris, and mud swamped homes and crops, affecting 200 households, according to OCHA. Several neighborhoods in the cities of Pointe-Noire and Brazzaville were affected by a heavy rainfall event on 29 November. This rainfall on top of already saturated soils, from an early start to the rainfall season in September, caused the water level of the river to rise 2.4 m above the riverbed, leading to the flooding of several villages. This situation forced thousands of people to leave their homes and lose their livelihoods, and the government declared a state of emergency, according to the IFRC.

4) EAST AFRICA—E. Bekele and W. M. Thiaw

East Africa, or the Greater Horn of Africa (GHA), spans the equator and extends 10°S–20°N and 20°–50°E. Its northern sector comprises Sudan, South Sudan, Ethiopia, Eritrea, Djibouti, and the northern two-thirds of Somalia. Southern Somalia, Kenya, northern Tanzania, Uganda, Rwanda, and Burundi are in its equatorial sector, while the southern sector encompasses central

and southern Tanzania. The region has a complex terrain, with elevation ranging from about 160 m below sea level at Ethiopia's northern exit of the Rift Valley to more than 5000 m above sea level at glaciated Mount Kilimanjaro. This complex topography is further typified by the presence of large lakes and is reflective of multi-faceted climate zones modulated by local and large-scale forcing such as the deep convective and moisture convergence zone, ENSO (El Niño-Southern Oscillation), the Indian Ocean dipole, the Madden Julian Oscillation, and tropical-extratropical interactions. Rainfall is bimodal in the equatorial sub-region, with two distinct rainfall seasons in March–May (MAM) and October–December (OND). Seasonal rainfall is unimodal in the northern and southern sectors, spanning November–April in the south and June–September in the north. The June–September rainfall over Ethiopia-Eritrea is locally known as "Kiremt" rains.

(i) Temperature

Annual mean temperatures exceeded 26°C over much of Sudan, Somalia, Djibouti, Eritrea, far eastern Ethiopia, and Kenya (Fig. 7.27a). Annual mean temperatures were less than 22°C in most of central Ethiopia. However, anomalously high annual temperatures (1.5–2°C above the mean) were observed across southwestern Ethiopia, southeastern South Sudan, northwestern Kenya, northern Uganda, and northern Sudan (Fig. 7.27b). Annual mean maximum temperatures exceeded 40°C locally in eastern Sudan and ranged between 34° and 40°C in other parts of the country. Eastern Kenya and much of Somalia, Djibouti, and Eritrea observed maximum temperatures between 34° and 38°C, while temperatures were less than 30°C in central and southern Ethiopia and in the Lake Victoria region.

Anomalously elevated temperatures, most prominent in central and southern Sudan, prevailed across much of the region between March and December 2021. Between December–February (DJF) 2020/21 and October–December (OND) 2021, mean temperatures were above normal over much of Sudan and South Sudan. Above-normal temperatures were also observed across much

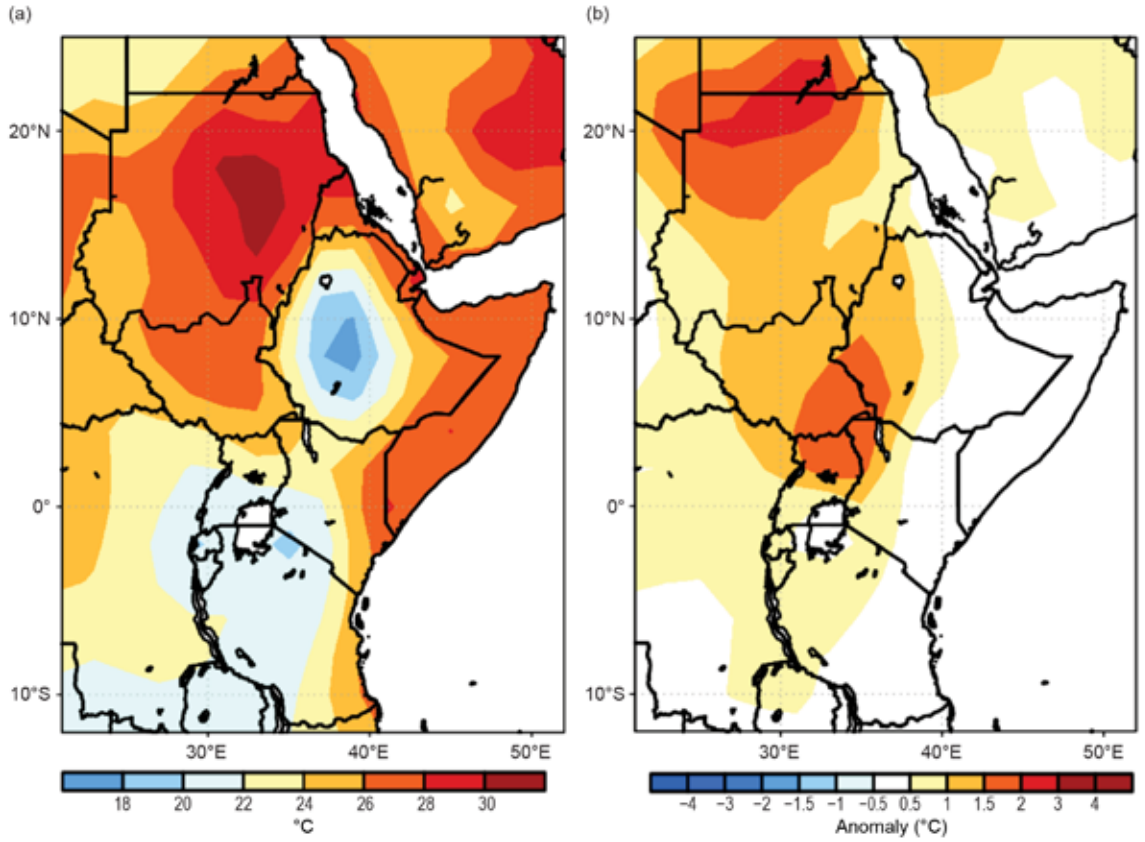

Fig. 7.27. Annual (a) mean temperature and (b) mean temperature anomalies (°C; base period 1991–2020) for East Africa in 2021. (Source: NOAA/NCEP.)

of Uganda, Rwanda, Burundi, western Kenya, western Tanzania, and parts of southeastern Ethiopia. Maximum temperatures were above normal over much of the region during OND, with the highest anomalies located over eastern Sudan, western areas of Ethiopia, eastern South Sudan, Uganda, and western Tanzania. The highlands of central Ethiopia exhibited the lowest annual minimum temperatures (Tmin), less than 12°C. Tmin ranged between 12° and 18°C across the rest of Ethiopia, southern Uganda and Kenya, and much of Tanzania, except for the coastline, and were 20–25°C over much of eastern Sudan, South Sudan, and Somalia.

(ii) Precipitation

Annual rainfall surpassed 1000 mm across western Ethiopia, portions of South Sudan, Uganda, Rwanda, Burundi, and northwestern Tanzania (Fig. 7.28a). Western Kenya, central Ethiopia, eastern South Sudan, northeastern Uganda, and much of Tanzania received rainfall between 600 mm and 1000 mm. Totals were less over northern Sudan, Eritrea, Djibouti, and northern Somalia, with rainfall amounts ranging between 50 mm and 600 mm. Overall, rainfall was below normal over much of equatorial East Africa (Fig. 7.28b). Rainfall deficits exceeded 250 mm over parts of southern Ethiopia, coastal Kenya, and southern Tanzania. Rainfall totals averaging 150–250 mm below the mean were recorded over parts of central and southeastern Ethiopia, southern Somalia, much of Kenya, Uganda, Rwanda, Burundi, and Tanzania. Kiremt rains (June–September) were 1–2 mm day^{-1} (~120–240 mm total) below normal over southwestern Ethiopia. The seasonal rains were generally below normal over northern and central Ethiopia, most of South Sudan, and Uganda (see Fig. 7.24).

Annual rainfall was below the 10th percentile over southern Ethiopia, southern Somalia, and portions of Kenya, northern Uganda and southern Tanzania. The most significant rainfall deficits, below the 3rd percentile, were observed over portions of southern Ethiopia, localized areas of southern Somalia, northern Uganda, and southern Tanzania. Most of equatorial East Africa received below-average rainfall during all seasons, with deficits most pronounced during OND over southern Ethiopia, southern Somalia, much of Kenya, and Tanzania. Rainfall was also below average over southwestern Ethiopia, South Sudan, Uganda, Rwanda, and Sudan.

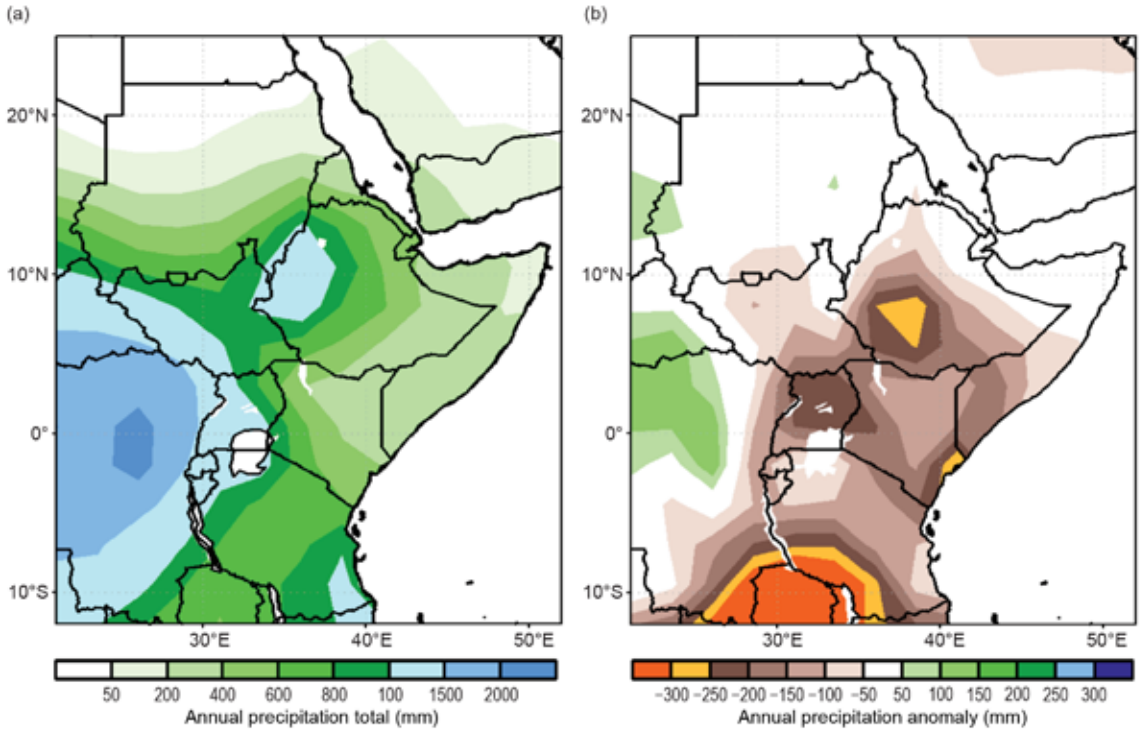

Fig. 7.28. Annual (a) total rainfall and (b) total rainfall anomaly (mm; base period 1991–2020) for East Africa. (Source: GPCP via NOAA/NCEP.)

(iii) Notable events and impacts

The annual total rainfall was the lowest on record in portions of equatorial East Africa (> 2 std. dev.), leading to three consecutive failed rainy seasons that resulted in one of the worst threats to food security in 35 years for more than 20 million people in eastern Africa, according to the U.S. Agency for International Development Famine Early Warning Systems Network (FEWS NET).

NOAA's satellite rainfall estimates (RFE2) indicated heavy downpours upstream of the Blue Nile and Baro–Akoba River basin in Ethiopia, with June–September accumulation exceeding 1000 mm, contributing to major inundations downstream in Sudan and South Sudan. The heavy rains resulted in significant increases in river levels that submerged low lying lands with significant impacts on livelihoods, food production, and drinking supplies. According to the United Nations, the flooding affected more than 835,000 people in 33 of South Sudan's 78 counties. The states of Jonglei, Unity, and Upper Niles suffered the worst impacts with 80% of the flood victims, including 305,000 in Jonglei State, 220,000 in Unity, and 141,000 in Upper Nile.

5) SOUTHERN AFRICA—A. C. Kruger, C. McBride, M. Robjhon, and W. M. Thiaw

Southern Africa covers the southern part of the African continent extending from about 5° to 35°S. It comprises Angola, Namibia, Zambia, Botswana, Zimbabwe, Malawi, South Africa, Lesotho, Eswatini, and Mozambique. The region is characterized by two main seasons. While the wet season spans from November of the predecessor year to April, the dry season lasts from May to October.

(i) Temperature

During 2021, annual mean temperatures averaged between 12° and 26°C in the region, with higher values exceeding 20°C across northern Namibia, Angola, northern Botswana, Zambia, northern Zimbabwe, Malawi, and Mozambique (Fig. 7.29a). The warmer regions included northwestern Angola and coastal Mozambique, where annual mean temperatures averaged 24–26°C. In contrast, the colder regions included much of Namibia, southern Botswana, central Zimbabwe, South Africa, Lesotho, and Eswatini, where annual mean temperatures averaged between 12°

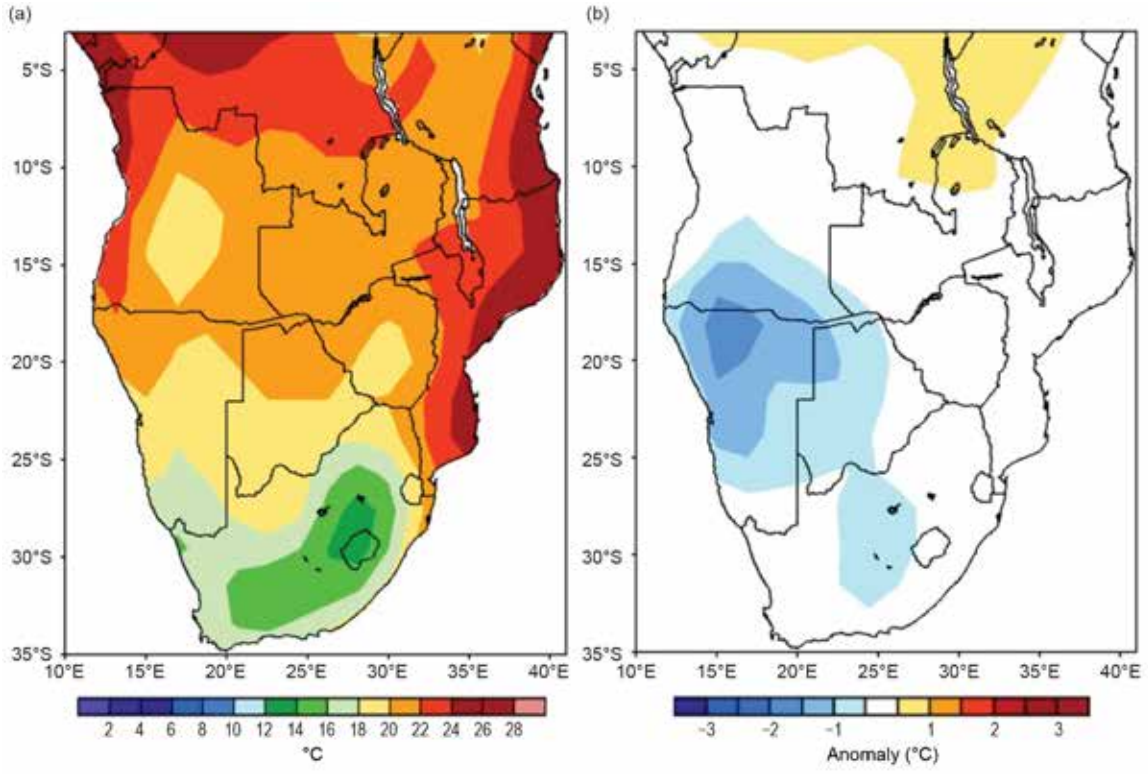

Fig. 7.29. Annual (a) mean temperature and (b) mean temperature anomaly (°C; base period 1991–2020) for southern Africa. (Source: NOAA/NCEP.)

and 20°C. The lowest annual mean temperatures registered over the interior of South Africa and Lesotho, and averaged between 12° and 16°C.

Annual mean temperatures were well below normal, with departures from the long-term average up to –2°C, over southern Angola, Namibia, and northwestern Botswana (Fig. 7.29b), ranking 2021 among the top 5% of the coldest years on record in these areas. Annual mean temperatures were near-normal elsewhere. An analysis of mean temperatures throughout the year show that below-normal mean temperatures persisted over southern Angola, Namibia, and parts of Botswana during all months, except for April, when near to above-normal mean temperatures were observed over the region. The coldest month was July, when well below-normal mean temperatures were observed over the region, with the largest departures from normal temperature, up to –3.5°C over parts of Angola, northeastern Namibia, and northwestern Botswana. On the seasonal time scale, mean temperatures remained below normal during DJF 2020/21, JJA, and SON over southern Angola and Namibia. Mean temperatures were above normal across central Angola, Zambia, Zimbabwe, Malawi, and northern Mozambique during SON.

South Africa experienced a somewhat warm year, which was quite mild compared to previous years. The warm year can be attributed, at least in part, to well-above normal rainfall over most of the country. The annual mean temperature anomalies for 2021, based on the data of 26 climate stations, was above average, making it approximately the 13th-hottest year on record since 1951 (Fig. 7.30). A warming trend of 0.16°C decade^{-1} is indicated for the country, statistically significant at the 5% level.

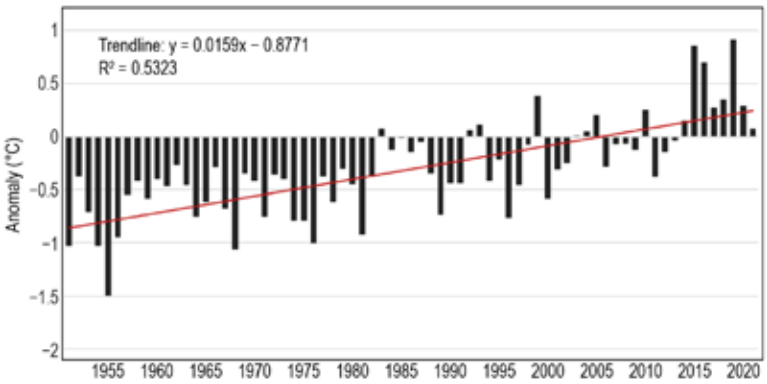

Fig. 7.30. Annual average surface temperature anomalies (°C; base period: 1991–2020) over South Africa based on 26 climate stations for the period 1951–2021. The linear trend is indicated by the red line. (Source: South African Weather Service.)

Annual maximum temperature (Tmax) averaged 20–34°C in the region. While Tmax ranged between 30° and 34°C in southern Angola, Namibia, southwestern Zambia, Botswana, western Zimbabwe, southern Malawi, and northern Mozambique, lower values averaging between 20° and 26°C were reported across much of South Africa, Lesotho, and Eswatini. Tmax was 0.5–1.5°C below normal over southern Angola, Namibia, southern Botswana, central South Africa, and Lesotho. Tmax was 0.5–1.5°C above normal farther north across northeastern Angola, Zambia, northern Zimbabwe, Malawi, and northern Mozambique.

Annual minimum temperature (Tmin) ranged from 4° to 24°C throughout the region, with values of less than 10°C in southern Namibia, South Africa, and Lesotho. Tmin was once again 0.5–2.5°C below normal over western portions of the region, including southern Angola, western Zambia, Namibia, and Botswana and near-normal elsewhere. Tmin ranked in the 3rd percentile over Namibia.

(ii) Precipitation

During 2021, annual rainfall was unevenly distributed across the region. While northern Angola and the eastern sector encompassing southern Malawi, Mozambique, Eswatini, and eastern South Africa had totals in excess of 800 mm, the central areas, including southern Angola, northeastern Namibia, Zambia, Botswana, central South Africa, Lesotho, and Zimbabwe received 400–800 mm. Limited accumulation of less than 400 mm was observed in the west across southwestern Angola, western Namibia, and northwestern South Africa (Fig. 7.31a).

Annual moisture deficits exceeded 250 mm across southern Angola, northern Namibia, Zambia, Malawi, and northern Mozambique, placing 2021 in the 3rd percentile in most areas. Annual rainfall was above normal over northern Angola, southwestern Botswana, central and northeastern South Africa, Eswatini, and southern Mozambique, with the largest surpluses of 150–200 mm over local areas in northern Angola and central South Africa (Fig. 7.31b).

An examination of the seasonal rainfall anomalies revealed an early onset of the rainfall season over eastern Angola and western Zambia in SON with departures 25 mm to 150 mm above the mean and ranking in the 90th percentile, while southwestern Angola and Mozambique experienced a slow start to the rainfall season. The peak of the rainfall season (DJF 2021/22) was extremely dry over southern Angola, Zambia, and northern Mozambique, with totals 150–250 mm below the mean and ranking in the lowest 3rd percentile. In contrast, eastern Namibia, Botswana, much of South Africa, Lesotho, Eswatini, Zimbabwe, and the southern two-thirds of Mozambique exhibited positive departures from the mean in the 50–350 mm range. Southern Mozambique had the highest moisture surpluses, up to +350 mm. Rainfall deficits (50–150 mm below the mean)

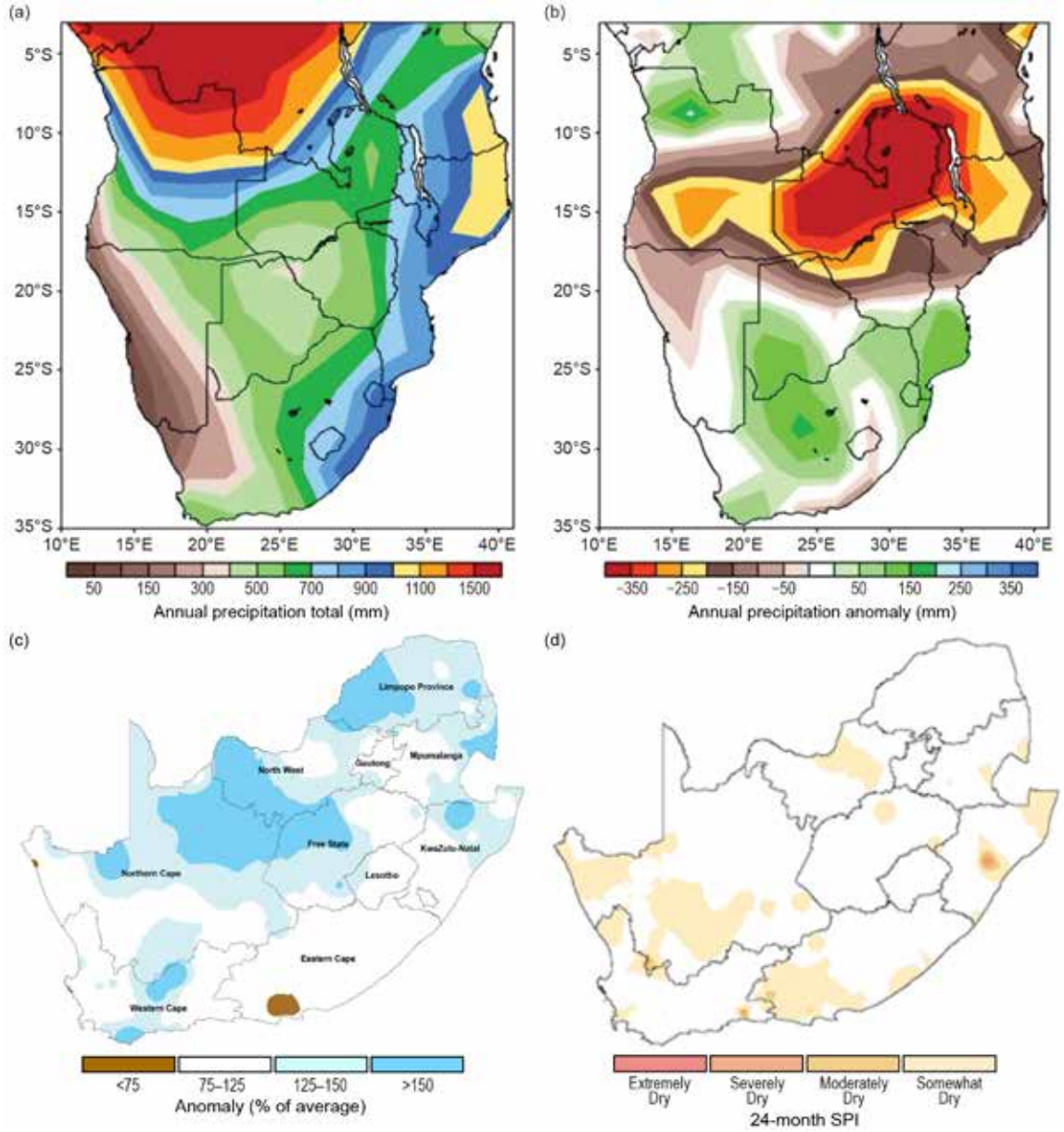

Fig. 7.31. Annual (a) rainfall totals and (b) rainfall anomaly (mm) for southern Africa. (c) Annual rainfall anomalies (% of average) for South Africa for 2021. (d) 24-month SPI map for South Africa ending December 2021. Base period for (a–c) is 1991–2020. (Sources: (a, b) GPCP via NOAA/NCEP and (c, d) South African Weather Service.)

prevailed toward the end of the rainfall season in MAM over much of the eastern sector from Zambia to eastern South Africa.

Figure 7.31c shows rainfall anomalies (expressed as percent of base period) for South Africa. The most significant feature of the rainfall during 2021 was the well-above normal rainfall received over extensive parts of South Africa. During 2021, ENSO was in a La Niña phase, which is associated with above-normal rainfall over most of the summer rainfall regions. The section of South Africa experiencing drought further decreased over the past year, due to the good rains in the early austral summer rainfall season of 2021/22, especially from November onwards. Figure 7.31d shows the 24-month SPI ending December 2021, which indicates that there were still some areas in the western and southern interior that could be considered somewhat dry, which shows persistence of the long-term drought this region has been experiencing (for almost a decade in some places).

The austral winter season (July–August) had unseasonal significant rainfall in the central and northwestern interior of South Africa, which persisted into spring. The early austral summer, starting in October, had well above-normal rainfall over especially the drought-stricken western interior, and spread to the south in November. In December, all of South Africa received above-normal rainfall. In many places, the monthly rainfall received were multiples of the normal rainfall totals. The early-summer rainfall season was, as a whole, characterized as above normal, except for some areas in the east and southeast of South Africa.

(iii) Notable events and impacts

Tropical Cyclone Eloise, with winds of around 140 km h^{-1} and gusts of up to 160 km h^{-1}, made landfall over the Sofala Province in Mozambique on 23 January and soaked several areas in the Sofala, Zambezia, Inhambane, and Manica provinces, with rainfall amounts up to 135 mm, according to the NOAA satellite rainfall estimates version 2 (RFE2). The resulting flooding affected 314,000 people, including 11 fatalities, according to United Nations Office for the Coordination of Humanitarian Affairs (OCHA). An estimated 600 classrooms and over 80 health centers needed repairs. In the aftermath of the storm, a low-pressure system brought heavy rains of about 135 mm during 14–15 February, according to the RFE2, and caused flooding over southern Mozambique, including the Maputo and Gaza provinces on 15 February. About 3000 homes were damaged or destroyed according to OCHA.

Extremely heavy rains of up to 105 mm drenched the Luanda area of Angola on 18–19 April, according the NOAA's CPC rainfall estimates by morphing technique (CMORPH), and triggered flash floods that affected more than 8000 people, including 14 reported fatalities and 12 injuries, and damaged over 1600 homes, according to the government of Angola.

In February northern parts of South Africa received substantial rain, but this was accompanied by much damage to infrastructure, mainly due to flash floods. In March, while it was hot in the eastern parts, with accompanying heat waves and record high temperatures, the Western Cape received high unseasonal rainfall, accompanied by flooding in places in the Cape Town metropole. The dry conditions in the western and southern interior were exacerbated in April with very low rainfall and abnormally high maximum temperatures. These conditions extended into May.

A winter storm brought extremely heavy rains (about 90 mm) over Cape Agulhas in the Western Cape Province of South Africa on 5 May and caused severe local flooding that damaged several homes and roads, and affected many people, according to local authorities in the province.

The high December rainfall totals were associated with a number of negative impacts. Of particular note, hundreds of families in Piet Retief, Mpumalanga, were left homeless after flash floods left a trail of damage and destruction on the 1st. The rain was accompanied by strong winds that blew roofs off houses and significant structural damages. Roads were also affected. At least two fatalities were reported on the 4th and 5th and at least two cars were swept away by floods on the 7th. Six people were killed and 44 injured after heavy rain affected Mthatha in the Eastern Cape

on the 9th. Seventy-seven families in the King Sabata Dalindyebo (KSD) Local Municipality lost their homes and 15 other families saw their houses collapse during heavy rain. Livestock were killed, and a preschool was damaged, along with power lines and other infrastructure.

6) WESTERN INDIAN OCEAN ISLAND COUNTRIES—G. Jumaux, K. R. Dhurmea, A. Abida, B. Andrade, M. Robjhon, and W. M. Thiaw

The Western Indian Ocean island countries consist of Madagascar, Seychelles, Comoros, Mayotte (France), Réunion (France), Mauritius, and Rodrigues (Mauritius). Overall, 2021 was warmer than normal (Fig. 7.32). Annual rainfall was below normal in Seychelles and Comoros and close to normal over the rest of the island countries (Fig. 7.32). There are two distinct main seasons: a warm and wet period spanning from November of the antecedent year to April, and a cold and dry season lasting from May to October.

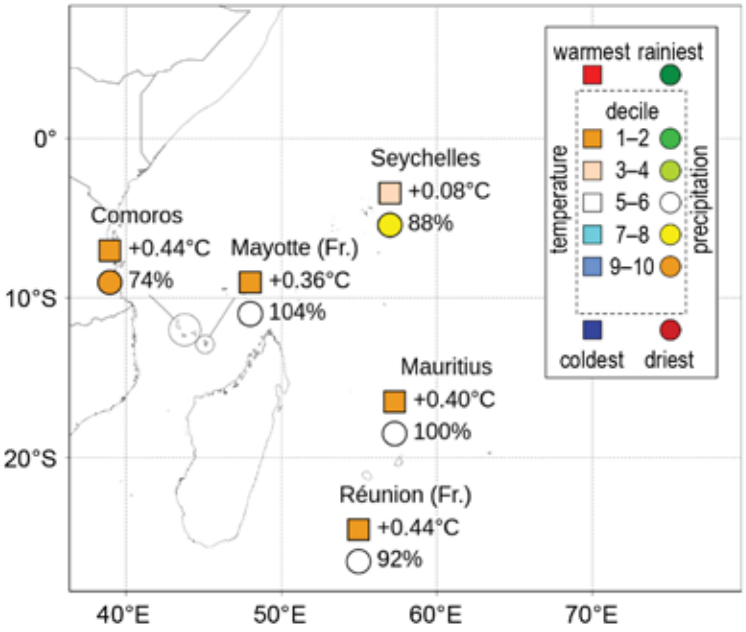

Fig. 7.32. Mean annual temperature anomalies (°C, squares), annual rainfall ratio to normal (%, circles), and their respective deciles for the western Indian Ocean island countries in 2021 (1991–2020 base period). (Sources: Météo France; and Meteorological Services of Mauritius, Seychelles, and Comoros.)

(i) Temperature

The annual mean temperature over Réunion Island (based on three stations) was 0.44°C above normal, the fifth highest since record keeping began in 1968 (Fig. 7.33). April and November, 0.9° and 0.8°C above normal respectively, were among the three warmest for their respective months. The annual minimum temperature anomaly was the second highest on record (+0.63°C), but 0.40°C below the record set in 2019. Maximum temperatures were near-normal during the cold season, but the annual average was still above normal (+0.26°C).

Over Mauritius, the annual mean temperatures (based on two stations at Vacoas and Plaisance) were above normal by 0.40°C, marking the eighth-warmest year since 1960. Both the maximum and minimum temperatures were above normal by 0.40°C. Mean temperatures were near-normal for most months (anomaly < +0.5°C), except for April, March, November, and December, where the anomaly exceeded +0.5°C. At Rodrigues, the mean temperature was near normal (+0.10°C). The maximum temperature was 0.30°C below normal, while the minimum was 0.50°C above normal.

In Comoros, the annual mean temperature for 2021 (based on four stations) was 27.1°C, which was 0.44°C above normal and the fourth-warmest year since 1991. The annual minimum

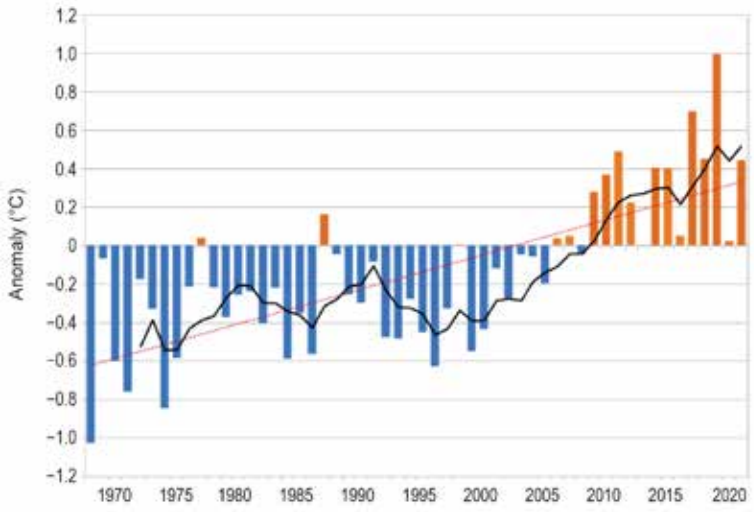

Fig. 7.33. Time series of Réunion Island annual mean temperature anomalies (°C; 1991–2020 base period) for the period 1968–2021. The black line is the 5-yr running mean and the red line represents the linear trend. (Source: Météo-France.)

temperature was 23.4°C, and the maximum temperature was 30.9°C. The absolute minimum temperature recorded was 17.4°C at Hahaya on 4 August. The absolute maximum temperature of 34.8°C was recorded at Hahaya on 28 December.

In Mayotte (Pamandzi Airport), the annual mean temperature was the seventh highest in the 61-year record, with at 27.41°C (0.36°C above normal). Five consecutive months from August to December were each among their five warmest on record.

At Seychelles International Airport, the annual mean temperature anomaly for 2021 was 0.08°C above normal, the 11th highest since 1972. Nearly all months were near-normal except March and October to December were above normal, and May was below normal.

Over Madagascar, annual mean temperatures averaged 20–26°C, with higher temperatures over the low-lying areas along the western and northern coasts and lower temperatures over the central highlands (Fig. 7.34a). Annual temperatures were slightly above normal with positive departures from the long-term mean ranging from +0.25° to +0.5°C across the western and central portions of the island (Fig. 7.34b). The annual mean temperature ranked between the 70th and 85th percentile over much of Madagascar, except for the mid-western sector, which had temperatures ranking in the 85th to 90th percentile.

An analysis of the temperatures throughout the year indicated that warmer-than-normal conditions dominated much of Madagascar during January–March and October–December when many areas experienced temperatures 1–2°C above normal, placing these months in the 90th to 97th percentiles. In contrast, the austral autumn season and latter part of the winter brought colder-than-normal conditions over the island.

On the seasonal time scale, DJF 2020/21 temperatures were well above normal throughout Madagascar, with the largest positive anomalies ranging from +1.25° to +1.5°C over the southern areas. March–May (MAM) brought changes with colder weather in the southern sector, near-normal conditions in the central areas, and elevated temperatures in the northeast. Warmer weather extended over central and northern Madagascar during September–November (SON) with the largest positive departures of +0.5° to +0.75°C observed in the Midwest.

Maximum temperatures (Tmax) ranged from 22° to 32°C over Madagascar with a steep east–west temperature gradient marked by values higher than 28°C in the west and lower than 26°C in the east. Tmax was 0.5–1°C above normal in the west-central and northwestern parts of the island. Tmin averaged 14–26°C over Madagascar and exceeded 20°C along the western and northern coasts and was above-normal across the northern two-thirds of the country, with departures from normal in the 0.25–0.75°C range. The largest positive anomalies (+0.5° to +0.75°C) were observed over western Madagascar ranked in the 90th to 97th percentiles.

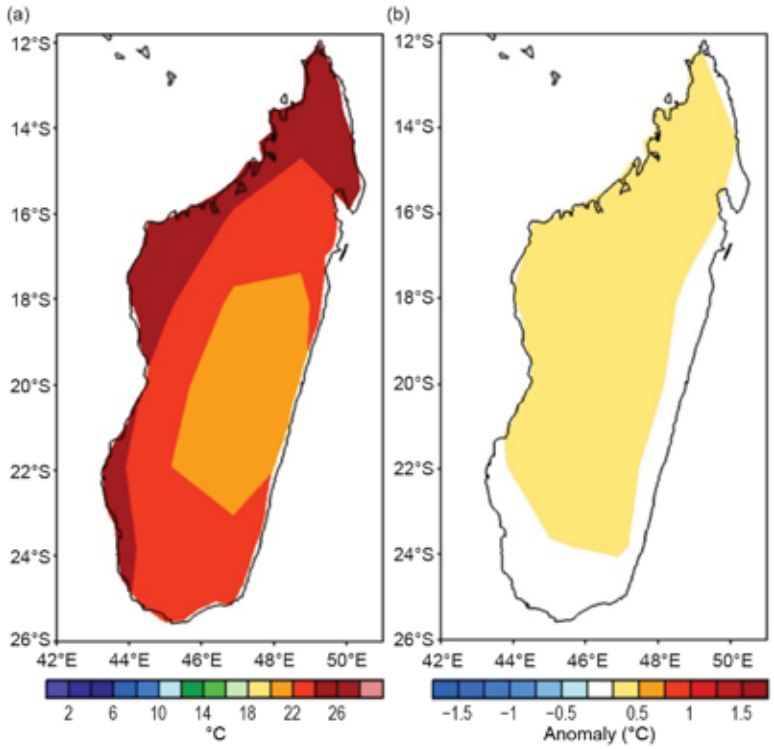

Fig. 7.34. Annual (a) mean temperature and (b) Annual mean temperature anomaly (°C; base period 1991–2020) for Madagascar. (Source: NOAA/NCEP.)

(ii) Precipitation

The annual rainfall total over Réunion Island was 92% of normal. Highlands and North Réunion Island experienced deficits during the rainy season (December–April), while the rainfall over East Réunion Island was close to normal. April was the wettest month of the year, reducing deficits just before the dry season (May–November) which was close to normal. April and August were among the wettest for their respective months over 50 years, at 220% and 200% of normal, respectively. Conversely, February and May were among the driest for their respective months, at 32% and 38% of normal. Remarkable rainfall intensities were recorded on the volcano and its southern flank (132 mm in 1 hour at La Crête station and 700 mm in 24 hours at Bellecombe-Jacob) on 28 August, which was quite unusual during the dry season.

In Mauritius, the mean annual rainfall total (based on 23 stations) was about 2025 mm, which was normal (average is 2018 mm); however, a marked seasonal variability was observed (Fig. 7.35a). The summer months January–March, which are the rain-bearing months, were all deficient in rainfall. February 2021 was the ninth driest on record and the driest in the last 19 years. November, another summer month, was the driest on record (since 1904), with only 11% of its normal rainfall recorded. Dry conditions prevailed until the first two weeks of April. The second half of April was exceptionally wet, recording most of the rainfall for the month with frequent floods and flash floods. Overall, April 2021 was the fifth wettest on record (since 1904) and the wettest in the last 19 years. A marked seasonal variability was observed at Rodrigues, with a wet winter and a dry summer. Most winter months had above-normal rainfall, except October. August was the wettest on record since 1954. All summer months had below-normal rainfall, except December, which was the third wettest in the last 35 years. March was the driest in the last 35 years and the second driest on record since 1954.

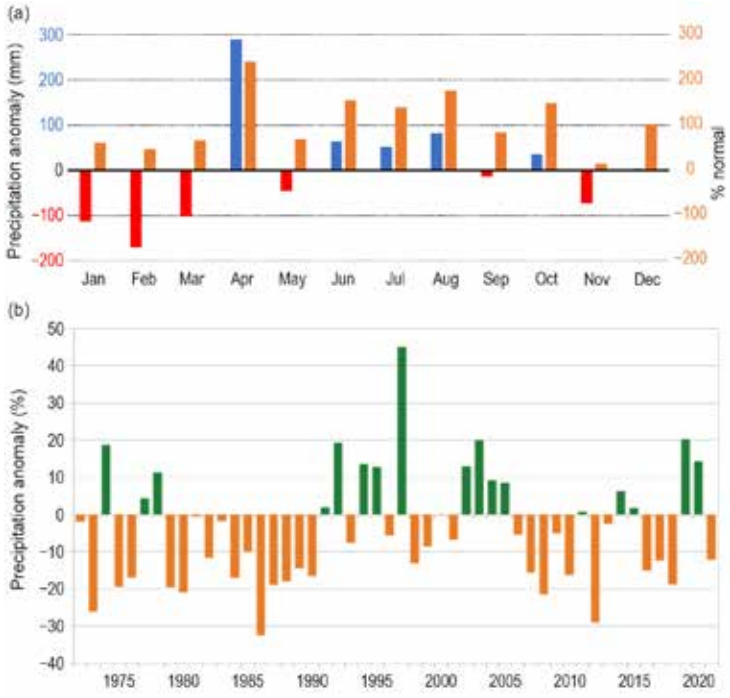

Fig. 7.35. (a) Monthly rainfall anomalies (mm; 1991–2020 base period) and percent of normal in Mauritius in 2021 (Source: Meteorological Services of Mauritius). (b) Annual rainfall anomaly time series (%; 1991–2020 base period) in Seychelles for the period 1972–2021. (Source: Seychelles Meteorological Authority.)

In Comoros, the total annual rainfall (average of three stations) was 1253 mm, which was 74% of normal and the fifth driest since 1991. The highest annual amount of rainfall compared to normal was recorded at the Moroni station at 112%. All months were below normal, except April and October.

In Mayotte, the total annual rainfall (average of two stations) was 1548 mm, which was 104% of normal. The total rainfall during the wet season was close to normal, but five consecutive months from May to September, during the dry season, were each below normal, leading to a 48% deficit in this period; this was the fifth driest such period in the 61-year record.

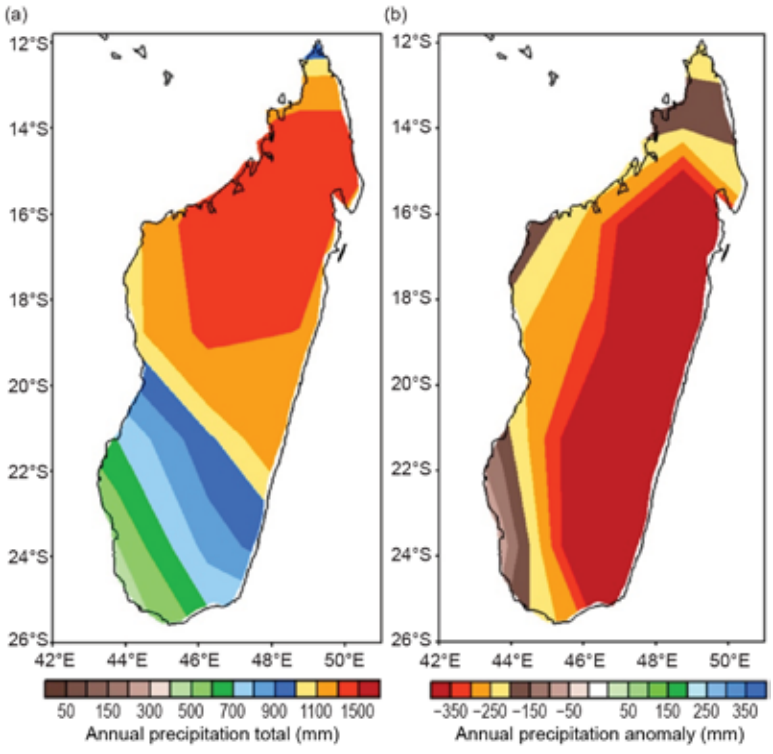

Fig. 7.36. Annual (a) rainfall total and (b) rainfall anomaly (mm; base period 1991–2020) for Madagascar. (Source: GPCP via NOAA/NCEP.)

In Seychelles, the total annual rainfall (2152 mm) was 88% of average, making 2021 the 20th-driest year on record since 1972 (Fig. 7.35b). Mainly related to the negative Indian Ocean dipole, all months between June and December had below-normal precipitation, except September.

In Madagascar, annual rainfall totals showed a north–south gradient, with a higher accumulation in excess of 1000 mm over the center and northern portions of the country and gradually decreasing amounts to about 400 mm in the southern areas (Fig. 7.36a). Annual rainfall was well below average, with departures varying from 50 mm to over 350 mm below the mean. The largest rainfall deficits surpassed 350 mm

over the eastern half of the interior of the island (Fig. 7.36b). The drier-than-normal conditions over central and eastern Madagascar placed 2021 among the top 3% driest over the past 30 years.

Examination of rainfall throughout the year indicated that drier-than-normal conditions persisted over Madagascar from January to May and October to December. The driest month was January, with deficits of 200–250 mm over eastern Madagascar.

Seasonal rainfall was well below average, with deficits between 25 and 350 mm across Madagascar during DJF 2020/21. The eastern half of the country was the driest region, with rainfall more than 100 mm below the mean, ranking in the 3rd percentile in coastal areas. The moisture deficits persisted and extended over the southern two-thirds of the island during MAM, while the northern and northeastern sectors registered rainfall surpluses. Rainfall deficits were observed over much of Madagascar during September–November, with the highest deficits of 50–150 mm, placing this season in the top 3% driest among such seasons.

(iii) Notable events and impacts

Tropical cyclones are the main natural hazard that can cause high impact flooding over the western Indian Ocean countries. With 12 named tropical storms and seven tropical cyclones, the November 2020–April 2021 tropical cyclone season was the fourth most active since 1998/99 (see section 4g6 for details).

Tropical storm Chalane, the first in the season made landfall in Fenoarivo Atsinanana in eastern Madagascar on 27 December 2020, causing flooding, infrastructure damage, and affected people in Toamasina, where rainfall accumulation totaled 351 mm during 26–27 December.

Tropical Cyclone Eloise made landfall as a tropical storm over Antalaha in northeastern Madagascar on 19 January, dumping 115 mm of rainfall, causing flooding with one fatality, destroying houses, and affecting ~1000 people in Antalaha, Maroantsetra, Vavatenina, and Toamasina, according to the United Nations Office for the Coordination of Humanitarian Affairs (UN OCHA). Eloise re-intensified into a tropical cyclone after crossing Madagascar and made landfall over central Mozambique four days later.

Extremely heavy rains (about 135 mm) fell during 11–17 February, triggering flooding and landslides, with one fatality reported and damaging many houses across several regions in central and western Madagascar, including the Alaotra Mangoro, Analamanga, Melaky, and Menabe. Nearly 1400 people were affected, according to the National Bureau of Risk and Disaster Management (BNGRC) in Madagascar.

The 2020/21 below-average rainfall season prolonged an unprecedented 6-year drought over southern and southwestern Madagascar, resulting in widespread food insecurity and malnutrition for over 1.14 million people over the Grand Sud, Great South, in Madagascar, according to the United Nations Fund for Population Activities.

f. Europe and the Middle East—P. Bissolli, Ed.

The region "Europe and the Middle East" in this context is defined by the so-called RA VI Region of WMO, which comprises 51 countries. The names of the countries are listed on the WMO website https://public.wmo.int/en/about-us/members. Throughout this section, 1991–2020 is the base period used for both temperature anomalies and precipitation percentages, unless otherwise specified. European countries conform to different standards applied by their individual national weather services. All seasons mentioned in this section refer to the Northern Hemisphere. More detailed information can be found in the *Monthly and Annual Bulletin on the Climate in RA VI – Europe and the Middle East*, provided by WMO RA VI Regional Climate Centre on Climate Monitoring (RCC-CM; http://www.dwd.de/rcc-cm). Anomaly information has been taken from Figs. 7.38–7.41 and aggregations of CLIMAT station data when national reports are not available. Appendix Table A7.1, at the end of this chapter, provides a list of included countries and the record lengths for both temperature and precipitation, along with their respective annual anomalies where available.

1) OVERVIEW

Based on the Global Historical Climate Network (GHCN) v4.0.1 dataset (Menne et al. 2018), Europe (36°–72°N, 23°W–60°E) experienced a slightly warmer-than-normal year with an anomaly of +0.2°C (Fig. 7.37) above the 1991–2020 average. This reflects the continuation of the long-term warming trend in Europe. Most of Europe had anomalies of close to normal, between −0.3°C and +0.5°C (Fig. 7.38). Only parts of southern Greece, most of Türkiye, west Kazakhstan, and Italy, and the Caucasus region were well above average with anomalies around +1.0°C. Türkiye reported its fourth-warmest year on record and west Kazakhstan its fifth warmest.

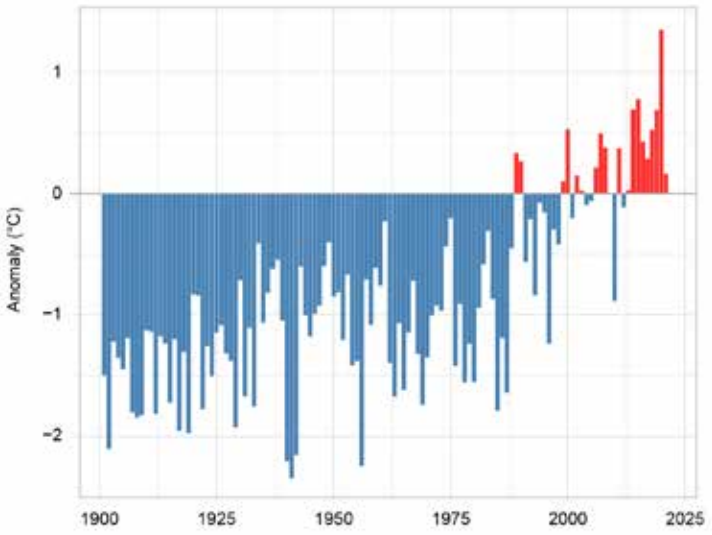

Fig. 7.37. Annual average land surface air temperature anomalies for the period 1900–2021 for Europe (36°–72°N, 10°W–60°E) relative to the 1991–2020 base period. (Source: GHCN version 4.0.1 dataset [Menne et al. 2018].)

Precipitation was also close to normal for many countries in Europe. For the southeastern part of Türkiye, the Middle East, west Kazakhstan, and areas around Caspian Sea, the year was characterized by a large precipitation deficit, as low as 40–60% of normal across wide regions (Fig. 7.39).

During winter 2020/21 (DJF), temperatures were above average or close to normal over most of the RA VI domain, except for European Russia, the United Kingdom, and Ireland (Fig. 7.40). Well-above-normal temperatures occurred over the southeast of RA VI and the western European Arctic with anomalies ranging from 1.0°C to 3.0°C above normal. The year started with a mild January (up to 4.0°C above normal) in southeastern Europe and the western European Arctic, and a generally colder January in Western Europe; a change of the prevailing atmospheric circulation with a significant weakening of the polar vortex took place in February, and a sharp air mass border developed over Europe with very cold air in the northern half and warm air in the southern half. Later, the cold air also moved to the southeast, which caused considerable variation in temperatures during February. Precipitation anomalies during winter (Fig. 7.41) were scattered; many parts of Europe were near normal, with local dry spots (as low as 40% of normal) in southern Spain, the west coast of Norway, the Baltic states, and the Middle East. Due to westerly weather conditions and cut-off lows, many parts of the Mediterranean and Eastern Europe, as well as south Caucasus received above normal precipitation—up to 160% of normal or more.

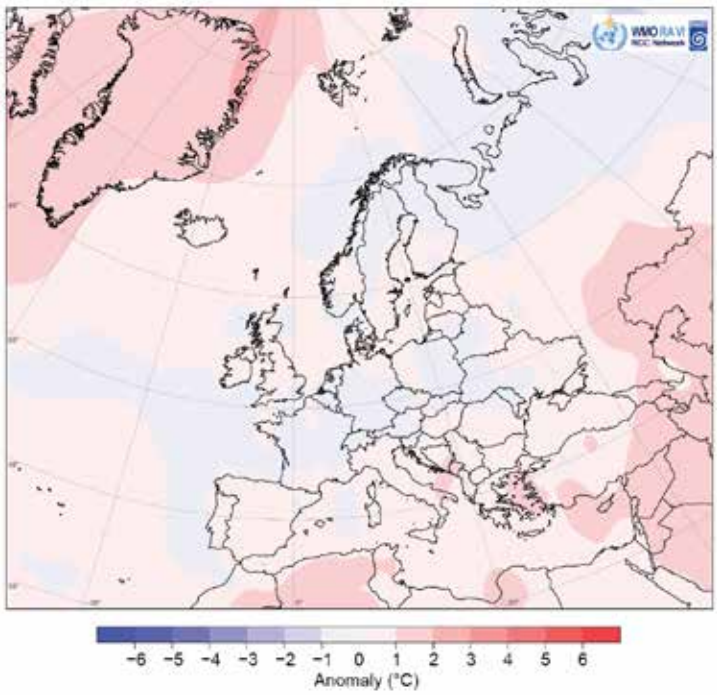

Fig. 7.38. Annual mean air temperature anomalies (°C; 1991–2020 base period) in 2021. (Source: interpolated climate station data over land and ship data over oceans; Deutscher Wetterdienst [DWD].) Since 1991–2020 normals were still not available for all stations, the 1991–2020 anomalies were computed from gridded 1981–2010 anomalies as a preliminary solution.

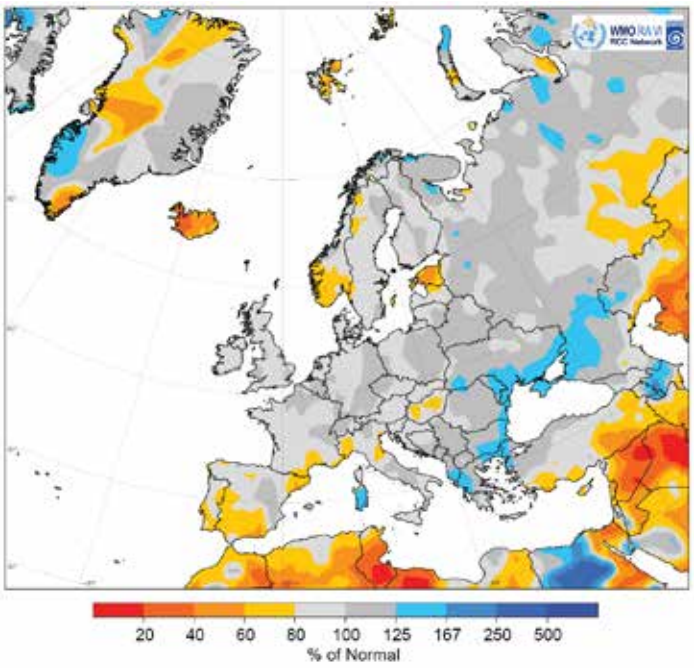

Fig. 7.39. European precipitation totals (% of 1991–2020 average) for 2021. Please note that data over Iceland should be interpreted with caution because it appears to be low compared with recent national data from the Icelandic Meteorological Service, which are not yet included in this analysis. A data check has been in progress at the time of publication of this report. Annual precipitation totals in Iceland were about 85–100% of normal in 2021. (Source: GPCC, created by DWD.)

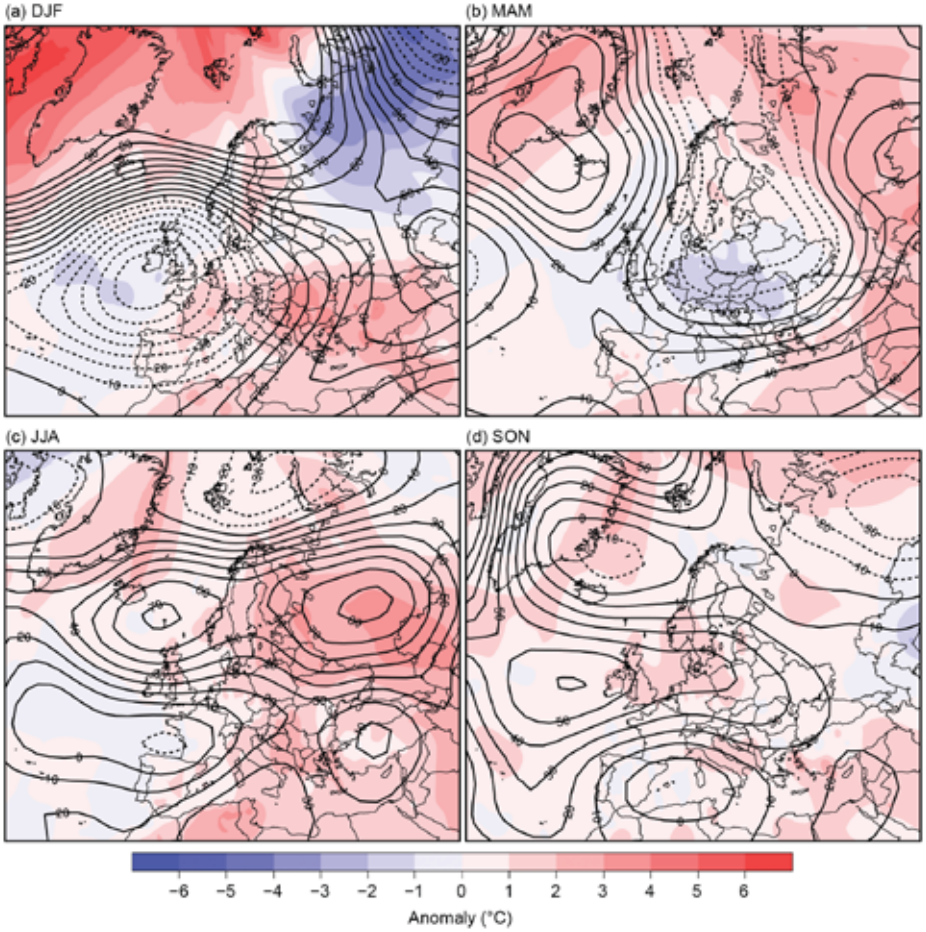

Fig. 7.40. Seasonal anomalies (1991–2020 base period) of 500-hPa geopotential height (contour; m) and surface air temperature (shading; °C) using data from the NCEP/NCAR reanalysis and DWD, respectively, for (a) DJF 2020/21, (b) MAM 2021, (c) JJA 2021, and (d) SON 2021.

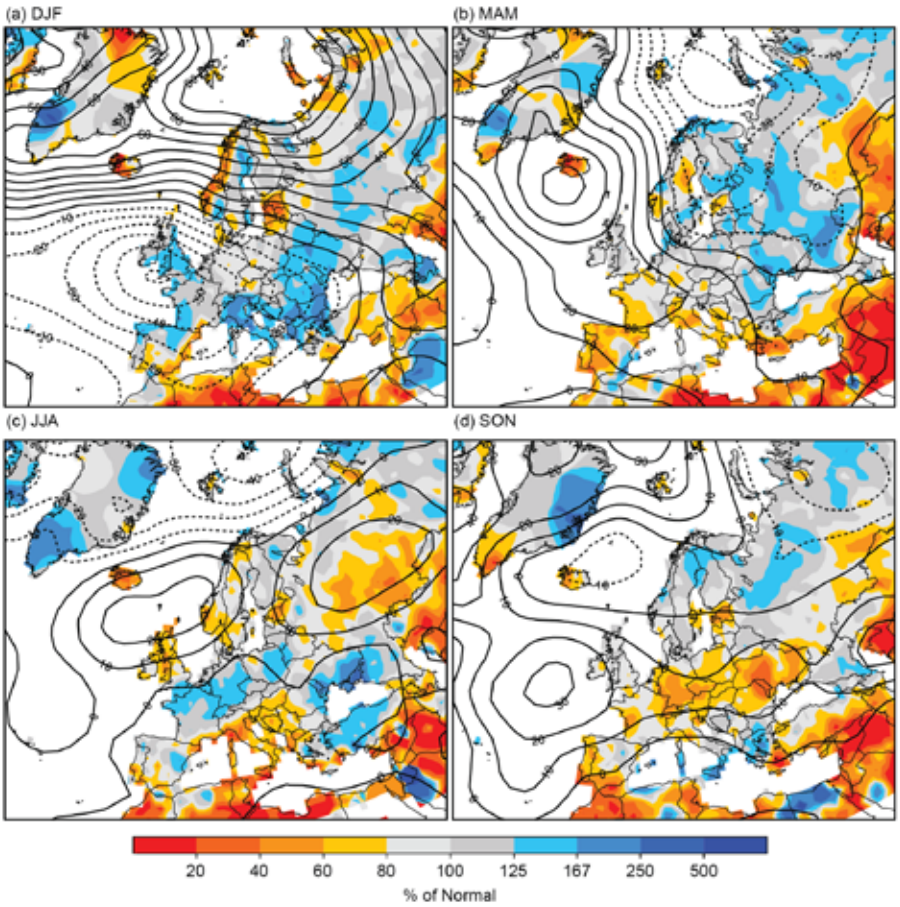

Fig. 7.41. Seasonal anomalies for 2021 (1991–2020 base period) of sea level pressure (hPa) from NCAR/NCEP reanalysis (contours) for (a) DJF 2020/21, (b) MAM 2021, (c) JJA 2021, and (d) SON 2021. Colored shading represents the percentage of seasonal mean precipitation for 2021 compared with the 1991–2020 mean from GPCC (Schneider et al. 2018). Please note that data over Iceland should be interpreted with caution because it appears to be low compared with recent national data from the Icelandic Meteorological Service, which are not yet included in this analysis. A data check has been in progress at the time of publication of this report.

Spring was dominated by below-normal air temperatures across most European areas, with anomalies exceeding –2.0°C or –3.0°C in Western and Central Europe. A strong area of high pressure was present over the North Atlantic and Greenland, and winds became more northerly than usual over northwestern Europe, bringing a persistent flow of cold polar air down to most of the continent, while also keeping the western part of Europe mostly dry. Spain, Portugal, Italy, and Greece received precipitation mostly around 60% of normal, while the Middle East had much higher precipitation deficits, as less than 20% of the normal rain fell in some areas. The situation was reversed northeast over western European Russia and Scandinavia, with southerly winds bringing warm air to the region. In May, low pressures and associated frontal weather systems prevailed over northwestern Europe, bringing much wetter conditions. Farther east, western European Russia saw a similar pressure pattern at the beginning of May, with strong and warm southerly winds bringing record warmth to the region (4.8°C above average), including to the fringes of the Arctic and west Kazakhstan.

Due to extended high-pressure influence, summer 2021 was the second-warmest summer on record (after 2010) for the RA VI region (+0.7°C anomaly) and for a number of countries, including Latvia (+2.6°C), Greece (+1.6°C), and Malta (+2.0°C). June was the second-warmest June on record for the RA VI region at 1.5°C above normal; particularly high anomalies were observed in Finland (+3.7°C) and western European Russia. The hottest temperatures were observed at the end of the season over the Mediterranean, the Balkan Peninsula, and Türkiye, exceeding 40°C

at times. During this hot spell, a new (provisional) European maximum temperature record was set in Sicily, Italy, where temperatures reached 48.8°C due to anticyclonic weather conditions. Characteristically for the blocking high pressure situation over Europe, summer in Italy and the Balkan states was dry, with precipitation totals as low as 60–80% of normal, while parts of Central Europe, Western Europe and Eastern Europe recorded close to normal or precipitation totals up to 167% of normal (locally even more) mainly due to higher low-pressure influence than usual and enhanced convective activity.

Autumn was warmer than average for most European countries, especially in the United Kingdom, Ireland, Denmark, and Mediterranean regions, where temperature anomalies exceeded +1.0°C (Fig. 7.40). In the Middle East, temperature anomalies also reached +1.0°C, while South Caucasus and West Kazakhstan reported a colder-than-normal autumn. Autumn precipitation was slightly below normal for Western Europe, parts of Scandinavia, and most of the Mediterranean countries, with local wet spots. Central Europe and the Iberian Peninsula received precipitation of around 60% of normal. Ukraine, Moldova, Türkiye, and the Middle East, where high-pressure influence was strong, were even drier for the season, with precipitation mostly 20–60% of normal.

December 2021 was again a warm month across most of Europe, except for Scandinavia and the Baltic Countries and northern Russia. It was wetter than normal during the month across much of Eastern Europe and the Balkan countries, but very dry for the season in eastern Iberia, Scandinavia, and the Middle East.

2) WESTERN EUROPE

This region includes Ireland (1981–2010 base period), the United Kingdom (1981–2010), Belgium, the Netherlands, Luxembourg, and France (1981–2010).

(i) Temperature

Ireland and France reported a slightly warmer year than normal, with anomalies of +0.5°C and +0.4°C, respectively, while it was slightly colder than normal for Belgium (–0.4°C) and Luxembourg (–0.4°C). A near-normal year was reported from the Netherlands and United Kingdom.

Except for the United Kingdom and Ireland (–0.2°C anomaly), all western European countries reported a warmer winter season than normal (France: +1.2°C, Belgium: +0.6°C, Luxembourg: +1.0°C, Netherlands: +0.5°C).

Spring started with near-average temperatures, but became cooler than average in April and May. Monthly temperature anomalies in April were around –3.0°C in Belgium, the Netherlands, and Luxembourg, setting new April records. Belgium had its coldest April since 1986 and its eighth coolest overall. The United Kingdom reported its coldest May since 1989 with an anomaly of –1.3°C, while Luxembourg reported its coolest spring since 2013, with an anomaly of –2.1°C.

At the beginning of summer, rapid warming occurred across Western Europe, where temperatures 2.0°C above normal were reported. The Netherlands had its warmest June on record (+2.0°C anomaly), France its fifth warmest (+2.0°C), and Belgium its third warmest (+1.9°C). July was the fifth warmest for the United Kingdom since the start of its record in 1884, at 1.5°C above normal.

Warm conditions continued across the region into autumn. September was warmer than normal for all countries: second warmest on record for the United Kingdom (+2.1°C anomaly) and third warmest for France in the past 50 years (+2.0°C). The seasonal mean was reduced, however, by a cool November. Overall, autumn ended with temperature anomalies of +0.3°C for Belgium, +0.4°C for France, +0.7°C for the Netherlands, –0.1°C for Luxembourg, +1.45°C for Ireland, and + 1.4°C for the United Kingdom. December 2021 was mild across the western European countries, with temperatures around +1.0°C above normal.

(ii) Precipitation

Annual precipitation totals were close to normal in the region, except for Belgium, which reported its third wettest year since 1991 (124% of normal).

The winter season was slightly wetter than normal for all countries, with 102–124% of normal precipitation. Only southeastern France received slightly below-normal precipitation. January was wetter than normal, with up to 140% of normal precipitation in France and 133% of normal in the United Kingdom.

Spring was near-normal in most places, except for France (80% of normal). Summer brought strong and persistent rainfall to France, Belgium, Luxembourg, and the Netherlands. Ireland and the United Kingdom reported below-average summer precipitation of around 75% of normal. In July, moist air flowed into Western Europe. Following extremely heavy precipitation, several severe weather events with flooding were reported from France, Belgium, Luxembourg, and the Netherlands. Belgium registered its highest July precipitation since 1991 (216% of normal), France reported its third-wettest July since 1955 (150% of normal), and Luxembourg reported its second-wettest July (264% of normal). In southern France, dry conditions set in with August, and the country received 60% of its normal precipitation for the month, marking its sixth-driest August on record.

This situation persisted into autumn; dry conditions extended into the Benelux countries, with precipitation totals between 52% and 86% of normal. Ireland and the United Kingdom each reported a slightly drier autumn than normal, with 86% and 96% of normal precipitation, respectively.

(iii) Notable events and impacts

During 18–21 January, Storm Christoph passed over northwestern Europe; minimum pressure fell to 950 hPa and wind gusts up to 190 km h^{-1} were recorded on exposed locations in the United Kingdom. Three-day precipitation totals reached 50% of the average January monthly rainfall in some areas, leading to record high river levels and flooding. This caused damage to bridges, roads, and power lines. On 21 January, the Dee River in North Wales reached its highest water level on record since the water gauge was installed in 1996. Approximately 2300 homes were evacuated. Following this storm, the United Kingdom experienced a rare thundersnow event, receiving up to 17 cm fresh snow on 24 January. Roads were closed and vehicles stranded.

During February, several Atlantic low-pressure systems brought heavy precipitation to France, the United Kingdom, and the Netherlands, leading to extensive traffic disruptions. Since soil was already saturated by rainfall, brought by Storm Christoph, the heavy rain in early February caused near-record river levels and widespread flooding. Southwestern France reported flooding, landslides, blocked roads, and damage to roads, bridges, and houses. During 12–13 February, cold air from the east caused extreme freezing rain in all of northern France. Ice layers reached a thickness up to 1 cm, making roads impassable for several hours.

On 31 March, Western Europe experienced unusually high maximum temperatures. France, Belgium, the Netherlands, and Luxembourg recorded local national record daily maximum temperatures around 25–30°C.

Conversely, during 6–8 April, many local cold records were set in France and Belgium as cold air flowed in from the North Sea due to a low-pressure area with central pressure 963.7 hPa in Överkalix-Svartbyn in northern Sweden. In southern France, frost caused considerable damage to agriculture.

During June, intense thunderstorms were observed across Belgium, the Netherlands, Luxembourg, the United Kingdom, and France. Heavy rain, tornados, tennis ball-sized hail, strong wind, and frequent lightning led to local flooding, roads blockages, and damage to agriculture and infrastructure.

From 12 to 15 July, Storm Bernd brought exceptionally high precipitation, leading to flooding, heavy damage to property, and casualties in the Netherlands, Belgium, Luxembourg, and France.

On 14–15 July, a total of more than 150 mm rain was measured in Limburg (southern Netherlands), which is more than double its normal precipitation total for July. Several stations in the provinces of Namur and Liège (southeastern Belgium) measured up to 271.5 mm rainfall in 48 hours. Liège City was completely flooded after the water level of the Meuse River rose. Approximately 2000 people were displaced, and at least 36 were killed. At the end of July, the Netherlands, Luxembourg, and the United Kingdom also experienced significant flooding.

During a heat wave in mid-August in southern France, local monthly record temperatures were set at multiple stations; for example, Valensole (located on a high plain in the Provence region in southern France) reported a maximum temperature of 37.5°C and La Chippa in Corsica reported 40.7°C.

During 2–3 October, northwestern France experienced extreme precipitation and strong winds. In the city of Nantes, a new daily record was set with a 24-hour total rainfall above 100 mm. Wind gusts up to 126 km h^{-1} caused power outages and blocked rail traffic.

At the end of December, above-normal temperatures were reported due to a high-pressure area in Western Europe. Local temperature records for December were set in Nimes (20.9°C) on 29 December and Marseille-Marignane (20.7°C) on 30 December in France.

3) CENTRAL EUROPE

This region includes Germany, Switzerland, Liechtenstein, Austria, Poland, Czechia, Slovakia (1981–2010), and Hungary.

(i) Temperature

Overall, Central Europe was around normal, with annual temperature anomalies ranging from −0.1°C to +0.4°C in 2021.

Winter 2020/21 was mostly mild. Switzerland reported a winter that ranked among its 10 warmest in some places (e.g., Geneva and Berne), at 0.5°C above normal on national average, while Slovakia reported an anomaly of +2.1°C. In February, several Atlantic low-pressure systems followed increasingly southerly tracks and brought warm air masses to southern parts of Central Europe, leading to temperature departures of +1.9°C in Austria, +2.1°C in Hungary, and +2.8°C in Switzerland. With Germany and Poland still under the influence of cold arctic air at the beginning of the month, their overall February temperatures were close to normal.

During spring, temperature anomalies were more than –1.0°C across the entire region. Switzerland reported its coolest spring in more than 30 years, at 1.6°C below normal. Hungary, Slovakia, Czechia, and Germany reported spring temperature departures ranging from –2.1°C to –1.7°C, while Poland and Austria observed departures near –1.0°C.

Summer was warmer than normal, with anomalies of +0.4°C to +2.0°C. Poland reported its fourth-warmest summer on record, at 1.0°C above normal. June was the warmest month of the season. Austria reported its third-warmest June since 1767, Poland its second warmest (+2.5°C), and Hungary reported its third-warmest June since 1901, with an anomaly of +2.2°C, and its warmest July, with an anomaly of +2.3°C. August was colder than normal everywhere, with anomalies ranging from −0.7°C to −1.6°C; Austria reported its coldest August since 2014 at 1.3°C below normal.

With a high-pressure system in place over Central Europe, autumn began with a warm September: anomalies of +1.7°C in Switzerland and +1.3°C in Austria, Germany, and Czechia. October was slightly colder than usual in the southern countries of the region, with anomalies between −0.5°C and −1.3°C, while Germany and Poland were slightly warmer than normal. The season ended with temperatures near-normal in November, but again warmer in the north and colder in the south. Overall, autumn was near-normal for many countries in Central Europe.

(ii) Precipitation

Precipitation was close to normal (90–116%) in the region for the year.

January was wetter than normal, with multiple storms passing over Europe; Switzerland and Germany received 202% and 130% of their normal precipitation, respectively. Austria reported 166% of normal, with the western part of the country measuring record high precipitation (Bregenz received as much as 500% of normal) and the northeastern part near-normal. In February, most countries reported near-normal precipitation, except Slovakia, which reported a slightly wetter February (130% of normal), and Austria and Switzerland reported a drier February (65% and 72% of normal, respectively). Overall, winter 2020/21 was near-normal for Czechia, Hungary, Poland, and Germany, while Austria, Switzerland, and Slovakia reported a slightly wetter winter season, up to 130% of normal.

During March, below-average precipitation was observed across much of Central Europe. Hungary reported a dry month, with 35% of its normal precipitation (locally even less than 10%). Austria and Slovakia also reported less than 50% of their normal precipitation. The season ended with a wetter-than-normal May, due to a trough over Central Europe. Czechia, Germany, Switzerland, Poland, and Slovakia received up to 140% of their normal precipitation, and Hungary and Austria received up to 120%. On average, spring precipitation was slightly below normal for many countries in the region.

Summer started with a drier-than-average June across many parts of Hungary, Slovakia, Poland, and Austria, while Germany received up to 130% of its normal precipitation. Switzerland received 108% of its normal June precipitation; however, there was a sharp contrast between northern and southern Switzerland, at 152% and 28% of average, respectfully. Precipitation did not exceed 40% of normal anywhere in Hungary, Austria, or Slovakia. Hungary reported 21% of its normal precipitation on average, making it the second-driest June since 1917. In July, due to multiple low-pressure systems bringing heavy convective precipitation to the region, Germany, Austria, Czechia, and Poland received up to 120% of their normal rainfall on average. Switzerland received 195% of its normal precipitation, which resulted in its wettest July on record since 1864. Wet conditions continued into August; Poland received up to 173% of normal precipitation, making this its second-wettest August in history. Overall, summer was wetter than normal for all countries, except Hungary (65% of normal).

The wet summer was followed by a drier-than-normal (widespread 58–70% of normal) autumn for most of Central Europe. In particular, September and October were very dry across Germany and the southeast of the region. Austria reported its driest September since 1975, with 52% of its normal precipitation. Czechia reported just 38% and 39% of its normal precipitation in September and October, respectively. Similarly, Slovakia reported just 38% of its normal precipitation in October.

(iii) Notable events and impacts

During 9–14 February, an extreme cold spell with snowstorms was reported in Germany, Switzerland, Austria, and Czechia. New monthly local records were set in central Germany (Thuringia region), with temperatures as low as –26.7°C. New all-time snow depth records were measured at several lowland stations in Germany, with snow depths of 60–70 cm, on 8–9 February. Southwesterly winds brought warm air to several parts of Central Europe, which caused considerable variation in temperatures. A new record February maximum temperature of 21.9°C was reached in Vaduz (Liechtenstein). On 26 February, several new high daily maximum temperatures for February were set at multiple stations: 22.1°C in Maków Podhalański (Poland), 20.8°C in Hurbanovo (Slovakia), and a new national February record of 22.4°C was set in Kiskunfélegyháza (Hungary). Additionally, a record-breaking temperature rise of 41.9°C within one week was reported in Göttingen (northern Germany), from –23.8°C on 14 February to 18.1°C on 21 February.

The ongoing warm airflow from the southwest caused record high temperatures in late March. On 31 March, a new national March record of 27.7°C in Rheinau-Memprechtshofen was set in Germany.

During 19–22 June, Switzerland and Germany experienced thunderstorms accompanied by sometimes heavy precipitation and exceptionally large hail events. Station Wädenswil in Switzerland received a 24-hour daily precipitation total of 62.6 mm. Station Root in Luzern County (Switzerland) reported 36.5 mm in 10 minutes. An F4 tornado struck several villages in southern Moravia (Czechia) on 24 June, with major damage and six deaths reported. This was the strongest tornado on record in the Czech Republic.

While a wet summer helped to replenish water resources after the preceding relatively dry years in many parts of Central Europe, Hungary continued to be affected by water scarcity in soils. The top 50 cm of soil dried out and soil moisture fell below the critical 40% level across almost the whole country due to the long-lasting drought situation.

Between 12 and 15 July, Storm Bernd (same as noted for Western Europe) brought heavy rainfall to Central Europe, which led to extreme flooding, particularly in western Germany where several towns were completely flooded. Water levels in rivers far exceeded historical records, locally 7–8 m above normal. The flooding caused heavy damage to property and infrastructure. Additionally, 179 people were killed in Germany, which was one of the deadliest weather events on record for the country. Several districts in western Germany declared a state of emergency, and hundreds of troops from the German army were deployed to help. Local precipitation records were exceeded in many places. More than double of the monthly normal rainfall was received within a few hours or days over entire river catchment areas.

In August, a new national daily wind gust record was set for Austria. The Tiszavasvar station in northeastern Hungary measured 121 km h^{-1}, the highest wind gust in a series dating from 1977. During 20 and 21 October, Storm Aurore brought severe weather to Central Europe, including wind gusts that surpassed 150 km h^{-1}.

4) THE NORDIC AND BALTIC COUNTRIES

This section includes Iceland, Norway, Denmark, Sweden, Finland, Estonia, Latvia, and Lithuania.

(i) Temperature

Temperatures across the Nordic and Baltic region in 2021 were mostly close to normal, with anomalies ranging from −0.4°C to +0.9°C.

Winter 2020/21 was near-normal, with anomalies between +1.1°C in Finland and −0.7°C in Norway. Temperatures varied considerably during February due to a change in the prevailing atmospheric circulation pattern mid-month. Sweden observed a new national February record for daily maximum temperature, but nevertheless monthly average temperatures for February were below normal across almost the entire country, similar to the other Nordic and Baltic Countries, with –3.2°C in Lithuania, –2.0°C in Norway, and –1.4°C in Denmark.

Spring was slightly warmer than normal, with anomalies up to +1.0°C in the Fenno-Scandinavian countries, while Denmark, Iceland, and the Baltic countries reported near- to slightly below-normal temperatures for the season.

In June, the northeastern part of the region experienced a heat wave that led to several record and near-record monthly anomalies in Estonia (+4.0°C, highest since 1961), Latvia (+3.6°C, highest since 1924), Finland (+ 3.7°C, highest since 1900), Lithuania (second highest since 1961), and Sweden (+3.4°C, second highest since 1860). Norway was also affected, with an anomaly of +2.3°C. July followed as the warmest on record for Latvia (+3.7°C) and Lithuania (+3.8°C), which resulted in the warmest summer on record for Latvia, with an average anomaly of +2.1°C, and second warmest summer for Finland, at +1.8°C. The summer season ended with temperatures slightly

below normal for August, ranging from near-normal to 1.2°C below normal in Denmark. Summer as a whole was the warmest on record at several locations in northeastern Iceland.

During autumn, temperatures were slightly above normal (around +1°C anomaly) in all Nordic and Baltic countries. Denmark reported its fifth-warmest autumn.

With temperature anomalies of –3.3°C in Estonia, –3.0°C in Latvia, –1.8°C in Norway, –3.6°C in Finland, and –2.2°C in Lithuania in December, 2021 ended rather cold in the region.

(ii) Precipitation

Annual total precipitation was mostly near-normal across the region, with considerable short-term variability. Winter 2020/21 brought a deficit of precipitation to most of the Nordic and Baltic countries, except Sweden where precipitation was near-normal on average, but distributed inhomogeneously. Due to a blocking high-pressure area expanding from Central Europe in February, especially dry conditions prevailed over southern Sweden and the Baltic countries. Latvia received less than 30% of its normal precipitation, resulting in its fifth-driest February in the record dating to 1924.

Dry conditions continued into spring. Sweden and the Baltic states reported a drier-than-normal March and April, while the season ended wetter than normal for most of the Nordic countries. In May, Latvia and Estonia each received nearly double their normal precipitation, while the national average in Finland, Sweden, and Denmark was around 125% of normal. For the other countries in the region, May was drier than normal.

During summer, overall precipitation was near to slightly below normal for all countries of the region, except Estonia and Iceland where the dry spring continued into summer. August was wetter than normal in Finland, Estonia, and Sweden, with around 150% of normal precipitation or higher. Denmark, Norway, and Iceland each reported a drier-than-normal August, though with high spatial variability of anomalies.

For autumn, Denmark and the Baltic states reported 90–95% of their normal precipitation while Fenno-Scandinavian countries received around 110% of normal. October was the third wettest for Finland, with 166% of its normal precipitation.

In December 2021, precipitation was below normal for all of the Nordic and Baltic States.

(iii) Notable events and impacts

In early February, cold arctic air moved into northern Europe. On 12 February, Denmark's coldest night in nine years was reported: –20.7°C in Horsens, on the eastern coast of Denmark. At the end of February warm air moved from southern to northern Europe, with new February records set in Sweden and Denmark. The station at Kalmar in southern Sweden reported a new national February record of 17.0°C. In Denmark, the temperature rose by 35.7°C in 11 days: from –20.7°C to 15.0°C on 22 February in Jyndevad. On 29 March, a new local record of 19.7°C was set at station Harstena (southeastern Sweden) where measurement started in 1942.

During 5–6 April, extreme snowfall was observed in Norway, with an April record of 25–41 cm of fresh snow in 24 hours (measurements commenced in 1896).

In June, Scandinavia and the Baltic countries experienced a heat wave, with high temperatures exceeding 30°C and reported tropical nights. Finland recorded the hot-weather threshold of 25°C on 25 days somewhere in Finland. Tampere (southern Finland) reported its highest temperature on record (33.2°C) on 22 June. New national June maximum records were also set for Estonia (34.6°C) and Latvia with a high minimum nighttime temperature (23.7°C), both on 23 June. The warmth continued in July; Liepaja in Latvia observed a new local record of 30.4°C on 2 July. Stations in northern Sweden, Norway, and Finland measured new local records above 30°C. Temperatures in northeastern Europe were high in the following 11 days. In Lithuania, temperatures above 30°C for more than 11 days had not been measured since 1961.

Later in summer, unusual warmth also reached Iceland. On 24 August, a station in Hallormsstadur (eastern Iceland) measured 29.4°C, which was the highest temperature ever recorded in August.

Temperatures remained high in autumn. On 8 September, Drammen (Norway) reached 28.6°C, 0.1°C above the previous September national record that was first set in 1906 in Austad, and later equaled in Meråker in 1958 and Drammen in 1991. On 4 October, a temperature of 16.2°C was measured in Abisko in northern Sweden, which was the highest October temperature in the station's history for more than 100 years.

During 18–19 November, Denmark observed a nighttime minimum temperature of 10°C, the highest night temperature ever recorded in the country that late in the year.

5) IBERIAN PENINSULA

This region includes Spain (1981–2010 base period), Portugal (1971–2000), and Andorra.

(i) Temperature

Spain and Portugal reported annual temperatures 0.5°C and 0.4°C above normal, respectively. Winter 2020/21 was slightly warmer than normal but with variations between months. While, January was cold overall, with an average temperature of 0.6°C below normal in Spain and 0.8°C below normal in Portugal, the season ended with a very warm February, the third warmest for Spain (2.5°C above normal) and fifth warmest for Portugal (1.7°C above normal).

Spring also was warmer than normal, as anomalies were up to +0.4°C for Spain and +1.0°C for Portugal. The season began with temperatures near-normal for March in Spain, while Portugal reported an anomaly of +0.7°C. While April was also normal in Spain, Portugal reported an anomaly of +1.9°C. May concluded the season with slightly above-normal temperatures on the Iberian Peninsula.

Summer was normal for both Spain and Portugal. During August, temperatures were above normal, but only Spain reported monthly anomalies close to +1.0°C, which marked its ninth-warmest August.

Autumn was also near-normal but with variation between months. October was warmer than average, with temperatures 1.0°C above normal in Spain and 1.5°C above normal in Portugal, while November was colder than average, with anomalies of –1.2°C for both countries.

The year ended with a warmer than normal December. Spain reported an anomaly of +1.9°C, while Portugal reported +1.7°C above normal, making this its fourth-warmest December on record.

(ii) Precipitation

Annual precipitation totals in Portugal and Spain were near-normal, with small deficits in the southern Andalusian region and in northeastern Spain. The main rainfalls occurred in winter, while autumn precipitation was below normal. Summer is climatologically a dry season anyway and spring was extremely dry.

February brought abundant rainfall but mainly in the northwest of the Peninsula where the mean precipitation was around 160% of normal in Portugal (third highest since 2000).

Spring set in with a strong precipitation deficit for the region, at 62% and 67% of normal for Portugal and Spain, respectively. This marked the fourth-driest spring on record for Spain.

Summer precipitation was near-normal for Spain (101% of normal) and below normal for Portugal (64%), with variations between months. Overall, June was wetter than normal, and July and August were drier than normal. Portugal received only 28% of its normal precipitation for the month, making it the fifth-driest August since 2000.

While autumn started with above-normal precipitation in September—160% of normal for Portugal and 133% for Spain—the season concluded with below-normal rainfall across most of

the region, except for northeastern Spain. Portugal reported its third-driest November on record with just 17% of its normal rainfall in November.

(iii) Notable events and impacts

A severe winter storm affected the Iberian Peninsula in early January. Storm Filomena brought abundant cooling, high precipitation totals with flooding, and large amounts of snow to Spain and Portugal. Central and northern areas of Spain came to a standstill following record snowfall up to 50 cm. On 6 January, Spain registered its national all-time lowest temperature in Catalan Pyrenees at –34.1°C. Some locations in the center of Spain also reported their lowest local temperature on record, including Toledo (–13.4°C) and Teruel (–21.0°C). Madrid Barajas International Airport was forced to suspend all flights on 9 January. Areas of the southern Andalusian region recorded heavy rainfall, with more than 200 mm total on 8 January. Flash flooding and damaged roads and homes were reported due to overflowing rivers. At least seven fatalities were reported from storm Filomena.

During summer, there were several significant warm episodes observed in mainland Spain. An intensive heat wave occurred from 11 to 16 August, with temperatures exceeding 40°C across much of southern Spain. A new national all-time maximum temperature record was set in Montoro on 14 August at 47.4°C. Additionally, a local all-time maximum temperature record was set in the capital of Spain, Madrid, at 42.7°C on 14 August.

Several heavy rain events with flash flooding occurred in eastern and southern Spain during autumn. The region around Montsia and Baix Ebre in eastern Spain recorded a 24-hour total of 233.5 mm of rain on 1 September. A 1-hour total of 112.4 mm was recorded in Huelva in southern Spain on 23 September. Eastern parts of Spain and the Balearic Islands were also affected by floods and heavy rainfall on 21 September (e.g., 24-hour total of 124 mm in Mura/Mallorca). Several roads were cut off or closed. On 22 October, a quasi-stationary low that developed over the central Mediterranean led to intense heavy rainfall up to 102 mm and subsequent flooding in Alicante (near the eastern coast of Spain). On 6 November, a low-pressure area developed over the western Mediterranean, which brought heavy precipitation and thunderstorms, particularly notable on the Balearic Islands, with 113 mm of rainfall reported in a 12-hour period on 11 November in Mallorca. Further heavy rainfall of over 150 mm in 24 hours caused severe flooding in northern Spain during 23–29 November.

6) CENTRAL MEDITERRANEAN REGION

This region includes Italy (1961–90 base period), Monaco (1981–2010), Malta (1981–2010), Slovenia (1981–2010), Croatia (1981–2010), Serbia (1981–2010), Montenegro (1981–2010), Bosnia and Herzegovina (1981–2010), Albania (1981–2010), North Macedonia (1981–2010), Greece (1981–2010), and Bulgaria.

(i) Temperature

Temperatures in the Mediterranean and Balkan States were well above normal for 2021, but were not as high as the record-breaking year of 2020. For Italy (+1.3°C anomaly), Serbia (+0.8°C), North Macedonia (+0.7°C), Albania (+0.4°C), Slovenia (+0.7°C), Greece (+1.2°C, fourth warmest on record), and Malta (+0.8°C, second warmest on record), 2021 was warm throughout the year.

An exceptionally warm winter, with widespread above-normal temperatures up to +3.0°C, was reported from the Mediterranean and Balkan States. Bulgaria and Greece each observed their second-warmest winter on record, with anomalies of +2.6°C and +2.1°C, respectively. Serbia reported its third-warmest winter, with an anomaly of +3.0°C. Both January and February were exceptionally warm, with above-average temperatures throughout the region. Anomalies up to +3.5°C in Bosnia and Herzegovina and +2.3°C in Italy were reported in February.

Except for Greece, Italy, and Malta (near-normal), spring was colder than average for the rest of the region. Bulgaria, Slovenia, and Serbia reported anomalies of –1.2°C or below, while Albania, Croatia, and North Macedonia reported slightly below-normal temperatures. Similar to Central and Eastern Europe, the lowest temperature anomalies occurred in April, up to –2.0°C.

During summer, the entire area experienced above-average temperatures. Greece and Malta each reported their second-warmest summer on record, at +1.6°C and +2.0°C, respectively, while North Macedonia reported its third warmest (+1.7°C) and Serbia, Italy, and Bulgaria their fifth warmest. June was the warmest month for the northwest part of the region, with many countries reporting anomalies close to or above +2.0°C; Italy reported its fourth-hottest June on record (+3.2°C). Conversely, July was the warmest month for the southeastern part of the region: second-warmest July on record for Serbia (+2.8°C) and Greece (+1.8°C), third warmest for Bulgaria (+2.2°C) and Malta (+1.7°C), and fourth warmest for Italy (+2.3°C). The season ended with a warmer-than-normal August for the whole region, except the northernmost areas. Greece and North Macedonia reported their hottest August on record, at 2.3°C above normal, while Malta reported its second-warmest August (+2.1°C).

Autumn temperatures were near-normal for the season across the region, but with variation in months. While the warmth continued in September, with anomalies of +2.1°C in Italy (fourth highest on record) and +1.6°C in Malta (second highest), October was colder than normal in the region, for example, 2.5°C below average in North Macedonia. November was warmer than normal, with anomalies between +0.5°C and +2.2°C in the central Mediterranean region.

(ii) Precipitation

Annual precipitation totals for 2021 were near or slightly above normal for the Mediterranean and Balkan countries. Elevated anomalies were observed around the Aegean Sea, southern Bulgaria, and Albania, where totals were around 160% of normal, which was mainly attributed to intense convective events that occurred during winter 2020/21. Drier-than-normal conditions were observed in northern Italy.

Winter was wet, especially in the Balkans and Italy. Serbia and Bulgaria each reported their fourth-wettest winter, with precipitation 160% and 175% of normal, respectively. January was the wettest winter month in the region. North Macedonia reported its wettest January on record, with 321% of normal precipitation. Bulgaria, Serbia, Albania, and northern Greece also observed totals up to 300% of normal. Additionally, localized precipitation totals of 500% were reported.

Due to developing strong high-pressure systems over the North Atlantic and Greenland in April, expanding to southeastern Europe, spring precipitation was mostly near- or drier than normal, except for Bulgaria (118% of normal) and Serbia (110%). Slovenia reported a wetter-than-normal May, with 214% of its normal precipitation due to low pressure over the North Sea progressing farther to southeastern Europe.

Summer continued with drier-than-normal conditions in the Mediterranean and Balkan regions. Italy received 50% of its normal rainfall and Slovenia, Croatia, Bosnia and Herzegovina, Albania, and North Macedonia reported 60–75% of their normal totals, while precipitation in Greece was near-normal. The season started wetter than normal for Greece and Bulgaria, while drought conditions—severe in some places—prevailed in most of Croatia, Sicily, and Malta, where precipitation totals were just 20–40% of normal in June. In July and August, the distribution of precipitation was scattered, with many regions reporting dry conditions. Northern Italy, Slovenia, and Serbia reported local wet spots.

During autumn, precipitation was near-normal for large parts of the region, with slightly wetter conditions reported for the southern parts of Italy and Greece; however, the season began with a drier-than-normal September throughout the region, with 30–40% of normal precipitation. October was wetter than normal, with precipitation 200–300% of normal in Greece, North Macedonia, and Bulgaria (fourth wettest on record), while Slovenia and Italy had below-normal

precipitation. The season ended with around 160% of normal precipitation for Italy, Croatia, and Bosnia and Herzegovina in November. For Macedonia, Greece, and Bulgaria, autumn ended with slightly below-normal precipitation.

(iii) Notable events and impacts

Several winter storms affected the western Mediterranean and the Balkan countries, followed by cold and warm extremes during winter. During 6–10 January, heavy rains caused landslide damage in southwest Italy and Albania. In mid-January, a storm low developed over the North Atlantic, causing heavy precipitation (over 200 mm in 24 hours on the Balkan Peninsula), followed by flooding in Albania, Montenegro, Serbia, Bulgaria, and northern Greece due to overflowing rivers. A state of emergency was declared in some municipalities in Serbia.

During February, many new temperature records were set in the Balkans and Mediterranean as a sharp air mass boundary developed over Europe with very warm air in the Mediterranean. Later, cold air flowed south from the northern half of Europe. On 4–6 February, Calabria in southern Italy reported 26°C and Sicily 29°C. Bilije in Slovenia reported 25.3°C and Knin in Croatia reported 26.4°C. In mid-February, Florina in northwestern Greece measured –25.1°C, its lowest temperature in the last 15 years for this time period. The Veneto Region in Italy recorded –28°C. Many other stations in the Mediterranean also recorded low temperatures. On 15 February, heavy snowfall with gale-force winds was reported in Greece, resulting in suspended transport and power outages. At least three people were killed.

Abnormally cold spring temperatures affected Balkan regions in early April. On 7 April, a record amount of snow was reported in the capital of Serbia (Belgrade), with 10 cm snow depth. A national April low temperature record of –20.6°C was set for Slovenia at station Nova vas Bloka.

Later in spring and summer, there were several significant warm episodes, with heat waves observed in Italy and the Balkan regions. At the end of March, new local March maximum temperature records were set: in the capital of Slovenia, Ljubljana reached 25.1°C, and Florence, Italy, reached 29.4°C. On 30 April, temperatures reached near-record levels, exceeding 30°C in Italy, Greece, Serbia, Albania, and North Macedonia. On the same day, a new April record for the warmest night in Europe was measured near Chania on the island of Crete (Greece). The temperature did not drop below 30°C.

A major heat wave occurred from 8 June, with temperatures exceeding 40°C across many Balkan cities, including Mostar (Bosnia), Shkoder (Albania), and Danilovgrad (Montenegro). A second heat wave followed on 11 August, with temperatures reaching 48.8°C in Sicily, Italy, and 47.1°C in Lagada, Greece. Large forest fires occurred in areas affected by the strong heat. On 13 August, more than 500 wildfires were burning across Italy. During these heatwaves, Greece also lost more than 56,000 hectares to fires. A state of emergency was declared.

On 4 October, record-breaking rainfall was measured in Liguria and Piedmont Regions in northern Italy. The Liguria environmental agency reported a national 1-hour record of 181 mm in Vicoromasso. The weather station in Cairo Montenotte reported 496 mm in 6 hours, which tied the previous Italian 6-hour rainfall record set in 2011. A new European 12-hour rainfall record was set in Rossiglione (northwest Italy), with a total of 740.6 mm, which is more than 50% of its annual average of 1270 mm. Roads and public places were closed as a consequence of flash floods and landslides.

Between 5 and 15 November, Medistorm Heli impacted the region, bringing abundant precipitation with thunderstorms, particularly notable on the western Mediterranean islands and the Mediterranean coasts. Sardinia received a 4-hour total of 100 mm, while a station on Sicily measured a 12-hour total of 271 mm. The storm caused flooding in Bosnia and Herzegovina, due to a heavy 24-hour rainfall of more than 100 mm. Several areas were left without electricity and homes were flooded.

7) EASTERN EUROPE

This region includes the European part of Russia (1981–2010), Belarus, Ukraine (1981–2010), Moldova, Romania (1981–2010), and western Kazakhstan (west of 50°E, 1981–2010).

(i) Temperature

The year was near-normal for eastern Europe, with temperature anomalies between −0.2°C and +0.9°C of average for most countries. West Kazakhstan, however, observed its fifth-warmest year on record, at 1.5°C above normal.

During winter, anomalies were above normal for Moldova, Romania, and Ukraine; Romania reported its second-warmest winter on record at 3.2°C above normal, equaling the record set in 2020. European Russia and West Kazakhstan reported a slightly colder winter than usual, at 1.6°C and 0.4°C below normal, respectively.

During spring, only European Russia (+1.5°C) and West Kazakhstan (+3.2°C; third-warmest spring) reported above-normal temperatures, while the other countries reported temperatures ranging from 1.6°C below normal in Moldova to near-normal in Belarus. April contained the largest negative anomalies of the season for Belarus (–2.2°C), Moldova (–2.5°C), Ukraine (–1.3°C), and Romania (–1.9°C). European Russia and West Kazakhstan, in contrast, reported a warmer-than-normal April, with anomalies of +2.3°C and +3.3°C, respectively. The season closed with a colder-than-normal May for most of the region, except for Kazakhstan (up to +6.6°C anomaly in the Atyrau region; warmest May on record) and European Russia (+2.3°C). Anomalies in Belarus and Moldova were more than –1.0°C, while Romania reported a closer-to-normal May (–0.7°C).

During summer, the entire region experienced temperatures 1.4–3.2°C above normal, except for Moldova, which was near-normal. Belarus and European Russia each reported their second-warmest summer on record, at 2.6°C and 2.5°C above normal, respectively. The season started with the warmest June on record for European Russia (+3.9°C anomaly) and the third-warmest June for West Kazakhstan (+4.0°C) and Belarus (+3.5°C). July was also a near-record warm month for Belarus (second warmest, +4.1°C), Romania (second warmest, +2.5°C), and Ukraine (fourth warmest, +3.1°C). August concluded the season with near-normal temperatures for Belarus, Moldova, and Romania. Temperature anomalies up to +2.0°C and above were reported from Ukraine, European Russia, and West Kazakhstan.

Autumn was near-normal, with anomalies between −0.3°C and +0.5°C throughout the region. September was colder than usual, and temperatures ranged from around 1.3°C below normal in Belarus to around 0.5°C below normal in West Kazakhstan. In October, only European Russia and Belarus reported slightly above-normal temperatures, while Moldova, Romania, Ukraine, and West Kazakhstan were slightly colder than normal. The season ended with a warmer-than-normal November across the entire region. Belarus reported its fifth-warmest November on record, with an anomaly of +2.4°C.

(ii) Precipitation

The year was near-normal across the region, with 98–111% of normal precipitation; western Kazakhstan reported a lower total of 47% of normal, which resulted in its third-driest year on record. The areas around the Caspian Sea received the least precipitation for the region.

During winter, European Russia and eastern Ukraine received near-normal precipitation. Moldova, Romania, and western Ukraine each reported around 150% of normal. Except for western Kazakhstan, which reported below-average precipitation, January was wetter than normal. Belarus, Ukraine, Moldova, and Romania received up to 180% of their normal precipitation, while European Russia reported near-normal precipitation. For Ukraine, European Russia, and western Kazakhstan, February was the wettest month of the season, with 150%, 180%, and 188% of their normal precipitation, respectively. Belarus, Moldova, and Romania reported a slightly wetter-than-normal February.

Spring was slightly wetter than normal for European Russia, Moldova, and Romania and was near-normal for Belarus and Ukraine. West Kazakhstan received only 35% of its normal precipitation, which resulted in its third-driest spring on record. During March, the areas near the Black Sea in Romania, European Russia, and Ukraine received above-normal precipitation, while Belarus and western Kazakhstan reported around 70% of normal precipitation. For Belarus, Ukraine, Moldova, European Russia, and Romania, May was the wettest month of the season, with nationally averaged precipitation around 150% of normal. West Kazakhstan, however, reported a very dry May, with average precipitation less than 15% of normal and even less in localized areas. Romania reported its driest April on record.

Summer was drier than normal for western Kazakhstan and slightly drier than normal for European Russia, at 27% and 82% of normal precipitation, respectively. Areas around the Caspian Sea received only 20% of their normal precipitation; however, precipitation was near- or slightly above normal for Belarus, Romania, and Ukraine. In Moldova, around 60% of the country received 100–170% of its normal precipitation, while the remaining 40% received 180–240% of normal. Although some areas, especially around the Black Sea received above-normal precipitation, June and July were drier than normal for most countries in the region. July rainfall was near-normal for Romania and Ukraine, but above normal for Moldova, with 100–250% of normal precipitation. Summer ended with above-normal precipitation in Belarus (around 180% of normal), Moldova (around 160%), and Romania and Ukraine (around 120%). Meanwhile, western Kazakhstan reported below 20% of its normal precipitation.

Belarus and European Russia reported near-normal rainfall for autumn. Moldova received only 15–35% of its normal precipitation; such a low total is observed on average once every 15–30 years. Romania and Ukraine received around 60% of its normal precipitation. The season started with above-normal precipitation in September for Belarus and southern European Russia, while Ukraine, Moldova, and Romania received around 60% of their normal totals. October was drier than normal throughout the region: Belarus, Ukraine, and Romania received 30–60% of normal precipitation on country average, while it was especially dry in south Belarus, Ukraine, Moldova, and southern European Russia where large areas received less than 20% of normal precipitation. In western Kazakhstan, rainfall was also very low—around 40% of normal. The season concluded with above-normal rainfall across Belarus and northern European Russia, with nationally averaged precipitation of 120% and 150% of normal in November, respectively, while the rest of the region received slightly less precipitation than normal. December saw well above-normal precipitation (125–250% of normal), particularly west and north of the Black Sea (Romania, Moldova, Ukraine).

(iii) Notable events and impacts

Early spring was characterized by unusually cold temperatures in Ukraine and Romania due to an Arctic air inflow over all of Europe, as reported earlier. Many stations in northern European Russia reported new daily low temperature records as minima fell below –30°C (e.g., in region Murmansk), and some minimum temperatures even dropped below –40°C in late March. Following this cold period, an extreme warm spell was observed over European Russia. On 13 April, a temperature of 22.6°C was measured in the capital of Russia (Moscow). This was the highest temperature for that day of the year since 1881. On 17 and 18 May, two more new daily high temperature records were broken in Moscow, at 30.6° and 30.8°C, respectively. Many other stations in Russia set new daily heat records of 30–35°C. On 22 May, a record temperature of 39.7°C was measured in Khasavyurt (southwestern Russia), which was a new national spring record. An additional new monthly record of 40.5°C was recorded in Novyj Ushtogan, West Kazakhstan, on the same day.

During 22–23 June, extremely high temperatures were again measured in European Russia. Many stations reported temperatures up to 35°C. On 22 June, Petrozavodsk (northwestern Russia) measured a maximum temperature of 34.3°C, which tied the previous station record set in 2010.

Moscow reported a maximum temperature of 34.8°C, which was the highest in June for the last 120 years.

Following heavy rain in July, overflowing rivers damaged roads, bridges, and power lines in the Krasnodar region (Russia) and Crimea. Approximately 177 people were displaced, and at least two people were killed.

8) MIDDLE EAST

This region includes Israel, Cyprus (1981–2010), Jordan, Lebanon (1981–2010), and Syria (1981–2010).

(i) Temperature

Overall, the year was warmer than usual across the Middle East, with temperatures 0.8–1.9°C above normal. It was the second-warmest year on record for Jordan (+1.3°C anomaly), third-warmest year for Cyprus (+1.3°C) and Syria (+1.9°C), and fourth warmest for Israel (+0.8°C).

Winter was warmer than normal for the region. Syria reported its second-warmest winter on record, with an anomaly of +2.5°C. Israel and Jordan each observed their third-warmest winter, at 1.7°C and 1.9°C above normal, respectively. January was the warmest month of the season, with anomalies +2.0°C or above. Syria reported its second warmest January, with an anomaly of +2.6°C. Cyprus (+2.0°C), Israel (+1.9°C), and Jordan (+1.9°C) reported their second-, fifth-, and fourth-warmest January on record, respectively. The season ended with ongoing above-normal temperatures (up to +2.0°C) in February.

Spring started with a near-normal March, except for Syria and Lebanon, which reported anomalies up to +1.5°C. April was warm throughout the region, with anomalies above +1.0°C. Jordan reported its third-warmest April on record, with an anomaly of +2.5°C. Above-normal temperatures continued into May: Israel and Cyprus each reported their third-warmest May (+2.0°C and +2.6°C, respectively), Jordan its second warmest (+2.9°C), while Syria had its warmest May on record (+3.5°C). Altogether, spring 2021 was the third warmest for Syria and second warmest for Jordan.

Summer temperatures ranged from 0.6°C above average in Israel to 1.7°C above average in Lebanon. June was near- to below normal across most of the region, as Cyprus reported its fourth coldest June. August was the warmest month of the season; anomalies for Cyprus, Syria, and Jordan were +2.0°C, which was the second highest for August for each country. Israel reported its third-warmest August, with an anomaly of +1.4°C. For Syria and Jordan, it was the fifth-warmest summer, at 1.5°C and 1.0°C above normal, respectively.

Autumn was warm for the entire Middle East; most countries observed temperatures around 1.0°C above normal. Cyprus reported its third-warmest November on record, with an anomaly of +2.6°C, while Israel, Lebanon, and Jordan reported also temperature anomalies above +2.0°C. During December, anomalies were mostly not quite as high but still well above +0.5°C. Syria observed an anomaly of +2.7°C, which tied its previous December record.

(ii) Precipitation

Annual precipitation totals were mostly below average across the Middle East (20–80% of normal (Fig. 7.39).

Winter was drier than normal; many areas received precipitation less than 80% of normal and less than 60% of normal in localized areas. During January, the northern and western parts of the region were wetter than normal. In February, many parts of Jordan were wetter than normal, while much of Syria and Lebanon received only 20–60% of their normal precipitation (even less in central Syria).

Spring was especially dry. Large parts of Israel and Jordan received below-normal precipitation, even beyond their dry season. Central and northern Israel received 50–80 mm in March and April combined. In Cyprus, precipitation was around 40% of normal. Lebanon and northwestern

Syria received little precipitation. All spring months were drier than normal for the Middle East, with precipitation totals mostly 0–30% of normal. As is typical, May was the driest month of the season, with no precipitation at all measured in Jordan, Cyprus, or Israel.

At the beginning of summer, only localized areas observed some precipitation in northern Jordan and Lebanon; otherwise the Middle East received precipitation well below 40% of normal or none at all. In July, it was dry as usual in Jordan, while some unseasonal precipitation fell across most of Israel and Lebanon. August, too, had some precipitation in the region, ranging from 125–250% of normal (except for northwestern Syria and Lebanon).

Autumn was drier than normal, with overall precipitation distributed inhomogeneously over the months. After a wetter-than-normal start in September, localized areas in Israel, Lebanon, and Jordan received about 10 mm of precipitation (monthly normal for September at most stations is 1–3 mm), large areas of the Middle East received well below 20% of their normal precipitation in October. For the most western parts of Syria, Lebanon, and Israel, precipitation was around 20–60% of normal in November, while the eastern parts of Jordan and Northern Cyprus received slightly above-normal precipitation.

(iii) Notable events and impacts

After a winter storm accompanied by heavy rain, northwestern Syria experienced flooding on 18 January. The floods made living conditions for over 120,000 displaced people living in tents difficult. At least one child was killed, and more than 22,000 tents were damaged or destroyed.

On 16 February, heavy snow and storms led to disrupted traffic and closed schools in the Middle East. A daily total of 15 cm snow was measured in Damascus (Syria) and 10–15 cm in Jerusalem (Israel), and gale force winds up to 100 km h^{-1} were reported in Lebanon.

During a spring heat wave, many countries in the Middle East reached near-record temperatures for that time of year. On 19 April, 42.7°C was measured at Besor Station in southern Israel, 35.6°C in Jerusalem, 38.0°C in Damascus (Syria), and 36.5°C in Jordan. On 3 May, Cyprus measured 39.1°C, and 44.6°C was reported from Israel and Jordan on 5 May. Significant rainfall occurred in northwestern Israel on 24 July with amounts of 10–30 mm, very unusual for this month.

Following a November with warm spells—high maximum temperatures for Cyprus (33.4°C), Lebanon (29°C), and Israel (33°C)—an exceptionally intense winter storm occurred in Israel in December. On 21 December, a daily total of 147 mm was measured in Mikve Yisrael, along the central coast of the country (third on record of more than 100 years of measurements at this station; the station record was set in 1938 with 199 mm). During 21–24 December, average total rainfall of 170–221 mm was reported at the area between Tel Aviv and Ben Gurion Airport, Israel.

9) TÜRKIYE AND SOUTH CAUCASUS

This region includes Türkiye, Armenia (1961–90), Georgia, and Azerbaijan.

(i) Temperature

Overall, the year was warmer than normal for the region, with annual temperatures 1.4–2.1°C above normal. Türkiye observed its fourth-warmest year on record, while Armenia observed its third warmest. The year started with a warmer-than-normal winter. Türkiye saw temperatures that were 1.3°C above normal, while anomalies for Armenia, Georgia, and Azerbaijan were around +2.0°C. Türkiye reported its second-warmest January on record with an anomaly of +2.7°C, while February was the warmest month in the period: +3.4°C in Armenia, +2.3°C in Georgia, and +1.5°C in Türkiye and Azerbaijan.

Spring started with a near-normal March. After a warmer-than-normal April for South Caucasus (anomalies +2.3°C to +4.0°C) and Türkiye (+1.3°C), May was also warmer than normal: the warmest May in the past 50 years in Türkiye (+2.6°C) and the warmest May on record for Armenia (+2.9°C).

Overall, spring was warmer than usual by up to 2.0°C in Armenia and Azerbaijan, while Türkiye reported temperature anomalies up to +1.5°C and Georgia a slightly warm anomaly of +0.6°C.

The above-normal temperatures in summer were dominated by a hot June in the South Caucasus region. In Armenia and Azerbaijan, anomalies were as high as +4.0°C and around +1.5°C in Georgia. For Türkiye, July was the hottest month in the season and the second-warmest July on record (+1.8°C anomaly). The season ended with temperatures well above normal in August across the region; anomalies were still above +2.0°C in large parts. Armenia observed its hottest summer on record, an average temperature anomaly of +2.5°C.

Autumn started with slightly below-normal temperatures in Türkiye and South Caucasus. For Türkiye, September temperatures were normal, while Armenia and Azerbaijan reported slightly above-normal temperatures (+0.5°C anomaly) and Georgia reported a below-normal anomaly of −0.5°C. October was colder than normal in northeastern Türkiye and South Caucasus. Anomalies were slightly below −1.0°C. The season ended with a warmer-than-normal November in the region, with anomalies up to +2.0°C.

(ii) Precipitation

With average precipitation totals 95% of normal, the year was near-normal for Türkiye and Georgia, while precipitation totals up to 80% of normal were reported in Armenia and 130% of normal in Azerbaijan. Distribution of precipitation was inhomogeneous in both time and space.

Winter was very wet in Azerbaijan, with precipitation up to 162% of normal. Winter was near-normal for Türkiye and Georgia and slightly below normal in Armenia (90%).

March was wetter than normal across the region. The Black Sea area received precipitation totals as high as 250–260% of normal, 150% of normal in Armenia. Overall, spring was wetter than normal for Azerbaijan (165% of normal), while Georgia reported a normal spring. Türkiye was drier than normal (75%), Armenia slightly drier than normal (90%).

Summer was drier than normal for Armenia, Azerbaijan, and Georgia with 70–95% of normal precipitation Türkiye received 123% of its normal precipitation. While some eastern regions in Türkiye were drier than normal, the national average was above normal due to wetter parts in the west. June was exceptionally dry in Armenia with the average precipitation total only 27 % of normal. Severe droughts were observed in the last week of June.

Autumn was wetter than normal for Georgia, with 115–155% of normal precipitation. Azerbaijan reported a near-normal autumn, while Türkiye observed a drier autumn than normal, with 86% of its normal precipitation, Armenia 75%. September was the wettest month in the season for Armenia in terms of anomalies, with 98% of normal precipitation, while October had 86% of normal. For Azerbaijan, October was the wettest month in the season, with 178% of normal precipitation. Georgia, Armenia, and Azerbaijan each reported a drier November than usual, with only about 50% of normal precipitation.

Overall, Türkiye and the South Caucasus reported an increase in extreme precipitation events over the year but with short duration and rather localized.

(iii) Notable events and impacts

During January and February, Türkiye experienced several winter storms with heavy rain and winds. During 6–10 January, the western Turkish province of Izmir Türkiye reported flash flooding that inundated streets, houses, and shops. The southern province of Antalya received around 98 mm of precipitation in 24 hours, causing severe flooding. On 2 February, Güzelyali station in Izmir Province reported a 6-hour rainfall total of 113 mm (February average is 102.3 mm). Subsequent flooding caused traffic disruption, heavy damage to residences, and at least two fatalities.

On 21 May, South Caucasus and Türkiye reported unusually high maximum temperatures. In Ambrolauria (Georgia) a maximum of 36.6°C was measured. Armenia reported a new local monthly May record of 36.1°C in the capital Yerevan. In Urfa, southeastern Türkiye, 40.4°C was

reported, which tied the previous May local record. Many other stations in southeastern Türkiye reported maximum temperatures around 40°C that day.

During summer, there were several significant warm episodes, with three heat waves exceeding 40°C observed in Türkiye and South Caucasus. A major heat wave occurred at the end of June, with new monthly temperature records set in Yerevan (Armenia), 41.1°C on 24 June, and in Baku (Azerbaijan), 40.4°C on 26 June. New monthly records were also set in Georgia and Türkiye. On 20 July, Tbilisi (Georgia) reported 40.6°C, which tied the previous July record set in 2018. Cizre (Türkiye) measured 49.1°C on the same day.

On 20 July, Cizre in southeastern Türkiye measured 49.1°C. This value sets a new national maximum temperature record for Türkiye.

During 28 July–3 August, wildfires broke out in southern Türkiye (especially notable in the provinces of Antalya and Mugla). More than 130 fires scorched at least 118,790 hectares, displaced more than 10,000 people, and killed at least eight people. On 3 August, a new local maximum temperature record of 45.1°C was reported at Aydin (also southern Türkiye). Meanwhile, due to a medistorm in the Black Sea region, heavy rainfall and flooding caused severe damage to infrastructure and houses in Türkiye, and at least 77 deaths were reported on 10 August.

On 1 December, Azerbaijan observed its hottest December day on record: 29.1°C at Lankaran.

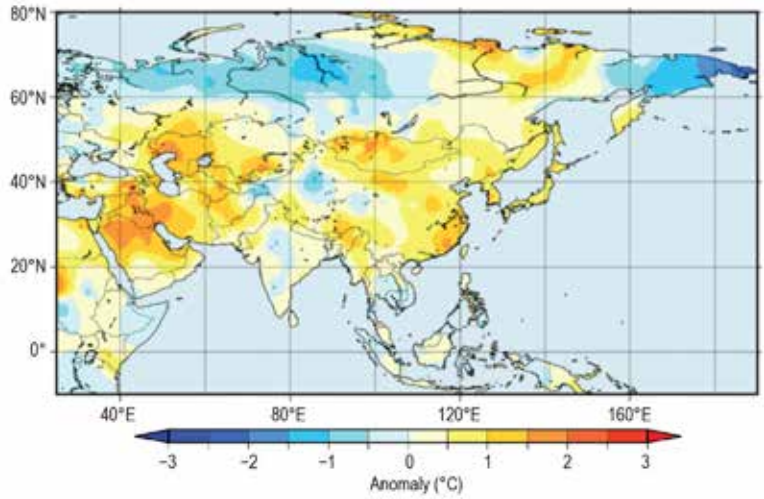

Fig. 7.42. Annual mean surface temperature anomalies (°C; 1991–2020 base period) over Asia in 2021. (Source: Japan Meteorological Agency.)

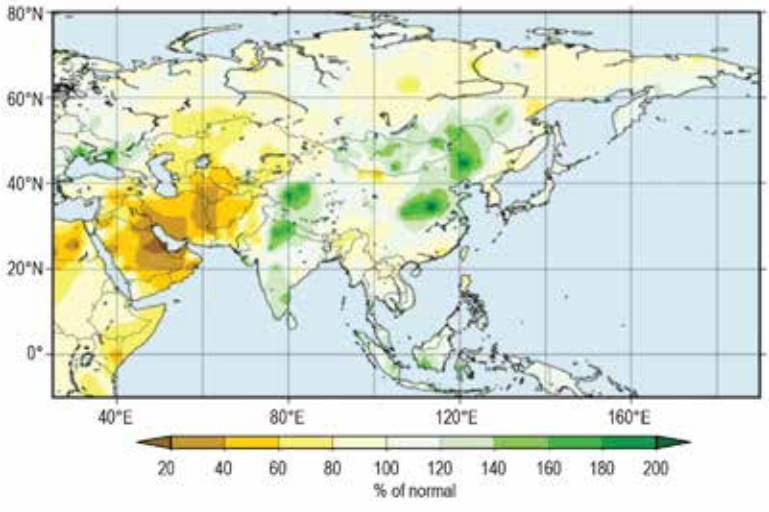

Fig. 7.43. Annual precipitation (% of normal; 1991–2020 base period) over Asia in 2021. (Source: Japan Meteorological Agency.)

g. Asia—Z. Zhu, Ed.

Throughout this section, the base periods for climatological normals and anomalies vary by region. The standard base period is 1991–2020, but earlier base periods are still in use in several countries and regions, and are noted as such in the analyses. All seasons in this section refer to the Northern Hemisphere, with winter referring to December–February 2020/21, unless otherwise noted.

1) OVERVIEW—Z. Zhu, P. Zhang, T.-C. Lee, A.-M. Setiawan, M. Hanafusa, Hir. Sato, Hit. Sato, S. Wakamatsu, K. Takahashi, G.-S. Im, D. Dulamsuren, M.-V. Khiem, and H.-P. Lam

Annual mean surface air temperatures during 2021 were above normal across most of Asia, with anomalies more than +1.0°C in southeastern China, part of western Mongolia, and Central and Southwest Asia (Fig. 7.42). Annual precipitation totals were above normal (> 120% of normal) in the northern part of eastern China and the Tibetan Plateau, Mongolia, parts of Indonesia, and northern and southern India, and below normal (< 80%) in Central and Southwest Asia (Fig. 7.43).

In winter, below-average temperatures dominated Siberia (Fig. 7.44a), while

temperatures were above normal in eastern China, the Tibetan Plateau, and northern Mongolia. Seasonal precipitation was below normal from eastern India to Myanmar (Fig. 7.44b) and much above normal in southwestern India, the Philippines, and in and around southern central Siberia. In spring, temperatures were above normal in western and southwestern Asia and from the southeast coast of China to northeast Asia (Fig. 7.44c). Much-above-normal precipitation prevailed from western China to India (Fig. 7.44d). In summer, above-average temperatures were observed from central Siberia to northern Japan and in western central Asia (Fig. 7.44e), and central China and

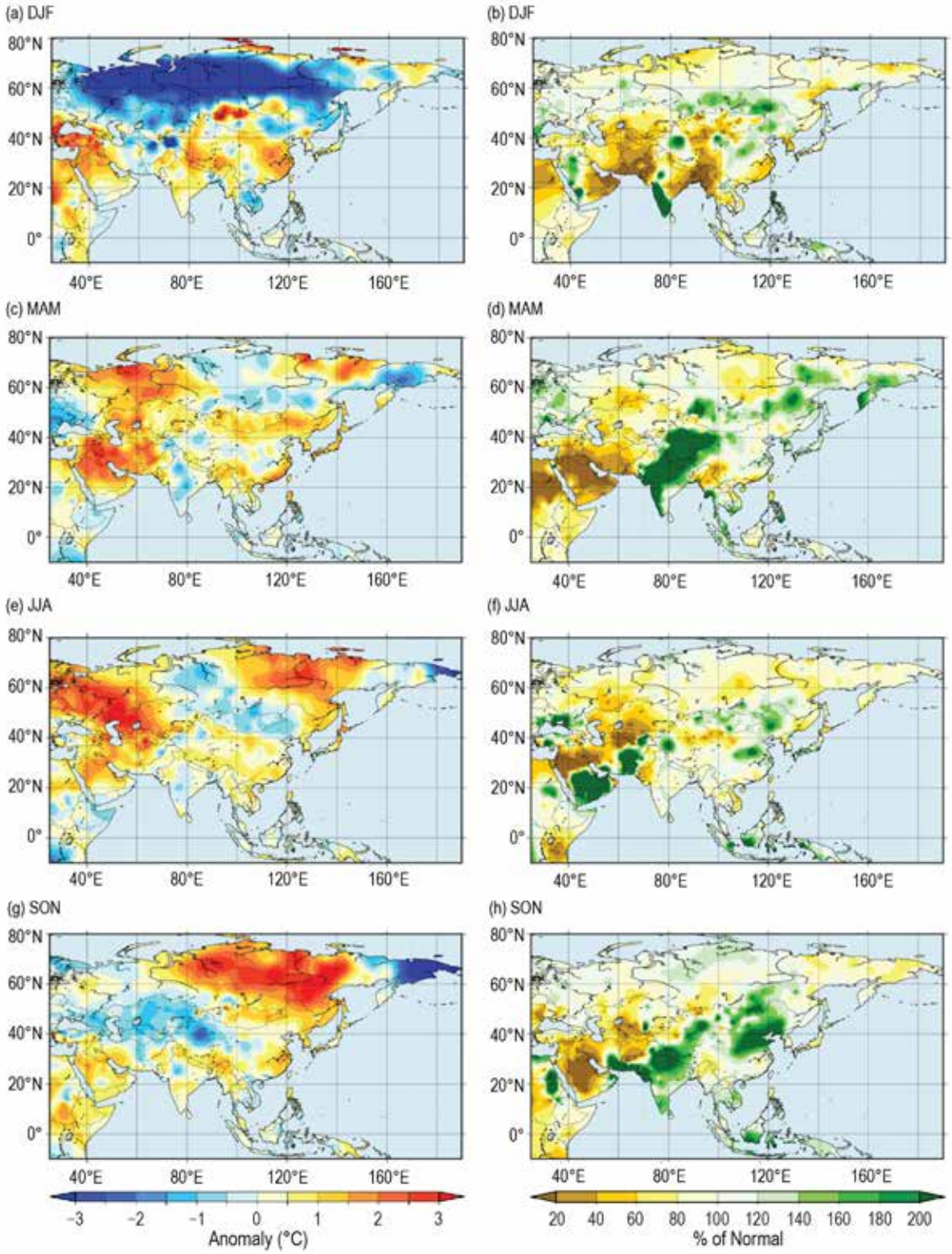

Fig. 7.44. Seasonal mean surface temperature anomalies (°C, left column) and seasonal precipitation ratios (% of normal, right column) over Asia in 2021 for (a), (b) winter, DJF; (c), (d) spring, MAM; (e), (f) summer, JJA; and (g), (h) autumn, SON. Anomalies and ratios are relative to 1991–2020. (Source: Japan Meteorological Agency.)

southern Japan experienced much-above-normal precipitation (Fig. 7.44f, see details in Sidebar 7.4). In autumn, above-average temperatures dominated Siberia, except for the easternmost region (Fig. 7.44g). Seasonal precipitation totals were much above normal in and around India and Tibet, and across Indonesia, eastern Mongolia, and northern China (Fig. 7.44h).

In winter, negative anomalies of 500-hPa geopotential height and 850-hPa temperature prevailed over Siberia (Fig. 7.45a). In spring, anti-cyclonic anomalies were dominant to the south of the Aleutian Islands at the 500-hPa and 850-hPa levels (Figs. 7.45c,d), accompanying positive 850-hPa temperature anomalies in Northeast Asia (Fig. 7.45c). In summer, significantly positive anomalies of 500-hPa geopotential height and 850-hPa temperature were observed from central Siberia to northern Japan (Fig. 7.45e). Convective activity was enhanced over the subtropical western North Pacific (Fig. 7.45f). In autumn, convective activity was enhanced from the northern Arabian Sea to the southern Indochina Peninsula and from the eastern tropical South Indian Ocean to the west of New Guinea, associated with a pair of 850-hPa cyclonic circulation anomalies straddling the equator in the tropical Indian Ocean (Fig. 7.45h).

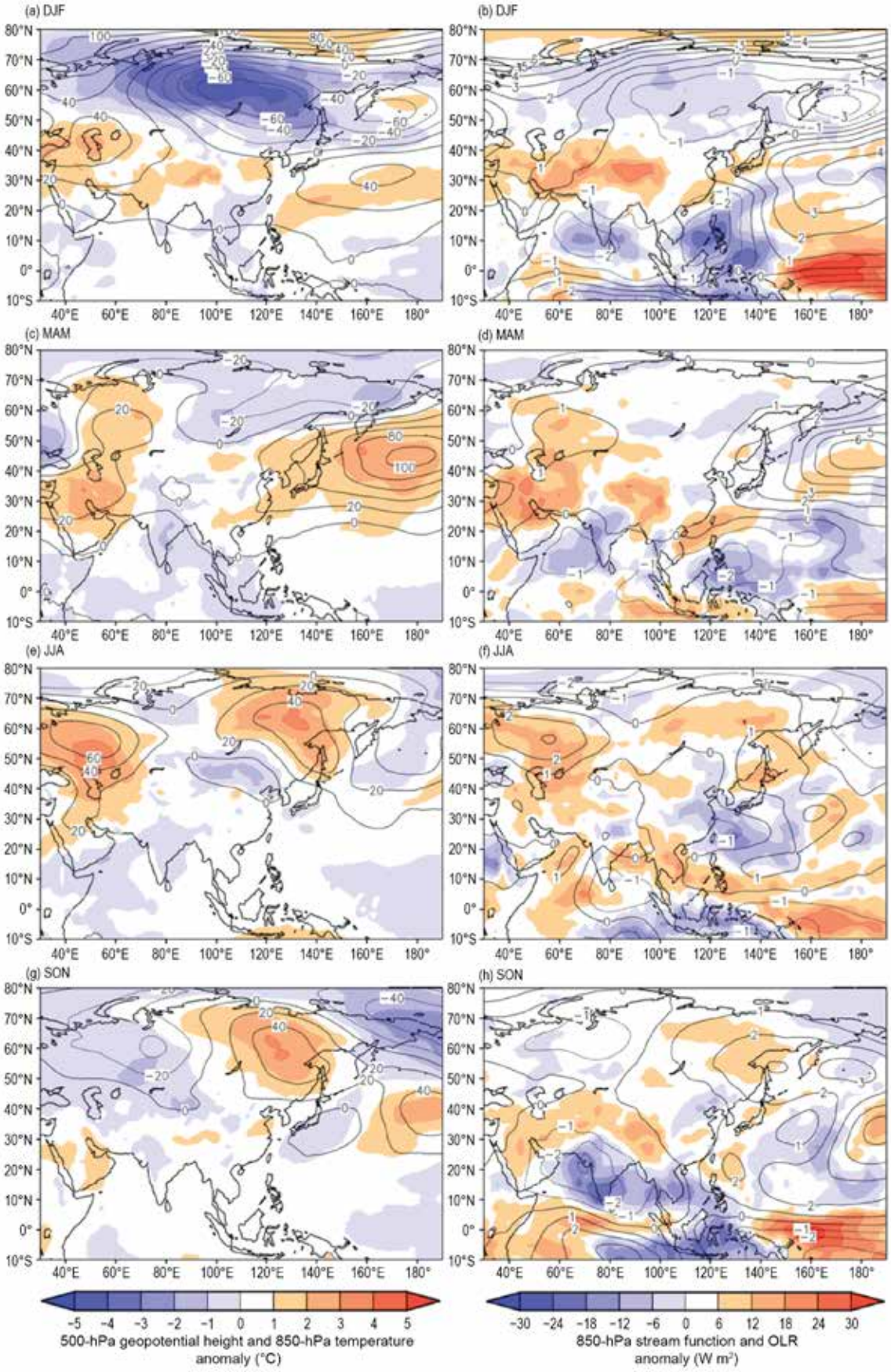

Fig. 7.45. Seasonal mean anomalies of atmospheric circulation variables in 2021 for (a), (b) winter, DJF; (c), (d) spring, MAM; (e), (f) summer, JJA; and (g), (h) autumn, SON. Left column: 500-hPa geopotential height (contour, gpm) and 850-hPa temperature (shading, °C). Right column: 850-hPa stream function (contour, 1 × 10^6 m^2 s^{-1}) using data from the JRA-55 reanalysis and OLR (shading, W m^{-2}) using data originally provided by NOAA. Anomalies are relative to 1991–2020. (Source: Japan Meteorological Agency.)

2) RUSSIA—M. Yu. Bardin and N. N. Korshunova

Estimates of climate features for Russia are obtained from hydrometeorological observations of the Roshydromet Observation Network. Anomalies are relative to the 1961–90 base period, and national rankings and percentiles are based on the 1936–2021 period of record. Note that the temperature database was extended significantly, which in some cases changed previous ranking. The boundary between Asian Russia and European Russia is considered to be 60°E.

(i) Temperature

The year 2021 in Russia was almost 2°C colder than the record warmest year of 2020, ranking 14th highest with annual mean temperature 1.3°C above normal (Fig. 7.46). Warm areas with anomalies above the 95th percentile were located in the Far East (Kamchatka, Sakhalin, lower Amur region) and the Lower Volga–Caspian region. The only small region with below-normal temperatures was in Chukotka.

Russia as a whole observed its record warmest summer with a temperature 2.0°C above normal; the previous two warmest summers occurred in 2016 and 2010. By region, Asian Russia was record warmest (1.66°C above normal), while European Russia was second warmest (2.92°C

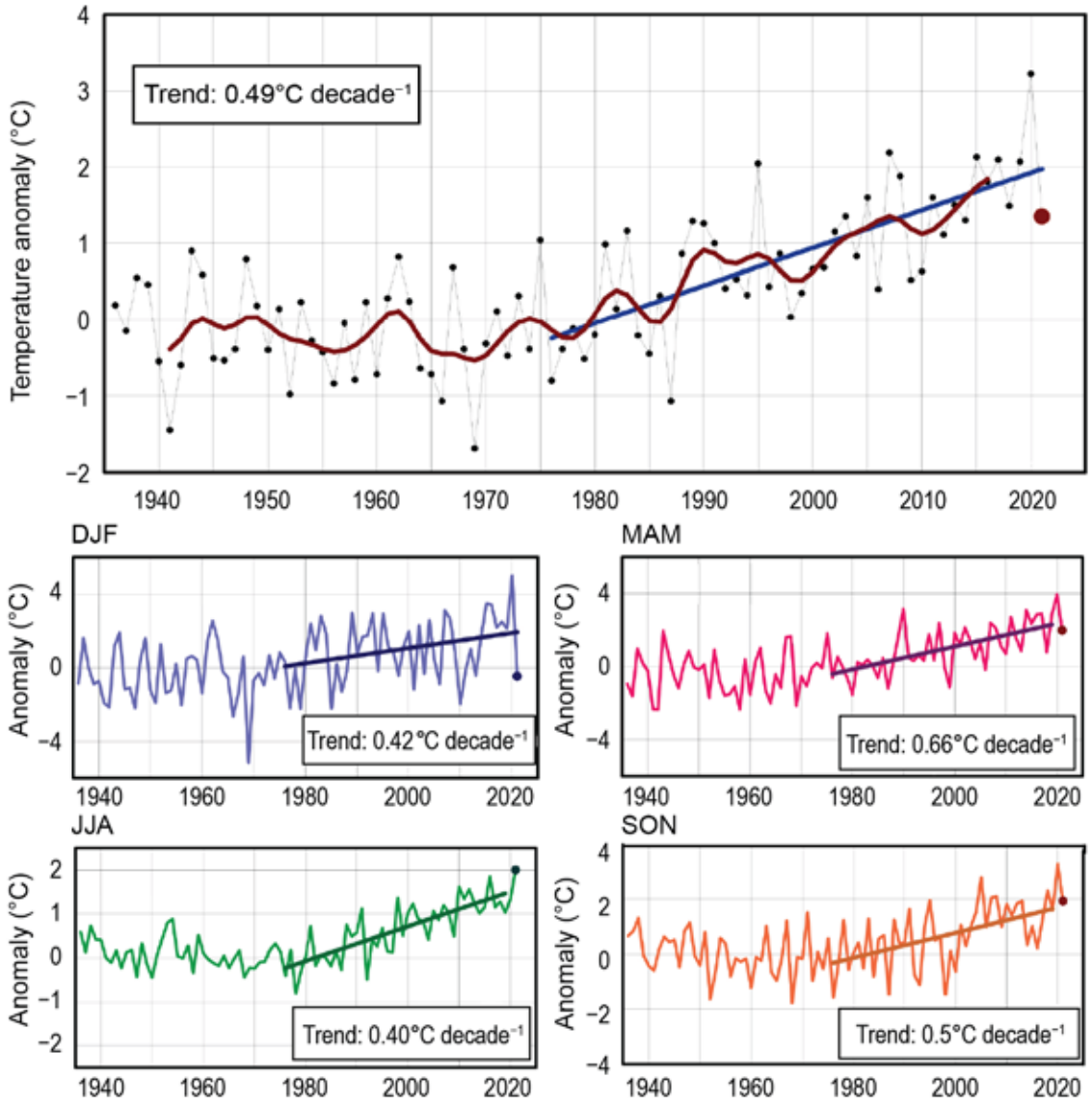

Fig. 7.46. Annual and seasonal mean temperature anomalies (°C; 1961–90 base period) averaged over the Russia territory for the period 1936–2021. The bold red line on the annual mean time series in (a) is an 11–point binomial filter. Linear trend b (°C decade^{-1}) is calculated for the period 1976–2021 for each panel.

above normal). This anomalous temperature pattern was mostly due to persistent anticyclonic circulation regimes observed simultaneously in European Russia and its eastern Asian part in the second half of June and first three weeks of August (Fig. 7.45e).

Abnormal summer warmth was compensated by a colder-than-normal winter: 0.46°C below normal, among the coldest 30% of all winters since 1936. Seasonal temperatures of 4–5°C below normal were observed in Siberia in the area of 60°–65°N, 60°–100°E (Fig. 7.45a). Above-average temperatures were reported only within narrow strips along the Arctic coast of Asian Russia, the Baikal and Amur regions along the southern borders of Russia, and in western European Russia. January was colder than normal in Asian Russia (2.6°C below normal), while February was colder than normal in European Russia (3.2°C below normal). The cold was especially noteworthy in the Northwestern Federal District, at 5.7°C below normal, ranking among its five coldest Februarys on record; at many stations, anomalies were below their fifth percentile (Fig. 7.46).

Spring was warmer than average (2.0°C above normal; 13th warmest on record) for Russia as a whole. Notably, May was abnormally warm over the vast areas encompassing eastern European Russia, the Urals, and western parts of Siberia, with temperature anomalies up to +6°C and temperatures above the 95th percentile at most stations. Autumn was also warmer than average for Russia as a whole (1.94°C above normal, seventh warmest on record), especially in eastern Asian Russia: up to 5°C above normal.

All of the seasons in Russia have warmed since the mid-1970s. Annual and seasonal trends were statistically significant at the 99% confidence level, except winter. Winters strongly warmed from the 1970s to the mid-1990s, and mostly leveled off or cooled thereafter (Fig. 7.46). However, the record warm winter of 2020 made the trend estimate for 1976–2021 formally statistically significant; this estimate should be treated with caution.

(ii) Precipitation

Across Russia as a whole, 2021 was among its 10-wettest years on record, with total precipitation about 107% of normal (Fig. 7.47). European Russia observed its sixth-wettest year, with 110% of normal precipitation. Asian Russia had 106% of normal precipitation, its 13th wettest. Spring was the third wettest on record, at 122% of normal, while summer was third driest, at 93% of normal. Winter and autumn were moderately wetter than average (11th and 12th-highest seasonal precipitation totals, respectively).

In winter, February was the second wettest on record (157% of normal precipitation); Asian Russia received 154% of average precipitation (second wettest on record) and European Russia received 159% of average (fifth wettest). February was wet across the southern latitudes of Russia, especially in the Baikal and Amur regions (≥ 260% of average), while polar regions were dry. Abnormal warmth in the Volga and the Southern Urals in May was accompanied by precipitation deficits that were 40–60% of normal.

In all summer months, precipitation deficits were observed across most of Russia. July (89% of average) and August (91% of average) were both among their five driest on record. Similar to May, anomalous warmth and rainfall deficit were observed simultaneously in the Volga and the Southern Urals. Strongly excessive precipitation was observed in southern European Russia, where a persistent cyclone caused heavy rains during 8–16 August (Fig. 7.48). Previous monthly and daily records were surpassed at many

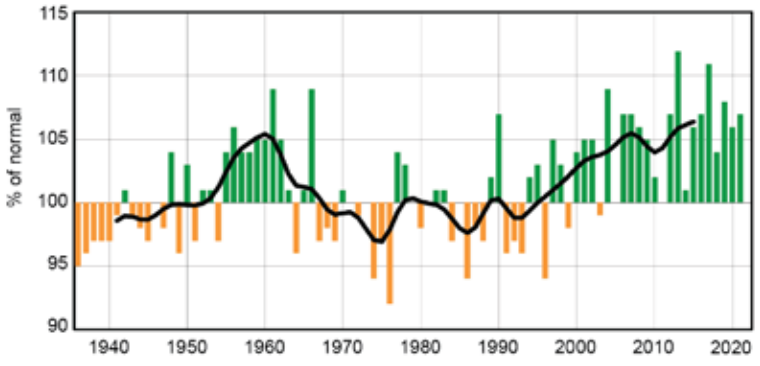

Fig. 7.47. Annual precipitation (% of normal; 1961–90 base period) averaged over the Russian territory for 1936–2021. The smoothed time series (11-point binomial filter) is shown as a bold black line.

stations. The heaviest rain was observed on 16 August in Temryuk (Krasnodar region): 355 mm (eight times its monthly normal), and monthly precipitation here totaled 596 mm (more than 13 times its normal). In Novorossiysk, maximum precipitation (110 mm) was recorded on 16 August.

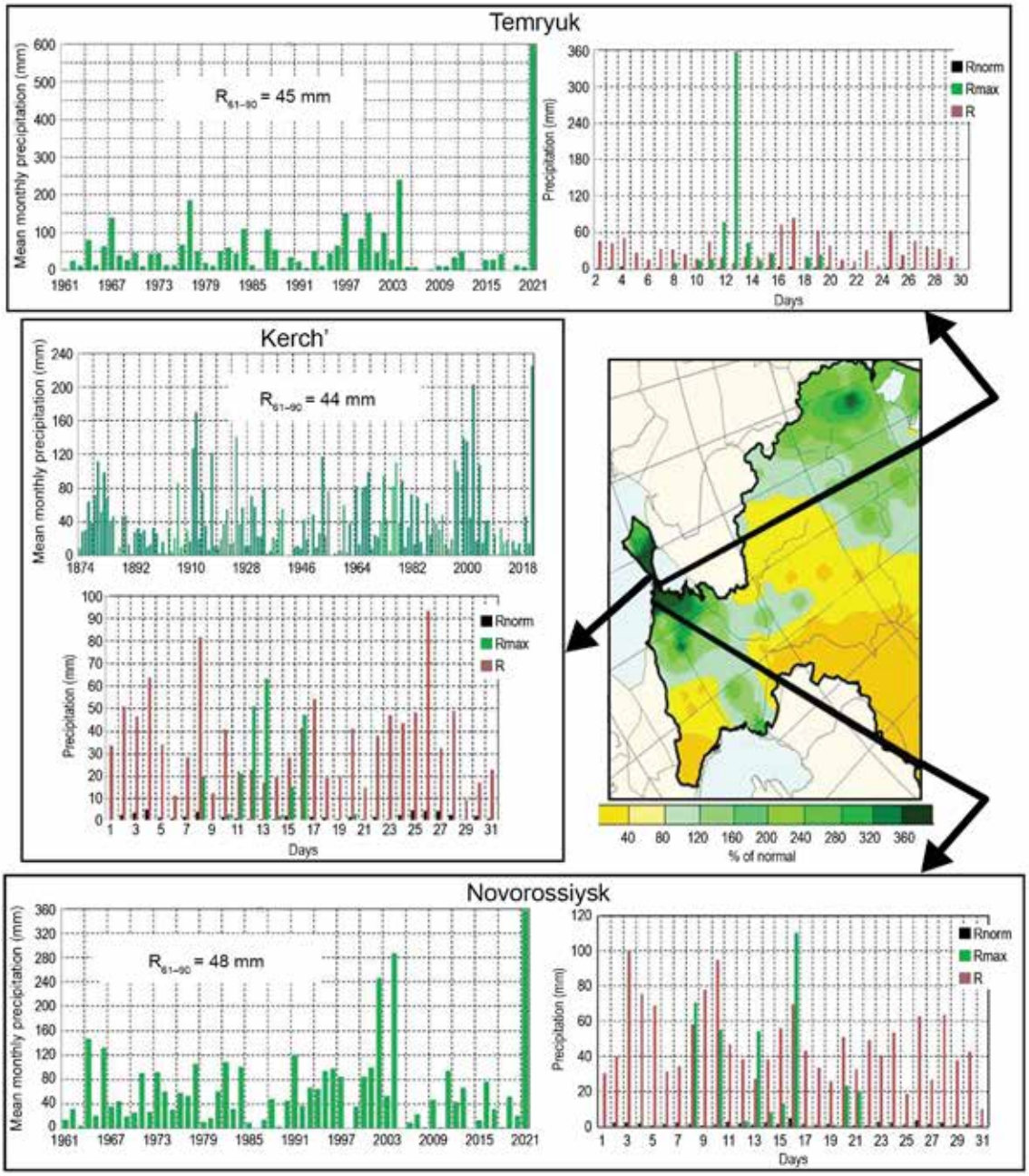

Fig. 7.48. Precipitation in Aug 2021 over southern regions of European Russia. The map shows the monthly precipitation (% of normal) and the insets provide the mean monthly precipitation (mm) in Kerch' (1874–2021) and Temryuk and Novorossiysk (1961–2021), and daily precipitation (mm): observed (R: green), along with the climatological normal (Rnorm, black) and the absolute maximum (Rmax, brick red) at these stations. R61–90 (mm) is the 1961–1990 normal precipitation for the month.

(iii) Notable events and impacts

On 8–9 April, easterly winds reached 33–38 m s^{-1} in the far eastern region of Petropavlovsk–Kamchatsky and up to 40–47 m s^{-1} along the nearby coastal regions, causing significant damage estimated at 7.1 million rubles to the city infrastructure.

On 12 May, wind speeds in Moscow and the Moscow region reached 20–24 m s^{-1}; leading to one fatality, four injuries, uprooting of 147 trees, and damage to dozens of cars.

On 17–18 June, heavy rain in Yalta, a city on the southern coast of the Crimean Peninsula, persisted for 16 hours, resulting in 133 mm rainfall accumulation. Pedestrian underpasses were inundated and many streets were completely flooded.

On 18 July, mudflow 100 m wide and up to 2.5 m thick descended along the bed of the Derekoika River. Traffic in the center of Yalta and the entrance to the city were completely diverted. A state of emergency was declared, and direct damage was about 15 billion rubles.

On 23 July, Khosta, part of Great Sochi, received 154 mm of precipitation in six hours. Runoff and river overflows in the Khosta region inundated roads, adjacent territories, a hospital, and ambulance substations. Mudflows affected the urban infrastructure in Kudepst, Matsesta, and Khosta.

From 5 August to 20 September, excessive rainfall led to flooding on the Amur River, impacting the Amur Region, Jewish Autonomous Region, and Khabarovsk Territory. Water levels in the river rose to 0.3–1.0 meters above the hazardous mark. A state of emergency was declared, as roads, communication lines, bridges, and houses were flooded.

On 17 October, heavy wet-snow precipitation (3–6 cm) was recorded on Sakhalin, accompanied by winds as high as 33–36 m s^{-1}. Dozens of villages lost power and heating. Rooftops were damaged in Aleksandrovsk–Sakhalinski, killing two people. Traffic was restricted and flights were delayed.

3) EAST AND SOUTHEAST ASIA—P. Zhang, T. C. Lee, A. M. Setiawan, M. Aurel, M. Hanafusa, Hir. Sato, S. Wakamatsu, G. S. Im, D. Dulamsuren, M.-V. Khiem, and H.-P. Lam

Countries/places considered in this section include China, Hong Kong (China), Indonesia, Japan, Korea, Mongolia, Singapore, and Vietnam. Unless otherwise noted, anomalies refer to the 1991–2020 base period.

(i) Temperature

Annual mean temperatures for 2021 across East and Southeast Asia are shown in Fig. 7.42. The annual mean air temperature for China was 10.5°C, 0.64°C above the 1991–2020 normal, the highest since the start of the record in 1951. It was also the warmest year in Hong Kong since its records began in 1884, with an annual mean temperature of 24.6°C which was 1.1°C above normal.

Annual mean temperatures were significantly above normal in northern and western Japan and above normal in eastern Japan and in Okinawa/Amami. The annual mean temperature over South Korea was 13.3°C (0.8°C above normal), which was the second highest since records began in 1973. Spring and autumn, in particular, were significantly warmer than normal.

The annual mean temperature over Mongolia was 1.7°C (2.3°C above average; also the second highest since 1940), The second-warmest February and third-warmest March on record contributed to this annual warmth.

Annual mean temperatures were above normal across Indonesia (0.4°C above the 1991–2020 normal), based on the record of 89 weather stations, marking the eighth-warmest year since start of the record in 1981. The highest temperature recorded in 2021 was 37.9°C on 22 October in Surabaya (East Java).

The annual mean temperature for Singapore was 27.9°C, which is 0.1°C above normal and marked the 10th warmest year on record. In January and August, below-average temperatures were associated with significantly above-average rainfall. Notably, January 2021 was the coolest January in the past 30 years, while August 2021 was the second coolest August in the past 20 years.

The monthly mean temperature was above normal across Vietnam for most months in 2021. Some stations in North and South Vietnam recorded historically high monthly mean temperatures, including: Dong Van (Ha Giang): 17.4°C (surpassing 17.1°C in 2015); Cao Lanh (Dong Thap): 28.7°C (28.3°C in 2015); Soc Trang: 28.6°C (28.2°C in 2017); Rach Gia (Kien Giang): 29.5°C (29.3°C in 2017).

(ii) Precipitation

Annual precipitation for 2021 as a percentage of normal over East and Southeast Asia is shown in Fig. 7.43. For China, the average annual precipitation total was 672.1 mm, 105.4% of its 1991–2020 normal. The annual precipitation total was highest in the 61-year record in both North China (154% of normal) and the Haihe River basin (174%). The precipitation in spring, summer, and autumn in total was also record high with 133% of its normal. The total annual rainfall for Hong Kong in 2021 was 2307.1 mm, 95% of its normal.

In Japan, annual precipitation totals were significantly above normal on the Pacific side of eastern Japan, and above normal on the Pacific side of northern Japan, the Sea of Japan side of eastern Japan, and in western Japan. The annual precipitation total in South Korea was 1244.5 mm, which was 93.7% of its normal of 1331.7 mm. Low-pressure systems, typhoons, and the Meiyu/Baiu/Changma fronts mainly affected the southern region; precipitation totals across the central region were below normal. Annual precipitation for Mongolia was 261.7 mm above normal, its fifth highest total since 1940.

The spatially averaged annual rainfall total for Indonesia was 2910 mm, placing 2021 as the second-wettest year since the start of the record in 1981. 2010 and 1998 were the wettest and the third wettest years, respectively, both of which experienced strong La Niñas in the second half of the years. The highest rainfall anomaly in 2021 was recorded at Sultan Iskandar Muda station, Banda Aceh, at about 249% of its 1991–2020 normal.

The annual total rainfall for Singapore in 2021 was well above average, resulting in the country's second wettest year since 1981. Average rainfall totals in January (480.5 mm) and August (426.2 mm) were at least twice their respective long-term monthly averages. The annual total rainfall at the Changi climate station of 2809.6 mm and the average total of 3167.7 mm across island-wide stations with long-term records was 133% and 125% of their respective long-term annual averages of 2113.3 mm and 2534.4 mm, respectively.

(iii) Notable events and impacts

In China, the Meiyu/Baiu/Changma season, which started later and ended earlier than the 1991–2020 normal, was eight days shorter overall, with 267.2 mm rainfall (78% of normal). However, the rainy season in North China in 2021 lasted 59 days, the second longest since the start of the record in 1961, with average total rainfall of 276.4 mm (203% of normal, the third highest on record). From 15 to 22 July, heavy precipitation fell in central and southern North China, the middle reaches of the Yellow River, and the upper reaches of the Huai River basins, with maximum cumulative precipitation records observed at 26 stations, including Zhengzhou in Henan (851 mm). During this period, Zhengzhou observed a maximum daily precipitation total of 624.1 mm, close to its 1981–2010 annual normal of 641 mm (see Sidebar 7.4). During September and October, the Weihe River, a tributary of the Yellow River, experienced its largest flood for this time of year since 1935. In 2021, under the control of the strong subtropical high, daily maximum temperatures exceeded 40°C at Toxon (46.5°C on 25 July) in Xinjiang, Fushun (41.5°C on 3 August) in Sichuan, and Mizhi and Yichuan (40.6°C on 31 July) in Shaanxi, breaking or equaling the historical record since 1961. From early November 2020 to early February 2021, due to scarce precipitation (20% to 50% of normal in most areas) and well-above-normal temperatures, moderate to severe meteorological drought developed rapidly in Jiangnan and South China, leading to less water storage in lakes and reservoirs and severe impacts on water resources and agricultural production in the concerned areas.

Hong Kong, China, experienced record-breaking monthly mean temperatures of 22.0°C in March, 29.0°C in May, and 29.7°C in September. Sixty-one hot nights (daily minimum temperature ≥ 28.0°C) and 54 very hot days (daily maximum temperature ≥ 33.0°C) were reported in 2021, both of which were the highest annual totals on record. Hong Kong was exceptionally dry during the first five months of 2021 with only 163.1 mm of rainfall, the second lowest amount on record for

this period. Tropical Cyclone Lionrock brought 329.7 mm of rainfall to Hong Kong on 8 October, the highest daily rainfall on record for that month. Tropical Cyclone Rai was the first super typhoon to occur in the South China Sea in December since 1961.

In central Vietnam, during 22–23 October, a new 24-hour record rainfall total of 488 mm in Tam Ky station (Quang Nam) was set, breaking the previous record of 381 mm on 20 October 2001. Additionally, Quang Ngai, Tra Khuc, and Chau O stations (Quang Ngai) observed record high totals of 532 mm, 576 mm, and 641 mm, respectively, compared to their previous records of 525 mm, 518 mm, and 439 mm on 29 September 2009.

In August, active stationary fronts formed between the Okhotsk High and the North Pacific Subtropical High, and moist air along these fronts brought record-breaking monthly precipitation amounts to western Japan.

South Korea observed its highest March monthly mean temperature (8.7°C; +2.6°C above normal) since the start of the record in 1973. As a result, the cherry blossoms bloomed 5–16 days earlier than normal across the country.

In Mongolia, 129 weather disasters/extreme events (strong winds, flash floods, heavy precipitation, etc.) were reported around the country in 2021. The most devastating of these was the strong winds and dust storms that spread across Mongolia on 13–15 March, which led to 10 fatalities, and more than 700 people were injured.

Tropical cyclone Seroja brought extremely heavy rainfall to Indonesia on 5 April, with daily rainfall totals of more than 200 mm recorded at many point observations. The heaviest rainfall was 460 mm, recorded in Tilong Dam, east of Kupang (East Nusa Tenggara provinces capital city).

In December, Typhoon Rai passed over Song Tu Tay station in Vietnam where maximum winds of 45.6 m s^{-1} (gusts of 56.8 m s^{-1}) were recorded. This was the highest wind speed observed in the Vietnam observation system in the last 40 years.

Sidebar 7.4: Unprecedented extreme rainfall over East Asia in July and August 2021—

Z. Zhu, X. Liu, R. Lu, S. Wakamatsu, and K. Takahashi

During July 2021, heavy rainstorms caused devastating floods across a wide range of areas in North China. On 20 July, a 1-hour precipitation total in Zhengzhou—the capital of Henan province in central China and home to more than 10 million people—reached 201.9 mm, breaking the record for the largest hourly precipitation in mainland China. The disastrous rainstorms inundated the city, leading to 380 fatalities or missing people.

The July mean precipitation anomalies (Fig. SB7.6a) showed two maximum centers > 8 mm day^{-1}: one in North China (red box) and one in the Yangtze River Delta. Steered by the dominant large-scale anomalous circulation, Typhoon In-fa (shown in Fig. SB7.6b) retained its status as a Category 2 storm, churning north of Taiwan and landing in the Yangtze River Delta; this led to the maximum center in the region. Meanwhile, a moist onshore flow from the East China Sea was induced by the dominant easterlies over the northern flank of Typhoon In-fa and southern flank of the westward-extended western North Pacific Subtropical High (WNPSH; Fig. SB7.6b). The easterly moisture belt formed an atmospheric river spanning thousands of miles, which continuously transported water vapor to North China. With the help of the unique terrain over North China, the windward upslope moisture flow contributed to the unprecedented extreme rainfall over North China (Figs. SB7.6c,d).

Large-scale rainfall anomalies were often directly linked with the anomalous atmospheric circulation, which was further induced by boundary layer forcing (e.g., sea surface temperatures [SST] and sea ice cover). Notably, positive SST anomalies were observed over the tropical Atlantic during July (Fig. SB7.6e), which was highest since the start of the record in 1979, and the topical Atlantic SST was historically correlated with North China rainfall (Fig. SB7.6d), suggesting its potential role in driving the abnormal North China rainfall. Associated with the tropical Atlantic SST is a circumglobal teleconnection (Branstator and Teng 2017) emanating from the North Atlantic to East Asia (Fig. SB7.6e). At the end of the teleconnection was an anticyclonic anomaly, leading to the westward-extended WNPSH, which was conducive to the transportation of water vapor into North China (Fig. SB7.6b).

In addition to the Atlantic SST anomaly, sea ice cover in the Laptev and East Siberian Seas was significantly below average in July 2021 (Fig. SB7.6f). Historically, sea ice cover in the Laptev and East Siberian Seas is negatively correlated with North China rainfall. The Arctic sea ice cover in July 2021 was the lowest since the start of the record in 1979 (see section 5d for details), which may have contributed to the positive North China rainfall anomaly (Fig. SB7.6d). The reduced sea ice cover could shift the polar vortex to southward and further enhance WNPSH over Northeast Asia and the moist onshore flow from the East China Sea, leading to the unprecedented North China rainfall in July (Fig. SB7.6f).

Monthly precipitation in August was above normal from central China to eastern Japan and in and around Mongolia. In particular, areas from western to eastern Japan experienced record-high rainfall, totaling as much as 1400 mm from mid-to-late August in association with a highly active stationary front over the region.

The widespread heavy rainfall in western and eastern Japan was partially attributed to the unusual formation of a stationary front during midsummer, which was related to a significant north–south temperature gradient in the lower troposphere between the Okhotsk High to the north of Japan and a southward-shifted WNPSH expanding to the south of Japan. The southward shift of the WNPSH that caused a large amount of water vapor flow into western and eastern Japan was related to the southward shift of the subtropical jet stream (STJ) over East Asia in the upper troposphere. Furthermore, significant southward meandering of the jet stream to the west of Japan was considered to have produced favorable conditions for updraft occurrence and persistent rainfall from western to eastern Japan. The southward shift of the STJ was likely affected by SST anomalies accompanying a negative phase of the Indian Ocean Dipole (Saji and Yamagata 2003) conditions (see section 4f) and related suppressed convection over the Asian summer monsoon region.

In conclusion, the simultaneous boundary forcings from different regions (both tropical and polar regions) led to unprecedented extreme rainfall in East Asia during the summer of 2021. Given that the Atlantic warming and Arctic Sea ice loss may be partly a manifestation of global warming, more extreme rainfall events are expected in the near future.

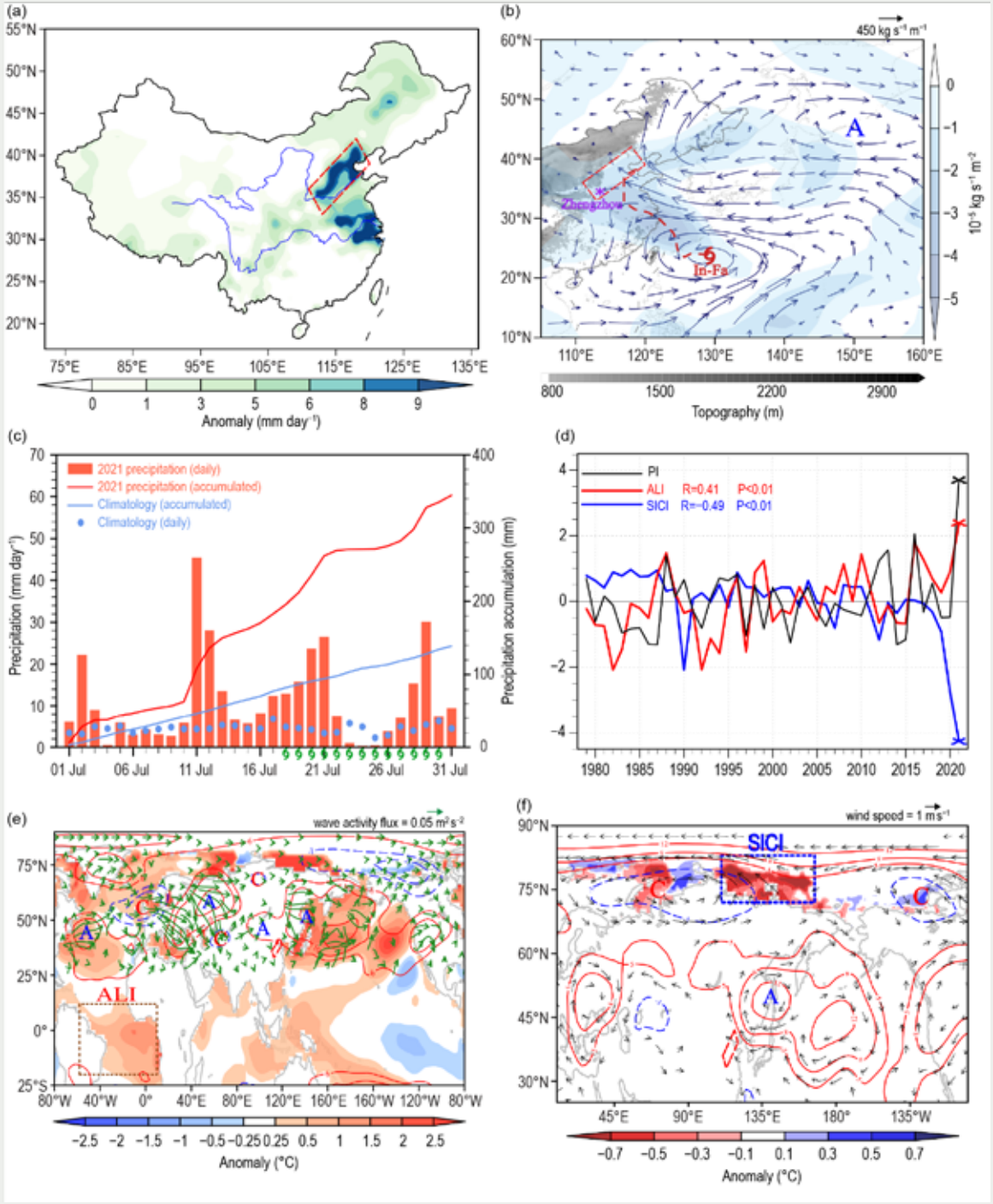

Fig. SB7.6. (a) Rainfall anomaly (shading, mm day^{-1}) in China for Jul 2021. (b) The 1000–700-hPa integrated moisture flux anomaly (vector, kg s^{-1} m^{-1}) and convergence (shading, × 10^{-5} kg s^{-1} m^{-2}) in July 2021; gray shading is topography (m), the dashed curve denotes the moving track of Typhoon In-fa, and the purple asterisk marks the city of Zhengzhou. (c) Evolution of the daily precipitation (mm day^{-1}) and accumulated precipitation (mm) averaged in Jul over North China. The green typhoon sign marks the duration of Typhoon In-fa. (d) The standardized time series of the North China precipitation index (PI, black, for averaged mean precipitation over North China), the tropical Atlantic sea surface temperature index (ALI, red, averaged mean SST over brown box in [e]), and the Arctic sea ice cover index (SICI, blue, averaged mean sea ice cover over black box in [f]) in July. The correlation coefficient between the PI and ALI (SICI) is shown in red (blue). (e) SST anomalies in Jul 2021 (shading, °C), and the regressed 500-hPa geopotential height (contour, gpm), wave activity flux (vector, m^2 s^{-2}) onto ALI. (f) Sea ice cover anomalies in Jul 2021 (shading, °C), and the regressed 500-hPa geopotential height (contour, gpm) and wind (vector, m s^{-1}) onto SICI. The letters A and C denote the centers of the anticyclonic and cyclonic anomalies, respectively. The dashed box in (a), (b), (e), and (f) outlines North China.

4) SOUTH ASIA—O. P. Sreejith, A. K. Srivastava, and M. Rajeevan

Countries in this section include Bangladesh, India, Pakistan, and Sri Lanka. Unless otherwise noted, climate anomalies are relative to the 1981–2010 base period.

(i) Temperature

In 2021, South Asia generally experienced above-normal temperatures. The annual mean land surface air temperature averaged over India was 0.44°C above normal, making 2021 the fifth-warmest year on record since nationwide records commenced in 1901 (Fig. 7.49). Seasonal mean temperatures were above normal for all seasons. The winter season (January–February, 0.78°C above average) and post-monsoon season (October–December, +0.42°C) mainly accounted for the above-normal annual temperature. The five-warmest years on record in order are: 2016 (+0.71°C), 2009 (+0.55°C), 2017 (+0.54°C), 2010 (+0.54°C), and 2021 (+0.44°C).

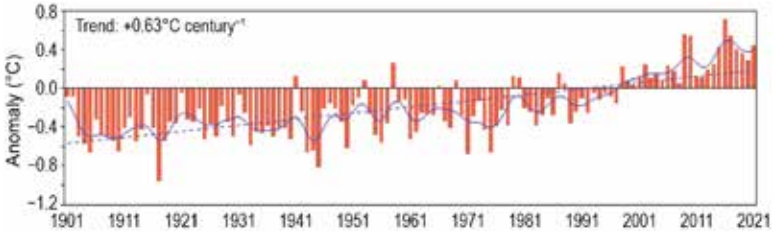

Fig. 7.49. Annual mean temperature anomalies (°C; 1981–2010 base period) averaged over India for the period 1901–2021. The smoothed time series (9-point binomial filter) is shown as a continuous blue line. The dotted blue line depicts the linear trend (°C century^{-1}).

(ii) Precipitation

The summer monsoon season (June–September) contributes about 75% of the annual precipitation over South Asia. In 2021, the summer monsoon set in over Kerala (southwestern parts of Indian peninsula) on 3 June (climatological normal is 1 June). The monsoon covered the entire country on 13 July (climatological normal is 8 July).

For India, the long-term average (LTA) of the summer monsoon rainfall, calculated using all data from 1961 to 2010, is 880 mm with a standard deviation of about 10%. However, over smaller regions, the standard deviation is much larger (around 19%). During 2021, the Indian summer monsoon rainfall (ISMR) averaged over India as a whole was 99% of its LTA value. Rainfall was fairly well distributed over the country, except for the eastern and northeastern regions. Seasonal rainfall was 96%, 104%, 111%, and 88% of LTA, respectively, over the homogeneous regions of Northwest India, Central India, South Peninsula, and East and Northeast India. On the monthly scale, rainfall for the country as a whole was above normal during June and September (110% and 135% of LTA, respectively) and below normal during July and August (93% and 76% of LTA, respectively). For the country as a whole, spatially-averaged rainfall was above or near-normal both at the beginning and end of the season (Figs.7.50, 7.51).

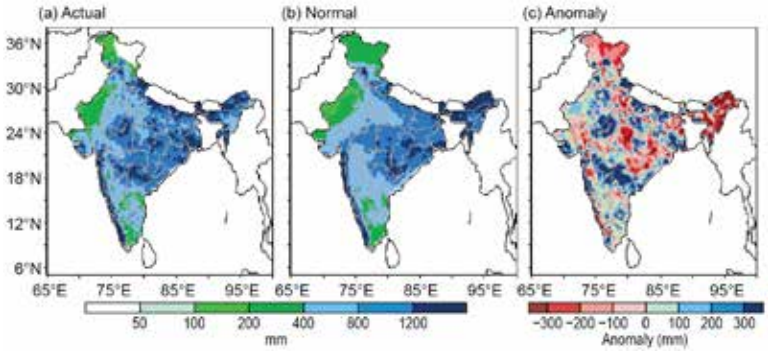

Fig. 7.50. Spatial distribution of (a) actual, (b) normal, and (c) anomalous monsoon seasonal (Jun–Sep) rainfall (mm) over India in 2021.

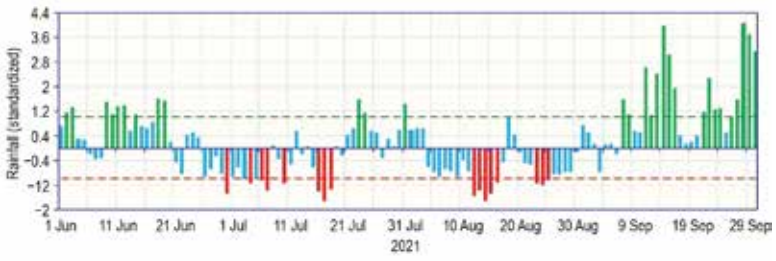

Fig. 7.51. Daily standardized rainfall time series averaged over the core monsoon zone of India for the period 1 Jun–30 Sep 2021.

Rainfall over India was below normal (68% of its LTA) during the winter season (January–February) and was above normal (118% and 144% of LTA) during the pre-monsoon season (March–May) and the post-monsoon season (October–December).

Pakistan, which is at the western edge of the pluvial region of the South Asian monsoon, received 60–70% of its annual rainfall during the summer monsoon season (July–September). The summer monsoon typically sets over eastern parts of Pakistan around 1 July, with a standard deviation of five days. In 2021, summer monsoon rainfall over Pakistan was normal (89% of LTA). Pakistan observed normal rainfall during July (104% of LTA), significantly below-normal rainfall during August (38%), and significantly above-normal rainfall during September (160%). During September, the monthly rainfall totals were generally above average throughout the country and significantly above average over South Pakistan and areas of Punjab province. The post-monsoonal rainfall (October–December) in 2021 was 89% of the LTA. However, in October, Pakistan as a whole received exceptionally above-normal rainfall (234.3% of its LTA), making it the fifth-wettest month on record since the start of the record in 1961. The unusually high rainfall totals during October were mainly associated with Severe Cyclonic Storm Shaheen, which formed at the beginning of the month, as well as subsequent passages of frequent westerly waves, with troughs affecting the region.

Bangladesh received normal rainfall (104% of its LTA) during its summer monsoon season in 2021 (May–September), while Sri Lanka received above-normal rainfall during its summer monsoon season.

Toward the end of the year, the northeast monsoon (NEM) set in over the southern Indian peninsula on 25 October and over Sri Lanka in late November. The NEM contributed 30–50% of the annual rainfall over the southern Indian peninsula and Sri Lanka as a whole. Seasonal rainfall over this region was exceptionally above normal (171% of LTA) and was the highest (579.1 mm) since the start of the record in 1901. The exceptionally above-normal rainfall during the season was mainly due to the frequent formation of many low-pressure systems. Northeast monsoon rainfall activity over Sri Lanka during October–December, however, was normal.

(iii) Notable events and impacts

In 2021, thunderstorms and lightning claimed around 800 lives across different parts of India. On 12 July, at least 74 people were killed by lightning strikes in Rajasthan, Uttar Pradesh, and Madhya Pradesh. At least 41 people—mostly women and children—were reportedly killed in Uttar Pradesh state. The highest death toll of 14 was recorded in the city of Allahabad. In Rajasthan, 11 people were killed when they were struck by lightning at Amer Fort near Jaipur.

Heavy rainfall and flood-related incidents claimed over 750 lives across different parts of India during the year. Of those lives lost, 215 were from Maharashtra, 143 from Uttarakhand, 55 from Himachal Pradesh, 53 from Kerala, and 46 from Andhra Pradesh.

In Bangladesh, continuous heavy rains from late July to early August caused severe floods, which claimed 21 lives. More than 2.6 million people were affected, and there was widespread loss of crops and houses.

During the monsoon season in June, 46 people died on the 16th and 17th due to severe floods in Nepal, and 10 people died in Bhutan. In another incident, during the first week of July, floods and landslides associated with heavy rains claimed 74 lives in Nepal. During 16–22 October, more than 100 people died due to floods and landslides resulting from heavy rains. In Sri Lanka, 26 people died due to floods associated with intense rainfall on 6–7 October.

During 2021, five tropical cyclones formed over the North Indian Ocean. Extremely Severe Cyclonic Storm Tauktae, which formed during the pre-monsoon season over the Arabian Sea, crossed the Saurashtra coast on 17 May. The storm claimed 144 lives, mainly from western India, stretching from Kerala in the far southern part of the country to Gujarat in the northwest. Severe Cyclonic Storm Yaas (23–28 May), which formed during the pre-monsoon season over the Bay of Bengal, crossed the north Odisha coast on 26 May, and caused nine fatalities. Over 1.3 million people in total were affected by the floods. Cyclonic Storm Gulab (24–28 September) crossed the north Andhra Pradesh/south Odisha coasts on 26 September, claiming 19 lives in the coastal

districts. See section 4g5 and Fig. 4.36 in The Tropics chapter for more details about the 2021 North Indian Ocean cyclone season. The tracks of these cyclonic storms are shown in Fig. 7.52.

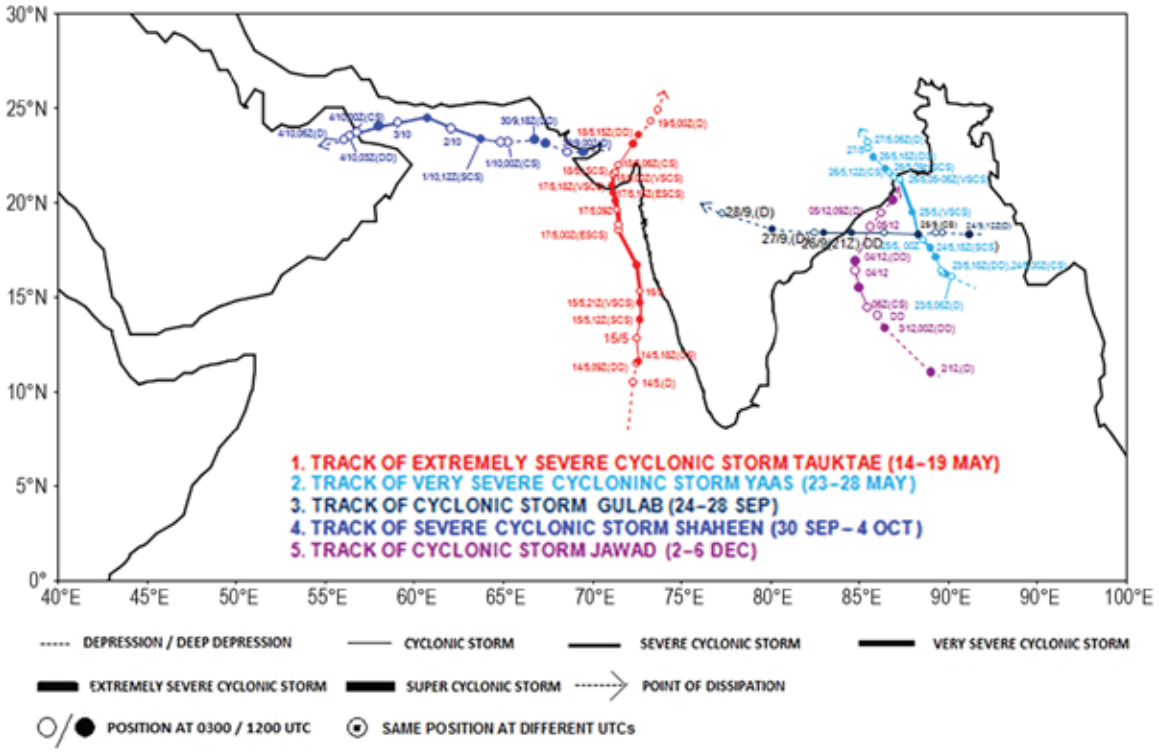

Fig. 7.52. Storm tracks of all cyclones that formed in the North Indian Ocean basin in 2021.

5) SOUTHWEST ASIA—A. Vazifeh, A. Fazl–Kazem, P. Asgarzadeh, and M. Mohammadi

This section only covers Iran. Climate anomalies are relative to a 1981–2010 base period for temperature and precipitation.

(i) Temperature

Based on synoptic station data analysis (around 500 stations), the annual average temperature for Iran in 2021 was 19.4°C, 1.9°C above normal. The annual maximum average temperature was 26.6°C, 2.2°C above normal, and the annual minimum average temperature was 12.2°C, 1.6°C above normal. West of the country, temperatures over the Zagros Mountains and plains in northern parts of the Persian Gulf were 1.6–2.5°C above normal, and all provinces were warmer than normal (Fig. 7.53).

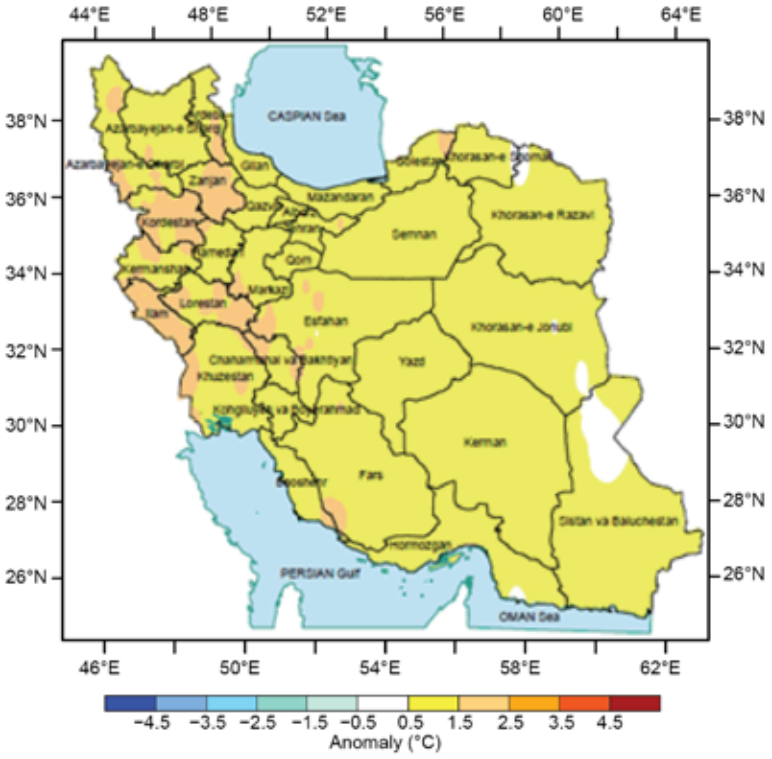

Fig. 7.53. Annual average temperature anomalies (°C; 1981–2010 base period) in Iran for 2021.

(ii) Precipitation

The average annual accumulated precipitation for all provinces in Iran was below normal (53.7% of normal), the lowest since 1991. The greatest deficits occurred in

the central Zagros Mountains in western and southwestern Iran, in the domains of the Alborz extending north, in the southern Caspian Sea, and in the south in provinces along the Persian Gulf. The three greatest deficits were observed in: Bushehr (24.8% of normal), Sistan va Baluchestan (26.3%), and Hormozgan (29.2%) provinces, all in southern and southeastern Iran (Fig. 7.54).

Thus, exceptional below-normal annual precipitation, together with above-normal temperatures, made 2021 the driest year on record since 1991, as shown by the standard precipitation index (SPI, Fig. 7.55).

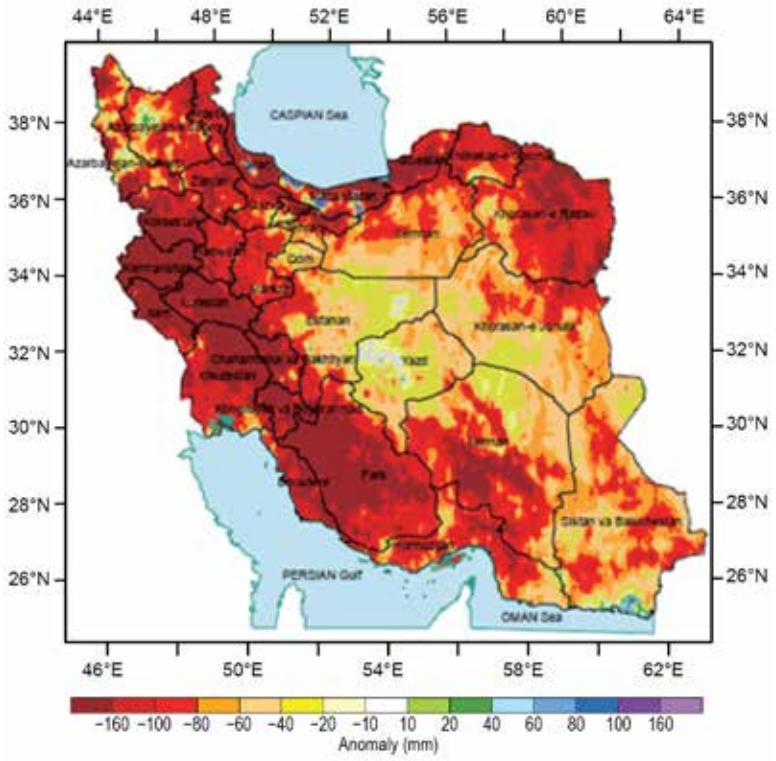

Fig. 7.54. Annual average precipitation anomalies (mm; 1981–2010 base period) in Iran for 2021.

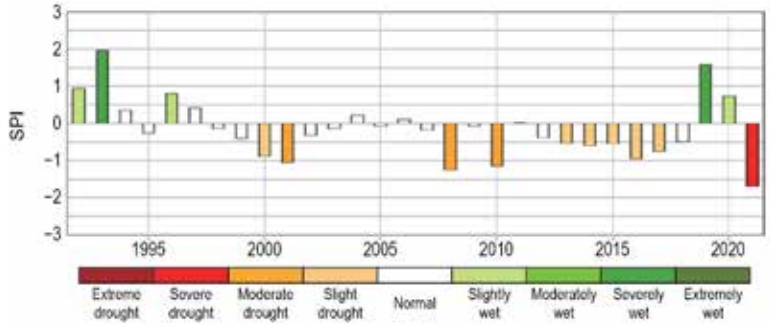

Fig. 7.55. Timeseries of the standard precipitation index (SPI) for Iran over the period 1992–2021.

6) CENTRAL ASIA—W. M. Thiaw, S. Fuhrman, and M. F. Zaheer

Central Asia is a landlocked, semi-arid region spanning a wide latitudinal area that extends from the northern temperate zone, with Russia at its northern border, to the southern subtropics. It exhibits a complex topography, ranging from vast plains to high mountains, with the Caspian Sea at its western edge. Its climate is diverse and is influenced by the strong inhomogeneity of the terrain. For the purpose of this analysis, Central Asia is defined as the region encompassing the countries of Afghanistan to the south; from east to west, Turkmenistan, Uzbekistan, Tajikistan, and Kyrgyzstan in the central part of the region; and Kazakhstan to the north. Unless otherwise specified, the climatological base period is 1991–2020 for both temperature and precipitation.

(i) Temperature

Climatologically, annual mean temperatures were lowest (0° to –10°C) over the central and southern areas of Tajikistan. The northern and east central areas encompassing northern Kazakhstan, Kyrgyzstan, western Tajikistan, and northeastern Afghanistan registered average temperatures (0° to 15°C). Mean temperatures were higher (15° to 25°C) over western Afghanistan, while they were (15° to 20°C) over eastern and western Turkmenistan.

During 2021, the annual mean temperature was between 15° and 25°C in western Afghanistan (Fig. 7.56a). Temperatures ranged between 15° and 20°C in eastern and western Turkmenistan, and between 0° and 15°C in the remainder of the region, except for the central and eastern areas of Tajikistan, where readings dipped to –20°C. Mean temperatures were 2–4°C below normal over the Afghanistan Panhandle extending into Tajikistan and eastern Kyrgyzstan (Fig. 7.56b), making 2021 one of the coldest years, in the 5th percentile based on the 1991–2020 period. Temperature departures from average ranged between –0.5° and –1.5°C in northeastern Kazakhstan, and northern Afghanistan, and westward to the border with Turkmenistan. In contrast, western Kazakhstan and southern Afghanistan registered 0.25° to 1°C above normal, with local areas observing mean annual temperatures in the 80th to 90th percentiles.

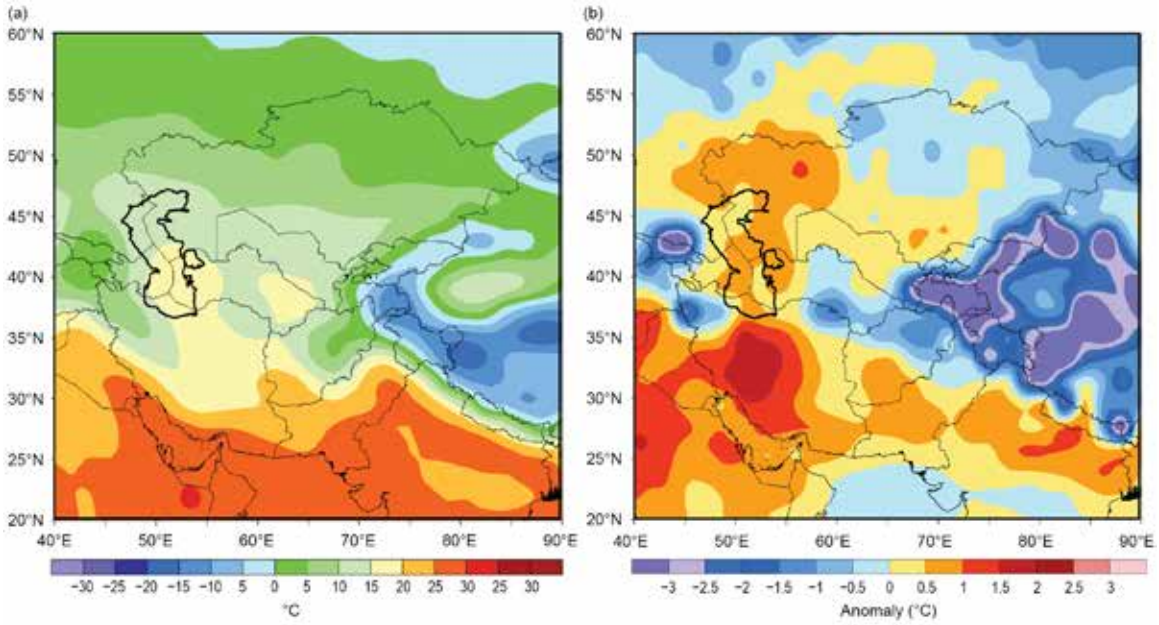

Fig. 7.56. Annual mean (a) climatological and (b) 2021 anomalous temperatures (°C) for Central Asia with respect to the 1991–2020 base period. (Source: NOAA/NCEP.)

An analysis of the evolution of temperature throughout the year shows that January was extremely cold in much of Central Asia, with temperatures hovering around –10°C in southern Kazakhstan and plunging to –20°C in the north, about 2–4°C below the mean over much of Kazakhstan. Mean temperatures were milder in February, ranging between –15°C in northern Kazakhstan to +15°C in the southern areas of the region. These were 0.5° to 3°C above the mean over much of the region, and in the 85th to 95th percentiles in southern Afghanistan.

During the spring and summer months, temperatures soared, and May was among the warmest months in the climatological period in the western two-thirds of Uzbekistan and much of Kazakhstan, with temperatures ranging between 15° and 30°C (4°C above the mean and in the 90th percentile) across this sub-region. Temperatures approached 40°C (≥ 2°C above the mean and exceeding the 85th percentile) in the southern tip of Afghanistan in July. Mean temperatures ranged between 30° and 35°C over much of the central and western sectors of the region from western Afghanistan northward into Turkmenistan, Uzbekistan, and southern Kazakhstan. These

were about 2–3°C above the mean and in the 90th percentile locally over eastern Turkmenistan and southeastern Kazakhstan. However, Tajikistan and Kyrgyzstan registered near-freezing temperatures as records indicated –5°C in eastern Tajikistan, while central Tajikistan and southern Kyrgyzstan registered 0° to +10°C. This was about 4°C below the mean and lower than the 5th percentile across Tajikistan.

Temperatures were more than 3°C below the mean across most of the mid-Central Asian countries from Kyrgyzstan and Tajikistan to Uzbekistan, including northern Afghanistan and southern Kazakhstan during October–December. This was below the 5th percentile in most areas in October and November. Freezing temperatures persisted in Tajikistan in December, falling to below –25°C (more than 3°C below the mean in far eastern Tajikistan).

The southern areas of Afghanistan and Kazakhstan, Turkmenistan, and Uzbekistan registered maximum temperatures (Tmax) between 40° and 45°C, but these were in the average range over most areas except for northwestern Kazakhstan where departures from normal ranged from +4° to +8°C. Tmax was lowest in Tajikistan, with departures ranging from 0° to –5°C (more than –8°C below the mean and less than the 3rd percentile) in August.

Annual minimum temperatures (Tmin) featured a steep east–west temperature gradient with the lowest temperatures between –20° and –30°C in eastern Tajikistan, more than 5°C below the mean, and less than the 3rd percentile. Tmin was average and hovered between 0° and 10°C in northern Kazakhstan. Tmin ranged from 0°C to 15°C from southern Kazakhstan southward to Uzbekistan and western Afghanistan. May exhibited the most elevated Tmin values (3–5°C above the mean) in the western half of Kazakhstan, while eastern Tajikistan registered Tmin values less than 5°C below the mean in November and December.

(ii) Precipitation

The climatological annual mean precipitation was variable across Central Asia and ranged from less than 200 mm over southwestern Afghanistan and central areas of Turkmenistan and Uzbekistan to 200–500 mm over central Afghanistan, far western Turkmenistan, extreme eastern Uzbekistan extending into Kyrgyzstan, and much of Kazakhstan. Precipitation was more than 500 mm over northeastern Afghanistan and Kazakhstan. Typically, winter and spring seasons accounted for the highest precipitation (rain and snow) amounts across the region, while the summer months tended to be drier.

Precipitation patterns in 2021 featured rainfall deficits across much of the region, except for a northeastern–central axis of Kazakhstan, where amounts ranged from 300 mm in the central areas to 750 mm in far northeastern sector (Fig. 7.57a), which was 25–50 mm above the mean across this sub-region (Fig. 7.57b). Deficits were highest over much of Afghanistan, the eastern areas of Turkmenistan and Uzbekistan, and western Tajikistan, where totals were as low as 10 mm to 50 mm (100–200 mm below the mean and in the 3rd percentile); in particular, totals were 300 mm below normal in southwestern Afghanistan. Totals averaged 50–150 mm (100–300 mm below the mean, below the 10th percentile) across the remainder of the sub-region. Examination of the evolution of precipitation throughout the year provided evidence of a dipole structure featuring above-average rainfall totals in northern Kazakhstan and below-average totals in the south in the areas encompassing the eastern sectors of Uzbekistan and Turkmenistan, along with Afghanistan, during winter. Precipitation totals in the north ranged from 100 mm to 300 mm (25–100 mm above the mean), and from less than 5 mm to 75 mm (50–200 mm below the mean, below 10th percentile) in the south. Much of the annual rainfall deficit was due to dryness in the winter through early spring. Precipitation was generally near-average across the region during the summer months through autumn.

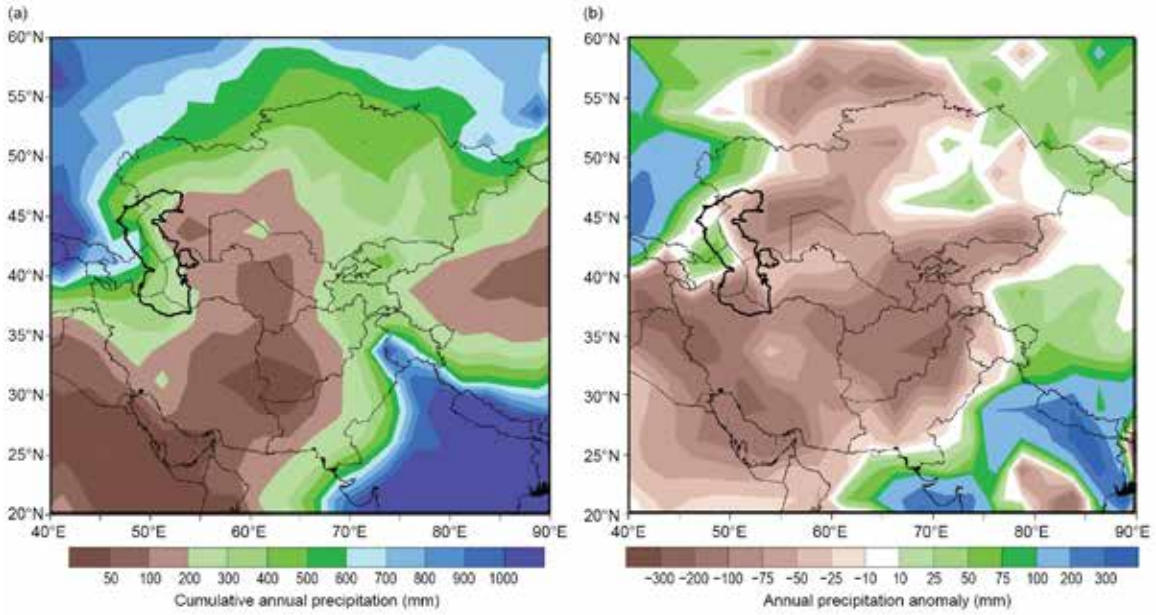

Fig. 7.57. Annual mean (a) climatological and (b) 2021 anomalous precipitation (mm) for Central Asia with respect to the 1991–2020 base period, GPCP data. (Source: NOAA/NCEP.)

(iii) Notable events and impacts

In central Afghanistan, 50–100 mm of rain fell during 27 April–3 May, according to NOAA's satellite rainfall estimates version 2 (RFE2), causing widespread flooding in the region. The Afghanistan National Disaster Management Authority reported 37 fatalities, along with the destruction of many homes that resulted in the displacement of more than 400 families.

The Aksy District in Jalal-Abad region of western Kyrgyzstan, close to the Uzbekistan border, experienced floods and landslides on 10 and 12 July due to heavy rains (~100 mm total). Kyrgyzstan's Ministry of Emergency reported that seven people were killed, and roads and four bridges were destroyed. Flood waters flowed downstream into the Namangan region of Uzbekistan, causing severe damage. The Ministry of Emergency Situations of the Republic of Uzbekistan reported eight fatalities and six injuries.

Large rainfall deficits were measured in Afghanistan during spring and autumn, with rainfall totals less than 50% of normal across the western two-thirds of the country and less than 30% of normal in the far southwest, according to data from the Global Precipitation Climatology Project (GPCP); these deficits led to a severe drought with significant impacts. The U.N. Food and Agriculture Organization estimated that wheat harvest in the region was about 20% less compared to the harvest in 2020. The U.S. Agency for International Development (USAID) projected that more than half of the country's population would be food insecure by winter 2021. In response to the humanitarian crisis, USAID disbursed more than $100 million (U.S. dollars) in food and nutrition assistance, essential healthcare, agriculture, and support to aid workers and access to critical relief supplies to care for more than 18.4 million vulnerable Afghans.

The spring drought in Afghanistan extended northward to Kazakhstan by the summer. Significant rainfall deficits were persistent here from April through August, especially in the western half of the country where totals were generally less than 50% of normal. A summer heat wave in the southern and western regions, with high record temperatures (including a reading on 7 July as high as 46.5°, which was 18° above the mean, according to the Kazakhstan Meteorological Service), exacerbated the situation. The drought, combined with the heat, resulted in the loss of thousands of livestock, depleted freshwater resources, and devastated crops. The Kazakhstan Ministry of Agriculture estimated crop yields were about 18% less compare to 2020. USAID provided Red Crescent of Kazakhstan with a grant in the amount of $100,000 (U.S. dollars) to support the population most affected by the drought.

h. Oceania—C. Ganter, Ed.

1) OVERVIEW

The region of Oceania (shown in Fig. 7.58) began 2021 with La Niña conditions in place. While regional assessments of La Niña differ slightly, conditions returned to a neutral El Niño–Southern Oscillation state in the middle of the year, with La Niña returning in the latter part of the year. La Niña typically leads to stark regional differences across the Oceania region, and 2021 reflected this, with drier conditions for some southwest Pacific Islands near the equator in the central and eastern part of the region and wetter conditions for eastern Australia. New Zealand experienced its typical warmer humid weather only during La Niña's return later in the year. The Micronesia region had a quiet year for typhoon activity, also typical of a La Niña influence. The negative Indian Ocean dipole, which was present through the middle of the year, was an additional factor contributing to Australia's wetter conditions, as was the positive Southern Annular Mode. New Zealand had its warmest year on record, with the climactic factors behind this discussed in Sidebar 7.5.

The BAMS *State of the Climate* editors and Micronesian co-authors would like to acknowledge the sad and sudden passing of Micronesian author Mark Lander in July 2022. Mark co-authored the Micronesian summary since its inclusion in the *State of the Climate* report in 2007, and he contributed immensely to the knowledge of how ENSO affects tropical storm, typhoon, and rainfall behavior in the North Pacific. Mark will be a huge loss to the tropical weather and climate community. Our thoughts and prayers are with his family during this solemn time.

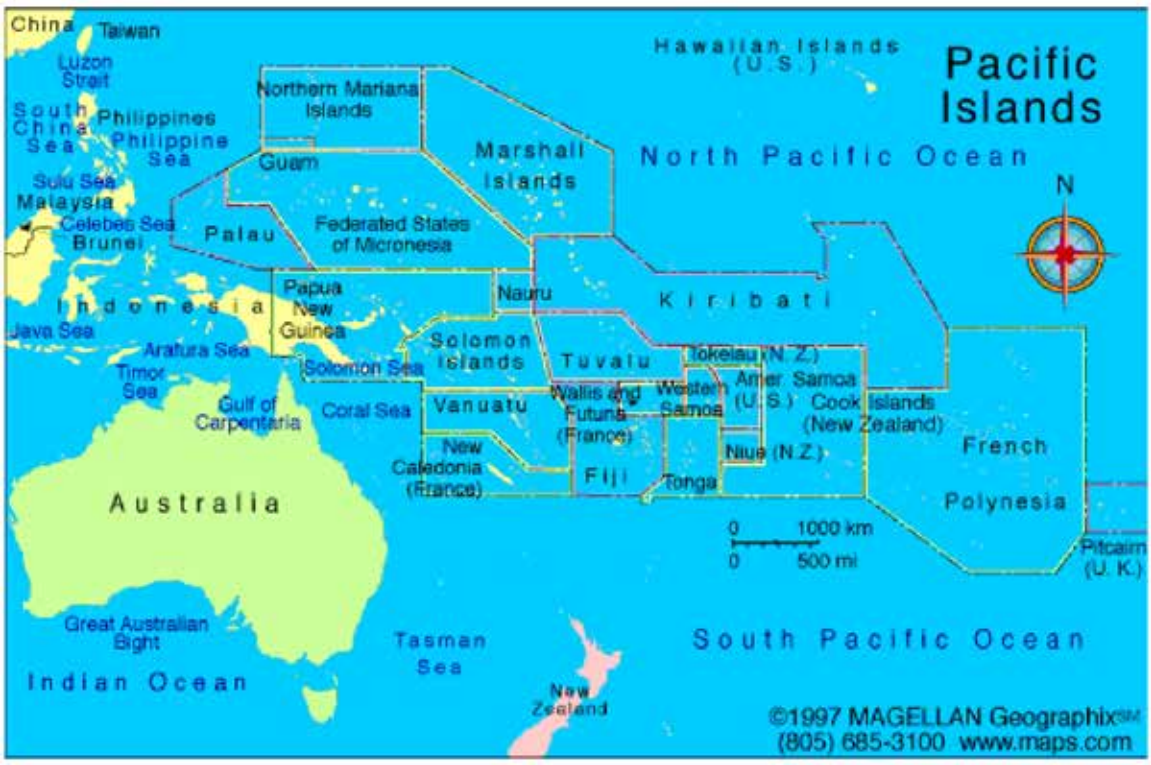

Fig. 7.58. The Oceania region as considered in this report includes the Pacific Islands from the Northern Mariana Islands in the western North Pacific to New Zealand in the south, Australia, Papua New Guinea, and Palau in the west, but excluding the islands of Indonesia, to French Polynesia in the east. (Source: https://www.infoplease.com/atlas/pacific-islands.)

2) NORTHWEST PACIFIC AND MICRONESIA—M. A. Lander, B. Bukunt, and C. P. Guard

This assessment covers the area from the date line west to 130°E, between the equator and 20°N. It includes the U.S.-Affiliated Islands of Micronesia, but excludes the western islands of Kiribati and nearby northeastern islands of Indonesia.

For much of Micronesia, the weather and climate of 2021 will be remembered for it being unusually quiet, with few extremes of wind, waves, or rainfall. There was a profound lack of tropical storms and typhoons in the western North Pacific basin, leading to quiet conditions throughout the region. Rainfall and temperature were near-average at most locations. Two La Niña characteristics stand out: (1) extreme dryness was confined to locations along the equator and (2) higher-than-normal sea levels exacerbated the magnitude of inundation from two high wave events in December.

(i) Temperature

Temperatures across Micronesia during 2021 varied regionally with both above- and below-average readings. The average 6-month maximum and minimum temperature anomalies are summarized in Table 7.1. Generally, warm daytime maximum temperatures are typically experienced in the Micronesian islands when skies are clear and winds are light; cooler temperatures occur when conditions are unusually cloudy, wet, and windy.

Table 7.1. Average 6-month temperature anomalies (Jan–Jun and Jul–Dec), and 6-month and annual rainfall totals and percent of average values for selected Micronesia locations during 2021. The average values are for the 1981–2010 base period. Latitudes and longitudes are approximate. "Kapinga" stands for Kapingamarangi Atoll in Pohnpei State, Federated States of Micronesia. The color fill of the boxes indicates: red for above average temperature and blue for below average; green for above average rainfall and yellow for below average rainfall. Note: extreme warmth at Saipan and at Yap are likely the result of ASOS sensor problems and a station relocation, respectively. The coolness at Palau may also be an effect of a relocation of the WSO Palau from the town of Koror to the international airport in Airai.

Location	Max Temp Min Temp		Rainfall (mm)							
	Jan–Jun	Jul–Dec	Jan–Jun	Jan–Jun	Jan–Jun	Jul–Dec	Jul–Dec	Jul–Dec	Jan–Dec	Jan–Dec
	°C	°C	AVG	2021	%	AVG	2021	%	2021	%
Saipan 15°N, 146°E	+1.87 +1.31	+0.69 +0.45	462.8	429.01	92.7	1306.1	1379.5	105.6	1808.5	102.2
Guam 13°N, 145°E	+0.06 +0.43	−0.04 +0.29	678.7	585.7	86.3	1813.6	1951.	107.6	2537.2	101.8
Yap 9°N, 138°E	−0.89 +1.24	−0.67 +1.40	1191.5	1662.8	139.5	1943.4	1689.4	86.9	3351.5	106.9
Palau 7°N, 134°E	−1.53 −0.35	−1.02 −0.67	1798.1	2170.4	120.7	2279.4	2525.3	110.8	4695.7	115.2
Chuuk 7°N, 152°E	−0.26 +0.68	−0.12 +0.75	1678.2	2102.9	125.3	1970.7	2122.7	110.7	4225.5	117.5
Pohnpei 7°N, 158°E	−0.70 +1.31	−0.49 +1.38	2361.2	3036.8	128.6	2308.4	2354.8	102.0	5391.6	115.5
Kapinga 1°N, 155°E	n/a	n/a	1880.6	1691.9	90.0	1485.1	1065.3	71.7	2757.2	81.9
Kosrae 5°N, 163°E	−0.19 −0.30	−0.23 +0.11	635.8	3941.3	149.5	2354.8	2686.0	114.1	6627.4	132.8
Majuro 7°N, 171°E	−0.14 +0.59	+0.23 +0.51	1459.0	2064.3	141.5	1875.0	1872.7	99.9	3937.0	118.1
Kwajalein 9°N, 168°E	+0.56 −0.05	+0.06 −0.04	898.4	831.9	92.6	1553.7	1319.8	84.9	2151.6	87.7

(ii) Precipitation

The average 6-month (January–June and July–December) and annual rainfall values for selected locations across Micronesia are summarized in Table 7.1. Three characteristics of the Micronesia regional precipitation during 2021 were particularly notable: (1) extreme dryness at Kapingamarangi; (2) a general tendency for wet conditions in central and western Micronesia, with drier conditions in the north (e.g., Saipan and Guam) and far east (e.g., Majuro and Kwajalein) for much of 2021; and (3) a record wet October at Guam.

Wet conditions across the average latitudes of the ITCZ (4°–8°N) are typical during La Niña. Also typical for La Niña is extreme dryness at Kapingamarangi and other locations along the equator. Dryness in eastern Micronesia (e.g., Majuro and Kwajalein) is often experienced during a prolonged La Niña event. Late in 2021, abundant rainfall returned to Kapingamarangi to help that island recover from the effects of long-term drought. On Guam, a large deficit of accumulated rainfall during a very dry 9-month period (January–September) was completely erased with record rainfall during October (Fig. 7.59).

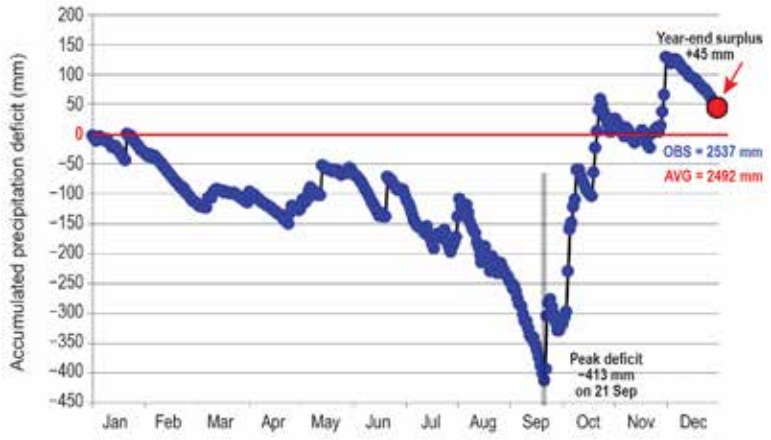

Fig. 7.59. Guam accumulated rainfall deficit for 2021. Gray line denotes lowest point in 2021.

(iii) Notable events and impacts

The Pacific climate system entered La Niña in the second half of 2020, and these conditions were present through much of 2021. During La Niña, prolonged dryness with accompanying drought is typically experienced at islands near the equator (e.g., at Kapingamarangi). In keeping with a typical response to La Niña, conditions were very dry at Kapingamarangi (1.1°N, 154.8°E). Prolonged dry conditions there led to severe drought conditions that impacted potable water supplies, local vegetation, and food crops. A few islands away from the equator (e.g., the northern Marshall Islands) also experienced some periods of unusual dryness, but the dryness in these locations was not accompanied by severe impacts.

Persistent dryness at Guam during January–September abruptly ended with very wet conditions in October. The 677.7 mm of rainfall observed at the Guam Weather Forecast Office was a modern-day (post-World War II) record. Contributors to this high rainfall total included some passing tropical disturbances and slow-moving diurnal island thunderstorms in light-wind (i.e., 'doldrum') conditions.

The western North Pacific typhoon season of 2021 was quiet (Fig. 7.60), which is typical for the Micronesia region during La Niña. The Joint Typhoon Warning Center (JTWC) upgraded only 10 of the basin's tropical cyclones to typhoon status—the fourth lowest annual total in its 62-year historical record (the Japan Meteorological Center reported only 9 typhoons). Within Micronesia, only Palau experienced some moderate effects (gales and high surf) when Tropical Storm Rai passed close by in December. Several tropical

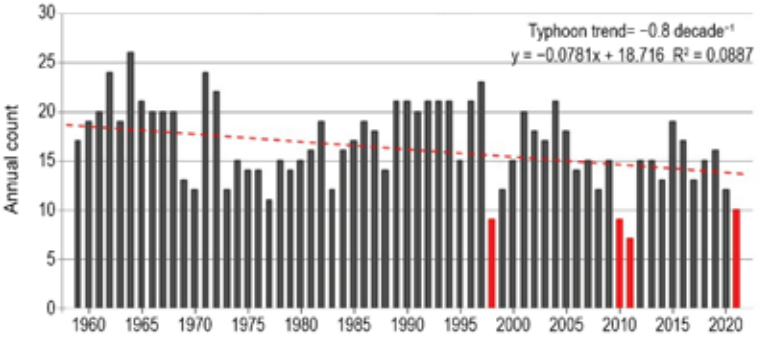

Fig. 7.60. JTWC annual count of typhoons in the western North Pacific Basin. The four lowest years are shaded red. The red dashed line indicates a general decreasing trend of typhoons occurrence over the six decades.

disturbances, including some that later became named tropical cyclones, made beneficial contributions to seasonal rainfall at islands across western Micronesia and at Guam. The island of Guam has not had a major typhoon (Category 3 or higher) since Typhoon Pongsona devastated the island in December 2002. See section 4g4 for more details on the 2021 western North Pacific tropical cyclone activity.

Much higher-than-average sea level across the tropical western Pacific is typical during La Niña. Indeed, sea level stands by the summer of 2021 were near their historical peaks throughout Micronesia. Time series of the sea level from two widely separated stations (Guam and Kwajalein) illustrate the strength of the coherence of the regional sea level, and the historical perspective of the very high stands during 2021 (Fig. 7.61). At Guam, the high stand reached during mid-2021 was the second highest in the historical record. Since 1998, the magnitude of sea level rise in the tropics of the western North Pacific has been among the highest in the world. The character of this rise was not gradual, but instead is best described as a step-function jump during 1998. The sea level increased by 30 cm from its low stand at the end of 1997 to a historically high stand at the end of 1998 (Fig. 7.61). Elevated sea levels then persisted to the present, with three major short-term dips during the 2002, 2015, and 2018 El Niño events. Very high sea level in the tropics of the western North Pacific is not a signal of climate change, but rather an artefact of a substantial increase in the strength of the Pacific trade-wind system (Merrifield et al. 2011). An abrupt increase in the strength of the trade winds in 1998 separates the recent historical climate of the western Pacific into two regimes: (1) weak trade winds, low sea level (1975–1998); and (2) strong trade winds, high sea level (1998–present).

During early December, two storm systems—Typhoon Nyatoh and an intense cut-off low to the northwest of Hawaii—churned up large waves that affected islands throughout the region. The large waves from these two concurrent storm events coincided with the monthly highest tides. In addition, due to La Niña conditions, the background sea level was 10–20 cm above average. Buoys in the region captured the long-period swell in real time. The following impacts were noted on the Kwajalein Atoll: flooding occurred on Roi Nemur and on Ebeye on 4–5 December; Yap Island and some of the outer islands received serious inundation, with water reported far inland; water inundation was reported up to 13 meters inland on some atolls of Chuuk State; and on Pohnpei, Nukuoro received inundation, and water penetrated 6 meters inland as far south as Kapingamarangi.

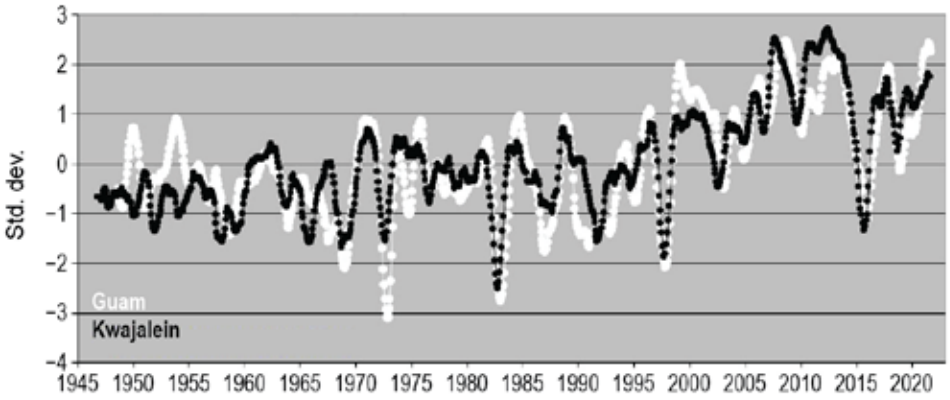

Fig. 7.61. Twelve-month moving average of the sea level anomaly at Guam (13.4°N, 144.8°E, white) and at Kwajalein (8.7°N, 167.7°E, black) during 1948 to present. Plotted values are normalized using their respective standard deviations. Note the continual high stands of the sea since 1998 at both stations. Note also the absolute historical high stands during 2010 through 2012 (a period of prolonged La Niña). At Guam, the high stand reached during mid-2021 was the second highest in the historical record. Strong El Niño events stand out as sharp dips. Note: y-axis is unitless due to normalization.

3) SOUTHWEST PACIFIC—E. Chandler

Countries considered in this section include American Samoa, Cook Islands, Fiji, French Polynesia, Kiribati, New Caledonia, Niue, Papua New Guinea (PNG), Samoa, Solomon Islands, Tonga, Tuvalu, Vanuatu, and Wallis and Futuna (Fig 7.58). The temperature analysis is based on the Climate Anomaly Monitoring System (CAMS) monthly surface air temperature anomalies. Anomalies are with respect to the 1991–2020 base period. The precipitation analysis is based on monthly analyses presented in the Climate and Oceans Support Program in the Pacific (COSPPac) Monthly Bulletin and COSPPac Online Climate Outlook Forum. The base period for precipitation is 1991–2020.

The year began with a mature La Niña event, with the tropical Pacific transitioning to a neutral ENSO state in the second quarter of the year. Sea surface temperatures were below average across the central and western equatorial Pacific during the first two months of 2021, before the cool regions retracted eastward and became patchy from March onwards as the equatorial water warmed. The tropical Pacific remained ENSO neutral during the middle months of the year before signs of La Niña re-emerged as the equatorial Pacific water again showed signs of cooling into the third quarter. Atmospheric indicators of the developing La Niña lagged the ocean cooling, although by October there was evidence of coupling, with trade winds strengthening and a reduction in cloud and rainfall near the date line.

Air temperatures and rainfall were both typical of a La Niña event at the beginning of 2021 and again as La Niña re-emerged toward the end of the year. Air temperatures began the year below normal along the equator, with warm anomalies in the far western Pacific. By March, air temperatures were near-normal in the equatorial Pacific and persisted until the last quarter of the year when above-normal temperatures became established to the east of the Maritime Continent and in a broad arc from PNG to French Polynesia. Rainfall was suppressed along the equator on and to the east of the dateline for most of the year, with the strongest anomalies in the western Pacific occurring at the start of 2021. In the off-equatorial South Pacific, positive rainfall anomalies were most evident along the South Pacific Convergence Zone (SPCZ) and at the beginning and end of the calendar year, coinciding with the southern wet season (approximately November to April). As expected, rainfall was more mixed for South Pacific countries during mid-year as ENSO-neutral conditions prevailed.

(i) Temperature

Air temperatures were below-normal along the equator at the start of 2021 and then warmed in this region during the first quarter of the year (Fig 7.62a). During January, a large region of temperatures 1–2°C below normal stretched from Nauru eastward past the Line Islands of Kiribati along the equator; however, by March this region had warmed to near-normal. A small region with air temperatures 1–2°C above normal was present in the far western Pacific near PNG during January, and a relatively large area covering the southern Cook Islands and southern French Polynesia had temperatures 1–3°C above normal. Both these regions returned to near-normal temperatures by March. The areas of above-normal temperatures during JFM were associated with above-normal SSTs in the same regions.

During April–June (AMJ), air temperatures across the equatorial Pacific remained close to normal. Small regions of air temperatures of 1–2°C below normal persisted in the far eastern Pacific near the coast of South America (Fig. 7.62b).

During July–September, the region covering the southern Cook Islands and southern French Polynesia warmed again, with temperature anomalies of +1° to +2°C (Fig. 7.62c). Warm anomalies of this magnitude were also present during August in a region around southern PNG. The region of warm air temperatures was associated with above-normal sea surface temperatures in the same area, with the highest anomalies near the southern Cook Islands and southern French

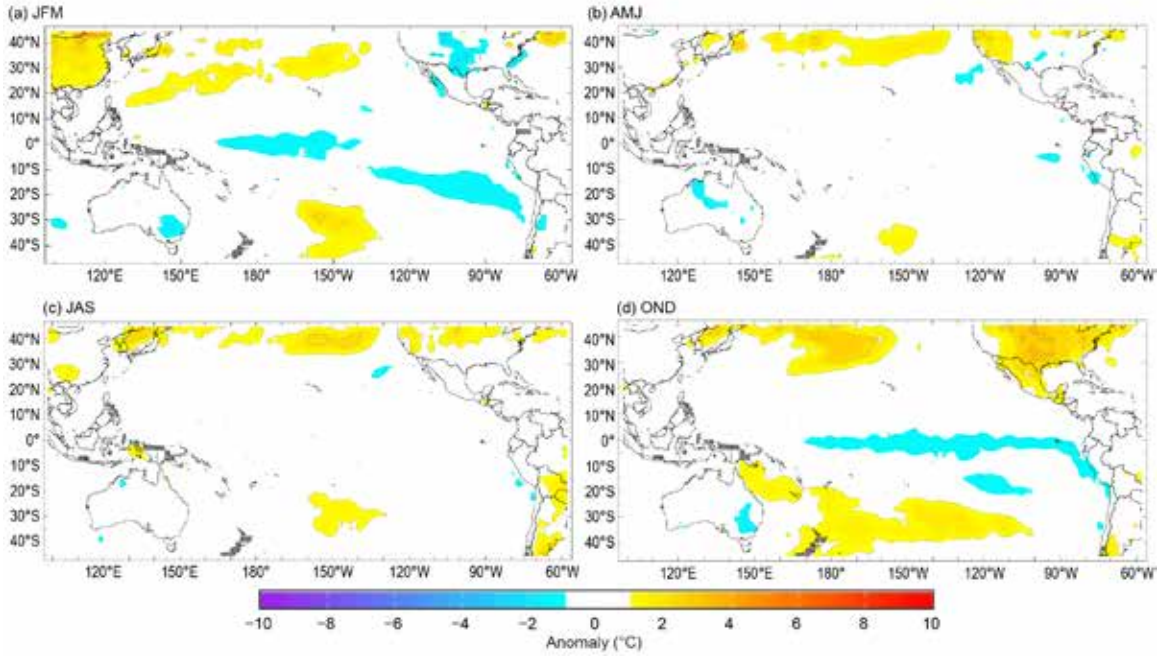

Fig. 7.62. Seasonal air temperature anomalies (°C) for (a) Jan–Mar, (b) Apr–Jun, (c) Jul–Sep, and (d) Oct–Dec. (Source: CAMS.)

Polynesia. Air temperatures across the equatorial Pacific were otherwise close to normal, with small areas of air temperatures 1–2°C below normal in the far eastern Pacific during September.

During the last quarter of the year, a region of positive anomalies (1–2°C above normal) in the South Pacific re-emerged near PNG and expanded southeastward in a narrow arc to encompass New Caledonia and as far south as New Zealand during November, although this weakened in spatial extent and strength by December. In contrast, the emerging La Niña contributed to regions of negative air temperature anomalies off the South American coast and extended along the eastern equatorial Pacific during October. The region of –1° to –2°C anomalies extended along the equator as far west as far as the date line by December, with a small region more than 3°C below normal observed in the far eastern Pacific (Fig. 7.62d).

(ii) Precipitation

Rainfall patterns at the start of the year reflected typical La Niña patterns across the tropical Pacific, including rainfall deficits along the equator in JFM and positive rainfall anomalies over most off-equatorial South Pacific Islands. The SPCZ was located to the south of its climatologically-normal position during JFM, bringing it closer to Vanuatu and Fiji (Figs. 7.63a–c). As a result of the SPCZ shifting south, a narrow band of positive rainfall anomalies was located between the Solomon Islands and Vanuatu, contributing to rainfall totals above the 90th percentile in Fiji, PNG, Tonga, and Vanuatu. Lemap (Vanuatu) recorded its third wettest JFM in its 61-year record (1294 mm). Conversely, the central and western equatorial regions from west of Nauru to eastern Kiribati experienced suppressed rainfall through the first quarter of 2021.

The SPCZ was close to its long-term average position during AMJ (Figs. 7.63d–f) as the tropical Pacific returned to ENSO neutral. The region experienced a mixed rainfall pattern during the second quarter of the year; during April there was a region of positive rainfall anomalies from PNG southeast through the Solomon Islands and New Caledonia, while negative rainfall anomalies were evident in a region straddling the date line during April and June. The southern Cook Islands, northwestern PNG, and Tonga all received rainfall above their 90th percentiles for the AMJ quarter. Rarotonga (Cook Islands) recorded its third wettest AMJ on record in its 123-year record (888 mm), as did Niuofo'ou (Tonga) in its 47 year-record (862 mm). Conversely, Samoa and the eastern Solomon Islands observed rainfall below their 10th percentiles during AMJ.

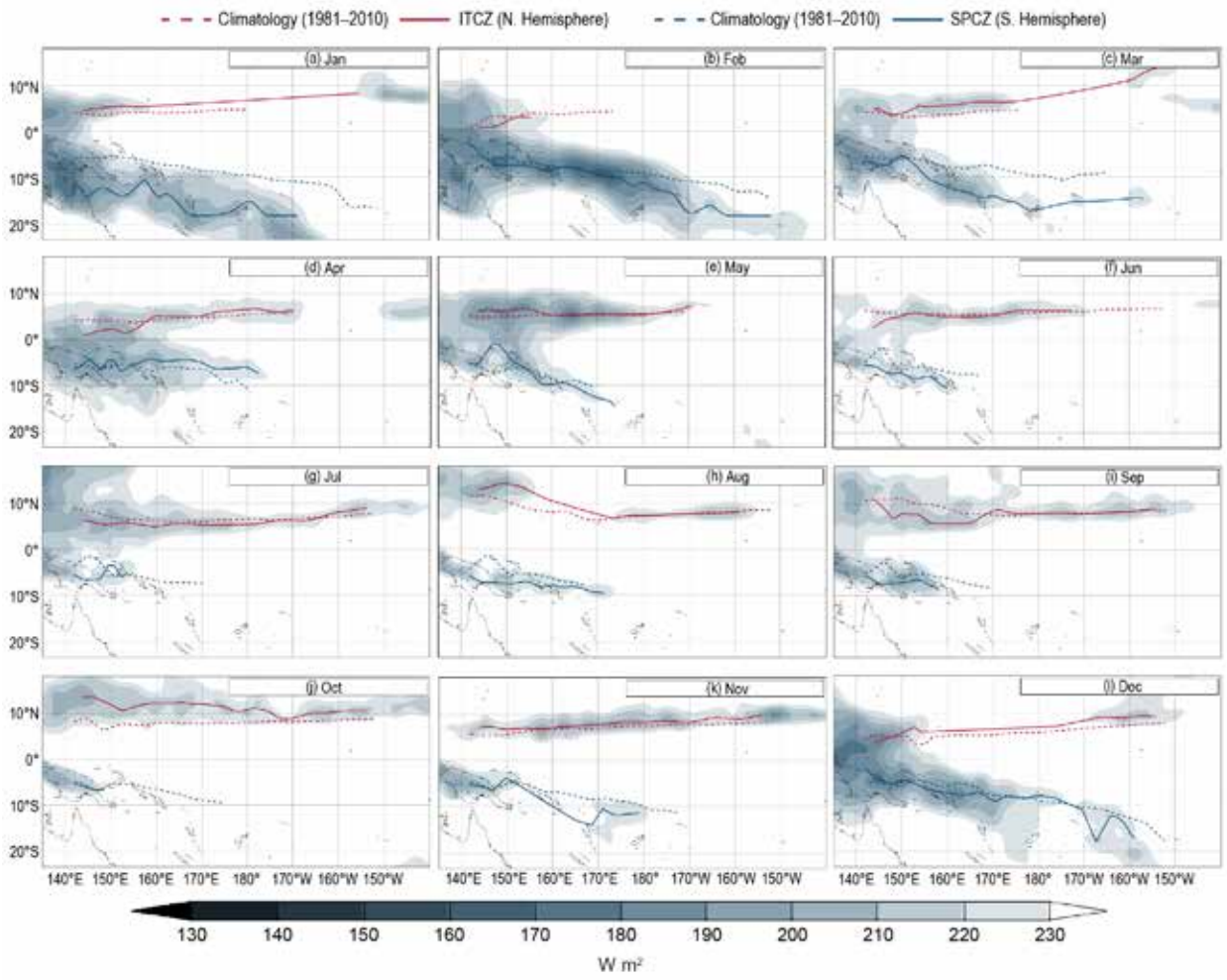

Fig. 7.63. South Pacific Convergence Zone (SPCZ) represented by 30-day average outgoing longwave radiation (OLR) monthly minimums for (a) Jan, (b) Feb, (c) Mar, (d) Apr, (e) May, (f) Jun, (g) Jul, (h) Aug, (i) Sep, (j) Oct, (k) Nov, and (l) Dec.

During JAS, the SPCZ was weak (Fig. 7.63g) before becoming more active and displaced to the south (compared to its usual position) during August and September (Figs. 7.63h,i) over the Solomon Islands, noting the SPCZ is not particularly active at this time of year during the South Pacific dry season. Weak cooling of the ocean surface occurred along the equator during this quarter as signs of another La Niña emerged. Notably, rainfall was suppressed in a large region around Nauru and Kiribati, which extended southward over Vanuatu and eastward over the northern Cook Islands by September. Niue recorded rainfall above its 90th percentile for the JAS quarter, and Faleolo (Samoa) recorded its third driest JAS on record in its 57-year record (86 mm).

Rainfall patterns during the last quarter of 2021 reflected the strengthening La Niña. Rainfall during October and November was suppressed along the equator, with the largest deficits occurring to the west of the date line. The SPCZ continued to be suppressed during October (Fig. 7.63j) before becoming increasingly active during November and December (Fig. 7.63k,l), as is typical for that time of the year. The active SPCZ near the date line in December was associated with enhanced rainfall and tropical cyclone activity in the South Pacific. The enhanced rainfall anomalies were highest in a broad region covering the PNG mainland, the northern Solomon Islands to Fiji and New Caledonia. Rainfall totals above the 90th percentile for OND were recorded in several areas, including Palau, PNG, and the Solomon Islands. Kirakira (Solomon Islands) recorded its wettest OND on record in its 53-year record (1417 mm). Conversely, Tarawa (Kiribati) recorded its second driest OND in its 74-year record (27 mm).

(iii) Notable events and impacts

Severe Tropical Cyclone Niran formed east of the Queensland coast of Australia and moved southeastward towards New Caledonia in early March. By 5 March, Niran had reached Category 5 tropical cyclone strength, with maximum 1-minute sustained winds of 260 km h^{-1} (140 kt) and a central pressure of 931 hPa. Niran was the second Category 5 storm of 2021 globally and the second Category 5 storm of the 2020/21 South Pacific cyclone season behind Tropical Cyclone Yasa which formed in December 2020. Despite not making landfall over New Caledonia, Niran passed close to its main island, Grande Terre, on 6 March; fortunately, the strongest winds remained offshore and, by this stage, it had weakened to a Category 3 storm. Niran continued to track to the southeast as it weakened and transitioned into an extratropical cyclone later that day. As Niran passed close to Grande Terre, gusts up to 150 km h^{-1} (81 kt) were recorded, with 69,000 households estimated to have lost electricity. There was damage to crops and, in the capital city Nouméa, many ships were forced aground along the coast. The damage caused by Niran was estimated at greater than $200 million (U.S. dollars), shared between Australia and New Caledonia (see section 4g7 for more details).

4) AUSTRALIA—S. Tobin and C. Ganter

For this section, monthly area-averaged temperatures are based on the ACORN-SAT dataset v2.2 (Trewin 2018), which begins in 1910. Daily temperatures and mapped temperature analyses are based on the Australian Water Availability Project (AWAP) dataset (Jones et al. 2009), which begins in 1910. Area-averaged rainfall values and mapped analyses use the Australian Gridded Climate Data (AGCD) dataset (Evans et al. 2020), which begins in 1900. Anomalies are based on the 1991–2020 average.

(i) Temperature

Due to the influence of La Niña, 2021 was Australia's coolest year since 2012 when the conclusion of the moderately strong 2011–12 La Niña brought cooler and wetter conditions for the first half of the year. The area-averaged annual mean temperature for 2021 was close to the 1991–2020 average (0.07°C below average), but overall was the 19th-highest in Australia's 112-year record. The annual nationwide mean maximum temperature (Fig. 7.64) was also 0.07°C below average, and the mean minimum temperature (Fig. 7.65) was 0.09°C below average.

In terms of annual anomalies, both mean annual maximum and minimum temperatures were above average for most of tropical northern Australia. Compared to the distribution across all 112 years of observations for 1910–2021, maximum temperatures were in the highest 10% of historical observations for most of the northern tropics, including the Kimberley in Western Australia, the Top End in the Northern Territory, and Queensland's Cape

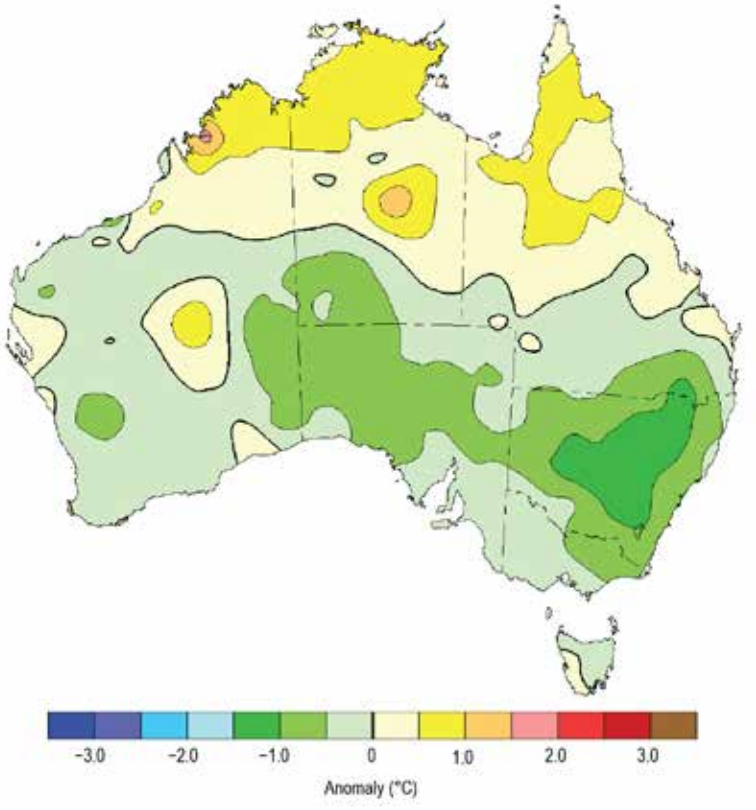

Fig. 7.64. Maximum temperature anomalies (°C; 1991–2020 base period) for Australia, averaged over 2021. Australian States/Territories are as follows, starting clockwise from the west: Western Australia, the Northern Territory, Queensland, New South Wales, Victoria, and South Australia, with the island of Tasmania in the southeast (Source: Australian Bureau of Meteorology.)

York Peninsula. However, much of central New South Wales west of the Great Dividing Range was in the bottom 30% of historical observations.

In terms of significant monthly anomalies, January brought heatwaves to the north of Western Australia and to southeast Australia. Mean temperatures were below average for much of the south and west in February. March and April were cooler than average across large parts of the mainland southeast, while much of the southern half of Western Australia was warmer than average during March, April, and May.

The northern tropics were warmer than average throughout the austral winter. July and August were particularly warm across much of the country, with the national mean temperature fourth and sixth highest on record for those months, respectively. Mean maximum temperatures were highest on record for large parts of northern Australia during July and for some areas along the northern coasts during August.

Warmth continued across the north into spring and early summer, with severe to extreme heatwave conditions in the Kimberley and Top End during October and parts of the north and west of Australia in November and December.

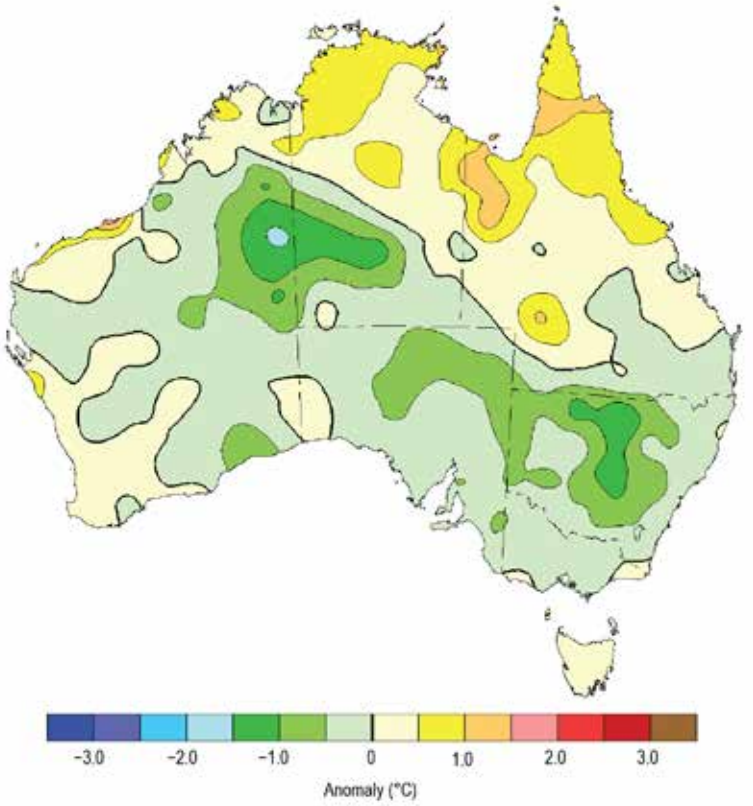

Fig. 7.65. Minimum temperature anomalies (°C; 1991–2020 base period) for Australia, averaged over 2021. (Source: Australian Bureau of Meteorology.)

(ii) Precipitation

Averaged across Australia, rainfall for 2021 was 507.8 mm, 4.5% above the 1991–2020 average of 486.0 mm. Compared to the distribution across all 122 years of observations for 1900–2021, annual rainfall was above average for eastern Victoria, much of New South Wales, inland southeast Queensland, much of the west of Western Australia, and much of the far northern tropics, including the Top End of the Northern Territory and Cape York Peninsula in Queensland (Fig. 7.66). Annual rainfall was below average for a few areas, including around the border of South Australia and Victoria.

Very-much-above-average rainfall in eastern Australia was largely a result of an exceptionally wet March and November,

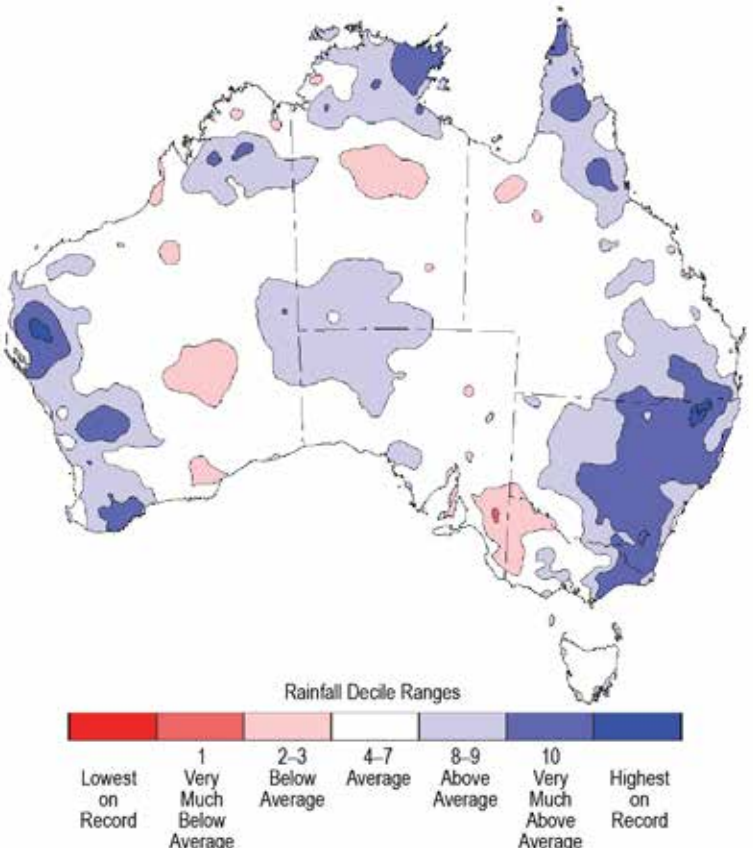

Fig. 7.66. Rainfall deciles for Australia for 2021, based on the 1900–2021 distribution. (Source: Australian Bureau of Meteorology.)

months both marked by flooding across large areas. Above-average rainfall in the west of Western Australia was a result of contributions spread across more of the year, mostly during February, March, May, and July.

La Niña was a dominant influence on Australia's climate during 2021, persisting through summer 2020/21, returning to neutral mid-year, and emerging again during austral spring. La Niña typically brings wetter conditions to much of northern and eastern Australia. A negative Indian Ocean dipole (IOD) during winter and spring also fueled above-average winter–spring rainfall over parts of southern Australia, as is typical of a negative IOD (Ashok et al. 2003). The third key influence for Australia was extended positive Southern Annular Mode conditions, with the strong positive value in June likely influencing drier conditions for southern Western Australia and western Tasmania. However, in Australia, the SAM influence varies strongly by season (Hendon et al. 2007). A positive SAM can also be promoted by La Niña in the spring and summer, which would have contributed to the extraordinarily persistent positive SAM during October–December 2021, a period during which the positive SAM likely contributed both to above-average rainfall across parts of eastern Australia and below-average rainfall over the west-facing coasts, such as southeast South Australia, western Victoria, and western Tasmania.

The year commenced with parts of southwest-to-central Western Australia and the southeastern quarter of Queensland affected by meteorological drought, with rainfall for the period commencing April 2020 in the lowest 10% of historical observations compared to all similar periods since 1900. Above-average rainfall during February resulted in a substantial lessening of deficiencies across much of Western Australia, with follow-up rain during March bringing further relief.

Rainfall during April 2021 was very low for the southeastern mainland. New South Wales observed its ninth-driest April on record and South Australia observed its seventh-driest.

The developing La Niña led to above-average rainfall becoming more widespread as the austral spring progressed. October rainfall was above or very much above average for large areas, and November rainfall was very much above average (highest 10% of historical observations for 1900 to 2021) for large areas of mainland Australia.

While deficiencies in Queensland contracted over the year across the Maranoa and Darling Downs in the inland south, closer to the coast serious or severe rainfall deficiencies persisted until November when very-much-above-average rainfall lifted totals across the Capricornia and Wide Bay and Burnett districts out of the lowest 10% of historical observations. Flooding occurred in numerous rivers in New South Wales and Queensland throughout November.

December rainfall was below average for most of Australia, and very much below average (lowest 10% of historical observations) for parts of the south coast and for most of Tasmania, which observed its sixth-driest December on record.

After commencing 2021 at 58% of capacity, water storages in the Murray–Darling Basin experienced significant filling over winter and spring, increasing to 90.7% by the end of the year, with some storages spilling or being operated to prevent spilling. However, storages in southeast Queensland remained low with the largest storage, Wivenhoe, only increasing from 39% to 47% during 2021. In northern Australia, the volume of water in Argyle Dam increased during 2021 but did not fill for the fourth consecutive year.

(iii) Notable events and impacts

Heatwave conditions affected most of mainland southeast Australia in the days leading up to 26 January. The hottest day was the 24th, with 45.3°C recorded at Port Augusta Aero in South Australia, 43.9°C at Ouyen in Victoria, and 43.6°C at Hay Airport in New South Wales. Sydney Observatory Hill recorded five consecutive days over 30°C from 22 to 26 January, only the ninth such instance since records began in 1859, but the third year in a row that this has occurred.

A major rain event affected many parts of eastern and central Australia in the second half of March. New South Wales observed its second-wettest March in the 122 year-record. Widespread

significant flooding resulted in coastal New South Wales, some adjacent parts of southeast Queensland and eastern Victoria, on some inland rivers in northern New South Wales and southern Queensland, and in eastern Tasmania. Data from the Insurance Council of Australia showed insured claims from this event reached more than $600 million AUD ($420 million US dollars) as of March 2022.

Severe tropical cyclone Seroja brought heavy rains and damaging winds to areas around Kalbarri and Geraldton in Western Australia during April. This was the farthest south a tropical cyclone has crossed the Western Australian coast since the 1950s (see section 4g7 for details).

Low temperatures, heavy rainfall, and damaging winds affected parts of Victoria on 7 and 8 June. The Victorian State Emergency Service received more than 9000 calls for assistance and power was cut to more than 200,000 homes. Repairs to the electrical supply and telecommunications networks took several weeks in some locations due to the severity of damage and large number of fallen trees. Many roads were closed due to flooding, particularly through Gippsland. Insured claims from this event approached $300 million AUD ($210 million US dollars) as of April 2022.

Australia's wettest November on record was due in part to record-high November rainfall at numerous sites in New South Wales and Queensland. Areas of flash flooding and riverine flooding affected eastern and southeast Australia, including large areas of Queensland and inland New South Wales.

The north of Western Australia experienced severe heatwave conditions several times during December, with parts of the northwest observing their hottest December on record, with respect to either mean maximum or mean minimum temperature. Marble Bar recorded a total of 16 days with maximum temperatures of 45°C or above, the highest count for December on record and the second-highest count for any month. Marble Bar also recorded 29 consecutive days of at least 42°C, exceeding the site's December record of 25 days in 1986. Slightly farther south, Geraldton Airport recorded six consecutive days with maximum temperatures at 40°C or above between 24 and 29 December, the longest such run in December and equal to the second-longest run for any month using composite site records that date 1941.

5) NEW ZEALAND—N. Fedaeff

In the following discussion, the base period is 1981–2010. The nationwide average temperature is based upon New Zealand's National Institute of Water and Atmospheric Research (NIWA) seven-station temperature series that began in 1909 (Mullan et al. 2010). All statistics are based on data available as of 12 January 2022.

(i) Temperature

According to NIWA's seven-station temperature series, 2021 was New Zealand's warmest year since records began in 1909. The annual nationwide average temperature was 13.56°C, 0.95°C above average. Mean annual temperatures were above average (+0.51°C to +1.20°C) across much of the country. Well-above-average temperatures (> 1.20°C) occurred in parts of Auckland, Bay of Plenty, Tasman, and Fiordland. Near-average (± 0.50°C of average) temperatures occurred in western Waikato, coastal Wairarapa, and parts of northern Canterbury and Otago (Fig. 7.67a, the named regions are shown in Fig. 7.68). There were several climate drivers that contributed to the record warm year, which are expanded upon in Sidebar 7.5.

The hottest spell of the year occurred over New Zealand from 25 to 28 January, with several locations observing record or near-record high daily maximum and daily minimum temperatures for January. The highest temperature of 2021 was 39.4°C and was recorded at Ashburton on 26 January. This became New Zealand's second-highest January temperature on record and equaled the country's 10th hottest temperature on record for any month. On 27 May, Dunedin airport recorded a minimum temperature of −8.8°C. This equaled the lowest temperature on record at

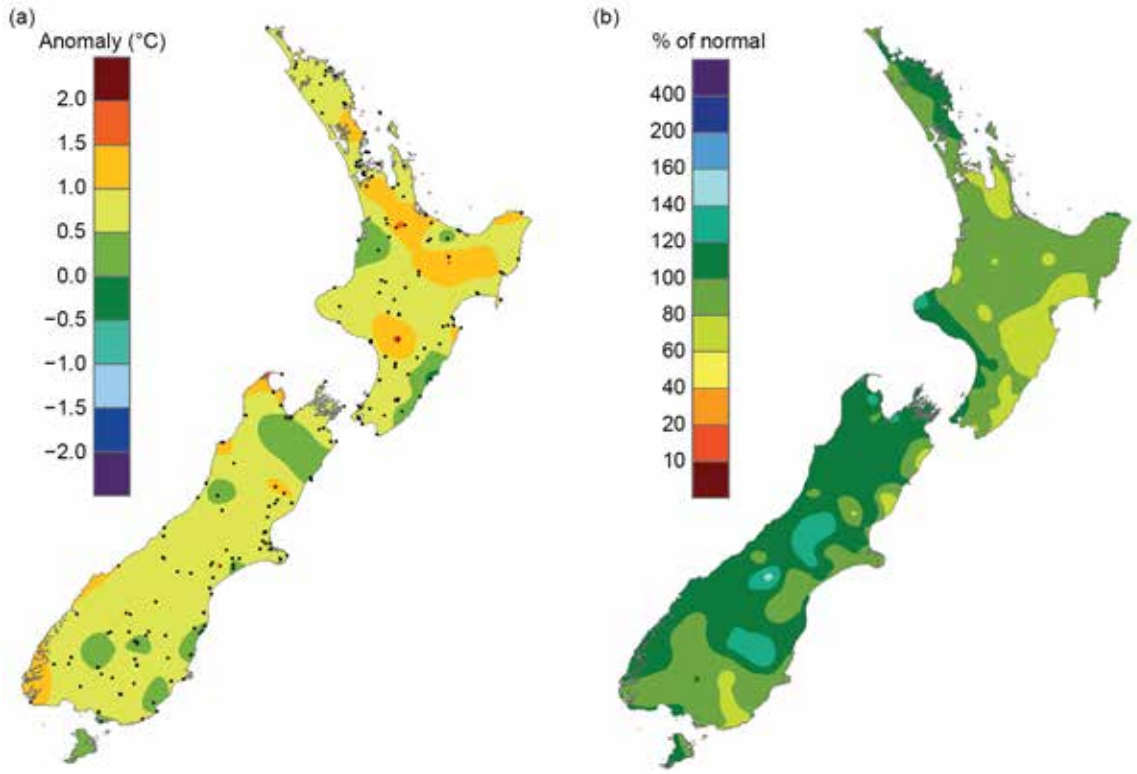

Fig. 7.67. 2021 annual (a) average temperature anomaly (°C) and (b) total rainfall (% of normal), relative to 1981–2010 base period. The dots on (a) represent the locations of climate stations used to create both the temperature and rainfall maps. (Source: NIWA.)

the site since records began in 1962. The lowest air temperature of the year was –10.8°C recorded at Tara Hills on 27 May.

(ii) Precipitation

In 2021, New Zealand rainfall was characterized by extended dry spells, under mainly anticyclonic conditions, interspersed with extreme rainfall events. Annual rainfall totals were near-normal (80–119% of normal) for most of the country. Above-normal rainfall (120–149%) occurred in the west of the lower North Island. Parts of Nelson, interior Canterbury, and Otago also experienced above-normal rainfall (Fig. 7.67b). Lake Tekapo experienced its third wettest year since records began in 1925, while Lauder and Greymouth experienced their fourth wettest (records began in 1924 and 1947, respectively). Conversely, Ohakune and Western Springs in Auckland experienced their third driest year on record (records began in 1948 and 1961, respectively). Of the regularly reporting rainfall gauges, the wettest location in 2021 was Cropp River, in the Hokitika River catchment (West Coast, South Island, 975 m above sea level), with an annual rainfall total of 14,090 mm. The driest of the regularly reporting rainfall sites in 2021 was Alexandra, which recorded 402 mm of rainfall for the year.

(iii) Notable events and impacts

See Fig. 7.68 for a schematic of notable events. The start of 2021 featured extended dry spells in the North Island. Meteorological drought (as defined by the NZ Drought Index [Mol et al. 2017]) developed in the Far North district during January and persisted through late February. Additionally, very dry to extremely dry conditions became widespread across large parts of the North Island, as well as Marlborough and northern Canterbury during February. Water restrictions were temporarily implemented in Northland, Auckland, Wairarapa, and the Hastings District.

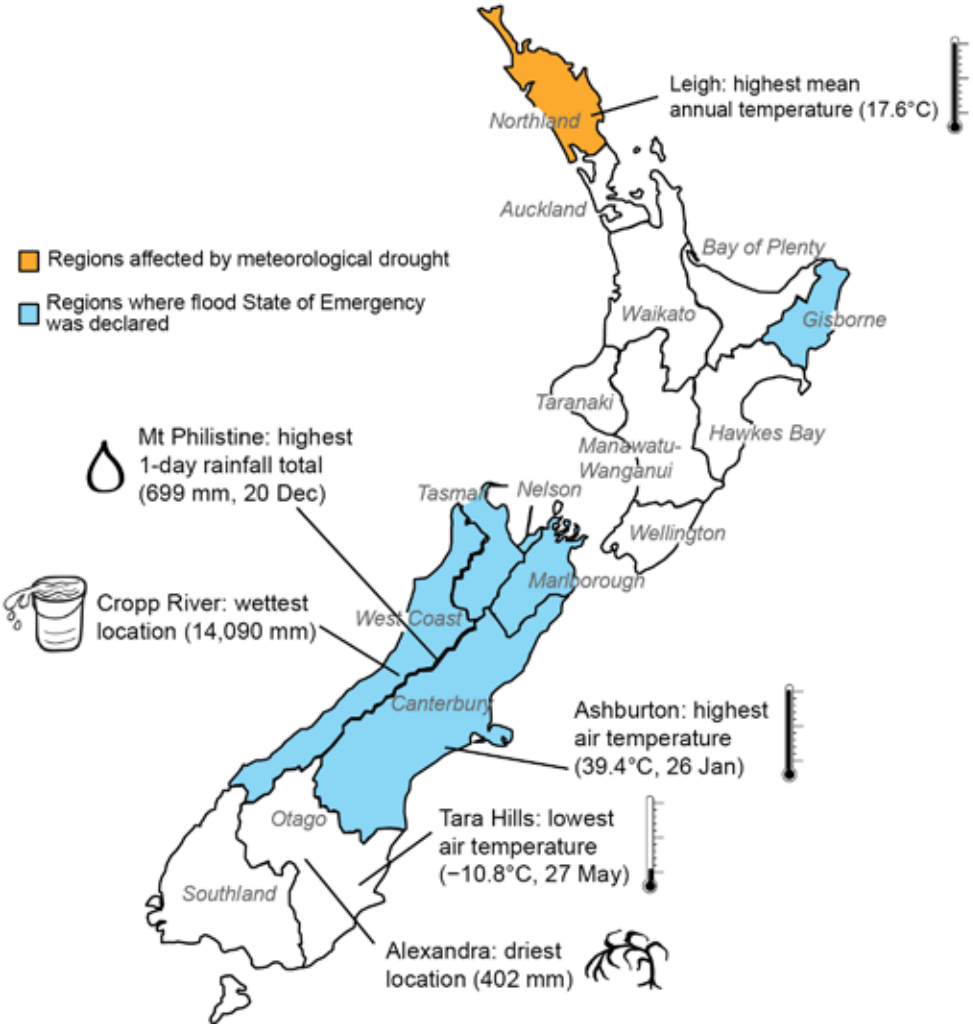

Fig. 7.68. Notable weather events and climate extremes for New Zealand in 2021. (Source: NIWA.)

Three flooding events during 2021 led to State of Emergency declarations. During 29–31 May, prolonged and heavy rain fell over Canterbury and set numerous 24-hour and 48-hour rainfall records for the month of May. Damage caused by the flooding was widespread, with many roads closed, bridges damaged and impassable, and farms suffering considerable impacts to infrastructure and livestock. The emergence of a negative Indian Ocean dipole event (see section 4f for details) and the presence of the active phase of the Madden Julian Oscillation in the Indian Ocean, Maritime Continent, and western Pacific during winter (see section 4c) were likely tropical sources of enhanced moisture supply available to the passing midlatitude cyclonic systems (Fauchereau et al. 2016; Ashok et al. 2007). The most notable flooding event occurred from 15 to 18 July, when an atmospheric river brought heavy rain to the West Coast, Tasman, Nelson, and Marlborough regions. This event led to the Buller River recording the highest flow rate for a New Zealand river. The flooding required evacuations and resulted in an estimated $132.4 million (New Zealand dollars; $91.8 million U.S. dollars) in privately insured damage according to the NZ Insurance Council. The third flooding event occurred during 3–5 November, when a slow-moving subtropical low caused persistent heavy rainfall that affected the eastern North Island and brought flooding and landslides to parts of Gisborne.

Sidebar 7.5: **New Zealand's hottest year on record**—N. Fedaeff

The year 2021 was New Zealand's warmest since records began in 1909. Separately, 12 locations across the country also observed their warmest year on record, and an additional 50 locations experienced an annual average temperature in their respective four highest on record (record lengths for each location are variable, ranging from 21 to 155 years).

Only three months (January, February, and September) had near-average temperatures (± 0.50°C of average), while nine months had above average temperatures (> 0.50°C). No months were cooler than average. Averaged daily data across the whole country based on NIWA's Virtual Climate Station Network shows that, for the country as a whole, 26% of days in 2021 featured below average temperatures, 19% of days had near-average temperatures, and 55% of days experienced above average temperatures.

There were several climate drivers that contributed to the record warm year. The Southern Annular Mode (SAM), an indicator of Southern Hemisphere climate variability, was positive 73% of the time during 2021. The positive SAM phase is associated with higher-than-normal air pressure around New Zealand, which tends to bring light winds, higher temperatures, and drier-than-usual weather to the country (Kidston et al. 2009). There have only been three other years (1993: 75%, 1998: 76%, and 2008: 74%) that have experienced a higher percentage of time in the positive SAM phase with the series extending back to 1979.

In line with the observations of the SAM index, annual mean sea level pressure for 2021 was higher than normal over the North Island and to the east of New Zealand. This was associated with more northerly quarter winds (winds from the northwest to northeast quadrant) than normal. The Trenberth M1 meridional index compares the mean sea level pressure between Hobart, Australia, and the Chatham Islands, New Zealand (Trenberth 1976; Salinger and Mullan 1999). Negative values are associated with northerly airflow. Based on this index, 2021 ranked 13th in terms of the strongest annual northerly airflow anomaly with records extending to 1909 (Fig. SB7.7).

During January and February, moderate La Niña conditions in the central Pacific (which began in October 2020) gradually eased. La Niña in New Zealand is often associated with northeasterly winds and warmer weather; however, the weather patterns at the start of 2021 were generally not consistent with those expected in La Niña. January featured more southwesterly winds than usual, and February featured more easterlies. Both months were some of New Zealand's coolest of the year (relative to the time of year). It is likely the atypical impacts can be attributed, in part, to a non-traditional central Pacific (CP) type of La Niña "modoki" (Capotondi et al. 2015), whereby the minimum sea surface temperature (SST) anomalies are located in the central Pacific rather than the east. Re-developing La Niña conditions during austral spring resulted in a transition from a westerly air flow, near-average temperatures, and widespread

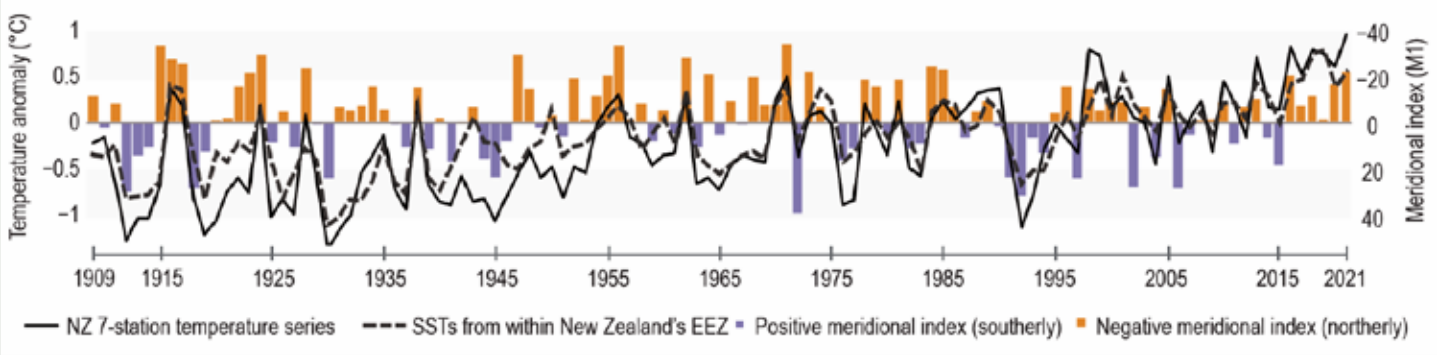

Fig. SB7.7. Timeseries of New Zealand seven-station temperature anomalies (°C, solid black line), sea surface temperature anomalies based on the New Zealand Exclusive Economic Zone (°C, dotted black line), and the Trenberth meridional index (M1) where negative values (orange bars) correspond with more northerly winds and positive values (purple bars) with more southerly winds. Note: the meridional index scale is reversed on the y-axis.

wet weather during September to more northeasterly winds during October–December, bringing frequent warm and humid weather and contributing to the country's fifth-warmest October, record warmest November, and fourth-warmest December. A warm end to the year was partially attributable to increasing coastal SSTs around New Zealand, particularly in November when marine heatwave (MHW) conditions emerged and persisted through the end of the year. During December, daily SSTs reached as high as 4–5°C above average around the western and northern North Island, qualifying as one of the strongest MHW events in the last four decades in the North Island's coastal waters. An area-weighted annual average of SSTs from within New Zealand's Exclusive Economic Zone based on ERSSTv5 (Huang et al. 2017) shows that SSTs for 2021 ranked third-warmest since at least 1909 (Fig. SB7.7).

Increasing global temperatures due to climate change are another key contributor to New Zealand's climate. The linear warming trend across the seven-station series from 1909–2021 is 1.07 ± 0.24°C century^{-1}. A study to discern the contribution of anthropogenic emissions to New Zealand's warmest year has not yet been carried out; however, seven of the past nine years have been among New Zealand's warmest on record.

Acknowledgments

Africa

- We would like to acknowledge the national and/or hydrometeorological services/bureaus of Morocco, Algeria, Egypt, Senegal (National Aviation and Meteorology Agency), Nigeria, South Africa, Madagascar, Seychelles, Comoros Mayotte (France), Reunion (France), and Mauritius.
- We acknowledge support by the NOAA-CPC International Desk. Global datasets from NCEP/NCAR and GPCP are acknowledged.
- Samson Hagos and Zhe Feng are supported by the U.S. Department of Energy Office of Science Biological and Environmental Research as part of the Atmospheric Systems Research (ASR) Program.

Europe

- Much of the information in this section is based on national climate reports kindly provided by the National Meteorological and Hydrological Services (NMHSs) of the WMO RA VI Region. The information has been compiled at the WMO RA VI Regional Climate Centre (RCC) Node on Climate Monitoring, located at Deutscher Wetterdienst (DWD) in Germany. The national contributions have been provided as part of the cooperation between NMHSs and the RCC.
- Specifically, we acknowledge the Instytut Meteorologii i Gospodarki Wodnej (IMGW) PIB in Poland for its kind cooperation with RCC in this subject.

APPENDIX 1: Chapter 7 – Acronyms

AGCD	Australian gridded climate data
AMJ	April–June
AWAP	Australian Water Availability Project
BNGRC	National Office for Risk and Disaster Management
CA	Central Africa
CA	Central America
CAMS	Climate Anomaly Monitoring System
CA-NWS	Central America National Weather Services
CAR	Central Africa Republic
CMORPH CPC	Morphing Technique
CONUS	contiguous United States
COSPPac	Climate and Oceans Support Program in the Pacific
CP	central Pacific
CPC	Climate Prediction Center
DJF	December–February
DRC	Democratic Republic of Congo
ECCC	Environment and Climate Change Canada
ENSO	El Niño–Southern Oscillation
GHA	Greater Horn of Africa
GHCN	Global Historical Climate Network
GPCC	Global Precipitation Climatology Centre
IDI	Integrated Drought Index
INPE	National Institute for Space Research
IO	Indian Ocean
ISMR	Indian summer monsoon rainfall
ITCZ	intertropical Convergence Zone
JAS	July–September
JFM	January–March
JJ	June–July
JJAS	June–September
JTWC	Joint Typhoon Warning Center
LTA	long-term average
MAM	March–May
NCEP/NCAR	National Centers for Environmental Prediction/ National Center for Atmospheric Research
NEM	Northeast monsoon
NH	Northern Hemisphere
NIWA	National Institute of Water and Atmospheric Research
OND	October–December
PNG	Papua New Guinea
RCC-CM	Regional Climate Centre on Climate Monitoring
RFE2	rainfall estimates version 2

SH	Southern Hemisphere
SON	September–November
SPCZ	South Pacific Convergence Zone
SPI	standardized precipitation index
SSA	Southern South America
SST	sea surface temperature
SSTA	sea surface temperature anomaly
TC	tropical cyclone
UN OCHA	United Nations Office for the Coordination of Humanitarian Affairs
WNPSH	western North Pacific Subtropical High

APPENDIX 2: Supplemental Materials

Table A7.1. Temporal coverage of nationally-averaged temperature and precipitation in-situ observations for Europe/WMO RA VI Region[5]. For some countries, only one station (preferably with long time series) has been used (name of the location in brackets). All records extend to the present. Missing values: no information available. Annual anomalies have been calculated from the 1991–2020 average if not otherwise mentioned in footnotes. Ranks are ordered for temperature from highest to lowest and for precipitation in green from wettest to driest and in red from driest to wettest.

Nation	Temperature start of record	Precipitation start of record	Source	Temperature Anomaly	Rank	Precipitation Anomaly	Rank
European average	1950	1950	GHCN[1,] data	—	—	—	—
Albania (Korce)	1963	1963	CLIMAT[2]	—	—-	—	—
Andorra	1950	1950	NMHS[3]	—	—	—	—
Armenia	1935	1935	NMHS	+2.1[6]	3	80%[6]	23
Austria	1767	1858	NMHS	−0.2	18	93%	12
Azerbaijan (Astara)	1991	1991	CLIMAT	—	—	—	—
Belarus	1881	1945	NMHS	+0.3[4]	26	112%[4]	9
Belgium (Ukkel-Uccle)	1883	1981	NMHS	−0.3	23	124%	7
Bosnia & Herzegovina (Banja Luka)	1955	1955	CLIMAT	—	—	—	—
Bulgaria	1930	1954 (Burgas)	NMHS/CLIMAT	+0.4	12	120%	7
Croatia (Split/Marjan)	1949	1949	CLIMAT	—	—	—	—
Cyprus (Nicosia)	1899	1899	NMHS	+1.3[4]	3	48%[4]	41
Czechia	1961	1961	NMHS	−0.3	26	100%	51
Denmark	1873	1874	NMHS	−0.4[4]	15	98%[4]	51
Estonia	1961	1961	NMHS	+1.2	8	102%	45
Finland (Helsinki)	1900	1961	NMHS	−0.1	32	104%	15
France	1900	1959	NMHS	+0.4[4]	20	99%[4]	32
Georgia	1956	1881 (Tbilisi)	NMHS	+1.0	6	126%	33
Germany	1881	1881	NMHS	−0.1	21	101%	53
Greece	1960	1949 (Athens)	NMHS/CLIMAT	+1.2[7]	4	105%[7]	42
Hungary	1901	1901	NMHS	+0.1	19	83%	20
Iceland (Stykkishólmur)	1846	1856	NMHS	+0.2	21	92%	84
Ireland	1900	1900	NMHS	+0.34	8	94%	41
Israel	1951	1950)	NMHS	+0.8	4	88%	24
Italy	1961	1949 (Alghero)	NMHS/CLIMAT	+1.36[6]	7	38%[6]	25
Jordan (Amman)	1981	1981	NMHS	+1.3	2	81%	23
Kazakhstan	1941	1941	NMHS	+1.5	5	47%	3
Latvia	1924	1924	NMHS	+0.2	20	99%	55
Lebanon (Beirut)	1949	1949	CLIMAT	—	—	—	—
Lithuania	1961	1887 (Vilnius)	NMHS	−0.1	21	101%	26
Luxembourg (Findel)	1947	1947	NMHS	−0.6	42	154%	52
Malta	1923	1923	NMHS/CLIMAT	+0.8	2	98%	46
Moldova (Chisinau)	1886	1891	NMHS	−0.2	12	111%	16
Monaco	not available	not available	—	—	—	—	—
Montenegro (Plevlja)	1955	1955	CLIMAT	—	—	—	—
Netherlands	1901	1901	NMHS	−0.1	21	106%	38

Table A7.1. Temporal coverage of nationally-averaged temperature and precipitation in-situ observations for Europe/WMO RA VI Region[5]. For some countries, only one station (preferably with long time series) has been used (name of the location in brackets). All records extend to the present. Missing values: no information available. Annual anomalies have been calculated from the 1991–2020 average if not otherwise mentioned in footnotes. Ranks are ordered for temperature from highest to lowest and for precipitation in green from wettest to driest and in red from driest to wettest.

Nation	Temperature start of record	Precipitation start of record	Source	Temperature Anomaly	Rank	Precipitation Anomaly	Rank
North Macedonia (Bitola)	1955	1955	CLIMAT	+0.7[4]	14	114%[4]	11
Norway	1900	1900	NMHS	−0.1	28	90%	50
Poland	1951	1951	NMHS (IMGW)[8]	−0.1	22	116%	25
Portugal	1931	1931	NMHS	+0.4[7]	25	78%[7]	17
Romania	1961	1954 (Bistrita)	NMHS/CLIMAT	+0.9	14	98%	36
Russia, European part	1936	1936	NMHS	+0.7	19	103%	28
Serbia	1951	1951	NMHS	—	—	96%	22
Slovakia	1951	1961	NMHS	+0.5[6]	18	98%[6]	28
Slovenia	1961	1961	NMHS	+0.1	17	93%	50
Spain	1961	1961	NMHS	+0.5[4]	10	89%[4]	14
Sweden	1860	1860	NMHS	+0.05	26	103%	24
Switzerland	1864	1864	NMHS	+0.2	21	105%	47
Syrian Arab Republic (Aleppo)	1960	1960	CLIMAT	+1.8	3	17%	2
Türkiye	1971	1949 (Adana)	NMHS	+1.0	4	91%	14
Ukraine	1891	1891	NMHS	+0.9	17	105%	50
United Kingdom	1884	1862	NMHS	+0.1	18	93%	80

[1] GHCN = Global Historical Climatology Network (Menne et al. 2018)
[2] CLIMAT station data as reported worldwide via the WMO Global Telecommunication System
[3] NMHS = National Meteorological and Hydrological Service; for individual names of NMHSs see https://public.wmo.int/en/about-us/members
[4] normal refers to 1981–2010
[5] https://public.wmo.int/en/about-us/members
[6] normal refers to 1961–1990
[7] normal refers to 1971–2000
[8] IMGW = Instytut Meteorologii i Gospodarki Wodnej PIB

References

Amador, J. A., 1998: A climatic feature of the tropical Americas: The trade wind easterly jet. *Top. Meteor. Oceanogr.*, **5**, 91–102.

——, 2008. The Intra-Americas Seas Low-Level Jet (IALLJ): Overview and future research. *Ann. N. Y. Acad. Sci.*, **1146**, 153–188, https://doi.org/10.1196/annals.1446.012.

——, E. J. Alfaro, H. G. Hidalgo, and B. Calderón, 2011: Central America [in "State of the Climate in 2010"]. *Bull. Amer. Meteor. Soc.*, **92**, S182–S183, https://doi.org/10.1175/1520-0477-92.6.S1.

——, E. R. Rivera, A. M. Durán-Quesada, G. Mora, F. Sáenz, B. Calderón, and N. Mora, 2016a: The easternmost tropical Pacific. Part I: A climate review. *Int. J. Trop. Biol*, **64** (S1), 1–22, https://doi.org/10.15517/rbt.v64i1.23407.

——, A. M. Durán-Quesada, E. R. Rivera, G. Mora, F. Sáenz, B. Calderón, and N. Mora, 2016b: The easternmost tropical Pacific. Part II: Seasonal and intraseasonal modes of atmospheric variability. *Int. J. Trop. Biol*, **64** (S1), 23–57, https://doi.org/10.15517/rbt.v64i1.23409.

——, H. G. Hidalgo, E. J. Alfaro, B. Calderón, and N. Mora, 2018: Central America [in "State of the Climate 2017"]. *Bull. Amer. Meteor. Soc.*, **99** (8), S199–S200, https://doi.org/10.1175/2018BAMSStateoftheClimate.1.

ANA, 2021a: HIDROWEB v3.2.6. Agência Nacional de Águas, https://www.snirh.gov.br/hidroweb/apresentacao.

——, 2021b: Sistema HIDRO – Telemetria. Agência Nacional de Águas, http://www.snirh.gov.br/hidrotelemetria/Mapa.aspx.

Ashok, K., Z. Guan, and T. Yamagata, 2003: Influence of the Indian Ocean dipole on the Australian winter rainfall. *Geophys. Res. Lett.*, **30**, 1821, https://doi.org/10.1029/2003GL017926.

——, H. Nakamura, and T. Yamagata, 2007: Impacts of ENSO and Indian Ocean dipole events on the Southern Hemisphere storm-track activity during austral winter. *J. Climate*, **20**, 3147–3163, https://doi.org/10.1175/JCLI4155.1.

Barichivich, J., E. Gloor, P. Peylin, R. J. W. Brienen, J. Schöngart, J.-C. Espinoza, and K. C. Pattnayak, 2018: Recent intensification of Amazon flooding extremes driven by strengthened Walker circulation. *Sci. Adv.*, **4**, eaat8785, https://doi.org/10.1126/sciadv.aat8785.

Branstator, G., and H. Teng, 2017: Tropospheric waveguide teleconnections and their seasonality. *J. Atmos. Sci.*, **74**, 1513–1532, https://doi.org/10.1175/JAS-D-16-0305.1.

Capotondi, A., and Coauthors, 2015: Understanding ENSO diversity. *Bull. Amer. Meteor. Soc.*, **96**, 921–938, https://doi.org/10.1175/BAMS-D-13-00117.1.

CLIMATEMPO, 2021: São Paulo registra duplo recorde de frio. 30 June, accessed 20 January 2022, https://www.climatempo.com.br/noticia/2021/06/30/sao-paulo-registra-duplo-recorde-de-frio-0627.

Cunha, A. P. M. A., and Coauthors, 2019: Extreme drought events over Brazil from 2011 and 2019. *Atmosphere*, **10**, 642, https://doi.org/10.3390/atmos10110642.

Espinoza, J.-C., J. A. Marengo, J. Ronchail, J. M. Carpio, L. N. Flores, and J. L. Guyot, 2014: The extreme 2014 flood in south-western Amazon basin: The role of tropical-subtropical South Atlantic SST gradient. *Environ. Res. Lett.*, **9**, 124007, https://doi.org/10.1088/1748-9326/9/12/124007.

——, ——, J. Schöngart, and J. C. Jimenez, 2022: The new historical flood of 2021 in the Amazon River compared to major floods of the 21st century: Atmospheric features in the context of the intensification of floods. *Wea. Climate Extremes*, **35**, 100406, https://doi.org/10.1016/j.wace.2021.100406.

Evans, A., D. Jones, R. Smalley, and S. Lellyett, 2020: An enhanced gridded rainfall analysis scheme for Australia. Bureau of Meteorology Research Rep. 041, 39 pp., www.bom.gov.au/research/publications/researchreports/BRR-041.pdf.

FAN, 2021: La sequedad de la vegetación a causa de las heladas aumentan el riesgo de incendios forestales en la Chiquitania. Fundación Amigos de la Naturaleza, 13 July, accessed 12 January 2022, http://incendios.fan-bo.org/Satrifo/la-sequedad-de-la-vegetacion-a-causa-de-las-heladas-aumentan-el-riesgo-de-incendios-forestales-en-la-chiquitania/.

Fauchereau, N., B. Pohl, and A. Lorrey, 2016: Extratropical impacts of the Madden–Julian oscillation over New Zealand from a weather regime perspective. *J. Climate*, **29**, 2161–2175, https://doi.org/10.1175/JCLI-D-15-0152.1.

Filizola, N., E. M. Larubesse, P. Fraizy, R. Souza, V. Guimarães, and J.-L. Guyot, 2014: Was the 2009 flood the most hazardous or the largest ever recorded in the Amazon? *Geomorphology*, **215**, 99–105, https://doi.org/10.1016/j.geomorph.2013.05.028.

Funk, C., and Coauthors, 2015a: The Climate Hazards Infrared Precipitation with Stations—A new environmental record for monitoring extremes. *Sci Data*, **2**, 150066, https://doi.org/10.1038/sdata.2015.66.

——, and Coauthors, 2015b: Climate Hazards InfraRed Precipitation with Station data-2.0 global monthly data. Climate Hazards Center, accessed 27 December 2021, https://data.chc.ucsb.edu/products/CHIRPS-2.0/global_monthly/netcdf/.

Harrigan, S., and Coauthors, 2020: GloFAS-ERA5 operational global river discharge reanalysis 1979–present. Earth Syst. *Sci. Data*, **12**, 2043–2060, https://doi.org/10.5194/essd-12-2043-2020.

——, and Coauthors, 2021: River discharge and related historical data from the Global Flood Awareness System, v3.1, Copernicus Climate Change Service (C3S) Climate Data Store (CDS), accessed 4 January 2022, https://cds.climate.copernicus.eu/cdsapp#!/dataset/cems-glofas-historical, https://doi.org/10.24381/cds.a4fdd6b9.

Hendon, H. H., D. W. Thompson, and M. C. Wheeler, 2007: Australian rainfall and surface temperature variations associated with the Southern Hemisphere annular mode. *J. Climate*, **20**, 2452–2467, https://doi.org/10.1175/JCLI4134.1.

Hidalgo, H. G., E. J. Alfaro, J. A. Amador, and A. Bastidas, 2019: Precursors of quasi-decadal dry-spells in the Central America Dry Corridor. *Climate Dyn.*, **53**, 1307–1322, https://doi.org/10.1007/s00382-019-04638-y.

Huang, B., and Coauthors, 2017: NOAA Extended Reconstructed Sea Surface Temperature (ERSST), version 5. NOAA National Centers for Environmental Information, accessed 2 February 2022, https://doi.org/10.7289/V5T72FNM.

Jones, D. A., W. Wang, and R. Fawcett, 2009: High-quality spatial climate datasets for Australia. *Aust. Meteor. Oceanogr. J.*, **58**, 233–248, https://doi.org/10.22499/2.5804.003.

Kidston, J., J. A. Renwick, and J. McGregor, 2009: Hemispheric-scale seasonality of the southern annular mode and impacts on the climate of New Zealand. *J. Climate*, **22**, 4759–4770, https://doi.org/10.1175/2009JCLI2640.1.

Koren, G., and Coauthors, 2018: Widespread reduction in sun-induced fluorescence from the Amazon during the 2015/2016 El Niño. *Philos. Trans. Roy. Soc.*, **B373**, 20170408, https://doi.org/10.1098/rstb.2017.0408.

Lehner, B., and G. Grill, 2013: Global river hydrography and network routing: baseline data and new approaches to study the world's large river systems. *Hydrol. Processes*, **27**, 2171–2186, https://doi.org/10.1002/hyp.9740.

Lewis, S. L., P. M. Brando, O. L. Phillips, G. M. F. van der Heijden, and D. Nepstad, 2011: The 2010 Amazon Drought. *Science*, **331**, 554, https://doi.org/10.1126/science.1200807.

Libonati, R., and Coauthors, 2022: Assessing the role of compound drought and heatwave events on unprecedented 2020 wildfires in the Pantanal. *Environ. Res. Lett.*, **17**, 015005, https://doi.org/10.1088/1748-9326/ac462e.

Magaña, V., J. A. Amador, and S. Medina, 1999: The midsummer drought over Mexico and Central America. *J. Climate*, **12**, 1577–1588, https://doi.org/10.1175/1520-0442(1999)012<1577:TMDOMA>2.0.CO;2.

Marengo, J. A., and Coauthors, 2021: Extreme drought in the Brazilian Pantanal in 2019–2020: Characterization, causes, and impacts. *Front. Water*, **3**, 639204, https://doi.org/10.3389/frwa.2021.639204.

Menne, M. J., C. N. Williams, and B. E. Gleason, 2018: The Global Historical Climatology Network monthly temperature dataset, version 4. *J. Climate*, **31**, 9835–9854, https://doi.org/10.1175/JCLI-D-18-0094.1.

Merrifield, M. A., P. R. Thompson, and M. A. Lander, 2012: Multidecadal sea level anomalies and trends in the western tropical Pacific. *Geophys. Res. Lett.*, **39**, L13602, https://doi.org/10.1029/2012GL052032.

Mol, A., A. Tait, and G. Macara, 2017: An automated drought monitoring system for New Zealand. *Wea. Climate*, **37**, 23–36, https://doi.org/10.2307/26735444.

Mullan, A. B., S. J. Stuart, M. G. Hadfield, and M. J. Smith, 2010: Report on the review of NIWA's "seven-station" temperature series. NIWA Information Series 78, 175 pp., https://niwa.co.nz/sites/niwa.co.nz/files/import/attachments/Report-on-the-Review-of-NIWAas-Seven-Station-Temperature-Series_v3.pdf.

Naumann, G., and Coauthors, 2021: The 2019–2021 extreme drought episode in La Plata Basin : A joint report from EC-JRC, CEMADEN, SISSA and WMO. EUR 30833 EN, Publications Office of the European Union, 44 pp.,https://data.europa.eu/doi/10.2760/773.

NOAA, 2022: U.S. billion-dollar weather and climate disasters. NOAA/National Centers for Environmental Information, https://www.ncei.noaa.gov/access/billions/.

ReliefWeb, 2021: Brazil: Floods - Dec 2021. Accessed 8 January 2022, https://reliefweb.int/disaster/fl-2021-000204-bra.

Rodriguez, A., R. Camargo, and V. Ibarnegaray, 2021: Cuantificación de áreas quemadas en Bolivia, con información de enero a octubre de 2021. Fundación Amigos de la Naturaleza, https://incendios.fan-bo.org/Satrifo/areas-quemadas-ago-2021/.

Saji, N. H., and T. Yamagata, 2003: Possible impacts of Indian Ocean Dipole mode events on global climate. *Climate Res.*, **25**, 151–169, https://doi.org/10.3354/cr025151.

Salinger, J. M., and A. B. Mullan, 1999: New Zealand climate: Temperature and precipitation variations and their links with atmospheric circulation. *Int. J. Climatol.*, **19**, 1049–1071, https://doi.org/10.1002/(SICI)1097-0088(199908)19:10<1049::AID-JOC417>3.0.CO;2-Z.

Satyamurty, P. C. P. Wanzeler da Costa, A. O. Manzi, and L. A. Candido, 2013: A quick look at the 2012 record flood in the Amazon Basin. *Geophys. Res. Lett.*, **40**, 1396–1401, https://doi.org/10.1002/grl.50245.

Schneider, U., P. Finger, A. Meyer-Christoffer, M. Ziese, and A. Becker, 2018: Global precipitation analysis products of the GPCC. Deutscher Wetterdienst, 15 pp., https://opendata.dwd.de/climate_environment/GPCC/PDF/GPCC_intro_products_v2018.pdf

Smith, A. B., 2020: U.S. billion-dollar weather and climate disasters, 1980–present (NCEI Accession 0209268). NOAA/National Centers for Environmental Information, accessed 27 March 2022, https://doi.org/10.25921/stkw-7w73.

——, 2022: 2021 U.S. billion-dollar weather and climate disasters in historical context. Climate.gov, https://www.climate.gov/news-features/blogs/beyond-data/2021-us-billion-dollar-weather-and-climate-disasters-historical.

Taylor, M., D. Enfield, and A. Chen, 2002: Influence of the tropical Atlantic versus the tropical Pacific on Caribbean rainfall. *J. Geophys. Res.*, **107**, 3127, https://doi.org/10.1029/2001JC001097. Trenberth, K. E., 1976: Fluctuations and trends in indices of the Southern Hemispheric circulation. *Quart. J. Roy. Meteor. Soc.*, **102**, 65–75, https://doi.org/10.1002/qj.49710243106.

Trewin, B., 2018: The Australian Climate Observations Reference Network–Surface Air Temperature (ACORN-SAT) version 2. Bureau of Meteorology Research Rep. No. 032, 57 pp., www.bom.gov.au/research/publications/researchreports/BRR-032.pdf.

van Schaik, E., L. Killaars, N. E. Smith, G. Koren, L. P. H. van Beek, W. Peters, and I. T. van der Laan-Luijkx, 2018: Changes in surface hydrology, soil moisture and gross primary production in the Amazon during the 2015/2016 El Niño. *Philos. Trans. Roy. Soc.*, **B373**, 20180084, https://doi.org/10.1098/rstb.2018.0084.

STATE OF THE CLIMATE IN 2021

RELEVANT DATASETS AND SOURCES

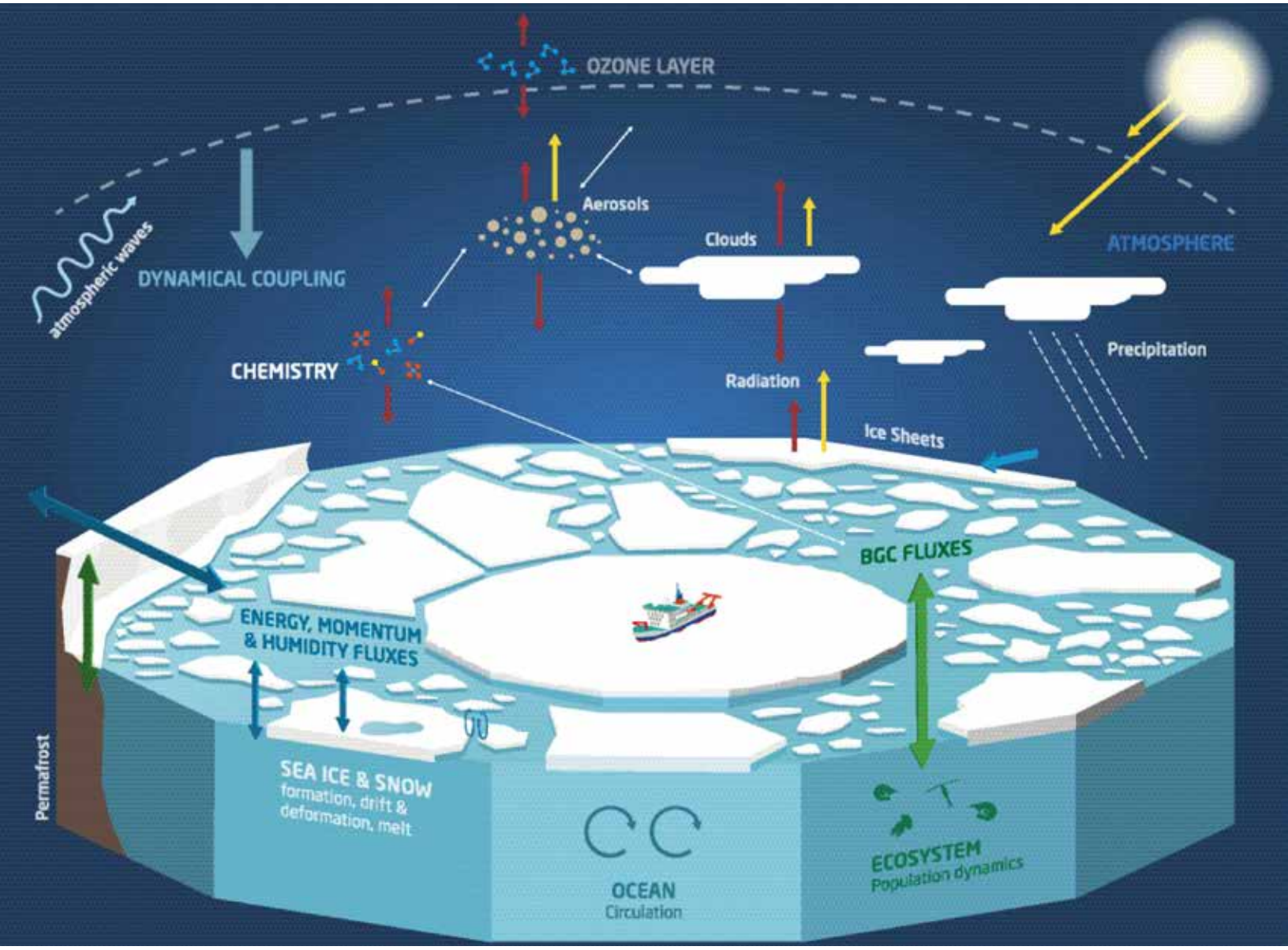

To learn more go to this website: https://mosaic-expedition.org/

Special Online Supplement to the *Bulletin of the American Meteorological Society*, Vol.103, No. 8, August 2022

https://doi.org/10.1175/2022BAMSStateoftheClimate_Chapter8.1
Corresponding author: Jessica Blunden / Jessica.Blunden@noaa.gov

8: RELEVANT DATASETS AND SOURCES

General Variable or Phenomenon	Specific dataset or variable	Source	Section
Aerosols	CAMS Reanalysis	https://ads.atmosphere.copernicus.eu/cdsapp#!/dataset/cams-global-radiative-forcing-auxilliary-variables?tab=overview	2g3
	MODIS Aerosol	https://modis.gsfc.nasa.gov/data/dataprod/mod04.php	2g3
	AATSR	https://earth.esa.int/eogateway/instruments/aatsr	2g3
Air-sea fluxes	CERES Energy Balanced and Filled	https://ceres.larc.nasa.gov/data/	3 e1
	CERES FLASHflux	https://ceres.larc.nasa.gov/data/	3e1
	Woods Hole Oceanographic Institute OAFlux	http://oaflux.whoi.edu	3e1, 3e2, 3e3
Albedo	MODIS	https://doi.org/10.5067/MODIS/MCD43C3.006	2h1
	MODIS (Greenland)	https://nsidc.org/data/MODGRNLD/versions/1	5e
Biomass, Greenness or Burning	GFAS v1.4	ftp://ftp.mpic.de/GFAS/sc17 (special reprocessing)	2h3
	Modis Fire Power Radiative Product	DOI:10.5067/MODIS/MOD14.006, DOI:10.5067/MODIS/MYD14.006	2h3
	Global Inventory Modeling and Mapping Studies (GIMMS) 3gv1	https://iridl.ldeo.columbia.edu/SOURCES/.NASA/.ARC/.ECOCAST/.GIMMS/.NDVI3g/.v1p0/index.html?Set-Language=en	5i
	MODIS MCD43A4	https://lpdaac.usgs.gov/products/mcd43a4v006/	5i
Cloud Properties	Aqua MODIS C6	http://dx.doi.org/10.5067/MODIS/MYD08_M3.006	2d6, 2h3
	Terra MODIS C6	http://dx.doi.org/10.5067/MODIS/MOD08_M3.006	2d6
	CALIPSO	http://www-calipso.larc.nasa.gov	6h
	CERES Aqua MODIS	https://doi.org/10.5067/Aqua/CERES/SSF1degMonth_L3.004A	2d6
	CLARA-A2	https://www.cmsaf.eu/EN/Home/home_node.html	2d6
	MISR	http://eosweb.larc.nasa.gov/PRODOCS/misr/level3/overview.html	2d6
	PATMOD	not publicly available	
	PATMOS-x/MODIS C6	available soon from NCEI	
Drought	CRU TS 4.05	https://crudata.uea.ac.uk/cru/data/hrg/cru_ts_4.05/	2d11
Land Evaporation	GLEAM v3.6	www.gleam.eu/	2d12
FAPAR	MERIS	https://earth.esa.int/eogateway/	2h2
	JRC TIP MODIS	https://fapar.jrc.ec.europa.eu/_www/	2h2
	SeaWiFS FAPAR	http://fapar.jrc.ec.europa.eu/	2h2
Geopotential Height	ERA5	https://www.ecmwf.int/en/forecasts/datasets/reanalysis-datasets/era5	5SB2, 6b
Glacier Mass, Area or Volume	GRACE / GRACE-FO	https://grace.jpl.nasa.gov/data/get-data/	5e, 5f, 6e
	World Glacier Monitoring Service	http://dx.doi.org/10.5904/wgms-fog-2020-08	2c3, 5f
	Glacier Front Line (Greenland)	https://doi.org/10.22008/promice/data/calving_front_lines	5e
Groundwater and terrestrial water storage	GRACE / GRACE-FO	https://podaac.jpl.nasa.gov/dataset/TELLUS_GRAC-GRFO_MASCON_CRI_GRID_RL06_V2	2d9, 5g

(cont.) Relevant datasets and sources

General Variable or Phenomenon	Specific dataset or variable	Source	Section
Humidity, [Near] Surface	ERA5	https://www.ecmwf.int/en/forecasts/datasets/reanalysis-datasets/era5	2d1
	HadISDH	www.metoffice.gov.uk/hadobs/hadisdh	2d1
	MERRA-2	https://gmao.gsfc.nasa.gov/reanalysis/MERRA-2/	2d1
	JRA-55 Atmospheric Reanalysis	http://jra.kishou.go.jp/JRA-55/index_en.html	2d1
Humidity, Upper Atmosphere	ERA5	https://www.ecmwf.int/en/forecasts/datasets/reanalysis-datasets/era5	2d3
	HIRS	https://www.ncei.noaa.gov/access/metadata/landing-page/bin/iso?id=gov.noaa.ncdc:C00951	2d3
Ice Sheet Characteristics	DMSP-SSMIS	https://nsidc.org/data/nsidc-0001	5d, 6d
	ERA5	https://www.ecmwf.int/en/forecasts/datasets/reanalysis-datasets/era5	6c
	ICESat-2	https://icesat-2.gsfc.nasa.gov/	5d2, 6e
	Cryosat-2	https://earth.esa.int/eogateway/missions/cryosat	5d2
	SMOS	https://earth.esa.int/eogateway/missions/smos	5d2
	MERRA-2	https://gmao.gsfc.nasa.gov/reanalysis/MERRA-2/	6c, 6h
	Modèle Atmosphérique Régionale surface mass	https://mar.cnrs.fr/	5e
	PROMICE (Greenland)	https://doi.org/10.22008/promice/data/aws	5e
	PROMICE (Greenland) Mass Balance	https://doi.org/10.22008/FK2/OHI23Z	5e
	DMI Weather Stations	http://polarportal.dk/en/weather/historisk-vejr/#:~:text=DMI%20has%20a%20number%20of,go%20back%20almost%20250%20years.&text=One%20cannot%20expect%20that%20temperature%20observations%20spanning%20centuries%20are%20homogeneous.	5e
	Ice Discharge (Greenland)	https://doi.org/10.22008/promice/data/ice_discharge/d/v02	5e
	RACMO	https://www.projects.science.uu.nl/iceclimate/models/racmo-model.php	5e
	ATLAS/ICESat-2 Land Height	https://nsidc.org/data/atl06/versions/5	6e
	GRACE - GRACE FO CRI	https://podaac.jpl.nasa.gov/dataset/TELLUS_GRAC-GRFO_MASCON_CRI_GRID_RL06_V2	6e
Lake Ice	Great Lakes Ice	www.glerl.noaa.gov/data/ice	2c4
	ERA5	https://doi.org/10.24381/cds.adbb2d47	2c4
Lake Temperature	ERA5	https://doi.org/10.24381/cds.adbb2d47	2b2
	NERC Globolakes, Copernicus Climate Service	https://cds.climate.copernicus.eu/cdsapp#!/dataset/satellite-lake-water-temperature?tab=overview	2b2
	MetOp A & B ATSR and AVHRR	https://navigator.eumetsat.int/product/EO:EUM:DAT:METOP:AVHRRL1	2b2
	Sentinel 3 SLSTR	https://sentinel.esa.int/web/sentinel/user-guides/sentinel-3-slstr/overview	2b2
	National Buoy Data Center Great Lakes Buoys	https://www.ndbc.noaa.gov/mobile/region.php?reg=great_lakes	2b2
Lake Water Levels	DAHITI	https://dahiti.dgfi.tum.de/en/31/time_series/	2d9

(cont.) Relevant datasets and sources

General Variable or Phenomenon	Specific dataset or variable	Source	Section
Modes of Variability	Indian Ocean Dipole Mode Index	https://psl.noaa.gov/gcos_wgsp/Timeseries/DMI/	4f
	Madden-Julian Oscillation (MJO) - Real-time Multivariate MJO	www.bom.gov.au/climate/mjo/graphics/rmm.74toRealtime.txt	4c
	Oceanic Nino Index (ONI)	www.cpc.ncep.noaa.gov/products/analysis_monitoring/ensostuff/ensoyears.shtml	4b, 4d1
	Southern Annular Mode (SAM)	www.antarctica.ac.uk/met/gjma/sam.html	6b
	Antarctic Oscillation (AAO)/Southern Annular Mode (SAM)	https://ftp.cpc.ncep.noaa.gov/cwlinks/norm.daily.aao.index.b790101.current.ascii	2e1, 2e2
Ocean Heat Content	CLIVAR and Carbon Hydrographic Data Office	https://cchdo.ucsd.edu/	3c
	CSIRO/ACE CRC/IMAS-UTAS estimate	www.cmar.csiro.au/sealevel/thermal_expansion_ocean_heat_timeseries.html	3c
	IAP/CAS	https://climatedataguide.ucar.edu/climate-data/ocean-temperature-analysis-and-heat-content-estimate-institute-atmospheric-physics	3c
	PMEL/JPL/JIMAR	http://oceans.pmel.noaa.gov	3c
	MRI/JMA	www.data.jma.go.jp/gmd/kaiyou/english/ohc/ohc_global_en.html	3c
	NCEI	https://www.ncei.noaa.gov/access/global-ocean-heat-content/	3c
	UK Met Office EN4.0.2	www.metoffice.gov.uk/hadobs/en4/download-en4-0-2-l09.html	3c
	Argo monthly climatology	https://sio-argo.ucsd.edu/RG_Climatology.html	3c, 3f, 6g1, 6g2
	Argo	https://usgodae.org/argo/argo.html	3c
Ocean Mass	GRACE	https://grace.jpl.nasa.gov/data/get-data	3f
Ocean Salinity	Aquarius V3.0	http://podaac.jpl.nasa.gov/aquarius	3d2
	Argo	https://usgodae.org/argo/argo.html	3c, 3d2
	Blended Analysis for Surface Salinity	ftp://ftp.cpc.ncep.noaa.gov/precip/BASS	3d2
	SMAP	https://podaac.jpl.nasa.gov/SMAP	3d2
	SMOS	https://earth.esa.int/eogateway/missions/smos	3d2
	World Ocean Atlas 2013	www.nodc.noaa.gov/OC5/woa13/	3d2, 3d3
	World Ocean Atlas 2018	https://www.ncei.noaa.gov/products/world-ocean-atlas	2d8
	NCEI salinity anomaly	https://www.ncei.noaa.gov/access/global-ocean-heat-content/	3d3
Ocean Chlorophyll	GlobColour	https://doi.org/10.48670/moi-00100	6g3
Outgoing Longwave Radiation	Daily OLR	https://www.ncei.noaa.gov/products/climate-data-records/outgoing-longwave-radiation-daily	2d8

(cont.) Relevant datasets and sources

General Variable or Phenomenon	Specific dataset or variable	Source	Section
Ozone, Total Column and Stratospheric	GOME/SCIAMACHY/GOME2 (GSG) Merged Total Ozone	http://www.iup.uni-bremen.de/UVSAT/datasets/merged-wfdoas-total-ozone	2g4
	GOME/SCIAMACHY/GOME2 (GTO) Merged Total Ozone	https://atmos.eoc.dlr.de/gto-ecv	2g4
	GOZCARDS ozone profiles	https://www.earthdata.nasa.gov/esds/competitive-programs/measures/gozcards	2g4
	Aura OMI/MLS	https://disc.gsfc.nasa.gov/datasets/ML2O3_004/summary	5j1, 6h
	Multi Sensor Reanalysis (MSR-2) of total ozone	http://www.temis.nl/protocols/O3global.html	2g4
	NASA BUV/SBUV v8.6 (MOD v8.6) Merged Ozone	http://acdb-ext.gsfc.nasa.gov/Data_services/merged	2g4
	Bodeker Scientific	http://www.bodekerscientific.com/data/total-column-ozone	5j1
	Ozone Mapping & Profiler Suite (OMPS)	https://ozoneaq.gsfc.nasa.gov/omps/	6h
	Ozonesonde	www.esrl.noaa.gov/gmd/dv/spo_oz	6h
	SAGE II/OSIRIS	dataset linked to Bourassa et al. (2018) doi:10.5194/amt-11-489-2018	2g4
	SAGE-SCIA-OMPS	dataset linked to Arosio et al., (2018) doi:10.5194/amt-2018-275	2g4
	SWOOSH	www.esrl.noaa.gov/csd/groups/csd8/swoosh/	2g4
	WOUDC Ground-based Ozone	ftp.tor.ec.gc.ca	2g4
	NDACC lidar, microwave and FTIR	ftp://ftp.cpc.ncep.noaa.gov/ndacc	2g4
	OMTO3	https://disc.gsfc.nasa.gov/datasets/OMTO3_003/summary	5j2
	TOMS	https://ozoneaq.gsfc.nasa.gov/data/toms/#	6h
Ozone, Tropospheric	Aura OMI/MLS	http://acd-ext.gsfc.nasa.gov/Data_services/cloud_slice/new_data.html	2g6
	NOAA Observatory Data	ftp://aftp.cmdl.noaa.gov/data/ozwv/SurfaceOzone/	2g6
	MERRA-2	http://gmao.gsfc.nasa.gov/reanalysis/MERRA-2/	5SB2, 6h
Permafrost	CALM Active Layer Thickness	www2.gwu.edu/~calm/	2c1, 5h2
	GTN-P global mean annual ground temperature data for permafrost	https://doi.org/10.1594/PANGAEA.884711	2c1
	Global Terrestrial Network for Permafrost (GTN-P)	http://gtnpdatabase.org/	2c1, 5h1
	Permafrost Temperature	http://permafrost.gi.alaska.edu/sites_map	5h1
	Permafrost Temperature at Chinese (QTP) sites	https://nsidc.org/data/GGD700/versions/1	2c1
	Permafrost Temperature at French sites	permafrance.osug.fr	2c1
	Permafrost Temperature at Norwegian sites	www.tspnorway.com	2c1
	Permafrost Temperature at Swiss sites (PERMOS)	www.permos.ch	2c1

(cont.) Relevant datasets and sources

General Variable or Phenomenon	Specific dataset or variable	Source	Section
Phenology	NDVI	https://modis.gsfc.nasa.gov/data/dataprod/mod13.php	2h4
	PhenoCam	http://phenocam.sr.unh.edu	2h4
	Harvard Forest	https://harvardforest1.fas.harvard.edu/exist/apps/datasets/showData.html?id=hf003	2h4
	Natures Calendar	https://naturescalendar.woodlandtrust.org.uk/	2h4
	German oak phenology data	https://opendata.dwd.de/	2h4
	UK Cumbrian lakes data	https://catalogue.ceh.ac.uk/documents/bf30d6aa-345a-4771-8417-ffbcf8c08c28/	2h4
Vegetation Optical Depth	VODCA	https://zenodo.org/record/2575599	2h5
Lightning	OTD	http://dx.doi.org/10.5067/LIS/OTD/DATA101	2S.1
	ISS LIS	http://dx.doi.org/10.5067/LIS/ISSLIS/DATA108	2S.1
	TRMM LIS	http://dx.doi.org/10.5067/LIS/LIS/DATA201	2S.1
Phytoplankton, Ocean Color	MODIS-Aqua	https://oceancolor.gsfc.nasa.gov/reprocessing/	3i
	SeaWiFS	https://oceancolor.gsfc.nasa.gov/reprocessing/	3i
Precipitation	Climate Extremes Index	https://www.ncdc.noaa.gov/extremes/cei/	2d5
	ERA5	https://www.ecmwf.int/en/forecasts/datasets/reanalysis-datasets/era5	2d5, 5b3
	GHCN v4	www.ncdc.noaa.gov/temp-and-precip/ghcn-gridded-products/precipitation	2d5
	GHCNDEX	www.climdex.org/	2d5
	GPCP	https://psl.noaa.gov/data/gridded/data.gpcp.html	2d4, 3e2, 4e, 4f
	GPCC	www.dwd.de/EN/ourservices/gpcc/gpcc.html	2d5
	European Climate & Assessment & Dataset	https://www.ecad.eu/	2d5
	CMAP	https://psl.noaa.gov/data/gridded/data.cmap.html	4d1
Pressure, Sea Level or Near-Surface	ERA5	https://www.ecmwf.int/en/forecasts/datasets/reanalysis-datasets/era5	2e1, 5b2, 5f,6b, 6SB.1
	NCEP/NCAR Reanalysis	www.esrl.noaa.gov/psd/data/gridded/data.ncep.reanalysis.html	2e1, 4f2
Sea Ice Age	EASE-Grid v4	https://nsidc.org/data/NSIDC-0611/versions/4	5d2
Sea Ice Duration	Near-Real-Time DMSP SSM/I-SSMIS Daily Polar Gridded	http://nsidc.org/data/nsidc-0081.html	5d3, 6f
	Nimbus-7 SMMR and DMSP SSM/I (Bootstrap)	http://nsidc.org/data/nsidc-0079.html	6f
	EASE Sea Ice Duration	https://nsidc.org/data/NSIDC-0611/versions/4	5d2

(cont.) Relevant datasets and sources

General Variable or Phenomenon	Specific dataset or variable	Source	Section
Sea Ice Extent / Area / Concentration	Nimbus-7 SMMR and DMSP SSM/I (Bootstrap)	http://nsidc.org/data/seaice_index/	5d1
	Nimbus-7 SMMR Sea Ice Concentration	https://nsidc.org/data/nsidc-0007	6d
	NSIDC Passive Microwave Sea Ice Concentration v4	https://nsidc.org/data/g02202	5d1
	NSIDC Sea Ice Extent	https://nsidc.org/data/g02135	5d1, 5d2
	NSIDC Passive Microwave Sea Ice Extent v2	https://nsidc.org/data/g10016	5d1
	GRACE , GRACE FO	https://grace.jpl.nasa.gov/data/get-data/	5e
Sea Level / Sea Surface Height	GRACE / GRACE-FO	https://grace.jpl.nasa.gov/data/get-data/	3f
	University of Texas Center for Space Research Gravity field	https://www.ncei.noaa.gov/access/global-ocean-heat-content/	3f
	NOAA Laboratory for Sea Level Altimetry	www.star.nesdis.noaa.gov/sod/lsa/SeaLevelRise/LSA_SLR_timeseries.php	3f
	CMEMS	http://marine.copernicus.eu/services-portfolio/access-to-products/?option=com_csw&view=details&product_id=SEALEVEL_GLO_PHY_L4_NRT_OBSERVATIONS_008_046	3f
	Argo	https://usgodae.org/argo/argo.html	3f
	NCEI steric sea level	https://www.ncei.noaa.gov/access/global-ocean-heat-content/	3f
	Tide Gauge	http://uhslc.soest.hawaii.edu/	3f
	AVISO	https://www.aviso.altimetry.fr/en/data.html	6g1
ocean currents	AOML climate indices	https://www.aoml.noaa.gov/phod/indexes/index.php	3g
	Ocean Surface Current Analysis - Real time (OSCAR)	https://www.esr.org/research/oscar/oscar-surface-currents/	3g
	Global Drifter Program	https://www.aoml.noaa.gov/phod/gdp/	3g
	Atlantic Ship of Opportunity XBT	https://www.aoml.noaa.gov/phod/goos/xbt_network/	3h
	RAPID array	https://rapid.ac.uk/rapidmoc/	3h
	MOVE array	http://www.oceansites.org/tma/move.html	3h
	OSNAP	https://www.o-snap.org/	3h
	SAMBA	http://www.oceansites.org/tma/samba.html	3h
	Florida Current transport	https://www.aoml.noaa.gov/phod/floridacurrent/data_access.php	3h
	Global Temperature and Salinity Profile Program (GTSPP)	https://www.ncei.noaa.gov/products/global-temperature-and-salinity-profile-programme	3h

(cont.) Relevant datasets and sources

General Variable or Phenomenon	Specific dataset or variable	Source	Section
Sea Surface Temperature	ERSSTv5	https://doi.org/10.7289/V5T72FNM	3b, 4b, 4e, 4g2
	HadISST	https://www.metoffice.gov.uk/hadobs/hadisst/	4e
	HadSST4	https://www.metoffice.gov.uk/hadobs/hadsst4/	2b3, 3b
	NOAA Optimum Interpolation SST (OISST) v2	https://www.ncei.noaa.gov/products/optimum-interpolation-sst	2b4, 3b, 4b1, 4d2, 4f, 4g3, 4g5, 4g6, 5c, 6f, 6g
	NOAA Optimum Interpolation SST (OISST) v2	https://psl.noaa.gov/data/gridded/data.noaa.oisst.v2.html	5c
	NOAA Daily Optimum Interpolated Temperature (DOISST)		3b
	MODIS Aqua	https://oceancolor.gsfc.nasa.gov/reprocessing	3i
Snow Properties	Crocus Snowpack Model	http://www.umr-cnrm.fr/spip.php?article265	5g
	NOAA Interactive Multi-sensor Snow and Ice Mapping System (Snow Cover Duration)	https://usicecenter.gov/Products/ImsHome	5g
	NOAA Snow Chart Data Record (Snow Cover Extent)	www.snowcover.org	2c5, 5g
	Northern Hemisphere (NH) Snow Cover Extent (SCE), Version 1	doi:10.7289/V5N014G9	2c5, 5g
	MERRA-2	http://gmao.gsfc.nasa.gov/reanalysis/MERRA-2/	5g
	Sentinel 3 SICE	http://snow.geus.dk/	5e
	Snow CCI	http://snow-cci.enveo.at/	5g
	ERA5	https://www.ecmwf.int/en/forecasts/datasets/reanalysis-datasets/era5	5g
Soil Moisture	ESA CCI SM	https://climate.esa.int/en/projects/soil-moisture/	2d10

(cont.) Relevant datasets and sources

General Variable or Phenomenon	Specific dataset or variable	Source	Section
Temperature, [Near] Surface	Antarctic Meteorological Research Center (AMRC) AWS	http://amrc.ssec.wisc.edu/data	6b, 6c
	Berkeley Earth	http://berkeleyearth.org/data/	2b1
	CRUTEM5	www.metoffice.gov.uk/hadobs/crutem5	5b1
	ERA5	https://www.ecmwf.int/en/forecasts/datasets/reanalysis-datasets/era5	2b1, 2b2, 2b4, 6b, 6SB1
	ERA5 Copernicus Climate Store	https://cds.climate.copernicus.eu	5h1
	GHCNDEX	www.climdex.org/	2b4, 4g3, 4g5, 4g6, 5c
	HadCRUT5 Global Temperature	https://www.metoffice.gov.uk/hadobs/hadcrut5/	2b1
	JRA-55 Atmospheric Reanalysis	http://jra.kishou.go.jp/JRA-55/index_en.html	2b1, 4f
	MERRA-2	http://gmao.gsfc.nasa.gov/reanalysis/MERRA-2/	6h
	NASA/GISS Global Temperature	https://data.giss.nasa.gov/gistemp/	2b1, 2b2, 2c4
	NCEP/NCAR Reanalysis	https://psl.noaa.gov/data/gridded/data.ncep.reanalysis.html	5b2, 5f
	NOAA/NCEI NOAAGlobalTemp	https://www.ncei.noaa.gov/products/land-based-station/noaa-global-temp	2b1
	Integrated Global Radiosonde Archive	https://www.ncei.noaa.gov/products/weather-balloon/integrated-global-radiosonde-archive	5f
Temperature, Upper Atmosphere	ERA5	https://www.ecmwf.int/en/forecasts/datasets/reanalysis-datasets/era5	2b4, 2b5, 6b, 6h
	JRA-55 Atmospheric Reanalysis	http://jra.kishou.go.jp/JRA-55/index_en.html	2b5
	MERRA-2	http://gmao.gsfc.nasa.gov/reanalysis/MERRA-2/	2b5, 6h
	RAOBCORE, RICH	https://imgw.univie.ac.at/forschung/klimadiagnose/raobcore/index.html	2b5
	RATPAC A2	https://www.ncei.noaa.gov/products/weather-balloon/radiosonde-atmospheric-temperature-products	2b5
	RSS v4.0	https://www.remss.com/measurements/upper-air-temperature/	2b5
	NOAA/NESDIS/STAR MSU v4.1	ftp://ftp.star.nesdis.noaa.gov/pub/smcd/emb/mscat/data/MSU_AMSU_v4.1	2b5
	UW MSU v1.0	https://pochedls.github.io/#!data.md	2b5
	UAH MSU v6.0	https://www.nsstc.uah.edu/public/msu/	2b5
	NCAR merged SSU+MLS satellite data	ftp://ftp.acom.ucar.edu/user/randel/SSUdata	2b6
	Stratospheric QBO data	https://acd-ext.gsfc.nasa.gov/Data_services/met/qbo/qbo.html	2b6
Nighttime marine Air Temperature	CLASSnmat	https://catalogue.ceda.ac.uk/uuid/9058edd550624de69a8b2a882d11b65c	2b3
	UAHNMAT	https://www.nsstc.uah.edu/climate/	2b3

(cont.) Relevant datasets and sources

General Variable or Phenomenon	Specific dataset or variable	Source	Section
TOA Earth Radiation Budget	CERES EBAF Ed4.1	https://ceres-tool.larc.nasa.gov/ord-tool/jsp/EBAF41Selection.jsp	2f1
	CERES FLASHflux	https://ceres-tool.larc.nasa.gov/ord-tool/jsp/FLASH_TISASelection.jsp	2f1
	TSIS TIM Level 3 Total Solar Irradiance 24-hour Means	doi:10.5067/TSIS/TIM/DATA306	2f1
Solar Transmission, Apparent	Mauna Loa Observatory	https://www.esrl.noaa.gov/gmd/webdata/grad/mloapt/mauna_loa_transmission.dat	2f2
	HYSPLIT	https://www.ready.noaa.gov/HYSPLIT.php	2f2
Trace Gases	Atmospheric Greenhouse Gas Index (AGGI)	www.esrl.noaa.gov/gmd/aggi	2g1
	Atmospheric Gas trends	www.esrl.noaa.gov/gmd/ccgg/trends	2g1
	CAMS Reanalysis (Carbon Monoxide)	https://ads.atmosphere.copernicus.eu/cdsapp#!/dataset/cams-global-radiative-forcing-auxilliary-variables?tab=overview	2g7
	Nitrous Oxide	www.esrl.noaa.gov/gmd/hats/combined/N2O.html	2g1
	Ozone-Depleting Gas Index (ODGI)	www.esrl.noaa.gov/gmd/odgi	2g2
Tropical Cyclone Data	HURDAT2	www.aoml.noaa.gov/hrd/hurdat/Data_Storm.html	4g2
	International Best Track Archive for Climate Stewardship (IBTrACS)	https://www.ncei.noaa.gov/products/international-best-track-archive	4g1, 4g3, 4g5, 4g6, 4g7
	JTWC Best-track Dataset	https://www.metoc.navy.mil/jtwc/jtwc.html?best-tracks	4b, 4e, 4g2 ,4g5, 4g6
	RSMC-Tokyo, JMA best-track data	www.jma.go.jp/jma/jma-eng/jma-center/rsmc-hp-pub-eg/besttrack.html	4g4
	Southwest Pacific Enhanced Archive of Tropical Cyclones (SPEArTC)	http://apdrc.soest.hawaii.edu/projects/speartc	4g8
	HURDAT US Hurricanes	http://www.aoml.noaa.gov/hrd/hurdat/All_U.S._Hurricanes.html	4SB.1
	Accumulated Cyclone Energy (ACE)	https://climatlas.com/tropical/	2e3
	Hurricane Glider Project	https://www.aoml.noaa.gov/hurricane-glider-project	4h
UV Radiation Data	NASA Aura Microwave Limb Sounder	https://mls.jpl.nasa.gov/	2g5
Water Vapor, Total Column	COSMIC	https://cdaac-www.cosmic.ucar.edu/	2d2
	ERA5	https://www.ecmwf.int/en/forecasts/datasets/reanalysis-datasets/era5	2d2, 6SB.1
	GNSS Ground-Based Total Column Water Vapor	https://doi.org/10.25326/18	2d2
	JRA-55 Atmospheric Reanalysis	http://jra.kishou.go.jp/JRA-55/index_en.html	2d2
	METOP A B C	https://www.eumetsat.int/our-satellites/metop-series	2d2

(cont.) Relevant datasets and sources

General Variable or Phenomenon	Specific dataset or variable	Source	Section
Wind, [Near] Surface	ERA5	https://www.ecmwf.int/en/forecasts/datasets/reanalysis-datasets/era5	2e2, 4e, 4g4, 4g5
	HadISD v3.3.0.202201p	www.metoffice.gov.uk/hadobs/hadisd/	2e2
	JRA-55 Atmospheric Reanalysis	http://jra.kishou.go.jp/JRA-55/index_en.html	4f
	MERRA-2	http://gmao.gsfc.nasa.gov/reanalysis/MERRA-2/	2e2
	RSS Radiometer winds	www.remss.com/measurements/wind	2e3
	Climate Forecast System Reanalysis (CFSR)	https://climatedataguide.ucar.edu/climate-data/climate-forecast-system-reanalysis-cfsr	4g3, 4g5, 4g6
Wind, Upper Atmosphere	ERA5	https://www.ecmwf.int/en/forecasts/datasets/reanalysis-datasets/era5	2e3, 4e, 6b
	ERA-Interim	www.ecmwf.int/en/research/climate-reanalysis/era-interim	2e3
	MERRA-2	http://gmao.gsfc.nasa.gov/reanalysis/MERRA-2/	2e3
River Discharge	QBO	https://www.geo.fu-berlin.de/met/ag/strat/produkte/qbo/index.html	2e3
	CaMA Flood	http://hydro.iis.u-tokyo.ac.jp/~yamadai/cama-flood/	2d7
	ELSE	offline	2d7
	DDM30	https://www.uni-frankfurt.de/45218101/DDM30	2d7